Multifunctional coordination compounds in Molecular Magnetism – Towards high density data storage

Dissertation

zur Erlangung des akademischen Grades

Doktor der Naturwissenschaften

im Promotionsfach Chemie

am Fachbereich Chemie, Pharmazie,

Geographie und Geowissenschaften der Johannes Gutenberg-Universität Mainz

vorgelegt von

Julian Eppelsheimer

geboren in Mainz

Mainz, 15.03.2022

Die vorliegende Arbeit wurde in der Zeit von Juli 2017 bis März 2022 am Department für Chemie der Johannes Gutenberg-Universität Mainz unter Betreuung von [redacted] angefertigt.

Hiermit versichere ich, dass ich diese Arbeit selbstständig verfasst und keine anderen als die angegebenen Quellen und Hilfsmittel verwendet habe.

Mainz, 15.03.2022

Ort, Datum



Unterschrift

Dekanin: [redacted]

Erste Berichterstatterin: [redacted]

Zweite Berichterstatterin: [redacted]

Prüfer: [redacted]

Danksagung

Zu Beginn möchte ich mich sehr gerne bei [redacted] bedanken, die es mir ermöglicht hat in ihrem Arbeitskreis an einem Thema meiner Wahl zu forschen. Vielen Dank für die hohe Entscheidungsfreiheit und das entgegengebrachte Vertrauen, nicht nur während der Promotion, sondern auch in jeglichen Phasen des Studiums. Ich habe über die Jahre hinweg stets Rückhalt und Unterstützung erhalten, sodass ich mich zu jedem Zeitpunkt gut betreut gefühlt habe.

Des Weiteren danke ich [redacted] für das zuverlässige Messen, Lösen und Verfeinern der Kristallstrukturen. Danke auch für die kritischen, wissenschaftlichen Diskussionen über Themen des molekularen Magnetismus und für die Unterstützung bei der Auswertung experimenteller Ergebnisse.

Ich danke [redacted] für die röntgenkristallographischen Messungen meiner Kristalle, [redacted] für die Unterstützung in der NMR-Spektroskopie und Massenspektrometrie und der gesamten analytischen Abteilung für sämtliche Analytik meiner synthetisierten Verbindungen. Danke auch an [redacted] aus der Gruppe von [redacted] von der Justus-Liebig-Universität Gießen für das Aufnehmen der Emissionsspektren.

Ein ganz großes Dankeschön an sämtliche Mitglieder und Ehemaligen des Arbeitskreises [redacted], die mich während der Promotion begleitet haben: [redacted], sowie allen Bachelor- und Masterstudenten. Vielen Dank für die angenehme und freundliche Atmosphäre, den fachlichen Austausch und die gemeinsamen Aktivitäten in der Freizeit.

Meinen zwei Bacheloranden [redacted] und [redacted] und meinem Modulanten [redacted] möchte ich für ihren Einsatz, ihre mitgebrachte Motivation und ihre Lernbereitschaft danken, die sie während ihrer Zeit im Arbeitskreis [redacted] zeigten.

Vielen Dank an meine Freunde, die mich während der gesamten Studien- und Promotionszeit begleitet und unterstützt haben. Für den entgegengebrachten Rückhalt und die stetige Ablenkung in stressigen Phasen bin ich sehr dankbar. Hierbei möchte ich besonders [redacted] hervorheben. Die gemeinsame Zeit in

sämtlichen Praktika, Vorlesungen und Seminaren werde ich nie vergessen. Insbesondere möchte ich mich bei meinem besten Freund [redacted] bedanken, der mit mir bis heute alle Meilensteine meines Lebens, Rücken an Rücken, gemeistert hat. Danke für die enge Freundschaft.

Meiner Freundin [redacted] möchte ich für Ihre nahezu unermüdliche Geduld, ihre geleistete Unterstützung in stressigen Phasen und für ihre liebevolle Zuneigung danken, die sie mir von Beginn an geschenkt hat. Danke für das Aufmuntern und die motivierenden Worte, wenn ich sie am meisten gebraucht habe.

Last but not least bedanke ich mich von ganzem Herzen bei meiner wundervollen Familie, die über all die Jahre hinweg bedingungslos an meiner Seite stand. Danke für die helfenden Hände in jeglichen Lebenslagen, die finanzielle und moralische Unterstützung und für eure Bereitschaft mir den Rücken freizuhalten – komme was wolle. Vielen Dank für all die Liebe, ich weiß sie wirklich zu schätzen.

Kurzzusammenfassung

Spin Crossover (SCO) Materialien werden durch Moleküle dargestellt, die durch externe Stimuli wie Temperatur-, Druckeinwirkung oder durch die Bestrahlung mit Licht zwischen einem elektronischen High-Spin- (HS) und Low-Spin-Zustand (LS) wechseln können. Im Falle eines Eisen(II) Ions ist der erstere paramagnetisch (S = 2), während der letztere diamagnetisch (S = 0) ist. Unter gewissen Bedingungen können solche Systeme eine Bistabilität aufweisen, was sie zu geeigneten Materialen für elektronische und spintronische Bauteile macht. Somit besitzen sie das Potential als Schlüsselelemente in molekularen Schaltern, Sensoren oder Datenspeichermedien zu fungieren. Diese Arbeit behandelt die Synthese und Untersuchung neuartiger 1,3,4-Oxadiazol-basierter Komplexverbindungen, welche Anwendung in den zuvor genannten Bereichen finden können. Die Strukturaufklärung dieser Komplexe wurde mittels Röntgenstrukturanalyse, NMR-/ IR-/ UV/Vis-Spektroskopie, Massenspektrometrie und Elementaranalyse gewährleistet. Der erste Teil der Arbeit handelt von der erfolgreichen Darstellung symmetrischer dinuklearer Eisen(II) Koordinationsverbindungen der Form $[Fe^{II}_2(\mu_2\text{-}\mathbf{L})_2](X)_4$ (X = BF_4^-, ClO_4^- oder $CF_3SO_3^-$). Hierbei stellt **L** einen 1,3,4-Oxadiazolbrückenliganden dar, dessen koordinierende Seitenarme gezielt modifiziert und angepasst wurden. Somit konnte der elektronische und sterische Einfluss verschiedener Substitutionsgruppen im Ligandensystem auf die molekularen magnetischen Eigenschaften mittels SQUID Magnetometrie untersucht werden. Hierbei zeigte sich deutlich, dass sämtliche dinuklearen Eisen(II) Verbindungen zwischen 2-300 K im [HS-HS] Zustand vorliegen und eine schwache intramolekulare antiferromagnetische Austauschwechselwirkung aufweisen. Im zweiten Teil der Arbeit wurden mononukleare Eisen(II) und Cobalt(II) Koordinationsverbindungen der Form $[M^{II}(\mathbf{L})(NCX)_2]$ (M = Fe und Co; X = S, Se und BH_3) synthetisiert und untersucht. Hier beschreibt **L** einen tetradentaten 1,3,4-Oxadiazolliganden, dessen nicht koordinierender aromatischer Rest in der 2-Position des Oxadiazols variiert wurde. Mittels Röntgenstrukturanalyse am Einkristall konnte in sämtlichen Komplexen ein hoher Grad an intermolekularen π-π-Wechselwirkungen gezeigt werden, was in den Verbindungen $[Fe^{II}(\mathbf{L})(NCBH_3)_2]$ zu abruptem SCO Verhalten führt. Darüber hinaus konnte in diesen ein TIESST Effekt und ein temperaturinduzierter zweistufiger Spinübergang beobachtet werden. Erste optische Messungen weisen stark auf ein erfolgreiches Zusammenspiel zwischen dem SCO Phänomen und den vorhandenen lumineszenten Eigenschaften hin. Die Komplexe des Typs $[Fe^{II}(\mathbf{L})(NCS)_2]$ und $[Fe^{II}(\mathbf{L})(NCSe)_2]$ verweilen dagegen im HS-Zustand über den kompletten gemessenen Temperaturbereich. Alle mononuklearen Verbindungen zeigen eine *easy-plane* Anisotropie. Der Austausch des Eisen(II) Ions gegen Kobalt(II) führte zur Darstellung neuer Einzelmolekülmagneten (engl. single ion magnets, SIMs), die neben den SCO Materialien eine tragende Rolle im Molekularen Magnetismus spielen.

Abstract

Spin crossover (SCO) materials are represented by molecules that can switch between a high-spin (HS) and low-spin (LS) electronic state by external stimuli such as exposure to temperature, pressure or irradiation with light. In the case of an iron(II) ion, the former is paramagnetic (S = 2) while the latter is diamagnetic (S = 0). Under certain conditions, such systems can exhibit bistability, which makes them suitable materials for electronic and spintronic devices. Thus, they have the potential to act as key elements in molecular switches, sensors or data storage media. This work deals with the synthesis of novel 1,3,4-oxadiazole based complex compounds, which can be used in the aforementioned fields. The structural elucidation of these complexes was ensured by X-ray structural analysis, NMR/ IR/ UV/Vis spectroscopy, mass spectrometry and elemental analysis. The first part of the work deals with the successful preparation and investigation of symmetrical dinuclear iron(II) coordination compounds of the form $[Fe^{II}_2(\mu_2\text{-}\mathbf{L})_2](X)_4$ (X = BF_4^-, ClO_4^- oder $CF_3SO_3^-$). Here, **L** represents a 1,3,4-oxadiazole bridge ligand whose coordinating side arms were specifically modified and adapted. Thus, the electronic and steric influence of different substitution groups in the ligand system on the molecular magnetic properties could be investigated by SQUID magnetometry. It was clearly shown that all dinuclear iron(II) compounds stay in the [HS-HS] state between 2-300 K and exhibit a weak intramolecular antiferromagnetic exchange interaction. In the second part of the work, mononuclear iron(II) and cobalt(II) coordination compounds of the form $[M^{II}(\mathbf{L})(NCX)_2]$ (M = Fe and Co; X = S, Se and BH_3) were synthesised and investigated. Here, **L** describes a tetradentate 1,3,4-oxadiazole ligand whose non-coordinating aromatic group in the 2-position of the oxadiazole was varied. By means of X-ray structure analysis on single crystals, a high degree of intermolecular π-π interactions could be shown in all complexes, which leads to abrupt SCO behaviour in the compounds $[Fe^{II}(\mathbf{L})(NCBH_3)_2]$. Furthermore, a TIESST effect and a temperature-induced two-step spin transition could be observed. First optical measurements strongly indicate a successful interplay between the SCO phenomenon and the present luminescent properties. In contrast, the complexes of the type $[Fe^{II}(\mathbf{L})(NCS)_2]$ and $[Fe^{II}(\mathbf{L})(NCSe)_2]$ remain in the HS state over the whole measured temperature range. All mononuclear compounds show an *easy-plane* anisotropy. The exchange of the iron(II) ion for cobalt(II) led to the synthesis of novel single ion magnets (SIMs), which play a major role in molecular magnetism alongside SCO materials.

Contents

1 Introduction **1**

1.1 The Spin Crossover Phenomenon 2

1.2 Further ways to induce Spin Crossover 6

1.2.1 Pressure 6

1.2.2 Light Induced Excited Spin State Trapping (LIESST) 6

1.3 Detecting the spin transition 8

1.3.1 Single Crystal X-Ray Structure Analysis 8

1.3.2 UV/Vis spectroscopy 9

1.3.3 ^{57}Fe Mössbauer Spectroscopy 10

1.3.4 Infrared Spectroscopy 11

1.3.5 Magnetic Measurements 11

1.4 Spin Transition Curves 13

1.5 The effects of solvent and non-coordinating anions on SCO 15

1.6 Dinuclear SCO active complexes 18

1.6.1 Dinuclear di-aza bridged SCO compounds 19

1.7 Luminescent Spin-Crossover Materials 22

2 Motivation **25**

3 Results and Discussion **27**

3.1 Dinuclear iron(II) complexes with 1,3,4-oxadiazole based ligands bearing five-membered heterocyclic aromatic sidearms ($L^{5,Y}$) 29

3.1.1 Synthesis of ligands $L^{5,Im}$ and $L^{5,TA}$ 30

3.1.2 Magnetic measurements of $[Fe_2(\mu2\text{-}L^{5,Im})_2](X)_4$-type complexes (C1 – C3) 31

3.1.3 Dinuclear complexes of type $[Fe_2(\mu2\text{-}L^{5,TA})_2](X)_4$ (C4 – C6) 36

3.1.4 Summarizing the influence of the ligand sidearm on the SCO activity in complexes C1 – C6. 45

3.2 Dinuclear iron(II) complexes with 1,3,4-oxadiazole based ligands bearing six-membered heterocyclic aromatic sidearms ($L^{6,Y}$) 47

3.2.1 Synthesis of ligands $L^{6,OMe}$, $L^{6,Cl}$ and $L^{6,N}$ 48

3.2.2 General discussion of bonding parameters of $[Fe_2(\mu2\text{-}L^{6,Y})_2](X)_4$-type complexes (C7 – C13). 52
3.2.3 Dinuclear iron(II) complexes of type $[Fe_2(\mu2\text{-}L^{6,OMe})_2](X)_4$ (C7 and C8) 55
3.2.4 Dinuclear iron(II) complexes of type $[Fe_2(\mu2\text{-}L^{6,Cl})_2](X)_4$ (C9 – C11) 62
3.2.5 Dinuclear iron(II) complexes of type $[Fe_2(\mu2\text{-}L^{6,N})_2](X)_4$ (C12 and C13) 68
3.3 Dinuclear iron(II) complexes of the asymmetric 1,3,4-oxadiazole based ligands ($L^{Py,Y}$). 73
3.3.1 Crystal structures of $[Fe_2(\mu2\text{-}L^{Py,1})_2](X)_4$-type complexes (C14 – C15) 75
3.3.2 Magnetic properties of $[Fe_2(\mu2\text{-}L^{Py,1})_2](X)_4$-type complexes (C14 – C15) 81
3.4 Oxadiazole – the too weak little brother to the thiadiazole? 83
3.4.1 Crystal structures of $[Fe(L)(NCX)_2]$-type complexes 84
3.5 Mononuclear coordination compounds of $L^{Py,1}$ 87
3.5.1 Solvatomorphs of $[Fe(L^{Py,1})(NCS)_2]$ (C16) 87
3.5.2 Solvatomorph of $[Fe(L^{Py,1})(NCSe)_2]$ (C17·3MeCN) 94
3.5.3 Solvatomorph of $[Fe(L^{Py,1})(NCBH_3)_2]$ (C18·1MeOH) 99
3.6 Mononuclear coordination compounds of L^{Ph} 105
3.6.1 Solvatomorphs of $[Fe(L^{Ph})(NCX)_2]$-type complexes (X = S, Se) (C19 – C20) 106
3.6.2 Solvatomorphs of $[Fe(L^{Ph})(NCBH_3)_2]$ (C21) 111
3.6.3 Nickel(II) complex of L^{Ph} 120
3.7 Mononuclear coordination compounds of L^{Naph} 125
3.7.1 Magneto-structural relationship in $[Fe(L^{Naph})(NCBH_3)_2] \cdot 4.5MeCN$ 126
3.7.2 Magneto-structural relationship in $[Fe(L^{Naph})(NCBH_3)_2] \cdot 3MeOH$ 132
3.8 Magneto-optical relationship in an oxadiazole-based SCO complex 141
3.8.1 Temperature dependent fluorescence of C23·3MeOH and C25 145
3.9 Cobalt(II) based mononuclear Single Ion Magnets (SIM) 149
3.9.1 $[Co(L^{Py,1})(NCS)_2] \cdot 1MeOH$ (C26) 149
3.9.2 $[Co(\eta^3\text{-}L^{Ph})(NCS)_2(MeOH)]$ (C27) 156
3.9.3 $[Co(\eta^3\text{-}L^{Naph})(NCS)_2]$ (C28) 160
4 Summary and Perspectives **165**
5 Short Outlook towards Catalysis **173**

6 Experimental section **177**

6.1 General Information 177

6.2 Instrumental Details 177

6.2.1 Elemental Analysis 177

6.2.2 Infrared Spectroscopy 177

6.2.3 Magnetic Measurements 178

6.2.4 Mass Spectrometry 178

6.2.5 NMR Spectroscopy 179

6.2.6 Optical Spectroscopy 179

6.2.7 X-Ray Structure Analysis 179

6.3 Ligand Synthesis 180

6.3.1 1,2-Bis(chloroacetyl)hydrazide (1) 180

6.3.2 2,5-Bis(chloromethyl)-1,3,4-oxadiazole (2) 181

6.3.3 2,5-Bis(azidomethyl)-1,3,4-oxadiazole (3) 182

6.3.4 2,5-Bis(aminomethyl)-1,3,4-oxadiazole (4) 183

6.3.5 2,5-Bis[(1*H*-imidazol-2-ylmethyl)amino]methyl-1,3,4-oxadiazole ($L^{5,Im}$) 184

6.3.6 2,5-Bis[(1,3-thiazol-2-ylmethyl)amino]methyl-1,3,4-oxadiazole ($L^{5,TA}$) 185

6.3.7 Methyl 4-methoxypicolinate (5) 186

6.3.8 4-Methoxy-2-(hydroxymethyl)pyridine (6) 187

6.3.9 2-Chloromethyl-4-methoxypyridine (7) 188

6.3.10 2-Azidomethyl-4-methoxypyridine (8) 189

6.3.11 (4-Methoxy-pyridin-2-yl)methylamine (9) 190

6.3.12 2,5-Bis[(4-methoxypyridin-2-ylmethyl)amino]methyl-1,3,4-oxadiazole ($L^{6,OMe}$) 191

6.3.13 4-Chloro-pyridine-2-carboxylic acid methyl ester (10) 192

6.3.14 (4-Chloropyridin-2-yl)methanol (11) 193

6.3.15 4-Chloro-2-chloromethyl pyridine (12) 194

6.3.16 2-(Azidomethyl)-4-chloropyridine (13) 195

6.3.17 (4-Chloropyridin-2-yl)methanamine (14) 196

6.3.18 2,5-Bis[(4-chloropyridin-2-ylmethyl)amino]methyl-1,3,4-oxadiazole ($L^{6,Cl}$) 197

6.3.19 Methyl pyrazine-2-carboxylate (15) 198
6.3.20 Pyrazin-2-ylmethanol (16) 199
6.3.21 2-Pyrazinemethylphthalimide (17) 200
6.3.22 2-(Aminomethyl)pyrazine (18) 201
6.3.23 2,5-Bis[(pyrazin-2-ylmethyl)amino]methyl-1,3,4-oxadiazole ($L^{6,N}$) 202
6.3.24 Pyridin-2-carboxylic acid hydrazide (19) 203
6.3.25 N'-(Chloroacetyl)-2-pyridinecarboxylic acid hydrazide hydrochloride (20) 204
6.3.26 2-(Chloromethyl)-5-(pyridin-2-yl)-1,3,4-oxadiazole (21) 205
6.3.27 Bis[(2-pyridyl)methyl]amine (22) 206
6.3.28 2-(2-Pyridyl)-5-[N,N-bis(2-pyridylmethyl)aminomethyl]-1,3,4-oxadiazole ($L^{Py,1}$)… 207
6.3.29 2-(2-Pyridyl)-5-[(2-pyridylmethyl)aminomethyl]-1,3,4-oxadiazole ($L^{Py,2}$) 208
6.3.30 Pyridin-2-yl-acetic acid hydrazide (23) 209
6.3.31 N'-(Chloroacetyl)-2-pyridylacetic acid hydrazide hydrochloride (24) 210
6.3.32 2-(Chloromethyl)-5-(pyridin-2-ylmethyl)-1,3,4-oxadiazole (25) 211
6.3.33 2-(Pyridin-2-ylmethyl)-5-[N,N-bis(2-pyridylmethyl)aminomethyl]-1,3,4-…….. oxadiazole ($L^{Py,3}$) 212
6.3.34 2-(Pyridin-2-ylmethyl)-5-[(2-pyridylmethyl)aminomethyl]-1,3,4-oxadiazole ($L^{Py,4}$). 213
6.3.35 Benzoic acid hydrazide (26) 214
6.3.36 N'-(2-chloroacetyl)benzohydrazide (27) 215
6.3.37 2-(Chloromethyl)-5-phenyl-1,3,4-oxadiazole (28) 216
6.3.38 2-Phenyl-5-[N,N-bis(2-pyridylmethyl)aminomethyl]-1,3,4-oxadiazole (L^{Ph}) 217
6.3.39 Methyl naphthalene-2-carboxylate (29) 218
6.3.40 2-Naphthohydrazide (30) 219
6.3.41 N'-(2-chloroacetyl)naphthalene-2-carbohydrazide (31) 220
6.3.42 2-(Chloromethyl)-5-(naphthalen-2-yl)-1,3,4-oxadiazole (32) 221
6.3.43 2-(Naphthalen-2-yl)-5-[N,N-bis(2-pyridylmethyl)aminomethyl]-1,3,4-…….. oxadiazole (L^{Naph}) 222
6.4 Complex Synthesis 223

6.4.1 $[Fe_2(\mu2\text{-}L^{5,Im})_2](BF_4)_4 \cdot 2MeCN$ (C1) 223
6.4.2 $[Fe_2(\mu2\text{-}L^{5,Im})_2](ClO_4)_4 \cdot 2MeCN$ (C2) 224
6.4.3 $[Fe_2(\mu2\text{-}L^{5,Im})_2](CF_3SO_3)_4 \cdot 2MeCN$ (C3) 225
6.4.4 $[Fe_2(\mu2\text{-}L^{5,TA})_2](BF_4)_4 \cdot 2MeCN$ (C4) 226
6.4.5 $[Fe_2(\mu2\text{-}L^{5,TA})_2](ClO_4)_4$ (C5) 227
6.4.6 $[Fe_2(\mu2\text{-}L^{5,TA})_2](CF_3SO_3)_4 \cdot 2MeCN$ (C6) 228
6.4.7 $[Fe_2(\mu2\text{-}L^{6,OMe})_2](ClO_4)_4 \cdot 2MeCN$ (C7) 229
6.4.8 $[Fe_2(\mu2\text{-}L^{6,OMe})_2](CF_3SO_3)_4 \cdot 2MeCN$ (C8) 230
6.4.9 $[Fe_2(\mu2\text{-}L^{6,Cl})_2](BF_4)_4$ (C9) 231
6.4.10 $[Fe_2(\mu2\text{-}L^{6,Cl})_2](ClO_4)_4$ (C10) 232
6.4.11 $[Fe_2(\mu2\text{-}L^{6,Cl})_2](CF_3SO_3)_4 \cdot 2MeCN$ (C11) 233
6.4.12 $[Fe_2(\mu2\text{-}L^{6,N})_2](BF_4)_4 \cdot 2MeCN$ (C12) 234
6.4.13 $[Fe_2(\mu2\text{-}L^{6,N})_2](ClO_4)_4 \cdot 2MeCN$ (C13) 235
6.4.14 $[Fe_2(\mu2\text{-}L^{Py,1})_2](BF_4)_4 \cdot 2MeNO_2$ (C14) 236
6.4.15 $[Fe_2(\mu2\text{-}L^{Py,1})_2](BF_4)_4 \cdot 2MeNO_2$ (C14') 237
6.4.16 $[Fe_2(\mu2\text{-}L^{Py,1})_2](ClO_4)_4 \cdot 2MeNO_2$ (C15) 238
6.4.17 $[Fe(py)_4(NCS)_2]$ 239
6.4.18 $[Fe(py)_4(NCSe)_2]$ 240
6.4.19 $[Fe(py)_4(NCBH_3)_2]$ 241
6.4.20 $[Fe(L^{Py,1})(NCS)_2] \cdot 1MeCN$ (C16·1MeCN) 242
6.4.21 $[Fe(L^{Py,1})(NCS)_2] \cdot 1MeOH$ (C16·1MeOH) 243
6.4.22 $[Fe(L^{Py,1})(NCSe)_2] \cdot 3MeCN$ (C17·3MeCN) 244
6.4.23 $[Fe(L^{Py,1})(NCBH_3)_2] \cdot 1MeOH$ (C18·1MeOH) 245
6.4.24 $[Fe(L^{Ph})(NCS)_2] \cdot 2MeCN$ (C19·2MeCN) 246
6.4.25 $[Fe(L^{Ph})(NCS)_2] \cdot 3MeOH$ (C19·3MeOH) 247
6.4.26 $[Fe(L^{Ph})(NCSe)_2] \cdot 2MeCN$ (C20·2MeCN) 248
6.4.27 $[Fe(L^{Ph})(NCSe)_2] \cdot 3MeOH$ (C20·3MeOH) 249
6.4.28 $[Fe(L^{Ph})(NCBH_3)_2] \cdot 1MeCN$ (C21·1MeCN) 250
6.4.29 $[Fe(L^{Ph})(NCBH_3)_2] \cdot 1.8MeOH$ (C21·1.8MeOH) 251

6.4.30 $[Ni(\eta3\text{-}L^{Ph})_2](ClO_4)_2$ (C22) 252

6.4.31 $[Fe(L^{Naph})(NCBH_3)_2] \cdot 4.5MeCN$ (C23·4.5MeCN) 253

6.4.32 $[Fe(L^{Naph})(NCBH_3)_2] \cdot 3MeOH$ (C23·3MeOH) 254

6.4.33 $[Zn(py)_4(NCBH_3)_2]$ (C24) 255

6.4.34 $[Zn(L^{Naph})(NCBH_3)_2]$ (C25) 256

6.4.35 $[Co(L^{Py,1})(NCS)_2] \cdot 1MeOH$ (C26) 257

6.4.36 $[Co(\eta3\text{-}L^{Ph})(NSC)_2(MeOH)]$ (C27) 258

6.4.37 $[Co(\eta3\text{-}L^{Naph})(NCS)_2]$ (C28) 259

Literature **261**

Appendix **279**

A IR Spectra 279

B NMR Spectra 301

C Mass Spectra 337

D Crystallographic Data 343

E Structural parameters of characterized coordination compounds 359

F Additional Figures and Tables 375

G Magnetic Measurements 437

H Complex coordinates 463

Curriculum Vitae **496**

Nomenclature

χ_M	Molar magnetic susceptibility
χ_g^{solv}	Mass susceptibility of the solvent in *Evans'* method
d	Distance
$\bar{d}$	Mean distance
Δ_o	Crystal field in a complex with octahedral coordination sphere
Δ_c	Critical crystal field
Δ_{HS}	Crystal field in a high spin complex
Δ_{LS}	Crystal field in a low spin complex
δ	Isomeric shift in Mössbauer spectroscopy
ΔE_Q	Quadrupole splitting energy in Mössbauer spectroscopy
E_P	Mean spin pairing energy
E	Energy
f	NMR spectrometer frequency
f_i	Vibrational force constant in the harmonic oscillator model of state i
Δf	NMR frequency shift
G	Gibbs free energy
g	*Landé* factor
γ_{HS}	Mole fraction of HS molecules
H	Enthalpy
$\hat{H}$	Total Energy operator "*Hamiltonian*"
J	Exchange coupling constant
k_B	*Boltzmann* constant:
L	Total orbit angular momentum
λ_{abs}	Absorption wavelength
λ_{em}	Emission wavelength
λ_{ex}	Excitation wavelength
m	Mass
m_{red}	Reduced mass
μ	Dipole moment
μ_B	*Bohr* magneton: $9.274 \cdot 10^{-24}\,JT^{-1}$
μ_{eff}	Effective magnetic moment
N_A	Avogadro constant: $6.022 \cdot 10^{23}\,mol^{-1}$
ν	Frequency
φ_i	Cis-angle in an octahedron

R	Gas constant : 8.3144598 $JK^{-1}mol^{-1}$
r	Metal-ligand distance
ρ_0	Density of the solvent in the *Evans'* Method
ρ_s	Density of the solution in the *Evans'* Method
S	Total spin angular momentum
S	Entropy
Σ_O	Octahedral distortion parameter
T	Temperature
τ	Relaxation time
U_{eff}	Effective energy barrier
V	Volume
W	Stabilization factor of the [HS-LS] state

CShM	Continuous Shape Measurement
DSC	Differential Scanning Calorimetric
EPR	Electron Paramegnetic Resonance
eq.	Equivalents: Molar ratios in chemical reactions
HS	High Spin
HMBC	Heteronuclear Multiple Bond Correlation
HSQC	Heteronuclear Single Quantum Correlation
IC	Internal Conversion
ISC	InterSystem Crossing
IR	Infrared
LIESST	Light Induced Excited Spin State Trapping
LS	Low Spin
MLCT	Metal to Ligand Charge Transfer
MuSR	Muon Spin Rotation
NFS	Nuclear Forward Scattering
PAS	Positron Annihilation Spectroscpoy
ppm	Parts per million
SCO	Spin crossover
SQUID	Superconducting Quantum Interference Device
TIP	Temperature Independent Paramagnetism
UV	Ultra violet (energy range of electromagnetic radiation 100-380 nm)
Vis	Visible (energy range of electromagnetic radiation 380-780 nm)
XAS	X-ray Absorption Spectroscopy
X-ray	Electromagnetic radiation with a wavelength range of 0.01 - 10 nm

bt	2,2'-Bi-2-thiazoline
bpp	2,6-Di(pyrazol-1-yl)pyridine
bpym	2,2'-Bipyrimidine
bzp	2,6-Bis(benzimidazole-2'-yl)pyridine
DABCO	1,4-Diazabicyclo[2.2.2]octane
DMSO	Dimethylsulfoxide
H_3L^{Me}	Tris[2-{[(2-methylimidazol-4-yl)methylidene]amino}ethyl]amine
hptrz	4-Heptyl-1,2,4-triazole
Hpy-DAPP	Bis[N-(2-pyridylmethyl)-3-amino-propyl](2-pyridyl-methyl)amine
l^2MTD	2,5-Bis[(1H-imidazol-2-ylmethyl)amino]methyl-1,3,4-thiadiazole
l^4MTD	2,5-Bis[(1*H*-imidazol-4-ylmethyl)-amino]methyl-1,3,4-thiadiazole
L1	N-salicylidene-4-amino-1,2,4-triazole
$L^{5,Im}$	2,5-Bis[(1H-imidazol-2-ylmethyl)amino]methyl-1,3,4-oxadiazole
$L^{5,TA}$	2,5-Bis[(1,3-thiazol-2-ylmethyl)amino]methyl-1,3,4-oxadiazole
$L^{6,Cl}$	2,5-Bis[(4-chloropyridin-2-ylmethyl)amino]-methyl-1,3,4-oxadiazole
$L^{6,N}$	2,5-Bis[(pyrazin-2-ylmethyl)amino]methyl-1,3,4-oxadiazole
$L^{6,OMe}$	2,5-Bis[(4-methoxypyridin-2-ylmethyl)amino]methyl-1,3,4-oxadiazole
$L^{6\text{-}OH}$	Tris{4-[(6-methanol)-2-pyridyl]-3-aza-3-butenyl}amine
L^{Naph}	2-(Naphthalen-2-yl)-5-[N,N-bis(2-pyridylmethyl)aminomethyl]-1,3,4-oxadiazole
$L^{Py,1}$	2-(2-Pyridyl)-5-[N,N-bis(2-pyridylmethyl)aminomethyl]-1,3,4-oxadiazole
$L^{Py,2}$	2-(2-Pyridyl)-5-[(2-pyridylmethyl)aminomethyl]-1,3,4-oxadiazole
$L^{Py,3}$	2-(Pyridin-2-ylmethyl)-5-[N,N-bis(2-pyridylmethyl)aminomethyl]-1,3,4-oxadiazole
$L^{Py,4}$	2-(Pyridin-2-ylmethyl)-5-[(2-pyridylmethyl)aminomethyl]-1,3,4-oxadiazole
L^{Ph}	2-Phenyl-5-[N,N-bis(2-pyridylmethyl)aminomethyl]-1,3,4-oxadiazole
NH_2trz	4-NH2-1,2,4-triazole
phen	1,10-Phenanthroline
pic	Picolylamine
PMAT	4-Amino-3,5-bis((2-pyridylmethyl)aminomethyl)-1,2,4-triazole
PMOD	2,5-Bis{[(2-pyridyl-methyl)amino]methyl}-1,3,4-oxadiazole
PMTDA	2,5-Bis((2-pyridylmethyl)aminomethyl)-1,3,4-thiadiazol
PPTD	2-(2-Pyridyl)-5-[N,N-bis(2-pyridyl-methyl)amino]methyl-1,3,4-thiadiazole
PSTD	2,5-Bis[(2-pyridylmethyl)thio]methyl-1,3,4-thiadiazole
terpy	2,2':6',2''-terpyridine
TMTD	2,5-Bis{[(thiazol-2-ylmethyl)-amino]-methyl}-1,3,4-thiadiazole
TPA	Tris(2-pyridylmethyl)amine

1 Introduction

Fifty-six years ago, *Gordon E. Moore* published a prediction that transistor density on integrated circuits (computer chips) will double every two years.[1] Well known as *Moore's law*, this statement suggests that computational progress will steadily become smaller, faster and cheaper. While this has been true for the last few decades, a discernible end is in sight. At some point, transistors will not be able to function within smaller circuits since miniaturization approaches its physical rather than its technological cap. This is mainly due to the limitation of thickness of the conduction oxide layer and inefficient heat dissipation.[2] To go beyond this critical point, bistable molecular switches might be the key to further enhance the performance of electronic components in the future. *Bistability* refers to the property of a system to exist in two thermodynamically stable states within a given range of equal physical parameters. The main focus of this research topic concentrates on molecular magnetism and electronically bistable molecules. The phenomenon of magnetism, caused by the movement of electric currents and magnetic moments of elementary particles, has become an inseparable part of everyday life. Hence, the application of magnetic materials range from telecommunications technology (memories, sensors) to acoustic components (microphones), magneto-mechanical machines (frictionless bearings, magnetic separators) and medical diagnostics (magnetic resonance imaging MRI).[3] Also for chemists, magnets play a major role in various analytical techniques (MS,[4] EPR,[5] NMR,[6] SQUID[7]). While the physical properties of classical bulk-magnets are based on magnetic domains,[8] molecular magnetism may arise from a single molecule.[9,10] Here, the first breakthrough was achieved by *Sessoli et al.* in 1993 with the publication "Magnetic bistability in a metal-ion cluster".[11] The reported manganese acetate cluster "$Mn_{12}O_{12}$" exhibits slow magnetic relaxation of magnetization and hysteretic behavior below 4 K. These kinds of materials are nowadays known as *single molecule magnets* (SMMs). Due to their present *bistability*, potential future applications range from high density data storages to quantum computing and spintronic devices.[12–17] In contrast to that, electronically bistable molecules can be triggered due to external stimuli such as temperature, pressure, light irradiation or chemical reactions.[2] Representatives of this substance class are complexes that exhibit valence tautomerism,[18] mixed valence[19] and spin crossover[20–25]. However, *bistability* alone is not sufficient to discuss such material as potential building block in molecular electronics. Furthermore, a respond function like the change in magnetic moment[20–25], colour,[26] dielectric constant,[27] electrical resistance[28] or refractive index[29] must be present. This work mainly deals with SCO materials, described in the following chapters.

1.1 The Spin Crossover Phenomenon

Octahedral coordinated metals of the first transition row with electron configuration $3d^4$ – $3d^7$ (Cr^{II}, Mn^{III}, Fe^{III}, Mn^{II}, Fe^{II}, Co^{III}, Co^{II}) can exhibit two different electronic ground states, depending on the present ligand field splitting energy.[30,31] If the octahedral ligand field is significantly larger than the spin pairing energy ($\Delta_o >> E_P$), the lower energy t_{2g}-orbitals are firstly occupied and the ground state of the central metal possesses the lowest possible total spin (low-spin, LS). However, if the ligand field is much smaller than the spin pairing energy ($\Delta_o << E_P$), the occupation of the d-orbitals follows *Hund's* first rule and the state with highest possible total spin (high-spin, HS) is populated.[32] This inevitably leads to the occupation of the antibonding e_g*-orbitals. In the case of the critical crystal field Δ_c where both energies are approximately equal, the spin ground state of the transition metal depends solely on external perturbations. The change of ground state due to the variation in temperature and pressure or caused by irradiation with electromagnetic light is called "spin crossover" (SCO) or "spin transition". However, it is important to point out that Δ_c is different for every coordinated metal center due to varying spin pairing energies.[30] Iron(II) coordination compounds take a special role in the field of SCO since they offer the only electron configuration (d^6) that allows for the switch between a diamagnetic LS state ($^1A_{1g}$, $S = 0$) and a paramagnetic HS state ($^5T_{2g}$, $S = 2$). This is especially interesting in terms of binary digital computing (0 *vs.* 1).[33] Figure 1.1 illustrates the energy diagram of electron configuration for the possible spin ground states in an octahedral d^6 system.

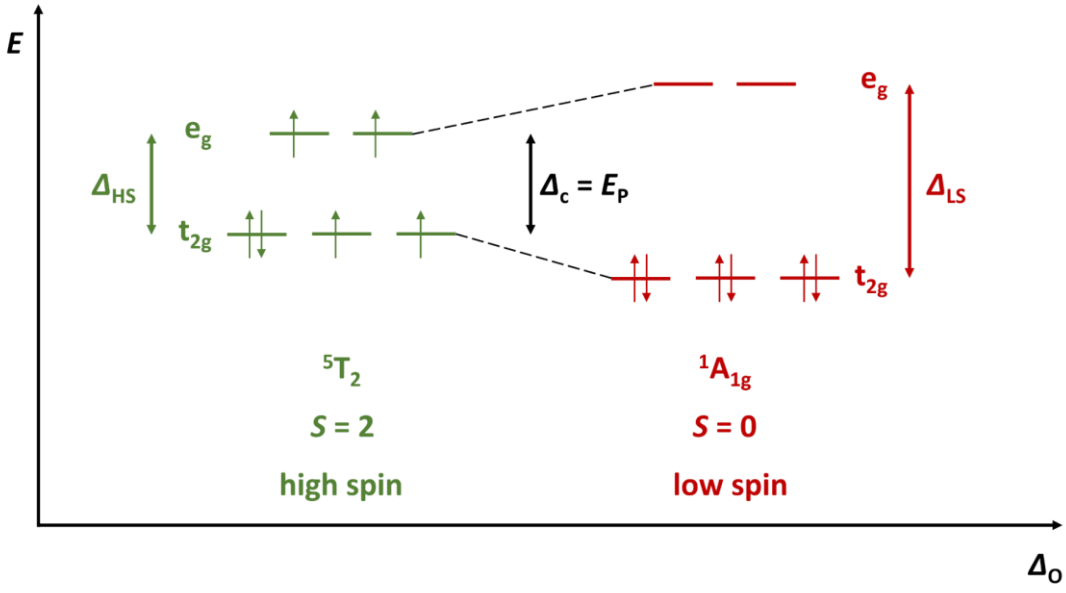


Figure 1.1 Schematic representation of ligand field splitting energies in octahedral complexes with $3d^6$ electron configuration. Due to the present coordination sphere, metal d-orbitals are split into e_g and t_{2g} subsets.

As this work mainly deals with the synthesis and characterization of iron(II) SCO compounds, all further theoretical discussions will be related to the d^6 system. The effect of ligand field strength on the energy of ground and excited states is expressed in the corresponding *Tanabe-Sugano* diagram.[34] Here, energy and ligand field are expressed through the *Racah* parameter *B* of the electron-electron repulsion.[35] Figure 1.2 shows the variation of chosen ground and excited states of a $3d^6$ ion with increasing octahedral ligand field. The electronic terms of the free ion, found at zero field, result from the *Russel-Saunders* coupling scheme ^{2S+1}L with the spin multiplicity $2S+1$ and the orbital momentum *L*.[36] Hence, the ground state is the ^{5}D term which possesses the highest spin multiplicity. The triplet and singlet terms (^{3}H and ^{1}I) are higher in energy since they exhibit larger electron-electron repulsion. Upon octahedral coordination, these terms are further split into ligand field terms. Hence, the ^{5}D term splits into the ligand field terms ^{5}E and $^5T_2$. Additionally, the ^{3}H term is split in the two triplet states $^3T_2$ and $^3T_1$ while the ^{1}I state splits into $^1T_2$, $^1T_1$ and $^1A_1$ ligand field components. In a weak octahedral ligand field, the $^5T_2(^5D)$ term displays the ground state and represents the HS state ($t_{2g}^4 e_g^2$) with $S = 2$. For increasing ligand field strengths, however, the $^1A_1(^1I)$ state is rapidly lowered in energy relative to the $^1T_1(^1I)$ state. Thus, at the critical ligand field Δ_c, the $^1A_1(^1I)$ term becomes the ground state, representing the LS state ($t_{2g}^6 e_g^0$) with $S = 0$. As discussed before, Δ_c marks the ligand field where Δ_o equals E_P. SCO complexes possess ligand field strength in vicinity close to Δ_c In this case, interconversion between HS and LS state can be triggered by external perturbations. Typical values of the ligand field splitting energy in SCO active complexes lie in the range of Δ_o^{HS} = 11500 – 12500 cm^{-1} and Δ_o^{LS} = 19000 – 21000 cm^{-1}.[31]

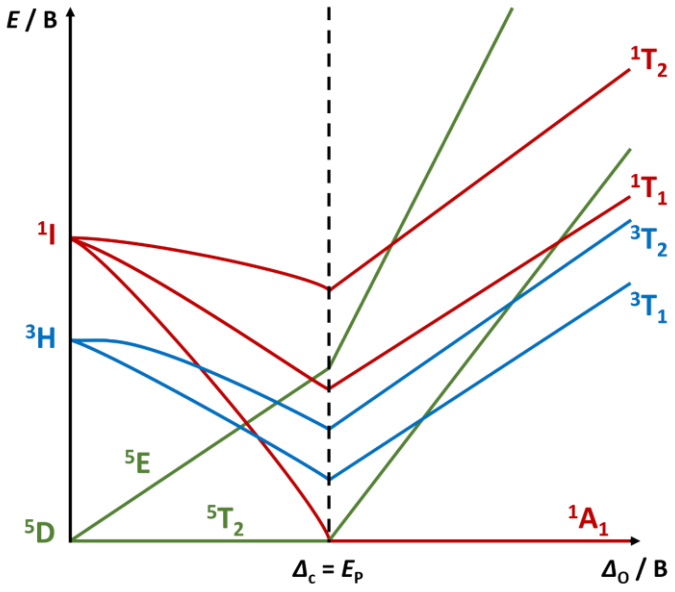


Figure 1.2 *Tanabe-Sugano* diagram for an octahedral coordinated $3d^6$ ion with chosen electronic terms. Quintet states are displayed in green, triplet states in blue and singlet states in red. The diagram was adopted from the work of *Tanabe* and *Sugano*.[34]

To understand the significance of the crossing point at Δ_c and the phenomenon of the thermal spin transition, it is insufficient to solely consider the *Tanabe-Sugano* diagram. This merely reflects the electronic energies of the excited states in relation to the ground state. However, the ligand field strength depends not only on the electronic nature of the ligands, but also on their metal-ligand distance. Hence, the ligand field splitting energy in octahedral complexes with neutral ligands can be estimated via Equation 1.1 with the dipole moment μ and the metal-ligand distance *r.*

$$\Delta_o \sim \frac{\mu}{r^6} \tag{1.1}$$

In general, the metal-ligand bond lengths in iron(II) high-spin complexes are much longer than those in the corresponding low-spin complexes. This can be explained by the occupation of antibonding e_g*-orbitals in the HS configuration. For SCO active compounds with a $\{N_6\}$ donor set, which is the most reported ligand set in literature, the metal-ligand bond distance varies between 1.95 – 2.00 Å and 2.12 – 2.18 Å for LS and HS complexes, respectively.[37,38] Therefore, the adiabatic potential wells of the $^5T_2$ and $^1A_1$ ground states are not only shifted with respect to their specific energies but also to their metal-ligand distances, shown in Figure 1.3. The resulting horizonal shift in the energy (*E*) *vs*. bond distance (*r*) plot is expressed by Δr_{HL}. Due to the stronger metal-ligand bond, the vibrational force constant f_{HS} is lower. This yields in a higher density of vibrational states in the $^5T_2$ (HS) state. In addition, the $^5T_2$ potential well is shifted vertically towards higher energy by ΔE_{HL} with respect to the $^1A_1$ state. The magnitude of ΔE_{HL} strongly depends on the properties of the coordinating ligands like strain, donor and acceptor strengths.

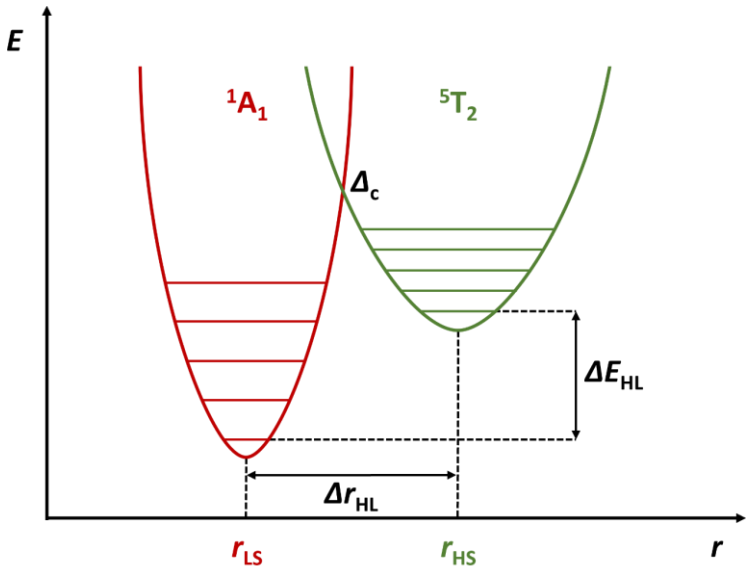


Figure 1.3 Schematic representation of the energy of the $^1A_1$ and $^5T_2$ potential wells in a d^6 system as a function of the metal-ligand bond distance *r*. Red marks the LS state ($^1A_1$), while green represents the HS term ($^5T_2$).

For SCO compounds, ΔE_{HL} is of the order of thermal energy. The intersection of both potential wells can be assigned to the critical ligand field splitting energy Δ_c, shown in the *Tanabe-Sugano* diagram in Figure 1.2. However, due to the pronounced difference in metal-ligand bond distances in the LS and HS state and the $\Delta_o \sim \mu \cdot r^{-6}$ correlation (Equation 1.1), Δ_c can never be the system's ground state ligand field. Hence, SCO active compounds *always* possess ligand field strengths in close vicinity. According to Figure 1.3, the zero-point energy of the LS state is lower compared to the HS state. Hence, the LS state is the electronic ground state and populated at very low temperature. Upon heating, the HS state will be populated at some point since it gets energetically accessible. Following this statement, the spin transition can be seen as a phase transition associated with a change in the Gibbs free energy *G*, which depends on the enthalpy and entropy Equation 1.2).[39]

$$G = -T \cdot S \tag{1.2}$$

During the spin transition at a critical temperature ($T = T_c$), the *difference* in the Gibbs free energy of the LS and HS state is null ($\Delta G = 0$). The change in enthalpy $\Delta H = H_{HS} - H_{LS}$ is usually in the range of 10 – 20 kJmol^{-1}, while the entropy change ($\Delta S = S_{HS} - S_{LS}$) is of the order 50 – 80 Jmol^{-1}K^{-1}.[40] Consequently, the electronic state with lower internal energy represents the ground state at lower temperature, where the entropy term is almost irrelevant. At higher temperature in contrast, *S* becomes increasingly important and starts to dominate the enthalpy term. The degree of freedom, and hence the entropy, is much greater in the HS than in the LS state. Therefore, approx. 25 % of the total entropy gain accompanying the SCO arises from the change in spin multiplicity, expressed by Equation 1.3.[41]

$$\Delta S_{mag} = R \cdot \ln\left(\frac{(2S+1)_{HS}}{(2S+1)_{LS}}\right) \tag{1.3}$$

Assuming a d^6 system with $S = 2$ for the HS and $S = 0$ for the LS state, ΔS_{mag} is equal to 13.4 J K mol^{-1}. This is attributed to the 15-fold degenerated $^5T_2$ state compared to the one-fold $^1A_1$ term. The major contribution, however, originates from changes in the intramolecular vibrations.[41,42] Hence, the SCO phenomenon can be seen as an entropy driven process.

1.2 Further ways to induce Spin Crossover

1.2.1 Pressure

Next to the temperature induced SCO, the application of pressure is a common and popular way to trigger the spin transition. The Gibbs free energy of a neat SCO system can be described with Equation 1.4.[43]

$$G(\gamma_{HS}, p, T) = \gamma_{HS}\left[\Delta F^0_{HL}(T) + p\Delta V^0_{HL}\right] - TS_{mix}(\gamma_{HS}) + G^{int}(\gamma_{HS}) \qquad (1.4)$$

Here, the high-spin mole fraction γ_{HS} of the random high-spin molecules is defined through $\gamma_{HS} = n_{HS}/(n_{HS} + n_{LS})$ with $\gamma_{LS} = 1 - \gamma_{HS}$. All γ_{HS}-independent terms are omitted for simplification. The free energy difference between the HS and the LS state in a given reference lattice in the absence of interactions at 1 bar is defined by the term $\Delta F^0_{HL}(T) = \Delta F^0_{HS}(T) - \Delta F^0_{LS}(T)$. This energy difference can be determined from transition curves (see Chapter 1.4) obtained for highly diluted mixed crystals, where the SCO active complex is doped into an isomorphous host lattice.[44,45] $\Delta V^0_{HL} = \Delta V^0_{HS} - \Delta V^0_{LS}$ displays the difference in volume between high and low-spin state, as the coordination spheres for both ground states differ. $S_{mix} = [\gamma_{HS} \cdot \ln(\gamma_{HS}) + (1 - \gamma_{HS}) \cdot \ln(1 - \gamma_{HS})]$ describes the mixing entropy for the neat SCO active compound, while G^{int} takes all interactions between the spin changing molecules in account. The resulting change in free energy of the HS and LS state can be directly understood phenomenologically by the afore described changes in metal-ligand bond lengths associated with the spin transition. In agreement with Equation 1.4, increasing the pressure will result in the destabilization of the HS state, as it possesses longer bond lengths and thus larger coordination volumes.[46] Hence, for a system at equilibrium, the transition temperature T_c is shifted to higher values since the energy gap between the LS and HS state becomes larger.[47,48]

1.2.2 Light Induced Excited Spin State Trapping (LIESST)

First evidence of the light-induced excited spin state trapping (LIESST) in an dissolved iron(II) SCO active compound was reported by *McGarvey et al.* in 1982.[49] Two years later, *Decurtins et al.* published the study about the exact same effect in the solid state.[50] The authors could show that it is possible to convert a low-spin state into a metastable high-spin state at low temperature due to the irradiation of green light. This phenomenon was further extended by *Hauser* at a later point in time, who showed the opposite effect upon using red light. This light-induced spin state switch from the HS to the LS state is referred to as reverse-LIESST effect.[51]

The rapid switching between two metastable states via light irradiation enables the usage of such material in electronic devices, where the change in temperature or pressure can be hard to realize.[52,53] Today, it is generally assumed that due to the large increase in metal-ligand bond lengths during the light-induced SCO, elastic interactions are of particular importance for the correct interpretation of the photo-magnetic findings.[52] Figure 1.4 illustrates the LIESST relevant electronic states in an octahedral SCO active Fe(II) complex, where the energy is plotted against the meta-ligand distance *r*(M-L). At low temperature, the thermodynamically stable LS ($^1A_1$) state can be excited via the spin allowed $^1A_1 \rightarrow {}^1T_1$ ($\lambda_{ex} \approx 515$ nm) or $^1A_1 \rightarrow$MLCT transition into the excited $^1T_1$ or MLCT state, respectively (orange arrows in Figure 1.4).[54,55] Such an accessible low-lying metal to ligand charge transfer (MLCT) state can be the product of a coordinated ligand possessing large π-systems. After excitation, the system relaxes via a cascade of processes, such as vibrational relaxation, internal conversion (IC) or intersystem crossing (ISC). Please note that the non-radiative pathways IC and ISC only occur between isoenergetic states and should thus be drawn in a horizontal manner. Hence, they usually result in vibrational excited states, followed by a non-radiative vibrational relaxation. However, for graphical simplification, these two steps have been combined in the shown curved arrows.

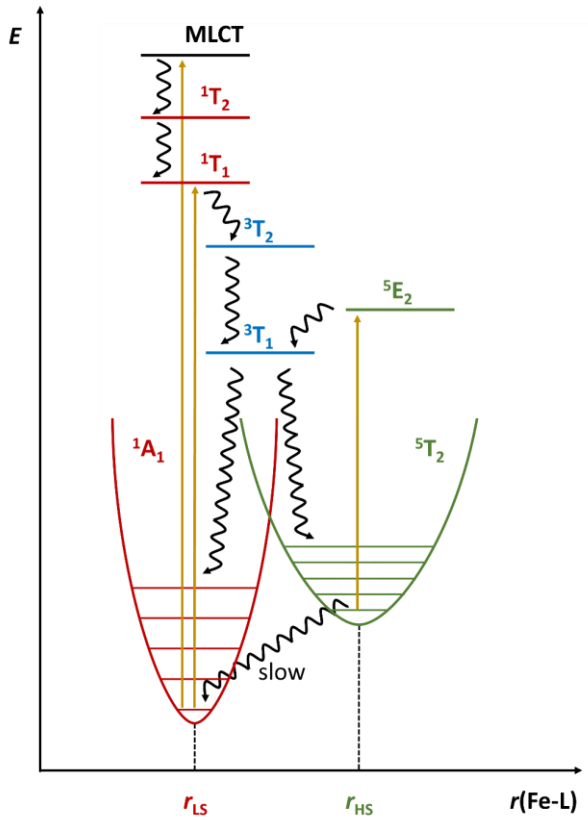


Figure 1.4 Simplified energy diagram of the electronic ground and excited states in Fe(II) SCO complexes. The energy of the harmonic potentials is displayed as a function of the metal-ligand distance *r*(Fe-L). The excited singlet, triplet and quintet states and the MLCT state are shown as horizontal lines for the sake of clarity. Straight arrows represent electronic transitions due to radiative excitation. Curved arrows, in contrast, represent combined radiative and non-radiative decay pathways.

According to the scheme in Figure 1.4, the $^3T_1$ can finally relax to the LS ($^1A_1$) or metastable HS ($^5T_2$) state. Therefore, a sufficient irradiation time is needed to populate the $^5T_2$ state. The occurrence of LIESST is ensured by the slow radiative direct decay from the $^5T_2$ state to the $^1A_1$ state. This allows for trapping of the system in the metastable state. However, if the thermal energy is high enough [*T*(LIESST)], the system will relax back to the ground state. In 2018, *Guionneau et al.* discussed the proper way to determine this temperature in the publication "A critical review of the T(LIESST) temperature in spin crossover materials – What it is and what it is not".[56] Once the system is successfully trapped in the $^5T_2$ state, it can be excited into the $^5E_2$ state due to irradiation with red light ($\lambda_{ex} \approx 820$ nm), which is referred to as reverse-LIESST effect (orange arrow in Figure 1.4).[51] Following the same relaxation cascade described above, the $^1A_1$ ground state can thus be populated with a sufficient irradiation time. The present activation energy for a LIESST active SCO system and the relating lifetime of the photoinduced HS state can be determined by kinetic measurements.[57]

1.3 Detecting the spin transition

The different electronic configuration of the HS state ($t_{2g}^4 e_g^2$) compared to the LS state (t_{2g}^6) results in a pronounced change of different physical parameters. Therefore, the detection of the SCO phenomenon can be achieved by various methods.

1.3.1 Single Crystal X-Ray Structure Analysis

Single crystal X-ray diffraction is a valuable technique to track the SCO phenomenon in a crystalline sample. In molecular spin crossover active compounds, the spin transition is associated with a pronounced change in the structural degrees of freedom.[58] Due to the different occupation of the antibonding e_g*-orbitals in the LS state compared to the HS state, molecular structural parameters differ for both forms. Firstly, the metal-ligand bond distances change, which becomes most evident in the case of the Fe(II) ion with a difference of $\Delta r_{HL} \approx 0.2$ Å.[37,38,58] This inevitably alters the volume of the octahedral coordination sphere in Fe(II)L_6 complexes. Therefore, the volume in the HS state takes typical values around $V_{O,HS} \approx 13$ Å³, while the coordination volume in the LS state is much smaller with $V_{O,LS} \approx 10$ Å³.[59] In contrast, the differentiation of the spin state for the Fe(III) or Co(II) ion can be more challenging with $\Delta r_{HL} \approx 0.15$ Å[60] and $\Delta r_{HL} \approx 0.09$ Å,[61] respectively. Secondly, the present metal-ligand angles change for both spin states. In general, the HS state possesses a more distorted coordination sphere compared to the more ideal octahedron of the LS state. This can be explained by the enhanced degree of freedom associated with the increased bond distances, combined with the anisotropic electron configuration in the high-spin state.

The distortion of the coordination sphere is usually quantified by continuous shape measurements (CShM)[62] or by applying the octahedral distortion parameter Σ_O. This value is defined as the sum over the absolute deviations of the twelve *cis*-angles φ_i from the ideal 90 ° angle (Equation 1.5).

$$\Sigma_O = \sum_{i=1}^{12} |90\,° - \varphi_i| \tag{1.5}$$

An ideal octahedron would thus have a distortion parameter of Σ_O = 0 °. The index was firstly introduced by *Hendrickson et al.* to measure small deviations of the coordination geometry in iron(II) HS complexes.[63] *Guionneau et al.* adopted this parameter and assigned coarse values to the high-spin and low-spin states.[64] Thus, FeN_6 HS complexes usually yield distortion parameters greater than 100 °, while they are smaller than 80 ° in the corresponding LS complexes. In addition to the coordination sphere of one SCO active molecule, single X-ray structure analysis can give an insight into the intermolecular interactions in the solid state, which can be crucial for the spin switching.

1.3.2 UV/Vis spectroscopy

Due to the fact that the electronic ground term changes in the course of spin crossover, the optical properties of the two states differ. As discussed for the LIESST effect in Chapter 1.2.2, the ligand field excitations in the HS and LS states are different for an octahedrally coordinated iron(II) ion. Thus, the $^1A_1$ (LS) state can be excited to the $^1T_1$ state with light of wavelength $\lambda_{ex} \approx 515$ nm.[54,55] In case this is the only absorption in the visible region, the coordination compound usually appears to have a violet colour.[20,65] In contrast, the energy difference between the $^5T_2$ (HS) ground state and the ^5E excited state is roughly equal to $\lambda_{ex} \approx 820$ nm[51] and thus outside the visible region (400 – 750 nm)[66]. Therefore, an octahedrally coordinated SCO complex can switch its colour from red/violet (HS) to pale-coloured/colourless (LS),[54,55] which can be tracked in UV/Vis studies. However, according to the selection rules of electronic transitions, such ligand field transitions are spin allowed but *Laporte* forbidden and thus often not easy to detect.[67] This not only complicates tracing the spin crossover but may also hinder the determination of the present ligand field strength. To overcome this obstacle, *Busch et al*. suggested to predict a possible spin transition in an octahedral iron(II) complex by studying the ligand field splitting of the analogous nickel(II) complex, possessing the same coordination sphere.[68] The comparison of different coordination compounds yielded in the mean $\Delta_o(Fe^{2+})/\Delta_o(Ni^{2+})$ ratio of 1.11, showing a decreasing trend for increasing ligand fields. *Shatruk et al*. recapped this observation and reported that ligand fields in the range of 11200 – 12400 cm^{-1} in octahedral nickel(II) complexes often lead to the observation of spin

transition in the corresponding iron(II) compounds.[69] For the more easily accessible nickel(II) complexes, the ligand field splitting energy can be simply estimated from the first spin-allowed d-d transition ($^3A_{2g} \rightarrow {}^3T_{2g}$) in the optical spectrum.[69] As SCO active compounds usually possess ligands with large π-systems, MLCT transitions often dominate the absorption spectra in the visible region. Hence, Fe(II) LS complexes do not mandatorily appear violet. However, the intensity of such MLCT bands can be used to track a possible SCO, since their intensity is directly correlated to the number of electrons in the t_{2g} orbitals for metal complexes with O_h symmetry.[70,71] Therefore, moving from the high-spin to the low-spin Fe(II) usually results in stronger MLCT absorption bands.[72]

1.3.3 ^{57}Fe Mössbauer Spectroscopy

Mössbauer spectroscopy displays the recoil-free nuclear resonant absorption and emission of γ-ray photons in solids and the accompanying hyperfine interaction in the chemical compound.[73] In 1966, *König et al.* used this method for the first time to track the spin crossover phenomenon in an iron(II) coordination compound.[74] The complex $[Fe(phen)_2(NCS)_2]$ was measured at 293 and 77 K. For the high temperature regime, the quadruple splitting ΔE_Q^{HS} is equal to 2.67(3) mms^{-1}, next to an isomeric shift of δ^{HS} = 0.98(3) mms^{-1}. At lower temperatures, these values decrease to ΔE_Q^{LS} = 0.34(6) mms^{-1} and δ^{LS} = 0.37(5) mms^{-1}. The isomeric shift δ is caused by the electrostatic interaction of the nuclear charge with the electron charge and hence describes the electron density around the nucleus. A pronounced quadrupole splitting ΔE_Q can be observed in case of an inhomogeneous electric field around the nucleus.[41,73] Since the electron distribution clearly differs for the HS and LS state in the iron(II) ion, both parameters vary between the $^5T_{2g}$ and $^1A_{1g}$ ground state.[73] Thus, zero field measurements of iron(II) SCO active complexes result in large HS quadrupole splitting energies $\Delta E_Q^{HS} \approx 2 - 3$ mms^{-1} and isomeric shifts $\delta^{HS} \approx 1$ mms^{-1}, while the values are much smaller for the corresponding LS species with $\Delta E_Q^{LS} \leq 1$ mms^{-1} and $\delta^{LS} \leq 0.5$ mms^{-1}.[75] *Ksenofontov et al.* could show that this spectroscopy method is especially suitable to distinguish between discrete [HS-LS] molecules and 1:1 mixtures of [HS-HS]:[LS-LS] molecules in dinuclear compounds.[20,76] Furthermore, the area fractions of the resonance lines are directly proportional to the HS/LS mole fractions and can be fitted with the *Lorentzian* fit.[77] By using Mössbauer spectroscopy in combination with various analytic methods, *Fürmeyer et al.* reported that the cooling rate is crucial when it comes to tracking of a phase transition associated with a SCO.[24] Thus, this technique is also very valuable to confirm phase changes during a spin transition in the solid state.

1.3.4 Infrared Spectroscopy

As the spin transition is accompanied by several structural changes due to different electronic configurations of HS and LS state, the electronic ground state can be monitored by temperature dependent infrared (IR) spectroscopy.[78] The additional occupation of antibonding e_g*-orbitals in the HS state results in weaker M-L bonds, which causes the shift of the M-L vibration bands to lower frequencies compared to the LS state. For an iron(II) coordination compound with a $\{N_6\}$ coordination sphere, the stretching frequencies of the M-L bonds lie in the range of approximately 250 – 500 cm^{-1}.[79] Additionally, the change in the M-L bond strengths can impact vibrational modes of the coordinated ligands. The pseudohalides NCS^- or $NCSe^-$ are good candidates for such studies, as their C-N stretching vibrations around 2000 cm^{-1} strongly depend on the spin state of the iron(II) center.[79,80] The increased Fe-N bond of the LS species strengthen the π-backbonding towards the ligand, which consequently results in partial depopulation of the antibonding π*(N-C) orbitals to compensate the charge deficit at the metal. Hence, the stretching N-C vibrational mode shifts to higher frequencies.[80]

1.3.5 Magnetic Measurements

The spin crossover phenomenon describes the change from a state with maximum unpaired electrons to a state with minimum unpaired electrons and vice versa. This change of the total spin inevitably leads to a change of the magnetic moment of the substance in an applied homogeneous magnetic field.[81] A popular instrument for measuring the temperature dependent magnetic susceptibility χ is the Superconducting QUantum Inteference Device (SQUID).[7] Due to the superconducting loops with *Josephson* junctions, very low magnetic fields can be determined, which allows for usage of very small sample masses in the order of milligrams. By customizing the sample holders, a variety of measurements series can be carried out under different conditions. Hence, it is possible to investigate a sample under inert atmosphere, in solution, under pressure or under light irradiation. For the most transition metals (Co(II) is an exception here), the effective magnetic moment μ_{eff} can be roughly calculated by using the spin-only formalism in Equation 1.6 with the *Landé* factor $g \approx 2$, the total spin S and the *Bohr* magneton μ_{B}.[67]

$$\mu_{\mathrm{eff}} = g\sqrt{S\,(S+1)}\,\mu_{\mathrm{B}} \tag{1.6}$$

The product of the molar magnetic susceptibility χ_M and temperature T is directly related to the magnetic moment via the *Boltzmann* constant k_{B}, the Avogadro number N_{A} and the Bohr magneton μ_{B}, as shown in Equation 1.7.[67]

$$\mu_{\text{eff}} = \sqrt{\frac{3\,k_{\text{B}}}{N_{\text{A}} \cdot {\mu_{\text{B}}}^2}\,\chi_M T} = 2.827915\,\sqrt{\chi_M T} \tag{1.7}$$

This correlation allows for comparing between theoretical values and the experimental values derived from the SQUID magnetometer. It is important to keep in mind that the experimental data usually exceed the calculated ones due to orbital contribution to the magnetic moment.[67,81] As Equation 1.6 shows, the higher the difference in *S* for HS and LS state, the higher the difference of the magnetic moment for both spin states. Hence, iron(II) ions (d^6) show the most pronounced SCO induced variation of the magnetic moment, since the total spin changes from *S* = 2 (HS) to *S* = 0 (LS). However, as the spin transition in a macroscopic sample does not occur instantly, the magnetic moment, or rather the $\chi_{\text{M}}T$ product, involves the contributions of HS and LS molecules, expressed by $\chi_{\text{M}}^{\text{HS}}$ and $\chi_{\text{M}}^{\text{LS}}$ (Equation 1.8).[41]

$$\chi_M T = \left(\gamma_{HS} \cdot \chi_{\text{M}}^{\text{HS}} + (1 - \gamma_{HS}) \cdot \chi_{\text{M}}^{\text{LS}}\right) T \tag{1.8}$$

Here, γ_{HS} describes the mole fraction of HS molecules. If the susceptibilities for the pure HS and LS states are known, γ_{HS} can be calculated and plotted against the temperature to produce the so-called spin transition curves. However, such curves are frequently expressed as $\chi_{\text{M}}T$ *vs*. *T* plots in literature, especially if the HS mole fraction is not accessible.

To determine the magnetic susceptibility in solution, the *Evans'* NMR method is commonly used.[82–85] Here, the samples are measured in deuterated solvents by using an NMR tube with two separate chambers. While the dissolved sample is placed in the inner chamber, the reference solvent is located in the outer tube. The NMR signals related to the solution in the inner chamber are consequently shifted by the value $\Delta\nu$ compared to those in the outer tube, as the paramagnetic substance induces an additional magnetic field. The magnetic mass susceptibility χ_g can thus be calculated via Equation 1.9.[86] Here, *m* is the sample mass, ν the spectrometer frequency, χ_g^{solv} the mass susceptibility of the solvent, ρ_0 the density of the solvent and ρ_s the density of the solution.

$$\chi_g = \frac{3\Delta\nu}{4\pi\nu m} + \chi_g^{solv} + \chi_g^{solv}\frac{\rho_0 - \rho_s}{m} \tag{1.9}$$

Further techniques to trace the SCO are X-ray Absorption Spectroscopy (XAS),[87,88] Electron Paramegnetic Resonance (EPR),[89] Muon Spin Rotation (MuSR),[90] Positron Annihilation Spectroscpoy (PAS),[91] Nuclear Forward Scattering (NFS)[92,93] or Differential Scanning Calorimetric (DSC).[94,95]

1.4 Spin Transition Curves

The fundamental theoretical approach of the SCO phenomenon, illustrated in Figure 1.5, suggests that the $^1A_1 \rightarrow {}^5T_2$ transition always occurs in an abrupt manner, since there are only two electronic states involved. While this is true for a single SCO active molecule, the situation in an ensemble of molecules can be completely different. Depending on the interactions between the SCO active centers, different transition temperatures of the molecules are possible. Spin transition curves are conventionally obtained by plotting the HS fraction (γ_{HS}) against the temperature (*T*). However, in literature, the temperature dependency of the $\chi_M T$ product is often discussed. The form of the spin transition curve strongly depends on the *degree of cooperativity*.[41,96] The spin switch is accompanied by drastic structural changes, which needs to be propagated within the crystal lattice to neighboring metal centers. The term *cooperativity* refers to any kind of intra- and intermolecular interactions that pass on the effects of the spin change. Figure 1.5 illustrates the most common spin transition curves in the form of γ_{HS} *vs*. *T* plots for an ensemble of SCO active centers. In case of weak intermolecular interaction and thus a low degree of cooperativity, the SCO appears to be gradual over a broad temperature range (Figure 1.5, a).[97,98] This *continuous* transition is primary observed in dissolved samples, as the present intermolecular interactions are very weak. The population of the $^5T_2$ ground state hence follows the *Boltzmann* distribution. In contrast, the abrupt spin transition (sometimes referred to as *discontinuous* transition) is the result of strong cooperativity (Figure 1.5, b).[99,100] Here, the switch in spin state appears in a narrow temperature regime.

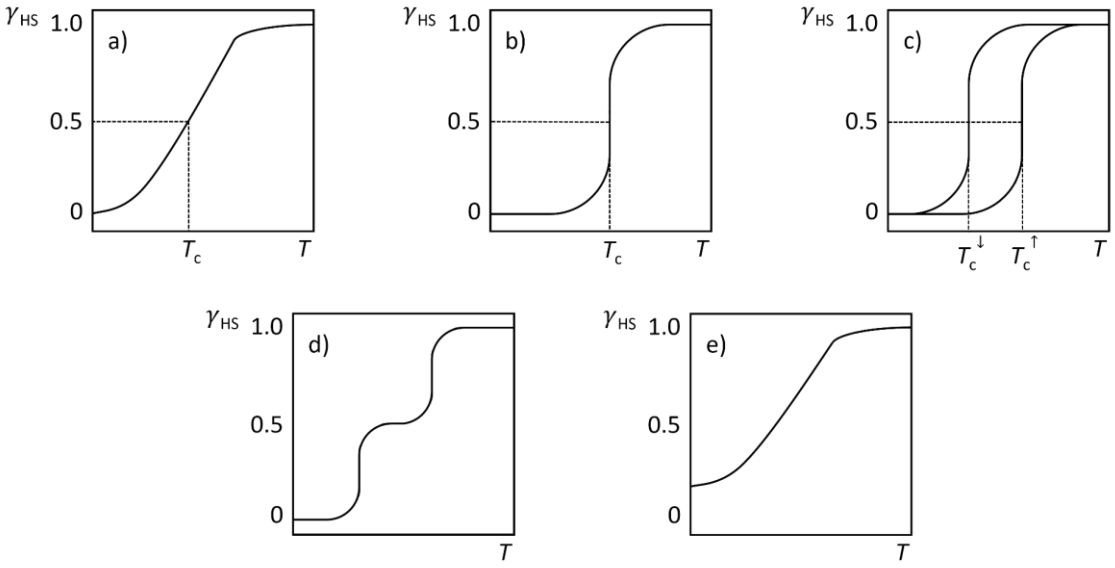


Figure 1.5 Schematic representation of the most common spin transition curves in form of γ_{HS} versus *T* plots: a) gradual, b) abrupt, c) abrupt with hysteresis, d) stepwise and e) incomplete. T_c represents the critical temperature, where equal amounts of HS and LS molecules are present.

If the *degree of cooperativity* is particularly high, a thermal hysteresis of the HS fraction (and thus of the magnetic moment) can occur (Figure 1.5, c). This situation is usually found in the crystalline phase where the SCO active molecules interact via classical and non-classical hydrogen bonding[101–107] or π-π-interactions[108,109], leading to long-range order of the metal centers. Another probable origin of an enhanced *degree of cooperativity* is the synergism between a spin transition and an order-disorder transition where disorder can be associated with solvate or counter ion molecules.[57,110–112] Metal dilution studies could show the impact of intermolecular interactions on the *degree of cooperativity* due to incorporation of further SCO inactive metals inside the crystal structure, as the spin transition curves changed from abrupt to gradual.[113–115] In case of a present hysteresis in the $\gamma_{HS}(T)$ function, the transition temperature during the cooling process ($T_c^{\downarrow}$) is lower than the one during the heating process ($T_c^{\uparrow}$), granting the system *bistability*. Thus, the system either stabilizes the $^5T_2$ or the $^1A_1$ state at a given temperature inside of the hysteresis loop. For the successful application as storage or memory devices, the associated 'memory-effect' is indispensable.[116] Hence, wide thermal hysteresis around room temperature are of particular interest, since such devices should work at ambient temperatures. *Gütlich et al*. proposed two general origins of a hysteric behavior. Either the spin change is associated by a phase transition or the SCO induced intramolecular structural changes are communicated effectively between the molecules.[41] In 2015, *S. Brooker* published a detailed review concerning thermally induced spin transitions in form of hysteresis. Fundamental topics such as kinetic aspects, hysteresis width dependencies and potential applications are discussed.[117] Stepwise SCO is observed in mononuclear as well as in polynuclear compounds among literature. As the two-step spin change (Figure 1.5, d) is the most foundational transition of this kind, further discussions will refer to this specific case. *Sorai et al.* attributed the phase transition without space group change to the SCO phenomenon as a fundamental characteristic. However, this does not apply for two-step spin transitions in mononuclear compounds.[118] For these cases, the stepwise character of the SCO is usually a result of symmetry breaking during the spin change.[119–125] Hence, such structures undergo two first-order phase transitions from the HS to the intermediate phase (IP) to the LS phase. A distinction can be made between two scenarios. In both cases, the space group of the IP differs from the one of the HS and LS phase. On the one hand, the HS and LS phase can exhibit the same space group. This could be shown by *Bürgi et al*. in 2003 by "…Uncovering the Nature of the Intermediate Phase of $[Fe(2\text{-pic})_3]Cl_2 \cdot EtOH$…".[126] While the space groups are $B2_1/c$ for the HS and LS phases in the $[Fe(2\text{-}\mathbf{pic})_3]Cl_2 \cdot EtOH$ complex (**pic** = picolylamine), the intermediate phase changes to $P2_1/c$.[126] This was interpreted in terms of short range interactions, leading to a preferred formation of HS/LS pairs during the SCO. On the other hand, all three phases can differ.

Iijima et al. for instance reported a two-step SCO in the compounds [Fe**H$_3$L^{Me}**]Cl·X (**H$_3$L^{Me}** = tris[2-{[(2-methylimidazol-4-yl)methylidene]amino}ethyl]amine, X = PF_6, AsF_6).[127] Here, the space group changes from $P2_1/n$ (HS) through $P2_1$ (IP) to $P2_1/n$ (LS). Such behavior was already published for the first time by *Tuchagues et al.* for the compound [Fe{5-NO_2-sal-N(1,4,7,10)}] in 1994.[128] Twelves years later, *Matouzenko et al.* reported a two-step spin change in [Fe(**Hpy-DAPP**)]$(BF_4)_2$ (**Hpy-DAPP** = {bis[N-(2-pyridylmethyl)-3-amino-propyl](2-pyridyl-methyl)amine}), where the space group remains the same for all phases.[129] This finding displays the first example of a step-wise SCO with a single iron(II) crystallographic site from high to very low temperatures. In this special case, the present disorder in the ligand system (generated in the lattice) induces two different geometries of the FeN_6 coordination sphere, leading to different transition temperatures. Next to mononuclear complexes, dinuclear SCO active compounds might stabilize an additional plateau in the spin transition curve as well. The intermediate phase can be a mixture of [HS-HS] and [LS-LS] molecules[130] or a distinct [HS-LS] complex.[20,76,131,132] Further details about bimetallic compounds are given in Chapter 1.6. An incomplete SCO with a significant retention of high-spin fraction at low temperature (Figure 1.5, e) might be the result of various reasons. Firstly, defects in the crystal structure can change the intermolecular interactions to the SCO active metal center. As the intrinsic ligand field splitting energy is very sensitive to the present environment, this might result in a too weak crystal field and hence in the partial absence of spin transition. A common example of this effect is the loss of lattice solvent, which tends to stabilize the HS state.[133] In addition to that, major structural changes which accompany a complete spin transition might not be accommodated for a particular lattice. As the conversion rate for the HS→LS change gets extremely small at low temperature, rapid cooling of the sample can lead to trapping of a partial HS phase. This kinetic effect is known as TIESST effect (Temperature Induced Excited Spin State Trapping) and results in a pronounced HS fraction (γ_{HS}).[134–136]

1.5 The effects of solvent and non-coordinating anions on SCO

Non-coordinating counter anions and solvent molecules can have a crucial effect on the spin transition behavior, as the SCO ability is very sensitive to the present intermolecular interactions inside the crystal structure. These kinds of interactions rarely occur directly between the SCO active molecules but are rather mediated via additional non-coordinating molecules. Classical as well as non-classical hydrogen bonds between anions/solvents and the metal bearing molecules can lead to intermolecular interaction pathways, which can change the occurrence of the spin transition drastically. Today, various examples of anion

dependent SCO compounds exist in literature. One of the first published examples is the compound [Fe(2-**pic**)$_3$]Cl$_2$·EtOH, which was discussed earlier with regards to its step-wise SCO ability. *Baker* and *Renovitch* reported the strong dependency of the thermally induced spin change characteristic on the nature of the anion (X = Cl$^-$, Br$^-$, I$^-$).[137] *Gütlich et al.* further investigated the chloride and bromide compounds in-depth, revealing the complete spin transition curves for both compounds.[38,138] While the chloride compound exhibits two-step SCO, the bromide complex shows hysteric behavior. In 2012, *Shores et al*. published the anion dependence SCO properties of the iron(II) complexes [Fe**L**$^{\mathbf{6\text{-}OH}}$]X$_2$ (**L**$^{\mathbf{6\text{-}OH}}$ = tris{4-[(6-methanol)-2-pyridyl]-3-aza-3-butenyl}amine, X = OTf$^-$, Br$^-$, I$^-$, BPh$_4^-$), as shown in Figure 1.6.[139] All compounds were measured in the solid phase using a SQUID magnetometer. The compound [Fe**L**$^{\mathbf{6\text{-}OH}}$](OTf)$_2$ exhibits a very abrupt and complete SCO at T_c = 173 K. Changing the counter ion from triflate to bromide resulted in [Fe**L**$^{\mathbf{6\text{-}OH}}$](Br)$_2$, which shows a spin transition at lower temperature (T_c = 113 K). Even though the spin change itself remains sharp and abrupt, a pronounced HS mole fraction can be found at lower temperatures. This example shows very well that non-coordinating anions might not only influence the transition temperature, but also the nature of the resulting spin transition curve. This becomes even more evident in the case of the [Fe**L**$^{\mathbf{6\text{-}OH}}$](I)$_2$ compound. While the critical spin transition temperature is shifted to T_c = 145 K, the transition itself becomes more gradual, albeit without any HS residues. The authors ascribed this behavior to present intermolecular hydrogen bonds in the solid state between the non-coordinating anions and complex cations. In order to prevent such interaction pathways, tetraphenylborate was introduced as counter ion.

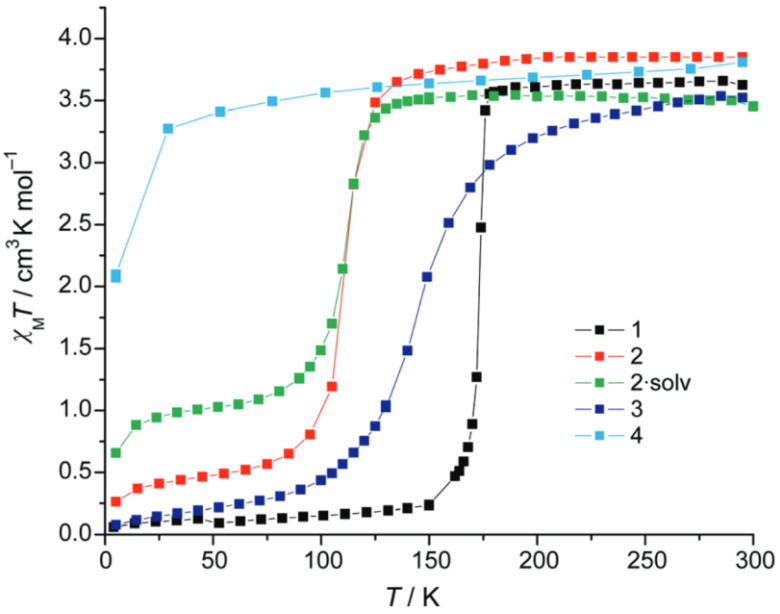


Figure 1.6 Temperature dependence of $\chi_M T$ for [Fe**L**$^{\mathbf{6\text{-}OH}}$]X$_2$ with X = OTf$^-$ (1), Br$^-$ (2), I$^-$ (3) and BPh$_4^-$ (4), as well as [Fe**L**$^{\mathbf{6\text{-}OH}}$](Br)$_2$ · 0.5MeOH (2·solv). The data points are connected via lines to guide the eye. Reprinted from literature with permission.[139]

The absence of any classical hydrogen bonds between the anions and the complex cations leads to a SCO inactive compound. Hence, [Fe**L**$^{\mathbf{6\text{-}OH}}$]$(BPh_4)_2$ remains in the high-spin state over the whole temperature range. The decrease of $\chi_M T$ below 29 K was attributed to zero-field splitting of the *S* = 2 system, which becomes evident at lower temperatures. In addition to the exchange of counter ions, the methanol solvatomorph of the bromide compound ([Fe**L**$^{\mathbf{6\text{-}OH}}$]$(Br)_2 \cdot 0.5MeOH$) was investigated with respect to its magnetic behavior. Compared to the solvent free compound, [Fe**L**$^{\mathbf{6\text{-}OH}}$]$(Br)_2 \cdot 0.5MeOH$ shows a drastically increased amount of HS molecules at lower temperature. This finding illustrates the fact that the SCO phenomenon might not only be influenced by the non-coordinating anion, but also by the non-coordinating solvent. In analogy to the anion related discussion, it has been extensively shown that the spin transition can also be drastically affected by intermolecular interactions induced by solvent molecules.[140–146] Hence, solvent molecules embedded in the lattice can affect the transition temperature (T_c),[147–153] as well as the *degree of cooperativity* and thus the nature of the spin transition.[107,154–157] Moreover, they might impose various crystal packing arrangements in the solid state, which in turn affects the metal center involving cooperative interactions. In some cases, the solvent effect can be reversibly triggered by de- and resolvation of the solid material.[158–161] A good example of this phenomenon was published by *Herold C*. in the group of *Prof. Dr. E. Rentschler.* The authors published the first dinuclear iron(II) SCO active compounds bearing the bridging 1,3,4-thiadiazole motif.[25] The hydrates $[Fe_2(\mu\text{-}\mathbf{PMTDA})_2](BF_4)_4 \cdot 2H_2O$ and $[Fe_2(\mu\text{-}\mathbf{PMTDA})_2](ClO_4)_4 \cdot 0.5H_2O$ (**PMTDA** = 2,5-bis((2-pyridylmethyl)aminomethyl)-1,3,4-thiadiazol) stabilize the [LS-LS] state at low temperature and exhibit incomplete SCO around room temperature. However, a modified complex synthesis resulted in the formation of two isostructural compounds with dimethylformamide as lattice solvent.[22] While both hydrate compounds crystallize in the $P2_1/n$ space group, $[Fe_2(\mu\text{-}\mathbf{PMTDA})_2](BF_4)_4 \cdot 4DMF$ and $[Fe_2(\mu\text{-}\mathbf{PMTDA})_2](ClO_4)_4 \cdot 4DMF$ crystallize in $P2_1$. The direct comparison of the solvatomorphs shows that the gradual spin transition of the DMF compounds occurs at higher temperatures, which displays a good example of how different solvents can affect the SCO phenomenon. However, heating the sample to higher temperatures and subsequent cooling does not result in the original [LS-LS] state, but in the stabilization of a [HS-LS] state. This gradual SCO step in both DMF compounds could be successfully explained by solvent loss, as present hydrogen bonds between the DMF molecules and complex cations influence the ligand field strength.[22] Moreover, the solvent free compound $[Fe_2(\mu\text{-}\mathbf{PMTDA})_2](BF_4)_4$ could be resolvated to show similar magnetic behavior as before annealing. This process could be successfully carried out several times, allowing a reversible manipulation of the spin state. The $[Fe_2(\mu\text{-}\mathbf{PMTDA})_2](X)_4$-type complexes, published by *Herold et al.*, display di-aza heterocycle bridged systems that will be discussed in-depth in the following chapter.

1.6 Dinuclear SCO active complexes

Polynuclear SCO compounds allow the combination of a magnetic exchange interaction between the spin-bearing centers and the SCO phenomenon. In this context, dinuclear compounds are of high interest, as they represent the smallest unit in which an intramolecular magnetic exchange interaction can prevail. Furthermore, due to the presence of two metal centers, the spin transition can occur in a step-like manner from the [HS-HS] via the [HS-LS] to the [LS-LS] state, resulting in an additional electronic state. This additional step makes them promising candidates for high order data storage and ternary processing.[162–165] In 1992, *Real et al.* published the first dinuclear iron(II) complex [Fe(**bt**)$(NCS)_2]_2$**bpym** (**bt** = 2,2'-bi-2-thiazoline and **bpym** = 2,2'-bipyrimidine), showing thermally induced two-step spin crossover with transition temperatures of $T_{c,1}$ = 197 K and $T_{c,2}$ = 163 K.[132] The bpym ligand acts as bridging ligand, allowing for an intramolecular interaction path inside of the dimeric specie. As the magnetic susceptibility data could not be used to determine the present magnetic interaction, the authors suggested a weak antiferromagnetic coupling based on similar systems.[166] Derived from the spin Hamiltonian $\hat{H} = -J \cdot S_1 S_2$, an intermolecular interaction of -4 cm^{-1} < J < 5 cm^{-1} was suggested. Based on theoretical calculations and Mössbauer spectroscopy, the authors suggested a different transition temperature for both metal ions. Hence, the SCO displays a [HS-HS]→[HS-LS]→[LS-LS]-transition, rather than a 1:1 mixture of [HS-HS] and [LS-LS] molecules in the intermediate state. This could be confirmed by *Ksenofontov et al.*, who published additional LIESST and dilution studies. They further highlighted the importance of short and long range intermolecular interactions for the energetic stabilization of the mixed intermediate HS-LS state.[167] In order to generalize the statement, whether the SCO in a dinuclear compound occurs in a one-step or two-step spin transition, *Real et al.* discussed the relevance of the enthalpy of the mixed [HS-LS] state.[132]

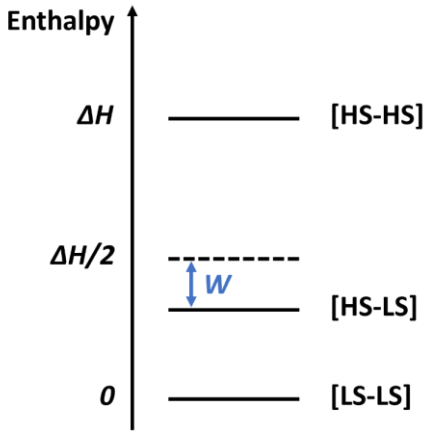


Figure 1.7 Schematic representation of [HS-HS], [HS-LS], [LS-LS] enthalpies. The enthalpy difference between [HS-HS] and [LS-LS] state is defined as ΔH. The difference of the [HS-LS] enthalpy to the average enthalpy of the [HS-HS] and [LS-LS] pairs is labeled as W.

Figure 1.7 represents the [HS-HS], [HS-LS] and [LS-LS] enthalpies relative to each other. The difference between [HS-HS] and [LS-LS] state is defined as ΔH, while W describes the difference of the [HS-LS] state to the average enthalpy of the [HS-HS] and [LS-LS] pairs. In the frame of this model a two-step SCO via the [HS-LS] state occurs, when the enthalpy of the [HS-LS] state ($H_{HS\text{-}LS}$) is smaller than the average enthalpy of the [HS-HS] and [LS-LS] pairs: $H_{HS\text{-}LS} < [(H_{HS\text{-}HS} + H_{LS\text{-}LS}) / 2]$ or $H_{HS\text{-}LS} < \Delta H/2$ (Figure 1.7). This enthalpy difference W thus needs to possess a stabilizing nature. Based on calculations, the relation $H_{HS\text{-}LS} < \Delta H/2$ is a necessary, but not sufficient, condition for the stepwise spin change. In addition to that, a pronounced *degree of cooperativity* is needed. Hence, the two-step character arises from a synergy between the intra- and intermolecular interactions.[168,169]

1.6.1 Dinuclear di-aza bridged SCO compounds

In 2005, *Klingele et al.* published "The first X-ray crystal structure determination of a dinuclear complex trapped in the [low spin-high spin] state: $[Fe^{II}_2(\mathbf{PMAT})_2](BF_4)_4 \cdot DMF$" (**PMAT** = 4-amino-3,5-bis((2-pyridylmethyl)aminomethyl)-1,2,4-triazole).[131] The authors observed a spin change from the [HS-HS] to the [HS-LS] state around T_c = 224 K with subsequent zero-field splitting of the residual HS iron(II) ions at very low temperature. Due to X-ray structure analysis, an inverse symmetrical complex cation could be determined at room temperature. As a consequence of the spin transition, the complex cation is converted to a symmetry broken complex with two crystallographic different iron(II) centers. Hence, the present Fe-N bond distances represent both, a HS and a LS iron(II) ion. Even though the space group remains the same, the inversion centers are shifted. While the complex cations are located on top of the centers of inversion for the high temperature phase, they are found in between two centers of inversion in the [HS-LS] phase. To fine-tune the ligand field splitting energy, the amino function in the 4-position of the 1,2,4-triazole moiety was substituted by various groups.[170] However, none of the 1,2,4-triazole based dinuclear complexes exhibit SCO to the [LS-LS] state. According to the authors, the too high strain in the complex cation, caused by the rigidity and wide biting angle of the ligand system, inhibits the conversion of both iron centers. To address this issue, *Herold et al.* modified the dinuclear compounds, published by the group of *S. Brooker*, by changing the 1,2,4-triazole moiety to the 1,3,4-thiadiazole group.[25] The novel complexes $[Fe_2(\mu\text{-}\mathbf{PMTDA})_2](X)_4 \cdot solv$ (X = BF_4^-, ClO_4^- and $CF_3SO_3^-$) are isostructural to the afore mentioned **PMAT** related complexes, representing the next family of di-aza bridged dinuclear compounds. The exchange of the ligand backbone was motivated by the fact that the larger sulphur atom should reduce the biting angle of the ligand system, increasing flexibility. Additionally, the changed electronic nature of the thiadiazole ring compared to the triazole moiety should result in a stronger ligand field. Both arguments were supposed to stabilize the [LS-LS] state at lower temperatures. However, as temperature dependent studies

of the magnetic moment showed, all three compound purely stabilize the diamagnetic state, showing only indications of a beginning SCO around room temperature. In a subsequent study, *Herold et al.* could show the impact of solvent effects on the spin crossover phenomenon.[22] As already described in Chapter 1.5, the compounds $[Fe_2(\mu\text{-}\mathbf{PMTDA})_2](BF_4)_4 \cdot 4DMF$ and $[Fe_2(\mu\text{-}\mathbf{PMTDA})_2](ClO_4)_4 \cdot 4DMF$ exhibit an incomplete SCO at higher temperatures as their analogous hydrate compounds.[25] Due to the loss of the dimethylformamide molecules, a temperature induced spin transition from the [HS-HS] to the [LS-LS] state could be triggered. In combination with X-ray structure analysis and Infrared spectroscopy, the authors reported that the DMF molecules form intermolecular hydrogen bonds to the complex cations, shifting electron density to the donor atoms while increasing the ligand field strength.[22] Hence, the loss of solvent results in a lower ligand field, which allows for SCO from the [HS-HS] to the [HS-LS] state. Once again, this finding shows the pronounced impact of intra- and intermolecular interactions on the spin change. While the **PMTDA** ligand displays a symmetrical chelating ligand, *D. Bittner* described the synthesis of the novel asymmetrical 1,3,4-thiadiazole based ligand **PPTD** (**PPTD** = 2-(2-pyridyl)-5-[N,N-bis(2-pyridyl-methyl)amino]methyl-1,3,4-thiadiazole).[171] This new ligand system was used to synthesize the next series of dinuclear 1,3,4-thiadiazole based iron(II) complexes with active SCO properties. The compounds $[Fe_2(\mu\text{-}\mathbf{PPTD})_2](BF_4)_4$ and $[Fe_2(\mu\text{-}\mathbf{PPTD})_2](ClO_4)_4$ were both isolated as microcrystalline solids and investigated with respect to their magnetic behavior. The tetrafluoroborate salt exhibits an abrupt and reversible one-step spin transition from the [HS-HS] to the [LS-LS] state. After heating the sample to 400 K with subsequent cooling, the magnetic data reveal an abrupt two-step SCO with transition temperatures near the original critical temperature. The change in the spin transition curve was attributed to partial solvent loss, which might result in a rearranged crystal structure. In contrast, the freshly prepared compound $[Fe_2(\mu\text{-}\mathbf{PPTD})_2](ClO_4)_4$ showed reversible and gradual two-step SCO right from the start. Hence, the sample exhibits spin transition from the [HS-HS] to the [LS-LS] state via an intermediate phase. After 14 days, the very same sample was remeasured under the same conditions. In analogy to the first measurement, the second one reveals a two-step spin transition, however, with different transition temperatures. Thus, the critical temperatures are shifted to higher temperatures. Further, the SCO appears to be more abrupt, indicating an increased *degree of cooperativity*. Also for this case, *Bittner* ascribed this phenomenon to the loss of lattice solvent. It was suggested that the higher transition temperatures result from an enhanced ligand field strength, arising from increased intermolecular interactions from the complex cation to the perchlorate anions. In case of the freshly prepared sample, these interaction paths might be blocked by the solvents. Recrystallization of both complexes yielded single crystals that were suitable for X-ray structure analysis, revealing solvent molecules inside the unit cells. However, as the synthesis differs, lattice solvents cannot be assumed with

certainty for the non-recrystallized compounds. *Fürmeyer* from our group used a different approach to stabilize the high-spin state of the 1,3,4-thiadiazole based compounds, published by *Herold et al.*. While the symmetrical nature of the ligand system was retained, the coordinating sidearms were varied to yield novel ligand systems. In this context, *Fürmeyer et al.* published the complex series $[Fe_2(\mu\text{-}\mathbf{TMTD})_2](X)_4 \cdot solv$ (**TMTD** = 2,5-bis{[(thiazol-2-ylmethyl)-amino]-methyl}-1,3,4-thiadiazole with X = BF_4^-, ClO_4^- and $CF_3SO_3^-$), showing anion dependent SCO behavior.[24] The triflate compound $[Fe_2(\mu\text{-}\mathbf{TMTD})_2](CF_3SO_3)_4 \cdot 2MeCN$ remains in the [LS-LS] state and shows incomplete and gradual spin transition above room temperature. In contrast, the complexes $[Fe_2(\mu\text{-}\mathbf{TMTD})_2](BF_4)_4 \cdot 3MeCN$ and $[Fe_2(\mu\text{-}\mathbf{TMTD})_2](ClO_4)_4 \cdot 3MeCN$ exhibit SCO below 300 K. While the tetrafluoroborate compound shows an abrupt spin change from the [HS-HS] to the [HS-LS] state, the perchlorate-balanced complex changes its spin state from the [HS-HS] to the [HS-LS] to the [LS-LS] state. The different magnetic behavior was ascribed to varying intermolecular hydrogen bonds between the anions and the complex cations in the crystalline state. The authors attributed the stabilization of the high-spin state to different geometric and electronic properties of the **TMTD** ligand compared to **PMTDA**, which results in a weaker ligand field in the related dinuclear complexes.[24] Mössbauer spectroscopy and X-ray structure analysis allowed *Fürmeyer et al.* to report that "the cooling rate is crucial to observe the phase transition associated with the SCO behavior".[24] This represents a remarkable finding of the *Rentschler* group, as crystallographic investigations are usually associated with rapid cooling or quenching of the sample. By changing the coordinating thiazole group with the imidazol-4-yl group, *Fürmeyer et al.* published another complex series of type $[Fe_2(\mu\text{-}\mathbf{I^4MTD})_2](X)_4 \cdot solv$ (**I⁴MTD** = 2,5-bis{[(1*H*-imidazol-4-ylmethyl)-amino]-methyl}-1,3,4-thiadiazole with X = BF_4^-, ClO_4^- and $CF_3SO_3^-$). In this series, $[Fe_2(\mu\text{-}\mathbf{I^4MTD})_2](BF_4)_4 \cdot THF$ exhibits an incomplete and gradual SCO, suggesting an intermediate [HS-LS] state at lower temperatures. Single crystal structure analysis, however, could show that the intermediate state corresponds to a 1:1 mixture of [HS-HS] and [LS-LS] molecules. The absence of the complete diamagnetic phase was attributed to the lack of "interlayer space" in the lattice, associated with the SCO induced phase transition. Next to the iron(II) based compounds, *Fürmeyer et al.* could further report the “First Cobalt(II) Spin Crossover Compound with N_4S_2-Donorset”.[172] Interestingly, the exchange of the secondary amine group in **PMTDA** with a sulfur atom resulted in the formation of the mononuclear SCO active compound $[Co(\mathbf{PSTD})_2](ClO_4)_2$ (**PSTD** = 2,5-bis[(2-pyridylmethyl)thio]methyl-1,3,4-thiadiazole). The preferred orientation of the ligands in the mononuclear complex was assigned to the large sulfur atom, which sterically hinders the formation of the related dinuclear coordination compound. *Köhler et al.* published the first 1,3,4-oxadiazole based dinuclear complex series with SCO active properties, by substituting the 1,3,4-thiadiazole group in **PMTDA** with the analogous oxadiazole moiety.[20] The

complexes of type $[Fe_2(\mu_2\text{-}\mathbf{PMOD})_2](X)_4 \cdot solv$ (**PMOD** = 2,5-bis{[(2-pyridyl-methyl)amino]methyl}-1,3,4-oxadiazole and X = BF_4^-, ClO_4^- or $CF_3SO_3^-$) show pronounced anion dependent behavior of their magnetic susceptibility. However, as these compounds play a crucial role for the motivation of this work, further details will be given in Chapter 2.

1.7 Luminescent Spin-Crossover Materials

In the past few years, various multifunctional materials have been reported with the aim to achieve luminescence signal modulation as a result of a present spin crossover phenomenon. To effectively couple luminescent and spin changing properties, two main synthetic strategies have been employed. The first approach includes the doping of luminescent entities (molecules or metal ions) into a SCO active material. However, due to its relatively small fraction, the luminophore will probe only some parts of the system. Hence, it cannot be guaranteed that the result inferred display the properties of the ensemble of the material. On the other hand, a sufficiently low concentration of dopant reduces the risk of an adverse interference with the SCO properties. In addition to that, as both components are usually independent, individual modification like fine-tuning the SCO properties might be easy to accomplish. This kind of “physical mixing” of two chemically separate entities includes various methods like the synthesis of doped nano-objects and thin films,[173,174] co-crystallization of structurally similar molecules[175] or the elaboration of nano-particles with a SCO core decorated by a luminescent shell.[176] Therefore, *Halcrow* and co-workers co-crystallized the SCO active compound $[Fe(\mathbf{bpp})_2](BF_4)_2$ (**bpp** = 2,6-di(pyrazol-1-yl)pyridine) with the structurally similar fluorescent complex $[Ru(\mathbf{terpy})_2](BF_4)_2$ (**terpy** = 2,2':6',2''-terpyridine).[175] Virtually complete spin transition could be observed in all iron(II) complexes, however, with changed transition temperature T_c. As the concentration of SCO active molecules in the lattice in reduced, cooperativity during the spin transition decreases as well. Thus, the narrow hysteresis loop of the pure $[Fe(\mathbf{bpp})_2](BF_4)_2$ complex vanishes with 5 % ruthenium complex ($[Fe(\mathbf{bpp})_2]_{0.95}[Ru(\mathbf{terpy})_2]_{0.05}(BF_4)_2$) and the SCO becomes more gradual with increasing dopant material. Pure $[Ru(\mathbf{terpy})_2](BF_4)_2$ exhibits strong fluorescence emission around 77 K. The material of composition $[Fe(\mathbf{bpp})_2]_{0.47}[Ru(\mathbf{terpy})_2]_{0.53}(BF_4)_2$ possesses both SCO and very weak fluorescence properties, albeit within different temperature regions. *Bousseksou et al.* combined the luminescent properties of rhodamine-110 (Rh-110) by doping a very low proportion (max. 3 %) into nano-particles of $[[Fe(\mathbf{NH_2trz})_3](OTs)_2]_n$ (**NH_2trz** = 4-NH2-1,2,4-triazole), dispersed in a reverse-micelle solution.[173] Following the thermal variation of the emission peak intensity at 540 nm, these particles show SCO between 288 and 318 K. The decrease in intensity while cooling the sample was assigned to the radiative energy transfer.

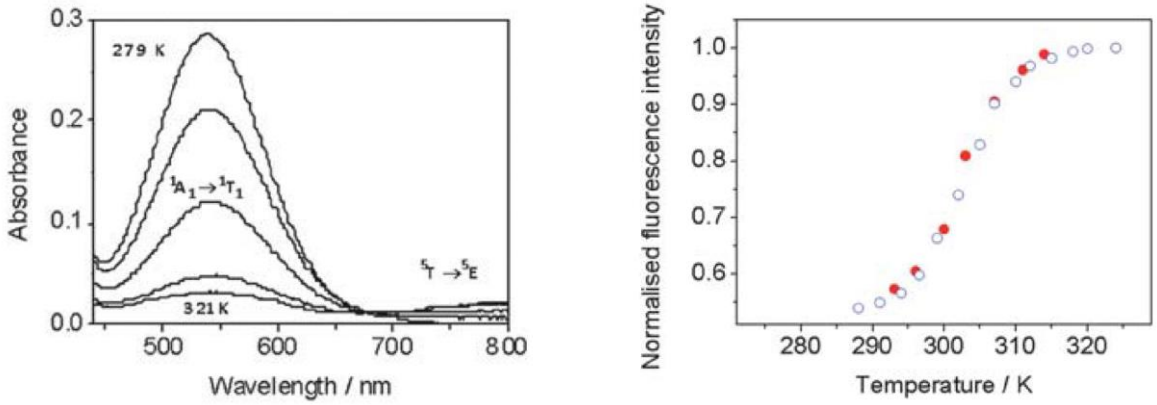


Figure 1.8 Left: Absorption spectra of an octane suspension of [Fe(**NH2trz**)$_3$](OTs)$_2$ nanoparticles at different temperatures. Right: Fluorescent thermometry around r.t. for a rhodamine-110 doped (0.01 %) [Fe(**NH2trz**)$_3$](OTs)$_2$ nanoparticle. The fluorescence intensity at 540 nm is shown for the heating (open symbols) and cooling (closed, red symbols) modes. Reprinted from literature with permission.[173]

Hence, the appearing singlet absorption band of the LS complex results in the observed quenching of luminescence (Figure 1.8). Two years later, *Bousseksou* and *Molnár et al.* published the fluorescent detection of spin transition in solid thin films and isolated nano-dots of [[Fe(**hptrz**)$_3$](OTs)$_2$]$_n$ (**hptrz** = 4-heptyl-1,2,4-triazole), doped with acridine orange.[174] In this case, the $^1A_{1g} \rightarrow {}^1T_{1g}$ absorption band of the iron(II) complex overlaps nearly perfect with the emission spectrum of acridine orange. Hence, the temperature dependency of the emission maximum at 500 nm was followed to track the spin change. An increased luminescence intensity between 293 and 323 K could be observed, showing no photobleaching in this regime. Again, the quenching mechanism was largely assigned to energy transfer between the luminophore and the iron(II) ions of the SCO complex.[174] In contrast, the second approach to generate luminescent spin crossover materials includes the combination of both compounds in one entity. Therefore, the luminophore might be a part of the ligand system,[177–180] a forming part of a mixed d-f metal molecular material[181] or might act as the counter ion to the cationic SCO molecule.[182] *Garcia et al.* substituted the well-known 1,2,4-triazole backbone to synthesize N-salicylidene-4-amino-1,2,4-triazole (**L1**), which exhibits strong emission in the solid state.[178] Complexation of Fe(NCS)$_2$ with **L1** yielded the crystalline dinuclear compound [Fe$_2$(**L1**)$_5$(NCS)$_4$] · 4MeOH. Temperature dependent magnetic measurements revealed the abrupt one-step SCO at T_c = 157(1) K and approx. 6 % residual HS fraction at very low temperatures, which was confirmed by Mössbauer spectroscopy. The high cooperativity during the spin transition was attributed to intra- and intermolecular interactions mediated by the triazole backbone and supramolecular interactions, respectively. Subsequently, the temperature dependent wavelengths of the emission maxima (λ_{ex} = 350 nm) were plotted alongside the spin transition curve, showing a remarkable correlation (Figure 1.9).

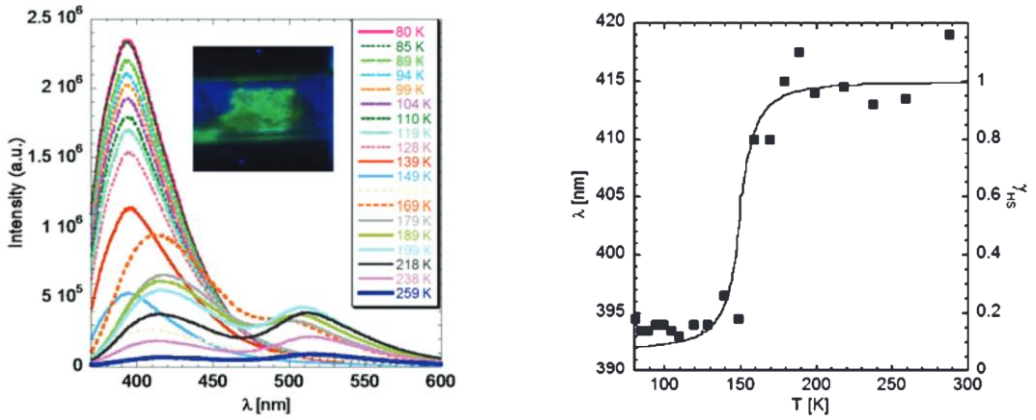


Figure 1.9 Left: Temperature-dependent emission spectra for $[Fe_2(\mathbf{L1})_5(NCS)_4] \cdot 4MeOH$ at λ_{ex} = 350 nm. The inset displays the fluorescence at 293 K. Right: Temperature dependence of the emission maximum of $[Fe_2(\mathbf{L1})_5(NCS)_4] \cdot 4MeOH$, which follows the spin transition curve from SQUID data. Reprinted from literature with permission.[178]

Hasegawa et al. reported the magneto-optical relationship in the two Fe(II) SCO complexes $[Fe(\mathbf{bzp}\text{-}H_2)_2](ClO_4)_2$ and $[Fe(\mathbf{bzp}\text{-}H)_2]$ (**bzp** = 2,6-bis(benzimidazole-2'-yl)pyridine). The authors used molecular orbital calculations to assign the electronic absorption spectra of the ligand system and the two related coordination compounds. In contrast, the fluorescent spectra of both complexes were used in the assignment of electronic transitions. $[Fe(bzp\text{-}H)_2]$ as well as $[Fe(\mathbf{bzp}\text{-}H_2)_2](ClO_4)_2$ both showed fluorescence in the HS and LS state, however, with increasing emission intensity on cooling. Using the *Boltzmann* equation, the proportions of high- and low-spin states could be estimated from the fluorescence spectra at different temperatures, which was in good agreement to other detection methods. Unlike the afore described examples, *Fabbrizzi et al.* reported a spin change in the fluorescent nickel(II) compound $[Ni(\mathbf{L2})X_2](ClO_4)_2$, where **L2** is the macrocyclic tetradentate 1,4,8,11-tetraazacyclo-tetradecane ligand with substituted naphthalene group.[180] As the perchlorate anions possess a non-coordinating character, the solid complex stabilizes the LS state due to its square-planar coordination geometry. Upon solvation in acetonitrile, the two apical sites of the complex are occupied by two solvent molecules. This results in an equilibrium between the square-planar LS and the octahedral HS form. Increasing temperature favors the endothermic HS→LS conversion, which is contrary to the "usual" SCO behavior. Between 300 and 338 K, the fluorescence intensity of the naphthalene moiety increases with increasing temperature (increasing LS proportion). This behavior displays an explicit interplay between spin state and luminescence, as emission intensity usually decays at higher temperature, known as thermal quenching.[183–185] The quenching mechanism was attributed to an energy transfer with double electron exchange. This involves the redistribution of electrons between the metal *d*-orbitals and the molecular orbitals of the photoexcited fluorophore.

2 Motivation

In 2016, *C. Köhler* from our group published a series of oxadiazole-based dinuclear iron(II) complexes of type $[Fe_2(\mu_2\text{-}\mathbf{PMOD})_2](X)_4$ (**PMOD** = 2,5-bis{[(2-pyridyl-methyl)amino]methyl}-1,3,4-oxadiazole and X = BF_4^-, ClO_4^- or $CF_3SO_3^-$).[20] Magnetic studies of these compounds revealed an anion dependent behavior of their magnetic susceptibility in the solid state. The tetrafluoroborate compound remains in the [HS-HS] state even at very low temperatures, while the perchlorate and triflate complexes exhibit thermally induced spin crossover (SCO) to the [HS-LS] state. At the time of writing this thesis, these two compounds were the only literature known oxadiazole coordinated SCO complexes. The spin transition in both iron(II) complexes occurs abruptly and is attributed to present hydrogen bonds between the complex cations and counter ions in the crystalline phase. Due to the high *degree of cooperativity*, structural changes associated with a spin change can be transferred very rapidly to adjacent molecules, resulting in a steep SCO curve. In the case of $[Fe_2(\mu_2\text{-}\mathbf{PMOD})_2](CF_3SO_3)_4 \cdot 2MeCN$, *cooperativity* seems to be strong enough to cause a thermal hysteresis of the magnetic moment ($T_c^{\downarrow}$ = 152 K and $T_c^{\uparrow}$ = 178 K), whereas the spin transition in $[Fe_2(\mu_2\text{-}\mathbf{PMOD})_2](ClO_4)_4 \cdot 2MeCN$ appears without hysteresis at $T_c^{\downarrow} = T_c^{\uparrow}$ 145 K. However, the SCO for both compounds led to the [HS-LS] state only. The authors attributed this to the fact that, after the first center undergoes structural changes due to the spin transition, there is a highly distorted coordination sphere for the second iron(II) ion. In general, dinuclear compounds take a special role in the field of SCO, as they display the smallest unit where spin transition and intramolecular magnetic interactions can occur simultaneously. Most interestingly, a stabilization of the [HS-HS], [HS-LS] and [LS-LS] state offers an additional magnetic spin state to the system. SCO compounds represent attractive candidates for numerous applications like display devices[65], sensors[186], molecular switches[116], high-density memory units[187], building blocks for molecular electronics or spintronics[188] and many more. However, the proper functionality of such complexes under ambient conditions requires a wide hysteresis (*bistability*) around room temperature.

This thesis aims to synthesize further SCO active oxadiazole based compounds with enhanced properties and can be divided into two parts. The first part deals with dinuclear iron(II) compounds that are inspired by the complex series $[Fe_2(\mu_2\text{-}\mathbf{PMOD})_2](X)_4$. To make these materials more suitable for applications, the coordinating side arms in the ligand system **PMOD** shall be varied, ranging from five membered to six membered aromatic heterocycles.

Additional hydrogen bonds may enhance the *degree of cooperativity*, which in turn can extend the thermal hysteresis of the magnetic moment found in $[Fe_2(\mu_2\text{-}\mathbf{PMOD})_2](CF_3SO_3)_4 \cdot 2MeCN$. On the other side, a shift of transition temperatures towards higher temperatures is the result of an increased octahedral ligand field splitting energy. Such stronger ligand fields might also yield in a two-step SCO, which is required for high order data storage and ternary processing.[162–165] This could clarify whether the absence of the [LS-LS] state in $[Fe_2(\mu_2\text{-}\mathbf{PMOD})_2](ClO_4)_4 \cdot 2MeCN$ and $[Fe_2(\mu_2\text{-}\mathbf{PMOD})_2](CF_3SO_3)_4 \cdot 2MeCN$ is solely due to the stiffness of the ligand or caused by a too weak ligand field.

The second part of this thesis deals with mononuclear oxadiazole related complexes. The major advantage over the analogous dinuclear coordination compounds is the more flexible coordination sphere since the oxadiazole moiety does not serve for bridging. This enhanced *degree of freedom* may lead to complexes with lower distortion of the octahedral coordination environment facilitating the spin transition. Although these compounds solely switch between the high-spin and low-spin state, various examples of multi-step spin transition curves are given in literature.[119–125] Most times, this phenomenon is attributed to symmetry-breaking in the crystalline phase. As the coordination of one metal ion requires only one binding pocket, diverse functional groups can be implemented into the ligand system quite easily. Such ligand design can result in the formation of multifunctional SCO complexes. For these materials, the interplay between the SCO phenomenon and luminescence extends the application potential for magneto-optical switches.[177,178,189–191] A successful combination of both properties would yield the first oxadiazole based coordination compound showing this kind of synergy.

In addition to the SCO materials, single molecule magnets (SMMs) and single ion magnets (SIMs) play a crucial role in molecular magnetism and are highly suitable for future applications as molecular spintronics or quantum computing.[12–17] In the field of transition metal SIMs, Co(II) takes the leading position as it exhibits a vast amount of preferred coordination geometries next to its large spin-orbit coupling.[192,193] Hence, switching from iron(II) to cobalt(II) might lead to novel oxadiazole based SIMs of which only a few exist in the literature.[194,195]

3 Results and Discussion

Parts of the results presented in the following chapter 3.1 (p. 29 – 46) have been submitted as manuscript on March 01, 2022 in *Crystals*.

Titel of the manuscript:

Three Novel Thiazole arm containing 1,3,4 Oxadiazole based [HS-HS] Fe(II) Di-Nuclear complexes

Summary:

The synthesis and magnetic property of three novel dinuclear Fe(II) complexes based on a new bridging 1,3,4 Oxadiazole ligand bearing coordinating thiadiazole side arms is described. In detail, the synthesis of 2,5-bis[(1,3-thiazol-2-ylmethyl)amino]methyl-1,3,4-oxadiazole (**L^{5,TA}**) is presented along with the preparation of three new dinuclear Fe(II) complexes with different counterions $[Fe^{II}_2(\mu_2\text{-}\mathbf{L^{5,TA}})_2](BF_4)_4 \cdot 2CH_3CN$ (**C4**), $[Fe^{II}_2(\mu_2\text{-}\mathbf{L^{5,TA}})_2](ClO_4)_4$ (**C5**) and $[Fe^{II}_2(\mu_2\text{-}\mathbf{L^{5,TA}})_2](CF_3SO_3)_4 \cdot 2CH_3CN$ (**C6**). The obtained complexes were characterized by single crystal X-Ray crystallography, SQUID magnetometry and IR spectroscopy. The structure of the crystalline material was determined at 120 K for **C4** and **C6**. The magnetic properties of all three complexes (**C4**-**C6**) were measured between 2-300 K and clearly show that all three complexes stay in the high spin state over the measured temperature range. The reason that all three compounds are locked in the high spin state [HS-HS] can be assigned to a combination of geometrical and electronic effects.

Contributions:

Julian Eppelsheimer: Concept development, ligand and complex synthesis. 1H-NMR and IR-spectroscopy, elemental analysis and mass spectrometry. Data analysis, manuscript preparation, figure preparation.

[redacted]: Concept development, manuscript preparation and correction.

[redacted]: X-ray analysis

[redacted]: Manuscript correction and scientific supervision.

3.1 Dinuclear iron(II) complexes with 1,3,4-oxadiazole based ligands bearing five-membered heterocyclic aromatic sidearms ($\mathbf{L^{5,Y}}$)

In a previous work, the axially coordinating pyridine rings in the $[Fe_2(\mu_2\text{-}\mathbf{PMOD})_2](X)_4$-type complexes (**PMOD** = 2,5-bis{[(2-pyridylmethyl)amino]methyl}-1,3,4-oxadiazole), published by *C. Köhler* and *E. Rentschler,*[20] were substituted by imidazol-2-yl groups.[196] The imidazole rings were supposed to form additional intermolecular hydrogen bonds via their free NH-groups to enhance the degree of cross linking. It is well known that such type of interaction in the solid state can lead to an enhanced *degree of cooperativity*, thus resulting in a wide thermal hysteresis of the magnetic moment.[101–107] Indeed, the crystal structures of the $[Fe_2(\mu_2\text{-}\mathbf{L^{5,Im}})_2](X)_4$-type complexes ($\mathbf{L^{5,Im}}$ = 2,5-bis[(1H-imidazol-2-ylmethyl)amino]methyl-1,3,4-oxadiazole) showed various hydrogen bonds between the complex cations and the non-coordinating anions (X = BF_4^-, ClO_4^- and $CF_3SO_3^-$). Due to the bridging nature of the counter ions, intermolecular one- and two-dimensional chains/networks are formed. The X-ray structures have already been described in the previous master thesis and will not be discussed any further at this point.[196] However, it is important to point out that all structures were measured at 173 K. At this temperature, the metal ligand bond lengths [*d*(M-L)], the octahedral distortion parameters [$\Sigma_O(FeN_6)$] and the continuous shape measurement values [CShM(O_h)] indicate a [HS-HS] state for all complexes. To study the complexes in terms of their spin crossover (SCO) behavior, the magnetic moment was measured in a temperature range between 300 K and 2 K throughout this work. Furthermore, a second ligand system with a thiazol-2-yl sidearm ($\mathbf{L^{5,TA}}$) was synthesized and used to form binuclear $[Fe_2(\mu_2\text{-}\mathbf{L^{5,TA}})_2](X)_4$-type complexes. The exchange of the NH group with a sulfur (S) atom in the heteroaromatic ring should allow for finetuning the ligand field, since thiazole and imidazole offer different σ- and π-character of resulting metal-ligand bonds.[197] All desired complexes of type $[Fe_2(\mu_2\text{-}\mathbf{L^{5,Y}})_2](X)_4$ ($\mathbf{L^{5,Y}}$ = $\mathbf{L^{5,Im}}$ or $\mathbf{L^{5,TA}}$) were synthesized by dissolving an equimolar amount of $\mathbf{L^{5,Y}}$ and FeX_2 (X = BF_4^-, ClO_4^-, $CF_3SO_3^-$) in acetonitrile separately, followed by the combination of both solutions. Slow evaporation or vapor diffusion yielded the coordination compounds as single crystals or microcrystalline powder (see Chapter 6.4 for details). The structural integrity was ensured by single-crystal X-ray diffraction or IR spectroscopy.

3.1.1 Synthesis of ligands $\mathbf{L}^{5,Im}$ and $\mathbf{L}^{5,TA}$

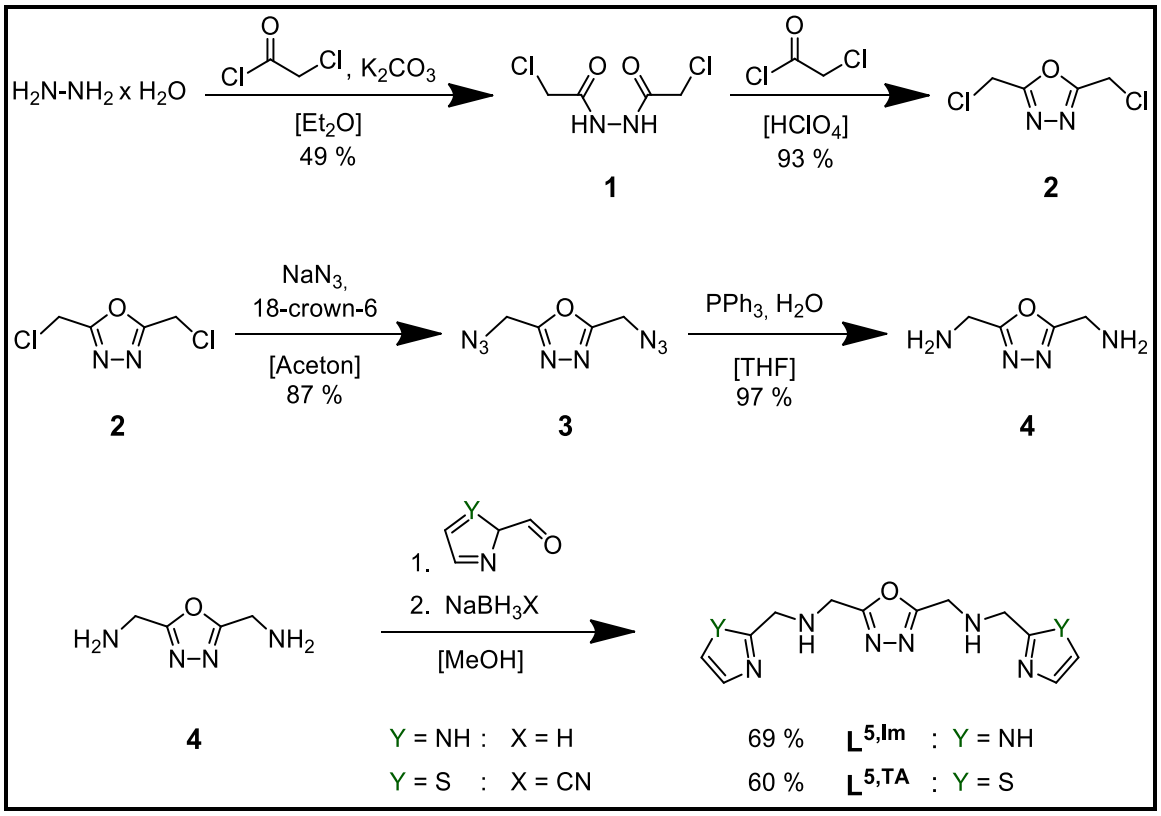


Figure 3.1 Synthesis of $\mathbf{L}^{5,Im}$ and $\mathbf{L}^{5,TA}$. Reduction of the in-situ formed imine species in the last step was done with either sodium borohydride or sodium cyanoborohydride. **1** – **4** have already been reported in a former work.[196] All yields refer to this work, except for $\mathbf{L}^{5,Im}$.

The synthesis of $\mathbf{L}^{5,Im}$ was described in a previous work.[196] The first two steps include the condensation reaction of hydrazine monohydrate and chloroacetyl chloride to 1,2-bis(chloracetyl)hydrazide (**1**), followed by the cyclization reaction to 2,5-bis(chloromethyl)-1,3,4-oxadiazole (**2**). This two-step synthesis is based on publications of *Nuyken et al* and *Liu et al*.[198,199] and is well established in the group of [redacted].[20,196] Nucleophilic substitution reaction of **2** with sodium azide results in the 2,5-bis(azidomethyl)-1,3,4-oxadiazole (**3**) with a good yield of 87 %. The *Staudinger reduction* of **3** with triphenylphosphine and water afforded 2,5-bis(aminomethyl)-1,3,4-oxadiazole (**4**) in a very good yield of 97 %, which served as precursor for the final step. Here, **4** was reacted with either 1H-imidazole-2-carboxaldehyde or thiazole-2-carboxaldehyde to form 2,5-bis[(1H-imidazol-2-ylmethyl)amino]-methyl-1,3,4-oxadiazole ($\mathbf{L}^{5,Im}$) or 2,5-bis[(1,3-thiazol-2-ylmethyl)amino]methyl-1,3,4-oxadiazole ($\mathbf{L}^{5,TA}$) in good yields (69 % and 60 %), respectively. The in-situ formed imine compound was reduced with sodium borohydride (for $\mathbf{L}^{5,Im}$) or sodium cyanoborohydride (for $\mathbf{L}^{5,TA}$) to the desired amine. Reductive amination of **4** with thiazole-2-carbaldehyde to form $\mathbf{L}^{5,TA}$,with sodium borohydride as reducing agent, was accompanied with low yield compared to $\mathbf{L}^{5,Im}$. Changing to sodium cyanoborohydride with catalytic amounts of acetic acid resulted in a better yield. The reaction was carried out by [redacted] in his bachelor thesis (Figure 3.1).[200]

3.1.2 Magnetic measurements of $[Fe_2(\mu_2\text{-}L^{5,Im})_2](X)_4$-type complexes (C1 – C3)

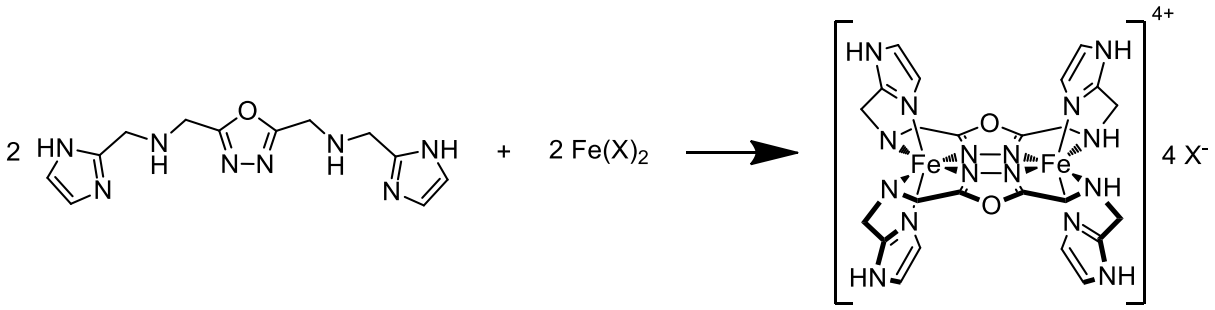


Figure 3.2 Synthesis of **C1** – **C3** by complexation of $Fe(X)_2$ [X = BF_4^- (**C1**), ClO_4^- (**C2**) and $CF_3SO_3^-$ (**C3**)] with $\mathbf{L^{5,Im}}$. The synthesis was already reported in a former work.[196]

The synthesis (Figure 3.2) and the crystal structures of $[Fe_2(\mu_2\text{-}\mathbf{L^{5,Im}})_2](BF_4)_4 \cdot 2MeCN$ (**C1**), $[Fe_2(\mu_2\text{-}\mathbf{L^{5,Im}})_2](ClO_4)_4 \cdot 2MeCN$ (**C2**) and $[Fe_2(\mu_2\text{-}\mathbf{L^{5,Im}})_2](CF_3SO_3)_4 \cdot 2MeCN$ (**C3**) have already been described and thus will not be discussed at this point.[196] All single-crystal X-ray diffraction measurements were performed at 173 K. Average bond lengths and distortion of the coordination spheres (see Figure F.2 – Figure F.4) indicate a [HS-HS] state of the complexes **C1** – **C3**. However, the temperature-dependent molar susceptibility of the complexes has not been measured yet. Therefore, **C1** – **C3** were freshly prepared for this work and investigated with respect to their magnetic properties in a temperature range from 300 K to 2 K. The $\chi_M T$ product of **C2** was plotted against the temperature (*T*) in Figure 3.3 (blue triangles). At 300 K, $\chi_M T$ is equal to 6.98 $cm^3mol^{-1}K$, which is higher than the *spin-only* value (6 $cm^3mol^{-1}K$) for two $S = 2$ spin centers with $g = 2$, following the *spin-only* formular with *n* equivalent spin centers (Equation 3.1).

$$\chi_M T = \frac{g^2}{8} \sum_{i=1}^{n} S_i(S_i + 1) \tag{3.1}$$

This higher experimental value can be explained by first-order spin-orbit coupling, which might occur in transition metal complexes with electronic T-terms as ground state (for iron(II): $^5T_{2g}$).[67] In this case, the orbitual moment *L* is not quenched and will couple with the spin *S* to the total angular momentum *J*, described by *Russel* and *Saunders*.[36] As shown in Figure 3.3, the cooling of the sample results in a continuous decrease of $\chi_M T$ to a value of 6.60 $cm^3mol^{-1}K$ at 31.8 K. Below this temperature, the $\chi_M T$ product drops significant faster to 1.38 $cm^3mol^{-1}K$ at 2 K.

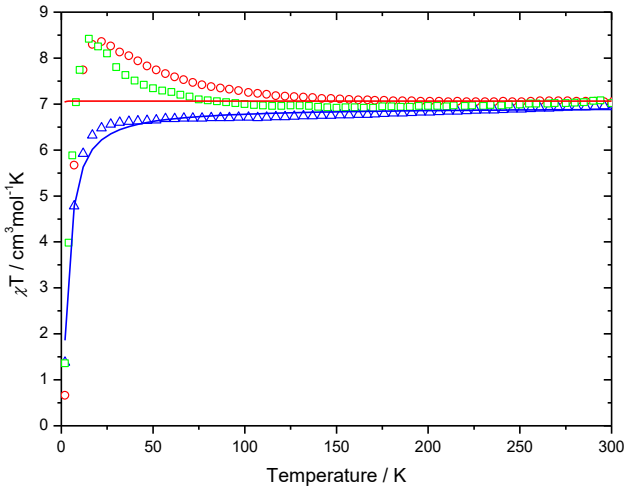


Figure 3.3 Temperature dependent behavior of **C1** (red open circles), **C2** (blue open triangles) and **C3** (green open squares) in form of the combined $\chi_M T$ *vs. T* plots. The blue solid line represents the best fit of the susceptibility data of **C2**. Red solid line illustrates the best simulation of the high temperature regime of **C1** using PHI.[201]

The overall decrease of $\chi_M T$ from high to low temperatures can be explained by an antiferromagnetic coupling between the two iron(II) centers, which are bridged by two 1,3,4-oxadiazole moieties. Data were fitted with the open source software PHI[201] using the Hamiltonian in Equation 3.2.

$$\hat{H} = \hat{H}_{EX} + \hat{H}_{ZEE} = -2J \cdot S_1 S_2 - g\mu_B HS \tag{3.2}$$

The *Heisenberg-Dirac-van Vleck* Hamiltonian $\hat{H}_{EX}$ takes the isotropic exchange coupling between the two iron(II) ions into account, while $\hat{H}_{ZEE}$ describes the *Zeeman Effect* as a small magnetic field of H = 0.1 T was applied. The best fit resulted in J = -0.38(2) and g = 2.149(4) with the isotropic g-factor $g = g_1 = g_2 = (g_x + g_y + g_z)/3$ and $S_1 = S_2 = 2$ (the errors correspond to the uncertainties gained from the fit using the "uncertainties" command in the ***params block). The small negative value for the exchange coupling parameter J describes a weak antiferromagnetic coupling between the oxadiazol-bridged iron(II) metals and is in good agreement with reported di-aza heterocycle bridged systems.[21,170,171,202–212] The rather weak superexchange interaction can be explained by the long pathway throughout the oxadiazol bridge. The goodness of the fit is described through the residual (R), which follows the sum of squares approach:

$$R = \sum_{i=1}^{points} (\chi_{exp} - \chi_{calc})^2 \tag{3.3}$$

Here, the residual is equal to R = 0.72, which is quite high compared to other fits of similar systems in literature.[171] This is mainly due to the deviation of the experimental values from the fit at lower temperature. It can be observed that the fit decreases faster below 30 K than the actual values. Each iron(II) center in **C1** – **C3** shows a high distortion of the octahedral coordination sphere, which is displayed by the octahedral distortion parameters ($\Sigma_O(FeN_6)_i$ > 120 °) and confirmed by the value of continuous shape measurements ($CShM(O_h)_i$ > 4.74) (Figure F.2 – Figure F.4). The octahedral distortion parameter Σ_O is defined as the sum over the absolute deviations of the twelve *cis*-angles φ_i from the ideal 90 ° angle (Equation 1.5).[63] An ideal octahedron would hence show a distortion parameter of Σ_O = 0 °. FeN_6 HS complexes usually yield parameters greater than 100 °, whereas the corresponding LS complexes exhibit values lower than 80 °. *Avnir et al.* have proposed, that symmetry[213] and shape[214] of a compound should be defined as continuous properties, leading to continuous symmetry measures (CSM) and continuous shape measures (CShM). This provides quantitative parameters to calibrate the deviation of structures from their given symmetry or shape.[62] These values are independent of the size or number of vertices. In general, the larger Σ_O and CShM, the greater the distortion of the coordination sphere. The present deviation in **C1** – **C3** will most likely result in a stronger spin-orbit coupling and hence in a pronounced magnetic anisotropy axis. Magnetic measurements have been performed in gelatin capsules without the use of eicosane. Due to this “non-blocked/unblocked” measuring method, the sample was not fixed and hence free to move. A possible anisotropy axis could lead to the macroscopic orientation of the crystallites in the external magnetic field, which usually leads to formally higher values of the magnetic moment than expected. The magnetic anisotropy of **C1** – **C3** has to be confirmed by magnetization data. The $\chi_M T$ product of $[Fe_2(\mu_2\text{-}\mathbf{L^{5,Im}})_2](CF_3SO_3)_4 \cdot 2MeCN$ (**C3**) was plotted versus the temperature as green squares in Figure 3.4. At 300 K, a $\chi_M T$ value of 7.02 $cm^3mol^{-1}K$ is found, which slightly drops to 6.92 $cm^3mol^{-1}K$ at 170 K. Below this temperature, $\chi_M T$ rises until it reaches its maximum at 15 K (8.42 $cm^3mol^{-1}K$), before it rapidly decreases towards 2 K. It appears that the maximum at 15 K is, also for this case, due to the orientation of the crystals in the magnetic field, since the $\chi_M T$ product firstly decreases from 300 K to 170 K. A ferromagnetic interaction between the centers seems not reasonable. Due to the fact that such behavior was also observed for other samples (see the following chapters), **C3** was remeasured using eicosane to prevent orientation of the crystallites in the applied magnetic field. The $\chi_M T$ product was plotted against the temperature in Figure 3.4 for both measurements to provide a good comparison. It can be observed that the curves are nearly identical in the temperature range between 300 K and 170 K. Below 170 K, the $\chi_M T$ product of the blocked measurement keeps on decreasing continuously, until it drops faster below a temperature of 30 K.

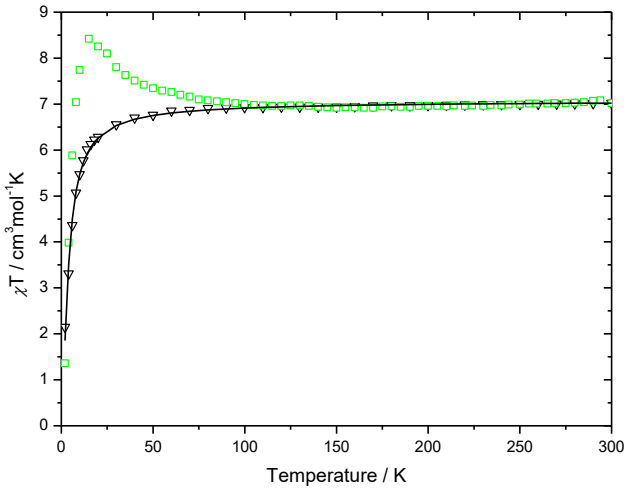


Figure 3.4 Temperature dependent behavior of **C3** measured in an unblocked way (green open squares) and with eicosane (black open triangles) in form of the combined $\chi_M T$ *vs. T* plots. The black solid line represents the best fit of the susceptibility data of **C3** (with eicosane) using PHI.[201]

This comparison shows that the rise of the $\chi_M T$ curve in the unblocked measurement of **C3** from 300 K to 170 K is not caused by a ferromagnetic interaction between the iron(II) centers. Rather, it appears to be caused by macroscopic alignment of the crystals within the applied magnetic field. The data of the eicosane-measurement of **C3** were fitted using the same Hamiltonian as before (Equation 3.2). The best fit resulted in J = -0.397(7) and g = 2.171(2) with a residual of R = 0.18. These values are very similar to those of **C2** and related systems in literature.[21,170,171,202–212] Again, the small negative value describes a weak antiferromagnetic coupling between the two metal ions through the bridging oxadiazol moiety. As expected, the *g*-factor of 2.171(2) is higher than 2.0, due to first order spin-orbit coupling. To avoid misinterpretation of the magnetic data of **C1**, $\chi_M T$ was simulated only considering the *Zeeman Effect* (Figure 3.3, solid red line), according to the Hamiltonian in Equation 3.4.

$$\hat{H} = \hat{H}_{ZEE} = -g\mu_B HS \tag{3.4}$$

The best simulation of the high temperature regime was achieved with *g*-factors of $g_1 = g_2 = 2.16$, which are close to the values for **C2** and **C3**. Regardless of the exchange interaction between the two iron(II) centers, all three complexes stabilize the [HS-HS] state even at low temperatures. *Fürmeyer et al.* could show that the ligand field strength in $[Fe_2(\mu_2\text{-}\mathbf{I^2MTD})_2](X)_4$-type complexes (**I²MTD** = 2,5-bis[(1H-imidazol-2-ylmethyl)amino]methyl-1,3,4-thiadiazole) is lower than in the complexes of type $[Fe_2(\mu_2\text{-}\mathbf{PMTD})_2](X)_4$ (**PMTD** = 2,5-bis[(2-pyridyl-methyl)amino]methyl-1,3,4-thiadiazole) (X = BF_4^-, ClO_4^- and $CF_3SO_3^-$), published by *Herold et al.*[24,25]

While the $[Fe_2(\mu_2\text{-}\mathbf{I}^2\mathbf{MTD})_2](X)_4$-type complexes remain in the [HS-HS] state between 2 K and 300 K, the compounds of type $[Fe_2(\mu_2\text{-}\mathbf{PMTD})_2](X)_4$ stabilize the diamagnetic [LS-LS] state, showing only the start of an incomplete SCO above room temperatures. The authors attribute this to the different angles between the heteroaromatic ring and the adjacent methylene group, visualized in Figure 3.5. Here, the angle α, formed by the pyridine ring, is approx. 120 °, whereas the angle β, formed by a five-membered ring, is approx. 125 °. Due to the stiffness of such ligand systems, the larger angle β results in longer Fe-N-bonds favoring the high-spin state. The same situation seems to apply for the analogous oxadiazole-based ligands $\mathbf{L}^{5,Im}$ and **PMOD**. In addition to that, imidazole is considered to generate a weaker ligand field than pyridine.[215] As expected, the exchange of the pyridine ring with the imidazole motif resulted in advanced cross-linking via hydrogen bonds between the complex cation, which should have led to a wider thermal hysteresis of the magnetic moment. However, due to the afore mentioned geometric and electronic changes in the ligand system, the SCO property of the $[Fe_2(\mu_2\text{-}\mathbf{L}^{5,Im})_2](X)_4$-type complexes was lost.

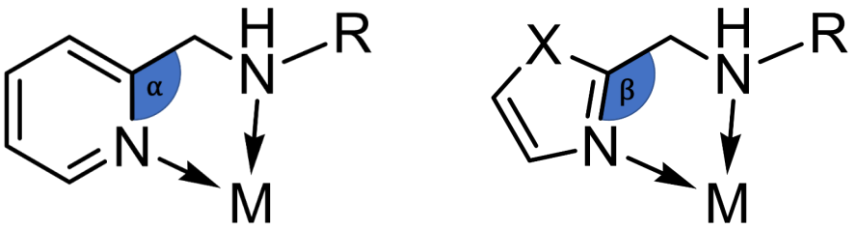
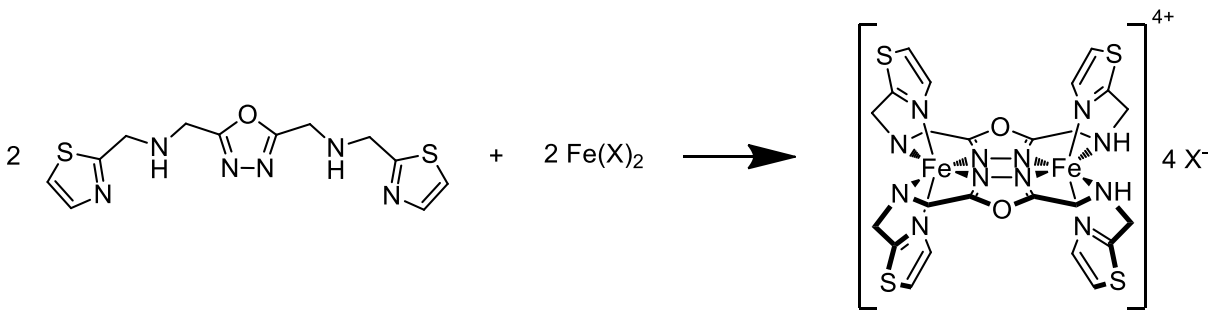


Figure 3.5 Scheme of different coordination angles between a 6-membered ring (left) and 5-membered ring (right) in the ligand side arm.

3.1.3 Dinuclear complexes of type $[Fe_2(\mu_2\text{-}L^{5,TA})_2](X)_4$ (C4 – C6)

Since the ligand field strength in the $[Fe_2(\mu_2\text{-}\mathbf{L^{5,Im}})_2](X)_4$-type complexes [X = BF_4^- (**C1**), ClO_4^- (**C2**) and $CF_3SO_3^-$ (**C3**)] appears to be too low for thermally induced SCO, the 1H-imidazol-2-yl group was exchanged for the 1,3-thiazol-2-yl moiety. Since the sulfur atom has a lower electronegativity than the NH-group, less electron density should be withdrawn from the coordinating nitrogen atom in the ring, resulting in a stronger σ-bonding. This could yield in SCO active oxadiazole bridged dinuclear iron(II) complexes with a five-membered aromatic ring in the apical coordination positions. The synthesis of 2,5-bis[(1,3-thiazol-2-ylmethyl)amino]methyl-1,3,4-oxadiazole ($\mathbf{L^{5,TA}}$) was already discussed in Chapter 3.1.1. Complexation reaction with different iron(II) salts under inert atmosphere resulted in the three compounds $[Fe_2(\mu_2\text{-}\mathbf{L^{5,TA}})_2](BF_4)_4 \cdot 2MeCN$ (**C4**), $[Fe_2(\mu_2\text{-}\mathbf{L^{5,TA}})_2](ClO_4)_4$ (**C5**) and $[Fe_2(\mu_2\text{-}\mathbf{L^{5,TA}})_2](CF_3SO_3)_4 \cdot 2MeCN$ (**C6**) (Figure 3.6).



$\mathbf{L^{5,TA}}$

C4 : X = BF_4^-
C5 : X = ClO_4^-
C6 : X = $CF_3SO_4^-$

Figure 3.6 Synthesis of **C4** – **C6** by complexation of $Fe(X)_2$ (X = BF_4^- (**C4**), ClO_4^- (**C5**) and $CF_3SO_3^-$ (**C6**) with $\mathbf{L^{5,TA}}$. The synthesis was initially performed by [redacted].[200]

While **C4** and **C6** were isolated as block shaped crystals that were suitable for single-crystal X-ray diffraction, **C5** could only be obtained as microcrystalline powder. However, comparison of the IR spectrum of **C5** with those of $\mathbf{L^{5,TA}}$, **C4** and **C6** indicates a successful synthesis of the desired compound (Figure 3.7). All three compounds **C4** – **C6** show a blueshift of the symmetric N-H stretching frequency [ν_s(N-H)] compared to the free ligand $\mathbf{L^{5,TA}}$ (3277 cm^{-1}). Here, the largest difference is found in **C4** (3333 cm^{-1}), followed by **C5** (3307 cm^{-1}) and **C6** (3278 cm^{-1}). In most cases, the coordination of a NHR_2 group to transition metals results in a redshift of the symmetric N-H stretching frequency.[216–218] However, there are also reported cases of a shift towards higher wavenumbers.[219] The different shifts of the symmetric N-H stretching frequency can be caused by varying hydrogen bonds to the secondary NHR_2 group of the ligand.

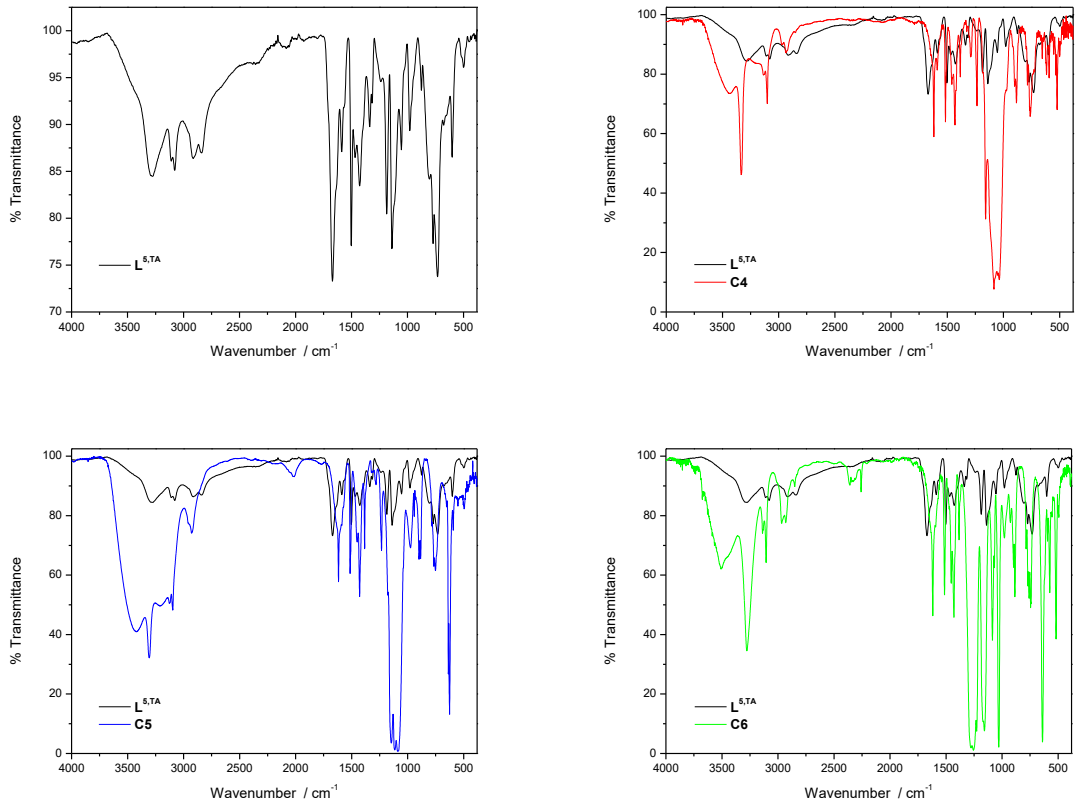


Figure 3.7 Comparison of IR spectra of $\mathbf{L^{5,TA}}$ (black line, top left) with **C4** (red line, top right), **C5** (blue line, bottom left) and **C6** (green line, bottom right). All complex spectra are overlayed onto the ligand spectra (black line). Difference in transmittance is mainly due to the use of different IR spectrometers.

In addition to the ν_s(N-H) band, the counter ion-specific IR bands are also clearly visible. Hence, **C4** shows very pronounced asymmetric B-F stretching bands $\nu_{as}(BF_4)$ at 1084 cm^{-1}, 1052 cm^{-1} and 1036 cm^{-1}. The IR band at 762 cm^{-1} can be assigned to the symmetric stretching mode $\nu_s(BF_4)$, while the bands at 522 cm^{-1}, 506 cm^{-1} and 500 cm^{-1} display deformation vibrations $\delta(BF_4)$.[220–223] **C5** shows vibration bands at 1147 cm^{-1}, 1115 cm^{-1} and 1086 cm^{-1}, which result from asymmetric stretching vibrations $\nu_{as}(ClO_4)$. In addition to that, an asymmetric bending band $\delta_{as}(ClO_4)$ at 625 cm^{-1} can be observed.[224–227] Based on the distinct N-H stretching vibration, the perchlorate specific bands and the ligand-like fingerprint region in the IR spectrum of **C5**, a successful synthesis of **C5** in the desired form of $[Fe_2(\mu_2\text{-}\mathbf{L^{5,TA}})_2](ClO_4)_4$ can be assumed. The IR spectrum of **C6** clearly shows symmetric and asymmetric stretching vibrations of the free triflate anion in the region of approx. 1020 cm^{-1} – 1300 cm^{-1} ($\nu_{as}(SO_3)$:= 1278 cm^{-1}, $\nu_s(CF_3)$: 1253 cm^{-1}, $\nu_{as}(CF_3)$: 1227 cm^{-1} and $\nu_s(SO_3)$: 1029 cm^{-1}). Next to that, bending virations can be found at 639 cm^{-1} [$\delta_s(SO_3)$], 573 cm^{-1} [$\delta_{as}(CF_3)$] and 517 cm^{-1} [$\delta_{as}(SO_3)$].[228–231]

Labelling scheme for $[Fe_2(\mu_2\text{-}L^{5,TA})_2]^{4+}$ complex cations:

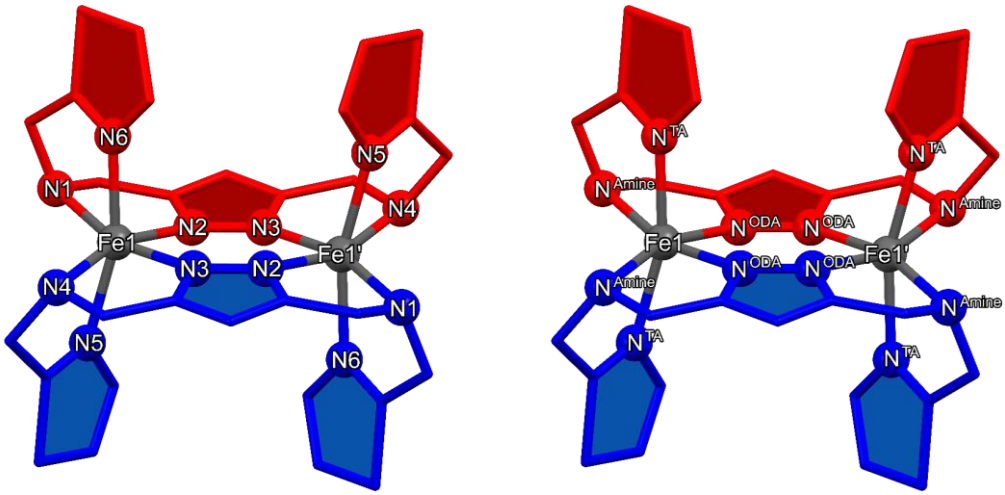


Figure 3.8 Left: Labelling scheme for $[Fe_2(\mu_2\text{-}L^{5,TA})_2]^{4+}$ complex cations. Right: Labeling scheme according to the coordinated functional group. *Cis*-axial coordination mode of the ligands is displayed by the colours red and blue.

$[Fe_2(\mu_2\text{-}L^{5,TA})_2](BF_4)_4 \cdot 2CH_3CN$ (C4) crystallizes in the triclinic space group $P\bar{1}$ with one formula unit in the unit cell. Crystallographic Data can be found in Table D.2. The coordination mode of the two $L^{5,TA}$ ligands is equivalent to the one in **C1** – **C3**, as illustrated in Figure 3.8. The two iron(II) ions are bridged by the 1,3,4-oxadiazole moieties of two opposing ligands. The secondary amine functions of both ligands are also coordinating in an equatorial way, thus saturating the horizontal vertices of both octahedral coordination spheres. In contrast, the vertical vacancies of the octahedron are occupied by the 1,3-thiazolyl groups. Both ligands coordinate in a *cis*-axial manner (Figure 3.8). The asymmetric unit consists of one ligand coordinated to an iron(II) centers, two perchlorate anions and one acetonitrile (Figure 3.9). To describe the complex cation itself, the labeling scheme illustrated in Figure 3.8 is applied. Since it is inverse symmetrical, the coordination spheres of both iron(II) centers are equivalent. Thus, only the coordination environment of Fe1 will be discussed. The mean distance between Fe1 and a secondary amine function [$\bar{d}$(Fe-N^{Amine}) = (d(Fe1-N1)+d(Fe1-N4))/2] is found to be 2.34 Å, which represent the longest Fe-N bond type. The next smaller average bond length can be found between the iron(II) ion and the oxadiazole nitrogen atom [$\bar{d}$(Fe-N^{ODA}) = (d(Fe1-N2)+d(Fe1-N3))/2 = 2.14 Å]. With an average value of $\bar{d}$(Fe-N^{TA}) = (d(Fe1-N5)+d(Fe1-N6))/2 = 2.13 Å, the bonds between the metal center and the thiazole ring are the shortest. While the amine group only offers σ-bonding, the metal-ligand bonds to the oxadiazol and thiazole moieties can have further π-backbonding character.[197,215,232]

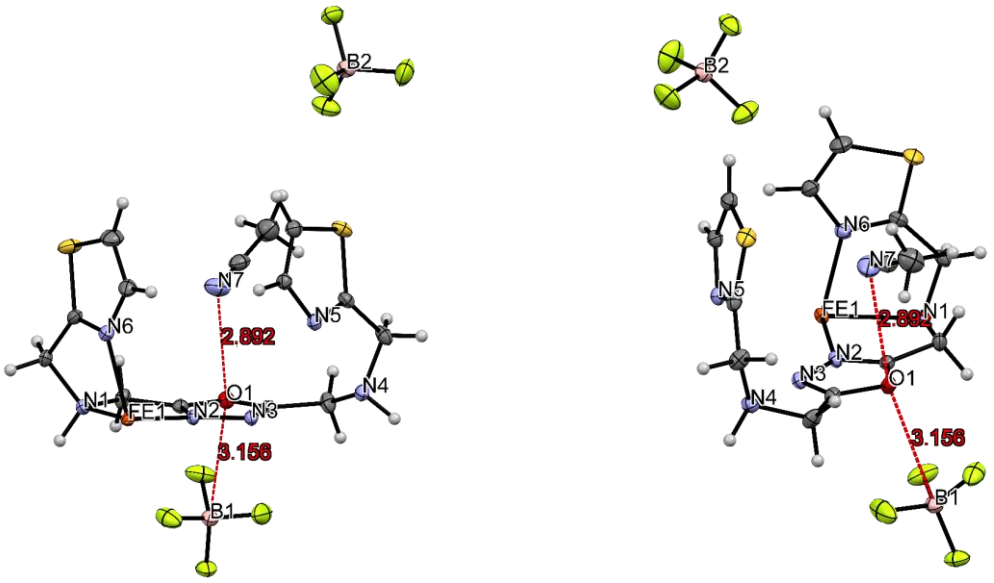


Figure 3.9 Asymmetric Unit of **C4** with front view (left) and side view (right). Measured distances are displayed as red dashed lines. ORTEP representation with atomic displacement parameters set to 50 % probability.

Therefore, the bond distances between Fe1 and the heteroaromatic compounds are shorter than those to the amine groups. The average Fe-N distance in the complex **C4** is found to be $\bar{d}$(Fe-N) = 2.21 Å. This value suggests a [HS-HS] state of the complex at the given temperature of 120 K. This assumption is supported by the very strong distortion of the coordination sphere. The octahedral distortion parameter $\Sigma_O(FeN_6)$ is equal to 123.9 °, displaying a very strong deviation of the ideal coordination octahedron. This is further confirmed by continuous shape measurement calculations, resulting in a value of $CShM(O_h)$ = 4.09 (Figure F.5). It is known from literature that high-spin iron(II) complexes have a larger distortion than low-spin complexes. Thus, the octahedral distortion parameter for LS complexes is usually less than 80 °, while it is greater than 100 ° for HS complexes.[63,64] This can be explained by the asymmetric electron configuration of the iron(II) ion in the high-spin state, compared to the symmetric population of the t_{2g}-orbitals of the low-spin specie. A detailed summary of all structural parameters can be found in Table E.2. The complex cation is located on top of a center of inversion in the middle of both *ab*-planes of the unit cell. Thus, half of the complex cation points into the unit cell while the other half formally lies outside of the unit cell (Figure F.6). One tetrafluoroborate and its symmetry generated pendant lie between the two halves of the two complex molecules The acetonitrile molecules are located between the thiazole rings above an oxadiazole unit. The distance between the oxadiazol-oxygen and the acetonitrile-nitrogen is equal to *d*(O1-N7) = 2.89 Å. On the opposing side of the oxadiazole ring, a non-coordinating tetrafluoroborate anion is located with *d*(O1-B1) = 3.16 Å (Figure 3.9).

This BF_4^- anion is involved in three hydrogen bonds, connecting the complex cations in a one-dimensional way. Due to the given symmetry, only these three unique intermolecular interactions must be described to fully characterize the hydrogen bond network. The first hydrogen bond can be found between the amine function of one ligand and a fluorine atom of the afore mentioned tetrafluoroborate. Here, the N1-H1···F1 distance is equal to 2.01 Å, with an N1-H1-F1 angle of 165.5 °. Two further fluorine atoms of the same BF_4^- anion form additional hydrogen bonds to a neighboring complex cation. The N4-H4···F4 distance is found to be 1.95 Å with an enclosed N4-H4-F4 angle of 165.5 °, while the N4-H4···F3 distance is equal to 2.65 Å. The N4-H4-F3 angle appears to be 129.9 °, which is approx. 36 ° smaller than the N4-H4-F4 angle (Figure 3.10). It is well known in literature that the N-H···F-BF_3 distances are shorter for angles close to 180 °.[233] All mentioned values are in line with published data in literature.[233,234] Due to the bridging nature of the BF_4^- counter ion, a one dimensional chain of complex cation is formed via hydrogen bonds (Figure F.7).

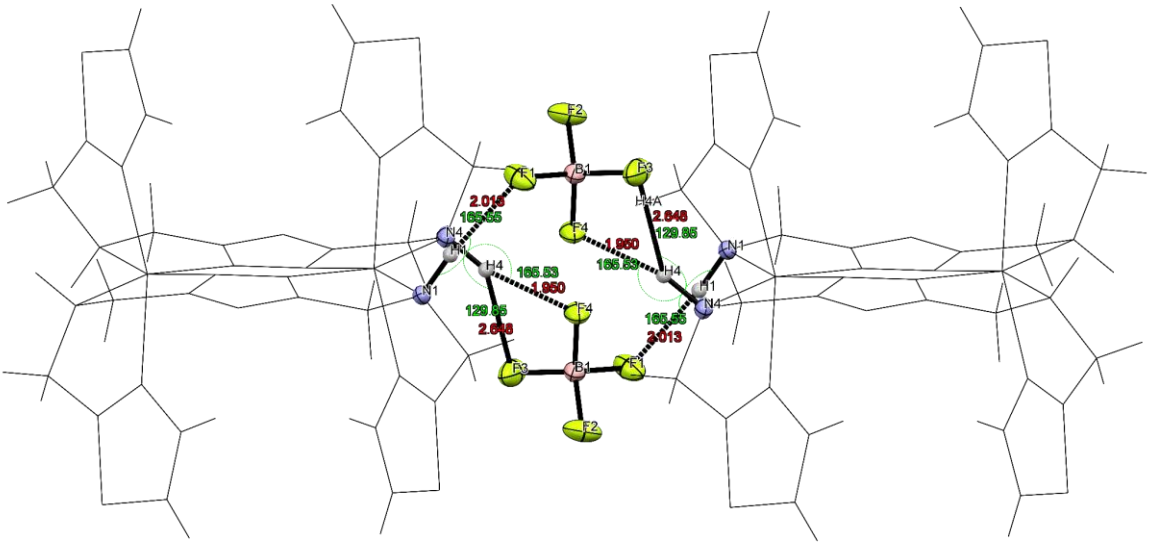


Figure 3.10 Unique hydrogen bonds (dashed black lines) in **C4** between complex cations and tetrafluoroborate anions. Acetonitrile molecules and irrelevant tetrafluoroborate anions are omitted for clarity. N-H···F distances are displayed in red. N-H-F angles are shown in green. ORTEP representation with atomic displacement parameters set to 50 % probability.

$[Fe_2(\mu_2\text{-}L^{5,TA})_2](CF_3SO_3)_4 \cdot 2CH_3CN$ (C6) crystallizes in the triclinic space group $P\bar{1}$ with one formular unit in the unit cell and displays the isostructural triflate compound to **C4**. Hence, the two ligands also coordinate in a *cis*-axial manner (Figure 3.8). Crystallographic Data can be found in Table D.3. Although the two structures are isostructural, they do not appear to be isomorphous. To clarify the terms “isostructural” and “isomorphous”, a definition of *Kálmán et al.* is used.[235] The authors defined that two structures can be seen as isostructural, if they exhibit the same crystal structure, but not necessarily the same chemical composition nor the same cell dimensions. On the other hand, two crystalline solids are said to be isomorphous, if both crystallize in the same space group and have the same unit-cell dimensions. The asymmetric unit consists of one $\mathbf{L}^{5,TA}$ molecule coordinated to an iron(II) ion, one acetonitrile and two trifluoromethanesulfonate anions (Figure 3.11).

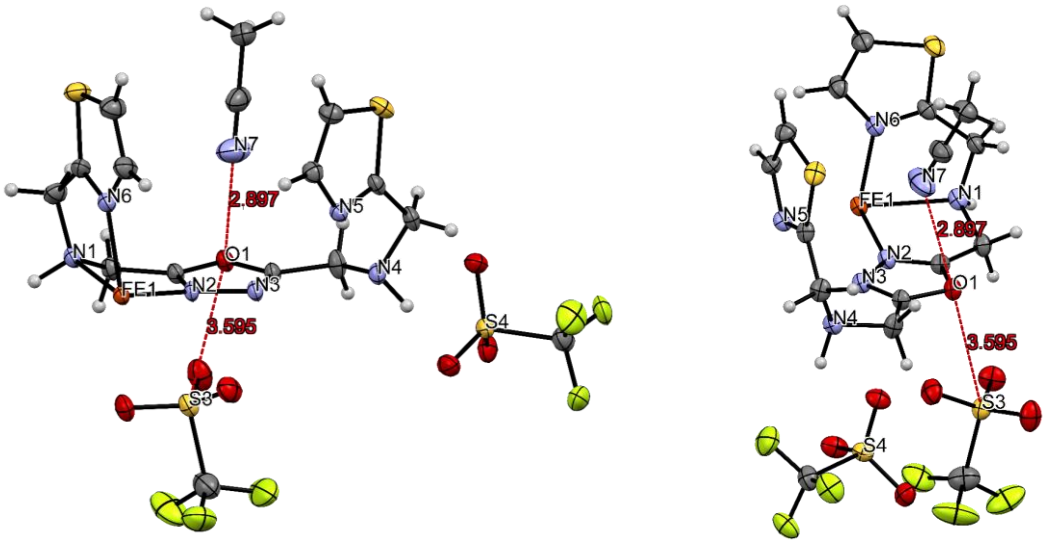


Figure 3.11 Asymmetric Unit of **C6** with front view (left) and side view (right). Measured distances are displayed as red dashed lines. ORTEP representation with atomic displacement parameters set to 50 % probability.

The description of the complex cation itself is analogous to that of **C4**. The longest average Fe-N bond type is displayed by $\bar{d}(\text{Fe-N}^{Amine})$ (2.36 Å), followed by $\bar{d}(\text{Fe-N}^{ODA})$ (2.14 Å) and $\bar{d}(\text{Fe-N}^{TA})$ (2.11 Å). These bond distances result in a mean Fe-N bond distance of 2.21 Å. The octahedral distortion parameter ($\Sigma_O(FeN_6)$ = 128 °) shows a larger distortion of the coordination sphere than found for **C4**, which is confirmed by continuous shape measurement ($CShM(O_h)$ = 4.57) (Figure F.8). In analogy, all those parameters point to a [HS-HS] state at the given temperature of 120 K. A complete list of all structural parameters can be found in Table E.2. Due to the present inversion center, one half of the unit cell is symmetry generated (Figure F.9). The complex cation is located in the middle of the unit cell on top of a center of inversion. Likewise to **C4**, the acetonitrile molecules lie between the thiazole rings above the oxadiazole moiety. The distance *d*(O1-N7) between the oxadiazole (O1) and the acetonitrile

(N7) equals to 2.90 Å. On the opposing side of the oxadiazole motif a triflate anion is located with *d*(O1-S3) = 3.60 Å (Figure 3.11). In contrast to **C4**, only two distinguishable hydrogen bonds between an amine function of the ligand and a triflate anion are found in **C6**. The first one can be found between N3-H3···O4 with a distance of 1.97 Å and an N3-H3-O4 angle of 161 °. Next to that, a second hydrogen bond N4-H4···O7 (2.05 Å) is formed, showing an N4-H4-O7 angle of 153 ° (Figure 3.12). All values are in agreement with the literature.[236] This time, the counter anions do not show any further hydrogen bonds to neighboring complex cation, thus offering no bridging nature.

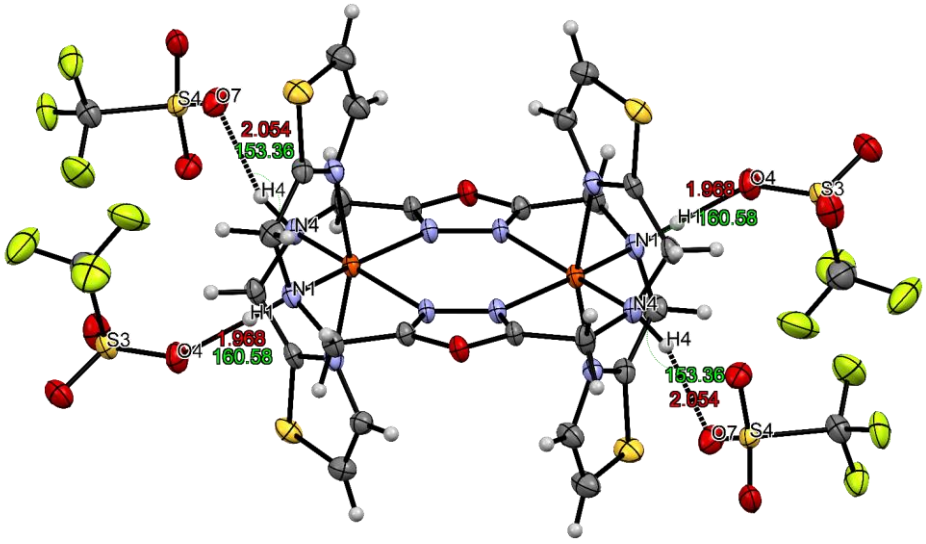


Figure 3.12 Unique hydrogen bonds (dashed black lines) in **C6** between complex cations and tetrafluoroborate anions. Acetonitrile molecules and irrelevant tetrafluoroborate anions are omitted for clarity. N-H···O distances are displayed in red. N-H-O angles are shown in green. ORTEP representation with atomic displacement parameters set to 50 % probability.

Magnetic properties of $[Fe_2(\mu_2\text{-}\mathbf{L^{5,TA}})_2](X)_4$ (X = ClO_4^-, $CF_3SO_3^-$) complexes

Magnetic measurements of **C4** – **C6** were carried out in a temperature range from 300-2 K at 0.1 T. Therefore, the magnetic susceptibility was determined and plotted as $\chi_M T$ product versus the temperature (*T*) for each complex (Figure 3.13). $[Fe_2(\mu_2\text{-}\mathbf{L^{5,TA}})_2](BF_4)_4 \cdot 2CH_3CN$ (**C4**) and $[Fe_2(\mu_2\text{-}\mathbf{L^{5,TA}})_2](CF_3SO_3)_4 \cdot 2CH_3CN$ (**C6**) were measured as colourless block shaped crystals, while $[Fe_2(\mu_2\text{-}\mathbf{L^{5,TA}})_2](ClO_4)_4$ (**C5**) was isolated and studied as microcrystalline powder. The $\chi_M T$ value of **C5** at 300 K is equal to 7.28 $cm^3mol^{-1}K$. This value is higher than the *spin-only* value, which is 6 $cm^3mol^{-1}K$ for two $S = 2$ spin centers with $g = 2$ (Equation 3.1). As already discussed for $[Fe_2(\mu_2\text{-}\mathbf{L^{5,Im}})_2](ClO_3)_4 \cdot 2CH_3CN$ (**C2**), the higher experimental value can be explained by first-order spin-orbit coupling due to the $^5T_{2g}$ ground state of both iron(II) centers.[67] The $\chi_M T$ value of **C5** decreases continuously to a value of 6.90 $cm^3mol^{-1}K$ at 50 K. Below 50 K, the $\chi_M T$ product drops significantly to 0.62 $cm^3mol^{-1}K$ at 2 K. The decline of $\chi_M T$ from high temperatures towards 2 K is caused by antiferromagnetic coupling between the oxadiazole-bridged iron(II) ions. Data were fitted with PHI,[201] using the spin Hamiltonian in Equation 3.2. The best fit resulted in $J = -0.66(2)$ and $g = 2.217(4)$ with the isotropic *g*-factor $g = g_1 = g_2 = (g_x + g_y + g_z)/3$ and $S_1 = S_2 = 2$, shown in Figure 3.13 (blue solid line).

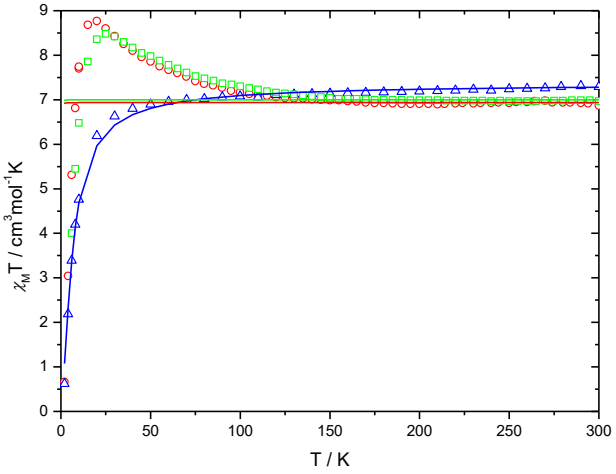


Figure 3.13 Temperature dependent behavior of **C4** (red open circles), **C5** (blue open triangles) and **C6** (green open squares) in form of the combined $\chi_M T$ *vs. T* plots. The blue solid line represents the best fit of the susceptibility data of **C5**. The red solid line and the green solid line show the best simulation of the high temperature regime of **C4** and **C6**, respectively.

Likewise to **C2**, the negative value for the exchange coupling parameter *J* represents a weak antiferromagnetic coupling between the iron(II) centers through the oxadiazol bridge. The *g*-factor of 2.217(4) is higher than 2.0, which is expected for systems showing first order spin-orbit coupling. The residual of the fit is equal to $R = 0.38$. The largest deviation of the fit from the experimental values takes place at lower temperatures. Again, this is attributed to the macroscopic orientation of the microcrystalline powder, since the sample was measured in a

non-blocked way. The octahedral distortion parameters [$\Sigma_O(FeN_6)$] of **C4** and **C6** are larger than 123 °, showing a large distortion of the coordination sphere. Comparing the structures of the $[Fe_2(\mu_2\text{-}\mathbf{L^{5,Im}})_2](X)_4$-type complexes, it can be assumed that the complex cation in $[Fe_2(\mu_2\text{-}\mathbf{L^{5,TA}})_2](ClO_4)_4$ (**C5**) also exhibits a large deviation of the coordination sphere from the ideal octahedron. High crystallographic anisotropy can lead to pronounced magnetic anisotropy, which in turn can cause the orientation of the crystals in the applied magnetic field. The resulting measured magnetic moment can therefore be formally higher than expected. Since **C3** showed completely different magnetic behavior while being studied in a blocked or non-blocked way in Chapter 3.1.2, **C4** and **C6** will not be investigated with respect to their coupling constant *J.* Both plots show a constant $\chi_M T$ value of approx. 7 $cm^3mol^{-1}K$ in the range of 300 – 150 K. Below 150 K, $\chi_M T$ starts to increase drastically, reaching its plateau at 20 K (8.77 $cm^3mol^{-1}K$) for **C4** and at 25 K (8.48 $cm^3mol^{-1}K$) for **C6**. Below these temperatures the curves decline rapidly towards zero, which can be ascribed to a combination of antiferromagnetic coupling between the iron(II) centers and to zero-field splitting (ZFS). However, since the crystals were measured in a non-blocked way, an alignment of the crystals with the magnetic field can occur (see Chapter 3.1.2). The effect on the measured magnetic moment in **C4** and **C6** should be larger than in **C5**, which was only isolated as microcrystalline powder. Thus, $\chi_M T$ was simulated solely taking the Zeeman effect into account ($\widehat{H} = \widehat{H}_{ZEE} = -g\mu_B HS$). The best simulations of the high temperature region for **C4** and **C6** are shown in Figure 3.13 as red and green solid line, respectively. The set isotropic *g*-factor ($g = g_1 = g_2$) of 2.15 (**C4**) and 2.16 (**C6**) represent in both cases spin-orbit coupled systems. Regardless of the magnetic coupling of both iron(II) centers, the complexes **C4** – **C6** do not exhibit SCO activity. Thus, all complexes of ligands $\mathbf{L^{5,Im}}$ and $\mathbf{L^{5,TA}}$ remain in the [HS-HS] state. The exchange of the imidazolyl group in the sidearms of $\mathbf{L^{5,Im}}$ with the thiazolyl moiety ($\mathbf{L^{5,TA}}$) did not lead to the desired SCO active dinuclear iron(II) compounds.

3.1.4 Summarizing the influence of the ligand sidearm on the SCO activity in complexes C1 – C6.

It is known, that the octahedral ligand field splitting energy (10*Dq*) is reciprocal to the metal-ligand distance (*r*) for neutral ligands ($10Dq \sim \mu/r^6$), where μ is the dipole moment of the ligand.[31] Accordingly, there should be mean metal-ligand bond length in the oxadiazole-bridged complexes, displaying a SCO suitable ligand field energy.[31] Looking at the average Fe-N bond lengths [$\bar{d}$(Fe-N)] in the oxadiazole-based complexes studied so far, the critical bond length for a SCO seems to be approx. 2.19 Å (Table 3.1). All compounds with $\bar{d}$(Fe-N) > 2.19 Å appear to stay in the [HS-HS] state even at very low temperatures.

Table 3.1 Summary of all average bond type lengths (in Å) of $[Fe_2(\mu_2\text{-}\mathbf{PMOD})_2](X)_4$-type complexes[20] and **C1** – **C6**. The overall average iron-nitrogen distance is described by $\bar{d}$(Fe-N). The superscript 'HC' describes the apically coordinating heterocycle.

	$\bar{d}$(Fe-N^{ODA})	$\bar{d}$(Fe-N^{Amine})	$\bar{d}$(Fe-N^{HC})	$\bar{d}$(Fe-N)	SCO
$[Fe_2(\mu_2\text{-}\mathbf{PMOD})_2](BF_4)_4$ · 2MeCN (173 K)[20]	2.14	2.32	2.14	2.20	No
$[Fe_2(\mu_2\text{-}\mathbf{PMOD})_2](ClO_4)_4$ · 4MeCN (193 K)[20]	2.12	2.28	2.14	2.18	Yes
$[Fe_2(\mu_2\text{-}\mathbf{PMOD})_2](CF_3SO_3)_4$ · 2MeCN (193 K)[20]	2.12	2.30	2.14	2.19	Yes
$[Fe_2(\mu_2\text{-}\mathbf{L^{5,Im}})_2](BF_4)_4$ · 2MeCN (**C1**) (173 K)[196]	2.15	2.43	2.08	2.22	No
$[Fe_2(\mu_2\text{-}\mathbf{L^{5,Im}})_2](ClO_4)_4$ · 2MeCN (**C2**) (173 K)[196]	2.13	2.42	2.08	2.22	No
$[Fe_2(\mu_2\text{-}\mathbf{L^{5,Im}})_2](CF_3SO_3)_4$ · 2MeCN (**C3**) (173 K)[196]	2.15	2.42	2.09	2.22	No
$[Fe_2(\mu_2\text{-}\mathbf{L^{5,TA}})_2](BF_4)_4$ · 2MeCN (**C4**) (120 K)	2.14	2.36	2.13	2.21	No
$[Fe_2(\mu_2\text{-}\mathbf{L^{5,TA}})_2](CF_3SO_3)_4$ · 2MeCN (**C6**) (120 K)	2.14	2.36	2.12	2.21	No

The reason for the absence of SCO is presumably due to the combination of geometrical constraints and electronic properties (mostly σ-donor and π-acceptor properties) of the ligand systems. Interestingly, the coordination of a 5-membered heteroaromatic ring in the apical positions (**C1** – **C6**) does not lead to longer axial bond lengths compared to the $[Fe_2(\mu_2\text{-}\mathbf{PMOD})_2](X)_4$-type complexes published by *Köhler et al.*.[20]

In fact, all complexes of $\mathbf{L^{5,Im}}$ and $\mathbf{L^{5,TA}}$ show smaller average Fe-N bond lengths to the axially coordinated aromatic heterocycle (HC) than the analogous iron(II) complexes of **PMOD,** expressed by [$\bar{d}$(Fe-N^{HC})]. It appears that the increased angle β (Figure 3.5) has more of an effect on the Fe-N^{Amine} bonds. While the average bond lengths to the oxadiazol moiety $\bar{d}$(Fe-N^{ODA}) are rather fixed at approx. 2.12 Å – 2.15 Å in every compound, the distances to the amine function $\bar{d}$(Fe-N^{Amine}) and the aromatic heterocycle in the axial position $\bar{d}$(Fe-N^{HC}) vary significantly. Thus, the axial bond distances in the [$Fe_2(\mu_2$-**PMOD**$)_2](X)_4$-type complexes ($\bar{d}$(Fe-N^{HC}) ≈ 2.14) are larger than those of **C1** – **C6**. However, at the same time, they exhibit the smallest bond distance of the iron(II) ion to the amine group ($\bar{d}$(Fe-N^{Amine}) ≈ 2.30). The change of the pyridyl moiety to the imidazole ring results in shorter apical bonds distances ($\bar{d}$(Fe-N^{HC}) ≈ 2.08) in complexes **C1** – **C3**. In contrast, the average distance to the amine function has increased significantly ($\bar{d}$(Fe-N^{Amine}) ≈ 2.42). In general, imidazole can be considered a moderate σ-donor and a weak π-acceptor.[215] Herein, the σ-donor and π-acceptor capabilities lie between those of saturated amines (e.g. ammonia) and aromatic amines, such as pyridine.[232] The series of coordinating ligands with increasing σ-donor ability follows the order pyridine (py) < imidazole (Im) < ammonia (NH_3), which is also the order of the decreasing π-acceptor capability (zero for NH_3).[232] *J. Reedijk* published a comparison between different "nitrogen-containing ligands" with respect to their ligand field strength in several transition metal complexes.[237] In this series, imidazole offers a lower ligand field than pyridine, which is ascribed to different π-acceptor properties. Thus, metal-ligand bond lengths to imidazole moieties should be larger than those to pyridine rings. However, the fact that complexes **C1** – **C3** have shorter axial bond lengths and significantly longer Fe-N^{Amin} distances than the [$Fe_2(\mu_2$-**PMOD**$)_2](X)_4$ complexes shows the great relevance of the altered ligand steric. Either way, the increased steric tension and the lower ligand field strength of $\mathbf{L^{5,Im}}$ lead to dinuclear iron(II) compounds without any SCO behavior. The exchange of the imidazolyl with the thiazolyl rest in **C4** – **C6** resulted in smaller values for the average metal-ligand bond distances, where $\bar{d}$(Fe-N) is approx. 2.22 Å in **C1** – **C3** and 2.20 Å in **C4** – **C6**. For azoles, the π-electron acceptor abilities increase in the order imidazole ≪ thiazole < pyrazole < 1,2,4-triazole, while the σ-basicity follows the reverse order.[197] Nevertheless, the most likely stronger π-backbonding to the thiazole ring in **C4** – **C6** still cannot compensate for the sterically unfavorable constraint of the five-membered ring in the ligand side arm, which again leads to SCO inactive complexes.

3.2 Dinuclear iron(II) complexes with 1,3,4-oxadiazole based ligands bearing six-membered heterocyclic aromatic sidearms ($L^{6,Y}$)

The SCO active compounds $[Fe_2(\mu_2\text{-}\mathbf{PMOD})_2](ClO4)_4 \cdot 4CH_3CN$ and $[Fe_2(\mu_2\text{-}\mathbf{PMOD})_2](CF_3SO_3)_4 \cdot 2CH_3CN$, published by *Köhler et al*., exhibit abrupt one-step SCO from the [HS-HS] to the [LS-HS] state below 180 K[20]. The latter complexes even shows a thermal hysteresis ($T_c^{\downarrow}$ = 152 K, $T_c^{\uparrow}$ = 178 K). However, most future applications of SCO materials as display devices, sensors or data storages will require room temperature bistability.[187,238–240] Higher ligand field strengths can shift the transition temperature to higher values, ideally to around 300 K. The missing spin transition from the [HS-LS] to the [LS-LS] state at lower temperature was attributed to elongated metal-ligand bond lengths of the second iron(II) ion, after the first center exhibits SCO. If the rigidity of the ligand is maintained and only a stronger ligand field is chosen, this could reveal whether steric hindrance alone or insufficient ligand field splitting energy causes the [LS-LS] state not to be reached. Therefore, three ligands $\mathbf{L^{6,Y}}$ with different para-substituted pyridyl sidearms [Y = (C-)OMe ($\mathbf{L^{6,OMe}}$), (C-)Cl ($\mathbf{L^{6,Cl}}$)and N ($\mathbf{L^{6,N}}$)] were synthesized. The substituents should influence the electron density in the aromatic ring, thus changing the resulting ligand field strength. Consequently, the transition temperature should then be shifted only by the different electronic nature of the ligand, the stiffness of the ligands should be the same as for **PMOD**. All these symmetrical ligands were used to successfully synthesize dinuclear iron(II) coordination compounds of type $[Fe_2(\mu_2\text{-}\mathbf{L^{6,Y}})_2](X)_4$ ($X = BF_4^-, ClO_4^-, CF_3SO_3^-$), as shown in Figure 3.14. Complex synthesis was done by dissolving equimolar amounts of ligand and iron(II) salt separately followed by the dropwise addition of the ligand solution to the metal salt under inert atmosphere. The resulting solution was then placed either for slow evaporation of the solvent or for vapor diffusion against a non-polar antisolvent. After different periods of time, the desired complexes could be isolated as single crystals or as microcrystalline powder (see Chapter 6.4 for synthetic details). Structure elucidation was either done by single-crystal X-ray diffraction or IR spectroscopy.

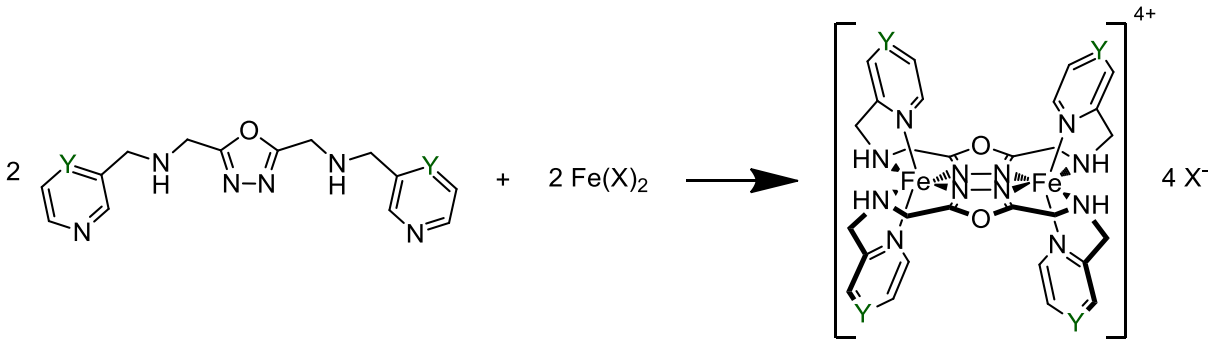


Figure 3.14 Synthesis of 1,3,4-oxadiazole based dinuclear iron(II) complexes with axially coordinating six-membered heterocyclic aromatic rings.

3.2.1 Synthesis of ligands $L^{6,OMe}$, $L^{6,Cl}$ and $L^{6,N}$

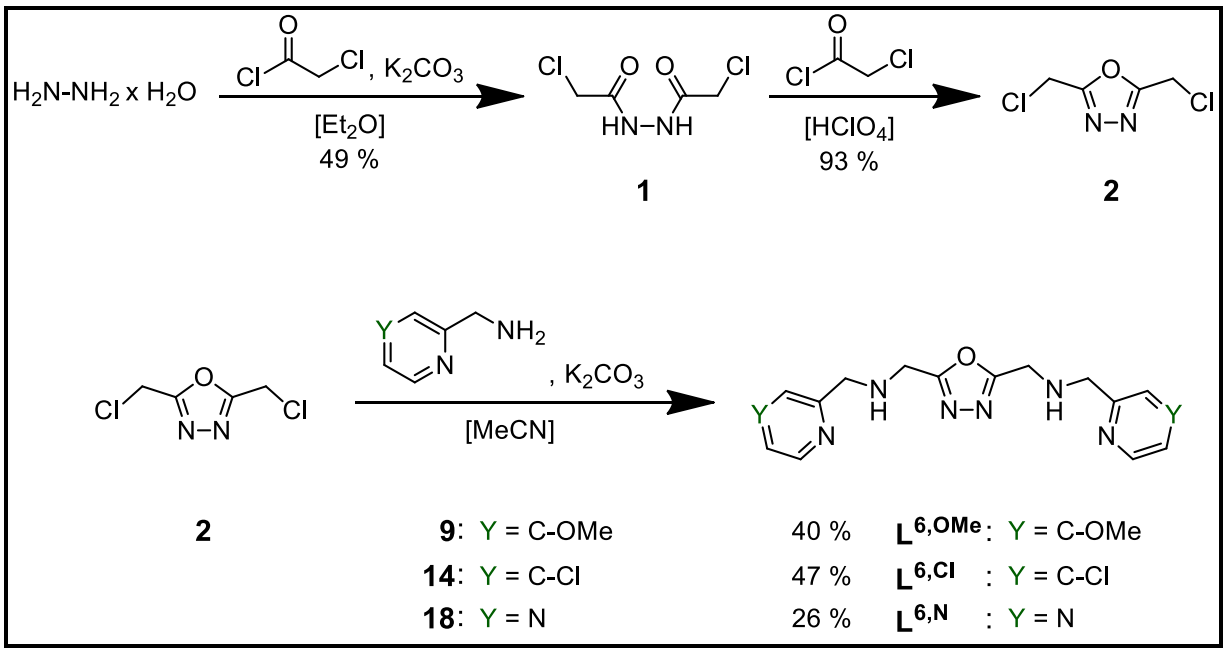


Figure 3.15 Synthesis of $L^{6,OMe}$, $L^{6,Cl}$ and $L^{6,N}$. Reaction conditions in the last steps were kept the same for all synthesized ligands. **1** and **2** were already reported in a former work.[196] All yields refer to this work.

The condensation reaction of hydrazine monohydrate and chloroacetyl chloride to form 1,2-Bis(chloracetyl)hydrazide (**1**), followed by the cyclization reaction to 2,5-bis(chloromethyl)-1,3,4-oxadiazole (**2**) was already described in Chapter 3.1.1. While **2** was converted to 2,5-bis(azidomethyl)-1,3,4-oxadiazole (**3**) in the synthesis for $L^{5,Im}$ and $L^{5,TA}$, here it serves directly as precursor for the synthesis of the desired ligands. The final nucleophilic substitution of the oxadiazole based compound **2** with a primary amine was described and published by *Köhler et al.*.[20] Following this reaction, the three ligands 2,5-bis[(4-methoxypyridin-2-ylmethyl)amino]methyl-1,3,4-oxadiazole ($L^{6,OMe}$), 2,5-bis[(4-chloropyridin-2-ylmethyl)amino]-methyl-1,3,4-oxadiazole ($L^{6,Cl}$) and 2,5-bis[(pyrazin-2-ylmethyl)amino]methyl-1,3,4-oxadiazole ($L^{6,N}$) were prepared in a nucleophilic reaction of **2** with (4-methoxy-pyridin-2-yl)methylamine (**9)**, (4-chloropyridin-2-yl)methylamine (**14**) or 2-(aminomethyl)pyrazine (**18**), respectively (Figure 3.15). While the yields for $L^{6,OMe}$ and $L^{6,Cl}$ are 40 % and 47 %, $L^{6,N}$ could only be isolated in a yield of 26 %. This was primarily caused by the final purification step including column chromatography. The retention factors R_f of the primary amine **18** and the desired ligand $L^{6,N}$ were nearly identical in various eluent mixtures, thus resulting in many mixed fractions. This problem was also evident in the synthesis of $L^{6,OMe}$ and $L^{6,Cl}$, but not as severe. To avoid this loss of product, many attempts were made to remove the primary amine by basic or acidic extraction, however, without success.

The distillative removal of the primary amines from the crude product resulted in the decomposition of the ligand. An improvement of the synthesis could be the exchange of functional groups. The 2,5-bis(aminomethyl)-1,3,4-oxadiazole (**4**) has already been used for the synthesis of $L^{5,Im}$ and $L^{5,Ta}$ and is easily accessible (see Chapter 3.1). The changed polarity and the presence of two amine functions could greatly increase the difference in retention times of the educts and the resulting ligand.

The synthesis of the required primary amines is already known in literature. (4-Methoxy-pyridin-2-yl)methylamine (**9**) could be obtained according to Figure 3.16. Therefore, methyl-4-methoxypicolinate (**5**) was synthesized in a one-step synthesis adopted from *Donohoe et al*., originally reported by *Sundber*g and *Jiang*.[241,242] After the completed reaction with thionyl chloride, the reaction residue was treated with methanol and heated to 70 °C for two additional days. This not only allowed the conversion of the intermediate acid chloride to the methyl ester, but also enabled the nucleophilic aromatic substitution at the 4-position of the pyridine ring to yield methyl-4-methoxypicolinate (**5**).[242] The rest of the synthesis follows the publication of *Fuchida et al.* with minor changes.[243] Thereby, the obtained ester **5** was reduced with sodium borohydride to the corresponding alcohol 4-methoxy-2-(hydroxymethyl)pyridine (**6**). The nucleophilic substitution reaction with thionyl chloride yielded 2-chloromethyl-4-methoxypyridine (**7**), which was subsequently reacted with sodium azide to 2-azidomethyl-4-methoxypyridine (**8**). (4-Methoxy-pyridin-2-yl)methylamine (**9**) could be obtained by the *Staudinger* reduction of **8** with triphenylphosphine and water.

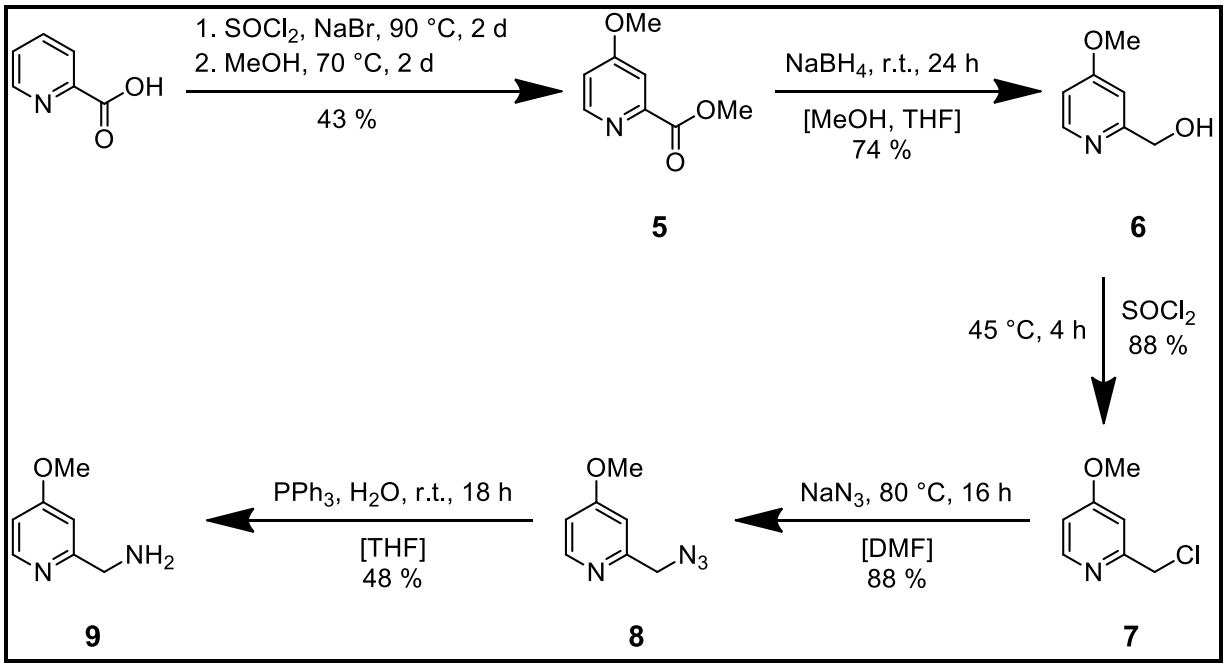


Figure 3.16 Synthesis scheme for (4-methoxy-pyridin-2-yl)methylamine **9**. The synthesis was taken from literature and slightly modified.[241,243,244]

(4-Chloropyridin-2-yl)methylamine (**14**) was obtained by using an equivalent route, shown in Figure 3.17. The most significant difference involves the synthesis of the ester compound methyl-4-chloropicolinate (**10**). In this synthetic step, the reaction mixture was stirred at room temperature for only 30 minutes after the addition of methanol. This only allowed for alcoholysis of the in situ formed 4-chloropicolinyl chloride to the methyl-4-chloropicolinate (**10**).[244] In both cases, for the synthesis of **5** and **10**, sodium bromide was added to facilitate the formation of the intermediate acid chloride.[242] Starting from the ester species, the yield of the synthesis of **14** is higher in each step compared to the synthesis of **9**. This could be caused by the different substitution groups in the 4-position of the pyridine. While the *+M*-effect of the methoxy function dominates, the *-I*-effect of halogens is stronger than their positive mesomeric effect.[245] This results in electron density being withdrawn from the aromatic ring, which in turn partially positively polarizes the methylene group in the 2-position. Nucleophilic attacks are thus facilitated.

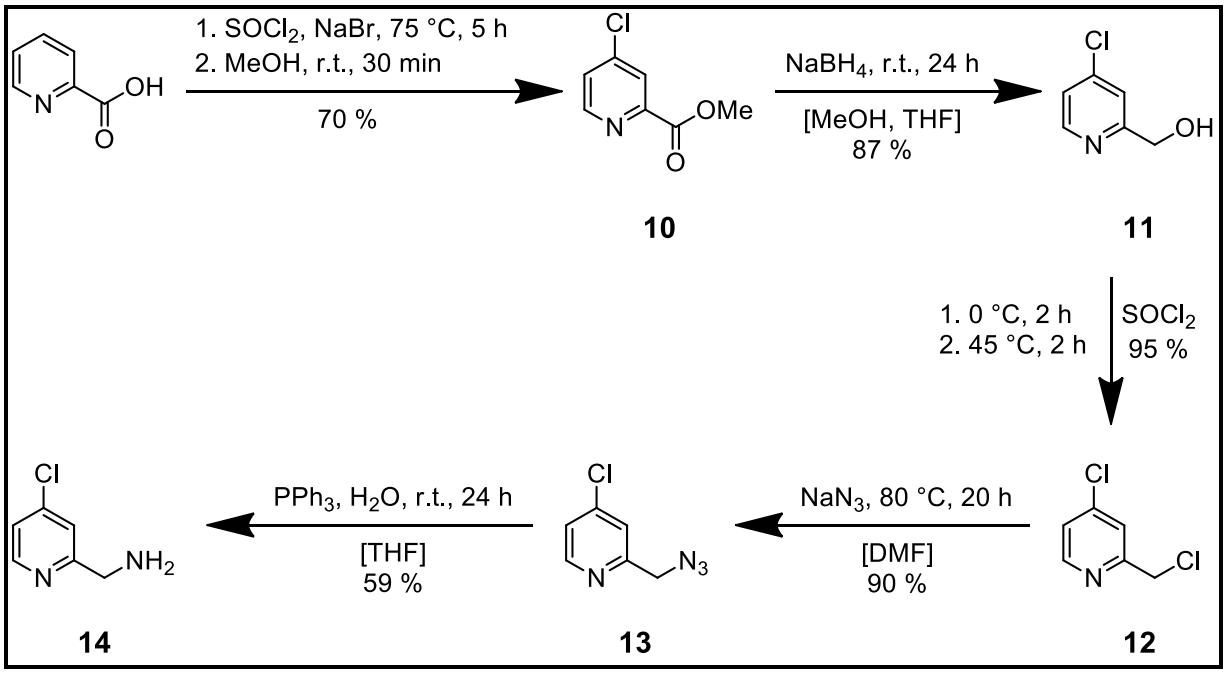


Figure 3.17 Synthesis scheme for (4-Chloropyridin-2-yl)methanamine **14**. The synthesis is already known in literature.[243,244,246] Modifications were done at some points.

2-(Aminomethyl)pyrazine (**18**) was synthesized by [redacted] in his bachelor thesis[247] according to a literature known route with adopted and modified procedures (see Figure 3.18).[248,249] Therefore, pyrazine-2-carboxylic acid was used in an esterification reaction to form methyl pyrazine-2-carboxylate (**15**), which was subsequently reduced with sodium borohydride to the corresponding alcohol compound pyrazin-2-ylmethanol (**16**).

2-Pyrazinemethylphthalimide (**17**) was then obtained via *Mitsunobu* reaction of **16** with diisopropyl azodicarboxylate (DIAD) and triphenylphosphine and was further hydrolyzed under basic conditions to the desired 2-(Aminomethyl)pyrazine (**18**). Please note that the *Ing-Manske* procedure is usually the milder method to convert N-alkyl phthalimides to primary amines.[250] In this case the N-alkyl phthalimide reacts with hydrazine to form the respective amine and phthalhydrazide. However, the separation of the hydrazide side product from **18** could not be achieved, which is why hydrolyzation of **17** was chosen as final step.

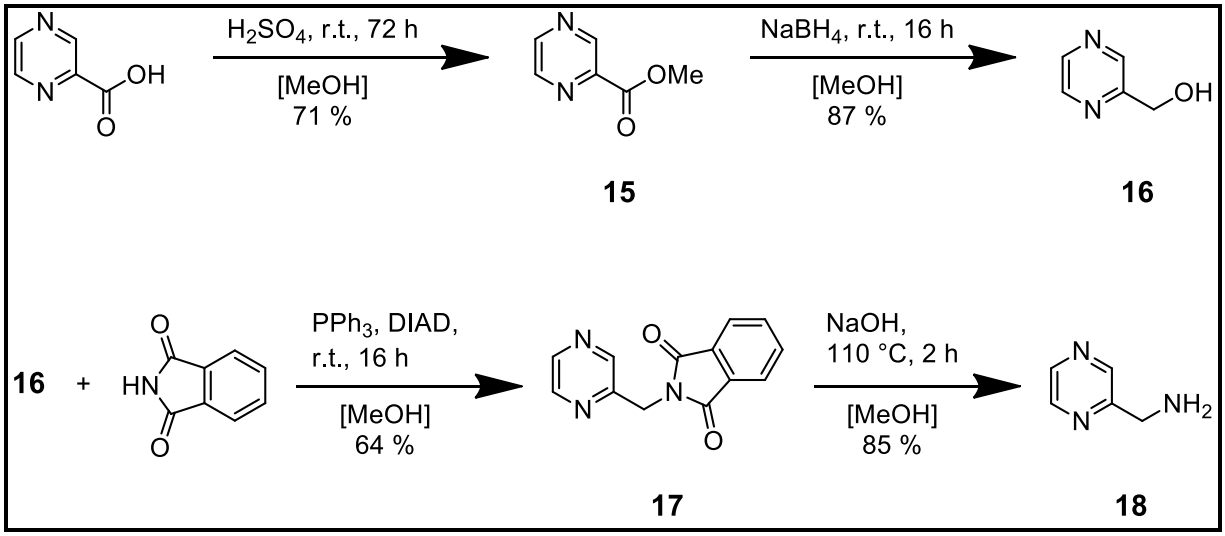


Figure 3.18 Synthesis scheme for 2-(aminomethyl)pyrazine **18**. The synthesis is already known in literature.[248,249]. Modifications were done at some points.

In summary, the precursor 2,5-bis(chloromethyl)-1,3,4-oxadiazole (**2**) was synthesized alongside the three primary amines **9**, **14** and **18** via literature known syntheses. Nucleophilic substitution of both chloride groups in **2** with the respective amines yielded the three novel ligands $L^{6,OMe}$, $L^{6,Cl}$ and $L^{6,N}$ in moderate yields. All three ligand systems are bearing the 1,3,4-oxadiazol motif and should form bridged dinuclear metal complexes of type $[Fe_2(\mu_2\text{-}L^{6,Y})_2](X)_4$ (X ≙ single charged anion), similar to those published by *Köhler et al.*.[20] The different functional groups in 4-position of the pyridine moiety are supposed to change the resulting ligand field strength, possibly enabling a thermal hysteresis loop of the magnetic moment around room temperature or a two-step spin crossover.

The following chapters will deal with the structure and magnetic properties of the prepared coordination compounds of $L^{6,OMe}$, $L^{6,Cl}$ and $L^{6,N}$. For this purpose, the general structural characteristics of the resulting complex cations shown by XRD analysis are described first. This description is followed by the detailed discussion of the crystal structure and magnetic properties of the individual complexes.

3.2.2 General discussion of bonding parameters of $[Fe_2(\mu_2\text{-}L^{6,Y})_2](X)_4$-type complexes (C7 – C13).

This chapter critically describes the structural characteristics of compounds **C7** – **C13** in a general manner. The exact structure and composition of each complex will be discussed at a later point. In all crystallographically studied $[Fe_2(\mu_2\text{-}\mathbf{L}^{6,Y})_2](X)_4$ coordination compounds the complex cation consists of two iron(II) centers, bridged by the nitrogen donor atoms of two 1,3,4-oxadiazole ligand backbones. The nitrogen atoms of the oxadiazoles and the secondary amines coordinate equatorially, thus forming the horizontal vertices of the two coordination octahedra. The pyridyl side arms are coordinating axially and form the apical corners of the polyhedra. Hereby, both pyridine rings of each ligand coordinate in *cis*-axial manner (Figure 3.19, left). Hence, the coordination mode of the ligands is the same as for the $\mathbf{L}^{5,Y}$ type ligands. The complex cation of every $\mathbf{L}^{6,Y}$ based complex [except for $[Fe_2(\mu_2\text{-}\mathbf{L}^{6,OMe})_2](CF_3SO_3)_4 \cdot 2CH_3CN$ (**C8**)] was built on a center of inversion. Therefore the $[Fe_2(\mu_2\text{-}\mathbf{L}^{6,Y})_2]^{4+}$ molecule can be described as inverse symmetrical (Figure 3.19, right). For the following discussion the labeling scheme of Figure 3.19 (left) is used. Due to the center of inversion, the coordination sphere of Fe1' is equivalent to Fe1 and won't be described additionally. **C8** is an exception here, as the complex cation shows no symmetry. However, even for this case, Fe1 and Fe1' are roughly equal, which allows the solely consideration of Fe1. In contrast to that, $[Fe_2(\mu_2\text{-}\mathbf{L}^{6,N})_2](BF_4)_4 \cdot 2MeCN$ (**C12**) shows even higher symmetry. A general trend considering the metal-ligand-bond distances and angles can be observed across all complexes. To provide a better overview, different metal-ligand bonds can be grouped together. Thus, the bonds Fe1-N1 and Fe1-N4 represent the bond of a secondary amine to the iron center ($Fe\text{-}N^{Amine}$). Fe1-N2 and Fe1-N3 both describe the bond of the oxadiazole nitrogen to the iron(II) ion ($Fe\text{-}N^{ODA}$).

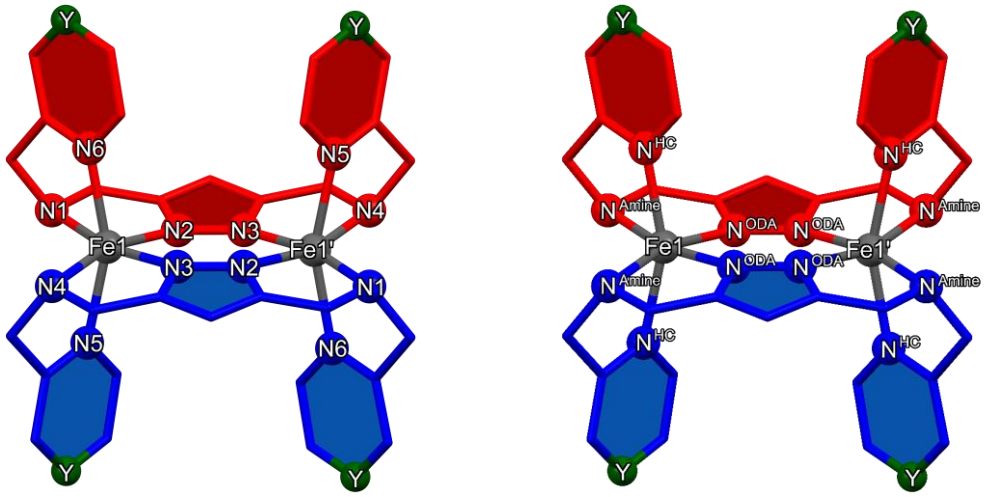


Figure 3.19 Left: Labelling scheme for all $[Fe_2(\mu_2\text{-}\mathbf{L}^{6,Y})_2]^{4+}$ complex cations (Y = C-OMe, C-Cl, N), except for **C8** and **C12**. Right: Labeling scheme according to the coordinated functional group. *Cis*-axial coordination mode of the ligands is displayed by the colours red and blue.

Fe1-N5 and Fe1-N6 will be summarized as Fe-N^{HC}, since they represent the binding of the apically coordinating heterocycle (HC) to the metal ion. The bond distances d(Fe-N^{Amine})$_i$ in complexes **C7** – **C13** ranges from 2.29 Å to 2.36 Å with an average of $\bar{d}$(Fe-N^{Amine}) = (2.33 ± 0.02) Å. Standard deviation was chosen as the error of the mean value, which is also a measure of dispersion of the individual values around the means. The value $\bar{d}$(Fe-N^{Amine}) shows the highest standard deviation, representing the metal-ligand bond type with the largest scattering in the considered complexes. A lower dispersion is found for the Fe-N^{ODA} and Fe-N^{HC} bonds with $\bar{d}$(Fe-N^{ODA}) = (2.14 ± 0.01) Å and $\bar{d}$(Fe-N^{HC}) = (2.14 ± 0.01) Å. Thus, the complexes differ mostly in their Fe-N^{Amine} bond. It becomes clear that Fe-N^{Amine} represents the longest metal-ligand bonds, whereas Fe-N^{ODA} and Fe-N^{HC} are roughly equal and much shorter (Figure 3.20). This trend of bond lengths was already observed for the $[Fe_2(\mu_2\text{-}\mathbf{L^{5,Y}})_2]^{4+}$ type complex cations. The difference can be attributed to the fact, that the amine function is known for its pure σ-donor character, while the oxadiazole and pyridine [pyrazine in case of $[Fe_2(\mu_2\text{-}\mathbf{L^{6,N}})_2](BF_4)_4 \cdot 2MeCN$ (**C12**) and $[Fe_2(\mu_2\text{-}\mathbf{L^{6,N}})_2](ClO_4)_4 \cdot 2MeCN$ (**C13**)] fragments can have further π-backbonding character.[232]

$$Fe\text{-}N^{Amin} \gg Fe\text{-}N^{ODA} \approx Fe\text{-}N^{HC}$$

Figure 3.20 General trend of metal-ligand bond lengths in the complexes **C7** - **C13**.

The substituents Y in the para-position of the pyridyl rest (Y = (C-)OMe, (C-)Cl, N) do not seem to influence the Fe-N^{HC} bond distance in the solid state in a reasoning way. Furthermore, all bond lengths indicate a high-spin iron(II) center. Accordingly, **C8**, $[Fe_2(\mu_2\text{-}\mathbf{L^{6,Cl}})_2](CF_3SO_3)_4 \cdot 2CH_3CN$ (**C11**) and **C13** are in the [HS-HS] state at 120 K, $[Fe_2(\mu_2\text{-}\mathbf{L^{6,OMe}})_2](ClO_4)_4 \cdot 2CH_3CN$ (**C7**) and **C12** at 173 K. A more detailed discussion about the magnetic properties of the afore mentioned complexes can be seen in the following chapters. To allow for further clear discussion, *cis*-angles have been categorized as shown in Table 3.2.

Table 3.2 The average of all grouped *cis*-angles of **C7** – **C13**. Standard deviation was chosen as error for the mean value. The notation L^a and L^b is used to clarify whether the angle is formed by nitrogen atoms of only one or two ligands.

$N^{Amin}(L^a)$-Fe-$N^{ODA}(L^a)$	$N^{ODA}(L^a)$-Fe-$N^{ODA}(L^b)$	$N^{Amin}(L^a)$-Fe-$N^{Amin}(L^b)$	$N^{Amin}(L^a)$-Fe-$N^{HC}(L^a)$	$N^{Amin}(L^a)$-Fe-$N^{HC}(L^b)$	$N^{ODA}(L^a)$-Fe-$N^{HC}(L^a)$	$N^{ODA}(L^a)$-Fe-$N^{HC}(L^b)$
N1-Fe1-N2 N3-Fe1-N4	N2-Fe1-N3	N4-Fe1-N1	N4-Fe1-N5 N1-Fe1-N6	N1-Fe1-N5 N4-Fe1-N6	N3-Fe1-N5 N2-Fe1-N6	N2-Fe1-N5 N3-Fe1-N6
75.1 ± 0.5	90.5 ± 0.5	120.9 ± 0.8	75.2 ± 0.2	90.7 ± 2.5	101.3 ± 2.8	98.7 ± 2.0

For this purpose, a distinction was made as to whether the nitrogen donor atoms forming the angle originate from only one [N(L^a)-Fe-N(L^a)] or two ligands [N(L^a)-Fe-N(L^b)]. For each angle group the average was calculated over the complexes **C7** – **C13**. To express the dispersion of the individual values around the mean, the standard deviation was given as error. Due to the bridging role of the oxadiazole group and the shape of the e_g^*-orbitals in the transition metal, the N^{ODA}(L^a)-Fe-N^{ODA}(L^b) angle is practically fixed at around 90 ° [(90.5 ± 0.5) °]. The angle formed by the oxadiazol and its methylene group in 2- and 5-position (N^{ODA}-C^{ODA}-CH_2) is about 125 ° for all oxadiazole backbones. Combined with the rigidity of the ligand and the rather fixed high-spin Fe-L bond lengths, this will compulsorily restrict the equatorial angles N^{Amin}(L^a)-Fe-N^{ODA}(L^a) and N^{Amin}(L^a)-Fe-N^{Amin}(L^b) to about (75.1 ± 0.5) ° and (120.9 ± 0.8) °, respectively. The latter represents the largest *cis*-angle in all considered complex. In fact, all of the afore mentioned angles lie in the equatorial plane and show a very low dispersion over all complexes (seen by the standard deviation). In contrast, the angles in the axial direction show a much larger variation. The mean values range from 90.7 ° to 101.3 ° with standard deviations between 2.0 ° and 2.8 °, respectively. N^{Amin}(L^a)-Fe-N^{HC}(L^a) is an exception here and is comparable to N^{Amin}(L^a)-Fe-N^{ODA}(L^a). Both angles are formed by the secondary amine and an adjacent donor atom of the same ligand, thus relying on the rigidity of the linking methylene group. Following this discussion, the complexes differ most in their geometry regarding the apical octahedral position. This trend can also be seen in the three *trans*-angles. While the two averages of the equatorial *trans*-angles are both about 162 ° (with standard deviations of 0.7 ° and 0.9 °), the mean of the axial *trans*-angles is 151.4 ° ± 4.7 °, showing the highest dispersion of all angles. Similar deviation of the *cis*-angles from 90 ° in all complexes results in octahedral distortion parameters above 120°°, which additionally indicates a [HS-HS] state the given temperature. A detailed list of selected bond lengths and angles can be found in Appendix E for all crystallographic studied $[Fe_2(\mu_2\text{-}\mathbf{L^{6,Y}})_2](X)_4$ complexes.

The following chapters will go into detail regarding the crystallographic and magnetic properties of each complex. Therefore, the $[Fe_2(\mu_2\text{-}\mathbf{L^{6,OMe}})_2](X)_4$-type complexes **C7** and **C8** will be described first in chapter 3.2.3, followed by the discussion of the $[Fe_2(\mu_2\text{-}\mathbf{L^{6,Cl}})_2](X)_4$-type compounds (**C9** – **C11**) in chapter 3.2.4. The last subchapter 3.2.5 will deal with the $[Fe_2(\mu_2\text{-}\mathbf{L^{6,N}})_2](X)_4$-type compounds **C12** and **C13**.

3.2.3 Dinuclear iron(II) complexes of type $[Fe_2(\mu_2\text{-}L^{6,OMe})_2](X)_4$ (C7 and C8)

$[Fe_2(\mu_2\text{-}L^{6,OMe})_2](ClO_4)_4 \cdot 2CH_3CN$ (C7) crystallizes in the triclinic space group $P\bar{1}$ with one formula unit in the unit cell. The crystal structure was measured at 173 K, the structure of the complex cation follows the discussion of Chapter 3.2.2. Crystallographic Data can be found in Table D.3. The asymmetric unit consists of an iron(II) center coordinated by one ligand, two perchlorate anions and an acetonitrile molecule (Figure 3.21).

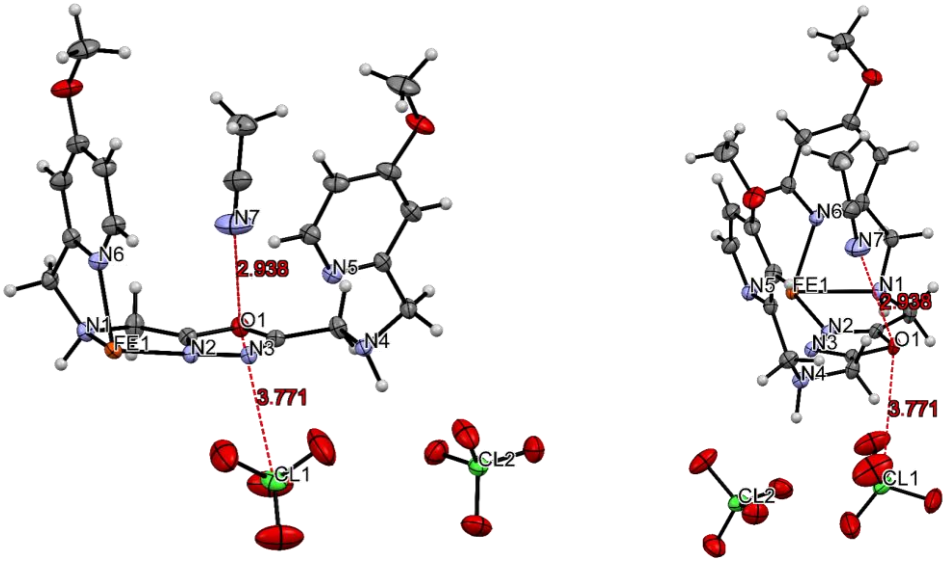


Figure 3.21 Asymmetric Unit of **C7** with front view (left) and side view (right). Measured distances are displayed as red dashed lines. ORTEP representation with atomic displacement parameters set to 50 % probability.

Both $Fe^{II}N_6$ coordination spheres are symmetry equivalent, showing an average Fe-N bond distance of $\bar{d}$(Fe-N) = 2.21 Å with an octahedral distortion parameter $\Sigma_O(FeN_6)$ of 143.3 °. Both values indicate an iron(II) ion in the HS, thus a [HS-HS] state for the complex cation at 173 K. The strong deviation of the coordination sphere from the ideal octahedron is further confirmed by continuous shape measurement with $CShM(O_h)$ = 5.75, displayed in Figure F.10. All structural parameters can be found in Table E.4. The influence of the methoxy function in the 4-position of the pyridyl moiety should most likely be reflected by the bond length of the pyridyl ring to the iron(II) center. Considering the two coordinating pyridyl rings, the average bond distance $\bar{d}(Fe\text{-}N^{Py})$ is equal to 2.13 Å. This value is only 0.01 Å shorter than the $\bar{d}(Fe\text{-}N^{Py})$ distance at 193 K of the corresponding unsubstituted compound $[Fe_2(\mu_2\text{-}\mathbf{PMODA})_2](ClO_4)_4 \cdot 4CH_3CN$, published by *Köhler et al.* (2.14 Å).[20] Thus, the difference is rather too small to allow for clear interpretation. The acetonitrile lies between the two coordinating pyridyl moieties above the oxadiazole ring. The distance between the oxadiazol-oxygen and the acetonitrile-nitrogen is equal to *d*(O1-N7) = 2.94 Å. Opposite the oxadiazole ring, a non-coordinating tetrafluoroborate anion is located with *d*(O1-B1) = 3.77 Å

(Figure 3.21). The remaining perchlorate lies in the corner of the unit cell, which is spanned by the translation vectors $\vec{a}$ and $\vec{b}$. Due to the present centers of inversion in the unit cell, the rest of the complex cation, two other counter ions as well as one solvent molecule are generated by symmetry (Figure F.11). All four amine functions form hydrogen bonds to neighboring perchlorate anions. These, in turn, exhibit further hydrogen bonds to the next complex cation, thus acting as bridging counter ions. Considering the symmetry, only three different interactions must be described (Figure 3.22). The first two hydrogen bonds can be found between N3-H3···O4 (2.08 Å) and N3-H3···O5 (2.60 Å), where O4 and O5 are two different oxygen atoms of the same perchlorate molecule. The measured distance between the hydrogen and the acceptor atom (here oxygen) often correlates with the enclosed angle. In this case, the found distances are reasonable values considering the N3-H3-O4 (155.0 °) and the N3-H3-O5 angle (133.1 °).[251] The former angle is closer to 180 °, thus resulting in the shorter hydrogen bond. The next interaction can be found between a third oxygen atom of the afore mentioned perchlorate and the amine function of a neighboring complex cation. The distance of the hydrogen bond N4-H4···O7 is equal to 2.02 Å along an N4-H4-O7 angle of 164.6 °. Again, the distance and angle are very well in line with the literature.[251] Considering the present symmetry, these hydrogen bonds result in a one-dimensional linkage of the complex cations (Figure F.12). This type of crosslinking via the perchlorate anion is often encountered in the literature for ligands of similar form.[20,22–25,196]

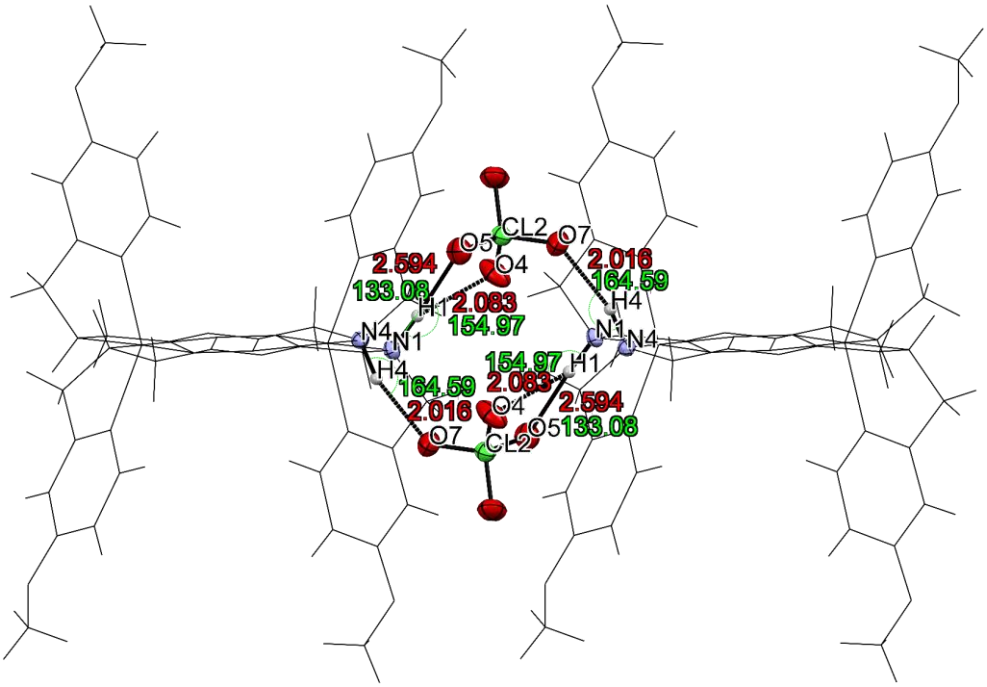


Figure 3.22 Unique hydrogen bonds (dashed black lines) in **C7** between complex cations and perchlorate anions. Acetonitrile molecules and irrelevant perchlorate anions are omitted for clarity. N-H···O distances are displayed in red. N-H-O angles are shown in green. ORTEP representation with atomic displacement parameters set to 50 % probability.

$[Fe_2(\mu_2\text{-}L^{6,OMe})_2](CF_3SO_3)_4 \cdot 2CH_3CN$ (C8) is isostructural to **C7** and also crystallizes in the triclinic space group $P\bar{1}$, but this time with two formula units inside of the unit cell. The crystal structure was measured at 120 K. Crystallographic Data can be found in Table D.4. Here, the complex cation is not located on top of a center of inversion. Thus, the asymmetric unit consist of the entire coordination cation, four triflate anions and two acetonitrile molecules (Figure 3.23). This results in two distinguishable iron(II) centers. The rest of the unit cell is generated by inversion symmetry (Figure F.13). Nevertheless, the coordination spheres for both the metal centers do not differ much and still follow the trend described in Chapter 3.2.2.

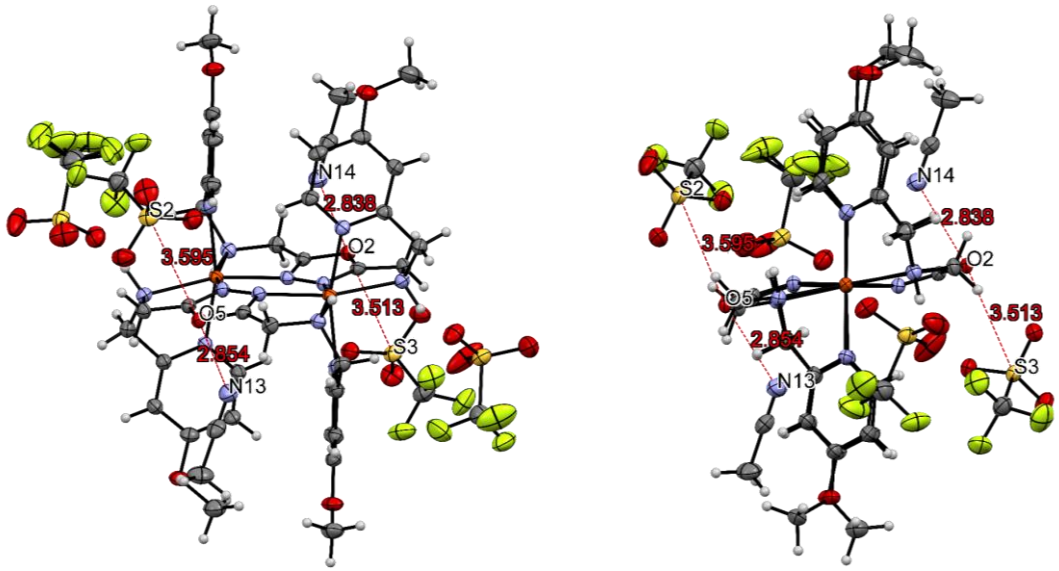


Figure 3.23 Asymmetric Unit of **C8** with front view (left) and view along the Fe-Fe-axis (right). Measured distances are displayed as red dashed lines. ORTEP representation with atomic displacement parameters set to 50 % probability.

The first iron(II) center shows an average metal to ligand distance of $\bar{d}$(Fe1-N) = 2.21 Å, combined with an octahedral distortion parameter $\Sigma_O(Fe1N_6)$ of 128.4 °. High deviation of the coordination sphere from the ideal octahedron is further confirmed by continuous shape measurements with $CShM(Fe1N_6,O_h)$ = 4.30. Similar values are found for the second iron(II) center with $\bar{d}$(Fe2-N) = 2.20 Å, $\Sigma_O(Fe2N_6)$ = 124.7 ° and $CShM\ (Fe2N_6,O_h)$ = 3.96 (see Figure F.14). All structural parameters can be found in Table E.3. All of the afore mentioned values refer to a [HS-HS] state at the given temperature of 120 K. The overall distortion seems to be less than in **C7**, which is most likely due to the lower deviation of the pyridine rings from the ideal apical positions. The *trans*-angles N^{Py}-Fe1-N^{Py} and N^{Py}-Fe2-N^{Py} (160.14(9) ° and 160.32(9) °, respectively) are approximately 16 ° larger than the N^{Py}-Fe-N^{Py} angle in **C7** (146.62(5) °). This can be explained by the orientation of the bulky methoxy-groups in the 4-position of the pyridine rings. While the methoxy functions of one ligand are directed toward each other in **C7**, they point away from each other in **C8**.

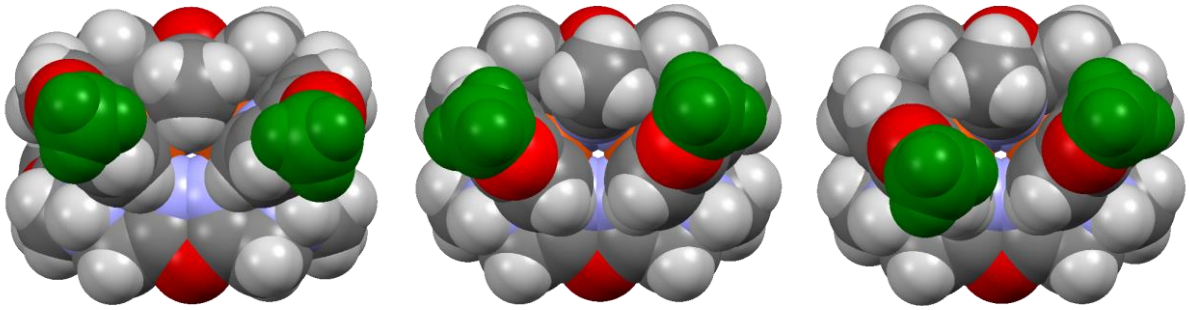


Figure 3.24 Molecular structure **C7** (left) and **C8** (middle and right) with view onto the 4-methoxypyridyl moieties as space filling model. The methyl group of the methoxy-function is displayed in green for clarity.

Hence, the pyridyl moieties have more space towards the acetonitrile molecule, which is located between them and above of the oxadiazole ring. This results in an N^{Py}-Fe1-N^{Py} angle closer to 180 °, compared to the complex **C7** (Figure 3.24) and thus in smaller distortion. The average iron pyridyl distance $\bar{d}$(Fe-N^{Py}) is equal to 2.14 Å, which is only 0.01 Å larger than in $[Fe_2(\mu_2\text{-}\mathbf{PMODA})_2](ClO_4)_4 \cdot 4CH_3CN$.[20] Thus, there seems to be no reasonable influence of the functional group in 4-position of the pyridyl ring on the pyridine-metal bond distance in the solid state. This might be due to the fact, that the ligand system is somehow rigid, leading to less freedom considering the apical bond distances. Likewise to **C7**, the acetonitrile molecules are located between the coordinating pyridyl rings of one ligand with distances of the acetonitrile-nitrogen and oxadiazole-oxygen of *d*(O2-N14) = 2.84 Å and *d*(O5-N13) = 2.85 Å. Please note that the labeling in **C8** does not follow the scheme in Figure 3.19, since the complex cation itself is not inverse symmetrical.

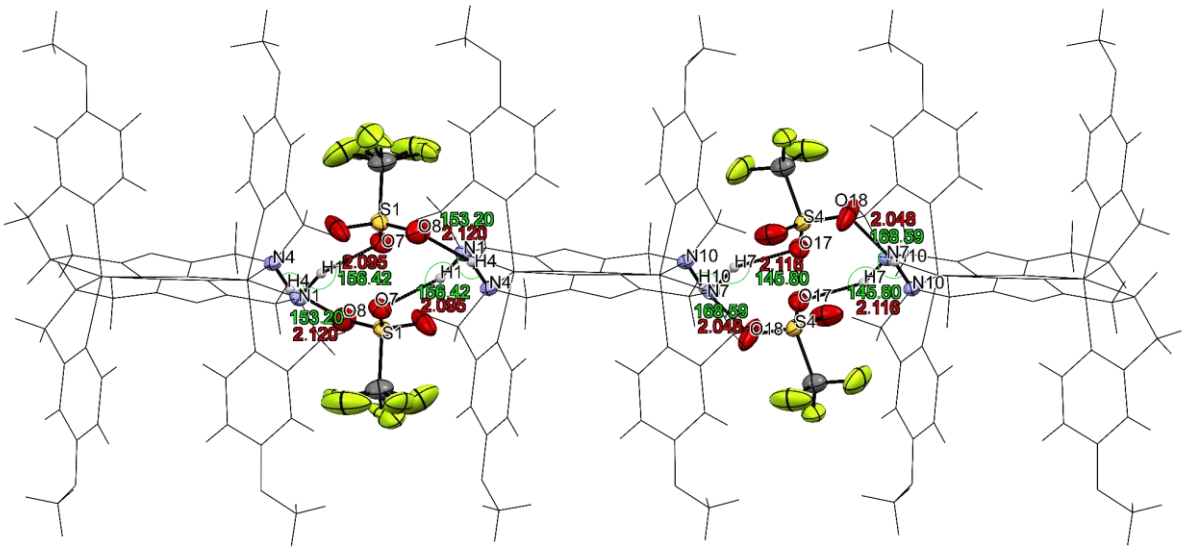


Figure 3.25 Unique hydrogen bonds (dashed black lines) in **C8** between complex cations and triflate anions. Acetonitrile molecules and irrelevant triflate anions are omitted for clarity. N-H···O distances are displayed in red. N-H-O angles are shown in green. ORTEP representation with atomic displacement parameters set to 50 % probability.

The space around the oxadiazole motif is filled by triflate anions with distances of *d*(O2-S3) = 3.51 Å and *d*(O5-S2) = 2.59 Å (Figure 3.23). The two remaining triflates can be found next to the complex cation, allowing for hydrogen bonds between the amin function of the ligand and the oxygen atoms of the anion. Due to the lack of symmetry of the complex cation, the hydrogen bonds to the amine functions are all distinguishable and differ slightly (Figure 3.25). Therefore, the first hydrogen bond can be found between the first amine function of ligand $\mathbf{L}^{6,OMe}$ and a bridging triflate anion between N3-H3···O11 (2.12 Å) with an enclosed N3-H3-O11 angle of 145.8 °. The same triflate molecule shows another hydrogen bond between a second oxygen atom and the amin function of a neighboring complex cation N10-H10···O10 (2.05 Å) along an N10-H10-O10 angle of 168.6 °. The same bridging situation applies to the second amine function of the ligand. Here, hydrogen bounds are found between N4-H4···O8 (2.12 Å) with an N4-H4-O8 angle of 153.2 ° and between N9-H9···O7 (2.10 Å), which yields in an angle of 156.4 °. All angles and distances of the mentioned hydrogen bonds are in agreement with the literature.[236] The present bridging nature of the triflate anions results in a one-dimensional network of complex cations via hydrogen bonds (Figure F.15).

Magnetic properties of $[Fe_2(\mu_2\text{-}\mathbf{L}^{6,OMe})_2](X)_4$-type complexes

Since just occasional crystals of **C8** were obtained, only $[Fe_2(\mu_2\text{-}\mathbf{L}^{6,OMe})_2](ClO_4)_4 \cdot 2CH_3CN$ (**C7**) was investigated with respect to its temperature-dependent magnetic moment at 0.1 T. Therefore, the molar susceptibility was determined and plotted as $\chi_M T$ product versus the temperature in Figure 3.26. At 300 K, the $\chi_M T$ value is equal to 6.96 $cm^3mol^{-1}K$ and slightly drops to 6.86 $cm^3mol^{-1}K$ at 170 K in a quite linear way.

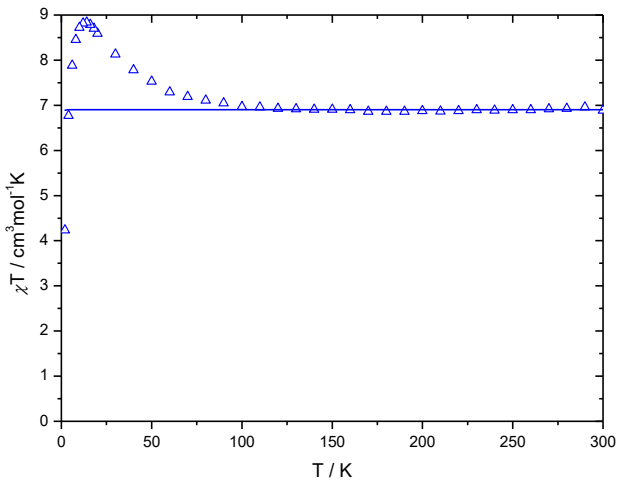


Figure 3.26 Resulting $\chi_M T$ *vs. T* plot of **C7** (blue open triangles). The blue solid line represents the best simulation of the high temperature regime of **C7** using PHI.[201]

Below this temperature, the $\chi_M T$ product rises until it reaches its maximum at 14 K (8.84 $cm^3mol^{-1}K$), before its drops again towards a value of 4.23 $cm^3mol^{-1}K$ at 2 K. The sample was measured without being embedded in eicosane or grease. Hence, the crystals with magnetic anisotropy axis may follow the orientation of the external magnetic field. This orientation effect results in the rise of $\chi_M T$ at lower temperatures. The rapid decrease of the $\chi_M T$ product below 14 K can be attributed to an antiferromagnetic coupling between the two bridged iron(II) centers or to zero-field splitting (or a combination of both). However, this is difficult to distinguish without magnetization data. The huge distortion of the coordination sphere in **C7** ($\Sigma_O(FeN_6)$ = 143.28 °, $CShM(O_h)$ = 5.75) could give rise to magnetic anisotropy, resulting in a pronounced value for the axial zero-field splitting parameter *D*. Due to the preferred direction of magnetization, macroscopic alignment of crystals in an external magnetic field may be enhanced. To avoid misinterpretation, the data were simulated by taking only the Zeeman effect into account (Equation 3.4) with $g = g_1 = g_2 = (g_x + g_y + g_z)/3$ and $S_1 = S_2 = 2$. The best simulation of the high temperature regime was obtained setting *g* to 2.15. The resulting plot is visualized as solid blue line in Figure 3.26. Deviation of the *g*-factor from 2.0 can be ascribed to the presence of first order spin-orbit coupling due to the unquenched orbital angular momentum in the $^5T_{2g}$ ground state.[67] The crystal structures of **C7** and **C8** already indicate a stabilization of the [HS-HS] state at 173 K and 120 K, respectively. The magnetic data of **C7** further show an absence of spin transition even at lower temperatures. Although this can not be said with complete certainty, **C8** most likely shows the same magnetic behavior. The desired shift of the spin transition occurring in the $[Fe_2(\mu_2\text{-}\mathbf{PMODA})_2](X)_4$-type complexes ($X = ClO_4^-$, $CF_3SO_3^-$) to higher temperatures by implementing a methoxy function in the 4-position of the pyridyl moiety could thus not be achieved. While sterically demanding ligand spheres in general lead to high-spin complexes[252–255], the relationship between the electronic character of the ligand on transition metal spin state is less straightforward. Thus, there are several examples in the literature, where electron-donating substituents stabilize either the low-spin[256,257] or the high-spin state[258–261] in various series of compounds. The methoxy group in *para*-position to the coordinating nitrogen should increase the electron density in the ring with its positive *mesomeric* effect (+*M*-effect), which in return should enhance the σ-binding to the iron(II) ion. However, it appears to be insufficient to only consider the σ-contributions to the metal-ligand bonding. *Halcrow et al.* showed the relationship between the *para*-substituent *Hammett* parameter (σ_p) and the energy of the d-orbitals for octahedral $[Fe(\mathbf{bpp^{X,H}})_2]^{2+}$-type complexes (**bpp^{X,H}** = 2,6-di{pyrazol-1-yl}pyridine with X-substitution in the 4-position of the pyridyl moiety).[262] *Hammett* constants were originally induced in 1937 to describe the effects of aromatic substitution in *meta*- (σ_m) or in *para*-position (σ_p) on the ionization of benzene like compounds.[263] Thus, σ_p represents the resonance and inductive effects on aromatic systems, while the *Hammett* constant of hydrogen $\sigma_p(H)$ is defined as zero. Tabulated values for various

substituents can be found in the literature.[264] *Halcrow et al.* could show, that electron-withdrawing subtitutions ($\sigma_p > 0$) lower the energy of all metal d-orbitals.[262] In case of the $[Fe(\mathbf{bpp^{X,H}})_2]^{2+}$-type complexes, the effect on the averaged t_{2g}-orbital energies is greater than for the e_g-orbitals, raising the ligand field splitting energy. On the other hand, electron-donating groups ($\sigma_p < 0$) seem to enhance the energy of the metal d-orbitals. Again, the effect on the t_{2g}-orbitals is more pronounced compared to the e_g-orbitals, which results in a lower ligand field splitting energy. Therefore, the relationship between T_c and the substitution pattern is a competition between the metal-ligand σ- and π-bonding effects. Electron-donating *para*-substituents can inductively increase the energy of the nitrogen lone pair in a pyridine moiety, resulting in a higher ligand field and thus stabilizing the LS state. However, the energy of the π*-molecule orbitals is *also enhanced*. This conversely lowers the ligand field by weakening the Fe-$N^{Pyridine}$ π-backbonding, favoring the HS state. In case of $[Fe_2(\mu_2\text{-}\mathbf{L^{6,OMe}})_2](ClO_4)_4 \cdot 2CH_3CN$ (**C7**), the Fe-L π-bonding effects seem to dominate, since the complex shows no SCO activity anymore but remains in the [HS-HS] state. Considering the complex series $[Fe_2(\mu_2\text{-}\mathbf{PMOD})_2](X)_4$, $[Fe_2(\mu_2\text{-}\mathbf{L^{5,Im}})_2](X)_4$ and $[Fe_2(\mu_2\text{-}\mathbf{L^{5,TA}})_2](X)_4$, it became apparent that the ligand field strength of perchlorate- and triflate-balanced complexes of same type is roughly equal. Therefore, it is to be expected that the complex $[Fe_2(\mu_2\text{-}\mathbf{L^{6,OMe}})_2](CF_3SO_3)_4 \cdot 2CH_3CN$ (**C8**) also stays in the [HS-HS] spin state even at low temperatures. This assumption is supported by the fact that the crystal structure of **C8** shows Fe-L bond lengths and distortion parameters referring to a high-spin state at 120 K. The introduction of the methoxy function ($\sigma_p(OMe) = -0.27$)[264] in the **PMOD** ligand seems to lower the ligand field splitting in **C7** and **C8,** compared to $[Fe_2(\mu_2\text{-}\mathbf{PMOD})_2](X)_4$ ($X = ClO_4^-, CF_3SO_3^-$). To cause the opposite effect and shift T_c to higher temperatures, an electron-withdrawing function must be incorporated in the *para*-position.

3.2.4 Dinuclear iron(II) complexes of type $[Fe_2(\mu_2\text{-}\mathbf{L^{6,Cl}})_2](X)_4$ (C9 – C11)

Due to the good synthetic accessibility of the precursor (4-chloropyridin-2-yl)methylamine (**14**), the ligand $\mathbf{L^{6,Cl}}$ was prepared, offering a chloride *para*-substitution (σ_p(Cl) = 0.23)[264] in the pyridine rings (see Chapter 3.2.1). $\mathbf{L^{6,Cl}}$ was consequently used to synthesize $[Fe_2(\mu_2\text{-}\mathbf{L^{6,Cl}})_2](BF_4)_4$ (**C9**) and $[Fe_2(\mu_2\text{-}\mathbf{L^{6,Cl}})_2](ClO_4)_4$ (**C10**) as microcrystalline powder. $[Fe_2(\mu_2\text{-}\mathbf{L^{6,Cl}})_2](CF_3SO_3)_4 \cdot 2MeCN$ (**C11**) could be isolated in form of single crystals, which were suitable for single-crystal X-ray analysis. IR spectroscopy confirmed the successful synthesis of complexes **C9** – **C11**. The IR spectra and assignment of the symmetric N-H valence vibration together with anion specific bands are shown in Figure F.16 and Table F.1, respectively.

$[Fe_2(\mu_2\text{-}\mathbf{L^{6,Cl}})_2](CF_3SO_3)_4 \cdot 2CH_3CN$ (C11) crystallizes in the triclinic space group $P\bar{1}$ with two formula units inside of the unit cell. The crystal structure was measured at 120 K. Crystallographic Data can be found in Table D.4. The complex is isostructural to $[Fe_2(\mu_2\text{-}\mathbf{L^{6,OMe}})_2](ClO_4)_4 \cdot 2CH_3CN$ (**C7**) and $[Fe_2(\mu_2\text{-}\mathbf{L^{6,OMe}})_2](CF_3SO_3)_4 \cdot 2CH_3CN$ (**C8**). Moreover, **C7** and **C11** seem to be isomorphous. To calculate the degree of isomorphism, the *unit-cell similarity index* (Π) can be used. It is calculated via Equation 3.5, where (a, b, c) and (a', b', c') are the reduced unit cell axes of the two compared structures, such that Π is always positive. In case of present isomorphism, Π should be very close to 0.[265–267]

$$\Pi = \frac{(a+b+c)}{(a'+b'+c')} - 1 \tag{3.5}$$

Here, Π(**C11**/**C7**) is equal to 0.02, which is close enough to zero to call the two structures not only isostructural, but also isomorphous.[265] Likewise to **C7**, the asymmetric unit consists of one iron(II) ion coordinated to one $\mathbf{L^{6,Cl}}$ molecule, next to one acetonitrile and two triflate anions (Figure 3.27). Both of the $Fe^{II}N_6$ coordination spheres are symmetry equivalent, showing an average Fe-N bond distance of 2.19 Å. This value is equal to the average Fe-N bond length in the SCO active complex $[Fe_2(\mu_2\text{-}\mathbf{PMOD})_2](ClO_4)_4 \cdot 4CH_3CN$ (2.19 Å), published by *Köhler et al.*, and shorter than the distances in the $\mathbf{L^{6,OMe}}$ related complexes **C7** (2.21 Å) and **C8** (2.21 Å). Assuming that the ligand field is stronger at shorter metal-ligand distances of the same coordination sphere ($\mathbf{L^{6,Cl}}$ *vs*. **PMOD**), the ligand field stabilization energy in **C11** should be suitable for SCO. However, the comparison of the octahedral coordination sphere [$\Sigma_O(FeN_6)$ and $CShM(O_h)$] shows that **C11** is more distorted than the SCO active **PMOD**-complexes (Table 3.3).Therefore, the ideal octahedral coordination sphere is illustrated in Figure 3.28.

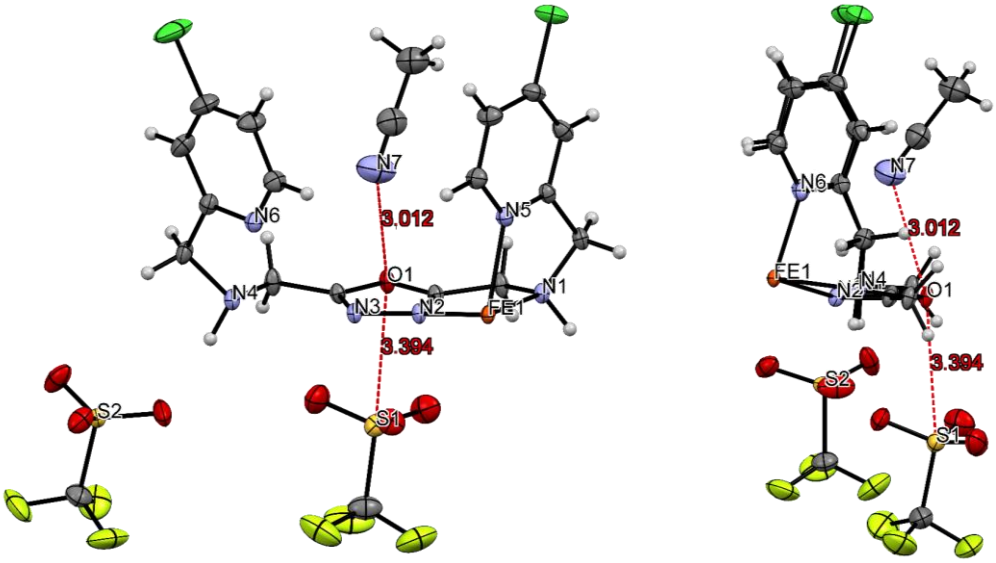


Figure 3.27 Asymmetric Unit of **C11** with front view (left) and side view (right). Measured distances are displayed as red dashed lines. ORTEP representation with atomic displacement parameters set to 50 % probability.

Table 3.3 Relevant structural parameters of the crystal structures of $[Fe_2(\mu_2\text{-}\mathbf{PMOD})_2](X)_4$- and $[Fe_2(\mu_2\text{-}\mathbf{L^{6,Cl}})_2](X)_4$-type complexes. The row "Temperature" refers to the temperature during the crystal structure analysis. All structural parameters of **C11** can be found in Table E.4.

	$[Fe_2(\mu_2\text{-}\mathbf{PMOD})_2](ClO_4)_4$ ·$4CH_3CN$[20]	$[Fe_2(\mu_2\text{-}\mathbf{PMOD})_2](CF_3SO_4)_4$ ·$2CH_3CN$[20]	$[Fe_2(\mu_2\text{-}\mathbf{L^{6,Cl}})_2](CF_3SO_3)_4$ ·$2CH_3CN$ (**C11**)
Temperature	193 K	193 K	120 K
$\bar{d}$(Fe-N)	2.18	2.19	2.19
$\Sigma_O(FeN_6)$	120.8	125.5	131.0
CShM(O_h)	3.79	3.91	4.67

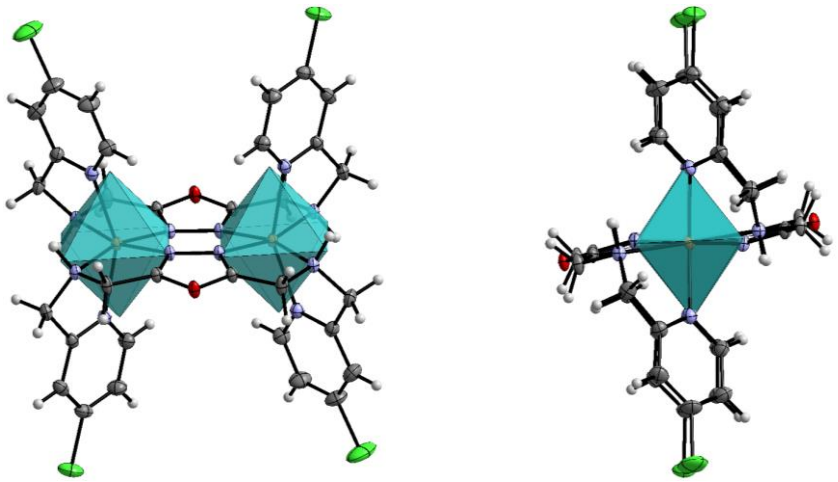


Figure 3.28 Molecular structure of **C11** and its ideal coordination octahedron with front view (left) and view onto the Fe-Fe axis (right), calculated with SHAPE.[62] Colour scheme: dark grey – C, green – Cl, grey – H, violet – N, red – O, orange – Fe. ORTEP representation with atomic displacement parameters set to 50 % probability.

Similar to the previous complexes, the acetonitrile molecule is located between the two pyridine rings above the oxadiazole ring (Figure 3.27). The distance between the oxadiazol-oxygen and the acetonitrile-nitrogen is equal to *d*(O1-N7) = 3.01 Å. Besides the oxadiazole ring lies one of the two triflate anions with a distance of the oxadiazole-oxygen to the triflate-sulfur of *d*(O1-S1) = 3.39 Å. The remaining triflate anion is located in the corner of the unit cell (Figure F.17). This trifluoromethanesulfonate anion is involved in three hydrogen bonds to the amine functions of neighboring complex cations, what results in the formation of a one-dimensional chain (Figure F.18). Thus, only the three unique intermolecular hydrogen bonds must be described to fully characterize the intermolecular network (Figure 3.29). The first hydrogen bond can be found between N1-H1···O5 (2.02 Å) in an N1-H1-O5 angle of 159.8 °. The same amine function forms another hydrogen bond to a second oxygen atom of the same triflate anion with a N1-H1···O6 distance of 2.48 Å. The N1-H1-O6 angle is equal to 121.6 °. In general, hydrogen bonds, which offer embedded angles unequal to 180 °, exhibit longer distances.[233] The same anion forms a third hydrogen bond the amin function of a neighboring complex cation between N4-H4···O4 (1.91 Å) with an enclosed N4-H4-O4 angle of 165.2 °. All angles and distances of the mentioned hydrogen bonds are in line with the literature.[233]

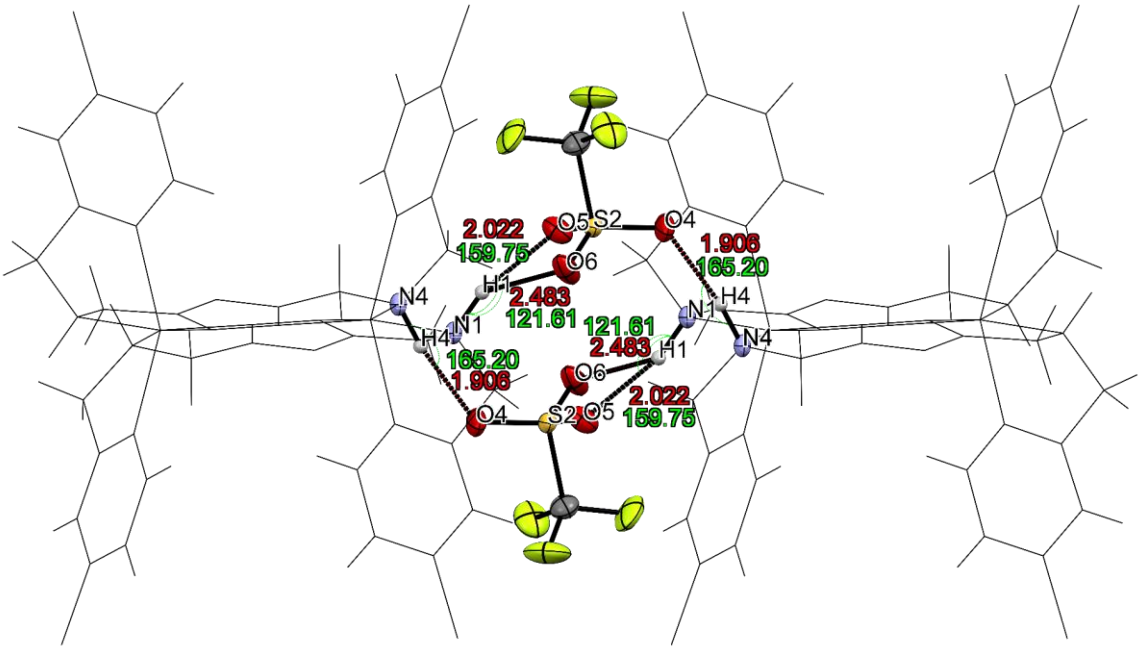


Figure 3.29 Unique hydrogen bonds (dashed black lines) in **C11** between complex cations and triflate anions. Acetonitrile molecules and irrelevant triflate anions are omitted for clarity. N-H···O distances are displayed in red. N-H-O angles are shown in green. ORTEP representation with atomic displacement parameters set to 50 % probability.

A closer look at the crystal structure of **C11** reveals a short contact between the *para*-substituted chlorine atom in $\mathbf{L}^{6,Cl}$ and the fluorine atom of a neighboring triflate anion. This intermolecular Cl1···F6 contact (3.11 Å) can be understood as an electrostatic attractive interaction (Figure 3.30), influencing the coordination sphere of **C11**. Thus, the larger deviation in **C11** from the ideal octahedron could be the result of packing effects in the solid state. Both the average Fe-N bond length and the distortion indicate a [HS-HS] state at 120 K.

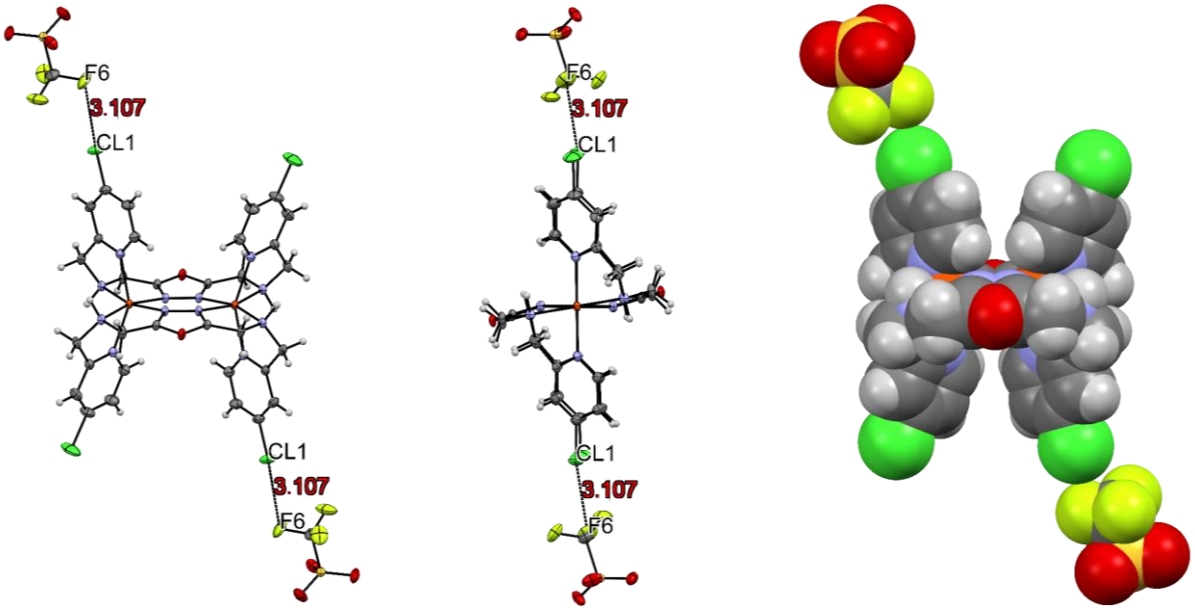


Figure 3.30 Short contact in **C11** between F6 and Cl1 in ORTEP representation (atomic displacement parameter set to 50 %) (left and middle) and in space fill representation (right). Colour scheme: dark grey – C, green – Cl, grey – H, violet – N, red – O, orange – Fe.

Magnetic properties of $[Fe_2(\mu_2\text{-}\mathbf{L^{6,Cl}})_2](X)_4$-type complexes (C9 – C11)

Temperature dependent magnetic behavior of the $[Fe_2(\mu_2\text{-}\mathbf{L^{6,Cl}})_2](X)_4$-type complexes was analyzed in a temperature range from 300-2 K at 0.1 T. Here, $[Fe_2(\mu_2\text{-}\mathbf{L^{6,Cl}})_2](BF_4)_4$ (**C9**) and $[Fe_2(\mu_2\text{-}\mathbf{L^{6,Cl}})_2](ClO_4)_4$ (**C10**) were measured as microcrystalline powder, while $[Fe_2(\mu_2\text{-}\mathbf{L^{6,Cl}})_2](CF_3SO_3)_4 \cdot 2MeCN$ (**C11**) could be investigated using single crystals. The molar susceptibility was determined and plotted as $\chi_M T$ product versus the temperature (Figure 3.31). At 300 K, the $\chi_M T$ value for **C10** is equal to 6.71 $cm^3mol^{-1}K$ and slightly drops to 6.58 $cm^3mol^{-1}K$ at 110 K in a linear way. Below this temperature, the $\chi_M T$ product increases again until it reaches its maximum at 40 K (6.62 $cm^3mol^{-1}K$), before its drops more pronouncedly. The overall decrease of $\chi_M T$ can be attributed to an antiferromagnetic coupling between the two iron(II) centers. As described in the previous chapters, the rise of $\chi_M T$ between 110 and 40 K can be the result of a macroscopic orientation of the sample with the applied magnetic field. The experimental data were fitted with PHI[201] by using the spin Hamiltonian in Equation 3.2. The best fit (Figure 3.31, blue solid line) resulted in J = -0.25(1) and g = 2.123(6) with an isotropic g-factor $g = g_1 = g_2 = (g_x + g_y + g_z)/3$ and $S_1 = S_2 = 2$. The small negative value for the exchange coupling parameter J describes a weak antiferromagnetic coupling between the iron(II) centers via the 1,3,4-oxadiazole moiety. The g-factor of 2.123(6) is slightly higher than 2.0, which can be ascribed to first order spin-orbit coupling in the $^5T_{2g}$ ground state.[67] The residual of the fit is equal to R = 0.94. Clearly the experimental values exceed the fit at lower temperatures. Due to possible orientation of the microcrystalline sample, the measured susceptibility is higher than expected, which results in the present deviation from the fit.

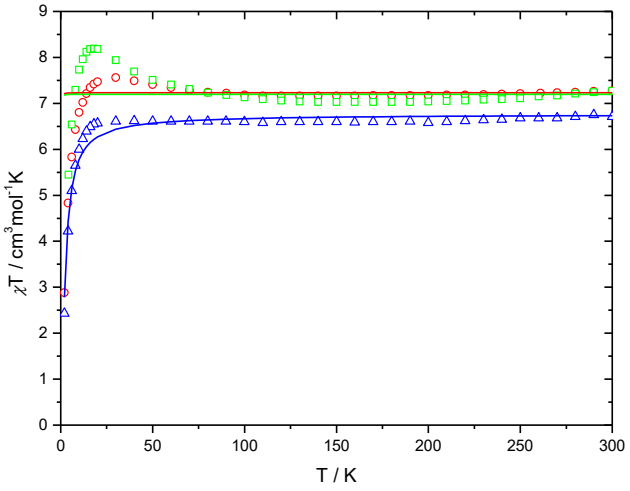


Figure 3.31 Temperature dependent behavior of **C9** (red open circles), **C10** (blue open triangles) and **C11** (green open quadrates) in form of the combined $\chi_M T$ *vs*. T plots. The blue solid line represents the best fit of the susceptibility data of **C10**; the red solid and the green solid lines show the best simulation of the high temperature regime of **C9** and **C11**, respectively, using PHI.[201]

Again, the $\chi_M T$ *vs*. *T* plots in Figure 3.31 indicate that the orientation effect of the sample in the magnetic field is not as strong for microcrystalline powders (**C9** and **C10**) as for single crystals (**C11**). The $\chi_M T$ values of **C9** and **C11** are equal to 7.27 $cm^3mol^{-1}K$ at 300 K. Both curves decrease towards 140 K. Below this temperature the plots start to rise again, reaching a maximum at 30 K (7.56 $cm^3mol^{-1}K$) for **C9** and at 18 K (8.19 $cm^3mol^{-1}K$) for **C11.** Further cooling towards 2 K leads to the decline $\chi_M T$. To avoid incorrect fitting, the high temperature regime for both compounds was simulated using PHI,[201] considering only the Zeeman effect ($\hat{H} = \hat{H}_{ZEE} = -g\mu_B HS$). The best simulation could be obtained with g = 2.20 (**C9**) and g = 2.19 (**C11**), assuming $g = g_1 = g_2 = (g_x + g_y + g_z)/3$ and $S_1 = S_2 = 2$. All three complexes **C9** – **C11** stabilize the [HS-HS] spin state at any temperature.

The crystal structure of **C11** shows a higher distortion of the complex cation compared to the SCO active **PMOD**-type complexes, which could be the result of intermolecular repulsion forces (Figure 3.30). Thus, packing effects could play an important role when implementing a functional group in the *para*-position of the axially coordinating pyridine rings. On the other hand, the continuous high-spin state for both iron(II) ions could also indicate a too weak ligand field strength to show thermally induced spin crossover. The chlorine function displays an electron-withdrawing substituent with $\sigma_p(Cl) = 0.23$[264]. Most of the literature known systems show a positive linear free energy relationship when T_c is plotted against the para-substituent *Hammett* parameter.[258–260,268] Thus, electron-withdrawing functions ($\sigma_p(Cl) > 0$) should increase the ligand field splitting energy. However, halogens might be the exception for this, as the electron-withdrawing nature most likely results from their strong negative inductive effect. In halogens, the negative inductive effect surpasses the positive mesomeric effect.[245] Consequently, due to their missing negative mesomeric effect, they might not lower the energy of the π*-orbitals in the pyridine ring. This consequently might not lead to stronger π-backbonding character of the metal-ligand-bond. The smaller average Fe-N bond distance in **C11** compared to $[Fe_2(\mu_2\text{-}\mathbf{L^{6,Cl}})_2](CF_3SO_3)_4 \cdot 2MeCN$, however, indicates a stronger binding and thus a stronger ligand field strength.

To avoid the steric demanding nature of a *para*-substituent, which could result in undesired packing effects, the pyridine ring was exchanged for a pyrazinyl group (**L^{6,N}**, Chapter 3.2.1). The resulting ligand **L^{6,N}** should also be capable to form oxadiazole-bridged dinuclear iron(II) complexes of type $[Fe_2(\mu_2\text{-}\mathbf{L^{6,N}})_2](X)_4$. Compared to the **PMOD** related complexes $[Fe_2(\mu_2\text{-}\mathbf{PMOD})_2](ClO_4)_4 \cdot 4CH_3CN$ and $[Fe_2(\mu_2\text{-}\mathbf{PMOD})_2](CF_3SO_3)_4 \cdot 2CH_3CN$, the targeted dinuclear iron(II) complexes of **L^{6,N}** should exhibit SCO at higher temperatures. This could result in room temperature hysteresis or in a two-step spin crossover, since pyrazine usually generate a stronger ligand field than pyridine.[248,269–275]

3.2.5 Dinuclear iron(II) complexes of type $[Fe_2(\mu_2\text{-}L^{6,N})_2](X)_4$ (C12 and C13)

Compared to pyridine, pyrazine is a stronger π-acceptor, but weaker σ-donor.[276] Thus, pyrazine is expected to stabilize the low-spin state, as the π-backbonding is usually more prominent than the dative σ-bonding, resulting in a stronger ligand field. Indeed, a lot of literature known systems confirm the anticipated effect, showing an increased T_c value for the pyrazine based complexes.[248,269–275] Therefore, the pyridine rings in **PMOD** were replaced by pyrazine moieties in $L^{6,N}$. The absence of steric demanding *para*-substituents should reduce the packing effects in the crystalline samples. Based on $L^{6,N}$, the two dinuclear iron(II) complexes $[Fe_2(\mu_2\text{-}L^{6,N})_2](BF_4)_4 \cdot 2MeCN$ (**C12**) and $[Fe_2(\mu_2\text{-}L^{6,N})_2](ClO_4)_4 \cdot 2MeCN$ (**C13**) were synthesized and isolated in form of single crystals, which were suitable for X-ray structure analysis.

$[Fe_2(\mu_2\text{-}L^{6,N})_2](BF_4)_4 \cdot 2MeCN$ (C12) crystallizes in the orthorhombic space group *Pbam* with two formula units per unit cell. The crystal structure was measured at 173 K. Crystallographic Data can be found in Table D.5. Due to the present centers of inversion and mirror/ glide planes, the asymmetric unit contains only one half of a ligand coordinated to one iron(II) ion, two tetrafluoroborate anions and one acetonitrile molecule (Figure 3.32, left). The rest of the unit cell is generated by symmetry (Figure F.19 and Figure F.20). It is noticeable that the crystal structure of **C12** exhibits disordering, in contrast to the structures discussed earlier.

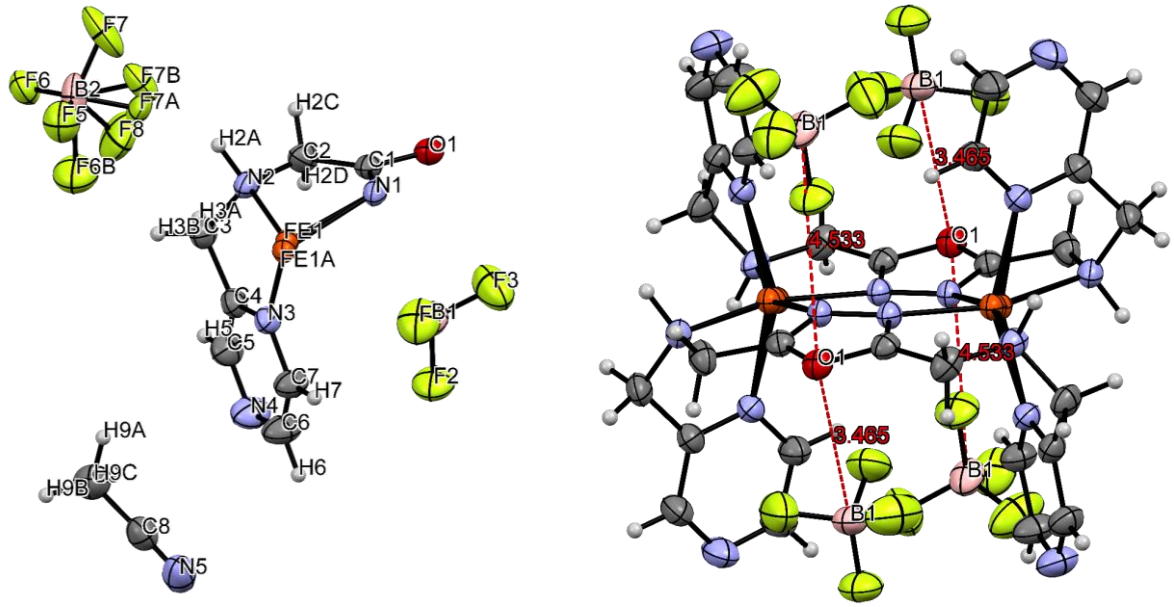


Figure 3.32 Asymmetric Unit of **C12** (left). Molecular structure of the complex cation of **C12** and chosen distances between the oxadiazole-motif and neighboring tetrafluoroborate anions. Acetonitrile molecules and irrelevant tetrafluoroborate anions are omitted for clarity (right). Measured distances are displayed as red dashed lines. ORTEP representation with atomic displacement parameters set to 50 % probability.

Thus, the iron(II) centers shows a static disorder between two positions in close proximity with an occupancy of 81(9) % (Fe1) and 9(4) % (Fe1A). In this work, all distances and angles involving the iron(II) ion in **C12** refer to Fe1. In addition to that, one tetrafluoroborate anion shows rotational disorder along its B2-F5 axis. Both $Fe^{II}N_6$ coordination spheres are symmetry equivalent with $\bar{d}$(Fe-N) = 2.21 Å, alongside with the bond distance to the axially coordinating pyrazine ring of d(Fe-N^{Pyr}) = 2.15 Å. The huge distortion of the coordination sphere is displayed by the octahedral distortion parameter ($\Sigma_O(FeN_6)$ = 133.0 °) and the resulting value of the continuous shape measurement (CShM(O_h) = 5.24), displayed in Figure F.21. All these values indicate a [HS-HS] state of the complex at 173 K. A summary of all structural parameters can be found in Table E.4. In contrast to all afore described structures, the packing of **C12** reveals that the acetonitrile molecules are not located between the two pyrazine rings, but beside the complex cation. Here, the space above and below the oxadiazole is filled with tetrafluoroborate anions with distances to the oxadiazol-oxygen (d(B1-O1)) of 4.53 Å and 3.47 Å (Figure 3.32, right). The complex cations are connected via hydrogen bonds between their amine function and neighboring tetrafluoroborate anions. Considering the present symmetry in addition to the disordered tetrafluoroborate anion ($B2F_4$), there are four hydrogen bonds with unique distances and angles to describe: N2-H2A···F8 (2.03 Å, 133.0 °), N2-H2A···F6 (1.20 Å, 160.3 °), N2-H2A···F7A (1.92 Å, 151.6 °) and N2-H2A···F7B (2.23 Å, 162.5 °) (Figure 3.33). All these distances and angles agree with the literature.[233,234] Due to the bridging nature of the tetrafluoroborate anions via hydrogen bonds, a one-dimensional chain is formed in the solid state (Figure F.22).

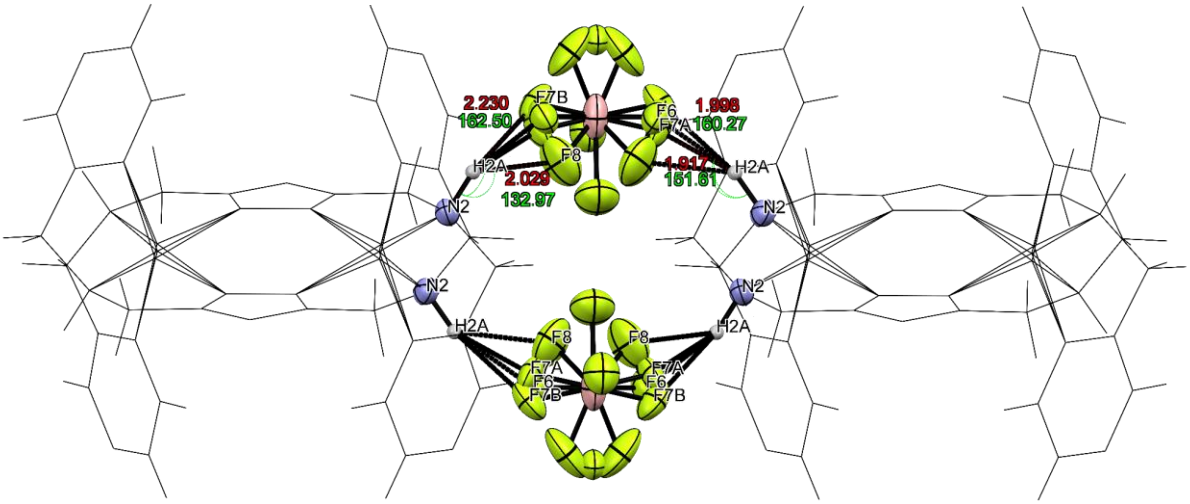


Figure 3.33 Unique hydrogen bonds (dashed black lines) in **C12** between complex cations and tetrafluoroborate anions. Acetonitrile molecules and irrelevant tetrafluoroborate anions are omitted for clarity. N-H···F distances are displayed in red. N-H-F angles are shown in green. ORTEP representation with atomic displacement parameters set to 50 % probability.

$[Fe_2(\mu_2\text{-}L^{6,N})_2](ClO_4)_4 \cdot 2MeCN$ (C13) is the isostructural complex to **C12** and crystallizes in the monoclinic space group *P*2/*c* with two formula units inside the unit cell. The crystal structure was measured at 120 K. Crystallographic data can be found in Table D.5. The asymmetric unit consists of one ligand molecule coordinated to the iron(II) center, next to two perchlorate and one acetonitrile molecule (Figure 3.34, left). The remaining atoms of the unit cell are generated by symmetry (Figure F.23). One of the perchlorate anions ($Cl1O_4$) shows rotational disorder around its Cl1-O4 axis, while the other perchlorate ($Cl2O_4$) shows disorder between two positions in close proximity. The coordination sphere, which is equal for both symmetry equivalent iron(II) centers, shows an average Fe-N bond distance of $\bar{d}$(Fe1-N) = 2.21 Å with a mean iron(II)-pyrazin distance of $\bar{d}$(Fe-N^{Pyr}) = 2.15 Å. Both values are slightly higher than in **C12**. The high distortion of the coordination sphere is displayed by the octahedral distortion parameter ($\Sigma_O(FeN_6)$ = 137.6 °). This pronounced distortion of the octahedron is further confirmed by continuous shape measurement with $CShM(O_h)$ = 5.50 (Figure F.24). A detailed summary of the structural parameters can be found in Table E.5. Both, the average Fe-N bond length as well as the calculated distortion in **C13** indicate a [HS-HS] state of the complex at 120 K.

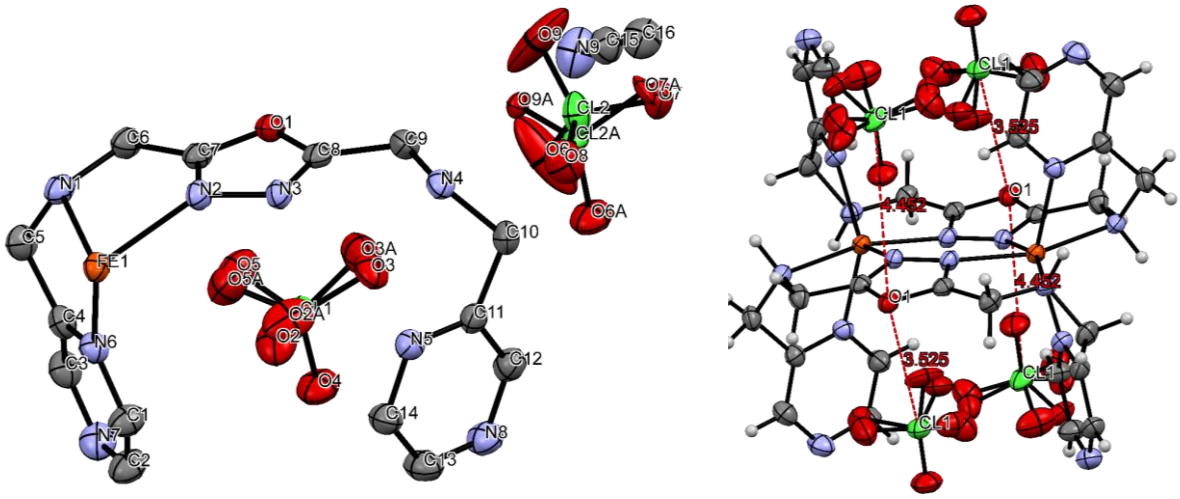


Figure 3.34 Asymmetric Unit of **C13** (left). Molecular structure of the complex cation of **C13** and chosen distances between the oxadiazole-motif and neighboring perchlorate anions. Acetonitrile molecules and irrelevant perchlorate anions are omitted for clarity (right). Measured distances are displayed as red dashed lines. ORTEP representation with atomic displacement parameters set to 50 % probability.

Similar to **C12**, the packing of **C13** reveals that the space above and below the oxadiazole ring is occupied by counter ions. The perchlorate anions show distances to the oxadiazol-oxygen of *d*(Cl1-O1) = 4.53 Å and *d*(Cl1-O1) = 3.53 Å (Figure 3.34, right). Due to the present disorder and symmetry, three unique hydrogen bonds between perchlorate ($Cl2O_4$) and complex cations are found (Figure 3.35).

The amine function of one complex cation therefore forms hydrogen bonds to the neighboring perchlorate between N1-H1···O7 (1.93 Å) with an N1-H1-O7 angle of 171.8 ° and between N1-H1···O7A (2.24 Å) with an N1-H1-O7A angle equal to 174.8 °. The same perchlorate forms an additional hydrogen bond to the amine function of the next complex cation between N4-H4···O6 (2.23 Å) with an enclosed angle of 129.7 °. This results in the formation of a one-dimensional intermolecular network of complex cations (Figure F.25). The bridging nature of the counter anion via hydrogen bonds is common for this type of dinuclear complex, as the afore discussed structures already showed. Again, all distances and angles involving the intermolecular hydrogen bonds are in line with the literature.[251]

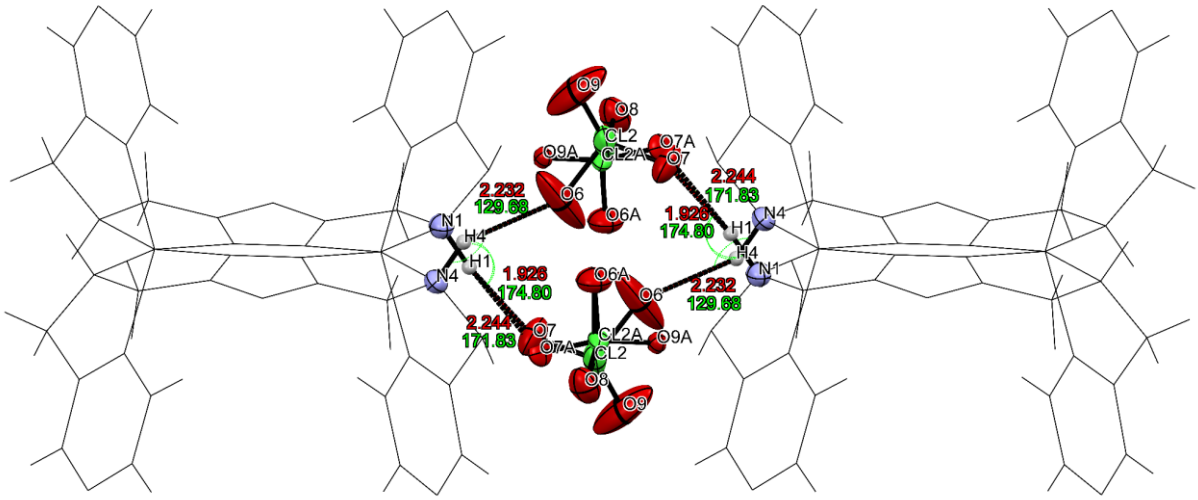


Figure 3.35 Unique hydrogen bonds (dashed black lines) in **C13** between complex cations and perchlorate anions. Acetonitrile molecules and irrelevant perchlorate anions are omitted for clarity. N-H···O distances are displayed in red. N-H-O angles are shown in green. ORTEP representation with atomic displacement parameters set to 50 % probability.

Magnetic properties of $[Fe_2(\mu_2\text{-}L^{6,N})_2](X)_4$–type complexes (C12 and C13)

Due to the very low yielded synthesis of **C13**, only $[Fe_2(\mu_2\text{-}L^{6,N})_2](BF_4)_4 \cdot 2MeCN$ (**C12**) was analyzed with regards to its temperature dependent magnetic behavior in a temperature range from 300-2 K at 0.1 T as single crystals. The molar susceptibility of **C12** was determined and plotted as $\chi_M T$ product versus the temperature (Figure 3.36). At 300 K, $\chi_M T$ is equal to 7.34 $cm^3mol^{-1}K$. As a result of first-order SOC, this experimental value is higher than the *spin-only* value (6 $cm^3mol^{-1}K$ for two $S = 2$ spin centers with $g = 2$ according to Equation 3.1). The $\chi_M T$ value of **C12** remains constant until 200 K, followed by the gradual increase to a value of 7.90 $cm^3mol^{-1}K$ at 80 K. Below this temperature, the $\chi_M T$ product starts to raise significantly to 11.67 $cm^3mol^{-1}K$ at 10 K, before it drops again to 9.41 $cm^3mol^{-1}K$ at 2 K. The overall increase of $\chi_M T$ towards lower temperatures with the pronounced maximum at 10 K can again be

ascribed to the macroscopic orientation of the single crystals inside of the gelatin capsule in the applied magnetic field (0.1 T). The pronounced decrease of $\chi_M T$ from 10-2 K can be attributed either to antiferromagnetic coupling, ZFS or to a combination of both. However, since no magnetization data are available, the magnetic data were simulated with PHI[201] solely taking the Zeeman effect into account (Equation 3.5). The best simulation of the high temperature regime was obtained with a set isotropic *g*-factor ($g = g_1 = g_2 = (g_x + g_y + g_z)/3$) of 2.22. This value indicates, as mentioned above, a spin-orbit coupled system. Independent of the orientation effect or magnetic coupling between the two oxadiazole-bridged iron(II) centers, this complex remains in the [HS-HS] state in the temperature range of 300-2 K as well. Hence, $[Fe_2(\mu_2\text{-}\mathbf{L^{6,N}})_2](BF_4)_4 \cdot 2MeCN$ (**C12**) shows no thermally induced SCO in the crystalline phase.

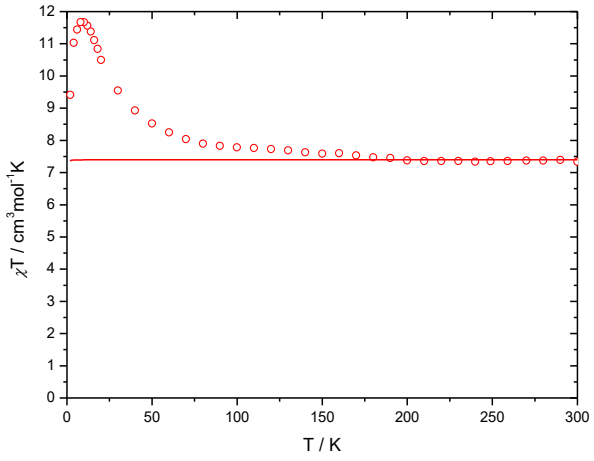


Figure 3.36 Temperature dependent behavior of **C12** (red open circles $\chi_M T$ *vs*. *T* plots. The red solid line shows the best simulation of the high temperature regime, done with PHI.[201]

The change to the pyrazine ring as apically coordinating group ($\mathbf{L^{6,N}}$) was supposed to strengthen the ligand field in the resulting dinuclear iron(II) complexes, while simultaneously reducing the steric demand of the heterocycle, compared to $\mathbf{L^{6,OMe}}$ and $\mathbf{L^{6,Cl}}$. This should result in less distorted $[Fe_2(\mu_2\text{-}\mathbf{L^{6,N}})_2](X)_4$-type complexes, since there is no steric demanding *para*-substituent that could exhibit intermolecular repulsive interactions to counter anions or solvent molecules. However, comparing both pyrazine-based complexes **C12** and **C13** to $[Fe_2(\mu_2\text{-}\mathbf{L^{6,Cl}})_2](CF_3SO_3)_4 \cdot 2CH_3CN$ (**C11**) reveals, that **C11** offers smaller bond lengths as well as a smaller distortion of the coordination sphere. According to the literature, pyrazine ligands can show larger bond distances to iron(II) ions than pyridine ligands.[277] However, the fact that the distortion in **C12** and **C13** is larger than in **C11** suggests that the deviation of the coordination sphere from the ideal octahedron is not related to the chosen *para*-substituent and cannot be influenced that easily in the solid state.

3.3 Dinuclear iron(II) complexes of the asymmetric 1,3,4-oxadiazole based ligands ($L^{Py,Y}$)

The dinuclear complexes of type $[Fe_2(\mu_2\text{-}\mathbf{L^{5,Y}})_2](X)_4$ and $[Fe_2(\mu_2\text{-}\mathbf{L^{6,Y}})_2](X)_4$ did not show the desired spin crossover phenomenon. To introduce a drastic change in electronic and geometrical properties, a new series of asymmetrical ligands $\mathbf{L^{Py,Y}}$ (Y = 1 – 4) was synthesized (Figure 3.37). The ligand design of $\mathbf{L^{Py,1}}$ was inspired by the analogous 1,3,4-thiadiazol based ligand system **PPTD** (**PPTD** = 2-(2-pyridyl)-5-[N,N-bis(2-pyridylmethyl)-aminomethyl]-1,3,4-thiadiazole), which was reported by *Bittner D.* in 2018.[171]

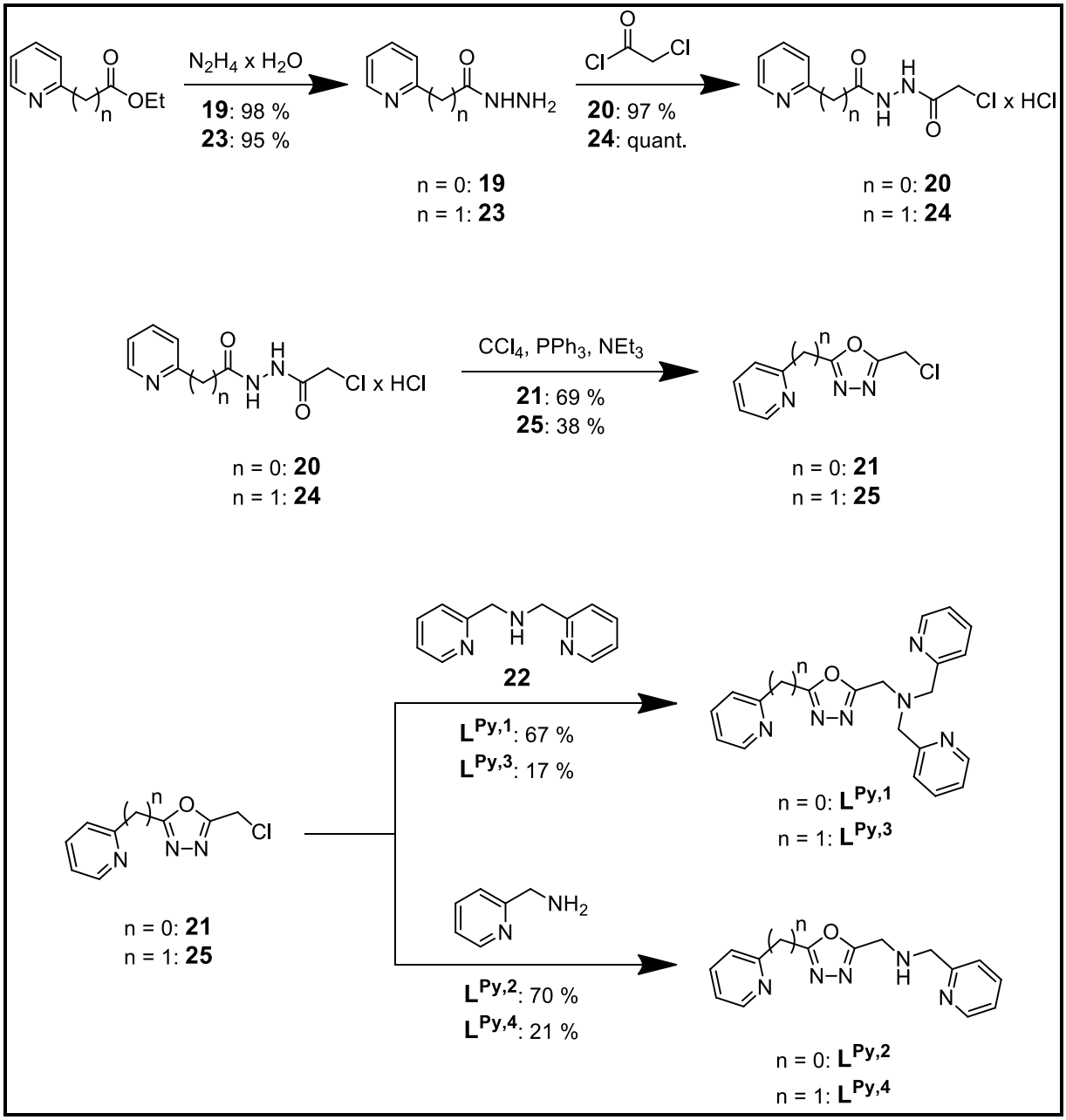


Figure 3.37 Synthesis scheme of $\mathbf{L^{Py,Y}}$ (Y = 1 – 4). The synthesis of **19**, **20**, **22** and **23** is already known in literature and was adapted with minor changes.[171,278]

The hydrazide compounds pyridin-2-carboxylic acid hydrazide (**19**) and pyridine-2-yl-acetic acid hydrazide (**23**) were synthesized in a nucleophilic substitution reaction of 2-pyridine carboxylate and ethyl 2-(pyridinyl-2)acetate with hydrazine monohydrate in very good yields (98 % for **19** and 95 % for **23**). Both synthesis were adapted from literature with minor changes.[171,278] Subsequent condensation reaction with chloroacetyl chloride resulted in N'-chloroacetyl-2-pyridinecarboxylic acid hydrazide hydrochloride (**20**) and N'-chloroacetyl-2-pyridylacetic acid hydrazide hydrochloride (**24**) with yields of 97 % and 100 %, respectively. The synthesis of **20** is literature known and was applied to the preparation of **24**.[278][171] Based on **20** and **24**, the two precursors 2-(chloromethyl)-5-(pyridin-2-yl)-1,3,4-oxadiazole (**21**) and 2-(chloromethyl)-5-(pyridin-2-ylmethyl)-1,3,4-oxadiazole (**25**) were synthesized in a ring-closure reaction with yields of 69 % (**21**) and 38 % (**25**). The combination of triphenylphosphine and carbon tetrachloride, together with triethylamine, has proven to be a useful variation of the *Mitsunobu* reaction, thus acting as a mild dehydrating system.[279–282] The lower yield in the synthesis of **25** compared to **21** can be ascribed to the increased steric hindrance of the additional methylene group between the oxadiazole and pyridine moiety in **25**. The reductive amination of pyridine-2-carboxaldehyde and 2-aminomethylpyridine with sodium borohydride is literature known and results in the secondary amine bis[(2-pyridyl)methyl]amine (**22**).[171] **21** was then reacted in a nucleophilic substitution reaction with **22** and 2-picolylamine to form the two ligand systems 2-(2-pyridyl)-5-[N,N-bis(2-pyridylmethyl)aminomethyl]-1,3,4-oxadiazole ($\mathbf{L^{Py,1}}$) and 2-(2-pyridyl)-5-[(2-pyridylmethyl)aminomethyl]-1,3,4-oxadiazole ($\mathbf{L^{Py,2}}$), respectively. The yields for both products are roughly equal with 67 % for $\mathbf{L^{Py,1}}$ and 70 % for $\mathbf{L^{Py,2}}$. In analogy, 2-(pyridin-2-ylmethyl)-5-[N,N-bis(2-pyridylmethyl)aminomethyl]-1,3,4-oxadiazole ($\mathbf{L^{Py,3}}$) and 2-(pyridin-2-ylmethyl)-5-[(2-pyridylmethyl)aminomethyl]-1,3,4-oxadiazole ($\mathbf{L^{Py,4}}$) were synthesized in the nucleophilic reactions of **25** with yields of 17 % and 21 %, respectively. Again, the lower yields in the synthesis of $\mathbf{L^{Py,3}}$ and $\mathbf{L^{Py,4}}$ compared to $\mathbf{L^{Py,1}}$ and $\mathbf{L^{Py,2}}$ is probably caused by the additional methylene group (n = 0 *vs*. n = 1, Figure 3.37). $\mathbf{L^{Py,1}}$ and $\mathbf{L^{Py,3}}$ offer a bidentate binding pocket between the oxadiazole and the pyridin-2-yl or pyridin-2-ylmethyl rest in 2-position. In 5-position, both ligand systems provide the condensed bis-(2-picolyl)amine group, which forms a tetradentate coordination pocket with the oxadiazole moiety. It should therefore be possible to synthesize dinuclear iron(II) complexes with two inverted ligands opposite to each other, such that the bidentate and tetradentate pockets provide the octahedral coordination environment. In contrast, $\mathbf{L^{Py,2}}$ and $\mathbf{L^{Py,4}}$ possess only a tridentate coordination pocket next to the bidentate one. This enables the use of coligands, such as substituted pyridines, to fine tune the ligand field of the resulting complexes. Negatively charged coligands like pyridine-3,5-dicarboxylate could additionally form neutral complexes without a second coordination sphere. The extra methylene group in $\mathbf{L^{Py,3}}$ and $\mathbf{L^{Py,4}}$ was supposed to offer a less sterically constrained binding pocket to stabilize the LS state.

3.3.1 Crystal structures of $[Fe_2(\mu_2\text{-}L^{Py,1})_2](X)_4$-type complexes (C14 – C15)

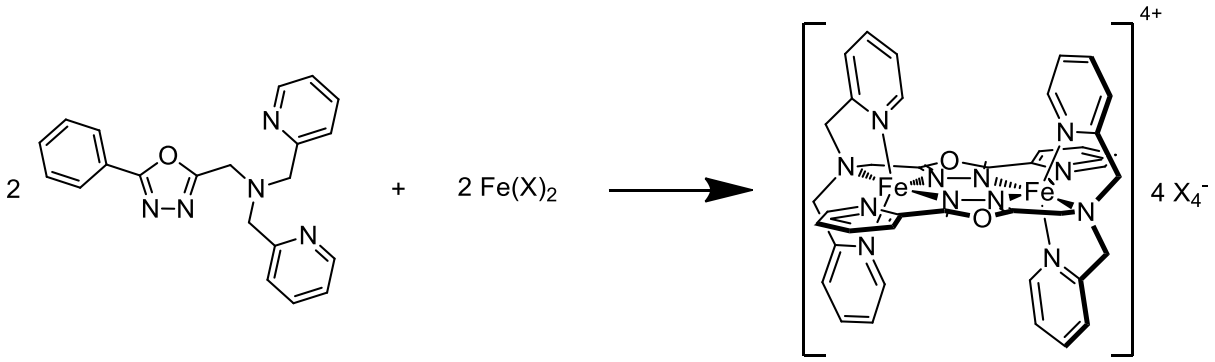


Figure 3.38 Synthesis of $[Fe_2(\mu_2\text{-}L^{Py,1})_2](X)_4$-type complexes (X = BF_4^-(**C14**, **C14'**), ClO_4^-(**C15**)).

During this work, only dinuclear transition metal complexes of $L^{Py,1}$ could be synthesized. Therefore, equimolar amounts of $L^{Py,1}$ and iron(II) salt were used to form $[Fe_2(\mu_2\text{-}L^{Py,1})_2](X)_4$-type complexes (X = BF_4^-, ClO_4^-) in an inert atmosphere (Figure 3.38). The resulting coordination compounds exhibit the same coordination mode as the 1,3,4-thiadiazole based complexes $[Fe_2(\mu_2\text{-}\mathbf{PPTD})_2](X)_4$-type (X = BF_4^-, ClO_4^-), reported by *Bittner D.*[171] The 2-(2-pyridyl)-1,3,4-oxadiazole moiety forms, together with the tertiary amine functions of two ligands, the four vertices of the coordination octahedra, where the oxadiazole rings bridge the two iron(II) ions. The apical positions of the octahedral coordination spheres are occupied by the remaining pyridyl rings, which bind *trans* to each other. For description of the crystal structures the labeling scheme in Figure 3.39 (left) is applied. All synthesized complexes show an inverse symmetrical complex cation, illustrated in Figure 3.39 (right).

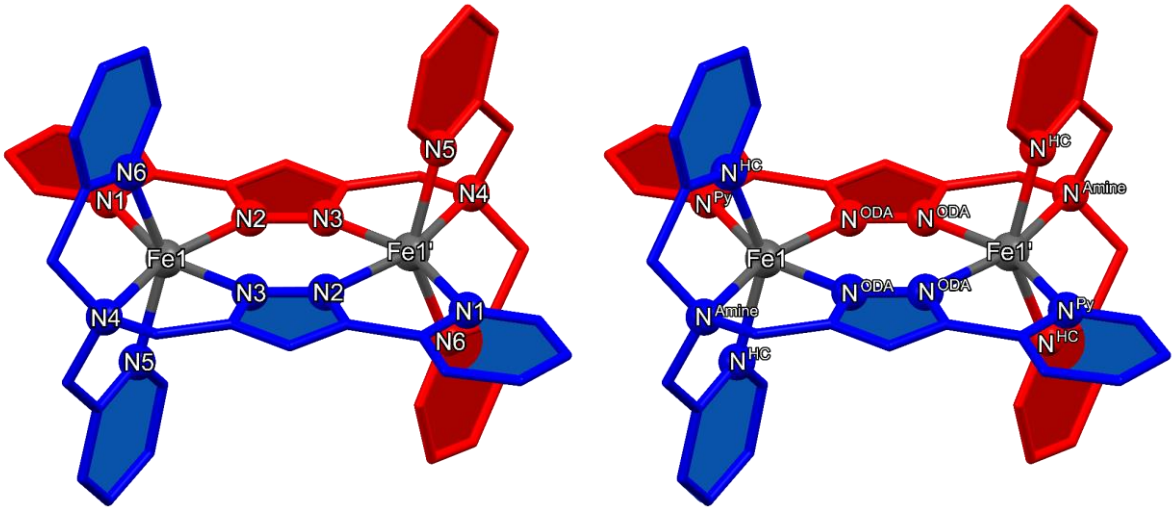


Figure 3.39 Left: Labelling scheme for all $[Fe_2(\mu_2\text{-}L^{Py,1})_2]^{4+}$ complex cations. Right: Labeling scheme according to the coordinated functional group. Coordination mode of the ligands is displayed by the colours red and blue.

$[Fe_2(\mu_2\text{-}L^{Py,1})_2](BF_4)_4 \cdot 2MeNO_2$ (C14) was prepared by separately dissolving equimolar amounts of $L^{Py,1}$ and $Fe(BF_4)_4 \cdot 6H_2O$ in acetone, followed by the combination of both solutions. The resulting orange precipitation was filtered and dissolved in nitromethane. Vapor diffusion against a mixture of diethyl ether, n-hexane and cyclohexane (1:1:1) yielded orange block shaped crystals of **C14**. The complex crystallized in the monoclinic space group $P2_1/n$ with two formula units inside the unit cell. The crystal structure was measured at 173 K and crystallographic data can be found in Table D.6. The asymmetric unit contains one ligand molecule coordinated to one iron(II) ion, one nitromethane molecule and two tetrafluoroborate anions (Figure 3.40). To describe the complex cation itself, the labeling scheme in Figure 3.39 is used. As the coordination environments of Fe1 and Fe1' are symmetry equivalent, only the $Fe1N_6$ octahedron will be discussed. The bond length to the tertiary amin is equal to $d(Fe\text{-}N^{Amine}) = d(Fe1\text{-}N4) = 2.3926(16)$ Å. Likewise to all before discussed complexes, this bond type represents the greatest metal-ligand bond distance in the present complex. The next smaller one can be found between the iron(II) center and the pyridyl moiety in 2-position of the oxadiazole with $d(Fe\text{-}N^{Py}) = d(Fe1\text{-}N1) = 2.3068(16)$ Å, which is followed by the oxadiazole-iron(II) bond type with $\bar{d}(Fe\text{-}N^{ODA}) = [d(Fe1\text{-}N2)+d(Fe1\text{-}N3))/2] = 2.15$ Å. The shortest metal-ligand bond lengths in **C14** are found between the apically coordinated heterocycles and the iron(II) center with a mean distance of $\bar{d}(Fe\text{-}N^{HC}) = [d(Fe1\text{-}N5)+d(Fe1\text{-}N6))/2] = 2.11$ Å. The variance in bond distances is caused by different σ- and π-contributions.[232] The average metal-ligand distance is equal to $\bar{d}(Fe\text{-}N) = 2.20$ Å, which is representative for a [HS-HS] structure at 173 K. This is further confirmed by the distortion of the octahedral coordination sphere with $\Sigma_O(FeN_6) = 150.5$ °) and $CShM(O_h) = 6.27$, displayed in Figure 3.41.

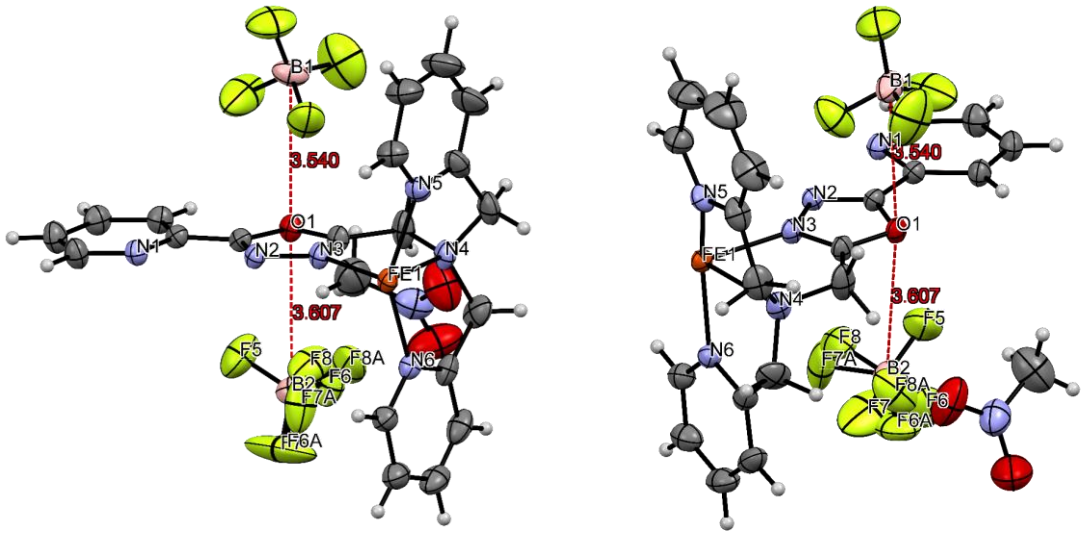


Figure 3.40 Asymmetric Unit of **C14** with different views. One tetrafluoroborate ($B2F_4$) shows rotational disorder around its B2-F5 axis. ORTEP representation with atomic displacement parameters set to 50 % probability.

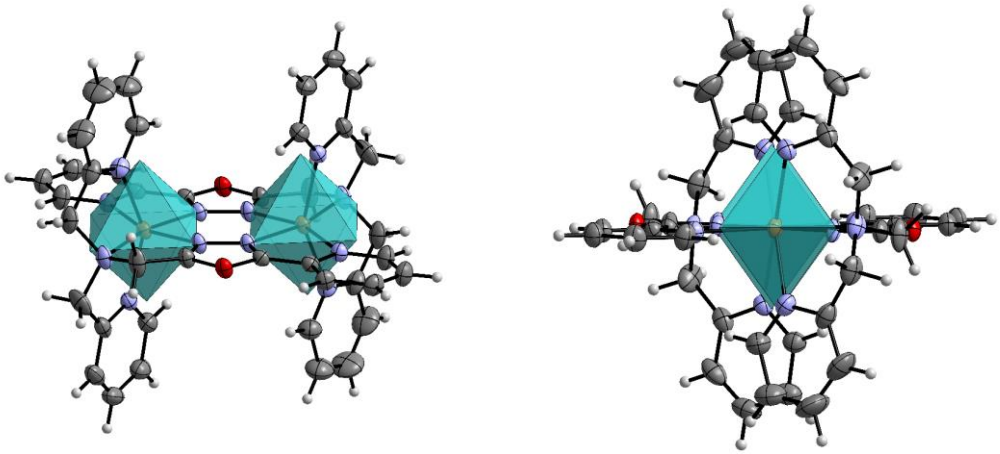


Figure 3.41 Molecular structure of **C14** and its ideal coordination octahedron with front view (left) and view along the Fe-Fe axis (right), calculated with SHAPE.[62] Colour scheme: dark grey – C, grey – H, violet – N, red – O, orange – Fe. ORTEP representation with atomic displacement parameters set to 50 % probability.

This deviation from the ideal coordination sphere is even higher than those in all described $[Fe_2(\mu_2\text{-}\mathbf{L^{5,Y}})_2](X)_4$- and $[Fe_2(\mu_2\text{-}\mathbf{L^{6,Y}})_2](X)_4$-type complexes. In first place, this can be attributed to the huge N1-Fe1-N4 angle between the two amine functions of both ligands and the iron center (125.01(6) °). In addition to that, the pyridine rings in the apical positions do not coordinate in a perpendicular way to the horizontal octahedron's base. Thus, the *trans*-angle between N5-Fe1-N6 is equal to 145.15(7) °, which differs very much from the ideal 180 °. This distortion is consequently reflected in all *cis*-angles to the apical pyridine rings, which results in the high value for $\Sigma_O(FeN_6)$. A detailed summary of the structural parameters can be found in Table E.5. Analogous to **C12** the space above and below the oxadiazole moiety is occupied by the tetrafluoroborate anions with distances to the oxadiazole-oxygen of *d*(B1-O1) = 4.53 Å and *d*(B2-O1) = 3.53 Å (Figure 3.40). One of the tetrafluoroborate anions shows rotational disorder around its B2-F5 axis. Due to the present centers of inversion, 2-fold screw axes and glide planes, the rest of the unit cell is symmetry generated (Figure F.26 and Figure F.27). Consequently, one complex cation is located in the middle of the unit cell, while eight additional ones are found on the corners of the unit cell. Since the ligand $\mathbf{L^{Py,1}}$ does not offer a free *NH*-function, no classical hydrogen bonds are found in the crystal structure.

$[Fe_2(\mu_2\text{-}\mathbf{L^{Py,1}})_2](BF_4)_4 \cdot 2MeNO_2$ (C14') was prepared by separately dissolving equimolar amounts of $\mathbf{L^{Py,1}}$ and $Fe(BF_4)_4 \cdot 6H_2O$ in acetonitrile, followed by the combination of both solutions. The reaction mixture was kept undisturbed until the solvent was completely evaporated. The resulting orange oil was dissolved in nitromethane. Slow evaporation yielded orange block shaped crystals of **C14'**, crystallized in the monoclinic space group $P2_1/c$ with four formula units inside the unit cell. The crystal structure was measured at 120 K.

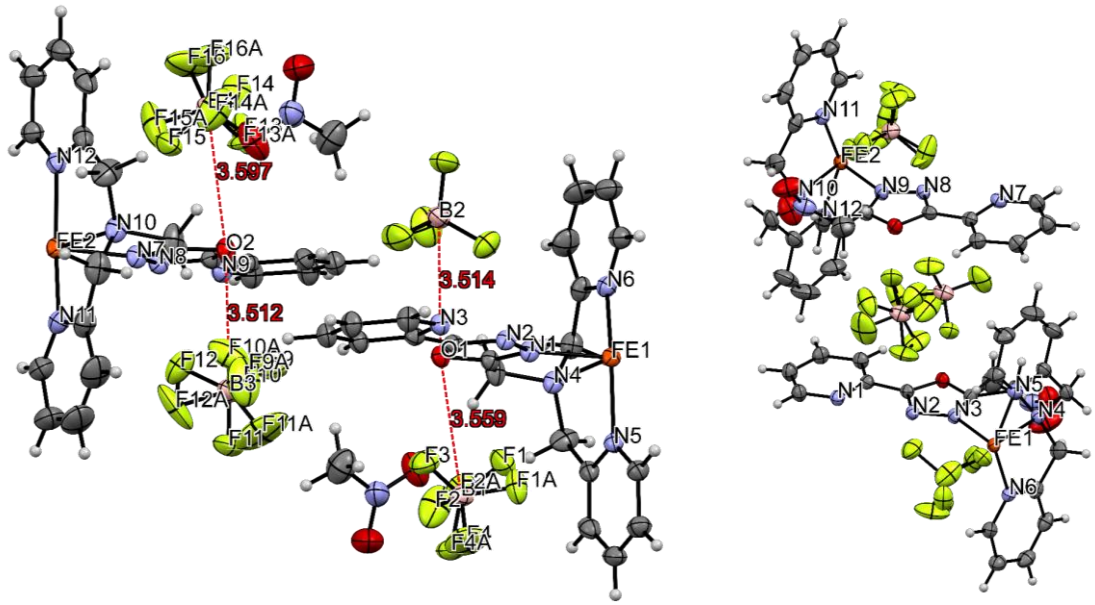


Figure 3.42 Asymmetric Unit of **C14'** with different views. One tetrafluoroborate ($B1F_4$) shows rotational disorder around its B1-F3 axis. $B3F_4$ and $B4F_4$ show disorder between two positions in close proximity. ORTEP representation with atomic displacement parameters set to 50 % probability.

The crystallographic data can be found in Table D.6. In contrast to **C14**, the asymmetric unit consists of two crystallographic distinguishable iron(II) centers, each coordinated by one ligand molecule. In addition to that, there are four tetrafluoroborate anions and two nitromethane molecules (Figure 3.42). The trend of metal-ligand bonds for both complex cations follows the order described for **C14**: $d(\text{Fe-N}^{\text{Amine}}) > d(\text{Fe-N}^{\text{Py}}) > \bar{d}(\text{Fe-N}^{\text{ODA}}) > \bar{d}(\text{Fe-N}^{\text{HC}})$. Table 3.4 shows a summary of the present bond distances.

Table 3.4 Bond distances in **C14'** for the complex cations with Fe1/Fe1 and Fe2/Fe2 in angstrom (Å).

Iron(II) ions	$d(\text{Fe-N}^{\text{Amine}})$	$d(\text{Fe-N}^{\text{Py}})$	$\bar{d}(\text{Fe-N}^{\text{ODA}})$	$\bar{d}(\text{Fe-N}^{\text{HC}})$	$\bar{d}(\text{Fe-N})$
Fe1/Fe1	2.3926(11)	2.3165(11)	2.15	2.10	2.20
Fe2/Fe2	2.3965(11)	2.3005(11)	2.15	2.10	2.20

The average metal-ligand distance in both distinguishable complex cations is approx. 2.2 Å, which represents a defined [HS-HS] structure at 120 K. The great distortion of the coordination spheres confirms this statement. The octahedral distortion parameters are equal to $\Sigma_O(Fe1N_6) = 150.2\ °$ and $\Sigma_O(Fe2N_6) = 151.9\ °$, while continuous shape measurements yield values of $CShM(Fe1N_6,O_h) = 6.29$ and $CShM(Fe2N_6,O_h) = 6.40$ (illustrated in Figure 3.43).

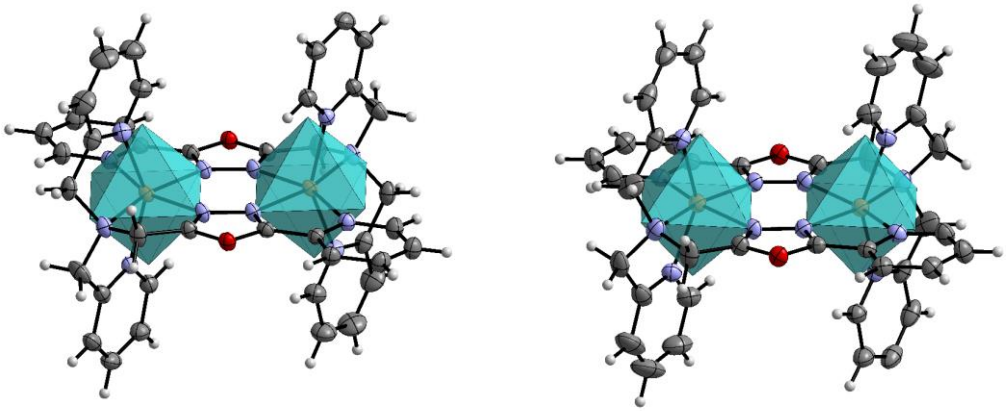


Figure 3.43 Molecular structure of the Fe1/Fe1 (left) and Fe2/Fe2 (right) complex cations in **C14'** and its ideal coordination octahedron, calculated with SHAPE.[62] Colour scheme: dark grey – C, grey – H, violet – N, red – O, orange – Fe. ORTEP representation with atomic displacement parameters set to 50 % probability.

The pronounced distortion in the complex cations of **C14'** follows the same explanation as for **C14**. A detailed summary of the structural parameters can be found in Table E.6. The whole unit cell (and thus the whole complex cation) is generated by symmetry due to the existing centers of inversion, 2-fold screw axes and glide planes (Figure F.28 and Figure F.29). It becomes apparent, that the complex cations (strictly speaking one-eighth of each complex cation) are located at the eight corners and at the center of the six faces of the unit cell (one-half of each complex cation). Three of four tetrafluoroborate anions show crystallographic disorder. Therefore, the first BF_4 molecule exhibits rotational disorder around its B1-F3 axis, while the other two counter ions ($B3F_4$ and $B4F_4$) show disorder between two positions in close proximity. In analogy to **C14**, the tetrafluoroborate anions are located above and below the oxadiazole rings of both ligand molecules with *d*(B1-O1) = 3.56 Å, *d*(B2-O1) = 3.51 Å, *d*(B3-O2) = 3.51 Å and *d*(B4-O2) = 3.60 Å (Figure 3.42)

$[Fe_2(\mu_2\text{-}L^{Py,1})_2](ClO_4)_4 \cdot 2MeNO_2$ (C15) is the isomorphous perchlorate compound to **C14**. Hence, it also crystallizes in the monoclinic space group $P2_1/n$ with two formula units inside of the unit cell. The *unit-cell similarity index* (see Equation 3.5) is found to be Π(**C15**/**C14**) = 0.004, which is very close the zero. The crystal structure was measured at 150 K, crystallographic data can be found in Table D.7. The asymmetric unit contains one ligand molecule coordinated to the iron(II) center, next to two perchlorate anions and one nitromethane molecule (Figure 3.44). One perchlorate molecule exhibits rotational disorder around its O7-Cl2 axis, while the other counter ion shows disorder between two positions in close proximity. The

distance of the oxadiazole-oxygen to the anions above and below the ring is equal to *d*(O1-Cl1) = 3.55 Å and *d*(O1-Cl2) = 3.62 Å (Figure 3.44). The structure of the symmetry generated complex cation and unit cell (Figure F.30 and Figure F.31) follows the description of **C14**.

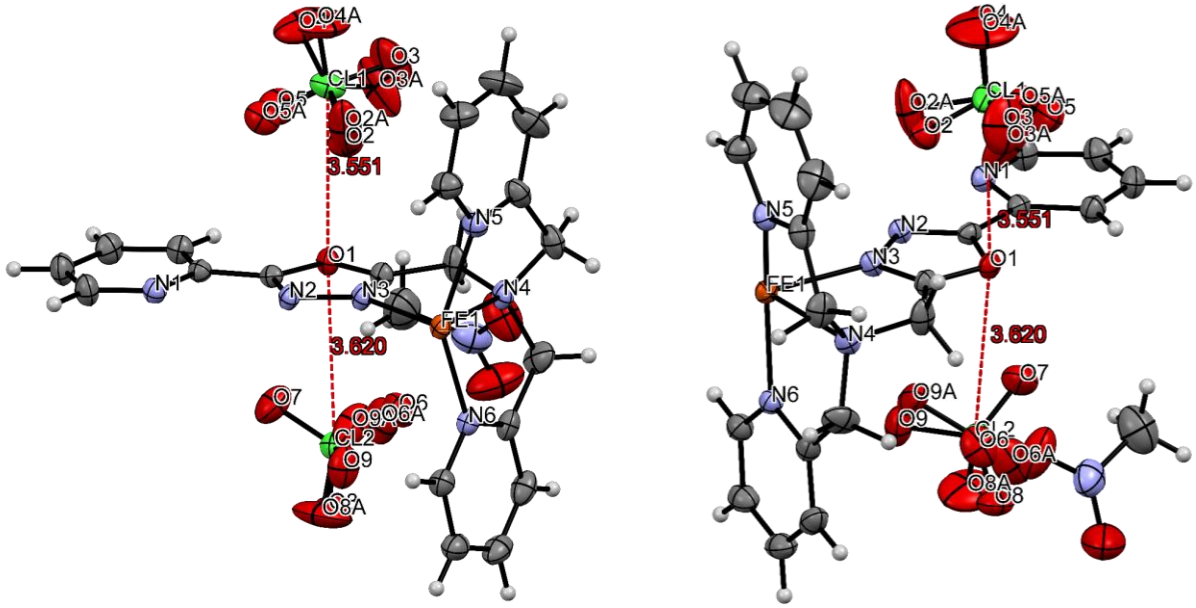


Figure 3.44 Asymmetric Unit of **C15** with different views. One perchlorate anion ($Cl2O_4$) shows rotational disorder around its Cl2-O7 axis. The other perchlorate molecule ($Cl1O_4$) exhibits disorder of its oxygen atoms between two positions in close proximity. ORTEP representation with atomic displacement parameters set to 50 % probability.

The order and magnitude of bond distances is the same as for **C14** and **C14'**. Thus, the bond length to the amine function is *d*(Fe-N^{Amine}) = 1.4291(15) Å. The next shorter bond is found between the iron(II) center and the equatorially coordinating pyridinyl moiety with *d*(Fe-N^{Py}) = 2.3100(12) Å, followed by $\bar{d}$(Fe-N^{ODA}) = 2.16 Å. The shortest bond type is represented by the binding of the axial coordinated pyridine rings with $\bar{d}$(Fe-N^{HC}) = 2.10 Å. The average metal-ligand bond lengths [$\bar{d}$(Fe-N)] is equal to 2.21 Å, which describes a [HS-HS] structure (at 150 K). The present spin state is further confirmed by the coordination sphere distortion with $\Sigma_O(FeN_6)$ = 153.7 ° and CShM(O_h) = 6.60 (Figure F.32). These values represent the highest deviation from the ideal coordination sphere for all complexes in this work. In analogy to **C14** and **C14'**, this can be explained by the N4-Fe1-N1 *cis*-angle (125.72(4) °) and the N5-Fe1-N6 *trans*-angle (143.83(5) °), which differ very much from 90 ° and 180 °, respectively. The detailed summary of all structural parameters can be found in Table E.5.

3.3.2 Magnetic properties of $[Fe_2(\mu_2\text{-}L^{Py,1})_2](X)_4$-type complexes (C14 – C15)

Temperature dependent magnetic behavior of the **C14** and **C15** was analyzed in a temperature range between 300 K and 2 K at 0.1 T. To avoid unwanted orientation effects in a present magnetic field (see Chapter 3.1 and Chapter 3.2), both samples were measured in a blocked way by using eicosane for fixation. The resulting $\chi_M T$ versus *T* plots are displayed in Figure 3.45 for **C14** (red open circles) and **C15** (blue open triangles). The $\chi_M T$ value of **C14** at 300 K is equal to 7.58 $cm^3mol^{-1}K$ and decreases in a gradual way to 7.36 $cm^3mol^{-1}K$ at 70 K. Below this temperature, $\chi_M T$ decreases more drastically to a value of 1.85 $cm^3mol^{-1}K$ at 2 K. Such temperature dependence typically reveals a rather weak antiferromagnetic exchange coupling between two Fe^{II} centers in the high-spin state. A similar magnetic behavior is found for **C15**. At 300 K the $\chi_M T$-product shows a value of 7.43 $cm^3mol^{-1}K$. This value decreases gradually to 7.26 $cm^3mol^{-1}K$ at 40 K with a slightly smaller slope compared to **C14**. Below 40 K, $\chi_M T$ drops significant faster until it reaches a value of 4.14 $cm^3mol^{-1}K$ at 2 K. It is noteworthy that due to the fixation of the crystals by eicosane, a macroscopic alignment of the sample along with the magnetic field does not occur. As discussed several times throughout this work, the pronounced drop of the $\chi_M T$ product at low temperature can be attributed to antiferromagnetic coupling, zero-field splitting or to a combination of both effects. Since no magnetization data are available for both complexes, experimental data were fitted considering only intramolecular exchange coupling between the two iron(II) ions with $\hat{H} = \hat{H}_{EX} + \hat{H}_{ZEE} = -2J \cdot S_1 S_2 - g\mu_B HS$ as spin Hamiltonian. The best fit for **C14** (Figure 3.45, blue solid line) resulted in J = -0.498(8) and g = 2.259(3) with the isotropic g-factor $g = g_1 = g_2 = (g_x + g_y + g_z)/3$ and $S_1 = S_2 = 2$. The residual is equal to R = 0.22.

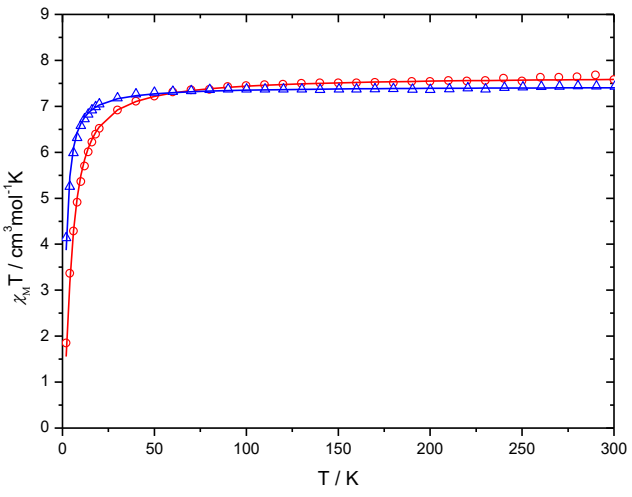


Figure 3.45 Temperature dependent behavior of **C14** (red open circles) and **C15** (blue open triangles) in form of the combined $\chi_M T$ *vs*. *T* plots. The solid lines represents the best fit of the susceptibility data for **C14** (red) and **C15** (blue), using PHI.[201]

For **C15**, the best fit resulted in J = -0.186(4) and g = 2.225(2), with R = 0.16. The small negative values of the exchange coupling parameters of **C14** (J = -0.498(8)) and **C15** (J = -0.186(4)) confirm the rather weak antiferromagnetic coupling between the 1,3,4-oxadiazole bridged iron(II) ions. The g-factors, which are greater than 2.0 in both compounds, describe typical S = 4/2 centers with an incompletely quenched orbital contribution. All values resulting from the fits are in good agreement with similar reported di-aza heterocycle bridged systems.[21,170,171,202–212] It is clearly evident, that $[Fe_2(\mu_2\text{-}\mathbf{L^{Py,1}})_2](ClO_4)_4 \cdot 2MeCN$ (**C14**) and $[Fe_2(\mu_2\text{-}\mathbf{L^{Py,1}})_2](BF_4)_4 \cdot 2MeCN$ (**C15**) do not show spin transition at any temperature. Once again, this finding demonstrates the more pronounced stabilization of the [HS-HS] state in dinuclear iron(II) oxadiazole-bridged complexes, compared to the analogous thiadiazole-bridged compounds. In 2018, *Bittner D.* reported the solvatomorphs of $[Fe_2(\mu_2\text{-}\mathbf{PPTD})_2](BF_4)_4$ and $[Fe_2(\mu_2\text{-}\mathbf{PPTD})_2](ClO_4)_4$, which represent the thiadiazole-based equivalents to **C14** and **C15**. Both **PPTD** related complexes exhibit SCO behavior in the high temperature regime.[171] The absence of spin transition in **C14** and **C15** is probably due to the combination of a smaller intrinsic ligand field strength of the oxadiazole moiety and a more constrained geometry of the ligand itself, which has already been reported by *Köhler C*.[20] This becomes evident in the distortion of the resulting iron(II) complexes. While the octahedral distortion parameters in $[Fe_2(\mu_2\text{-}\mathbf{PPTD})_2](BF_4)_4$ and $[Fe_2(\mu_2\text{-}\mathbf{PPTD})_2](ClO_4)_4$ show a value of approx. 120 ° for both [HS-HS] structures[171], **C14** and **C15** offer a much larger deviation of the ideal coordination sphere with values around 150 °. However, it is difficult to say whether the absence of the SCO is due to an insufficient ligand field strength or caused by a too distorted coordination sphere. A spin switch is inevitably accompanied by shrinking of metal-ligand bond lengths. However, if the coordination sphere is too distorted this might not be possible, resulting in a constant [HS-HS] state. To solve this indeterminacy, three similar ligand systems to $\mathbf{L^{Py,1}}$ were synthesized (Figure 3.37). $\mathbf{L^{Py,2}}$ possess only a tridentate coordination pocked next to its bidentate one. This leaves room for a coordinating coligand, which could result in the appropriate ligand field strength to show thermally induced SCO. In addition to that, the use of negatively charged coligands like pyridine-3,5-dicarboxylate could yiled in the formation of neutral complexes that are suitable for sublimation on surfaces. This might lead to spin switchable films, that are especially desired for various applications.[283] $\mathbf{L^{Py,3}}$ was designed to have an additional methylene group between the pyridin-2-yl rest and the oxadiazole ring. Thus, the coordination sphere of the metal center might be less distorted, enabling a possible spin transition. $\mathbf{L^{Py,4}}$ provides both, a free coordination site alongside to its tridentate binding pocket and the extra methylene group. However, it was not possible to synthesize any transition metal complexes of $\mathbf{L^{Py,2}}$, $\mathbf{L^{Py,3}}$ and $\mathbf{L^{Py,4}}$ yet.

3.4 Oxadiazole – the too weak little brother to the thiadiazole?

All oxadiazole based complexes described in the previous chapter stabilized the [HS-HS] spin state at any given temperature. Also, at the time of writing the complexes $[Fe_2(\mu_2\text{-}\mathbf{PMOD})_2](ClO_4)_4 \cdot 4CH_3CN$ and $[Fe_2(\mu_2\text{-}\mathbf{PMOD})_2](CF_3SO_3)_4 \cdot 2CH_3CN$ are the *only* literature known *oxadiazole-coordinated* systems that show SCO activity. This leads to the question: Is the spin transition in $[Fe_2(\mu_2\text{-}\mathbf{PMOD})_2](ClO_4)_4 \cdot 4CH_3CN$ and $[Fe_2(\mu_2\text{-}\mathbf{PMOD})_2](CF_3SO_3)_4 \cdot 2CH_3CN$ just an extra-ordinary coincidence that seems to never happen again?

To give the oxadiazole one last chance to prove its relevance in the field of spin crossover, $\mathbf{L^{Py,1}}$ was used to synthesize a series of mononuclear iron(II) complexes of type $[Fe(\mathbf{L^{Py,1}})(NCX)_2]$ (X = S, Se or BH_3) (Figure 3.46). Due to the fact that the donor strength in the pseudohalide series rises in the order NCS < NCSe ≪ $NCBH_3$, the resulting ligand field splitting can be fine-tuned.[210,259] Additionally, the use of two monodentate coligands should yield in a less sterically stressed coordination sphere around the iron(II) ion. Complex synthesis was done by dissolving equimolar amounts of $\mathbf{L^{Py,1}}$ and $[Fe^{II}(py)_4(NCX)_2]$ (X = S, Se or BH_3) separately in either acetonitrile or methanol under inert atmosphere, followed by the dropwise combination of both solutions. After a short time, the desired complexes crystallized in form of orange block-shaped single crystals or as microcrystalline powder (see Chapter 6.4 for details). Structure elucidation was achieved by single-crystal X-ray diffraction and IR spectroscopy. The iron(II) precursors $[Fe^{II}(pyridine)_4(NCS)_2]$ and $[Fe^{II}(pyridine)_4(NCSe)_2]$ were prepared through a modified method from literature. $Fe^{II}(SO_4)_2$ x $7(H_2O)$, together with $NH_4(SCN)$ or KSeCN, was dissolved in water, containing excess pyridine.[284] The synthesis of $[Fe^{II}(pyridine)_4(NCBH_3)_2]$ was adopted from the published method of *Nakano et al.*, dissolving $Fe^{II}(BF_4)_2$ x $6(H_2O)$, $NaBH_3CN$ and excess pyridine in water.[206] The precipitated iron(II) starting materials were filtered under inert atmosphere and used without further analytics (see Chapter 6.4).

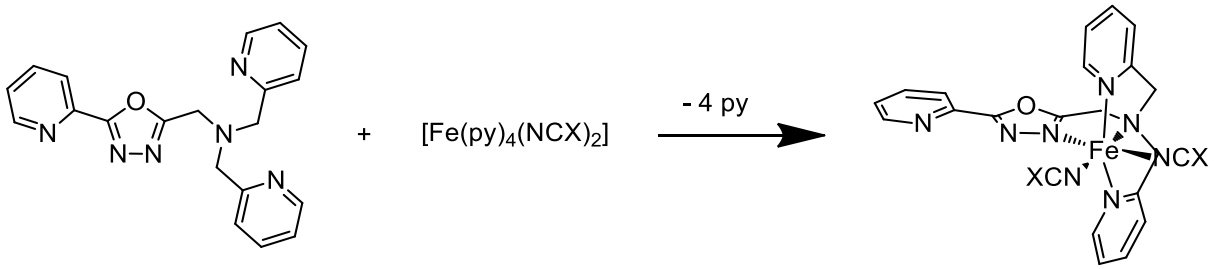


Figure 3.46 Synthesis of mononuclear $[Fe_2(\mathbf{L^{Py,1}})(NCX)_2]$-type complexes (X = S, Se, BH_3). The reactions took place in either dry methanol or dry acetonitrile in an inert atmosphere at room temperature.

3.4.1 Crystal structures of [Fe(L)(NCX)$_2$]-type complexes

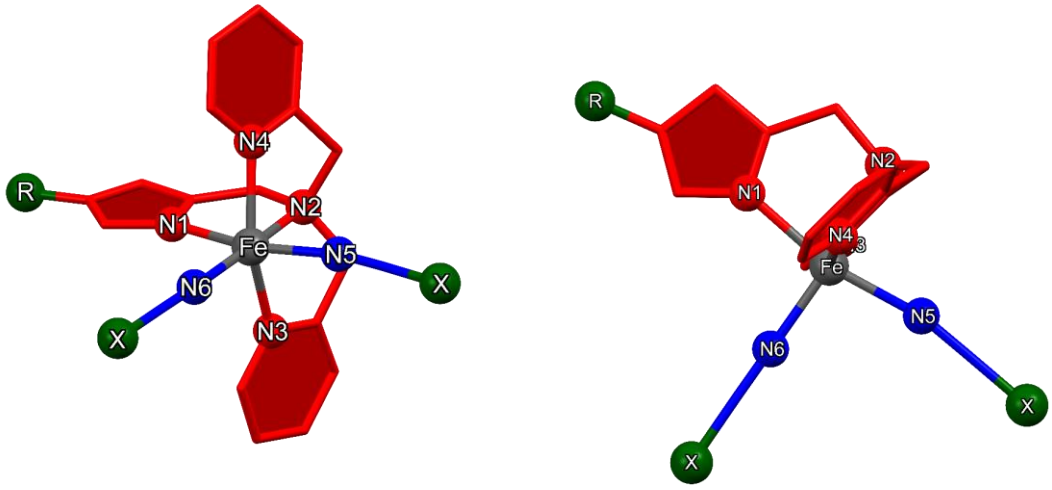


Figure 3.47 Labelling scheme for all mononuclear iron(II) complexes in this work with front view (left) and view along the N4-Fe-axis (right). The used ligand is displayed in red while the coligands are shown in blue. Variable groups are illustrated in green (R = aryl rest; X = S, Se, BH_3).

To describe the molecular structures of [Fe(**L**)(NCX)$_2$]-type complexes (**L** ≙ tetradentate ligand), the labeling scheme in Figure 3.47 is used. The coordination sphere in this kind of complexes is saturated with two coligands, whereas only one ligand molecule coordinates via its tetradentate binding pocket. One nitrogen of the oxadiazole ring shapes, together with the amine function and the two coligands, the equatorial base of the coordination octahedron. Thus, the pseudohalides (NCS, NCSe or $NCBH_3$) exhibit a *cis*-configuration. The apical positions of the octahedron are occupied by the *trans*-coordinating pyridyl moieties. Regarding the metal-ligand bond distances, a general trend can be observed:

$$\text{Fe-N6} < \text{Fe-N5} < \text{Fe-N3} \approx \text{Fe-N4} \approx \text{Fe-N1} < \text{Fe-N2}$$

Figure 3.48 General trend of metal-ligand bond lengths in [Fe(**L**)(NCX)$_2$]-type complexes.

The largest bond distance is represented by the bond between the iron(II) center and the amin function [d(Fe-N^{Amine}) = d(Fe-N2)]. This is completely reasonable, since the sp^3 hybridized amine nitrogen is known for its pure σ-donor character.[232] The next shorter bond distance can be found between the metal center and the oxadiazole motif. This bond length is roughly equal to the bond lengths of the axially coordinating pyridine rings [d(Fe-N3) ≈ d(Fe-N4) ≈ d(Fe-N1)]. The smaller distances compared to the amine function can be attributed to the additional π-backbonding to aromatic systems, which further strengthens the metal-ligand bond. The shortest bond lengths are found between the iron(II) ion and the negatively charged coligands (NCS, NCSe and $NCBH_3$). Firstly, this can be ascribed to the negative charge of the

coordinated pseudohalides, which results in a strong electrostatic attraction. Secondly, both coligands are monodentate and hence not affected by a steric stiffness of backbone functions. Moreover, the Fe-N6 bond is slightly shorter than the Fe-N5 bond. The coordination of two *trans* ligands with different π-acceptor strengths leads to a weakening of the π-backbonding and thus to a prolongation of the metal-ligand bond of the *weaker* π-acceptor. Accordingly, the oxadiazole nitrogen exhibits a *trans influence* on the pseudohalide nitrogen (N5), which is manifested in the prolongation of the Fe-N5 bond.[285] As expected, the use of two monodentate independent coligands leads to a higher *degree of freedom*, which is reflected in a smaller distortion of the coordination sphere. Thus, the octahedral distortion parameter [$\Sigma_O(FeN_6)$] of these mononuclear HS species range between 93 ° and 108 °, which is significantly smaller than the values discussed in earlier chapters. Here, the largest deviation from the ideal coordination sphere takes place at the apical positions and involves the *trans* coordinating pyridine rings. This is displayed by the N3-Fe-N4 *trans* angle, which is approx. 150 ° for all mononuclear iron(II) high-spin complexes.

Due to the absence of counter anions and free NH-groups, intermolecular classical hydrogen bonds are no longer observed. However, as the ligand systems contain several aromatic groups, pronounced π-π stacking in the crystalline phase can be found. In general, π-π interactions between aromatic systems can be broadly classified into two categories: Parallel stacked (either cofacial stacked or parallel displaced) or edge-to-face (T-shaped).[286] To determine whether two roughly parallel oriented aromatic rings are stacked attractively in crystal structures, different geometrical parameters have to be calculated (Figure 3.49, left).[287] Here, two three-dimensional planes A and B are defined by two opposing aromatic rings with centers Q and O.

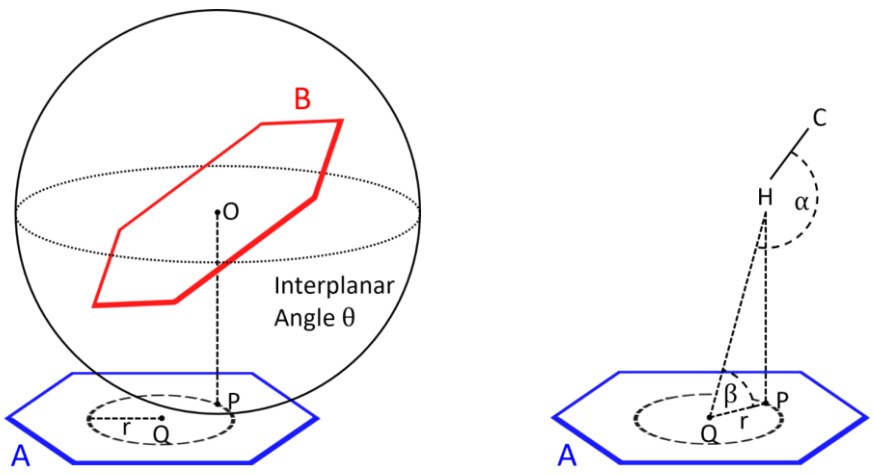


Figure 3.49 Schematic diagram of π-π interactions with relevant geometrical parameters. Left: Parameters used to describe a parallel-wise π-π stacking of two aromatic rings. Right: Parameters used for the description of a T-shaped π-π interaction.

The coordinates of a center correspond to the mean value of all positional vectors of the ring forming atoms. To calculate the corresponding planes, which include the aromatic rings, the least-squares approach was used. The angle between both planes is defined as the *interplanar angle* θ, which can vary between 0 ° (parallel) and 90 °(perpendicular). P is defined as the intersection of the line $\vec{x} = \overrightarrow{O} + a \cdot \vec{n}$ with plane A, where $\overrightarrow{O}$ is the positional vector of center O and $\vec{n}$ is the normal vector of plane A. Hence, the vector $\overrightarrow{PO}$ is perpendicular to plane A. The resulting distance $\overline{PO}$ represents the *interplanar distance* d_{AB}. The *offset r* of both aromatic rings can now be described by the distance $\overline{QP}$. Therefore, the assignment of plane A and B was done in such way, that the *offset r* is as small as possible. The statistical analysis of π-π interactions in crystal structures by *Saha B. K.* et al. showed that the *interplanar distance* d_{AB} statistically varies between 3.0 Å and 6.0 Å, depending on the *interplanar angle* θ.[287] The maximal value of the *offset r* was defined as 3.6 Å. This value is the sum of two quantities: i) the mean distance of a hydrogen atom attached to its six membered aromatic ring (~2.4 Å). ii) the van der Waals radius of a hydrogen atom (~1.2 Å). Thus, 3.6 Å displays the largest distance from an aromatic center where any kind of interaction could still occur. To simplify figures that represent packing of complex molecules in the solid state, *center-to-center distances* ($d_{QO} = \overline{QO}$) (in some publications also referred to as *centroid-to-centroid distance*) are used.

The orthogonal T-shaped π-π interaction can be seen as a non-classical C-H···π hydrogen bond.[288–291] *Malone* et al. categorized such Donor-H···π interactions (Donor = O, N, S, sp^2 C and sp^3 C) into categories of Type I – V (Table F. 2), depending on geometrical parameters shown in Figure 3.49 (right). To assign such T-shaped π-π interactions to a specific category, the schematic diagram changes slightly. While the aromatic ring A (with Q and P) still represents a three-dimensional plane, B is exchanged for the C-H-motif to put the focus on the hydrogen atom. The *interaction distance* d_{QH} from the center of A (≙ Q) to the hydrogen atom is defined by $\overline{QH}$, while the *offset r* is still expressed by the distance between Q and P ($r = \overline{QP}$). Additionally, two relevant angles are introduced. The angle α is defined by the angle enclosed between the vectors $\overrightarrow{HC}$ and $\overrightarrow{HQ}$, whereas β describes the angle between $\overrightarrow{QP}$ and $\overrightarrow{QH}$. According to the study of *Malone F. et al.*, the sp^2 C-H··· π interaction type shows a preference for type III. For the sake of clarity, intermolecular T-shaped π-π interactions are expressed only with the *interaction distance* d_{QH} in packing related figures.

3.5 Mononuclear coordination compounds of $L^{Py,1}$

3.5.1 Solvatomorphs of [Fe($L^{Py,1}$)$(NCS)_2$] (C16)

[Fe($L^{Py,1}$)$(NCS)_2$] · 1MeCN (C16·1MeCN) was synthesized by dissolving an equimolar amount of [Fe$(py)_4(NCS)_2$] and **$L^{Py,1}$** in acetonitrile separately. Both solutions were combined and the resulting reaction was kept undisturbed at room temperature. Slow evaporation of the solvent yielded yellow block shaped crystals that were suitable for X-ray structure analysis. The compound crystallizes in the monoclinic space group $P2_1/c$ with four formula units inside of the unit cell. The crystal structure was measured at 120 K, crystallographic data can be found in Table D.7. The asymmetric unit consist of one complex molecule next to one acetonitrile (Figure F.33, left). The remaining atoms inside of the unit cell are generated by symmetry due to the present centers of inversion, two-fold screw axes and glide planes (Figure F.33, right). The structure of the complex molecule as well as the trend of bond lengths follow the description in Chapter 3.4.1. Here, the average metal-ligand bond distance is equal $\bar{d}$(Fe-N) = 2.18 Å, which represents a defined HS structure at 120 K (Table E.7). This statement is strengthened by the distortion of the octahedral coordination sphere with $\Sigma_O(FeN_6)$ = 102.3 ° and CShM(O_h) = 1.31, displayed in Figure 3.50. Both values are significantly smaller than those reported in earlier stages of this work. As already discussed in Chapter 3.4.1, this finding is based on the coordination of two independent, monodentate coligands with no steric strain. **C16**·1MeCN shows π-π stacking between the pyridyl rings attached to the amine function with A (N4, C16, C17, C18, C19, C20) and B (N3, C11, C12, C13, C14, C15) (A and B refer to the schematic diagram in Figure 3.49). The *interplanar distance* d_{AB} is equal to 3.94 Å, accompanied by an *interplanar angle* of θ = 15.8 ° and an *offset* of *r* = 1.75 Å (Figure 3.51).

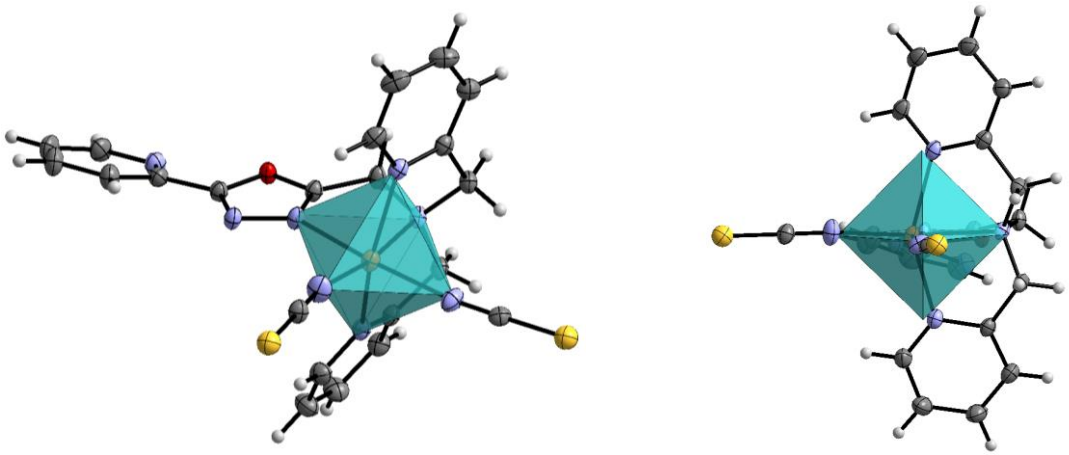


Figure 3.50 Molecular structure of **C16**·1MeCN and its ideal coordination octahedron with front view (left) and view along the Fe-N5 axis (right), calculated with SHAPE.[62] Colour scheme: dark grey – C, grey – H, violet – N, red – O, yellow – S, orange – Fe. ORTEP representation with atomic displacement parameters set to 50 % probability.

These parameters agree with literature known values reported for π-π stacking in crystalline phases.[287] Packing of **C16**·1MeCN reveals that, due to this intermolecular π-π interaction, one-dimensional chains along the b-axis are formed (Figure F.34 and Figure F.35).

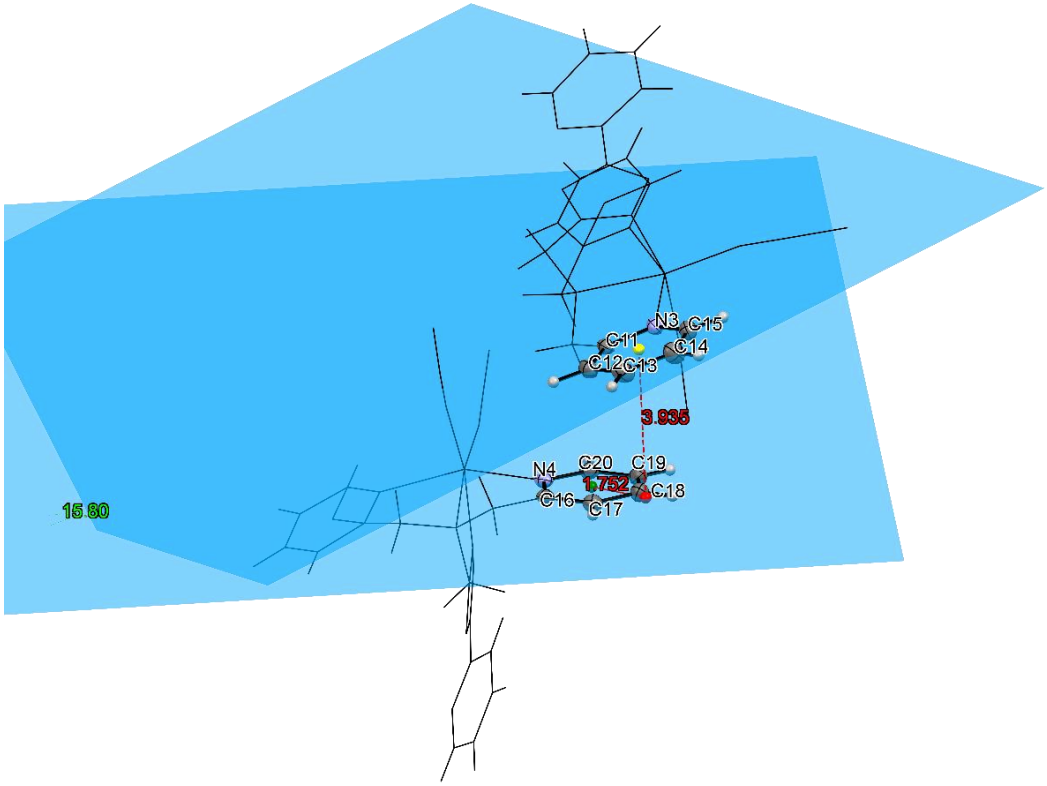


Figure 3.51 π-π interaction in **C16**·1MeCN. Least-squares mean plane A is defined by N4, C16, C17, C18, C19 and C20. Plane B is defined by N3, C11, C12, C13, C14 and C15. Green point – center of the aromatic ring in A. Yellow point – center of the aromatic ring in B. Red point – orthogonal intersection of the aromatic center in B onto plane A. *Offset r* = 1.752Å, *interplanar distance* d_{AB} = 3.959Å, *interplanar angle* θ = 15.80 °. ORTEP representation with atomic displacement parameters set to 50 % probability.

[Fe($L^{Py,1}$)$(NCS)_2$] · 1MeOH (C16·1MeOH) was synthesized in a similar way as **C16**·1MeCN, except that methanol was used as solvent. The compound crystallizes in the monoclinic space group *C*2/*c* with eight formula units inside of the unit cell. Crystallographic data gathered at 120 K can be found in Table D.7. The asymmetric unit contains one complex and one methanol molecule (Figure F.36). The residual atoms in the unit cell are symmetry generated by the centers of inversion, two-fold screw/ rotation axes and glide planes (Figure F.37 and Figure F.38). Analogous to **C16**·1MeCN the complex molecule itself shows the trend of bond lengths, described in Chapter 3.4.1. The mean metal-ligand bond distance is equal to $\bar{d}$(Fe-N) = 2.18 Å. The distortion, expressed by $\Sigma_O(FeN_6)$ = 108.6 ° and CShM(O_h) =1.45, is slightly higher than in **C16**·1MeCN. This can be ascribed to the additional intermolecular π-π interactions in the lattice. The coordinated pyridine ring (N4, C16, C17, C18, C19, C20) slightly bends towards the C6-H6 fragment to exhibit an attractive interaction.

Deviation of the coordination sphere from the ideal octahedron is displayed in Figure 3.52, which, in combination with the present bond distances, is representative for a high-spin state at 120 K. Structural details are summarized in Table E.7. Although the complex molecule is isostructural to **C16**·1MeCN, the packing of both complexes and thus the intermolecular interactions differ. Therefore, three unique intermolecular π-π interactions in the solid phase can be observed.

The first interaction displays a parallel-like stacking between two pyridin-2-yl moieties (at the 2-position of the oxadiazole ring) of two complex molecules with N8, C3, C4, C5, C6 and C7 for plane A and B. The *interplanar distance* is equal to d_{AB} = 3.46 Å, combined with an *interplanar angle* of θ = 23.7 ° and an *offset* of *r* = 1.62 Å (Figure 3.53). The thus formed dimer additionally exhibits a T-shape like π-π interaction between the pyridin-2-yl rest at the 2-position of the oxadiazole and the pyridine ring attached to the amine function. The non-classical C-H···π hydrogen bond is formed between C6-H6 and the plane A with N4, C16, C17, C18, C19 and C20 (see schematic diagram in Figure 3.49). The interaction can be categorized as type III (Table F. 2), with an *interaction distance* of d_{QH} = 2.97 Å, an *offset* of *r* = 0.72 Å and the two angles α = 147.3 ° and β = 76.0 ° (Figure F.39). In addition to that, a second T-shape like π-π interaction between two “dimers” of type V can be found, with d_{QH} = 3.05 Å, *r* = 1.55 Å, α = 136.1 ° and β = 59.4 ° (Figure F.40). Due to these intermolecular interactions, a one-dimensional network of “complex dimers” is formed (Figure 3.54).

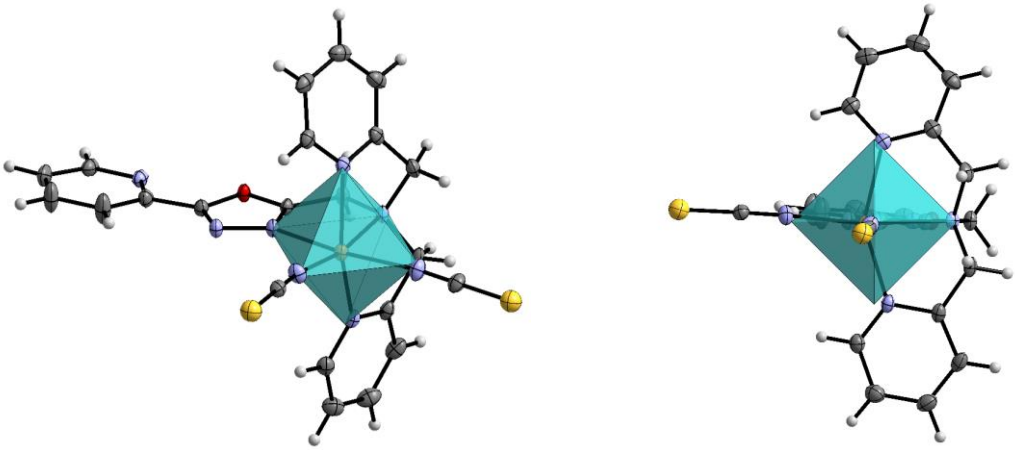


Figure 3.52 Molecular structure of **C16**·1MeOH and its ideal coordination octahedron with front view (left) and view along the Fe-N5 axis (right), calculated with SHAPE.[62] Colour scheme: dark grey – C, grey – H, violet – N, red – O, yellow – S, orange – Fe. ORTEP representation with atomic displacement parameters set to 50 % probability.

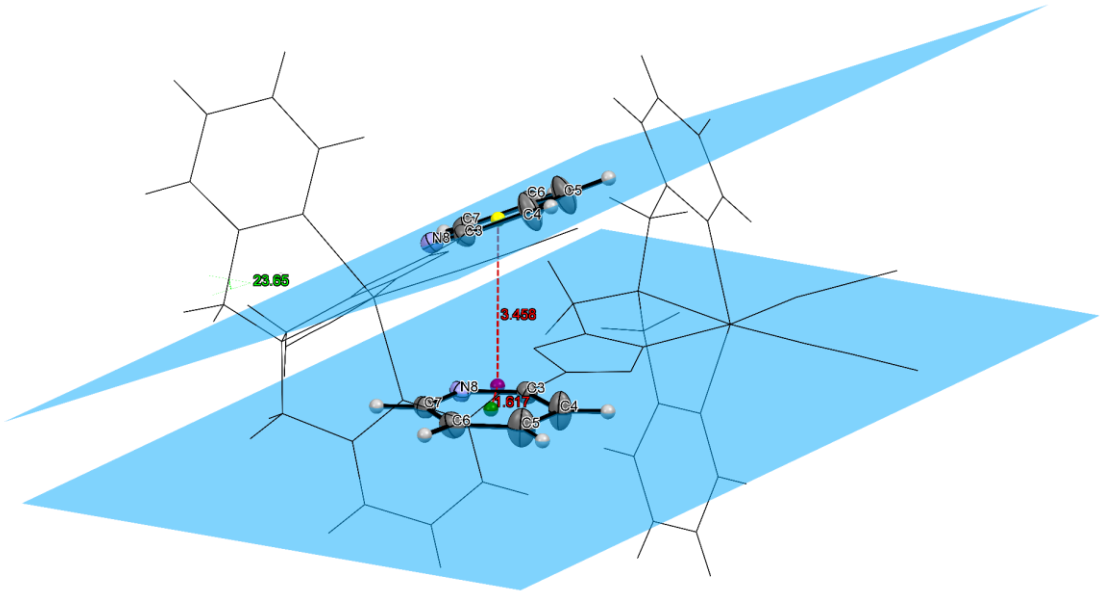


Figure 3.53 π-π interaction in **C16**·1MeOH. Least-squares mean plane A is defined by N8, C3, C4, C5, C6 and C7. Plane B is defined by N8, C3, C4, C5, C6 and C7 of an adjacent molecule. Green point – center of the aromatic ring in A. Yellow point – center of the aromatic ring in B. Purple point – orthogonal intersection of the aromatic center in B onto plane A. *Offset r* = 1.617Å, *interplanar distance* d_{AB} = 3.485Å, *interplanar angle* θ = 23.65 °. ORTEP representation with atomic displacement parameters set to 50 % probability.

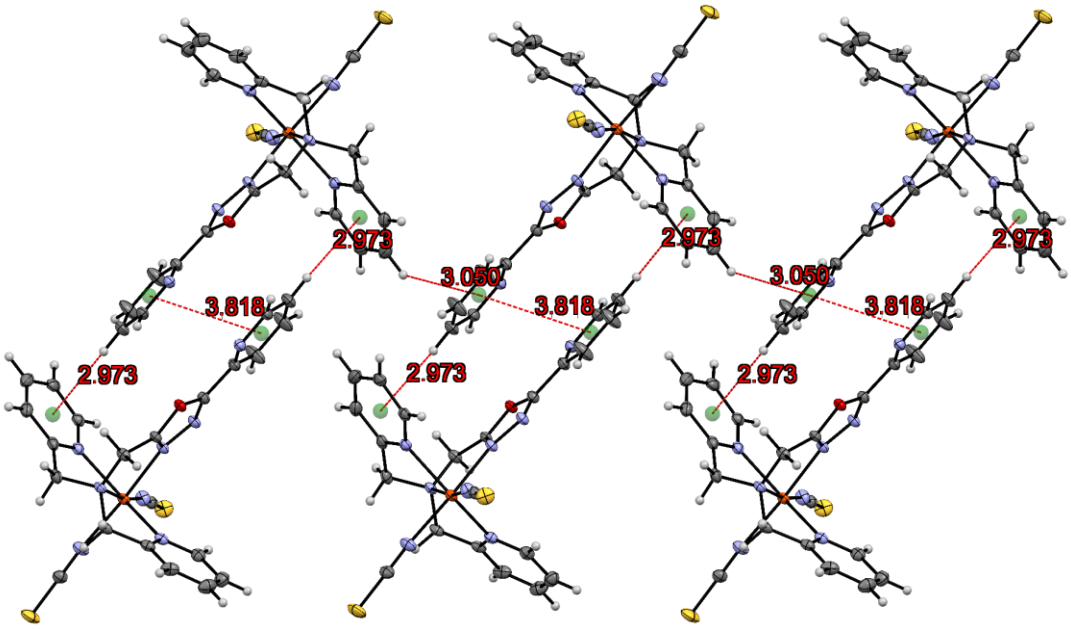


Figure 3.54 One-dimensional network of "complex dimers" in **C16**·1MeOH. Red dashed lines represent intermolecular distances. Colour scheme: dark grey – C, grey – H, violet – N, red – O, yellow – S, orange – Fe. ORTEP representation with atomic displacement parameters set to 50 % probability.

Magnetic properties of C16·1MeCN and C16·1MeOH

C16·1MeCN and **C16**·1MeOH were analyzed as single crystals with respect to their temperature dependent magnetic behavior in a temperature range from 300-2 K. Eicosane was used to fix the samples inside of the gelatin capsule. The molar susceptibilities are plotted as $\chi_M T$ product versus the temperature for **C16**·1MeCN (red open circles) and **C16**·1MeOH (blue open triangles) in Figure 3.55. At 300 K, the $\chi_M T$ value of **C16**·1MeCN is equal to 3.80 $cm^3mol^{-1}K$, which is higher than the *spin-only* value of 3 $cm^3mol^{-1}K$ for one $S = 2$ spin centers with $g = 2$ (Equation 3.1). The higher experimental value can be attributed to first-order spin-orbit coupling due to the $^5T_{2g}$ ground state.[67]

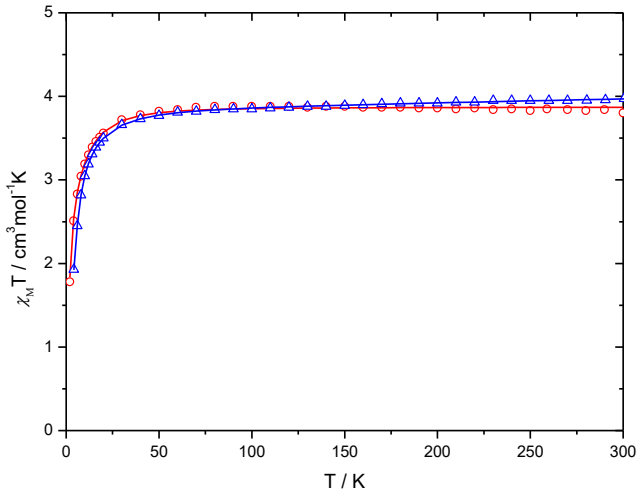


Figure 3.55 Temperature dependent magnetic behavior of **C16**·1MeCN (red open circles) and **C16**·1MeOH (blue open triangles) in form of the combined $\chi_M T$ *vs*. *T* plots. The solid lines represents the best fit of the susceptibility data for **C16**·1MeCN (red) and **C16**·1MeOH (blue), using PHI.[201]

Starting at 300 K, $\chi_M T$ remains nearly constant to 60 K and falls significantly below this temperature to a value of 1.78 $cm^3mol^{-1}K$ at 2 K. This drop of the $\chi_M T$ product can be ascribed to zero-field splitting in the iron(II) center. In order to provide more detailed information about the magnetic anisotropy and thus about the zero-field splitting parameters *D* and *E*, additional magnetization data were recorded between 2 K and 10 K with magnetic fields ranging from 0.1 T to 7 T. The resulting data of **C16**·1MeCN are either visualized as magnetization (*M*) versus field (*H*) plots (Figure 3.56) or in form of magnetization (*M*) versus field/temperature (*H*/*T*) plots, also known as the reduced magnetization (Figure 3.57). The magnetization at the lowest temperature (2K) and highest field (7 T) is equal to 3.11 $N_A\mu_B$. This value is lower than the expected saturated magnetization (M_{sat}) of 4 $N_A\mu_B$ for one isolated iron(II) ion ($g = 2$, $S = 2$), calculated with Equation 3.6.

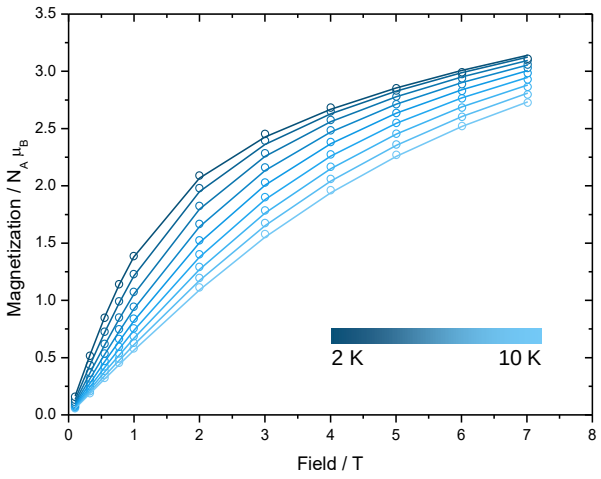


Figure 3.56 Temperature and field dependent magnetization measurement of **C16**·1MeCN in form of *M vs*. *H* plot (open circles). Solid lines represent the best fit using PHI.[201]

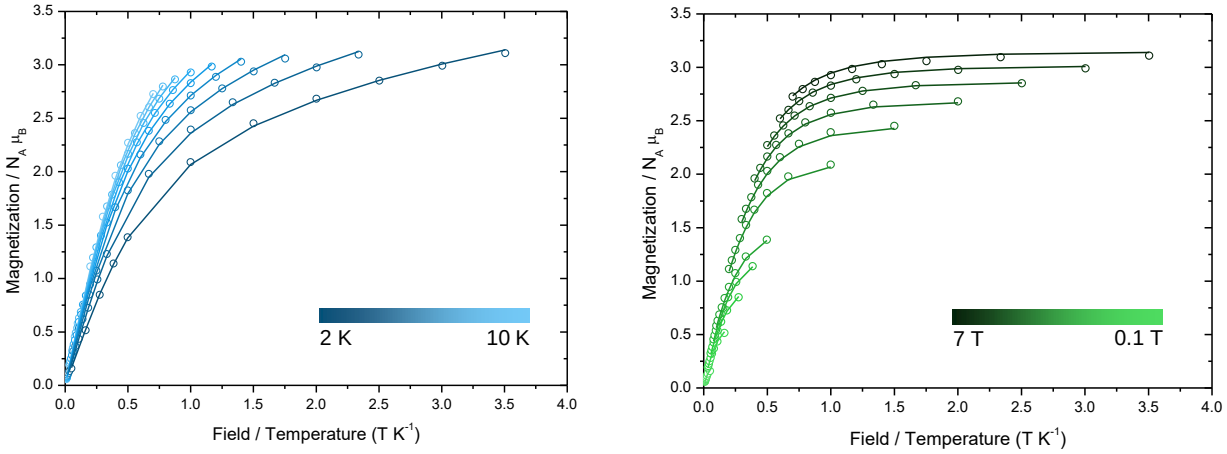


Figure 3.57 Temperature and field dependent magnetization measurement of **C16**·1MeCN in form of *M vs*. *H*/*T* plots (open circles). Solid lines represent the best fit using PHI.[201]

$$M_{sat} = \sum_i g_i \cdot S_i \cdot N_A \mu_B \tag{3.6}$$

The experimental curves of the reduced magnetization for equal temperatures (Figure 3.57, left) and equal magnetic fields (Figure 3.57, right) do not superimpose, which indicates the presence of magnetic anisotropy. To quantify the underlying parameter, susceptibility and magnetization data were fitted simultaneously using the program PHI.[201]

The spin Hamiltonian in Equation 3.7 with the axial (*D*) and rhombic (*E*) zero-field splitting parameter, an isotropic *g*-factor and a spin-state of *S* = 2 was applied.

$$\hat{H} = D\left[\hat{S}_z^2 - S(S+1)/3\right] + E\left(\hat{S}_y^2 - \hat{S}_x^2\right) + g\mu_B HS \tag{3.7}$$

The best fit resulted in *g* = 2.2715(5), *D* = 8.66(2) cm^{-1} and *E* = 2.36(1) cm^{-1} with a residual of $R = 0.5 \cdot 10^{-3}$ and is visualized as solid lines in the corresponding plots. The value of *g* above 2.0 describes a spin-orbit coupled system, which is expected for an $^5T_{2g}$ ground state with an incompletely quenched orbital momentum. The positive value for the parameter *D* refers to an *easy-plane* type of magnetic anisotropy. Next to that, $E \neq 0$ is representative for additional transverse magnetic anisotropy. The absolute ratio |*E*/*D*|, which can vary in the range of $0.3 \geq |E/D| \geq 0$, is equal to 0.27. All values are in good agreement with literature known parameters of distorted octahedral HS Fe(II) systems.[292] In analogy, the $\chi_M T$ product of **C16**·1MeOH at 300 K is equal to 3.97 $cm^3mol^{-1}K$ and slightly drops to 3.81 $cm^3mol^{-1}K$ at 60 K. Below 60 K, the $\chi_M T$ value decreases very fast to 1.93 $cm^3mol^{-1}K$ at 4 K. Next to that, magnetization at 4 K and 7 T is equal to 3.09 $N_A\mu_B$, which, also for this **C16** solvatomorph, can be attributed to zero-field splitting (Figure G.17). This is further confirmed by the experimental curves of the reduced magnetization for equal temperatures (Figure G.18) and equal magnetic fields (Figure G.19), which do not follow the Brillouin function and thus do not superimpose. Susceptibility and magnetization data were fitted simultaneously with PHI[201] by using the spin Hamiltonian in Equation 3.7. Best fit with an isotropic *g*-factor, *S* = 2 and a present TIP (temperature independent paramagnetism) of $\chi_{TIP} = 0.9 \cdot 10^{-5}$ cm^3mol^{-1} yielded *g* = 2.2842(6), *D* = 11.12(1) cm^{-1} and *E* = 0.36(8) cm^{-1} with a residual of $R = 0.6 \cdot 10^{-4}$. Likewise to **C16**·1MeCN, the increased *g*-value can be attributed to first-order spin orbit coupling due to orbital momentum of the $^5T_{2g}$ ground state. The system exhibits an *easy-plane* type of magnetic anisotropy combined with transverse anisotropy of |*E*/*D*| = 0.03. Both solvatomorphs of **C16** remain in the high-spin state until very low temperatures. The octahedral distortion parameter $\Sigma_O(FeN_6)$ is at the lower regime of the typical range for HS complexes. Thus, the absence of a thermally induced SCO is most likely due to an insufficient ligand field.

3.5.2 Solvatomorph of [Fe($L^{Py,1}$)$(NCSe)_2$] (C17·3MeCN)

[Fe($L^{Py,1}$)$(NCSe)_2$] · 3MeCN (C17·3MeCN) was prepared in the same manner as **C16**·1MeCN, using the iron(II) precursor [Fe$(py)_4(NCSe)_2$] as starting material. The compound crystallizes in the monoclinic space group $P2_1/c$ with four formula units inside of the unit cell. The crystal structure was measured at 173 K. Crystallographic data can be found in Table D.8. There are one complex and three acetonitrile molecules in the asymmetric unit (Figure F.41). Due to the present centers of inversion, two-fold screw axes and glide planes, the rest of the unit cell is generated by symmetry (Figure F.42). The structure and the bond length trend of the complex cation is analogous to the discussion in Chapter 3.4.1. The distortion of the coordination sphere is slightly lower than in the complexes **C16**·1MeCN and **C16**·1MeOH with $\Sigma_O(FeN_6)$ = 100.3 ° and CShM(O_h) = 1.26. Next to the average metal-ligand bond distance of $\bar{d}$(Fe-N) = 2.17 Å, these value represent a high-spin iron(II) complex. A summary of all structural parameters is given in Table E.7. Deviation of the coordination sphere from the ideal octahedron is displayed in Figure 3.58.

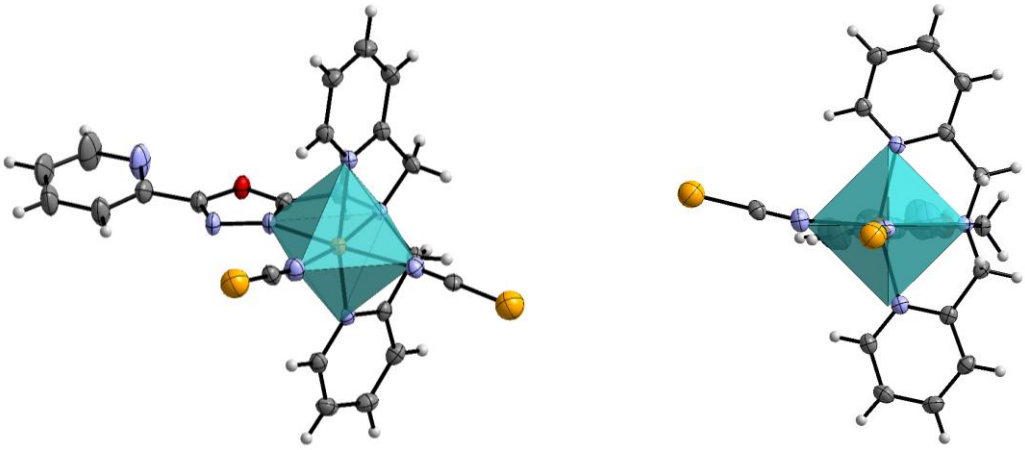


Figure 3.58 Molecular structure of **C17**·3MeCN and its ideal coordination octahedron with front view (left) and view along the Fe-N5 axis (right), calculated with SHAPE.[62] Colour scheme: dark grey – C, grey – H, violet – N, red – O, bright orange – Se, orange – Fe. ORTEP representation with atomic displacement parameters set to 50 % probability.

The packing of **C17**·3MeCN reveals, that the solvent molecules are always next to the oxadiazol-pyridyl moieties, resulting in a layer-like structure (Figure F.43 and Figure F.44). Three unique intermolecular π-π interactions in the crystalline phase can be found. The first parallel-like π-π stacking occurs between two pyridine-2-yl moieties (attached to the amine function) of two adjacent molecules. This kind of interaction results in the formation of a one-dimensional chain along the b-axis in the crystal lattice and was already observed in the complex **C16**·1MeCN (Figure 3.59).

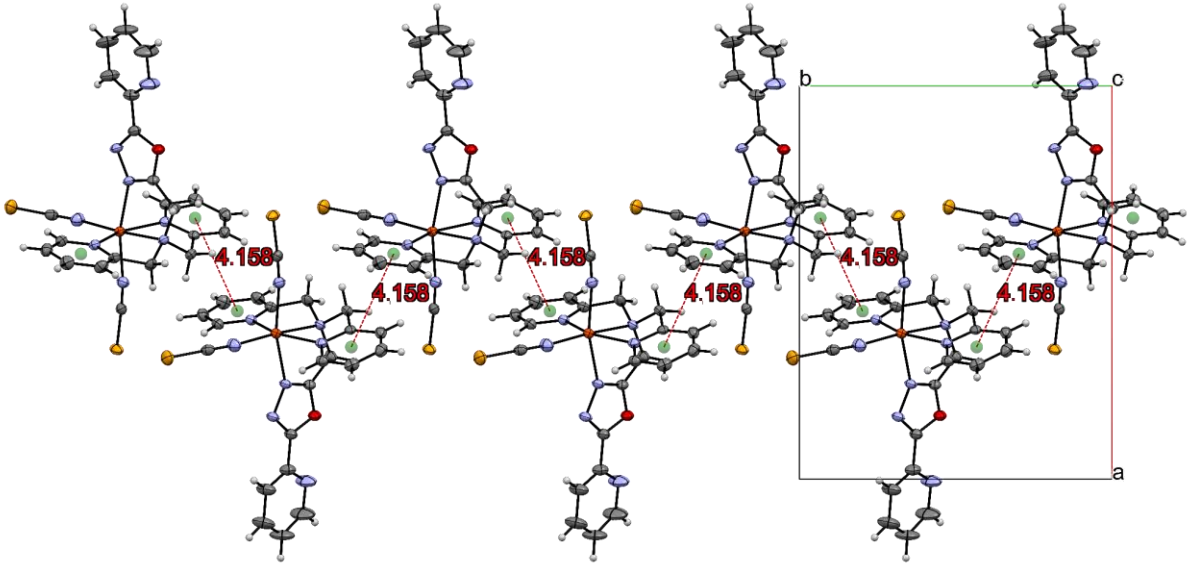


Figure 3.59 One-dimensional chain of complex molecules in **C17**·3MeCN due to intermolecular π-π stacking along the b-axis. The centers of involved aromatic rings are displayed as green points. Red dashed lines and numbers represent the distance between two centers.

The least-squares mean plane A is formed by N4, C16, C17, C18, C19 and C20, plane B includes N3, C11, C12, C13, C14 and C15. The *interplanar distance* is equal to d_{AB} = 4.03 Å, combined with an *interplanar angle* of θ = 23.9 ° and an *offset* of *r* = 1.04 Å (Figure 3.60).

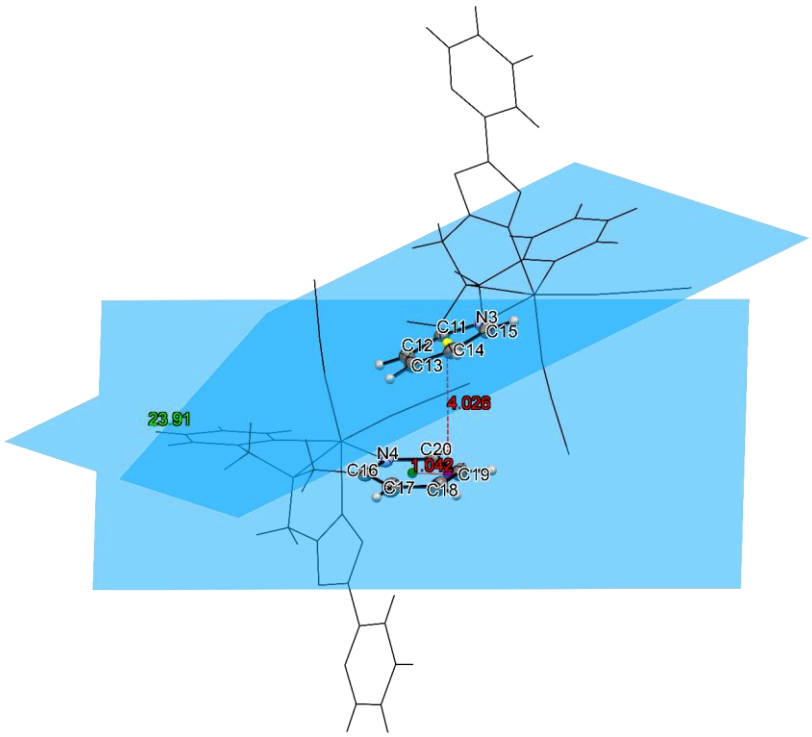


Figure 3.60 π-π interaction in **C17**·3MeCN. Least-squares mean plane A is defined by N4, C16, C17, C18, C19 and C20. Plane B is defined by N3, C11, C12, C13, C14 and C15 of an adjacent molecule. Green point – center of the aromatic ring in A. Yellow point – center of the aromatic ring in B. Purple point – orthogonal intersection of the aromatic center in B onto plane A.

The oxadiazole-pyridine moieties are aligned roughly orthogonal with respect to the chain direction and stack with the oxadiazole-pyridine fragments of neighboring chains. Here, each oxadiazole interacts with the opposing pyridine ring. Plane A includes N8, C1, C2, C3, C4 and C5, while the least-squares mean plane B is formed by the oxadiazole atoms O1, C6, N7, N1 and C7. Next to the *interplanar distance* d_{AB} = 3.75 Å, the *offset* is equal to r = 1.46 Å with an *interplanar angle* of θ = 8.1 ° (Figure F.45). In addition to that, a second π-π interactions between the same molecules takes place. The pyridine (attached to the oxadiazole) shows an intermolecular T-shape π-π interactions to the pyridine moiety, which is attached to the amine function. The involved C-H fragment is labeled as C2-H2, plane A includes N3, C11, C12, C13, C14 and C15. The interaction can be categorized as type III (see Chapter 3.4.1). The *interaction distance* is equal to d_{QH} = 2.73 Å combined with an *offset* of r = 0.61 Å and the two angles α = 147.8 ° and β = 77.2 ° (Figure F.46). This results in a crosslinking of the afore mentioned one-dimensional chains of complex molecules, such that a two-dimensional network is formed (Figure 3.61).

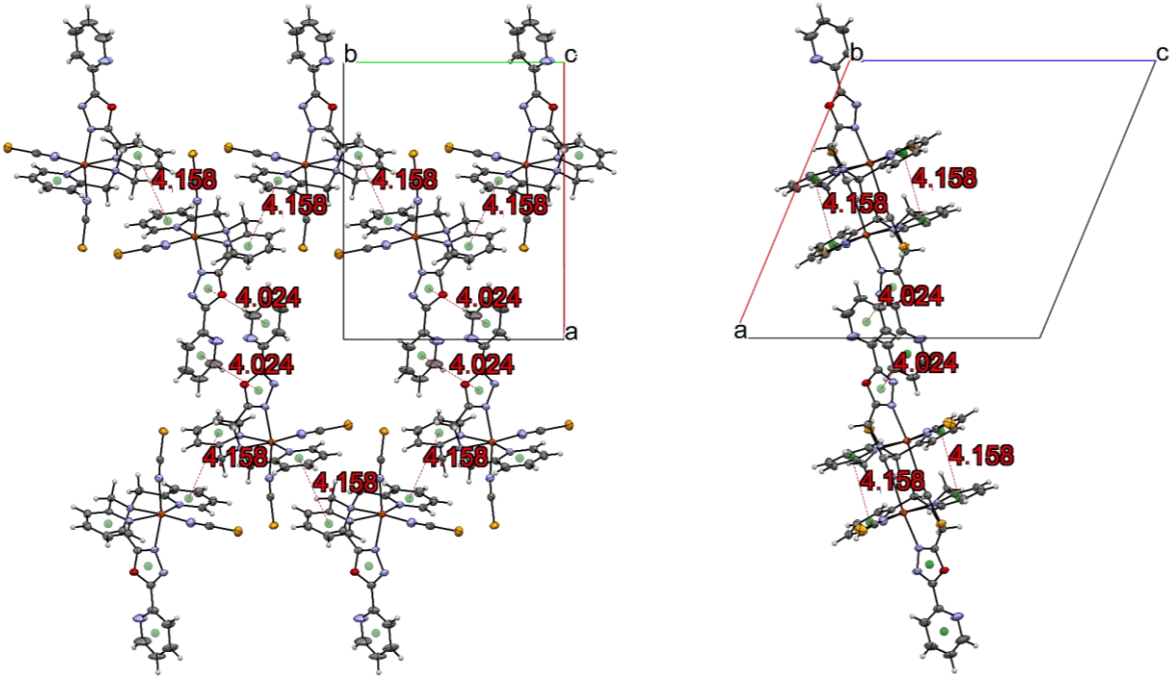


Figure 3.61 Two-dimensional network of complex molecules in **C17**·3MeCN due to intermolecular π-π interactions with view along the c-axis (left) and b-axis (right). The centers of involved aromatic rings are displayed as green points. Distances are displayed as red dashed lines and numbers. Solvent molecules are omitted for better vision.

Magnetic properties of C17·3MeCN

The magnetic behavior of single crystals of **C17**·3MeCN was investigated in an eicosane-blocked manner in a temperature range between 300 K and 2 K. The temperature dependency of the molar susceptibility is displayed in form of combined $\chi_M T$ *vs*. *T* and χ_M *vs*. *T* plots in Figure 3.62.

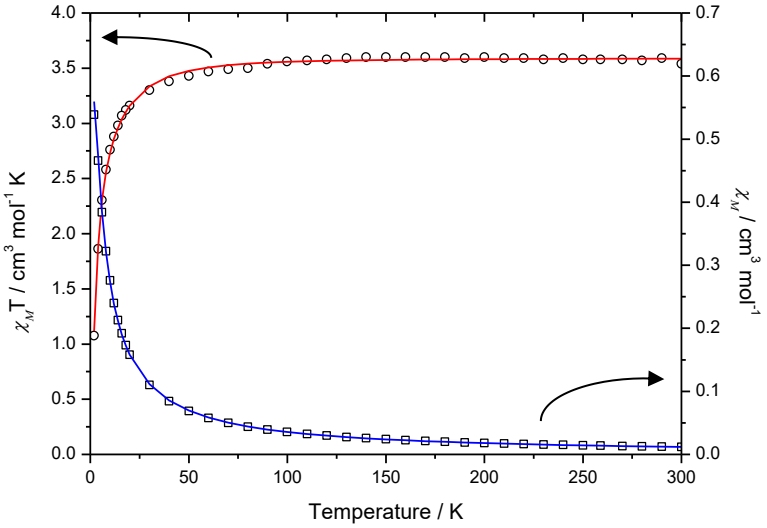


Figure 3.62 Temperature dependent magnetic behavior of **C17**·3MeCN in the form of combined $\chi_M T$ *vs*. *T* (left values, open circles) and χ_M *vs*. *T* plots (right values, open squares). Solid lines represent the best fit for $\chi_M T$ *vs*. *T* (red) and χ_M *vs*. *T* (blue), using PHI.[201]

Since complexes **C16**·1MeCN and **C16**·1MeOH already showed significant zero-field splitting, additional magnetization data were taken from 2 K to 10 K between 0.1 T and 7 T. Again, the resulting data are either visualized as magnetization (*M*) versus field (*H*) plots (Figure G.20) or in form of magnetization (*M*) versus field/temperature (*H*/*T*) plots (Figure G.21 and Figure G.22). This allows for fitting of the data including an axial (*D*) and transverse anisotropy (*E*) parameter. As expected, the $\chi_M T$ product stays nearly constant at a value of 3.54 cm^{3}mol^{-1}K until it starts to decrease significantly below a temperature of 90 K, which can be ascribed to zero-field splitting. This statement is reinforced by the magnetization at 2 K and 7 T, which is equal to 2.65 $N_A\mu_B$ (saturation magnetization of an *S* = 2 system with a *g*-factor of 2.0 should be 4.00 $N_A\mu_B$). Additionally, the experimental values of the reduced magnetization for equal temperatures (Figure G.21) and equal magnetic fields (Figure G.22) do not superimpose, which further indicates the presence of magnetic anisotropy. Susceptibility and magnetization data were fitted simultaneously with PHI, using the Hamiltonian in Equation 3.7 with *S* = 2 and an isotropic *g*-factor. The best fit resulted in *g* = 2.188(2), *D* = 12.74(9) cm^{-1} and *E* = 2.83(8) cm^{-1} with a residual of *R* = 1.4 · 10^{-3}. The fit is

displayed as solid lines in the corresponding plots. Similar to **C16**·1MeCN, the parameters describe a spin-orbit coupled Fe(II) high-spin system with an *easy-plane* type of magnetic anisotropy and an |*E*/*D*| ratio of 0.22, which is in line with literature.[292] Considering the low distortion in the complexes **C16**·1MeCN, **C16**·1MeOH and **C17**·3MeCN, it is very likely that the absence of SCO can be assigned to the present ligand field splitting energy, which seems to be too low. Using cyanoborohydride as coligand could solve this problem, as it offers the strongest ligand field in the group of used pseudohalides.

3.5.3 Solvatomorph of [Fe($\mathbf{L^{Py,1}}$)$(NCBH_3)_2$] (C18·1MeOH)

[Fe($L^{Py,1}$)$(NCBH_3)_2$] · 1MeOH (C18·1MeOH) was prepared by using $\mathbf{L^{Py,1}}$ and $[Fe(py)_4(NCBH_3)_2]$ as starting materials. The compound crystallizes in the monoclinic space group *C*2/*c* with eight formula units inside of the unit cell. The crystal structure was measured at 173 K, crystallographic data can be found in Table D.9. The asymmetric unit consists of one complex and one methanol molecule (Figure F.47). The unit cell is constructed by symmetry operations through the present centers of inversion, two-fold rotation and screw axes and glide planes (Figure F.48 and Figure F.49). It should be noted that the obtained crystallographic data are of rather bad quality with R_{int} = 19.8 %, $R_1[I \geq 2\sigma(I)]$ = 20.8 % and wR_2 = 43.3 %. Analogous to the afore described mononuclear iron(II) complexes, **C18**·1MeOH offers the molecular structure discussed in Chapter 3.4.1. An average metal-ligand bond distance of $\bar{d}$(Fe-N) = 2.17 Å is found, which is representative for an iron(II) high-spin structure at 173 K (Table E.8). However, the distortion of the octahedral coordination sphere is very low compared the solvatomorphs of **C16** and **C17**. Thus, the octahedral distortion parameter $\Sigma_O(FeN_6)$ is found to be 93 °, next to CShM(O_h) = 1.17 (Figure 3.63). Such distortion is usually too large for a pure LS state of an FeN_6 coordination sphere, but also too low for pure HS state. This finding could be explained by a superposition of LS and HS molecules in the crystal structure at the given temperature of 173 K and could hint towards a spin transition.

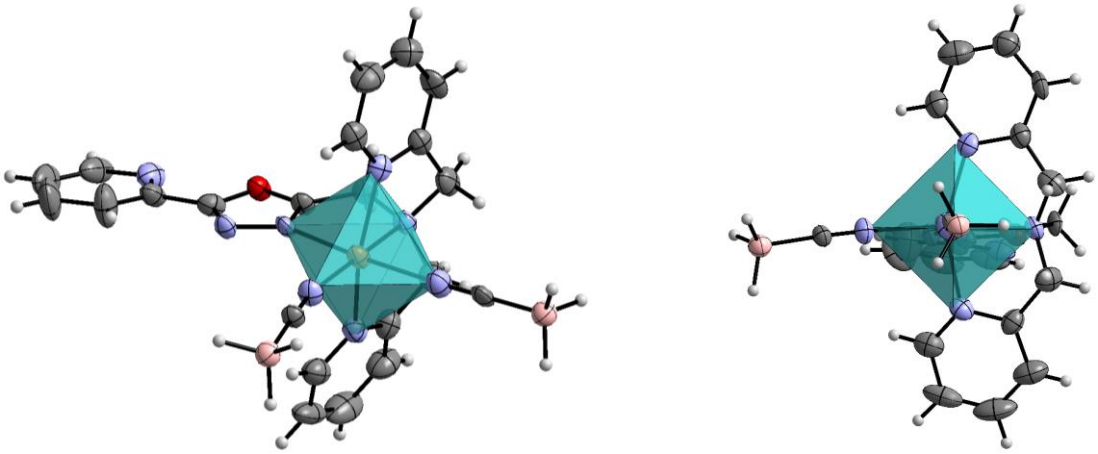


Figure 3.63 Molecular structure of **C18**·1MeOH and its ideal coordination octahedron with front view (left) and view along the Fe-N5 axis (right), calculated with SHAPE.[62] Colour scheme: dark grey – C, grey – H, violet – N, red – O, bright orange – Se, orange – Fe. ORTEP representation with atomic displacement parameters set to 50 % probability.

Three unique intermolecular π-π interactions can be found in the crystalline phase of **C18**·1MeOH. The first non-classical C-H···π hydrogen bond links complex molecules along the c-axis and takes place between an axially coordinated pyridine ring and the pyridyl moiety in 2-position of the oxadiazole. Here, the involved C-H moiety is labeled as C13-H13, while the least-squares mean plane A involves N8, C3, C4, C5, C6 and C7.

This interaction can be categorized as type III (see Chapter 3.4.1). Next to the *interaction distance* of d_{QH} = 2.9 Å, an *offset* of r = 0.7 Å is found. The two relevant angles are equal to α = 145 ° and β = 76 ° (Figure 3.64).

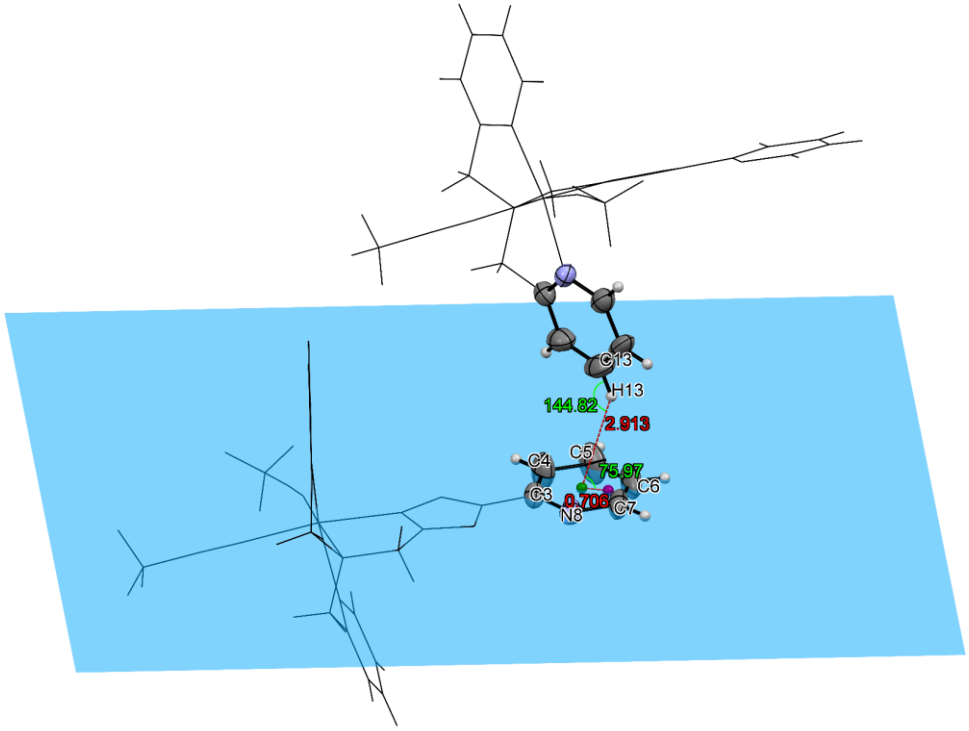


Figure 3.64 C-H···π interaction in **C18**·1MeOH. Least-squares plane A is defined by N8, C3, C4, C5, C6 and C7. Interacting C-H fragment is labeled as C13-H13. Green point – center of the aromatic ring in A. Purple point – orthogonal intersection of H13 onto plane A. *Offset* r = 0.706 Å, *interaction distance* d_{QH} = 2.913 Å, α = 144.82 ° and β = 75.97 °. ORTEP representation with atomic displacement parameters set to 50 % probability.

This one-dimensional chain is connected to a neighboring chain through two additional π-π interactions. The first one can be described as parallel π-π stacking between the pyridine rings attached to the oxadiazole moiety of two molecules. Least-squares mean planes A and B are defined through N8, C3, C4, C5, C6 and C7. The *interplanar distance* is equal to d_{AB} = 3.3 Å, next to an *offset* of r = 1.9 Å. Both planes are exactly parallel to each other, meaning that the *interplanar angle* θ is zero (Figure F.50). The second crosslinking π-π interactions can be found between the same molecules as described before. Consequently, the pyridine (attached to the oxadiazole) exhibits an intermolecular T-shape π-π interactions to the pyridine ring, which is attached to the amine function. The C-H fragment is labeled as C6-H6, while the involved plane A is defined through N3, C11, C12, C13, C14 and C15. The interaction can be categorized as type V. The present geometric parameters are d_{QH} = 3.2 Å, r = 1.1 Å, α = 155 ° and β = 69 ° (Figure F.51).

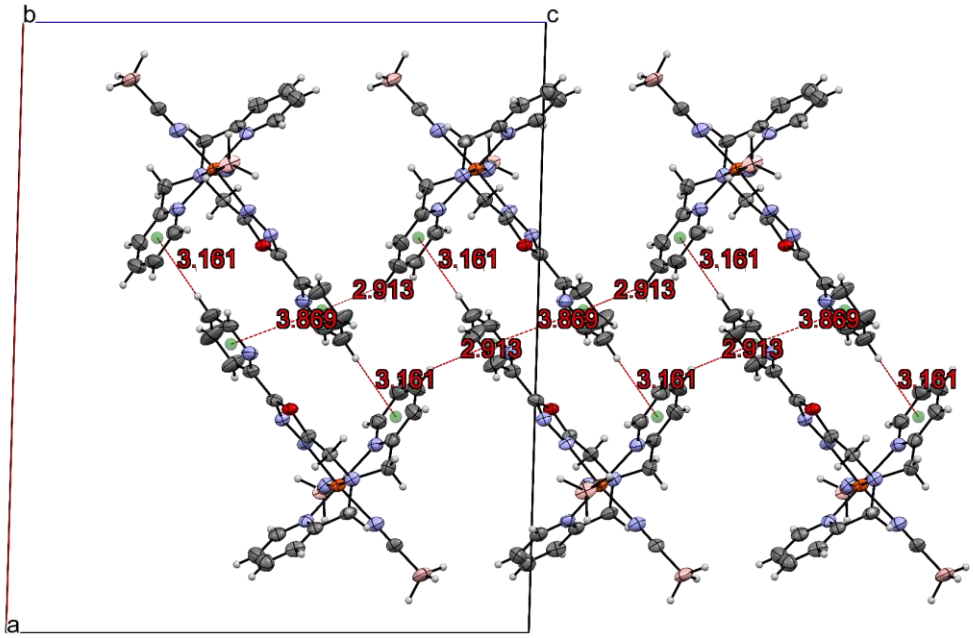


Figure 3.65 One-dimensional network of "complex dimers" in **C18**·1MeOH. Red dashed lines represent intermolecular distances. Colour scheme: pink – B, dark grey – C, grey – H, violet – N, red – O, orange – Fe. ORTEP representation with atomic displacement parameters set to 50 % probability.

Due to these three unique intermolecular interactions, a one-dimensional chain of "dimers" is formed along the c-axis (Figure 3.65), which is similar to the network of complex molecules in the packing of **C16**·1MeOH. The solvent molecules are located in channels between the described chains along the c-axis (Figure 3.66).

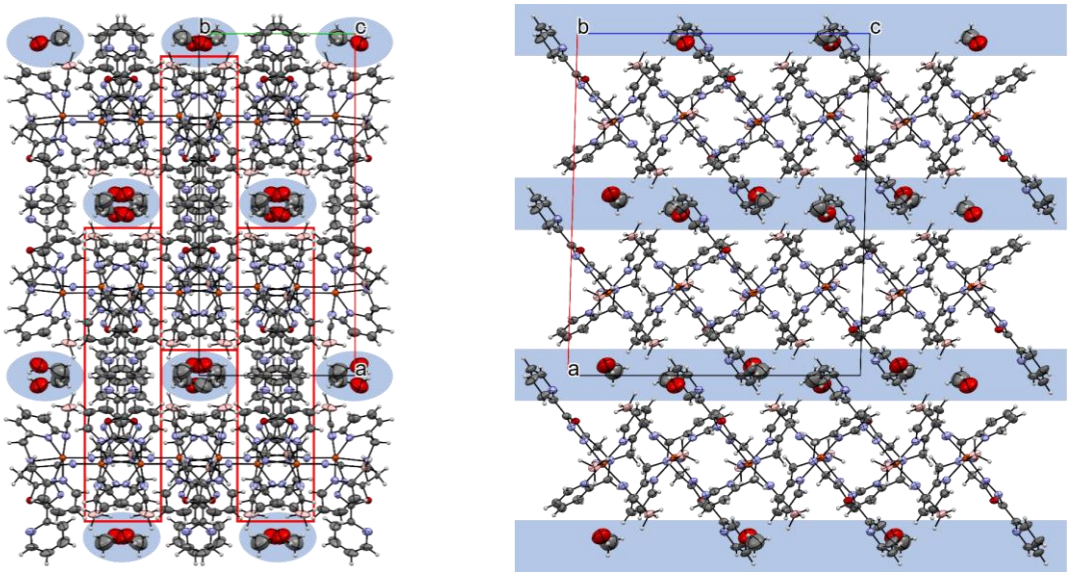


Figure 3.66 Packing of **C18**·1MeOH with view along the c-axis (left) and view along the b-axis (right). Red rectangles mark the one-dimensional chains of complex molecules along the c-axis. Blue areas illustrate the channel of solvent molecules. Colour scheme: pink – B, dark grey – C, grey – H, violet – N, red – O, orange – Fe. ORTEP representation with atomic displacement parameters set to 50 % probability.

Magnetic properties of C18·1MeOH

To investigate the possible SCO of **C18**·1MeOH in the crystalline phase, the molar susceptibility was determined in a temperature range between 300 K and 2 K. The resulting $\chi_M T$ *vs*. *T* plot is displayed in Figure 3.67. The $\chi_M T$ product stays constant from 300 K to 200 K at 3.85 $cm^3mol^{-1}K$. Below 200 K, $\chi_M T$ indeed decreases significantly to 2.68 $cm^3mol^{-1}K$ at 140 K. Further cooling leads to a minor drop of the $\chi_M T$ product to 2.30 $cm^3mol^{-1}K$ at 40 K, before it falls again significantly to 0.95 $cm^3mol^{-1}K$ at 2 K. Consequently, the magnetic moment of **C18**·1MeOH primarily changes between 300 K and 200 K and between 40 K and 2 K. The first decrease of $\chi_M T$ can be ascribed to an incomplete temperature induced spin crossover in the solid phase. Assuming that the plateau is reached at 80 K (2.43 $cm^3mol^{-1}K$), only 47 % of the complex molecules switched from the HS to the LS state. The second major decrease of $\chi_M T$ at very low temperatures can be attributed to zero-field splitting of the remaining HS molecules (*S* = 2 systems with $^5T_{2g}$ ground state). The solvatomorphs of **C16** and **C17** showed substantial *easy-plane* type magnetic anisotropy. Thus, it is very likely that the residual HS molecules of **C18**·1MeOH show the same magnetic behavior at low temperatures. Increasing the temperature from 2 K to 300 K leads to the same magnetic behavior. However, the spin transition temperature slightly shifts towards higher temperature. The critical transition temperature T_c can be seen in the first derivative of $\chi_M T$ with respect to *T* (Figure G.23). A transition temperature of $T_c^{\downarrow}$ = 160 K is found for the cooling process of the system. Increasing the temperature from low to high temperatures results in the critical temperature $T_c^{\uparrow}$ = 170 K, thus providing the system a thermal hysteresis of approx. 5 K.

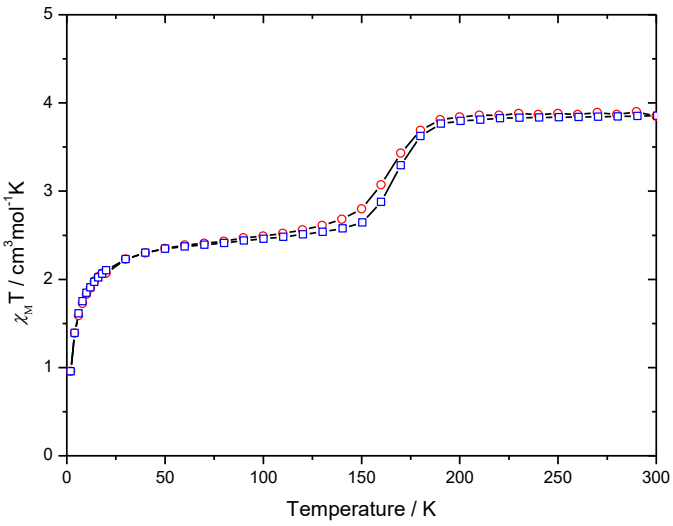


Figure 3.67 Temperature dependent magnetic behavior of **C18**·1MeOH in the form of a $\chi_M T$ *vs*. *T* plot. Measurement was done from 300-2 K (red open circles) and 2-300 K (blue open squares). Experimental points are connected through a solid line for clarity.

Spin transitions in form of thermal hysteresis are often observed in systems with a high *degree of cooperativity*, which describes the prolongation of the spin transition in the lattice. Intermolecular interactions, like the present π-π interactions, can enhance this *cooperativity*.[109] It is well known in literature, that an incomplete SCO can occur due to defects in the crystal lattice. Especially the loss of lattice solvent molecules tends to stabilize the HS state.[133] In order to avoid this effect, freshly prepared single crystals of **C18**·1MeOH were remeasured in mother liquor, such that the crystals have not been exposed to air at any time. The $\chi_M T$ *vs*. *T* plot is displayed in Figure 3.68. The sample was measured from 300 K to 70 K to 400 K, followed by a subsequent measurement down to 2 K. The $\chi_M T$ product stays constant from 300 K to 200 K at approx. 3.8 cm^{3}mol^{-1}K. Starting at this temperature, the $\chi_M T$ value decreases very abruptly to 0.24 cm^{3}mol^{-1}K at 150 K. Below this temperature, $\chi_M T$ runs into a plateau at 0.15 cm^{3}mol^{-1}K. The subsequent measurement towards 400 K resulted in the same magnetic behavior of the sample. Thus, the first derivative of $\chi_M T$ with respect to *T* (Figure G.24) yields a transition temperature of $T_c^{\downarrow} = T_c^{\uparrow} = 165$ K. The abrupt transition from high- to low-spin can be explained by the afore described intermolecular π-π interactions in the crystal structure of **C18**·1MeOH, which yields in a high *degree of cooperativity*. Lowering the temperature from 400 K to 30 K results in a gradual increase of $\chi_M T$ from 3.85 cm^{3}mol^{-1}K to 4.40 cm^{3}mol^{-1}K, followed by the significant drop of the $\chi_M T$ product to 2.23 cm^{3}mol^{-1}K at 2 K. Heating the sample to 400 K leads to the evaporation of the mother liquor and the lattice solvents. The loss of solvent molecules most likely induced defects in the crystal lattice to such extend, that a spin crossover is no longer possible in the solid state.

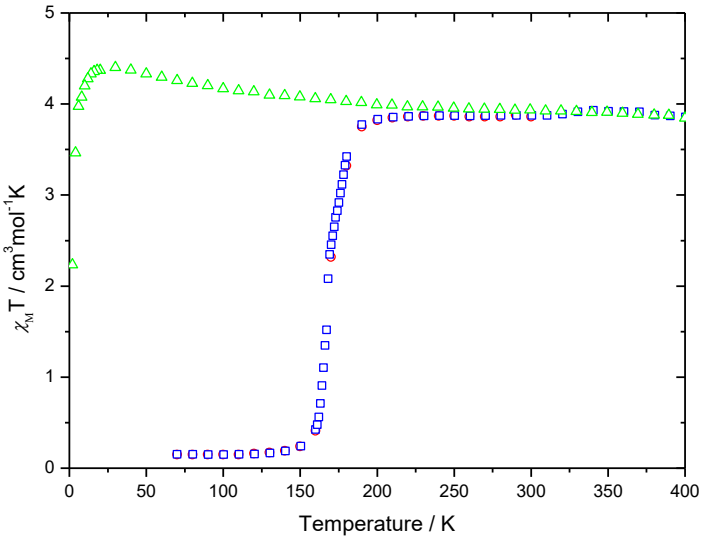


Figure 3.68 Temperature dependent magnetic behavior of single crystals of **C18**·1MeOH in mother liquor in the form of a $\chi_M T$ *vs*. *T* plot. Measurement was done from 300-70 K (red open circles), 70-400 K (blue open squares) and 400-2 K (green open triangles).

The gradual rise of the magnetic moment towards 30 K can be explained by the orientation of the sample inside of the magnetic field, since the sample was not embedded in eicosane. Below 30 K the effect of zero-field splitting becomes apparent.

At the time of writing this work, **C18**·1MeOH is thus the third reported oxadiazole-coordinated complex (next to the compounds $[Fe_2(\mu_2\text{-}\mathbf{PMOD})_2](ClO_4)_4 \cdot 4CH_3CN$ and $[Fe_2(\mu_2\text{-}\mathbf{PMOD})_2](CF_3SO_3)_4 \cdot 2CH_3CN$)[20] that shows a thermally induced SCO. As expected, the use of two monodentate coligands with sufficient ligand field strength led to a mononuclear complex with low distortion and a suitable ligand field splitting energy. Both properties allowed the spin transition from the HS to the LS state, which has not been observed for the former discussed dinuclear coordination compounds. The pyridine ring in the 2-position of the oxadiazole moiety does not participate in the coordination of the metal center. Assuming that the ligand field strength is nearly independent of this pyridinyl group, two novel ligand systems with different aromatic rings were synthesized. Different intermolecular interaction might lead to a changed spin transition behavior.

3.6 Mononuclear coordination compounds of L^{Ph}

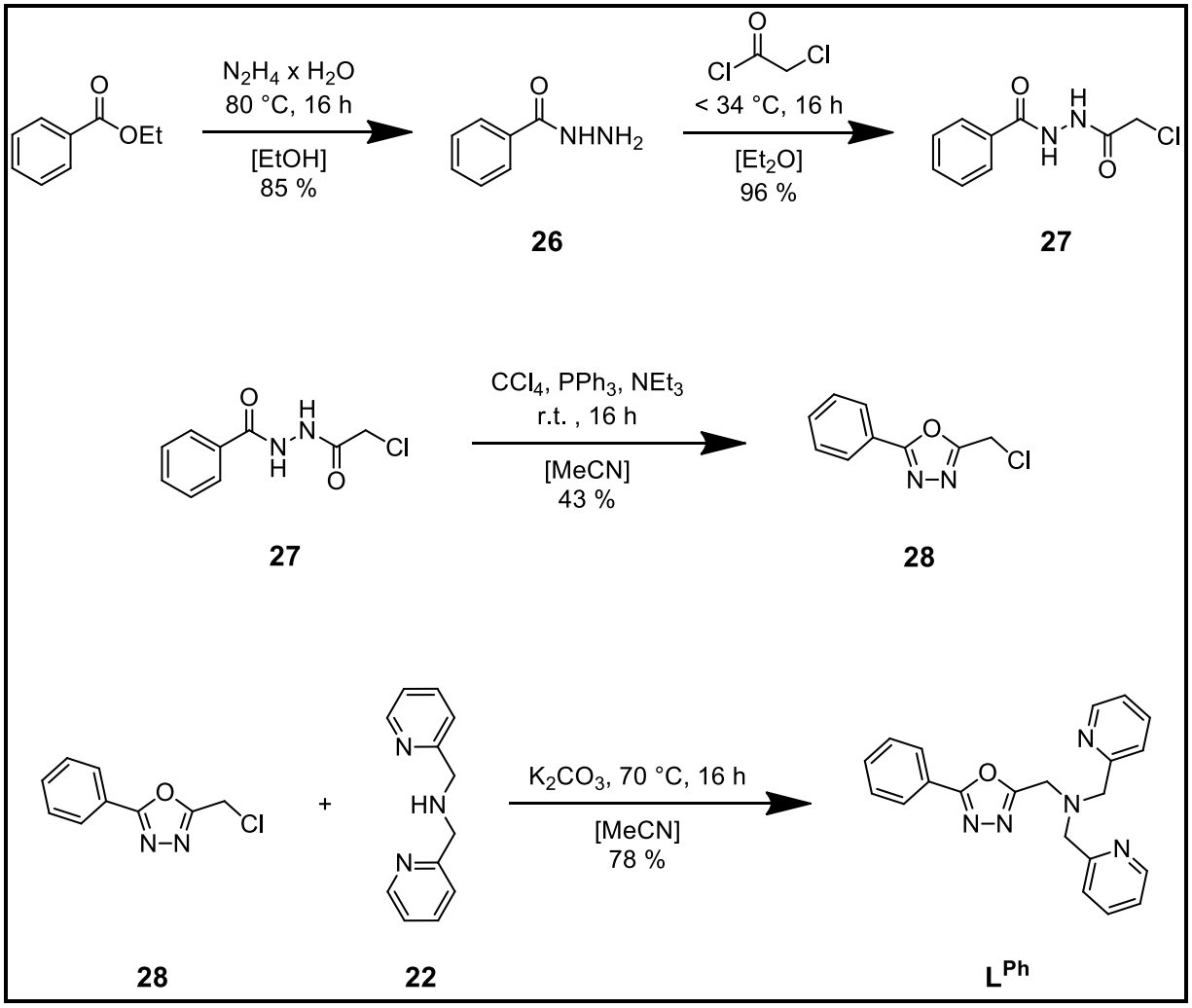


Figure 3.69 Synthesis scheme of L^{Ph}. The synthesis of **26** is already known in literature and was adapted with minor changes.[293]

Inspired by the ligand system 2-(2-pyridyl)-5-[N,N-bis(2-pyridylmethyl)aminomethyl]-1,3,4-oxadiazole ($L^{Py,1}$), the novel ligand 2-phenyl-5-[N,N-bis(2-pyridylmethyl)aminomethyl]-1,3,4-oxadiazole (L^{Ph}) was synthesized in a 4-step synthesis (Figure 3.69). The synthetic route is similar to that of $L^{Py,1}$, except that ethyl benzoate was used as starting material. Benzoic acid hydrazide (**26**) was synthesized in a nucleophilic reaction of ethyl benzoate with hydrazine monohydrate in a yield of 85 %.[293] The following condensation reaction with chloroacetyl chlorid yielded N'-(2-chloroacetyl)benzohydrazide (**27**) in 96 % yield. The hydrazide compound **27** was used in a ring-closure reaction to form 2-(chloromethyl)-5-phenyl-1,3,4-oxadiazole (**28**) in a yield of 43 %. Analogous to the oxadiazole precursor **21** and **25**, the ring-closing was achieved by the use of the three-component system triphenylphosphine, carbon tetrachloride and triethylamine.[279–282] In the final step, L^{Ph} could be synthesized in a nucleophilic reaction of **28** and **22** in 78 % yield, using potassium carbonate as base.

The difference between **L**^{Ph} and **L**^{Py,1} is the aryl group in the 2-position of the oxadiazole. The pyridyl rest in **L**^{Py,1} was hence replaced by a phenyl group. This was done for two major reasons. Firstly, the effect of a different aryl group on the spin crossover phenomenon can be investigated. As shown in Chapter 3.5.3, the presence of π-π interactions are decisive for the appearance of the spin transition in the crystalline phase. A change of the aromatic system can lead to different intermolecular interactions, which ideally results in higher *degree of cooperativity*. Secondly, **L**^{Ph} only offers one tetradentate coordination pocket. A complexation reaction with, for instance, a transition metal perchlorate salt should no longer yield dinuclear complexes such as [Fe$_2$(μ_2-**L**^{Py,1})$_2$](ClO$_4$)$_4$ · 2MeNO$_2$ (**C15**). Rather, mononuclear complexes should be formed with weakly coordinating coligands like methanol, acetonitrile or perchlorate. This could allow to use of such complexes in the field of catalysis.

3.6.1 Solvatomorphs of [Fe(L^{Ph})(NCX)$_2$]-type complexes (X = S, Se) (C19 – C20)

Analogous to **L**^{Py,1}, **L**^{Ph} was used to synthesize solvatomorphs of [Fe(**L**^{Ph})(NCS)$_2$] and [Fe(**L**^{Ph})(NCSe)$_2$] to investigate the effect of the (changed) aryl group on the resulting ligand field strength. Thus, [Fe(py)$_4$(NCS)$_2$] and [Fe(py)$_4$(NCSe)$_2$] were used as starting materials to prepare the complexes [Fe(**L**^{Ph})(NCS)$_2$] · 2MeCN (**C19**·2MeCN)/[Fe(**L**^{Ph})(NCS)$_2$] · 3MeOH (**C19**·3MeOH) and [Fe(**L**^{Ph})(NCSe)$_2$] · 2MeCN (**C20**·2MeCN)/[Fe(**L**^{Ph})(NCSe)$_2$] · 3MeOH (**C20**·3MeOH), respectively. All four complexes are isomorphous, differing only in the lattice solvent molecules and crystalize in the monoclinic space group *C*2/*c* with 8 formula units inside of the crystal structure. The asymmetric unit contains one complex molecule, next to two or three solvent molecules. The molecular structure of the complex molecules agrees with the discussion Chapter 3.4.1. Average metal-ligand distances [$\bar{d}$(Fe-N)] as well as the distortion [Σ_O(FeN$_6$) and CShM(O$_h$)] of the complex molecules of **C19**·2MeCN, **C19**·3MeOH, **C20**·2MeCN and **C20**·3MeOH indicate a HS state at a temperature of 173 K. Relevant parameters and references are summarized in Table 3.5. Three unique intermolecular π-π interactions can be found. The first parallel-like π-π stacking takes place between two pyridine rings of two neighboring molecules, which results in a one-dimensional chain along the b-axis, similar to [Fe(**L**^{Py,1})(NCSe)$_2$] · 3MeCN (**C17**·3MeCN). As an example, this is shown for **C19**·2MeCN in Figure 3.70. Since the oxadiazole-phenyl rests are pointing approx. orthogonal to the chain direction, they can stack with the oxadiazole-phenyl fragments of adjacent chains. In addition to that, a T-shape π-π interactions between the phenyl ring and a pyridine moiety can be found between two chains. This type of crosslinking results in intermolecular connection of complex molecules in two dimensions Hence, a two-dimensional network of complex molecules via π-π interactions is formed in the crystalline phase of the solvatomorphs of **C19** and **C20**. Figure 3.71 illustrates this for the **C19**·2MeCN compound.

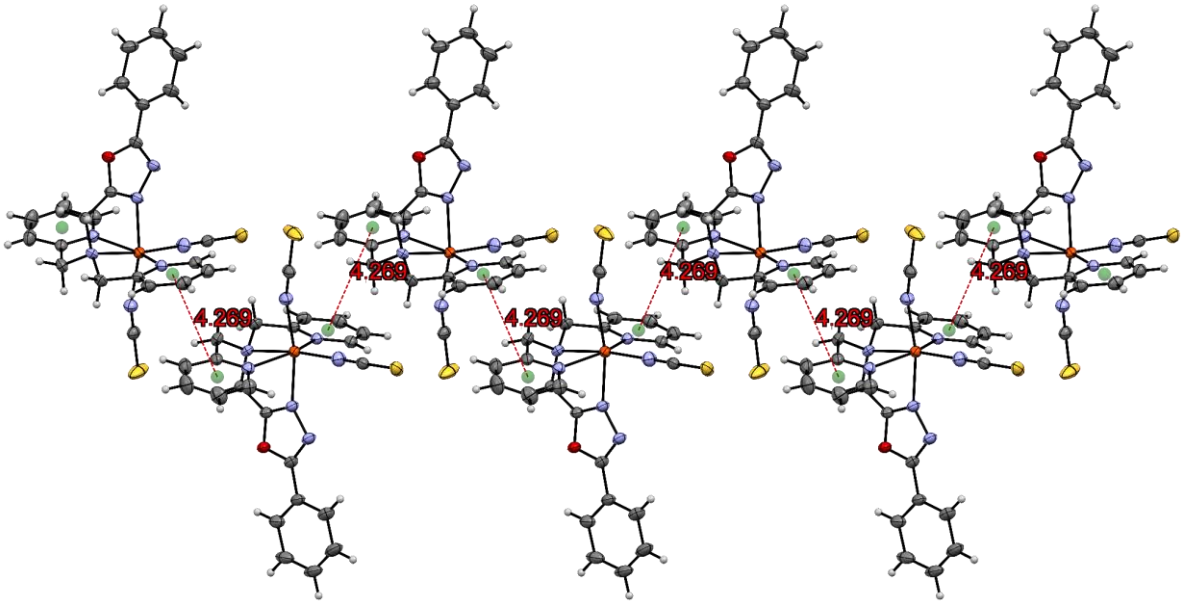


Figure 3.70 One-dimensional chain of complex molecules in **C19**·2MeCN due to intermolecular π-π stacking. The centers of involved aromatic rings are displayed as green points. Red dashed lines and numbers represent the distance between two centers. Colour scheme: dark grey – C, grey – H, violet – N, red – O, bright orange – Se, orange – Fe. ORTEP representation with atomic displacement parameters set to 50 % probability.

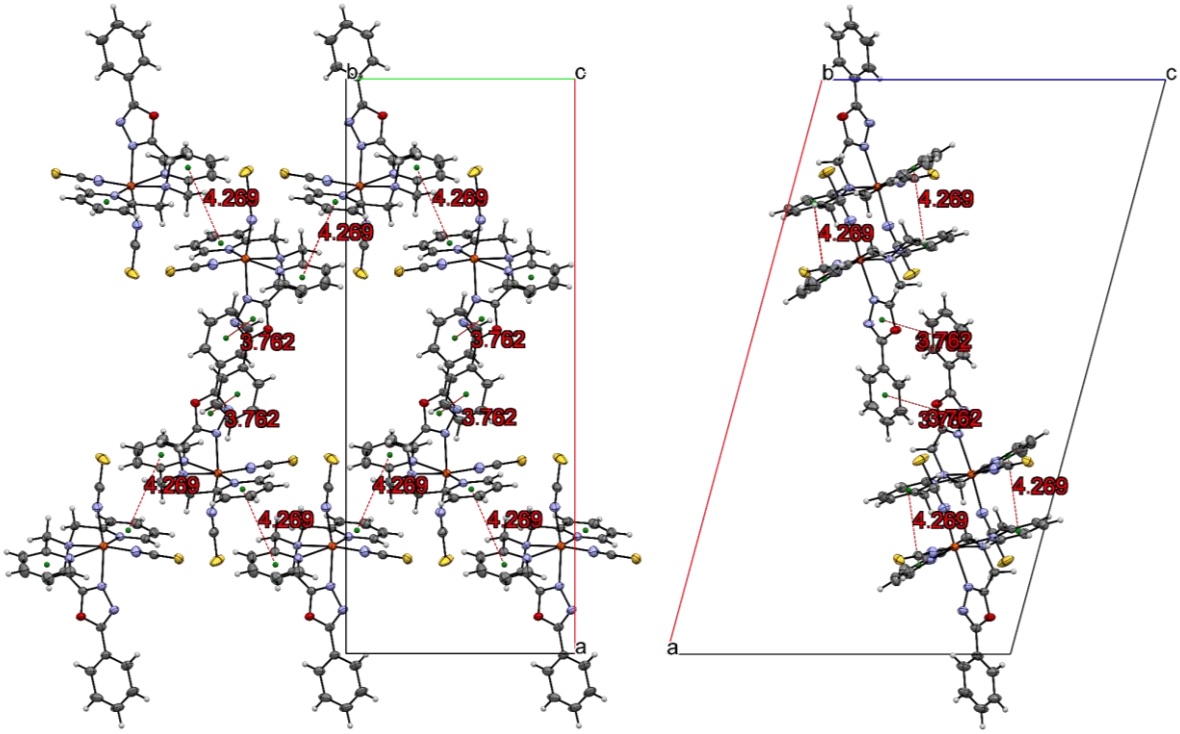


Figure 3.71 Two-dimensional network of complex molecules in **C19**·2MeCN due to intermolecular π-π interactions with view along the c-axis (left) and b-axis (right). The centers of involved aromatic rings are displayed as green points. Distances are displayed as red dashed lines and numbers. Solvent molecules are omitted for better vision. Colour scheme: dark grey – C, grey – H, violet – N, red – O, bright orange – Se, orange – Fe. ORTEP representation with atomic displacement parameters set to 50 % probability.

Table 3.5 Important parameters and internal references of **C19**·2MeCN, **C19**·3MeOH, **C20**·2MeCN and **C20**·3MeOH.

	[Fe(**L**^{Ph})(NCS)$_2$] · 2MeCN (**C19**·2MeCN)	[Fe(**L**^{Ph})(NCS)$_2$] · 3MeOH (**C19**·3MeOH)	[Fe(**L**^{Ph})(NCSe)$_2$] · 2MeCN (**C20**·2MeCN)	[Fe(**L**^{Ph})(NCSe)$_2$] · 3MeOH (**C20**·3MeOH)
Crystallographic data	Table D.9	Table D.10	Table D.10	Table D.11
Unit Cell	Figure F.52	Figure F.58	Figure F.64	Figure F.70
Π(**CX**/**C19**·2MeCN)	0.000	0.011	0.008	0.003
Pyridine-Pyridine-π-π interaction	d_{AB} = 4.09 Å *r* = 1.24 Å θ = 18.4 ° Figure F.53	d_{AB} = 3.98 Å *r* = 1.13 Å θ = 16.9 ° Figure F.59	d_{AB} = 4.18 Å *r* = 1.35 Å θ = 17 ° Figure F.65	d_{AB} = 4.03 Å *r* = 1.26 Å θ = 16.8 ° Figure F.71
Phenyl-Oxadiazole-π-π interaction	d_{AB} = 3.27 Å *r* = 1.87 Å θ = 2.7 ° Figure F.54	d_{AB} = 3.27 Å *r* = 1.93 Å θ = 5.6 ° Figure F.60	d_{AB} = 3.26 Å *r* = 1.85 Å θ = 3 ° Figure F.66	d_{AB} = 3.26 Å *r* = 1.91 Å θ = 5.9 ° Figure F.72
Phenyl-Pyridyl-π-π interaction (T-shape)	d_{QH} = 2.91 Å *r* = 0.36 Å α = 147.7 ° β = 82.9 ° Figure F.55	d_{QH} = 2.75 Å *r* = 0.11 Å α = 156.6 ° β = 87.7 ° Figure F.61	d_{QH} = 2.94 Å *r* = 0.32 Å α = 149 ° β = 84 ° Figure F.67	d_{QH} = 2.74 Å *r* = 0.12 Å α = 156.8 ° β = 87.5 ° Figure F.73
Two-dimensional network	Figure F.56	Figure F.62	Figure F.68	Figure F.74
$\bar{d}$(Fe-N)	2.18 Å	2.18 Å	2.17 Å	2.18 Å
Σ_O(FeN$_6$) | CShM(O$_h$)	105.1 ° | 1.44	104.2 ° | 1.38	101 ° | 1.41	99.6 ° | 1.33
Visualization of distortion	Figure F.57	Figure F.63	Figure F.69	Figure F.75
Structural parameters	Table E.8	Table E.8	Table E.9	Table E.9

Magnetic properties of the solvatomorphs of C19 and C20

Solvatomorphs of **C19** and **C20** have been investigated with respect to their temperature dependent magnetic behavior. Therefore, the molar susceptibilities were determined in a temperature range from 300-2 K and plotted as χ_M *vs*. *T* or $\chi_M T$ *vs*. *T* plots in Figure 3.72. Additionally, magnetization data were taken from 2-10 K in external fields of 0.1 – 7 T. All samples were embedded in eicosane to prevent a macroscopic orientation of single-crystals in the gelatin capsule. The complexes [Fe($\mathbf{L}^{Py,1}$)(NCS)$_2$] (**C16**·1MeCN/ **C16**·1MeOH) and [Fe($\mathbf{L}^{Py,1}$)(NCSe)$_2$] (**C17**·3MeCN) stabilized the HS state at any temperature. Since the aryl group in the 2-position of the oxadiazole does not coordinate at the iron(II) center, the solvatomorphs of **C19** and **C20** are also expected to show no SCO. Indeed, all complexes show a $\chi_M T$-value between 3.75-4.00 cm^{3}mol^{-1}K that stays constant until approx. 50 K. Below this temperature, the $\chi_M T$ decreases significantly, which can be ascribed to the effect of ZFS on the magnetic moment. Thus, no spin transition can be observed for the crystalline samples. Fitting was done by applying the spin Hamiltonian in Equation 3.7 to susceptibility and magnetization data simultaneously in PHI.[201] Here, axial (*D*) and transverse magnetic anisotropy (*E*) were assumed, as well as an isotropic *g*-factor of the *S* = 2 systems.

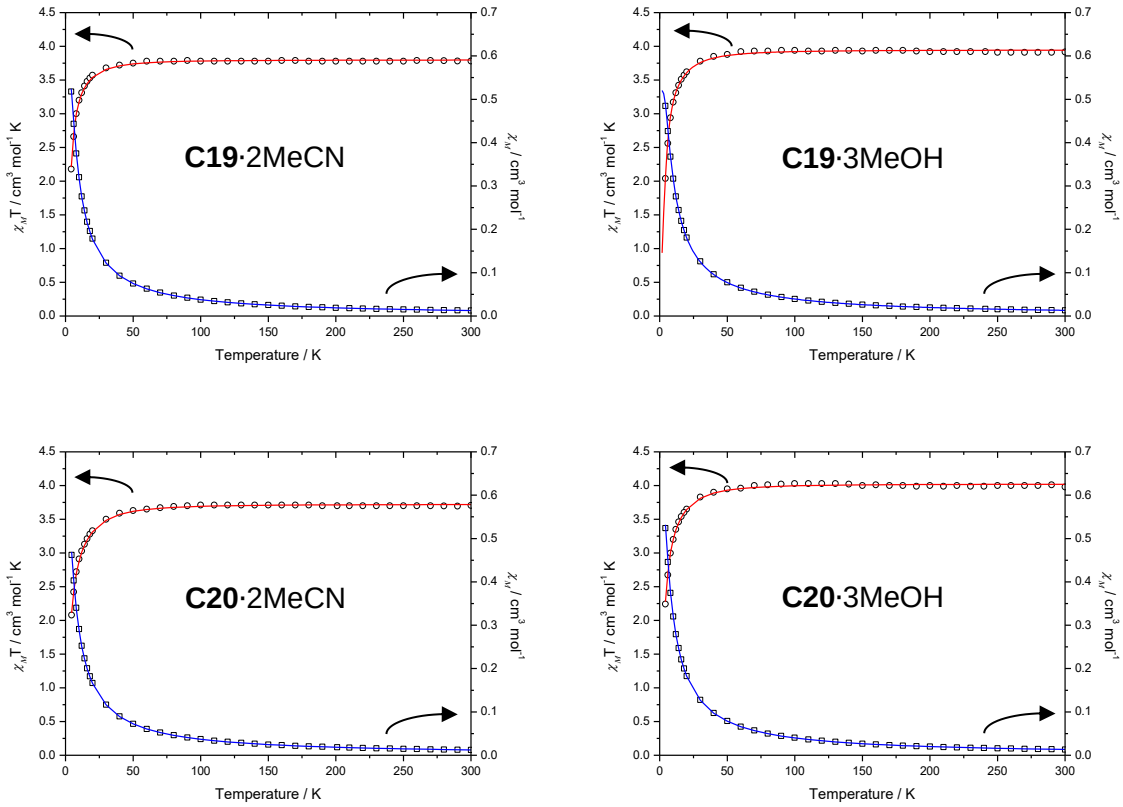


Figure 3.72 Temperature dependent magnetic behavior of **C19**·2MeCN (top left), **C19**·3MeOH (top right), **C20**·2MeCN (bottom left) and **C20**·3MeOH (bottom right) in the form of combined $\chi_M T$ *vs*. *T* (left values, red open circles) and χ_M *vs*. *T* plots (right values, blue open squares).

The results of the fitting are recapped in Table 3.6. All complexes offer a *g*-factor around 2.3, which can be attributed to first-order spin-orbit coupling of the $^5T_{2g}$ ground state due to incomplete quenching of the orbital momentum.[67] The positive values of the axial distortion parameter *D* vary between 9.9(1) and 12.02(2) cm^{-1}. Such values reveal an *easy-plane* type of magnetic anisotropy and are the result of a compressed distortion of the O_h symmetry.[292] Further, a transverse magnetic anisotropy is present in the solvatomorphs of **C19** and **C20**, with values for *E* between 0.5(1) and 2.4(1) cm^{-1}. Since these mononuclear iron(II) complexes are isostructural and isomorphous, similar parameters were expected. All values are in good agreement with those of literature for octahedral coordinated iron(II) complexes.[292,294]

Table 3.6 Fitting results and references of the solvatomorphs of **C19** and **C20**. Fitting was done by applying the spin Hamiltonian in Equation 3.7 to susceptibility and magnetization data simultaneously in PHI.[201]

	C19·2MeCN	**C19**·3MeOH	**C20**·2MeCN	**C20**·3MeOH
g-factor	2.254(2)	2.293(1)	2.227(1)	2.3156(5)
D / cm^{-1}	9.9(1)	10.63(4)	12.02(8)	10.85(3)
E / cm^{-1}	1.7(1)	0.5(1)	2.4(1)	1.82(3)
E/*D* ratio	0.17	0.05	0.20	0.17
Residual *R*	$5.1 \cdot 10^{-3}$	$0.1 \cdot 10^{-3}$	$0.3 \cdot 10^{-3}$	$0.4 \cdot 10^{-3}$
M vs. *H* plot	Figure G.25	Figure G.28	Figure G.31	Figure G.34
M vs. *H*/*T* plots	Figure G.26 & Figure G.27	Figure G.29 & Figure G.30	Figure G.32 & Figure G.33	Figure G.35 & Figure G.36

The exchange of the pyridyl group with a phenyl rest in the 2-position of the oxadiazol led to different packing in the crystalline phase, yet the coordination mode of the ligand is unchanged. Therefore, the magnetic behavior in the solid state did not change. The ligand field strength of NCS and NCSe is still too low to generate a ligand field splitting energy suitable for SCO, which results in a constant high-spin state.

3.6.2 Solvatomorphs of [Fe(L^{Ph})(NCBH$_3$)$_2$] (C21)

Compounds [Fe(**L**^{Ph})(NCBH$_3$)$_2$] · 1MeCN (**C21**·1MeCN) and [Fe(**L**^{Ph})(NCBH$_3$)$_2$] · 1.8MeOH (**C21**·1.8MeOH) were synthesized by using the precursor [Fe(py)$_4$(NCBH$_3$)$_2$], since the **L**^{Ph}-based complexes **C19** and **C20** show no thermally induced spin transition. The coordination compounds were isolated in form of block shaped single-crystals that were suitable for X-ray structure analysis. To analyze the temperature dependent magnetic behavior, the molar susceptibility of both complexes was determined in a temperature range from 400-2 K and plotted as $\chi_M T$ *vs*. *T* plots. Figure 3.73 illustrates the magnetic measurement of **C21**·1MeCN in form of the resulting $\chi_M T$ *vs*. *T* plot. Data were taken from 300-130 K, followed by the subsequent measurements between 130-400 K and 400-2 K. The $\chi_M T$ value at 300 K is equal to 3.72 cm^{3}mol^{-1}K and stays constant upon cooling down to 250 K. The further decrease of the temperature results in a significant drop of the $\chi_M T$. The $\chi_M T$ product at 170 K is equal to 0.08 cm^{3}mol^{-1}K and decreases furthermore to a value of 0.04 cm^{3}mol^{-1}K at 130 K. This behavior of the magnetic moment illustrates a very abrupt SCO from the HS to the LS state of the mononuclear iron(II) complex **C21**·1MeCN. Heating the sample from 130 K to 300 K results in the same curve for $\chi_M T$. The value of $\chi_M T$ at 300 K (3.73 cm^{3}mol^{-1}K) stays constant to a temperature of 400 K. Lowering the temperature leads to a slight decrease of the $\chi_M T$ product to 3.66 cm^{3}mol^{-1}K at 250 K. Below this temperature, $\chi_M T$ starts to decrease more significantly. At 210 K however, the slope starts to flatten (see the enlarged plot in Figure G.37 in the Appendix).

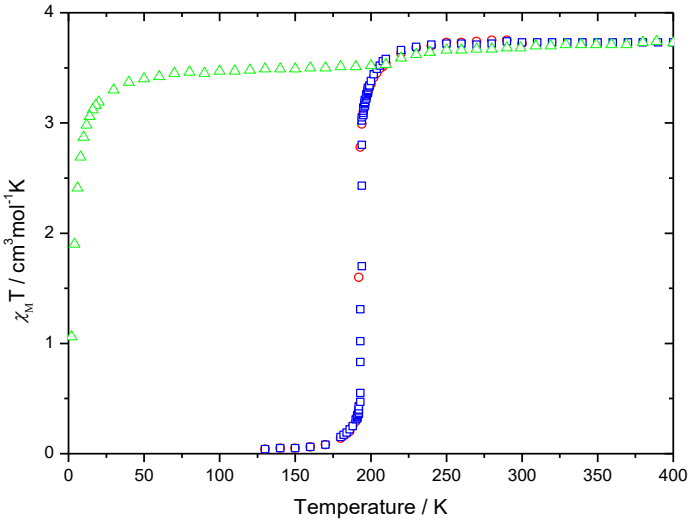


Figure 3.73 Temperature dependent magnetic behavior of single crystals of **C21**·1MeCN in the form of a $\chi_M T$ *vs*. *T* plot. Measurement was done from 300-130 K (red open circles), 130-400 K (blue open squares) and 400-2 K (green open triangles).

Thus, the magnetic moment falls only slightly until a temperature of 50 K is reached. At the low temperature regime, the value of $\chi_M T$ drops very fast towards 1.06 cm^{3}mol^{-1}K. The measurement from 400 K to 2 K shows an incomplete spin transition, where only approximately 5 % of the HS molecules in the lattice switch to the low-spin state. At lower temperature, the effect of ZFS on the magnetic moment becomes visible. The absence of the SCO ability upon solvent loss is a literature known phenomenon and has already been observed in **C18**·1MeOH.[133] The first derivative of $\chi_M T$ with respect to the temperature *T* reveals a transition temperature of $T_c^{\downarrow} = T_c^{\uparrow}$ = 194 K (Figure G.38), which is 29 K higher than the critical temperature in **C18**·1MeOH ($T_c^{\downarrow} = T_c^{\uparrow}$ = 165 K). *Formally*, the ligand field in **C21**·1MeCN is therefore higher than in **C18**·1MeOH. However, as discussed in the Chapters 3.1 – 3.3, the SCO is also dependent on the packing in the solid state. For this reason, the temperature only gives a limited indication of the ligand field strength. Furthermore, it is noticeable that the spin transition in **C21**·1MeCN is even more abrupt than in **C18**·1MeOH. The *degree of cooperativity* has thus been increased. Such curve progression of the SCO is most likely due to a pronounced connectivity of complex molecules in the lattice. To get an insight into the packing of **C21**·1MeCN in the crystalline state, X-ray structure analysis was performed at 240 K (HS state according to Figure 3.73) and 120 K (LS state).

Crystal structure of C21·1MeCN

The X-ray structure analysis of a single crystal of **C21**·1MeCN was performed at 240 K. Crystallographic Data can be found in Table D.11. The compound crystallizes in the monoclinic space group *C*2/*c* with 8 formula units inside of the unit cell, which comprises a volume of 5476.0(7) Å^3. The asymmetric unit is defined by one complex molecule next to one acetonitrile molecule, that shows disorder between two positions in close proximity (Figure F.76). The residual molecules in the unit cell are symmetry generated through the present centers of inversion, 2-fold rotation and screw axes, and glide planes (Figure F.77 and Figure F.78). The structure and the bond-length tendency follow the general discussion of Chapter 3.4.1 for mononuclear complexes. As expected from the magnetic data, the structure of **C21**·1MeCN at 240 K reflects a HS structure. This statement is based on the average metal-ligand distance of $\bar{d}$(Fe-N) = 2.18 Å and the distortion of the octahedral coordination sphere with Σ_O(FeN$_6$) = 97.3 ° and CShM(O$_h$) = 1.24. All structural parameters are given in Table E.9. In analogy to the afore described mononuclear iron(II) complexes, the largest deviation from the ideal coordination sphere arises from the apically coordinated pyridine moieties with an enclosed *trans*-angle of 151.6 ° (*vs*. 180 ° in an ideal octahedron). It is noticeable that the distortion of the complex molecule of **C21**·1MeCN at 240 K is greater than that of **C18**·1MeOH at 173 K. According to the magnetic data in Figure 3.68, this finding is probably attributed to the fact that the structure of **C18**·1MeOH shows a superposition of HS and LS molecules at

173 K. Comparison of the molecular structure and cell parameters shows that **C21**·1MeCN crystalizes isomorphous to the $\mathbf{L}^{Py,1}$-based complex **C18**·1MeOH with Π(**C18**·1MeOH/**C21**·1MeCN) = 0.019. Due to that fact, the intermolecular connections between the complex molecules are roughly equal. Three unique π-π interactions can be found in the crystalline state, leading to a one-dimensional chain of complex molecules along the c-axis, illustrated in Figure 3.74.

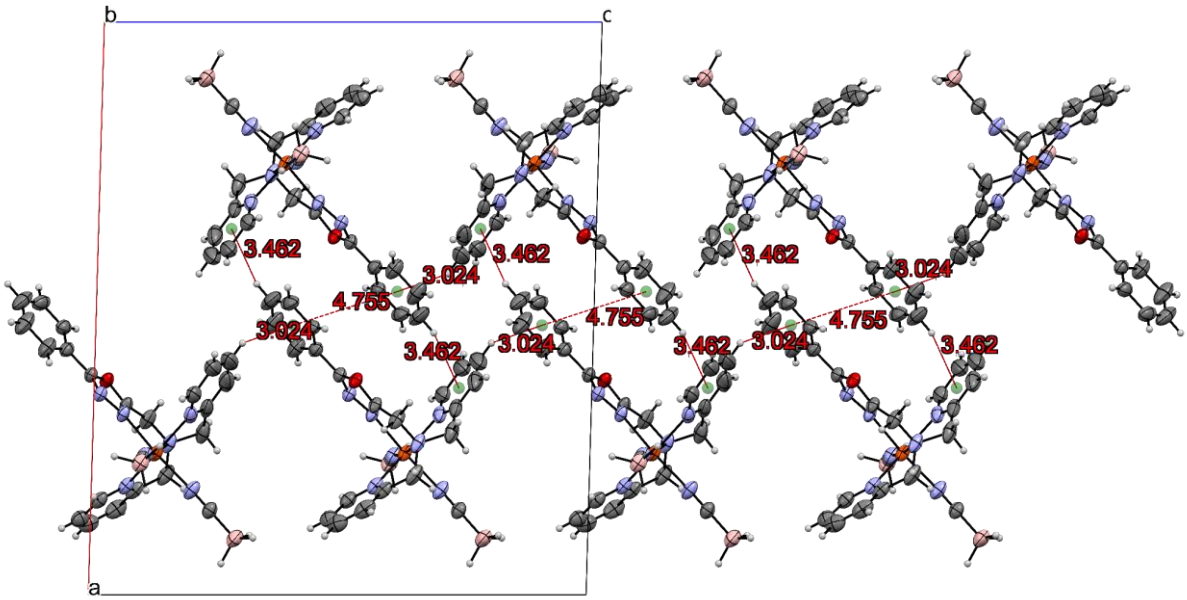


Figure 3.74 One-dimensional network of "complex dimers" in **C21**·1MeCN. Red dashed lines represent intermolecular distances. Colour scheme: pink – B, dark grey – C, grey – H, violet – N, red – O, orange – Fe. ORTEP representation with atomic displacement parameters set to 50 % probability.

The first interaction can be described as non-classical C-H···π hydrogen bond between complex molecules along the c-axis. Here, the pyridyl group points onto the π-system of the phenyl ring. The involved C-H moiety is labeled as C19-H19, whereas the least-squares mean plane A includes C1, C2, C3, C4, C5 and C6. The interaction can be categorized as type III (see Chapter 3.4.1). Hence, the *interaction distance* is equal to d_{QH} = 3.02 Å next to an *offset* of *r* = 1.19 Å and the two angles α = 130.2 ° and β = 66.8 ° (Figure 3.75). Due to two additional π-π interactions, two adjacent chains are crosslinked. The first interaction is defined through a parallel stacking of the phenyl groups of two complex molecules. Therefore, the least-squares mean planes A and B are defined by C1, C2, C3, C4, C5 and C6. Since both planes are orientated parallel to each other, the *interplanar angle* θ is equal to 0. The *interplanar distance* is equal to d_{AB} = 3.16 Å, next to an *offset* of *r* = 3.55 Å (Figure F.79). This *offset* is clearly larger than those described until this point. However, it is still below the maximum value of 3.6 Å, reported by *Saha* et al..[287] Furthermore, a second intermolecular T-shape π-π interaction can be found between the same two complex molecules mentioned above.

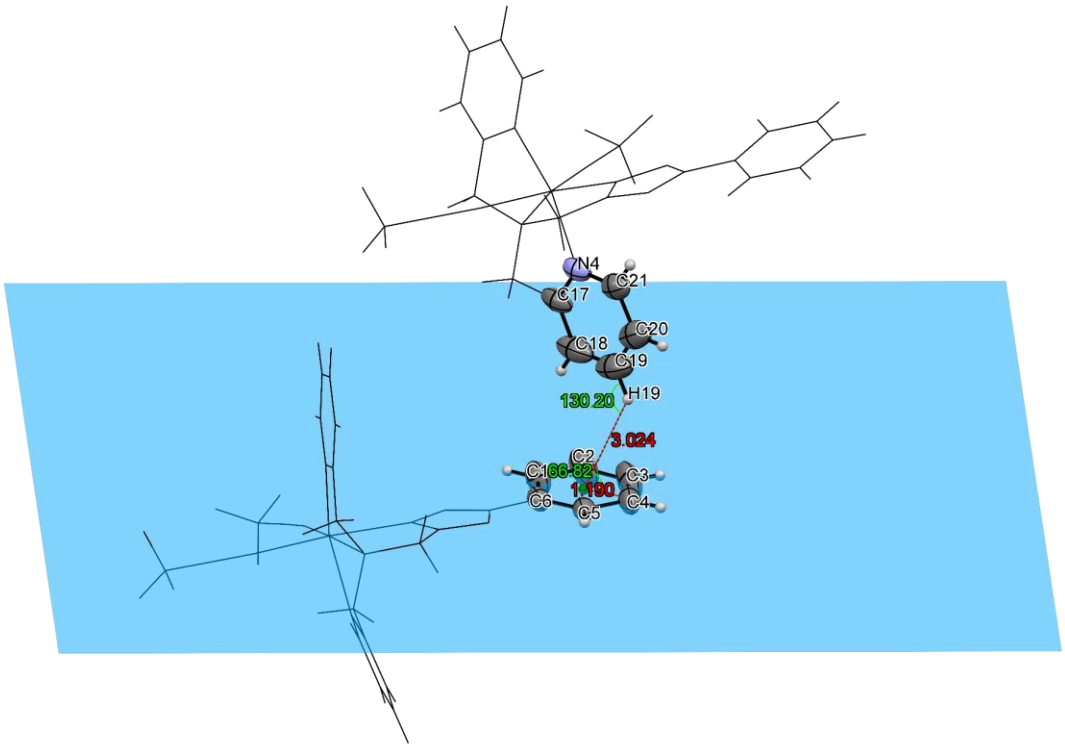


Figure 3.75 C-H···π interaction in **C21**·1MeCN (240 K). Least-squares plane A is defined by C1, C2, C3, C4, C5 and C6. Interacting C-H fragment is labeled as C19-H19. Green point – center of the aromatic ring in A. Purple point – orthogonal intersection of H19 onto plane A. *Offset r* = 1.19 Å, *interaction distance* d_{QH} = 3.02 Å, α = 130.2 ° and β = 66.8 °. ORTEP representation with atomic displacement parameters set to 50 % probability.

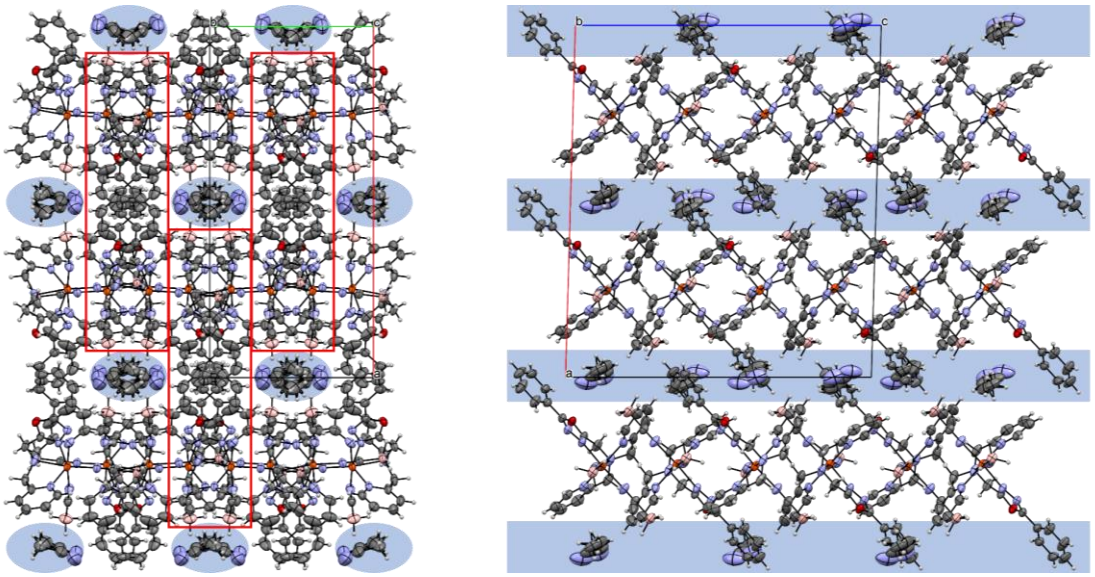


Figure 3.76 Packing of **C21**·1MeCN with view along the c-axis (left) and view along the b-axis (right). Red rectangles mark the one-dimensional chains of complex molecules along the c-axis. Blue areas illustrate the channel of solvent molecules. Colour scheme: pink – B, dark grey – C, grey – H, violet – N, red – O, orange – Fe. ORTEP representation with atomic displacement parameters set to 50 % probability.

Here, the phenyl group exhibits a non-classical C-H···π hydrogen bond of type V (see Chapter 3.4.1) to a pyridine function. The involved plane A includes N4, C17, C18, C19, C20 and C21, while the interacting C-H fragment is labeled as C4-H4. An *interaction distance* of d_{QH} = 3.42 Å is found next to an *offset* of r = 0.93 Å. The involved angles are α = 131.1 ° and β = 74.1 ° (Figure F.80). Solvent molecules can be found in channels in between the one-dimensional chains along the c-axis, which is illustrated in Figure 3.76.

The second single-crystal X-ray structure analysis of **C21**·1MeCN was performed at 120 K. Crystallographic Data can be found in Table D.12. Decreasing the temperature below the spin transition temperature does not yield in a phase change of the system. The compound still crystallizes in the monoclinic space group *C*2/*c* with eight formula units in the unit cell. However, the cell parameters changed to such extent, that the volume of the unit cell shrinks from 5476.0(7) Å³ to 5112.9(2) Å³. This is a reduction of the cell volume of approx. 7 %, which can be explained by the contraction of the FeN_6 coordination sphere in consequence of the SCO. According to literature, this volume reduction varies between 0 – 10 %.[58,295] It is noteworthy that the acetonitrile molecule in the asymmetric unit does not show disorder anymore (Figure F.81). This is consistent with the fact, that crystalline phases at low temperature show an higher degree of order.[296] Due to the changed cell parameters, intermolecular distances of π-π interactions changed as well. Thus, the iron(II)-iron(II) distances are shorter in the one-dimensional chain of complex molecules compared to those at 240 K (Figure 3.77).

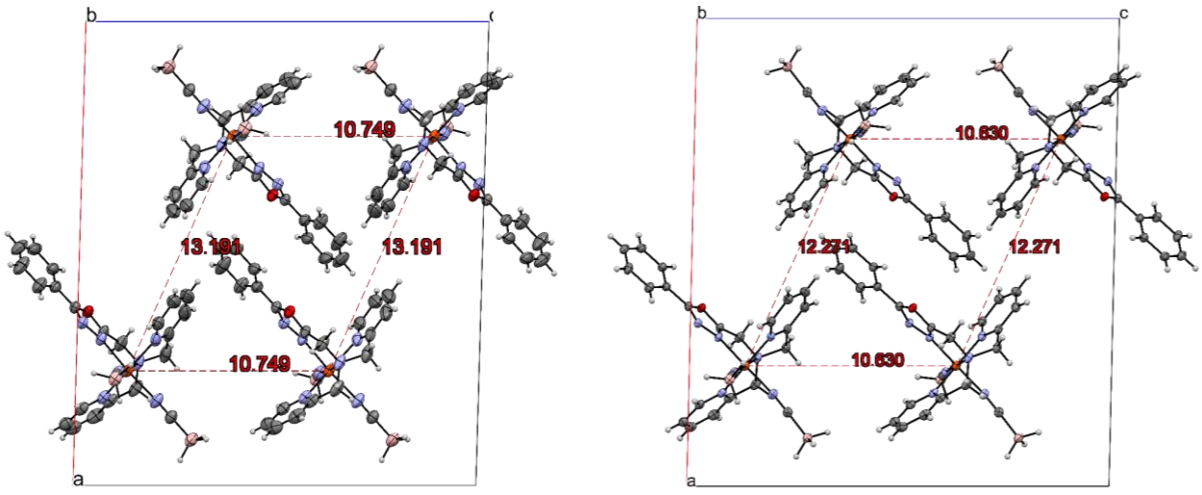


Figure 3.77 One-dimensional network of "complex dimers" in **C21**·1MeCN at 240 K (left) and 120 K (right). Unit cell changes are remarkably more pronounced along the a-axis, which corresponds to the interdimer short contacts. Red dashed lines represent intermolecular distances between iron(II) centers. Colour scheme: pink – B, dark grey – C, grey – H, violet – N, red – O, orange – Fe. ORTEP representation with atomic displacement parameters set to 50 % probability.

As expected, the coordination sphere of the iron(II) centers in the LS state differs to the one in the HS complex molecules. In the low-spin state, only the bonding t_{2g}-orbitals are occupied. Thus, there is no contribution of the antibonding e_g^*-orbitals to the metal-ligand bonds, which results in shorter bond distances. Next to that, the isotropic occupation of the t_{2g}-orbitals leads to smaller distortion of the coordination sphere in octahedral systems. The complex molecule of **C21**·1MeCN at 120 K shows an average metal-ligand bond length of $\bar{d}$(Fe-N) = 1.97 Å, which is 0.21 Å shorter than the mean bond distance at 240 K. The average Fe-N bond lengths in LS Fe(II)N_6 complexes usually are between 1.95 Å and 2.00 Å.[37,38] The deviation from the ideal coordination sphere of the LS molecules can be described with $\Sigma_O(FeN_6)$ = 49.4 ° and CShM(O_h) = 0.32. A comparison of the coordination sphere of both spin states is illustrated in Figure 3.78. The detailed summary of all structural parameters can be found in Table E.10.

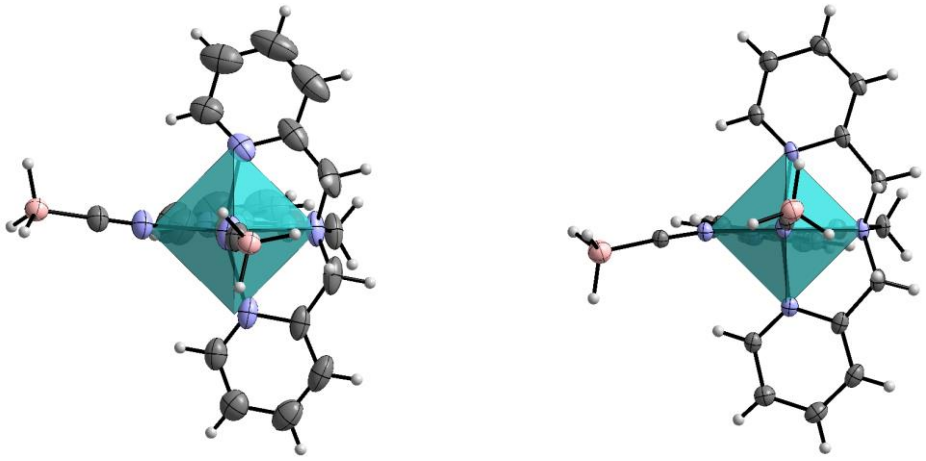


Figure 3.78 Molecular structure of **C21**·1MeCN and its ideal coordination octahedron with view along the Fe-N5 axis at 240 K (left) and 120 K (right), calculated with SHAPE.[62]. ORTEP representation with atomic displacement parameters set to 50 % probability.

[Fe($\mathbf{L^{Ph}}$)($\mathbf{NCBH_3)_2}$] · 1.8MeOH (C21·1.8MeOH) was synthesized in a similar way to **C21**·1MeCN with methanol as reaction solvent. The compound was investigated with single-crystal X-ray structure analysis at 173 K. Crystallographic data can be found in Table D.12. **C21**·1.8MeOH crystallizes in the monoclinic space group *C*2/*c* with eight formula units inside of the unit cell. However, due to disorder, solvent molecules could not be refined properly, which is why the SQUEEZE routine was applied.[297] The structure at the given temperature represents a LS structure of **C21**·1.8MeOH. Thus, the average metal-ligand bond length is equal to $\bar{d}$(Fe-N) = 1.98 Å accompanied by a low distortion of the coordination sphere with $\Sigma_O(FeN_6)$ = 50 ° and CShM(O_h) = 0.33 (Figure 3.79). The detailed summary of all structural parameters can be found in Table E.10. Since the cell parameter of SCO active species depend on the spin state of the metal center(s), the crystal structure of **C21**·1.8MeOH has to be compared to the structure of **C21**·1MeCN at 120 K.

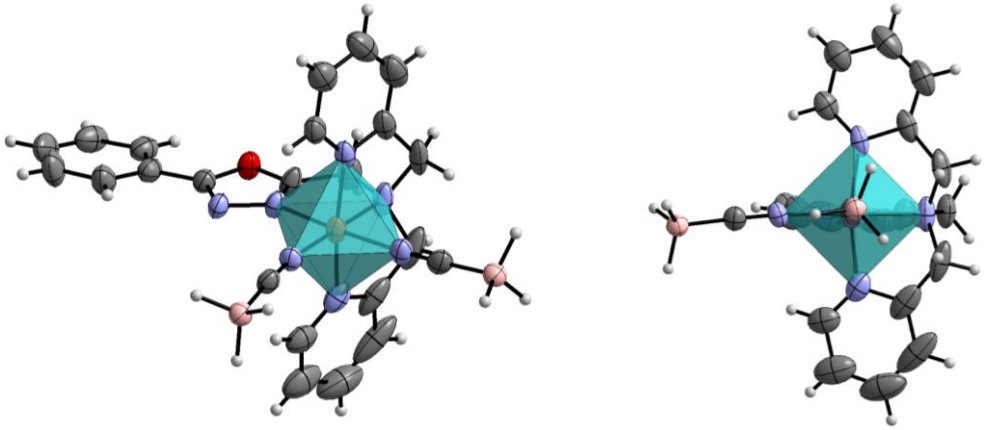


Figure 3.79 Molecular structure of **C21**·1.8MeOH and its ideal coordination octahedron with front view (left) and view onto the Fe-N5 axis (right), calculated with SHAPE.[62] ORTEP representation with atomic displacement parameters set to 50 % probability.

Both complexes are isomorphous with a *unit-cell similarity index* of Π(**C21**·1.8MeOH/**C21**·1MeCN) = 0.007. In analogy to the acetonitrile solvatomorph, three unique π-π interactions can be observed, leading to the formation of a one-dimensional chain of "dimer" complex molecules along the c-axis (Figure F.82). Relevant parameters of the intermolecular π-π interactions are summarized in Table F.3 with references to the corresponding figures. Figure 3.80 displays the packing of **C21**·1.8MeOH with view along the c-axis (left) and view along the b-axis (right). The afore mentioned chains of complex molecules are exemplarily marked with red rectangles for better understanding. Blue areas illustrate the solvent channels, where the (squeezed) methanol molecules are located.

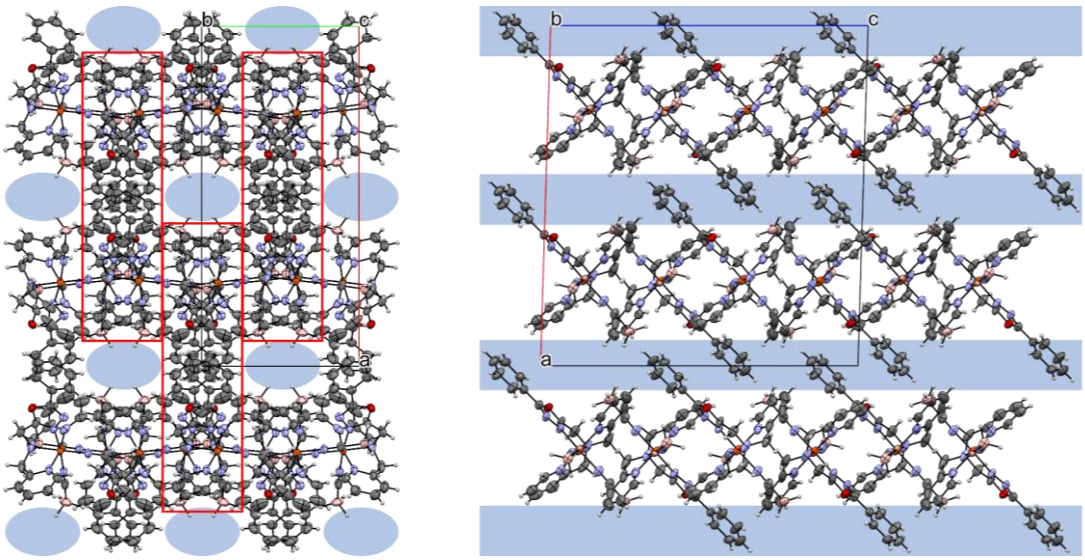


Figure 3.80 Packing of **C21**·1.8MeOH with view along the c-axis (left) and view along the b-axis (right). Red rectangles mark the one-dimensional chains of complex molecules along the c-axis. Blue areas illustrate the channel of solvent molecules. Colour scheme: pink – B, dark grey – C, grey – H, violet – N, red – O, orange – Fe. ORTEP representation with atomic displacement parameters set to 50 % probability.

Magnetic properties of C21·1.8MeOH

Temperature dependent magnetic behavior of **C21**·1.8MeOH was analyzed in four sequential measurements. The sample was set at 10 K and measured in the following sequences: 1) 10-300 K, 2) 300-90 K, 3) 90-400 K and 4) 400-2 K. The resulting $\chi_M T$ versus T plot is illustrated in Figure 3.81. At the start of the measurement (10 K), the $\chi_M T$ value is equal to 0.04 $cm^3mol^{-1}K$, which is representative for a pure iron(II) low-spin state. This value stays constant until 130 K. Above this temperature, $\chi_M T$ starts to rise significantly to a value of 3.52 $cm^3mol^{-1}K$ at 210 K. Further heating to 300 K only leads to a slightly increased $\chi_M T$ product of 3.63 $cm^3mol^{-1}K$. This value is higher than the *spin-only* value of a $S = 2$ system (3.00 $cm^3mol^{-1}K$), which can be explained by SOC of the $^5T_{2g}$-ground state. The temperature dependent behavior of $\chi_M T$ describes an abrupt SCO from the LS to the HS state of the mononuclear iron(II) complex **C21**·1.8MeOH. The transition temperature in the first heating sequence is equal to $T_c^{\uparrow(1)}$ = 173 K. Cooling the sample to 90 K with subsequent heating to 400 K results in the same magnetic behavior, except a slightly shifted transition temperature. Thus, the critical temperature is shifted to $T_c^{\downarrow(1)} = T_c^{\uparrow(2)}$ = 166 K, which is fairly equal to the one in **C18**·1MeOH ($T_c^{\downarrow} = T_c^{\uparrow}$ = 165 K). This discrepancy of 7 K can be attributed to a different measurement sequence and thus to a different scan rate. In the temperature range between 10 K and 130 K during the first heating sequence, the magnetic moment was taken in 40 K steps leading to a faster heating rate compared to the subsequent cycle. It is well documented in literature that different scan rates in magnetic measurements can lead to different transition temperatures of the SCO active sample.[117]

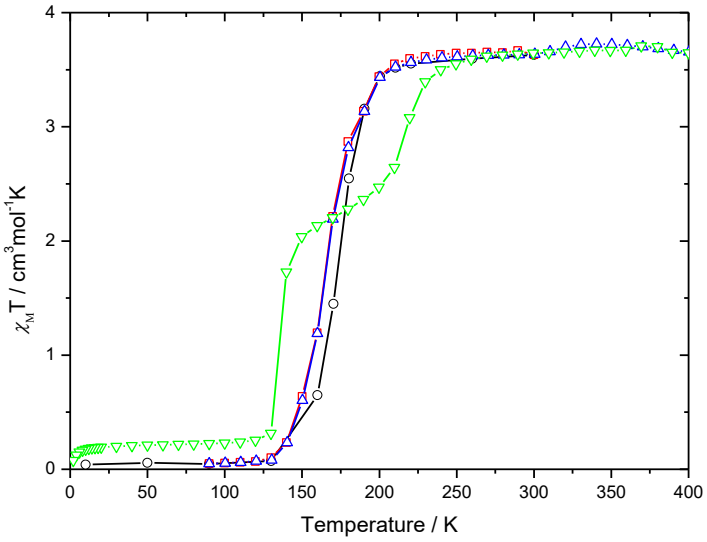


Figure 3.81 Temperature dependent magnetic behavior of single crystals of **C21**·1.8MeOH in the form of a $\chi_M T$ *vs*. T plot. Measurement was done from 10-300 K (black open circles), 300-90 K (red open squares), 90-400 K (blue open triangles) and 400-2 K (green open triangles).

At 400 K, the $\chi_M T$ value of the HS species is slightly increased to 3.66 $cm^3mol^{-1}K$. While cooling thereafter, $\chi_M T$ product surprisingly starts to decrease at a higher temperature of 260 K until it forms a plateau between 200 and 150 K. Below 150 K, the magnetic moment drops again significantly to a value of 0.31 $cm^3mol^{-1}K$ at 130 K. Further cooling to 10 K results in the constant $\chi_M T$ value of approximately 0.2 $cm^3mol^{-1}K$. At very low temperatures, the magnetic moment drops again to 0.08 $cm^3mol^{-1}K$ at 2 K. This temperature dependent behavior of $\chi_M T$ illustrates a two-step spin crossover from the HS to the LS state over an intermediate state. In consideration of the $\chi_M T$ product of 0.2 $cm^3mol^{-1}K$ at low temperatures, 95 % of the HS molecules transitioned to the LS state. The final drop of the magnetic moment below 10 K can be ascribed to ZFS of the remaining S = 2 high-spin molecules. The transition temperatures of the two-step SCO ($T_c^{\downarrow(2)}$ = 215 K and $T_c^{\downarrow(3)}$ = 137 K) are nearly equally distributed around the original transition temperature of $T_c^{\downarrow(1)}$ = 166 K. Since **C21**·1.8MeOH shows the same magnetic behavior during the first three measurement sequences, the two-step SCO is most likely a result of the heating process towards 400 K. Here, **C21**·1.8MeOH differs drastically from **C21**·1MeCN, which remains almost completely in the HS state after being heated to 400 K. Solvent effects on the nature of spin crossover are well known in literature and numerously reported.[133,154–157] In addition, solvatomorphs of a SCO active compound might behave differently after annealing at 400 K.[298] It is difficult to evaluate whether the solvent loss in **C21**·1.8MeOH during the measurement sequence is only partial or complete. It might be possible that upon (partial) desolvation, the compound undergoes a crystallographic structural phase transition, which in return leads to the two-step nature of the SCO.[298] The single-crystals of **C21**·1.8MeOH were not suitable for singe-crystal X-ray structure analysis after being heated to high temperatures. Thus, a comparison of crystal structures was not possible. In order to still make a qualitative statement about the crystalline phases before and after the loss of solvents, powder X-ray diffraction (PXRD) was employed. However, this was only successful for a freshly prepared sample of **C21**·1.8MeOH before temperature treatment. The measurement still provides a good insight into the phase purity of the bulk material, since experimental data are in good agreement with the simulation derived from the measured crystal structure (Figure F.86).

To wrap up chapter 3.6.1 and 3.6.2, the exchange of the non-coordinating aryl group in $\mathbf{L^{Py,1}}$ led to the new ligand $\mathbf{L^{Ph}}$. As expected, the slight change of intermolecular π-π interactions resulted in different magnetic behavior of the SCO active mononuclear iron(II) complexes. Thus, [Fe($\mathbf{L^{Ph}}$)($NCBH_3$)$_2$] · 1MeCN (**C21**·1MeCN) exhibits a very abrupt spin crossover at a higher transition temperature than [Fe($\mathbf{L^{Py,1}}$)($NCBH_3$)$_2$] · 1MeOH (**C18**·1MeCN), while [Fe($\mathbf{L^{Ph}}$)($NCBH_3$)$_2$] · 1.8MeOH (**C21**·1.8MeOH) shows a two-step spin transition after heating the sample to 400 K.

3.6.3 Nickel(II) complex of L^{Ph}

The ligand system L^{Ph} is the result of a substitution of the pyridyl group in 2-position of the oxadiazole with a phenyl group. This was done for two major reasons. The effect of the changed aryl group on the SCO in the [Fe(**L**)(NCBH$_3$)$_2$]·solv-type complexes (**L** = $L^{Py,1}$ and L^{Ph}) could be shown in Chapter 3.4.2. In addition to different intermolecular interactions, L^{Ph} only offers one tetradentate coordination pocket. Therefore, the formation of dinuclear oxadiazole-bridged complexes is not possible anymore. Complexation of metal salts with weakly coordinating counter anions should result in the formation of mononuclear complexes. Saturation of the octahedral vacancies could be achieved by coordination of weakly coordinating coligands as methanol, acetonitrile or counter anions. These kind of coordination compounds are already known in literature and used in catalysis reactions like lactide polymerization,[299,300] olefine epoxidation[301] or alkane hydroxylation.[302–308] Consequently, L^{Ph} was used in a complexation reaction with Ni(II) perchlorate hexahydrate in methanol. After four weeks, slow evaporation of the solvent yielded violet block shaped crystals that were suitable for X-ray structure analysis. However, the structure of the resulting complex differs from the expectation.

[Ni(η³-L^{Ph})$_2$](ClO$_4$)$_2$ (C22) crystallizes in the triclinic space group $P\bar{1}$ with two formula units in the unit cell. Crystallographic Data can be found in Table D.13. The crystal structure was taken at 173 K. The asymmetric unit includes one complex cation next to two non-coordinating perchlorate anions, while the residual of the unit cell is generated by symmetry due to the presence of an inversion center (Figure F.87). Figure 3.82 illustrates the structure of the complex cation.

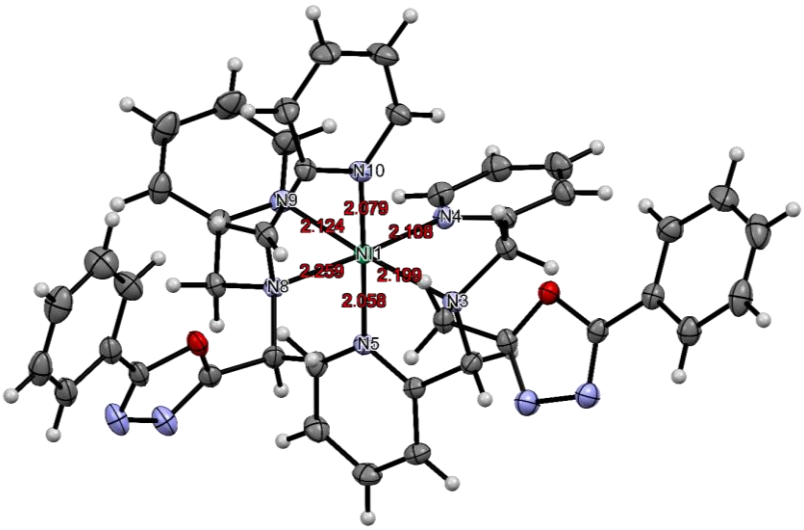


Figure 3.82 Molecular structure of **C22**. Bond distances are displayed in red. Colour scheme: dark grey – C, grey – H, violet – N, red – O, green – Ni. ORTEP representation with atomic displacement parameters set to 50 % probability.

The nickel(II) ion is coordinated by two ligand molecules. Here, both ligands bind with their bis(2-picolyl)amino function to the metal center. The pyridyl groups of one $\mathbf{L^{Ph}}$ molecule exhibit a *cis*-configuration. In addition to that, the amine functions of both ligand molecules are also coordinated *cis*-wise. Interestingly, the oxadiazole moiety does not bind to the nickel(II) ion in any way. The present bond lengths can be categorized in three groups. The smallest bond distances are found between the nickel(II) and the pyridyl groups in the axial positions (N5 and N10) with distances between 2.06 Å ≤ *d*(Ni-N) ≤ 2.08 Å. The next longer metal-ligand bonds are found to the pyridine rings, which are coordinated *trans* to the amine functions (N4 and N9) with 2.11 Å ≤ *d*(Ni-N) ≤ 2.12 Å. The longest bonds are formed to the amine functions (N3 and N8) with 2.20 Å ≤ *d*(Ni-N) ≤ 2.26 Å, which can be explained by the pure σ-donor character of the amine, while the pyridine fragments exhibit further π-backbonding character.[232] Compared to the described mononuclear iron(II) HS complexes, the ligand sphere of **C22** is less distorted with $\Sigma_O(NiN_6)$ = 99.2 ° and CShM(O_h) = 1.47 (Figure 3.83). This finding can be explained by the isotropic electron configuration of a S = 1 system in an octahedral ligand field [$t_{2g}(6)\ e_g^*(2)$]. A full summary of the structural parameters can be found in Table E.12.

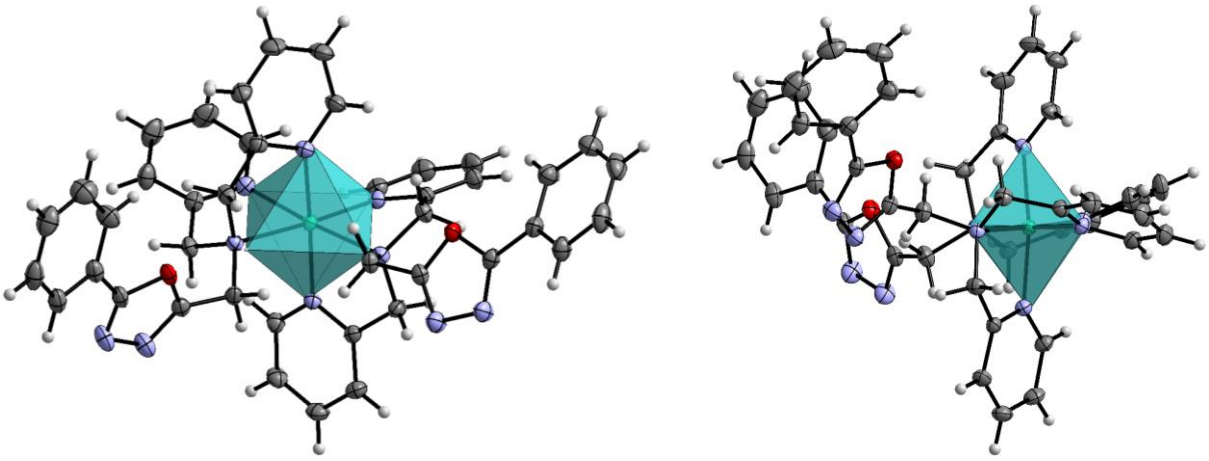


Figure 3.83 Molecular structure of **C22** and its ideal coordination octahedron with front view (left) and side view (right), calculated with SHAPE.[62] Colour scheme: dark grey – C, grey – H, violet – N, red – O, bright orange – Se, green – Ni. ORTEP representation with atomic displacement parameters set to 50 % probability.

In the packing of **C22**, two unique π-π interactions are present, leading to the formation of a "dimer" of complex cations. The first one takes place between two pyridyl groups and is of parallel nature. The least-squares mean planes A and B are defined through the atoms N5, C17, C18, C19, C20 and C21 of two neighboring molecules. Both planes are orientated parallel so the *interplanar angle* θ is equal to zero. The *interplanar distance* is equal to d_{AB} = 3.40 Å, combined with an *offset* of *r* = 1.66 Å (Figure F.88). The second T-shape π-π interactions can be found between the same two molecules. Here, the pyridine ring, which is involved in the first interaction, is pointing onto another pyridyl group of the adjacent complex cation.

This non-classical C-H···π hydrogen bond can be categorized as type II (see Chapter 3.4.1). Plane A includes N4, C12, C13, C14, C15 and C16, while the interacting C-H fragment is labeled as C19-H19. An *interaction distance* of d_{QH} = 2.82 Å is found, next to an *offset* of r = 0.78 Å. The two relevant angles are α = 170.3 ° and β = 74.0 ° (Figure 3.84).

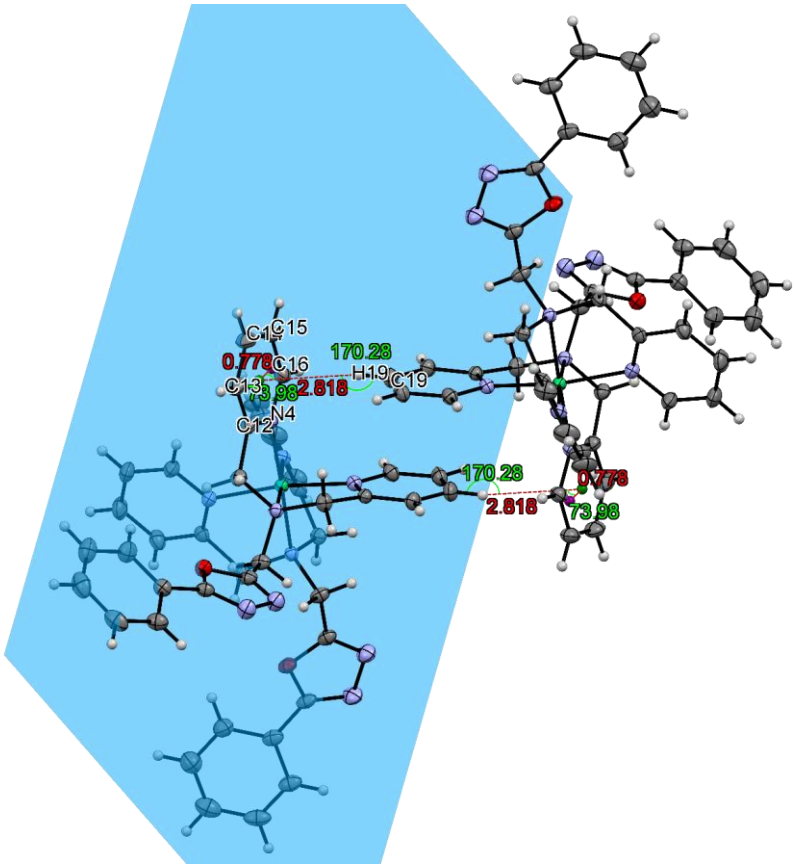


Figure 3.84 C-H···π interaction in **C22**. Least-squares plane A is defined by N4, C12, C13, C14, C15 and C16. Interacting C-H fragment is labeled as C19-H19. Green point – center of the aromatic ring in A. Purple point – orthogonal intersection of H19 onto plane A. *Offset* r = 0.78 Å, *interaction distance* d_{QH} = 2.82 Å, α = 170.3 ° and β = 74.0 °. ORTEP representation with atomic displacement parameters set to 50 % probability.

The resulting "dimer" is illustrated in Figure 3.85. The preferred coordination of a second ligands molecule compared to two methanol molecules is most likely caused by the thermodynamical chelating effect of the ligand system $\mathbf{L}^{Ph}$.[309] Since there are no weak metal-ligand bonds in **C22**, the compound was not analyzed with respect to its catalytic activity towards alkane hydroxylation.

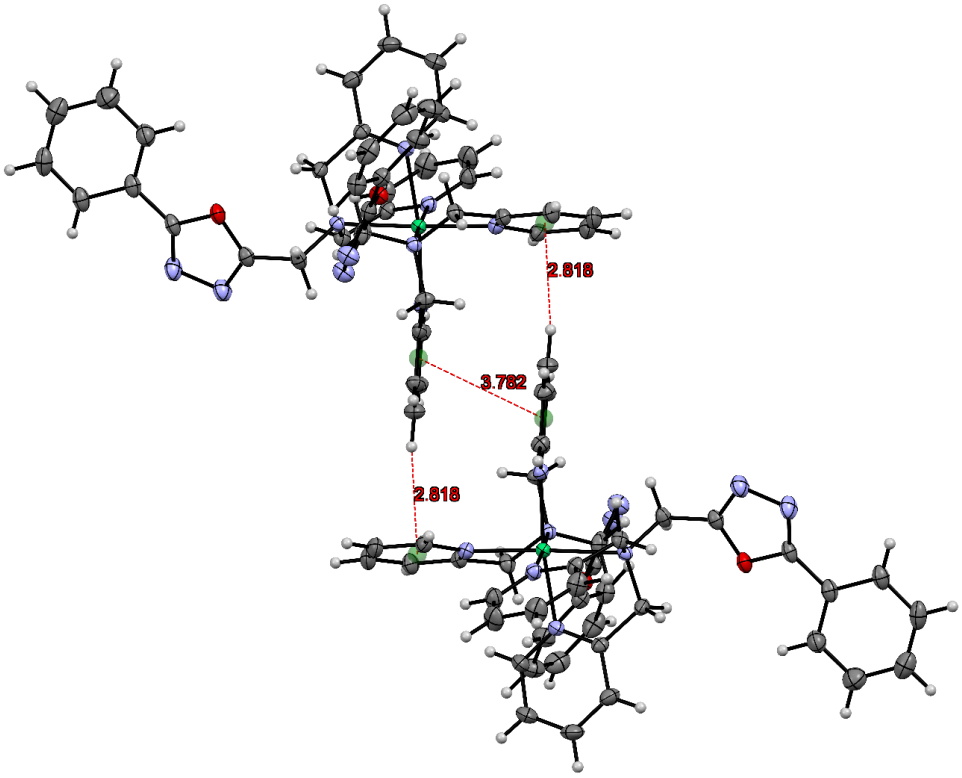


Figure 3.85 Intermolecular π-π interactions between two complex cations in the packing of **C22**. Red dashed lines and numbers represent intermolecular distances. Colour scheme: pink – B, dark grey – C, grey – H, violet – N, red – O, orange – Fe. ORTEP representation with atomic displacement parameters set to 50 % probability.

3.7 Mononuclear coordination compounds of L^{Naph}

In the last years, research in the field of SCO did not only focus on the spin crossover phenomenon itself but also on understanding multifunctional systems. Therefore, the SCO can be seen as a function coupled to another feature, i.e. liquid crystallinity[310], magnetic ordering[311], conductivity[312] or luminescence[178,189–191,313–315]. Since the mononuclear iron(II) complexes of type [Fe(**L**)$(NCBH_3)_2$]·solv (**L** = $L^{Py,1}$ and L^{Ph}) showed SCO at similar transition temperatures, it can be assumed that the ligand field is roughly independent of the aryl group in the 2-position of the oxadiazole backbone. Rather, slightly shifted transition temperatures and different natures of the SCO are most likely the result of packing effects in the crystalline solid state. The novel ligand system L^{Naph} (Figure 3.86) was designed by implementing the 2-naphthyl group in the 2-position of the 1,3,4-oxadiazole. Naphthalene is known for its remarkably long lifetime fluorescence with very low self-quenching.[316–321] Thus, iron(II) coordination compounds of type [Fe(L^{Naph})$(NCBH_3)_2$]·solv could represent the first ODA-based multifunctional SCO compounds with interplay between fluorescence and spin-state.

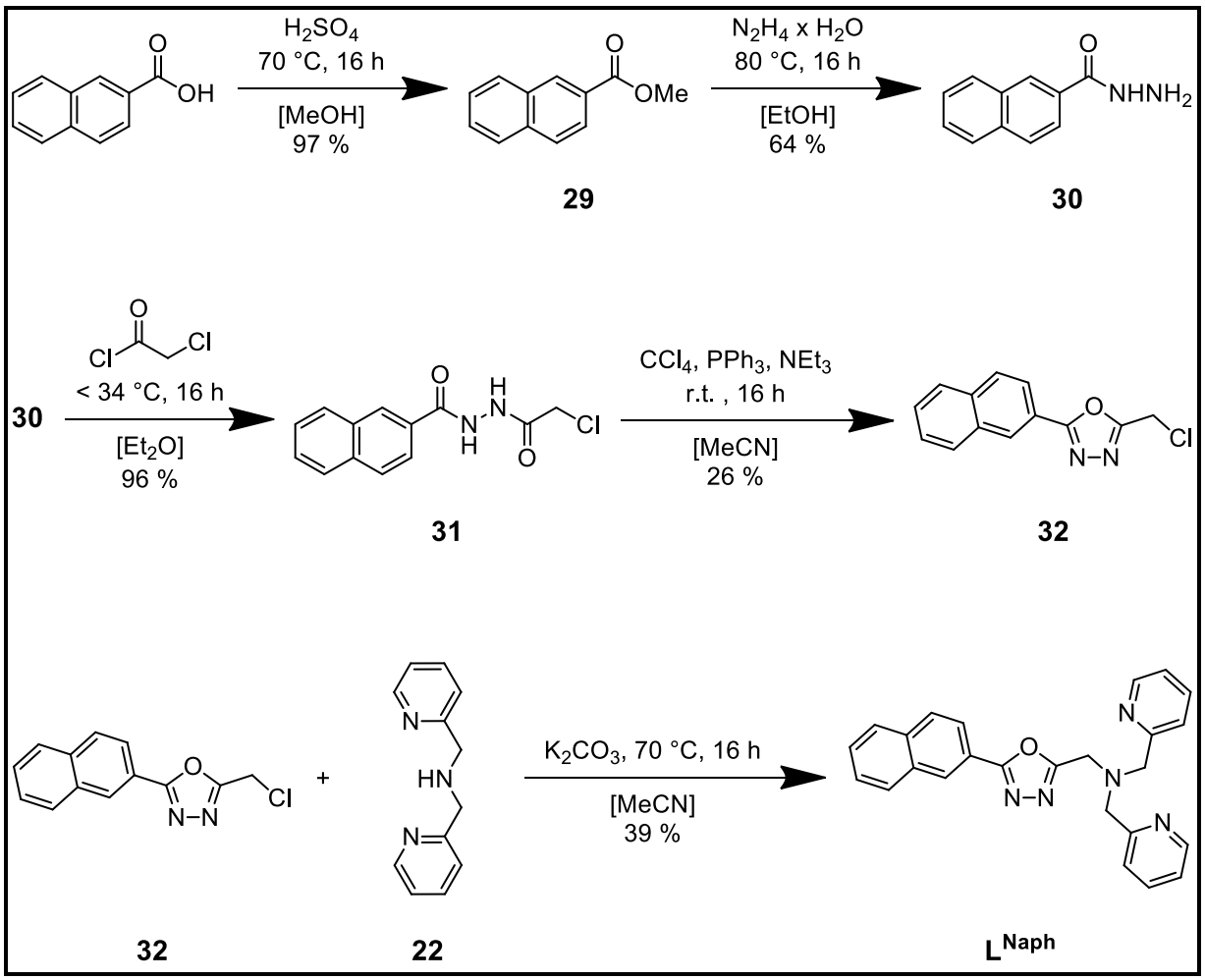


Figure 3.86 Synthesis scheme of L^{Naph}. The synthesis of **29** is already known in literature and was adapted with minor changes.[322]

The synthetic route of 2-(Naphthalen-2-yl)-5-[N,N-bis(2-pyridylmethyl)aminomethyl]-1,3,4-oxadiazole (**L**$^{\mathbf{Naph}}$) is based on the synthesis of **L**$^{\mathbf{Py,1}}$ and **L**$^{\mathbf{Ph}}$. In the first step, 2-naphthoic acid was converted to methyl naphthalene-2-carboxylate (**29**) in a literature known Fischer esterification in a very good yield.[322] 2-Naphthohydrazide (**30**) was synthesized in a subsequent nucleophilic reaction of **29** with hydrazine monohydrate in a yield of 64 %. The following condensation reaction with chloroacetyl chlorid yielded N'-(2-chloroacetyl)naphthalene-2-carbohydrazide (**31**) in 96 %. As described several times before, such hydrazide compound can be used in a ring-closure reaction to form the corresponding 1,3,4-oxadiazole compound. Thus, 2-(Chloromethyl)-5-(naphthalen-2-yl)-1,3,4-oxadiazole (**32**) could be isolated with a yield of 26 %. Ring-closing was achieved by the use of the three-component system triphenylphosphine, carbon tetrachloride and triethylamine.[279–282] In the fifth and final step, **L**$^{\mathbf{Naph}}$ was isolated after a nucleophilic reaction of **32** and **22** in 39 % yield, using potassium carbonate as base.

Analogous to **L**$^{\mathbf{Ph}}$ and **L**$^{\mathbf{Py,1}}$, **L**$^{\mathbf{Naph}}$ was used to synthesize mononuclear iron(II) complexes. Since the coordination compounds of type [Fe(**L**)(NCS)$_2$]·solv (**C16**, **C19**) and [Fe(**L**)(NCSe)$_2$]·solv (**C17**, **C20**) with **L** = **L**$^{\mathbf{Py,1}}$ and **L**$^{\mathbf{Ph}}$ do not show temperature induced SCO, it can be assumed that similar magnetic behavior applies for the analogous **L**$^{\mathbf{Naph}}$ based compounds. Thus, **L**$^{\mathbf{Naph}}$ was only used in a complexation reaction with the iron(II) precursor [Fe(py)$_4$(NCBH$_3$)$_2$] in either acetonitrile or methanol under inert atmosphere. Slow evaporation of the solvent resulted in the formation of [Fe(**L**$^{\mathbf{Naph}}$)(NCBH$_3$)$_2$] · 4.5MeCN (**C23**·4.5MeCN) and [Fe(**L**$^{\mathbf{Naph}}$)(NCBH$_3$)$_2$] · 3MeOH (**C23**·3MeOH) in form of single-crystals.

3.7.1 Magneto-structural relationship in [Fe(L$^{\mathbf{Naph}}$)(NCBH$_3$)$_2$] · 4.5MeCN

[Fe(**L**$^{\mathbf{Naph}}$)(NCBH$_3$)$_2$] · 4.5MeCN (**C23**·4.5MeCN) was investigated with respect to its temperature dependent magnetic behavior between 400-2 K in a magnetic field of 0.1 T. The determined magnetic susceptibility is shown in Figure 3.87 in form of the resulting $\chi_M T$ versus *T* plot. The sample was set at 300 K and measured in the following sequences: 1) 300-2 K, 2) 2-400 K, 3) 400-2 K and 4) 2-400 K. At the beginning of the measurement (300 K), the $\chi_M T$ value is equal to 4.04 cm^{3}mol^{-1}K, which represents a spin-orbit coupled *S* = 2 system. Until a temperature of 150 K is reached, $\chi_M T$ stays nearly constant. Below this temperature, the $\chi_M T$ product decreases to a minimum of 0.91 cm^{3}mol^{-1}K at 70 K. Further cooling results in a gradual increase of $\chi_M T$ to 1.16 cm^{3}mol^{-1}K at 10 K. Between 10 K and 2 K, the $\chi_M T$ value drops again to 0.71 cm^{3}mol^{-1}K. The first decrease of the magnetic moment between 150 K and 70 K can be ascribed to a reasonably abrupt SCO. The first derivative of $\chi_M T$ with respect to the temperature *T* reveals a spin transition temperature of $T_c^{\downarrow}$ = 111 K (Figure G.39).

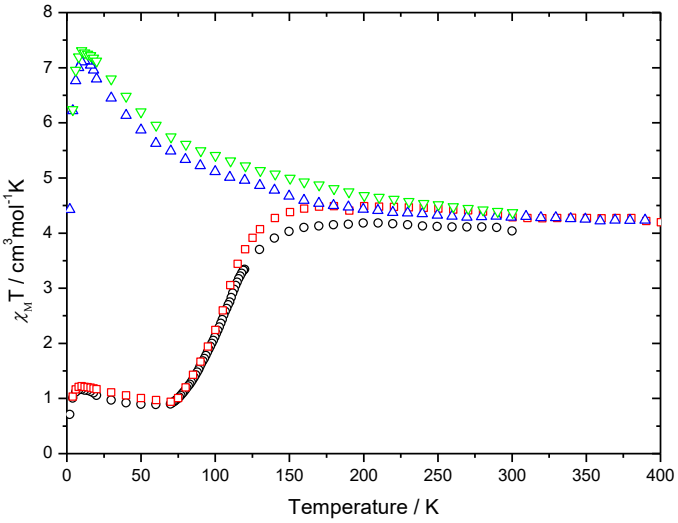


Figure 3.87 Temperature dependent magnetic behavior of single crystals of **C23**·4.5MeCN in the form of a $\chi_M T$ *vs*. *T* plot. Measurement was done from 300-2 K (black open circles), 2-400 K (red open squares), 400-2 K (blue open triangles) and 2-300 K (green open triangles).

The $\chi_M T$ value of 0.92 cm^{3}mol^{-1}K at 70 K indicates, that approx. 77 % of the HS molecules in the crystalline state changed to the LS state. The rise of the magnetic moment from 70 K to 10 K can be ascribed to macroscopic orientation of the crystalline sample in the applied magnetic field (0.1 T). Below 10 K, the effect of ZFS in the remaining HS molecules on $\chi_M T$ is visible, which inevitably indicates a pronounced magnetic anisotropy. Such preferred direction of magnetization may indeed result in a macroscopic alignment of the crystals with the magnetic field. Heating the sample to 400 K yields in the same magnetic behavior with slightly increased values for $\chi_M T$. This finding can also be explained by the different alignment of the sample in the gelatin capsule, compared to the previous measurement sequence. Thus, $\chi_M T$ at 300 K (4.28 cm^{3}mol^{-1}K) is slightly higher than at the start of the measurement. The first derivative, displayed in Figure G.39, yields a transition temperature of $T_c^{\uparrow}$ = 110 K. Until the temperature of 400 K is reached, the $\chi_M T$ product remains reasonably the same. Repeated cooling of the sample leads to a gradual increasement of $\chi_M T$ to a value of 7.13 cm^{3}mol^{-1}K at 12 K. Lower temperatures yield in another drop of the $\chi_M T$ product to 4.42 cm^{3}mol^{-1}K at 2 K. After heating the sample to 400 K, no spin transition of **C23**·4.5MeCN is observed. Thus, 100 % of the complex molecules remain in the HS state even at lower temperature. The higher amount of HS molecules explains the enhanced orientation of the sample in the magnetic field, compared to the previous cooling sequence. Again, the drop of the magnetic moment below 12 K can be attributed to ZFS. Final heating of the sample leads to the same progression of $\chi_M T$. To further investigate this unusual magnetic behavior, a freshly sample of **C23**·4.5MeCN was analyzed in a slightly changed measuring routine.

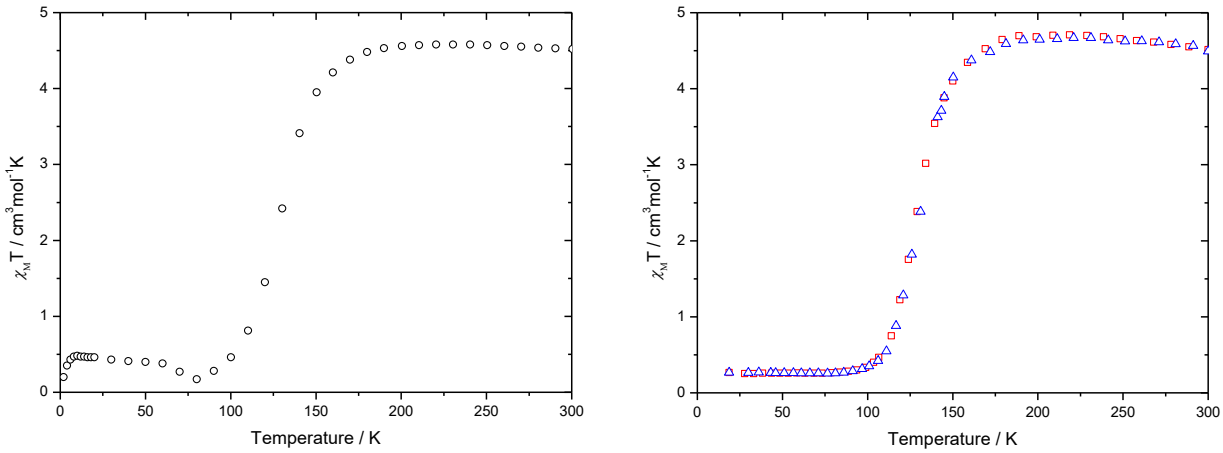


Figure 3.88 Temperature dependent magnetic behavior of freshly prepared single crystals of **C23**·4.5MeCN in the form of $\chi_M T$ *vs*. *T* plots. Right: Measurement between 2-300 K (black circles). Left: Measurement between 300-20 K (red open squares) and 20-300 K (blue open triangles).

The $\chi_M T$ versus *T* plot of the first sequence is illustrated in Figure 3.88 (left). **C23**·4.5MeCN was set very quickly at 10 K without an external magnetic field. Afterwards, a magnetic field of 0.1 T was applied and the sample cooled to 2 K. Starting at this temperature, the measurement routine towards 300 K was started. At 2 K, $\chi_M T$ is equal to 0.20 cm^{3}mol^{-1}K and rises with increasing temperature to 0.48 cm^{3}mol^{-1}K at 10 K. This value of $\chi_M T$ remains nearly constant until a temperature of 60 K is reached. Above 60 K, the $\chi_M T$ product decreases again to a minimum of 0.17 cm^{3}mol^{-1}K at 80 K. Further heating to 200 K causes a significant rise of the $\chi_M T$ value (4.56 cm^{3}mol^{-1}K), which stays roughly constant to 300 K. This measurement offers many aspects to discuss. This time, approximately 96 % of the HS complex molecules switched their spin state to the *S* = 0 state. Next to that, the thermally induced SCO is more abrupt than before with a shifted transition temperature of $T_c^{\uparrow(1)}$ = 130 K. This shows again that the SCO phenomenon depends not only on the molecular structure, but also on the macroscopic nature of the substance. Additionally, the sample of **C23**·4.5MeCN used in the first measurement (Figure 3.87) may have already lost lattice solvents to some extent. The plateau of $\chi_M T$ between 10 K and 60 K looks like the afore described macroscopic orientation of the sample at first glance. However, a subsequent measurement of the magnetic moment from 300 K to 20 K and vice versa reveals that such effect is not observed (Figure 3.88, right). This suggests that the fast cooling of **C23**·4.5MeCN to 10 K entailed a trapping of HS molecules in the crystalline phase, also referred to as TIESST effect.[134–136] This statement is strengthened by the fact, that the $\chi_M T$ drops above 60 K, which is representative for the relaxation of the system. According to the $\chi_M T$ value at 10 K (0.48 cm^{3}mol^{-1}K), approx. 10 % of the complex molecules are trapped in the paramagnetic HS state. Yet, the subsequent measurement in Figure 3.88 (right) reveals that the spin transition itself is not fully completed

with 5 % of remaining HS molecules. The derivative of $\chi_M T$ with respect to the temperature shows the same transition temperature as before $T_c^{\downarrow(1)} = T_c^{\uparrow(2)} = 130$ K (Figure G.40). Thus, the fraction of *trapped* high-spin complex molecules is probably lower than 10 %. Afterwards, the sample was heated from 300 K to 400 K to 300 K with the measurement routine used in the first analysis, which ensures an equal heating period. Once 300 K was reached again, the external magnetic field was removed and the sample cooled to 2 K. This method is similar to the known *zero-field-cooling* (ZFC) and should lead to less macroscopic movement of the crystalline sample.[323] At a temperature of 2 K, a low magnetic field of 0.02 T was applied and the sample heated towards 300 K (Figure 3.89, black open circles). $\chi_M T$ rises from 2.66 cm^{3}mol^{-1}K at 2 K to 4.85 cm^{3}mol^{-1}K at 10 K. Above this temperature, the $\chi_M T$ product decreases gradually to 4.28 cm^{3}mol^{-1}K at 110 K. The lower maximum of $\chi_M T$ at 10 K compared to the one in Figure 3.87 indeed indicates less orientation of the single-crystals in the applied field. Further heating does not yield in major changes of the magnetic moment. Cooling the sample from 300 K to 120 K at 0.02 T still results in the constant $\chi_M T$ value (Figure 3.89, red open squares). The magnetic field was changed to a slightly higher value of 0.1 T and $\chi_M T$ determined towards 2 K (Figure 3.89, blue open triangles). Since 0.1 T is still considered a weak magnetic field, linearity between the magnetic susceptibility and magnetization should still be valid ($\chi \cdot H = M$). However, the $\chi_M T$ product at 110 K at 0.1 T (4.69 cm^{3}mol^{-1}K) is remarkably higher than at 0.02 T and rises to a value of 6.02 cm^{3}mol^{-1}K at 10 K. For very low temperatures, the effect of ZFS can be observed. This field-dependency of $\chi_M T$ clearly indicates the macroscopic alignment of the sample along the field direction, which explains the unusual magnetic behavior of **C23**·4.5MeCN in Figure 3.87.

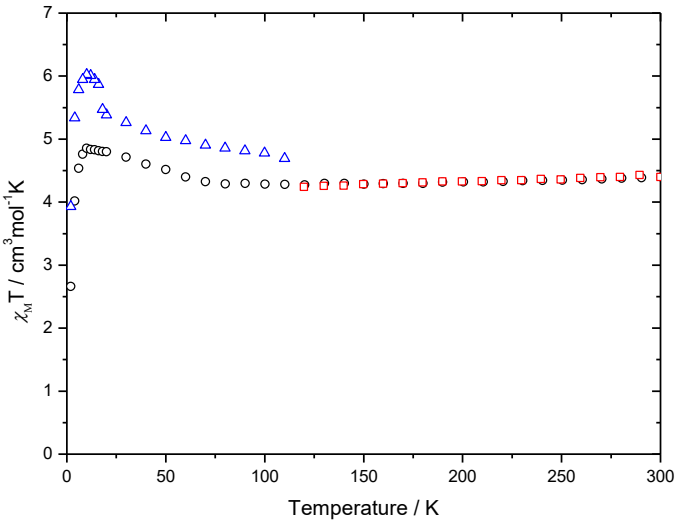


Figure 3.89 Temperature dependent magnetic behavior of **C23**·4.5MeCN after heating to 400 K in the form of a $\chi_M T$ *vs.* *T* plot. Sample was *zero-field-cooled* to 2 K. Measurement was done from 2-300 K at 0.02 T (black open circles), 300-120 K at 0.02 T (red open squares) and 110-2 K at 0.1 T (blue open triangles).

[Fe($\mathbf{L^{Naph}}$)$(NCBH_3)_2$] · 4.5MeCN (C23·4.5MeCN) crystallizes in the monoclinic space group *C*2/*c* with eight formula units in the unit cell. Crystallographic data can be found in Table D.13. The structure was determined at 220 K. The compound is isomorphous to the solvatomorphs of [Fe($\mathbf{L^{Ph}}$)$(NCX)_2$] (X = S,Se) **C19**·2MeCN, **C19**·3MeOH, **C20**·2MeCN and **C20**·3MeOH with Π(**C23**·4.5MeCN/**C19**·2MeCN) = 0.059. This value is higher than the *unit-cell similarity indices* stated in Table 3.5. The greater value can be explained by the longer a-axis of the unit cell of **C23**·4.5MeCN, which is caused by the larger aromatic naphthalene group compared to a phenyl group. The asymmetric unit consists of the complex molecule next to solvent molecules. However, since the acetonitrile molecules show strong disorder, no proper refinement was possible. Thus, the SQUEEZE routine had to be applied.[297] The unit cell is generated by symmetry (Figure F.89 and Figure F.90). Structure and bond lengths trend still follow the description of Chapter 3.4.1. An average metal-ligand distance of $\bar{d}$(Fe-N) = 2.18 Å is found, which represents a complex molecule in the high-spin state. This statement is reinforced by the present distortion of the coordination sphere with $\Sigma_O(FeN_6)$ = 92.4 ° and CShM(O_h) = 1.28 (Figure 3.90). A detailed summary of coordination parameters can be found in Table E.10. The crystallographic HS state is in accordance with the magnetic data at 220 K.

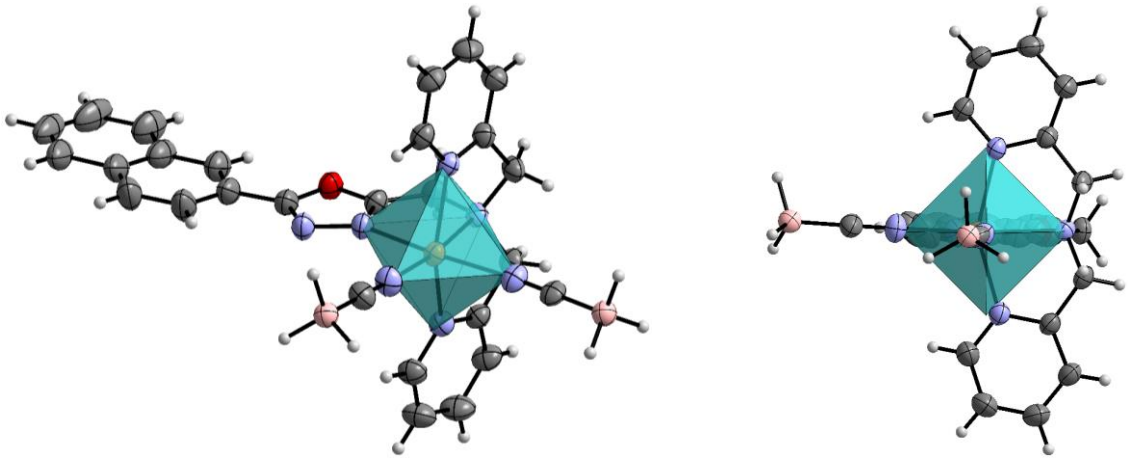


Figure 3.90 Molecular structure of **C23**·4.5MeCN and its ideal coordination octahedron with front view (left) and view along the Fe-N5 axis (right), calculated with SHAPE.[62] Colour scheme: dark grey – C, grey – H, violet – N, red – O, bright orange – Se, orange – Fe. ORTEP representation with atomic displacement parameters set to 50 % probability.

Due to the isomorphism to **C19**·2MeCN, packing of the molecules in the crystalline phase is equal. Therefore, three unique intermolecular π-π interactions can be found. One parallel-wise π-π stacking can be found between two pyridyl groups of two adjacent molecules. The least-squares mean plane A is defined by the atoms N4, C16, C17, C18, C19 and C20, while plane B includes N3, C21, C22, C23, C24 and C25. An *interplanar distance* of d_{AB} = 3.93 Å is found, next to an *interplanar angle* of θ = 15.6 ° and an *offset* of *r* = 1.25 Å (Figure 3.91).

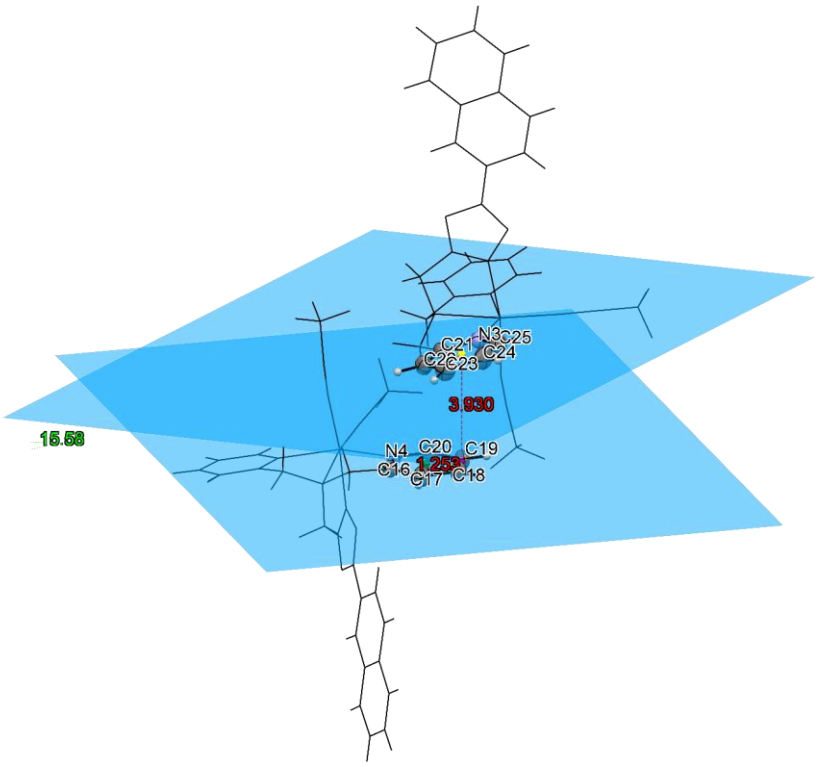


Figure 3.91 π-π interaction in **C23**·4.5MeCN Least-squares mean plane A is defined by N4, C16, C17, C18, C19 and C20. Plane B is defined by N3, C21, C22, C23, C24 and C25 of an adjacent molecule. Green point – center of the aromatic ring in A. Yellow point – center of the aromatic ring in B. Purple point – orthogonal intersection of the aromatic center in B onto plane A. *Offset* r = 1.25 Å, *interplanar distance* d_{AB} = 3.93 Å, *interplanar angle* θ = 15.6 °. ORTEP representation with atomic displacement parameters set to 50 % probability.

This interaction results in the formatting of a one-dimensional chain along the b-axis. Due to the naphthyl groups, neighboring chains are connected via two additional π-π interactions. Thus, a second parallel π-π stacking between two naphthalene rings can be observed. Here, the least-squares mean planes A and B include the atoms C1, C2, C7, C8, C9 and C10. Since both aromatic systems are oriented parallel, the *interplanar angle* is equal to zero. The *offset* is equal to r = 1.56 Å, combined with an *interplanar distance* of d_{AB} = 3.42 Å. (Figure F.91). The third intermolecular interaction involves the same complex molecules as before and displays a non-classical C-H··· π hydrogen bond between the naphthyl group and a pyridyl rest. Plane A includes N4, C16, C17, C18, C19 and C20 while the donor function is labeled as C5-H5. This T-shaped π-π interaction can be categorized as type I (see Chapter 3.4.1). The *interaction distance* is equal to d_{QH} = 2.79 Å combined with an *offset* of r = 0.24 Å and the two angles α = 160.7 ° and β = 85.2 ° (Figure F.92). Since the orientation of the naphthyl groups in the one-dimensional chain is alternating, this kind of connectivity yields a two-dimensional network of complex molecules, shown in Figure 3.92.

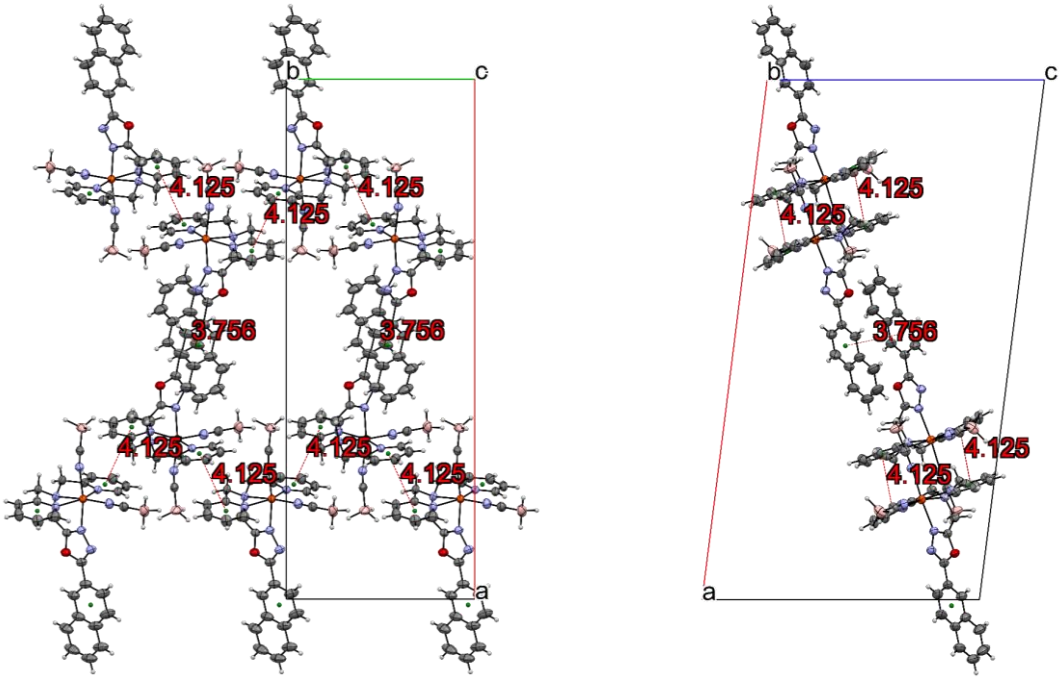


Figure 3.92 Two-dimensional network of complex molecules in **C23**·4.5MeCN due to intermolecular π-π interactions with view along the c-axis (left) and b-axis (right). The centers of involved aromatic rings are displayed as green points. Distances are displayed as red dashed lines and numbers. Solvent molecules are treated with the SQUEEZE routine.[297]

This type of crosslinking can ensure the transfer of structural changes associated with the spin transition from one molecule to another and explains the abrupt SCO of compound **C23**·4.5MeCN in the crystalline phase. In addition to that, packing reveals solvent channels between the naphthyl groups along the c-axis.

3.7.2 Magneto-structural relationship in [Fe(L$^{\mathbf{Naph}}$)(NCBH$_3$)$_2$] · 3MeOH

Analogous to **C23**·4.5MeCN, the temperature dependent magnetic behavior of [Fe(**L**$^{\mathbf{Naph}}$)(NCBH$_3$)$_2$] · 3MeOH (**C23**·3MeOH) was measured in a temperature range between 400 K and 2 K. $\chi_M T$ was plotted against the temperature in Figure 3.93. Single crystals of **C23**·3MeOH were set at 300 K and measured while lowering the temperature to 2 K (Figure 3.93, left, black open squares). At 300 K, a $\chi_M T$ product of 3.45 cm^{3}mol^{-1}K can be observed, which can be ascribed to SOC of the $^5T_{2g}$ ground state. Cooling of the sample leads to an abrupt and complete spin crossover to the diamagnetic $^1A_{1g}$ low-spin state. The first derivative of $\chi_M T$ with respect to *T* yields a transition temperature of $T_c^{\downarrow}$ = 207 K (Figure G.41), representing the highest value throughout this work. Heating the sample up to 400 K results in the same magnetic behavior with $T_c^{\uparrow} = T_c^{\downarrow}$ = 207 K (Figure 3.93, left, red open circles). At 400 K, a $\chi_M T$ value of 3.55 cm^{3}mol^{-1}K can be found.

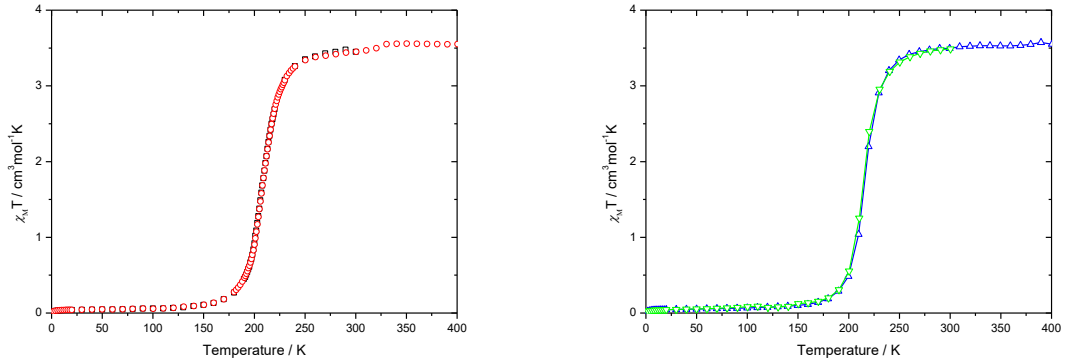


Figure 3.93 Temperature dependent magnetic behavior of single crystals of **C23**·3MeOH in the form of $\chi_M T$ *vs*. *T* plots. Left: Measurement between 300-2 K (black open squares) and 2-400 K (red open circles). Right: Subsequent measurement between 400-2 K (blue open triangles) and 2-300 K (green open triangles).

The subsequent measuring routine from 400 K to 2 K to 300 K results in the same temperature dependency of the magnetic moment (Figure 3.93 right). In contrast to the afore discussed mononuclear iron(II) SCO active compounds, the magnetic behavior of **C23**·3MeOH seems to be independent of eventual solvent loss. However, it might be possible that the time at higher temperature was not sufficient to remove lattice solvents. The measured sample was exposed to air and stored for 5 days. During this time, neither the morphology of the single crystals changed, nor cracks were observed. This finding suggests the absence of solvent loss.

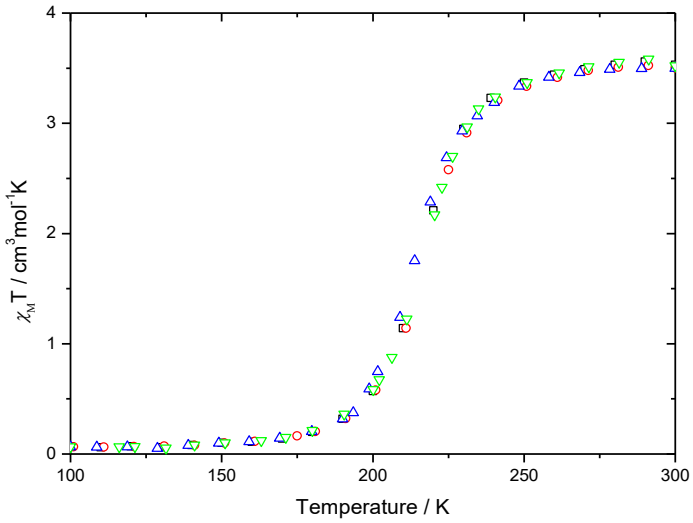


Figure 3.94 Temperature dependent magnetic behavior of single crystals of **C23**·3MeOH after five days under air in the form of the resulting $\chi_M T$ *vs*. *T* plot. Magnetic susceptibility was determined between 300-100 K (black open circles), 100-300 K (red open squares), 300-100 K (blue open squares) and 100-300 K (green open triangles).

Furthermore, there was no colour change of the orange crystals, indicating chemical inertness to atmospheric oxygen. The single-crystals of **C23**·3MeOH were placed in a gelatin capsule and measured once again in the SQUID magnetometer to investigate possible changes of the magnetic behavior. The sample was cycled four times in a temperature regime between 300 K and 100 K, illustrated in Figure 3.94. There is no significant change of $\chi_M T$ observable compared to the first measurement. Thus, the SCO capability of **C23**·3MeOH seems to be stable after exposure to air and high temperatures. Additionally, the nature of the spin transition is consistent, showing an abrupt spin switch of complex molecules to the LS state.

[Fe(L$^{\mathbf{Naph}}$)(NCBH$_3$)$_2$] · 3MeOH (C23·3MeOH) was firstly investigated in a single-crystal structure analysis at 220 K. Crystallographic Data can be found in Table D.14. The compound crystallizes in the monoclinic space group *C*2/*c* with eight formula units inside the unit cell. One complex molecule and three methanol molecules are defining the asymmetric unit (Figure F.93). Due to the centers of inversion, two-fold rotation and screw axes, and glide planes, the unit cell is generated by symmetry (Figure F.94 and Figure F.95). The crystalline phase of **C23**·3MeOH differs from **C23**·4.5MeCN. While the acetonitrile solvatomorph of **C23** crystallizes in the same manner as the thiocyanate and selenocyanate compounds **C19** and **C20**, **C23**·3MeOH shows isomorphism to the cyanoborohydride compounds **C18** and **C21**. Here, a *unit-cell similarity index* of Π(**C23**·3MeOH/**C21**·1MeCN) = 0.056 can be found. The larger aromatic naphthyl group in **C23**·3MeOH causes an enlargement of the a- and b-axes of the unit cell, compared to **C21**·1MeCN. This results in an increased value for Π. The structural properties of the complex molecule itself correspond to those described in Chapter 3.4.1.

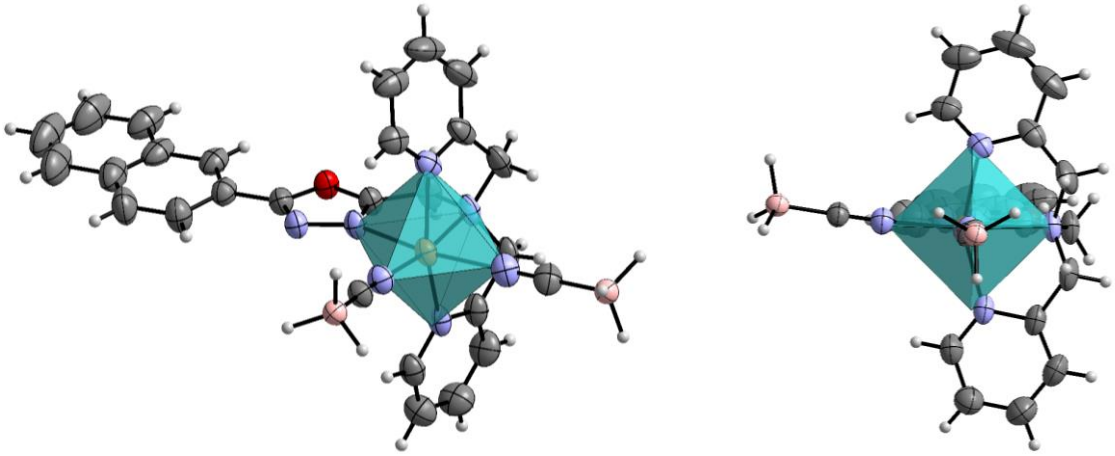


Figure 3.95 Molecular structure of **C23**·3MeOH and its ideal coordination octahedron with front view (left) and view along the Fe-N5 axis (right), calculated with SHAPE.[62] Colour scheme: dark grey – C, grey – H, violet – N, red – O, bright orange – Se, orange – Fe. ORTEP representation with atomic displacement parameters set to 50 % probability.

At 220 K, a mean metal-ligand distance of $\bar{d}$(Fe-N) = 2.17 Å can be found, representing a high-spin iron(II) center. This spin state is further confirmed by the present distortion of the octahedral coordination sphere with $\Sigma_O(FeN_6)$ = 94.0 ° and CShM(O_h) = 1.14 (Figure 3.95). Similar to the isomorphous solvatomorphs of **C18** and **C21**, the greatest deviation from the ideal coordination sphere is caused by the apical pyridine moieties, forming a *trans*-angle of 152.7 °. Due to different packing of the solvatomorphs of **C23**, intermolecular interactions between the complex molecules differ. In the case of **C23**·3MeOH, three different types of π-π interactions are present in the crystalline phase. The first intermolecular non-classical C-H···π-hydrogen bond can be found between the C-H function of a pyridyl group and the π-system of the naphthyl group. The least-squares mean plane A is formed by the atoms C2, C3, C4, C5, C6 and C7, while the interacting C-H function is labeled as C18-H18. Next to an *interaction distance* of d_{QH} = 2.94 Å, an *offset* of *r* = 1.26 Å can be found. The relevant geometrical angles are α = 159.5 ° and β = 64.6 ° (Figure 3.96). Thus, this C-H···π hydrogen bond can be classified as Typ II (see Chapter 3.4.1) and causes a one-dimensional chain of complex molecules along the c-axis. Analogous to the solvatomorphs of **C18** and **C21**, two neighboring chains are crosslinked via two additional π-π interactions. Firstly, a parallel stacking between the naphthalene rings of two complex molecules can be observed.

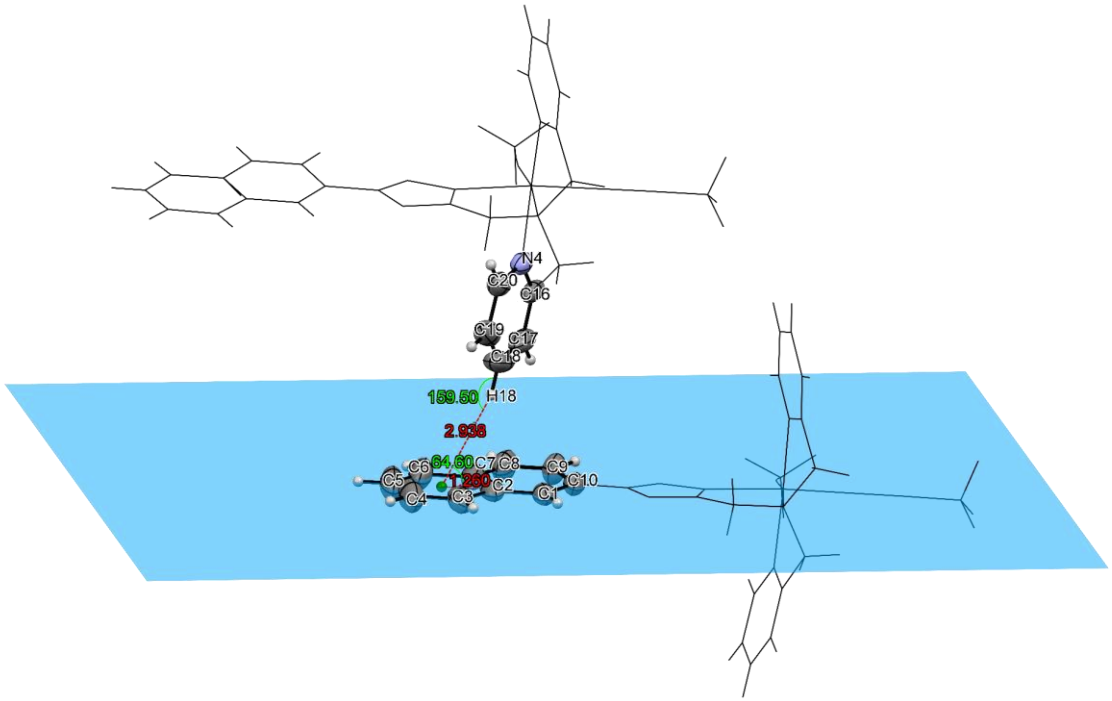


Figure 3.96 C-H···π interaction in **C23**·3MeOH (240 K). Least-squares plane A is defined by C2, C3, C4, C5, C6 and C7. Interacting C-H fragment is labeled as C18-H18. Green point – center of the aromatic ring in A. Purple point – orthogonal intersection of H18 onto plane A. *Offset* *r* = 1.26 Å, *interaction distance* d_{QH} = 2.94 Å, α = 159.5 ° and β = 64.6 °. ORTEP representation with atomic displacement parameters set to 50 % probability.

Least-squares mean plan A is defined through C2, C3, C4, C5, C6 and C7, while plane B includes C1, C2, C7, C8, C9 and C10. The *interplanar angle* θ is equal to 1.8 °. Next to that, an *interplanar distance* of d_{AB} = 3.40 Å and an *offset* of *r* = 2.14 Å can be found (Figure F.96). In addition to that, a second intermolecular T-shape π-π interaction is present between the same two complex molecules. Therefore, the naphthyl group exhibits a non-classical C-H···π hydrogen bond of type II (see Chapter 3.4.1) to a pyridine ring. The involved plane A includes N4, C16, C17, C18, C19 and C20, while the interacting C-H fragment is labeled as C5-H5. The *interaction distance* is equal to d_{QH} = 2.96 Å with an *offset* of *r* = 0.93 Å. The involved angles are α = 152.3 ° and β = 71.7 ° (Figure F.97). Due to these three unique intermolecular interactions, the same one-dimensional chain of "dimers" as in **C18** and **C21** is formed along the c-axis (Figure 3.97).

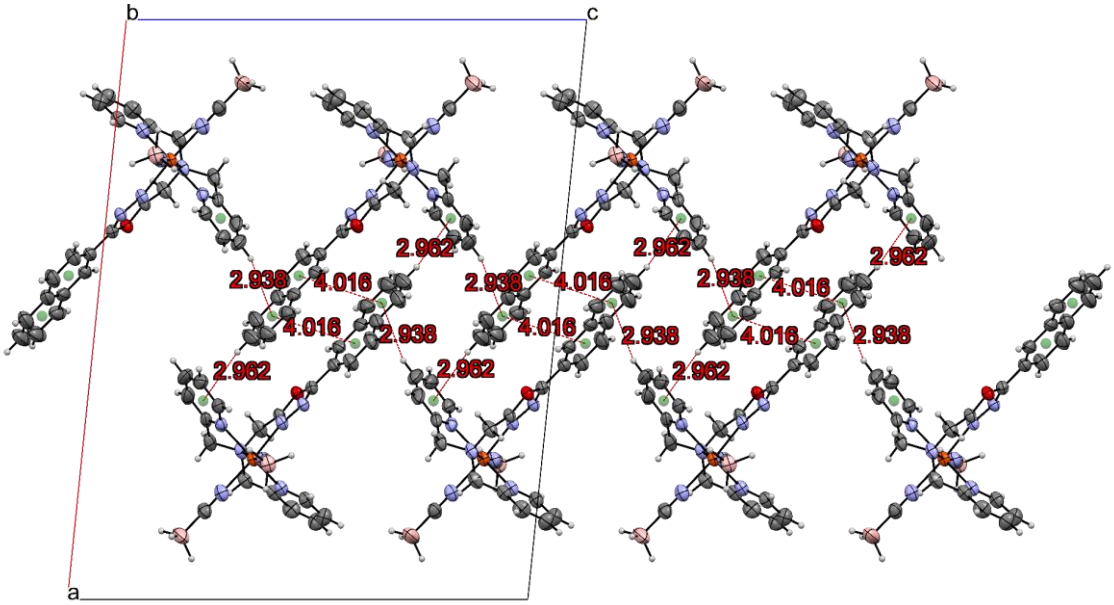


Figure 3.97 One-dimensional network of "complex dimers" in **C23**·3MeOH. Red dashed lines represent intermolecular distances. Colour scheme: pink – B, dark grey – C, grey – H, violet – N, red – O, orange – Fe. ORTEP representation with atomic displacement parameters set to 50 % probability.

With regard to the spin state of the iron(II) center, crystallographic data match with the magnetic measurements, shown in Figure 3.93. The abruptness of the spin transition can be explained by the intermolecular π-π interactions, which result in the chain-like ordering of complex molecules along the c-axis. Thus, structural changes associated with the SCO (primarily the contraction of the octahedral coordination sphere) can be transferred to neighboring molecules quite easily. Once again, solvent channels are formed between adjacent chains of complex molecules (Figure 3.98).

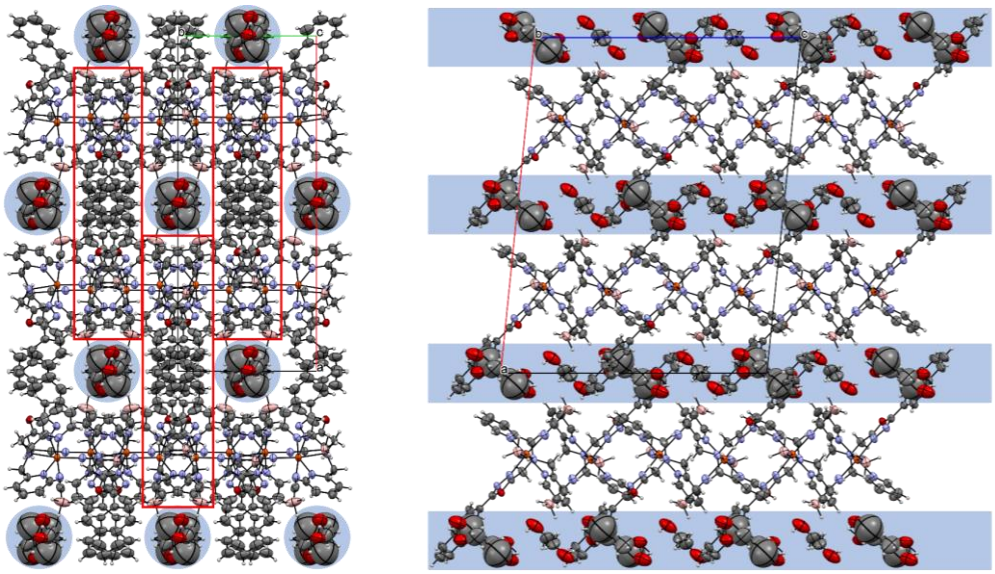


Figure 3.98 Packing of **C23**·3MeOH with view along the c-axis (left) and view along the b-axis (right). Red rectangles mark the one-dimensional chains of complex molecules along the c-axis. Blue areas illustrate the channel of solvent molecules. Colour scheme: pink – B, dark grey – C, grey – H, violet – N, red – O, orange – Fe. ORTEP representation with atomic displacement parameters set to 50 % probability.

For comparison, a second single-crystal X-ray structure analysis of **C23**·3MeOH was performed at 120 K. Crystallographic Data can be found in Table D.14. At the given temperature, the compound is still crystallized in the monoclinic space group *C*2/*c* with eight formula units in the unit cell. Nevertheless, the cell volume decreased from 6164.9(3) Å³ to 5835.1(3) Å³, which displays a reduction of the cell volume of about 5 %. This can be attributed to the fact, that the octahedral coordination sphere of low-spin iron(II) ions is smaller compared to high-spin iron(II) ions, since there is no occupation of antibonding e_g*-orbitals.

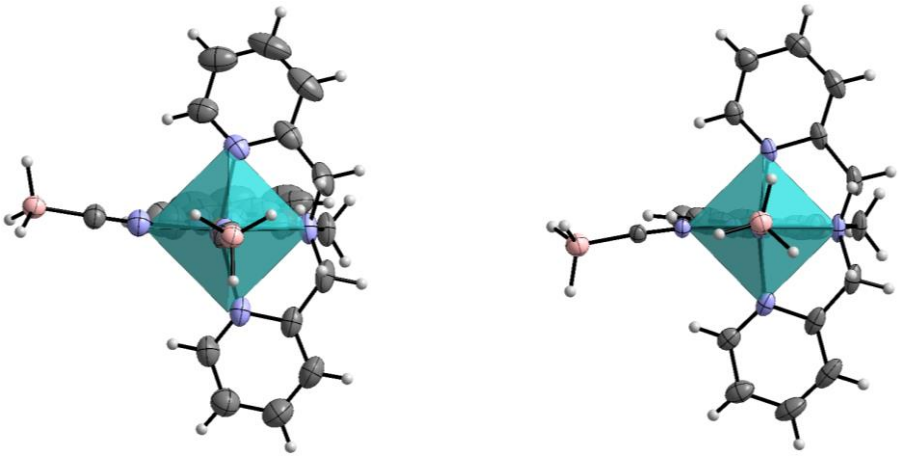


Figure 3.99 Molecular structure of **C23**·3MeOH and its ideal coordination octahedron with view along the Fe-N5 axis at 220 K (left) and 120 K (right), calculated with SHAPE.[62]. Colour scheme: pink – B, dark grey – C, grey – H, violet – N, red – O, orange – Fe. ORTEP representation with atomic displacement parameters set to 50 % probability.

Furthermore, since the occupation of the bonding t_{2g}-orbitals in LS Fe(II) is perfectly isotropic, deviation of the octahedral coordination sphere from the ideal one should be smaller. Indeed, a lower distortion of the N_6-coordination sphere is found in the low-spin species at 120 K. The octahedral distortion parameter is equal to $\Sigma_O(FeN_6)$ = 47.0 °, accompanied by the continuous shape value of $CShM(O_h)$ = 0.30. Figure 3.99 shows that the major difference arises from the position of the apical coordinated pyridyl groups. Thus, the embedded *trans*-angle increases from 152.75(5) ° (at 220 K) to 166.83(6) ° (at 120 K), closing the gap to the ideal 180 °. A detailed summary of structural parameters of **C23**·3MeOH for both temperatures can be found in Table E.11. As expected, the crystallographic and magnetic data also agree at 120 K with regards to the present spin state. The small change of cell parameters consequently results in a variation of the intermolecular distances. Figure 3.100 illustrates the iron(II)-iron(II) distances in the one-dimensional chain of complex molecules along the c-axis. In the HS state at 220 K, distances of 10.94 Å and 14.21 Å are found. At 120 K, these distances decreased to 10.87 Å and 13.42 Å, respectively. In addition to the intermolecular distances, intramolecular metal-ligand bond lengths changed as well. The mean metal-ligand distance is equal to 1.97 Å, which is 9 % shorter than the average distance in the HS state. This reduction of the FeN_6 coordination sphere is in good agreement with the literature.[58,295]

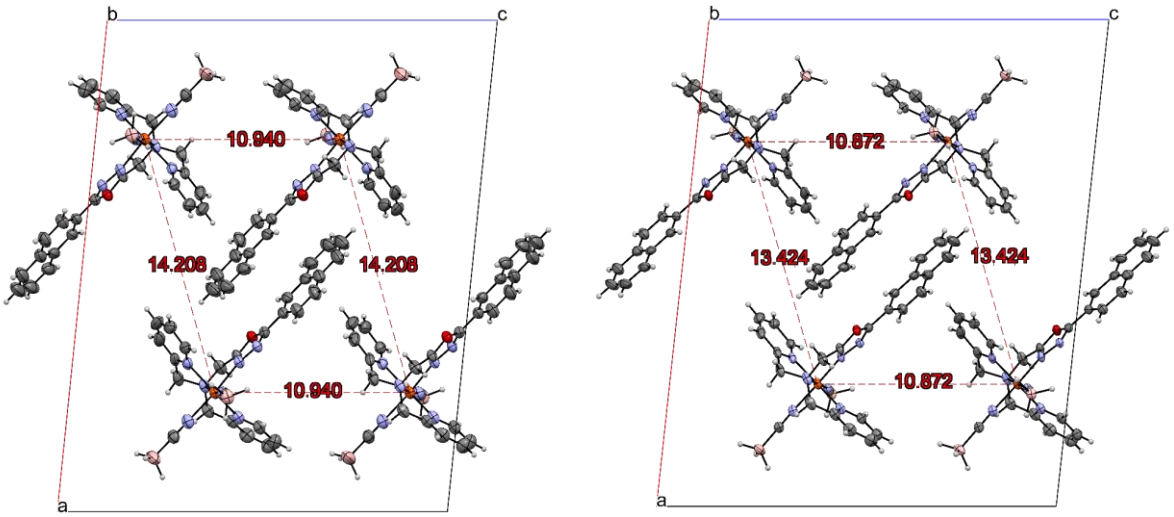


Figure 3.100 One-dimensional network of "complex dimers" in **C23**·3MeOH at 220 K (left) and 120 K (right). Unit cell changes are remarkably more pronounced along the a-axis, which corresponds to the interdimer short contacts. Red dashed lines represent intermolecular distances between iron(II) centers. Colour scheme: pink – B, dark grey – C, grey – H, violet – N, red – O, orange – Fe. ORTEP representation with atomic displacement parameters set to 50 % probability.

In summary,complexation of **L**$^{\mathbf{Naph}}$ led to the formation of the two SCO active monomers [Fe(**L**$^{\mathbf{Naph}}$)$(NCBH_3)_2$] · 4.5MeCN (**C23**·4.5MeCN) and [Fe(**L**$^{\mathbf{Ph}}$)$(NCBH_3)_2$] · 3MeOH (**C21**·3MeOH). Both compounds exhibit an abrupt spin transition, which can be ascribed to intermolecular π-π interactions in the crystal lattice. **C23**·4.5MeCN shows a trapped ratio of HS molecules when cooled to very low temperatures in a fast manner. This effect is known as TIESST effect (temperature induced excited spin state trapping). However, heating the compound to 400 K most likely results in the loss of lattice solvent, which stabilized the HS state even at lower temperatures. **C21**·3MeOH, in contrast, keeps its SCO ability after being heated towards higher temperatures. Additionally, exposing the coordination compound to air for five days does not influence the magnetic behavior either. Thus, the complex still shows a spin transition at approx. 207 K, offering the highest transition temperature throughout this work.

3.8 Magneto-optical relationship in an oxadiazole-based SCO complex

In the recent years, multifunctional materials, that allow modulation of the luminescence signal by using the spin crossover phenomenon, have become increasingly popular. This interest is motivated by a variety of different goals. Firstly, the energy transfer mechanism between the luminophore and the SCO active complex upon spin switching is not completely understood until now. More importantly, however, a luminescent signal may also be used to track the spin state of the SCO material. Indeed, the detection of emission is more efficient and easier to implement than other common techniques like magnetometry, optical absorption etc. **L^{Naph}** was designed to have a SCO suitable tetradentate binding pocket as well as the naphthyl group, acting as luminophore. In order to find a suitable excitation wavelength, the ligand system was studied with regards to its absorption in the UV/Vis region. Thus, various UV/Vis spectra of various concentrated solutions of **L^{Naph}** in n-butyronitril were recorded. Here, the starting concentration was equal to 8 mmol/l. For each additional measurement, the concentration was halved by diluting the solution. Figure F.105 in the appendix shows the combined spectra of all measurements. To allow for better comparison with literature known spectra, the absorption (in arbitrary units) was plotted against the wavelength (in nm). Figure 3.101 illustrates the penultimate measurement of the series with a concentration of 0.03 mmol/l. Absorption takes place in the region between 200 nm and 350 nm. For higher wavelength than 350 nm, no absorbance was detected anymore. The observed different maxima are summarized in Table 3.7 alongside with their corresponding molar extinction coefficients (ε[$M^{-1}cm^{-1}$]). Due to the different aromatic groups in **L^{Naph}**, the present absorption pattern can be attributed to a mixture of $\pi \rightarrow \pi^*$ transitions. According to literature, pure naphthalene shows absorption bands with maxima at 257, 265, 275, 283 and 285 nm, when measured in isooctane.[324]

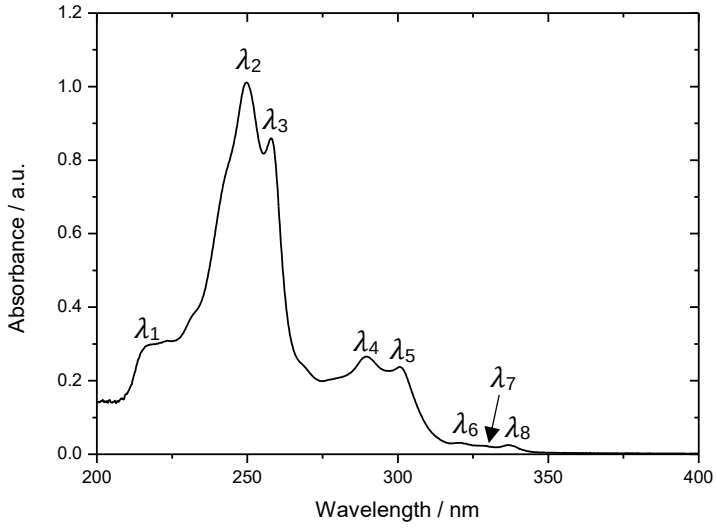


Figure 3.101 UV/Vis spectrum of **L^{Naph}** in n-butyronitril (c = 0.03 mmol/l).

Table 3.7 Summary of the present absorption maxima λ_i in the UV/Vis spectrum of $\mathbf{L^{Naph}}$ in n-butyronitril with corresponding molar extinction coefficients (ε) in $M^{-1}cm^{-1}$.

	λ_1	λ_2	λ_3	λ_4	λ_5	λ_6	λ_7	λ_8
λ_{abs} / nm	216	249	258	289	300	320	328	337
ε / $M^{-1}cm^{-1}$	15084	79001	67250	13506	11902	1068	775	850

The very high molar extinction coefficients for λ_2 (79001 $M^{-1}cm^{-1}$) and λ_3 (67250 $M^{-1}cm^{-1}$) are most likely caused by the superposition of different absorptions bands in this particular area. To investigate the luminescent properties of the system, a solution of $\mathbf{L^{Naph}}$ in n-butyronitril was excited by UV-radiation at room temperature. In order to examine the influence of the exciting wavelength, the solution was irradiated with light of wavelengths $\lambda_{ex,1}$ = 249 nm or $\lambda_{ex,2}$ = 289 nm. The resulting emission band wavelengths of the fluorescence spectra were independent of the exciting energy, which is in line with the literature known property of pure naphthalene.[316] Figure 3.102 illustrates the combined intensity versus wavelength plots of absorption and emission spectra of $\mathbf{L^{Naph}}$ with normalized intensities. There are two emission maxima at $\lambda_{em,1}$ = 344 nm and $\lambda_{em,2}$ = 361 nm, next to a shoulder at $\lambda_{em,3}$ = 379 nm. This spectrum looks very similar to the one of pure naphthalene, which shows emission peaks at approx. 323 nm, 334 nm and 349 nm.[321,325] This redshift of maxima could be explained by the aromatic 1,3,4-oxadiazole in 2-position of the naphthalene ring, which results in a larger conjugated π-system. Thus, energy of the π*-orbitals decreases, resulting in the emission of light of lower energy (higher wavelength). *Paun et al.* published the optical properties of a series of 2,5-disubstituted 1,3,4-oxadiazoles, including compounds with the naphthyl group in 2-position.[326]

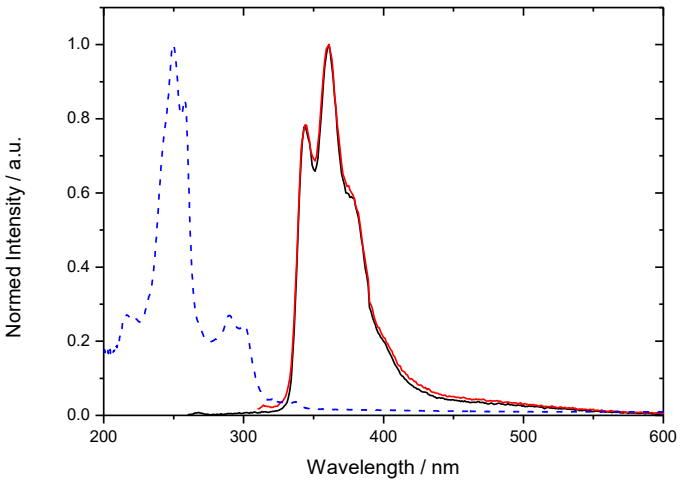


Figure 3.102 Combined intensity versus wavelength plot of absorption (blue dashed line) and emission spectra with excitation wavelengths of $\lambda_{ex,1}$ = 249 nm (black solid line) and $\lambda_{ex,2}$ = 289 nm (red solid line) of $\mathbf{L^{Naph}}$ in n-butyronitril.

Indeed, these systems exhibit redshifted emission maxima as well, compared to pure naphthalene. Thus, the emission spectra are nearly equal to the one of $\mathbf{L^{Naph}}$. Since **C23**·3MeOH shows abrupt SCO with no HS residue, the compound is ideal to be investigated for its photo-magnetic properties. In addition to that, the complex seems to be inert against atmospheric oxygen and keeps its SCO capability after being exposed to high and low temperatures. Consequently, absorption of **C23**·3MeOH in n-butyronitril was measured between 250 nm and 1000 nm. Starting with a concentration of c_1 = 1 mmol/l, a total of seven measurements were performed, with the concentration being halved from measurement to measurement by diluting the solution. Since the molar extinction factors (ε) of the absorption bands differ heavily, the spectra are shown in a combined plot in Figure 3.103 to illustrate every absorption band. Concentration independent absorption maxima are highlighted with red vertical lines.

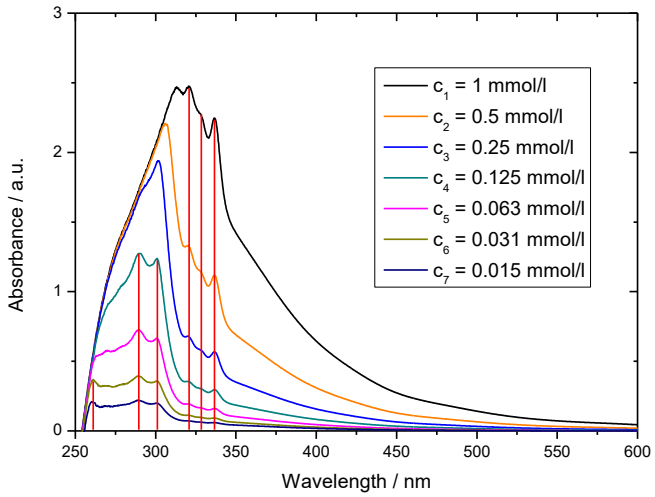


Figure 3.103 UV/Vis spectra of **C23**·3MeOH in n-butyronitril for different concentrations. From measurement to measurement, the concentration was halved by diluting the solution. There is no absorption observable between 600-1000 nm.

The observed absorption bands for **C23**·3MeOH in n-butyronitril (Table 3.8) represent ligand centered transitions and are in very good agreement with those of $\mathbf{L^{Naph}}$. In contrast to the spectrum of the free ligand, the spectra of the coordination compound show further absorptions above 350 nm, even though no well-resolved absorption band is observed.

Table 3.8 Summary of the present absorption maxima λ_i in the UV/Vis spectra of $\mathbf{L^{Naph}}$ in n-butyronitril with corresponding molar extinction coefficients ε in $M^{-1}cm^{-1}$.

	λ_1	λ_2	λ_3	λ_4	λ_5	λ_6
λ_{abs} / nm	258	289	301	320	328	337
ε / $M^{-1}cm^{-1}$	2657	2729	3192	12488	13588	12890

This could be an indication of a MLCT transition, which is known to appear between approx. 350 and 600 nm for mononuclear octahedral iron(II) complexes with aromatic ligands.[327–330] [Fe(**TPA**)$(NCMe)_2](ClO_4)_2$ (**TPA** = tris(2-pyridylmethyl)amine) for instance, which offers a similar coordination sphere to **C23**·3MeOH, exhibits MLCT absorption bands around 370, 389 and 506 nm.[331–333]

It is well known from literature that the intensity of fluorescence itself is temperature dependent and decreases from low to high temperatures, which is referred to as thermal quenching.[183–185] To distinguish between the effect of temperature and the effect of spin state on the fluorescence, an analogous diamagnetic Zn(II) complex was synthesized. Therefore, zinc(II) sulfate hydrate was firstly reacted with four equivalents pyridine and two equivalents sodium cyanoborohydride in water, which yielded $[Zn(py)_4(NCBH_3)_2]$ (**C24**) as a colourless solid. It can be assumed, that the zinc(II) complex offers the same octahedral coordination geometry as the literature known compounds $[Zn(py)_4(NCS)_2]$ and $[Zn(py)_4(NCSe)_2]$.[334] Structure elucidation was achieved by IR and NMR spectroscopy (see Chapter 6.4.33). The subsequent complexation of **C24** with $\mathbf{L^{Naph}}$ resulted in the formation of microcrystalline needles of the desired zinc(II) coordination compound $[Zn(\mathbf{L^{Naph}})(NCBH_3)_2]$ (**C25**). Similar to **C24**, the IR spectrum of **C25** shows the prominent ν(B-H) and ν(C≡N) stretching bands at 2353 cm^{-1} and 2190 cm^{-1}, respectively. Next to that, a consistent fingerprint region to the IR spectrum of $\mathbf{L^{Naph}}$ can be found (Figure A.40). ^{1}H-NMR studies of **C25** in d^6-DMSO further confirm the successful synthesis and isolation of the desired complex (see Chapter 6.4.34). Absorption of **C25** in n-butyronitril was measured from 250 – 1000 nm, shown in Figure 3.104.

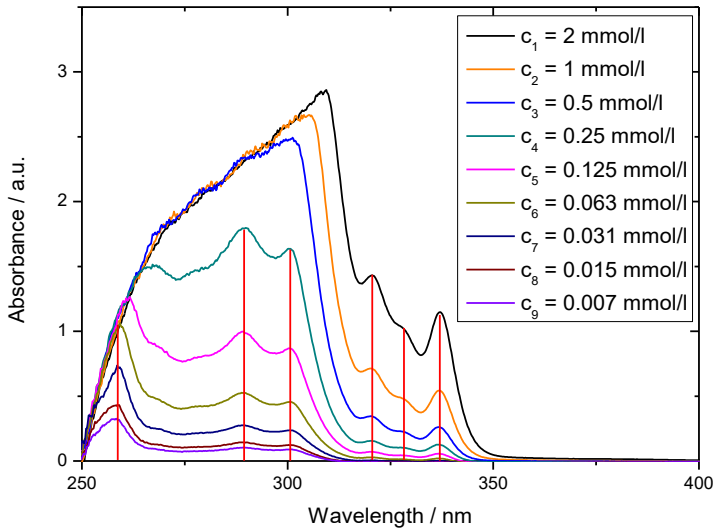


Figure 3.104 UV/Vis spectra of **C25** in n-butyronitril for different concentrations. From measurement to measurement, the concentration was halved by diluting the solution. There is no absorption observable between 400-1000 nm.

Complex **C25** exhibits ligand centered transition bands at the exact wavelengths as **C23**·3MeOH and is thus showing the absorption pattern of $\mathbf{L}^{\mathbf{Naph}}$. This finding additionally confirms the successful synthesis of the desired complex in form of [Zn($\mathbf{L}^{\mathbf{Naph}}$)($NCBH_3$)$_2$]. Furthermore, it is noticeable that **C25** shows no absorption above 350 nm, resulting in colourless crystals/ solutions.

3.8.1 Temperature dependent fluorescence of C23·3MeOH and C25

The SCO in solution can differ significantly to the one observed in the crystalline state. While spin transition in the solid can occur in an abrupt and complete manner, the same compound may show a considerable HS residue at low temperatures in solution.[335] In addition to that, solvation of the SCO active molecules might result in a more gradual spin transition due to weaker intermolecular interactions.[336] Considering these two arguments, luminescence measurements of **C23**·3MeOH and **C25** (for comparison) were performed on single-crystals by [redacted] in the group of [redacted] in Giessen (Germany). Firstly, photoluminescence of both complexes was measured at room temperature and at 77 K (temperature of liquid nitrogen). The resulting emission spectra are shown in Figure 3.105, plotting the normalized intensity versus the wavelength. Both samples were irradiated with light of wavelength 300 nm. The spectrum of **C23**·3MeOH at 77 K is very close to the one of $\mathbf{L}^{\mathbf{Naph}}$ in solution. Here, two well-resolved absorption maxima at $\lambda_{em,1}$ = 343 nm and $\lambda_{em,2}$ = 359 nm can be observed, next to one shoulder-like maximum at $\lambda_{em,3}$ = 378 nm. Wavelengths are in good agreement with those of $\mathbf{L}^{\mathbf{Naph}}$. Measuring the same sample at room temperature slightly shifts $\lambda_{em,1}$ and $\lambda_{em,2}$ to 348 nm and 359 nm, respectively. The shoulder-like emission band is not resolved anymore.

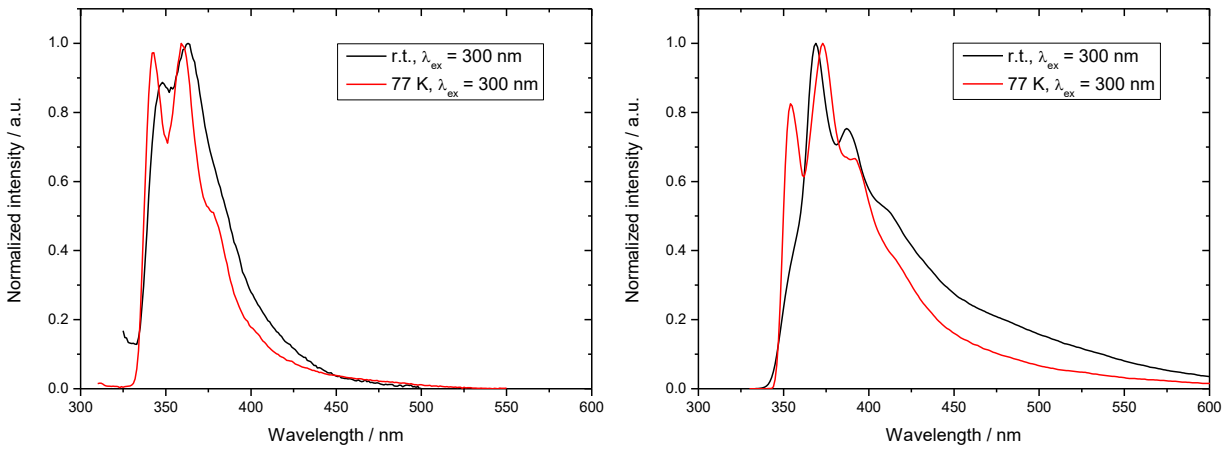


Figure 3.105 Emission spectra of **C23**·3MeOH (left) and **C25** (right) between 300 nm and 600 nm. Samples were excited with λ_{ex} = 300 nm. Measurements were done at 77 K (red solid lines) and at room temperature (black solid lines). The emission of **C23**·3MeOH below 330 nm is above zero due to overcorrection of spectra since emission intensity was rather low.

Similar to **C23**·3MeOH, the emission spectrum of **C25** at 77 K resembles roughly the luminescence of $\mathbf{L}^{\mathbf{Naph}}$. However, emission bands are shifted more pronouncedly. Thus, three well-resolved emission maxima at $\lambda_{em,1}$ = 354 nm, $\lambda_{em,2}$ = 373 nm and $\lambda_{em,3}$ = 392 nm (shoulder) can be found. In addition to that, a fourth shoulder-like band at $\lambda_{em,4}$ = 414 nm becomes apparent. Remeasuring the sample at room temperature reveals a different shape of the emission band. The emission maxima $\lambda_{em,2}$ and $\lambda_{em,3}$ shift to 369 nm and 387 nm, respectively, while $\lambda_{em,1}$ and $\lambda_{em,4}$ remain unchanged. However, the relative intensity of $\lambda_{em,1}$ drastically decreases, whereas that of $\lambda_{em,4}$ increases. To further investigate the dependency of *emission intensity* from temperature, two additional series of measurements were carried out. Therefore, the cuvette, containing either **C23**·3MeOH or **C25,** was adjusted in a Dewar assembly half-filled with liquid nitrogen. Afterwards, emission spectra were recorded using the same parameters with a delay of 10 min between each measurement. Altogether, 20 spectra were recorded for each compound. Thus, the last spectra were measured in a Dewar already warmed up to room temperature. However, sample temperature could not be controlled during that time. Furthermore, as for both compounds different parameters (slits, substance amount, and exact position of the cuvette in the beam) were used, no comparison of the absolute intensity between them is possible. The resulting plots are illustrated in Figure 3.106 (left for **C23**·3MeOH and right for **C25**). Considering the shape and intensity of emission bands in both samples, it can be assumed that room temperature was reached after approx. 60 min. After this time, the spectra do not significantly differ anymore. For both samples, the overall intensity of emission decreases with increasing temperature. For **C25**, this can be ascribed to thermal quenching of luminescence.[183–185] In the case of **C23**·3MeOH, however, this effect could be combined with a potential interplay between the SCO and luminescence.

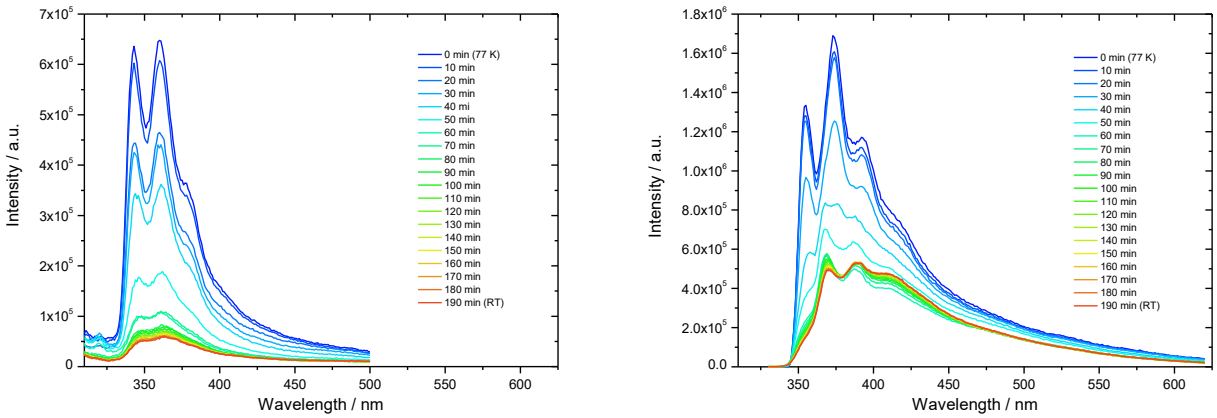


Figure 3.106 Emission spectra of **C23**·3MeOH (left) and **C25** (right) between 310 nm and 625 nm for a series of time related measurements. During the measured 190 min, liquid nitrogen was allowed to evaporate, which results in a heating of the sample.

To compare the progression of luminescence quenching, the normalized intensity of the most pronounced emission maximum $\lambda_{em,2}$ (359 nm in **C23**·3MeOH and 373 nm in **C25**) is plotted against the time for both compounds.[177,189,190] The resulting plots are visualized in Figure 3.107. The normalized intensity of $\lambda_{em,2}$ in [Zn(**L**$^{\mathbf{Naph}}$)$(NCBH_3)_2$] (**C25**) decreases only slightly in the first 20 min to 94 %. Afterwards, the intensity drops continuously to a value of 34 % at 60 min. After this time, significant changes of the intensity can no longer be observed, indicating a present room temperature in the experimental system. This time period can not only be presumed by the plot in Figure 3.107, but also due to the emission spectra in Figure 3.106. In contrast, the behavior of [Fe(**L**$^{\mathbf{Naph}}$)$(NCBH_3)_2$] · 3MeOH (**C23**·3MeOH) is somehow different. While the percentage of intensity after 10 min is approximately the same as for **C25**, the value drops pronouncedly to 72 % at 20 min. This displays a difference of Δ = 22 % to the value of **C25** at that exact same time. After that, the normalized intensity decreases progressively until it plateaus at about 60 min, showing the same behavior as **C25**. However, it results in a plateau at around 10 % intensity, which is clearly lower compared to the analogous zinc(II) complex. Interestingly, this gap between the plateaus of both compounds (marked as Δ in Figure 3.107) is exactly the offset of emission intensity between the two complexes at 20 min. This finding hints towards a significant impact of the SCO on the fluorescence in **C23**·3MeOH, assuming a spin transition from the LS to the HS state between 10 and 20 min. After 30 min, the progression of intensity is analogous to **C25** (vertically shifted by Δ), which in contrast does not change its diamagnetic $^1A_{1g}$ ground state. Thus, it can be assumed that the overall decrease of intensity in **C23**·3MeOH between 20 and 60 min is attributed to thermal quenching.

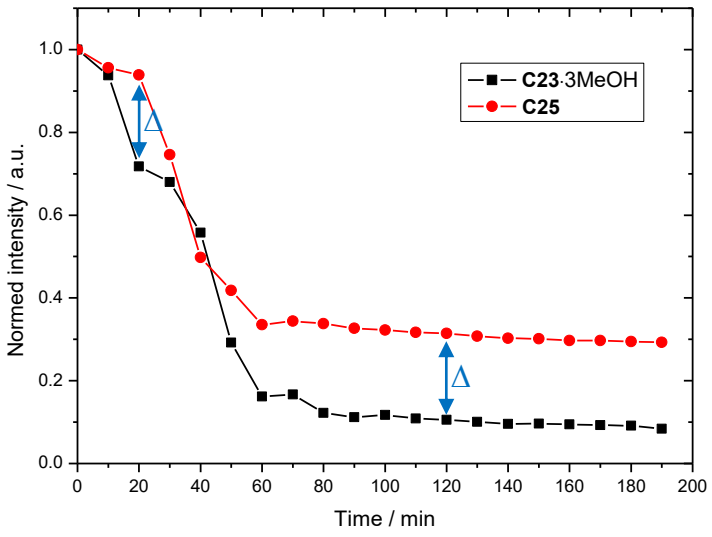


Figure 3.107 Normalized intensity of $\lambda_{em,2}$ vs. time for **C23**·3MeOH ($\lambda_{em,2}$ = 359 nm, black squares) and **C25** ($\lambda_{em,2}$ = 359 nm, red circles). The offset Δ is attributed to the present SCO in Fe(II) from LS to HS.

The drop between 10 and 20 min, on the other hand, is most likely due to the change from the diamagnetic $^1A_{1g}$ to the paramagnetic $^5T_{2g}$ state in the iron(II) ion. Quenching of luminescence in the presence of paramagnetic transition metals is well known in literature.[180,337–341] Thus, the pronounced decrease of the $\lambda_{em,2}$-intensity in **C23**·3MeOH at 20 min can indeed be attributed to the switch from the diamagnetic LS to the paramagnetic HS state. Comparison between **C23**·3MeOH and its analogous zinc(II) complex **C25** reveals, that the overall decrease in emission intensity is probably a combination of SCO and thermal quenching. Published SCO systems with fluorescent ligands shows similar temperature dependent behavior of luminescence as [Fe(**L**$^{\mathbf{Naph}}$)$(NCBH_3)_2$] · 3MeOH.[177,178,189,313–315] However, further temperature-controlled experiments are required to determine the exact relationship between emission intensity and SCO more precisely. If the correlation between photoluminescence and SCO is further confirmed, **C23**·3MeOH would be the first oxadiazole-based complex showing such a property.

3.9 Cobalt(II) based mononuclear Single Ion Magnets (SIM)

In the last few years, research has focused more and more on the realization of Single Ion Magnets (SIM), since controlling the anisotropic axes in multinuclear clusters (SMMs) can be an extremely difficult task. Six-coordinate Co(II) complexes with distorted octahedral (O_h) symmetry are known to exhibit large |*D*| values owing to the unquenched orbital contribution in the t_{2g} set and energetically low-lying excited states. Hence, they play an important role in the field of transition metal SIMs. Formation of the mononuclear iron(II) complexes of type [Fe(**L**)$(NCS)_2$] · solv (**L** = $\mathbf{L^{Py,1}}$, $\mathbf{L^{Ph}}$, $\mathbf{L^{Naph}}$) inspired the synthesis of the analogous cobalt(II) coordination compounds to study their potential SIM behavior.

3.9.1 [Co($\mathbf{L^{Py,1}}$)$(NCS)_2$] · 1MeOH (C26)

Complexation of $Co(SCN)_2$ with $\mathbf{L^{Py,1}}$ in methanol yielded the Co(II) coordination compound [Co($\mathbf{L^{Py,1}}$)$(NCS)_2$] · MeOH (**C26**) with the expected molecular structure. The compound crystallizes in the monoclinic space group *I*2/*a* with eight formula units inside the unit cell. The structure was recorded at 120 K, crystallographic data can be found in Table D.15. Likewise to the isostructural iron(II) compound **C16**·MeOH, the asymmetric unit contains one complex unity next to one methanol molecule (Figure F.98). The complex molecule exhibits the expected coordination mode. Thus, one nitrogen donor atom of the 1,3,4-oxadiazole, the tertiary amine and the two thiocyanate coligands form the equatorial base of the coordination octahedron. The apical vacancies are saturated by the pyridine rings of the bis-2-picolylamine moiety. Similar to **C16**·MeOH, the trend of bond lengths in **C26** follows the description of Chapter 3.4.1 and can be explained by different σ- and π-contributions of the metal-ligand bonds. Thus, a distorted coordination geometry can be found in the crystalline packing with an octahedral distortion parameter equal to $\Sigma_O(CoN_6)$ = 94.1. This deviation of the coordination sphere from the ideal one is further confirmed by the continuous shape measurement value CShM(O_h) = 1.04 (Figure 3.108). These values are in good agreement with literature,[342,343] representing a high-spin CoN_6 system, which is also confirmed by the average metal-ligand bond length of $\bar{d}$(Co-N) = 2.13 Å .[344] This value is 0.05 Å smaller than the mean metal-ligand distance in the isostructural iron(II) complex **C16**·MeOH, which can be explained by the greater effective nuclear charge of cobalt(II). Since both compounds show anisotropic electron configurations ($^4T_{1g}$ for d^7-Co^{II} and $^5T_{2g}$ for d^6-Fe^{II}), the lower distortion compared to **C16**·MeOH [CShM(O_h) = 1.31] could be the result of a lower *degree of freedom* owing to shorter bonds. Due to π-π interactions, one-dimensional chains along the c-axis can be found (Figure F.102), arranged in the same manner as in **C23**·3MeOH. Parameters of the unique interactions as summarized in Table F.4 with references to the corresponding figures.

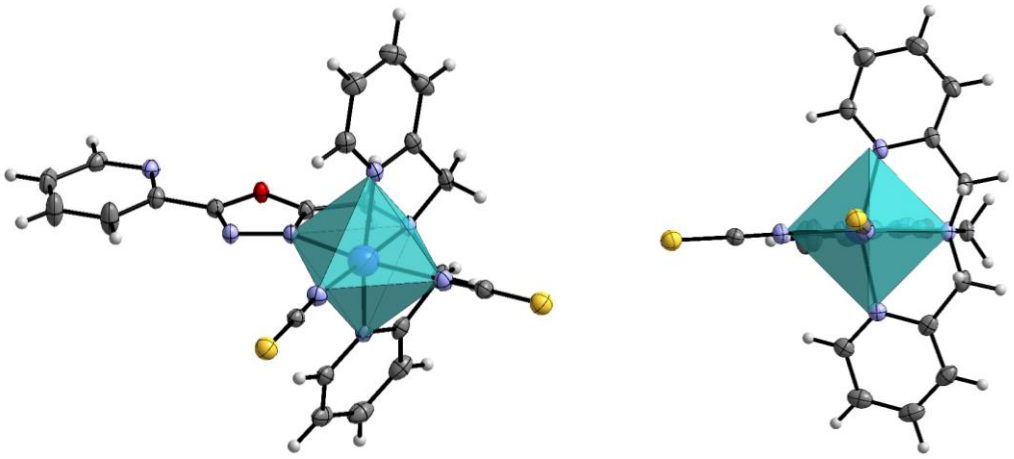


Figure 3.108 Molecular structure of **C26** and its ideal coordination octahedron with front view (left) and view along the Co-N5 axis (right), calculated with SHAPE.[62] Colour scheme: dark grey – C, grey – H, violet – N, red – O, yellow – S, purple – Co. ORTEP representation with atomic displacement parameters set to 50 % probability.

Magnetic properties of C26

To investigate **C26** towards its potential SIM behavior, the direct current (dc) magnetic properties were determined firstly. Hence, the magnetic susceptibility of sample was measured in the temperature range of 2-300 K with an applied magnetic field of 0.1 T. Since pronounced anisotropy was expected for this kind of system, single-crystals of **C26** were blocked with eicosane to prevent macroscopic movement. The combined χ_M *vs*. *T* and $\chi_M T$ *vs*. *T* plots are shown in Figure 3.109 (top left). At 300 K, a $\chi_M T$ product of 2.77 $cm^3mol^{-1}K$ can be found, which is significantly higher than the *spin-only* value for an isolated S = 3/2 Co(II) ion with *g* = 2 (1.88 $cm^3mol^{-1}K$, Equation 3.1). However, this value is within the expected range for a cobalt(II) high-spin ion (*S* = 3/2) with orbital angular momentum contribution.[343,345–347] Upon cooling, the $\chi_M T$ value decreases in a continuously manner to 1.62 $cm^3mol^{-1}K$ at 2.0 K, hinting towards significant zero-field splitting (ZFS) and thermal depopulation of excited *Kramer's* doublets.[343,345–347] To quantify the magnetic anisotropy correctly, additional magnetization data were collected between 2-10 K from 0.1 T to 7 T. The resulting data are visualized in *M vs*. *H* (Figure 3.109, top right) and *M vs*. *H*/*T* plots, also known as the reduced magnetization (Figure 3.109, bottom left and right). The broadening of the magnetization isotherms in the *M vs*. *H* plot towards higher fields confirms the present contribution of orbital momentum. Furthermore, the magnetization at the lowest temperature (2K) and highest field (7 T) is equal to 2.22 $N_A\mu_B$, which is lower than the expected saturated magnetization (M_{sat}) of 3 $N_A\mu_B$ for *g* = 2 and *S* = 3/2 (Equation 3.6). This difference is mainly caused be a present magnetic anisotropy. The reduced magnetization, which does not follow the Brillouin function, further confirms this statement (Figure 3.109, bottom).[348]

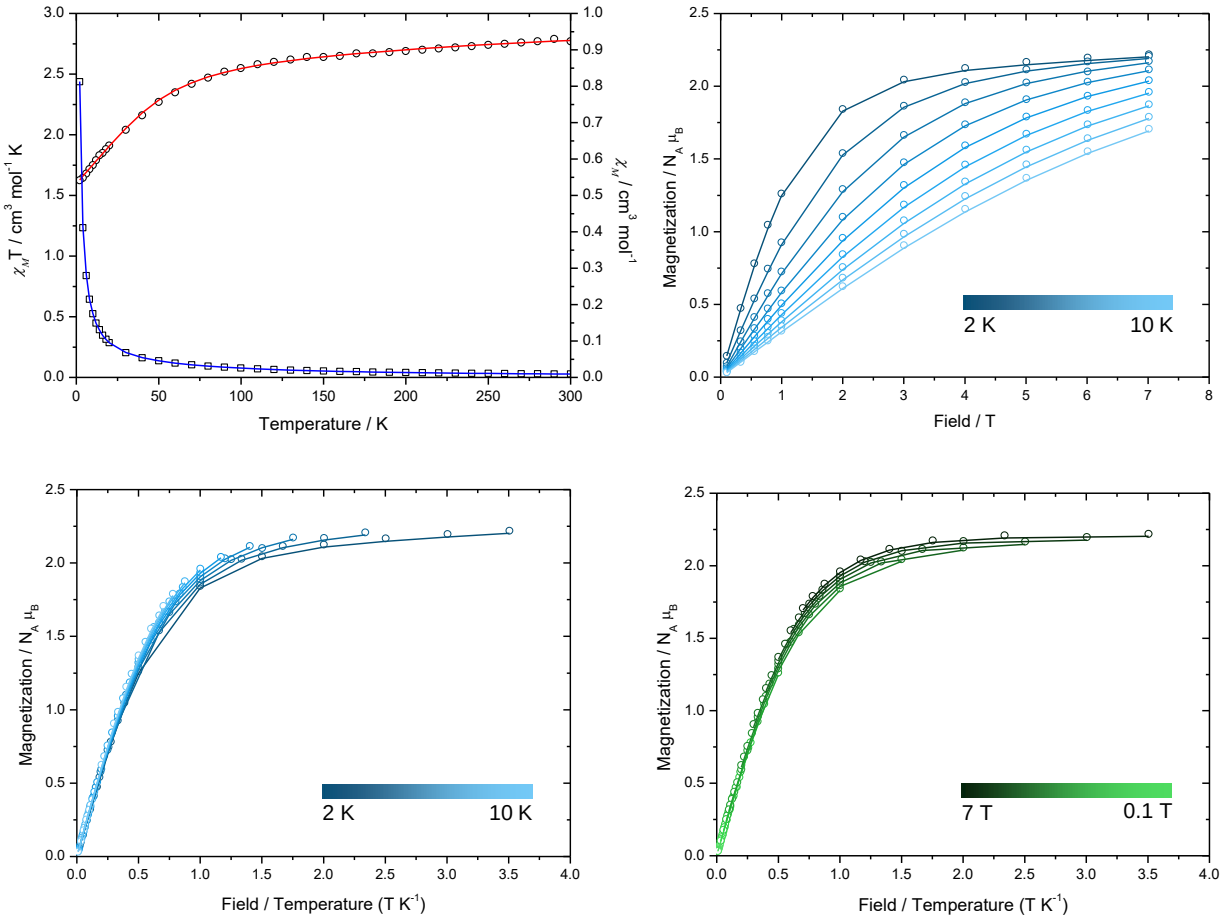


Figure 3.109 Temperature dependent magnetic behavior of **C26**. Top left: Combined $\chi_M T$ vs *T* (left values, open circles) and χ_M vs *T* (right values, open squares). Top right: *M* vs *H* plot. Bottom: *M* vs. *H/T* plots. Solid lines represent the best fits, using PHI.[201]

To fully understand the present SOC and ZFS effects in an Co(II) complex, a short theoretical recap of the fundamentals is considered essential to clarify the following approach. The electronic ground term of an octahedrally coordinated HS Co(II) ion is the orbital triplet $^4T_{1g}$. According to the T-P isomorphism, this term can be seen as the term with fictitious orbital angular momentum L = 1 (M_L = 0, ±1)[349]. An axial crystal field (caused by the tetragonal component of the distortion) splits the $^4T_{1g}$ term into an orbital doublet ^4E_g (M_L = ±1) and orbital singlet $^4A_{2g}$ (M_L = 0). In addition to that, SOC further splits the ^4E_g term into four *Kramers doublets*, which is attributed to the first-order effect. Second-order effect, in contrast, causes the mixture of ^4E_g and $^4A_{2g}$, resulting in the splitting of the $^4A_{2g}$-term. In case of lower symmetries than D_{4h}, the rhombic component of the crystal field further splits the ^4E_g term. A positive axial field yields a $^4A_{2g}$ ground state which causes a positive anisotropy (*easy-plane* anisotropy).[347] The *Figgis approach* is strictly used for systems with unquenched orbital angular momentum, relying the T-P isomorphism.[350] This Hamiltonian (Equation 3.8) takes SOC, the low-symmetry crystal field and Zeeman interaction into account.

Therefore, it includes the axial field Δ, the rhombic field δ, the SOC parameter λ and the orbital reduction factor α.

$$\hat{H} = \alpha\lambda\hat{L}\cdot\hat{S} + \Delta\left[\hat{L}_z^2 - L(L+1)/3\right] + \delta\left(\hat{L}_y^2 - \hat{L}_x^2\right) + \beta H\left(-\alpha\hat{L} + g\hat{S}\right) \quad (3.8)$$

For HS Co(II) complexes, the spin-orbit coupling parameter λ is negative due to more than half-filled 3d-orbitals. The value of λ in octahedrally coordinated Co(II) ion ranges between -180 cm and -90 cm^{-1}.[347] The orbital reduction factor α ($\alpha = \kappa \cdot A$) describes the reduction of orbital angular momentum ($L \leq 1$) caused by two factors: Delocalization of the unpaired electrons towards the ligands (due to κ) and admixture of the excited $^4T_{1g}(^4P)$ term with the $^4T_{1g}$ (^4F) ground term due to second-order SOC.[347] The reduction factor κ lies in the range of $0 \leq \kappa \leq 1$ and originates from the covalency of the meta-ligand bond. Values towards 1 describe a pure ionic bond type with isolated spins.[351,352] As the mixing of excited and ground states with equal symmetry is crystal field dependent, *A* describes the weak and strong field situation with *A* = 3/2 and *A* = 1, respectively.[347] Hence, the orbital reduction factor α can vary between 0 and 1.5. As mentioned above, an axial distortion causes a symmetry reduction from O_h to D_{4h} symmetry. The crystal field parameter Δ is defined by the energy gap between the $^4A_{2g}$ and ^4E_g term arising from the split $^4T_{1g}$ ground term. Further rhombic distortion is described by the parameter δ, which describes the splitting of the orbital doublet ^4E_g by definition, values of δ cannot be greater than $|\delta| \leq |\Delta|/3$.[346] Hence, susceptibility and magnetization data of **C26** were fitted simultaneously using the *Figgis approach* in Equation 3.8 with PHI.[201] The resulting fits are displayed in the corresponding plots as solid lines (Figure 3.109). To reduce the amount of fitting variables and thus prohibit overparameterization, values for λ = -180 cm^{-1} and α = 1.0 (localized spins with weak admixture between the $^4T_{1g}$ (^4P) and $^4T_{1g}$ (^4F) term) were kept constant. Best fit for *S* = 3/2, an isotropic *g*-factor and a present *TIP* of χ_{TIP} = 350 · 10^{-6} cm^3mol^{-1} resulted in *g* = 2.087(1), Δ = 236(2) cm^{-1} and δ = 61(21) cm^{-1}. The residual *R* of the fit is equal to 0.57 · 10^{-4}. The chosen *TIP* value is still below the common range for Co(II) complexes (400 – 600 · 10^{-6} cm^3mol^{-1}).[353] The model reveals an *easy-plane* type of magnetic anisotropy with a δ/Δ ratio of 0.26. However, this needs to be treated with caution, since the error of δ is approx. a third of the value itself. Nevertheless, the energy differences Δ and δ are in line with literature.[81,345–347] Subsequently, these values were used to simulate the *Zeeman splitting* of the magnetic terms in an applied magnetic field. The resulting simulation is illustrated in Figure 3.110 in form of an energy (*E*) versus field (*H*) plot. Additionally, percentage composition of the two lowest *Kramers doublet* states was calculated with PHI,[201] shown in Table F.5 in appendix.

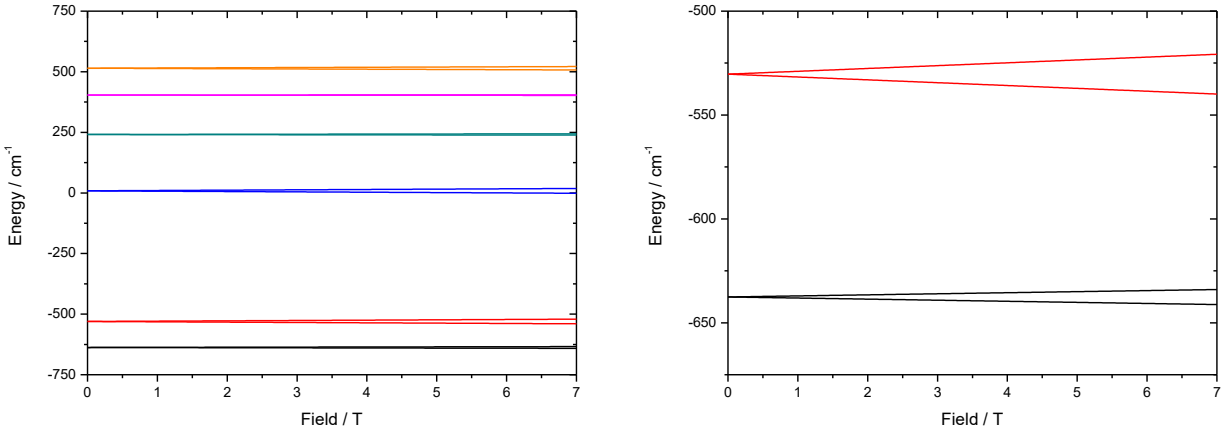


Figure 3.110 Left: Simulation of the *Zeeman splitting* in **C26** between 0 and 7 T, calculated with PHI.[201] Right: Zoom into the energy region from -675 cm^{-1} to -500 cm^{-1}.

Due to the positive axial crystal field parameter Δ, the ground term proves to be the orbit singlet $^4A_{2g}$-term, which is well-separated from the excited term ^4E_g.[347] This ground term is further split by second-order spin-orbit coupling, resulting in the two *Kramers doublets* M_S = ±1/2 and M_S = ±3/2 (at zero field). These states, which are illustrated as black and red lines in Figure 3.110 respectively, are consequently affected by the *Zeeman Effect* in an external magnetic field.[67] Indeed, calculation of the percentage composition of the eigenstates with PHI[201] confirms the isolated M_S = ±1/2 and M_S = ±3/2 states with M_L = 0 (Table F.5). Hence, at *low temperatures*, the system can be treated as a *spin-only S* = 3/2 system with no orbital contribution. Therefore, *Pardo et al*. suggested to fit low-temperature magnetization data of the compound [Co(**dmphen**)$_2$(NCS)$_2$] with the spin Hamiltonian in Equation 3.7.[345]

$$\hat{H} = D\left[\hat{S}_z^2 - S(S+1)/3\right] + E\left(\hat{S}_y^2 - \hat{S}_x^2\right) + g\mu_B HS \qquad (3.7)$$

Fitting of the magnetization data of **C26** with the afore described spin Hamiltonian resulted in g = 2.429(1), D = 48.7(7) cm^{-1} and E = 7.7(2) cm^{-1} for S = 3/2 (Figure G.42 – Figure G.44 in the Appendix). The sign of the zero-field parameters D and E are in accordance with the sign of the axial and rhombic crystal field parameters Δ and δ. Thus, the compound shows *easy-plane* anisotropy with additional transverse ZFS contribution ($|E/D|$ = 0.16). The increased g-factor refers to the contribution of the orbital angular momentum in the assumed $^4T_{1g}$ ground term. All parameters are in line with published values for HS Co(II) complexes with pseudo-octahedral coordination geometry.[342,343,345,346,354–358] The magnetic anisotropy is in good agreement with the distorted coordination sphere ($\Sigma_O(CoN_6)$ = 94.1 and CShM(O_h) = 1.04) of the complex molecule in the crystalline state.

In the classical SMM/ SIM picture, a system with D > 0 offers no energy barrier, since the spin is free to rotate within the *easy-plane*. However, in-plane anisotropy given by the $E(\hat{S}_y^2 - \hat{S}_x^2)$ term might result in the presence of out-of-phase signals (χ_M'') and hence in SIM behavior.[345] The alternating-current (ac) magnetic susceptibility of **C26** was measured at 2 K under different applied fields in the range of 0 T to 0.3 T. While no χ_M'' signal was observed under zero dc field, non-zero out-of-phase signals appeared when a small dc field was applied. Considering that the correct determination of an energy barrier requires maxima in the Cole-Cole plot, further measurements were made with an applied field of 0.28 T. At this field, the maxima were the most pronounced. Hence, the ac data of **C26** were collected from 1.9 K to 3.0 K with frequencies varying between 4 and 1400 Hz. Figure 3.111 (top left) illustrates the resulting χ_M'' versus χ_M' plot ("Cole-Cole plot"), where χ_M' and χ_M'' are the in-phase and out-of-phase molar magnetic susceptibilities. Both, χ_M' and χ_M'' show temperature- and frequency-dependent behavior (Figure 3.111 bottom). At 1.9 K, χ_M'' shows a maximum at 565 Hz, which shifts towards higher frequencies with increasing temperature.

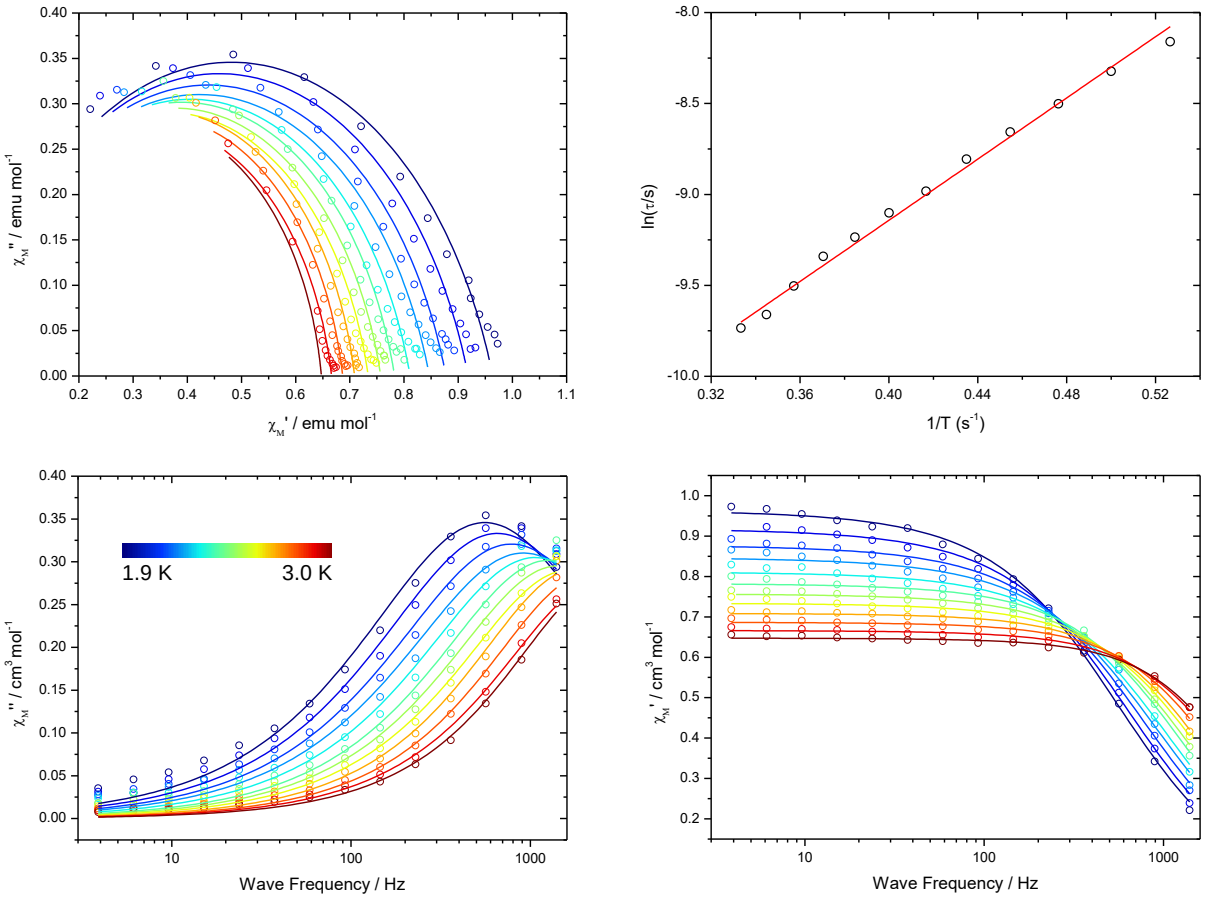


Figure 3.111 The ac susceptibility measurements of **C26** under an applied field of 0.28T between 1.9 K and 3.0 K. Top left: Cole-Cole (χ_M'' versus χ_M') plot. Top right: Arrhenius (ln(τ) vs. T^{-1}) plot. Bottom left: frequency-dependent in-phase signal χ_M'. Bottom right: frequency-dependent out-of-phase signal χ_M''. Solid lines represent the best fit using CC-FIT2.[359]

Hence, a maximum of χ_M'', when plotted against χ_M' or ν (wave frequency), can only be observed below 2.4 K. Above that temperature, no more maxima are present due to the frequency limit of the SQUID magnetometer of 1400 Hz. Data were fitted with the open-source program CC-FIT2 by *Reta* and *Chilton*.[359] It is important to note that data processing was done with the option "--discard_off" activated. Hence, temperatures with no observable maximum in χ_M'' are still taken into account during the evaluation process. The ac susceptibility data were fitted with the generalized Debye model,[359] illustrated as solid lines in the corresponding plots in Figure 3.111. The resulting temperature-dependent relaxation times τ are plotted in form of the Arrhenius plot in Figure 3.111 (top right). Since temperatures with no observable maximum in χ_M'' were considered in the evaluation, fitting of ln(τ) was performed assuming only the pure thermally activated Orbach process to prevent misinterpretation:

$$\tau^{-1} = \tau_0^{-1} \cdot \exp\left(-\frac{U_{\text{eff}}}{k_{\text{B}}T}\right) \tag{3.9}$$

The obtained parameters are U_{eff} = 8 K (≙ 5.6 cm^{-1}) and $\tau_0 = 3.98 \cdot 10^{-6}$ s. The ln(τ) values at high temperatures (≙ low 1/*T*-regime) do not follow the linear trend, as they are slightly smaller than expected. This is most likely caused by inaccurate determination of τ due to the missing maxima in χ_M''. Greater values would yield in a smaller slope of the fitting function and thus a smaller U_{eff} and higher τ_0. Nevertheless, this activation barrier agrees well with literature known values of octahedral Co(II) systems with similar *D* and *E* values.[343,345,354] The pathway and origin of slow relaxation in pseudo-octahedral Co(II) with *easy-plane* anisotropy is discussed very frequently in literature. *Pardo et al.* suggested for the first time that the origin of energy barrier in the complex [Co(**dmphen**)$_2$(NCS)$_2$] is not caused by the classical axial anisotropy barrier, but due to the transverse anisotropy [$U_{\text{eff}} = E(S^2\text{-}1/4) = 2E$ for $S = 3/2$]. This barrier would prevent the spin-flip from +x (or +y) to −x (or −y) in the *xy* plane.[345] As **C26** shows a significant *E*/*D* ratio of 0.16, this could be a valid explanation for the present energy barrier. The theoretical value of U_{eff} caused by the present transverse anisotropy (E = 7.7(2) cm^{-1}) would be equal to U_{eff} = 15.4 cm^{-1}. This discrepancy between theoretical and experimental value could be caused by tunneling processes, that were excluded in the fitting of τ. In Co(II), hyperfine interaction of the M_S = 1/2 state with the I = 7/2 nuclear spin additionally results in a manifold of 16 states. Some of these states provide the appropriate energy to allow for direct transition.[354] Also, energy splitting caused by the hyperfine interaction enhances the relaxation probability of QTM via spin-lattice relaxation, since the density of lattice phonons increases with energy.[360]

3.9.2 [Co(η³-L^{Ph})(NCS)$_2$(MeOH)] (C27)

As the mononuclear Co(II) complex [Co(**L^{Py,1}**)(NCS)$_2$] · 1MeOH (**C26**) exhibits SIM behavior under an applied magnetic field of 0.28 T, Co(SCN)$_2$ was reacted with **L^{Ph}** to synthesize the second cobalt(II) compound in this work. Therefore, equimolar amounts of Co(SCN)$_2$ and **L^{Ph}** were dissolved separately in methanol. Combination of both solutions with subsequent slow evaporation of the solvent yielded [Co(η^3-**L^{Ph}**)(NCS)$_2$(MeOH)] (**C27**) as purple single-crystals. X-ray structure analysis was performed at 173 K. The resulting crystallographic data can be seen in Table D.15. **C27** is not isostructural to complex **C26,** as the coordination mode of **L^{Ph}** differs. Hence, **L^{Ph}** only coordinates via its bis-(2-picolyl)amine moiety such that the pyridine rings are coordinated in a *cis* manner. The equatorial positions of the coordination octahedron are thus occupied by the amine function, one pyridinyl group and by two thiocyanate coligands. One apical position is filled with the remaining pyridine ring, while a methanol molecule coordinates in the *trans* position. Similar to the **L^{Ph}**-based nickel(II) complex **C22**, the oxadiazole backbone does not bind to the cobalt(II) ion resulting in a CoN_5O_1 coordination sphere (Figure 3.112). Bond distances can be roughly categorized in three groups. The longest bond lengths can be found between the Co(II) ion and the amine function (Co1-N1) or methanol molecule (Co1-O1) with 2.27 Å and 2.21 Å, respectively. While the amine nitrogen offers almost pure σ-donor contribution to the resulting metal-ligand bond [232], oxygen in general exhibits larger bond distance to transition metals compared to nitrogen donor atoms.[67] The next shorter metal-ligand bonds can be found to the pyridine rings with distances of *d*(Co1-N5) = 2.15 Å and *d*(Co1-N2) = 2.10 Å, which exhibit additional π-backbonding character.[232] Due to enhanced electrostatic attraction, the smallest bond lengths are formed to the negatively charged thiocyanate coligands with *d*(Co1-N3) = 2.04 Å and *d*(Co1-N4) = 2.06 Å.

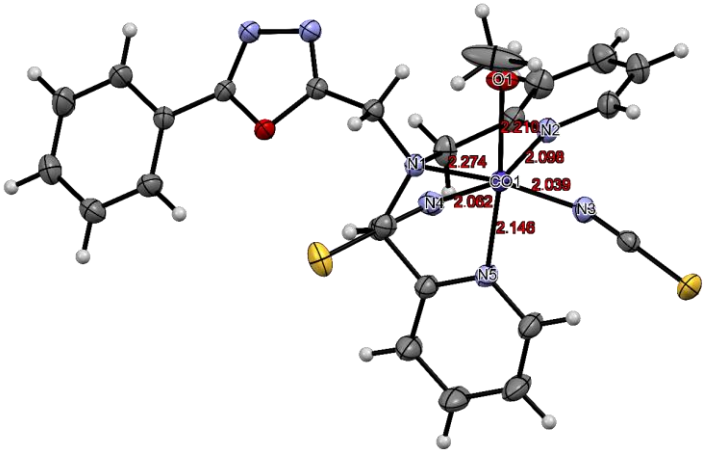


Figure 3.112 Molecular structure of **C27**. Bond distances are displayed in red. Colour scheme: dark grey – C, grey – H, violet – N, red – O, yellow – S, purple – Co. ORTEP representation with atomic displacement parameters set to 50 % probability.

The average cobalt(II)-ligand bond distance is equal to $\bar{d}$(Co-L) = 2.14 Å and thus slightly larger than in the cobalt(II) complex **C26**. Combined with the present distortion of $\Sigma_O(CoN_5O_1)$ = 83.3 ° and CShM(O_h) = 1.01 (Figure 3.113), this represents a Co(II) ion in the high-spin state.[342–344] The detailed compilation of structural parameters can be found in Table E.13. [Co(η^3-**L^{Ph}**)(NCS)$_2$(MeOH)] crystalizes in the triclinic space group $P\bar{1}$. The asymmetric unit includes one complex molecule. Symmetry operation due to the present center of inversion yields in a second complex unity in the unit cell (Figure F.103).

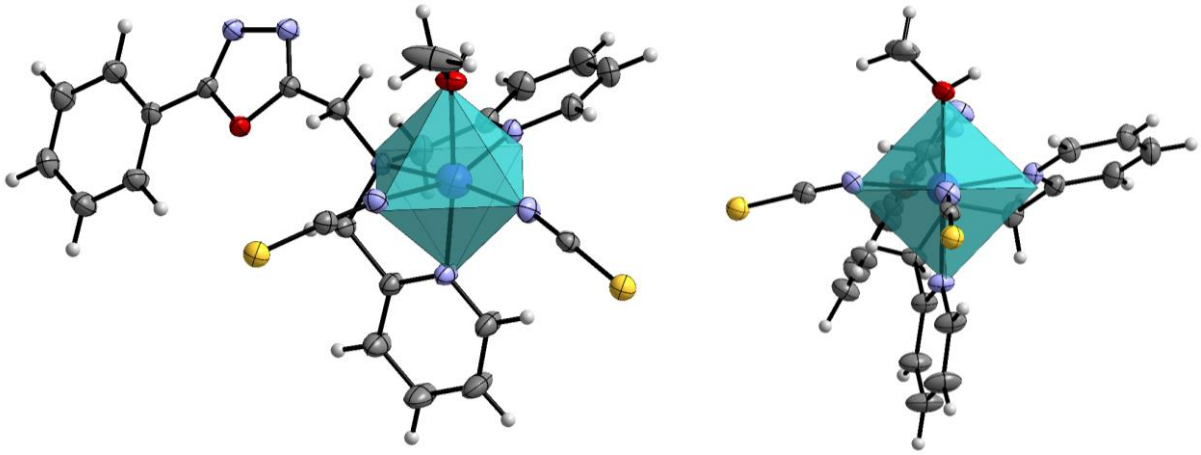


Figure 3.113 Molecular structure of **C27** and its ideal coordination octahedron with front view (left) and view along the Co-N3 axis (right), calculated with SHAPE.[62] Colour scheme: dark grey – C, grey – H, violet – N, red – O, yellow – S, purple – Co. ORTEP representation with atomic displacement parameters set to 50 % probability.

Magnetic properties of C27

Since **C26** already showed SIM behavior, **C27** was investigated with respect to its magnetic properties as well. Thus, the sample was measured under a dc field of 0.1 T to determine its magnetic susceptibility in a temperature range of 2 K – 300 K. The combined χ_M *vs*. *T* and $\chi_M T$ *vs*. *T* plots are visualized in Figure 3.114. Next to that, magnetization data were collected between 2 K and 10 K in a magnetic field varying from 0.1 T to 7 T (Figure 3.114). Single-crystals were blocked with eicosane during both measurements. Since both susceptibility and magnetization data confirm the same magnetic behavior as seen in **C26**, data were fitted simultaneously with the spin Hamiltonian suggested by *Figgis,* shown in Equation 3.8.[350] Likewise, the same values for λ = -180 cm^{-1}, α = 1.0 and χ_{TIP} = 350 · 10^{-6} cm^{3}mol^{-1} were kept constant. However, no rhombic crystal field (δ) was found, which is why the transverse term $\left(E\left(\hat{S}_y^2 - \hat{S}_x^2\right)\right)$ was removed from the spin Hamiltonian. The best fit resulted in *g* = 2.307(2) and Δ = 142(4) cm^{-1}. The resulting fits are displayed in the corresponding plots as solid lines (Figure 3.114). As the simulation of the *Zeeman splitting* in Figure G.45 shows, the two *Kramers doublets* M_S = ±1/2 and M_S = ±3/2 (resulting from second-order spin-orbit coupling of the $^4A_{2g}$ term) are also for this compound well-separated from higher excited states.

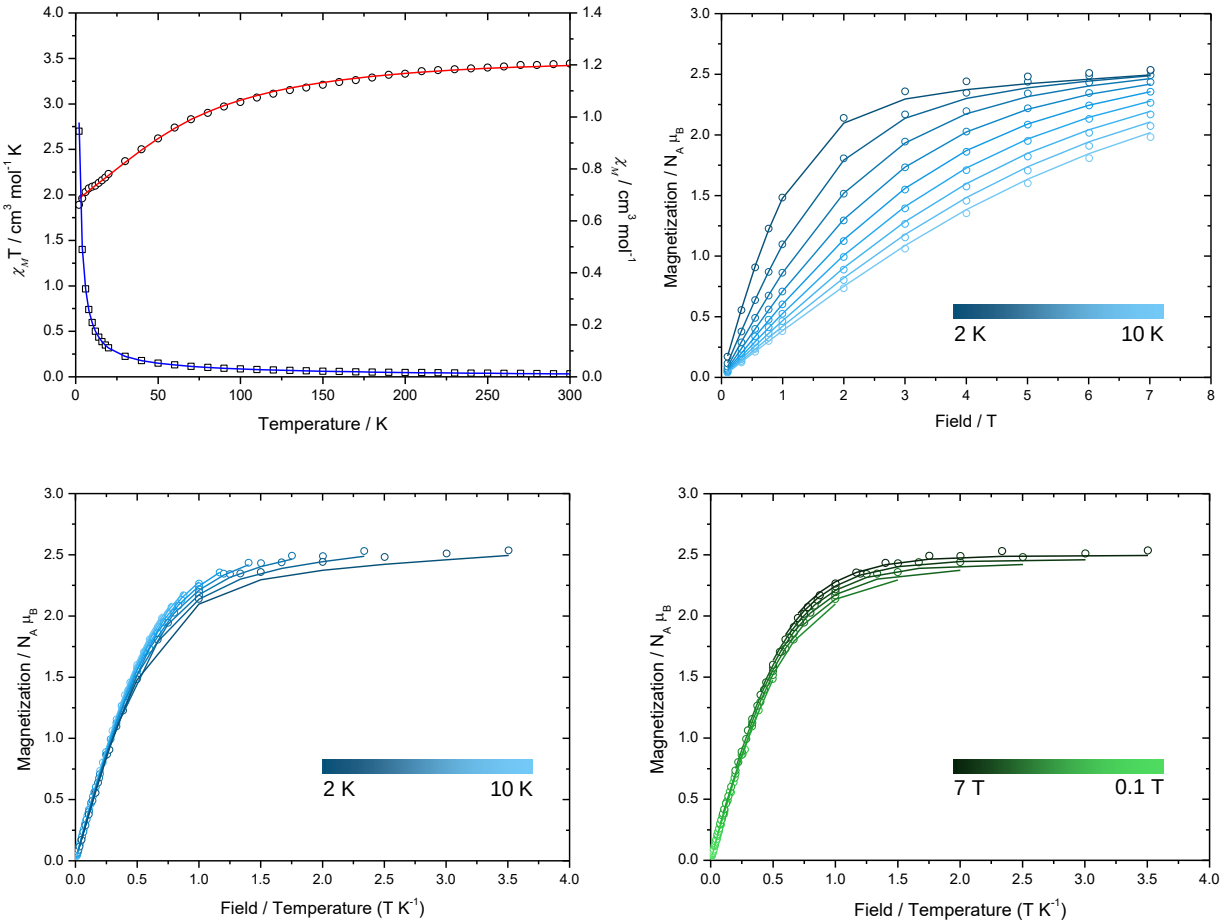


Figure 3.114 Temperature dependent magnetic behavior of **C27**. Top left: Combined $\chi_M T$ vs *T* (left values, open circles) and χ_M vs *T* plots (right values, open squares). Top right: *M* vs *H* plot. Bottom: *M* vs. *H/T* plots. Solid lines represent the best fits, using PHI.[201]

However, this separation is not as prominent as in **C26**, which is attributed to the lower axial crystal field parameter Δ. Consequently, magnetization data (which display low-temperature data) were fitted in PHI[201] with the spin Hamiltonian in Equation 3.10, as shown in Figure G.47 – Figure G.49 in appendix.

$$\hat{H} = D\left[\hat{S}_z^2 - S(S+1)/3\right] + g\mu_B HS \tag{3.10}$$

The resulting fit parameters are g = 2.679(8) and D = 46(4) cm^{-1} for S = 3/2 with a residual of R = 0.82. Again, the sign of the zero-field parameters D is in accordance with the sign of the axial crystal field parameters Δ. The slightly lower value of D in comparison to **C26** may be ascribed to the lower distortion [Σ_O(**C27**) = 83.3 ° versus Σ_O(**C26**) = 91.1 °]. This difference seems reasonable, since the coordination of an additional methanol molecule causes less steric strain. Hence, the compound shows an *easy-plane* type of anisotropy.

The alternating-current (ac) magnetic susceptibility of **C27** was determined between 1.9 K and 3.2 K under an applied magnetic field of 0.16 T. While at zero field, no out-of-phase signal χ_M'' was observed, the signal was the most pronounced at 0.16 T. As there are no observable maxima in the Cole-Cole plot (Figure G.50), the effective energy barrier U_{eff} was estimated by the following equation:[361]

$$\ln\left(\frac{\chi_M''}{\chi_M'}\right) = \ln(2\pi\nu\tau_0) + \frac{U_{\text{eff}}}{k_B}\cdot\frac{1}{T} \qquad (3.11)$$

The relaxation time strictly follows the *Arrhenius law*, which results in the neglection of χ_s in the generalized Debye model. This approach is based on several simplifications and assumptions. A pure thermal relaxation via the Orbach process is assumed, which excludes tunneling processes. However, it yields a rough approximation of the effective energy barrier. Figure 3.115 shows the resulting $\ln(\chi_M''/\chi_M')$ versus 1/*T* plot of chosen frequencies. Experimental data were fitted using the program Origin7.5, illustrated as solid lines.

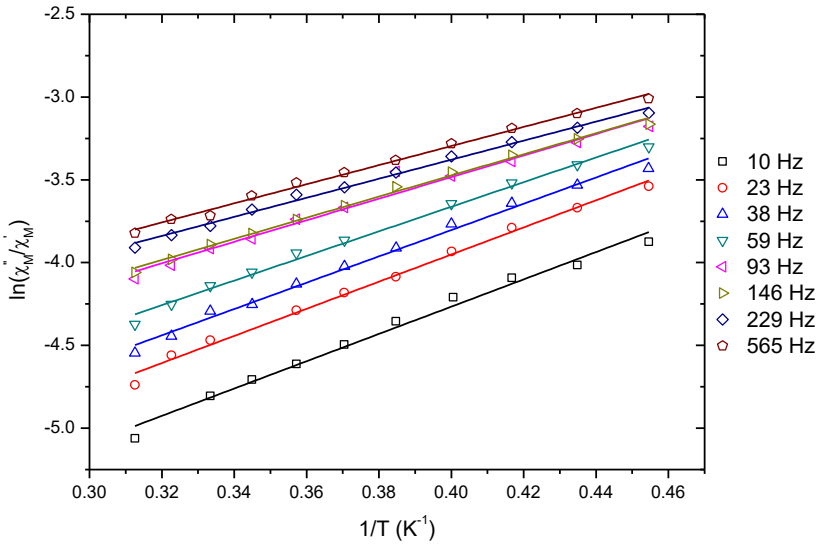


Figure 3.115 Visualization of the $\ln(\chi_M''/\chi_M')$ versus 1/*T* plot of **C27** with an applied field of 0.16 T. Open symbols represent experimental data, solid line the according fits, using Origin7.5.

This approach leads to the reasonable effective energy barrier of U_{eff} = 4.9 K (≙ 3.4 cm^{-1}) with and $\tau_0 = 3.8 \cdot 10^{-6}$ s. Unlike **C26**, the effective energy barrier in **C27** cannot be attributed to a present in-plane rhombic anisotropy. Also, the positive D parameter offers no *easy-axis* anisotropy, that could explain the occurrence of an out-of-phase signal χ_M'' with the fitted energy barrier. However, the occurrence of χ_M'' may be attributed to a present phonon bottleneck process, which can occur in a one-phonon direct relaxation process.[362,363]

3.9.3 [Co(η³-L^{Naph})(NCS)$_2$] (C28)

The third cobalt(II) complex in this work was synthesized in analogy to **C26** and **C27** by complexation of $Co(SCN)_2$ with the ligand **L^{Naph}**. Single-crystal X-ray structure analysis was performed at a temperature of 120 K. The resulting crystallographic data are summarized in Table D.16. While **C26** and **C27** exhibit an octahedral coordination sphere, the cobalt(II) ion in **C28** is only five coordinated. The molecular structure is shown in Figure 3.116.

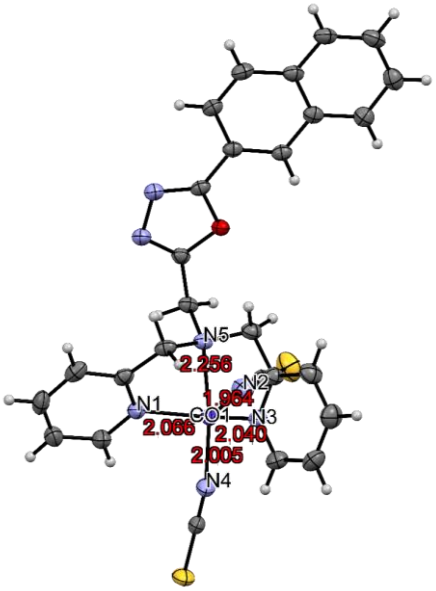


Figure 3.116 Asymmetric unit of **C28**. Bond distances are displayed in red. Colour scheme: dark grey – C, grey – H, violet – N, red – O, yellow – S, purple – Co. ORTEP representation with atomic displacement parameters set to 50 % probability.

Continuous shape measurements[62] revealed that the present structure is closer to a trigonal bipyramidal (TBP) than to a square pyramidal (SPY) geometry with CShM(D_{3h}) = 1.24 and CShM(C_{4v}) = 4.39, illustrated in Figure 3.117. Therefore, the two pyridine rings coordinate *cis*-wise and form together with one thiocyanate coligand the equatorial base of the triangular bipyramid. The axial positions are occupied by the second thiocyanate and the amin function of **L^{Naph}**. The bond distances to the pyridine rings and thiocyanate coligands are roughly equal to 2.0 Å. The amin function, in contrast, shows a longer bond distance of *d*(Co1-N2) = 2.26 Å. This results in an axial elongation of the coordination sphere and lowers the symmetry from D_{3h} towards C_{3v}, which explains the calculated CShM value. A full summary of structural parameters is listed in Table E.13 The present distortion is further confirmed by the angular structural parameter τ = 0.7, introduced by *Addison et al*. in 1984.[364] This distortion parameter was suggested for five coordinated centric molecules and proposed as an index of trigonality. It can be calculated via $\tau = (\beta - \alpha) / 60$ °, where β is the angles closest to 180 °, while α is the next smaller L-M-L angle.

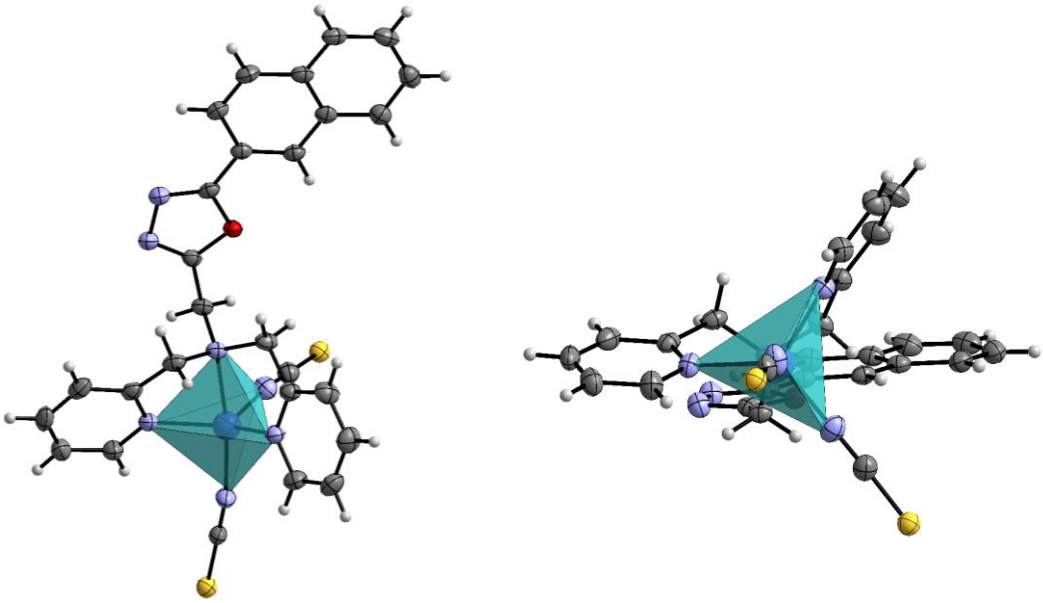


Figure 3.117 Molecular structure of **C28** and its ideal coordination polyeder with front view (left) and view along the Co-N4 axis (right), calculated with SHAPE.[62] Colour scheme: dark grey – C, grey – H, violet – N, red – O, yellow – S, purple – Co. ORTEP representation with atomic displacement parameters set to 50 % probability.

For ideal trigonal bipyramidal systems τ is equal to 1, while it is zero for square pyramidal compounds. The value of τ = 0.7 in **C28** describes a distorted coordination geometry close to the D_{3h} symmetry and is in line with literature known Co(II) TBP systems.[365,366] The average bond distance is equal to $\bar{d}$(Co-L) = 2.07 Å, representing a Co(II) HS metal center. [Co(η^3-**L^{Naph}**)(NCS)$_2$] crystallizes in the orthorhombic space group *Pbca* with eight formula units inside the unit cell (Figure F.104). The asymmetric unit is defined by one complex molecule (Figure 3.116). One unique parallel-like intermolecular π-π interaction can be found between the naphthyl groups of two adjacent molecules. Hence, the least-squares plane A is defined by C2, C3, C4, C5, C6 and C7, while plane B includes C1, C2, C7, C8, C9 and C10. The *interplanar distance* is equal to d_{AB} = 3.45 Å, combined with an *interplanar angle* of θ = 5.9 ° and an *offset* of *r* = 1.57 Å (Figure 3.118).

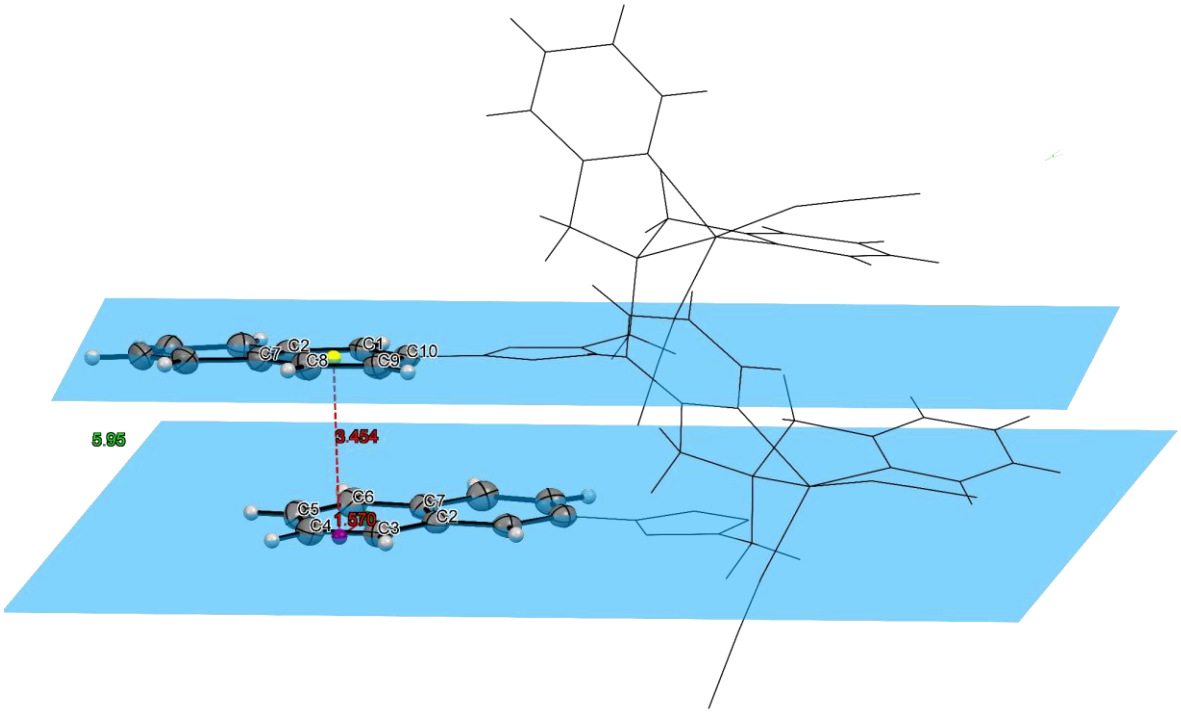


Figure 3.118 π-π interaction in **C28**. Least-squares mean plane A is defined by C2, C3, C4, C5, C6 and C7. Plane B is defined by C1, C2, C7, C8, C9 and C10 of an adjacent molecule. Green point – center of the aromatic ring in A. Purple point – orthogonal intersection of the aromatic center in B onto plane A. *Offset r* = 1.68 Å, *interplanar distance* d_{AB} = 3.44 Å, *interplanar angle* θ = 22.2 °. ORTEP representation with atomic displacement parameters set to 50 % probability.

This π-π stacking results in a one-dimensional chain of complex molecules along the a-axis, where the chains are aligned in a zigzag-like manner (Figure 3.119).

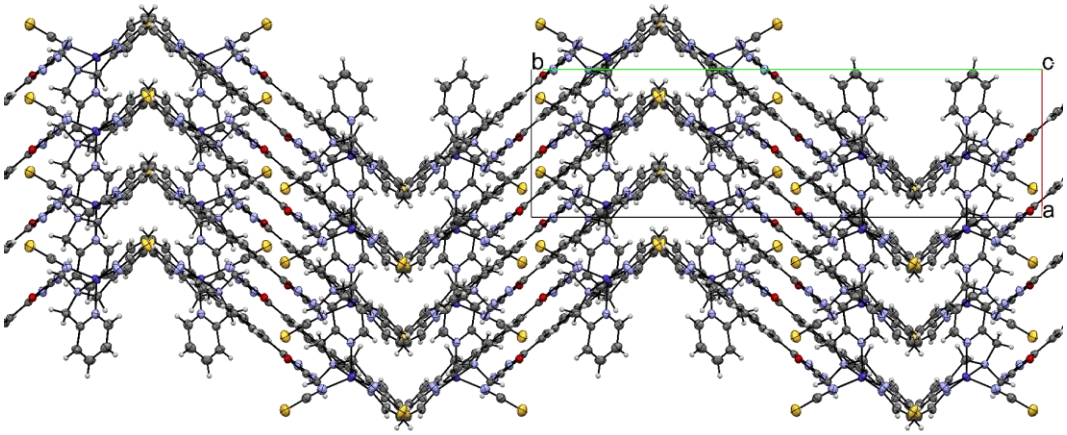


Figure 3.119 Zigzag-like alignment of the complex molecules in **C28** due to the present π-π stacking between the naphthyl groups of two adjacent molecules. One-dimensional chains are formed along the a-axis. Colour scheme: dark grey – C, grey – H, violet – N, red – O, yellow – S, purple – Co. ORTEP representation with atomic displacement parameters set to 50 % probability.

Magnetic properties of C28

Temperature and field dependent magnetic data of **C28** were measured between 2-300 K, shown in Figure 3.120. [Co(η^3-**L**$^{\mathbf{Naph}}$)(NCS)$_2$] as a d^7 system in a trigonal bipyramidal ligand field (D_{3h} symmetry) offers the orbital singlet $^4A_2'$ as electronic ground term.[367–369] This term remains lowest in energy even for the present distortion towards C_{3v} symmetry, seen in the crystallographic data.[370] In contrast to **C26** and **C27**, prominent first-order spin orbit coupling should therefore not be expected in **C28**. Indeed, the resulting $\chi_M T$ *vs*. *T* plot (Figure 3.120, top left) does not resemble the magnetic behavior of the octahedral coordinated Co(II) monomers. At 300 K, the $\chi_M T$ product is equal to 2.54 cm^{3}mol^{-1}K and decreases linearly to 2.38 cm^{3}mol^{-1}K at 30 K. Below this temperature, $\chi_M T$ drops significantly to 1.73 cm^{3}mol^{-1}K at 2 K. The value around room temperature is higher than the *spin-only* value (Equation 3.1) for S = 3/2 and g = 2, which is equal to 1.88 cm^{3}mol^{-1}K. This can be attributed to the contribution of the angular momentum of the excited states to the present $^4A_2'$ ground state.[365] The linear decrease of the magnetic moment from 300 K towards 30 K is most likely the result of temperature independent paramagnetism (TIP) in the Co(II) ion.

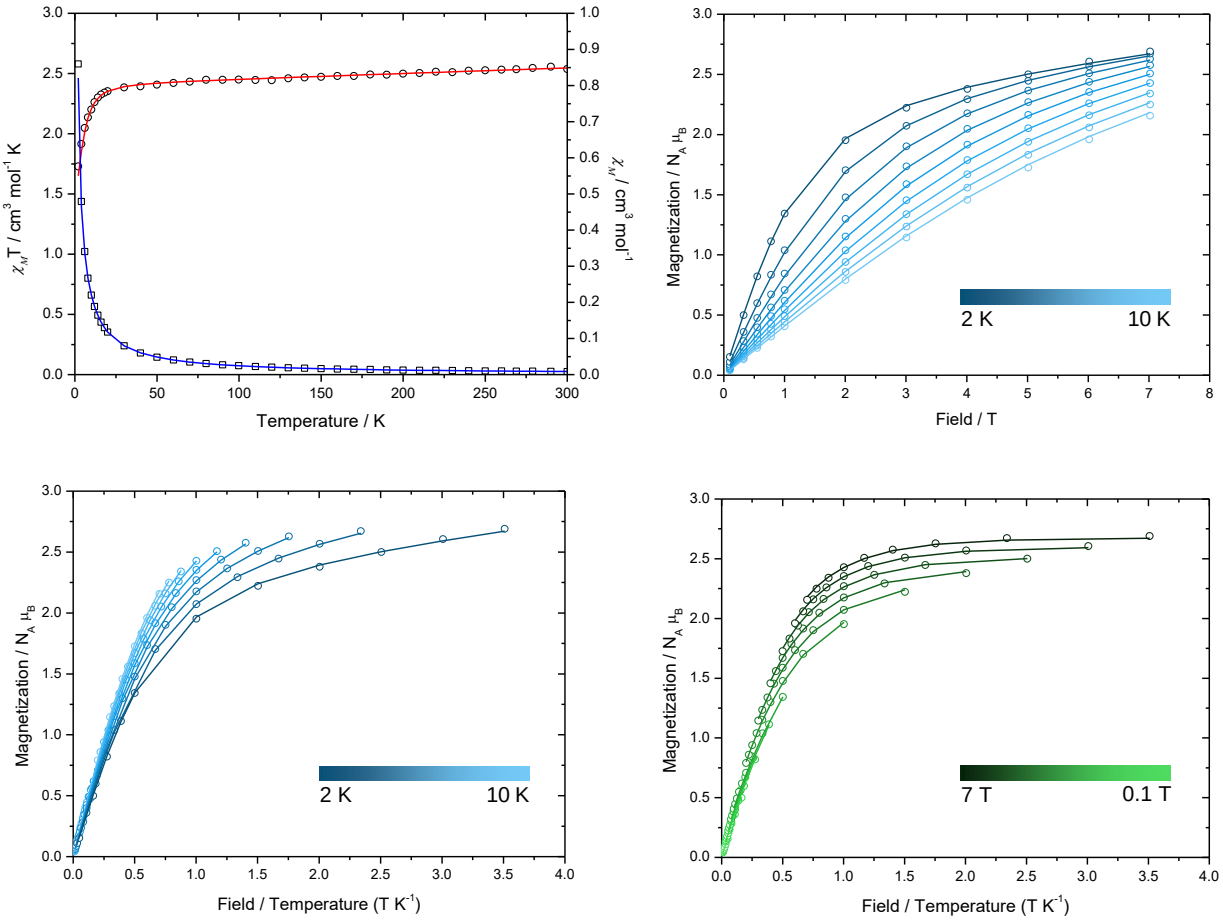


Figure 3.120 Temperature dependent magnetic behavior of **C28**. Top left: Combined $\chi_M T$ vs *T* (left values, open circles) and χ_M vs *T* plots (right values, open squares). Top right: *M* vs *H* plot. Bottom: *M* vs. *H/T* plots. Solid lines represent the best fits, using PHI.[201]

The pronounced drop at very low temperatures reflects the effect of ZFS on the magnetic moment, when only the lowest magnetic states are occupied (*Boltzmann distribution*)[67]. The present ZFS is also supported by the fact that the experimental curves in the *M vs*. *H* plot (Figure 3.120, top right) do not reach the saturation magnetization of 3 $N_A\mu_B$. Furthermore, the experimental values in the reduced magnetization do not superimpose. Thus, they do not follow the *Brillouin function*. Susceptibility and magnetization data were fitted simultaneously with the spin Hamiltonian in Equation 3.10, using PHI.[201] Best fit for S = 3/2 and an isotropic *g*-factor yielded $g = 2.267(1)$ and $D = 6.3(2)$ cm^{-1} with a residual of $R = 1.25 \cdot 10^{-3}$. The temperature independent paramagnetism was kept constant with a value of $\chi_{TIP} = 460 \cdot 10^{-6}$ cm^3mol^{-1}, which is a plausible value for a Co(II) HS ion.[353] The slightly increased *g*-value represents the present contribution of the orbital angular momentum of higher states, while the positive *D* parameter indicates an *easy-plane* type of anisotropy. Interestingly, the sign and value of *D* fits very well in the τ versus *D*-correlation for $Co(II)L_5$ (TBP) complexes with neutral tripodal N-donor ligands, published by *Massoud et al.. Murrie et al*. stated that the main contribution to *D* in trigonal bipyramidal Co(II) complexes arises from the mixing of the ground state with the excited state $^4E''$.[369] Since such TBP Co(II) complexes like $[CoCl_3$(**DABCO**)(**HDABCO**)] (**DABCO**=1,4-diazabicyclo[2.2.2]octane) with positive *D* and non-existent *E* values can exhibit SIM behavior,[369] **C28** was investigated with respect to its alternating-current susceptibility. However, no out-of-phase χ_M'' signal was observed, even under various applied static fields. Thus, compound **C28** does not show SIM behavior like **C26** and **C27**.

4 Summary and Perspectives

The aim of the present work was to synthesize new 1,3,4-oxadiazole-related SCO compounds based on the $[Fe_2(\mu_2\text{-}\mathbf{PMOD})_2](X)_4$-type series, published by *C. Köhler* from our group in 2016 (**PMOD** = 2,5-bis{[(2-pyridyl-methyl)amino]methyl}-1,3,4-oxadiazole). The work is divided into two parts. First, the synthesis of novel dinuclear 1,3,4-oxadiazole based coordination compounds is described and discussed, followed by the synthesis and discussion of mononuclear complexes. In total, 35 new coordination compounds, characterized by X-ray structural analysis, NMR, IR and optical spectroscopy, mass spectrometry, elemental analysis and SQUID magnetometry, are presented.

With the aim of obtaining new dinuclear iron-spin crossover complexes, in the first part of the work, the coordinating sidearms of the **PMOD** ligand were modified either by substituting the pyridyl group with a five membered heterocycle or by implementing a functional group in the 4-position of the pyridine ring. The five membered aromatic imidazole ring offers an additional NH group, which can enhance the degree of cross linking in the crystalline phase via further hydrogen bonds. This in turn should lead to wide a hysteresis of the magnetic moment in the resulting SCO compounds. Therefore, the new ligand 2,5-bis[(1H-imidazol-2-ylmethyl)amino]methyl-1,3,4-oxadiazole ($\mathbf{L^{5,Im}}$) was synthesized (Figure 4.1). The dinuclear iron(II) complexes of type $[Fe_2(\mu_2\text{-}\mathbf{L^{5,Im}})_2](X)_4 \cdot 2MeCN$ [X = BF_4^- (**C1**), ClO_4^- (**C2**) and $CF_3SO_3^-$ (**C3**)] were synthesized in a previous work and characterized by single-crystal X-ray structure analysis.[196] The crystal structures revealed a pronounced network of complex cations via hydrogen bonds to the non-coordinating anions. Coordination parameters such as average bond distances and distortions of the coordination sphere indicate a [HS-HS] state at a temperature above 120 K.

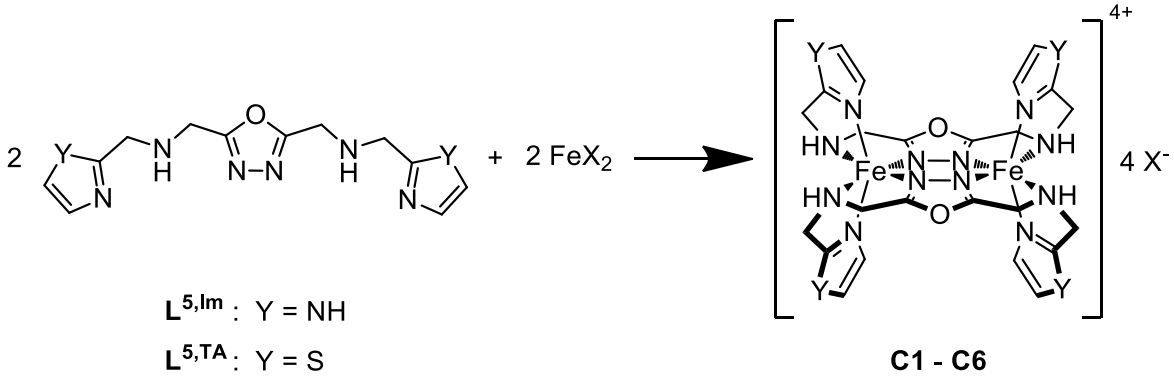


Figure 4.1 Synthesis of the dinuclear iron(II) complexes $[Fe_2(\mu_2\text{-}\mathbf{L})_2](X)_4$ (**L** = $\mathbf{L^{5,Im}}$ or $\mathbf{L^{5,TA}}$) (**C1** - **C6**).

Magnetic studies of **C1** – **C3** in this work confirmed the absence of a thermally induced SCO. The complexes remain in the magnetic [HS-HS] state over the measured temperature range. Presumably, the lack of SCO activity is caused by the combination of highly distorted coordination spheres and too weak ligand field splitting energies.

The imidazol-2-yl group was substituted with the thiazol-2-yl group, yielding the novel ligand system 2,5-bis[(1,3-thiazol-2-ylmethyl)amino]-methyl-1,3,4-oxadiazole (**L^{5,TA}**) (Figure 4.1). Thiazole provides a stronger ligand field than 2-imidazole due to its higher π-electron acceptor ability.[197] **L^{5,TA}** coordinates as expected, leading to the dinuclear complexes $[Fe_2(\mu_2\text{-}\mathbf{L}^{5,TA})_2](X)_4 \cdot 2MeCN$ [X = BF_4^- (**C4**), ClO_4^- (**C5**) and $CF_3SO_3^-$ (**C6**)]. Structural elucidation and magnetic studies revealed similar magnetic behavior as for **C1** – **C3**. However, a detailed analysis of the crystallographic data shows the desired trend of stabilization of the low spin state. First, the average metal-ligand bond distances decreased, indicating stronger metal-ligand bonds and thus a stronger ligand field. Second, the distortion of the octahedral coordination sphere was also smaller in the **L^{5,TA}** related complexes. Future work should follow this reasonable trend and further increase the π-backbonding to the axially coordinated heterocycle. For azoles, the π-electron acceptor abilities increase in the order imidazole ≪ thiazole < pyrazole < 1,2,4-triazole. Hence, the introduction of the 1,2,4-triazolyl group seems to be a promising way. This group would offer a free NH-function to provide further hydrogen bonding while strengthening the ligand field. Since 1H-[1,2,4]triazole-3-carbaldehyde is commercially available, the synthesis of the suggested ligand could follow the same route used for **L^{5,Im}** and **L^{5,TA}**. However, the product must be handled with care as such high nitrogen to carbon ratio is prone to explosions!

The implementation of a methoxy function in the 4-position of the pyridyl group in **PMOD** led to the successful synthesis of the new bridging ligand 2,5-bis[(4-methoxypyridin-2-ylmethyl)amino]methyl-1,3,4-oxadiazole (**L^{6,OMe}**) (Figure 4.2).

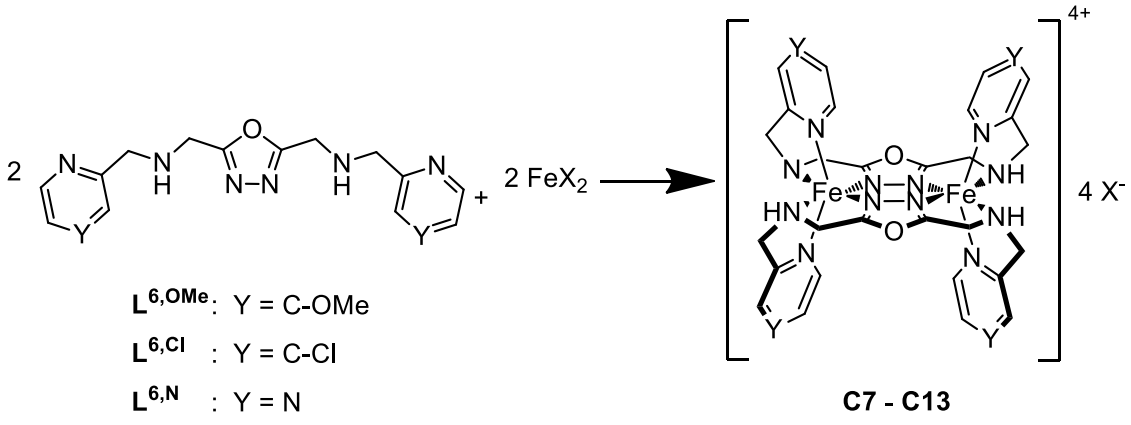


Figure 4.2 Synthesis of the dinuclear iron(II) complexes $[Fe_2(\mu_2\text{-}\mathbf{L})_2](X)_4$ (**L** = **L^{6,Cl}**, **L^{6,OMe}** or **L^{6,N}**) (**C7** - **C13**).

In contrast to **L^{5,Im}** and **L^{5,TA}**, the coordinating sidearm in **L^{6,OMe}** consists of the six membered pyridine ring. The functional group in the 4-position should shift the transition temperature in the [$Fe_2(\mu_2$-**PMOD**$)_2](X)_4$-type SCO compounds toward room temperature. Two dinuclear iron(II) complexes of the desired type [$Fe_2(\mu_2$-**L^{6,OMe}**$)_2](X)_4$ [X = ClO_4^- (**C7**) and $CF_3SO_3^-$ (**C8**)] were synthesized from this ligand. Both formed single crystals suitable for X-ray structure analysis. Magnetic studies revealed a temperature independent [HS-HS] state for both compounds. A possible explanation is the bonding situation of the complexes. Electron-donating *para*-substituents raise the energy of the nitrogen lone pair, resulting in a stronger ligand field strength. At the same time, they also lift the energy of the π* molecule orbitals, which results in a smaller ligand field splitting energy due to weaker π-backbonding. For the compounds **C7** and **C8**, the latter contribution seems to have the stronger effect, as both complexes show no thermal SCO.

The ligand 2,5-bis[(4-chloropyridin-2-ylmethyl)amino]-methyl-1,3,4-oxadiazole (**L^{6,Cl}**) (Figure 4.2) was synthesized to provoke the opposite effect, seen in **C7** and **C8**. Therefore, the electron donating methoxy group was exchanged with the electron withdrawing chloride group. As expected, isostructural complexes of type [$Fe_2(\mu_2$-**L^{6,Cl}**$)_2](X)_4$ [X = BF_4^- (**C9**), ClO_4^- (**C10**) and $CF_3SO_3^-$ (**C11**)] have formed upon coordination. Structural elucidation was done via IR spectroscopy and single-crystal X-ray structure analysis. Temperature dependent measurements of the magnetic moment revealed a stabilization of the [HS-HS] state of **C9** – **C11** as well. Although the average metal-ligand bond distance in **C11** of 2.19 Å corresponds to the one in the SCO active complex [$Fe_2(\mu_2$-**PMOD**$)_2](CF_3SO_3)_4 \cdot 2$MeCN in the [HS-HS] state, the distortion of the coordination environment is higher. This was explained by the intermolecular attractive interactions between the chloride function and the non-coordinating triflate anions.

The last modification of the **PMOD** ligand studied was the substitution of the pyridin-2-yl group with the pyrazin-2-yl group, resulting in the successful synthesis of 2,5-bis[(pyrazin-2-ylmethyl)amino]methyl-1,3,4-oxadiazole (**L^{6,N}**) (Figure 4.2). Pyrazine exhibits a stronger π-electron acceptor ability and stronger ligand field strength than pyridine.[276] The ligand **L^{6,N}** was used to form the two coordination compounds [$Fe_2(\mu_2$-**L^{6,N}**$)_2](X)_4$ [X = BF_4^- (**C12**) and ClO_4^- (**C13**)]. X-ray structure analysis and SQUID magnetometry revealed the temperature independent [HS-HS] state for both complexes.

In the solid state, packing effects seem to play too large a role to allow the transition temperature to be manipulated specifically by the electronic nature of the ligand. In future works, it would therefore be interesting to study the magnetic behavior of the complexes

C1 - **C13** in solution, where cooperative and packing effects are negligible. The *Evan's* NMR method is well suited for this task.[82–85] Due to the ionic nature of these compounds, a protic polar solvent like methanol should be suitable for such studies. The alcohol should dissolve the iron(II) complexes down to its melting point of 175 K, providing a comfortable wide temperature range for these studies.

In addition, the new oxadiazole bridging ligand 2-(2-pyridyl)-5-[N,N-bis(2-pyridylmethyl)amino-methyl]-1,3,4-oxadiazole ($\mathbf{L^{Py,1}}$) was synthesized (Figure 4.3), inspired by the dinuclear SCO active iron(II) complexes of type $[Fe_2(\mu_2\text{-}\mathbf{PPTD})_2](X)_4$ (**PPTD** = 2-(2-pyridyl)-5-[N,N-bis(2-pyridylmethyl)-aminomethyl]-1,3,4-thiadiazole), reported by *D. Bittner.* from our group.[171] Complexation of this novel asymmetric ligand led to the successful formation of the dinuclear complexes $[Fe_2(\mu_2\text{-}\mathbf{L^{Py,1}})_2](X)_4$ [X = BF_4^- (**C14**, **C14'**) and ClO_4^- (**C15**)]. X-ray structure analysis and magnetic measurements showed the absence of SCO activity. Hence, the systems remain in the [HS-HS] state until very low temperatures. This could be attributed to the highest distortion found throughout this work with values of the octahedral distortion parameter of $\Sigma_O(FeN_6) > 150$ °. As the asymmetric $\mathbf{L^{Py,1}}$ ligand offers a tetradentate binding pocket, steric strain in the coordination octahedron can be released by the coordination of two additional monodentate coligands. This leads to the formation of mononuclear complexes, where the coordination sphere is saturated by the tetradentate binding pocket of $\mathbf{L^{Py,1}}$ and two monodentate ligands. Therefore, the second part of this work deals with the formation of mononuclear coordination compounds.

In the second part of this work, the successful synthesis and characterization of mononuclear iron(II) and cobalt(II) complexes is reported. The coordination of the literature known precursors $[Fe^{II}(py)_4(NCX)_2]$ (X = S, Se or BH_3) with $\mathbf{L^{Py,1}}$ results in the desired coordination compounds of type $[Fe(\mathbf{L^{Py,1}})(NCX)_2]$ (Figure 4.4).

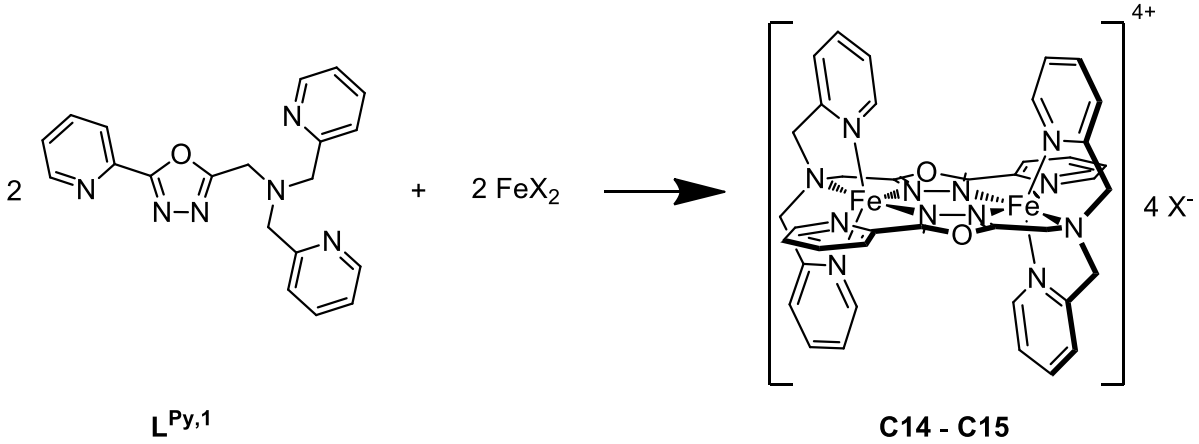
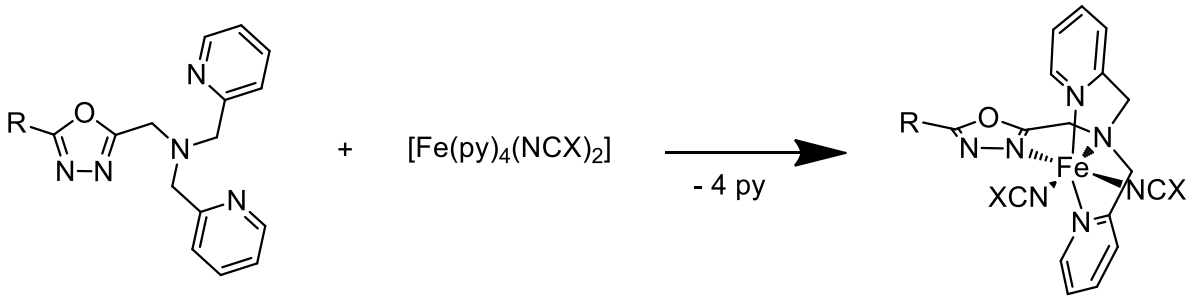


Figure 4.3 Synthesis of the dinuclear iron(II) complexes $[Fe_2(\mu_2\text{-}\mathbf{L^{Py,1}})_2](X)_4$ (**C14** - **C15**).

Hence, the tetradentate binding pocket of $\mathbf{L^{Py,1}}$ coordinates alongside with two pseudohalides (NCX = NCS, NCSe and $NCBH_3$). Here, the two coligands exhibit a *cis*-configuration, while the pyridine moieties coordinate axially in a *trans* manner. This type of coordination mode not only causes a low distorted coordination environment, but also offers the possibility to fine-tune the ligand field strength. As single crystal structure analysis and magnetic studies showed, the solvatomorphs of $[Fe(\mathbf{L^{Py,1}})(NCS)_2]$ (**C16**·1MeOH, **C16**·1MeCN) and $[Fe(\mathbf{L^{Py,1}})(NCSe)_2]$ (**C17**·3MeCN) represent high spin compounds with pronounced *easy-plane* type anisotropy. In contrast, $[Fe(\mathbf{L^{Py,1}})(NCBH_3)_2] \cdot 1MeOH$ (**C18**·1MeOH) exhibits an incomplete SCO with a thermal hysteresis with $T_c^{\downarrow}$ = 160 K and $T_c^{\uparrow}$ = 170 K, providing a hysteresis width of approx. 5 K. This magnetic behavior is the result of a high *degree of cooperativity* due to intermolecular π-π interactions between the pyridyl groups of the complex molecules in the solid phase. The measurement of a freshly prepared sample of **C18**·1MeOH in mother liquor showed a complete and abrupt SCO at $T_c^{\downarrow} = T_c^{\uparrow}$ = 165 K, however, without a thermal hysteresis. Nevertheless, the high steepness of the transition curve can be ascribed to the intermolecular π-π interactions as well. Therefore, **C18**·1MeOH represents the third 1,3,4-oxadiazole based SCO compound reported in literature, next to $[Fe_2(\mu_2\text{-}\mathbf{PMOD})_2](ClO_4)_4 \cdot 2MeCN$ and $[Fe_2(\mu_2\text{-}\mathbf{PMOD})_2](CF_3SO_3)_4 \cdot 2MeCN$ from our group.[20] Compared to the perchlorate compound, the transition temperature is shifted by 20 K towards higher temperatures.

The pyridine ring in the 2-position of the oxadiazole was substituted with a phenyl group to synthesize the novel ligand system 2-phenyl-5-[N,N-bis(2-pyridylmethyl)amino-methyl]-1,3,4-oxadiazole ($\mathbf{L^{Ph}}$), as the bidentate coordination pocket in $\mathbf{L^{Py,1}}$ does not coordinate in the mononuclear complexes (Figure 4.4). The study of the magneto-structural relationship in $[Fe(\mathbf{L^{Py,1}})(NCBH_3)_2] \cdot 1MeOH$ (**C18**·1MeOH) showed that intermolecular π-π interactions play a crucial role for the spin transition in this type of complexes.



$\mathbf{L^{Py,1}}$: Y = 2-pyridyl

$\mathbf{L^{Ph}}$: Y = 2-phenyl

$\mathbf{L^{Naph}}$: Y = 2-naphthyl

X = S, Se, BH_3

C16 - C21, **C23**

Figure 4.4 Synthesis of the mononuclear iron(II) complexes $[Fe(\mathbf{L})(NCX)_2]$ ($\mathbf{L}$ = $\mathbf{L^{Py,1}}$, $\mathbf{L^{Ph}}$ or $\mathbf{L^{Naph}}$ and X = S, Se, BH_3) (**C16** - **C21, C23**).

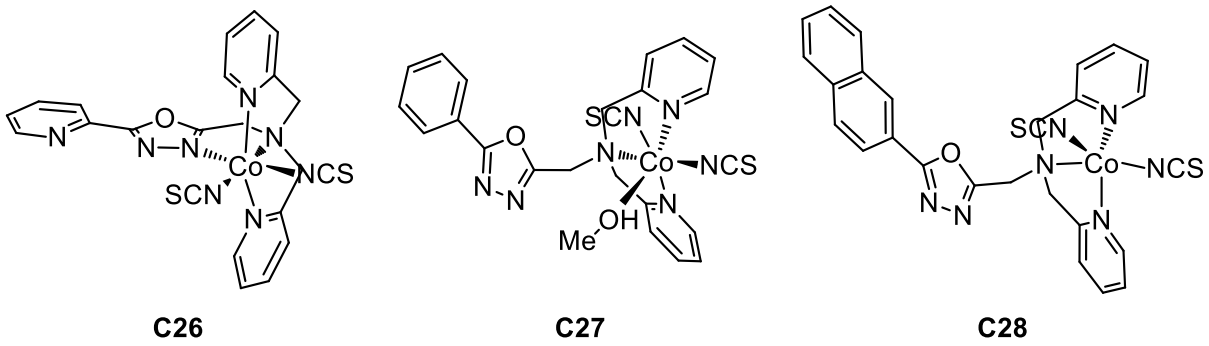
Thus, the exchange of aromatic systems can result in different SCO properties. The related mononuclear complexes were synthesized in the same manner as for $\mathbf{L^{Py,1}}$ and characterized by X-ray structure analysis and SQUID magnetometry. As expected, the solvatomorphs of type [Fe($\mathbf{L^{Ph}}$)$(NCS)_2$] (**C19**·2MeCN, **C19**·3MeOH) and [Fe($\mathbf{L^{Ph}}$)$(NCSe)_2$] (**C20**·2MeCN, **C20**·3MeOH) are isostructural to the analogous $\mathbf{L^{Py,1}}$ based complexes [Fe($\mathbf{L^{Py,1}}$)$(NCS)_2$] (**C16)** and [Fe($\mathbf{L^{Py,1}}$)$(NCSe)_2$] (**C17)**, respectively. Both solvatomorphs represent high-spin iron(II) complexes with *easy-plane* type anisotropy. Similar to the SCO active compound [Fe($\mathbf{L^{Py,1}}$)$(NCBH_3)_2$] · 1MeOH (**C18**·1MeOH), the isostructural solvatomorphs of [Fe($\mathbf{L^{Ph}}$)$(NCBH_3)_2$] (**C21**·1MeCN, **C21**·1.8MeOH) also exhibit thermally induced SCO. Both, **C18** and **C21**, possess a coordination sphere saturated with cyanoborohydride (H_3BCN^-). **C21**·1MeCN shows a very abrupt SCO at $T_c^{\downarrow} = T_c^{\uparrow} = 194$ K with a nearly vertical transition curve. Thus, the spin transition temperature has shifted by 29 K compared to **C18**·1MeOH, which can be explained by the changed ligand field splitting energy of $\mathbf{L^{Ph}}$ compared to $\mathbf{L^{Py,1}}$. In addition, T_c also surpasses the ones in the **PMOD** related SCO compounds. **C21**·1.8MeOH offers a very similar transition temperature as **C18**·1MeOH with $T_c^{\uparrow} = T_c^{\downarrow} = 166$ K. However, this temperature is furthermore increased to $T_c^{\uparrow} = 173$ K in case of a higher scan rate. After the heating procedure at 400 K, the sample shows a two-step spin crossover at $T_c^{\downarrow(1)} = 215$ K and $T_c^{\downarrow(2)} = 137$ K. This work thus demonstrates the first literature known two-step SCO of an 1,3,4-oxadiazole based complex. The altered nature of the spin transition was assigned to a solvent loss induced crystallographic structural phase transition. However, this could not be proven via X-ray structure analysis, as the single crystals were not suitable anymore for additional studies. In future works, the exact annealing temperature, leading to the two-step SCO in **C21**·1.8MeOH, should be determined. In case of a lower temperature and shorter heating time, the single crystals might be suitable for further crystallographic studies to confirm the crystallographic symmetry breaking.

The solvatomorphs of type [Fe(**L**)$(NCBH_3)_2$] (**L** = $\mathbf{L^{Py,1}}$ and $\mathbf{L^{Ph}}$) illustrate that the non-coordinating group in the 2-position of the 1,3,4-oxadiazole can influence the nature of the spin change due to cooperative effects in the lattice. This led to the formation of the final ligand 2-(Naphthalen-2-yl)-5-[N,N-bis(2-pyridylmethyl)aminomethyl]-1,3,4-oxadiazole ($\mathbf{L^{Naph}}$), which bears the napthalen-2-yl group in the 2-position of the oxadiazole (Figure 4.4). The complexation of $[Fe^{II}(py)_4(NCBH_3)_2]$ with $\mathbf{L^{Naph}}$ led to the solvatomorphs of [Fe($\mathbf{L^{Naph}}$)$(NCBH_3)_2$] (**C23**·4.5MeCN, **C23**·3MeOH), which has been characterized by X-ray structure analysis, SQUID magnetometry and optical spectroscopy. As expected, **C23**·4.5MeCN also shows reversible SCO ($T_c^{\downarrow} = T_c^{\uparrow} = 130$ K) in an abrupt manner, which again is related to intermolecular π-π interactions between the aromatic groups of the complex molecules. Fast quenching of

the sample to very low temperatures reveals the presence of a TIESST effect, where approximately 10 % of the complex molecules are trapped in the HS state. At 80 K, the system shows relaxation into the LS state. After heating to 400 K, no SCO activity is found anymore upon cooling. The methanol solvatomorph **C23**·3MeOH, in contrast, shows reversible abrupt spin transition even after heating to 400 K or exposing to air for several days. With a transition temperature of $T_c^{\downarrow} = T_c^{\uparrow} = 207$ K, it represents the 1,3,4-oxadiazole based complex with the highest critical temperature in literature. These findings make **C23**·3MeOH an ideal candidate for temperature dependent optical measurements, since naphthalene is known for its long lifetime fluorescence with very low self-quenching.[316–321] To distinguish between the thermal quenching of fluorescence and a potential magneto-optical interplay, the isostructural diamagnetic complex [Zn(**L**$^{\mathbf{Naph}}$)$(NCBH_3)_2$] (**C25**) was synthesized and characterized by NMR, IR and optical spectroscopy. Comparison of the temperature dependent emission spectra of both compounds, the iron(II) and zinc(II) ones, strongly hints towards a successful synergism between the SCO and the emission in **C23**·3MeOH. Future studies are necessary to assign the correct temperature to the discrepancy-point of both series of emission spectra. If the proposed synergism in **C23**·3MeOH proves to be true, the complex would be one of a few coordination compounds to show such interplay.[177,178,189,313–315] Also, future works should focus on the synthesis of novel ligand systems with different emitting heterocycles in the 2-position of the oxadiazole. Hence, aromatic systems like anthracene, phenanthrene or quinoline could easily be introduced via the same synthetic route used for **L**$^{\mathbf{Naph}}$.[371,372] Furthermore, the SCO complexes **C18**, **C21** and **C23** should be investigated with respect to their potential LIESST property. This would be particularly interesting for **C23**, since magneto-optical synergism could be studied without undesired temperature effects.

In the last part of this work, **L**$^{\mathbf{Py,1}}$, **L**$^{\mathbf{Ph}}$ and **L**$^{\mathbf{Naph}}$ were used to coordinate $Co(SCN)_2$. Cobalt(II) is known for its large spin-orbit coupling in various coordination geometries.[192,193] This usually results in pronounced magnetic anisotropy, which in turn yields an effective anisotropy barrier of the magnetization. The resulting coordination products were successfully characterized in single-crystal X-ray structure analysis and magnetic studies. Unexpectedly, all three complexes exhibit different coordination spheres (Figure 4.5). The compound [Co(**L**$^{\mathbf{Py,1}}$)$(NCS)_2$] · 1MeOH (**C26**) is isostructural to the mononuclear iron(II) compounds and shows *easy-plane* anisotropy with additional transvers anisotropy (D = 48.7(7) cm^{-1} and E = 7.7(2) cm^{-1}). Alternating current magnetic measurements revealed an effective energy barrier of U_{eff} = 8 K for the magnetization reversal, attributed to a transverse type of energy barrier. In contrast, [Co(**L**$^{\mathbf{Ph}}$)$(NCS)_2$(MeOH)] (**C27**) shows a very different octahedral sphere. Here, the oxadiazole moiety itself does not coordinate, so that the appropriate notation is [Co(η^3-**L**$^{\mathbf{Ph}}$)$(NCS)_2$(MeOH)]. The coordination environment is saturated with one additional

methanol molecule. This compound exhibits only a small anisotropy barrier of U_{eff} = 4.9 K, which was assigned to the missing transverse anisotropy (D = 46(4) cm^{-1}, E = 0 cm^{-1}). Finally, the complex [Co(η^3-**L^{Naph}**)(NCS)$_2$] (**C28**) exhibits a trigonal bipyramidal geometry with *easy-plane* anisotropy (D = 6.3(2) cm^{-1}). However, no SIM behavior was observed for this compound. In future works, both monodentate isothiocyanates in **C26**, **C27** and **C28** could be substituted with bulkier bidentate coligands like sulfate, oxalate, nitrate or acetylacetonate. This can lead to a more distorted coordination sphere in the cobalt(II) complexes. It is well known that the present distortion of the coordination geometry is crucial for the magnetic anisotropy and the relating SIM behavior.



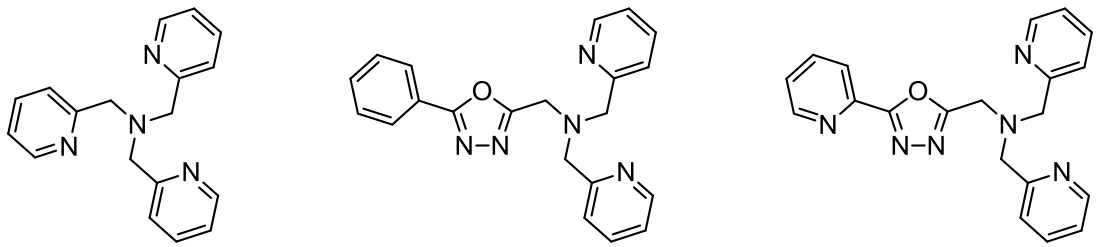
C26 **C27** **C28**

Figure 4.5 Molecular structure of the mononuclear cobalt(II) complexes **C26** – **C28**.

In summary, 35 novel transition metal complexes based on the 1,3,4-oxadiazole ligand system were described, showing various properties such as abrupt or two-step SCO, TIESST effect, magneto-optical synergism or even SIM behavior. These compounds extend the previously published 1,3,4-oxadiazole based complexes in the field of molecular magnetism. Future work should especially focus on additional investigations and modification of the synthesized SCO materials to make them more viable for applications. Implementation of functional groups in the coordinating heterocycles may lead to room temperature hysteresis of the magnetic moment. Finally, the cobalt compounds should be investigated with respect to their catalytic activity. Therefore, Chapter 5 gives a short outlook towas alkane hydroxylation.

5 Short Outlook towards Catalysis

While the ligand 2-Phenyl-5-[N,N-bis(2-pyridylmethyl)aminomethyl]-1,3,4-oxadiazole (**L^{Ph}**) allows for the synthesis of mononuclear SCO/ SIM compounds, it is also capable to generate transition metal complexes suitable for catalysis.[373] Tetradentate N4 ligands are extensively used for the synthesis of various metal complex catalysts in challenging catalytic processes. The field of application includes lactide polymerization,[299,300] olefine epoxidation,[301] bondage cleaving,[374] arene dihydroxylation[375] and many more. However, this short outlook shall focus on the well-known transition metal catalyzed alkane hydroxylation.[302–308] Frequently encountered ligands in this area are derivatives of **TPA** (TPA = tris(2-pyridylmethyl)amine), whose molecular structure strongly resembles **L^{Ph}** (Figure 5.1). Both ligands exhibit one tetradentate coordination pocket. Since most of the commonly used transition metals favor the octahedral coordination sphere, two vacancies can be occupied by different independent coligands. Since such molecular catalysts need to cleave and build metal-ligand bonds in a reversible manner, weakly coordinating coligands such as solvent molecules or weakly coordinating mono- or bidentate anions dominate the field. Figure 5.1 shows the synthesized system 2-(2-Pyridyl)-5-[N,N-bis(2-pyridylmethyl)amino-methyl]-1,3,4-oxadiazole (**L^{Py,1}**). Since this ligand possesses an additional bidentate binding pocket, complexation of metal salts of type $M^{II}X_2$ results in the formation of dinuclear compound like $[Fe_2(\mu_2\text{-}\mathbf{L}^{Py,1})_2](ClO_4)_4 \cdot 2MeNO_2$ (**C15**). Hence, weakly coordinating coligands do not bind to the metal center. Therefore, the pyridin-2-yl group in the 2-position of the oxadiazole was substituted with the phenyl group to remove the bidentate binding pocket. With that being done, complexes of **L^{Ph}** should exhibit similar structures compared to the **TPA** related compounds.



TPA **L^{Ph}** **L^{Py,1}**

Figure 5.1 Comparison of the molecular structure of **TPA**, **L^{Ph}** and **L^{Py,1}**.

In 2016 and 2017, *Itoh et al*. published a series of transition metal complexes of **TPA** and related derivates along with their catalytic activity in the alkene-hydroxylation.[303–305] Here, the used transition metals varied between manganese(II), iron(II), cobalt(II) and nickel(II), while the coordination octahedron was saturated with nitrates, acetates or solvent molecules. The studies focused on the hydroxylation of cyclohexane to cyclohexanol with *m*-CPBA (meta-chloroperoxybenzoic acid) as oxidant, shown in Figure 5.2.

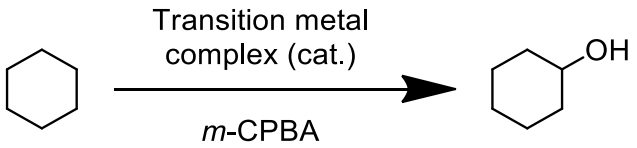


Figure 5.2 Catalyzed hydroxylation of cyclohexane to cyclohexanol with *m*-CPBA, done by *Itoh et al*..[303–305]

The oxidation of cyclohexane to the corresponding alcohol with *m*-CPBA is also possible in the absence of any metal catalyst, however, only under vigorous reaction conditions like high temperature, long reaction times and high concentrations of *m*-CPBA.[376] As the nickel(II) compound $[Ni^{II}(\mathbf{TPA})(OAc)(H_2O)]BPh_4$ showed the highest turnover number (TON = moles of product/moles of catalyst)[303] in the series, $\mathbf{L^{Ph}}$ was reacted with nickel(II) perchlorate hexahydrate in methanol. This should result in the formation of a mononuclear nickel(II) complex with weakly coordinated perchlorate or methanol molecules. However, slow evaporation of the solvent yielded $[Ni(\eta^3\text{-}\mathbf{L^{Ph}})_2](ClO_4)_2$ (**C22**) as single crystals. In this complex, the nickel(II) center is coordinated by two $\mathbf{L^{Ph}}$ ligands via the bis-(2-picolyl)amine group. Hence, the oxadiazole ring does not participate to the coordination sphere. Since the chelate complex offers no weak metal-ligand bond, **C22** was not investigated with respect to its catalytic properties. Similar to that, the complexation of $Co(SCN)_2$ with $\mathbf{L^{Ph}}$ yielded in $[Co(\eta^3\text{-}\mathbf{L^{Ph}})(NCS)_2(MeOH)]$ (**C27**). Again, $\mathbf{L^{Ph}}$ coordinates via its bis-(2-picolyl)amine group, whereas the oxadiazole moiety does not bind to the metal center. However, in contrast to **C22**, the three remaining vacancies of the coordination octahedron are occupied by two isothiocyanate and one methanol molecules. As Figure 5.3 shows, *Itoh et al.* suggested a catalytic mechanism, where only one coordination bond needs to be cleaved for a subsequent end-on coordination of the *m*-CPBA.[303] The following O-O bond homolysis results in a radical species, which reacts with cyclohexane directly to yield cyclohexanol. Consequently, **C27** was used as catalyst in the exact same reaction, as it offers a weakly coordinated methanol ligand. Therefore, complex **C27** (8 µmol), solved in acetonitrile, was added to a mixture of cyclohexane (15 mmol), *m*-CPBA (2 mmol) and nitrobenzene (50 µmol) in dichloromethane. The reaction was done under inert atmosphere to exclude atmospheric oxygen.[304]

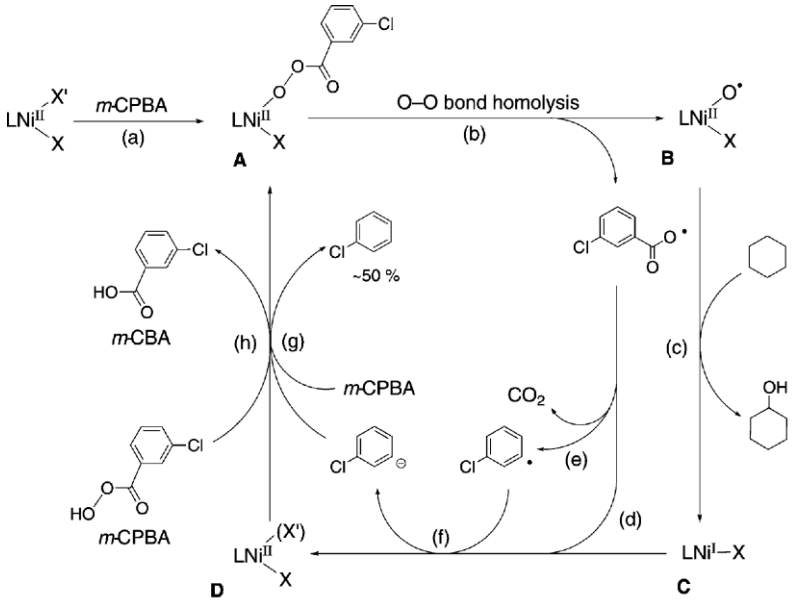


Figure 5.3 Proposed mechanism of the catalyzed reaction of cyclohexane to cyclohexanol. Reproduced from literature with permission.[304]

After one hour, an aliquot of the reaction mixture was taken and quenched with triphenylphosphine. The amount of cyclohexanol was determined via gas chromatography (GC) analysis, done by [redacted] in the group of [redacted] at Johannes Gutenberg University Mainz. Therefore, a calibration curve was used by plotting the area ratio of cyclohexanol and nitrobenzene against the amount of cyclohexanol for seven calibration standards (Figure F.113). Indeed, GC analysis revealed 32 µmol of formed cyclohexanol. Hence, the total turnover number of the catalyst reached a value of TON = 12 within 1 hour. After a reaction time of 24 hours, the TON increased to 50, indicating an incomplete reaction in the first probe. In contrast, the same reaction without the addition of **C27** yielded no desired product under equivalent conditions. All chromatograms are represented in Figure F.106 – Figure F.115. This comparison shows that [Co(η^3-**L**$^{\mathbf{Ph}}$)(NCS)$_2$(MeOH)] (**C27**) certainly catalyzes the hydroxylation of cyclohexane to cyclohexanol. Subsequent mass spectrometry (GC-MS) further confirmed the successful formation of cyclohexanol and revealed the additional presence of chlorobenzene, *m*-CBA, triphenylphosphine and triphenylphosphine oxide. The formation of m-chlorobenzoic acid (*m*-CBA) is most likely caused by the quenching process with triphenylphosphine, which also explains the presence of triphenylphosphine oxide. However, chlorobenzene is a side product in the suggested mechanism by *Itoh et al*., shown in Figure 5.3. Compared to the turnover number of [Ni^{II}(**TPA**)(OAc)(H$_2$O)]BPh$_4$ with TON = 587, the catalytic activity of **C27** is clearly lower. This might be caused due to irreversible redox processes at the cobalt(II) center, which could be investigated in cyclic voltammetry studies. In conclusion, this experiment lays the foundation of further catalytic studies with oxadiazole based metal catalysts. Hence, compounds like **C27** should not only be studied with respect to their physical, but also with respect to their chemical properties.

6 Experimental section

6.1 General Information

The commercially available chemicals were purchased by Acros Organics, Fisher Scientific, Roth, Merck and TCI and used without any further purification. The synthesis of 2,5-Bis[(1H-imidazol-2-ylmethyl)amino]methyl-1,3,4-oxadiazole (**$L^{5,Im}$**) and its corresponding metal complexes **C1**, **C2** and **C3** has already been reported in a former work, however, without magnetic data.[196] 2,5-Bis[(1,3-thiazol-2-ylmethyl)amino]methyl-1,3,4-oxadiazole (**$L^{5,TA}$**) and its associated iron(II) complexes **C4**, **C5** and **C6** were synthesized by [redacted] during his bachelor thesis.[200] 2,5-Bis[(pyrazin-2-ylmethyl)amino]methyl-1,3,4-oxadiazole (**$L^{6,N}$**) and its coordination compounds **C12** and **C13** were synthesized by [redacted] in his bachelor thesis.[247]

6.2 Instrumental Details

6.2.1 Elemental Analysis

All elemental analysis were done by the micro-analytical laboratory at the Johannes Gutenberg University Mainz using a Foss Heraeus Vario EL elemental analyzer.

6.2.2 Infrared Spectroscopy

Infrared spectra were recorded either on a JASCO FT/IR-4200 in form of potassium bromide pellets, on a Nicolet 5700 FT-IR-Spectrometer with an attached Smart Orbit ATR probe head from Thermo Electron Cooperation or on ALPHA II FTIR Spectrometer of the company BRUKER at the Johannes Gutenberg University Mainz. The measurements were done in a range of 400 cm^{-1} to 4000 cm^{-1} at room temperature. The background was measured prior to the samples and has been subtracted from the spectra. Visualization of the data was done by using the program Origin7.5.

6.2.3 Magnetic Measurements

Magnetic data of the alternation current (ac) and direct current (dc) measurements were obtained from a Quantum Design SQUID magnetometer MPMSXL in a temperature range between 2 K and 300 K at various magnetic fields. The samples were placed in a gelatin capsule and mounted inside a plastic straw The data were then collected over a length of 4 cm with 24 data points. The ac data of **C36** were obtained from a Quantum Design MPMS-XL-5 SQUID magnetometer at the TU Kaiserslautern. The sample was prepared as described above. The contribution of the temperature dependent volume magnetization of the capsule and the straw were determined experimentally and subtracted from the measured samples. Some of the measurements were carried out under the use of eicosane, which was placed on top of the samples in the gelatin capsule. In these cases, the prior experimentally determined magnetic contribution of the eicosane was subtracted from the obtained data. The molar susceptibility was calculated from the corrected volume magnetization M_v.

$$\chi = \frac{\partial M}{\partial H} \tag{6.1}$$

$$\chi_M = \frac{M_v \cdot M(\mathrm{g/mol})}{H(\mathrm{Oe}) \cdot m(\mathrm{g})} \tag{6.2}$$

The diamagnetic compound of the molar susceptibility was considered by Equation 6.3, which approximately results in values close to those deriving from Pascal's constants.

$$\chi_{M,para} = \chi_M - \chi_{M,dia} = \chi_M - \left(-\frac{M}{2} \cdot 10^6\ \mathrm{cm^3 mol^{-1}}\right) \tag{6.3}$$

The magnetic susceptibility and magnetization data were fitted using the program PHI.[201] The ac data were fitted with the program CC-Fit2.[359] All Plots have been visualized with Origin7.5.

6.2.4 Mass Spectrometry

All mass spectra were recorded by the analytics department of the Johannes Gutenberg University Mainz. FD mass measurements were performed on a Thermo Fischer DFS, while ESI mass spectra were recorded on an Agilent QTOF-MS with positive ion mode. The samples were prepared by dissolving in appropriate solvents. The spectra were plotted in Origin7.5.

6.2.5 NMR Spectroscopy

^{1}H-NMR (400 MHz), ^{13}C-NMR (101 MHz), ^{1}H-^{1}H-COSY, ^{1}H-^{13}C-HMBC and ^{1}H-^{13}C-HSQC spectra were recorded on a Bruker DRX 400 at Johannes Gutenberg University Mainz at room temperature. Samples were dissolved in appropriate deuterated solvent. The raw data were processed and visualized in MestReNova14.0. Chemical shifts were reported in parts per million while the solvent residual peaks have been used as an internal standard: $CDCl_3$: ^{1}H - 7.26 ppm (singlet), ^{13}C - 77.16 ppm (triplet); DMSO-d_6: ^{1}H - 2.50 ppm (quintet), ^{13}C - 39.52 ppm (septet); MeOD-d_4: ^{1}H - 3.30 ppm (quintet), ^{13}C - 49.00 ppm (septet).

6.2.6 Optical Spectroscopy

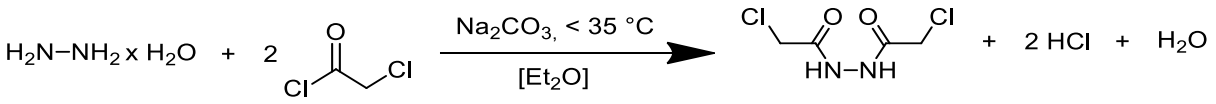
UV-Vis spectra in solution were recorded on a JASCO V-570 UV/Vis/NIR spectrometer at the Johannes Gutenberg University Mainz. For all measurements, a quartz glass cell with an optical path length of 1 cm was used. Therefore, the sample was dissolved in a chosen solvent. Background correction and measurements were performed with the software Jasco Spectra Manager. For the photoluminescence investigations substances were filled in a spectroscopically pure quartz cuvettes and flushed with argon. For measurements at 77 K, a special quartz glass Dewar assembly (HORIBA) was filled with liquid nitrogen. Excitation and emission spectra were recorded using the HORIBA Jobin Yvon Spex Fluorolog 3 spectrometer equipped with a UV Xe short-arc lamp (450 W, USHIO), double-grated excitation and emission monochromators, a photomultiplier tube (R928P), and a TCSPC (time-correlated single-photon counting) upgrade using a FluoroEssence™ software. Emission spectra were corrected for the spectral response of the monochromators and the detector using spectral corrections provided by the manufacturer.

6.2.7 X-Ray Structure Analysis

X-ray crystallographic data were collected at Johannes Gutenberg University Mainz by Regine Jung Pothmann from the crystallography department using a SMART APEX II CCD diffractometer with graphite monochromated Mo-Kα radiation, by Dieter Scholmeyer from the crystallography department using a Stoe IPDS 2T diffractometer with Mo-Kα radiation or by Dr. Luca Carrella from the chemistry department using a STOE STADIVARI diffractometer with Mo- Kα radiation. Any further compound specific details are given in the corresponding XRD tables in appendix D. The crystal structures were solved by using SHELXS/T/D[377–379] and SHELXL[380], implemented in Olex2[381]. Structure visualization was done with Mercury4.2 and Diamond3. Continuous Shape Measurements (CShM) were carried out with SHAPE2.1 and displayed with Diamond3.

6.3 Ligand Synthesis

6.3.1 1,2-Bis(chloroacetyl)hydrazide (1)



1

185.01 g/mol

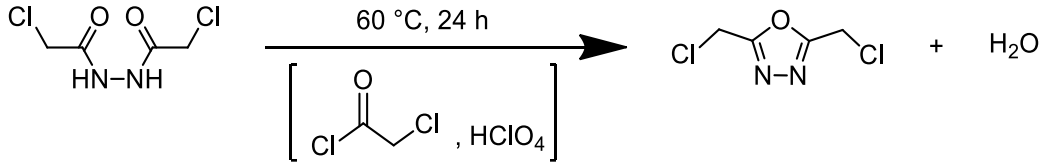
Preparation: **REN-JE-101**

Compound **1** was prepared by using a modified procedure from the literature.[199] Hydrazine hydrate (25.03 g, 0.50 mol, 1 eq) was dissolved in 200 ml diethyl ether. To this solution, chloroacetyl chloride (56.47 g, 0.50 mol, 1 eq), dissolved in 150 ml diethyl ether, was added under cooling and vigorous stirring such that the temperature did not exceed 35 °C. A colourless suspension had formed, which was stirred for 30 minutes after complete addition of the chloroacetyl chloride. 100 ml of deionized water were added followed by the portionwise addition of sodium carbonate (53.10 g, 0.50 mol, 1 eq). Afterwards, another equivalent of chloroacetyl chloride (56.47 g, 0.50 mol, 1 eq), again dissolved in 150 ml diethyl ether, was slowly added. After stirring at room temperature for 12 hours, the colourless solid was filtered, washed with cold diethyl ether, and recrystallized in ethyl acetate. **1** was isolated as a colourless powder (45.13 g, 0.24 mol, 48 %). **^{1}H-NMR** (400 MHz, DMSO, δ (ppm)): 10.47 (s, 2H, N*H*), 4.15 (s, 4H, CH_2) (Figure B.1). **^{13}C-NMR** (101 MHz, DMSO, δ (ppm)): 165.09 (O=*C*), 41.25 (*C*H_2) (Figure B.2). **FT-IR**: $\tilde{\upsilon}$ (cm^{-1}) = 3176, 3034, 2979, 2956, 2891, 1701, 1606, 1491, 1437, 1405, 1306, 1252, 1222, 1112, 1007, 934, 918, 792, 713, 639, 577, 538, 490, 460 (Figure A.1). **FD-MS**: m/z = 184.00 (100.00 %), 185.00 (6.98 %), 185.99 (45.67 %) (Figure C.1). **EA** (%): Calc. (found) C 25.97 (25.90), H 3.27 (3.01), N 15.14 (15.43).

Literature:

[199] S. Liu, L. Zhang, X. Liu, New J. Chem. 2013, 37, 821.

6.3.2 2,5-Bis(chloromethyl)-1,3,4-oxadiazole (2)



1

185.01 g/mol

2

166.99 g/mol

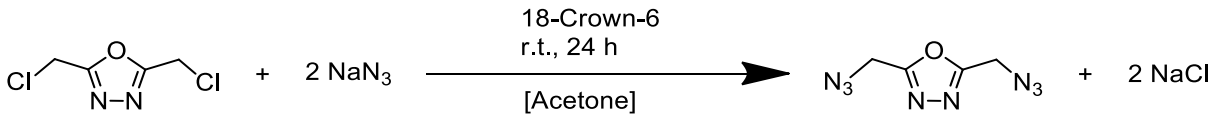
Preparation: **REN-JE-026**

Compound **2** was prepared by using a modified procedure from the literature.[199] Perchloric acid (60 %, 8.75 g) and chloroacetyl chloride (30.00 g, 270.25 mmol, 5 eq) were added and heated at a temperature of 60 °C until a uniform phase was formed. **1** (10.00 g, 54.05 mmol, 1 eq) was then added in portions with stirring, whereupon it dissolved completely after a short time. After 24 hours of vigorous stirring, the yellow solution was added to a 150 ml ice-water mixture and the pH was adjusted to 9.0 with a saturated sodium carbonate solution. The reaction mixture was extracted three times with 100 ml of diethyl ether. The combined extracts were washed with a 10 % sodium carbonate solution, dried over sodium sulfate and taken to dryness under reduced pressure yielding a bright yellow oil. **2** was isolated from the crude product by column chromatography (SiO_2, cyclohexane/ ethyl acetate (3:1), R_f = 0.3) as a colourless oil (8.38 g, 50.18 mmol, 93 %). **^{1}H-NMR** (400 MHz, $CDCl_3$, δ (ppm)): 4.68 (s, 4H, CH_2) (Figure B.3). **^{13}C-NMR** (101 MHz, $CDCl_3$, δ (ppm)): 163.70 (C^{ODA}), 32.75 (CH_2) (Figure B.4). **FT-IR**: $\tilde{\upsilon}$ (cm^{-1}) = 3029 (w), 2969 (w), 1582 (s), 1565 (s), 1427 (s), 1382 (s), 1269 (m), 1233 (s), 1154 (m), 1038 (m), 989 (s), 968 (m), 918 (w), 886 (w), 780 (vs), 760 (vs), 719 (s), 654 (vs), 616 (s) (Figure A.2). **EA** (%): Calc. (found) C 28.77 (28.70), H 2.41 (2.79), N 16.78 (16.76).

Literature:

[199] S. Liu, L. Zhang, X. Liu, New J. Chem. 2013, 37, 821.

6.3.3 2,5-Bis(azidomethyl)-1,3,4-oxadiazole (3)



2 166.99 g/mol

3 180.13 g/mol

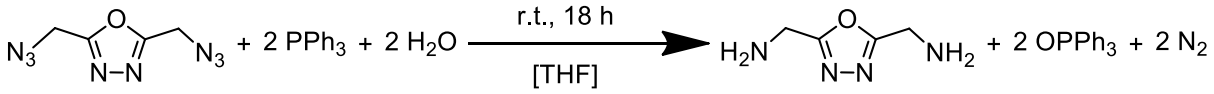
Preparation: **REN-JE-056**

Compound **3** was prepared according to a procedure from the literature.[196] **2** (19.68 g, 118.00 mmol, 1 eq), sodium azide (41.49 g, 638.00 mmol, 5.4 eq), and 18-crown-6 (2.81 g, 11.00 mmol, 0.09 eq) were suspended in 200 ml of acetone and stirred at room temperature for 18 hours. The suspension was filtered and the filtrate was freed from solvent under reduced pressure, yielding a yellowish crude product. **3** was isolated as a colourless oil by column chromatography (SiO_2, dichloromethane/ diethyl ether (4:1), R_f = 0.6) (18.42 g, 102.26 mmol, 87 %). **^{1}H-NMR** (400 MHz, $CDCl_3$, δ (ppm)): 4.75 (s, 4H, CH_2) (Figure B.5). **^{13}C-NMR** (101 MHz, $CDCl_3$, δ (ppm)): 162.95 (C^{ODA}), 44.18 (CH$_2$) (Figure B.6). **FT-IR**: $\tilde{\upsilon}$ (cm^{-1}) = 3004 (w), 2941 (w), 2858 (vw), 2180 (sh, s), 2093 (vs), 1585 (m), 1566 (m), 1435 (m), 1394 (m), 1333 (m), 1257 (s), 1181 (s), 1043 (w), 980 (m), 944 (m), 889 (m), 789 (m), 687 (m), 649 (m), 555 (m) (Figure A.3). **FD-MS**: m/z = 180.12 (100.00 %), 181.13 (12.80 %) (Figure C.2). **EA** (%): Calc. (found) C 26.67 (26.71), H 2.24 (2.23), N 62.21 (61.82).

Literature:

[196] J. Eppelsheimer, *Eisen(II) Spin-Crossover Verbindungen mit 1,3,4-Oxadiazol-Brückenliganden*, Masterarbeit, Mainz 2017.

6.3.4 2,5-Bis(aminomethyl)-1,3,4-oxadiazole (4)



3 180.13 g/mol

4 128.14 g/mol

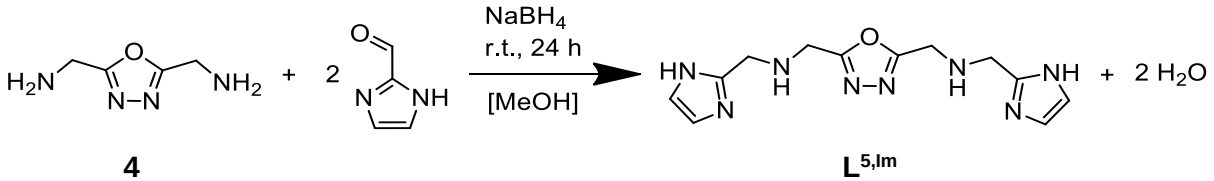
Preparation: **REN-JE-058**

Compound **4** was prepared according to a procedure from the literature.[196] **3** (5.00 g, 27.76 mmol, 1 eq) was dissolved in 250 ml tetrahydrofuran and triphenylphosphine (17.47 g, 66.62 mmol, 2.4 eq) was added in portions while stirring. After completed addition and gas evolution, 17 ml of deionized water were added to the solution. The reaction was stirred at room temperature for 18 hours. The solvent was then removed, whereupon a yellow solid was obtained as crude product. **4** was isolated as a brown solid by column chromatography with discontinuous gradient elution (SiO_2, chloroform/ methanol (4:1) → chloroform/ methanol/ triethylamine (80:20:1) → chloroform/ methanol/ triethylamine (67:33:1)) (3.44 g, 26.85 mmol, 97 %). **^{1}H-NMR** (400 MHz, $CDCl_3$, δ (ppm)): 4.05 (s, 4H, C*H*$_2$), 1.64 (s, 4H, N*H*$_2$) (Figure B.7). **^{13}C-NMR** (101 MHz, MeOD, δ (ppm)): 167.57 (*C*^{ODA}), 35.90 (*C*H$_2$) (Figure B.8). **FT-IR**: $\tilde{\upsilon}$ (cm^{-1}) = 3373 (s), 3304 (s), 3067 (m), 2967 (m), 2927 (m), 2848 (m), 2555 (w), 1663 (s), 1606 (s), 1572 (vs), 1550 (vs), 1438 (s), 1374 (m), 1339 (s), 1219 (m), 1176 (s), 1094 (s), 1005 (w), 980 (s), 960 (m), 899 (s), 871 (vs), 772 (m), 697 (w), 661 (w), 625 (w), 497 (w), 486 (w), 440 (w) (Figure A.4). **FD-MS**: m/z = 128.08 (54.91 %), 129.09 (100.00 %) (Figure C.3). **EA** (%): Calc. (found) C 37.49 (37.05), H 6.29 (7.21), N 43.73 (42.12).

Literature:

[196] J. Eppelsheimer, *Eisen(II) Spin-Crossover Verbindungen mit 1,3,4-Oxadiazol-Brückenliganden*, Masterarbeit, Mainz 2017.

6.3.5 2,5-Bis[(1*H*-imidazol-2-ylmethyl)amino]methyl-1,3,4-oxadiazole ($L^{5,Im}$)



4 128.14 g/mol

$L^{5,Im}$ 288.32 g/mol

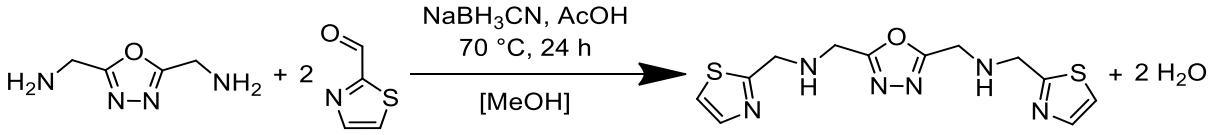
Preparation: **REN-JE-039**

Compound $L^{5,Im}$ was prepared according to a procedure from the literature.[196] To a solution of **4** (3.00 g, 23.41 mmol, 1 eq) in 250 ml methanol was added 1H-imidazole-2-carboxaldehyde (4.95 g, 51.51 mmol, 2.2 eq), dissolved in 250 ml methanol. The reaction mixture was stirred for 24 hours. Sodium borohydride (4.42 g, 117.05 mmol, 5 eq) was then added to the yellow solution under cooling. The reaction was stirred again for 24 hours at room temperature. The solvent was removed under reduced pressure, yielding a brown oil as crude product. $L^{5,Im}$ was isolated as a brown solid by column chromatography with continuous gradient elution (SiO_2, chloroform/ methanol (4:1) → methanol) (4,67 g, 16,20 mmol, 69 %). **^{1}H-NMR** (400 MHz, MeOD, δ (ppm)): 6.97 (s, 4H, *H*C=C*H*), 3.99 (s, 4H, CH_2), 3.91 (s, 4H, CH_2) (Figure B.9). **^{13}C-NMR** (101 MHz, MeOD, δ (ppm)): 165.93, 146.15, 121.44, 44.97, 42.12 (Figure B.10). **FT-IR**: $\tilde{\upsilon}$ (cm^{-1}) = 3326, 3145, 3110, 3051, 2968, 2891, 2809, 2736, 2661, 2386, 2348, 1664, 1565, 1493, 1458, 1438, 1424, 1369, 1339, 1326, 1288, 1260, 1234, 1219, 1199, 1147, 1128, 1065, 1005, 980, 969, 914, 875, 814, 756, 736, 703, 678, 665, 622, 483, 472, 452, 438, 419 (Figure A.5). **FD-MS**: m/z = 289.34 (100.00 %), 290.35 (16.03 %) (Figure C.4).

Literature:

[196] J. Eppelsheimer, *Eisen(II) Spin-Crossover Verbindungen mit 1,3,4-Oxadiazol-Brückenliganden*, Masterarbeit, Mainz 2017.

6.3.6 2,5-Bis[(1,3-thiazol-2-ylmethyl)amino]methyl-1,3,4-oxadiazole ($L^{5,TA}$)



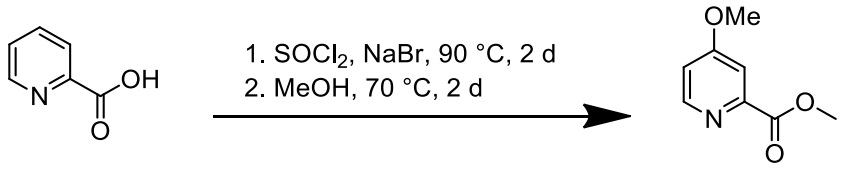
4 128.14 g/mol

$L^{5,TA}$ 322.41 g/mol

Preparation: **REN-LM-010**

To a solution of **4** (2.52 g, 19.7 mmol, 1 eq), thiazole-2-carbaldehyde (4.70 g, 41.55 mmol, 2.1 eq) and acetic acid (2,37 ml, 2,49 g, 41.55 mmol, 2.1 eq) in 1000 ml methanol was added sodium cyanoborohydride (6.19 g, 98.50 mmol, 5 eq) slowly in portions. Afterwards the reaction mixture was refluxed for 24 hours. The solvent was removed under reduced pressure, yielding a brown oil as crude product. **$L^{5,TA}$** was isolated as brown oil by column chromatography (SiO_2, chloroform/ methanol (19:1)) (3.82 g, 11.84 mmol, 60 %). **^{1}H-NMR** (400 MHz, $CDCl_3$, COSY, δ (ppm)): 7.73 (d, 2H, *H*C=CH), 7.29 (d, 2H, HC=C*H*), 4.23 (s, 4H, TA-C*H*$_2$), 4.12 (s, 4H, ODA-C*H*$_2$) (Figure B.11, Figure B.13). **^{13}C-NMR** (101 MHz, $CDCl_3$, HSQC, HMBC, δ (ppm)): 169.84 (TA*C*^{2}), 165.39 (ODA*C*$^{2/5}$), 142,6 (H*C*=CH), 119.30 (HC=*C*H), 49.97 (TA-*C*H$_2$), 43.06 (ODA-*C*H$_2$) (Figure B.12, Figure B.14, Figure B.15). **FT-IR**: $\tilde{\upsilon}$ (cm^{-1}) = 3277, 3109, 3079, 2913, 2838, 1670, 1587, 1502, 1468, 1427, 1337, 1315, 1238, 1185, 1138, 1054, 979, 875, 804, 771, 731, 677, 601, 499 (Figure A.6). **FD-MS**: m/z = 323.08 (100.00 %), 324.08 (15.63 %), 325.07 (9.37 %) (Figure C.5).

6.3.7 Methyl 4-methoxypicolinate (5)



5

123.11 g/mol 167.16 g/mol

Preparation: **REN-JE-156**

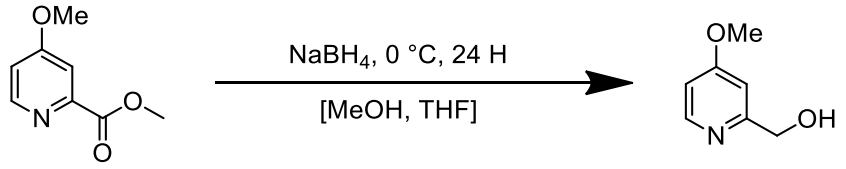
Compound **5** was prepared according to a modified procedure from the literature.[241,246] Picolinic acid (15.704 g, 128.00 mmol, 1 eq) and sodium bromide (1.31 g, 12.80 mmol, 0.1 eq) were suspended in 110 mL of thionyl chloride and stirred vigorously at 90 °C for 2 days. The excess of thionyl chlorid was removed completely under reduced pressure. The residue was cooled to 0 °C and 50 ml of methanol were added cautiously. The resulting reaction mixture was stirred at 70 °C for further 2 days. Afterwards, the solvent was removed in vacuo and the residue dissolved in 100 ml of dichloromethane. Sodium carbonate (20.28 g, 191 mmol, 1.5 eq) was added and the mixture was stirred for 3 hours. 100 ml of water were added and the mixture was extracted five times with chloroform. The combined organic extracts were dried over magnesium sulfate, filtered and concentrated. The crude product was purified by column chromatography (SiO_2, cyclohexane/ ethyl acetate (1:1)) to give **5** as brown oil (9.19 g, 55.04 mmol, 43 %). **^{1}H-NMR** (400 MHz, $CDCl_3$, δ (ppm)): 8.54 (d, 1H, pyC*H*), 7.67 (d, 1H, pyC*H*), 6.97 (m, 1H, pyC*H*), 4.00 (s, 3H, CH_3), 3.91 (s, 3H, CH_3) (Figure B.16).

Literature:

[241] T. J. Donohoe, D. J. Johnson, L. H. Mace, R. E. Thomas, J. Y. K. Chiu, J. S. Rodrigues, R. G. Compton, C. E. Banks, P. Tomcik, M. J. Bamford, O. Ichihara, Organic & biomolecular chemistry 2006, 4, 1071.

[246] T. J. Donohoe, M. J. Connolly, L. Walton, Organic letters 2009, 11, 5562.

6.3.8 4-Methoxy-2-(hydroxymethyl)pyridine (6)



5
167.16 g/mol

6
139.15 g/mol

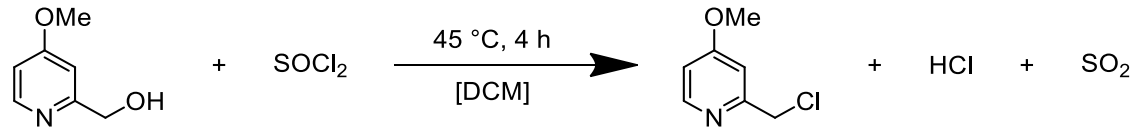
Preparation: **REN-JE-161**

Compound **6** was prepared according to a modified procedure from the literature.[243] To a cooled (0 °C) suspension of **5** (9.00 g, 53.86 mmol, 1 eq) and calcium chloride (5.09 g, 134.64 mmol, 2.5 eq) in dry methanol-tetrahydrofuran (2:1, 100 ml) was added sodium borohydride (5.97 g, 157.94 mmol, 2 eq) in portions under an inert atmosphere. The reaction mixture was stirred for 24 hours at room temperature. The solvent was removed under reduced pressure. 200 ml of water and 200 ml of chloroform were added and the mixture was stirred for 1 hour. The remaining solid was filtered and the aqueous and organic phases were separated. The aqueous phase was extracted three more times with chloroform. The combined organic phases were dried over magnesium sulfate. The solvent was removed under reduced pressure to yield **6** as yellow oil which crystallizes after several hours (5.54 g, 39.82 mmol, 74 %). **^{1}H-NMR** (400 MHz, $CDCl_3$, δ (ppm)): 8.35 (d, 1H, pyC*H*), 6.78 - 6.72 (m, 2H, pyC*H*), 4.71 (s, 2H, CH_2) (Figure B.17).

Literature:

[243] H. Fuchida, S. Tabata, N. Shindo, I. Takashima, Q. Leng, Y. Hatsuyama, I. Hamachi, A. Ojida, BCSJ 2015, 88, 784.

6.3.9 2-Chloromethyl-4-methoxypyridine (7)



6

139.15 g/mol

7

157.60 g/mol

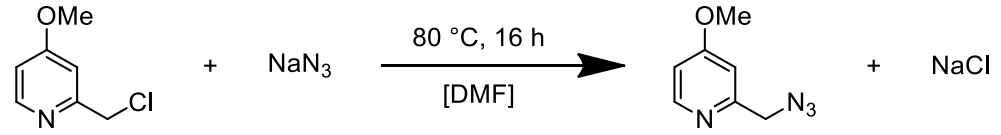
Preparation: **REN-JE-164**

Compound **7** was prepared according to a modified procedure from the literature.[243] To a cooled (0 °C) solution of **6** (5.00 g, 35.94 mmol, 1 eq) in 30 ml of dry dichloromethane was added thionyl chloride (15.98 ml, 220.33 mmol, 6 eq) dropwise. The reaction mixture was stirred for 4 hours at 45 °C before it was taken to dryness under reduced pressure. The residue was dissolved in a sat. sodium bicarbonate solution and extracted 4 times with dichloromethane. The combined organic extracts were dried over magnesium sulfate and the solvent was removed under reduced pressure to yield **7** as a red oil (4.97 g, 31.57 mmol, 88 %). **^{1}H-NMR** (400 MHz, $CDCl_3$, δ (ppm)): 8.46 (d, 1H, pyC*H*), 7.51 (d, 1H, pyC*H*), 7.26 - 7.25 (m, 1H, pyC*H*), 4.65 (s, 2H, CH_2) (Figure B.18).

Literature:

[243] H. Fuchida, S. Tabata, N. Shindo, I. Takashima, Q. Leng, Y. Hatsuyama, I. Hamachi, A. Ojida, BCSJ 2015, 88, 784.

6.3.10 2-Azidomethyl-4-methoxypyridine (8)



7
157.60 g/mol

8
164.16 g/mol

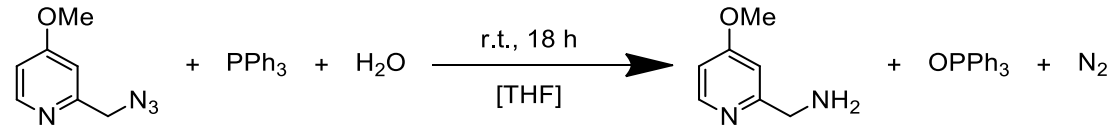
Preparation: **REN-JE-166**

Compound **8** was prepared according to a modified procedure from the literature.[243] To a solution of **7** (4.98 g, 31.61 mmol, 1 eq) in 120 ml dimethylformamide was added sodium azide (15.24 ml, 234.42 mmol, 3 eq) in portions. The reaction mixture was stirred for 16 hours at 80 °C. After dilution with 50 ml of saturated sodium bicarbonate solution, the mixture was extracted with ethyl acetate, until the ethyl acetate phase was nearly colourless. The combined organic extracts were dried over magnesium sulfate and the solvent was removed under reduced pressure to yield **8** as a brown oil (4.59 g, 27.94 mmol, 88 %). **^{1}H-NMR** (400 MHz, $CDCl_3$, δ (ppm)): 8.40 (d, 1H, pyC*H*), 6.87 (d, 1H, pyC*H*), 6.77 - 6.75 (m, 1H, pyC*H*), 4.45 (s, 2H, CH_2), 3.87 (s, 3H, CH_3) (Figure B.19).

Literature:

[243] H. Fuchida, S. Tabata, N. Shindo, I. Takashima, Q. Leng, Y. Hatsuyama, I. Hamachi, A. Ojida, BCSJ 2015, 88, 784.

6.3.11 (4-Methoxy-pyridin-2-yl)methylamine (9)



8

164.16 g/mol

9

138.17 g/mol

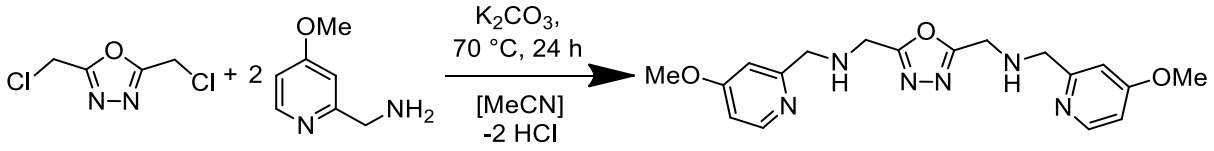
Preparation: **REN-JE-168**

Compound **9** was prepared according to a modified procedure from the literature.[243] **8** (4.59 g, 27.94 mmol, 1 eq) was dissolved in 100 ml tetrahydrofuran. To this solution triphenylphosphine (18.34 g, 69.92 mmol, 2.5 eq) was added portionwise. The reaction mixture was stirred for 1 hours at room temperature before 9 ml of water were added. The solution was stirred for further 17 hours. After removal of the solvent under reduced pressure, the residue was purified by column chromatography with discontinuous gradient elution (SiO_2, chloroform/ methanol (9:1) → chloroform/ methanol (4:1) to yield **9** as yellow oil (1.87 g, 13.53 mmol, 48 %). **^{1}H-NMR** (400 MHz, $CDCl_3$, δ (ppm)): 8.34 (d, 1H, pyC*H*), 6.80 (d, 1H, pyC*H*), 6.69 - 6.67 (m, 1H, pyC*H*), 3.93 (s, 2H, CH_2), 3.83 (s, 3H, CH_3), 2.80 (s, 2H, NH_2) (Figure B.20).

Literature:

[243] H. Fuchida, S. Tabata, N. Shindo, I. Takashima, Q. Leng, Y. Hatsuyama, I. Hamachi, A. Ojida, BCSJ 2015, 88, 784.

6.3.12 2,5-Bis[(4-methoxypyridin-2-ylmethyl)amino]methyl-1,3,4-oxadiazole ($L^{6,OMe}$)



2 166.99 g/mol

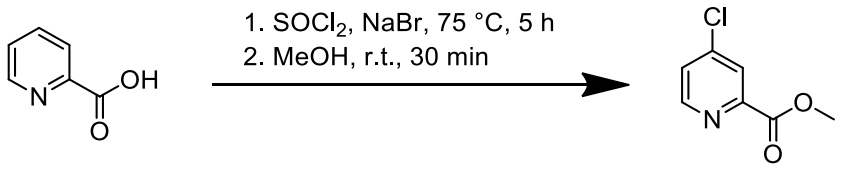
9 138.17 g/mol

$L^{6,OMe}$ 370.41 g/mol

Preparation: **REN-JE-171**

9 (1.52 g, 10.98 mmol, 2.5 eq) and potassium carbonate (3.04 g, 21.95 mmol, 5 eq) were dissolved in 150 ml acetonitrile under an inert atmosphere. To this mixture, a solution of **2** (0.79 g, 4.39 mmol, 1 eq) in 20 ml acetonitrile was added dropwise at 70 °C. The reaction was stirred for 24 h at given temperature. The solid was filtered and the solvent removed under reduced pressure, resulting in a brown oil as crude product. **$L^{6,OMe}$** could be isolated by column chromatography (ALOX (neutral), chloroform/ methanol (9:1)) as a brown oil (650 mg, 1.76 mmol, 40 %). **^{1}H-NMR** (400 MHz, $CDCl_3$, δ (ppm)): 8.27 - 8.25 (m, 2H, pyC*H*), 6.75 (d, 2H, pyC*H*), 6.62 - 6.60 (m, 2H, pyC*H*), 3.96 (s, 4H, CH_2), 3.83 (s, 4H, CH_2), 3.75 (s, 6H, CH_3) (Figure B.21). **FT-IR**: $\tilde{\upsilon}$ (cm^{-1}) = 3291, 3271, 3249, 3234, 3217, 3049, 3010, 2973, 2942, 2841, 1670, 1636, 1594, 1566, 1483, 1459, 1427, 1303, 1288, 1244, 1190, 1157, 1123, 1031, 992, 825, 782, 758, 556, 533, 472, 446 (Figure A.8). **ESI-MS**: m/z = 371.18 (100.00 %), 372.19 (19.99 %), 373.19 (2.56 %) (Figure C.7).

6.3.13 4-Chloro-pyridine-2-carboxylic acid methyl ester (10)



10

123.11 g/mol 171.58 g/mol

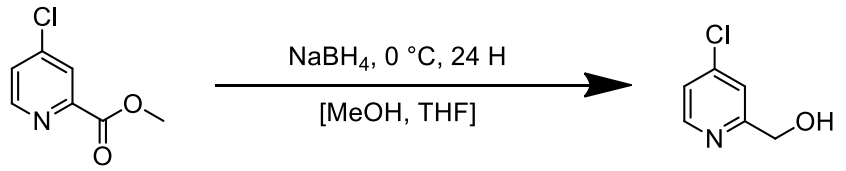
Preparation: **REN-JE-179**

Compound **10** was prepared according to a modified procedure from the literature.[244] Picolinic acid (20 g, 162 mmol, 1 eq) and sodium bromide (33.43 g, 325 mmol, 2 eq) were suspended in 81 ml of thionyl chloride and refluxed for 5 hours. The solvent was removed by distillation under reduced pressure. 160 ml of absolute methanol were added under cooling and the reaction mixture was stirred at room temperature for 30 minutes. Afterwards, methanol was removed under reduced pressure and the residue was taken up in 200 ml of a 5 % aqueous solution of sodium bicarbonate. The solution was extracted three times with 100 ml chloroform. The combined organic layers were dried over magnesium sulfate and freed from solvent under reduced pressure. The residue was purified by column chromatography (SiO_2, cyclohexane/ ethyl acetate (4:1)) to afford **10** as a yellow solid (19.55 g, 113.96 mmol, 70 %). **^{1}H-NMR** (400 MHz, $CDCl_3$, δ (ppm)): 8.64 (d, 1H, pyC*H*), 8.14 (d, 1H, pyC*H*), 7.51 - 7.26 (m, 1H, pyC*H*), 4.02 (s, 3H, CH_3) (Figure B.22).

Literature:

[244] J. G. Lewis, D.V. Patel, S. K. Anandan, M. F. Gordeev, *LINCOMYCIN DERIVATIVES POSSESSING ANTIBACTERIAL ACTIVITY: Patent Application Publication* **2004**.

6.3.14 (4-Chloropyridin-2-yl)methanol (11)



10
171.58 g/mol

11
143.57 g/mol

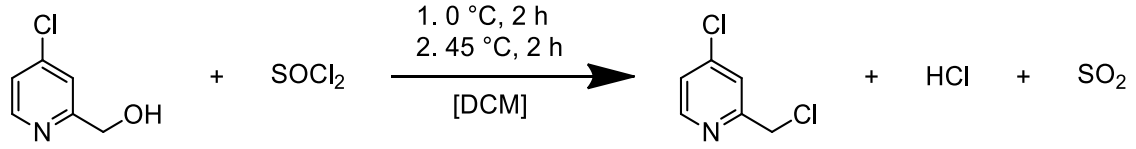
Preparation: **REN-JE-182**

Compound **11** was prepared according to a modified procedure from the literature.[243] To a cooled (0 °C) suspension of **10** (13.55 g, 78.97 mmol, 1 eq) and calcium chloride (35.06 g, 315.89 mmol, 4 eq) in methanol-tetrahydrofuran (2:1, 150 ml) was added sodium borohydride (5.97 g, 157.94 mmol, 2 eq) in portions. The reaction mixture was stirred for 24 hours at room temperature. After cooling to 0 °C, 50 ml of water were added and the solution was stirred for another two hours. Afterwards, the solvent was removed completely under reduced pressure. The residue was taken up in ca. 200 ml water and extracted three times with 100 ml chloroform each time. The combined organic extracts were dried over magnesium sulfate and taken to dryness. **11** could be isolated as yellow solid (9.84 g, 68.56 mmol, 87 %). **^{1}H-NMR** (400 MHz, $CDCl_3$, δ (ppm)): 8.43 (d, 1H, pyC*H*), 7.33 (s, 1H, pyC*H*), 7.21 (d, 1H, pyC*H*), 4.74 (s, 2H, CH_2) (Figure B.23).

Literature:

[243] H. Fuchida, S. Tabata, N. Shindo, I. Takashima, Q. Leng, Y. Hatsuyama, I. Hamachi, A. Ojida, BCSJ 2015, 88, 784.

6.3.15 4-Chloro-2-chloromethyl pyridine (12)



11

143.57 g/mol

12

162.01 g/mol

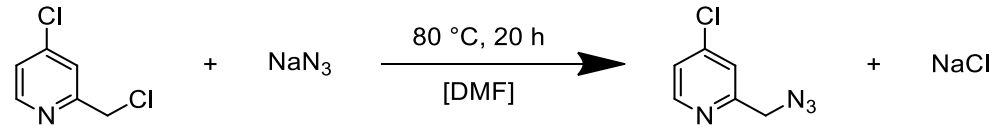
Preparation: **REN-JE-186**

Compound **12** was prepared according to a modified procedure from the literature.[243] To a cooled (0 °C) solution of **11** (11.84 g, 82.49 mmol, 1 eq) in 100 ml dichloromethane was added thionyl chloride (36.00 ml, 494.94 mmol, 6 eq) dropwise. The reaction mixture was stirred for 2 hours at 0 °C. Afterwards the solution was heated up to 45 °C and stirred at given temperature for another 2 hours. The reaction mixture was taken to dryness under reduced pressure. The residue was dissolved in a sat. sodium bicarbonate solution and extracted 4 times with chloroform. The combined organic extracts were dried over magnesium sulfate and the solvent was removed under reduced pressure to yield **12** as a brown oil (12.66 g, 78.11 mmol, 95 %). **^{1}H-NMR** (400 MHz, $CDCl_3$, δ (ppm)): 8.46 (d, 1H, $_{py}CH$), 7.51 (d, 1H, $_{py}CH$), 7.26 - 7.25 (m, 1H, $_{py}CH$), 4.65 (s, 2H, CH_2) (Figure B.24).

Literature:

[243] H. Fuchida, S. Tabata, N. Shindo, I. Takashima, Q. Leng, Y. Hatsuyama, I. Hamachi, A. Ojida, BCSJ 2015, 88, 784.

6.3.16 2-(Azidomethyl)-4-chloropyridine (13)



12 162.01 g/mol

13 168.58 g/mol

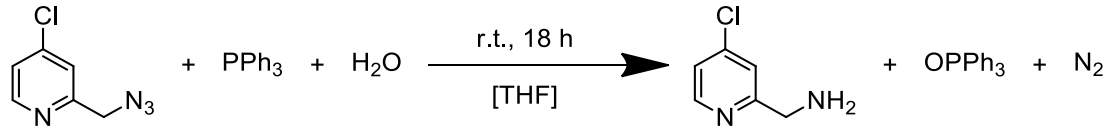
Preparation: **REN-JE-187**

Compound **13** was prepared according to a modified procedure from the literature.[243] To a solution of **12** (12.66 g, 78.14 mmol, 1 eq) in 250 ml dimethylformamide was added sodium azide (15.24 ml, 234.42 mmol, 3 eq) in portions. The reaction mixture was stirred for 20 hours at 80 °C. The solvent was removed under reduced pressure. The residue was dissolved in a sat. sodium bicarbonate solution and extracted with a hexane - ethyl acetate mixture (1:1) until the aqueous phase was colourless. The combined organic extracts were dried over magnesium sulfate and the solvent was removed under reduced pressure to yield **13** as a brown oil (11.84 g, 70.53 mmol, 90 %). **^{1}H-NMR** (400 MHz, $CDCl_3$, δ (ppm)): 8.48 (d, 1H, $_{py}CH$), 7.38 (d, 1H, $_{py}CH$), 7.27 - 7.25 (m, 1H, $_{py}CH$), 4.49 (s, 2H, CH_2) (Figure B.25).

Literature:

[243] H. Fuchida, S. Tabata, N. Shindo, I. Takashima, Q. Leng, Y. Hatsuyama, I. Hamachi, A. Ojida, BCSJ 2015, 88, 784.

6.3.17 (4-Chloropyridin-2-yl)methanamine (14)



13

168.58 g/mol

14

142.59 g/mol

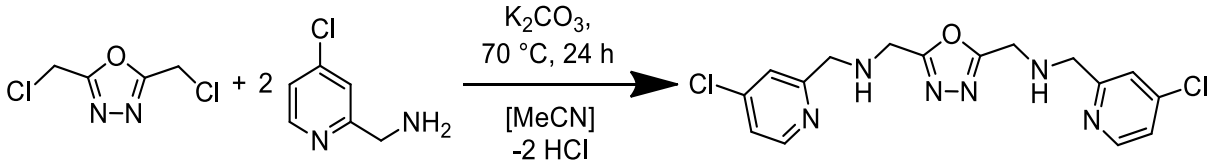
Preparation: **REN-JE-188**

Compound **14** was prepared according to a modified procedure from the literature.[243] **13** (1.72 g, 10.20 mmol, 1 eq) was dissolved in 20 ml tetrahydrofuran. To this solution triphenylphosphine (4.01 g, 15.30 mmol, 1.5 eq) was added portionwise. The reaction mixture was stirred for 2 hours at room temperature before 2 ml of water were added. The solution was stirred for further 16 hours. After removal of the solvent under reduced pressure, the residue was purified by column chromatography (SiO_2, chloroform/ methanol (19:1)) to yield **14** as yellow oil (0.86 g, 6.03 mmol, 59 %). **^{1}H-NMR** (400 MHz, MeOD, δ (ppm)): 8.47 (d, 1H, pyC*H*), 7.55 (s, 1H, pyC*H*), 7.55 - 7.38 (m, 1H, pyC*H*), 4.03 (s, 2H, CH_2) (Figure B.26).

Literature:

[243] H. Fuchida, S. Tabata, N. Shindo, I. Takashima, Q. Leng, Y. Hatsuyama, I. Hamachi, A. Ojida, BCSJ 2015, 88, 784.

6.3.18 2,5-Bis[(4-chloropyridin-2-ylmethyl)amino]methyl-1,3,4-oxadiazole ($L^{6,Cl}$)



2 166.99 g/mol

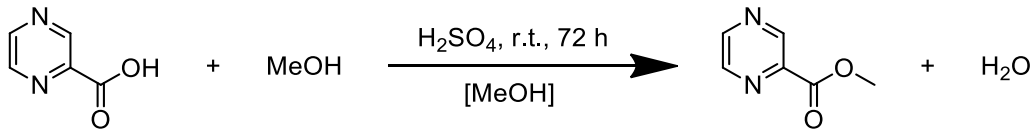
14 142.59 g/mol

$L^{6,Cl}$ 379.25 g/mol

Preparation: **REN-JE-189**

14 (860 mg, 6.03 mmol, 2.5 eq) and potassium carbonate (1.67 g, 12.05 mmol, 5 eq) were dissolved in 60 ml acetonitrile under an inert atmosphere. To this mixture, a solution of **2** (403 mg, 2.41 mmol, 1 eq) in 10 ml acetonitrile was added dropwise at 70 °C. The reaction was stirred for 24 h at given temperature. The solid was filtered and the solvent removed under reduced pressure, resulting in a brown oil as crude product. **$L^{6,Cl}$** could be isolated by column chromatography (SiO_2, chloroform/ methanol (19:1)) as a brown oil (428 mg, 1.13 mmol, 47 %). **^{1}H-NMR** (400 MHz, $CDCl_3$, δ (ppm)): 8.44 (d, 2H, py*CH*), 7.36 (d, 2H, py*CH*), 7.21 - 7.19 (m, 2H, py*CH*), 4.07 (s, 4H, Py-CH_2), 3.98 (s, 4H, ODA-CH_2) (Figure B.27). **^{13}C-NMR** (101 MHz, $CDCl_3$, HSQC, HMBC, δ (ppm)): 165.50 (ODA$C^{2/5}$), 160.37 (pyC^1), 150.29 (py*C*), 144.69 (py*C*), 123.65 (py*C*), 122.67 (py*C*), 53.66 (Py-CH_2), 43.21 (ODA-CH_2) (Figure B.28, Figure B.29, Figure B.30). **FT-IR**: $\tilde{\upsilon}$ (cm^{-1}) = 3245, 3047, 2919, 2727, 2661, 2335, 2314, 1714, 1673, 1634, 1574, 1555, 1528, 1464, 1444, 1392, 1344, 1242, 1192, 1126, 1101, 1028, 989, 951, 891, 808, 703, 651, 560, 545, 529, 515, 433, 410 (Figure A.7). **ESI-MS**: m/z = 379.08 (25.52 %), 380.09 (4.86 %), 381.08 (17.00 %) (Figure C.6).

6.3.19 Methyl pyrazine-2-carboxylate (15)



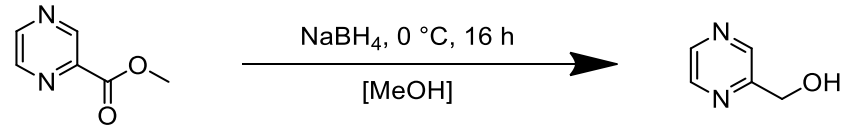
15

124.10 g/mol 138.12 g/mol

Preparation: **REN-JE-133**

Pyrazine-2-carboxylic acid (10.00 g, 72.90 mmol, 1 eq) was suspended in 56 ml methanol. 16 ml of conc. sulfuric acid were added dropwise at a temperature of 0 °C. Afterwards, the reaction was stirred at room temperature for 72 hours. The solution was added cautiously to a aqueous sodium bicarbonate solution (33 g sodium bicarbonate in 150 ml water) and stirred for 1 hour. The solid was filtered and the solvent has been removed under reduced pressure. The residue was dissolved in 200 ml water and the aqueous phase was extracted three times with 100 ml chloroform. The organic extracts were combined, extracted one time with 100 ml of brine and freed from solvent. Purification of the crude product by column chromatography (SiO_2, cyclohexane/ ethyl acetate (1:1)) yielded **15** as a yellow solid (7.11 g, 51.48 mmol, 71 %). **^{1}H-NMR** (400 MHz, $CDCl_3$, δ (ppm)): 9.33 (d, 1H, pyrC*H*), 8.78 (d, 1H, pyrC*H*), 8.73 - 8.72 (m, 1H, pyrC*H*), 4.05 (s, 3H, CH_3) (Figure B.31). **FT-IR**: $\tilde{\upsilon}$ (cm^{-1}) = 2966, 2923, 2856, 1604, 1485, 1440, 1383, 1236, 1178, 1145, 1120, 1109, 1086, 1018, 764, 636, 630, 625 (Figure A.9).

6.3.20 Pyrazin-2-ylmethanol (16)



15
138.12 g/mol

16
110.11 g/mol

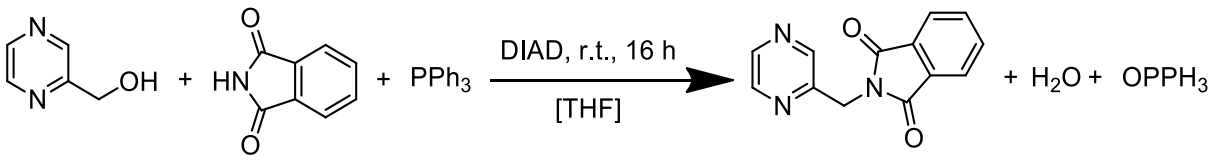
Preparation: **REN-JE-174**

Compound **16** was prepared according to a modified procedure from the literature.[248] To a cooled (0 °C) solution of **15** (4.67 g, 33.85 mmol, 1 eq) in 325 ml methanol was added sodium borohydride (5.12 g, 135.21 mmol, 4 eq) in portions. After complete addition, the reaction mixture was stirred for 16 hours at room temperature. 18 ml of water were added to quench the reaction. Afterwards, the solvent was removed completely under reduced pressure. The crude product was suspended in 550 ml chloroform and stirred vigorously overnight. The solid was filtered and the filtrate freed from solvent under reduced pressure to yield 16 as a yellow oil (3.24 g, 29.43 mmol, 87 %). **^{1}H-NMR** (400 MHz, $CDCl_3$, δ (ppm)): 8.64 (s, 1H, pyrC*H*), 8.54 - 8.51 (m, 2H, pyrC*H*), 4.85 (s, 2H, CH_2) (Figure B.32).

Literature:

[248] H. L. C. Feltham, M. G. Cowan, J. A. Kitchen, G. N. L. Jameson, S. Brooker, *Supramolecular Chemistry* 2018, *30*, 296.

6.3.21 2-Pyrazinemethylphthalimide (17)



16 138.12 g/mol

17 239.23 g/mol

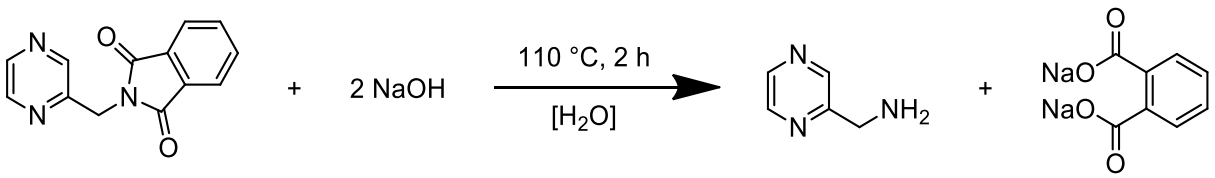
Preparation: **REN-JE-196**

Compound **17** was prepared according to a modified procedure from the literature.[248] To a cooled (0 °C) suspension of **16** (2.20 g, 20.00 mmol, 1 eq), triphenylphosphine (6.08 g, 23.19 mmol, 1.16 eq) and phthalimide (3.53 g, 23.99 mmol, 1.20 eq) in 160 ml tetrahydrofuran was added diisopropyl azodicarboxylate (4.85 g, 23.99 mmol, 1.20 eq) dropwise. After complete addition, the reaction mixture was stirred for 16 hours at room temperature and taken to dryness under reduced pressure. The resulting oil was treated with 25 ml of ethanol, stirred for 30 min and again taken to dryness under reduced pressure. The crude product was dissolved in 200 ml of hot ethanol and left to cool and evaporate to ca. 100 ml overnight at room temperature. The resulting yellow crystals were filtered and washed with cold methanol, yielding **17** as pure product (3.07 g, 12.82 mmol, 64 %). **^{1}H-NMR** (400 MHz, $CDCl_3$, δ (ppm)): 8.66 (s, 1H, pyrC*H*), 8.48 - 8.48 (m, 2H, pyrC*H*), 7.92 - 7.87 (m, 2H, phthalimidC*H*), 7.77 - 7.73 (m, 2H, phthalimidC*H*), 5.06 (s, 2H, CH_2) (Figure B.33).

Literature:

[248] H. L. C. Feltham, M. G. Cowan, J. A. Kitchen, G. N. L. Jameson, S. Brooker, *Supramolecular Chemistry* 2018, *30*, 296.

6.3.22 2-(Aminomethyl)pyrazine (18)



17

239.23 g/mol

18

109.13 g/mol

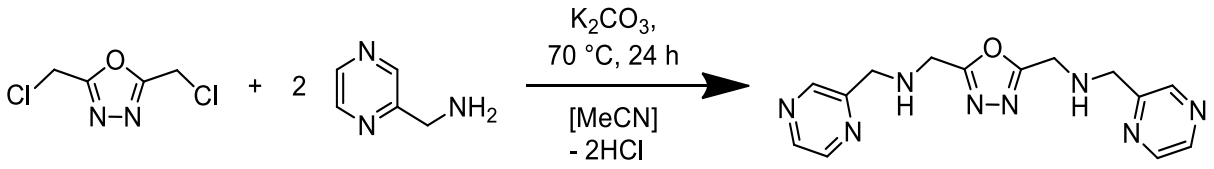
Preparation: **REN-PS-18**

Compound **18** was prepared according to a modified procedure from the literature.[249] To a solution of sodium hydroxide (50.50 g, 1.28 mol, 70 eq) in 260 ml of water was added **17** (4.38 g, 18.31 mmol, 1 eq). The reaction was refluxed for 2 hours and allowed to cool to room temperature. The solid was filtered and the filtrate extracted 15 times with chloroform. The combined organic extracts were combined, dried over magnesium sulfate and freed from solvent under reduced pressure to yield **18** as yellow oil (1.70 g, 15.60 mmol, 85 %). **^{1}H-NMR** (400 MHz, MeOD, δ (ppm)): 8.64 (d, 1H, pyrC*H*), 8.59 - 8.58 (m, 1H, pyrC*H*), 8.49 - 8.48 (m, 1H, pyrC*H*), 3.97 (s, 2H, CH_2) (Figure B.34).

Literature:

[249] XENON PHARMACEUTICALS INC., S. LIU, T. FOCKEN, N. CHAHAL, Z. ZHANG, OBALLA, Renata, Marcella, J. FONAREV, BIARYL ETHER SULFONAMIDES AND THEIR USE AS THERAPEUTIC AGENTS, 2013.

6.3.23 2,5-Bis[(pyrazin-2-ylmethyl)amino]methyl-1,3,4-oxadiazole ($L^{6,N}$)



2 166.99 g/mol

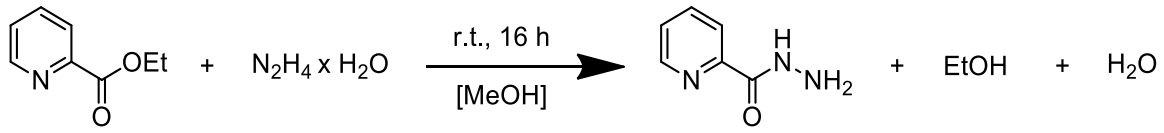
18 109.13 g/mol

$L^{6,N}$ 312.33 g/mol

Preparation: **REN-JE-140**

18 (300 mg, 2.75 mmol, 2.2 eq) and potassium carbonate (864 mg, 6.25 mmol, 5 eq) were dissolved in 35 ml acetonitrile under an inert atmosphere. To this mixture, a solution of **2** (209 mg, 1.25 mmol, 1 eq) in 5 ml acetonitrile was added dropwise at 70 °C. The reaction was stirred for 24 h at given temperature. The solid was filtered and the solvent removed under reduced pressure, resulting in a brown oil as crude product. **$L^{6,N}$** could be isolated by column chromatography (SiO_2, chloroform/ methanol (9:1)) as a brown oil (100 mg, 0.32 mmol, 26 %). **^{1}H-NMR** (400 MHz, MeOD, δ (ppm)): 8.68 (s, 2H, pyrC*H*), 8.58 - 8.57 (m, 2H, pyrC*H*), 8.50 - 8.49 (m, 2H, pyrC*H*), 4.09 (s, 4H, ODA-CH_2), 4.04 (s, 4H, Pyr-CH_2) (Figure B.35). **^{13}C-NMR** (101 MHz, MeOD, HSQC, HMBC, δ (ppm)): 165.98 (ODA$C^{2/5}$), 154.86 (pyrC^1), 144.08 (pyr*C*), 143.99 (pyr*C*), 142.99 (pyr*C*), 51.05 (Pyr-*C*H_2), 42.42 (ODA-*C*H_2) (Figure B.36, Figure B.37, Figure B.38).

6.3.24 Pyridin-2-carboxylic acid hydrazide (19)



19

151.16 g/mol 137.14 g/mol

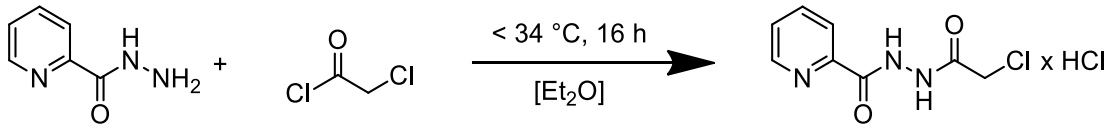
Preparation: **REN-JE-228**

Compound **19** was prepared according to a procedure from the literature.[171] To a solution of ethyl 2-pyridine carboxylate (13.82 g, 91.43 mmol, 1 eq) in 125 ml methanol was added hydrazine monohydrate (13.73 g, 274.27 mmol, 3 eq). The reaction was stirred for 16 hours at room temperature. Afterwards, the mixture was taken to dryness under reduced pressure yielding **19** as a pale beige solid (12.24 g, 89.25 mmol, 98 %). **^{1}H-NMR** (400 MHz, DMSO, δ (ppm)): 9.86 (s, 1H, N*H*), 8.61 - 8.60 (m, 1H, pyC*H*), 7.98 - 7.97 (m, 2H, pyC*H*), 7.58 - 7.55 (m, 1H, pyC*H*), 4.61 (s, 2H, NH_2) (Figure B.39).

Literature:

[171] Denis Bittner, 1,3,4-Thiadiazol based bis-multidentate ligands for bridged bimetallic complexes with individually adjustable coordination pockets, Mainz 2018.

6.3.25 N'-(Chloroacetyl)-2-pyridinecarboxylic acid hydrazide hydrochloride (20)



19

137.14 g/mol

20

250.09 g/mol

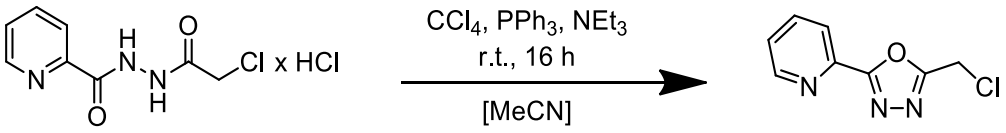
Preparation: **REN-JE-228**

Compound **20** was prepared according to a modified procedure from the literature.[171] **19** (12.24 g, 89.25 mmol, 1 eq) was suspended in 500 ml diethyl ether and cooled to 0 °C. To this solution was added chloroacetyl chloride (11.08 g, 7.90 ml, 98.18 mmol, 1.1 eq) dropwise keeping the temperature below 34 °C. The reaction mixture was stirred for 16 hours at room temperature. The colourless solid was filtered and washed with cold diethyl ether to yield **20** as colourless solid (21.65 g, 86.5 mmol, 97 %). **^{1}H-NMR** (400 MHz, DMSO, δ (ppm)): 9.86 (s, 1H, N*H*), 8.61 - 8.60 (m, 1H, pyC*H*), 7.98 - 7.97 (m, 2H, pyC*H*), 7.58 - 7.55 (m, 1H, pyC*H*), 4.61 (s, 2H, NH_2) (Figure B.40).

Literature:

[171] Denis Bittner, *1,3,4-Thiadiazol based bis-multidentate ligands for bridged bimetallic complexes with individually adjustable coordination pockets*, Dissertation, Mainz 2018.

6.3.26 2-(Chloromethyl)-5-(pyridin-2-yl)-1,3,4-oxadiazole (21)



20
250.09 g/mol

21
195.61 g/mol

Preparation: **REN-JE-229**

20 (10.00 g, 39.98 mmol, 1 eq) was dissolved in 500 ml acetonitrile under an inert atmosphere. To this solution triphenylphosphine (20.97 g, 79.99 mmol, 2 eq), triethylamine (12.14 g, 16.63 ml, 119.94 mmol, 3 eq) and carbon tetrachloride (24.61 g, 15.48 ml, 159.95 mmol, 4 eq) were added simultaneously. The reaction was stirred for 16 hours keeping the inert atmosphere. The solvent was removed completely to yield a black solid as crude product. Column chromatography (SiO_2, chloroform) afforded 23.66 g of a mixture of the desired product **21** and triphenylphosphine oxide (TPPO) as beige solid which was used without any more purification for further reactions. Proton nuclear magnetic resonance spectroscopy showed a molar ratio n(TPPO) / n(**21**) equal to 2.40. Therefor **21** was isolated with a yield of 69 % (5.36 g, 27.70 mmol), next to triphenylphosphine oxid (18.30 g, 65.76 mmol). **^{1}H-NMR** (400 MHz, $CDCl_3$, δ (ppm)): 8.80 (d, 1H, pyC*H*), 8.27 (d, 1H, pyC*H*), 7.93 - 7.89 (m, 1H, pyC*H*), 7.93 - 7.44 (m, 37H, pyC*H* + TPPO), 4.81 (s, 2H, CH_2) (Figure B.41).

Yield calculation by NMR spectroscopy:

$$\frac{\mathrm{n(TPPO)}}{\mathrm{n}(21)} = \frac{(37-1)/15}{1} = \frac{2.4}{1}$$

$$\mathrm{n(TPPO)} = 2.4\,\mathrm{n}(21)$$

$$\mathrm{m(total)} = \mathrm{m(TPPO)} + \mathrm{m}(21) = 23.66\,\mathrm{g}$$

$$\mathrm{n(TPPO)} * \mathrm{M(TPPO)} + \mathrm{n}(21) * \mathrm{M}(21) = 23.66\,\mathrm{g}$$

$$2.4\,\mathrm{n}(21) * \mathrm{M(TPPO)} + \mathrm{n}(21) * \mathrm{M}(21) = 23.66\,\mathrm{g}$$

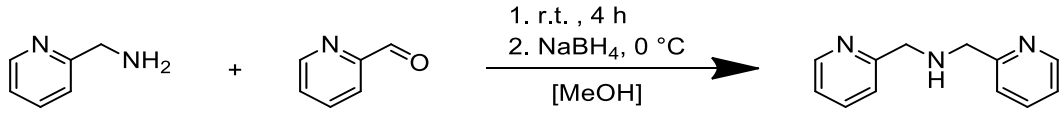
$$\mathrm{n}(21)\big(2.4\,\mathrm{M(TPPO)} + \mathrm{M}(21)\big) = 23.66\,\mathrm{g}$$

$$\mathrm{n}(21) = \frac{23.66\,\mathrm{g}}{2.4\,\mathrm{M(TPPO)} + \mathrm{M}(21)} = \frac{23.66\,\mathrm{g}}{2.40 * 278.29\frac{\mathrm{g}}{\mathrm{mol}} + 195.61\frac{\mathrm{g}}{\mathrm{mol}}}$$

$$\mathrm{n}(21) = 0.02740\ \mathrm{mol} \rightarrow \mathrm{m}(21) = 5.36\,\mathrm{g}$$

$$\mathrm{n(TPPO)} = 2.4\,\mathrm{n}(21) = 0.06576\ \mathrm{mol} \rightarrow \mathrm{m(TPPO)} = 18.30\,\mathrm{g}$$

6.3.27 Bis[(2-pyridyl)methyl]amine (22)



22

108.14 g/mol 107.11 g/mol 199.25 g/mol

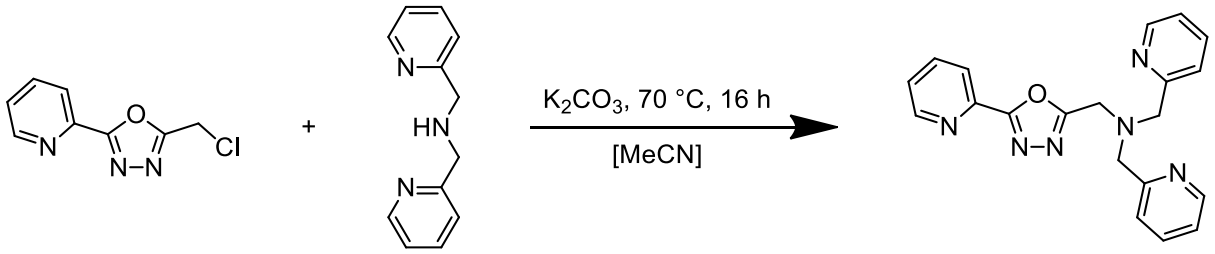
Preparation: **REN-JE-155**

Compound **22** was prepared according to a modified procedure from the literature.[171] Pyridine-2-carboxaldehyde (3.21 g, 30.00 mmol, 1.0 eq) and 2-aminomethylpyridine (3.24 g, 30.00 mmol, 1.0 eq) were dissolved in 200ml methanol and stirred at room temperature for 4 hours. After cooling the mixture to 0 °C, sodium borohydride (3.03 g, 80.10 mmol, 2.67 eq) was added portionwise and the reaction mixture stirred for 16 hours at room temperature. The solvent was removed under reduced pressure. The residue was taken up in 100 ml of water and extracted four times with 60 ml chloroform. The combined organic extracts were dried over magnesium sulfate and taken to dryness to afford **22** as orange oil (5.85 g, 29.34 mmol, 98 %). **^{1}H-NMR** (400 MHz, $CDCl_3$, δ (ppm)): 8.54 (d, 2H, pyC*H*), 7.65 - 7.61 (m, 2H, pyC*H*), 7.34 (d, 2H, pyC*H*), 7.16 - 7.13 (m, 2H, pyC*H*), 3.97 (s, 4H, CH_2) (Figure B.42).

Literature:

[171] Denis Bittner, *1,3,4-Thiadiazol based bis-multidentate ligands for bridged bimetallic complexes with individually adjustable coordination pockets*, Dissertation, Mainz 2018.

6.3.28 2-(2-Pyridyl)-5-[N,N-bis(2-pyridylmethyl)aminomethyl]-1,3,4-oxadiazole ($L^{Py,1}$)



21 195.61 g/mol

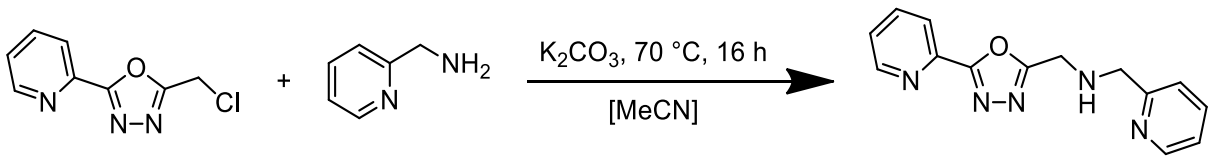
22 199.25 g/mol

$L^{Py,1}$ 358.40 g/mol

Preparation: **REN-JE-208**

22 (6.03 g, 30.27 mmol, 1.5 eq) and potassium carbonate (6.98 g, 50.45 mmol, 2.5 eq) were suspended in 400 ml acetonitrile under an inert atmosphere and heated to 70 °C. To this solution was added **21** (3.95 g, 20.18 mmol, 1 eq), together with its side product triphenylphosphine oxide (19.67 g, 70.65 mmol) (see Chapter 6.3.26), dissolved in 250 ml of acetonitrile. The reaction mixture was stirred vigorously at 70 °C for 16 hours. The solid was filtered and the filtrate freed from solvent under reduced pressure to afford a brown solid as crude product. Column chromatography (SiO_2, chloroform/ methanol (29:1)) yielded **$L^{Py,1}$** as an orange oil which crystallizes after several days (4.87 g, 19.93 mmol, 67 %). **^{1}H-NMR** (400 MHz, $CDCl_3$, COSY, δ (ppm)): 8.77 (d, 1H, pyC*H*), 8.53 (d, 2H, pyC*H*), 8.22 (d, 1H, pyC*H*), 7.88 (td, 1H, pyC*H*), 7.68 - 7.63 (m, 2H, pyC*H*), 7.58 (d, 2H, pyC*H*), 7.46 (dd, 1H, pyC*H*), 7.17 - 7.14 (m, 2H, pyC*H*), 4.19 (s, 2H, ODA-CH_2), 4.04 (s, 4H, Py-CH_2) (Figure B.43, Figure B.45). **^{13}C-NMR** (101 MHz, $CDCl_3$, HSQC, HMBC, δ (ppm)): 165.00, 164.28, 158.22, 150.25, 149.20, 143.42, 137.25, 136.64, 125.87, 123.30, 123.13, 122.30, 59.76 (*C*H_2), 47.97 (*C*H_2) (Figure B.44, Figure B.46, Figure B.47). **FT-IR**: $\tilde{\upsilon}$ (cm^{-1}) = 3055, 3008, 2984, 2946, 2917, 2887, 2838, 1675, 1587, 1567, 1557, 1545, 1515, 1473, 1456, 1431, 1375, 1365, 1360, 1340, 1323, 1308, 1297, 1286, 1247, 1220, 1148, 1100, 1087, 1045, 1022, 1012, 994, 974, 959, 894, 868, 856, 844, 797, 787, 777, 753, 743, 708, 659, 640, 632, 617, 610, 506, 487, 477, 461 (Figure A.10). **ESI-MS**: m/z = 359.17 (100.00 %), 360.17 (47.24 %), 361.17 (5.97 %) (Figure C.8).

6.3.29 2-(2-Pyridyl)-5-[(2-pyridylmethyl)aminomethyl]-1,3,4-oxadiazole ($L^{Py,2}$)



21 — 195.61 g/mol

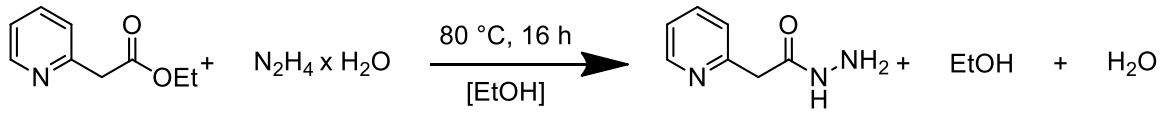
108.14 g/mol

$L^{Py,2}$ — 267.29 g/mol

Preparation: **REN-JE-232**

2-Picolylamin (2.37 ml, 2.49 g, 23.01 mmol, 1.5 eq) and potassium carbonate (5.31 g, 38.35 mmol, 2.5 eq) were suspended in 300 ml acetonitrile under an inert atmosphere and heated to 70 °C. To this solution was added **21** (3.00 g, 15.34 mmol, 1 eq), together with its side product triphenylphosphine oxide (10.80 g, 38.81 mmol) (see Chapter 6.3.26), dissolved in 200 ml of acetonitrile. The reaction mixture was stirred vigorously at 70 °C for 16 hours. The solid was filtered and the filtrate freed from solvent under reduced pressure to afford a brown solid as crude product. Column chromatography (SiO_2, chloroform/ methanol (19:1)) yielded **$L^{Py,2}$** as an orange oil (2.87 g, 10,74 mmol, 70 %). **^{1}H-NMR** (400 MHz, $CDCl_3$, COSY, HSQC, HMBC, δ (ppm)): 8.73 (d, 1H, pyC*H*), 8.50 (d, H, pyC*H*), 8.20 (d, 1H, pyC*H*), 7.85 (td, 1H, pyC*H*), 7.60 (td, 1H, pyC*H*), 7.45 - 7.41 (m, 1H, pyC*H*), 7.28 (d, 1H, pyC*H*), 7.13 - 7.10 (m, 1H, pyC*H*), 4.18 (s, 2H, ODA-CH_2), 4.01 (s, 2H, py-CH_2) (Figure B.48, Figure B.50). **^{13}C-NMR** (101 MHz, $CDCl_3$, HSQC, HMBC, δ (ppm)): 166.11 (ODA$C^{2/5}$), 164.28, 158.45 (CH_2-pyC^2), 150.26, 149.42, 143.43, 137.37, 136.65, 125.88, 123.12, 122.43, 122.24 (CH_2-pyC^3)), 77.42, 77.10, 76.78, 54.03 (py-CH_2), 43.29 (ODA-CH_2) (Figure B.49, Figure B.51, Figure B.52). **FT-IR**: $\tilde{\upsilon}$ (cm^{-1}) = 3309, 3054, 3008, 2921, 2921, 2838, 1673, 1673, 1645, 1645, 1645, 1645, 1645, 1645, 1645, 1645, 1645, 1645, 1645, 1645, 1588, 1567, 1518, 1472, 1458, 1432, 1378, 1283, 1245, 1148, 1099, 1045, 1014, 994, 969, 844, 793, 742, 707, 655, 618, 506, 476, 401 (Figure A.11). **ESI-MS**: m/z = 268.12 (100.00 %), 269.12 (24.99 %), 270.12 (1.98 %) (Figure C.9).

6.3.30 Pyridin-2-yl-acetic acid hydrazide (23)



23

165.19 g/mol 151.17 g/mol

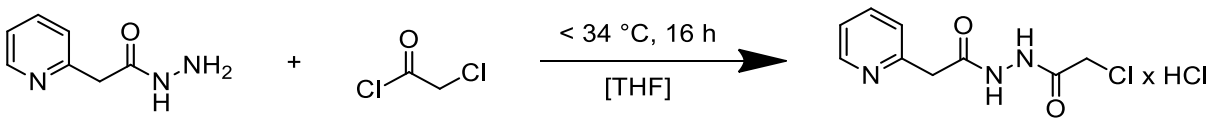
Preparation: **REN-JE-142**

Compound **23** was prepared according to a modified procedure from the literature.[278] To a solution of ethyl 2-(pyridinyl-2)acetate (2.50 g, 15.13 mmol, 1 eq) in 25 ml methanol was added hydrazine monohydrate (2.20 ml, 2.27 g, 45.39 mmol, 3 eq). The reaction was stirred for 16 hours at 80 °C. Afterwards, the mixture was taken to dryness under reduced pressure. The residual of water was co-evaporated with toluene yielding **23** as a pale beige solid (2.17 g, 14.38 mmol, 95 %). **^{1}H-NMR** (400 MHz, DMSO, δ (ppm)): 9.25 (s, 1H, N*H*), 8.60 (d, 1H, pyC*H*), 7.74 - 7.70 (m, 1H, pyC*H*), 7.33 (d, 1H, pyC*H*), 7.25 - 7.22 (d, 1H, pyC*H*), 4.24 (s, 2H, NH_2), 3.54 (s, 2H, CH_2) (Figure B.53).

Literature:

[278] Y. Uto, Y. Ueno, Y. Kiyotsuka, Y. Miyazawa, H. Kurata, T. Ogata, M. Yamada, T. Deguchi, M. Konishi, T. Takagi, S. Wakimoto, J. Ohsumi, European Journal of Medicinal Chemistry 2010, 45, 4788.

6.3.31 N'-(Chloroacetyl)-2-pyridylacetic acid hydrazide hydrochloride (24)



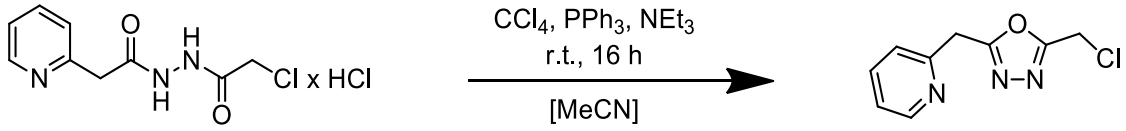
23
151.17 g/mol

24
264.11 g/mol

Preparation: **REN-JE-144**

23 (708 mg, 4.23 mmol, 1 eq) was suspended in 28 ml tetrahydrofuran and cooled to 0 °C. Chloroacetyl chloride (717 mg, 0.51 ml, 6.35 mmol, 1.5 eq) dissolved in 7 ml tetrahydrofuran was added dropwise keeping the temperature below 34 °C. The reaction mixture was stirred for 16 hours at room temperature. The colourless solid was filtered and washed with cold diethyl ether to yield **24** as colourless solid (1.12 g, 4.23 mmol, quant.). **^{1}H-NMR** (400 MHz, DMSO, δ (ppm)): 10.50 (s, 1H, N*H*), 10.44 (s, 1H, N*H*), 8.74 (d, 1H, pyC*H*), 8.28 - 8.24 (m, 1H, pyC*H*), 7.78 (d, 1H, pyC*H*), 7.71 (t, 1H, pyC*H*), 4.14 (s, 2H, CH_2), 3.96 (s, 2H, CH_2) (Figure B.54).

6.3.32 2-(Chloromethyl)-5-(pyridin-2-ylmethyl)-1,3,4-oxadiazole (25)



24

264.11 g/mol

25

209.63 g/mol

Preparation: **REN-JE-145**

24 (200 mg, 0.76 mmol, 1 eq) was dissolved in 20 ml acetonitrile under an inert atmosphere. To this solution triphenylphosphine (430 g, 1.64 mmol, 2.2 eq), triethylamine (165 mg, 0.23 ml, 1.64 mmol, 2.2 eq) and carbon tetrachloride (504 mg, 0.32 ml, 3.28 mmol, 4.3 eq) were added simultaneously. The reaction was stirred for 16 hours keeping the inert atmosphere. The solvent was removed completely to yield a black solid as crude product. Column chromatography (SiO_2, chloroform) afforded 68 mg of a mixture of the desired product **25** and triphenylphosphine oxide (TPPO) as beige solid which was used without any more purification for further reactions. Proton nuclear magnetic resonance spectroscopy showed a molar ratio n(TPPO) / n(**25**) equal to 0.08. Therefor **25** was isolated with a yield of 38 % (61 mg, 0.29 mmol), next to triphenylphosphine oxid (7 mg, 0.02 mmol). **^{1}H-NMR** (400 MHz, $CDCl_3$, δ (ppm)): 8.57 (d, 1H, pyC*H*), 7.72 - 7.67 (m, 1H, pyC*H*), 7.67 - 7.43 (m, 1.19H, TPPO), 7.32 (d, 1H, pyC*H*), 7.25 - 7.22 (m, 1H, pyC*H*), 4.67 (s, 2H, CH_2), 4.44 (s, 2H, CH_2) (Figure B.55).

Yield calculation by NMR spectroscopy:

$$\frac{\mathrm{n(TPPO)}}{\mathrm{n(25)}} = \frac{1.19/15}{1} = \frac{0.08}{1}$$

$$\mathrm{n(TPPO)} = 0.08\,\mathrm{n(25)}$$

$$\mathrm{m(total)} = \mathrm{m(TPPO)} + \mathrm{m(25)} = 68\ \mathrm{mg}$$

$$\mathrm{n(TPPO)} * \mathrm{M(TPPO)} + \mathrm{n(25)} * \mathrm{M(25)} = 68\ \mathrm{mg}$$

$$0.08\,\mathrm{n(25)} * \mathrm{M(TPPO)} + \mathrm{n(25)} * \mathrm{M(25)} = 68\ \mathrm{mg}$$

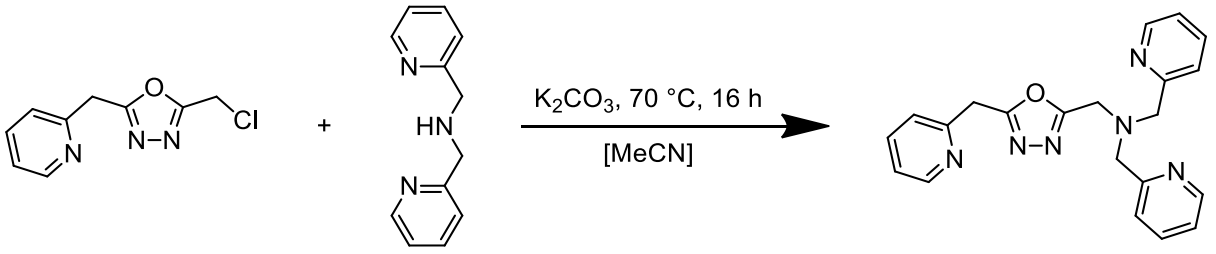
$$\mathrm{n(25)}\big(0.08\,\mathrm{M(TPPO)} + \mathrm{M(25)}\big) = 68\ \mathrm{mg}$$

$$\mathrm{n(25)} = \frac{68\ \mathrm{mg}}{0.08\,\mathrm{M(TPPO)} + \mathrm{M(25)}} = \frac{68\ \mathrm{mg}}{0.08 * 278.29\,\frac{\mathrm{g}}{\mathrm{mol}} + 209.63\,\frac{\mathrm{g}}{\mathrm{mol}}}$$

$$\mathrm{n(25)} = 0.29\ \mathrm{mmol} \rightarrow \mathrm{m(25)} = 61\ \mathrm{mg}$$

$$\mathrm{n(TPPO)} = 0.08\,\mathrm{n(25)} = 0.02\ \mathrm{mmol} \rightarrow \mathrm{m(TPPO)} = 7\ \mathrm{mg}$$

6.3.33 2-(Pyridin-2-ylmethyl)-5-[N,N-bis(2-pyridylmethyl)aminomethyl]-1,3,4-oxadiazole ($L^{Py,3}$)



25 209.63 g/mol

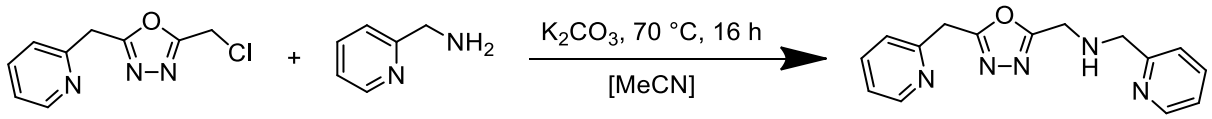
22 199.25 g/mol

$L^{Py,3}$ 372.42 g/mol

Preparation: **REN-JE-157**

22 (1.01 g, 5.04 mmol, 1.5 eq) and potassium carbonate (1.16 g, 8.40 mmol, 2.5 eq) were suspended in 70 ml acetonitrile under an inert atmosphere and heated to 70 °C. To this solution was added **25** (704 mg, 3.36 mmol, 1 eq), together with its side product triphenylphosphine oxide (12.96 g, 4.66 mmol) (see Chapter 6.3.32), dissolved in 150 ml of acetonitrile. The reaction mixture was stirred vigorously at 70 °C for 16 hours. The solid was filtered and the filtrate freed from solvent under reduced pressure to afford a brown solid as crude product. Column chromatography (SiO_2, chloroform/ methanol (29:1)) yielded **$L^{Py,3}$** as an orange oil (208 mg, 0.56 mmol, 17 %). **^{1}H-NMR** (400 MHz, $CDCl_3$, δ (ppm)): 8.56 - 8.52 (d, 3H, pyCH), 7.70 - 7.61 (m, 3H, pyCH), 7.49 (d, 2H, pyCH), 7.32 - 7.14 (m, 4H, pyCH), 4.41 (s, 2H, CH_2), 4.02 (s, 2H, CH_2), 3.94 (s, 4H, CH_2) (Figure B.56). **^{13}C-NMR** (101 MHz, $CDCl_3$, δ (ppm)): 164.85, 164.75, 158.27, 154.13, 149.75, 149.22, 137.03, 136.61, 123.24, 122.53, 122.29, 77.39, 77.07, 76.76, 59.78, 47.88, 34.54 (Figure B.57).

6.3.34 2-(Pyridin-2-ylmethyl)-5-[(2-pyridylmethyl)aminomethyl]-1,3,4-oxadiazole ($L^{Py,4}$)



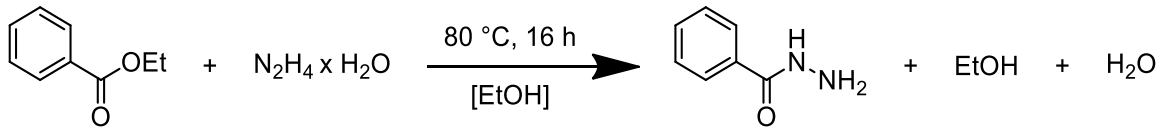
25 $L^{Py,4}$

209.63 g/mol 108.14 g/mol 281.31 g/mol

Preparation: **REN-JE-151**

2-Picolylamin (0.74 ml, 773 mg, 7.16 mmol, 1.5 eq) and potassium carbonate (3.29 g, 23.85 mmol, 5 eq) were suspended in 50 ml acetonitrile under an inert atmosphere and heated to 70 °C. To this solution was added **25** (1.00 g, 4.77 mmol, 1 eq), together with its side product triphenylphosphine oxide (18.39 g, 66.12 mmol) (see Chapter 6.3.32), dissolved in 150 ml of acetonitrile. The reaction mixture was stirred vigorously at 70 °C for 16 hours. The solid was filtered and the filtrate freed from solvent under reduced pressure to afford a brown solid as crude product. Column chromatography (SiO_2, chloroform/ methanol (19:1)) yielded $L^{Py,4}$ as a brown oil (275 mg, 0.98 mmol, 21 %). **^{1}H-NMR** (400 MHz, $CDCl_3$, δ (ppm)): 8.57 - 8.54 (m, 2H, $_{py}CH$), 7.69 - 7.31 (m, 2H, $_{py}CH$), 7.31 - 7.28 (m, 2H, $_{py}CH$), 7.23 - 7.16 (m, 2H, $_{py}CH$), 4.39 (s, 2H, CH_2), 4.06 (s, 2H, CH_2), 3.97 (s, 2H, CH_2) (Figure B.58).

6.3.35 Benzoic acid hydrazide (26)



26

150.17 g/mol 136.15 g/mol

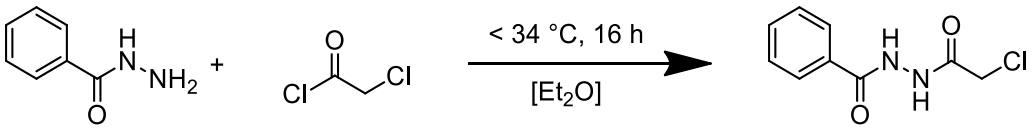
Preparation: **REN-JE-245**

Compound **26** was prepared according to a modified procedure from the literature.[293] To a solution of ethyl benzoate (30.00 g, 0.2 mol, 1.0 eq) in 200 ml methanol was added hydrazine monohydrate (50.00 ml, 51.50 g, 1.03 mol, 5.1 eq). The reaction was stirred for 16 hours at 80 °C. Afterwards, the mixture was taken to dryness under reduced pressure and the residual of water was co-evaporated with toluene. The pale yellow solid was then suspended in 200 ml of diethyl ether and stirred for 30 minutes. The solid was filtered, washed with cold diethyl ether and dried on air to yield **19** as a pale beige solid (23.65 g, 0.17 mol, 85 %). **^{1}H-NMR** (400 MHz, DMSO, δ (ppm)): 9.78 (s, 1H, N*H*), 7.83 - 7.80 (m, 2H, PhC*H*), 7.53 - 7.42 (m, 3H, PhC*H*), 3.69 (s, 8H, NH_2 + H_2O) (Figure B.59).

Literature:

[293] Hoon Choi, Wheesahng Yun, Jung-hun Lee, Seoul Jang, Sang Won Park, Dong Hwan Kim, Kyoung Pyo Seon, Jung-mi Hyun, Kwiwan Jeong, Jin-mo Ku, Tae-gyu Nam, Med Chem Res 2019, 28, 2142.

6.3.36 N'-(2-chloroacetyl)benzohydrazide (27)



26

136.15 g/mol

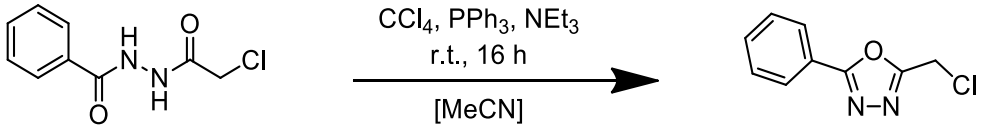
27

212.63 g/mol

Preparation: **REN-JE-246**

26 (23.50 g, 172.57 mmol, 1 eq) was suspended in 600 ml diethyl ether and cooled to 0 °C. To this solution was added chloroacetyl chloride (23.38 g, 16.47 ml, 207.08 mmol, 1.2 eq), dissolved in 150 ml diethyl ether, dropwise keeping the temperature below 34 °C. The reaction mixture was stirred for 16 hours at room temperature. The colourless solid was filtered and washed with cold diethyl ether to yield **27** as colourless solid (35.09 g, 165.80 mmol, 96). The product was used for further reactions without analytics.

6.3.37 2-(Chloromethyl)-5-phenyl-1,3,4-oxadiazole (28)



27
212.63 g/mol

28
194.62 g/mol

Preparation: **REN-JE-247**

27 (15.00 g, 70.88 mmol, 1 eq) was dissolved in 500 ml acetonitrile under an inert atmosphere. To this solution triphenylphosphine (37.18 g, 141.76 mmol, 2 eq), triethylamine (21.51 g, 29.47 ml, 212.64 mmol, 3 eq) and carbon tetrachloride (43.61 g, 27.43 ml, 283.52 mmol, 4 eq) were added simultaneously. The reaction was stirred for 16 hours keeping the inert atmosphere. The solvent was removed completely to yield a black solid as crude product. Column chromatography (SiO_2, chloroform) afforded 30.33 g of a mixture of the desired product **25** and triphenylphosphine oxide (TPPO) as beige solid which was used without any more purification for further reactions. Proton nuclear magnetic resonance spectroscopy showed a molar ratio n(TPPO) / n(**25**) equal to 2.87. Therefor **25** was isolated with a yield of 43 % (5.94 g, 30.51 mmol), next to triphenylphosphine oxid (24.39 g, 87.56 mmol). **^{1}H-NMR** (400 MHz, $CDCl_3$, δ (ppm)): 8.08 (d, 2H, PhC*H*), 7.69 - 7.44 (m, 46H, 3PhC*H* + TPPO), 4.78 (s, 2H, CH_2) (Figure B.60).

Yield calculation by NMR spectroscopy:

$$\frac{\mathrm{n(TPPO)}}{\mathrm{n}(28)} = \frac{(46-3)/15}{1} = \frac{2.87}{1}$$

$$\mathrm{n(TPPO)} = 2.87\ \mathrm{n}(28)$$

$$\mathrm{m(total)} = \mathrm{m(TPPO)} + \mathrm{m}(28) = 30.33\ \mathrm{g}$$

$$\mathrm{n(TPPO)} * \mathrm{M(TPPO)} + \mathrm{n}(28) * \mathrm{M}(28) = 30.33\ \mathrm{g}$$

$$2.87\ \mathrm{n}(28) * \mathrm{M(TPPO)} + \mathrm{n}(28) * \mathrm{M}(28) = 30.33\ \mathrm{g}$$

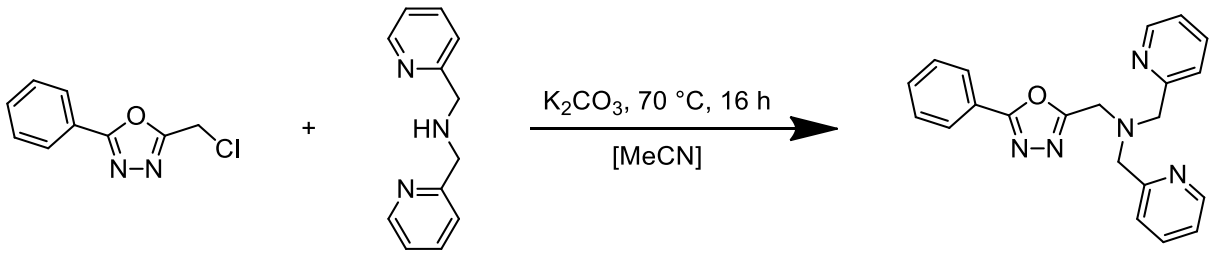
$$\mathrm{n}(28)\big(2.87\ \mathrm{M(TPPO)} + \mathrm{M}(28)\big) = 30.33\ \mathrm{g}$$

$$\mathrm{n}(28) = \frac{30.33\ \mathrm{g}}{2.87\ \mathrm{M(TPPO)} + \mathrm{M}(28)} = \frac{30.33\ \mathrm{g}}{2.87 * 278.29\frac{\mathrm{g}}{\mathrm{mol}} + 194.62\frac{\mathrm{g}}{\mathrm{mol}}}$$

$$\mathrm{n}(28) = 0.03051\ \mathrm{mol} \rightarrow \mathrm{m}(28) = 5.94\ \mathrm{g}$$

$$\mathrm{n(TPPO)} = 2.87\ \mathrm{n}(28) = 0.08756\ \mathrm{mol} \rightarrow \mathrm{m(TPPO)} = 24.39\ \mathrm{g}$$

6.3.38 2-Phenyl-5-[N,N-bis(2-pyridylmethyl)aminomethyl]-1,3,4-oxadiazole (L^{Ph})



28 194.62 g/mol

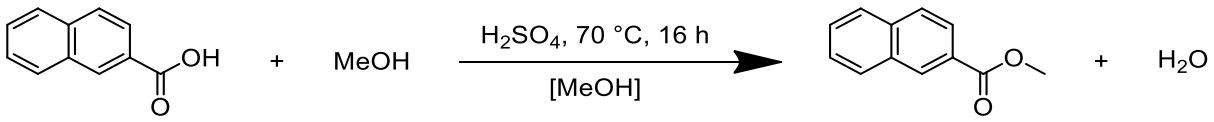
22 199.25 g/mol

L^{Ph} 357.41 g/mol

Preparation: **REN-JE-249**

22 (9.12 g, 45.77 mmol, 1.5 eq) and potassium carbonate (10.56 g, 76.28 mmol, 2.5 eq) were suspended in 250 ml acetonitrile under an inert atmosphere and heated to 70 °C. To this solution was added **28** (5.97 g, 30.51 mmol, 1 eq), together with its side product triphenylphosphine oxide (24.36 g, 87.56 mmol) (see Chapter 6.3.26), dissolved in 400 ml of acetonitrile. The reaction mixture was stirred vigorously at 70 °C for 16 hours. The solid was filtered and the filtrate freed from solvent under reduced pressure to afford a brown solid as crude product. Column chromatography (SiO_2, chloroform/ methanol (49:1)) yielded **L^{Ph}** as bright brown oil which crystallizes after several days (7.94 g, 22.21 mmol, 78 %). **^{1}H-NMR** (400 MHz, $CDCl_3$, δ (ppm)): 8.56 - 8.54 (m, 2H, pyC*H*), 8.05 - 8.03 (m, 2H, pyC*H*), 8.69 (dt, 2H, pyC*H*), 7.60 - 7.48 (m, 5H, PhC*H* + pyC*H*), 7.20 - 7.16 (m, 2H, pyC*H*), 4.15 (s, 2H, ODA-CH_2), 4.06 (s, 4H, Py-CH_2) (Figure B.61). **^{13}C-NMR** (101 MHz, $CDCl_3$, δ (ppm)): 165.11, 164.02, 158.22, 149.18, 136.62, 131.70, 129.00, 126.89, 123.75, 123.19, 122.30, 59.90 (*C*H_2), 47.95 (*C*H_2) (Figure B.62). **FT-IR**: $\tilde{\upsilon}$ (cm^{-1}) = 3061, 3009, 2948, 2932, 2900, 2853, 1673, 1607, 1589, 1561, 1548, 1490, 1473, 1447, 1433, 1412, 1393, 1367, 1355, 1326, 1311, 1287, 1249, 1206, 1150, 1128, 1085, 1070, 1044, 1007, 994, 984, 975, 958, 942, 919, 896, 877, 831, 771, 755, 744, 706, 685, 652, 641, 631, 612, 514, 488, 471, 445, 403 (Figure A.12). **ESI-MS**: m/z = 358.17 (100.00 %), 359.17 (29.34 %), 360.17 (3.41 %) (Figure C.10).

6.3.39 Methyl naphthalene-2-carboxylate (29)



29

172.18 g/mol 186.21 g/mol

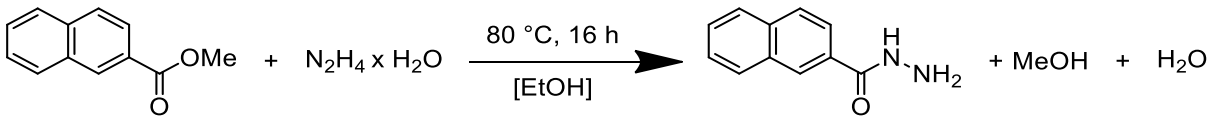
Preparation: **REN-JE-261**

Compound **29** was prepared according to a modified procedure from the literature.[322] To a solution of 2-naphthoic acid (25.83 g, 150.00 mmol, 1.0 eq) in 150 ml ethanol was added sulfuric acid (conc., 7.5 ml). The reaction was stirred for 16 hours at 80 °C. Afterwards, the solvent was removed under reduced pressure. 200 ml of water were added and the pH value was set to 9 with sodium bicarbonate. The aqueous phase was extracted four times with dichloromethane. The combined organic extracts were dried over magnesium sulfate and freed from solvent under reduced pressure to afford **29** as a colourless solid (27.07 g, 145.30 mmol, 97 %). **^{1}H-NMR** (400 MHz, DMSO, δ (ppm)): 8.63 (s, 1H, NaphCH), 8.13 (d, 1H, NaphCH), 8.04 - 7.96 (m, 3H, NaphCH), 7.68 - 7.59 (m, 2H, NaphCH), 3.91 (s, 3H, CH_3) (Figure B.63).

Literature:

[322] L. Ma, L. Yuan, C. Xu, G. Li, M. Tao, W. Zhang, Synthesis 2012, 45, 45.

6.3.40 2-Naphthohydrazide (30)



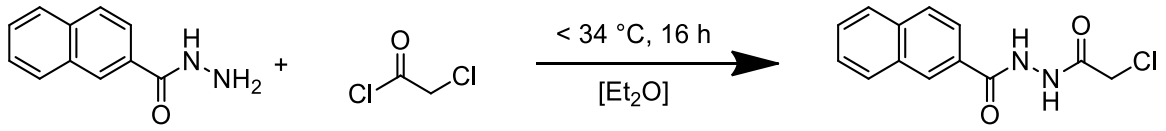
29
186.21 g/mol

30
186.21 g/mol

Preparation: **REN-JE-262**

To a solution of ethyl 2-naphthoate (27.07 g, 145.30 mmol, 1.0 eq) in 250 ml ethanol was added hydrazine monohydrate (50.00 ml, 41.20 g, 0.82 mol, 5.6 eq). The reaction was stirred for 16 hours at 80 °C. Afterwards, the mixture was concentrated under reduced pressure to 75 % of its volume. The resulting solid was filtered and washed with cold diethyl ether to yield **30** as white powder (17.56 g, 94.33 mmol, 64 %). **^{1}H-NMR** (400 MHz, DMSO, δ (ppm)): 9.94 (s, 1H, N*H*), 8.43 (s, 1H, NaphC*H*), 8.02 - 7.90 (m, 4H, NaphC*H*), 7.62 - 7.56 (m, 2H, NaphC*H*), 4.58 (s, 2H, N*H*$_2$) (Figure B.64).

6.3.41 N'-(2-chloroacetyl)naphthalene-2-carbohydrazide (31)



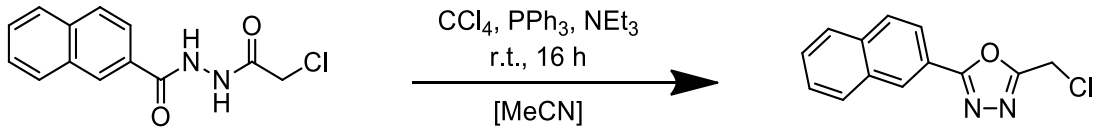
30
186.21 g/mol

31
262.69 g/mol

Preparation: **REN-JE-263**

30 (17.56 g, 94.33 mmol, 1 eq) was suspended in 600 ml diethyl ether and cooled to 0 °C. To this solution was added chloroacetyl chloride (12.78 g, 9.00 ml, 113.18 mmol, 1.2 eq), dissolved in 150 ml diethyl ether, dropwise keeping the temperature below 34 °C. The reaction mixture was stirred for 16 hours at room temperature. The colourless solid was filtered and washed with cold diethyl ether to yield **31** as colourless solid (23.72 g, 90.29 mmol, 96 %). **^{1}H-NMR** (400 MHz, DMSO, δ (ppm)): 10.71 (s, 1H, N*H*), 10.48 (s, 1H, N*H*), 8.52 (s, 1H, NaphC*H*), 8.11 - 7.93 (m, 4H, NaphC*H*), 7.66 - 7.59 (m, 2H, NaphC*H*), 4.24 (s, 2H, CH_2) (Figure B.65).

6.3.42 2-(Chloromethyl)-5-(naphthalen-2-yl)-1,3,4-oxadiazole (32)



31
262.69 g/mol

32
244.68 g/mol

Preparation: **REN-JE-264**

31 (23.72 g, 90.29 mmol, 1 eq) was dissolved in 500 ml acetonitrile under an inert atmosphere. To this solution triphenylphosphine (47.36 g, 180.58 mmol, 2 eq), triethylamine (18.27 g, 25.03 ml, 180.58 mmol, 2 eq) and carbon tetrachloride (55.56 g, 34.94 ml, 361.16 mmol, 4 eq) were added simultaneously. The reaction was stirred for 16 hours keeping the inert atmosphere. The solvent was removed completely to yield a black solid as crude product. Column chromatography (SiO_2, chloroform) afforded **32** (1.88 g, 7.68 mmol) as a pale red solid, next to 17.06 g of a mixture of the desired product **32** and triphenylphosphine oxide (TPPO). Proton nuclear magnetic resonance spectroscopy showed a molar ratio n(TPPO) / n(**32**) equal to 2.91. Therefor **32** was isolated with a yield of 26 % (5.83 g, 23.86 mmol), next to triphenylphosphine oxid (24.36 g, 87.56 mmol). **^{1}H-NMR** (*pure*, 400 MHz, $CDCl_3$, δ (ppm)): 8.59 (s, 1H, NaphC*H*), 8.16 - 8.13 (m, 1H, NaphC*H*), 7.99 - 7.90 (m, 3H, NaphC*H*), 7.64 - 7.57 (m, 2H, NaphC*H*), 4.83 (s, 2H, CH_2) (Figure B.66). **^{1}H-NMR** (*mixture*, 400 MHz, $CDCl_3$, δ (ppm)): 8.57 (s, 1H, NaphC*H*), 8.14 - 8.12 (m, 1H, NaphC*H*), 7.98 - 7.88 (m, 3H, NaphC*H*), 7.69 - 7.43 (m, 45.70H, 2NaphC*H* + TPPO), 4.81 (s, 2H, CH_2) (Figure B.67).

Yield calculation by NMR spectroscopy:

$$\frac{\mathrm{n(TPPO)}}{\mathrm{n(32)}} = \frac{(45.70-2)/15}{1} = \frac{2.91}{1}$$

$$\mathrm{n(TPPO)} = 2.91\ \mathrm{n(32)}$$

$$\mathrm{m(total)} = \mathrm{m(TPPO)} + \mathrm{m(32)} = 17.06\ \mathrm{g}$$

$$\mathrm{n(TPPO)} * \mathrm{M(TPPO)} + \mathrm{n(32)} * \mathrm{M(32)} = 17.06\ \mathrm{g}$$

$$2.91\ \mathrm{n(32)} * \mathrm{M(TPPO)} + \mathrm{n(32)} * \mathrm{M(32)} = 17.06\ \mathrm{g}$$

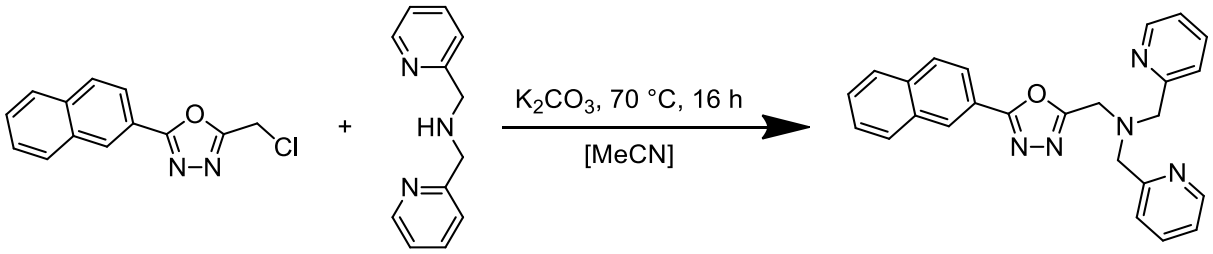
$$\mathrm{n(32)}\big(2.91\ \mathrm{M(TPPO)} + \mathrm{M(32)}\big) = 17.06\ \mathrm{g}$$

$$\mathrm{n(32)} = \frac{17.06\ \mathrm{g}}{2.91\ \mathrm{M(TPPO)} + \mathrm{M(32)}} = \frac{17.06\ \mathrm{g}}{2.91 * 278.29\frac{\mathrm{g}}{\mathrm{mol}} + 244.68\frac{\mathrm{g}}{\mathrm{mol}}}$$

$$\mathrm{n(32)} = 0.01618\ \mathrm{mol} \rightarrow \mathrm{m(32)} = 3.96\ \mathrm{g}$$

$$\mathrm{n(TPPO)} = 2.91\ \mathrm{n(32)} = 0.04708\ \mathrm{mol} \rightarrow \mathrm{m(TPPO)} = 13.10\ \mathrm{g}$$

6.3.43 2-(Naphthalen-2-yl)-5-[N,N-bis(2-pyridylmethyl)aminomethyl]-1,3,4-oxadiazole (L^{Naph})



32 244.68 g/mol

22 199.25 g/mol

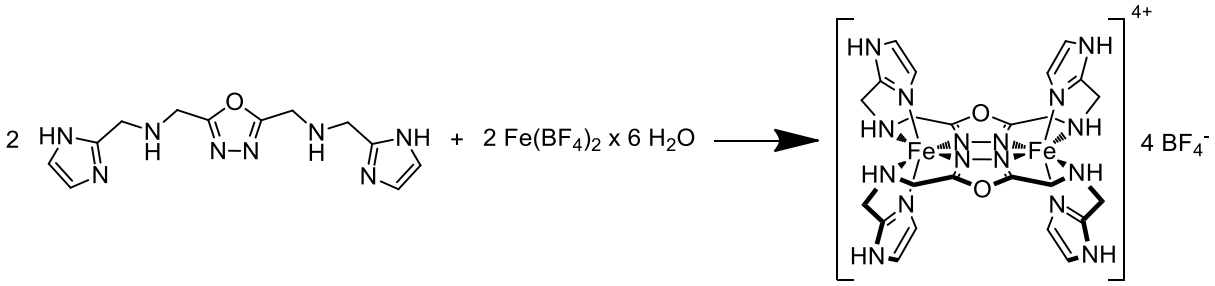
L^{Naph} 407.47 g/mol

Preparation: **REN-JE-265**

22 (7.13 g, 35.79 mmol, 1.5 eq) and potassium carbonate (8.25 g, 59.65 mmol, 2.5 eq) were suspended in 250 ml acetonitrile under an inert atmosphere and heated to 70 °C. To this solution was added **32** (5.83 g, 23.86 mmol, 1 eq), together with its side product triphenylphosphine oxide (13.10 g, 47.08 mmol) (see Chapter 6.3.42), dissolved in 400 ml of acetonitrile. The reaction mixture was stirred vigorously at 70 °C for 16 hours. The solid was filtered and the filtrate freed from solvent under reduced pressure to afford a brown solid as crude product. Column chromatography (SiO_2, chloroform/ methanol (39:1)) yielded **L^{Naph}** as bright brown oil which crystallizes after several days (3.82 g, 9.37 mmol, 39 %). **^{1}H-NMR** (400 MHz, $CDCl_3$, δ (ppm)): 8.56 - 8.51 (m, 3H), 8.11 - 8.08 (m, 1H), 7.96 - 7.93 (m, 2H), 7.89 - 7.86 (m, 1H), 7.69 - 7.65 (m, 2H), 7.59 - 7.54 (m, 4H), 7.17 - 7.14 (m, 2H), 4.18 (s, 2H, ODA-CH_2), 4.07 (s, 4H, Py-CH_2) (Figure B.68). **^{13}C-NMR** (101 MHz, $CDCl_3$, δ (ppm)): 165.42, 164.17, 158.22, 149.18, 136.81, 134.71, 132.80, 129.05, 128.89, 128.00, 127.44, 127.13, 123.38, 123.23, 122.41, 121.03, 59.97 (CH_2), 48.12 (CH_2). (Figure B.69). **FT-IR**: $\tilde{\upsilon}$ (cm^{-1}) = 3076, 3057, 3002, 2951, 2929, 2899, 2849, 1607, 1588, 1563, 1544, 1509, 1469, 1447, 1430, 1409, 1392, 1368, 1360, 1325, 1309, 1282, 1271, 1242, 1218, 1187, 1147, 1125, 1088, 1071, 1044, 1018, 987, 975, 962, 945, 908, 894, 879, 867, 846, 818, 767, 750, 721, 655, 630, 613, 593, 552, 540, 507, 473, 456, 425, 404 (Figure A.13). **ESI-MS**: m/z = 408.19 (100.00 %), 409.19 (40.55 %), 410.19 (5.81 %) (Figure C.11).

6.4 Complex Synthesis

6.4.1 $[Fe_2(\mu_2\text{-}L^{5,Im})_2](BF_4)_4 \cdot 2MeCN$ (C1)



$L^{5,Im}$ **C1**

288.31 g/mol 337.55 g/mol 1035.53 g/mol

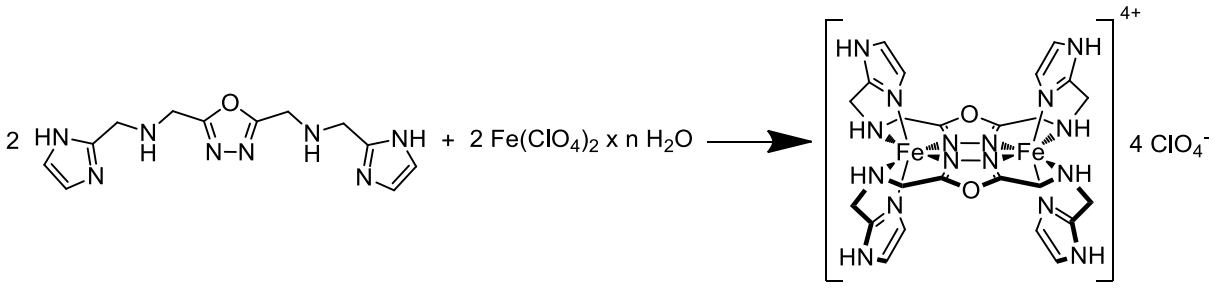
Preparation: **REN-JE-053-03**

Compound **C1** was prepared according to a procedure from the literature.[196] The following reaction was carried out in a glovebox under an inert atmosphere. **$L^{5,Im}$** (29 mg, 0,1 mmol, 1 eq) was dissolved in 0.7 ml methanol and 1.3 ml of acetonitrile. To this solution $Fe(BF_4)_2 \cdot 6H_2O$ (34 mg, 0,1 mmol, 1 eq), dissolved in 2 ml acetonitrile, was added dropwise. The reaction was set for vapour diffusion against tetrahydrofuran and kept undisturbed at room temperature. After two weeks, colourless plate shaped crystals have formed that were suitable for X-ray structure analysis (Table D.1, $P\bar{1}$). The crystals were collected by filtration, washed with diethyl ether and dried at atmospheric pressure to yield **C1** (20.22 mg, 0.020 mmol, 20 %). **FT-IR**: $\tilde{\upsilon}$ (cm^{-1}) = 3353 (vs), 3198 (s), 2923 (w), 2856 (w), 2752 (vw), 2662 (vw), 2362 (vw), 2070 (vw), 1617 (w), 1565 (w), 1488 (w), 1444 (w), 1372 (w), 1346 (vw), 1297 (vw), 1223 (w), 1159 (m), 1123 (vs), 1083 (vs), 1037 (vs), 934 (vw), 891 (w), 770 (w), 663 (w), 533 (w), 521 (w) (Figure A.14).

Literature:

[196] J. Eppelsheimer, Eisen(II) Spin-Crossover Verbindungen mit 1,3,4-Oxadiazol-Brückenliganden, Masterarbeit, Mainz 2017.

6.4.2 $[Fe_2(\mu_2\text{-}L^{5,Im})_2](ClO_4)_4 \cdot 2MeCN$ (C2)



$L^{5,Im}$ **C2**

288.31 g/mol 272.76 g/mol 1086.11 g/mol

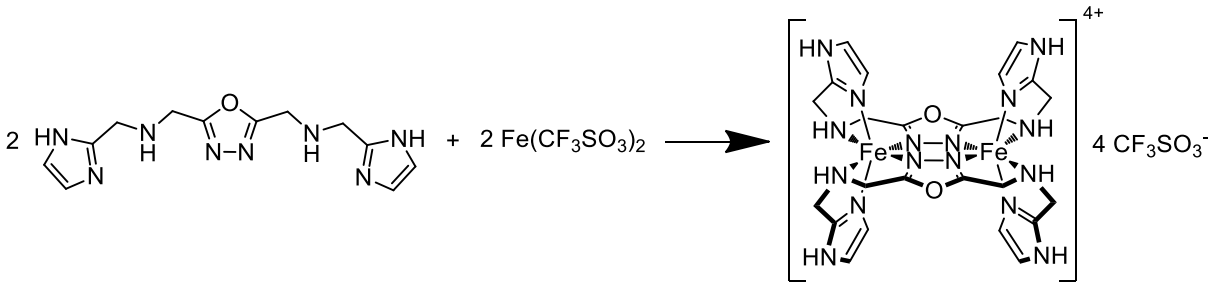
Preparation: **REN-JE-055-05**

Compound **C2** was prepared according to a procedure from the literature.[196] The following reaction was carried out in a glovebox under an inert atmosphere. **$L^{5,Im}$** (29 mg, 0,1 mmol, 1 eq) was dissolved in 0.7 ml methanol and 1.3 ml of acetonitrile. To this solution $Fe(ClO_4)_2 \cdot nH_2O$ (27 mg, 0,1 mmol, 1 eq), dissolved in 2 ml acetonitrile, was added dropwise. The reaction was set for vapour diffusion against tetrahydrofuran and kept undisturbed at room temperature. After two weeks, colourless block shaped crystals have formed that were suitable for X-ray structure analysis (Table D.1, *Pbca*). The crystals were collected by filtration, washed with diethyl ether and dried at atmospheric pressure to yield **C2** (27.24 mg, 0.025 mmol, 25 %). **FT-IR**: $\tilde{\upsilon}$ (cm^{-1}) = 3328 (s), 3212 (m), 3136 (m), 2927 (w), 2856 (w), 2749 (vw), 2672 (vw), 2475 (vw), 2362 (vw), 2020 (vw), 1617 (w), 1589 (w), 1570 (w), 1489 (w), 1445 (w), 1381 (w), 1348 (vw), 1284 (vw), 1229 (w), 1144 (vs), 1120 (vs), 1108 (vs), 1089 (vs), 1011 (w), 940 (vw), 892 (w), 760 (w), 663 (w), 636 (m), 626 (s) (Figure A.15).

Literature:

[196] J. Eppelsheimer, Eisen(II) Spin-Crossover Verbindungen mit 1,3,4-Oxadiazol-Brückenliganden, Masterarbeit, Mainz 2017.

6.4.3 $[Fe_2(\mu_2\text{-}L^{5,Im})_2](CF_3SO_3)_4 \cdot 2MeCN$ (C3)



$L^{5,Im}$		C3
288.31 g/mol	353.98 g/mol	1284.58 g/mol

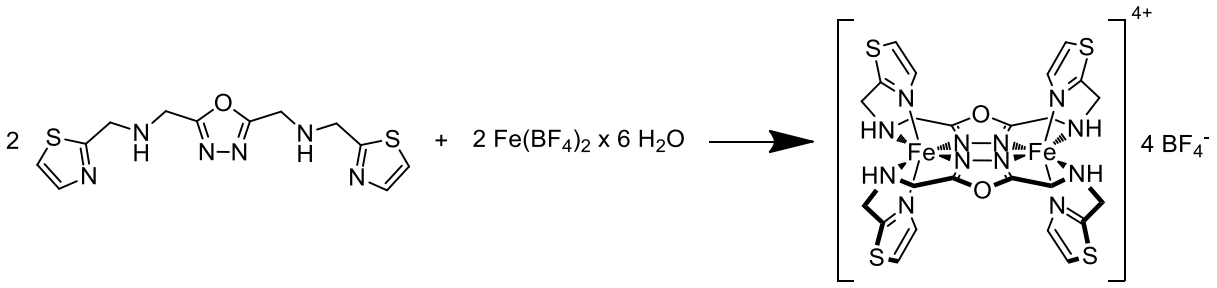
Preparation: **REN-JE-044-01**

Compound **C3** was prepared according to a procedure from the literature.[196] The following reaction was carried out in a glovebox under an inert atmosphere. $L^{5,Im}$ (29 mg, 0,1 mmol, 1 eq) was dissolved in 0.7 ml methanol and 1.3 ml of acetonitrile. To this solution $Fe(CF_3SO_3)_2$ (35 mg, 0,1 mmol, 1 eq), dissolved in 3 ml acetonitrile, was added dropwise. The reaction was kept undisturbed for two weeks at room temperature. Slow evaporation of the solvent afforded colourless block shaped crystals that were suitable for X-ray structure analysis (Table D.2, $P2_1/n$). The crystals were collected by filtration, washed with diethyl ether and dried at atmospheric pressure to yield **C3** (23.20 mg, 0.018 mmol, 18 %). **FT-IR**: $\tilde{\upsilon}$ (cm^{-1}) = 3308 (s), 3259 (m), 3159 (w), 3127 (m), 2965 (w), 2937 (w), 2872 (vw), 2752 (vw), 2672 (vw), 1643 (w), 1610 (m), 1573 (m), 1494 (w), 1451 (w), 1425 (w), 1380 (w), 1295 (vs), 1276 (vs), 1254 (vs), 1235 (vs), 1184 (m), 1159 (s), 1136 (w), 1107 (w), 1097 (w), 1083 (w), 1029 (vw), 1014 (w), 975 (vw), 895 (w), 779 (m), 769 (m), 741 (vw), 668 (w), 636 (vs), 578 (w), 548 (vw), 521 (w), 512 (w). (Figure A.16).

Literature:

[196] J. Eppelsheimer, Eisen(II) Spin-Crossover Verbindungen mit 1,3,4-Oxadiazol-Brückenliganden, Masterarbeit, Mainz 2017.

6.4.4 $[Fe_2(\mu_2\text{-}L^{5,TA})_2](BF_4)_4 \cdot 2MeCN$ (C4)



$L^{5,TA}$ **C4**

322.41 g/mol 337.55 g/mol 1103.73 g/mol

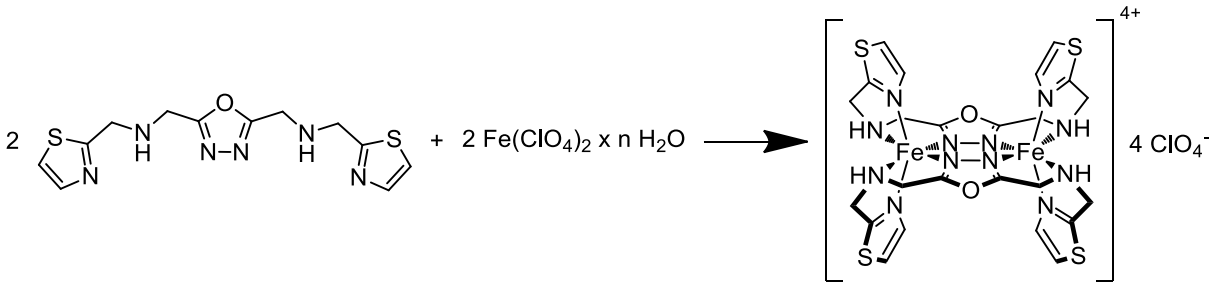
Preparation: **REN-JE-224-03**

Compound **C4** was prepared according to a procedure from the literature.[200] The following reaction was carried out in a glovebox under an inert atmosphere. **$L^{5,TA}$** (32 mg, 0,1 mmol, 1 eq) was dissolved in 2 ml of acetonitrile. To this solution $Fe(BF_4)_2 \cdot 6H_2O$ (34 mg, 0,1 mmol, 1 eq), dissolved in 2 ml acetonitrile, was added dropwise. The reaction was set for vapour diffusion against diethyl ether and kept undisturbed at room temperature. After three days, colourless block shaped crystals have formed that were suitable for X-ray structure analysis (Table D.2, $P\bar{1}$). The crystals were collected by filtration, washed with diethyl ether and dried at atmospheric pressure to yield **C4** (23.79 mg, 0.022 mmol, 22 %). **FT-IR**: $\tilde{\upsilon}$ (cm^{-1}) = 3442 (m), 3333 (s), 3101 (m), 2935 (w), 1619 (m), 1589 (m), 1516 (m), 1459 (w), 1421 (m), 1384 (w), 1296 (w), 1235 (w), 1159 (s), 1084 (vs), 1037 (vs), 901 (w), 884 (w), 786 (w), 762 (m), 655 (w), 617 (w), 594 (w), 522 (w) (Figure A.17). **EA** (%): Calc. (found) C 26.12 (26.18), H 2.56 (2.35), N 15.23 (15.33).

Literature:

[200] Lasse Moormann, Auswirkungen von 1,3,4-Oxadiazolen auf das Spin-Crossover Verhalten von dinuklearen Eisen(II)- und Cobalt(II)-Verbindungen, Bachelorarbeit, Mainz 2018.

6.4.5 $[Fe_2(\mu_2\text{-}L^{5,TA})_2](ClO_4)_4$ (C5)



$L^{5,TA}$		C5
322.41 g/mol	272.76 g/mol	1154.31 g/mol

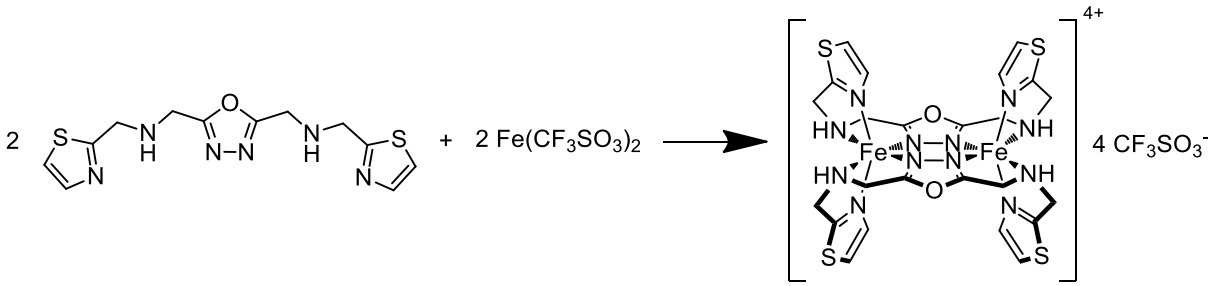
Preparation: **REN-LM-012-2a**

Compound **C5** was prepared according to a procedure from the literature.[200] The following reaction was carried out in a glovebox under an inert atmosphere. $L^{5,TA}$ (32 mg, 0,1 mmol, 1 eq) was dissolved in 2 ml of acetonitrile. To this solution $Fe(ClO_4)_2 \cdot nH_2O$ (27 mg, 0,1 mmol, 1 eq), dissolved in 2 ml acetonitrile, was added dropwise. The reaction was set for vapour diffusion against diethyl ether and kept undisturbed at room temperature. After one hour, colourless microcrystalline needles had formed. The crystals were collected by filtration, washed with diethyl ether and dried at atmospheric pressure to yield **C5** (17.76 mg, 0.015 mmol, 15 %). **FT-IR**: $\tilde{\upsilon}$ (cm^{-1}) = 3422 (s), 3307 (vs), 3125 (m), 3097 (m), 2938 (w), 1617 (m), 1513 (m), 1451 (m), 1429 (m), 1384 (m), 1282 (m), 1233 (m), 1146 (vs), 1115 (vs), 1088 (vs), 974 (w), 897 (m), 884 (m), 637 (s), 626 (vs), 593 (w) (Figure A.18). **EA** (%): Calc. (found) C 24.97 (25.01), H 2.45 (2.40), N 14.56 (14.63).

Literature:

[200] Lasse Moormann, Auswirkungen von 1,3,4-Oxadiazolen auf das Spin-Crossover Verhalten von dinuklearen Eisen(II)- und Cobalt(II)-Verbindungen, Bachelorarbeit, Mainz 2018.

6.4.6 $[Fe_2(\mu_2\text{-}L^{5,TA})_2](CF_3SO_3)_4 \cdot 2MeCN$ (C6)



$L^{5,TA}$ **C6**

322.41 g/mol 353.98 g/mol 1352.78 g/mol

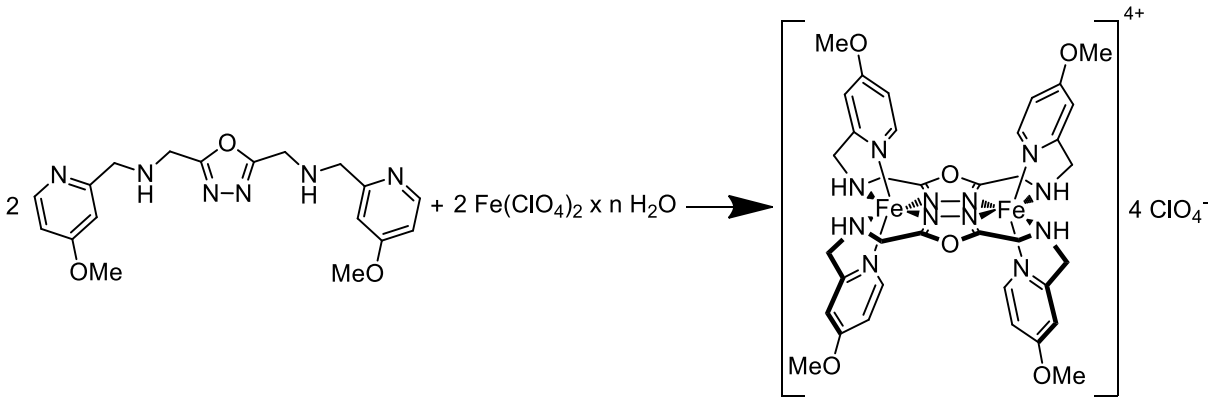
Preparation: **REN-LM-012-1b**

Compound **C6** was prepared according to a procedure from the literature.[200] The following reaction was carried out in a glovebox under an inert atmosphere. **$L^{5,TA}$** (32 mg, 0,1 mmol, 1 eq) was dissolved in 2 ml of acetonitrile. To this solution $Fe(CF_3SO_3)_2$ (35 mg, 0,1 mmol, 1 eq), dissolved in 2 ml acetonitrile, was added dropwise. The reaction was set for vapour diffusion against diethyl ether and kept undisturbed at room temperature. After one week, colourless block shaped crystals have formed that were suitable for X-ray structure analysis (Table D.3, $P\bar{1}$). The crystals were collected by filtration, washed with diethyl ether and dried at atmospheric pressure to yield **C6** (22.54 mg, 0.017 mmol, 17 %). **FT-IR**: $\tilde{\upsilon}$ (cm^{-1}) = 3509 (m), 3277 (s), 3138 (w), 3106 (m), 2967 (w), 2930 (w), 2850 (w), 2359 (w), 2258 (w), 1618 (s), 1513 (m), 1454 (m), 1429 (s), 1384 (w), 1277 (vs), 1255 (vs), 1227 (vs), 1158 (vs), 1086 (s), 1029 (vs), 979 (w), 886 (m), 786 (w), 770 (m), 759 (m), 7435 (m), 639 (vs), 594 (w), 574 (m), 518 (s) (Figure A.19). **EA** (%): Calc. (found) C 26.79 (26.42), H 2.39 (2.05), N 13.67 (13.54).

Literature:

[200] Lasse Moormann, Auswirkungen von 1,3,4-Oxadiazolen auf das Spin-Crossover Verhalten von dinuklearen Eisen(II)- und Cobalt(II)-Verbindungen, Bachelorarbeit, Mainz 2018.

6.4.7 $[Fe_2(\mu_2\text{-}L^{6,OMe})_2](ClO_4)_4 \cdot 2MeCN$ (C7)



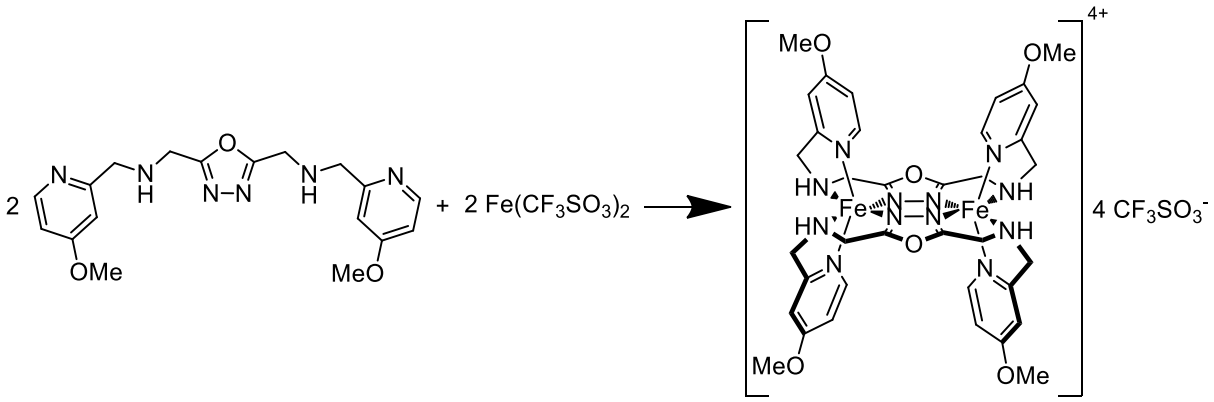
$L^{6,OMe}$ **C7**

370.41 g/mol 272.76 g/mol 1250.30 g/mol

Preparation: **REN-JE-172-02**

The following reaction was carried out in a glovebox under an inert atmosphere. **$L^{6,OMe}$** (37 mg, 0,1 mmol, 1 eq) was dissolved in 2.5 ml of acetonitrile. To this solution $Fe(ClO_4)_2 \cdot nH_2O$ (27 mg, 0,1 mmol, 1 eq), dissolved in 2.5 ml acetonitrile, was added dropwise. The reaction was kept undisturbed for four weeks at room temperature. Slow evaporation of the solvent afforded colourless block shaped crystals that were suitable for X-ray structure analysis (Table D.3, $P\bar{1}$). The crystals were collected by filtration, washed with diethyl ether and dried at atmospheric pressure to yield **C7** (10.29 mg, 0.008 mmol, 8 %). **FT-IR**: $\tilde{\upsilon}$ (cm^{-1}) = 3290, 2953, 2931, 1613, 1582, 1562, 1497, 1473, 1456, 1436, 1426, 1349, 1318, 1297, 1263, 1240, 1227, 1194, 1164, 1071, 1035, 1009, 989, 931, 901, 867, 850, 829, 793, 769, 729, 667, 650, 619, 592, 575, 541, 506, 451 (Figure A.20).

6.4.8 $[Fe_2(\mu_2\text{-}L^{6,OMe})_2](CF_3SO_3)_4 \cdot 2MeCN$ (C8)



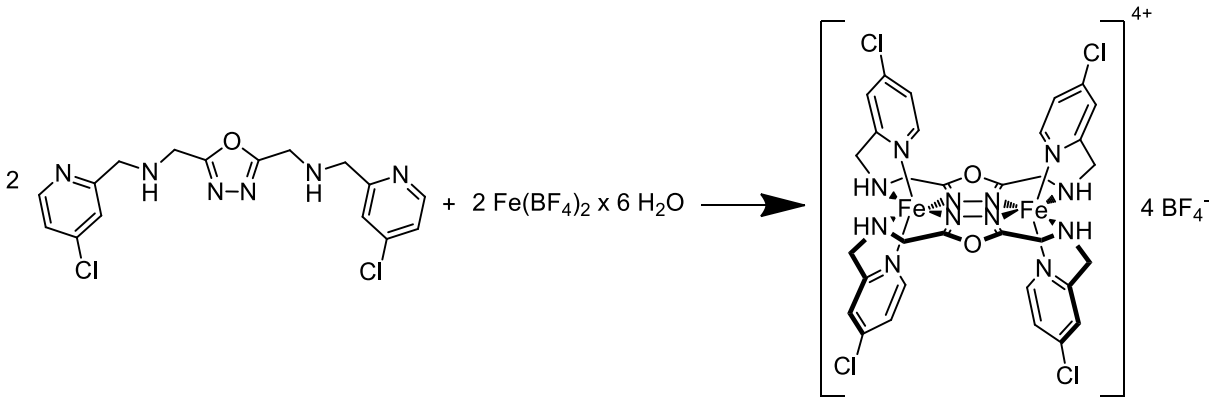
$L^{6,OMe}$ **C8**

307.41 g/mol 353.98 g/mol 1448.78 g/mol

Preparation: **REN-JE-172-04**

The following reaction was carried out in a glovebox under an inert atmosphere. **$L^{6,OMe}$** (37 mg, 0,1 mmol, 1 eq) was dissolved in 2.5 ml of acetonitrile. To this solution $Fe(CF_3SO_3)_2$ (35 mg, 0,1 mmol, 1 eq), dissolved in 2.5 ml acetonitrile, was added dropwise. The reaction was set for vapour diffusion against diethyl ether and kept undisturbed at room temperature. After one week, pale yellow block shaped crystals have formed that were suitable for X-ray structure analysis (Table D.4, $P\bar{1}$). The crystals were collected by filtration, washed with diethyl ether and dried at atmospheric pressure to afford **C8**. No yield was determined, as only a few single crystals were obtained. **FT-IR**: $\tilde{\upsilon}$ (cm^{-1}) = 3271, 2955, 2932, 1612, 1564, 1502, 1455, 1428, 1330, 1251, 1224, 1194, 1161, 1089, 1025, 937, 900, 869, 854, 843, 827, 793, 772, 760, 732, 672, 635, 574, 543, 516, 453, 431 (Figure A.21).

6.4.9 $[Fe_2(\mu_2\text{-}L^{6,Cl})_2](BF_4)_4$ (C9)



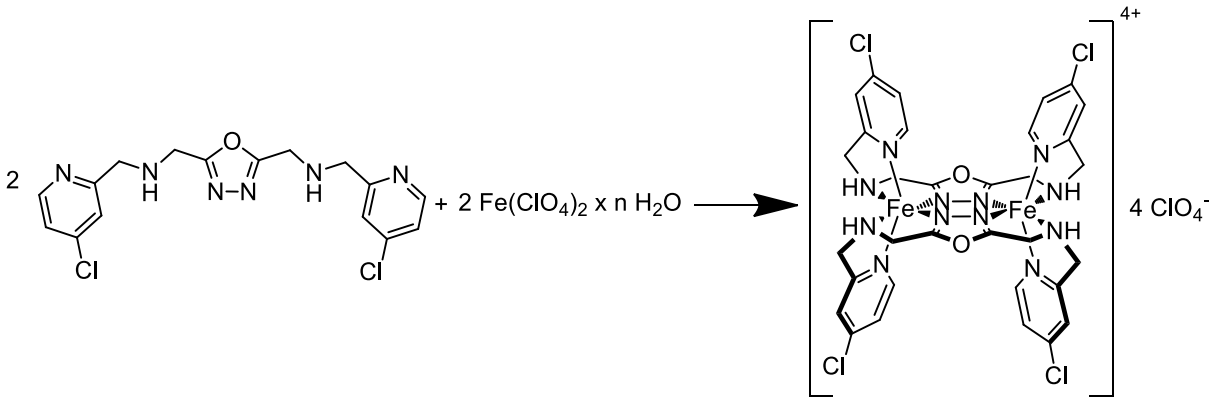
$L^{6,CL}$ **C9**

379.24 g/mol 337.55 g/mol 1217.40 g/mol

Preparation: **REN-JE-191-03**

The following reaction was carried out in a glovebox under an inert atmosphere. **$L^{6,CL}$** (38 mg, 0,1 mmol, 1 eq) was dissolved in 2.5 ml of acetonitrile. To this solution $Fe(BF_4)_2 \cdot 6H_2O$ (34 mg, 0,1 mmol, 1 eq), dissolved in 2.5 ml acetonitrile, was added dropwise. The reaction was kept undisturbed for four weeks at room temperature. Slow evaporation of the solvent afforded colourless block shaped crystals. The crystals were collected by filtration, washed with diethyl ether and dried at atmospheric pressure to yield **C9** (13.41 mg, 0.011 mmol, 11 %). **FT-IR**: $\tilde{\upsilon}$ (cm^{-1}) = 3423 (m), 2925 (vw), 1603 (s), 1569 (m), 1482 (w), 1440 (m), 1384 (w), 1304 (vw), 1272 (vw), 1199 (w), 1083 (vs), 1036 (vs), 919 (vw), 770 (w), 706 (vw), 644 (vw), 533 (w), 521 (w), 421 (vw) (Figure A.22).

6.4.10 $[Fe_2(\mu_2\text{-}L^{6,Cl})_2](ClO_4)_4$ (C10)



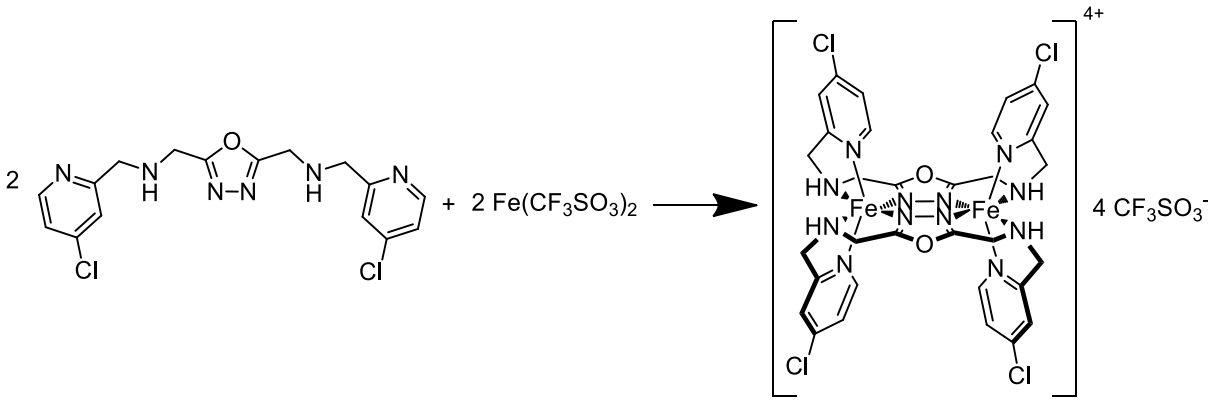
$L^{6,CL}$ **C10**

379.24 g/mol 272.76 g/mol 1267.98 g/mol

Preparation: **REN-JE-191-02**

The following reaction was carried out in a glovebox under an inert atmosphere. **$L^{6,CL}$** (38 mg, 0,1 mmol, 1 eq) was dissolved in 2.5 ml of acetonitrile. To this solution $Fe(ClO_4)_2 \cdot nH_2O$ (27 mg, 0,1 mmol, 1 eq), dissolved in 2.5 ml acetonitrile, was added dropwise. The reaction was kept undisturbed for four weeks at room temperature. Slow evaporation of the solvent afforded colourless block shaped crystals. The crystals were collected by filtration, washed with diethyl ether and dried at atmospheric pressure to yield **C10** (21.16 mg, 0.017 mmol, 17 %). **FT-IR**: $\tilde{\upsilon}$ (cm^{-1}) = 3443, 3306, 3120, 2925, 1617, 1603, 1558, 1482, 1474, 1450, 1418, 1384, 1349, 1301, 1281, 1250, 1234, 1219, 1144, 1134, 1121, 1115, 1108, 1088, 1022, 993, 965, 940, 907, 855, 839, 794, 742, 717, 636, 624, 542, 530, 465, 438 (Figure A.23).

6.4.11 $[Fe_2(\mu_2\text{-}L^{6,Cl})_2](CF_3SO_3)_4 \cdot 2MeCN$ (C11)



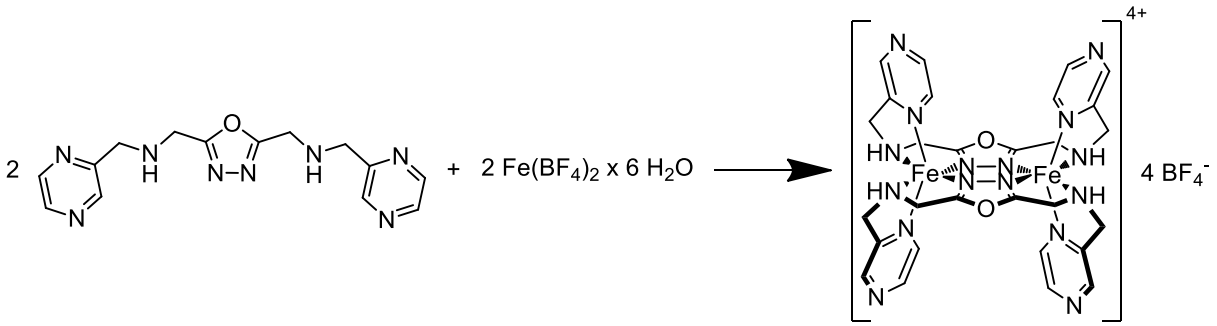
$L^{6,CL}$ **C11**

379.24 g/mol 353.98 g/mol 1466.45 g/mol

Preparation: **REN-JE-191-01**

The following reaction was carried out in a glovebox under an inert atmosphere. **$L^{6,CL}$** (38 mg, 0,1 mmol, 1 eq) was dissolved in 2.5 ml of acetonitrile. To this solution $Fe(CF_3SO_3)_2$ (35 mg, 0,1 mmol, 1 eq), dissolved in 2.5 ml acetonitrile, was added dropwise. The reaction was kept undisturbed for four weeks at room temperature. Slow evaporation of the solvent afforded colourless block shaped crystals that were suitable for X-ray structure analysis (Table D.4, $P\bar{1}$). The crystals were collected by filtration, washed with diethyl ether and dried at atmospheric pressure to yield **C11** (35.75 mg, 0.024 mmol, 24 %). **FT-IR**: $\tilde{\upsilon}$ (cm^{-1}) = 3238, 3110, 3043, 2950, 2930, 2257, 1659, 1617, 1598, 1557, 1478, 1459, 1443, 1415, 1374, 1350, 1245, 1223, 1160, 1116, 1096, 1026, 937, 908, 870, 854, 835, 796, 758, 739, 716, 661, 634, 574, 540, 532, 516, 494, 440, 406 (Figure A.24).

6.4.12 $[Fe_2(\mu_2\text{-}L^{6,N})_2](BF_4)_4 \cdot 2MeCN$ (C12)



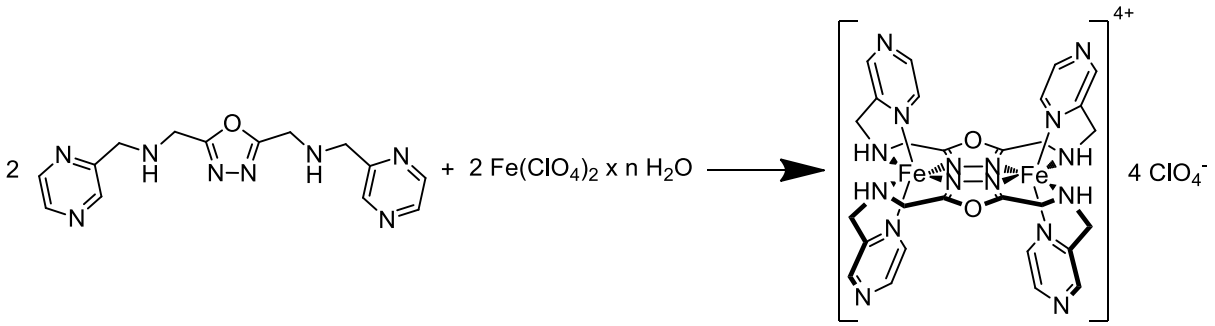
$L^{6,N}$ **C12**

312.33 g/mol 337.55 g/mol 1083.57 g/mol

Preparation: **REN-JE-214-05**

The following reaction was carried out in a glovebox under an inert atmosphere. **$L^{6,N}$** (31 mg, 0,1 mmol, 1 eq) was dissolved in 2.5 ml of acetonitrile. To this solution $Fe(BF_4)_2 \cdot 6H_2O$ (34 mg, 0,1 mmol, 1 eq), dissolved in 0.5 ml methanol and 2.0 ml acetonitrile, was added dropwise. The reaction was kept undisturbed for four weeks at room temperature. Slow evaporation of the solvent afforded colourless block shaped crystals that were suitable for X-ray structure analysis (Table D.5, *Pbam*). The crystals were collected by filtration, washed with diethyl ether and dried at atmospheric pressure to yield **C12** (23.30 mg, 0.022 mmol, 22 %). **FT-IR**: $\tilde{\upsilon}$ (cm^{-1}) = 3271, 2955, 1790, 1598, 1530, 1448, 1416, 1363, 1305, 1243, 1201, 1153, 1089, 930, 902, 833, 752, 667, 622, 456, 410 (Figure A.25).

6.4.13 $[Fe_2(\mu_2\text{-}L^{6,N})_2](ClO_4)_4 \cdot 2MeCN$ (C13)



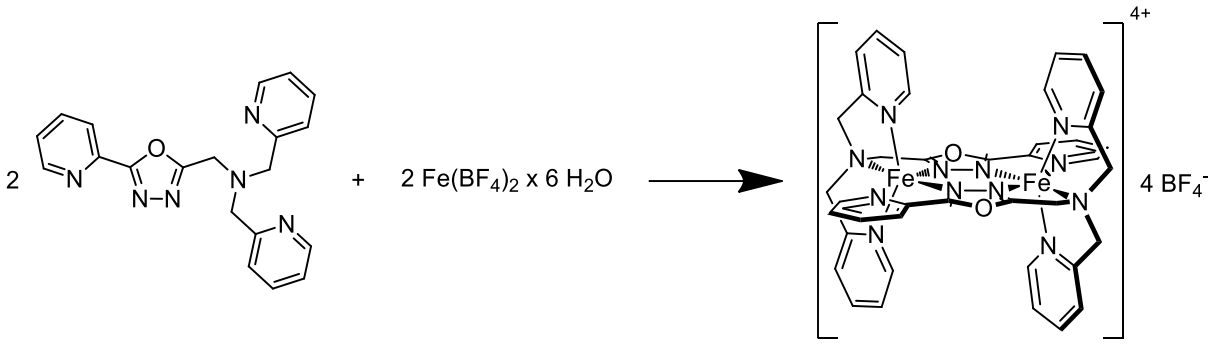
$L^{6,N}$ **C13**

312.33 g/mol 272.76 g/mol 1134.15 g/mol

Preparation: **REN-JE-214-06**

The following reaction was carried out in a glovebox under an inert atmosphere. **$L^{6,N}$** (31 mg, 0,1 mmol, 1 eq) was dissolved in 2.5 ml of acetonitrile. To this solution $Fe(ClO_4)_2 \cdot nH_2O$ (27 mg, 0,1 mmol, 1 eq), dissolved in 0.5 ml methanol and 2.0 ml acetonitrile, was added dropwise. The reaction was kept undisturbed for four weeks at room temperature. Slow evaporation of the solvent afforded colourless plate shaped crystals that were suitable for X-ray structure analysis (Table D.5, $P2_1/c$). The crystals were collected by filtration, washed with diethyl ether and dried at atmospheric pressure to afford **C13**. No yield was determined, as only a few single crystals were obtained. **FT-IR**: $\tilde{\upsilon}$ (cm^{-1}) = 3423, 3273, 2920, 2851, 1781, 1633, 1601, 1529, 1479, 1448, 1415, 1384, 1303, 1242, 1148, 1121, 1108, 1092, 1042, 1021, 941, 904, 835, 636, 625, 424, 416 (Figure A.26).

6.4.14 $[Fe_2(\mu_2\text{-}L^{Py,1})_2](BF_4)_4 \cdot 2MeNO_2$ (C14)



$L^{Py,1}$		**C14**
358.40 g/mol	337.55 g/mol	1175.70 g/mol

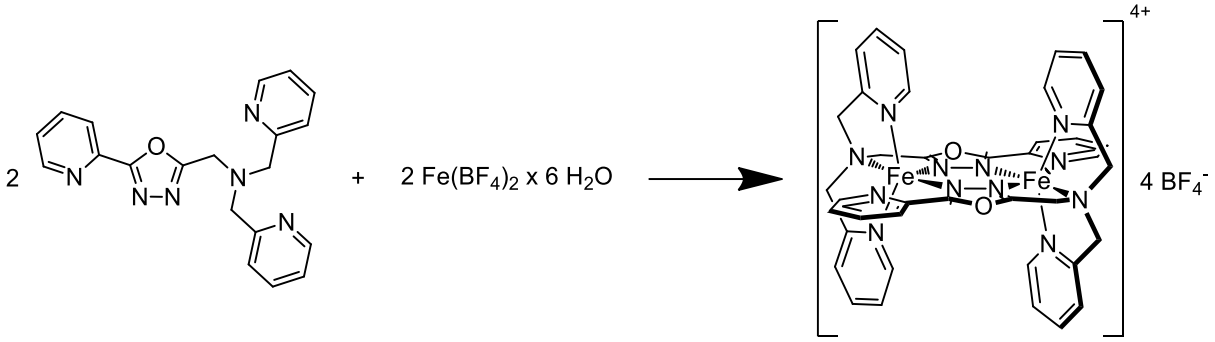
Preparation: **REN-JE-213-2**

Compound **C14** was prepared according to an adapted procedure from the literature.[171] The following reaction was carried out in a glovebox under an inert atmosphere. $L^{Py,1}$ (108 mg, 0,3 mmol, 1 eq) was dissolved in 5.0 ml of acetone. To this solution $Fe(BF_4)_2 \cdot 6H_2O$ (102 mg, 0,3 mmol, 1 eq), dissolved in 10 ml acetone, was added dropwise. After complete addition, an orange solid precipitated. The solid was filtered and dissolved in 6 ml of nitromethane. The solution was set for vapour diffusion against a mixture of diethyl ether, n-hexane and cyclohexane (1:1:1) and kept undisturbed at room temperature. After four weeks, orange block shaped crystals have formed that were suitable for X-ray structure analysis (Table D.6, $P2_1/n$). The crystals were collected by filtration, washed with diethyl ether and dried at atmospheric pressure to afford **C14** (21 mg, 0.018, 18 %). **FT-IR**: $\tilde{\upsilon}$ (cm^{-1}) = 3077, 2924, 2853, 1697, 1652, 1608, 1554, 1485, 1444, 1412, 1362, 1290, 1248, 1083, 1053, 1021, 973, 928, 898, 861, 794, 763, 724, 707, 647, 620, 533, 500, 474, 461, 416 (Figure A.27).

Literature:

[171] Denis Bittner, 1,3,4-Thiadiazol based bis-multidentate ligands for bridged bimetallic complexes with individually adjustable coordination pockets, Dissertation, Mainz 2018.

6.4.15 $[Fe_2(\mu_2\text{-}L^{Py,1})_2](BF_4)_4 \cdot 2MeNO_2$ (C14')



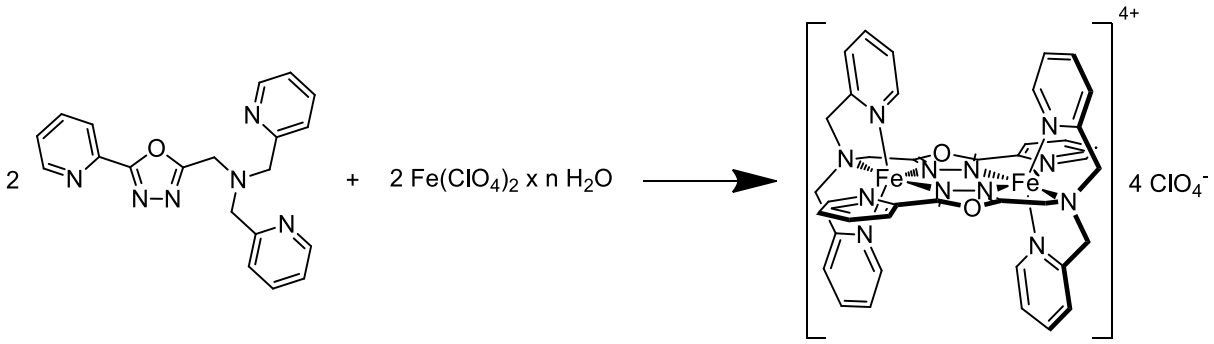
$L^{Py,1}$ | | **C14'**

358.40 g/mol | 337.55 g/mol | 1175.70 g/mol

Preparation: **REN-JE-212-2**

The following reaction was carried out in a glovebox under an inert atmosphere. **$L^{Py,1}$** (36 mg, 0,1 mmol, 1 eq) was dissolved in 2.5 ml of acetonitrile. To this solution $Fe(BF_4)_2 \cdot 6H_2O$ (34 mg, 0,1 mmol, 1 eq), dissolved in 2.5 ml acetonitrile, was added dropwise. The reaction was kept undisturbed for four weeks at room temperature. After complete evaporation of the solvent an orange oil had formed, which was again dissolved in 2 ml of nitromethane. Slow evaporation yielded orange block shaped crystals after four weeks that were suitable for X-ray structure analysis (Table D.6, $P2_1/c$). The crystals were collected by filtration, washed with diethyl ether and dried at atmospheric pressure to afford **C14'** (13.99 mg, 0.012 mmol, 12 %). **FT-IR**: $\tilde{\upsilon}$ (cm^{-1}) = 3078, 3043, 2961, 2934, 2911, 1610, 1586, 1573, 1555, 1487, 1460, 1444, 1429, 1383, 1375, 1362, 1318, 1312, 1292, 1253, 1236, 1164, 1151, 1069, 1019, 1001, 963, 948, 907, 897, 887, 877, 842, 834, 799, 778, 761, 747, 732, 716, 706, 665, 648, 619, 549, 511, 485, 457, 419, 409 (Figure A.28).

6.4.16 $[Fe_2(\mu_2\text{-}L^{Py,1})_2](ClO_4)_4 \cdot 2MeNO_2$ (C15)



$L^{Py,1}$ **C15**

358.40 g/mol 272.76 g/mol 1226.29 g/mol

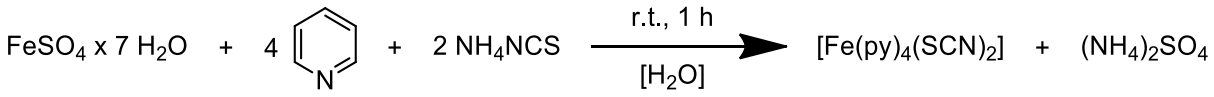
Preparation: **REN-JE-213-3**

Compound **C16** was prepared according to an adapted procedure from the literature.[171] The following reaction was carried out in a glovebox under an inert atmosphere. **$L^{Py,1}$** (36 mg, 0,1 mmol, 1 eq) was dissolved in 2.5 ml of acetone. To this solution $Fe(ClO_4)_2 \cdot nH_2O$ (27 mg, 0,1 mmol, 1 eq), dissolved in 2.5 ml acetone, was added dropwise. The reaction was set for vapour diffusion against a mixture of diethyl ether, n-hexane and cyclohexane (1:1:1). After one day brown microcrystalline needles had formed. The crystals were filtered and dissolved in 2 ml of nitromethane. The solution was again set for vapour diffusion against the 1:1:1 mixture of diethyl ether, n-hexane and cyclohexane, yielding orange block shaped crystals that were suitable for X-ray structure analysis (Table D.7, $P2_1/n$). The crystals were collected by filtration, washed with diethyl ether and dried at atmospheric pressure to afford **C15** (5.01 mg, 0.004 mmol, 5 %). **FT-IR**: $\tilde{\upsilon}$ (cm^{-1}) = 3079, 2961, 2935, 2005, 1652, 1636, 1609, 1587, 1572, 1555, 1517, 1506, 1487, 1459, 1443, 1430, 1375, 1362, 1319, 1312, 1292, 1253, 1224, 1163, 1151, 1072, 1021, 1003, 962, 948, 930, 897, 886, 878, 835, 799, 761, 748, 716, 706, 665, 648, 620, 511, 485, 458, 419, 409 (Figure A.29).

Literature:

[171] Denis Bittner, 1,3,4-Thiadiazol based bis-multidentate ligands for bridged bimetallic complexes with individually adjustable coordination pockets, Dissertation, Mainz 2018.

6.4.17 $[Fe(py)_4(NCS)_2]$

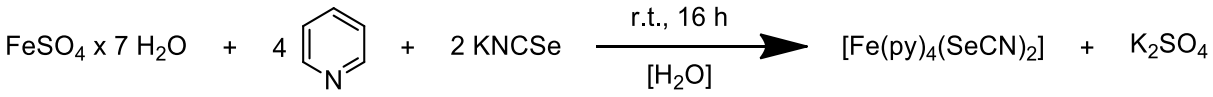


278.01 g/mol 488.41 g/mol

Preparation: **REN-XL-015**

The following reaction was carried out under an inert atmosphere using schlenk technique. Iron(II) sulfate heptahydrate (2.78 g, 10.0 mmol, 1 eq) and pyridine (3.92 g, 50 mmol, 5 eq) were dissolved in 60 ml degassed water. This solution was added to solution of ammonium thiocyanate (1.60 g, 21.0 mmol, 2.1 eq) in 20 ml degassed water. The resulting yellow suspension was stirred for one hour. The solid was filtered and dried in vacuo to yield $[Fe(py)_4(NCS)_2]$ as a yellow powder (4.30 g, 8.80 mmol, 88 %). The product was used without any further analytics.

6.4.18 $[Fe(py)_4(NCSe)_2]$

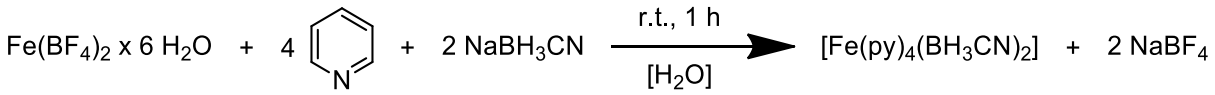


278.01 g/mol 582.20 g/mol

Preparation: **REN-XL-022**

The following reaction was carried out under an inert atmosphere using schlenk technique. Iron(II) sulfate heptahydrate (3.22 g, 11.6 mmol, 1 eq) and pyridine (6.78 g, 85.7 mmol, 7.4 eq) were dissolved in 80 ml degassed water. To this solution, potassium selenocyanate (3.34 g, 23.2 mmol, 2 eq), dissolved in 20 ml degassed water, was added dropwise. The resulting pale green suspension was stirred for 16 hours. The solid was filtered and dried in vacuo to yield $[Fe(py)_4(NCSe)_2]$ as a yellow-green powder. No yield was determined. The product was used without any further analytics.

6.4.19 $[Fe(py)_4(NCBH_3)_2]$

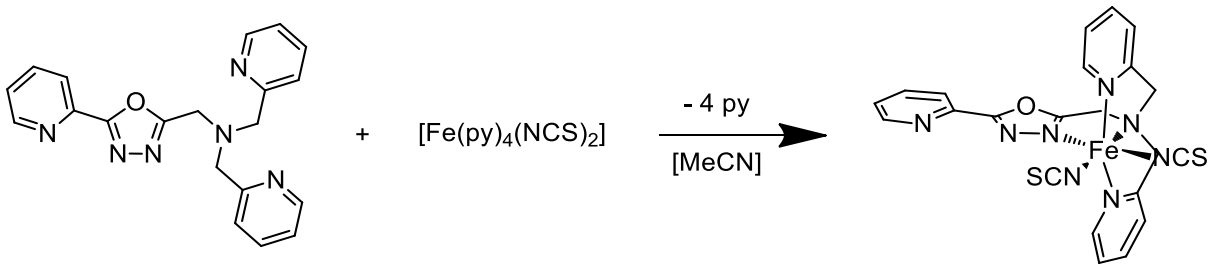


377.55 g/mol 451.95 g/mol

Preparation: **REN-XL-016**

The following reaction was carried out under an inert atmosphere using schlenk technique. Iron(II) tetrafluoroborate hexahydrate (2.00 g, 5.80 mmol, 1 eq) and pyridine (1.82 g, 23.0 mmol, 4 eq) were dissolved in 18 ml degassed water. To this solution sodium cyanoborohydride (0.72 g, 11.5 mmol, 2 eq) was added in portions. The resulting yellow suspension was stirred for one hour. The solid was filtered and dried in vacuo to yield $[Fe(py)_4(NCBH_3)_2]$ as a yellow powder. No yield was determined. The product was used without any further analytics.

6.4.20 $[Fe(L^{Py,1})(NCS)_2] \cdot 1MeCN$ (C16·1MeCN)

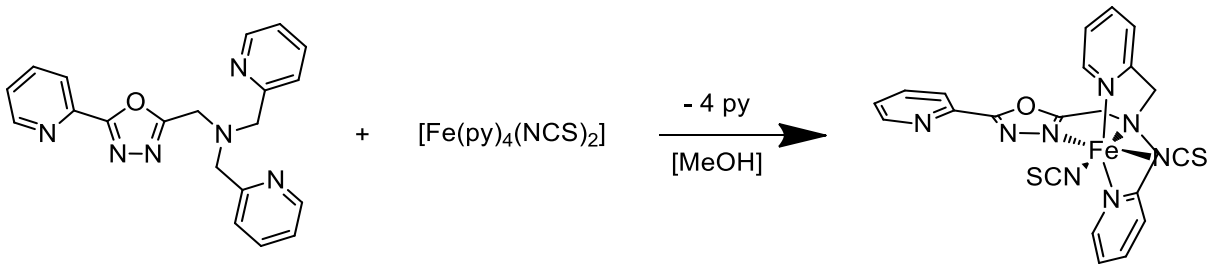


$L^{Py,1}$		**C16·1MeCN**
358.40 g/mol	488.41 g/mol	530.41 g/mol

Preparation: **REN-JE-234-2**

The following reaction was carried out in a glovebox under an inert atmosphere. $[Fe(py)_4(NCS)_2]$ (49 mg, 0.1 mmol, 1 eq) was dissolved in 3 ml acetonitrile and stirred for 15 minutes. The solution was filtered with a syringe filter, to remove unsolved particles. The filtrate was added to a solution of $L^{Py,1}$ (36 mg, 0.1 mmol, 1 eq) in 2 ml acetonitrile. The solution was kept undisturbed and set for slow evaporation of the solvent. After one day yellow block shaped crystals had formed that were suitable for X-ray structure analysis (Table D.7, $P2_1/c$). The crystals were collected by filtration, washed with diethyl ether and dried at atmospheric pressure to afford **C16·1MeCN** (13.45 mg, 0.025 mmol, 25 %).

6.4.21 $[Fe(L^{Py,1})(NCS)_2] \cdot 1MeOH$ (C16·1MeOH)

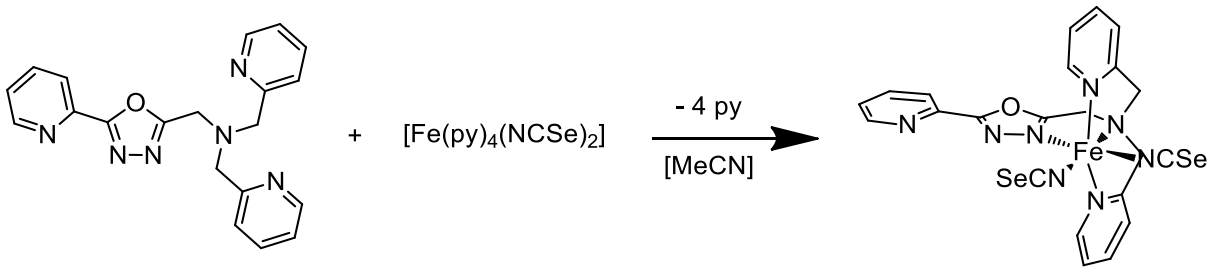


$L^{Py,1}$		**C16**·1MeCN
358.40 g/mol	488.41 g/mol	530.41 g/mol

Preparation: **REN-JE-234-3**

The following reaction was carried out in a glovebox under an inert atmosphere. $[Fe(py)_4(NCS)_2]$ (49 mg, 0.1 mmol, 1 eq) was dissolved in 3 ml methanol and stirred for 15 minutes. The solution was filtered with a syringe filter, to remove unsolved particles. The filtrate was added to a solution of $L^{Py,1}$ (36 mg, 0.1 mmol, 1 eq) in 2 ml methanol. The solution was kept undisturbed and set for slow evaporation of the solvent. After one day yellow block shaped crystals had formed that were suitable for X-ray structure analysis (Table D.8, *C*2/*c*). The crystals were collected by filtration, washed with diethyl ether and dried at atmospheric pressure to afford **C16**·1MeCN (23.54 mg, 0.044 mmol, 44 %).

6.4.22 $[Fe(L^{Py,1})(NCSe)_2] \cdot 3MeCN$ (C17·3MeCN)

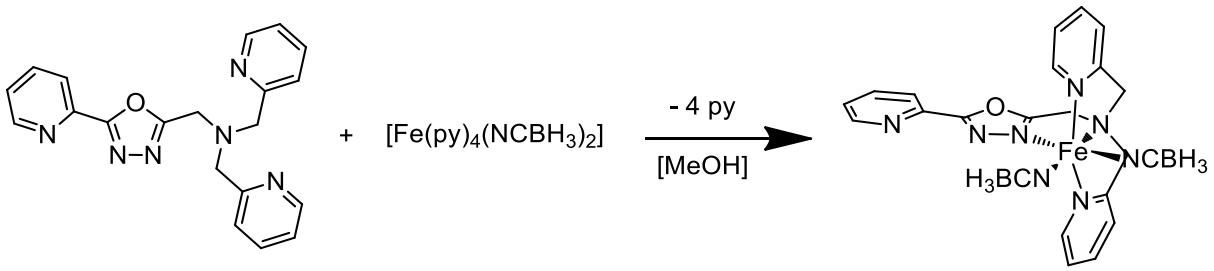


$L^{Py,1}$		**C17**·3MeCN
358.40 g/mol	582.20 g/mol	624.20 g/mol

Preparation: **REN-XL-030-2**

The following reaction was carried out in a glovebox under an inert atmosphere. $[Fe(py)_4(NCSe)_2]$ (58 mg, 0.1 mmol, 1 eq) was dissolved in 3 ml acetonitrile and stirred for 15 minutes. The solution was filtered with a syringe filter, to remove unsolved particles. The filtrate was added to a solution of $L^{Py,1}$ (36 mg, 0.1 mmol, 1 eq) in 2 ml acetonitrile. The solution was kept undisturbed and set for slow evaporation of the solvent. After one week yellow block shaped crystals had formed that were suitable for X-ray structure analysis (Table D.8, $P2_1/c$). The crystals were collected by filtration, washed with diethyl ether and dried at atmospheric pressure to afford **C17**·3MeCN (29.54 mg, 0.047 mmol, 47 %). **FT-IR**: $\tilde{\upsilon}$ (cm^{-1}) = 3054, 2904, 2846, 2684, 2307, 2198, 2163, 2059, 1946, 1601, 1569, 1552, 1475, 1457, 1440, 1425, 1410, 1386, 1350, 1332, 1301, 1280, 1247, 1153, 1118, 1097, 1048, 1017, 992, 972, 957, 899, 882, 852, 817, 795, 757, 737, 705, 640, 619, 532, 509, 480, 418 (Figure A.30).

6.4.23 $[Fe(L^{Py,1})(NCBH_3)_2] \cdot 1MeOH$ (C18·1MeOH)

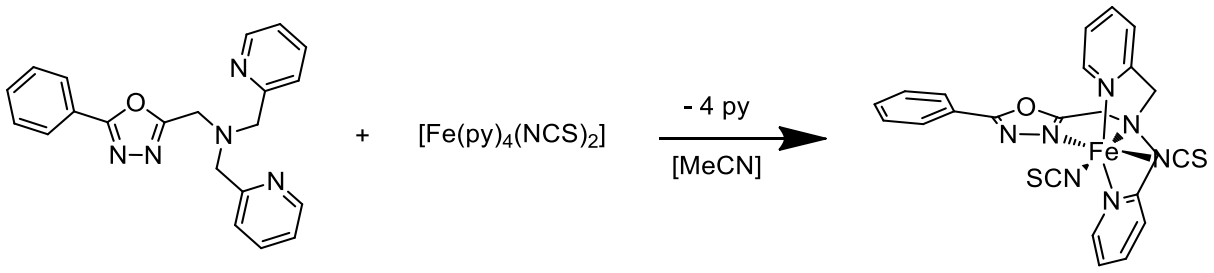


$L^{Py,1}$		**C18**·1MeOH
358.40 g/mol	451.95 g/mol	493.95 g/mol

Preparation: **REN-XL-030-3**

The following reaction was carried out in a glovebox under an inert atmosphere. $[Fe(py)_4(NCBH_3)_2]$ (45 mg, 0.1 mmol, 1 eq) was dissolved in 3 ml methanol and stirred for 15 minutes. The solution was filtered with a syringe filter, to remove unsolved particles. The filtrate was added to a solution of $L^{Py,1}$ (36 mg, 0.1 mmol, 1 eq) in 2 ml methanol. The solution was kept undisturbed and set for slow evaporation of the solvent. After one week yellow block shaped crystals had formed that were suitable for X-ray structure analysis (Table D.9, *C*2/*c*). The crystals were collected by filtration, washed with diethyl ether and dried at atmospheric pressure to afford **C18**·1MeOH (16.98 mg, 0.034 mmol, 34 %).

6.4.24 $[Fe(L^{Ph})(NCS)_2] \cdot 2MeCN$ (C19·2MeCN)

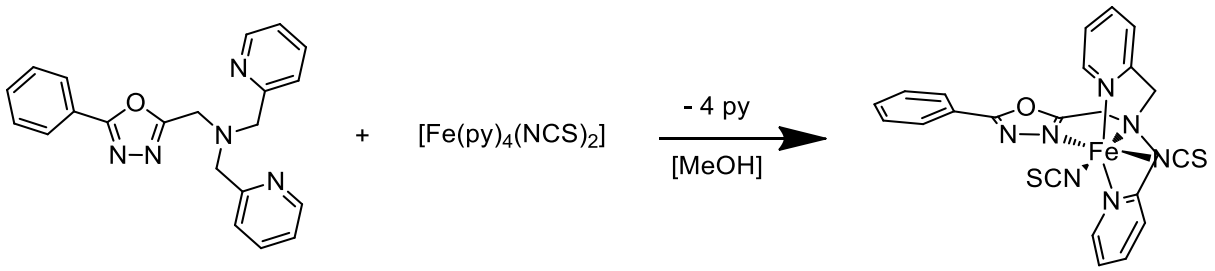


L^{Ph}		**C19**·2MeCN
357.41 g/mol	488.41 g/mol	529.42 g/mol

Preparation: **REN-JE-259-4**

The following reaction was carried out in a glovebox under an inert atmosphere. $[Fe(py)_4(NCS)_2]$ (49 mg, 0.1 mmol, 1 eq) was dissolved in 3 ml acetonitrile and stirred for 15 minutes. The solution was filtered with a syringe filter, to remove unsolved particles. The filtrate was added to a solution of L^{Ph} (36 mg, 0.1 mmol, 1 eq) in 2 ml acetonitrile. The solution was kept undisturbed and set for slow evaporation of the solvent. After one day yellow block shaped crystals had formed that were suitable for X-ray structure analysis (Table D.9, *C*2/*c*). The crystals were collected by filtration, washed with diethyl ether and dried at atmospheric pressure to afford **C19**·2MeCN (27.91 mg, 0.053 mmol, 53 %). **FT-IR**: $\tilde{\upsilon}$ (cm^{-1}) = 3061, 3008, 2906, 2849, 2059, 1971, 1602, 1590, 1570, 1554, 1479, 1439, 1387, 1368, 1351, 1333, 1314, 1300, 1285, 1247, 1224, 1152, 1121, 1099, 1069, 1047, 1018, 993, 974, 956, 927, 898, 881, 853, 798, 778, 756, 736, 707, 690, 640, 614, 510, 477, 435, 418, 404 (Figure A.31).

6.4.25 $[Fe(L^{Ph})(NCS)_2] \cdot 3MeOH$ (C19·3MeOH)

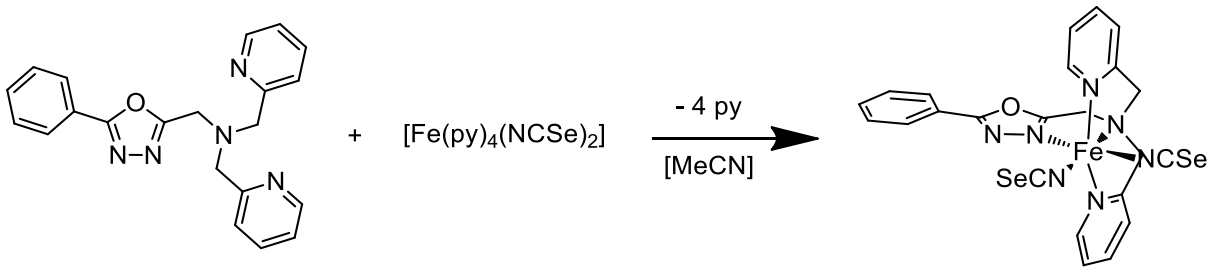


L^{Ph}		**C19**·3MeOH
357.41 g/mol	488.41 g/mol	529.42 g/mol

Preparation: **REN-JE-259-4**

The following reaction was carried out in a glovebox under an inert atmosphere. $[Fe(py)_4(NCS)_2]$ (49 mg, 0.1 mmol, 1 eq) was dissolved in 3 ml methanol and stirred for 15 minutes. The solution was filtered with a syringe filter, to remove unsolved particles. The filtrate was added to a solution of L^{Ph} (36 mg, 0.1 mmol, 1 eq) in 2 ml methanol. The solution was kept undisturbed and set for slow evaporation of the solvent. After one day yellow block shaped crystals had formed that were suitable for X-ray structure analysis (Table D.10, *C*2/*c*). The crystals were collected by filtration, washed with diethyl ether and dried at atmospheric pressure to afford **C19**·3MeOH (29.79 mg, 0.056 mmol, 56 %). **FT-IR**: $\tilde{\upsilon}$ (cm^{-1}) = 2907, 2849, 2058, 1970, 1602, 1572, 1554, 1479, 1439, 1387, 1351, 1314, 1300, 1284, 1245, 1153, 1121, 1098, 1069, 1042, 1018, 992, 975, 955, 927, 898, 881, 853, 817, 801, 779, 757, 735, 708, 689, 640, 510, 476, 419 (Figure A.32).

6.4.26 $[Fe(L^{Ph})(NCSe)_2] \cdot 2MeCN$ (C20·2MeCN)

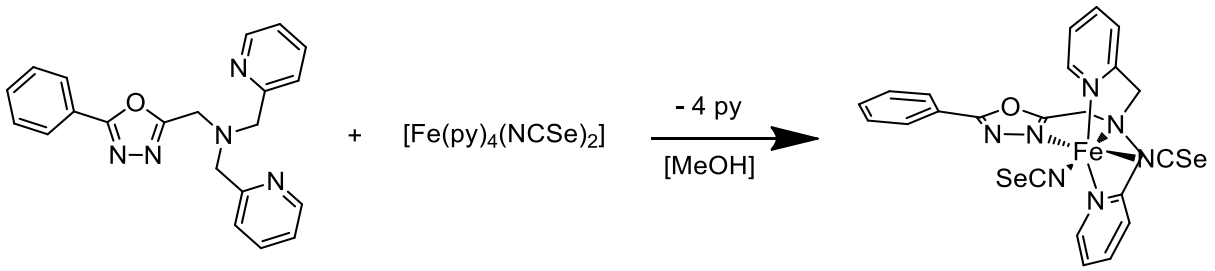


L^{Ph}		**C20**·2MeCN
357.41 g/mol	582.20 g/mol	623.21 g/mol

Preparation: **REN-XL-025-2**

The following reaction was carried out in a glovebox under an inert atmosphere. $[Fe(py)_4(NCSe)_2]$ (58 mg, 0.1 mmol, 1 eq) was dissolved in 3 ml acetonitrile and stirred for 15 minutes. The solution was filtered with a syringe filter, to remove unsolved particles. The filtrate was added to a solution of L^{Ph} (36 mg, 0.1 mmol, 1 eq) in 2 ml acetonitrile. The solution was kept undisturbed and set for slow evaporation of the solvent. After one day yellow block shaped crystals had formed that were suitable for X-ray structure analysis (Table D.10, *C*2/*c*). The crystals were collected by filtration, washed with diethyl ether and dried at atmospheric pressure to afford **C20**·2MeCN (45.63 mg, 0.073 mmol, 73 %). **FT-IR**: $\tilde{\upsilon}$ (cm^{-1}) = 2945, 2903, 2847, 2060, 1970, 1944, 1602, 1579, 1572, 1555, 1480, 1450, 1439, 1386, 1350, 1333, 1313, 1300, 1283, 1248, 1224, 1152, 1120, 1113, 1099, 1069, 1047, 1034, 1019, 992, 974, 966, 956, 898, 880, 850, 817, 779, 756, 736, 707, 690, 640, 511, 479, 418 (Figure A.33).

6.4.27 [Fe(L^{Ph})(NCSe)$_2$] · 3MeOH (C20·3MeOH)



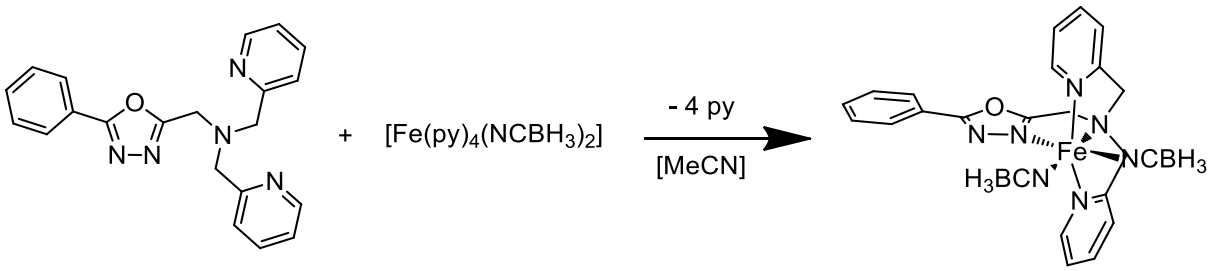
L^{Ph} | [Fe(py)$_4$(NCSe)$_2$] | **C20**·3MeOH

357.41 g/mol | 582.20 g/mol | 623.21 g/mol

Preparation: **REN-XL-025-1**

The following reaction was carried out in a glovebox under an inert atmosphere. [Fe(py)$_4$(NCSe)$_2$] (58 mg, 0.1 mmol, 1 eq) was dissolved in 3 ml methanol and stirred for 15 minutes. The solution was filtered with a syringe filter, to remove unsolved particles. The filtrate was added to a solution of **L^{Ph}** (36 mg, 0.1 mmol, 1 eq) in 2 ml methanol. The solution was kept undisturbed and set for slow evaporation of the solvent. After one day yellow block shaped crystals had formed that were suitable for X-ray structure analysis (Table D.11, *C*2/*c*). The crystals were collected by filtration, washed with diethyl ether and dried at atmospheric pressure to afford **C20**·3MeOH (51.26 mg, 0.073 mmol, 82 %). **FT-IR**: $\tilde{\upsilon}$ (cm^{-1}) = 3059 3026 2905 2854 2696 2065 1604 1571 1554 1482 1442 1384 1351 1312 1285 1248 1178 1154 1119 1098 1069 1051 1019 991 974 957 898 881 850 817 759 735 709 690 642 509 478 419 (Figure A.34).

6.4.28 $[Fe(L^{Ph})(NCBH_3)_2] \cdot 1MeCN$ (C21·1MeCN)

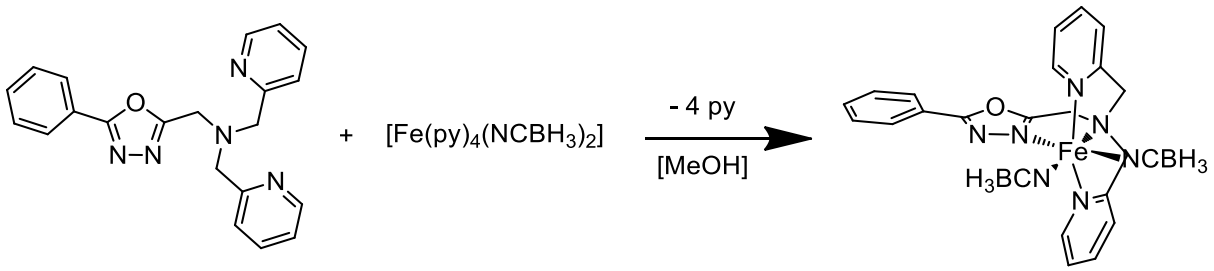


L^{Ph}		**C21**·1MeCN
357.41 g/mol	451.95 g/mol	492.96 g/mol

Preparation: **REN-XL-023-3**

The following reaction was carried out in a glovebox under an inert atmosphere. $[Fe(py)_4(NCBH_3)_2]$ (45 mg, 0.1 mmol, 1 eq) was dissolved in 3 ml acetonitrile and stirred for 15 minutes. The solution was filtered with a syringe filter, to remove unsolved particles. The filtrate was added to a solution of L^{Ph} (36 mg, 0.1 mmol, 1 eq) in 2 ml acetonitrile. The solution was kept undisturbed and set for slow evaporation of the solvent. After two days yellow block shaped crystals had formed that were suitable for X-ray structure analysis (Table D.11 and Table D.12, *C*2/*c*). The crystals were collected by filtration, washed with diethyl ether and dried at atmospheric pressure to afford **C21**·1MeCN (27.38 mg, 0.056 mmol, 56 %). **FT-IR**: $\tilde{\upsilon}$ (cm^{-1}) = 3030, 2958, 2919, 2352, 2328, 2177, 1604, 1584, 1574, 1557, 1481, 1440, 1427, 1390, 1355, 1333, 1320, 1304, 1287, 1250, 1223, 1153, 1118, 1112, 1098, 1052, 1044, 1021, 988, 960, 892, 883, 855, 817, 776, 764, 735, 704, 686, 642, 510, 480, 418 (Figure A.35).

6.4.29 $[Fe(L^{Ph})(NCBH_3)_2] \cdot 1.8MeOH$ (C21·1.8MeOH)

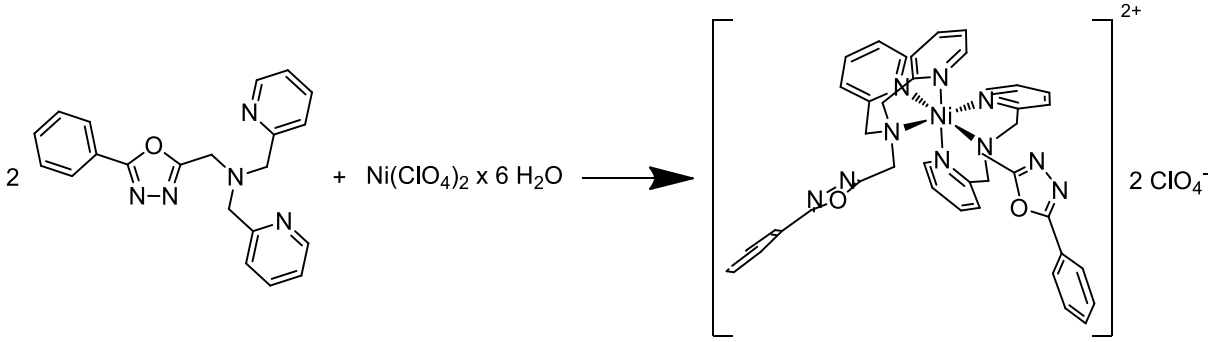


L^{Ph}		**C21**·1.8MeOH
357.41 g/mol	451.95 g/mol	492.96 g/mol

Preparation: **REN-JE-256-5**

The following reaction was carried out in a glovebox under an inert atmosphere. $[Fe(py)_4(NCBH_3)_2]$ (45 mg, 0.1 mmol, 1 eq) was dissolved in 3 ml methanol and stirred for 15 minutes. The solution was filtered with a syringe filter, to remove unsolved particles. The filtrate was added to a solution of L^{Ph} (36 mg, 0.1 mmol, 1 eq) in 2 ml methanol. The solution was kept undisturbed and set for slow evaporation of the solvent. After two days orange plate shaped crystals had formed that were suitable for X-ray structure analysis (Table D.12, *C*2/*c*). The crystals were collected by filtration, washed with diethyl ether and dried at atmospheric pressure to afford **C21**·xMeOH (29.33 mg, 0.053 mmol, 53 %). **FT-IR**: $\tilde{\upsilon}$ (cm^{-1}) = 2980, 2928, 2338, 2179, 1605, 1575, 1558, 1541, 1521, 1507, 1488, 1477, 1457, 1445, 1425, 1419, 1305, 1244, 1154, 1124, 1113, 1096, 1054, 1045, 1020, 959, 940, 881, 852, 762, 738, 706, 688, 669, 644, 511, 493, 476, 417 (Figure A.36).

6.4.30 $[Ni(\eta^3\text{-}L^{Ph})_2](ClO_4)_2$ (C22)



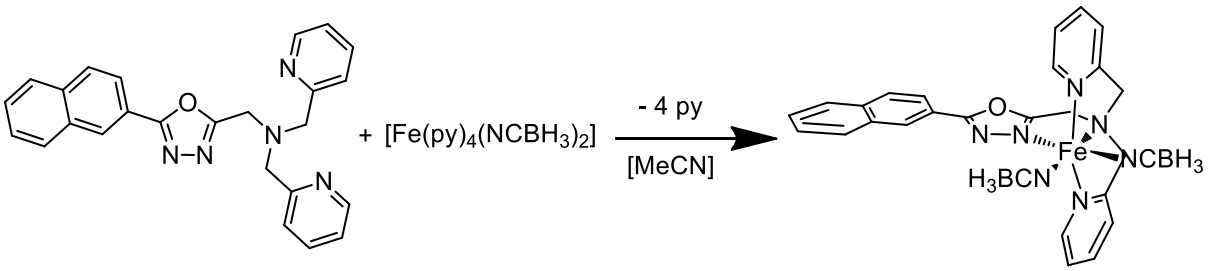
L^{Ph} **C22**

357.41 g/mol 365.69 g/mol 972.41 g/mol

Preparation: **REN-JE-253-10**

Nickel(II) perchlorate hexahydrate (37 mg, 0.1 mmol, 1 eq) was dissolved in 3 ml methanol. To this solution **L^{Ph}** (36 mg, 0.1 mmol, 1 eq), dissolved in 2 ml methanol, was added. The reaction was kept undisturbed and set for slow evaporation of the solvent. After four weeks, violet block shaped crystals (**C22**) had formed that were suitable for X-ray structure analysis (Table D.13, $P\bar{1}$). Since only a few crystals were obtained, yield was not determined and no further analysis done.

6.4.31 [Fe(L^{Naph})($NCBH_3$)$_2$] · 4.5MeCN (C23·4.5MeCN)



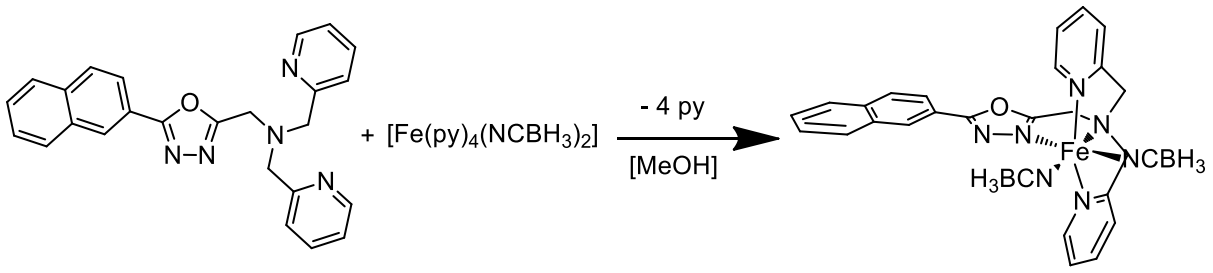
L^{Naph} **C23**·4.5MeCN

407.47 g/mol 451.95 g/mol 543.02 g/mol

Preparation: **REN-JE-266-2**

The following reaction was carried out in a glovebox under an inert atmosphere. [Fe(py)$_4$($NCBH_3$)$_2$] (45 mg, 0.1 mmol, 1 eq) was dissolved in 3 ml acetonitrile and stirred for 15 minutes. The solution was filtered with a syringe filter, to remove unsolved particles. The filtrate was added to a solution of **L^{Naph}** (41 mg, 0.1 mmol, 1 eq) in 2 ml acetonitrile. The solution was kept undisturbed and set for slow evaporation of the solvent. After two days yellow block shaped crystals had formed that were suitable for X-ray structure analysis (Table D.13, *C*2/*c*). The crystals were collected by filtration, washed with diethyl ether and dried at atmospheric pressure to afford **C23**·4.5MeCN (38.48 mg, 0.051 mmol, 52 %). **FT-IR**: $\tilde{\upsilon}$ (cm^{-1}) = 2970, 2929, 2915, 2338, 2192, 2177, 1634, 1605, 1573, 1549, 1507, 1489, 1476, 1458, 1445, 1425, 1350, 1316, 1306, 1255, 1229, 1193, 1155, 1139, 1125, 1112, 1096, 1055, 1043, 1020, 994, 984, 964, 940, 902, 892, 881, 863, 849, 820, 755, 738, 718, 645, 596, 508, 476, 418 (Figure A.37).

6.4.32 $[Fe(L^{Naph})(NCBH_3)_2] \cdot 3MeOH$ (C23·3MeOH)



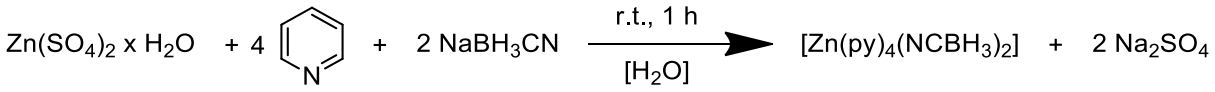
L^{Naph} + $[Fe(py)_4(NCBH_3)_2]$ → **C23**·3MeOH

407.47 g/mol + 451.95 g/mol → 543.02 g/mol

Preparation: **REN-JE-266-2**

The following reaction was carried out in a glovebox under an inert atmosphere. $[Fe(py)_4(NCBH_3)_2]$ (45 mg, 0.1 mmol, 1 eq) was dissolved in 3 ml methanol and stirred for 15 minutes. The solution was filtered with a syringe filter, to remove unsolved particles. The filtrate was added to a solution of **L^{Naph}** (41 mg, 0.1 mmol, 1 eq) in 2 ml methanol. The solution was kept undisturbed and set for slow evaporation of the solvent. After two days yellow block shaped crystals had formed that were suitable for X-ray structure analysis (Table D.14, *C*2/*c*). The crystals were collected by filtration, washed with diethyl ether and dried at atmospheric pressure to afford **C23**·3MeOH (38.00 mg, 0.070 mmol, 70 %). **FT-IR**: $\tilde{\upsilon}$ (cm^{-1}) = 2974, 2928, 2916, 2861, 2356, 2340, 2194, 2177, 1970, 1634, 1604, 1574, 1549, 1445, 1426, 1387, 1361, 1350, 1316, 1306, 1256, 1230, 1193, 1155, 1125, 1111, 1096, 1044, 1055, 1020, 994, 984, 977, 963, 940, 902, 892, 863, 849, 821, 754, 738, 718, 683, 669, 660, 645, 596, 540, 508, 477, 456, 418 (Figure A.38).

6.4.33 $[Zn(py)_4(NCBH_3)_2]$ (C24)



C24

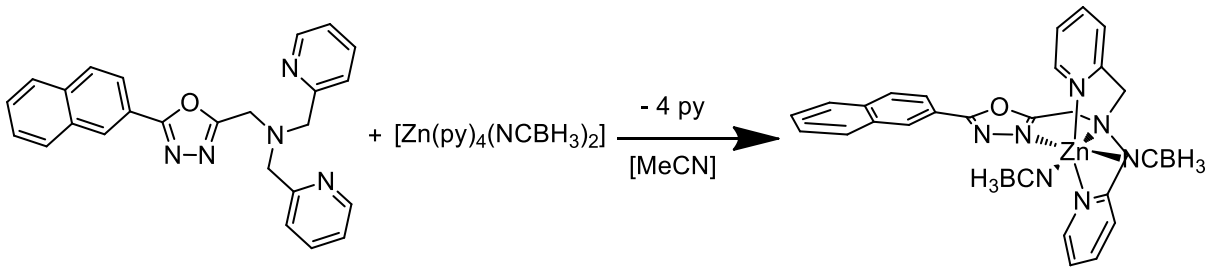
407.47 g/mol

461.48 g/mol

Preparation: **REN-JE-270**

Zinc(II) sulfate hydrate (2.00 g, 11.14 mmol, 1 eq), pyridine (3.52 g, 3.59 ml, 44.56 mmol, 4 eq) and sodium cyanoborohydride (1.40 g, 22.28 mmol, 2 eq) were suspended in 50 ml water. The reaction mixture was stirred for one hour, during which a colourless solid had formed. The solid was filtered and dried in vacuo to yield **C24** as colourless powder (1.79 g, 3.87 mmol, 35 %). **^{1}H-NMR** (400 MHz, DMSO, δ (ppm)): 8.58 - 8.56 (m, 8H, pyC*H*), 7.82 - 7.78 (m, 4H, pyC*H*), 7.41 - 7.38 (m, 8H, pyC*H*), 0.56 - 0.10 (m, 6H, B*H*3) (Figure B.70). **FT-IR**: $\tilde{\upsilon}$ (cm^{-1}) = 2980, 2341, 2184, 1598, 1575, 1558, 1541, 1520, 1507, 1487, 1457, 1440, 1397, 1216, 1153, 1120, 1068, 1038, 1008, 860, 765, 753, 697, 626, 420 (Figure A.39).

6.4.34 $[Zn(L^{Naph})(NCBH_3)_2]$ (C25)

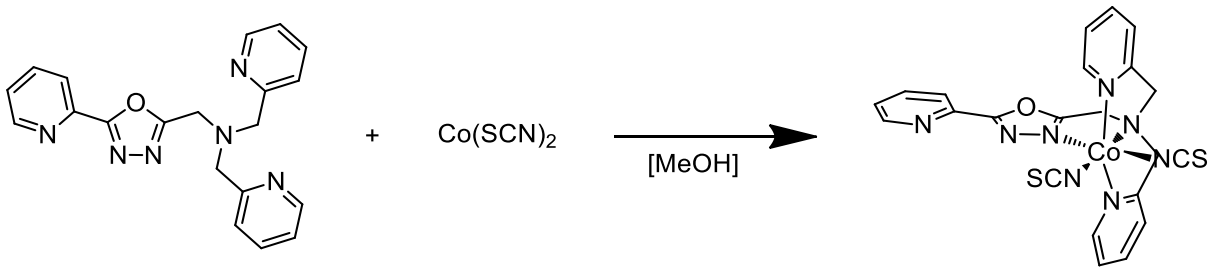


L^{Naph}	C24	C25
407.47 g/mol	451.95 g/mol	543.02 g/mol

Preparation: **REN-JE-271-1**

C24 (45 mg, 0.1 mmol, 1 eq) was dissolved in 3 ml acetonitrile and stirred for 15 minutes. The solution was filtered with a syringe filter, to remove unsolved particles. The filtrate was added to a solution of L^{Naph} (41 mg, 0.1 mmol, 1 eq) in 2 ml acetonitrile. The solution was kept undisturbed and set for slow evaporation of the solvent. After one day, colourless microcrystalline needles had formed. The crystals were collected by filtration, washed with diethyl ether and dried at atmospheric pressure to yield **C25** (23.48 mg, 0.042 mmol, 42 %). **^{1}H-NMR** (400 MHz, DMSO, δ (ppm)): 8.71 - 8.65 (m, 3H), 8.21 - 8.07 (m, 6H), 7.70 - 7.64 (m, 6H), 4.55 (d, 2H, ODA-CH_2), 4.27 - 4.23 (m, 4H, Py-CH_2), 0.56 - 0.05 (m, 6H, BH_3) (Figure B.71). **FT-IR**: $\tilde{\upsilon}$ (cm^{-1}) = 3056, 2941, 2867, 2353, 2340, 2200, 2190, 1607, 1573, 1559, 1539, 1508, 1489, 1481, 1455, 1443, 1389, 1371, 1338, 1312, 1292, 1270, 1222, 1159, 1145, 1123, 1114, 1096, 1075, 1055, 1026, 997, 987, 967, 954, 910, 864, 846, 823, 795, 767, 752, 733, 723, 683, 652, 632, 593, 529, 502, 492, 476, 458, 418 (Figure A.40).

6.4.35 $[Co(L^{Py,1})(NCS)_2] \cdot 1MeOH$ (C26)



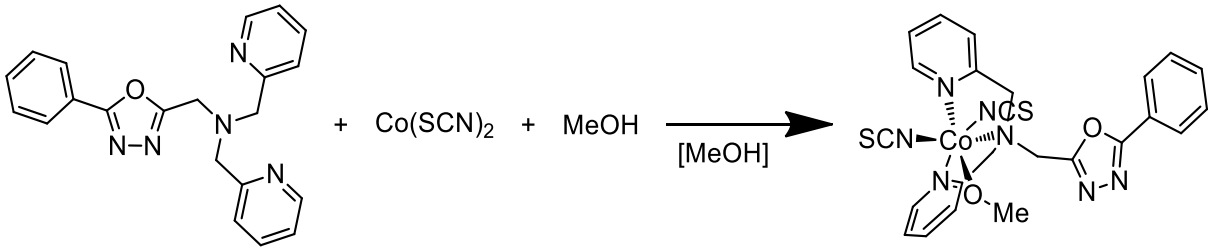
$L^{Py,1}$ **C26**

358.40 g/mol 175.10 g/mol 533.49 g/mol

Preparation: **REN-JE-240-1**

Cobalt(II) thiocyanate (18 mg, 0.1 mmol, 1 eq) was dissolved in 3 ml methanol. To this solution **$L^{Py,1}$** (36 mg, 0.1 mmol, 1 eq), dissolved in 2 ml methanol, was added. After complete addition, a green solid precipitated, which was filtered. The filtrate was kept undisturbed and set for slow evaporation of the solvent. After a few days violet block shaped crystals had formed that were suitable for X-ray structure analysis (Table D.15, *I*2/*a*). The crystals were collected by filtration, washed with diethyl ether and dried at atmospheric pressure to afford **C26** (6.44 mg, 0.012 mmol, 12 %). **FT-IR**: $\tilde{\upsilon}$ (cm^{-1}) = 2970, 2906, 2323, 2073, 1646, 1636, 1603, 1571, 1556, 1540, 1508, 1481, 1439, 1386, 1350, 1308, 1284, 1250, 1154, 1120, 1100, 1071, 1047, 1020, 993, 975, 956, 897, 880, 859, 820, 797, 779, 756, 735, 707, 691, 641, 511, 476, 419 (Figure A.41).

6.4.36 $[Co(\eta^3\text{-}L^{Ph})(NSC)_2(MeOH)]$ (C27)



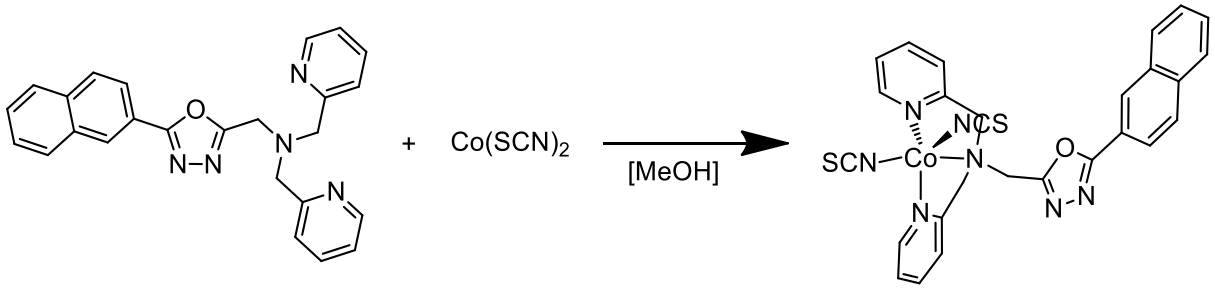
L^{Ph} + $Co(SCN)_2$ + MeOH → **C27**

357.41 g/mol + 175.10 g/mol → 564.55 g/mol

Preparation: **REN-JE-251-1**

Cobalt(II) thiocyanate (18 mg, 0.1 mmol, 1 eq) was dissolved in 3 ml methanol. To this solution **L^{Ph}** (36 mg, 0.1 mmol, 1 eq), dissolved in 2 ml methanol, was added. The reaction was kept undisturbed and set for slow evaporation of the solvent. After a few days violet plate shaped crystals had formed that were suitable for X-ray structure analysis (Table D.15, $P\bar{1}$). The crystals were collected by filtration, washed with diethyl ether and dried at atmospheric pressure to afford **C27** (16.22 mg, 0.029 mmol, 29 %). **FT-IR**: $\tilde{\upsilon}$ (cm^{-1}) = 2971, 2906, 2851, 2073, 1636, 1603, 1582, 1555, 1518, 1481, 1439, 1421, 1350, 1313, 1300, 1284, 1249, 1224, 1153, 1115, 1101, 1071, 1047, 1020, 993, 975, 956, 898, 880, 852, 799, 779, 756, 736, 707, 691, 641, 597, 512, 482, 460, 419 (Figure A.42).

6.4.37 $[Co(\eta^3\text{-}L^{Naph})(NCS)_2]$ (C28)



L^{Naph}		**C28**
407.47 g/mol	175.10 g/mol	582.57 g/mol

Preparation: **REN-JE-272-1**

L^{Naph} (41 mg, 0.1 mmol, 1 eq) was dissolved in 4 ml methanol and filled in a test tube with screw cap. The solution was layered carefully with 3 ml of methanol. On top, Cobalt(II) thiocyanate (18 mg, 0.1 mmol, 1 eq), dissolved in 4 ml methanol, was layered in such way that the different phases don't mix. The reaction was kept undisturbed. After a few days purple needle shaped crystals had formed that were suitable for X-ray structure analysis (Table D.16, *Pbca*). The crystals were collected by filtration, washed with diethyl ether and dried at atmospheric pressure to afford **C28** (13.74 mg, 0.024 mmol, 24 %). **FT-IR**: $\tilde{\upsilon}$ (cm^{-1}) = 3054, 2914, 2071, 2047, 1867, 1627, 1604, 1570, 1559, 1537, 1508, 1478, 1439, 1386, 1365, 1346, 1333, 1306, 1290, 1262, 1239, 1221, 1195, 1157, 1129, 1103, 1093, 1072, 1054, 1025, 994, 984, 966, 955, 939, 910, 897, 859, 845, 822, 793, 768, 753, 733, 724, 682, 650, 631, 592, 527, 502, 492, 475, 414 (Figure A.43).

Literature

[1] G. E. Moore, *IEEE Solid-State Circuits Soc. Newsl.* **2006**, *11*, 33.

[2] V. I. Minkin, *Russ Chem Bull* **2008**, *57*, 687.

[3] W. Plass, *Chem. Unserer Zeit* **1998**, *32*, 323.

[4] M. L. Gross, in *Mass Spectrometry*, Vol. 193, Elsevier **1990**, p. 131.

[5] F. Muller, M. A. Hopkins, N. Coron, M. Grynberg, L. C. Brunel, G. Martinez, *Review of Scientific Instruments* **1989**, *60*, 3681.

[6] E. Danieli, J. Perlo, B. Blümich, F. Casanova, *Angewandte Chemie International Edition* **2010**, *49*, 4133.

[7] K. Gramm, L. Lundgren, O. Beckman, *Phys. Scr.* **1976**, *13*, 93.

[8] D. J. Craik, R. S. Tebble, *Rep. Prog. Phys.* **1961**, *24*, 116.

[9] D. Gatteschi, *Adv. Mater.* **1994**, *6*, 635.

[10] E. Coronado, *Nat Rev Mater* **2020**, *5*, 87.

[11] R. Sessoli, D. Gatteschi, A. Caneschi, M. A. Novak, *Nature* **1993**, *365*, 141.

[12] L. Bogani, W. Wernsdorfer, *Nature materials* **2008**, *7*, 179.

[13] M. Hołyńska (Ed.), *Single-Molecule Magnets: Molecular architectures and building blocks for spintronics*, Wiley-VCH Verlag GmbH & Co. KGaA, Weinheim, Germany **2018**.

[14] J. Camarero, E. Coronado, *J. Mater. Chem.* **2009**, *19*, 1678.

[15] J. M. Clemente-Juan, E. Coronado, A. Gaita-Ariño, *Chem. Soc. Rev.* **2012**, *41*, 7464.

[16] K. Katoh, H. Isshiki, T. Komeda, M. Yamashita, *Coordination Chemistry Reviews* **2011**, *255*, 2124.

[17] K. Hymas, A. Soncini, *Phys. Rev. B* **2019**, *99*, 245404.

[18] D. M. Adams, D. N. Hendrickson, *J. Am. Chem. Soc.* **1996**, *118*, 11515.

[19] N. Guihery, G. Durand, M.-B. Lepetit, *Chemical Physics* **1994**, *183*, 45.

[20] C. Köhler, E. Rentschler, *Eur. J. Inorg. Chem.* **2016**, *2016*, 1955.

[21] Christian Herold, *Spin-Crossover Systems based on 1,3,4-Thiadiazoles*, Mainz **2016**.

[22] C. F. Herold, S. I. Shylin, E. Rentschler, *Inorg. Chem.* **2016**, *55*, 6414.

[23] F. Fürmeyer, L. Carrella, E. Rentschler, *Crystals* **2020**, *10*, 448.

[24] F. Fürmeyer, L. M. Carrella, V. Ksenofontov, A. Möller, E. Rentschler, *Inorg. Chem.* **2020**, *59*, 2843.

[25] C. F. Herold, L. M. Carrella, E. Rentschler, *Eur. J. Inorg. Chem.* **2015**, *2015*, 3632.

[26] O. Kahn, J. Kröber, C. Jay, *Adv. Mater.* **1992**, *4*, 718.

[27] A. Bousseksou, G. Molnár, P. Demont, J. Menegotto, *J. Mater. Chem.* **2003**, *13*, 2069.

[28] M. Matsuda, H. Tajima, *Chem. Lett.* **2007**, *36*, 700.

[29] P. Gamez, J. S. Costa, M. Quesada, G. Aromí, *Dalton Trans* **2009**.

[30] J. S. Griffith, L. E. Orgel, *Q. Rev., Chem. Soc.* **1957**, *11*, 381.

[31] P. Gütlich, A. Hauser, H. Spiering, *Angew. Chem.* **1994**, *106*, 2109.

[32] F. Hund, *Z. Physik* **1927**, *40*, 742.

[33] A. A. Sawchuk, T. C. Strand, *Proc. IEEE* **1984**, *72*, 758.

[34] Y. Tanabe, S. Sugano, *J. Phys. Soc. Jpn.* **1954**, *9*, 766.

[35] G. Racah, *Phys. Rev.* **1942**, *62*, 438.

[36] H. N. Russell, F. A. Saunders, *ApJ* **1925**, *61*, 38.

[37] A. Hauser, in *Spin Crossover in Transition Metal Compounds I*, Vol. 233 (Eds.: P. Gütlich, H. A. Goodwin), Springer Berlin Heidelberg. Berlin, Heidelberg **2004**, p. 49.

[38] L. Wiehl, G. Kiel, C. P. Koehler, H. Spiering, P. Guetlich, *Inorg. Chem.* **1986**, *25*, 1565.

[39] W. B. Jensen, *ChemTexts* **2016**, *2*.

[40] E. König, in *Complex Chemistry*, Vol. 76 (Eds.: M. J. Clarke, J. B. Goodenough, J. A. Ibers, C. K. Jørgensen, D. M. P. Mingos, J. B. Neilands, G. A. Palmer, D. Reinen, P. J. Sadler, R. Weiss, R. J. P. Williams), Springer Berlin Heidelberg. Berlin, Heidelberg **1991**, p. 51.

[41] P. Gütlich, H. A. Goodwin (Eds.), *Spin Crossover in Transition Metal Compounds I*, Springer Berlin Heidelberg, Berlin, Heidelberg **2004**.

[42] M. Sorai, in *Spin crossover in transition metal compoundsn3* (Eds.: P. Gütlich, H. A. Goodwin, K. Boukheddaden, P. Gütlich), Springer. Berlin [u.a.] **2004**, p. 153.

[43] J. Jeftic, R. Hinek, S. C. Capelli, A. Hauser, *Inorg. Chem.* **1997**, *36*, 3080.

[44] H. Spiering, E. Meissner, H. Köppen, E. W. Müller, P. Gütlich, *Chemical Physics* **1982**, *68*, 65.

[45] R. Jakobi, H. Spiering, L. Wiehl, E. Gmelin, P. Guetlich, *Inorg. Chem.* **1988**, *27*, 1823.

[46] V. Ksenofontov, A. B. Gaspar, P. Gütlich, in *Spin Crossover in Transition Metal Compounds III*, Vol. 235, Springer-Verlag. Berlin/Heidelberg **2004**, p. 23.

[47] S. Usha, R. Srinivasan, C. Rao, *Chemical Physics* **1985**, *100*, 447.

[48] J. A. Real, A. B. Gaspar, M. C. Muñoz, *Dalton Trans* **2005**.

[49] J. J. McGravey, I. Lawthers, *J. Chem. Soc., Chem. Commun.* **1982**.

[50] S. Decurtins, P. Gütlich, C. P. Köhler, H. Spiering, A. Hauser, *Chemical Physics Letters* **1984**, *105*, 1.

[51] A. Hauser, *Chemical Physics Letters* **1986**, *124*, 543.

[52] A. Hauser, in *Spin crossover in transition metal compounds*, Vol. 234 (Eds.: P. Gütlich, H. A. Goodwin), Springer. Berlin, [London] **2004**, p. 155.

[53] J.-F. Létard, *J. Mater. Chem.* **2006**, *16*, 2550.

[54] A. F. Holleman, E. und Nils Wiberg, G. Fischer, *Lehrbuch der Anorganischen Chemie*, Walter de Gruyter, Berlin • New York **2007**.

[55] A. Hauser, *Coordination Chemistry Reviews* **1991**, *111*, 275.

[56] G. Chastanet, C. Desplanches, C. Baldé, P. Rosa, M. Marchivie, P. Guionneau, *Chem.Sq.* **2018**, *2*, 2.

[57] C.-C. Wu, J. Jung, P. K. Gantzel, P. Gütlich, D. N. Hendrickson, *Inorg. Chem.* **1997**, *36*, 5339.

[58] E. Collet, P. Guionneau, *Comptes Rendus Chimie* **2018**, *21*, 1133.

[59] A. L. Thompson, V. A. Money, A. E. Goeta, J. A. Howard, *Comptes Rendus Chimie* **2005**, *8*, 1365.

[60] D. J. Harding, P. Harding, W. Phonsri, *Coordination Chemistry Reviews* **2016**, *313*, 38.

[61] I. Krivokapic, M. Zerara, M. L. Daku, A. Vargas, C. Enachescu, C. Ambrus, P. Tregenna-Piggott, N. Amstutz, E. Krausz, A. Hauser, *Coordination Chemistry Reviews* **2007**, *251*, 364.

[62] S. ALVAREZ, P. ALEMANY, D. CASANOVA, J. CIRERA, M. LLUNELL, D. AVNIR, *Coordination Chemistry Reviews* **2005**, *249*, 1693.

[63] J. K. McCusker, A. L. Rheingold, D. N. Hendrickson, *Inorg. Chem.* **1996**, *35*, 2100.

[64] P. Guionneau, M. Marchivie, G. Bravic, J.-F. Létard, D. Chasseau, in *Spin crossover in transition metal compounds*, Vol. 234 (Eds.: P. Gütlich, H. A. Goodwin), Springer. Berlin, [London] **2004**, p. 97.

[65] O. Kahn, *Science* **1998**, *279*, 44.

[66] B. DEUTCH, O. L. RASMUSSEN, *Physiol Plant* **1974**, *30*, 64.

[67] L. H. Gade, *Koordinationschemie*, John Wiley & Sons, Hoboken **2012**.

[68] M. A. Robinson, J. D. Curry, D. H. Busch, *Inorg. Chem.* **1963**, *2*, 1178.

[69] H. Phan, J. J. Hrudka, D. Igimbayeva, L. M. Lawson Daku, M. Shatruk, *J. Am. Chem. Soc.* **2017**, *139*, 6437.

[70] C. Dubroca, *Chemical Physics Letters* **1972**, *15*, 207.

[71] H. R. Chang, J. K. McCusker, H. Toftlund, S. R. Wilson, A. X. Trautwein, H. Winkler, D. N. Hendrickson, *J. Am. Chem. Soc.* **1990**, *112*, 6814.

[72] A. E. Thorarinsdottir, A. I. Gaudette, T. D. Harris, *Chemical science* **2017**, *8*, 2448.

[73] N. N. Greenwood, *Mössbauer Spectroscopy*, Springer Netherlands, Dordrecht **1971**.

[74] E. König, K. Madeja, *Chem. Commun. (London)* **1966**, *0*, 61.

[75] P. Gütlich, Y. Garcia, H. A. Goodwin, *Chem. Soc. Rev.* **2000**, *29*, 419.

[76] V. Ksenofontov, H. Spiering, S. Reiman, Y. Garcia, A. Gaspar, N. Moliner, J. Real, P. Gütlich, *Chemical Physics Letters* **2001**, *348*, 381.

[77] F.-L. Yang, B. Li, T. Hanajima, Y. Einaga, R.-B. Huang, L.-S. Zheng, J. Tao, *Dalton Trans* **2010**, *39*, 2288.

[78] J. H. Takemoto, B. Hutchinson, *Inorg. Chem.* **1973**, *12*, 705.

[79] P. Gütlich, A. Hauser, H. Spiering, *Angewandte Chemie International Edition* **1994**, *33*, 2024.

[80] M. Sorai, S. Seki, *Journal of Physics and Chemistry of Solids* **1974**, *35*, 555.

[81] W. Haase, *Berichte der Bunsengesellschaft für physikalische Chemie* **1994**, *98*, 1208.

[82] K. de Buysser, G. G. Herman, E. Bruneel, S. Hoste, I. van Driessche, *Chemical Physics* **2005**, *315*, 286.

[83] E. M. Schubert, *J. Chem. Educ.* **1992**, *69*, 62.

[84] C. Piguet, *J. Chem. Educ.* **1997**, *74*, 815.

[85] D. Ostfeld, I. A. Cohen, *J. Chem. Educ.* **1972**, *49*, 829.

[86] R. W. Hogue, H. L. C. Feltham, R. G. Miller, S. Brooker, *Inorg. Chem.* **2016**, *55*, 4152.

[87] C. Hannay, M.-J. Hubin-Franskin, F. Grandjean, V. Briois, A. Polian, S. Trofimenko, G. J. Long, *Inorg. Chem.* **1997**, *36*, 5580.

[88] N. A. Young, *J. Chem. Soc., Dalton Trans.* **1996**.

[89] N. E. Domracheva, A. V. Pyataev, V. E. Vorobeva, E. M. Zueva, *The journal of physical chemistry. B* **2013**, *117*, 7833.

[90] N. Shioyasu, K. Kagetsu, K. Mishima, M. K. Kubo, T. Tominaga, K. Nishiyama, K. Nagamine, *Hyperfine Interact* **1994**, *84*, 477.

[91] A. Vértes, K. Süvegh, R. Hinek, P. Gütlich, *Hyperfine Interact* **1994**, *84*, 483.

[92] H. Grünsteudel, H. Paulsen, W. Meyer-Klaucke, H. Winkler, A. X. Trautwein, H. F. Grünsteudel, A. Baron, A. I. Chumakov, R. Rüffer, H. Toftlund, *Hyperfine Interact* **1998**, *113*, 311.

[93] H. Paulsen, H. Grünsteudel, W. Meyer-Klaucke, M. Gerdan, H. F. Grünsteudel, A. I. Chumakov, R. Rüffer, H. Winkler, H. Toftlund, A. X. Trautwein, *Eur. Phys. J. B* **2001**, *23*, 463.

[94] R. Kulmaczewski, J. Olguín, J. A. Kitchen, H. L. C. Feltham, G. N. L. Jameson, J. L. Tallon, S. Brooker, *J. Am. Chem. Soc.* **2014**, *136*, 878.

[95] T. Nakamoto, Z. C. Tan, M. Sorai, *Inorg. Chem.* **2001**, *40*, 3805.

[96] S. Vela, H. Paulsen, *Inorg. Chem.* **2018**, *57*, 9478.

[97] R. Kulmaczewski, O. Cespedes, M. A. Halcrow, *Inorg. Chem.* **2017**, *56*, 3144.

[98] D. Savard, C. Cook, G. D. Enright, I. Korobkov, T. J. Burchell, M. Murugesu, *CrystEngComm* **2011**, *13*, 5190.

[99] S. E. Lazaro, A. Alkaş, S. J. Lee, S. G. Telfer, K. S. Murray, W. Phonsri, P. Harding, D. J. Harding, *Dalton Trans* **2019**, *48*, 15515.

[100] H. Zenno, F. Kobayashi, M. Nakamura, Y. Sekine, L. F. Lindoy, S. Hayami, *Dalton Trans* **2021**, *50*, 7843.

[101] T. Fujinami, M. Koike, N. Matsumoto, Y. Sunatsuki, A. Okazawa, N. Kojima, *Inorg. Chem.* **2014**, *53*, 2254.

[102] H. Hagiwara, N. Matsumoto, S. Iijima, M. Kojima, *Inorganica Chimica Acta* **2011**, *366*, 283.

[103] H. Hagiwara, S. Okada, *Chem. Commun.* **2016**, *52*, 815.

[104] N. Li, J.-P. Xue, J.-L. Liu, Y.-Y. Wang, Z.-S. Yao, J. Tao, *Dalton Trans* **2020**, *49*, 998.

[105] M. Shatruk, H. Phan, B. A. Chrisostomo, A. Suleimenova, *Coordination Chemistry Reviews* **2015**, *289-290*, 62.

[106] B. Weber, W. Bauer, J. Obel, *Angewandte Chemie International Edition* **2008**, *47*, 10098.

[107] B. Weber, W. Bauer, T. Pfaffeneder, M. M. Dîrtu, A. D. Naik, A. Rotaru, Y. Garcia, *Eur. J. Inorg. Chem.* **2011**, *2011*, 3193.

[108] J.-F. Létard, P. Guionneau, E. Codjovi, O. Lavastre, G. Bravic, D. Chasseau, O. Kahn, *J. Am. Chem. Soc.* **1997**, *119*, 10861.

[109] Z. J. Zhong, J.-Q. Tao, Z. Yu, C.-Y. Dun, Y.-J. Liu, X.-Z. You, *J. Chem. Soc., Dalton Trans.* **1998**.

[110] M. Mikami, M. Konno, Y. Saito, *Acta Crystallogr B Struct Sci* **1980**, *36*, 275.

[111] E. Koenig, G. Ritter, S. K. Kulshreshtha, J. Waigel, L. Sacconi, *Inorg. Chem.* **1984**, *23*, 1241.

[112] E. Koenig, G. Ritter, S. K. Kulshreshtha, S. M. Nelson, *Inorg. Chem.* **1982**, *21*, 3022.

[113] M. Sorai, J. Ensling, P. Gütlich, *Chemical Physics* **1976**, *18*, 199.

[114] T. Tayagaki, A. Galet, G. Molnar, M. C. Muñoz, A. Zwick, K. Tanaka, J.-A. Real, A. Bousseksou, *The journal of physical chemistry. B* **2005**, *109*, 14859.

[115] H. Spiering, N. Willenbacher, *J. Phys.: Condens. Matter* **1989**, *1*, 10089.

[116] M. B. Duriska, S. M. Neville, B. Moubaraki, J. D. Cashion, G. J. Halder, K. W. Chapman, C. Balde, J.-F. Létard, K. S. Murray, C. J. Kepert, S. R. Batten, *Angew. Chem.* **2009**, *121*, 2587.

[117] S. Brooker, *Chem. Soc. Rev.* **2015**, *44*, 2880.

[118] M. Sorai, M. Nakano, Y. Miyazaki, *Chem. Rev.* **2006**, *106*, 976.

[119] Z.-Y. Li, J.-W. Dai, Y. Shiota, K. Yoshizawa, S. Kanegawa, O. Sato, *Chem. Eur. J.* **2013**, *19*, 12948.

[120] S. Bonnet, M. A. Siegler, J. S. Costa, G. Molnár, A. Bousseksou, A. L. Spek, P. Gamez, J. Reedijk, *Chemical communications (Cambridge, England)* **2008**.

[121] M. Nihei, H. Tahira, N. Takahashi, Y. Otake, Y. Yamamura, K. Saito, H. Oshio, *J. Am. Chem. Soc.* **2010**, *132*, 3553.

[122] T. Sato, K. Nishi, S. Iijima, M. Kojima, N. Matsumoto, *Inorg. Chem.* **2009**, *48*, 7211.

[123] A. J. Simaan, M.-L. Boillot, E. Rivière, A. Boussac, J.-J. Girerd, *Angew. Chem.* **2000**, *112*, 202.

[124] J. Tang, J. Sánchez Costa, S. Smulders, G. Molnár, A. Bousseksou, S. J. Teat, Y. Li, G. A. van Albada, P. Gamez, J. Reedijk, *Inorg. Chem.* **2009**, *48*, 2128.

[125] B. J. C. Vieira, J. T. Coutinho, I. C. Santos, L. C. J. Pereira, J. C. Waerenborgh, V. da Gama, *Inorg. Chem.* **2013**, *52*, 3845.

[126] D. Chernyshov, M. Hostettler, K. W. Törnroos, H.-B. Bürgi, *Angew. Chem. Int. Ed.* **2003**, *42*, 3825.

[127] M. Yamada, H. Hagiwara, H. Torigoe, N. Matsumoto, M. Kojima, F. Dahan, J.-P. Tuchagues, N. Re, S. Iijima, *Chem. Eur. J.* **2006**, *12*, 4536.

[128] D. Boinnard, A. Bousseksou, A. Dworkin, J. M. Savariault, F. Varret, J. P. Tuchagues, *Inorg. Chem.* **1994**, *33*, 271.

[129] G. S. Matouzenko, D. Luneau, G. Molnár, N. Ould-Moussa, S. Zein, S. A. Borshch, A. Bousseksou, F. Averseng, *European Journal of Inorganic Chemistry* **2006**, *2006*, 2671.

[130] K. Nakano, S. Kawata, K. Yoneda, A. Fuyuhiro, T. Yagi, S. Nasu, S. Morimoto, S. Kaizaki, *Chemical communications (Cambridge, England)* **2004**.

[131] M. H. Klingele, B. Moubaraki, J. D. Cashion, K. S. Murray, S. Brooker, *Chemical communications (Cambridge, England)* **2005**.

[132] J. A. Real, H. Bolvin, A. Bousseksou, A. Dworkin, O. Kahn, F. Varret, J. Zarembowitch, *J. Am. Chem. Soc.* **1992**, *114*, 4650.

[133] A. Craze, M. Bhadbhade, C. Kepert, L. Lindoy, C. Marjo, F. Li, *Crystals* **2018**, *8*, 376.

[134] A. Arroyave, A. Lennartson, A. Dragulescu-Andrasi, K. S. Pedersen, S. Piligkos, S. A. Stoian, S. M. Greer, C. Pak, O. Hietsoi, H. Phan, S. Hill, C. J. McKenzie, M. Shatruk, *Inorg. Chem.* **2016**, *55*, 5904.

[135] N. Paradis, G. Chastanet, J.-F. Létard, *Eur. J. Inorg. Chem.* **2012**, *2012*, 3618.

[136] N. F. Sciortino, S. M. Neville, J.-F. Létard, B. Moubaraki, K. S. Murray, C. J. Kepert, *Inorg. Chem.* **2014**, *53*, 7886.

[137] G. A. Renovitch, W. A. Baker, *J. Am. Chem. Soc.* **1967**, *89*, 6377.

[138] H. Köppen, E. W. Müller, C. P. Köhler, H. Spiering, E. Meissner, P. Gütlich, *Chemical Physics Letters* **1982**, *91*, 348.

[139] C. M. Klug, A. M. McDaniel, S. R. Fiedler, K. A. Schulte, B. S. Newell, M. P. Shores, *Dalton Trans* **2012**, *41*, 12577.

[140] K. Dankhoff, C. Lochenie, F. Puchtler, B. Weber, *Eur. J. Inorg. Chem.* **2016**, *2016*, 2136.

[141] M. B. Duriska, S. M. Neville, B. Moubaraki, J. D. Cashion, G. J. Halder, K. W. Chapman, C. Balde, J.-F. Létard, K. S. Murray, C. J. Kepert, S. R. Batten, *Angewandte Chemie International Edition* **2009**, *48*, 2549.

[142] M. Fumanal, F. Jiménez-Grávalos, J. Ribas-Arino, S. Vela, *Inorg. Chem.* **2017**, *56*, 4475.

[143] D. J. Harding, W. Phonsri, P. Harding, I. A. Gass, K. S. Murray, B. Moubaraki, J. D. Cashion, L. Liu, S. G. Telfer, *Chem. Commun.* **2013**, *49*, 6340.

[144] C. Lochenie, W. Bauer, A. P. Railliet, S. Schlamp, Y. Garcia, B. Weber, *Inorg. Chem.* **2014**, *53*, 11563.

[145] M. Steinert, B. Schneider, S. Dechert, S. Demeshko, F. Meyer, *Inorg. Chem.* **2016**, *55*, 2363.

[146] X.-R. Wu, H.-Y. Shi, R.-J. Wei, J. Li, L.-S. Zheng, J. Tao, *Inorg. Chem.* **2015**, *54*, 3773.

[147] C. Rajadurai, Z. Qu, O. Fuhr, B. Gopalan, R. Kruk, M. Ghafari, M. Ruben, *Dalton Trans* **2007**.

[148] Y.-C. Chuang, C.-T. Liu, C.-F. Sheu, W.-L. Ho, G.-H. Lee, C.-C. Wang, C.-C. Wang, Y. Wang, *Inorg. Chem.* **2012**, *51*, 4663.

[149] M. Bartel, A. Absmeier, G. N. L. Jameson, F. Werner, K. Kato, M. Takata, R. Boca, M. Hasegawa, K. Mereiter, A. Caneschi, W. Linert, *Inorg. Chem.* **2007**, *46*, 4220.

[150] S. Bonnet, G. Molnár, J. Sanchez Costa, M. A. Siegler, A. L. Spek, A. Bousseksou, W.-T. Fu, P. Gamez, J. Reedijk, *Chem. Mater.* **2009**, *21*, 1123.

[151] G. A. Craig, J. S. Costa, O. Roubeau, S. J. Teat, G. Aromí, *Chem. Eur. J.* **2012**, *18*, 11703.

[152] R.-J. Wei, J. Tao, R.-B. Huang, L.-S. Zheng, *Inorg. Chem.* **2011**, *50*, 8553.

[153] W. Zhang, F. Zhao, T. Liu, M. Yuan, Z.-M. Wang, S. Gao, *Inorg. Chem.* **2007**, *46*, 2541.

[154] A. Ferguson, M. A. Squire, D. Siretanu, D. Mitcov, C. Mathonière, R. Clérac, P. E. Kruger, *Chem. Commun.* **2013**, *49*, 1597.

[155] A. M. Greenaway, E. Sinn, *J. Am. Chem. Soc.* **1978**, *100*, 8080.

[156] M. Hostettler, K. W. Törnroos, D. Chernyshov, B. Vangdal, H.-B. Bürgi, *Angew. Chem. Int. Ed.* **2004**, *43*, 4589.

[157] K. A. Schulte, S. R. Fiedler, M. P. Shores, *Aust. J. Chem.* **2014**, *67*, 1595.

[158] A. Lennartson, P. Southon, N. F. Sciortino, C. J. Kepert, C. Frandsen, S. Mørup, S. Piligkos, C. J. McKenzie, *Chem. Eur. J.* **2015**, *21*, 16066.

[159] R. G. Miller, S. Brooker, *Chemical science* **2016**, *7*, 2501.

[160] M. Steinert, B. Schneider, S. Dechert, S. Demeshko, F. Meyer, *Angewandte Chemie International Edition* **2014**, *53*, 6135.

[161] H. Wang, C. Sinito, A. Kaiba, J. S. Costa, C. Desplanches, P. Dagault, P. Guionneau, J.-F. Létard, P. Negrier, D. Mondieig, *Eur. J. Inorg. Chem.* **2014**, *2014*, 4927.

[162] M. J. Murphy, K. A. Zenere, F. Ragon, P. D. Southon, C. J. Kepert, S. M. Neville, *J. Am. Chem. Soc.* **2017**, *139*, 1330.

[163] Y.-Y. Peng, S.-G. Wu, Y.-C. Chen, W. Liu, G.-Z. Huang, Z.-P. Ni, M.-L. Tong, *Inorg. Chem. Front.* **2020**, *7*, 1685.

[164] N. F. Sciortino, K. A. Zenere, M. E. Corrigan, G. J. Halder, G. Chastanet, J.-F. Létard, C. J. Kepert, S. M. Neville, *Chemical science* **2017**, *8*, 701.

[165] C.-J. Zhang, K.-T. Lian, S.-G. Wu, Y. Liu, G.-Z. Huang, Z.-P. Ni, M.-L. Tong, *Inorg. Chem. Front.* **2020**, *7*, 911.

[166] A. Real, J. Zarembowitch, O. Kahn, X. Solans, *Inorg. Chem.* **1987**, *26*, 2939.

[167] A. B. Gaspar, V. Ksenofontov, S. Reiman, P. Gütlich, A. L. Thompson, A. E. Goeta, M. C. Muñoz, J. A. Real, *Chem. Eur. J.* **2006**, *12*, 9289.

[168] A. B. Gaspar, V. Ksenofontov, J. A. Real, P. Gütlich, *Chemical Physics Letters* **2003**, *373*, 385.

[169] V. Ksenofontov, A. B. Gaspar, V. Niel, S. Reiman, J. A. Real, P. Gütlich, *Chem. Eur. J.* **2004**, *10*, 1291.

[170] J. A. Kitchen, J. Olguín, R. Kulmaczewski, N. G. White, V. A. Milway, G. N. L. Jameson, J. L. Tallon, S. Brooker, *Inorg. Chem.* **2013**, *52*, 11185.

[171] Denis Bittner, *1,3,4-Thiadiazol based bis-multidentate ligands for bridged bimetallic complexes with individually adjustable coordination pockets*, Dissertation, Mainz **2018**.

[172] F. Fürmeyer, D. Münzberg, L. M. Carrella, E. Rentschler, *Molecules (Basel, Switzerland)* **2020**, *25*, 855.

[173] L. Salmon, G. Molnár, D. Zitouni, C. Quintero, C. Bergaud, J.-C. Micheau, A. Bousseksou, *J. Mater. Chem.* **2010**, *20*, 5499.

[174] C. M. Quintero, I. A. Gural'skiy, L. Salmon, G. Molnár, C. Bergaud, A. Bousseksou, *J. Mater. Chem.* **2012**, *22*, 3745.

[175] C. A. Tovee, C. A. Kilner, J. A. Thomas, M. A. Halcrow, *CrystEngComm* **2009**, *11*, 2069.

[176] S. Titos-Padilla, J. M. Herrera, X.-W. Chen, J. J. Delgado, E. Colacio, *Angewandte Chemie International Edition* **2011**, *50*, 3290.

[177] R. González-Prieto, B. Fleury, F. Schramm, G. Zoppellaro, R. Chandrasekar, O. Fuhr, S. Lebedkin, M. Kappes, M. Ruben, *Dalton Trans.* **2011**, *40*, 7564.

[178] Y. Garcia, F. Robert, A. D. Naik, G. Zhou, B. Tinant, K. Robeyns, S. Michotte, L. Piraux, *J. Am. Chem. Soc.* **2011**, *133*, 15850.

[179] M. Hasegawa, F. Renz, T. Hara, Y. Kikuchi, Y. Fukuda, J. Okubo, T. Hoshi, W. Linert, *Chemical Physics* **2002**, *277*, 21.

[180] M. Engeser, L. Fabbrizzi, M. Licchelli, D. Sacchi, *Chem. Commun.* **1999**.

[181] C. Edder, C. Piguet, J.-C. G. Bünzli, G. Hopfgartner, *Chem. Eur. J.* **2001**, *7*, 3014.

[182] H. Matsukizono, K. Kuroiwa, N. Kimizuka, *Chem. Lett.* **2008**, *37*, 446.

[183] X. Wang, O. S. Wolfbeis, R. J. Meier, *Chem. Soc. Rev.* **2013**, *42*, 7834.

[184] J. Yuan, M.-J. Liu, S.-Q. Wu, X. Zhu, N. Zhang, O. Sato, H.-Z. Kou, *Inorg. Chem. Front.* **2019**, *6*, 1170.

[185] J. Yuan, S.-Q. Wu, M.-J. Liu, O. Sato, H.-Z. Kou, *J. Am. Chem. Soc.* **2018**, *140*, 9426.

[186] Y. Garcia, V. Ksenofontov, P. Gütlich, *Hyperfine Interactions* **2002**, *139/140*, 543.

[187] J.-F. Létard, P. Guionneau, L. Goux-Capes, in *Spin crossover in transition metal compoundsn3* (Eds.: P. Gütlich, H. A. Goodwin, K. Boukheddaden, P. Gütlich), Springer. Berlin [u.a.] **2004**, p. 221.

[188] S. Sanvito, *Chem. Soc. Rev.* **2011**, *40*, 3336.

[189] B. Benaicha, K. van Do, A. Yangui, N. Pittala, A. Lusson, M. Sy, G. Bouchez, H. Fourati, C. J. Gómez-García, S. Triki, K. Boukheddaden, *Chemical science* **2019**, *10*, 6791.

[190] S. Ghosh, S. Kamilya, T. Pramanik, M. Rouzières, R. Herchel, S. Mehta, A. Mondal, *Inorg. Chem.* **2020**, *59*, 13009.

[191] Helena J. Shepherd, Carlos M. Quintero, Gábor Molnár, Lionel Salmon, Azzedine Bousseksou, in *Spin-Crossover Materials*, John Wiley & Sons, Ltd **2013**, p. 347.

[192] A. Sarkar, S. Dey, G. Rajaraman, *Chem. Eur. J.* **2020**, *26*, 14036.

[193] S. Tripathi, A. Dey, M. Shanmugam, R. S. Narayanan, V. Chandrasekhar, in *Organometallic Magnets*, Vol. 64 (Eds.: V. Chandrasekhar, F. Pointillart), Springer International Publishing. Cham **2019**, p. 35.

[194] P. Zoufalý, E. Čižmár, J. Kuchár, R. Herchel, *Molecules (Basel, Switzerland)* **2020**, *25*.

[195] P. Zoufalý, A. Kliuikov, E. Čižmár, I. Císařová, R. Herchel, *European Journal of Inorganic Chemistry* **2021**, *2021*, 1190.

[196] J. Eppelsheimer, *Eisen(II) Spin-Crossover Verbindungen mit 1,3,4-Oxadiazol-Brückenliganden*, Masterarbeit, Mainz **2017**.

[197] B. Barszcz, M. Gabryszewski, J. Kulig, B. Lenarcik, *J. Chem. Soc., Dalton Trans.* **1986**.

[198] R. Zhang, R. Jordan, O. Nuyken, *Macromol. Rapid Commun.* **2003**, *24*, 246.

[199] S. Liu, L. Zhang, X. Liu, *New J. Chem.* **2013**, *37*, 821.

[200] Lasse Moormann, *Auswirkungen von 1,3,4-Oxadiazolen auf das Spin-Crossover-Verhalten von dinuklearen Eisen(II)- und Cobalt(II)-Verbindungen*, Bachelorarbeit, Mainz **2018**.

[201] N. F. Chilton, R. P. Anderson, L. D. Turner, A. Soncini, K. S. Murray, *Journal of computational chemistry* **2013**, *34*, 1164.

[202] B. Ding, Y. Y. Liu, Y. Wang, J.-G. Ma, Z. Niu, W. Shi, P. Cheng, *Inorganic Chemistry Communications* **2013**, *31*, 44.

[203] J. A. Kitchen, A. Noble, C. D. Brandt, B. Moubaraki, K. S. Murray, S. Brooker, *Inorg. Chem.* **2008**, *47*, 9450.

[204] A.-M. Li, T. Hochdörffer, J. Wolny, V. Schünemann, E. Rentschler, *Magnetochemistry* **2018**, *4*, 34.

[205] A.-M. Li, T. Hochdörffer, J. A. Wolny, V. Schünemann, E. Rentschler, *Eur. J. Inorg. Chem.* **2018**, *2018*, 4190.

[206] K. Nakano, N. Suemura, S. Kawata, A. Fuyuhiro, T. Yagi, S. Nasu, S. Morimoto, S. Kaizaki, *Dalton transactions (Cambridge, England 2003)* **2004**.

[207] A. Noble, J. Olguín, R. Clérac, S. Brooker, *Inorg. Chem.* **2010**, *49*, 4560.

[208] O. Roubeau, P. Gamez, S. J. Teat, *Eur. J. Inorg. Chem.* **2013**, *2013*, 934.

[209] I. Sánchez-Molina, A. Moneo-Corcuera, D. Nieto-Castro, J. Benet-Buchholz, J. R. Galán-Mascarós, *European Journal of Inorganic Chemistry* **2021**, *2021*, 112.

[210] C. J. Schneider, J. D. Cashion, B. Moubaraki, S. M. Neville, S. R. Batten, D. R. Turner, K. S. Murray, *Polyhedron* **2007**, *26*, 1764.

[211] H. S. Scott, T. M. Ross, B. Moubaraki, K. S. Murray, S. M. Neville, *Eur. J. Inorg. Chem.* **2013**, *2013*, 803.

[212] S. Zaiter, C. Kirk, M. Taylor, Y. M. Klein, C. E. Housecroft, N. F. Sciortino, J. E. Clements, R. I. Cooper, C. J. Kepert, S. M. Neville, *Dalton transactions (Cambridge, England 2003)* **2019**, *48*, 7337.

[213] H. Zabrodsky, S. Peleg, D. Avnir, *J. Am. Chem. Soc.* **1992**, *114*, 7843.

[214] S. Alvarez, D. Avnir, M. Llunell, M. Pinsky, *New J. Chem.* **2002**, *26*, 996.

[215] M. Andersson Trojer, A. Movahedi, H. Blanck, M. Nydén, *Journal of Chemistry* **2013**, *2013*, 1.

[216] G. F. Svatos, C. Curran, J. V. Quagliano, *J. Am. Chem. Soc.* **1955**, *77*, 6159.

[217] M. V. Stackelberg, *Z. Anorg. Chem.* **1947**, *253*, 136.

[218] J. Fujita, K. Nakamoto, M. Kobayashi, *J. Am. Chem. Soc.* **1956**, *78*, 3295.

[219] V. Kumar, V. Kumar, N. Upadhyay, S. Sharma, *3 Biotech* **2015**, *5*, 791.

[220] M. Boumediene, B. Haddad, A. Paolone, M. Drai, D. Villemin, M. Rahmouni, S. Bresson, O. Abbas, *Journal of Molecular Structure* **2019**, *1186*, 68.

[221] N. E. Heimer, R. E. Del Sesto, Z. Meng, J. S. Wilkes, W. R. Carper, *Journal of Molecular Liquids* **2006**, *124*, 84.

[222] R. L. Hunt, B. S. Ault, *Spectrochimica Acta Part A: Molecular Spectroscopy* **1981**, *37*, 63.

[223] S. A. Katsyuba, E. E. Zvereva, A. Vidis, P. J. Dyson, *The Journal of Physical Chemistry A* **2007**, *111*, 352.

[224] Y. Chen, Y.-H. Zhang, L.-J. Zhao, *Phys. Chem. Chem. Phys.* **2004**, *6*, 537.

[225] J. L. Bishop, R. Quinn, M. D. Dyar, *The American mineralogist* **2014**, *99*, 1580.

[226] J. Hanley, V. F. Chevrier, R. S. Barrows, C. Swaffer, T. S. Altheide, *J. Geophys. Res. Planets* **2015**, *120*, 1415.

[227] AGARWAL R.K., KUMAR A., *SYNTHESIS, PHYSICO-CHEMICAL AND BIOLOGICAL PROPERTIES OF SOME MIXED LIGAND COMPLEXES OF TRIVALENT LANTHANIDES WITH 4 [N-4'-DIMETHYLAMINO-BENZALIDENE)AMINO] ANTIPYRINETHIOSEMICARBAZONE AND PYRIDINE*, JOURNAL OF APPLIED CHEMICAL RESEARCH (JACR) **2011**.

[228] W. Harhouri, C. Mchiri, S. Najmudin, C. Bonifácio, H. Nasri, *Acta Crystallographica Section E: Crystallographic Communications* **2016**, *72*, 720.

[229] D. H. Johnston, D. F. Shriver, *Inorg. Chem.* **1993**, *32*, 1045.

[230] N. N. Mobarak, N. Ramli, M. P. Abdullah, A. Ahmad, AIP Publishing LLC **2013**, p. 843.

[231] J. M. Alía, Y. Díaz^de Mera, H. Edwards, F. J. García, E. E. Lawson, *Journal of Molecular Structure* **1997**, *408-409*, 439.

[232] R. J. Sundberg, R. B. Martin, *Chem. Rev.* **1974**, *74*, 471.

[233] S. J. Grabowski, *Crystals* **2020**, *10*, 460.

[234] C. G. Marcellus, R. T. Oakley, A. W. Cordes, W. T. Pennington, *Can. J. Chem.* **1984**, *62*, 1822.

[235] A. Kálmán, L. Párkányi, G. Argay, *Acta Cryst B* **1993**, *49*, 1039.

[236] N. Qureshi, D. S. Yufit, K. M. Steed, J. A. K. Howard, J. W. Steed, *CrystEngComm* **2016**, *18*, 5333.

[237] J. Reedijk, *Recl. Trav. Chim. Pays-Bas* **1969**, *88*, 1451.

[238] I. Boldog, A. B. Gaspar, V. Martínez, P. Pardo-Ibañez, V. Ksenofontov, A. Bhattacharjee, P. Gütlich, J. A. Real, *Angewandte Chemie International Edition* **2008**, *47*, 6433.

[239] M. M. Khusniyarov, *Chemistry (Weinheim an der Bergstrasse, Germany)* **2016**, *22*, 15178.

[240] I. Šalitroš, N. T. Madhu, R. Boča, J. Pavlik, M. Ruben, *Monatsh Chem* **2009**, *140*, 695.

[241] T. J. Donohoe, D. J. Johnson, L. H. Mace, R. E. Thomas, J. Y. K. Chiu, J. S. Rodrigues, R. G. Compton, C. E. Banks, P. Tomcik, M. J. Bamford, O. Ichihara, *Organic & biomolecular chemistry* **2006**, *4*, 1071.

[242] R. J. Sundberg, S. Jiang, *Organic Preparations and Procedures International* **1997**, *29*, 117.

[243] H. Fuchida, S. Tabata, N. Shindo, I. Takashima, Q. Leng, Y. Hatsuyama, I. Hamachi, A. Ojida, *BCSJ* **2015**, *88*, 784.

[244] J. G. Lewis, D.V. Patel, S. K. Anandan, M. F. Gordeev, *LINCOMYCIN DERIVATIVES POSSESSING ANTIBACTERIAL ACTIVITY: Patent Application Publication* **2004**.

[245] D. T. Clark, J. N. Murrell, J. M. Tedder, *J. Chem. Soc.* **1963**.

[246] T. J. Donohoe, M. J. Connolly, L. Walton, *Organic letters* **2009**, *11*, 5562.

[247] Patrick Schafforz, *Koordinative Verknüpfung von 1,3,4-Oxadiazol-basierten Eisen(II)-Spin-Crossover Verbindungen*, Bachelorarbeit, Mainz **2019**.

[248] H. L. C. Feltham, M. G. Cowan, J. A. Kitchen, G. N. L. Jameson, S. Brooker, *Supramolecular Chemistry* **2018**, *30*, 296.

[249] XENON PHARMACEUTICALS INC., S. LIU, T. FOCKEN, N. CHAHAL, Z. ZHANG, OBALLA, Renata, Marcella, J. FONAREV, *BIARYL ETHER SULFONAMIDES AND THEIR USE AS THERAPEUTIC AGENTS* **2013**.

[250] H. R. Ing, R. H. F. Manske, *J. Chem. Soc.* **1926**, *129*, 2348.

[251] P. T. Muthiah, B. Umadevi, N. Stanley, G. Bocelli, A. Cantoni, *Acta Crystallogr E Struct Rep Online* **2002**, *58*, o59-o61.

[252] E. C. Constable, G. Baum, E. Bill, R. Dyson, R. van Eldik, D. Fenske, S. Kaderli, D. Morris, A. Neubrand, M. Neuburger, D. R. Smith, K. Wieghardt, M. Zehnder, A. D. Zuberbühler, *Chem. Eur. J.* **1999**, *5*, 498.

[253] J. Elhaik, D. J. Evans, C. A. Kilner, M. A. Halcrow, *Dalton transactions (Cambridge, England 2003)* **2005**.

[254] V. Martínez, A. B. Gaspar, M. C. Muñoz, G. V. Bukin, G. Levchenko, J. A. Real, *Chemistry (Weinheim an der Bergstrasse, Germany)* **2009**, *15*, 10960.

[255] M. G. Simmons, L. J. Wilson, *Inorg. Chem.* **1977**, *16*, 126.

[256] H.-J. Lin, D. Siretanu, D. A. Dickie, D. Subedi, J. J. Scepaniak, D. Mitcov, R. Clérac, J. M. Smith, *J. Am. Chem. Soc.* **2014**, *136*, 13326.

[257] J. G. Park, I.-R. Jeon, T. D. Harris, *Inorg. Chem.* **2015**, *54*, 359.

[258] B. J. Houghton, R. J. Deeth, *Eur. J. Inorg. Chem.* **2014**, *2014*, 4573.

[259] K. Nakano, N. Suemura, K. Yoneda, S. Kawata, S. Kaizaki, *Dalton transactions (Cambridge, England 2003)* **2005**.

[260] I. Prat, A. Company, T. Corona, T. Parella, X. Ribas, M. Costas, *Inorg. Chem.* **2013**, *52*, 9229.

[261] M. F. Tweedle, L. J. Wilson, *J. Am. Chem. Soc.* **1976**, *98*, 4824.

[262] L. J. Kershaw Cook, R. Kulmaczewski, R. Mohammed, S. Dudley, S. A. Barrett, M. A. Little, R. J. Deeth, M. A. Halcrow, *Angewandte Chemie International Edition* **2016**, *55*, 4327.

[263] L. P. Hammett, *J. Am. Chem. Soc.* **1937**, *59*, 96.

[264] C. Hansch, A. Leo, R. W. Taft, *Chem. Rev.* **1991**, *91*, 165.

[265] S. Ranjan, R. Devarapalli, S. Kundu, S. Saha, S. Deolka, V. R. Vangala, C. M. Reddy, *IUCrJ* **2020**, *7*, 173.

[266] M. A. Oliveira, M. L. Peterson, D. Klein, *Crystal Growth & Design* **2008**, *8*, 4487.

[267] P. A. Wood, M. A. Oliveira, A. Zink, M. B. Hickey, *CrystEngComm* **2012**, *14*, 2413.

[268] K. Takahashi, Y. Hasegawa, R. Sakamoto, M. Nishikawa, S. Kume, E. Nishibori, H. Nishihara, *Inorg. Chem.* **2012**, *51*, 5188.

[269] L. J. K. Cook, F. Tuna, M. A. Halcrow, *Dalton transactions (Cambridge, England 2003)* **2013**, *42*, 2254.

[270] B. A. Leita, S. M. Neville, G. J. Halder, B. Moubaraki, C. J. Kepert, J.-F. Létard, K. S. Murray, *Inorg. Chem.* **2007**, *46*, 8784.

[271] B. J. Childs, D. C. Craig, K. A. Ross, M. L. Scudder, H. A. Goodwin, *Aust. J. Chem.* **1994**, *47*, 891.

[272] R. J. Smithson, C. A. Kilner, A. R. Brough, M. A. Halcrow, *Polyhedron* **2003**, *22*, 725.

[273] Z. Yan, J.-Y. Li, T. Liu, Z.-P. Ni, Y.-C. Chen, F.-S. Guo, M.-L. Tong, *Inorg. Chem.* **2014**, *53*, 8129.

[274] R. Mohammed, G. Chastanet, F. Tuna, T. L. Malkin, S. A. Barrett, C. A. Kilner, J.-F. Létard, M. A. Halcrow, *Eur. J. Inorg. Chem.* **2013**, *2013*, 819.

[275] J. England, R. Gondhia, L. Bigorra-Lopez, A. R. Petersen, A. J. P. White, G. J. P. Britovsek, *Dalton transactions (Cambridge, England 2003)* **2009**.

[276] K. B. Wiberg, D. Nakaji, C. M. Breneman, *J. Am. Chem. Soc.* **1989**, *111*, 4178.

[277] H. L. Feltham, A. S. Barltrop, S. Brooker, *Coordination Chemistry Reviews* **2017**, *344*, 26.

[278] Y. Uto, Y. Ueno, Y. Kiyotsuka, Y. Miyazawa, H. Kurata, T. Ogata, M. Yamada, T. Deguchi, M. Konishi, T. Takagi, S. Wakimoto, J. Ohsumi, *European Journal of Medicinal Chemistry* **2010**, *45*, 4788.

[279] R. C. Storr, T. L. Gilchrist (Eds.), *Hetarenes and related ring systems*, G. Thieme, Stuttgart **2004**.

[280] M. J. Taschner, in *Encyclopedia of reagents for organic synthesis*, Wiley. Chichester **1995**.

[281] P. Brown, D. J. Best, N. J. Broom, R. Cassels, P. J. O'Hanlon, T. J. Mitchell, N. F. Osborne, J. M. Wilson, *Journal of medicinal chemistry* **1997**, *40*, 2563.

[282] M. G. Thomas, M. de Rycker, R. J. Wall, D. Spinks, O. Epemolu, S. Manthri, S. Norval, M. Osuna-Cabello, S. Patterson, J. Riley, F. R. C. Simeons, L. Stojanovski, J. Thomas, S. Thompson, C. Naylor, J. M. Fiandor, P. G. Wyatt, M. Marco, S. Wyllie, K. D. Read, T. J. Miles, I. H. Gilbert, *Journal of medicinal chemistry* **2020**, *63*, 9523.

[283] K. S. Kumar, M. Ruben, *Angewandte Chemie International Edition* **2021**, *60*, 7502.

[284] J.-Q. Tao, Z.-G. Gu, T.-W. Wang, Q.-F. Yang, J.-L. Zuo, X.-Z. You, *Inorganica Chimica Acta* **2007**, *360*, 4125.

[285] B. Pinter, V. van Speybroeck, M. Waroquier, P. Geerlings, F. de Proft, *Phys. Chem. Chem. Phys.* **2013**, *15*, 17354.

[286] C. A. Hunter, J. K. M. Sanders, *J. Am. Chem. Soc.* **1990**, *112*, 5525.

[287] A. Banerjee, A. Saha, B. K. Saha, *Crystal Growth & Design* **2019**, *19*, 2245.

[288] M. J. Calhorda, *Chem. Commun.* **2000**.

[289] Christoph Janiak, Savas¸ Temizdemir, Sebastian Dechert, Werner Deck, Frank Girgsdies, Jürgen Heinze, Mario J. Kolm, Tobias G. Scharmann, Oliver M. Zipffel, *European Journal of Inorganic Chemistry* **2000**, *2000*, 1229.

[290] J. F. Malone, C. M. Murray, M. H. Charlton, R. Docherty, A. J. Lavery, *Faraday Trans.* **1997**, *93*, 3429.

[291] Y. Umezawa, S. Tsuboyama, K. Honda, J. Uzawa, M. Nishio, *BCSJ* **1998**, *71*, 1207.

[292] N. J. Higdon, A. T. Barth, P. T. Kozlowski, R. G. Hadt, *The Journal of chemical physics* **2020**, *152*, 204306.

[293] Hoon Choi, Wheesahng Yun, Jung-hun Lee, Seoul Jang, Sang Won Park, Dong Hwan Kim, Kyoung Pyo Seon, Jung-mi Hyun, Kwiwan Jeong, Jin-mo Ku, Tae-gyu Nam, *Med Chem Res* **2019**, *28*, 2142.

[294] R. Boča, *Coordination Chemistry Reviews* **2004**, *248*, 757.

[295] P. Guionneau, *Dalton Trans* **2014**, *43*, 382.

[296] R. F. Mueller, in *Mineralogy*, Kluwer Academic Publishers. Dordrecht **1981**, p. 344.

[297] A. L. Spek, *Acta Crystallogr C Struct Chem* **2015**, *71*, 9.

[298] W.-Q. Gao, Y.-S. Meng, C.-H. Liu, Y. Pan, T. Liu, Y.-Y. Zhu, *Dalton Trans.* **2019**, *48*, 6323.

[299] A. D. Schwarz, Z. Chu, P. Mountford, *Organometallics* **2010**, *29*, 1246.

[300] A. D. Schwarz, A. L. Thompson, P. Mountford, *Inorg. Chem.* **2009**, *48*, 10442.

[301] E. Hao, Z. Wang, L. Jiao, S. Wang, *Dalton Trans* **2010**, *39*, 2660.

[302] M. Balamurugan, R. Mayilmurugan, E. Suresh, M. Palaniandavar, *Dalton Trans* **2011**, *40*, 9413.

[303] T. Nagataki, Y. Tachi, S. Itoh, *Chemical communications (Cambridge, England)* **2006**.

[304] T. Nagataki, K. Ishii, Y. Tachi, S. Itoh, *Dalton Trans* **2007**.

[305] T. Nagataki, S. Itoh, *Chem. Lett.* **2007**, *36*, 748.

[306] Y. Morimoto, S. Bunno, N. Fujieda, H. Sugimoto, S. Itoh, *J. Am. Chem. Soc.* **2015**, *137*, 5867.

[307] F. Li, M. Wang, C. Ma, A. Gao, H. Chen, L. Sun, *Dalton Trans* **2006**.

[308] I. Terao, S. Horii, J. Nakazawa, M. Okamura, S. Hikichi, *Dalton Trans* **2020**, *49*, 6108.

[309] R. D. Hancock, A. E. Martell, *Comments on Inorganic Chemistry* **1988**, *6*, 237.

[310] Y. Galyametdinov, V. Ksenofontov, A. Prosvirin, I. Ovchinnikov, G. Ivanova, P. Gütlich, W. Haase, *Angew. Chem. Int. Ed.* **2001**, *40*, 4269.

[311] I. Gudyma, K. Boboshko, K. Boukheddaden, *Physics Letters A* **2020**, *384*, 126677.

[312] A. Rotaru, I. A. Gural'skiy, G. Molnár, L. Salmon, P. Demont, A. Bousseksou, *Chem. Commun.* **2012**, *48*, 4163.

[313] Y. Jiao, J. Zhu, Y. Guo, W. He, Z. Guo, *J. Mater. Chem. C* **2017**, *5*, 5214.

[314] C. Lochenie, K. Schötz, F. Panzer, H. Kurz, B. Maier, F. Puchtler, S. Agarwal, A. Köhler, B. Weber, *J. Am. Chem. Soc.* **2018**, *140*, 700.

[315] C.-F. Wang, M.-J. Sun, Q.-J. Guo, Z.-X. Cao, L.-S. Zheng, J. Tao, *Chem. Commun.* **2016**, *52*, 14322.

[316] I. B. Berlman, A. Weinreb, *Molecular Physics* **1962**, *5*, 313.

[317] F. M. Behlen, D. B. McDonald, V. Sethuraman, S. A. Rice, *The Journal of chemical physics* **1981**, *75*, 5685.

[318] G. Grabner, K. Rechthaler, B. Mayer, G. Köhler, K. Rotkiewicz, *The Journal of Physical Chemistry A* **2000**, *104*, 1365.

[319] J. B. Aladekomo, J.B. Birks, *Proc. R. Soc. Lond. A* **1965**, *284*, 551.

[320] N. Mataga, M. Tomura, H. Nishimura, *Molecular Physics* **1965**, *9*, 367.

[321] C. A. Parker, *Spectrochimica Acta* **1963**, *19*, 989.

[322] L. Ma, L. Yuan, C. Xu, G. Li, M. Tao, W. Zhang, *Synthesis* **2012**, *45*, 45.

[323] P. A. Joy, P. S. A. Kumar, S. K. Date, *J. Phys.: Condens. Matter* **1998**, *10*, 11049.

[324] E. D. Amstutz, *J. Org. Chem.* **1952**, *17*, 1508.

[325] H. Maeda, T. Maeda, K. Mizuno, *Molecules (Basel, Switzerland)* **2012**, *17*, 5108.

[326] A. Paun, C. Paraschivescu, M. Matache, V. Parvulescu, *Synthesis* **2016**, *48*, 606.

[327] T. Reuter, A. Kruse, R. Schoch, S. Lochbrunner, M. Bauer, K. Heinze, *Chem. Commun.* **2021**, *57*, 7541.

[328] S. M. Fatur, S. G. Shepard, R. F. Higgins, M. P. Shores, N. H. Damrauer, *J. Am. Chem. Soc.* **2017**, *139*, 4493.

[329] J. D. Braun, I. B. Lozada, C. Kolodziej, C. Burda, K. M. E. Newman, J. van Lierop, R. L. Davis, D. E. Herbert, *Nat. Chem.* **2019**, *11*, 1144.

[330] W. Zhang, K. S. Kjær, R. Alonso-Mori, U. Bergmann, M. Chollet, L. A. Fredin, R. G. Hadt, R. W. Hartsock, T. Harlang, T. Kroll, K. Kubiček, H. T. Lemke, H. W. Liang, Y. Liu, M. M. Nielsen, P. Persson, J. S. Robinson, E. I. Solomon, Z. Sun, D. Sokaras, T. B. van Driel, T.-C. Weng, D. Zhu, K. Wärnmark, V. Sundström, K. J. Gaffney, *Chemical science* **2017**, *8*, 515.

[331] S. Furukawa, Y. Hitomi, T. Shishido, T. Tanaka, *Inorganica Chimica Acta* **2011**, *378*, 19.

[332] Y. Hitomi, S. Furukawa, M. Higuchi, T. Shishido, T. Tanaka, *Journal of Molecular Catalysis A: Chemical* **2008**, *288*, 83.

[333] C. Kim, K. Chen, J. Kim, L. Que, *J. Am. Chem. Soc.* **1997**, *119*, 5964.

[334] G. Bhosekar, J. Boeckmann, I. Jeß, C. Näther, *Z. anorg. allg. Chem.* **2010**, *636*, 2595.

[335] S. De, S. Tewary, D. Garnier, Y. Li, G. Gontard, L. Lisnard, A. Flambard, F. Breher, M.-L. Boillot, G. Rajaraman, R. Lescouëzec, *Eur. J. Inorg. Chem.* **2018**, *2018*, 414.

[336] W. Nicolazzi, A. Bousseksou, *Comptes Rendus Chimie* **2018**, *21*, 1060.

[337] W. Yang, X. Chen, H. Su, W. Fang, Y. Zhang, *Chem. Commun.* **2015**, *51*, 9616.

[338] A. T. Wrobel, T. C. Johnstone, A. Deliz Liang, S. J. Lippard, P. Rivera-Fuentes, *J. Am. Chem. Soc.* **2014**, *136*, 4697.

[339] J. Rosenthal, S. J. Lippard, *J. Am. Chem. Soc.* **2010**, *132*, 5536.

[340] V. V. Volchkov, V. L. Ivanov, B. M. Uzhinov, *J Fluoresc* **2010**, *20*, 299.

[341] J. H. Chang, Y. M. Choe, Y. G. Sin, *Bulletin of the Korean Chemical Society* **2001**, *22*, 527.

[342] J. Acharya, A. Swain, A. Chakraborty, V. Kumar, P. Kumar, J. F. Gonzalez, O. Cador, F. Pointillart, G. Rajaraman, V. Chandrasekhar, *Inorg. Chem.* **2019**, *58*, 10725.

[343] D. Sertphon, K. S. Murray, W. Phonsri, J. Jover, E. Ruiz, S. G. Telfer, A. Alkaş, P. Harding, D. J. Harding, *Dalton Trans* **2018**, *47*, 859.

[344] J. Matsumoto, T. Suzuki, Y. Kajita, H. Masuda, *Dalton Trans* **2012**, *41*, 4107.

[345] J. Vallejo, I. Castro, R. Ruiz-García, J. Cano, M. Julve, F. Lloret, G. de Munno, W. Wernsdorfer, E. Pardo, *J. Am. Chem. Soc.* **2012**, *134*, 15704.

[346] A. V. Palii, D. V. Korchagin, E. A. Yureva, A. V. Akimov, E. Y. Misochko, G. V. Shilov, A. D. Talantsev, R. B. Morgunov, S. M. Aldoshin, B. S. Tsukerblat, *Inorg. Chem.* **2016**, *55*, 9696.

[347] F. Lloret, M. Julve, J. Cano, R. Ruiz-García, E. Pardo, *Inorganica Chimica Acta* **2008**, *361*, 3432.

[348] R. Herchel, L. Váhovská, I. Potočňák, Z. Trávníček, *Inorg. Chem.* **2014**, *53*, 5896.

[349] J. S. Griffith, *The theory of transition-metal ions*, Cambridge University Press, Cambridge **2009**.

[350] B. N. Figgis, M. Gerloch, J. Lewis, F. E. Mabbs, G. A. Webb, *J. Chem. Soc., A* **1968**.

[351] A. S. Chakravarty, *Introduction to the magnetic properties of solids*, Wiley, New York **1980**.

[352] S. Sugano, R. G. Shulman, *Phys. Rev.* **1963**, *130*, 517.

[353] A. Earnshaw, *Introduction to Magnetochemistry*, Elsevier Science, Burlington **1968**.

[354] S. Gómez-Coca, A. Urtizberea, E. Cremades, P. J. Alonso, A. Camón, E. Ruiz, F. Luis, *Nat Commun* **2014**, *5*, 4300.

[355] S. Mandal, S. Mondal, C. Rajnák, J. Titiš, R. Boča, S. Mohanta, *Dalton Trans* **2017**, *46*, 13135.

[356] D. Aravena, D. Venegas-Yazigi, E. Ruiz, *Inorg. Chem.* **2016**, *55*, 6405.

[357] M. A. Palacios, J. Nehrkorn, E. A. Suturina, E. Ruiz, S. Gómez-Coca, K. Holldack, A. Schnegg, J. Krzystek, J. M. Moreno, E. Colacio, *Chem. Eur. J.* **2017**, *23*, 11649.

[358] C. Rajnák, F. Varga, J. Titiš, J. Moncol, R. Boča, *Inorg. Chem.* **2018**, *57*, 4352.

[359] D. Reta, N. F. Chilton, *Phys. Chem. Chem. Phys.* **2019**, *21*, 23567.

[360] A. Abragam, B. Bleaney, *Electron paramagnetic resonance of transition ions*, Clarendon Press, Oxford **2013**.

[361] C. V. Topping, S. J. Blundell, *J. Phys.: Condens. Matter* **2019**, *31*, 13001.

[362] K. Uchida, G. Cosquer, K. Sugisaki, H. Matsuoka, K. Sato, B. K. Breedlove, M. Yamashita, *Dalton Trans* **2019**, *48*, 12023.

[363] T. T. da Cunha, V. M. M. Barbosa, W. X. C. Oliveira, E. F. Pedroso, D. M. A. García, W. C. Nunes, C. L. M. Pereira, *Inorg. Chem.* **2020**, *59*, 12983.

[364] A. W. Addison, T. N. Rao, J. Reedijk, J. van Rijn, G. C. Verschoor, *J. Chem. Soc., Dalton Trans.* **1984**.

[365] S. S. Massoud, R. C. Fischer, F. A. Mautner, M. M. Parfait, R. Herchel, Z. Trávníček, *Inorganica Chimica Acta* **2018**, *471*, 630.

[366] I. Nemec, H. Liu, R. Herchel, X. Zhang, Z. Trávníček, *Synthetic Metals* **2016**, *215*, 158.

[367] J.-W. Lim, M. Mikuriya, H. Sakiyama, *BCSJ* **2001**, *74*, 2131.

[368] L. Sacconi, *Pure and Applied Chemistry* **1968**, *17*, 95.

[369] M. A. Hay, A. Sarkar, G. A. Craig, L. Bhaskaran, J. Nehrkorn, M. Ozerov, K. E. R. Marriott, C. Wilson, G. Rajaraman, S. Hill, M. Murrie, *Chemical science* **2019**, *10*, 6354.

[370] L. Banci, A. Bencini, C. Benelli, D. Gatteschi, C. Zanchini, in *Structures versus Special Properties*, Vol. 52, Springer Berlin Heidelberg. Berlin, Heidelberg **1982**, p. 37.

[371] N. Nijegorodov, R. Mabbs, *Spectrochimica Acta Part A: Molecular and Biomolecular Spectroscopy* **2002**, *58*, 349.

[372] W. R. Dawson, M. W. Windsor, *J. Phys. Chem.* **1968**, *72*, 3251.

[373] M. Stradiotto, R. Lundgren, *Ligand design in metal chemistry: Reactivity and catalysis*, Wiley, Chichester, West Sussex, UK **2016**.

[374] D. Wang, E. R. Farquhar, A. Stubna, E. Münck, L. Que, *Nat. Chem.* **2009**, *1*, 145.

[375] Y. Feng, C. Ke, G. Xue, L. Que, *Chemical communications (Cambridge, England)* **2009**.

[376] A. Bravo, H.-R. Bjorsvik, F. Fontana, F. Minisci, A. Serri, *J. Org. Chem.* **1996**, *61*, 9409.

[377] G. M. Sheldrick, *Acta Cryst A* **2015**, *71*, 3.

[378] G. M. Sheldrick, *Acta Crystallogr A Found Crystallogr* **2008**, *64*, 112.

[379] S. Fortier, *Direct Methods for Solving Macromolecular Structures*, Springer Netherlands, Dordrecht **1998**.

[380] G. M. Sheldrick, *Acta Crystallogr C Struct Chem* **2015**, *71*, 3.

[381] O. V. Dolomanov, L. J. Bourhis, R. J. Gildea, J. A. K. Howard, H. Puschmann, *J Appl Crystallogr* **2009**, *42*, 339.

[382] *Spin-Crossover Materials*, John Wiley & Sons, Ltd **2013**.

Appendix

A IR Spectra

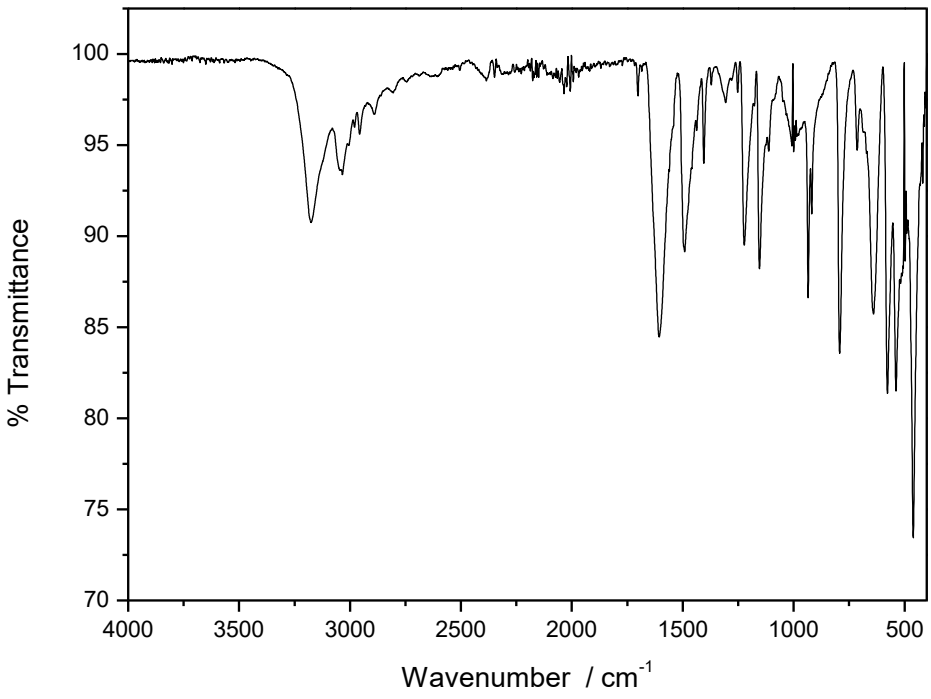


Figure A.1 IR spectrum of 1,2-Bis(chloroacetyl)hydrazide (**1**).

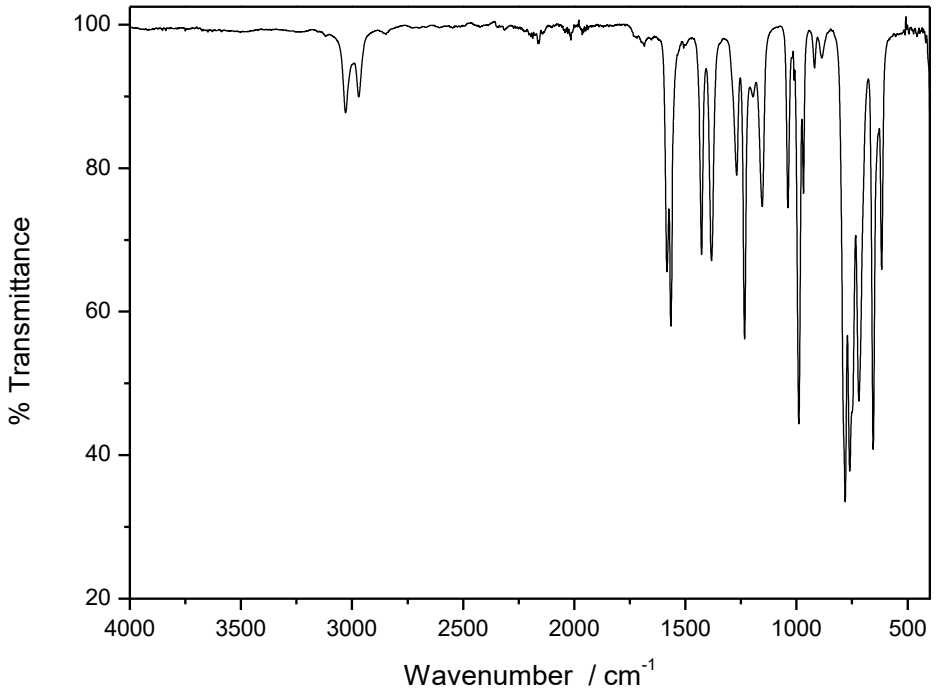


Figure A.2 IR spectrum of 2,5-Bis(chloromethyl)-1,3,4-oxadiazole (**2**).

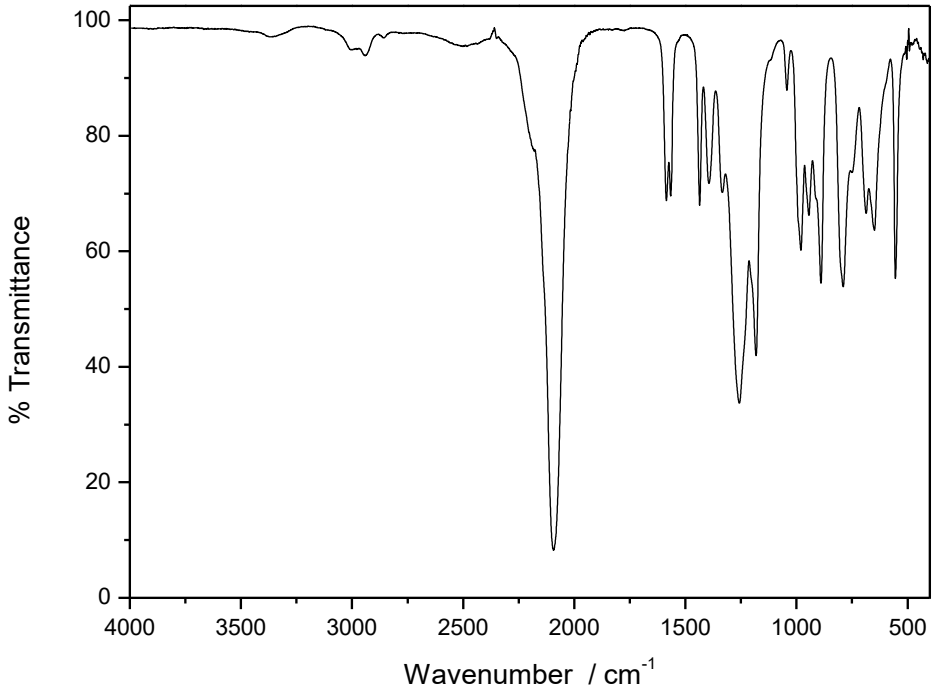


Figure A.3 IR spectrum of 2,5-Bis(azidomethyl)-1,3,4-oxadiazole (**3**).

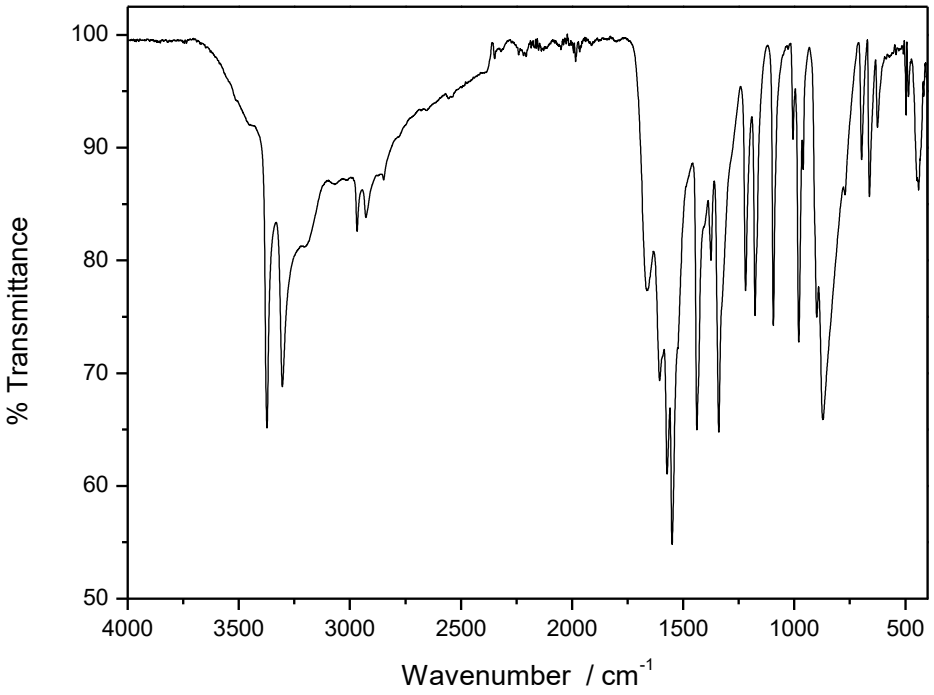


Figure A.4 IR spectrum of 2,5-Bis(aminomethyl)-1,3,4-oxadiazole (**4**).

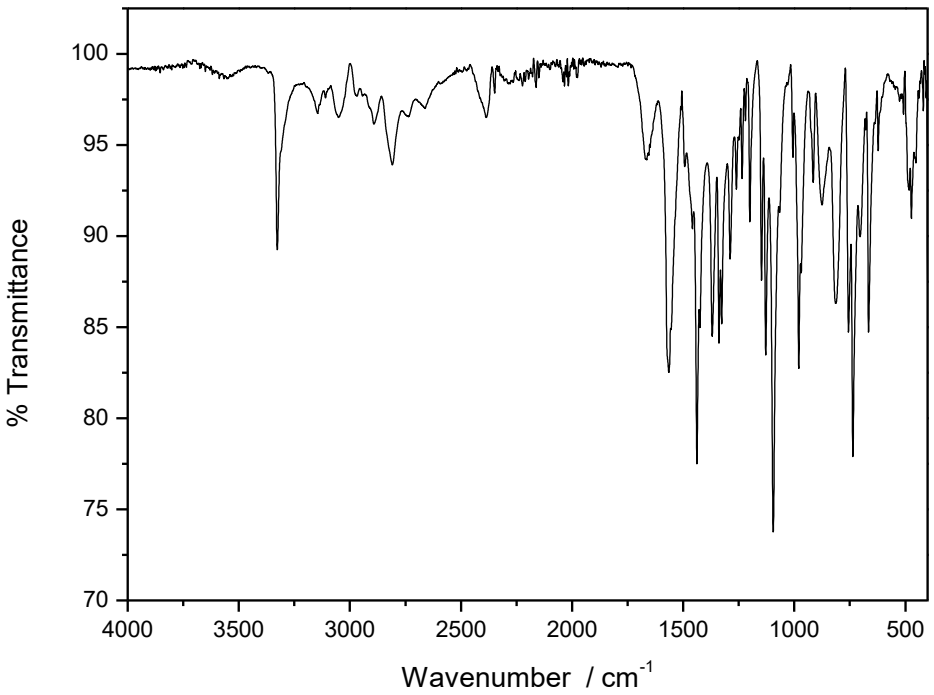


Figure A.5 IR spectrum of 2,5-Bis[(1*H*-imidazol-2-ylmethyl)amino]methyl-1,3,4-oxadiazole ($\mathbf{L^{5,Im}}$).

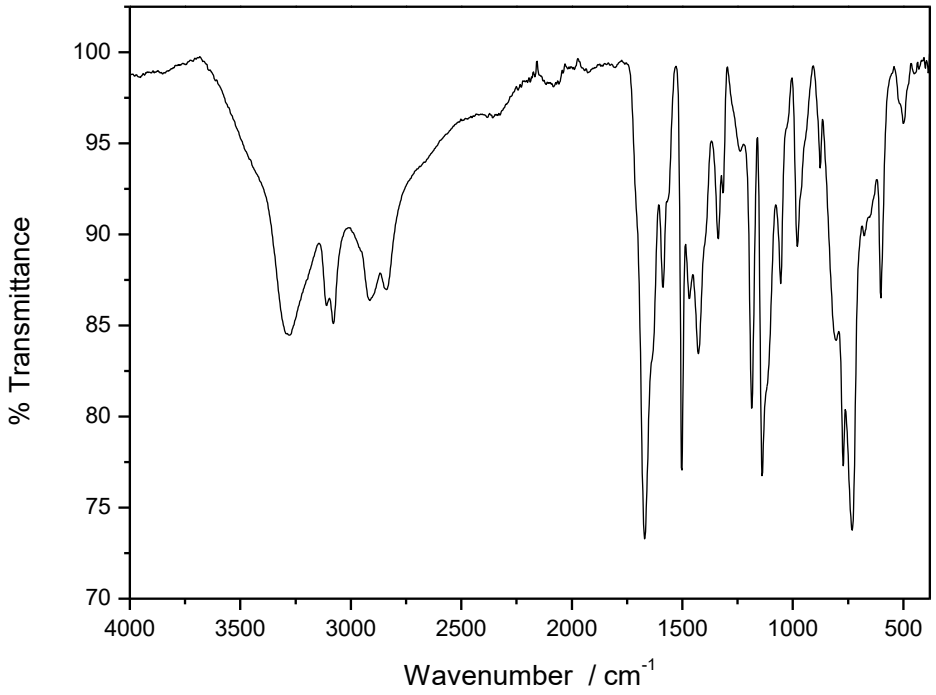


Figure A.6 IR spectrum of 2,5-Bis[(1,3-thiazol-2-ylmethyl)amino]methyl-1,3,4-oxadiazole ($\mathbf{L^{5,TA}}$).

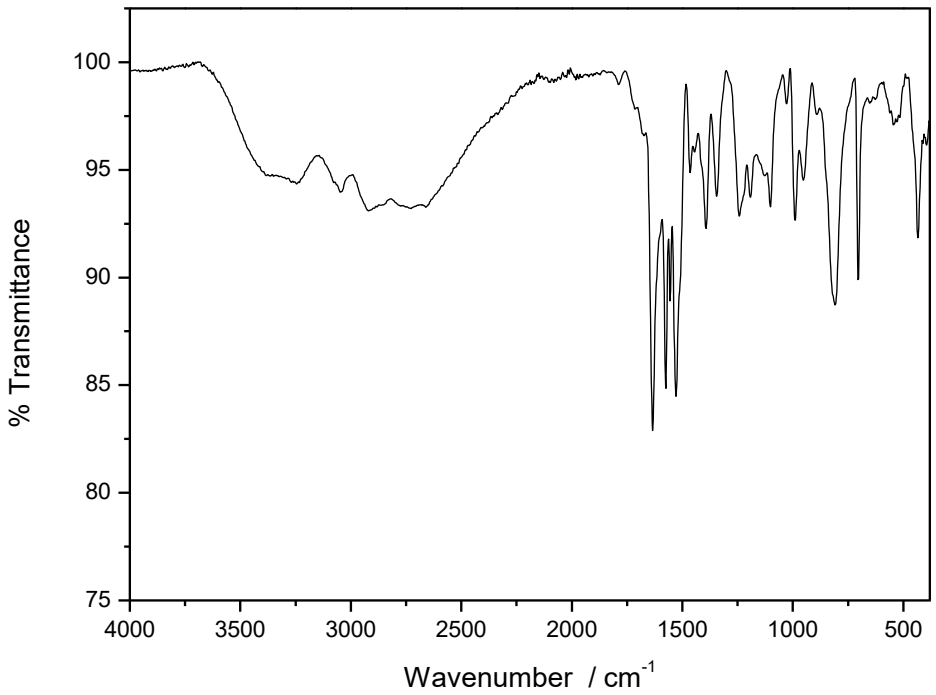


Figure A.7 IR spectrum of 2,5-Bis[(4-chloropyridin-2-ylmethyl)amino]methyl-1,3,4-oxadiazole ($\mathbf{L^{6,Cl}}$).

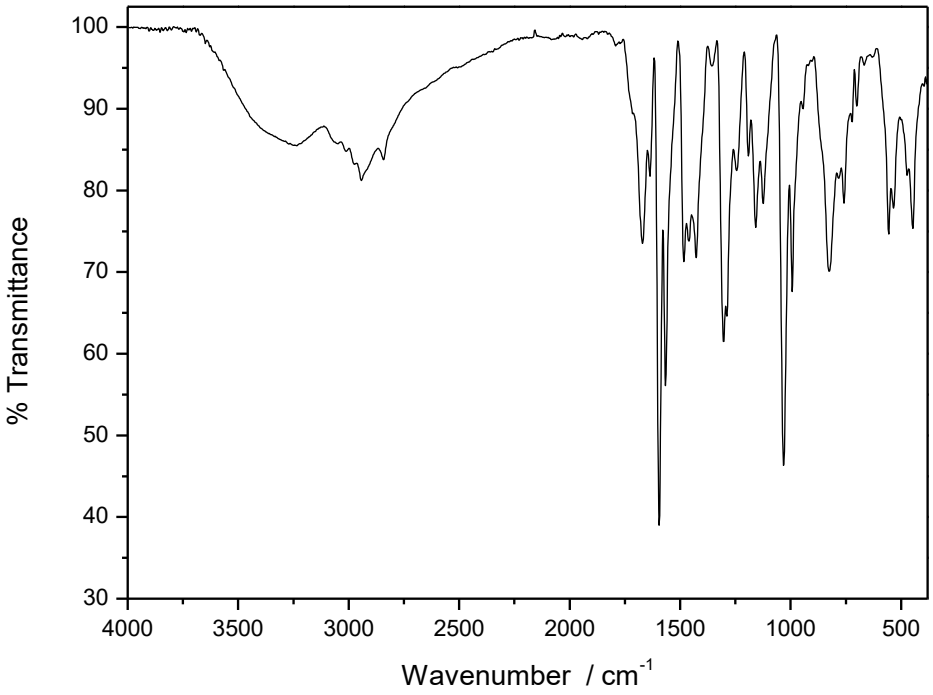


Figure A.8 IR spectrum of 2,5-Bis[(4-methoxypyridin-2-ylmethyl)amino]methyl-1,3,4-oxadiazole ($\mathbf{L^{6,OMe}}$).

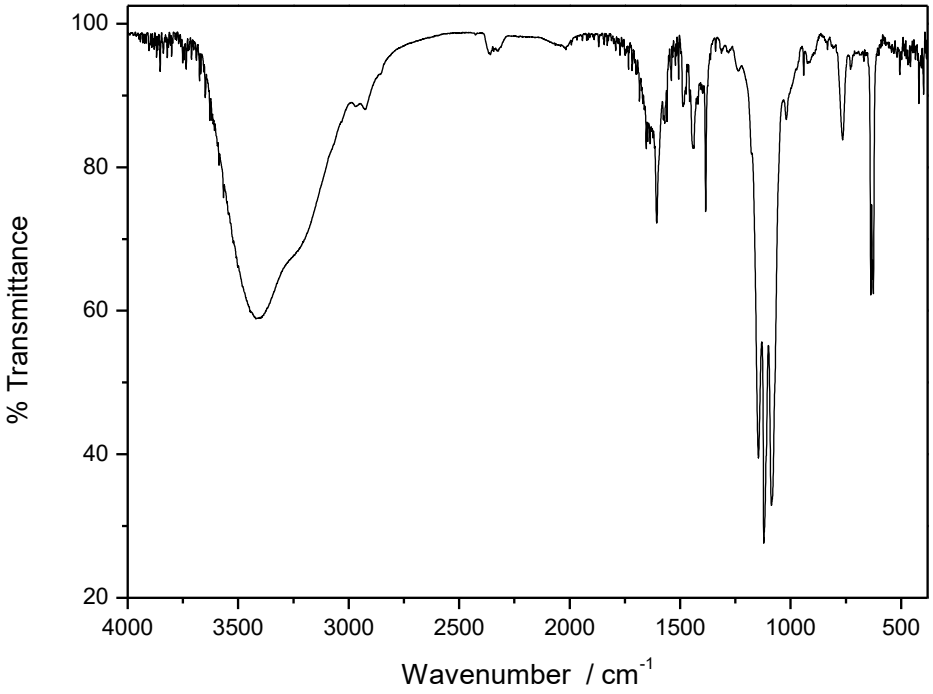


Figure A.9 IR spectrum of Methyl pyrazine-2-carboxylate (**15**).

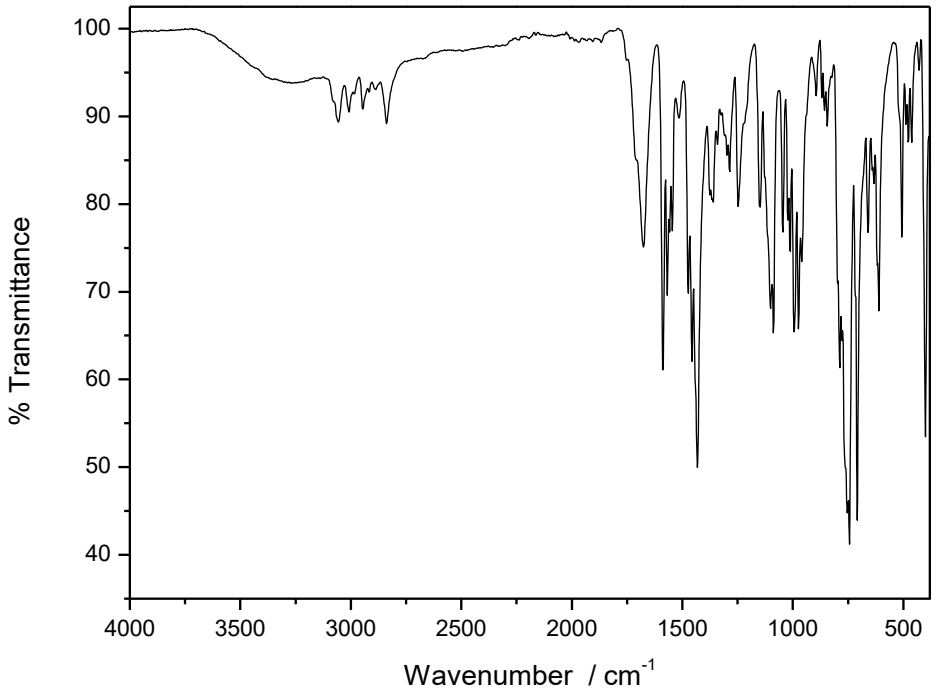


Figure A.10 IR spectrum of 2-(2-Pyridyl)-5-[N,N-bis(2-pyridylmethyl)aminomethyl]-1,3,4-oxadiazole ($\mathbf{L}^{\mathbf{Py,1}}$).

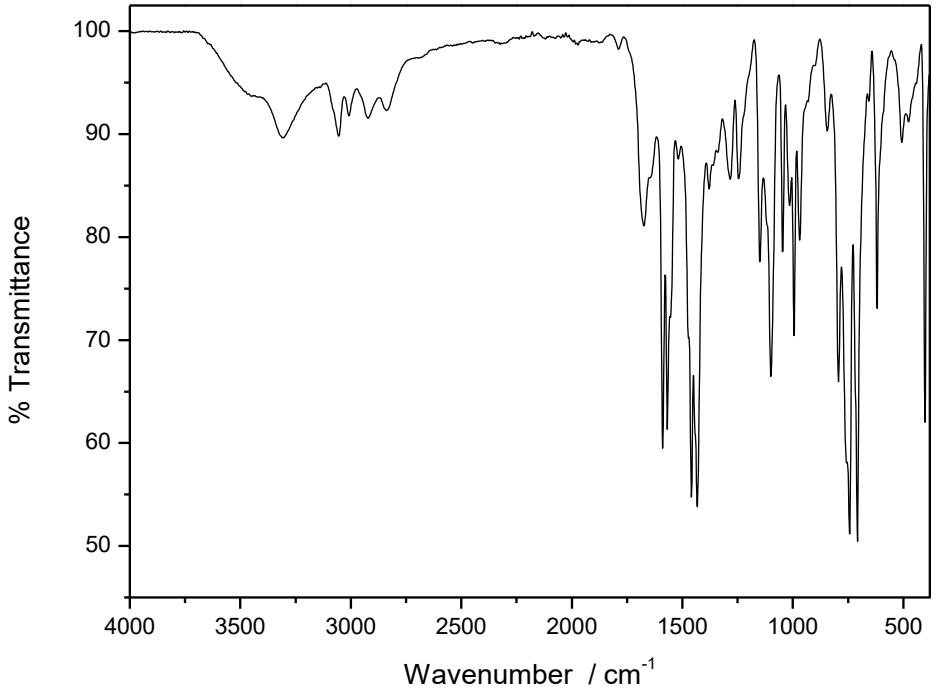


Figure A.11 IR spectrum of 2-(2-Pyridyl)-5-[(2-pyridylmethyl)aminomethyl]-1,3,4-oxadiazole ($\mathbf{L}^{\mathbf{Py,2}}$).

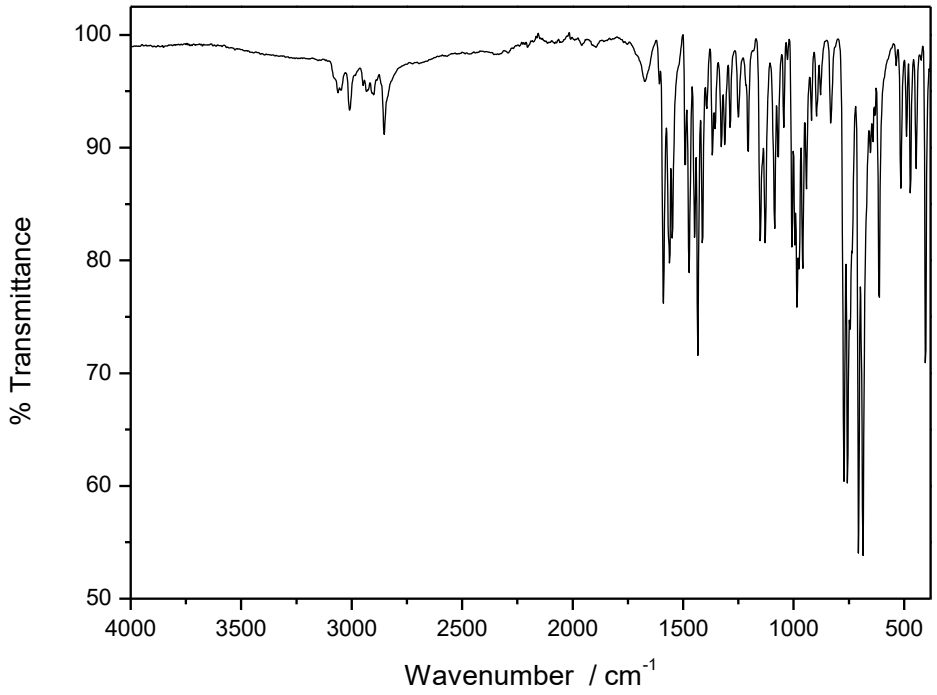


Figure A.12 IR spectrum of 2-Phenyl-5-[N,N-bis(2-pyridylmethyl)aminomethyl]-1,3,4-oxadiazole (**L^{Ph}**).

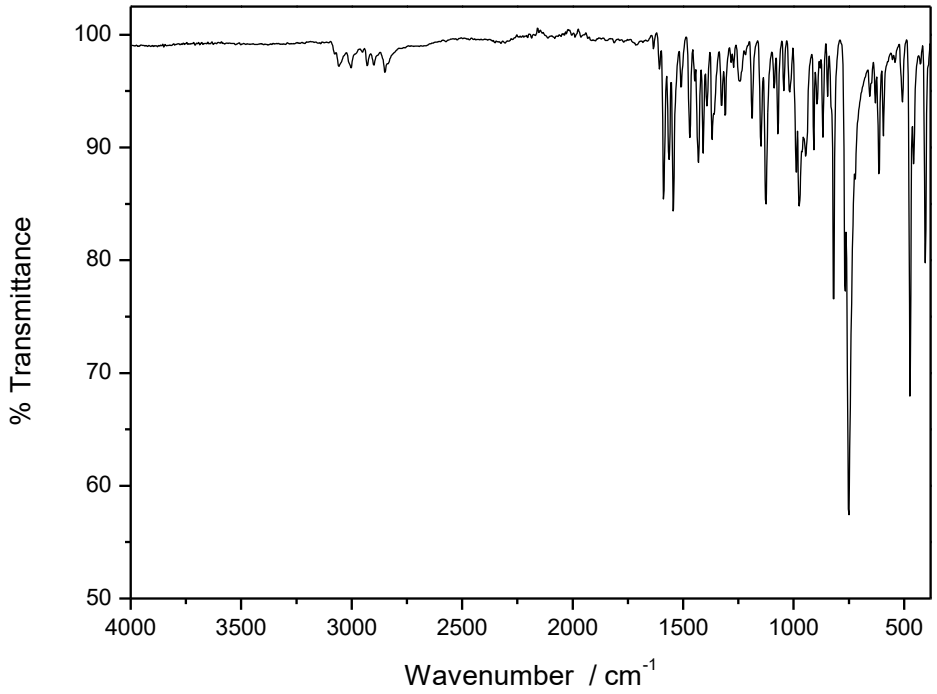


Figure A.13 IR spectrum of 2-(Naphthalen-2-yl)-5-[N,N-bis(2-pyridylmethyl)aminomethyl]-1,3,4-oxadiazole (**L^{Naph}**).

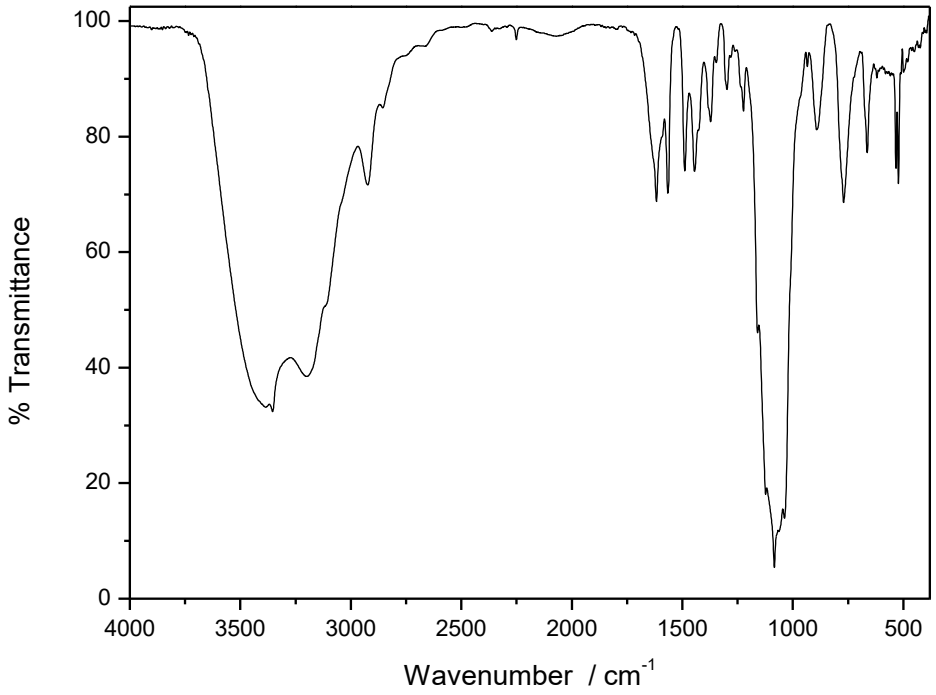


Figure A.14 IR spectrum of $[Fe_2(\mu_2\text{-}\mathbf{L^{5,Im}})_2](BF_4)_4 \cdot 2MeCN$ (**C1**).

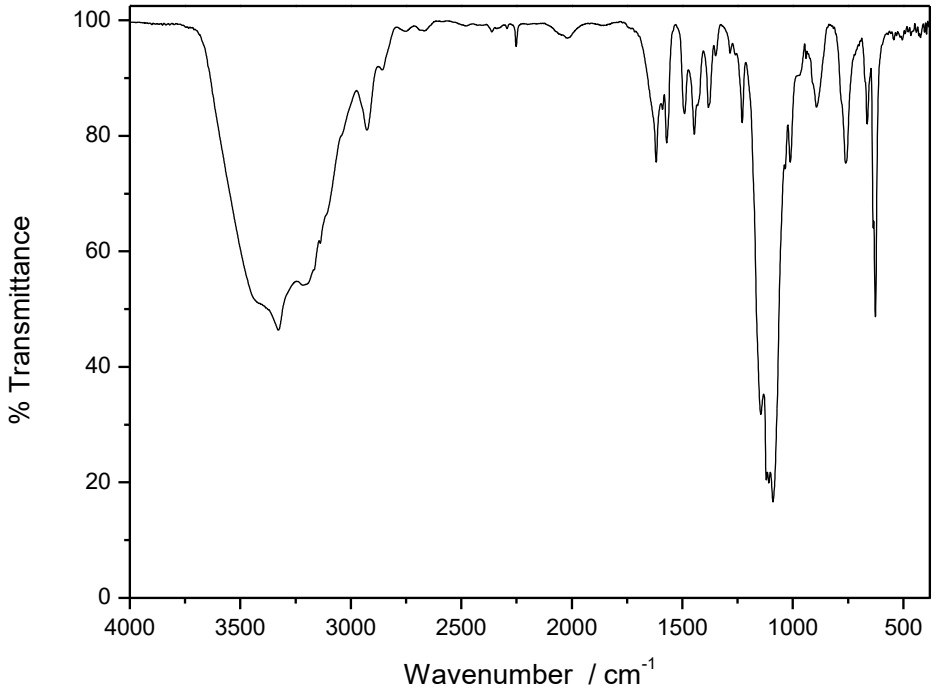


Figure A.15 IR spectrum of $[Fe_2(\mu_2\text{-}\mathbf{L^{5,Im}})_2](ClO_4)_4 \cdot 2MeCN$ (**C2**).

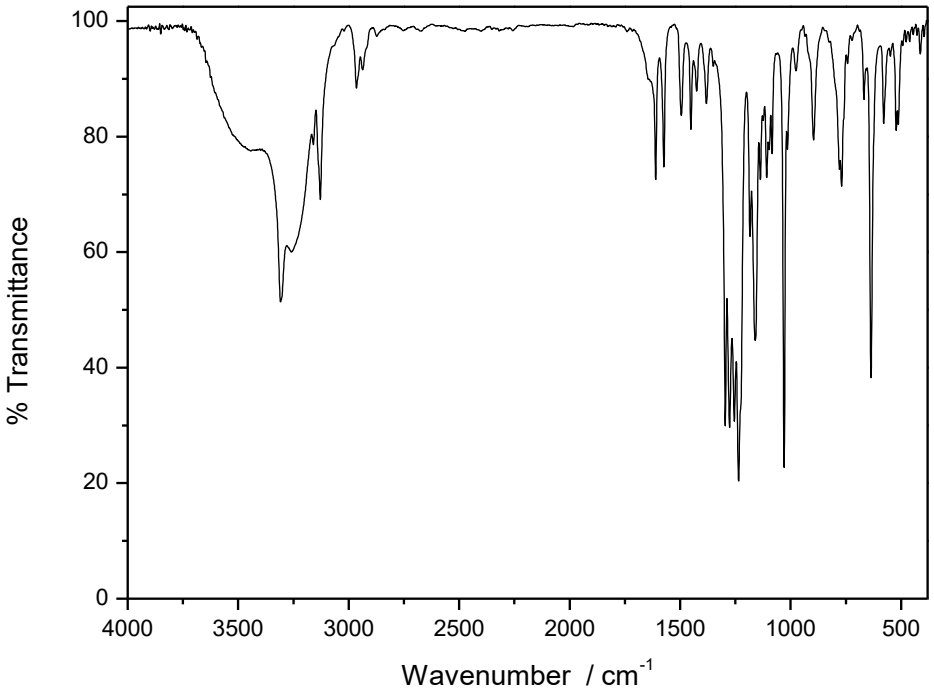


Figure A.16 IR spectrum of $[Fe_2(\mu_2\text{-}\mathbf{L}^{\mathbf{5,Im}})_2](CF_3SO_3)_4 \cdot 2MeCN$ (**C3**).

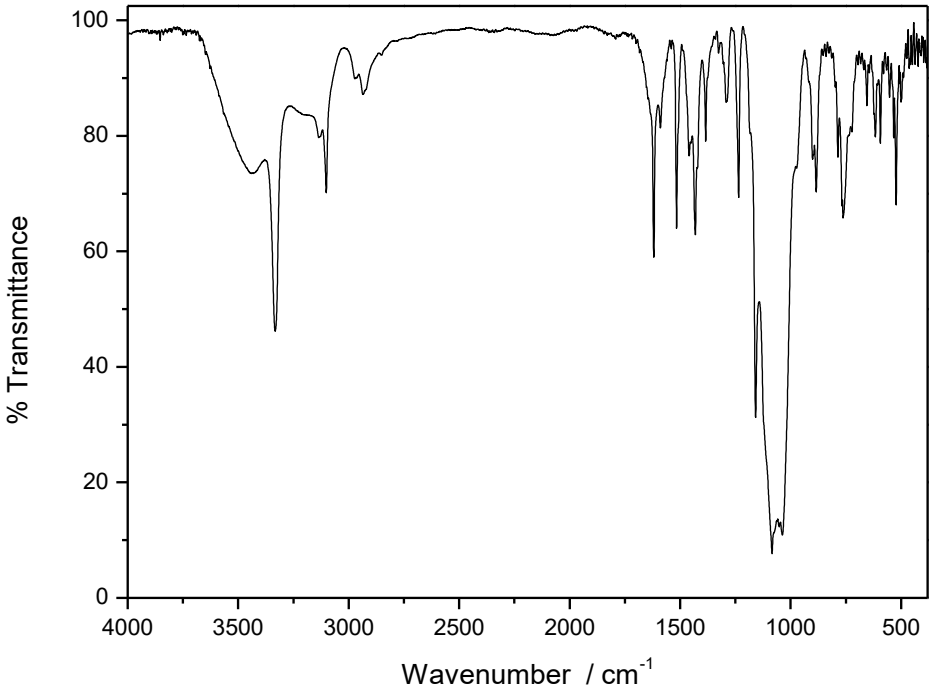


Figure A.17 IR spectrum of $[Fe_2(\mu_2\text{-}\mathbf{L}^{\mathbf{5,TA}})_2](BF_4)_4 \cdot 2MeCN$ (**C4**).

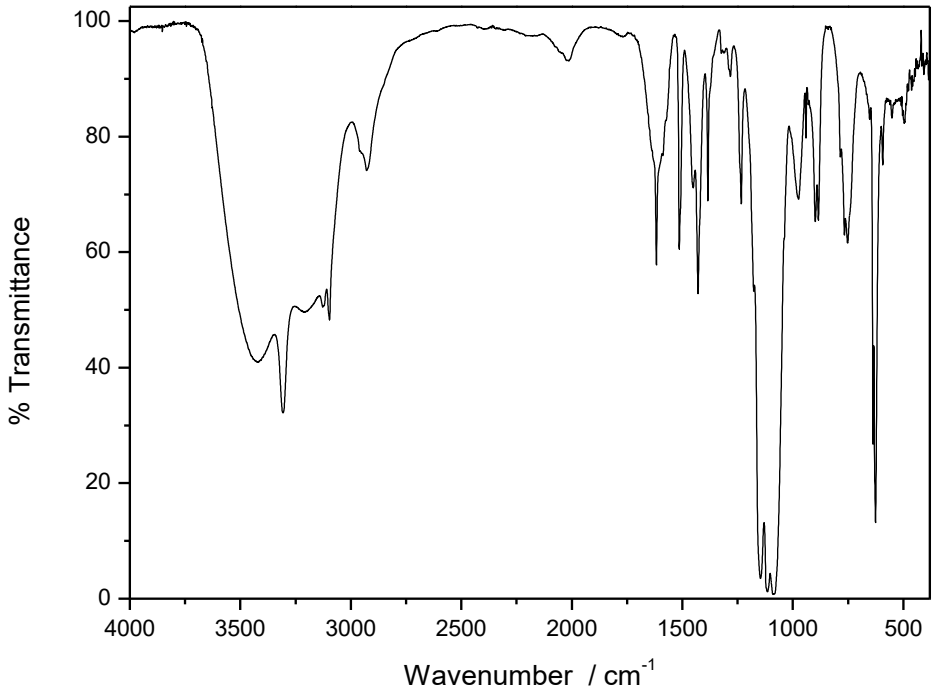


Figure A.18 IR spectrum of $[Fe_2(\mu_2\text{-}\mathbf{L}^{\mathbf{5,TA}})_2](ClO_4)_4$ (**C5**).

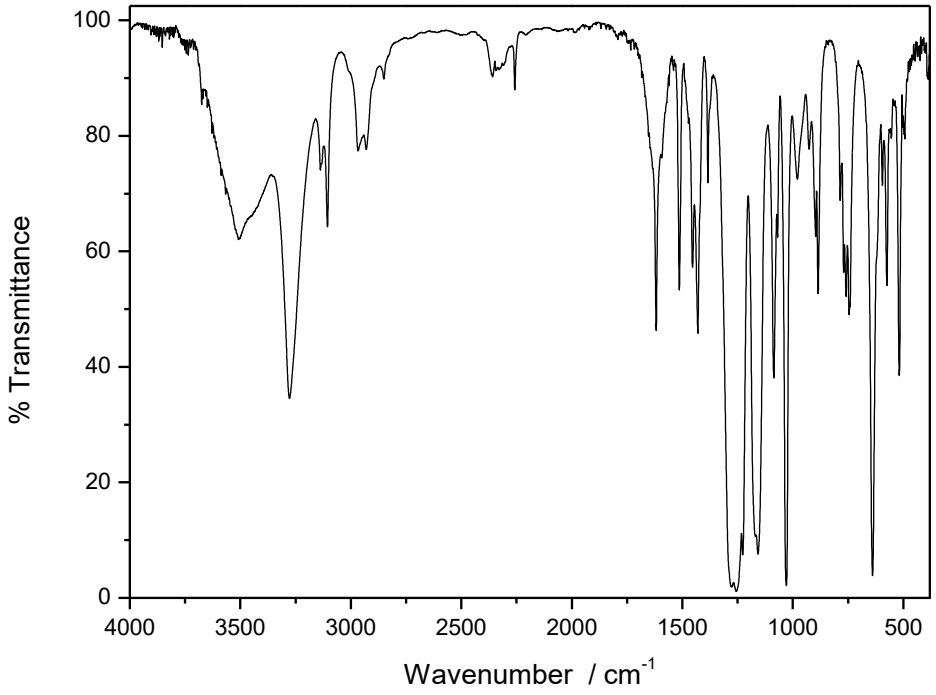


Figure A.19 IR spectrum of $[Fe_2(\mu_2\text{-}\mathbf{L}^{\mathbf{5,TA}})_2](CF_3SO_3)_4 \cdot 2MeCN$ (**C6**).

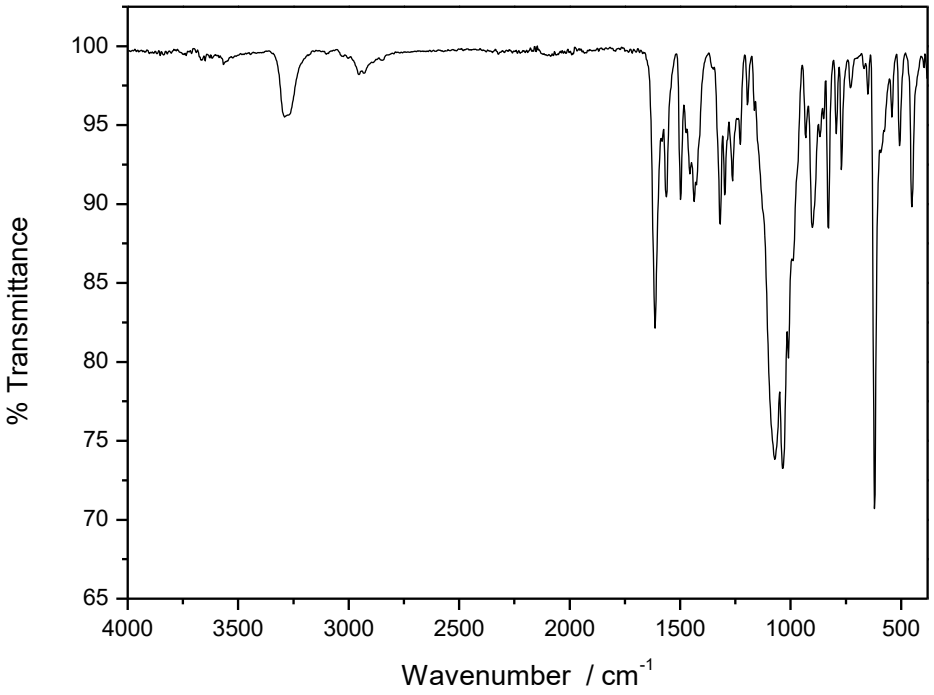


Figure A.20 IR spectrum of $[Fe_2(\mu_2\text{-}\mathbf{L^{6,OMe}})_2](ClO_4)_4$ (**C7**).

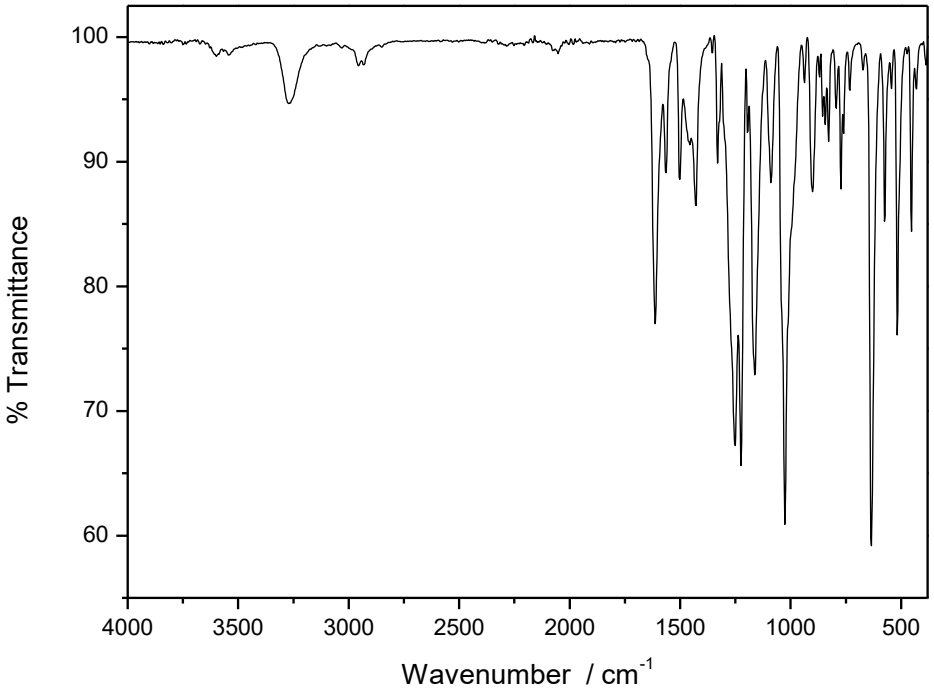


Figure A.21 IR spectrum of $[Fe_2(\mu_2\text{-}\mathbf{L^{6,OMe}})_2](CF_3SO_3)_4$ (**C8**).

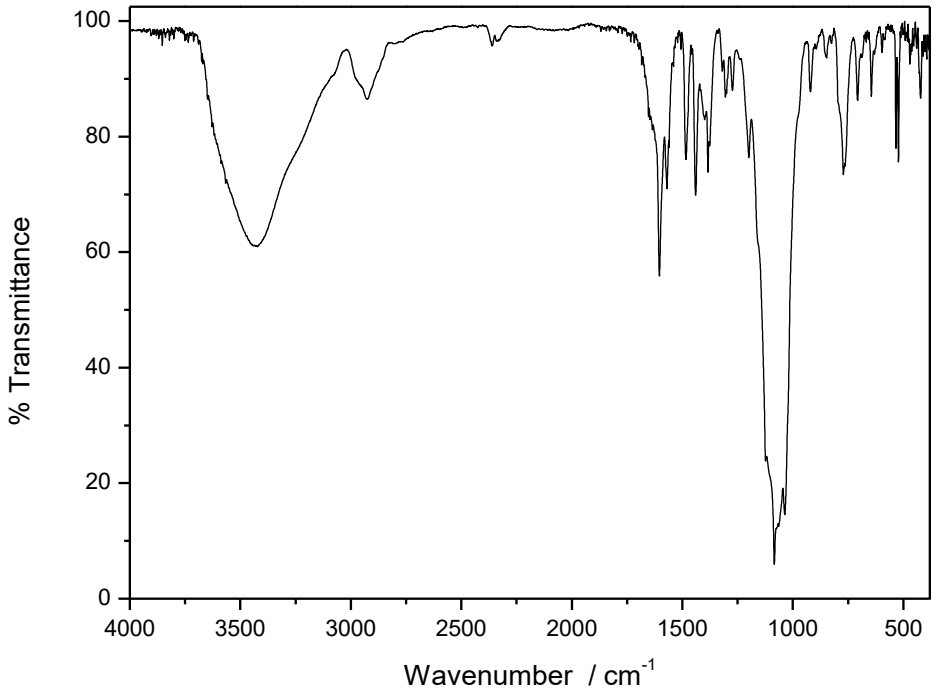


Figure A.22 IR spectrum of $[Fe_2(\mu_2\text{-}\mathbf{L}^{\mathbf{6,Cl}})_2](BF_4)_4$ (**C9**).

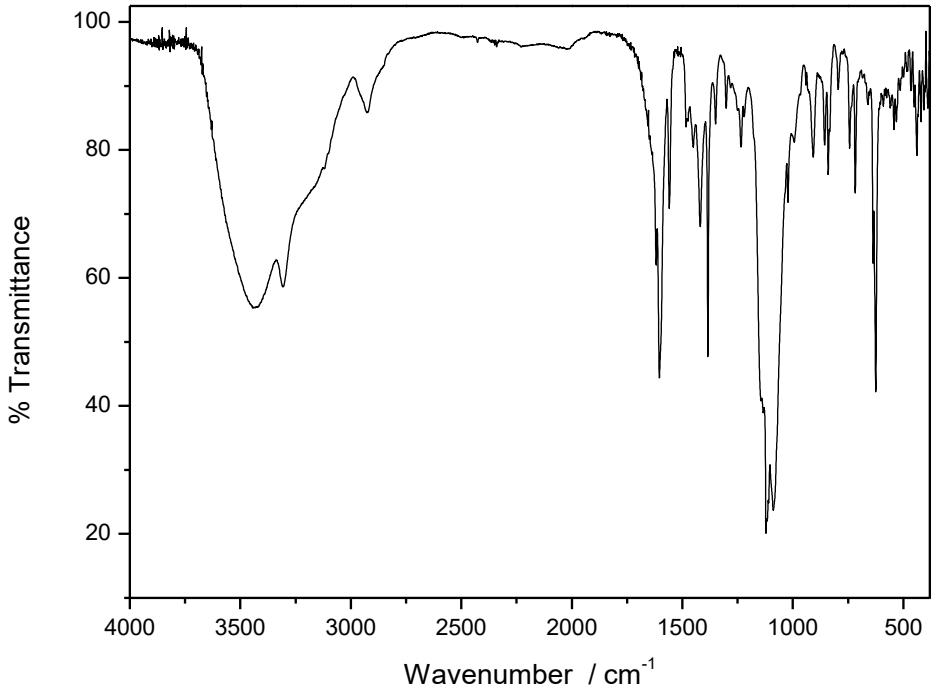


Figure A.23 IR spectrum of $[Fe_2(\mu_2\text{-}\mathbf{L}^{\mathbf{6,Cl}})_2](ClO_4)_4$ (**C10**).

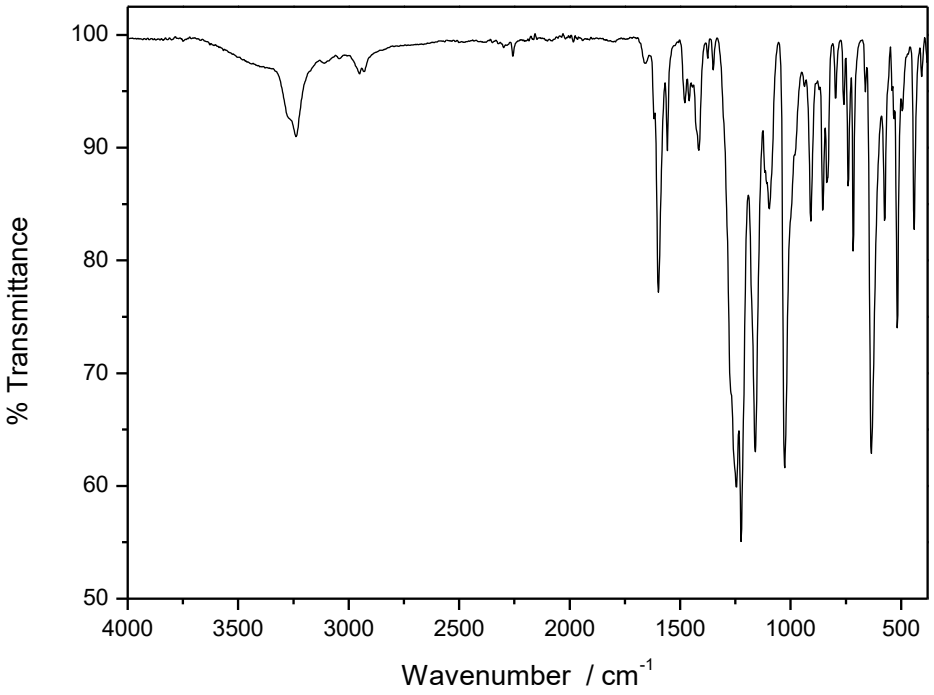


Figure A.24 IR spectrum of $[Fe_2(\mu_2\text{-}\mathbf{L^{6,Cl}})_2](CF_3SO_3)_4$ (**C11**).

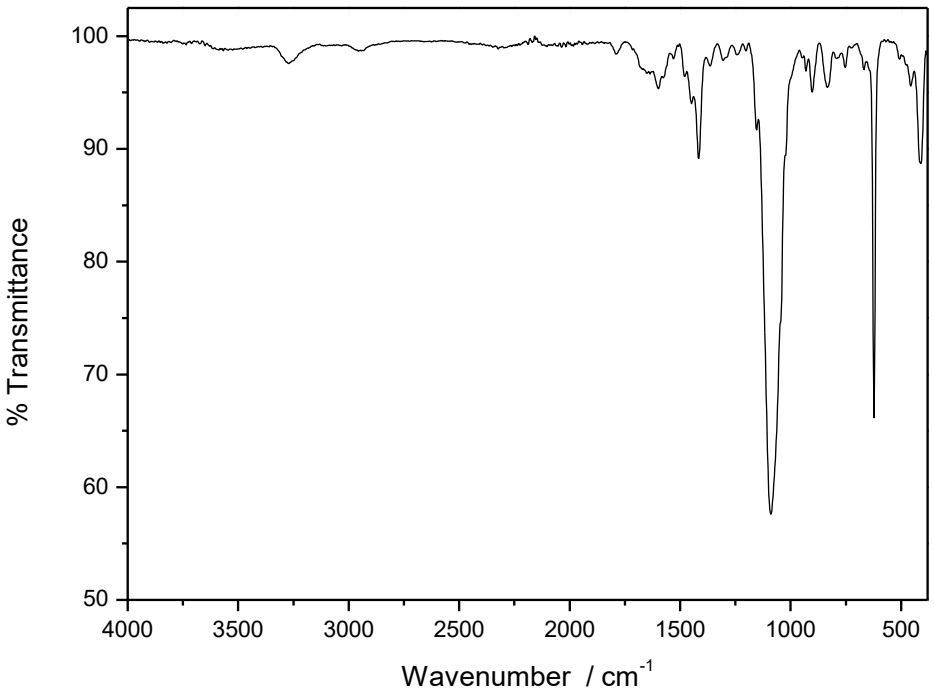


Figure A.25 IR spectrum of $[Fe_2(\mu_2\text{-}\mathbf{L^{6,N}})_2](BF_4)_4$ (**C12**).

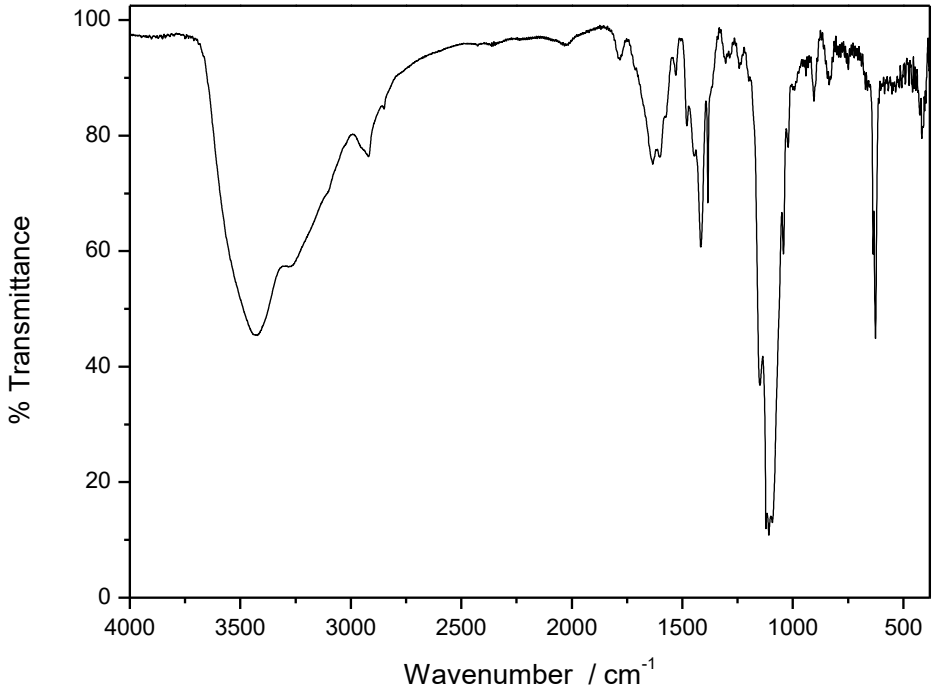


Figure A.26 IR spectrum of $[Fe_2(\mu_2\text{-}\mathbf{L}^{\mathbf{6,N}})_2](ClO_4)_4$ (**C13**).

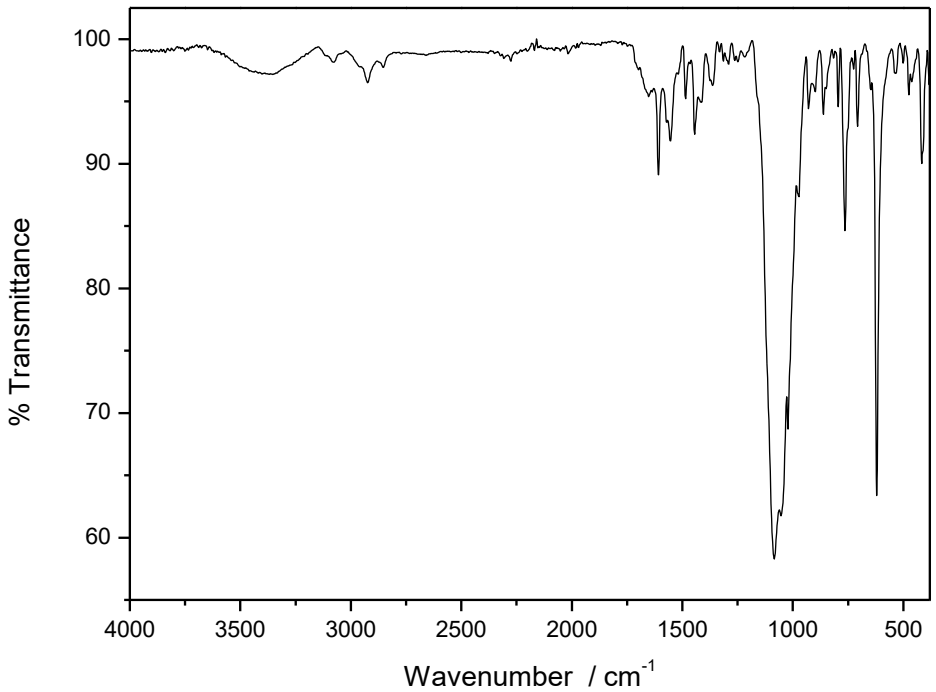


Figure A.27 IR spectrum of $[Fe_2(\mu_2\text{-}\mathbf{L}^{\mathbf{Py,1}})_2](BF_4)_4{\cdot}2MeNO_2$ (**C14**).

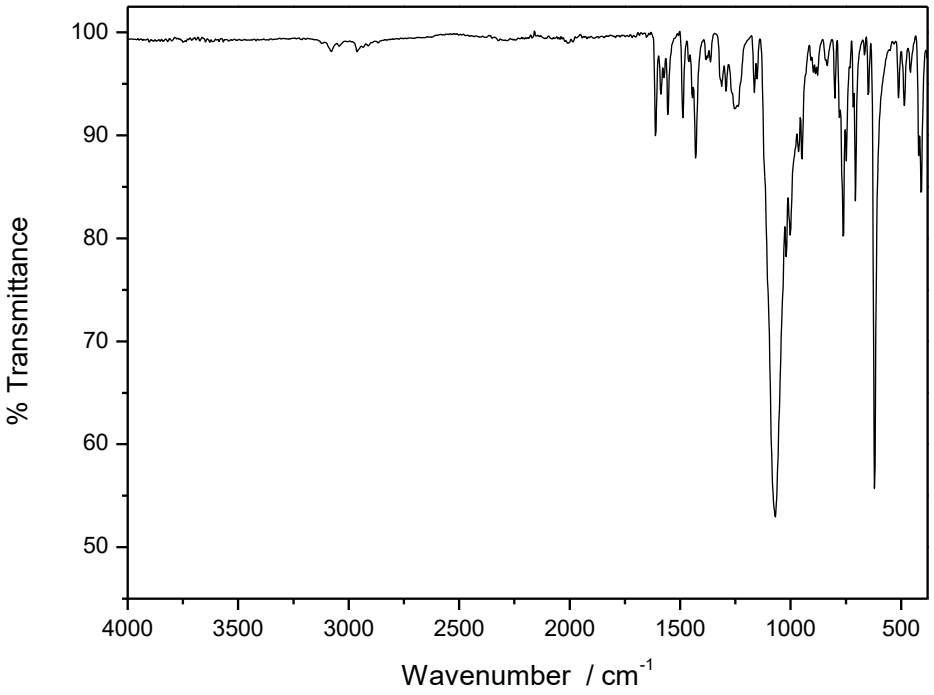


Figure A.28 IR spectrum of $[Fe_2(\mu_2\text{-}\mathbf{L}^{\mathbf{Py,1}})_2](BF_4)_4 \cdot 2MeNO_2$ (**C14'**).

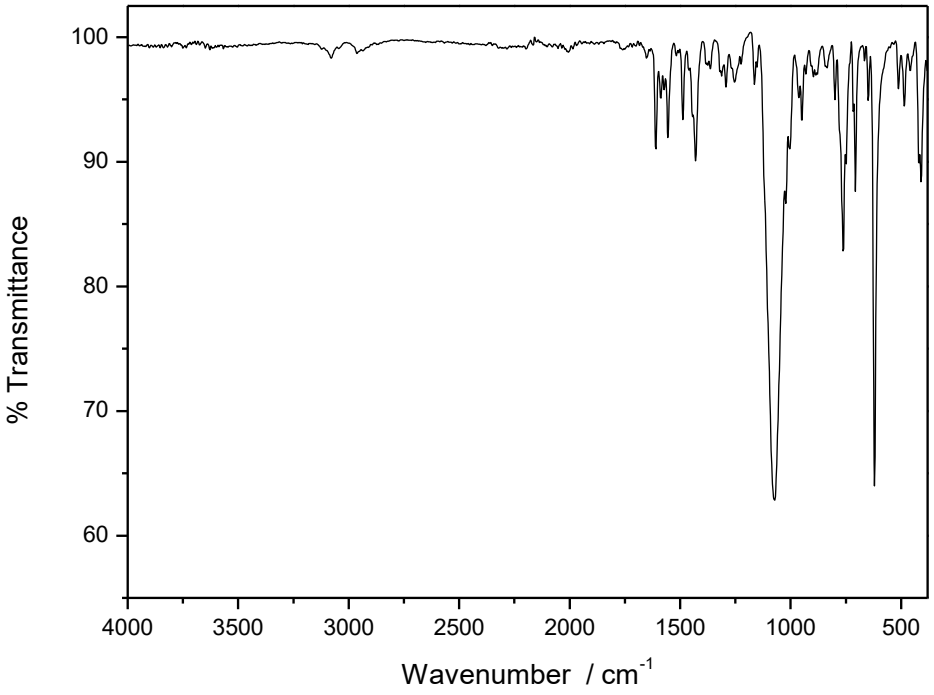


Figure A.29 IR spectrum of $[Fe_2(\mu_2\text{-}\mathbf{L}^{\mathbf{Py,1}})_2](ClO_4)_4 \cdot 2MeNO_2$ (**C15**).

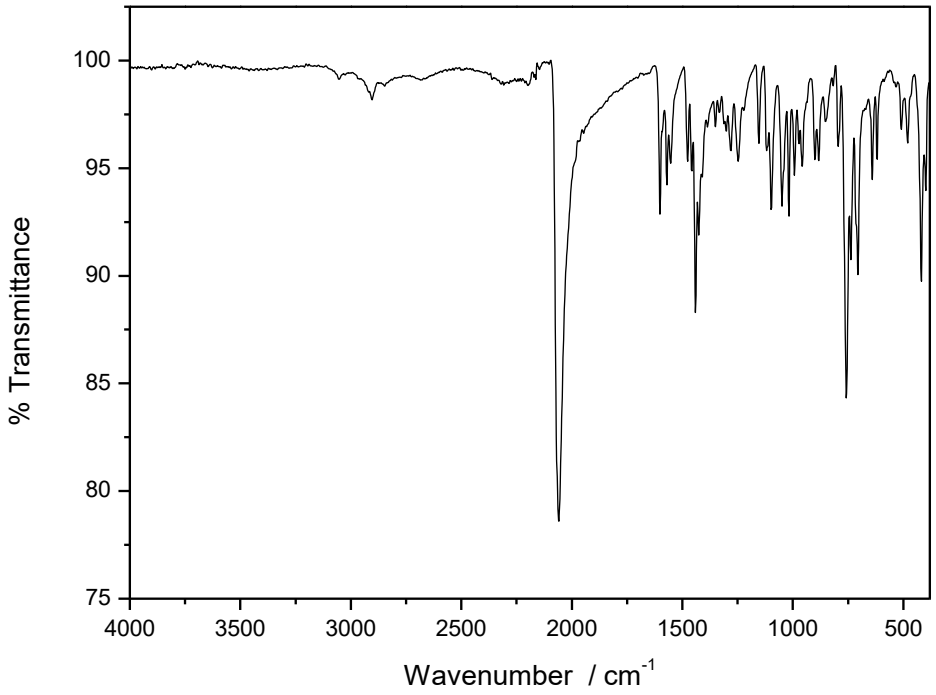


Figure A.30 IR spectrum of [Fe(**L**^{Py,1})(NCSe)$_2$]·3MeCN (**C17**·3MeCN).

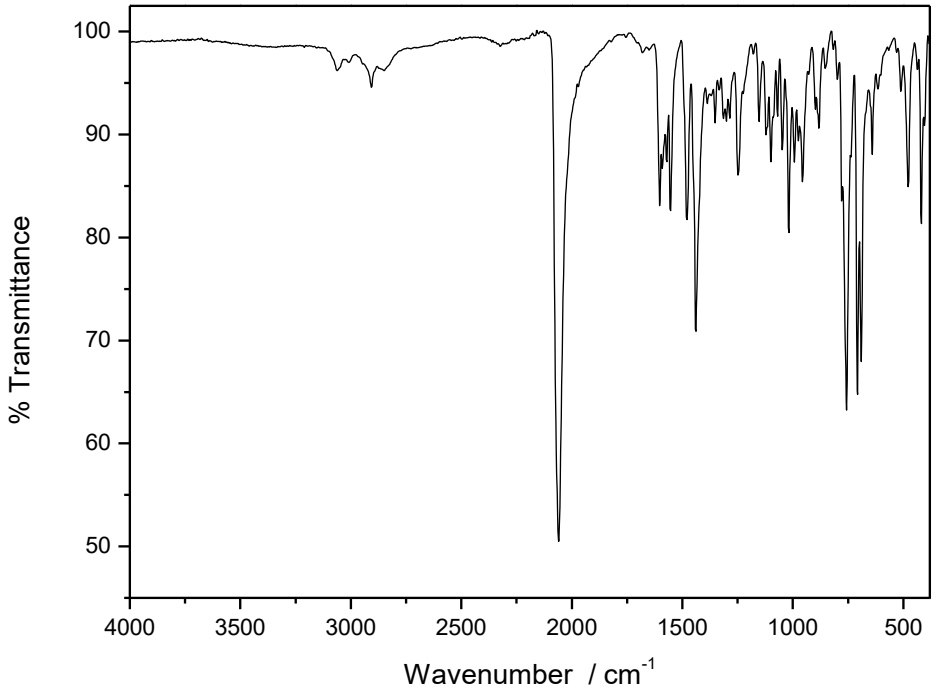


Figure A.31 IR spectrum of [Fe(**L**^{Ph})(NCS)$_2$] · 2MeCN (**C19**·2MeCN).

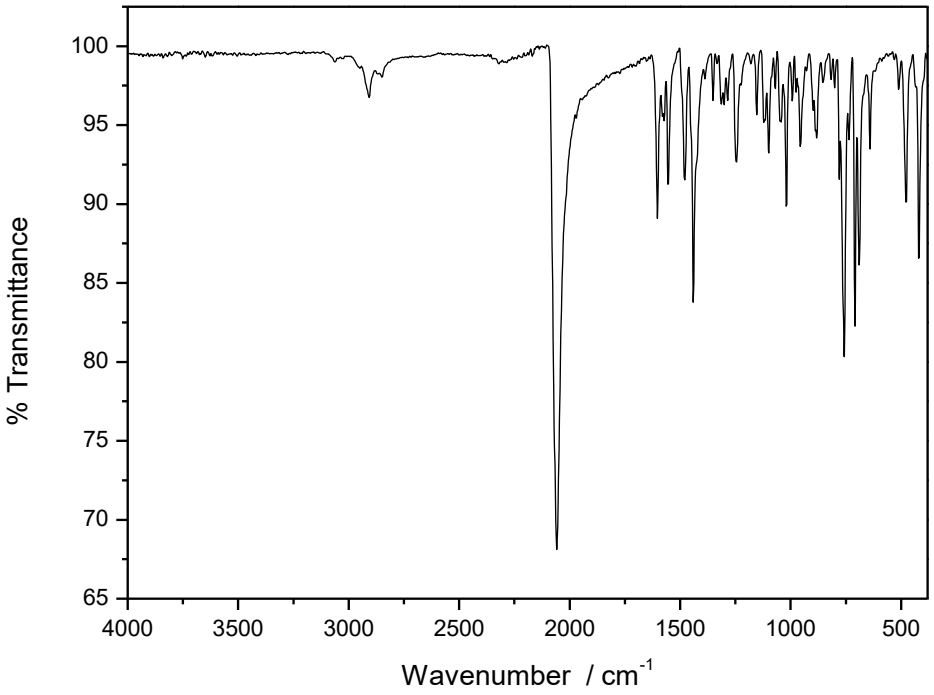


Figure A.32 IR spectrum of [Fe(**L**^{Ph})$(NCS)_2$] · 3MeOH (**C19**·3MeOH).

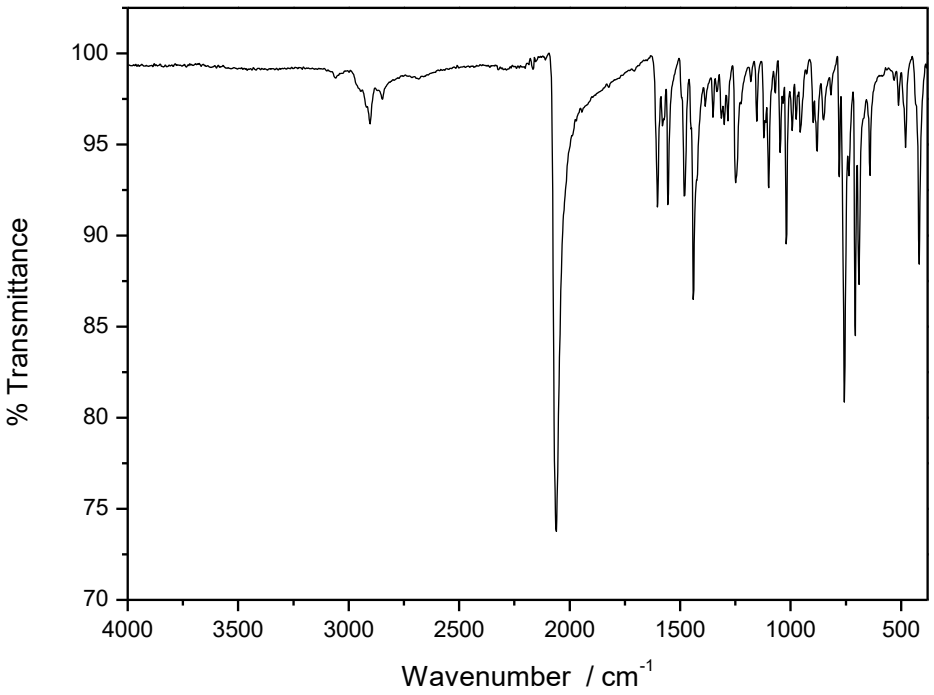


Figure A.33 IR spectrum of [Fe(**L**^{Ph})$(NCSe)_2$] · 2MeCN (**C20**·2MeCN).

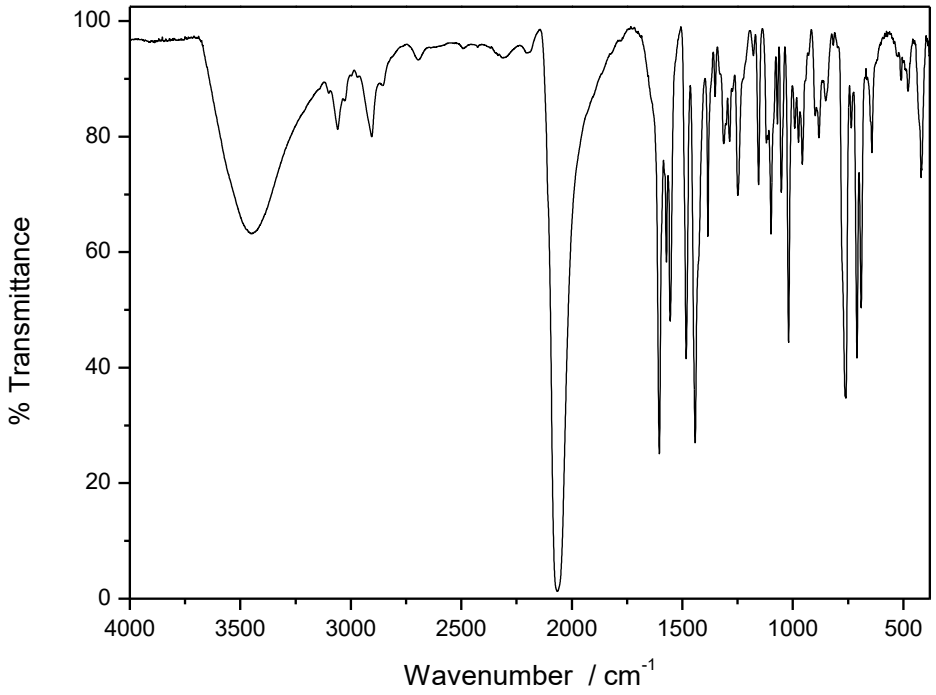


Figure A.34 IR spectrum of [Fe(**L**^{Ph})$(NCSe)_2$] · 3MeOH (**C20**·3MeOH).

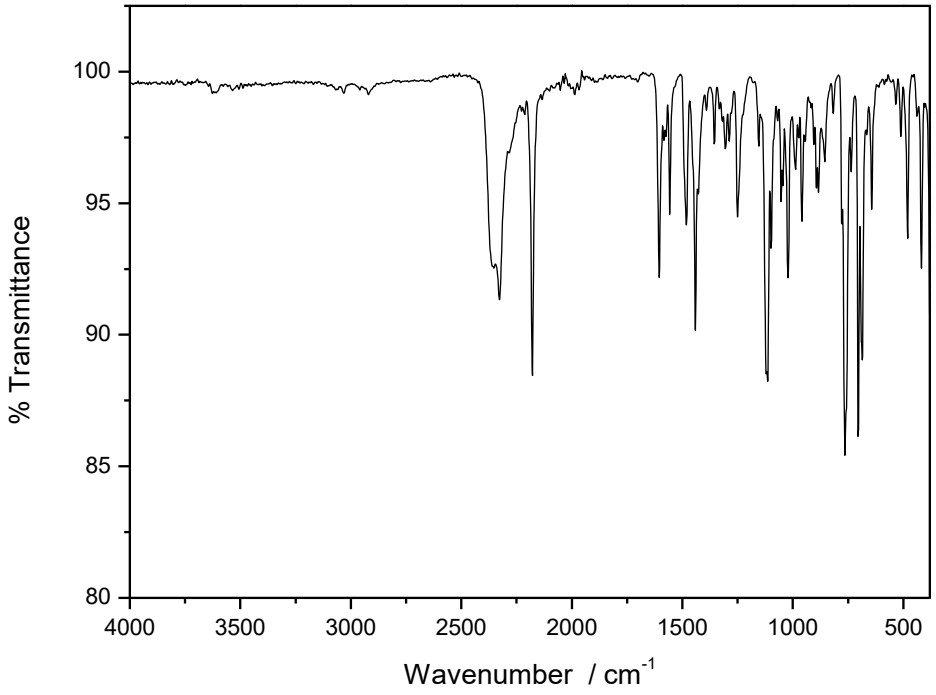


Figure A.35 IR spectrum of [Fe(**L**^{Ph})$(NCBH_3)_2$] · 1MeCN (**C21**·1MeCN).

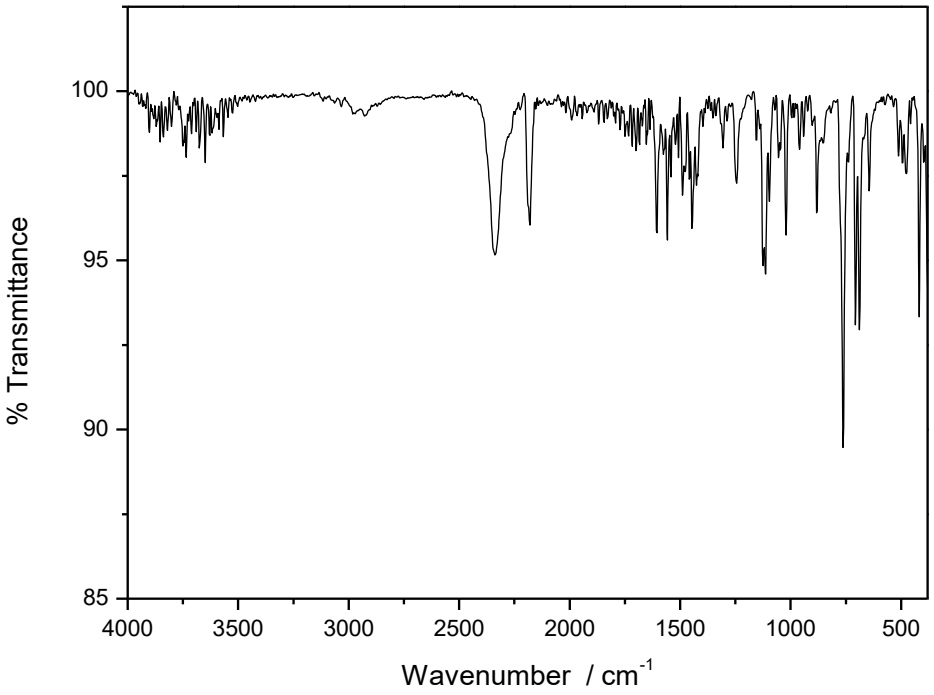


Figure A.36 IR spectrum of [Fe(**L^{Ph}**)$(NCBH_3)_2$] · xMeOH (**C21**·1.8MeOH).

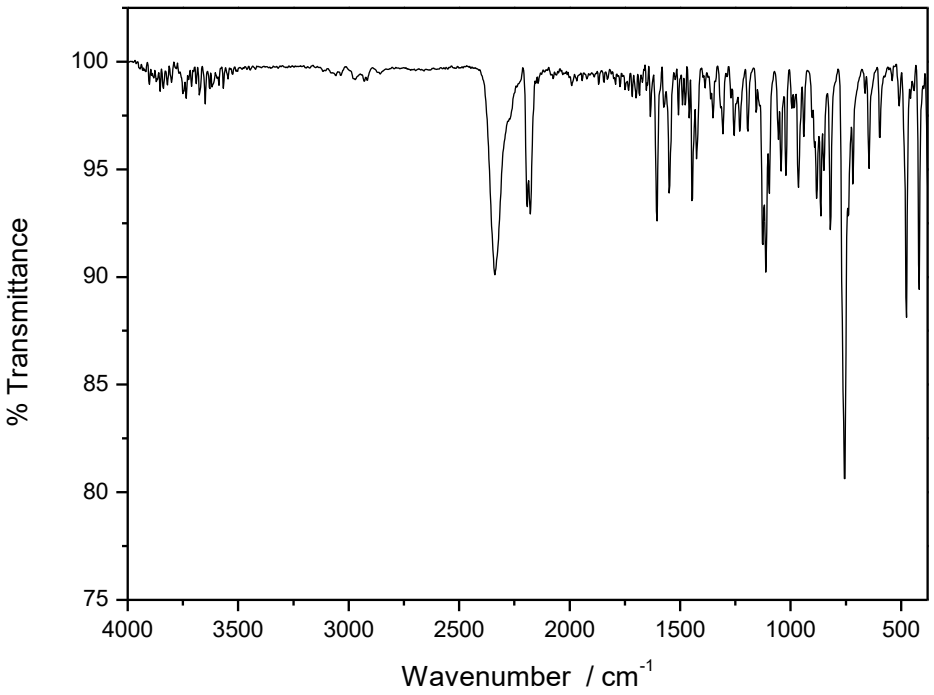


Figure A.37 IR spectrum of [Fe(**L^{Naph}**)$(NCBH_3)_2$] · xMeCN (**C23**·4.5MeCN).

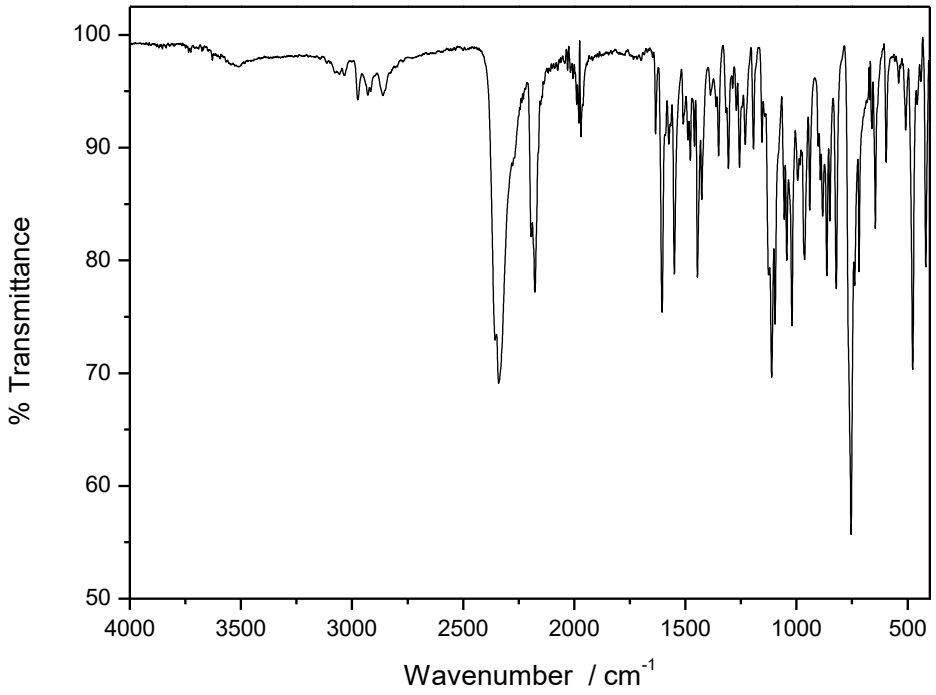


Figure A.38 IR spectrum of [Fe($\mathbf{L}^{\mathbf{Naph}}$)($NCBH_3$)$_2$] · 3MeOH (**C23**·3MeOH).

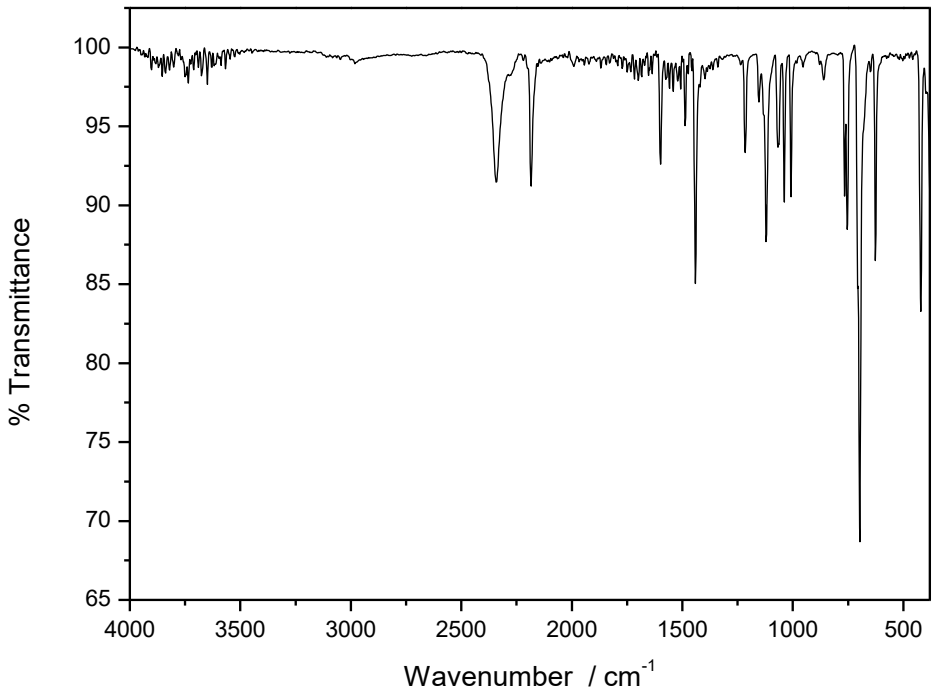


Figure A.39 IR spectrum of [Zn(py)$_4$($NCBH_3$)$_2$] (**C24**).

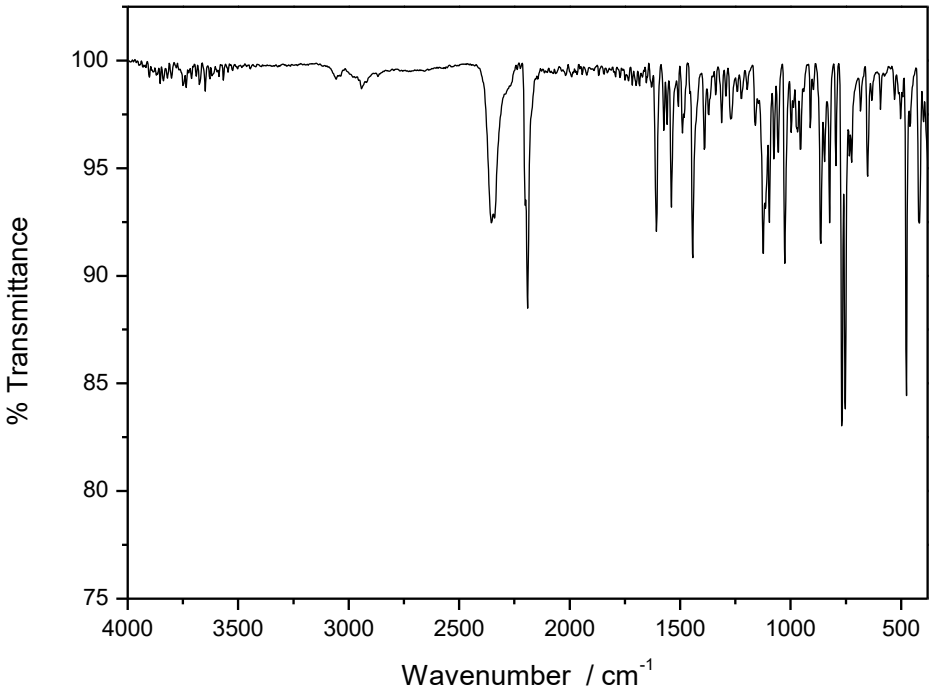


Figure A.40 IR spectrum of [Zn($\mathbf{L}^{\mathbf{Naph}}$)$(NCBH_3)_2$] (**C25**).

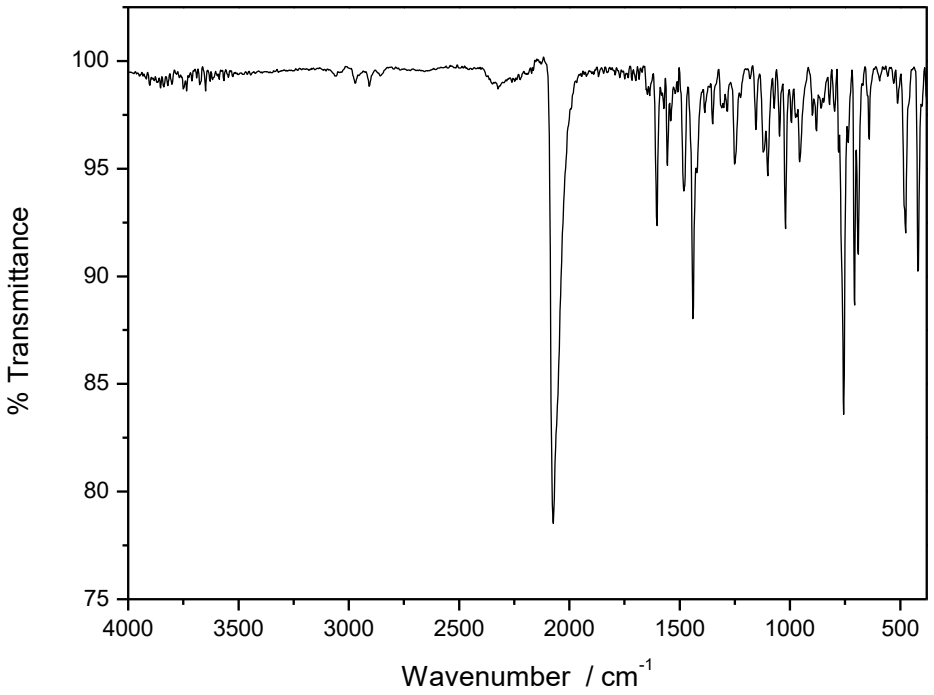


Figure A.41 IR spectrum of [Co($\mathbf{L}^{\mathbf{Py,1}}$)$(NCS)_2$] · 1MeOH (**C26**).

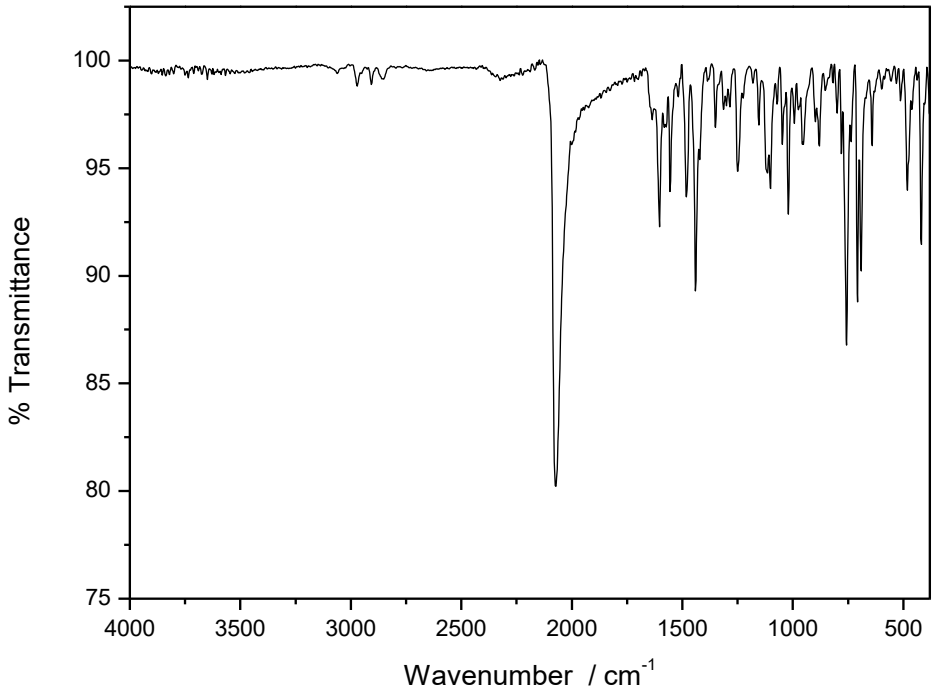


Figure A.42 IR spectrum of [Co(η^3-L^{Ph})$(NCS)_2$(MeOH)] (**C27**).

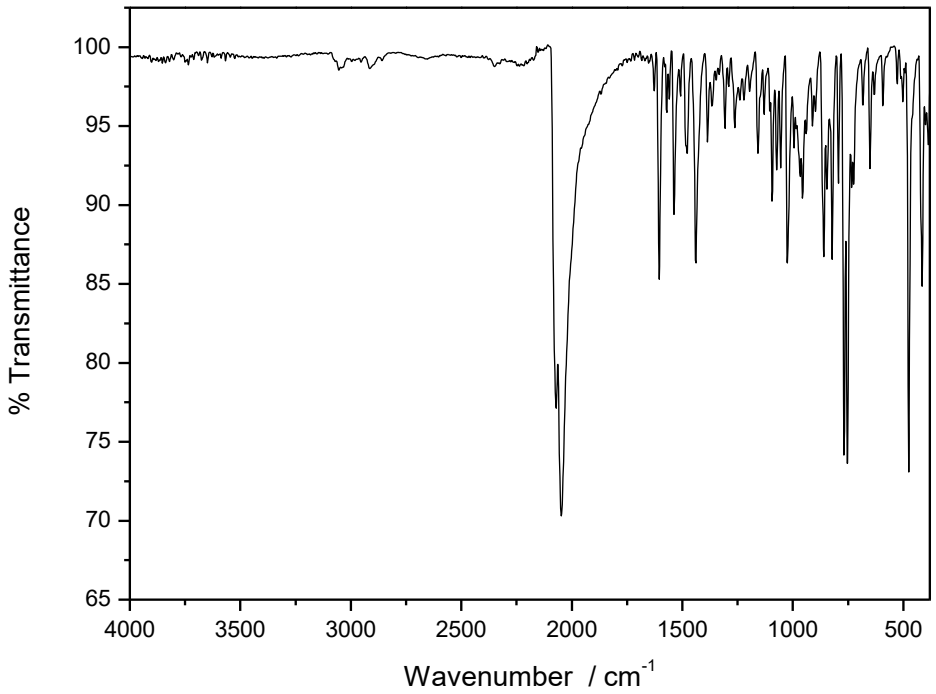


Figure A.43 IR spectrum of [Co(η^3-L^{Naph})$(NCS)_2$] (**C28**).

B NMR Spectra

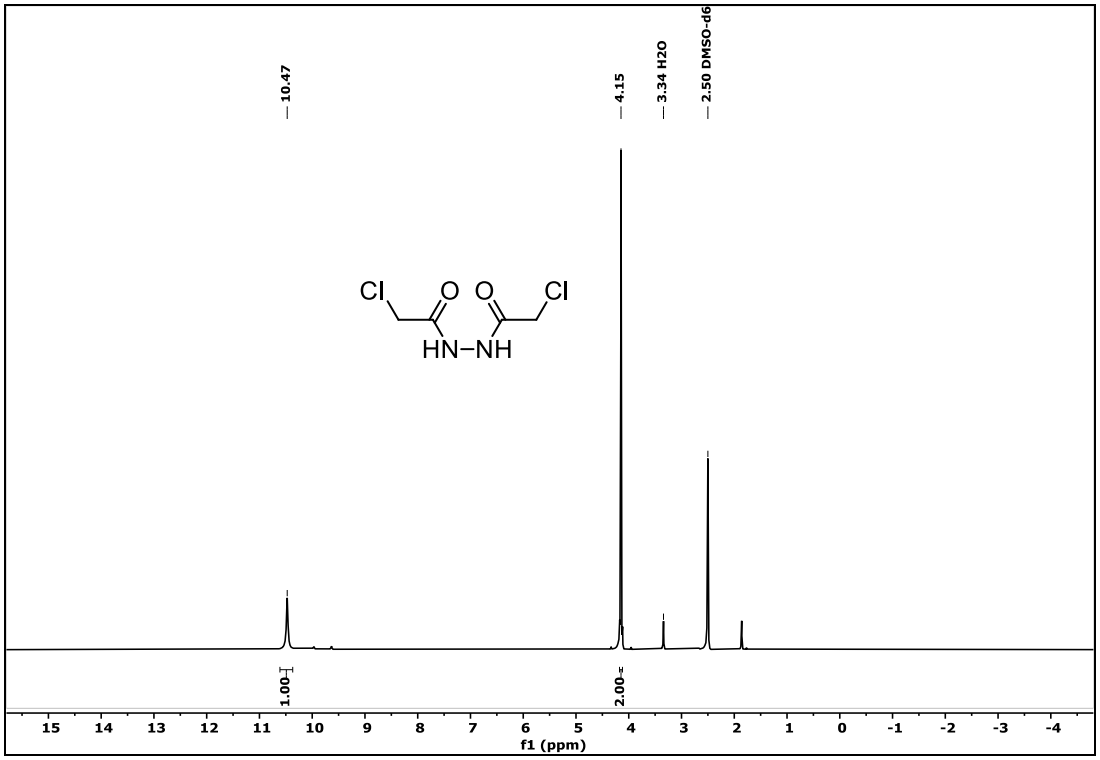


Figure B.1 ^{1}H-NMR spectrum of 1,2-Bis(chloroacetyl)hydrazide (**1**) in DMSO-d_6.

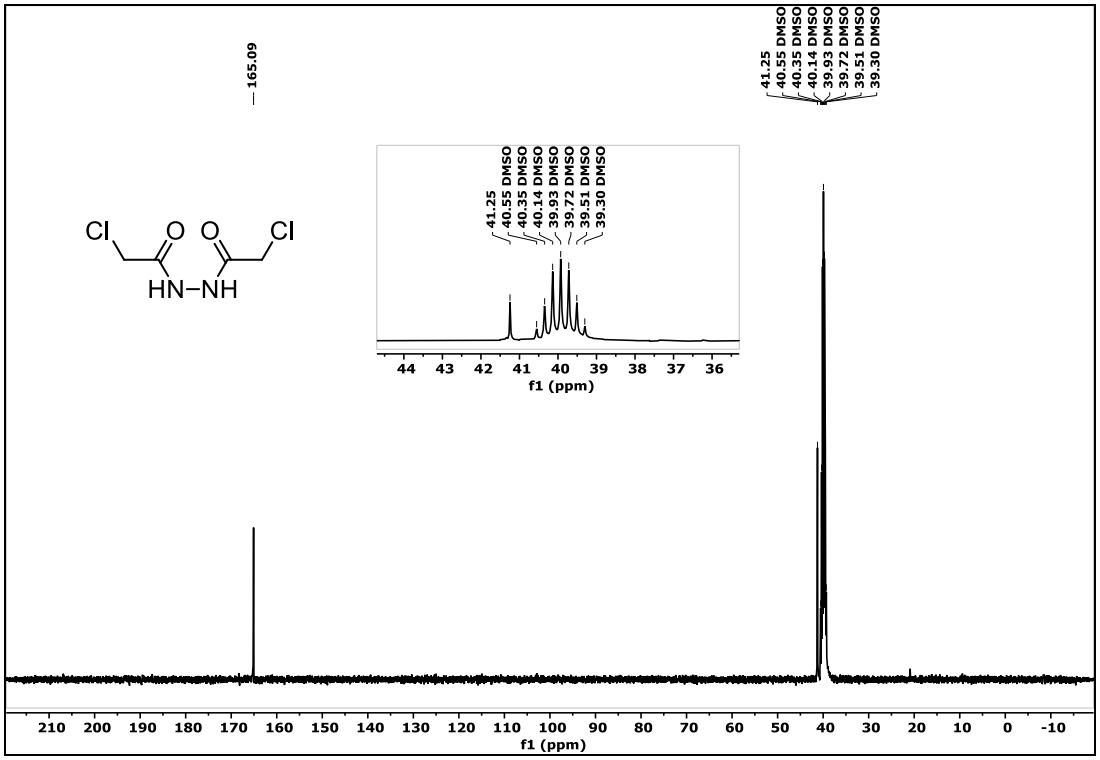


Figure B.2 ^{13}C-NMR spectrum 1,2-Bis(chloroacetyl)hydrazide (**1**) in DMSO-d_6.

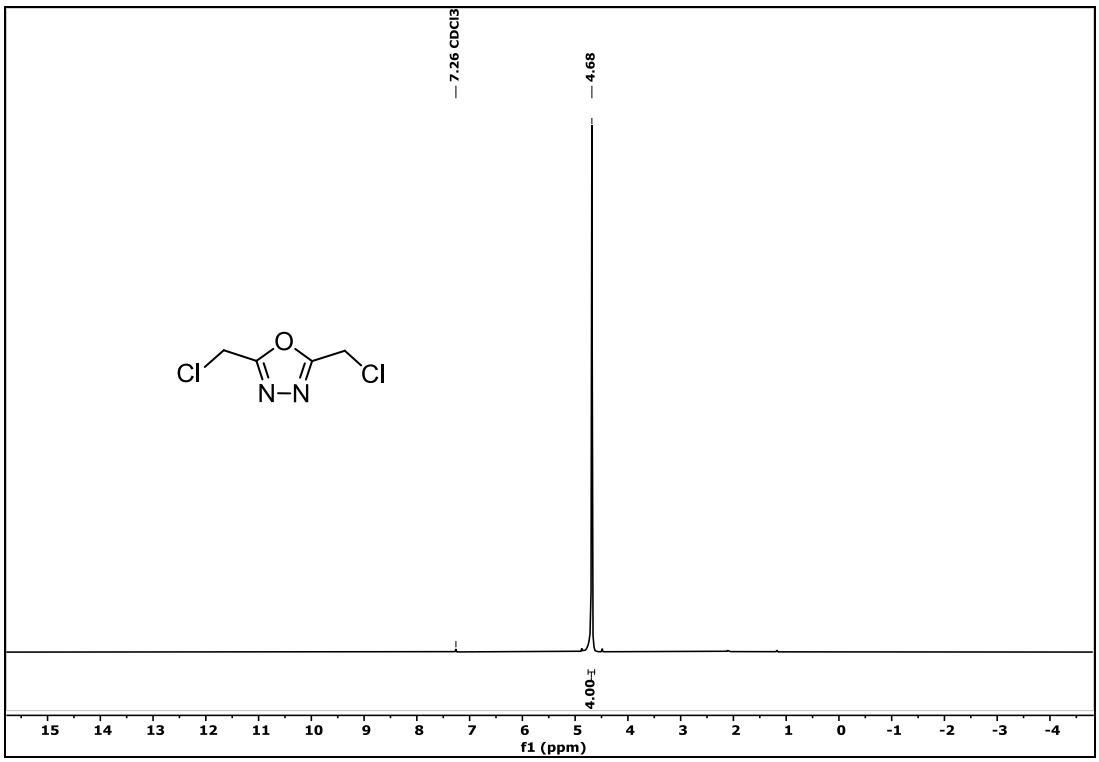


Figure B.3 ^{1}H-NMR spectrum of 2,5-Bis(chloromethyl)-1,3,4-oxadiazole (**2**) in $CDCl_3$.

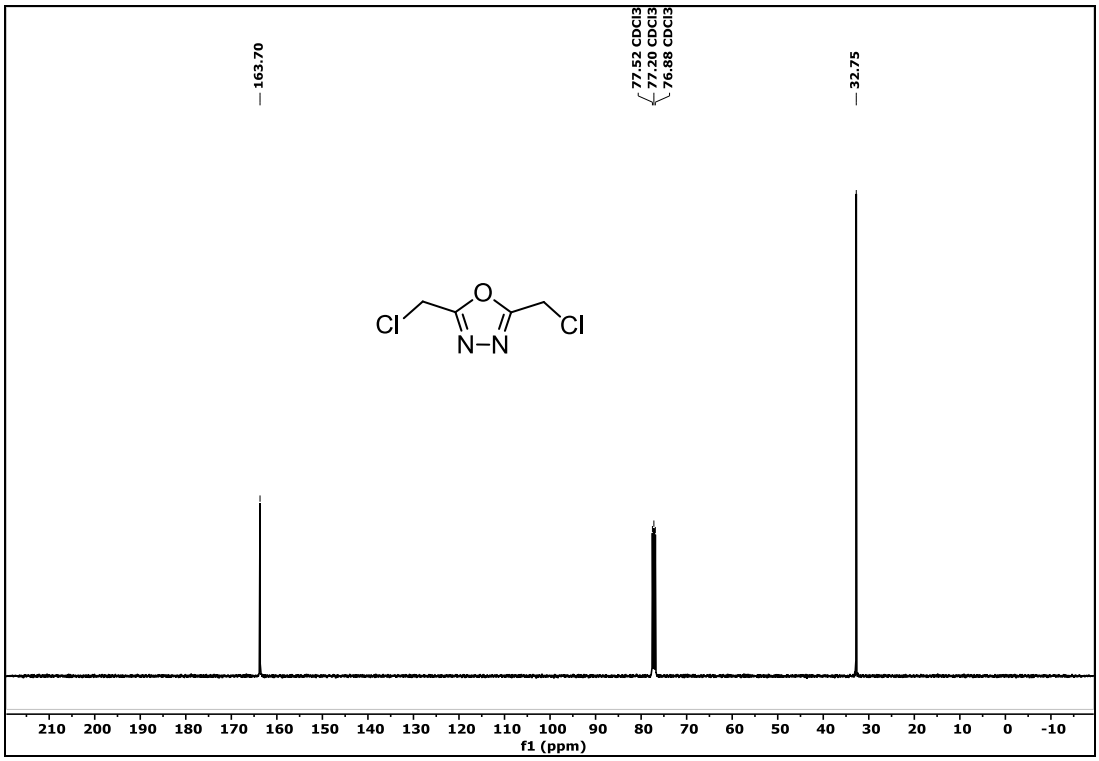


Figure B.4 ^{13}C-NMR spectrum of 2,5-Bis(chloromethyl)-1,3,4-oxadiazole (**2**) in $CDCl_3$.

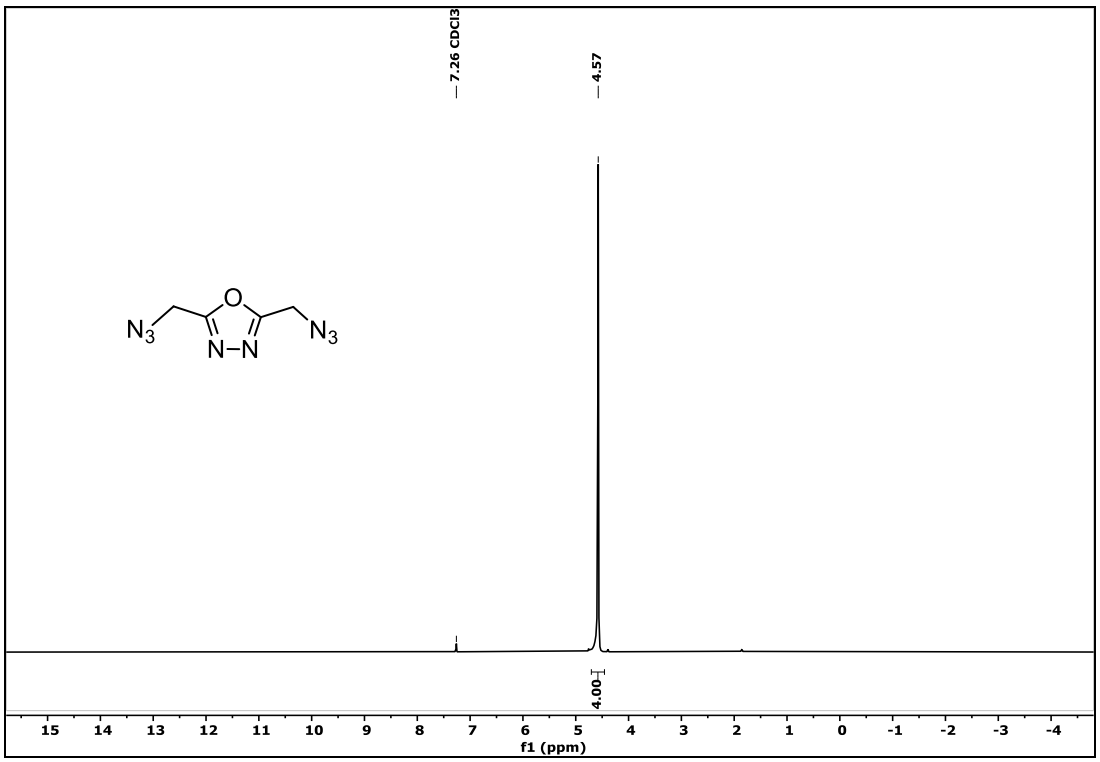


Figure B.5 ^{1}H-NMR spectrum of 2,5-Bis(azidomethyl)-1,3,4-oxadiazole (**3**) in $CDCl_3$.

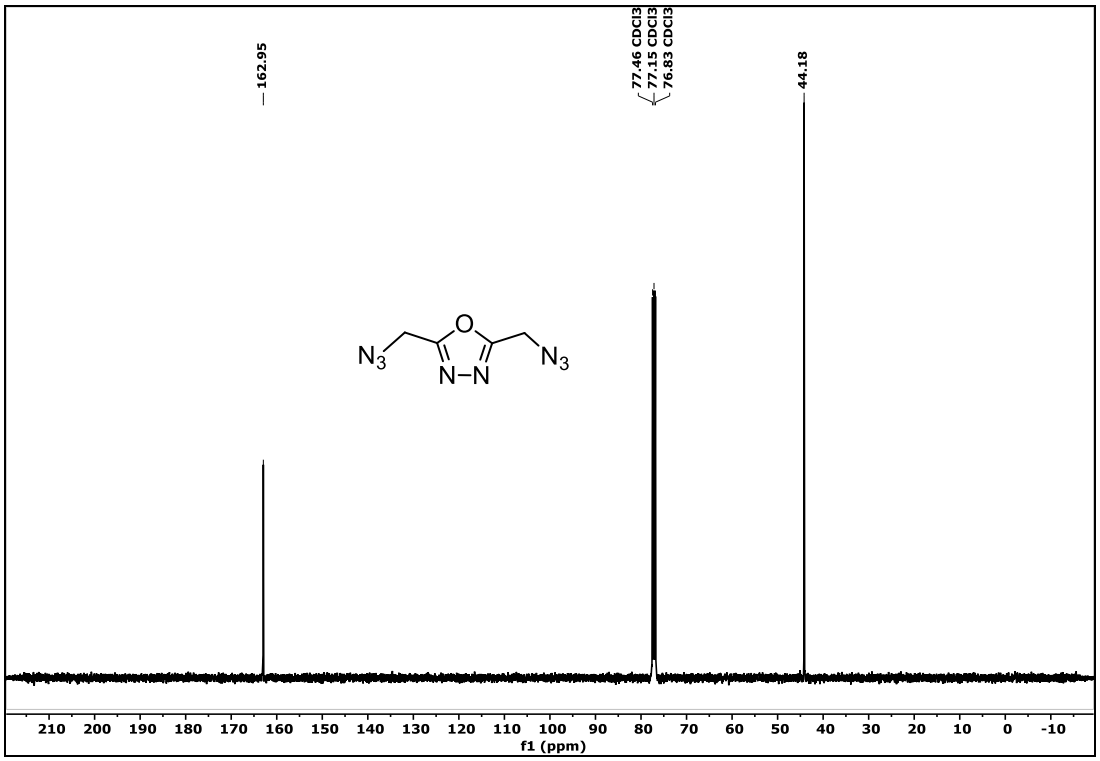


Figure B.6 ^{13}C-NMR spectrum of 2,5-Bis(azidomethyl)-1,3,4-oxadiazole (**3**) in $CDCl_3$.

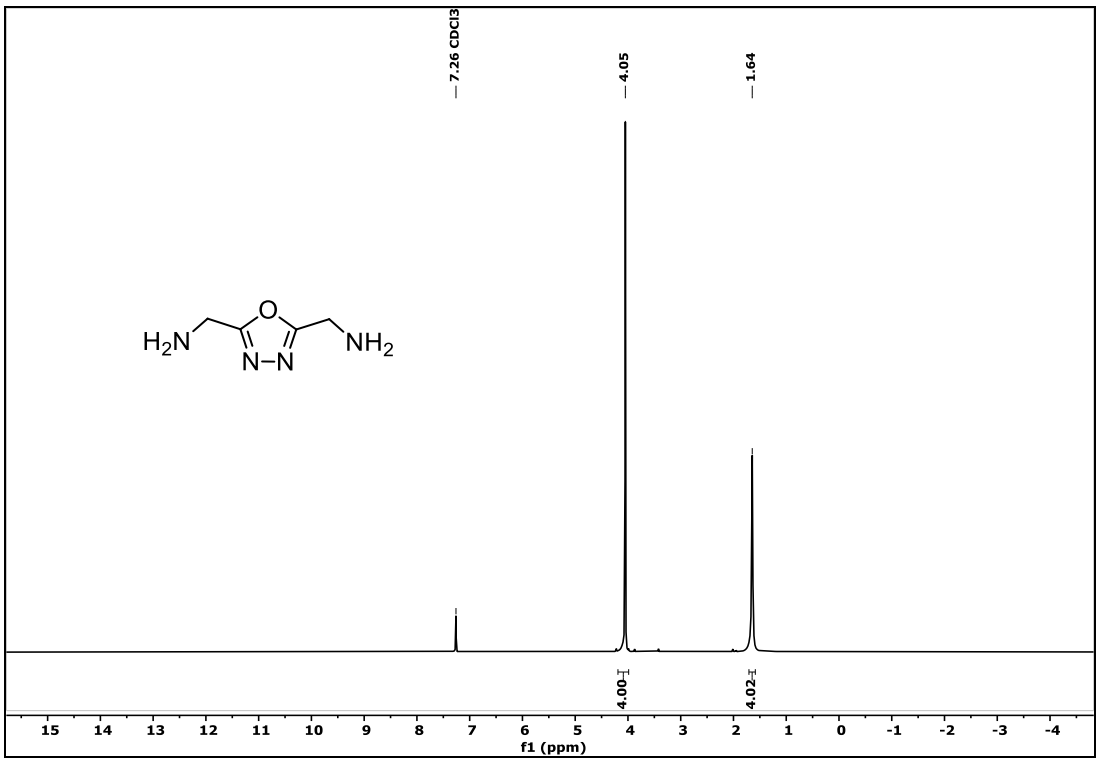


Figure B.7 ^{1}H-NMR spectrum of 2,5-Bis(aminomethyl)-1,3,4-oxadiazole (**4**) in $CDCl_3$.

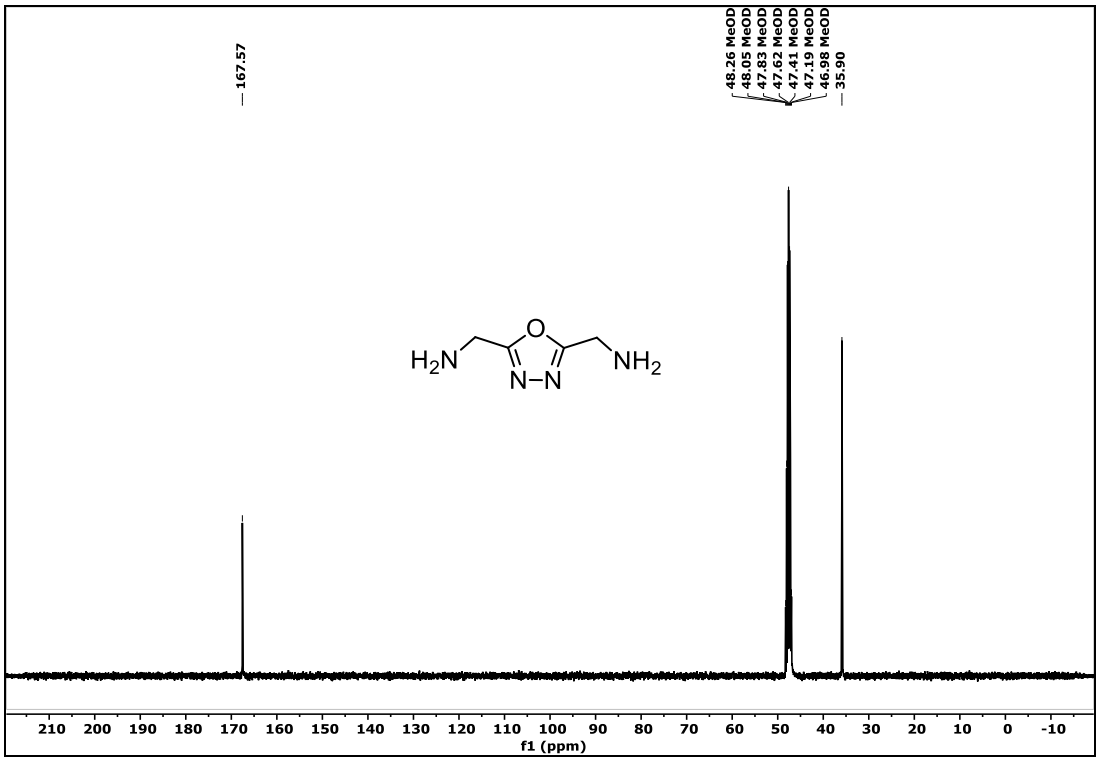


Figure B.8 ^{13}C-NMR spectrum of 2,5-Bis(aminomethyl)-1,3,4-oxadiazole (**4**) in CD_3OD.

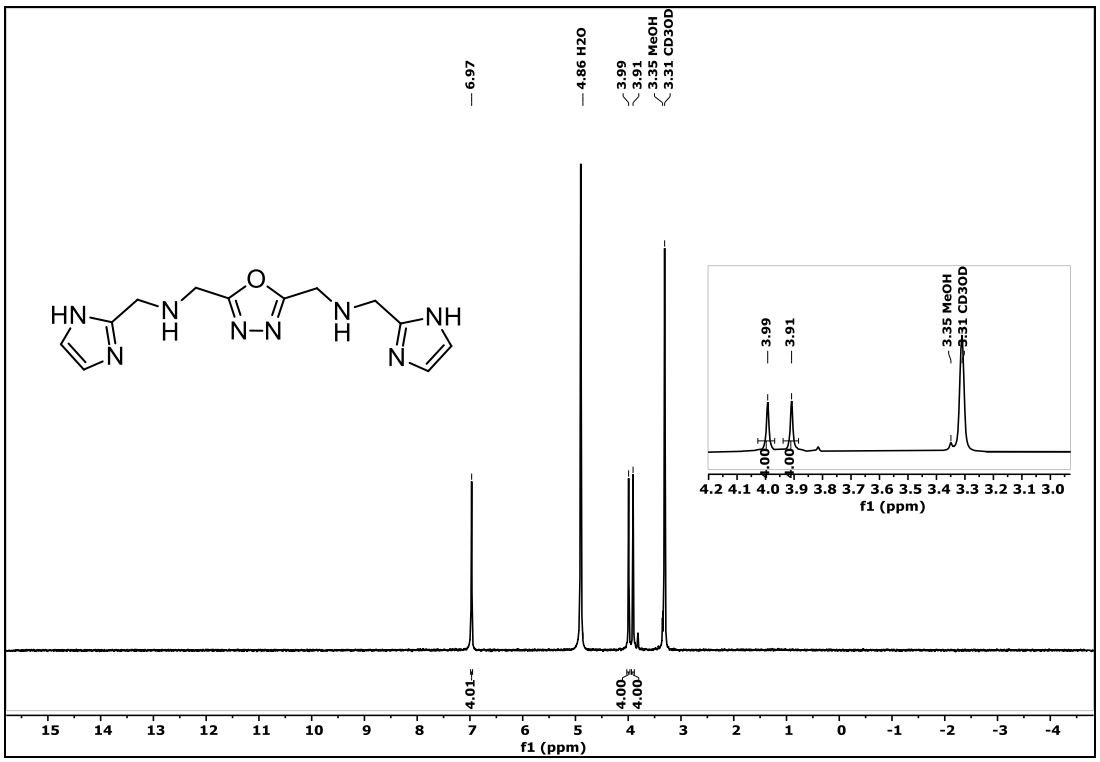


Figure B.9 ^{1}H-NMR spectrum of 2,5-Bis[(1H-imidazol-2-ylmethyl)amino]methyl-1,3,4-oxadiazole (**L^{5,Im}**) in CD_3OD.

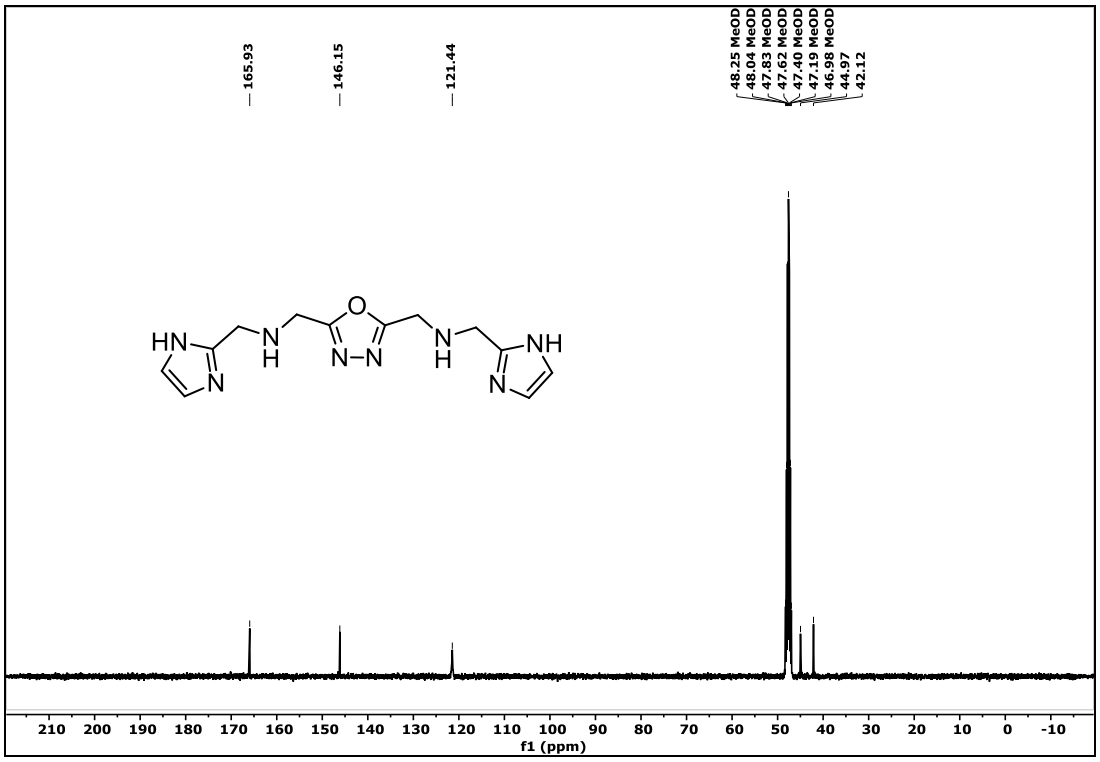


Figure B.10 ^{13}C-NMR spectrum of 2,5-Bis[(1H-imidazol-2-ylmethyl)amino]methyl-1,3,4-oxadiazole (**L^{5,Im}**) in CD_3OD.

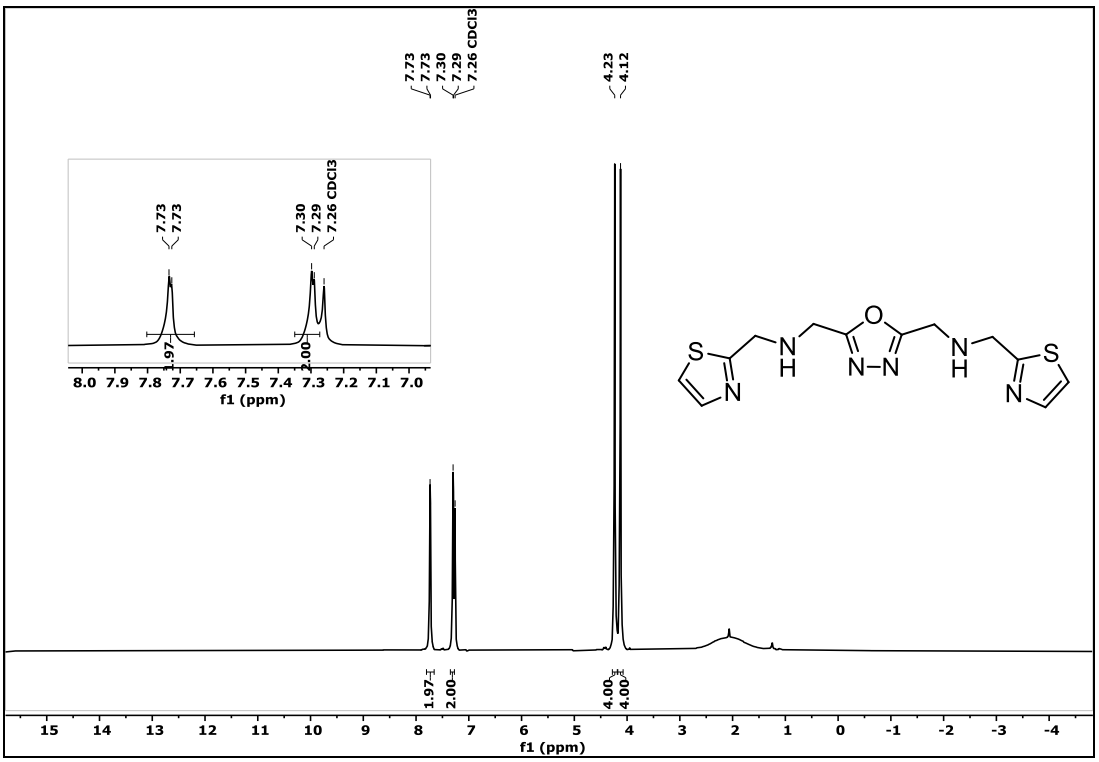


Figure B.11 ^{1}H-NMR spectrum of 2,5-Bis[(1,3-thiazol-2-ylmethyl)amino]methyl-1,3,4-oxadiazole (**L^{5,TA}**) in $CDCl_3$.

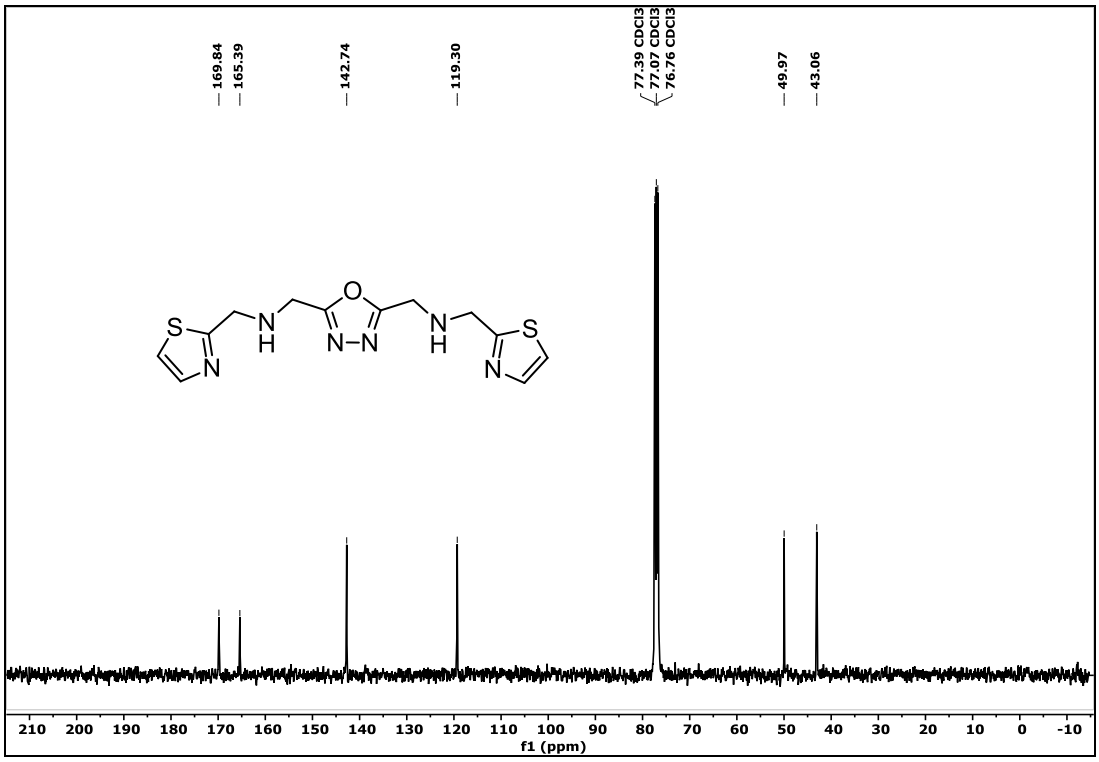


Figure B.12 ^{13}C-NMR spectrum of 2,5-Bis[(1,3-thiazol-2-ylmethyl)amino]methyl-1,3,4-oxadiazole (**L^{5,TA}**) in $CDCl_3$.

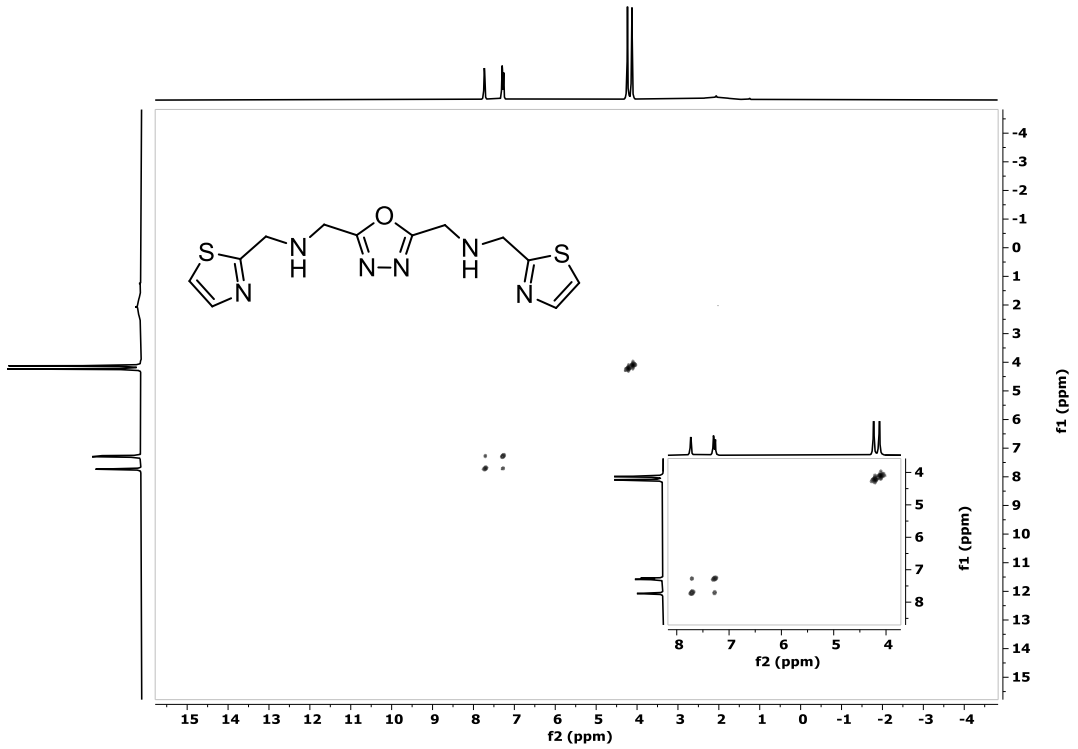


Figure B.13 ^{1}H-^{1}H-COSY spectrum of 2,5-Bis[(1,3-thiazol-2-ylmethyl)amino]methyl-1,3,4-oxadiazole (**L**^{5,TA}) in $CDCl_3$.

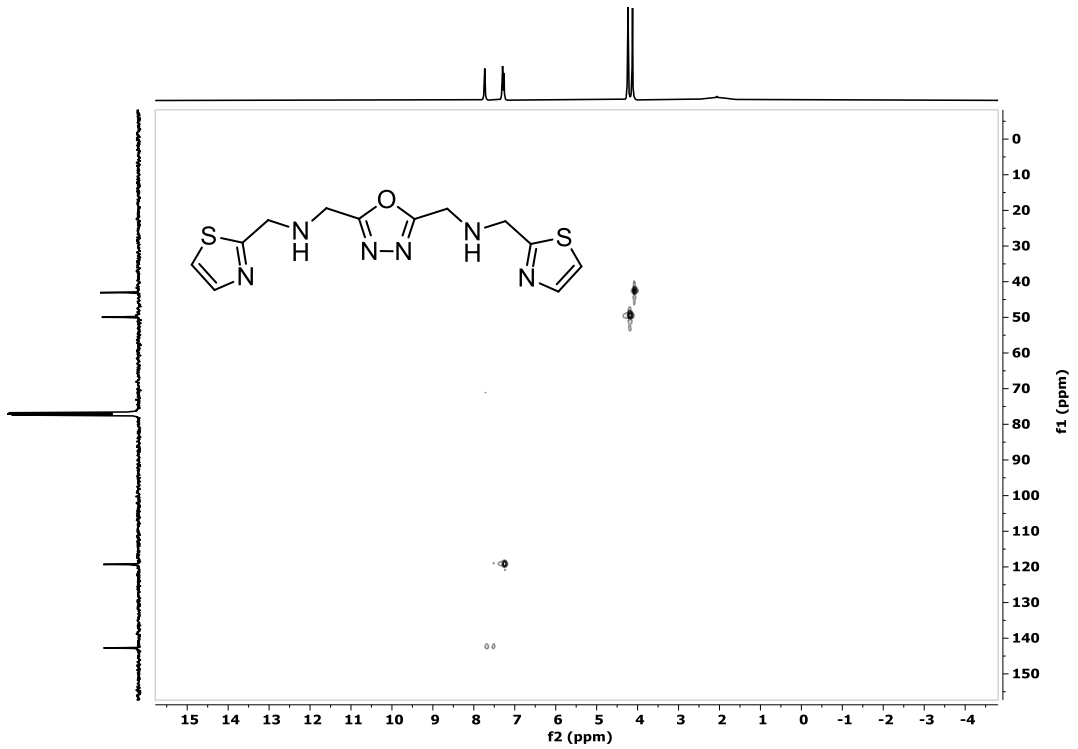


Figure B.14 ^{1}H-^{13}C-HSQC spectrum of 2,5-Bis[(1,3-thiazol-2-ylmethyl)amino]methyl-1,3,4-oxadiazole (**L**^{5,TA}) in $CDCl_3$.

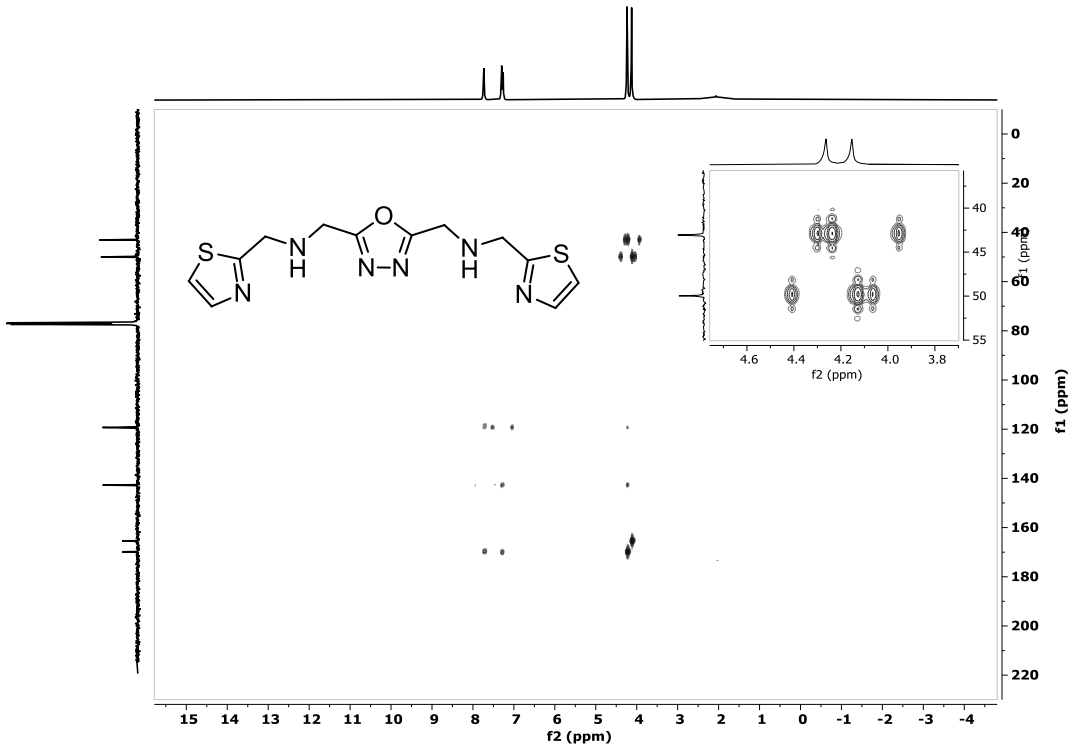


Figure B.15 ^{1}H-^{13}C-HMBC spectrum of 2,5-Bis[(1,3-thiazol-2-ylmethyl)amino]methyl-1,3,4-oxadiazole ($\mathbf{L}^{5,TA}$) in $CDCl_3$.

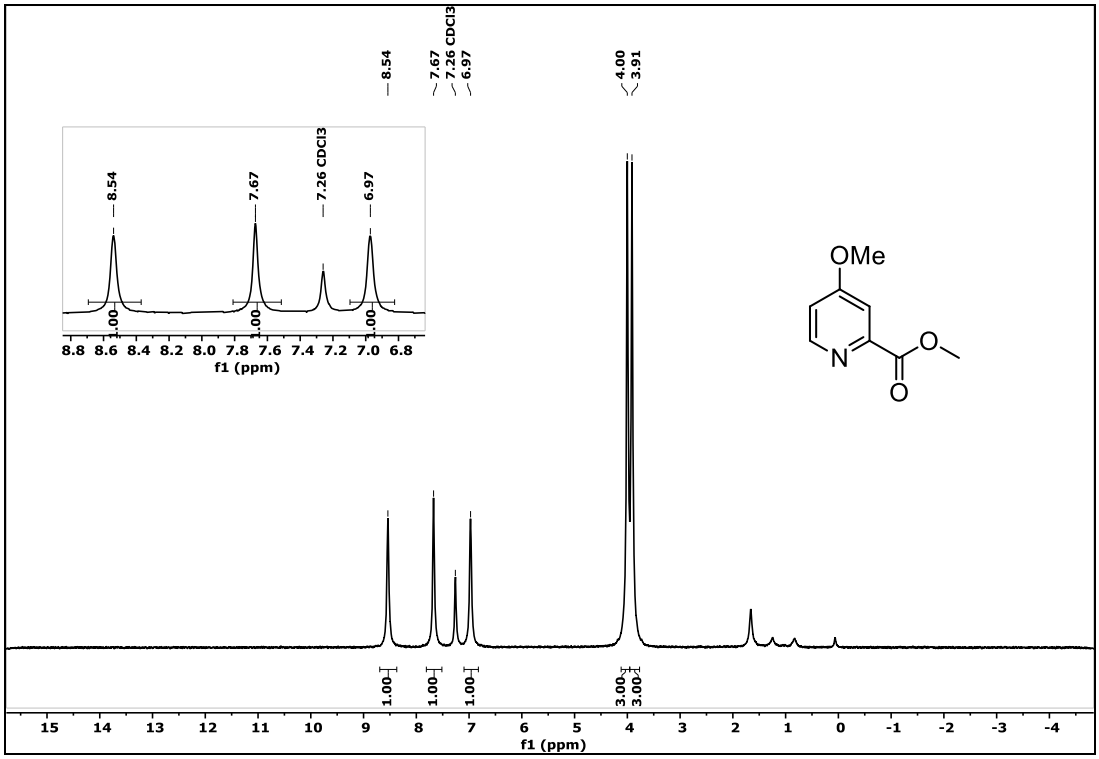


Figure B.16 ^{1}H-NMR spectrum of Methyl 4-methoxypicolinate (**5**) in $CDCl_3$.

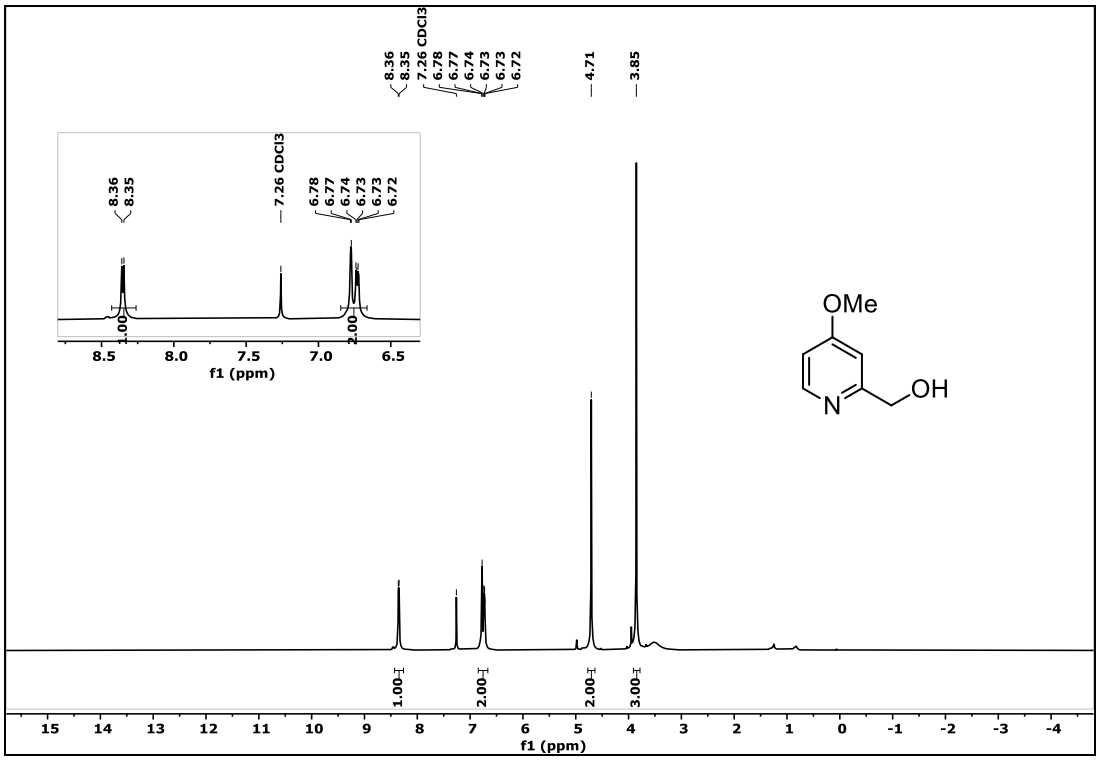


Figure B.17 ^{1}H-NMR spectrum of 4-Methoxy-2-(hydroxymethyl)pyridine (**6**) in $CDCl_3$.

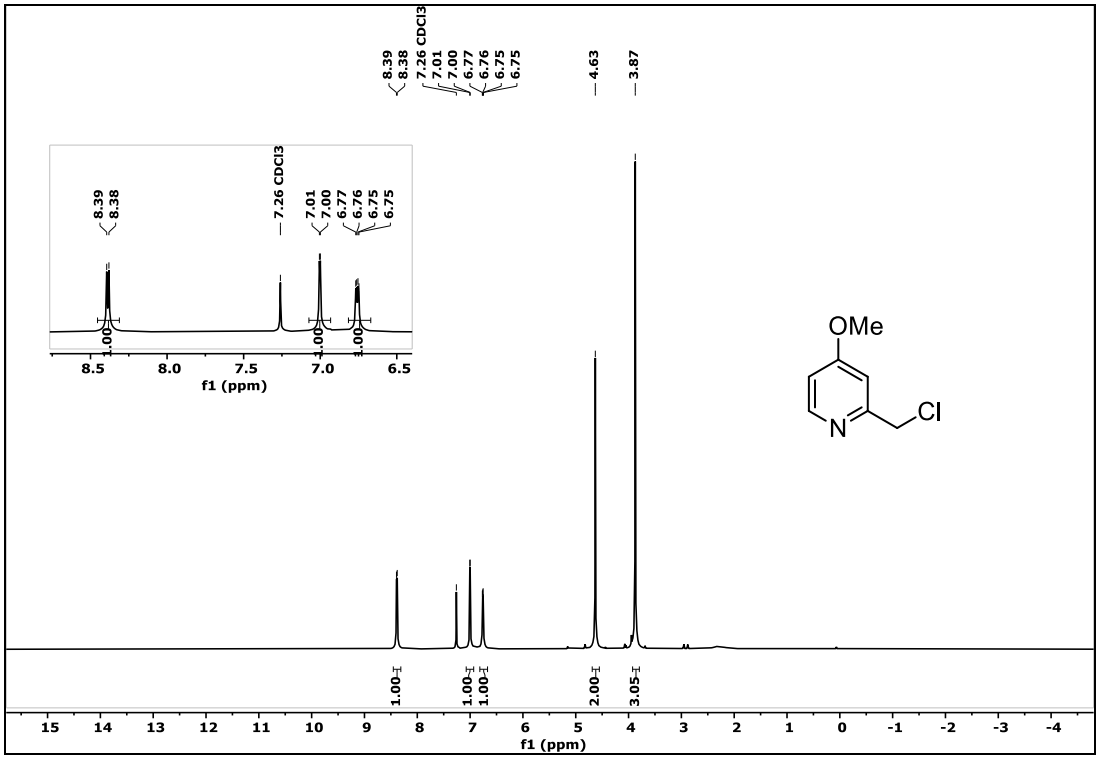


Figure B.18 ^{1}H-NMR spectrum of 2-Chloromethyl-4-methoxypyridine (**7**) in $CDCl_3$.

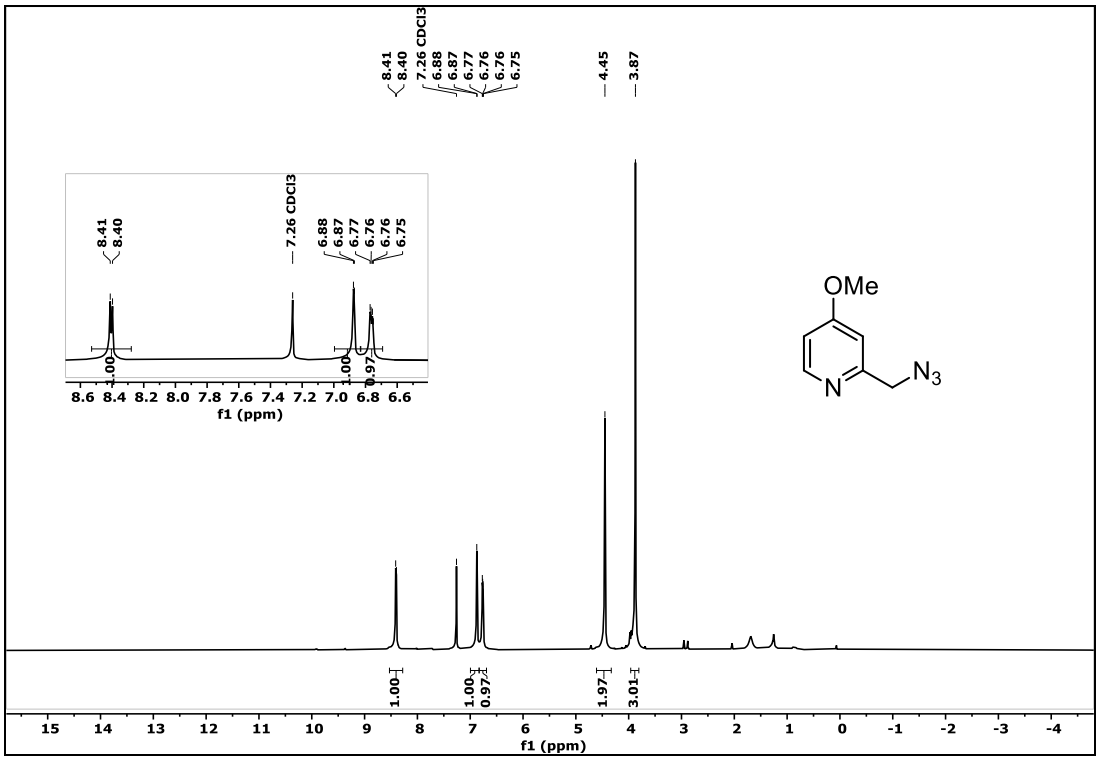


Figure B.19 ^{1}H-NMR spectrum of 2-Azidomethyl-4-methoxypyridine (**8**) in $CDCl_3$.

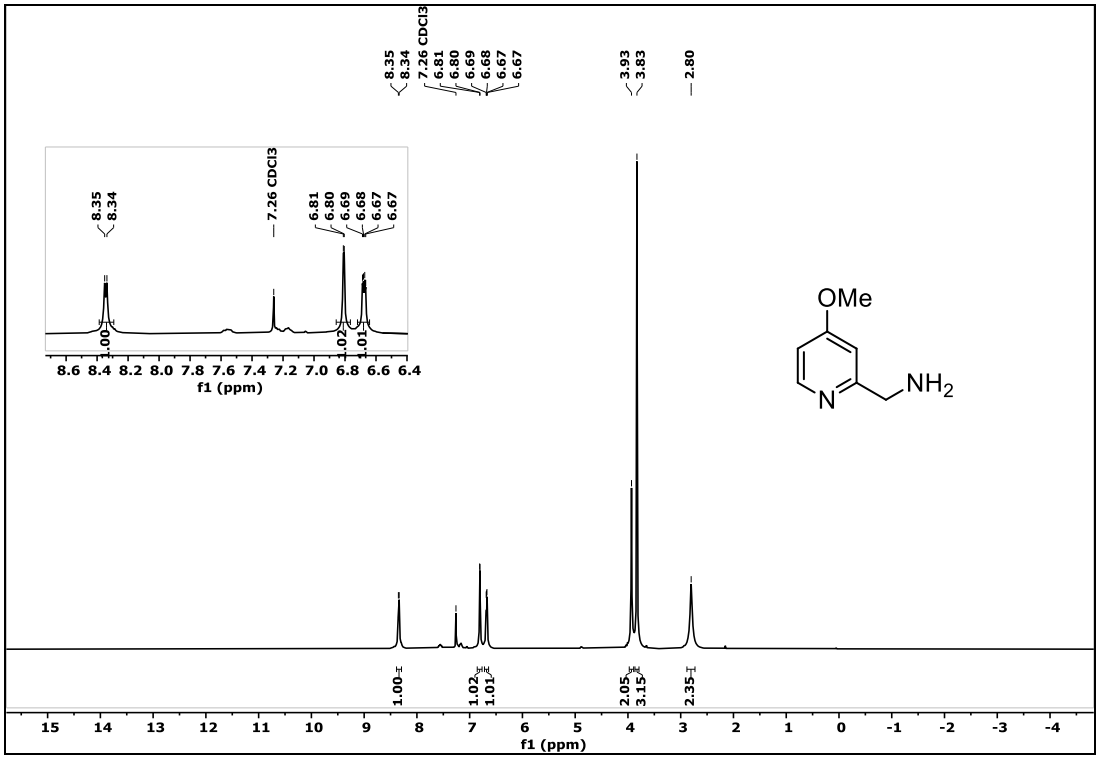


Figure B.20 ^{1}H-NMR spectrum of (4-Methoxy-pyridin-2-yl)methylamine (9) in $CDCl_3$.

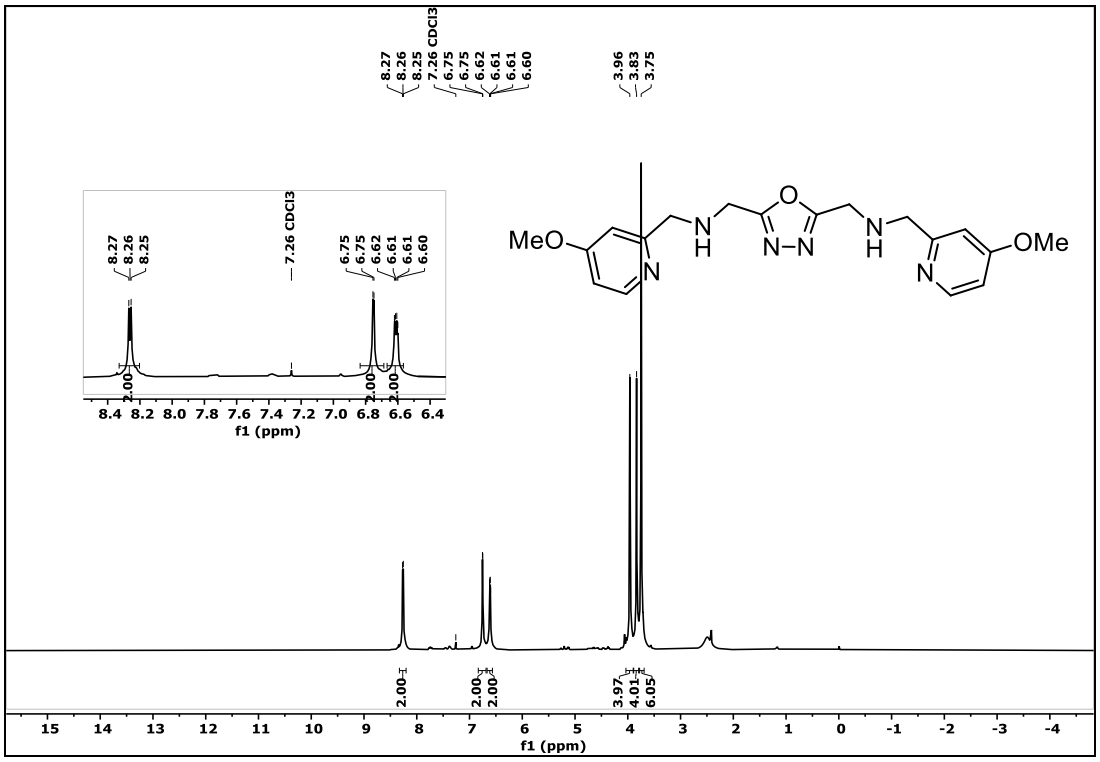


Figure B.21 ^{1}H-NMR spectrum of 2,5-Bis[(4-methoxypyridin-2-ylmethyl)amino]methyl-1,3,4-oxadiazole (**L^{6,OMe}**) in $CDCl_3$.

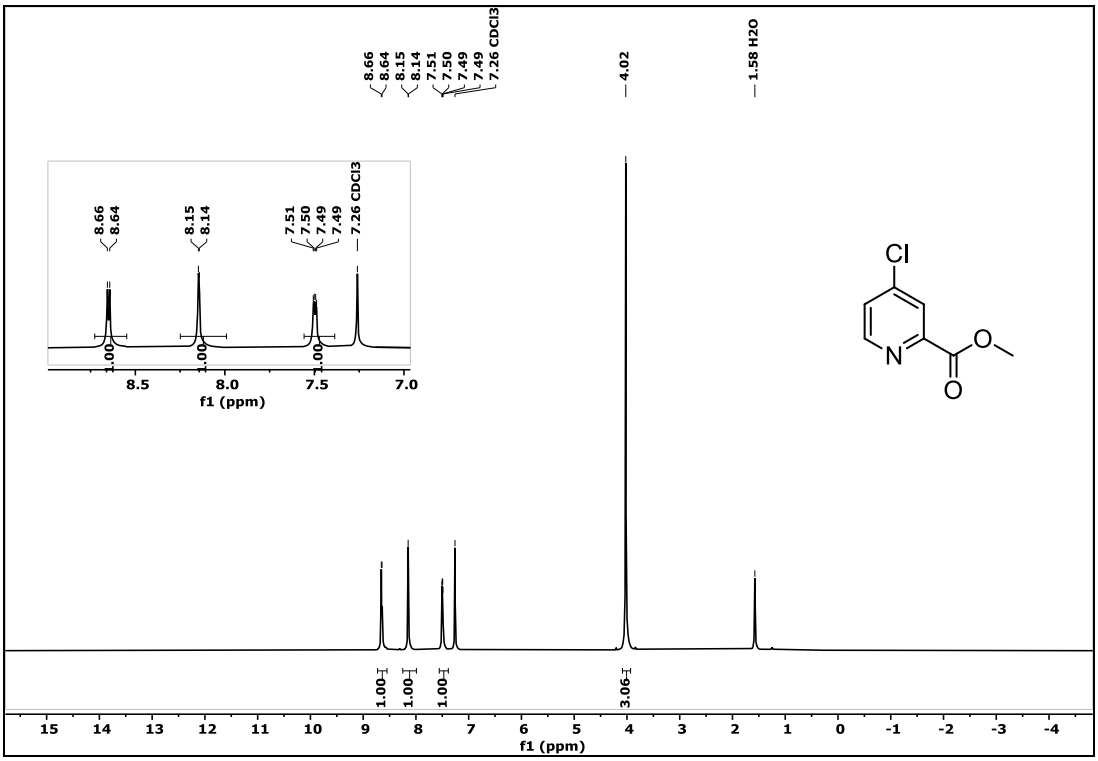


Figure B.22 ^{1}H-NMR spectrum of 4-Chloro-pyridine-2-carboxylic acid methyl ester (**10**) in $CDCl_3$.

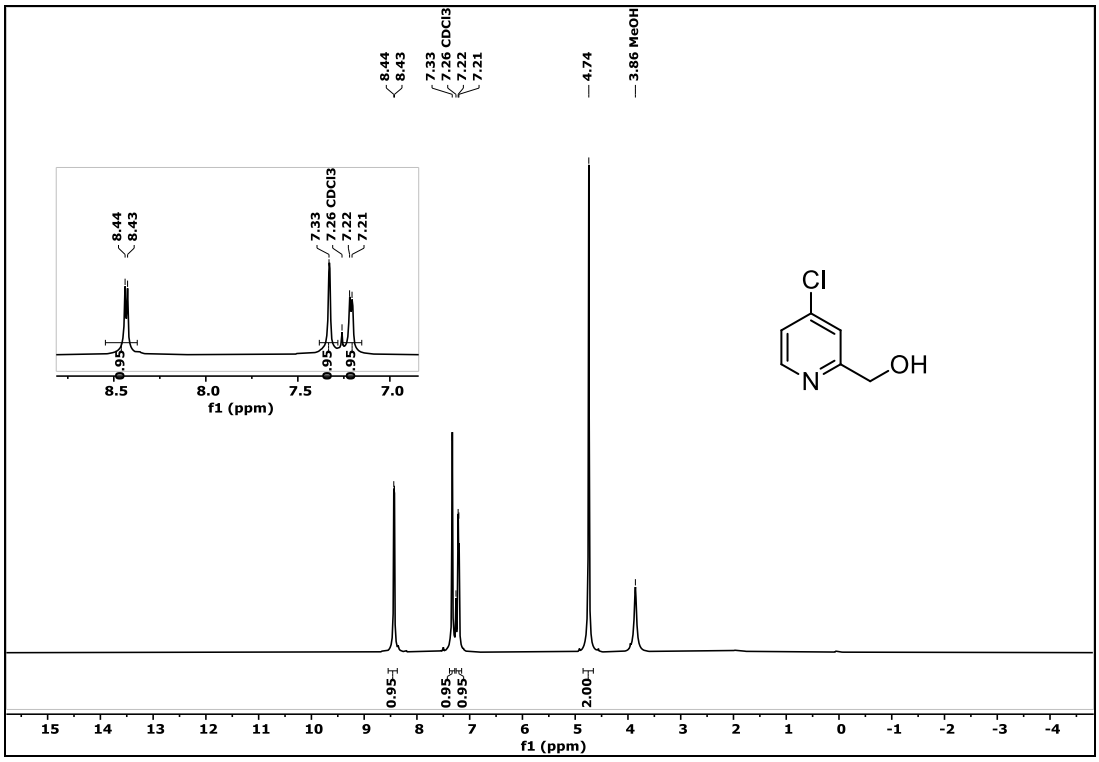


Figure B.23 ^{1}H-NMR spectrum of (4-Chloropyridin-2-yl)methanol (**11**) in $CDCl_3$.

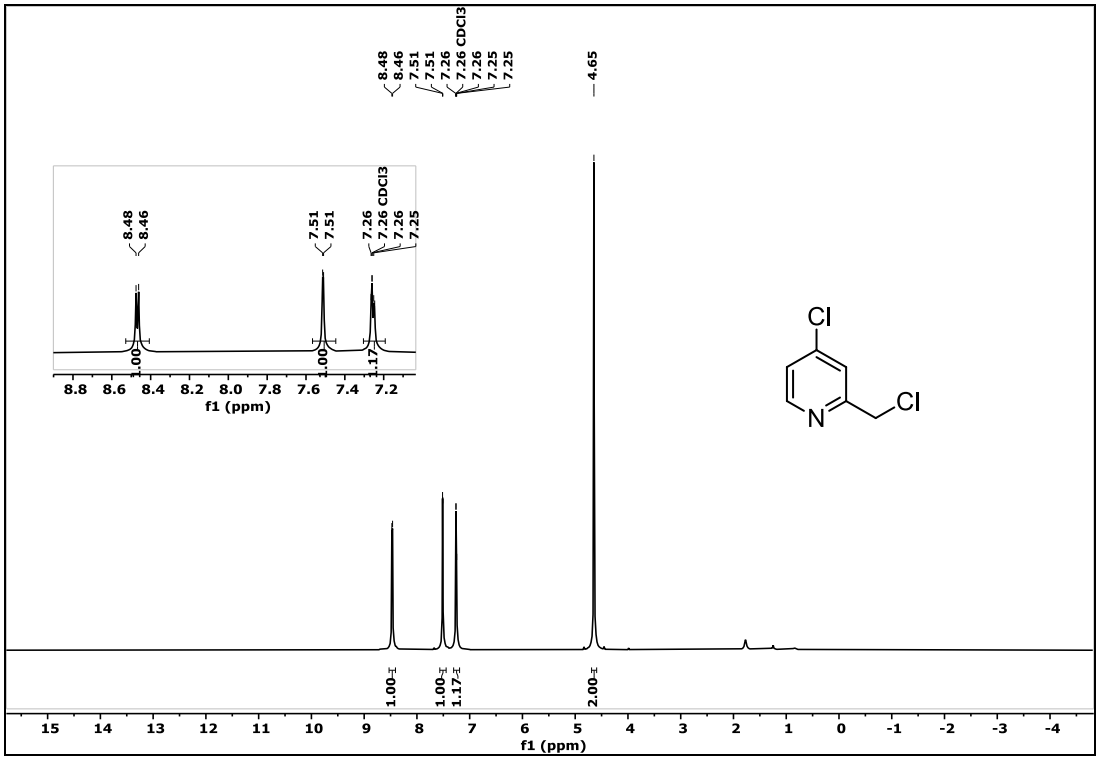


Figure B.24 ^{1}H-NMR spectrum of 4-Chloro-2-chloromethyl pyridine (**12**) in $CDCl_3$.

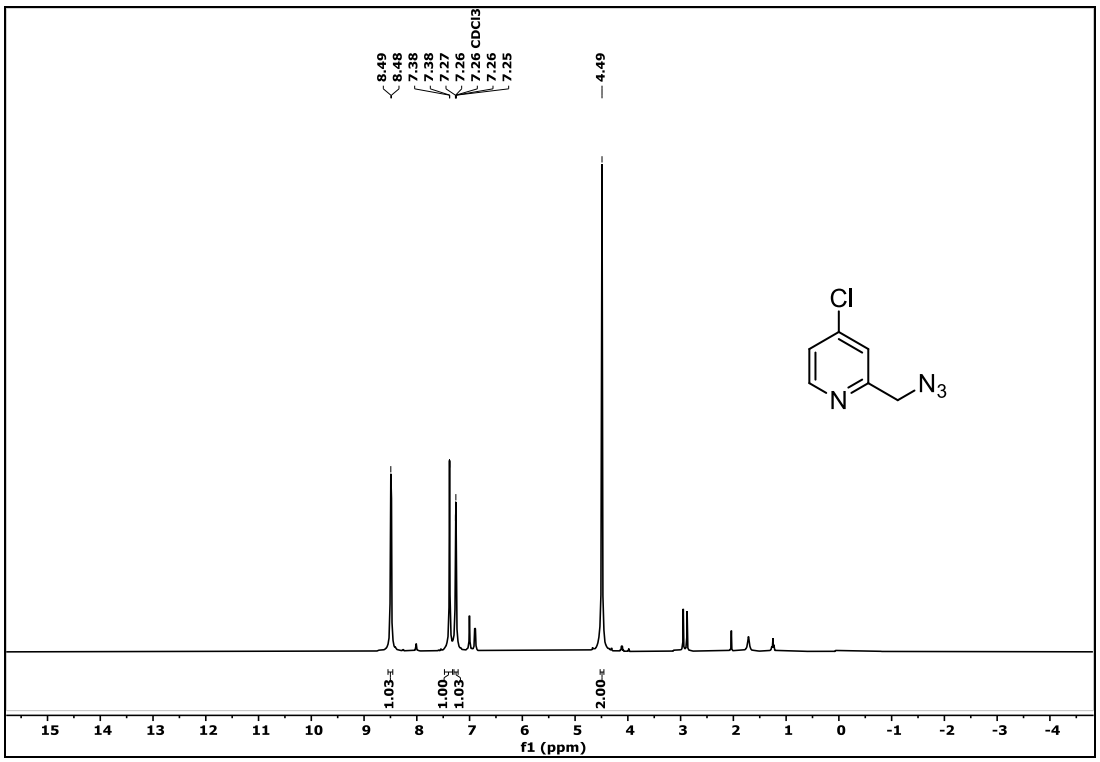


Figure B.25 ^{1}H-NMR spectrum of 2-(Azidomethyl)-4-chloropyridine (**13**) in $CDCl_3$.

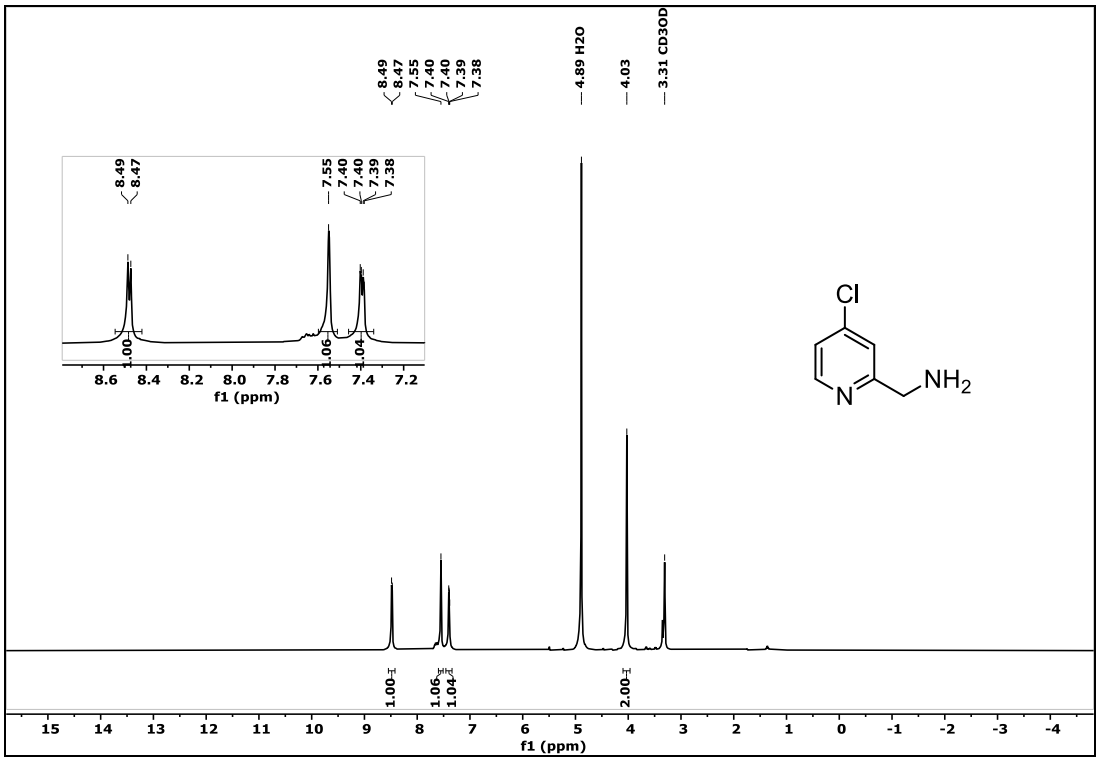


Figure B.26 ^{1}H-NMR spectrum of (4-Chloropyridin-2-yl)methanamine (**14**) in CD_3OD.

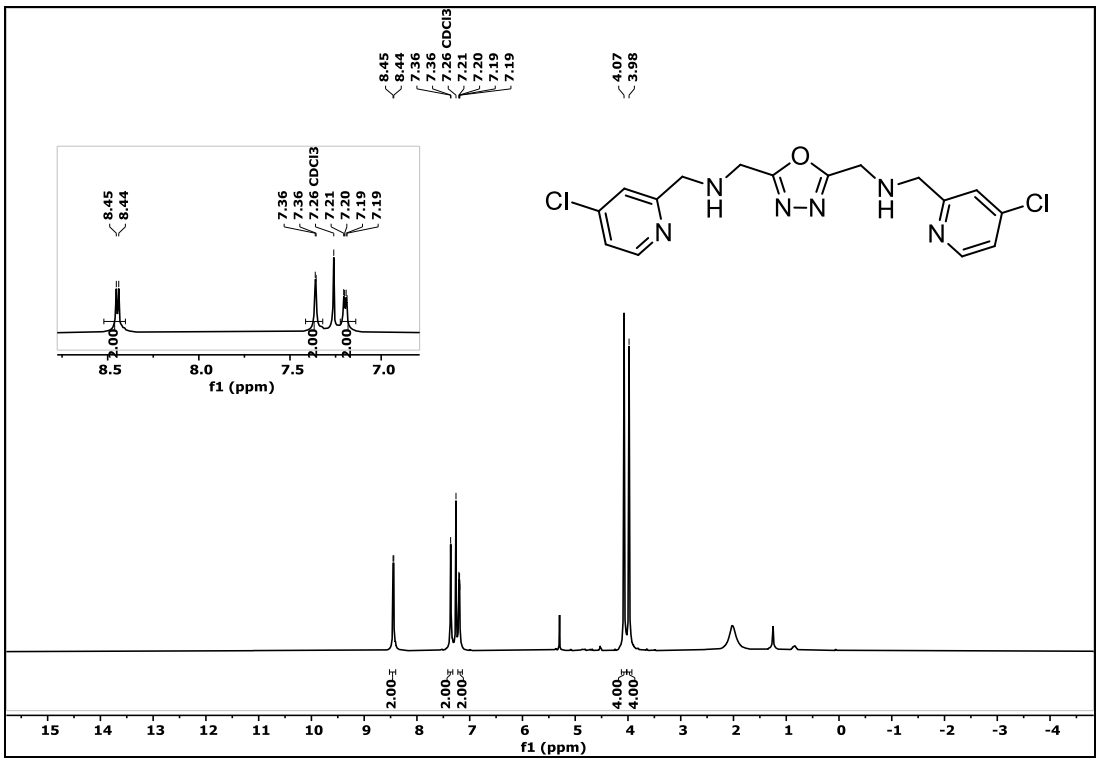


Figure B.27 ^{1}H-NMR spectrum 2,5-Bis[(4-chloropyridin-2-ylmethyl)amino]methyl-1,3,4-oxadiazole (**L^{6,Cl}**) in $CDCl_3$.

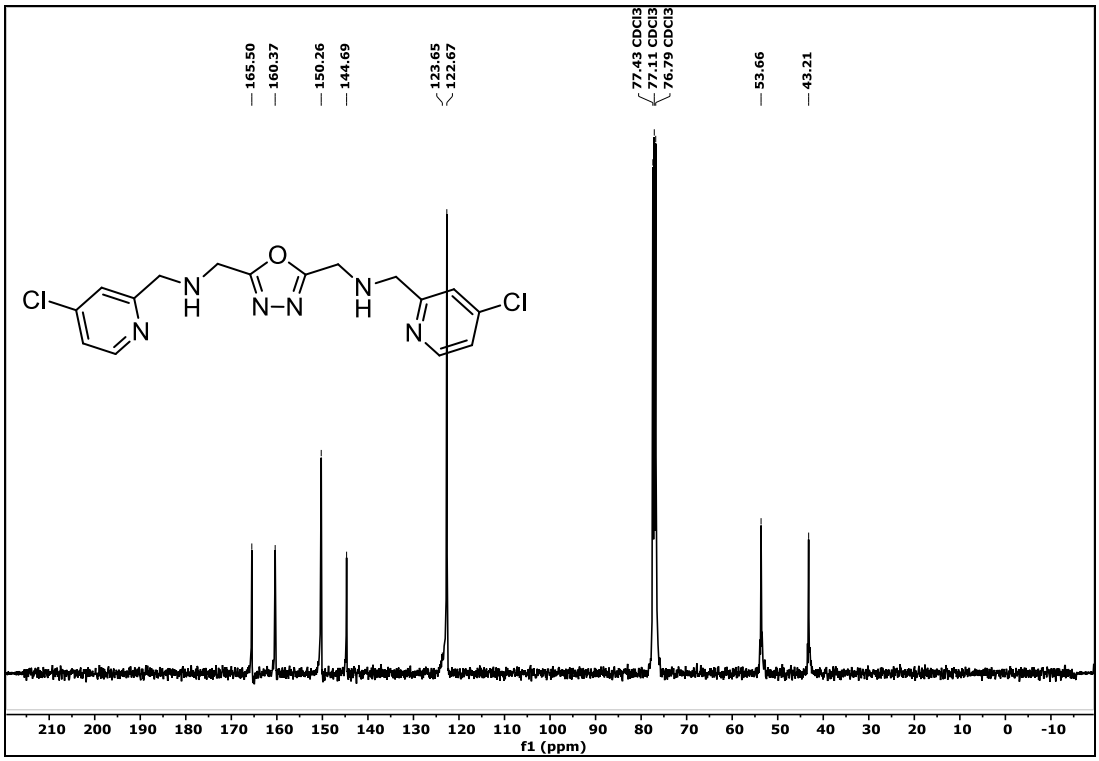


Figure B.28 ^{13}C-NMR spectrum 2,5-Bis[(4-chloropyridin-2-ylmethyl)amino]methyl-1,3,4-oxadiazole (**L^{6,Cl}**) in $CDCl_3$.

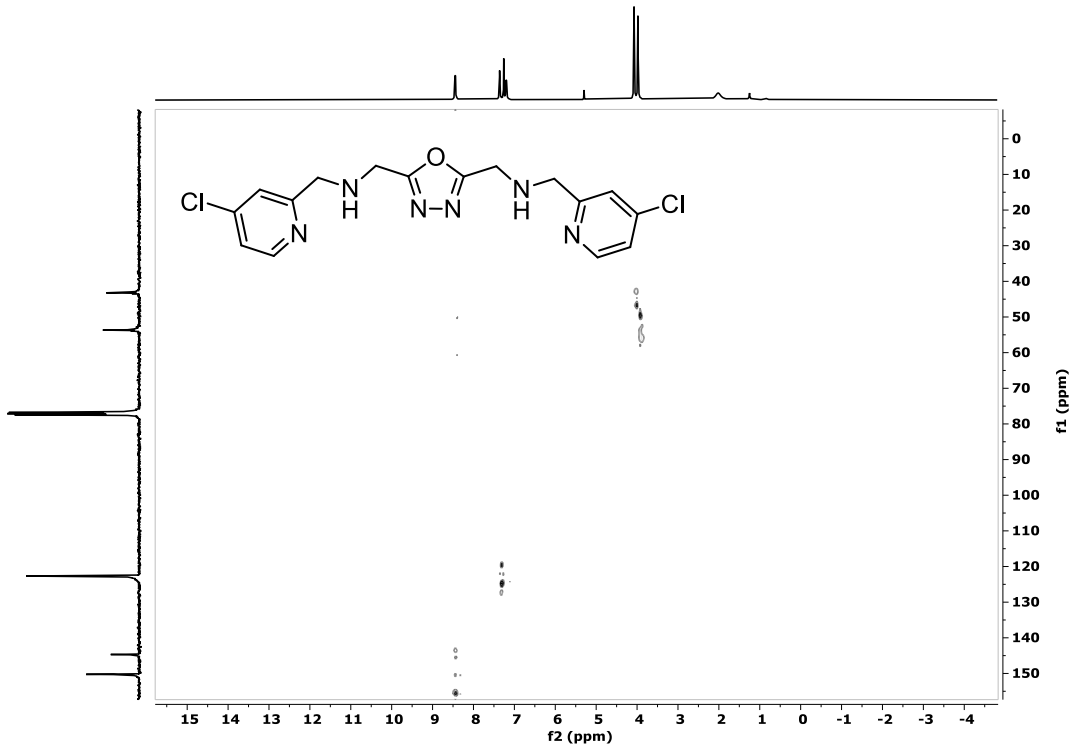


Figure B.29 ^{1}H-^{13}C-HSQC spectrum of 2,5-Bis[(1,3-thiazol-2-ylmethyl)amino]methyl-1,3,4-oxadiazole ($\mathbf{L^{6,Cl}}$) in $CDCl_3$.

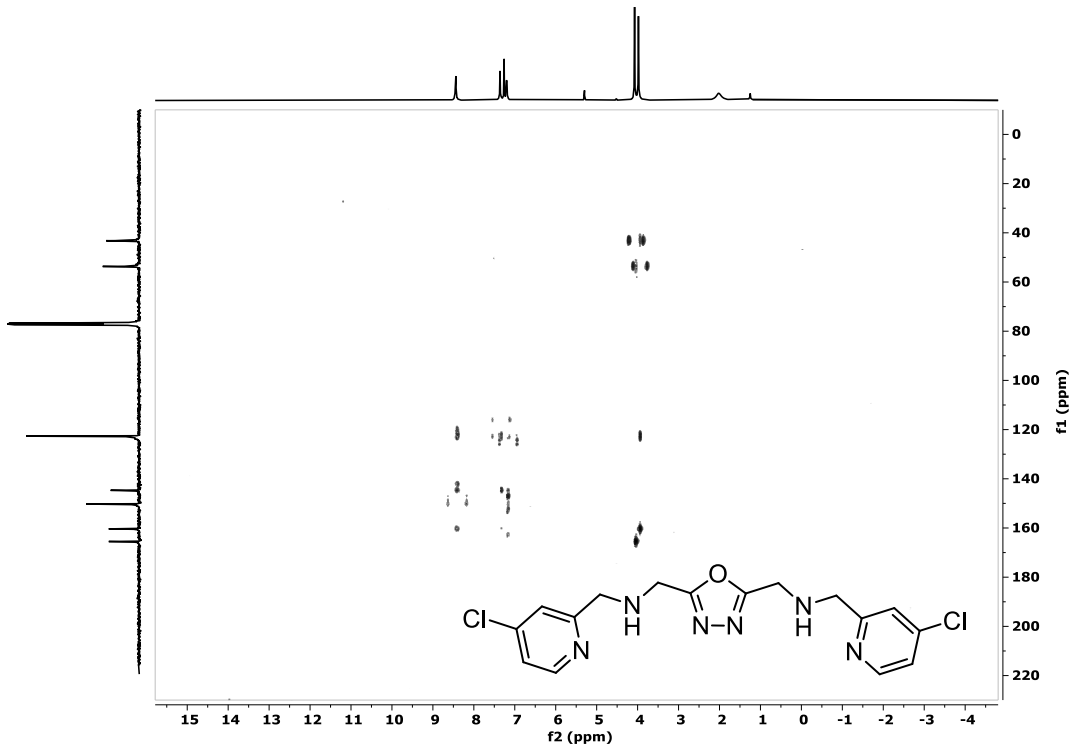


Figure B.30 ^{1}H-^{13}C-HMBC spectrum of 2,5-Bis[(1,3-thiazol-2-ylmethyl)amino]methyl-1,3,4-oxadiazole ($\mathbf{L^{6,Cl}}$) in $CDCl_3$.

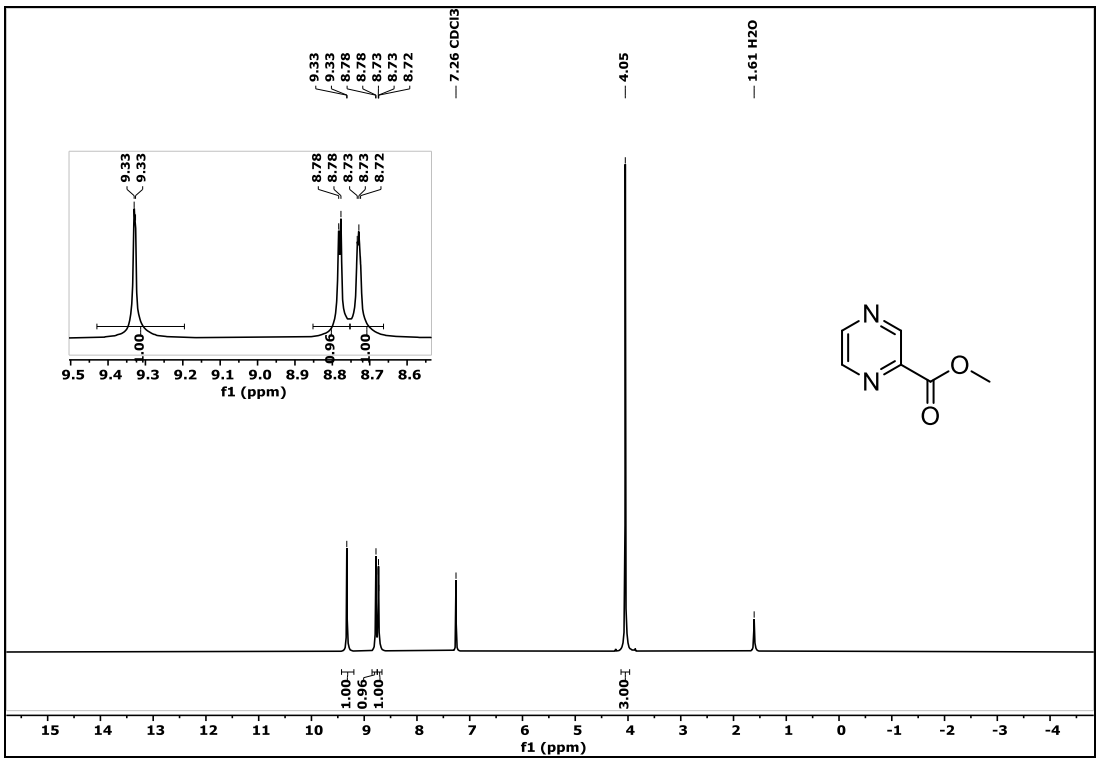


Figure B.31 ^{1}H-NMR spectrum of Methyl pyrazine-2-carboxylate (**15**) in $CDCl_3$.

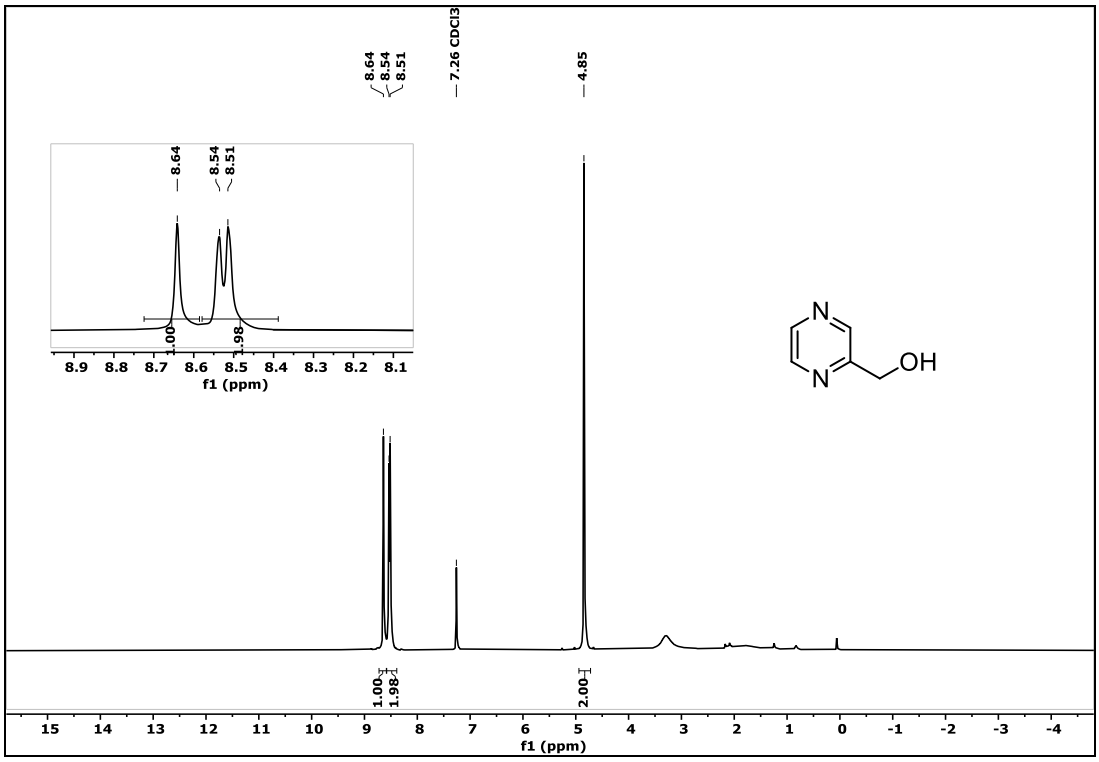


Figure B.32 ^{1}H-NMR spectrum of Pyrazin-2-ylmethanol (**16**) in $CDCl_3$.

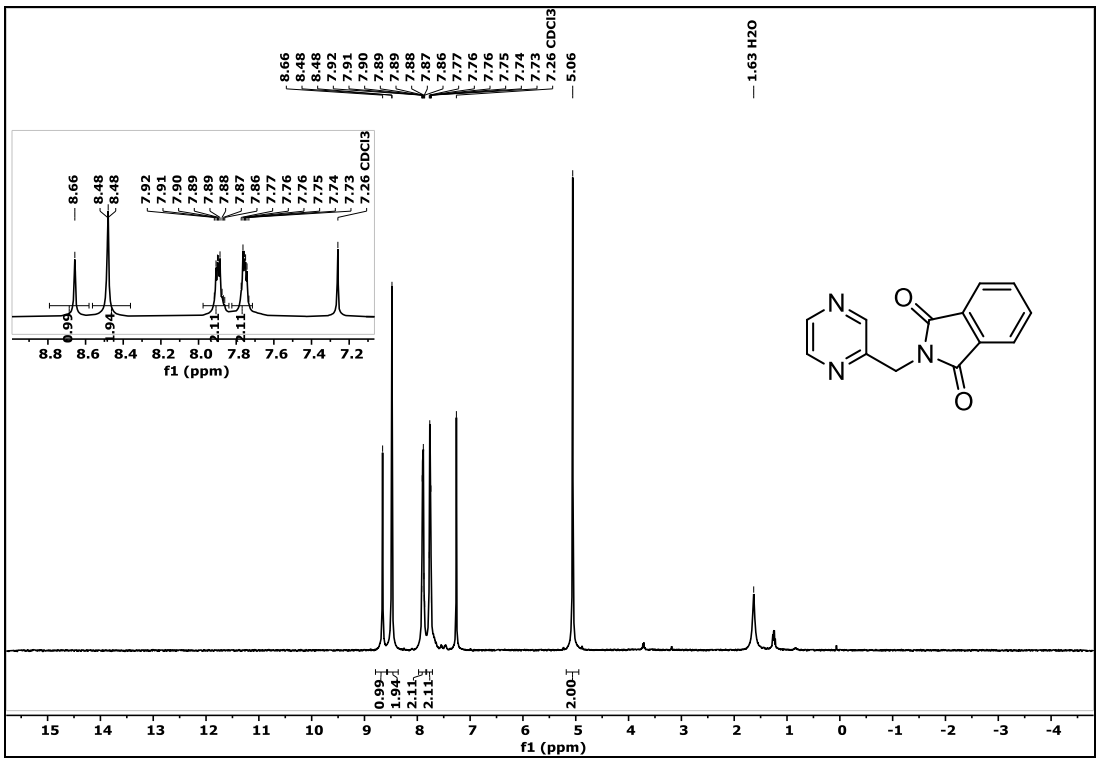


Figure B.33 ^{1}H-NMR spectrum of 2-Pyrazinemethylphthalimide (**17**) in $CDCl_3$.

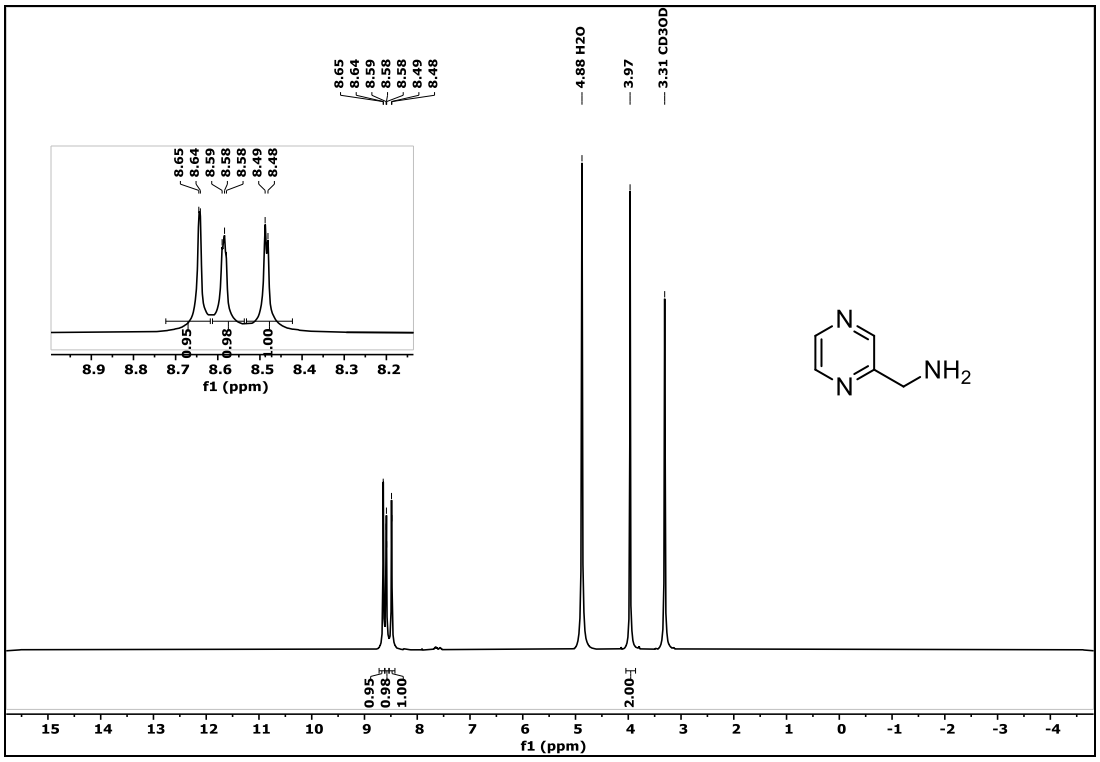


Figure B.34 ^{1}H-NMR spectrum of 2-(Aminomethyl)pyrazine (**18**) in CD_3OD.

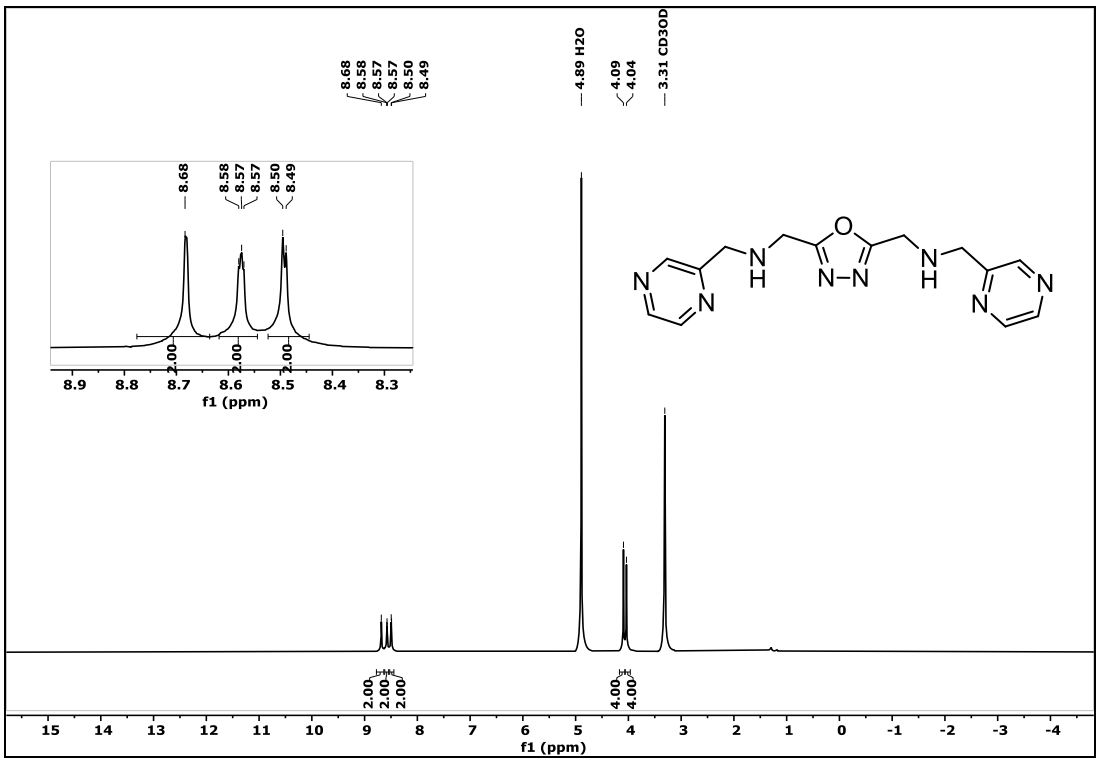


Figure B.35 ^{1}H-NMR spectrum of 2,5-Bis[(pyrazin-2-ylmethyl)amino]methyl-1,3,4-oxadiazole (**L^{6,N}**) in CD_3OD.

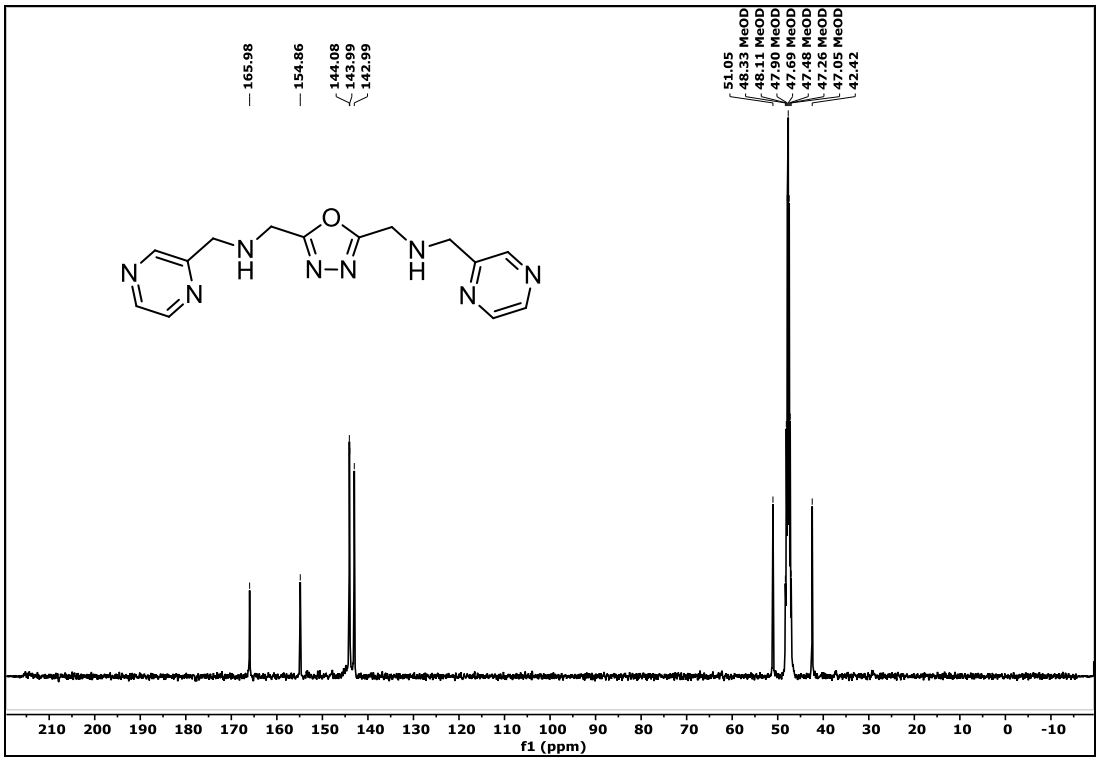


Figure B.36 ^{13}C-NMR spectrum of 2,5-Bis[(pyrazin-2-ylmethyl)amino]methyl-1,3,4-oxadiazole (**L^{6,N}**) in CD_3OD.

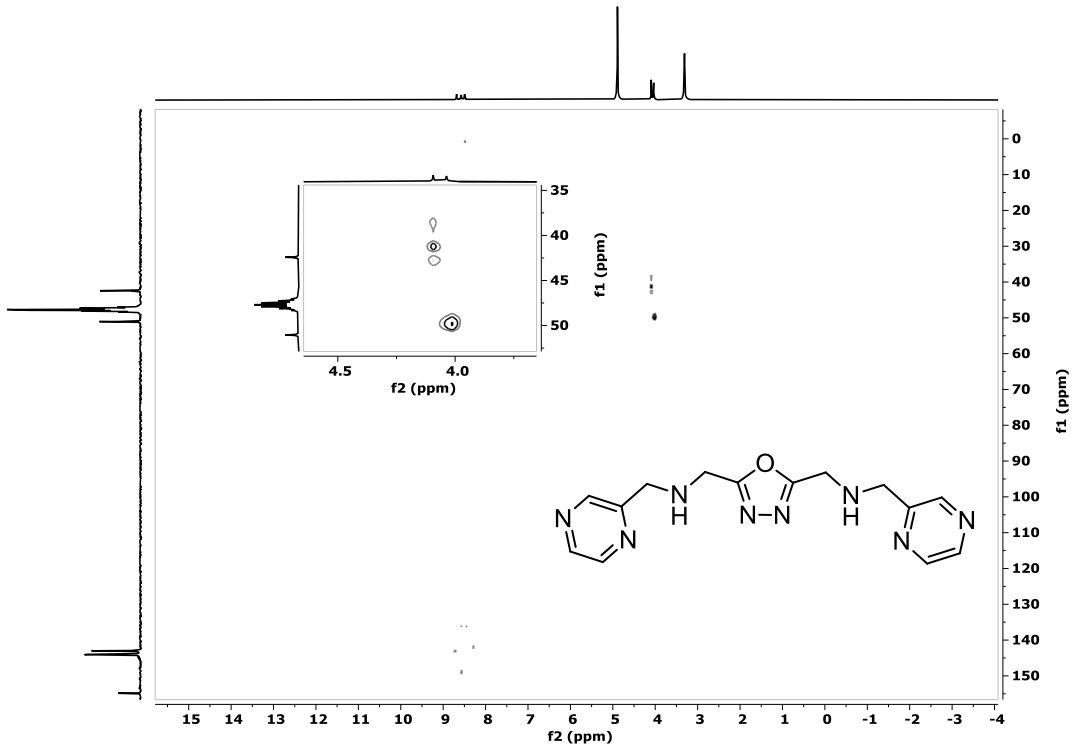


Figure B.37 ^{1}H-^{13}C-HSQC spectrum of 2,5-Bis[(pyrazin-2-ylmethyl)amino]methyl-1,3,4-oxadiazole ($L^{6,N}$) in CD_3OD.

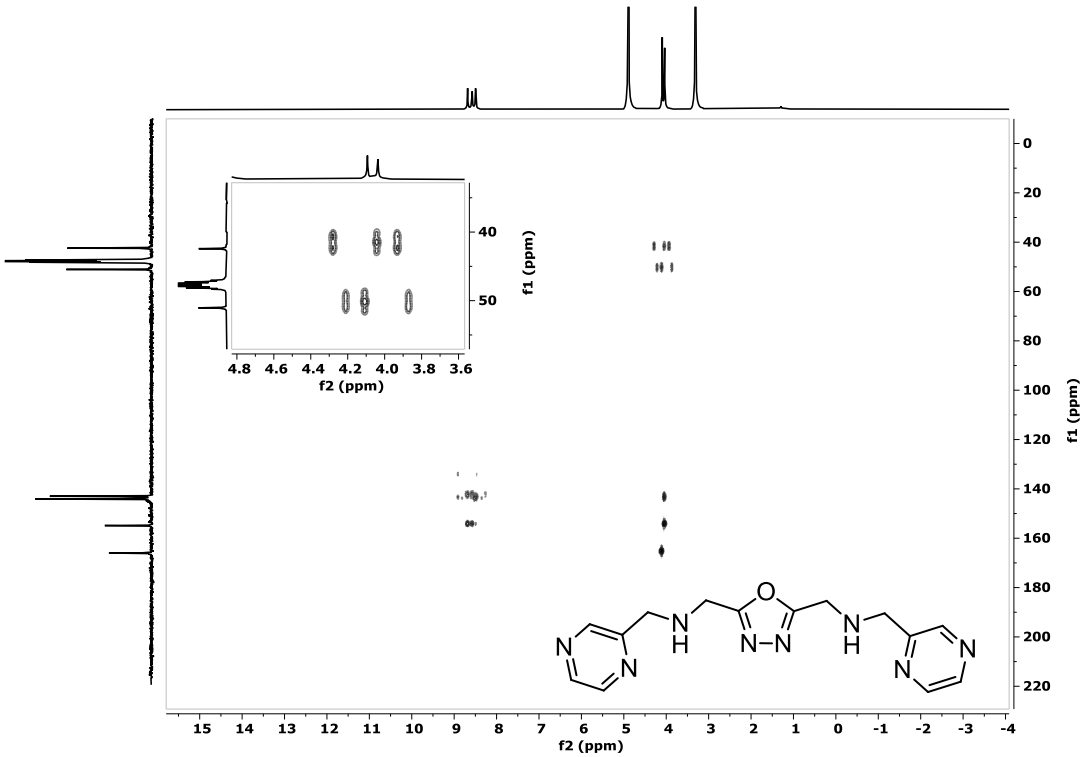


Figure B.38 ^{1}H-^{13}C-HMBC spectrum of 2,5-Bis[(pyrazin-2-ylmethyl)amino]methyl-1,3,4-oxadiazole ($L^{6,N}$) in CD_3OD.

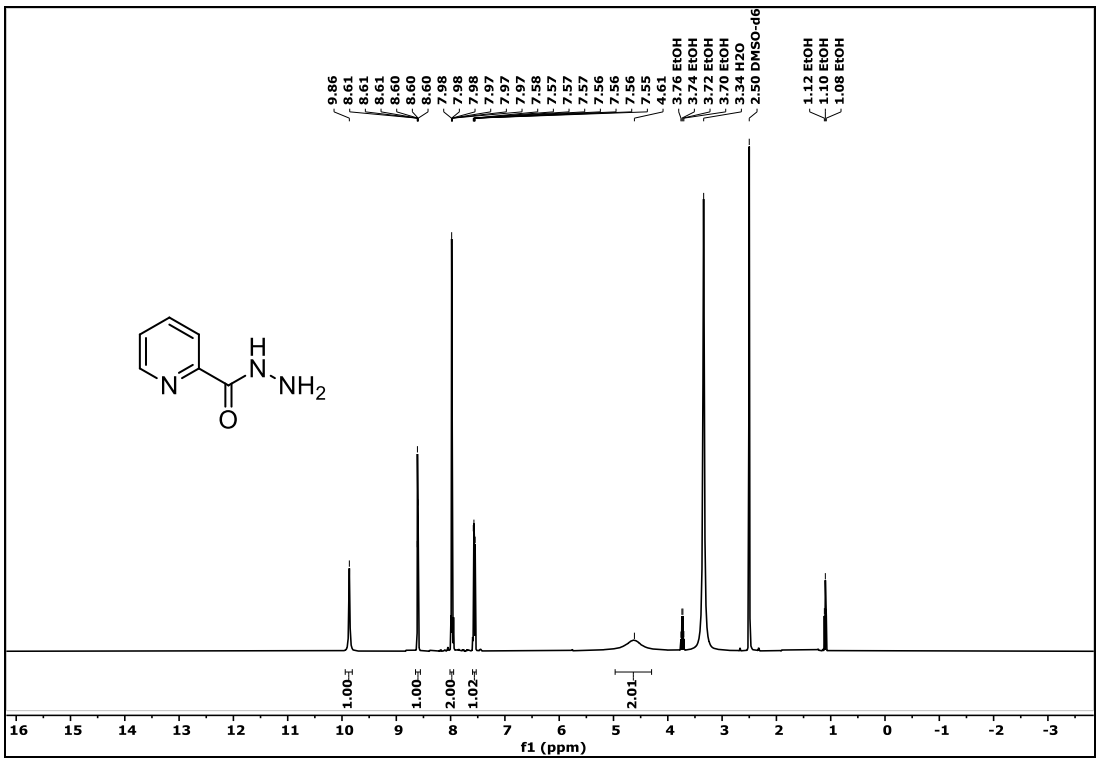


Figure B.39 [1]H-NMR spectrum of Pyridin-2-carboxylic acid hydrazide (**19**) in DMSO-d_6.

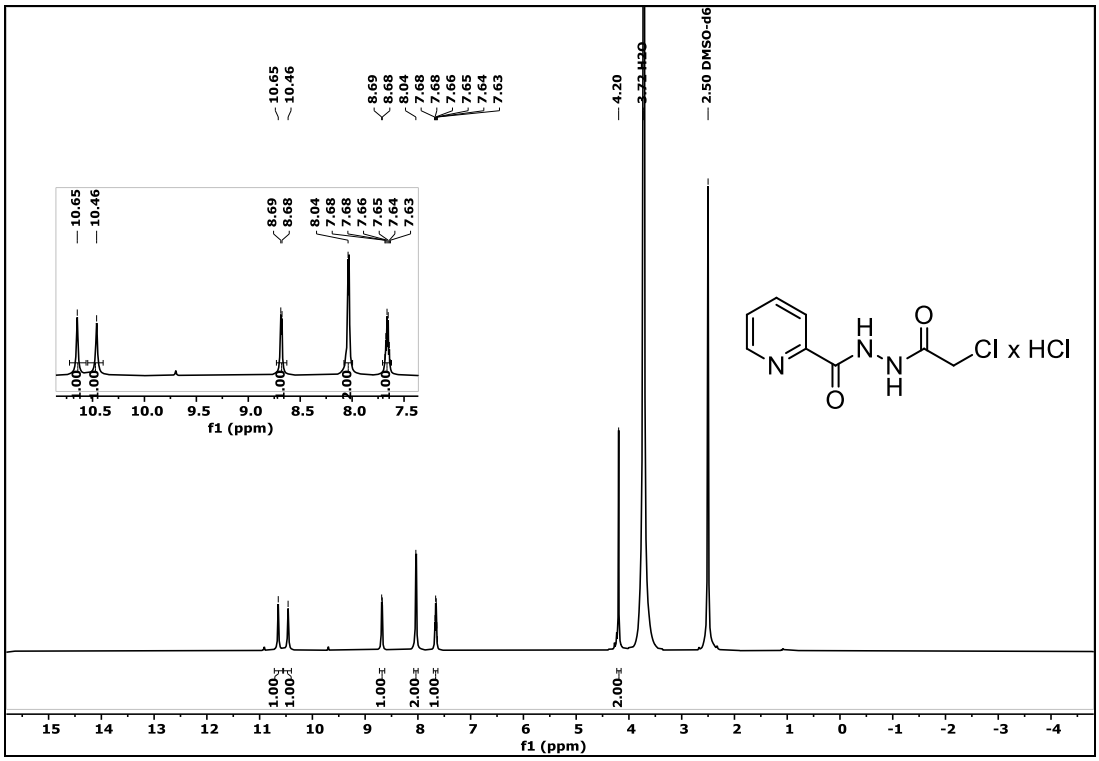


Figure B.40 [1]H-NMR spectrum of N'-(Chloroacetyl)-2-pyridinecarboxylic acid hydrazide hydrochloride (**20**) in DMSO-d_6.

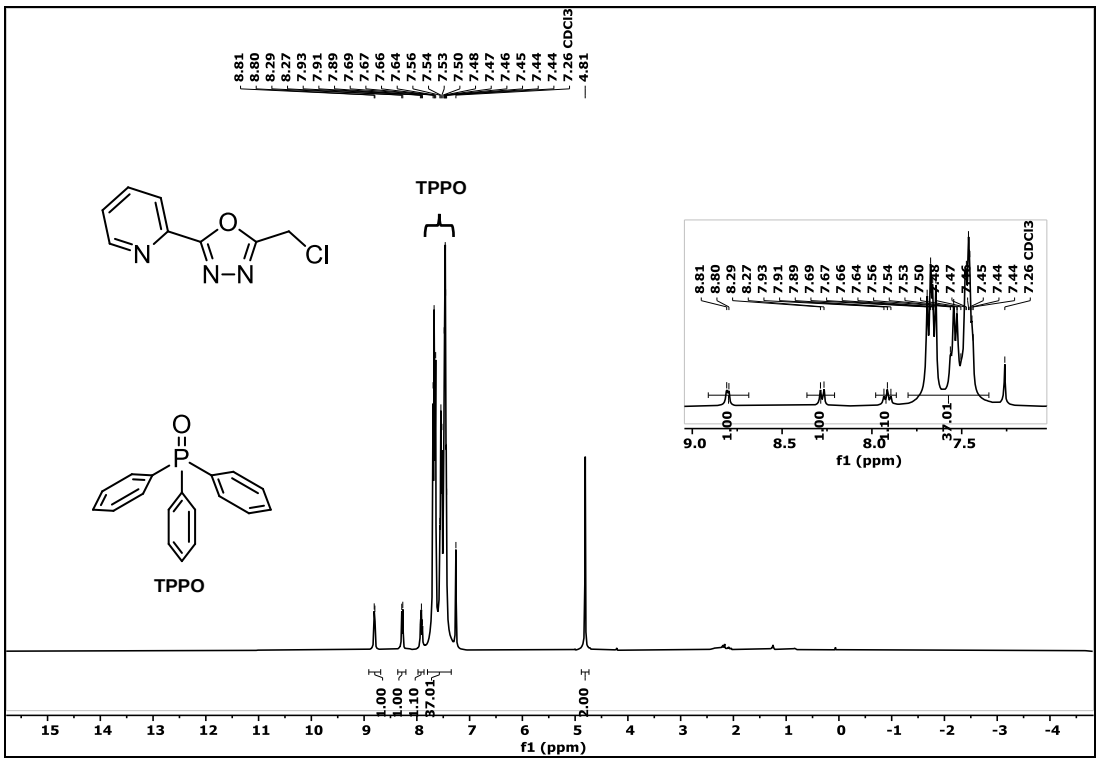


Figure B.41 [1]H-NMR spectrum of 2-(Chloromethyl)-5-(pyridin-2-yl)-1,3,4-oxadiazole (**21**) and TPPO in $CDCl_3$.

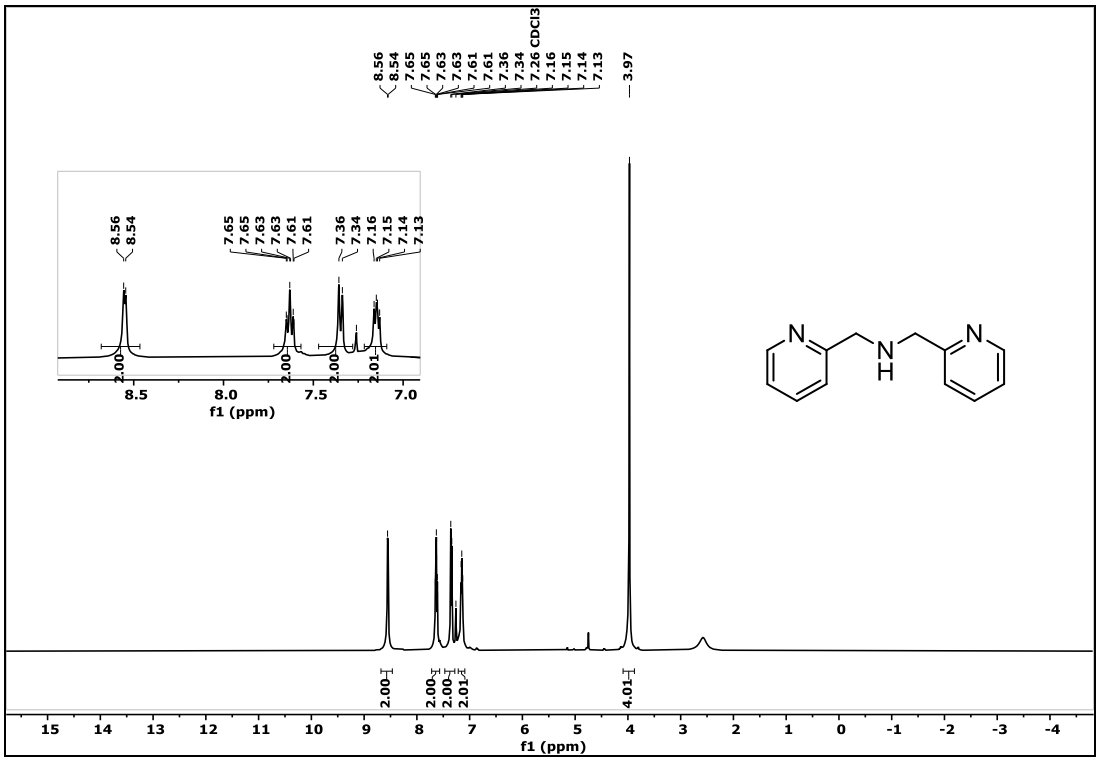


Figure B.42 [1]H-NMR spectrum of Bis[(2-pyridyl)methyl]amine (**22**) in $CDCl_3$.

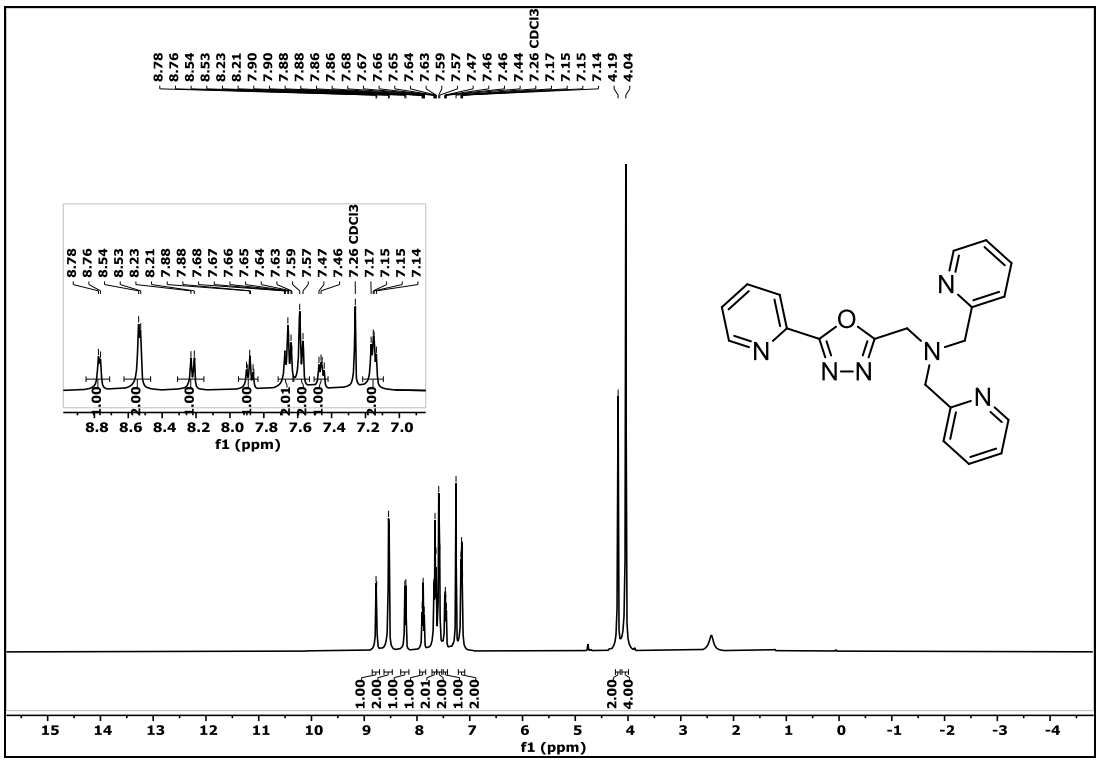


Figure B.43 ^{1}H-NMR spectrum of 2-(2-Pyridyl)-5-[N,N-bis(2-pyridylmethyl)aminomethyl]-1,3,4-oxadiazole ($\mathbf{L^{Py,1}}$) in $CDCl_3$.

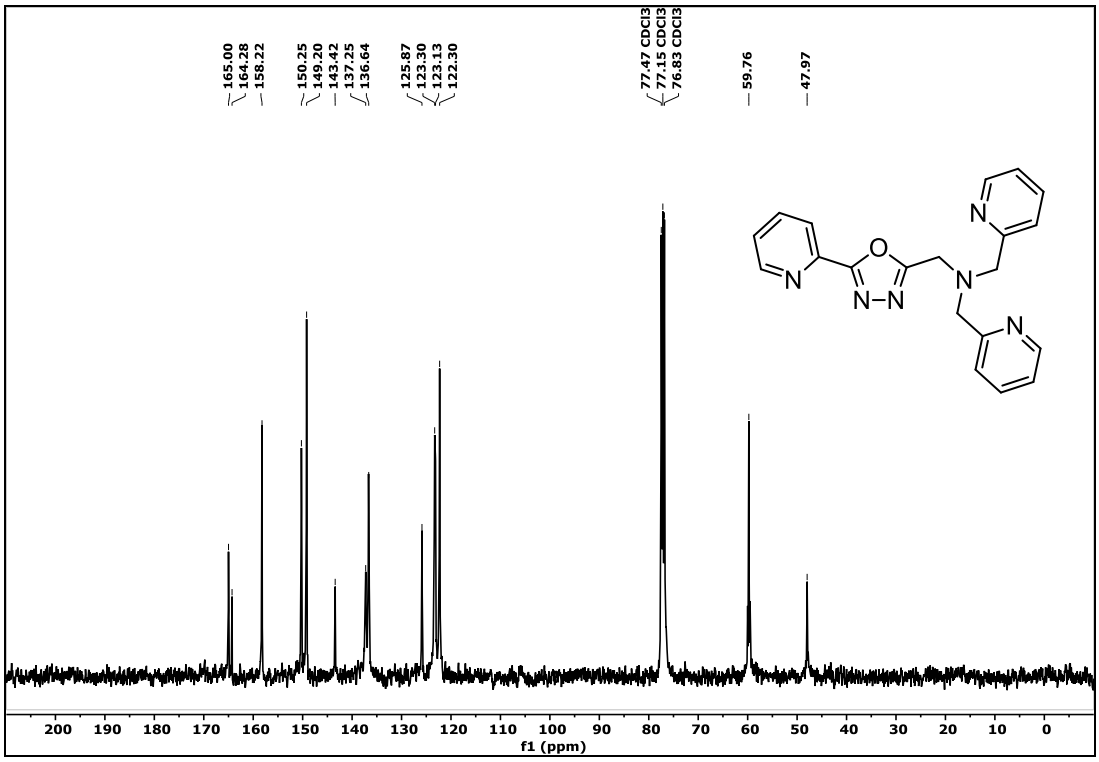


Figure B.44 ^{13}C-NMR spectrum of 2-(2-Pyridyl)-5-[N,N-bis(2-pyridylmethyl)aminomethyl]-1,3,4-oxadiazole ($\mathbf{L^{Py,1}}$) in $CDCl_3$.

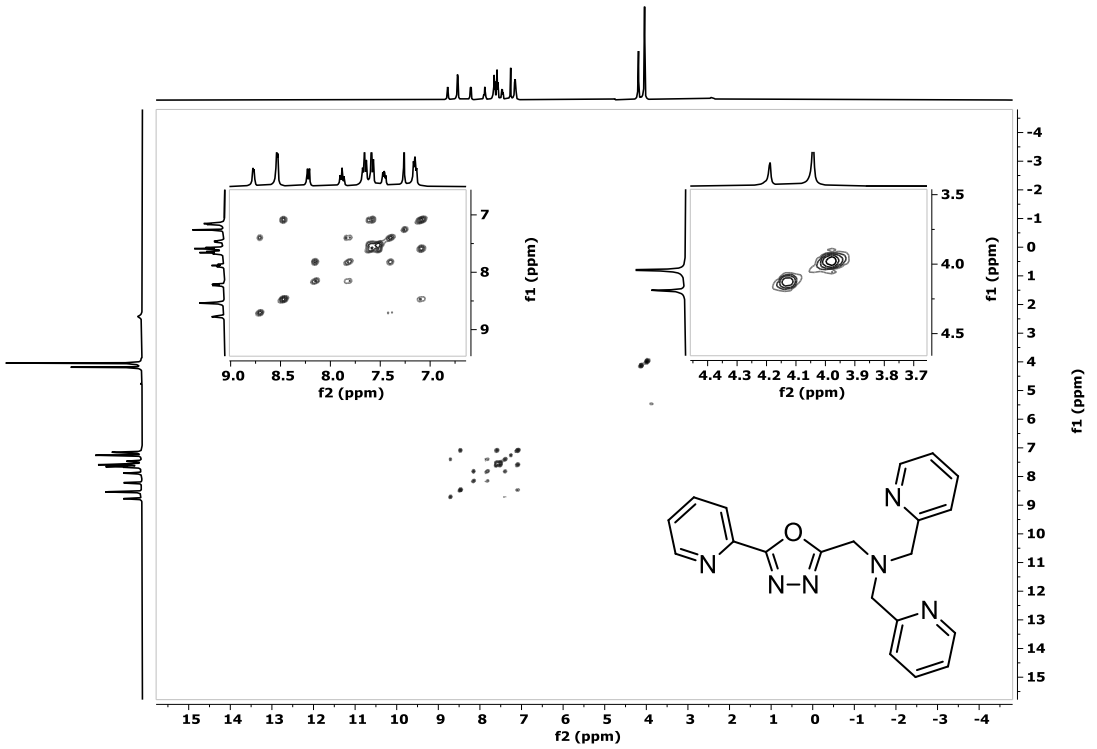


Figure B.45 ^{1}H-1H-COSY spectrum of 2-(2-Pyridyl)-5-[N,N-bis(2-pyridylmethyl)aminomethyl]-1,3,4-oxadiazole (**L^{Py,1}**) in $CDCl_3$.

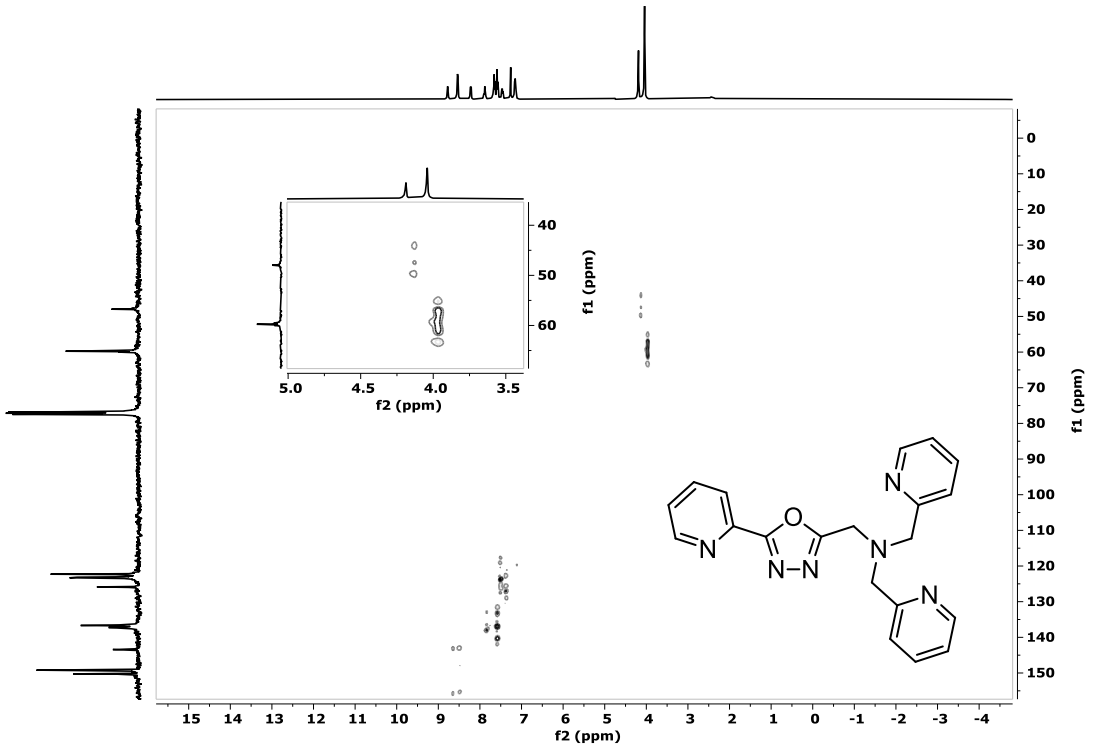


Figure B.46 ^{1}H-^{13}C-HSQC spectrum of 2-(2-Pyridyl)-5-[N,N-bis(2-pyridylmethyl)aminomethyl]-1,3,4-oxadiazole (**L^{Py,1}**) in $CDCl_3$.

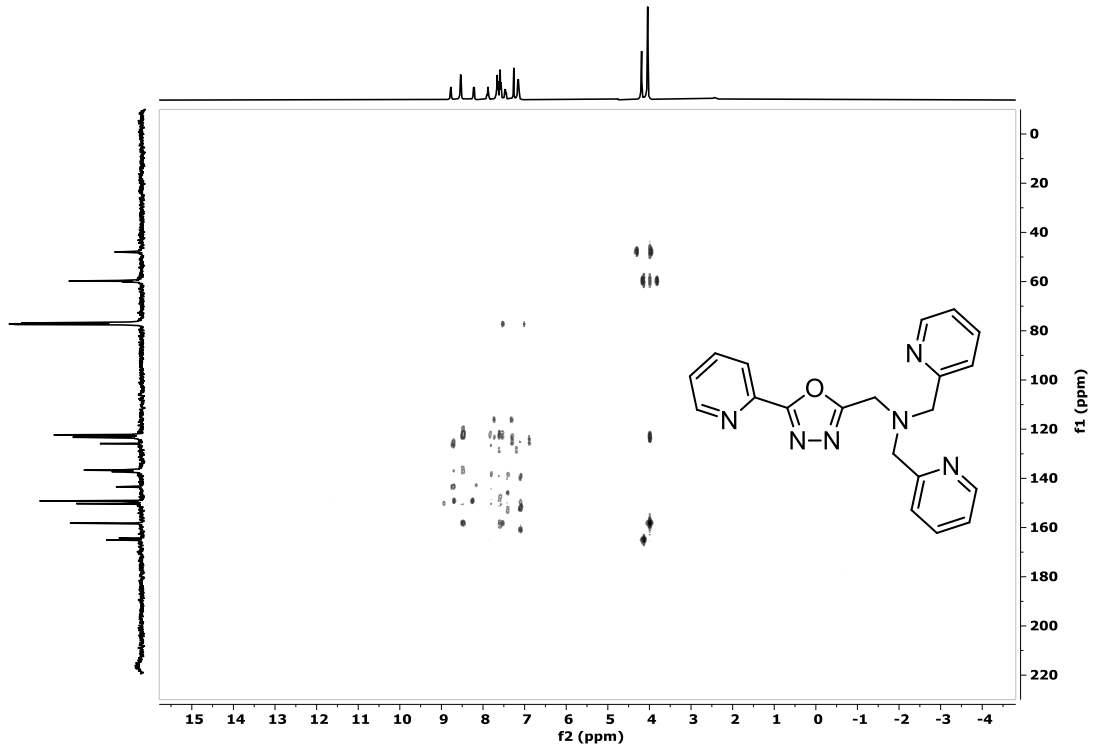


Figure B.47 ^{1}H-^{13}C-HMBC spectrum of 2-(2-Pyridyl)-5-[N,N-bis(2-pyridylmethyl)aminomethyl]-1,3,4-oxadiazole (**L**^{Py,1}) in $CDCl_3$.

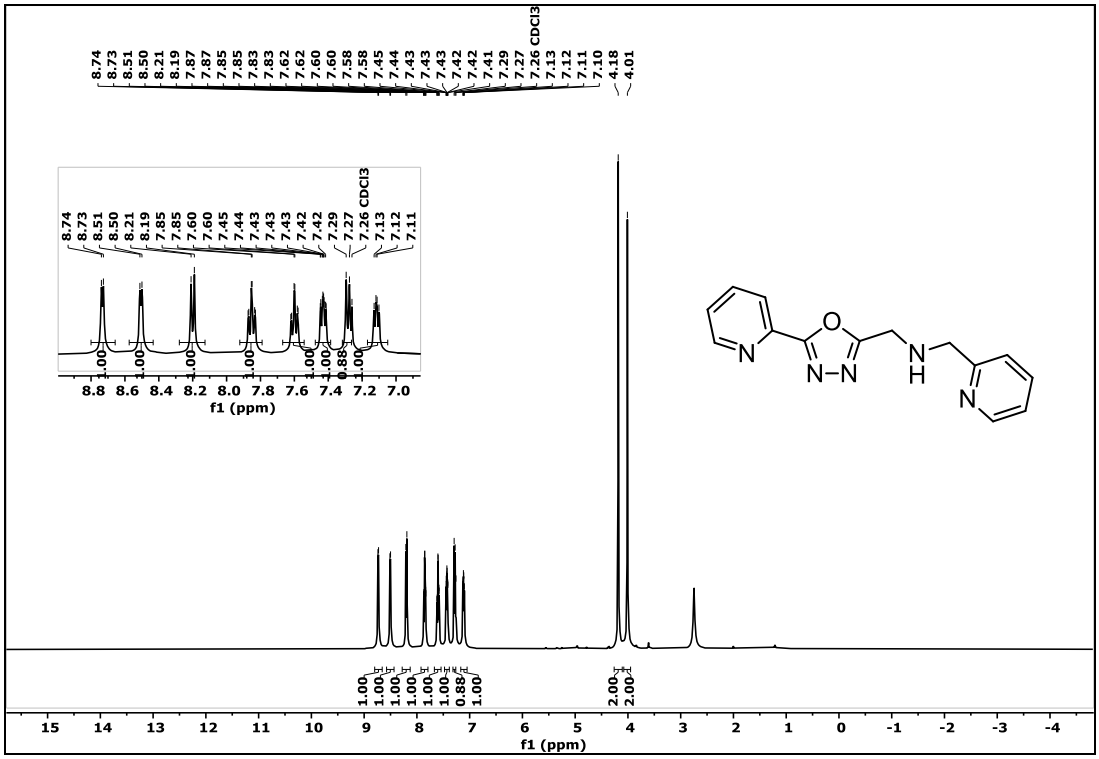


Figure B.48 ^{1}H-NMR spectrum of 2-(2-Pyridyl)-5-[(2-pyridylmethyl)aminomethyl]-1,3,4-oxadiazole (**L**^{Py,2}) in $CDCl_3$.

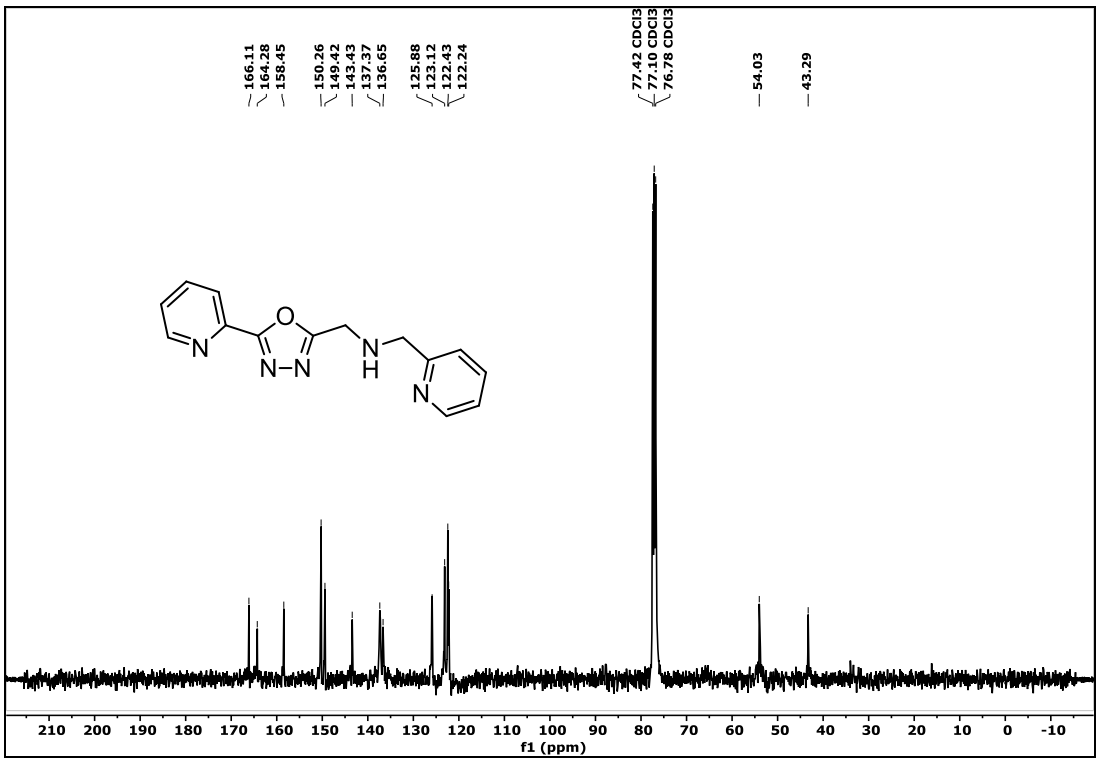


Figure B.49 ^{13}C-NMR spectrum of 2-(2-Pyridyl)-5-[(2-pyridylmethyl)aminomethyl]-1,3,4-oxadiazole (**L^{Py,2}**) in $CDCl_3$.

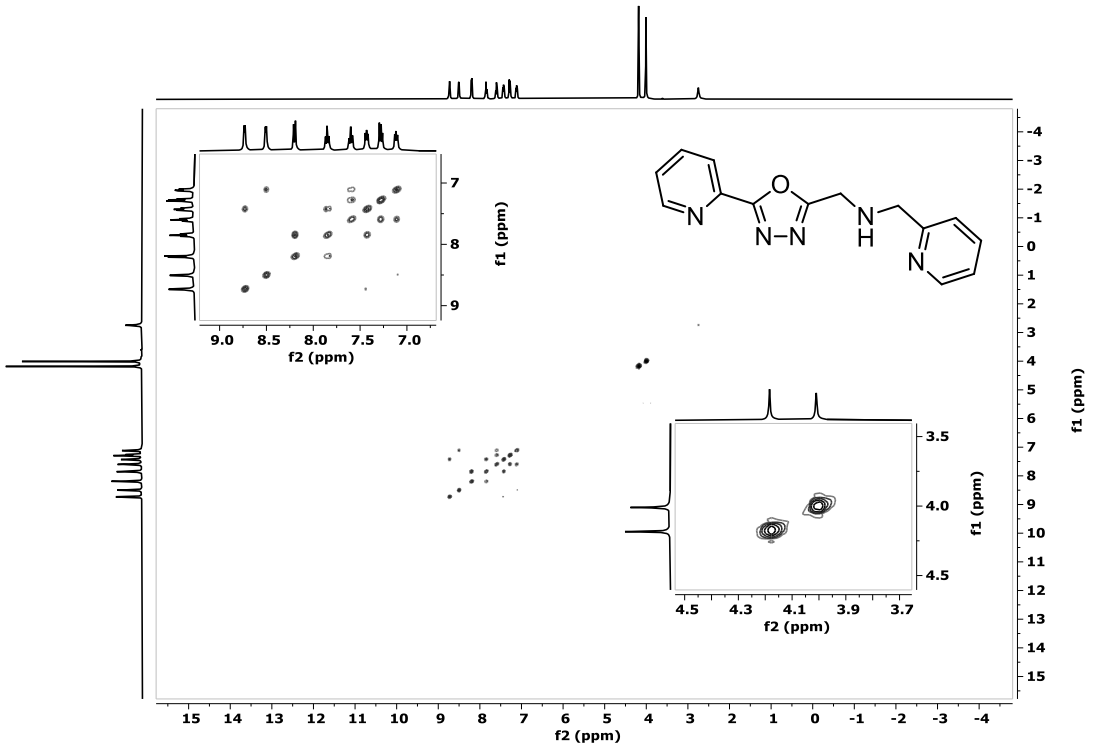


Figure B.50 ^{1}H-^{1}H-COSY spectrum of 2-(2-Pyridyl)-5-[(2-pyridylmethyl)aminomethyl]-1,3,4-oxadiazole (**L^{Py,2}**) in $CDCl_3$.

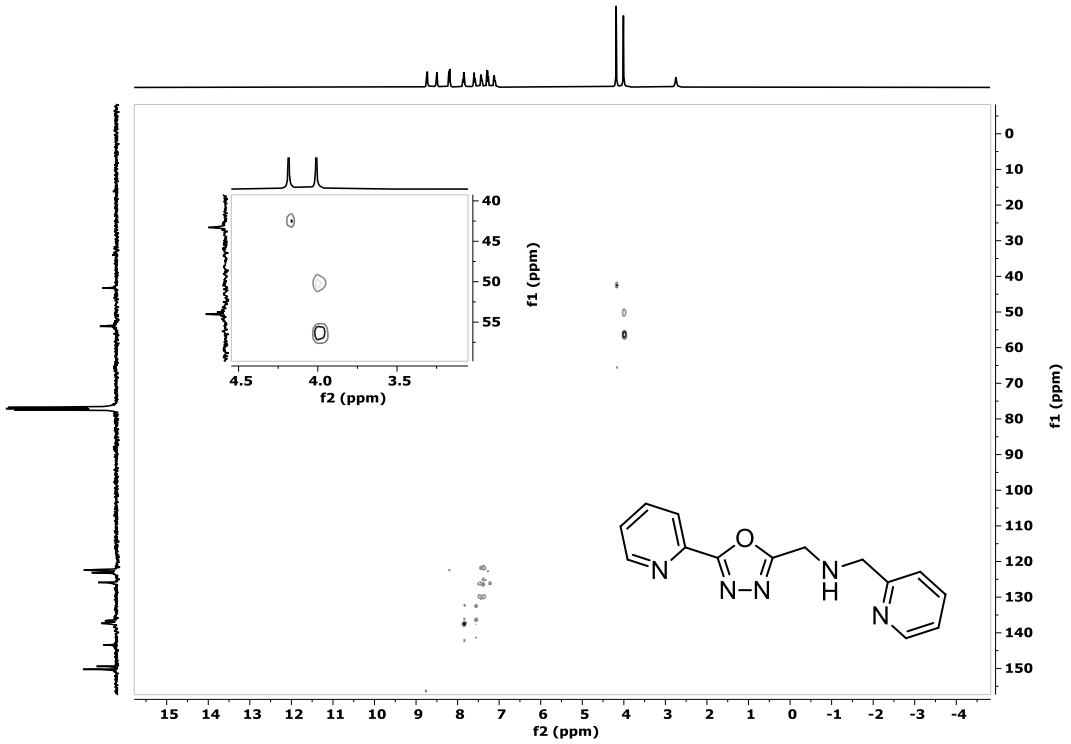


Figure B.51 ^{1}H-^{13}C-HSQC spectrum of 2-(2-Pyridyl)-5-[(2-pyridylmethyl)aminomethyl]-1,3,4-oxadiazole ($\mathbf{L}^{\mathbf{Py,2}}$) in $CDCl_3$.

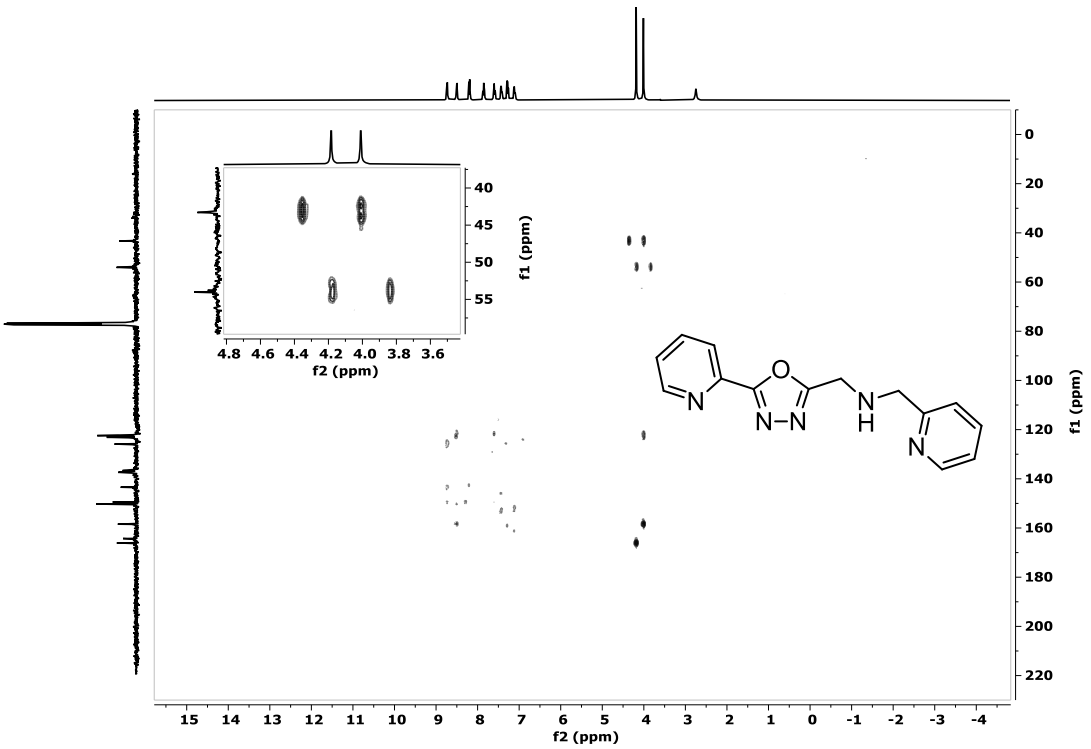


Figure B.52 ^{1}H-^{13}C-HMBC spectrum of 2-(2-Pyridyl)-5-[(2-pyridylmethyl)aminomethyl]-1,3,4-oxadiazole ($\mathbf{L}^{\mathbf{Py,2}}$) in $CDCl_3$.

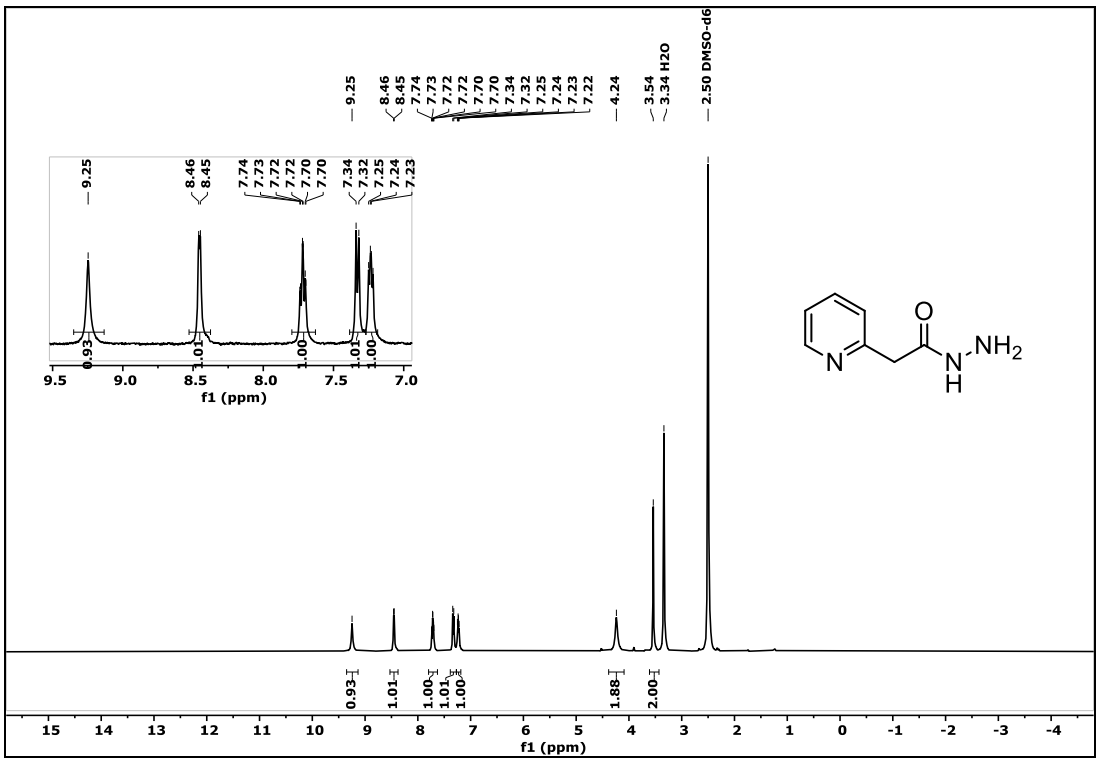


Figure B.53 ^{1}H-NMR spectrum of Pyridin-2-yl-acetic acid hydrazide (**23**) in DMSO-d_6.

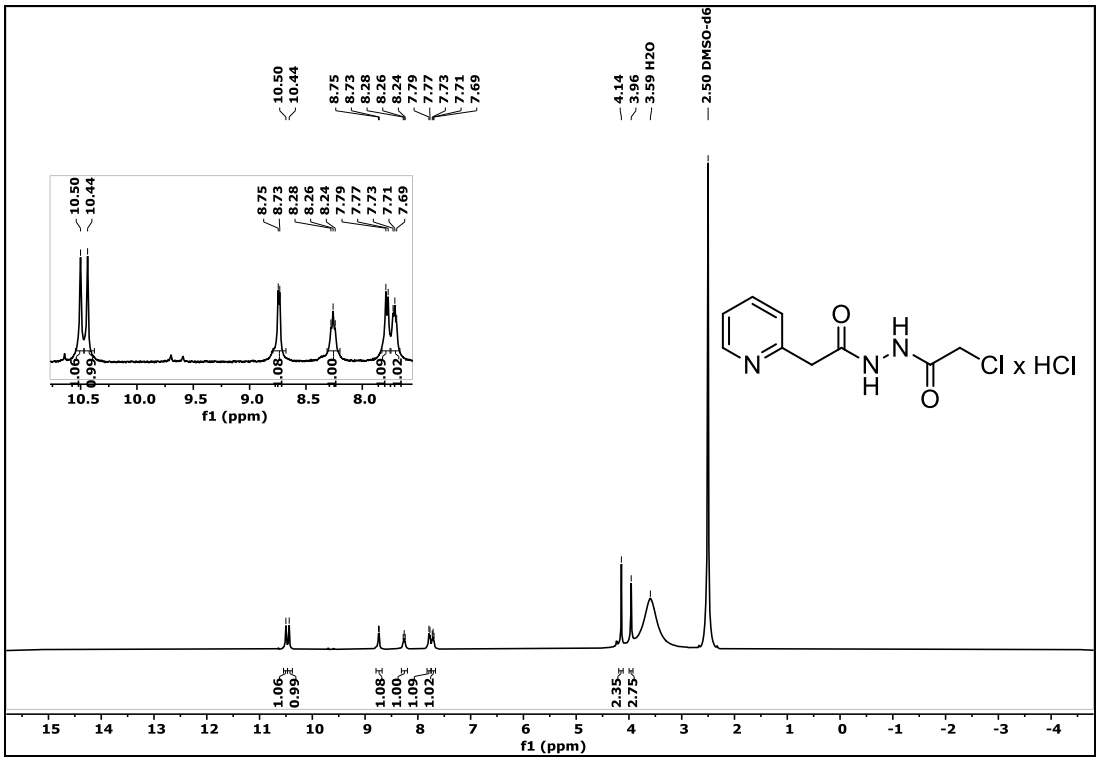


Figure B.54 ^{1}H-NMR spectrum of N'-(Chloroacetyl)-2-pyridylacetic acid hydrazide hydrochloride (**24**) in DMSO-d_6.

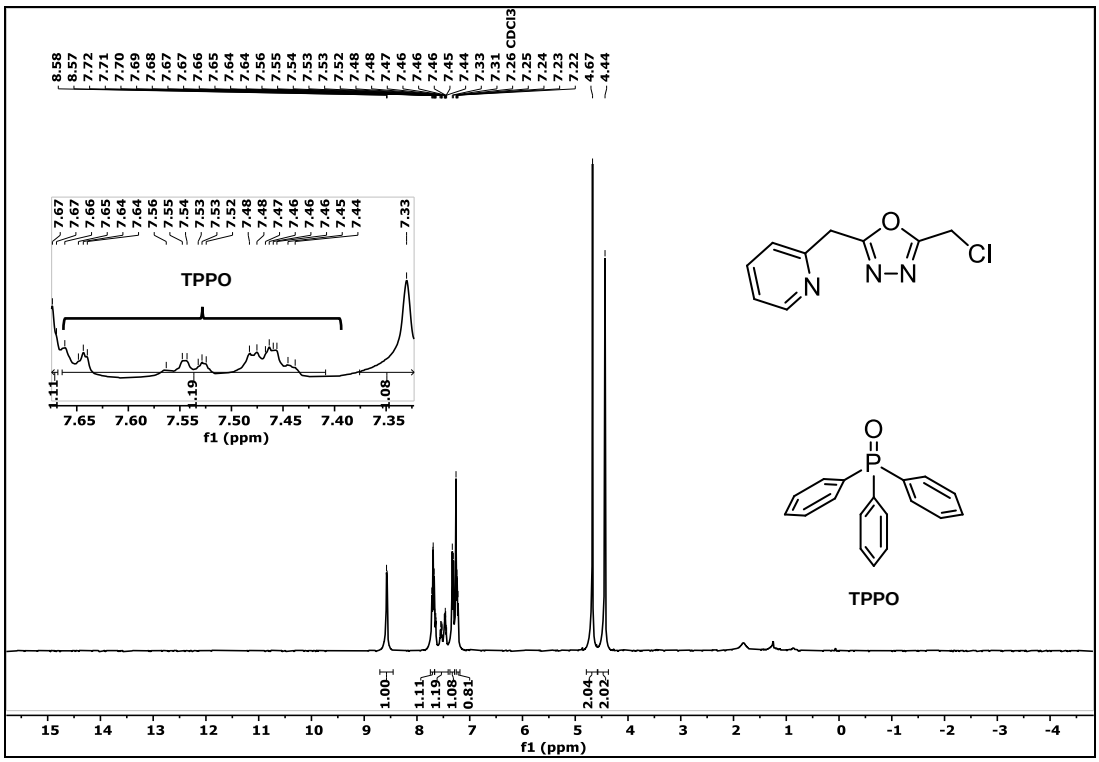


Figure B.55 ^{1}H-NMR spectrum of 2-(Chloromethyl)-5-(pyridin-2-ylmethyl)-1,3,4-oxadiazole (**25**) and TPPO in $CDCl_3$.

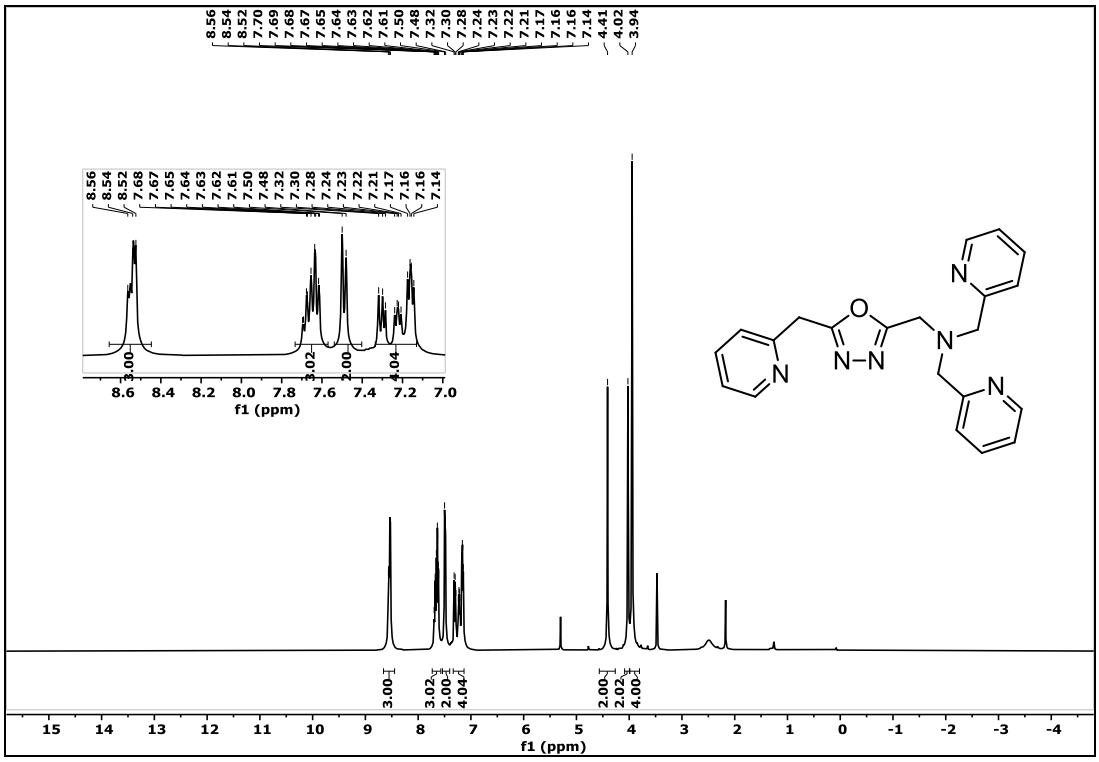


Figure B.56 ^{1}H-NMR spectrum of 2-(Pyridin-2-ylmethyl)-5-[N,N-bis(2-pyridylmethyl)aminomethyl]-1,3,4-oxadiazole ($\mathbf{L^{Py,3}}$) in $CDCl_3$.

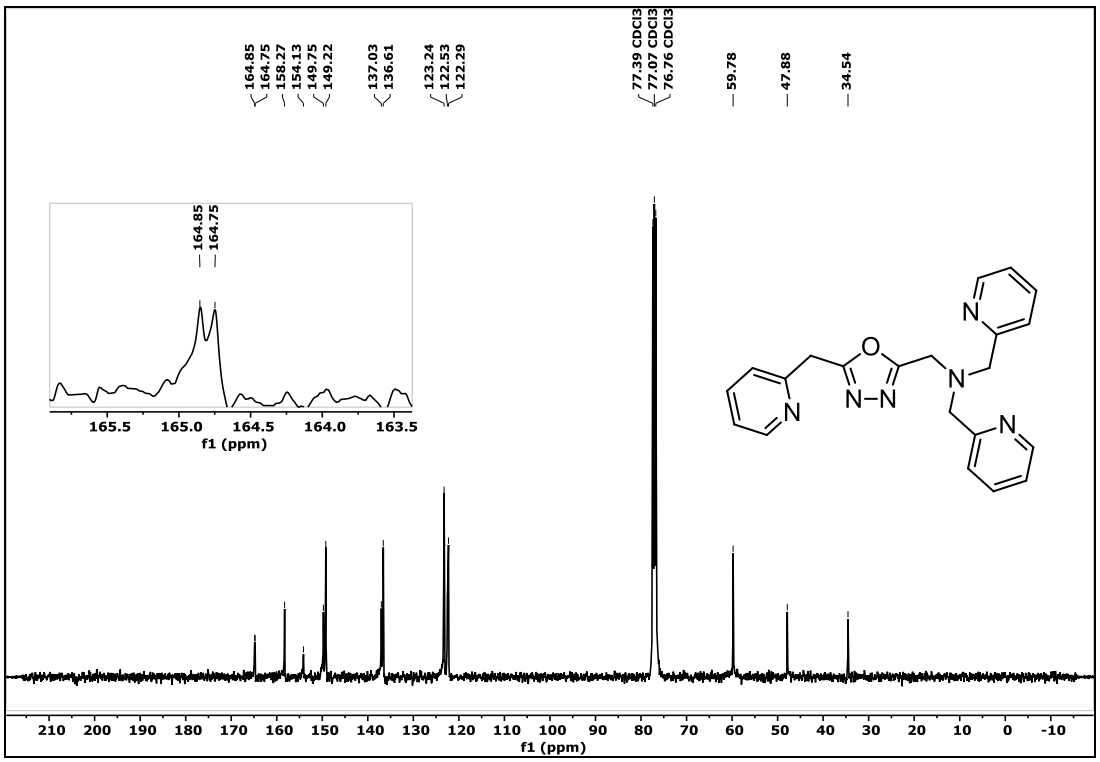


Figure B.57 ^{13}C-NMR spectrum of 2-(Pyridin-2-ylmethyl)-5-[N,N-bis(2-pyridylmethyl)aminomethyl]-1,3,4-oxadiazole (**L^{Py,3}**) in $CDCl_3$.

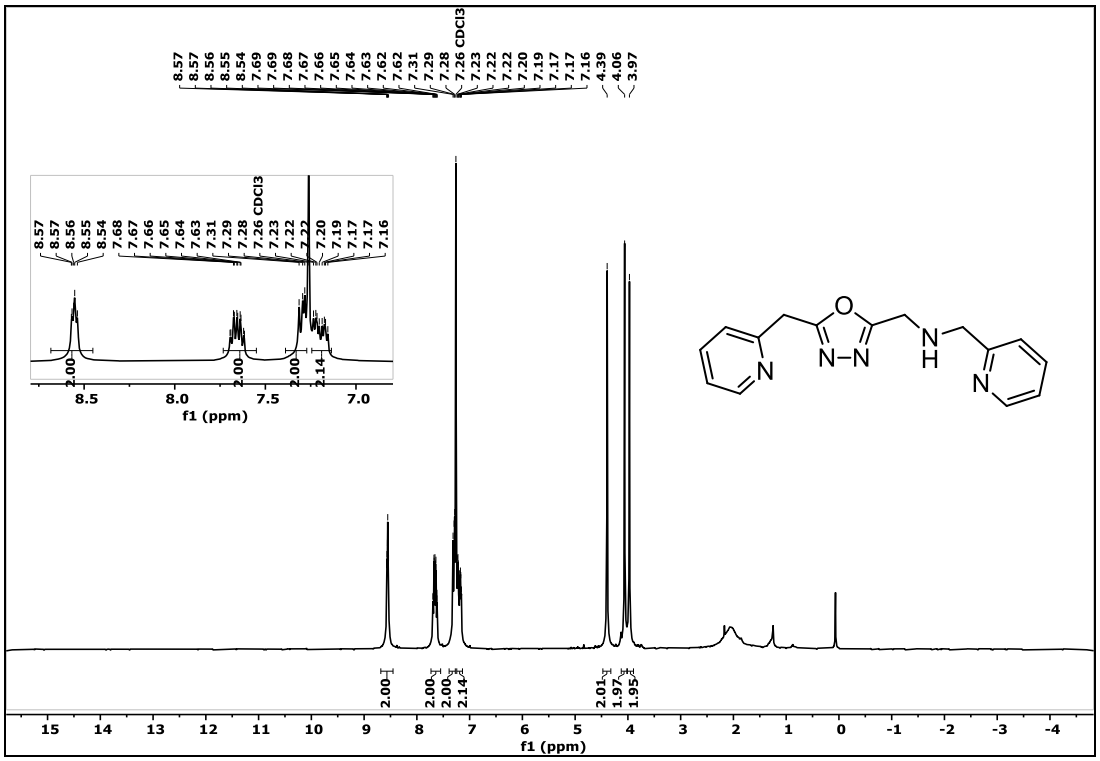


Figure B.58 ^{1}H-NMR spectrum of 2-(Pyridin-2-ylmethyl)-5-[(2-pyridylmethyl)aminomethyl]-1,3,4-oxadiazole (**L^{Py,4}**) in $CDCl_3$.

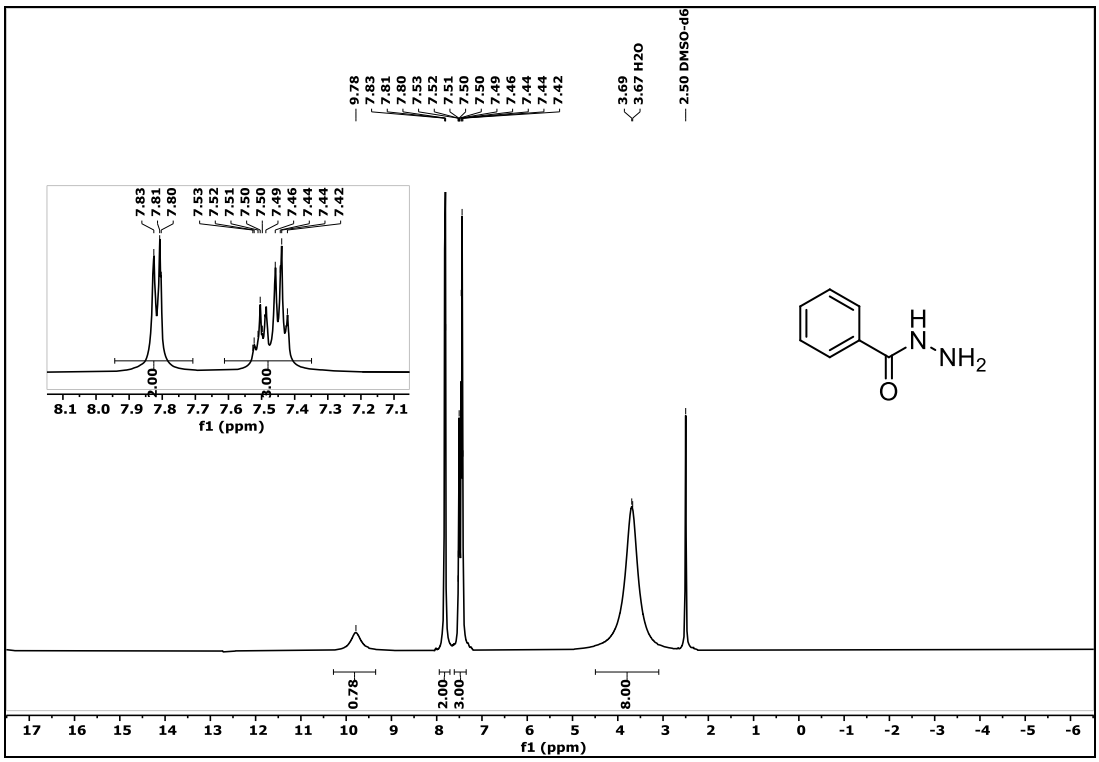


Figure B.59 [1]H-NMR spectrum of Benzoic acid hydrazide (**26**) in DMSO-d_6.

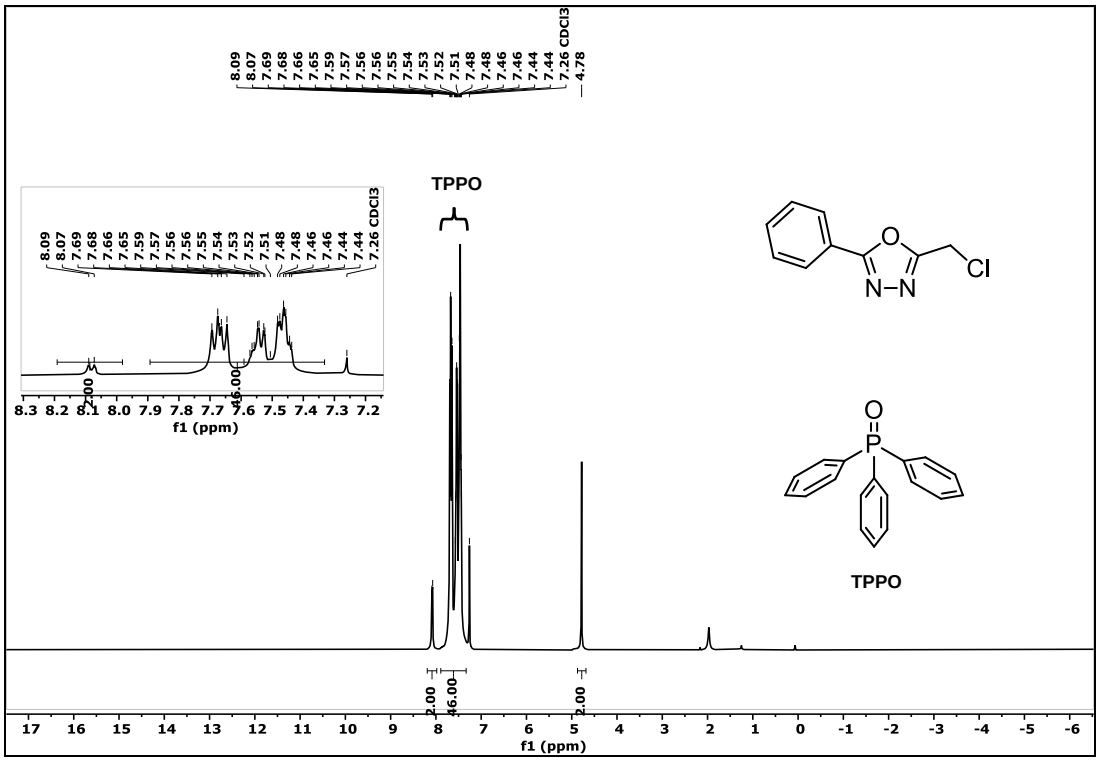


Figure B.60 [1]H-NMR spectrum of 2-(Chloromethyl)-5-phenyl-1,3,4-oxadiazole (**28**) and TPPO in $CDCl_3$.

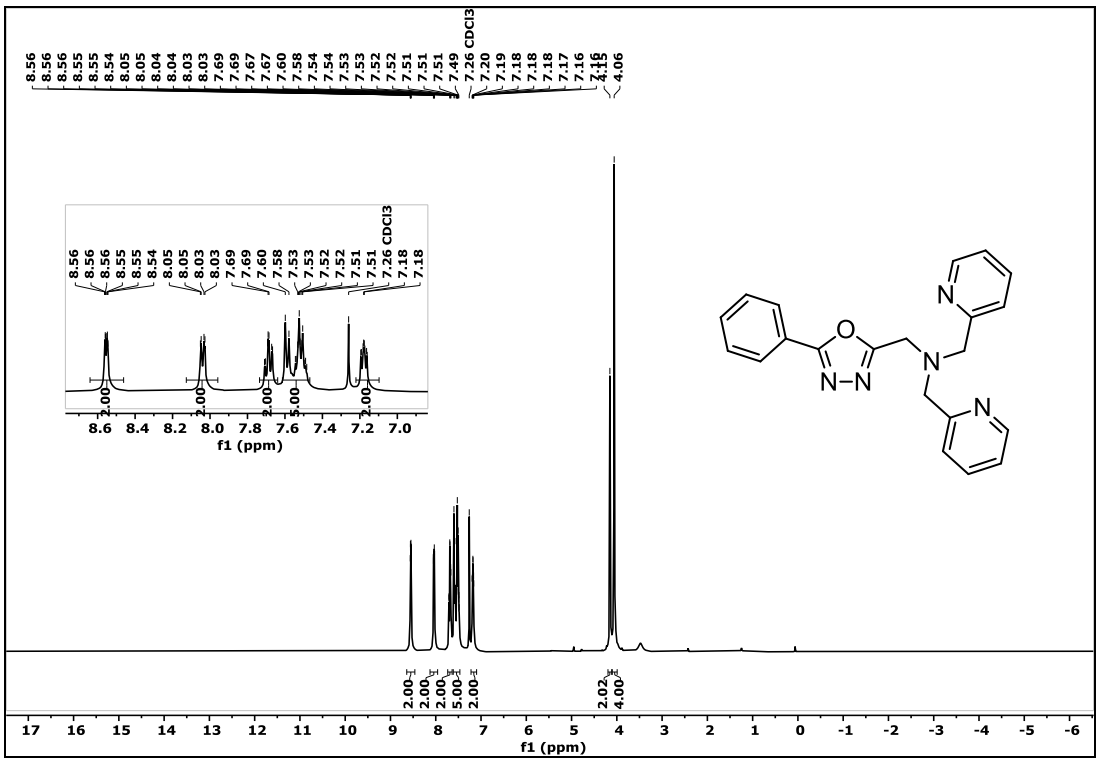


Figure B.61 ^{1}H-NMR spectrum of 2-Phenyl-5-[N,N-bis(2-pyridylmethyl)aminomethyl]-1,3,4-oxadiazole (**L^{Ph}**) in $CDCl_3$.

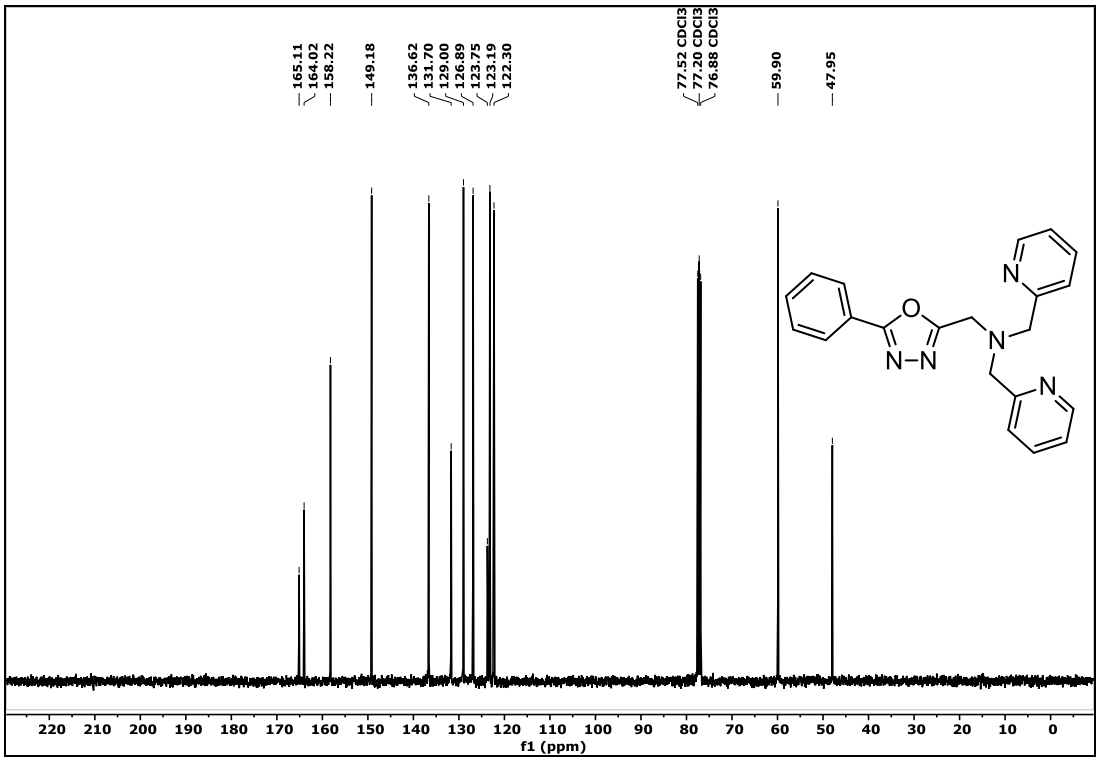


Figure B.62 ^{13}C-NMR spectrum of 2-Phenyl-5-[N,N-bis(2-pyridylmethyl)aminomethyl]-1,3,4-oxadiazole (**L^{Ph}**) in $CDCl_3$.

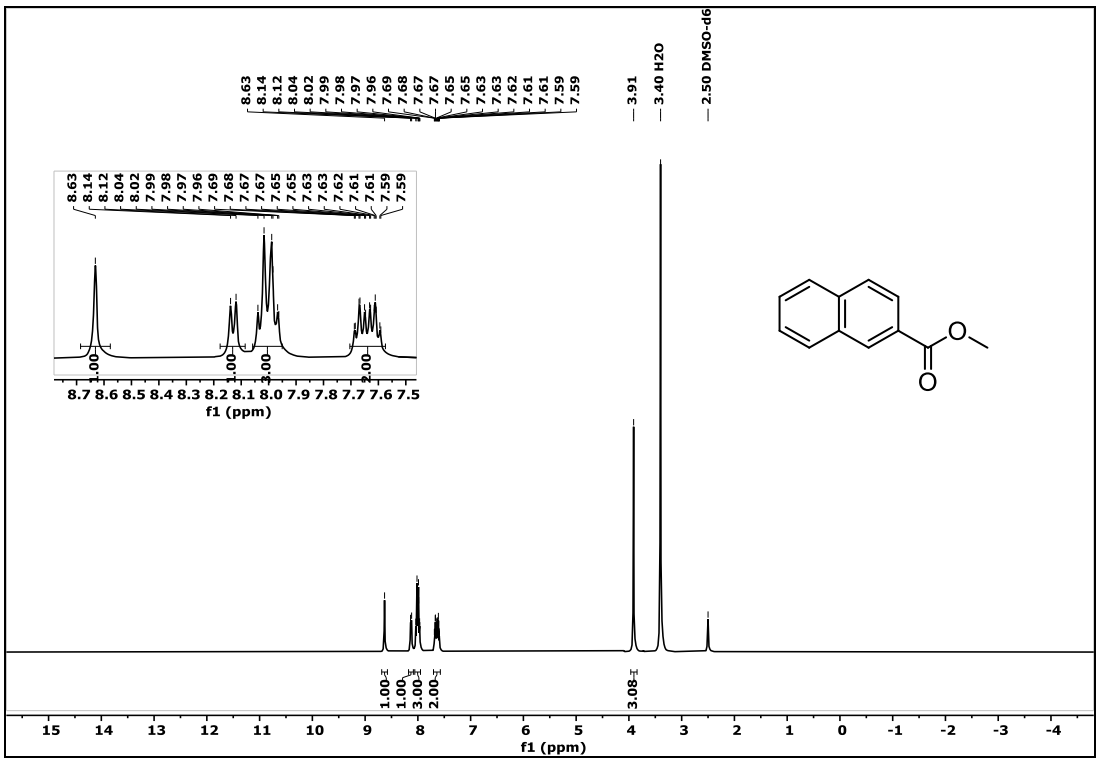


Figure B.63 ^{1}H-NMR spectrum of Methyl naphthalene-2-carboxylate (**29**) in DMSO-d_6.

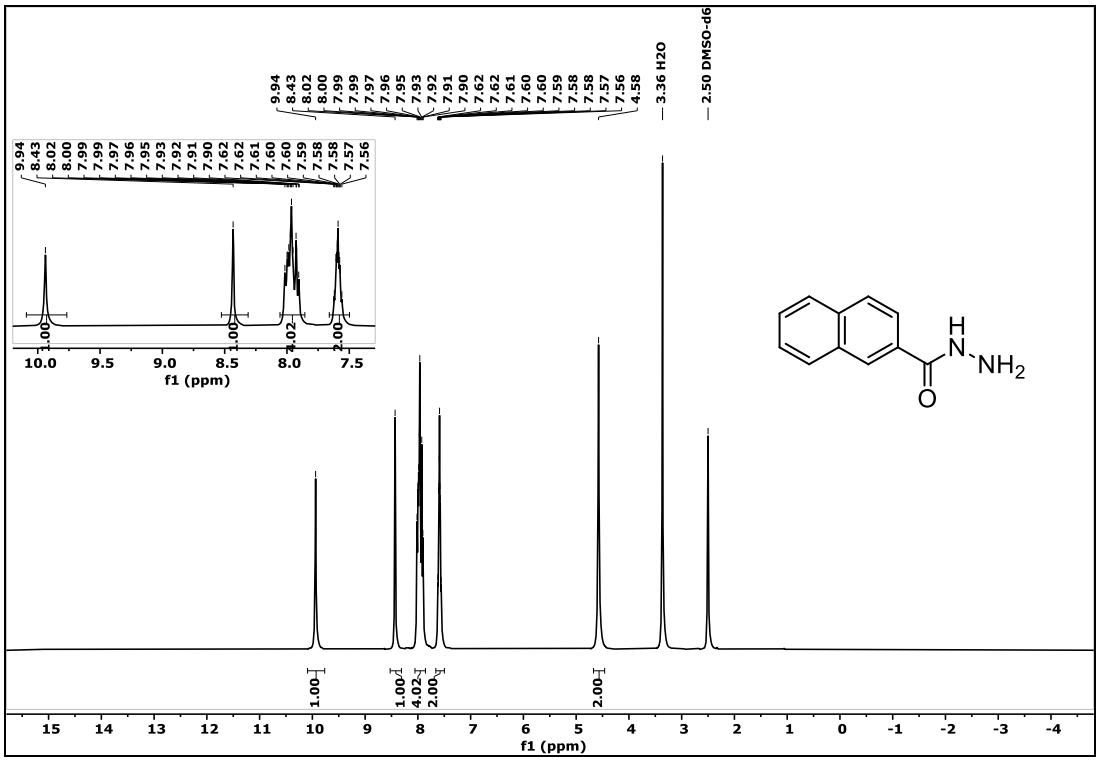


Figure B.64 ^{13}H-NMR spectrum of 2-Naphthohydrazide (**30**) in DMSO-d_6.

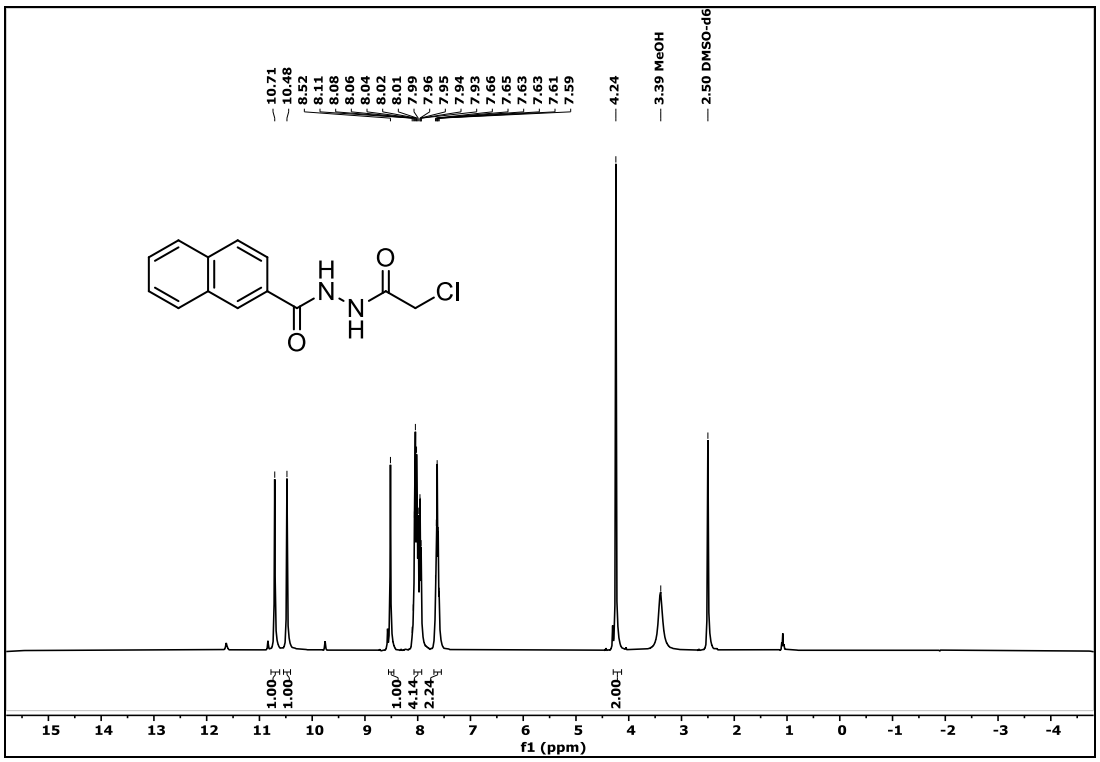


Figure B.65 ^{1}H-NMR spectrum of N'-(2-chloroacetyl)naphthalene-2-carbohydrazide (**31**) in DMSO-d_6.

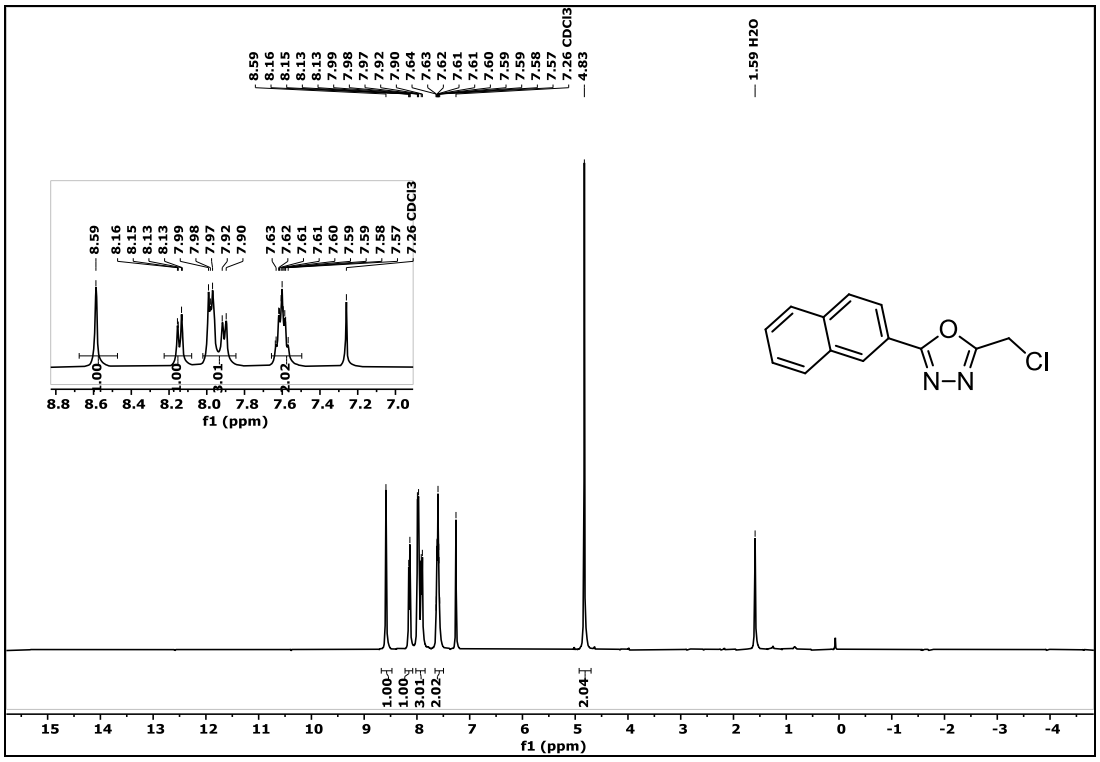


Figure B.66 ^{1}H-NMR spectrum of 2-(Chloromethyl)-5-(naphthalen-2-yl)-1,3,4-oxadiazole (**32**) in $CDCl_3$.

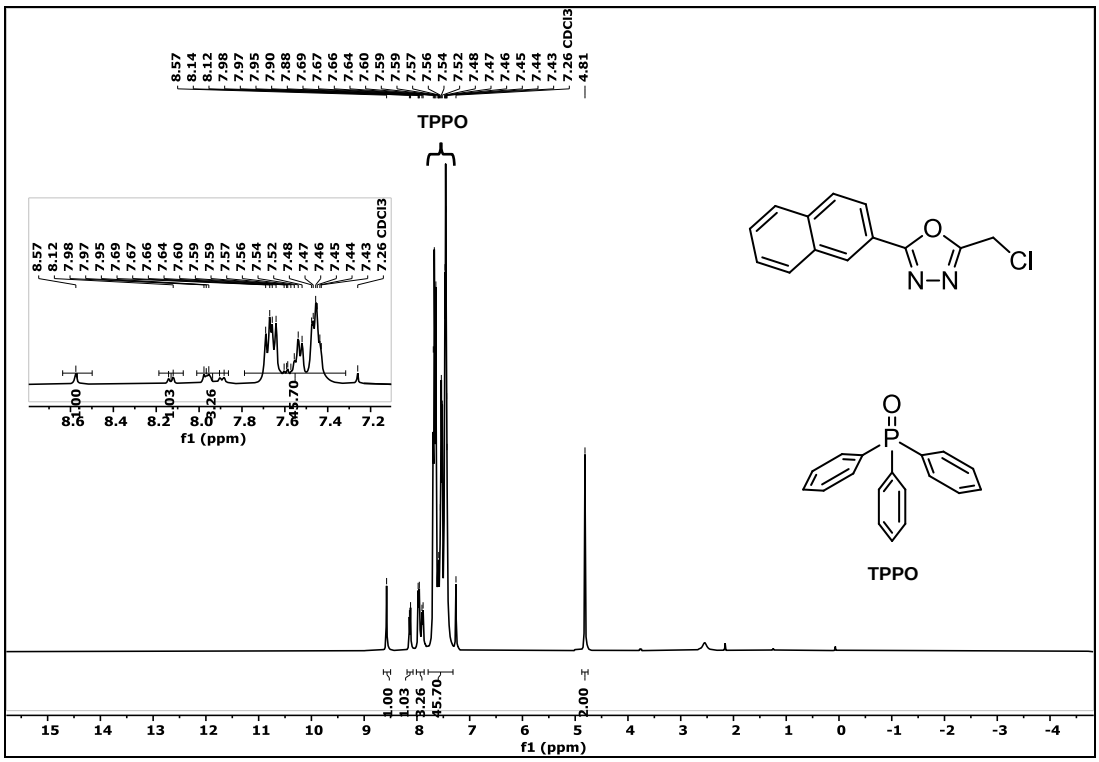


Figure B.67 ^{1}H-NMR spectrum of 2-(Chloromethyl)-5-(naphthalen-2-yl)-1,3,4-oxadiazole (**32**) and TPPO in $CDCl_3$.

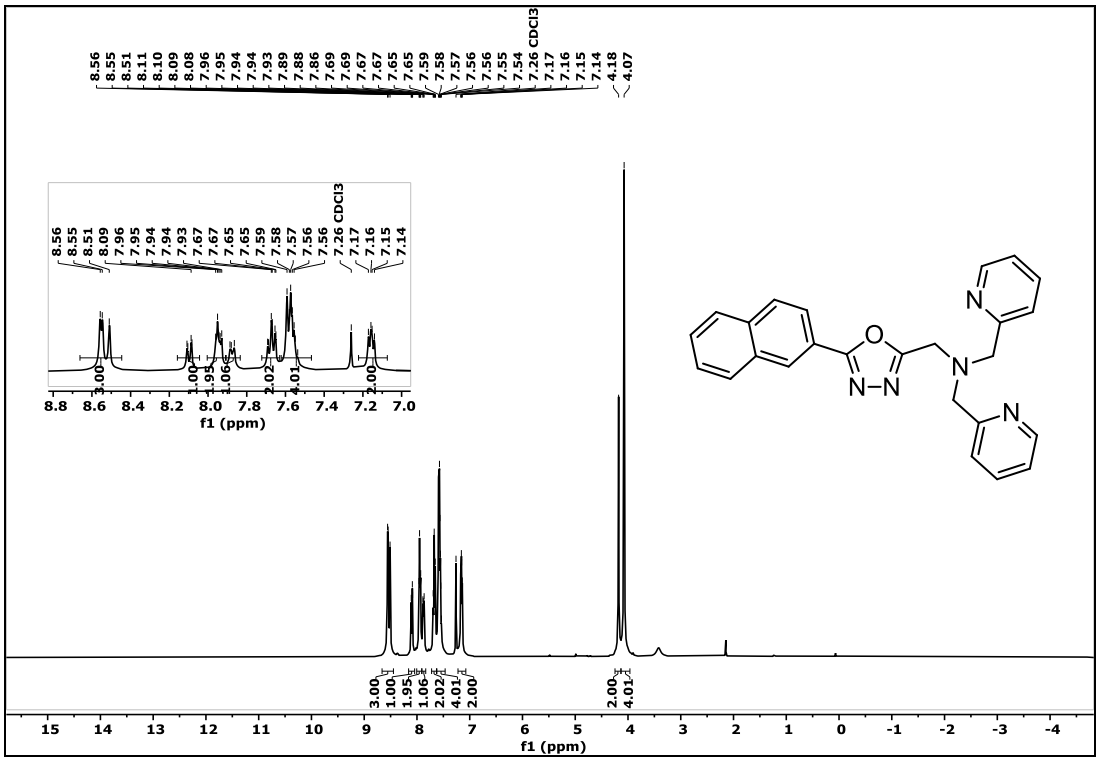


Figure B.68 ^{1}H-NMR spectrum of 2-(Naphthalen-2-yl)-5-[N,N-bis(2-pyridylmethyl)aminomethyl]-1,3,4-oxadiazole ($\mathbf{L}^{\mathbf{Naph}}$) in $CDCl_3$.

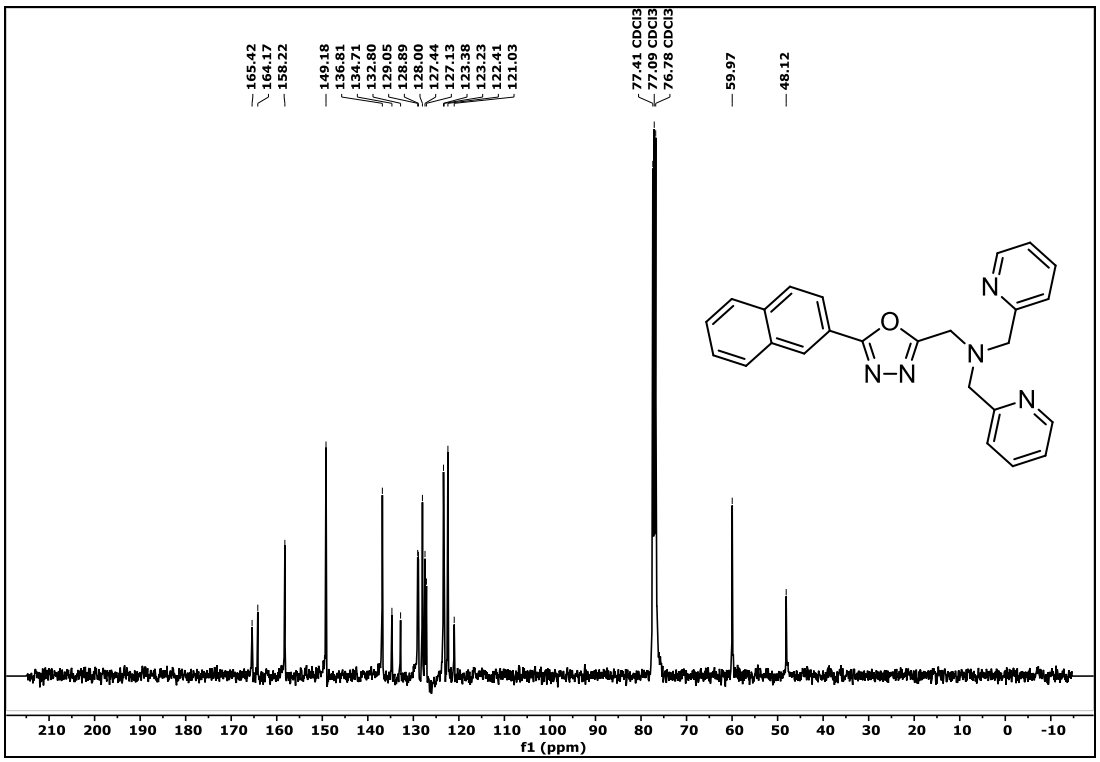


Figure B.69 ^{13}C-NMR spectrum of 2-(Naphthalen-2-yl)-5-[N,N-bis(2-pyridylmethyl)aminomethyl]-1,3,4-oxadiazole (**L^{Naph}**) in $CDCl_3$.

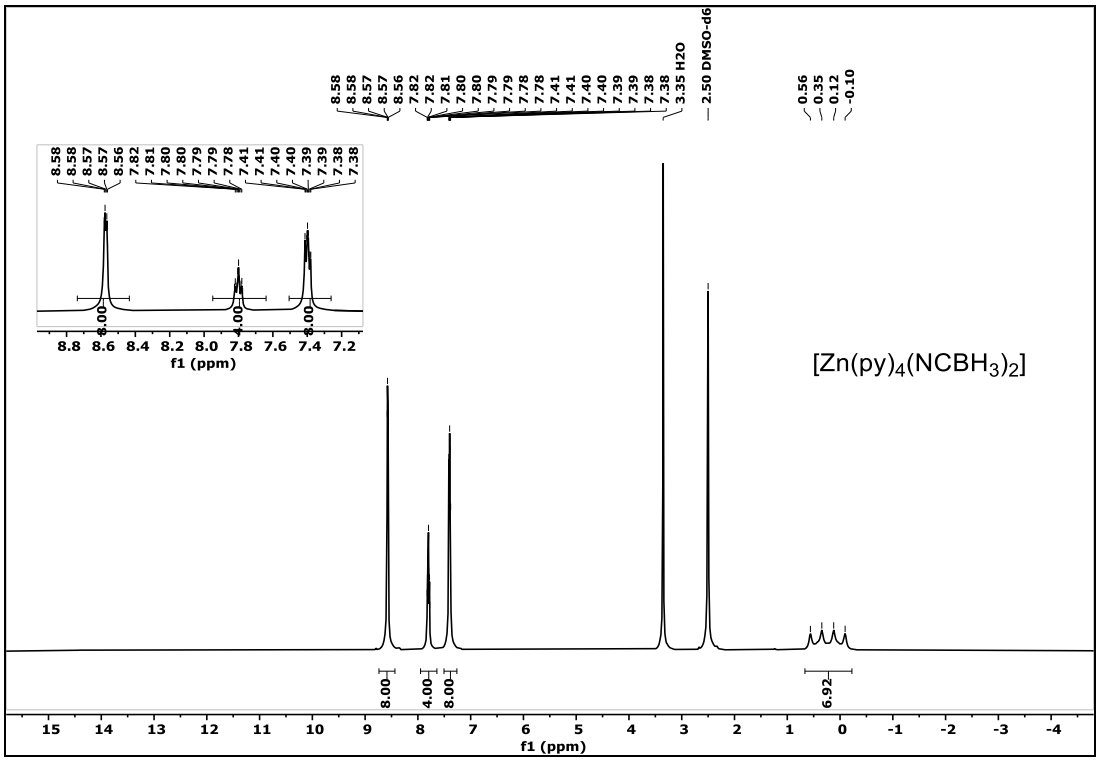


Figure B.70 ^{13}H-NMR spectrum of $[Zn(py)_4(NCBH_3)_2]$ (**C24**) in DMSO-d_6.

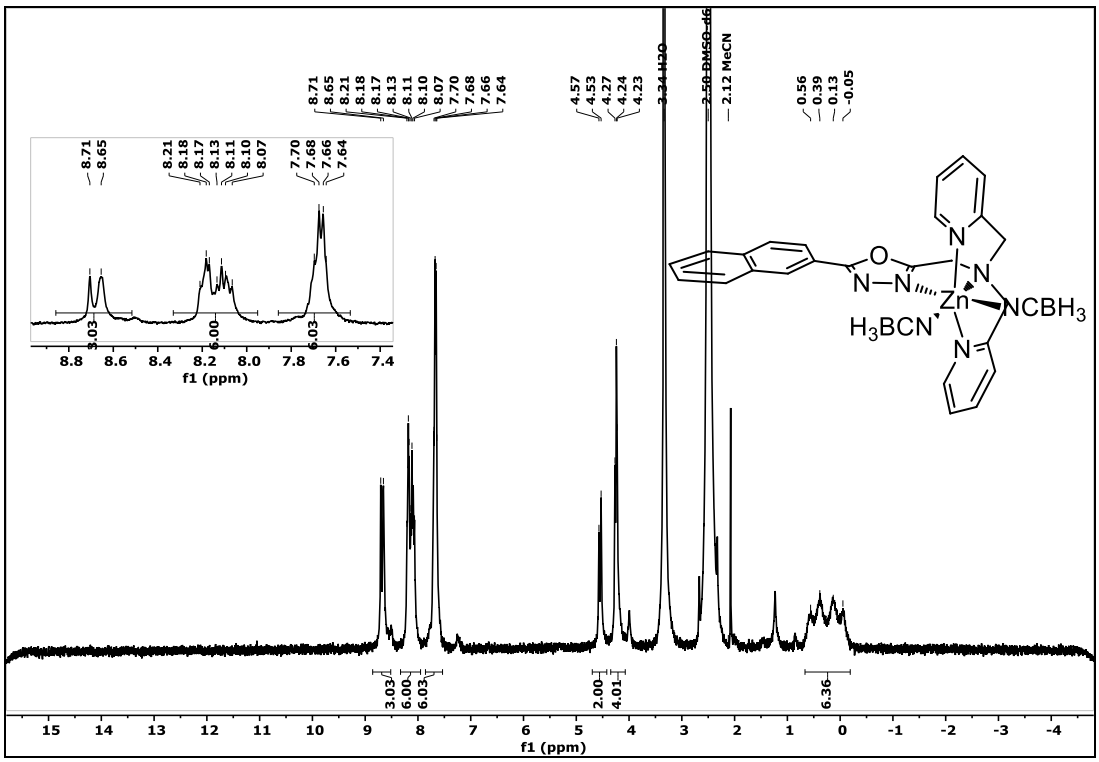


Figure B.71 ^{1}H-NMR spectrum of [Zn(**L^{Naph}**)(NCBH$_3$)$_2$] (**C25**) in DMSO-d$_6$.

C Mass Spectra

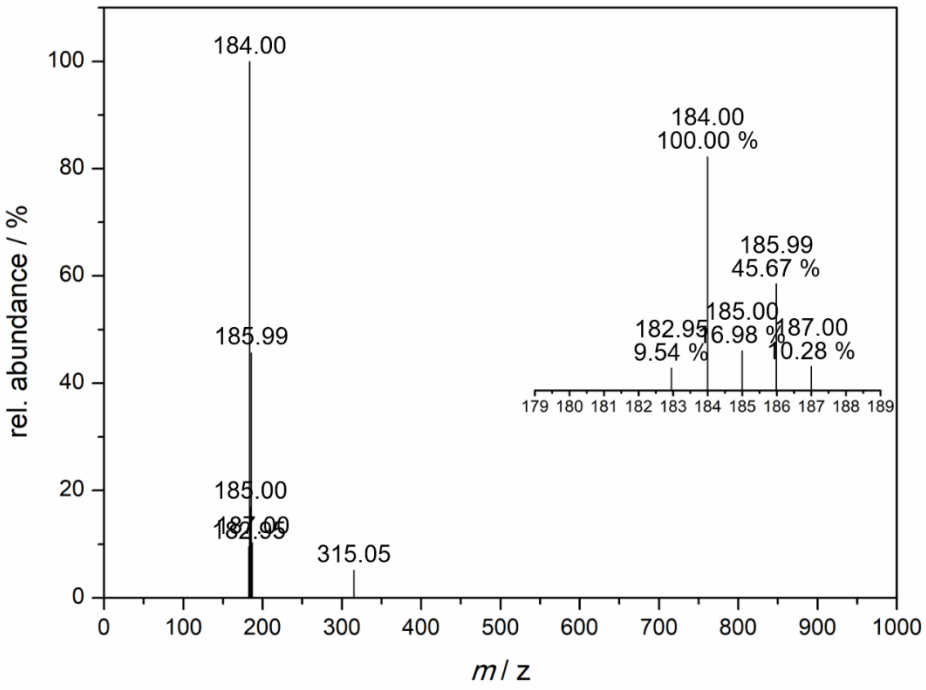


Figure C.1 FD mass spectrum of 1,2-Bis(chloroacetyl)hydrazide (**1**).

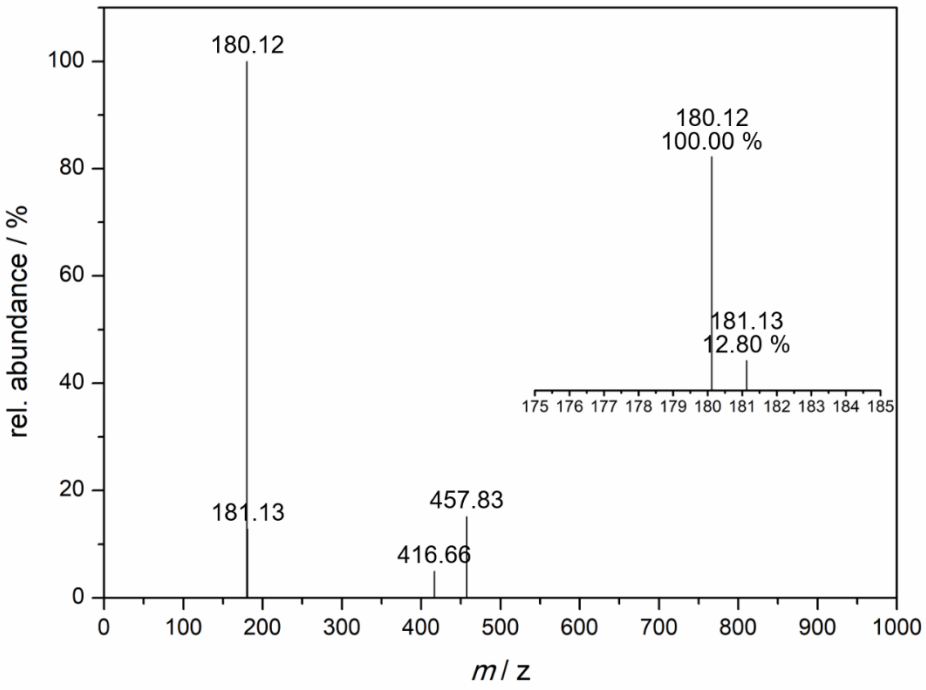


Figure C.2 FD mass spectrum of 2,5-Bis(azidomethyl)-1,3,4-oxadiazole (**3**).

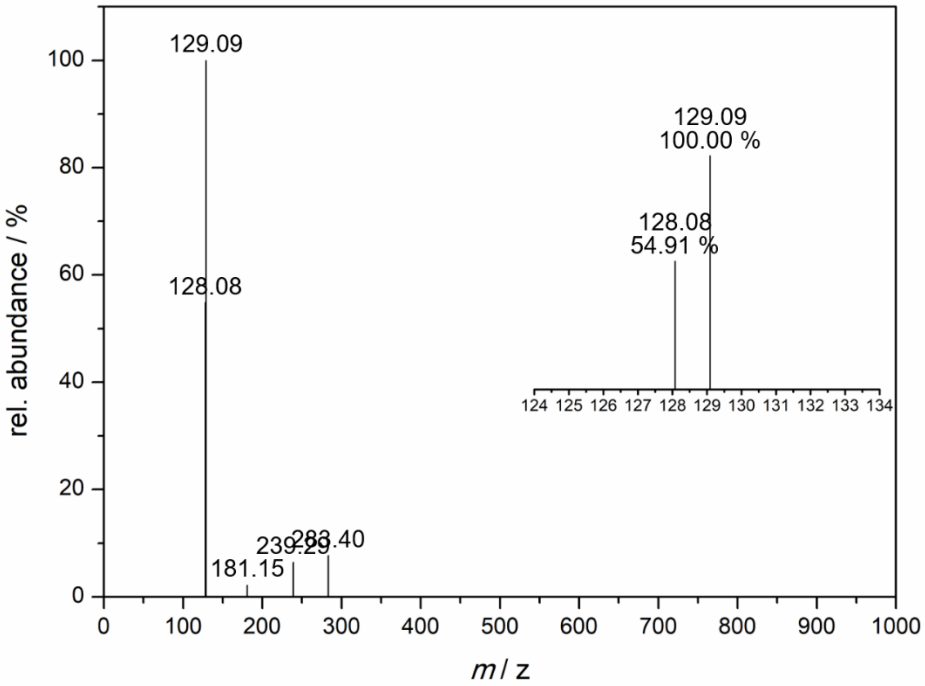


Figure C.3 FD mass spectrum of 2,5-Bis(aminomethyl)-1,3,4-oxadiazole (**4**)

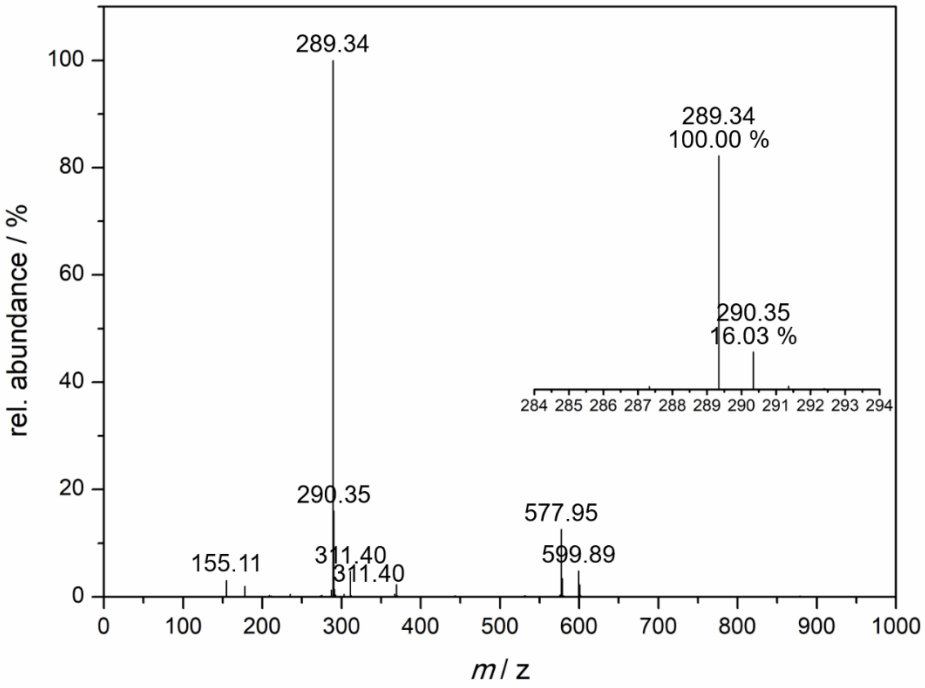


Figure C.4 FD mass spectrum of 2,5-Bis[(1H-imidazol-2-ylmethyl)amino]methyl-1,3,4-oxadiazole ($\mathbf{L^{5,Im}}$).

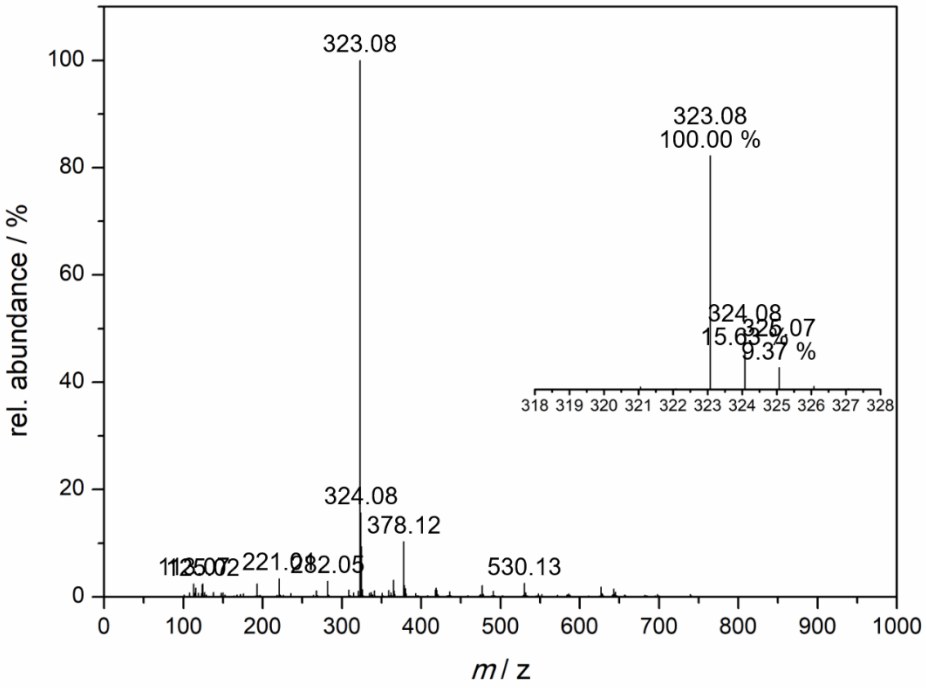


Figure C.5 FD mass spectrum of 2,5-Bis[(1,3-thiazol-2-ylmethyl)amino]methyl-1,3,4-oxadiazole (**L^{5,TA}**).

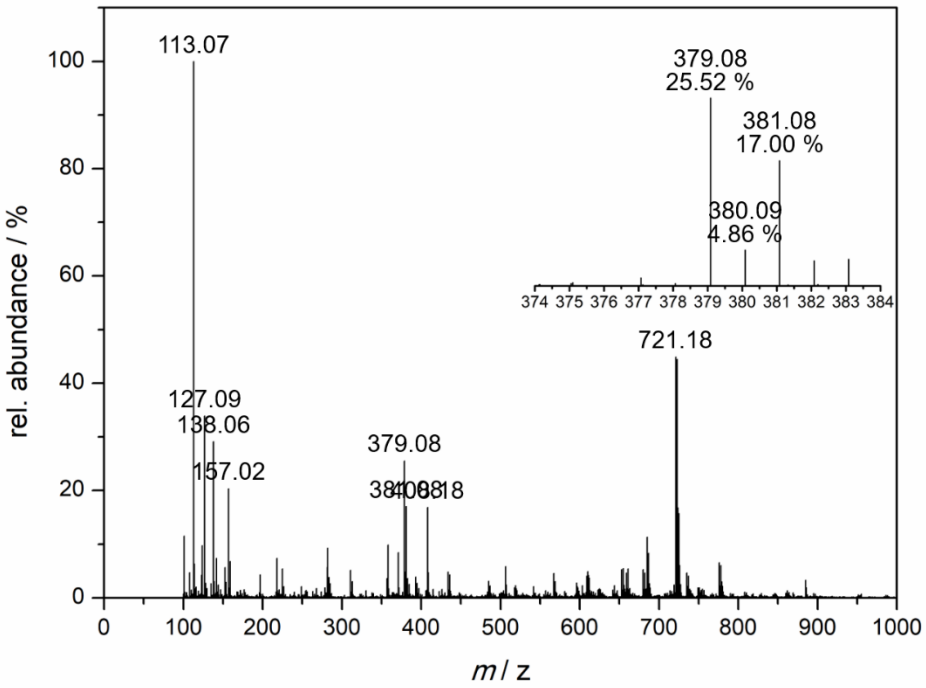


Figure C.6 ESI mass spectrum of 2,5-Bis[(4-chloropyridin-2-ylmethyl)amino]methyl-1,3,4-oxadiazole (**L^{6,Cl}**).

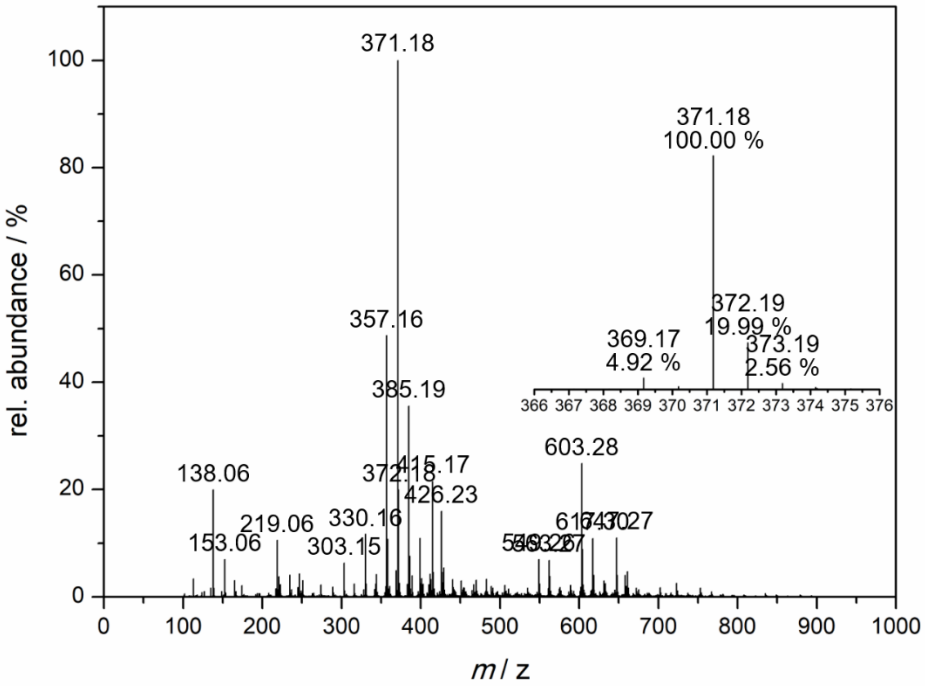


Figure C.7 ESI mass spectrum of 2,5-Bis[(4-methoxypyridin-2-ylmethyl)amino]methyl-1,3,4-oxadiazole ($\mathbf{L^{6,OMe}}$).

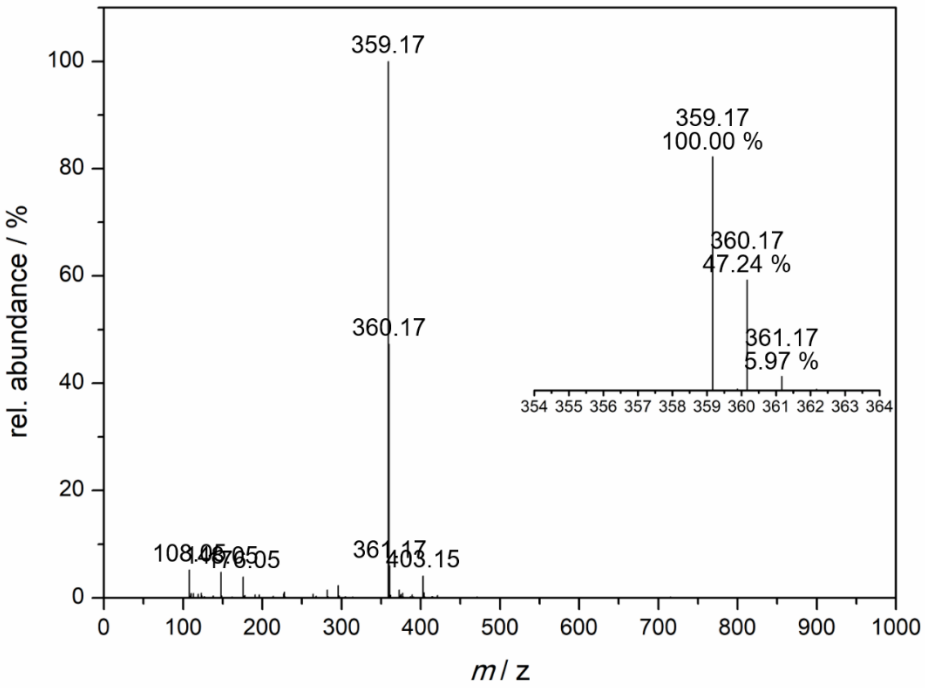


Figure C.8 ESI mass spectrum of 2-(2-Pyridyl)-5-[N,N-bis(2-pyridylmethyl)aminomethyl]-1,3,4-oxadiazole ($\mathbf{L^{Py,1}}$).

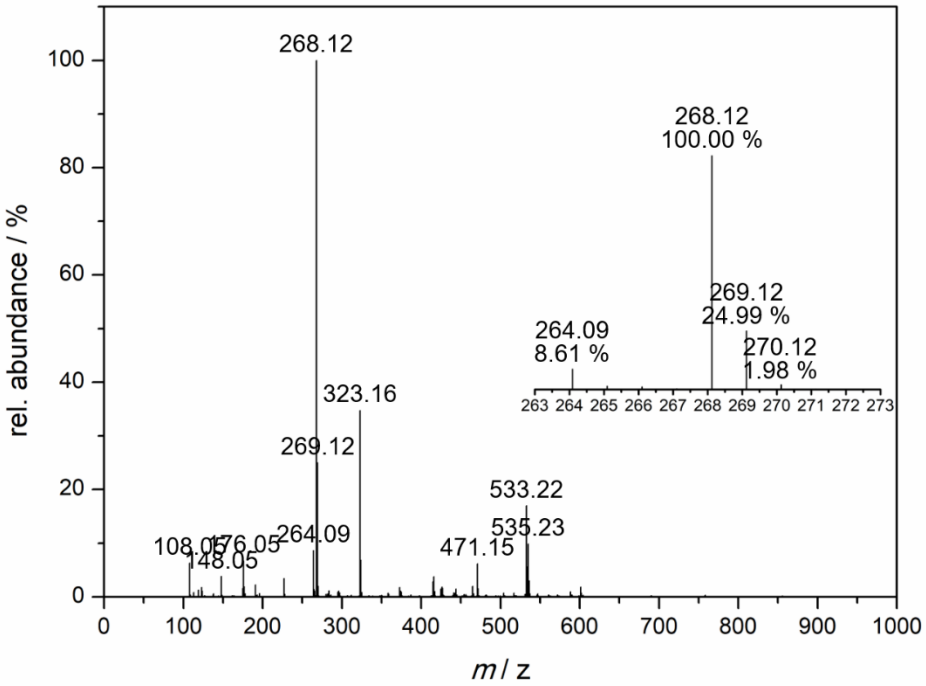


Figure C.9 ESI mass spectrum of 2-(2-Pyridyl)-5-[N,N-bis(2-pyridylmethyl)aminomethyl]-1,3,4-oxadiazole ($\mathbf{L^{Py,2}}$).

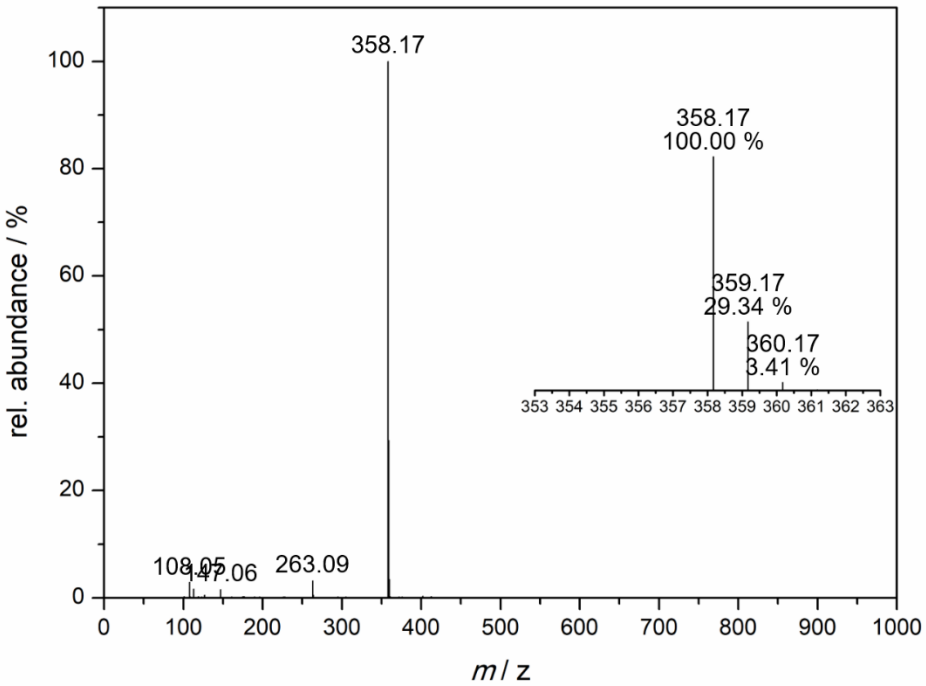


Figure C.10 ESI mass spectrum of 2-Phenyl-5-[N,N-bis(2-pyridylmethyl)aminomethyl]-1,3,4-oxadiazole ($\mathbf{L^{Ph}}$).

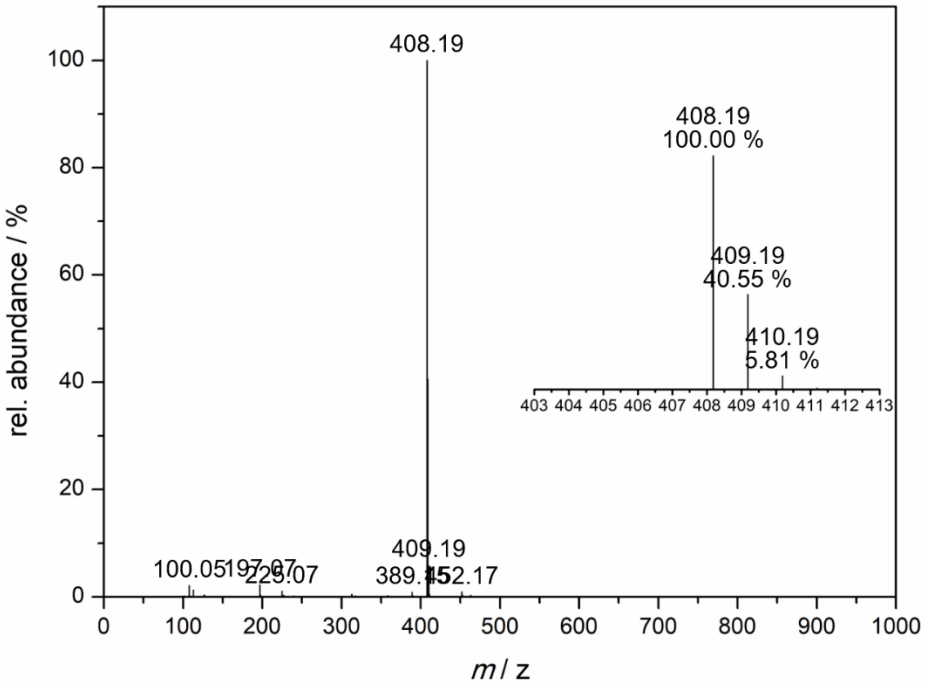


Figure C.11 ESI mass spectrum of 2-(Naphthalen-2-yl)-5-[N,N-bis(2-pyridylmethyl)aminomethyl]-1,3,4-oxadiazole (**L**$^{\mathbf{Naph}}$).

D Crystallographic Data

Table D.1 Crystallographic Data of **C1** and **C2**.

Compound	**C1**	**C2**
Empirical formula	$C_{28}H_{38}B_4F_{16}Fe_2N_{18}O_2$	$C_{28}H_{38}Cl_4Fe_2N_{18}O_{18}$
Formula weight / g mol^{-1}	1117.70	1168.26
Crystal size / mm	0.27 x 0.18 x 0.03	0.17 x 0.16 x 0.1
Crystal system	triclinic	orthorhombic
Space group	$P\bar{1}$	*Pbca*
Unit cell dimensions		
a / Å	9.8790(11)	12.5264(5)
b / Å	11.0981(12)	17.1932(7)
c / Å	11.6164(12)	21.2316(8)
α / °	64.523(3)	90
β / °	73.415(3)	90
γ / °	78.551(3)	90
Volume / Å	1097.7(2)	4572.6(3)
Z	1	4
$\rho_{calc.}$ / g cm^{-1}	1.691	1.697
μ / mm^{-1}	0.783	0.960
F(000)	564	2384
Temperature / K	173.15	173.15
Diffractometer	Bruker SMART APEX2	Bruker SMART APEX2
Radiation	Mo-Kα	Mo-Kα
θ – range for data collection / °	$1.994 < \theta < 27.956$	$1.918 < \theta < 27.987$
Index ranges	-12 < h < 12	-16 < h < 16
	-8 < k < 14	-22 < k < 22
	-12 < l < 15	-28 < l < 27
Collected reflections	9856	61828
Independent reflections	5204	5508
Completeness	0.987	0.998
Max. and min. transmission	1.0537 and 0.8274	0.7456 and 0.6923
R_{int}	0.0476	0.0784
R_{sigma}	0.0788	0.0347
Data/ restraints/ parameters	5204 / 27 / 342	5508 / 0 / 336
Goodness-of-fit on F^2	0.909	1.011
Final R_1 [$I \geq 2\sigma(I)$]	0.0431	0.0416
Final wR_2 [$I \geq 2\sigma(I)$]	0.0840	0.0951
Final R_1 [*alldata*]	0.0737	0.0771
Final wR_2 [*alldata*]	0.0923	0.1131

Table D.2 Crystallographic Data of **C3** and **C4**.

Compound	**C3**	**C4**
Empirical formula	$C_{32}H_{38}F_{12}Fe_2N_{18}O_{14}S_4$	$C_{28}H_{34}B_4F_{16}Fe_2N_{14}O_2S_4$
Formula weight / g mol^{-1}	1366.74	1185.87
Crystal size / mm	0.45 x 0.34 x 0.18	0.21 x 0.17 x 0.13
Crystal system	monoclinic	triclinic
Space group	$P2_1/n$	$P\bar{1}$
Unit cell dimensions		
a / Å	14.0235(5)	10.0069(4)
b / Å	12.7973(5)	10.5646(5)
c / Å	15.6316(6)	11.9159(5)
α / °	90	111.523(3)
β / °	109.2310(10)	89.855(3)
γ / °	90	107.989(3)
Volume / Å	2648.75(17)	1105.84(9)
Z	2	1
$\rho_{calc.}$ / g cm^{-1}	1.714	1.781
μ / mm^{-1}	0.825	0.962
F(000)	1384	596
Temperature / K	173.15	120(2)
Diffractometer	Bruker SMART APEX2	STOE STADIVARI
Radiation	Mo-Kα	Mo-Kα
θ – range for data collection / °	$1.694 < \theta < 27.931$	$2.157 < \theta < 30.551$
Index ranges	-18 < h < 18	-14 < h < 14
	-16 < k < 15	-14 < k < 14
	-20 < l < 20	-16 < l < 16
Collected reflections	27352	18186
Independent reflections	6341	6053
Completeness	0.998	0.894
Max. and min. transmission	1.0433 and 0.6877	0.8681 and 0.3816
R_{int}	0.0706	0.0207
R_{sigma}	0.0546	0.0276
Data/ restraints/ parameters	6341 / 0 / 374	6053 / 0 / 317
Goodness-of-fit on F^2	0.967	1.045
Final R_1 [$I \geq 2\sigma(I)$]	0.0359	0.0275
Final wR_2 [$I \geq 2\sigma(I)$]	0.0838	0.0692
Final R_1 [*alldata*]	0.0526	0.0376
Final wR_2 [*alldata*]	0.0906	0.0717

Table D.3 Crystallographic Data of **C6** and **C7**.

Compound	**C6**	**C7**
Empirical formula	$C_{32}H_{34}F_{12}Fe_2N_{14}O_{14}S_8$	$C_{40}H_{50}Cl_4Fe_2N_{14}O_{22}$
Formula weight / g mol^{-1}	1434.91	1332.44
Crystal size / mm	0.61 x 0.373 x 0.14	0.3 x 0.217 x 0.16
Crystal system	triclinic	triclinic
Space group	$P\bar{1}$	$P\bar{1}$
Unit cell dimensions		
a / Å	10.4594(8)	10.5754(6)
b / Å	10.5736(8)	11.9621(6)
c / Å	12.6476(10)	12.8565(7)
α / °	103.871(6)	72.880(4)
β / °	91.204(6)	68.092(4)
γ / °	100.026(6)	64.573(4)
Volume / Å	1334.33(18)	1345.20(14)
Z	1	1
$\rho_{calc.}$ / g cm^{-1}	1.786	1.645
μ / mm^{-1}	0.972	0.831
F(000)	724	684
Temperature / K	120(2)	173(2)
Diffractometer	STOE IPDS 2T	STOE STADIVARI
Radiation	Mo-Kα	Mo-Kα
θ – range for data collection / °	2.502 < θ < 28.151	2.225 < θ < 30.593
Index ranges	-12 < h < 13	-15 < h < 15
	-14 < k < 13	-17 < k < 17
	-16 < l < 16	-18 < l < 18
Collected reflections	11758	22606
Independent reflections	6440	7362
Completeness	0.988	0.889
Max. and min. transmission	0.8776 and 0.6109	0.8633 and 0.4584
R_{int}	0.0521	0.0181
R_{sigma}	0.0517	0.0249
Data/ restraints/ parameters	6440 / 0 / 371	7362 / 0 / 373
Goodness-of-fit on F^2	1.047	1.045
Final R_1 [$I \geq 2\sigma(I)$]	0.0622	0.0306
Final wR_2 [$I \geq 2\sigma(I)$]	0.1589	0.0775
Final R_1 [*alldata*]	0.0778	0.0414
Final wR_2 [*alldata*]	0.1743	0.0814

Table D.4 Crystallographic Data of **C8** and **C11**.

Compound	**C8**	**C11**
Empirical formula	$C_{44}H_{50}F_{12}Fe_2N_{14}O_{18}S_4$	$C_{40}H_{38}Cl_4F_{12}Fe_2N_{14}O_{14}S_4$
Formula weight / g mol^{-1}	1530.92	1548.58
Crystal size / mm	0.14 x 0.117 x 0.1	0.2 x 0.133 x 0.1
Crystal system	triclinic	triclinic
Space group	$P\bar{1}$	$P\bar{1}$
Unit cell dimensions		
a / Å	10.4649(3)	10.5568(3)
b / Å	17.3014(5)	11.8417(4)
c / Å	18.8815(6)	13.6741(4)
α / °	77.180(3)	81.358(2)
β / °	73.656(2)	80.467(2)
γ / °	73.224(2)	66.682(2)
Volume / Å	3103.84(17)	1541.32(9)
Z	2	1
$\rho_{calc.}$ / g cm^{-1}	1.638	1.668
μ / mm^{-1}	0.717	0.886
F(000)	156	78
Temperature / K	120	120(2)
Diffractometer	STOE STADIVARI	STOE STADIVARI
Radiation	Mo-Kα	Mo-Kα
θ – range for data collection / °	2.090 < θ < 30.576	2.115 < θ < 30.725
Index ranges	-14 < h < 14	-15 < h < 14
	-23 < k < 24	-16 < k < 17
	-24 < l < 26	-17 < l < 19
Collected reflections	51323	25385
Independent reflections	16808	8489
Completeness	0.883	0.885
Max. and min. transmission	0.9735 and 0.4705	0.8323 and 0.3991
R_{int}	0.0408	0.0176
R_{sigma}	0.0499	0.0235
Data/ restraints/ parameters	16808 / 51 / 881	8489 / 0 / 407
Goodness-of-fit on F^2	0.999	1.020
Final R_1 [$I \geq 2\sigma(I)$]	0.0569	0.0350
Final wR_2 [$I \geq 2\sigma(I)$]	0.1571	0.0849
Final R_1 [*alldata*]	0.0904	0.0473
Final wR_2 [*alldata*]	0.1788	0.0903

Table D.5 Crystallographic Data of **C12** and **C13**.

Compound	**C12**	**C13**
Empirical formula	$C_{32}H_{36}B_4F_{16}Fe_2N_{18}O_2$	$C_{32}H_{38}Cl_4Fe_2N_{18}O_{18}$
Formula weight / g mol^{-1}	1163.73	1216.30
Crystal size / mm	0.18 x 0.147 x 0.1	0.1 x 0.06 x 0.03
Crystal system	orthorhombic	monoclinic
Space group	*Pbam*	$P2_1/c$
Unit cell dimensions		
a / Å	15.7492(3)	13.0808(4)
b / Å	11.3827(3)	11.6105(3)
c / Å	13.0409(2)	15.7389(6)
α / °	90	90
β / °	90	90.349(3)
γ / °	90	90
Volume / Å	2337.82(8)	2390.30(13)
Z	2	2
$\rho_{calc.}$ / g cm^{-1}	1.653	1.690
μ / mm^{-1}	0.739	0.922
F(000)	1172	124
Temperature / K	173(2)	120
Diffractometer	STOE STADIVARI	STOE STADIVARI
Radiation	Mo-Kα	Mo-Kα
θ – range for data collection / °	2.208 < θ < 30.741	1.754 < θ < 27.000
Index ranges	-21 < h < 22	-16 < h < 16
	-13 < k < 16	-14 < k < 14
	-18 < l < 18	-20 < l < 20
Collected reflections	37370	33684
Independent reflections	3620	5208
Completeness	0.955	0.986
Max. and min. transmission	0.5401 and 0.2929	0.9838 and 0.6045
R_{int}	0.0355	0.0490
R_{sigma}	0.0174	0.0262
Data/ restraints/ parameters	3620 / 112 / 236	5208 / 120 / 401
Goodness-of-fit on F^2	1.271	1.041
Final R_1 [$I \geq 2\sigma(I)$]	0.0414	0.0369
Final wR_2 [$I \geq 2\sigma(I)$]	0.1003	0.0891
Final R_1 [*alldata*]	0.0580	0.0445
Final wR_2 [*alldata*]	0.1098	0.0934

Table D.6 Crystallographic Data of **C14** and **C14'**.

Compound	**C14**	**C14'**
Empirical formula	$C_{42}H_{42}B_4F_{16}Fe_2N_{14}O_6$	$C_{42}H_{42}B_4F_{16}Fe_2N_{14}O_6$
Formula weight / g mol^{-1}	1297.83	1297.83
Crystal size / mm	0.22 x 0.21 x 0.2	0.41 x 0.397 x 0.37
Crystal system	monoclinic	monoclinic
Space group	$P2_1/n$	$P2_1/c$
Unit cell dimensions		
a / Å	12.4037(8)	19.1371(3)
b / Å	16.0937(10)	16.0100(3)
c / Å	13.5145(9)	17.3627(3)
α / °	90	90
β / °	95.767(5)	94.9110(10)
γ / °	90	90
Volume / Å	2684.1(3)	5300.14(16)
Z	2	4
$\rho_{calc.}$ / g cm^{-1}	1.606	1.626
μ / mm^{-1}	0.656	0.665
F(000)	1312	2624
Temperature / K	173(2)	120(2)
Diffractometer	STOE STADIVARI	STOE STADIVARI
Radiation	Mo-Kα	Mo-Kα
θ – range for data collection / °	$2.080 < \theta < 30.790$	$2.088 < \theta < 30.805$
Index ranges	-17 < h < 17	-27 < h < 27
	-22 < k < 23	-22 < k < 22
	-18 < l < 18	-24 < l < 24
Collected reflections	45459	97357
Independent reflections	7690	15302
Completeness	0.915	0.922
Max. and min. transmission	0.9946 and 0.5021	0.9413 and 0.3959
R_{int}	0.0312	0.0352
R_{sigma}	0.0244	0.0285
Data/ restraints/ parameters	7690 / 51 / 408	15302 / 209 / 861
Goodness-of-fit on F^2	1.052	0.942
Final R_1 [$I \geq 2\sigma(I)$]	0.0487	0.0372
Final wR_2 [$I \geq 2\sigma(I)$]	0.1364	0.0956
Final R_1 [*alldata*]	0.0641	0.0529
Final wR_2 [*alldata*]	0.1465	0.1006

Table D.7 Crystallographic Data of **C15** and **C16**·1MeCN.

Compound	**C15**	**C16**·1MeCN
Empirical formula	$C_{42}H_{42}Cl_4Fe_2N_{14}O_{22}$	$C_{24}H_{21}FeN_9OS_2$
Formula weight / g mol^{-1}	1348.39	571.47
Crystal size / mm	0.2 x 0.147 x 0.08	0.15 x 0.093 x 0.06
Crystal system	monoclinic	monoclinic
Space group	$P2_1/n$	$P2_1/c$
Unit cell dimensions		
a / Å	12.5361(4)	15.4394(3)
b / Å	16.0432(6)	11.5893(2)
c / Å	13.6085(5)	23.9234(4)
α / °	90	90
β / °	95.600(3)	141.138(2)
γ / °	90	90
Volume / Å	2723.87(17)	2685.90(11)
Z	2	4
$\rho_{calc.}$ / g cm^{-1}	1.644	1.413
μ / mm^{-1}	0.822	0.752
F(000)	1376	1176
Temperature / K	150(2)	120
Diffractometer	STOE STADIVARI	STOE STADIVARI
Radiation	Mo-Kα	Mo-Kα
θ – range for data collection / °	1.968 < θ < 30.803	2.102 < θ < 30.782
Index ranges	-16 < h < 17	-21 < h < 22
	-21 < k < 22	-16 < k < 16
	-19 < l < 19	-34 < l < 31
Collected reflections	31060	48282
Independent reflections	7639	7725
Completeness	0.895	0.919
Max. and min. transmission	0.6837 and 0.5083	0.9853 and 0.6395
R_{int}	0.0246	0.0221
R_{sigma}	0.0307	0.0181
Data/ restraints/ parameters	7639 / 18 / 445	7725 / 0 / 335
Goodness-of-fit on F^2	1.036	1.053
Final R_1 [$I \geq 2\sigma(I)$]	0.0328	0.0259
Final wR_2 [$I \geq 2\sigma(I)$]	0.0793	0.0708
Final R_1 [*alldata*]	0.0509	0.0336
Final wR_2 [*alldata*]	0.0842	0.0730

Table D.8 Crystallographic Data of **C16**·1MeOH and **C17**·3MeCN.

Compound	**C16**·1MeOH	**C17**·3MeCN
Empirical formula	$C_{23}H_{22}FeN_8O_2S_2$	$C_{28}H_{27}FeN_{11}OSe_2$
Formula weight / g mol^{-1}	562.45	747.37
Crystal size / mm	0.365 x 0.322 x 0.25	0.38 x 0.293 x 0.24
Crystal system	monoclinic	monoclinic
Space group	*C*2/*c*	$P2_1/c$
Unit cell dimensions		
a / Å	30.6049(8)	16.8096(5)
b / Å	10.7652(2)	12.3242(2)
c / Å	22.5293(6)	17.0638(5)
α / °	90	90
β / °	135.8290(10)	112.630(2)
γ / °	90	90
Volume / Å	5172.1(2)	3262.85(15)
Z	8	4
$\rho_{calc.}$ / g cm^{-1}	1.445	1.521
μ / mm^{-1}	0.782	2.733
F(000)	232	1496
Temperature / K	120	173
Diffractometer	STOE STADIVARI	STOE STADIVARI
Radiation	Mo-Kα	Mo-Kα
θ – range for data collection / °	1.910 < θ < 30.683	2.098 < θ < 31.109
Index ranges	-43 < h < 43	-24 < h < 24
	-15 < k < 15	-17 < k < 17
	-31 < l < 32	-20 < l < 23
Collected reflections	43687	60603
Independent reflections	7316	61872
Completeness	0.911	0.907
Max. and min. transmission	0.9697 and 0.4942	0.8343 and 0.3674
R_{int}	0.0264	0.0422
R_{sigma}	0.0231	0.0381
Data/ restraints/ parameters	7316 / 0 / 327	9526 / 0 / 391
Goodness-of-fit on F^2	1.048	0.946
Final R_1 [$I \geq 2\sigma(I)$]	0.0261	0.0293
Final wR_2 [$I \geq 2\sigma(I)$]	0.0694	0.0645
Final R_1 [*alldata*]	0.0340	0.0529
Final wR_2 [*alldata*]	0.0714	0.0688

Table D.9 Crystallographic Data of **C18**·1MeOH and **C19**·2MeCN.

Compound	**C18**·1MeOH	**C19**·2MeCN
Empirical formula	$C_{23}H_{28}B_2FeN_8O_3$	$C_{27}H_{25}FeN_9OS_2$
Formula weight / g mol^{-1}	526.00	611.53
Crystal size / mm	0.13 x 0.097 x 0.08	0.32 x 0.207 x 0.11
Crystal system	monoclinic	monoclinic
Space group	*C*2/*c*	*C*2/*c*
Unit cell dimensions		
a / Å	24.0771(16)	30.6059(10)
b / Å	10.9789(7)	11.7584(5)
c / Å	20.5964(18)	17.6574(6)
α / °	90	90
β / °	91.607(6)	105.110(3)
γ / °	90	90
Volume / Å	5442.3(7)	6134.8(4)
Z	8	8
$\rho_{calc.}$ / g cm^{-1}	1.284	1.324
μ / mm^{-1}	0.589	0.664
F(000)	2192	2528
Temperature / K	293(2)	173
Diffractometer	STOE STADIVARI	STOE STADIVARI
Radiation	Mo-Kα	Mo-Kα
θ – range for data collection / °	1.978 < θ < 30.601	1.864 < θ < 30.969
Index ranges	-34 < h < 32	-38 < h < 43
	-15 < k < 14	-16 < k < 16
	-29 < l < 28	-25 < l < 25
Collected reflections	110056	56051
Independent reflections	7483	8963
Completeness	0.894	0.919
Max. and min. transmission	0.9935 and 0.4279	0.9852 and 0.2527
R_{int}	0.1980	0.0282
R_{sigma}	0.0539	0.0266
Data/ restraints/ parameters	7483 / 54 / 327	8963 / 18 / 414
Goodness-of-fit on F^2	1.199	1.028
Final R_1 [$I \geq 2\sigma(I)$]	0.2075	0.0384
Final wR_2 [$I \geq 2\sigma(I)$]	0.4245	0.1236
Final R_1 [*alldata*]	0.2252	0.0498
Final wR_2 [*alldata*]	0.4328	0.1291

Table D.10 Crystallographic Data of **C19**·3MeOH and **C20**·2MeCN.

Compound	**C19**·3MeOH	**C20**·2MeCN
Empirical formula	$C_{26}H_{31}FeN_7O_4S_2$	$C_{27}H_{25}FeN_9OSe_2$
Formula weight / g mol^{-1}	625.55	705.33
Crystal size / mm	0.32 x 0.203 x 0.11	1.1 x 0.73 x 0.29
Crystal system	monoclinic	monoclinic
Space group	*C*2/*c*	*C*2/*c*
Unit cell dimensions		
a / Å	30.0687(6)	30.7836(16)
b / Å	11.8250(2)	11.8309(4)
c / Å	17.4007(4)	17.8246(10)
α / °	90	90
β / °	103.8190(10)	105.213(4)
γ / °	90	90
Volume / Å	6008.0(2)	6264.2(5)
Z	8	8
$\rho_{calc.}$ / g cm^{-1}	1.383	1.496
μ / mm^{-1}	0.684	2.841
F(000)	2608	2816
Temperature / K	173	173
Diffractometer	STOE STADIVARI	STOE STADIVARI
Radiation	Mo-Kα	Mo-Kα
θ – range for data collection / °	1.858 < θ < 30.675	1.853 < θ < 25.998
Index ranges	-33 < h < 41	-37 < h < 37
	-16 < k < 16	-14 < k < 14
	-24 < l < 24	-21 < l < 21
Collected reflections	54013	42183
Independent reflections	55105	56025
Completeness	0.929	1.000
Max. and min. transmission	0.9852 and 0.2636	0.8170 and 0.1557
R_{int}	0.0333	0.0989
R_{sigma}	0.0302	0.0579
Data/ restraints/ parameters	8650 / 55 / 372	6163 / 36 / 387
Goodness-of-fit on F^2	0.967	1.064
Final R_1 [$I \geq 2\sigma(I)$]	0.0340	0.0703
Final wR_2 [$I \geq 2\sigma(I)$]	0.0955	0.1916
Final R_1 [*alldata*]	0.0455	0.0875
Final wR_2 [*alldata*]	0.0992	0.2016

Table D.11 Crystallographic Data of **C20**·3MeOH and **C21**·1MeCN @240 K.

Compound	**C20**·3MeOH	**C21**·1MeCN @240 K
Empirical formula	$C_{26}H_{31}FeN_7O_4Se_2$	$C_{25}H_{28}B_2FeN_8O$
Formula weight / g mol^{-1}	719.35	534.02
Crystal size / mm	0.62 x 0.567 x 0.52	0.7 x 0.5 x 0.2
Crystal system	monoclinic	monoclinic
Space group	*C*2/*c*	*C*2/*c*
Unit cell dimensions		
a / Å	30.1566(14)	23.819(2)
b / Å	11.9304(4)	11.1057(7)
c / Å	17.6430(9)	20.7090(17)
α / °	90	90
β / °	104.259(4)	91.611(7)
γ / °	90	90
Volume / Å	6152.0(5)	5476.0(7)
Z	8	8
$\rho_{calc.}$ / g cm^{-1}	1.553	1.295
μ / mm^{-1}	2.899	0.584
F(000)	2896	2224
Temperature / K	173	240
Diffractometer	STOE STADIVARI	STOE STADIVARI
Radiation	Mo-Kα	Mo-Kα
θ – range for data collection / °	1.844 < θ < 30.818	1.968 < θ < 30.718
Index ranges	-43 < h < 43	-33 < h < 34
	-16 < k < 15	-15 < k < 15
	-25 < l < 24	-29 < l < 28
Collected reflections	55051	45829
Independent reflections	56480	47171
Completeness	0.918	0.927
Max. and min. transmission	0.8299 and 0.2057	0.9107 and 0.1064
R_{int}	0.0537	0.0391
R_{sigma}	0.0453	0.0292
Data/ restraints/ parameters	8872 / 16 / 414	7890 / 99 / 366
Goodness-of-fit on F^2	0.961	1.080
Final R_1 [$I \geq 2\sigma(I)$]	0.0394	0.0387
Final wR_2 [$I \geq 2\sigma(I)$]	0.0989	0.1116
Final R_1 [*alldata*]	0.0653	0.0580
Final wR_2 [*alldata*]	0.1063	0.1185

Table D.12 Crystallographic Data of **C21**·1MeCN @120 K and **C21**·1.8MeOH.

Compound	**C21**·1MeCN @120 K	**C21**·1.8MeOH
Empirical formula	$C_{25}H_{28}B_2FeN_8O$	$C_{23}H_{25}B_2FeN_7O$
Formula weight / g mol^{-1}	534.02	492.97
Crystal size / mm	0.7 x 0.5 x 0.2	0.09 x 0.061 x 0.014
Crystal system	monoclinic	monoclinic
Space group	*C*2/*c*	*C*2/*c*
Unit cell dimensions		
a / Å	22.9994(7)	22.8924(11)
b / Å	10.7119(2)	10.6084(5)
c / Å	20.7583(6)	21.3529(10)
α / °	90	90
β / °	91.282(2)	91.711(4)
γ / °	90	90
Volume / Å	5112.9(2)	5183.3(4)
Z	8	8
$\rho_{calc.}$ / g cm^{-1}	1.387	1.263
μ / mm^{-1}	0.625	0.610
F(000)	2224	2048
Temperature / K	120	173
Diffractometer	STOE STADIVARI	STOE STADIVARI
Radiation	Mo-Kα	Mo-Kα
θ – range for data collection / °	1.963 < θ < 30.816	1.908 < θ < 25.998
Index ranges	-32 < h < 32	-28 < h < 28
	-15 < k < 14	-13 < k < 13
	-29 < l < 28	-26 < l < 26
Collected reflections	38963	36965
Independent reflections	40193	48257
Completeness	0.915	1.000
Max. and min. transmission	0.9675 and 0.2137	0.9724 and 0.2162
R_{int}	0.0386	0.1275
R_{sigma}	0.0254	0.0794
Data/ restraints/ parameters	7340 / 0 / 337	5097 / 0 / 309
Goodness-of-fit on F^2	1.076	1.148
Final R_1 [$I \geq 2\sigma(I)$]	0.0436	0.0730
Final wR_2 [$I \geq 2\sigma(I)$]	0.1185	0.2355
Final R_1 [*alldata*]	0.0509	0.1168
Final wR_2 [*alldata*]	0.1236	0.2505

Table D.13 Crystallographic Data of **C22** and **C23**·4.5MeCN.

Compound	**C22**	**C23**·4.5MeCN
Empirical formula	$C_{42}H_{38}Cl_2N_{10}NiO_{10}$	$C_{27}H_{27}B_2FeN_7O$
Formula weight / g mol^{-1}	972.43	543.02
Crystal size / mm	0.2 x 0.127 x 0.09	0.64 x 0.603 x 0.54
Crystal system	triclinic	monoclinic
Space group	$P\bar{1}$	*C*2/*c*
Unit cell dimensions		
a / Å	11.4143(5)	33.6829(10)
b / Å	13.8757(6)	12.1127(2)
c / Å	15.1788(6)	17.7933(5)
α / °	107.094(3)	90
β / °	92.643(3)	97.121(2)
γ / °	113.147(3)	90
Volume / Å	2076.81(16)	7203.5(3)
Z	2	8
$\rho_{calc.}$ / g cm^{-1}	1.555	1.001
μ / mm^{-1}	0.670	0.444
F(000)	1004	2256
Temperature / K	173	220
Diffractometer	STOE STADIVARI	STOE STADIVARI
Radiation	Mo-Kα	Mo-Kα
θ – range for data collection / °	1.809 < θ < 30.752	1.788 < θ < 30.882
Index ranges	-13 < h < 16	-47 < h < 42
	-19 < k < 19	-17 < k < 17
	-21 < l < 21	-25 < l < 22
Collected reflections	38909	66234
Independent reflections	38909	67906
Completeness	0.889	0.919
Max. and min. transmission	0.9593 and 0.5015	0.9664 and 0.3474
R_{int}	0.0185	0.0351
R_{sigma}	0.0272	0.0307
Data/ restraints/ parameters	11523 / 0 / 586	10447 / 0 / 345
Goodness-of-fit on F^2	1.081	0.972
Final R_1 [$I \geq 2\sigma(I)$]	0.0383	0.0359
Final wR_2 [$I \geq 2\sigma(I)$]	0.1054	0.1023
Final R_1 [*alldata*]	0.0487	0.0470
Final wR_2 [*alldata*]	0.1094	0.1054

Table D.14 Crystallographic Data of **C23**·3MeOH @220 K and **C23**·3MeOH @120 K.

Compound	**C23**·3MeOH @220 K	**C23**·3MeOH @120 K
Empirical formula	$C_{28.25}H_{32.25}B_2FeN_7O_{2.50}$	$C_{28.50}H_{33}B_2FeN_7O_{2.50}$
Formula weight / g mol^{-1}	587.33	591.09
Crystal size / mm	0.2 x 0.187 x 0.18	0.23 x 0.19 x 0.15
Crystal system	monoclinic	monoclinic
Space group	*C*2/*c*	*C*2/*c*
Unit cell dimensions		
a / Å	26.7229(7)	26.0632(7)
b / Å	10.9749(2)	10.5691(2)
c / Å	21.1290(6)	21.3067(6)
α / °	90	90
β / °	95.813(2)	96.182(2)
γ / °	90	90
Volume / Å	6164.9(3)	5835.1(3)
Z	8	8
$\rho_{calc.}$ / g cm^{-1}	1.266	1.346
μ / mm^{-1}	0.528	0.558
F(000)	2454	2472
Temperature / K	220	120
Diffractometer	STOE STADIVARI	STOE STADIVARI
Radiation	Mo-Kα	Mo-Kα
θ – range for data collection / °	1.938 < θ < 31.123	1.923 < θ < 30.771
Index ranges	-38 < h < 36	-36 < h < 37
	-15 < k < 15	-15 < k < 15
	-30 < l < 30	-30 < l < 30
Collected reflections	56550	51641
Independent reflections	58044	53070
Completeness	0.908	0.929
Max. and min. transmission	0.9893 and 0.4678	0.9090 and 0.2842
R_{int}	0.0364	0.0308
R_{sigma}	0.0318	0.0291
Data/ restraints/ parameters	9010 / 38 / 404	8470 / 31 / 403
Goodness-of-fit on F^2	0.977	1.078
Final R_1 [$I \geq 2\sigma(I)$]	0.0455	0.0444
Final wR_2 [$I \geq 2\sigma(I)$]	0.1354	0.1316
Final R_1 [*alldata*]	0.0638	0.0573
Final wR_2 [*alldata*]	0.1438	0.1369

Table D.15 Crystallographic Data of **C26** and **C27**.

Compound	**C26**	**C27**
Empirical formula	$C_{23}H_{22}CoN_8O_2S_2$	$C_{24}H_{23}CoN_7O_2S_2$
Formula weight / g mol^{-1}	565.53	564.54
Crystal size / mm	0.1 x 0.08 x 0.06	0.3 x 0.18 x 0.06
Crystal system	monoclinic	triclinic
Space group	*I*2/*a*	$P\bar{1}$
Unit cell dimensions		
a / Å	22.3904(5)	8.4664(5)
b / Å	10.6597(2)	11.5196(6)
c / Å	21.4977(5)	13.8175(7)
α / °	90	90.126(4)
β / °	91.833(2)	94.539(4)
γ / °	90	106.148(4)
Volume / Å	5128.34(19)	1289.97(12)
Z	8	2
$\rho_{calc.}$ / g cm^{-1}	1.465	1.453
μ / mm^{-1}	0.870	0.863
F(000)	2328	582
Temperature / K	120	173
Diffractometer	STOE STADIVARI	STOE STADIVARI
Radiation	Mo-Kα	Mo-Kα
θ – range for data collection / °	1.896 < θ < 30.595	1.841 < θ < 30.808
Index ranges	-30 < h < 31	-12 < h < 10
	-14 < k < 15	-16 < k < 16
	-30 < l < 30	-19 < l < 19
Collected reflections	44588	22441
Independent reflections	7336	7130
Completeness	0.930	0.881
Max. and min. transmission	0.9915 and 0.3508	0.9427 and 0.2992
R_{int}	0.0236	0.0237
R_{sigma}	0.0229	0.0277
Data/ restraints/ parameters	7336 / 0 / 327	7130 / 3 / 329
Goodness-of-fit on F^2	1.054	1.033
Final R_1 [$I \geq 2\sigma(I)$]	0.0262	0.0301
Final wR_2 [$I \geq 2\sigma(I)$]	0.0708	0.0774
Final R_1 [*alldata*]	0.0365	0.0387
Final wR_2 [*alldata*]	0.0732	0.0808

Table D.16 Crystallographic Data of **C28**.

Compound	**C28**
Empirical formula	$C_{27}H_{21}CoN_7OS_2$
Formula weight / g mol^{-1}	582.56
Crystal size / mm	0.46 x 0.173 x 0.027
Crystal system	orthorhombic
Space group	*Pbca*
Unit cell dimensions	
a / Å	8.57830(10)
b / Å	29.6409(6)
c / Å	20.7495(3)
α / °	90
β / °	90
γ / °	90
Volume / Å	5275.95(14)
Z	8
$\rho_{calc.}$ / g cm^{-1}	1.467
μ / mm^{-1}	0.844
F(000)	2392
Temperature / K	120
Diffractometer	STOE STADIVARI
Radiation	Mo-Kα
θ – range for data collection / °	$1.689 < \theta < 31.190$
Index ranges	-12 < h < 12
	-37 < k < 42
	-29 < l < 29
Collected reflections	63632
Independent reflections	63632
Completeness	0.921
Max. and min. transmission	0.9922 and 0.2683
R_{int}	0.0738
R_{sigma}	0.0493
Data/ restraints/ parameters	7887 / 0 / 343
Goodness-of-fit on F^2	0.930
Final R_1 [$I \geq 2\sigma(I)$]	0.0441
Final wR_2 [$I \geq 2\sigma(I)$]	0.1172
Final R_1 [*alldata*]	0.0757
Final wR_2 [*alldata*]	0.1316

E Structural parameters of characterized coordination compounds

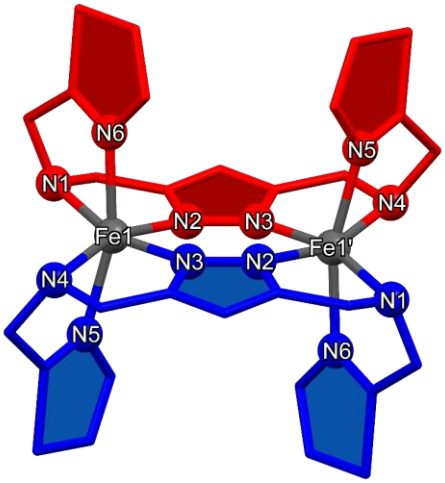


Figure E.1 Labelling scheme for **C1**, **C2**, **C3**, **C4** and **C6**. Colour scheme is set to different ligand molecules.

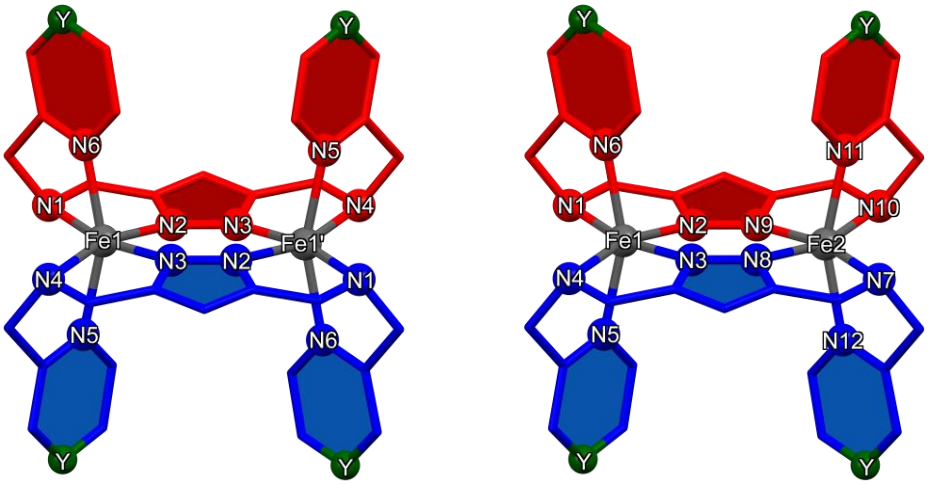


Figure E.2 Labelling scheme for **C7**, **C11**, **C12**, **C13** (left) and **C8** (right). Colour scheme is set to different ligand molecules. Green represents variable functional groups. Substitution group Y is marked in green (Y = (C-)OMe, (C-)Cl, N).

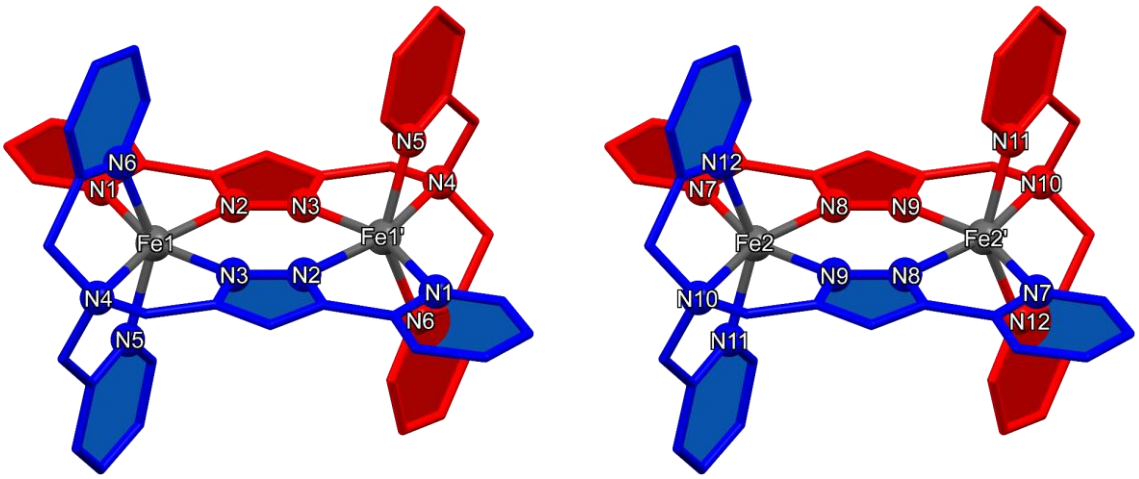


Figure E.3 Labelling scheme for **C14**, **C15** (left) and **C14'** (left and right). Colour scheme is set to different ligand molecules.

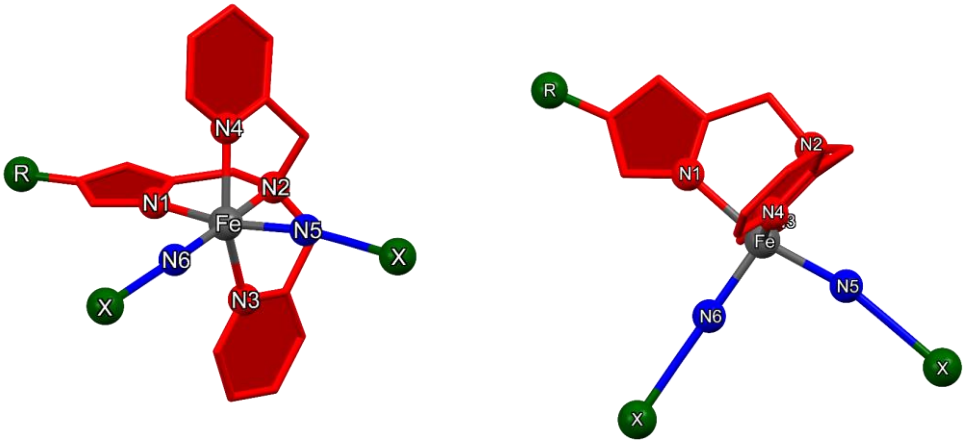


Figure E.4 Labelling scheme for solvatomorphs of **C16**, **C17, C18**, **C19, C20**, **C21** and **C23** with different views. Colour scheme is set to different ligand molecules. Green represents variable functional groups (R = aryl group, X = S, Se or BH_3).

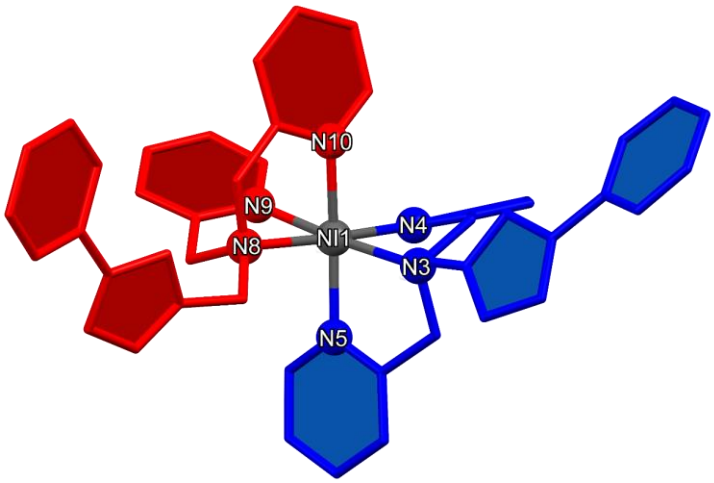


Figure E.5 Labelling scheme for **C22**. Colour scheme is set to different ligand molecules.

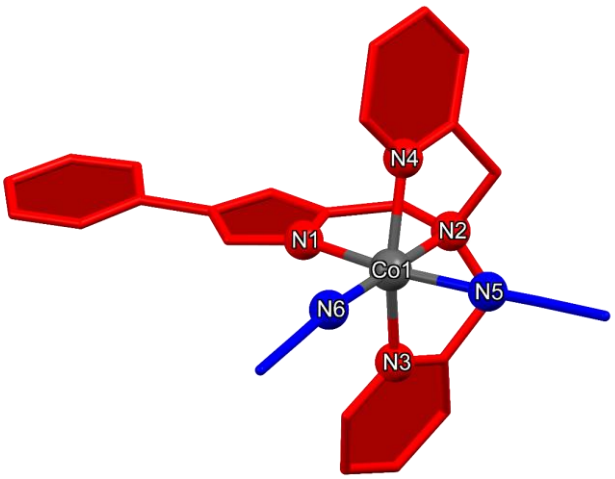


Figure E.6 Labelling scheme for **C26**. Colour scheme is set to different ligand molecules.

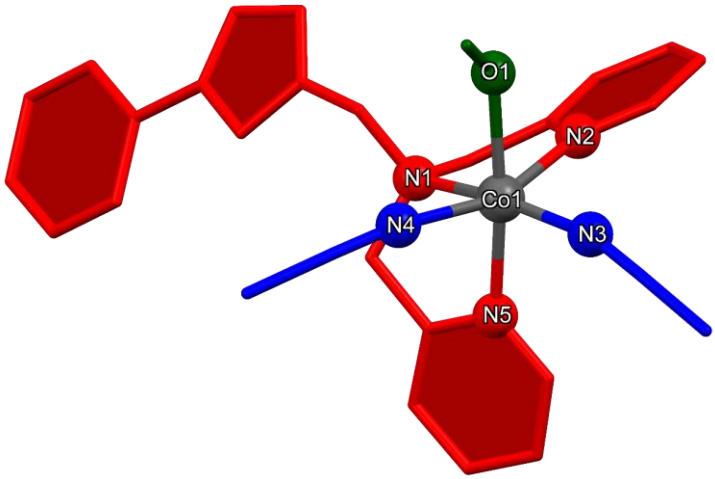


Figure E.7 Labelling scheme for **C27**. Colour scheme is set to different ligand molecules.

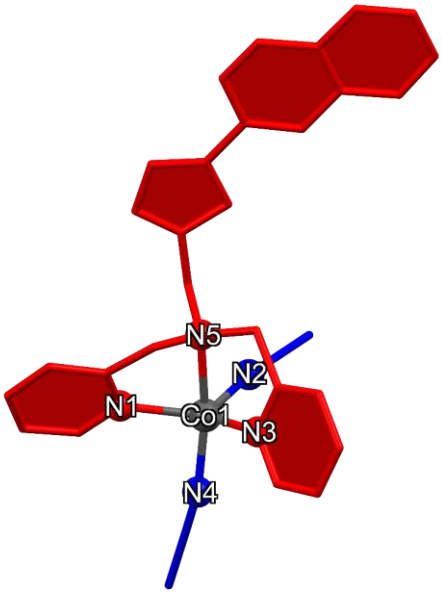


Figure E.8 Labelling scheme for **C28**. Colour scheme is set to different ligand molecules.

Table E.1 Selected bond lengths and angles of complexes **C1, C2** and **C3**.[196] Labeling of the atoms follows the scheme in Figure E.1. Since Fe1 and Fe1' are symmetry equivalent, the term Fe will be used.

	C1	**C2**	**C3**
	173 K	173 K	173 K
Bond / Å			
Fe-N1	2.4190(20)	2.422(2)	2.4592(16)
Fe-N2	2.1377(19)	2.138(2)	2.1429(16)
Fe-N3	2.1510(20)	2.130(2)	2.1612(16)
Fe-N4	2.4490(18)	2.418(2)	2.3815(17)
Fe-N5	2.0873(19)	2.081(2)	2.0851(16)
Fe-N6	2.0780(20)	2.077(2)	2.0839(16)
$\overline{\text{Fe-N}}$	2.22	2.21	2.22
cis-Angles / °			
N1-Fe-N2	72.98(7)	74.08(8)	72.52(6)
N2-Fe-N3	93.47(7)	93.90(8)	91.65(6)
N3-Fe-N4	74.35(7)	74.26(8)	73.67(6)
N4-Fe-N1	120.90(8)	119.29(8)	124.74(6)
N1-Fe-N5	102.25(7)	91.12(8)	94.65(6)
N2-Fe-N5	97.36(7)	98.75(8)	95.45(6)
N3-Fe-N5	92.29(8)	101.45(8)	102.14(6)
N4-Fe-N5	74.62(7)	74.79(8)	76.39(6)
N1-Fe-N6	75.17(8)	75.27(8)	75.97(6)
N2-Fe-N6	100.28(7)	102.96(8)	95.90(6)
N3-Fe-N6	95.02(8)	97.67(8)	91.04(6)
N4-Fe-N6	89.91(8)	88.44(8)	96.46(6)
trans-Angles / °			
N1-Fe-N3	161.13(7)	163.90(8)	158.01(7)
N2-Fe-N4	164.85(8)	164.71(8)	160.93(6)
N5-Fe-N6	160.43(8)	149.87(9)	162.32(7)
Distortion			
$\Sigma_O(FeN_6)$ / °	134.5	138.3	133.5
$CShM(O_h)$	4.75	5.23	5.17
Torsions / °			
Fe-N2-N3-Fe1'	15.8	0.9	10.9

Table E.2 Selected bond lengths and angles of complexes **C4** and **C6**[381]. Labeling of the atoms follows the scheme in Figure E.1. Since Fe1 and Fe1' are symmetry equivalent, the term Fe will be used.

	C4	**C6**
	120 K	120 K
Bond / Å		
Fe-N1	2.3627(11)	2.370(3)
Fe-N2	2.1303(11)	2.145(3)
Fe-N3	2.1408(11)	2.132(3)
Fe-N4	2.3495(12)	2.357(3)
Fe-N5	2.1289(11)	2.121(3)
Fe-N6	2.1259(11)	2.106(3)
$\overline{\text{Fe-N}}$	2.21	2.21
cis-Angles / °		
N1-Fe-N2	74.57(4)	74.69(10)
N2-Fe-N3	90.63(4)	90.67(10)
N3-Fe-N4	75.64(4)	74.47(10)
N4-Fe-N1	120.95(4)	122.24(10)
N1-Fe-N5	97.88(4)	96.63(10)
N2-Fe-N5	94.31(4)	92.48(11)
N3-Fe-N5	94.61(4)	95.11(11)
N4-Fe-N5	76.26(4)	76.07(10)
N1-Fe-N6	75.80(4)	75.84(11)
N2-Fe-N6	98.43(4)	101.61(11)
N3-Fe-N6	95.53(4)	96.75(11)
N4-Fe-N6	93.83(4)	93.41(11)
trans-Angles / °		
N1-Fe-N3	161.24(4)	161.56(10)
N2-Fe-N4	162.43(4)	160.07(11)
N5-Fe-N6	163.60(4)	161.42(11)
Distortion		
$\Sigma_O(FeN_6)$ / °	123.9	128
$CShM(O_h)$	4.09	4.57
Torsions / °		
Fe-N2-N3-Fe1'	9.03(18)	10

Table E.3 Selected bond lengths and angles of complex **C8**. Labeling of the atoms follows the scheme in Figure E.2 (right).

$[Fe_2(\mu_2\text{-}\mathbf{L}^{6,OMe})_2](CF_3SO_3)_4 \cdot 2CH_3CN$ (**C8**) 120 K			
Bond / Å		Bond / Å	
Fe1-N1	2.344(2)	Fe2-N7	2.334(2)
Fe1-N2	2.153(2)	Fe2-N8	2.140(2)
Fe1-N3	2.144(2)	Fe2-N9	2.134(2)
Fe1-N4	2.328(2)	Fe2-N10	2.318(2)
Fe1-N5	2.133(2)	Fe2-N11	2.142(2)
Fe1-N6	2.147(2)	Fe2-N12	2.153(2)
$\overline{\text{Fe1-N}}$	2.21	$\overline{\text{Fe2-N}}$	2.20
cis-Angles / °		*cis*-Angles / °	
N1-Fe1-N2	74.50(8)	N7-Fe2-N8	75.02(8)
N2-Fe1-N3	90.88(8)	N8-Fe2-N9	91.28(8)
N3-Fe1-N4	75.44(8)	N9-Fe2-N10	75.73(8)
N4-Fe1-N1	120.97(8)	N10-Fe2-N7	119.49(8)
N1-Fe1-N5	96.46(8)	N7-Fe2-N11	94.08(8)
N2-Fe1-N5	95.56(8)	N8-Fe2-N11	95.26(8)
N3-Fe1-N5	96.40(8)	N9-Fe2-N11	96.92(8)
N4-Fe1-N5	75.53(8)	N10-Fe2-N11	75.91(8)
N1-Fe1-N6	75.26(8)	N7-Fe2-N12	75.49(8)
N2-Fe1-N6	99.42(8)	N8-Fe2-N12	97.98(8)
N3-Fe1-N6	96.34(8)	N9-Fe2-N12	97.28(8)
N4-Fe1-N6	93.06(8)	N10-Fe2-N12	94.51(8)
trans-Angles / °		*trans*-Angles / °	
N1-Fe1-N3	161.37(8)	N7-Fe2-N9	163.17(8)
N2-Fe1-N4	162.46(8)	N8-Fe2-N10	163.04(8)
N5-Fe1-N6	160.14(9)	N11-Fe2-N12	160.32(9)
Distortion		Distortion	
$\Sigma_O(Fe1N_6)$ / °	128.4	$\Sigma_O(Fe2N_6)$ / °	124.7
$CShM(O_h)$	4.30	$CShM(O_h)$	3.96
Torsions / °			
Fe1-N2-N9-Fe2	5.0(3)		
Fe1-N3-N8-Fe2	0.5(3)		

Table E.4 Selected bond lengths and angles of complexes **C7, C11** and **C12**. Labeling of the atoms follows the scheme in Figure E.2 (left). Since Fe1 and Fe1' are symmetry equivalent, the term Fe will be used.

	C7 173 K	**C11** 120 K	**C12** 173 K
Bond / Å			
Fe-N1	2.3571(12)	2.2925(14)	2.3333(19)
Fe-N2	2.1443(12)	2.1249(13)	2.1440(20)
Fe-N3	2.1560(11)	2.1256(13)	2.1440(20)
Fe-N4	2.3208(12)	2.2937(14)	2.3333(19)
Fe-N5	2.1340(13)	2.1511(15)	2.1450(16)
Fe-N6	2.1170(12)	2.1472(14)	2.1450(16)
$\overline{\text{Fe-N}}$	2.21	2.19	2.21
cis-Angles / °			
N1-Fe-N2	74.53(4)	75.98(5)	75.17(6)
N2-Fe-N3	90.94(4)	90.72(5)	90.12(11)
N3-Fe-N4	74.20(4)	75.06(5)	75.17(6)
N4-Fe-N1	121.44(4)	119.39(5)	120.92(12)
N1-Fe-N5	86.99(4)	88.78(5)	90.00(7)
N2-Fe-N5	102.82(5)	100.59(5)	98.97(7)
N3-Fe-N5	106.38(5)	103.41(5)	102.26(7)
N4-Fe-N5	74.72(4)	75.25(5)	75.10(6)
N1-Fe-N6	75.43(4)	75.44(5)	75.10(6)
N2-Fe-N6	99.54(5)	97.98(5)	102.26(7)
N3-Fe-N6	97.65(5)	97.25(5)	98.97(7)
N4-Fe-N6	90.38(4)	92.20(5)	90.00(7)
trans-Angles / °			
N1-Fe-N3	162.31(4)	163.53(5)	162.26(9)
N2-Fe-N4	163.18(4)	163.50(5)	162.26(9)
N5-Fe-N6	146.62(5)	151.89(6)	149.77(14)
Distortion			
$\Sigma_O(FeN_6)$ / °	143.3	131.03	133.0
$CShM(O_h)$	5.75	4.67	5.24
Torsions / °			
Fe-N2-N3-Fe1'	3.32(19)	2.60(20)	0.00

Table E.5 Selected bond lengths and angles of complexes **C13**, **C14** and **C15**. Labeling of the atoms follows the scheme in Figure E.2 (left) for **C13** and Figure E.3 (left) for **C14** and **C15.** Since Fe1 and Fe1' are symmetry equivalent, the term Fe will be used.

	C13	**C14**	**C15**
	120 K	173 K	150 K
Bond / Å			
Fe-N1	2.314(2)	2.3068(16)	2.3100(12)
Fe-N2	2.151(2)	2.1590(15)	2.1683(11)
Fe-N3	2.150(2)	2.1430(16)	2.1494(12)
Fe-N4	2.359(2)	2.3926(16)	2.4010(12)
Fe-N5	2.144(2)	2.1067(18)	2.1026(14)
Fe-N6	2.147(2)	2.1044(17)	2.0975(13)
$\overline{\text{Fe-N}}$	2.21	2.20	2.21
cis-Angles / °			
N1-Fe-N2	75.45(8)	72.94(6)	72.80(4)
N2-Fe-N3	89.75(8)	87.24(6)	86.81(4)
N3-Fe-N4	74.66(8)	74.97(6)	74.74(4)
N4-Fe-N1	121.54(8)	125.01(6)	125.72(4)
N1-Fe-N5	88.63(9)	86.70(6)	86.87(5)
N2-Fe-N5	98.59(9)	108.88(7)	108.18(5)
N3-Fe-N5	102.87(9)	94.99(7)	95.17(5)
N4-Fe-N5	74.95(8)	75.80(7)	75.73(5)
N1-Fe-N6	75.25(9)	93.96(6)	93.05(5)
N2-Fe-N6	102.92(9)	104.55(6)	106.28(5)
N3-Fe-N6	99.74(9)	96.17(6)	97.40(5)
N4-Fe-N6	90.64(8)	75.44(7)	75.14(5)
trans-Angles / °			
N1-Fe-N3	162.58(9)	159.48(6)	159.04(5)
N2-Fe-N4	160.97(8)	162.03(6)	161.49(5)
N5-Fe-N6	148.68(8)	145.15(7)	143.83(5)
Distortion			
$\Sigma_O(FeN_6)$ / °	137.6	150.5	153.7
$CShM(O_h)$	5.50	6.27	6.60
Torsions / °			
Fe-N2-N3-Fe1'	2.90(40)	5.6(3)	5.9

Table E.6 Selected bond lengths and angles of complex **C14'**. Labeling of the atoms follows the scheme in Figure E.3 (left and right). Since Fe1 and Fe1' are symmetry equivalent, the term Fe will be used.

$[Fe_2(\mu_2\text{-}\mathbf{L^{Py,1}})_2](BF_4)_4 \cdot 2MeNO_2$ (**C14'**) 120 K			
Bond / Å		Bond / Å	
Fe1-N1	2.3165(11)	Fe2-N7	2.3005(11)
Fe1-N2	2.1601(10)	Fe2-N8	2.1590(10)
Fe1-N3	2.1458(10)	Fe2-N9	2.1420(11)
Fe1-N4	2.3926(11)	Fe2-N10	2.3965(11)
Fe1-N5	2.1041(11)	Fe2-N11	2.0966(11)
Fe1-N6	2.1010(11)	Fe2-N12	2.1027(12)
$\overline{\text{Fe1-N}}$	2.20	$\overline{\text{Fe2-N}}$	2.20
cis-Angles / °		*cis*-Angles / °	
N1-Fe1-N2	72.68(4)	N7-Fe2-N8	72.91(4)
N2-Fe1-N3	87.41(4)	N8-Fe2-N9	87.48(4)
N3-Fe1-N4	74.87(4)	N9-Fe2-N10	74.87(4)
N4-Fe1-N1	125.07(4)	N10-Fe2-N7	125.04(4)
N1-Fe1-N5	87.19(4)	N7-Fe2-N11	94.07(4)
N2-Fe1-N5	107.38(4)	N8-Fe2-N11	103.89(4)
N3-Fe1-N5	95.28(4)	N9-Fe2-N11	97.10(4)
N4-Fe1-N5	75.79(4)	N10-Fe2-N11	75.24(4)
N1-Fe1-N6	93.47(4)	N7-Fe2-N12	86.36(4)
N2-Fe1-N6	106.26(4)	N8-Fe2-N12	109.98(5)
N3-Fe1-N6	95.93(4)	N9-Fe2-N12	94.43(4)
N4-Fe1-N6	75.27(4)	N10-Fe2-N12	75.72(5)
trans-Angles / °		*trans*-Angles / °	
N1-Fe1-N3	159.70(4)	N7-Fe2-N9	159.30(4)
N2-Fe1-N4	162.25(4)	N8-Fe2-N10	161.96(4)
N5-Fe1-N6	144.90(4)	N11-Fe2-N12	144.60(5)
Distortion		Distortion	
$\Sigma_O(Fe1N_6)$ / °	150.2	$\Sigma_O(Fe2N_6)$ / °	151.9
CShM(O_h)	6.29	CShM(O_h)	6.40
Torsions / °		Torsions / °	
Fe1-N2-N3-Fe1'	5.08(19)	Fe2-N8-N9-Fe2'	7.2(2)

Table E.7 Selected bond lengths and angles of complexes **C16**·1MeCN, **C16**·1MeOH and **C17**·3MeCN. Labeling of the atoms follows the scheme in Figure E.4. Since Fe1 and Fe1' are symmetry equivalent, the term Fe will be used.

	C16·1MeCN 120 K	**C16**·1MeOH 120 K	**C17**·3MeCN 173 K
Bond / Å			
Fe-N1	2.2268(9)	2.2143(9)	2.2039(13)
Fe-N2	2.2952(9)	2.3191(9)	2.3108(13)
Fe-N3	2.2197(9)	2.1799(10)	2.1698(13)
Fe-N4	2.2042(10)	2.1978(10)	2.1764(13)
Fe-N5	2.1008(10)	2.1251(10)	2.1054(15)
Fe-N6	2.0297(11)	2.0316(10)	2.0616(15)
$\overline{\text{Fe-N}}$	2.18	2.18	2.17
cis-Angles / °			
N1-Fe-N2	76.32(3)	75.95(3)	75.61(5)
N2-Fe-N5	89.89(4)	90.79(4)	90.86(5)
N5-Fe-N6	97.94(4)	95.66(4)	95.41(6)
N6-Fe-N1	96.22(4)	97.67(4)	98.46(6)
N1-Fe-N3	81.39(3)	85.70(3)	84.68(5)
N2-Fe-N3	76.31(3)	74.81(3)	75.47(5)
N5-Fe-N3	90.00(4)	89.49(4)	87.48(5)
N6-Fe-N3	107.22(4)	112.98(4)	109.20(6)
N1-Fe-N4	88.05(3)	81.60(3)	87.71(5)
N2-Fe-N4	73.12(3)	74.36(3)	75.61(5)
N5-Fe-N4	93.36(4)	96.36(4)	93.46(5)
N6-Fe-N4	102.59(4)	97.08(4)	99.50(6)
trans-Angles / °			
N1-Fe-N5	165.10(4)	166.67(4)	165.70(5)
N2-Fe-N6	171.35(4)	169.86(4)	172.31(5)
N3-Fe-N4	149.23(3)	148.67(3)	151.08(5)
Distortion			
$\Sigma_O(FeN_6)$ / °	102.3	108.6	100.3
CShM(O_h)	1.31	1.45	1.26

Table E.8 Selected bond lengths and angles of complexes **C18**·1MeOH, **C19**·2MeCN and **C19**·3MeOH. Labeling of the atoms follows the scheme in Figure E.4. Since Fe1 and Fe1' are symmetry equivalent, the term Fe will be used.

	C18·1MeOH 173 K	**C19**·2MeCN 173 K	**C19**·3MeOH 173 K
Bond / Å			
Fe-N1	2.202(8)	2.1851(14)	2.2082(12)
Fe-N2	2.299(9)	2.3038(13)	2.3028(11)
Fe-N3	2.175(9)	2.2100(14)	2.2149(12)
Fe-N4	2.148(9)	2.2158(13)	2.1996(12)
Fe-N5	2.129(10)	2.0972(15)	2.1143(13)
Fe-N6	2.066(10)	2.0601(15)	2.0487(12)
$\overline{\text{Fe-N}}$	2.17	2.18	2.18
cis-Angles / °			
N1-Fe-N2	77.1(3)	77.21(5)	76.65(4)
N2-Fe-N5	91.3(4)	91.50(5)	90.46(5)
N5-Fe-N6	93.0(4)	96.34(6)	96.67(5)
N6-Fe-N1	98.4(3)	95.09(6)	96.46(5)
N1-Fe-N3	81.7(3)	82.47(5)	86.62(4)
N2-Fe-N3	76.7(4)	73.89(5)	74.13(4)
N5-Fe-N3	93.4(4)	90.77(6)	93.65(5)
N6-Fe-N3	97.9(4)	107.77(6)	101.45(5)
N1-Fe-N4	90.0(3)	86.30(5)	82.38(4)
N2-Fe-N4	75.6(3)	74.16(5)	74.46(4)
N5-Fe-N4	89.4(4)	94.40(5)	90.51(5)
N6-Fe-N4	109.5(4)	103.27(6)	109.21(5)
trans-Angles / °			
N1-Fe-N5	168.1(4)	168.07(6)	166.54(5)
N2-Fe-N6	173.3(3)	171.94(6)	171.88(5)
N3-Fe-N4	152.2(4)	147.73(5)	148.34(4)
Distortion			
$\Sigma_O(FeN_6)$ / °	93.0	105.1	104.2
$CShM(O_h)$	1.17	1.44	1.38

Table E.9 Selected bond lengths and angles of complexes **C20**·2MeCN, **C20**·3MeOH and **C21**·1MeCN. Labeling of the atoms follows the scheme in Figure E.4. Since Fe1 and Fe1' are symmetry equivalent, the term Fe will be used.

	C20·2MeCN 173 K	**C20**·3MeOH 173 K	**C21**·1MeCN 240K
Bond / Å			
Fe-N1	2.177(4)	2.198(2)	2.2055(11)
Fe-N2	2.292(4)	2.2897(19)	2.3125(12)
Fe-N3	2.213(4)	2.196(2)	2.1582(14)
Fe-N4	2.204(4)	2.208(2)	2.1621(15)
Fe-N5	2.092(5)	2.118(2)	2.1385(14)
Fe-N6	2.068(5)	2.063(2)	2.0699(13)
$\overline{\text{Fe-N}}$	2.17	2.18	2.17
cis-Angles / °			
N1-Fe-N2	77.82(15)	77.23(7)	76.29(4)
N2-Fe-N5	92.26(17)	91.01(8)	91.08(5)
N5-Fe-N6	95.0(2)	95.35(9)	93.66(5)
N6-Fe-N1	95.00(18)	96.61(8)	98.86(5)
N1-Fe-N3	87.20(17)	82.84(8)	88.39(5)
N2-Fe-N3	74.49(15)	74.81(7)	75.23(5)
N5-Fe-N3	94.23(18)	90.45(8)	88.80(5)
N6-Fe-N3	103.67(18)	108.19(9)	110.68(5)
N1-Fe-N4	82.89(17)	87.42(8)	83.01(5)
N2-Fe-N4	74.35(15)	74.71(7)	76.43(5)
N5-Fe-N4	90.46(18)	93.21(8)	93.73(6)
N6-Fe-N4	106.78(18)	101.74(8)	97.40(5)
trans-Angles / °			
N1-Fe-N5	169.23(17)	167.63(8)	167.37(5)
N2-Fe-N6	172.60(18)	172.91(8)	172.47(5)
N3-Fe-N4	148.64(16)	149.35(8)	151.59(5)
Distortion			
$\Sigma_O(FeN_6)$ / °	100.7	99.6	97.3
CShM(O_h)	1.41	1.33	1.24

Table E.10 Selected bond lengths and angles of complexes **C21**·1MeCN, **C21**·1.8MeOH and **C23**·4.5MeCN. Labeling of the atoms follows the scheme in Figure E.4. Since Fe1 and Fe1' are symmetry equivalent, the term Fe will be used.

	C21·1MeCN 120K	**C21**·1.8MeOH 173K	**C23**·4.5MeCN 220K
Bond / Å			
Fe-N1	1.9651(12)	1.979(5)	2.1731(10)
Fe-N2	2.0352(13)	2.045(5)	2.2870(10)
Fe-N3	1.9668(13)	1.985(6)	2.1733(10)
Fe-N4	1.9699(14)	1.970(6)	2.1985(10)
Fe-N5	1.9517(13)	1.952(5)	2.1434(12)
Fe-N6	1.9359(13)	1.936(5)	2.0819(11)
$\overline{\text{Fe-N}}$	1.97	1.98	2.18
cis-Angles / °			
N1-Fe-N2	83.05(5)	82.5(2)	77.64(4)
N2-Fe-N5	90.95(5)	91.0(2)	92.12(4)
N5-Fe-N6	89.85(5)	89.7(2)	93.86(5)
N6-Fe-N1	96.18(5)	96.88(19)	96.52(4)
N1-Fe-N3	86.99(5)	86.9(2)	86.42(4)
N2-Fe-N3	83.98(6)	83.2(2)	75.34(4)
N5-Fe-N3	93.44(6)	92.2(2)	88.79(4)
N6-Fe-N3	94.14(5)	95.8(2)	108.50(5)
N1-Fe-N4	90.30(5)	90.3(2)	87.55(4)
N2-Fe-N4	82.83(5)	82.7(2)	75.48(3)
N5-Fe-N4	87.90(5)	89.0(2)	92.13(4)
N6-Fe-N4	99.03(5)	98.3(2)	100.53(4)
trans-Angles / °			
N1-Fe-N5	173.91(5)	173.43(19)	169.50(4)
N2-Fe-N6	178.00(6)	178.8(2)	172.94(4)
N3-Fe-N4	166.76(5)	165.9(2)	150.82(4)
Distortion			
$\Sigma_O(FeN_6)$ / °	49.4	50.5	92.4
$CShM(O_h)$	0.32	0.33	1.28

Table E.11 Selected bond lengths and angles of complexes **C23**·3MeOH. Labeling of the atoms follows the scheme in Figure E.4. Since Fe1 and Fe1' are symmetry equivalent, the term Fe will be used.

	C23·3MeOH 220K	**C23**·3MeOH 120K
Bond / Å		
Fe-N1	2.2049(14)	1.9660(14)
Fe-N2	2.2872(13)	2.0311(14)
Fe-N3	2.1438(16)	1.9653(16)
Fe-N4	2.1570(15)	1.9675(16)
Fe-N5	2.1473(18)	1.9531(15)
Fe-N6	2.0513(15)	1.9349(14)
$\overline{\text{Fe-N}}$	2.17	1.97
cis-Angles / °		
N1-Fe-N2	76.51(5)	82.76(6)
N2-Fe-N5	91.83(6)	91.51(6)
N5-Fe-N6	93.31(6)	89.53(6)
N6-Fe-N1	98.17(6)	96.20(6)
N1-Fe-N3	88.30(5)	87.55(6)
N2-Fe-N3	76.29(6)	83.88(7)
N5-Fe-N3	89.91(6)	91.96(6)
N6-Fe-N3	109.93(6)	94.63(6)
N1-Fe-N4	83.00(5)	90.06(6)
N2-Fe-N4	76.58(6)	82.97(7)
N5-Fe-N4	93.43(6)	89.13(6)
N6-Fe-N4	96.87(6)	98.50(6)
trans-Angles / °		
N1-Fe-N5	168.30(5)	174.27(6)
N2-Fe-N6	171.92(6)	178.21(7)
N3-Fe-N4	152.75(5)	166.83(6)
Distortion		
$\Sigma_O(FeN_6)$ / °	93.0	47.0
CShM(O_h)	1.14	0.30

Table E.12 Selected bond lengths and angles of complexes **C22** and **C26**. Labeling of the atoms follows the scheme in Figure E.5 for **C22** and Figure E.6 for **C26**.

	C22 173 K		**C26** 120 K
Bond / Å		Bond / Å	
Ni1-N3	2.1988(14)	Co1-O1	2.1690(9)
Ni1-N4	2.1080(14)	Co1-N1	2.2514(10)
Ni1-N5	2.0585(14)	Co1-N2	2.1405(10)
Ni1-N8	2.2594(13)	Co1-N3	2.1193(10)
Ni1-N9	2.1237(14)	Co1-N4	2.1017(10)
Ni1-N10	2.0792(14)	Co1-N5	2.0120(11)
$\overline{\text{Ni1-N}}$	2.14	$\overline{\text{Co1-N}}$	2.13
cis-Angles / °		*cis*-Angles / °	
N3-Ni1-N4	77.38(5)	N1-Co1-N2	78.22(3)
N3-Ni1-N8	105.62(5)	N2-Co1-N3	90.51(4)
N8-Ni1-N9	77.84(5)	N3-Co1-N4	94.32(4)
N9-Ni1-N4	99.07(5)	N4-Co1-N1	96.93(4)
N3-Ni1-N5	81.31(5)	N1-Co1-N5	82.56(4)
N8-Ni1-N5	92.37(5)	N2-Co1-N5	76.18(4)
N9-Ni1-N5	101.48(5)	N3-Co1-N5	95.06(4)
N4-Ni1-N5	89.80(5)	N4-Co1-N5	99.09(4)
N3-Ni1-N10	94.92(5)	N1-Co1-O1	86.45(4)
N8-Ni1-N10	81.64(5)	N2-Co1-O1	76.67(4)
N9-Ni1-N10	82.74(6)	N3-Co1-O1	90.78(4)
N4-Ni1-N10	96.46(5)	N4-Co1-O1	107.50(4)
trans-Angles / °		*trans*-Angles / °	
N3-Ni1-N9	175.55(5)	N1-Co1-N3	168.73(4)
N4-Ni1-N8	176.53(5)	N2-Co1-N4	173.54(4)
N5-Ni1-N10	171.84(5)	N5-Co1-O1	152.26(4)
Distortion		Distortion	
$\Sigma_O(Ni1N_6)$ / °	99.21	$\Sigma_O(Co1N_5O_1)$ / °	94.1
CShM(O_h)	1.47	CShM(O_h)	1.04

Table E.13 Selected bond lengths and angles of complexes **C27** and **C28**. Labeling of the atoms follows the scheme in Figure E.7 for **C27** and Figure E.8 for **C28**.

	C27 173 K		**C28**
Bond / Å		Bond / Å	
Co1-N1	2.2098(10)	Co1-N1	2.0657(18)
Co1-N2	2.2739(11)	Co1-N2	1.964(2)
Co1-N3	2.0978(12)	Co1-N3	2.0400(19)
Co1-N4	2.0393(12)	Co1-N4	2.005(2)
Co1-N5	2.0623(12)	Co1-N5	2.2556(17)
Co1-N6	2.1464(12)		
$\overline{\text{Co1-N}}$	2.14	$\overline{\text{Co1-N}}$	2.07
cis-Angles / °		*cis*-Angles / °	
N1-Co1-N2	78.18(4)	N1-Co1-N2	125.81(8)
N2-Co1-N5	96.66(5)	N2- Co1-N3	107.32(8)
N5-Co1-N6	99.26(5)	N3-Co1-N1	119.26(7)
N6-Co1-N1	88.68(4)	N1-Co1-N4	94.91(8)
N1-Co1-N3	75.07(4)	N2-Co1-N4	101.89(9)
N2-Co1-N3	98.97(5)	N3-Co1-N4	101.35(8)
N5-Co1-N3	93.92(5)	N1-Co1-N5	76.67(7)
N6-Co1-N3	92.20(5)	N2-Co1-N5	88.52(8)
N1-Co1-N4	97.90(4)	N3-Co1-N5	77.61(7)
N2-Co1-N4	80.48(4)		
N5-Co1-N4	93.20(5)		
N6-Co1-N4	86.36(4)		
trans-Angles / °		*trans*-Angles / °	
N1-Fe-N5	166.75(4)	N4-Co1-N5	169.27(8)
N2-Fe-N6	159.85(5)		
N3-Fe-N4	172.87(4)		
Distortion		Distortion	
$\Sigma_O(Co1N_6)$ / °	83.34	$\tau(Co1N_5)$	0.7
CShM(O_h)	1.41	CShM(D_{3h})[a]	1.24

F Additional Figures and Tables

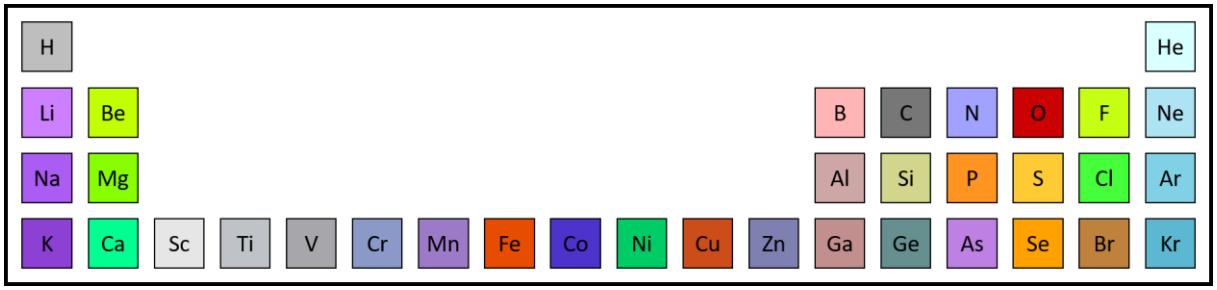


Figure F.1 Colour code for crystallographic figures used in this work, if not stated differently.

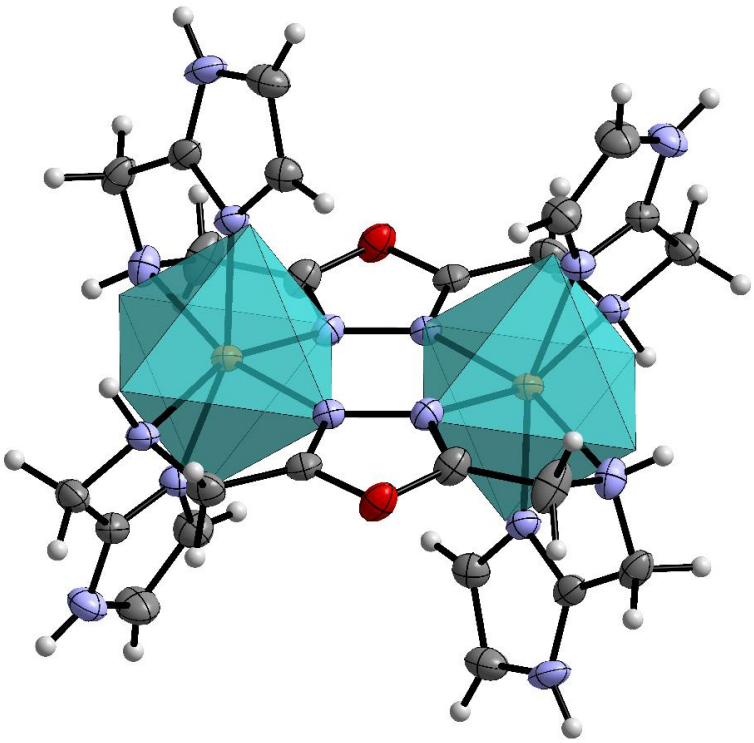


Figure F.2 Molecular structure of **C1** and its calculated ideal coordination octahedron (SHAPE). ORTEP representation with atomic displacement parameters set to 50 % probability.

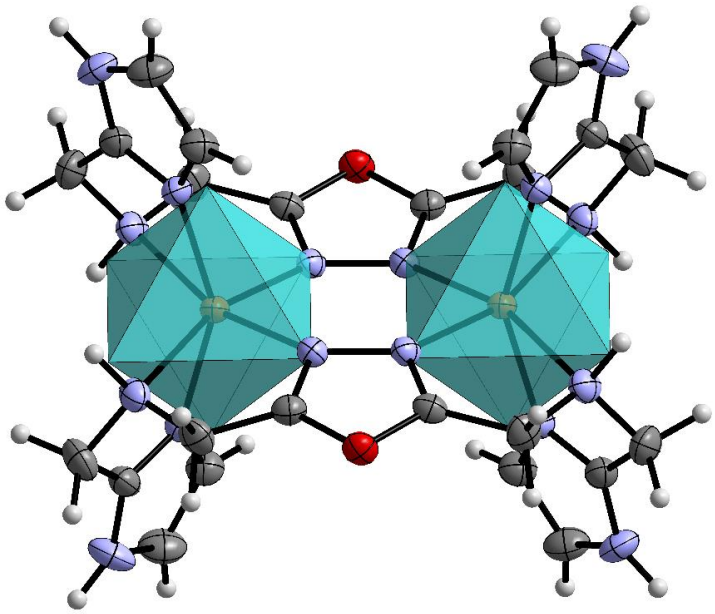


Figure F.3 Molecular structure of **C2** and its calculated ideal coordination octahedron (SHAPE). ORTEP representation with atomic displacement parameters set to 50 % probability.

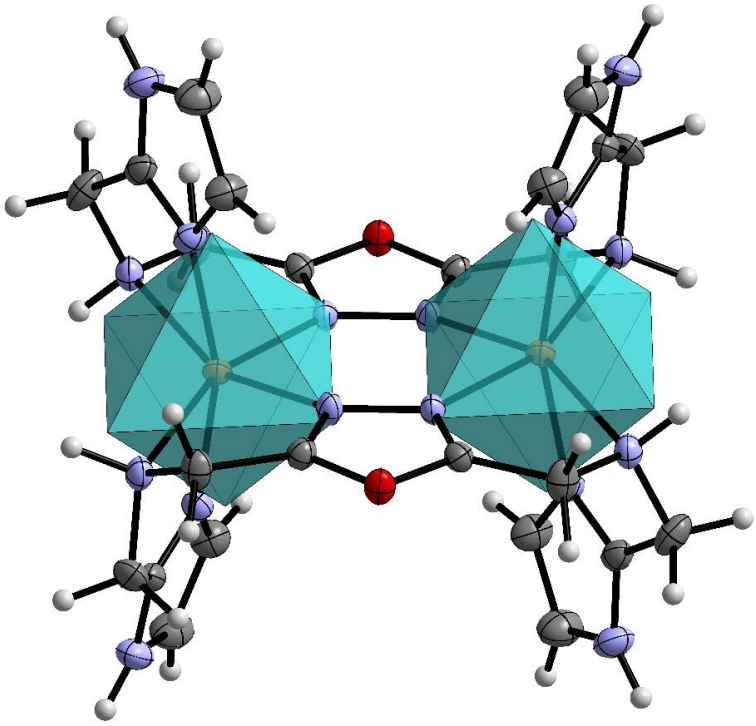


Figure F.4 Molecular structure of **C3** and its calculated ideal coordination octahedron (SHAPE). ORTEP representation with atomic displacement parameters set to 50 % probability.

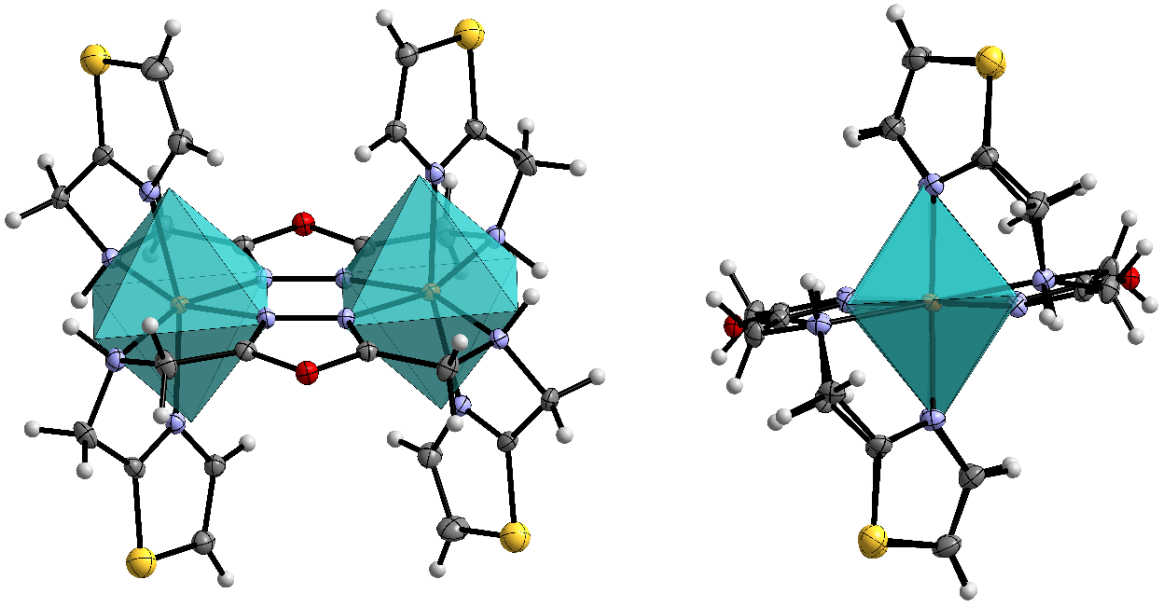


Figure F.5 Molecular structure of **C4** and its ideal coordination octahedron with front view (left) and view along the Fe-Fe axis (right), calculated with SHAPE.[62] Colour scheme: dark grey – C, grey – H, violet – N, red – O, yellow – S, orange – Fe. ORTEP representation with atomic displacement parameters set to 50 % probability.

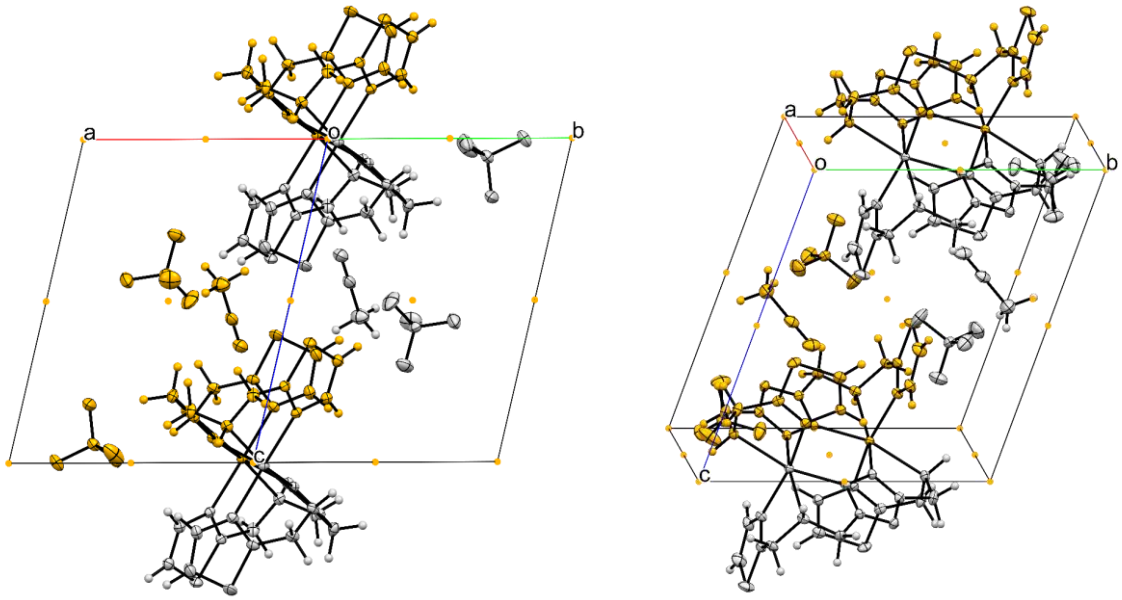


Figure F.6 Unit cell of **C4** with view along the bisector of γ (left) and perspective (right). The colour scheme is set according to symmetry equivalent moieties. Yellow dots represent a center of inversion. ORTEP representation with atomic displacement parameters set to 50 % probability.

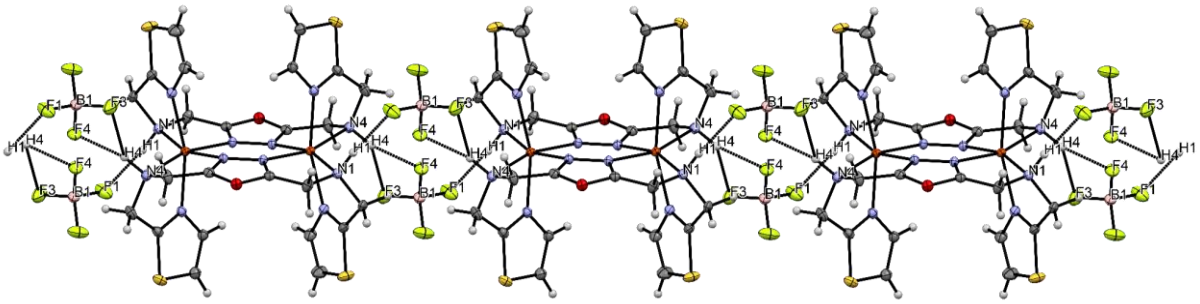


Figure F.7 One-dimensional network of complex cations via hydrogen bonds (dashed black lines) in **C4**. Acetonitrile molecules and irrelevant tetrafluoroborate anions are omitted for clarity. ORTEP representation with atomic displacement parameters set to 50 %[382] probability.

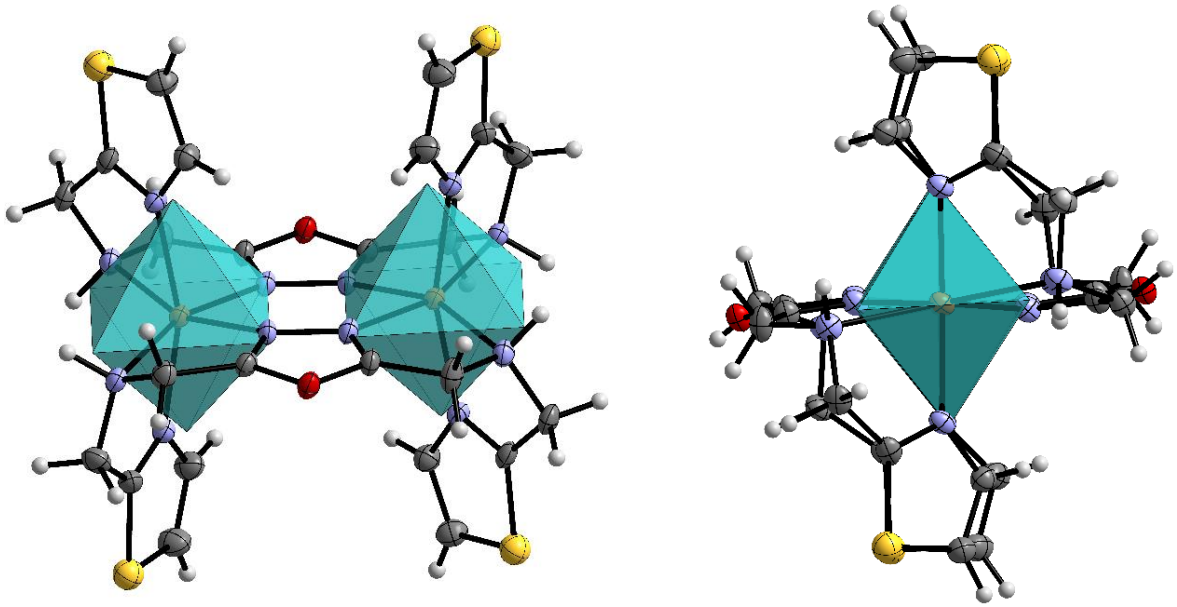


Figure F.8 Molecular structure of **C6** and its ideal coordination octahedron with front view (left) and view along the Fe-Fe axis (right), calculated with SHAPE.[62] Colour scheme: dark grey – C, grey – H, violet – N, red – O, yellow – S, orange – Fe. ORTEP representation with atomic displacement parameters set to 50 % probability.

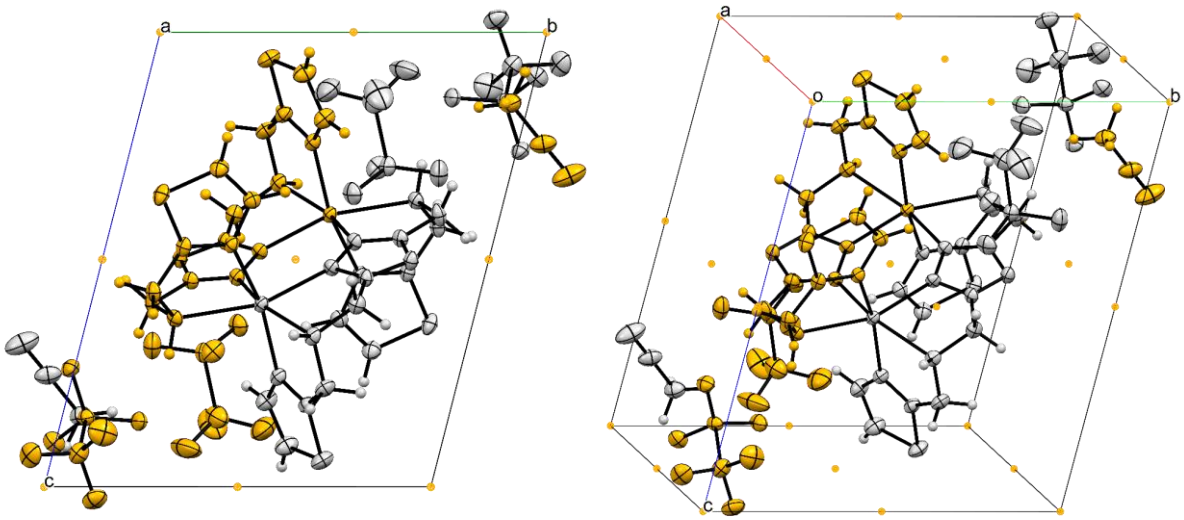


Figure F.9 Unit cell of **C6** with view along the a-axis (left) and perspective (right). The colour scheme is set according to symmetry equivalent moieties. Yellow dots represent a center of inversion. ORTEP representation with atomic displacement parameters set to 50 % probability.

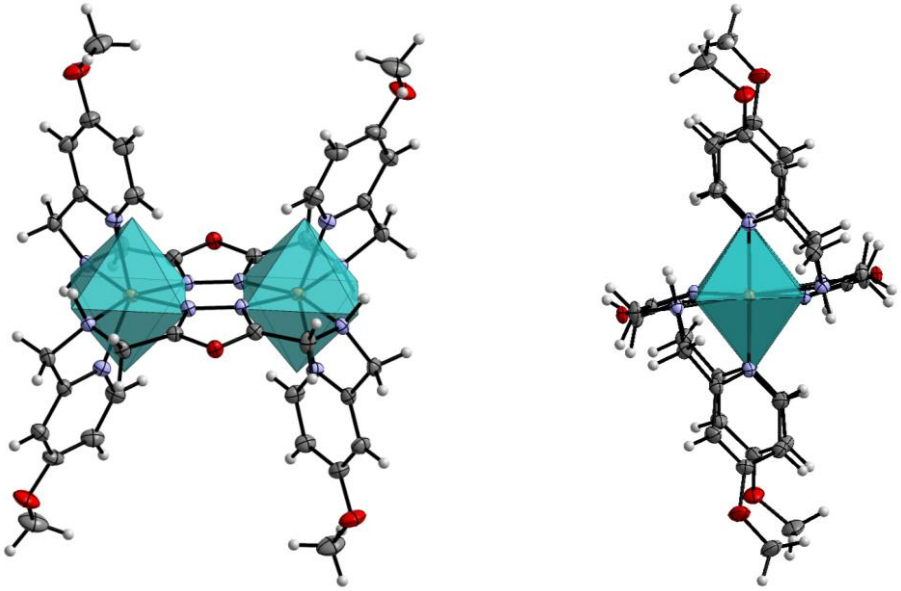


Figure F.10 Molecular structure of **C7** and its ideal coordination octahedron with front view (left) and view along the Fe-Fe axis (right), calculated with SHAPE.[62] Colour scheme: dark grey – C, grey – H, violet – N, red – O, orange – Fe. ORTEP representation with atomic displacement parameters set to 50 % probability.

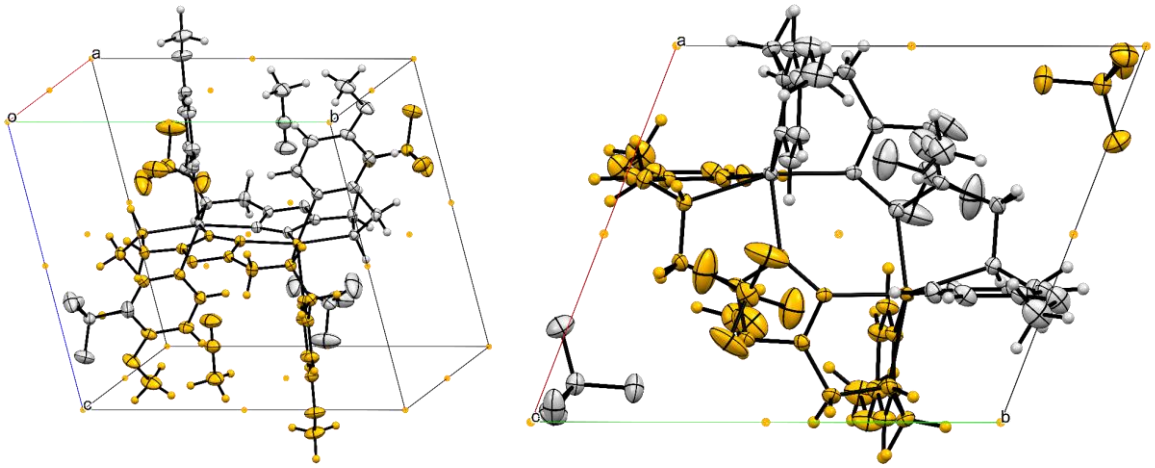


Figure F.11 Unit cell of **C7** perspective (left) and with view along the c-axis (right). The colour scheme is set according to symmetry equivalent moieties. Yellow dots represent a center of inversion. ORTEP representation with atomic displacement parameters set to 50 % probability.

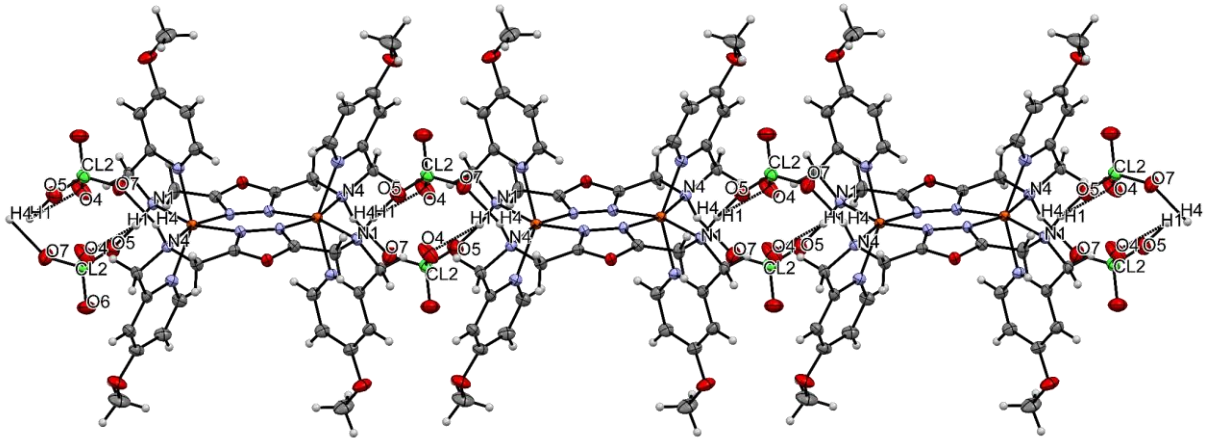


Figure F.12 One-dimensional network of complex cations via hydrogen bonds (dashed black lines) in **C7**. Acetonitrile molecules and irrelevant perchlorate anions are omitted for clarity. ORTEP representation with atomic displacement parameters set to 50 % probability.

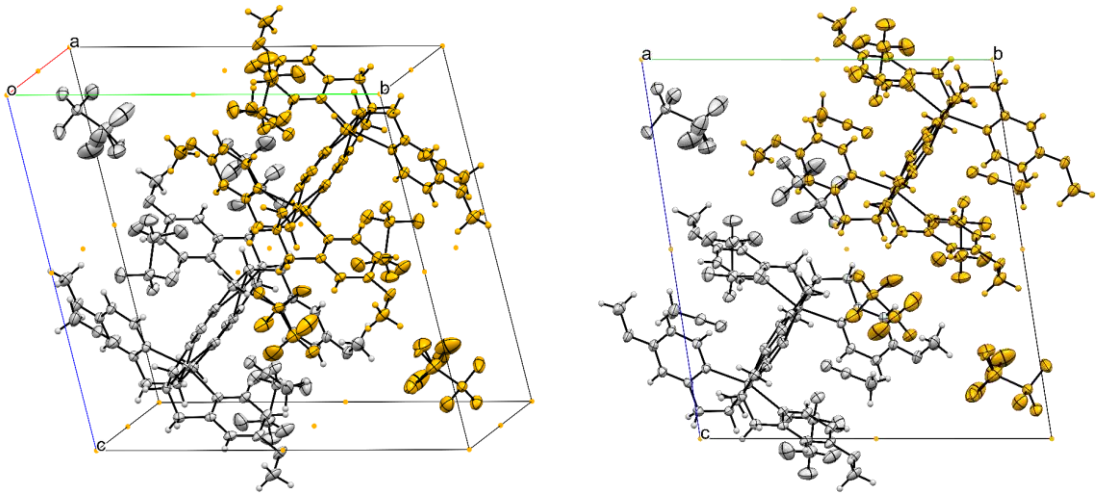


Figure F.13 Unit cell of **C8** perspective (left) and with view along the a-axis (right). The colour scheme is set according to symmetry equivalent moieties. Yellow dots represent a center of inversion. ORTEP representation with atomic displacement parameters set to 50 % probability.

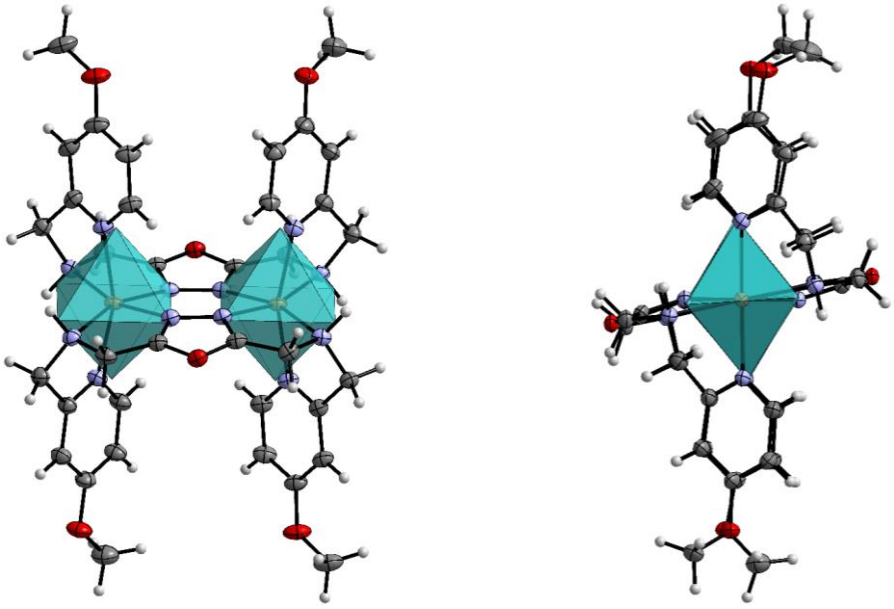


Figure F.14 Molecular structure of **C8** and its ideal coordination octahedron with front view (left) and view along the Fe-Fe axis (right), calculated with SHAPE.[62] Colour scheme: dark grey – C, grey – H, violet – N, red – O, orange – Fe. ORTEP representation with atomic displacement parameters set to 50 % probability.

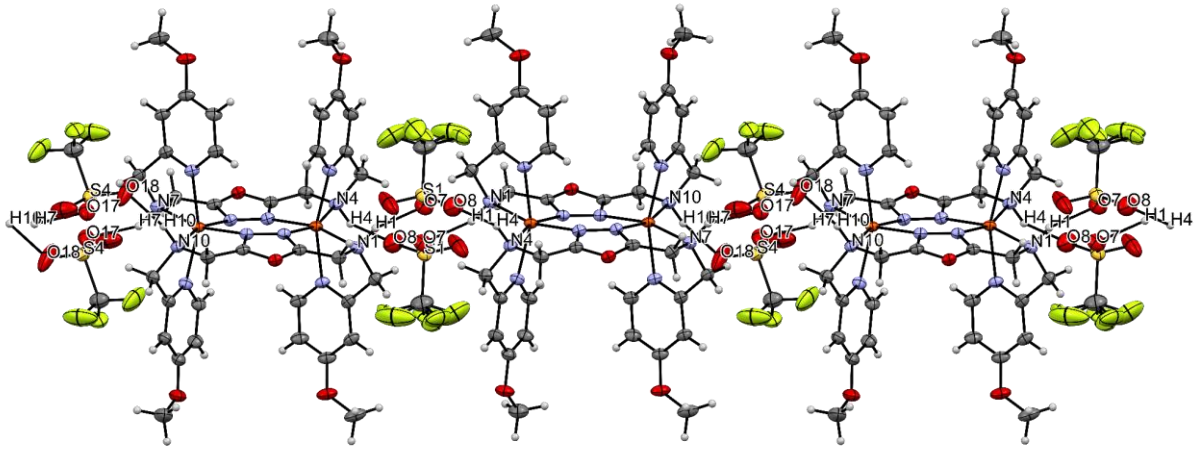


Figure F.15 One-dimensional network of complex cations via hydrogen bonds (dashed black lines) in **C8**. Acetonitrile molecules and irrelevant triflate anions are omitted for clarity. ORTEP representation with atomic displacement parameters set to 50 % probability.

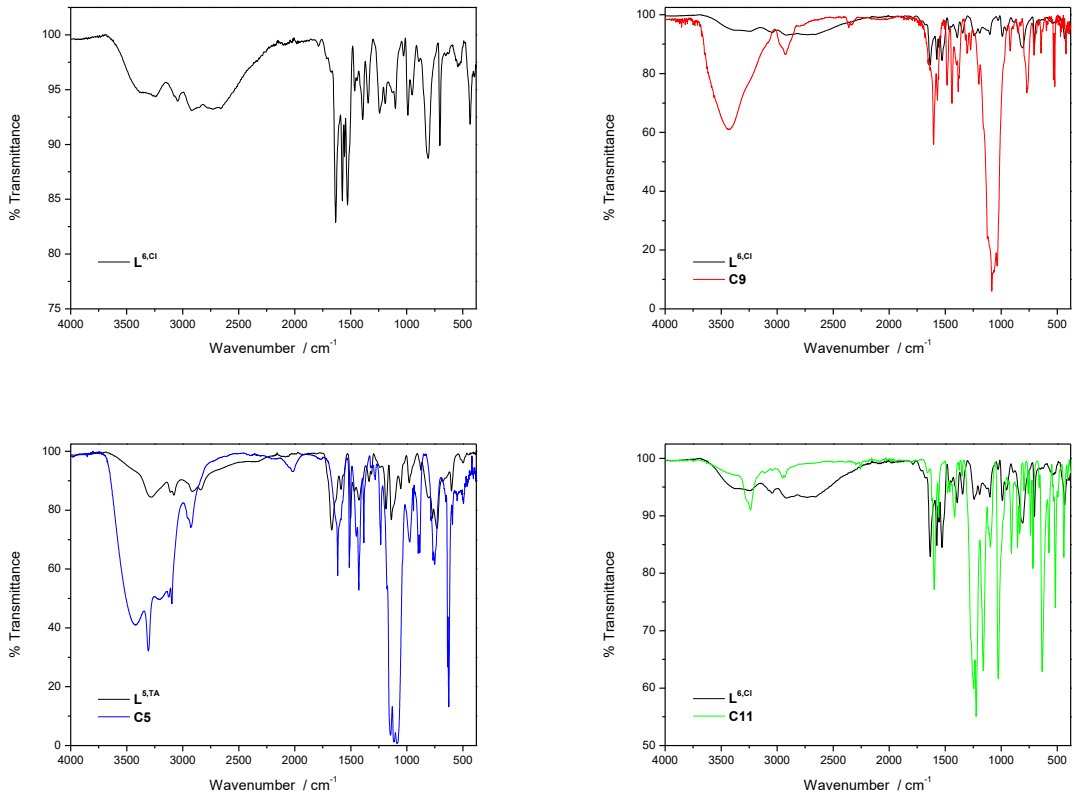


Figure F.16 Comparison of IR spectra of $\mathbf{L^{6,Cl}}$ (black line, top left) with **C9** (red line, top right), **C10** (blue line, bottom left) and **C11** (green line, bottom left). All complex spectra were overlayed on the ligand IR spectra (black line). Difference in transmittance is mainly due to the use of different IR spectrometers.

Table F.1 Relevant IR vibration bands of $L^{6,Cl}$ and complexes C9 - C11.

Compound	Relevant infrared bands / cm^{-1}
$\mathbf{L^{6,Cl}}$	3277 (ν_s(N-H))
$[Fe_2(\mu_2\text{-}\mathbf{L^{6,Cl}})_2](BF_4)_4$ (**C9**)	3233 (ν_s(N-H)), 1083 ($\nu_{as}(BF_4)$), 1063 ($\nu_{as}(BF_4)$), 1036 ($\nu_{as}(BF_4)$), 762 ($\nu_s(BF_4)$), 533 ($\delta(BF_4)$), 521 ($\delta(BF_4)$)
$[Fe_2(\mu_2\text{-}\mathbf{L^{6,Cl}})_2](ClO_4)_4$ (**C10**)	3305 (ν_s(N-H)), 1144 ($\nu_{as}(ClO_4)$), 1134 ($\nu_{as}(ClO_4)$), 1121 ($\nu_{as}(ClO_4)$), 1115 ($\nu_{as}(ClO_4)$), 1109 ($\nu_{as}(ClO_4)$), 1088 ($\nu_{as}(ClO_4)$), 625 ($\delta_{as}(ClO_4)$)
$[Fe_2(\mu_2\text{-}\mathbf{L^{6,Cl}})_2](CF_3SO_3)_4 \cdot 2CH_3CN$ (**C11**)	3236 (ν_s(N-H)), 1271 ($\nu_{as}(SO_3)$), 1246 ($\nu_s(CF_3)$), 1223 ($\nu_{as}(CF_3)$), 1026 ($\nu_s(SO_3)$), 634 ($\delta_s(SO_3)$), 574 ($\delta_{as}(CF_3)$), 517 ($\delta_{as}(SO_3)$)

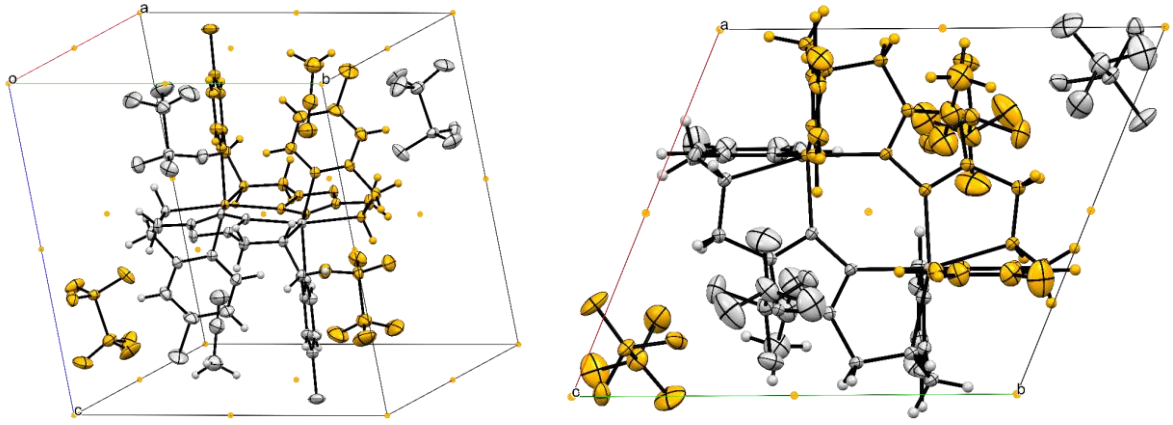


Figure F.17 Unit cell of **C11** perspective (left) and with view along the c-axis (right). The colour scheme is set according to symmetry equivalent moieties. Yellow dots represent a center of inversion. ORTEP representation with atomic displacement parameters set to 50 % probability.

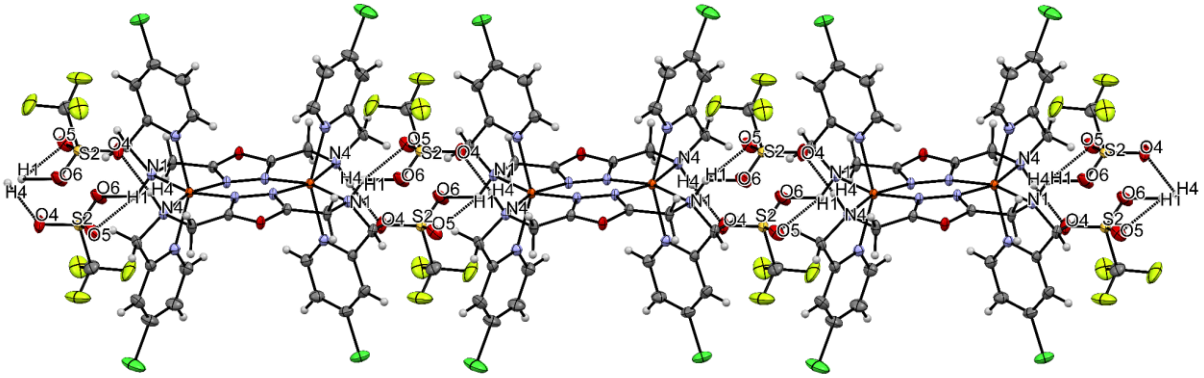


Figure F.18 One-dimensional network of complex cations via hydrogen bonds (dashed black lines) in **C11**. Acetonitrile molecules and irrelevant triflate anions are omitted for clarity. ORTEP representation with atomic displacement parameters set to 50 % probability.

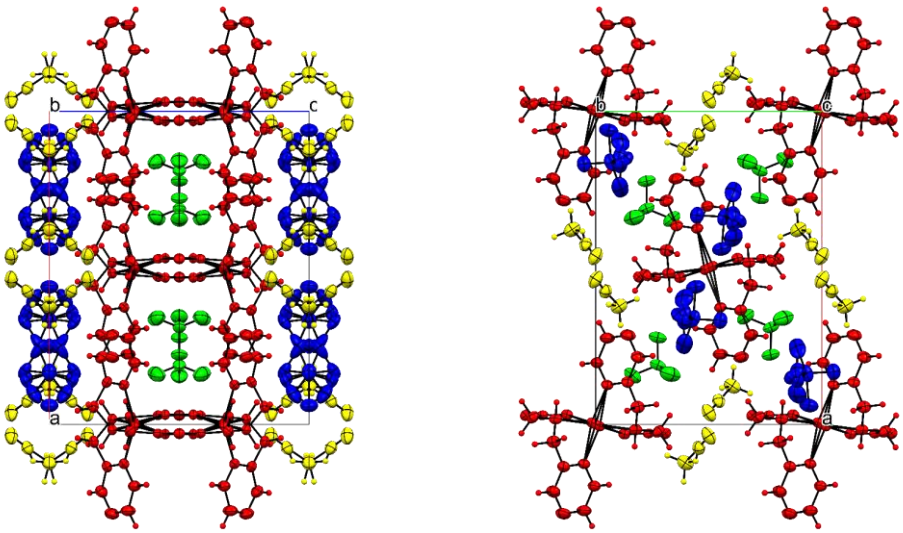


Figure F.19 Unit cell of **C12** with view along the b-axis (left) and view along the c-axis (right). The colour scheme is set according to symmetry equivalent molecules. ORTEP representation with atomic displacement parameters set to 50 % probability.

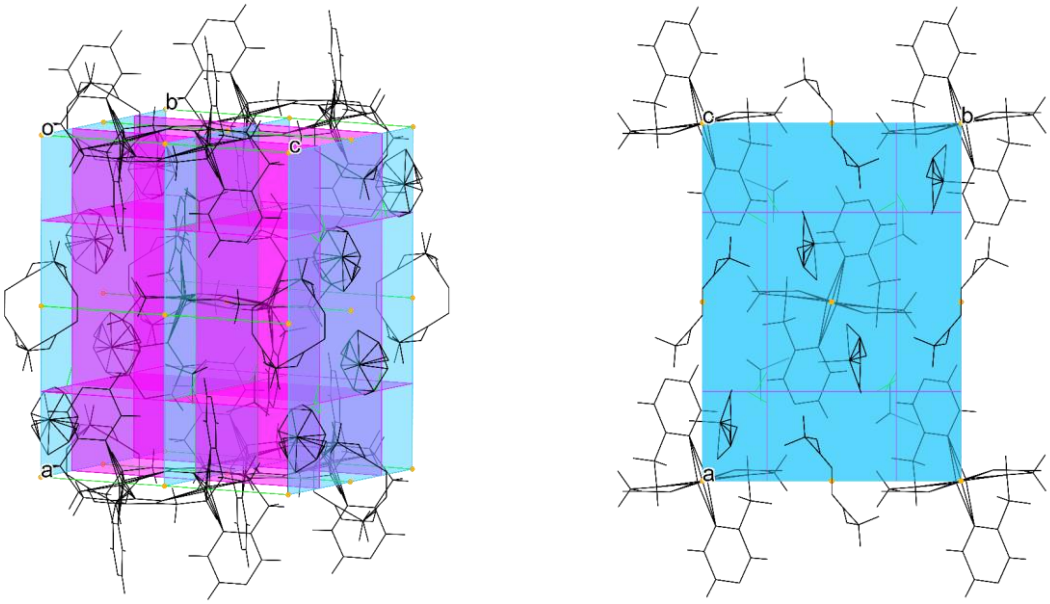


Figure F.20 Illustration of the present symmetry elements in **C12**. Molecules are displayed in the wireframe model for better vision. Left: Perspective view onto the Unit Cell. Right: View along the c-axis of the Unit Cell. Center of Inversion – yellow dots, Two-fold Axis – green lines, Mirror Planes – blue planes, Glide Planes – purple planes.

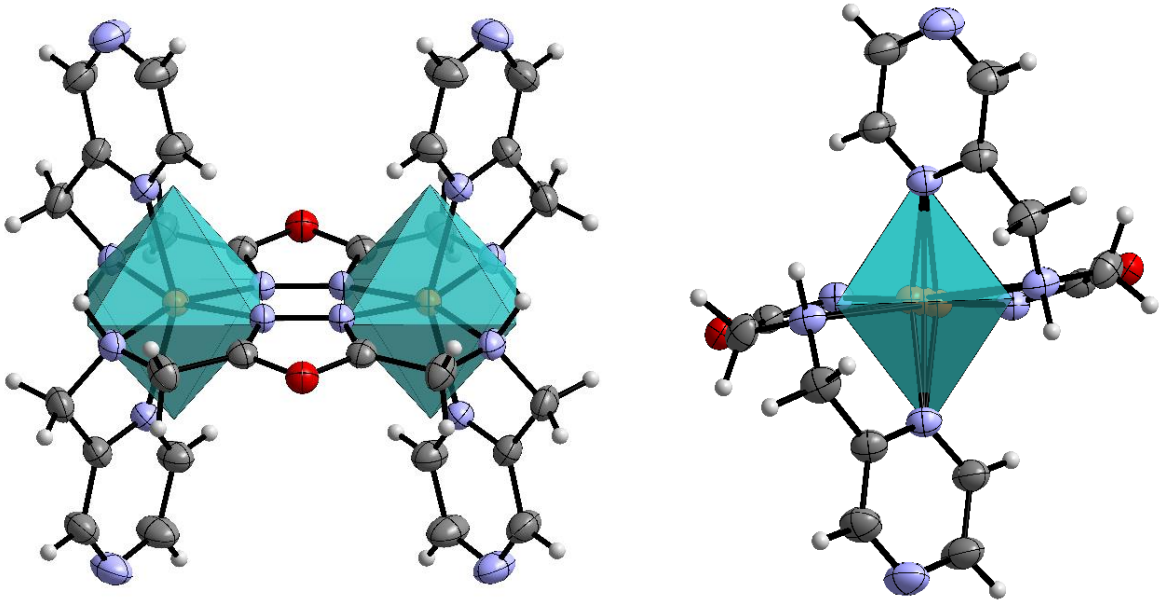


Figure F.21 Molecular structure of **C12** and its ideal coordination octahedron with front view (left) and view along the Fe-Fe axis (right), calculated with SHAPE.[62] Colour scheme: dark grey – C, grey – H, violet – N, red – O, orange – Fe. ORTEP representation with atomic displacement parameters set to 50 % probability.

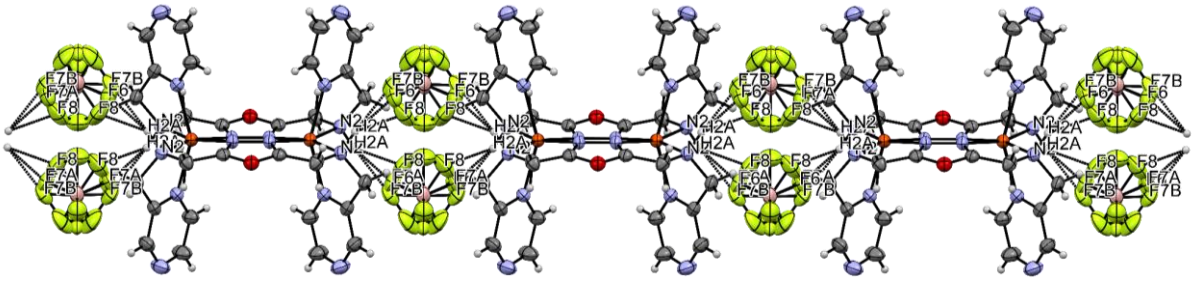


Figure F.22 One-dimensional network of complex cations via hydrogen bonds (dashed black lines) in **C12**. Acetonitrile molecules and irrelevant tetrafluoroborate anions are omitted for clarity. ORTEP representation with atomic displacement parameters set to 50 % probability.

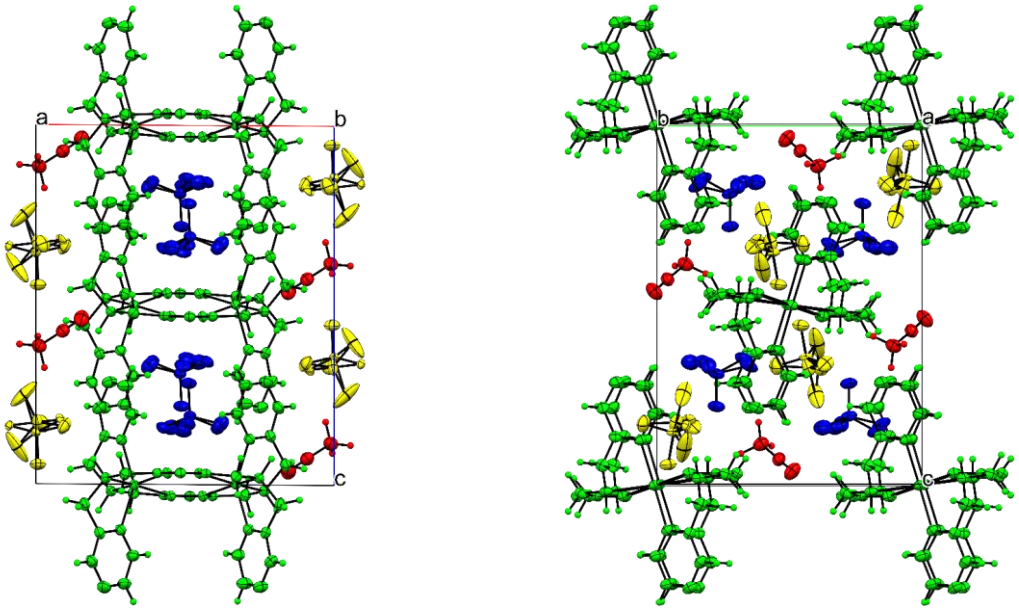


Figure F.23 Unit cell of **C13** with view along the b-axis (left) and view along the a-axis (right). The colour scheme is set according to symmetry equivalent molecules. ORTEP representation with atomic displacement parameters set to 50 % probability.

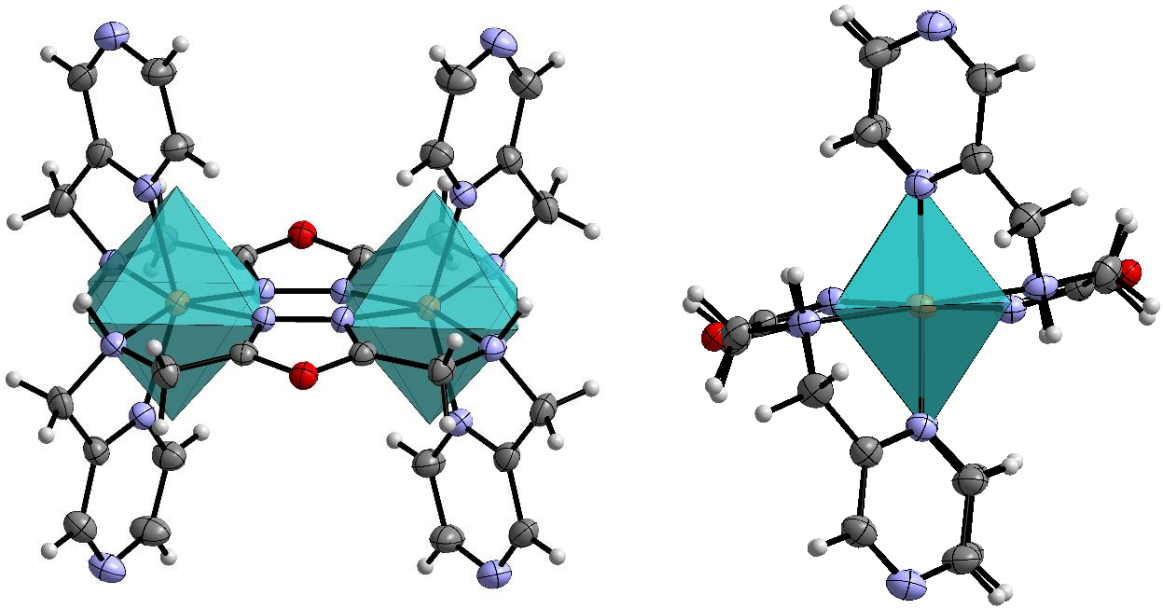


Figure F.24 Molecular structure of **C13** and its ideal coordination octahedron with front view (left) and view along the Fe-Fe axis (right), calculated with SHAPE.[62] Colour scheme: dark grey – C, grey – H, violet – N, red – O, orange – Fe. ORTEP representation with atomic displacement parameters set to 50 % probability.

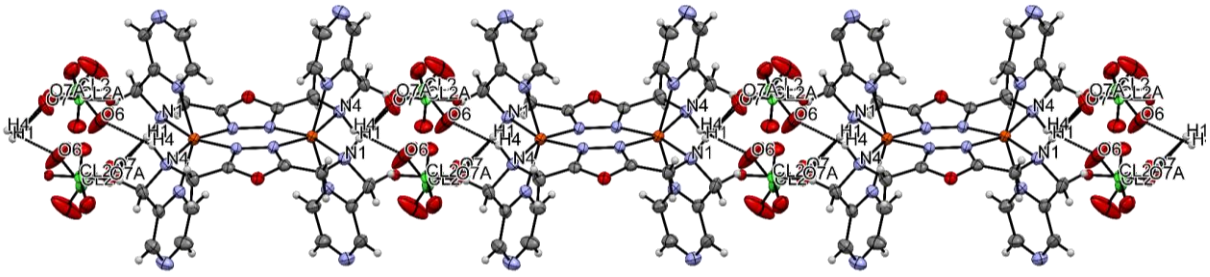


Figure F.25 One-dimensional network of complex cations via hydrogen bonds (dashed black lines) in **C13**. Acetonitrile molecules and irrelevant perchlorate anions are omitted for clarity. ORTEP representation with atomic displacement parameters set to 50 % probability.

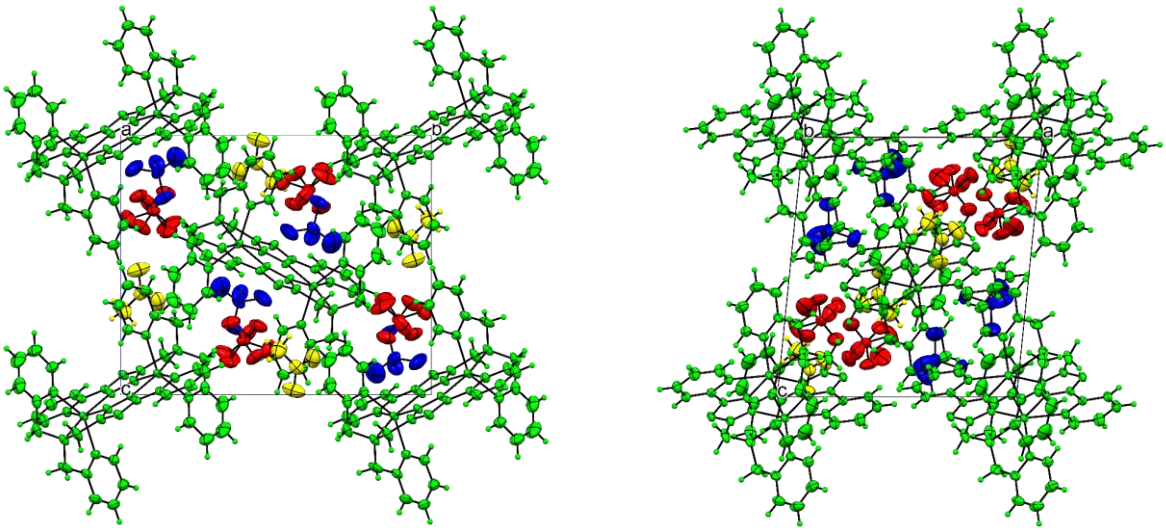


Figure F.26 Unit cell of **C14** with view along the a-axis (left) and view along the b-axis (right). The colour scheme is set according to symmetry equivalent molecules. ORTEP representation with atomic displacement parameters set to 50 % probability.

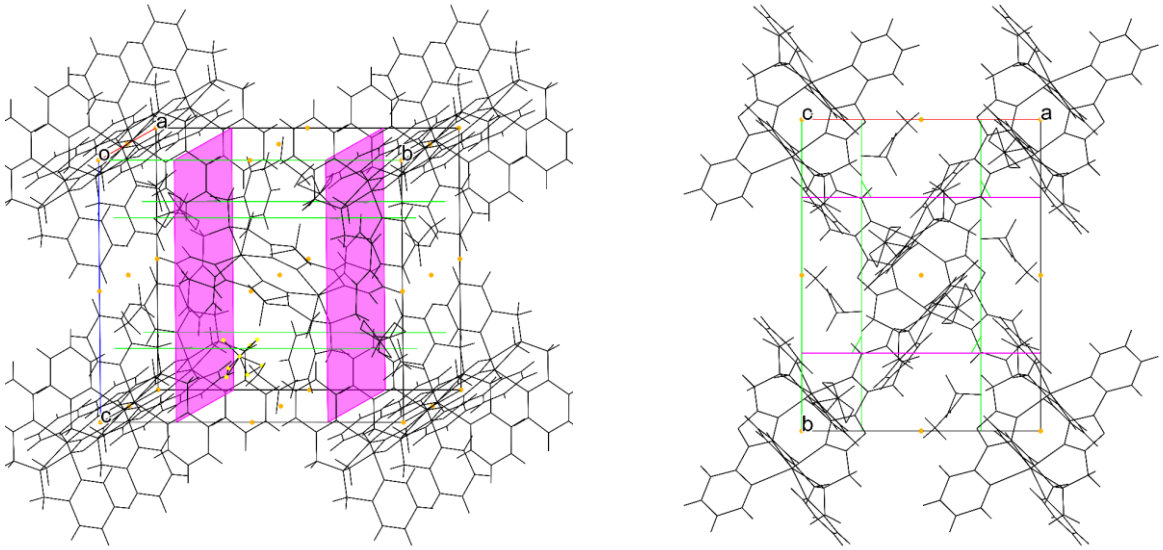


Figure F.27 Illustration of the present symmetry elements in **C14**. Molecules are displayed in the wireframe model for better vision. Left: Perspective view onto the Unit Cell. Right: View along the c-axis of the Unit Cell. Center of Inversion – yellow dots, Two-fold Axis – green lines, Mirror Glide Planes – purple planes.

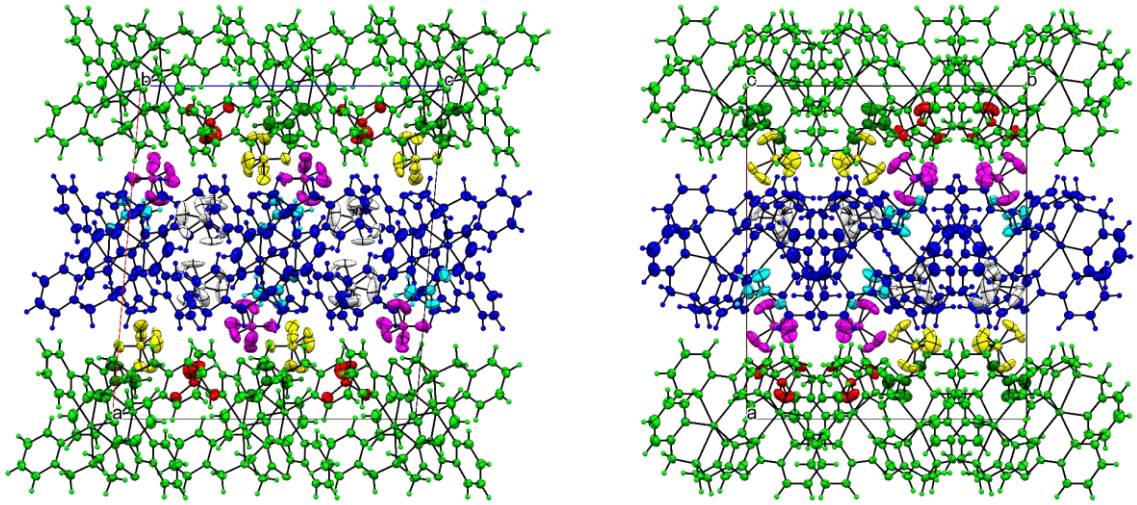


Figure F.28 Unit cell of **C14'** with view along the b-axis (left) and view along the c-axis (right). The colour scheme is set according to symmetry equivalent molecules. ORTEP representation with atomic displacement parameters set to 50 % probability.

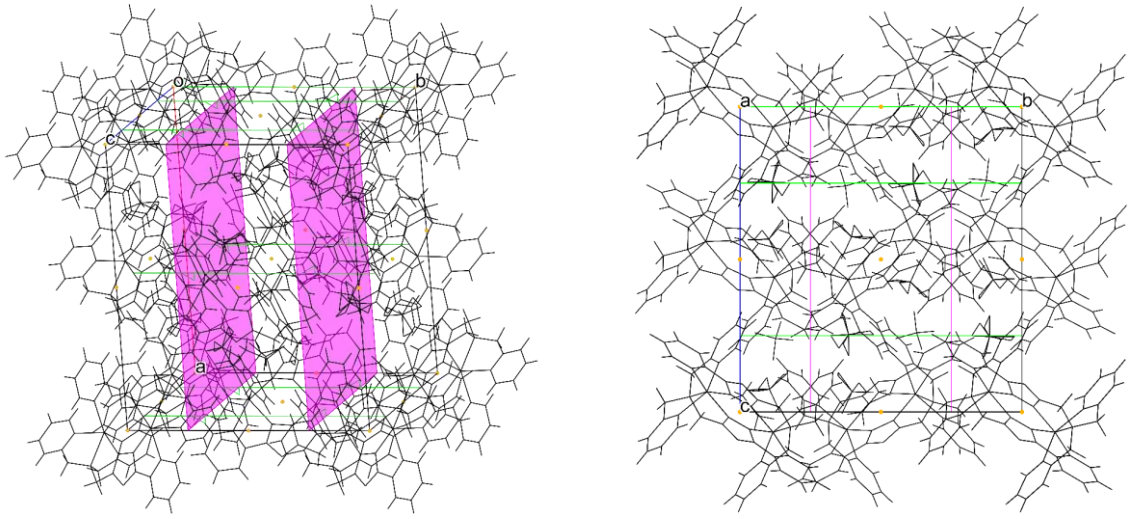


Figure F.29 Illustration of the present symmetry elements in **C14'**. Molecules are displayed in the wireframe model for better vision. Left: Perspective view onto the Unit Cell. Right: View along the c-axis of the Unit Cell. Center of Inversion – yellow dots, Two-fold Axis – green lines, Mirror Glide Planes – purple planes.

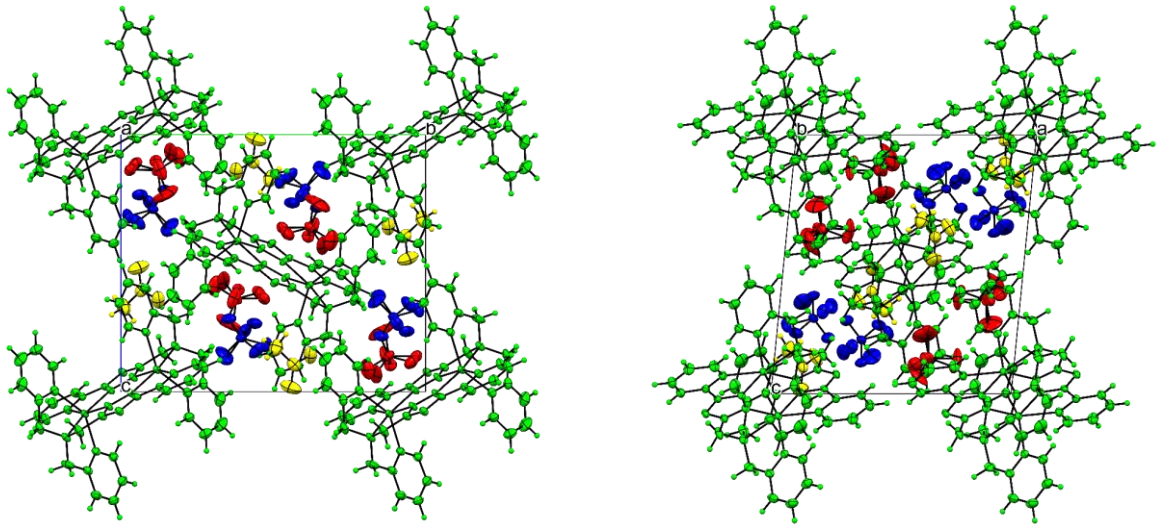


Figure F.30 Unit cell of **C15** with view along the a-axis (left) and view along the b-axis (right). The colour scheme is set according to symmetry equivalent molecules. ORTEP representation with atomic displacement parameters set to 50 % probability.

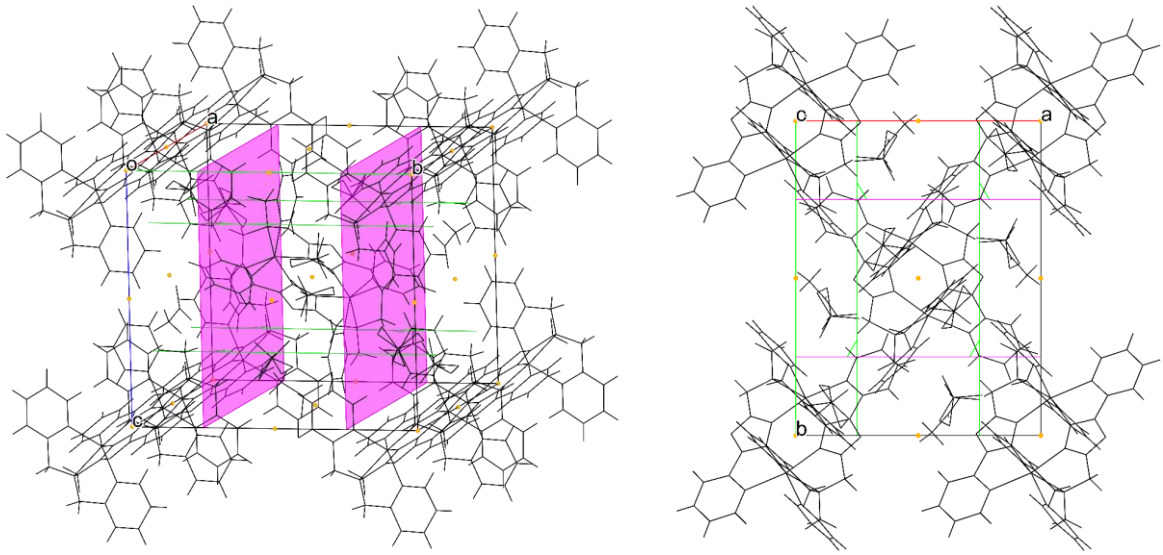


Figure F.31 Illustration of the present symmetry elements in **C15**. Molecules are displayed in the wireframe model for better vision. Left: Perspective view onto the Unit Cell. Right: View along the c-axis of the Unit Cell. Centers of Inversion – yellow dots, Two-fold Axis – green lines, Mirror Glide Planes – purple planes.

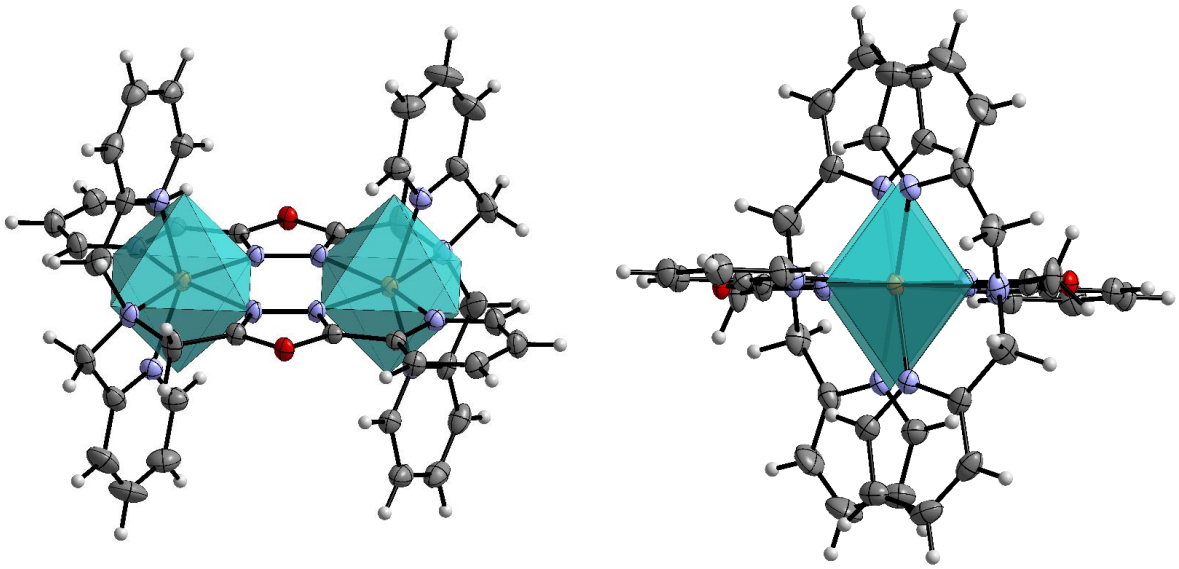


Figure F.32 Molecular structure of **C15** and its ideal coordination octahedron with front view (left) and view along the Fe-Fe axis (right), calculated with SHAPE.[62] Colour scheme: dark grey – C, grey – H, violet – N, red – O, orange – Fe. ORTEP representation with atomic displacement parameters set to 50 % probability.

Table F. 2 Categorization of non-classical Donor-H···π hydrogen bonds in Type I – V after *Malone et al.*[290] Parameters are defined in Figure 3.49.

Type	d_{QH} / Å	α / °	β / °	*offset r* / *Å*
I	≤ 3.05	≥ 53	150 – 180	≤ 0.5
II	≤ 3.05	≥ 53	150 – 180	0.5 < *r* < 1.4
III	≤ 3.05	≥ 53	< 150	≤ 1.4
IV	≤ 3.05	40 – 60	130 – 150	1.4 ≤ *r* ≤ 1.5
V	≤ 4.00	≤ 90	90 – 180	> 1.4
VI	≤ 4.00	≤ 90	< 90	> 1.4

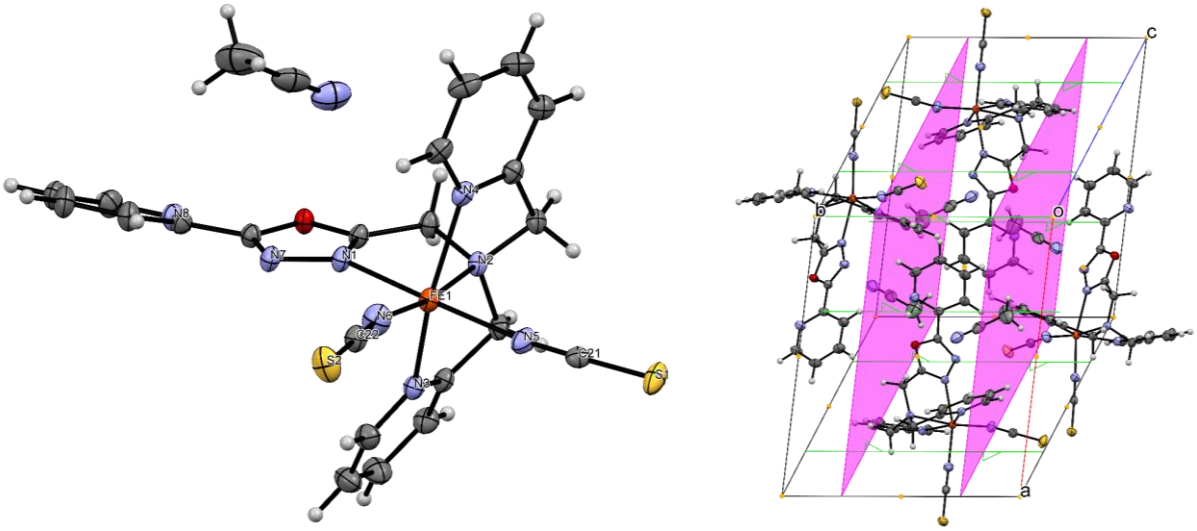


Figure F.33 Left: Asymmetric Unit of **C16**·1MeCN. Right: Perspective view onto the unit cell of **C16**·1MeCN with present symmetry elements. Centers of Inversion – yellow dots, Two-fold Axis – green lines, Mirror Glide Plane – purple planes. ORTEP representation with atomic displacement parameters set to 50 % probability

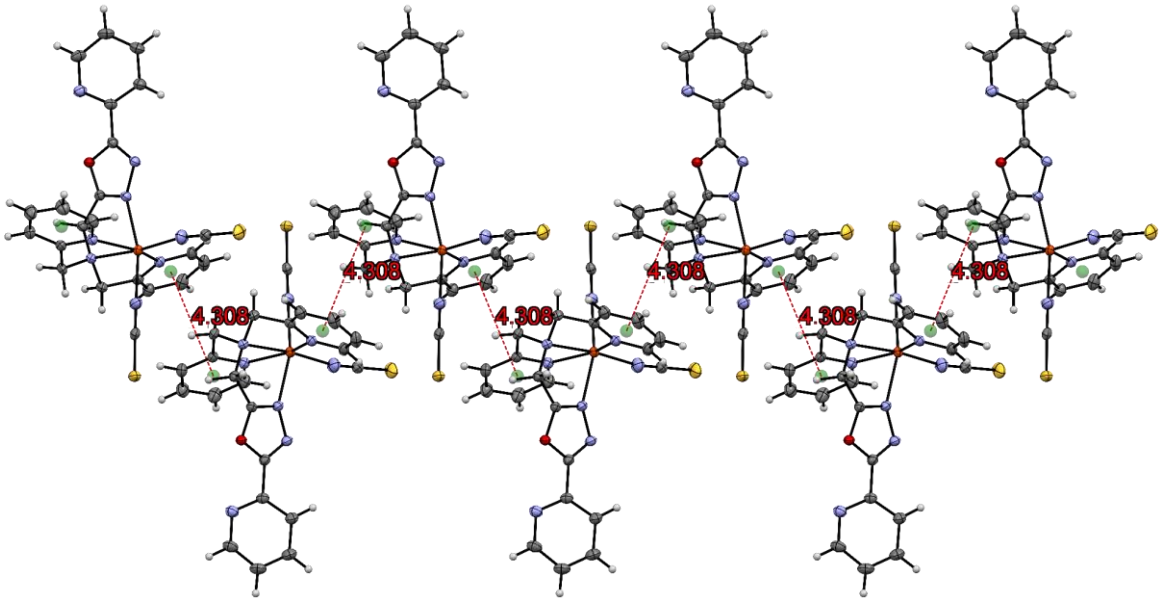


Figure F.34 One dimensional chain formed by π-π interactions in **C16**·1MeCN. Colour scheme was set according to symmetry equivalent molecules. Green points – centers of aromatic rings involved in π-π interactions. Red dashed lines – center-to-center distance. Distances between the centers of two interacting aromatic rings are displayed in red. ORTEP representation with atomic displacement parameters set to 50 % probability.

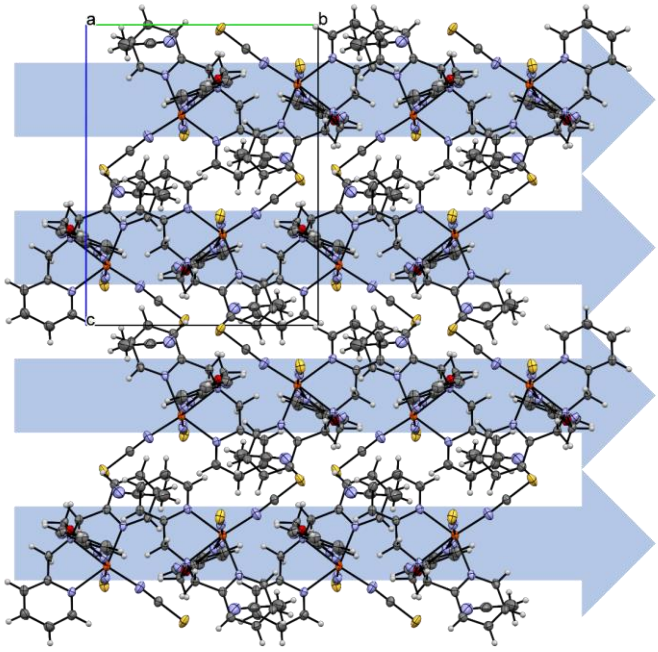


Figure F.35 One dimensional chain formed by π-π interactions in the packing of **C16**·1MeCN with view along the a-axis. Blue arrows indicate the chains along the b-axis. ORTEP representation with atomic displacement parameters set to 50 % probability.

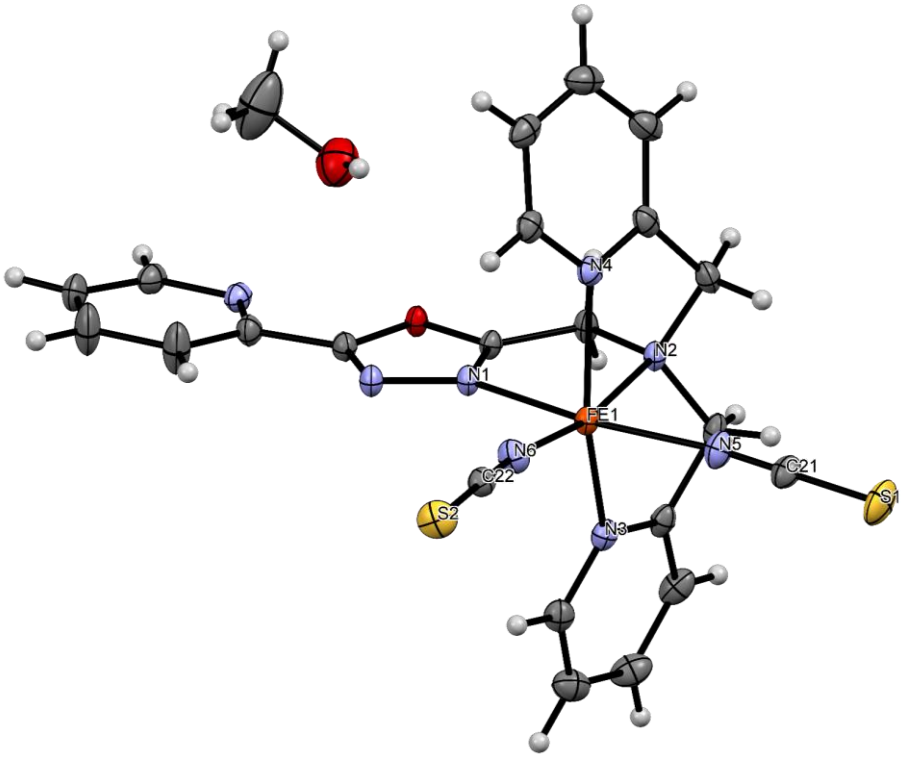


Figure F.36 Asymmetric Unit of **C16**·1MeOH. ORTEP representation with atomic displacement parameters set to 50 % probability.

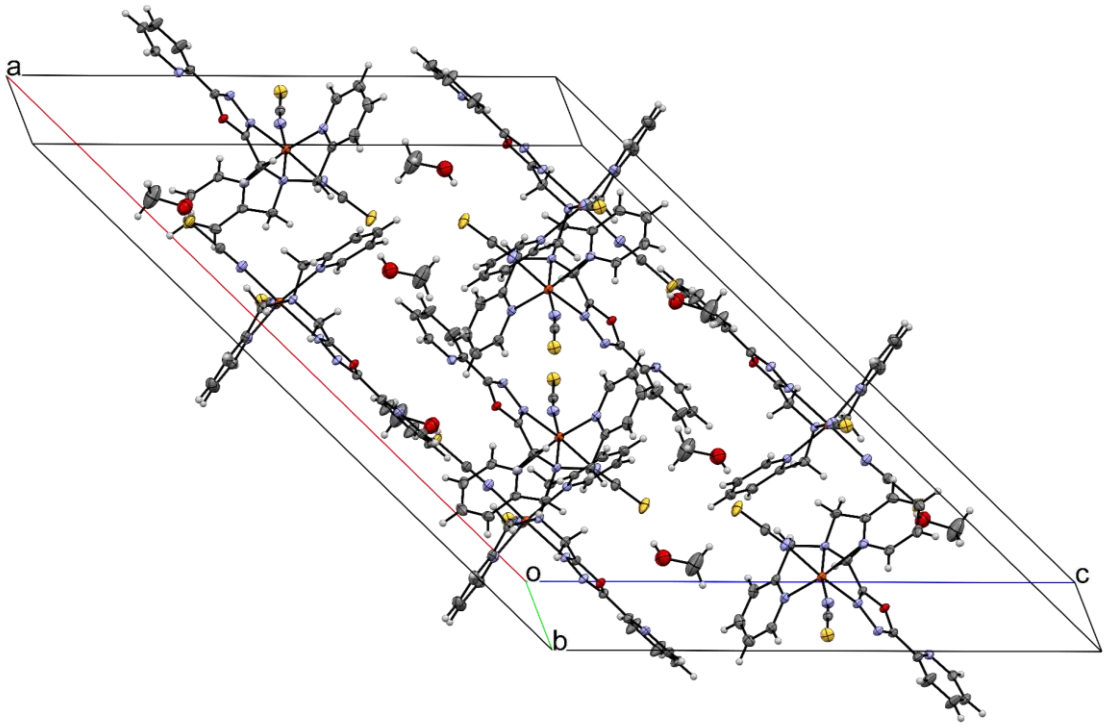


Figure F.37 Perspective view onto the unit cell of **C16**·1MeOH. ORTEP representation with atomic displacement parameters set to 50 % probability.

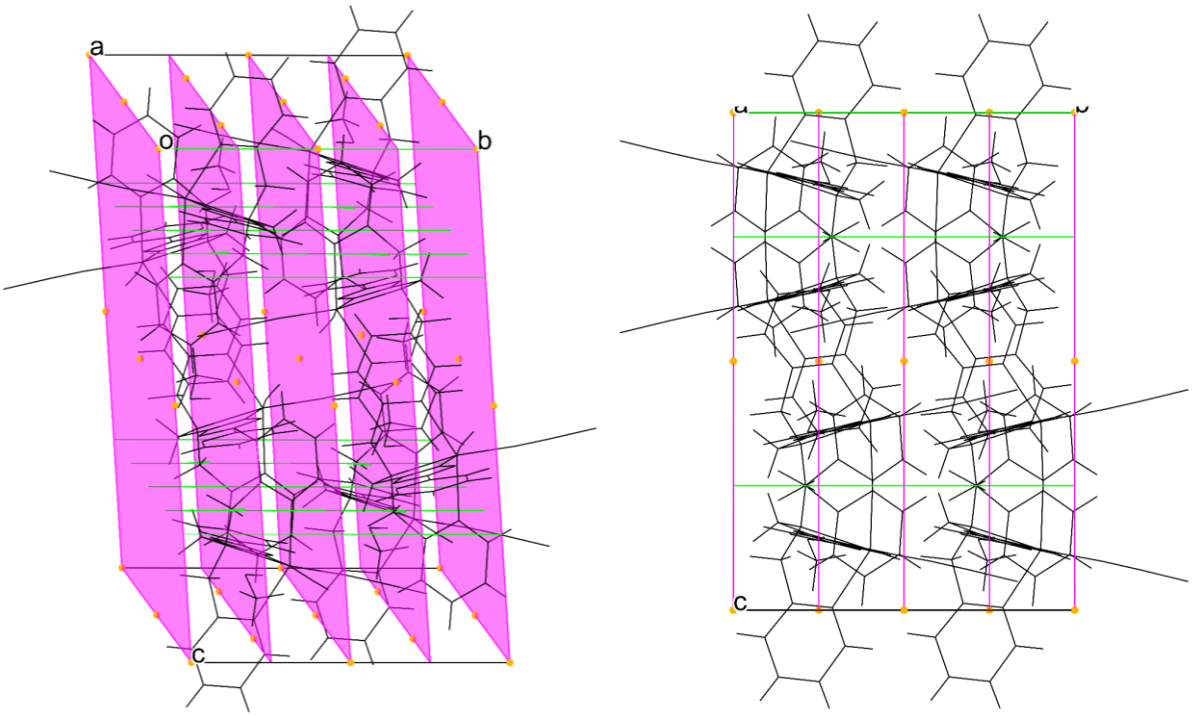


Figure F.38 Unit cell of **C16**·1MeOH with present symmetry elements with perspective view (left) and view along the a-axis (right). Centers of Inversion – yellow dots, Two-fold Axis – green lines, Mirror Glide Planes – purple planes. Molecules are displayed in the wireframe model for better vision.

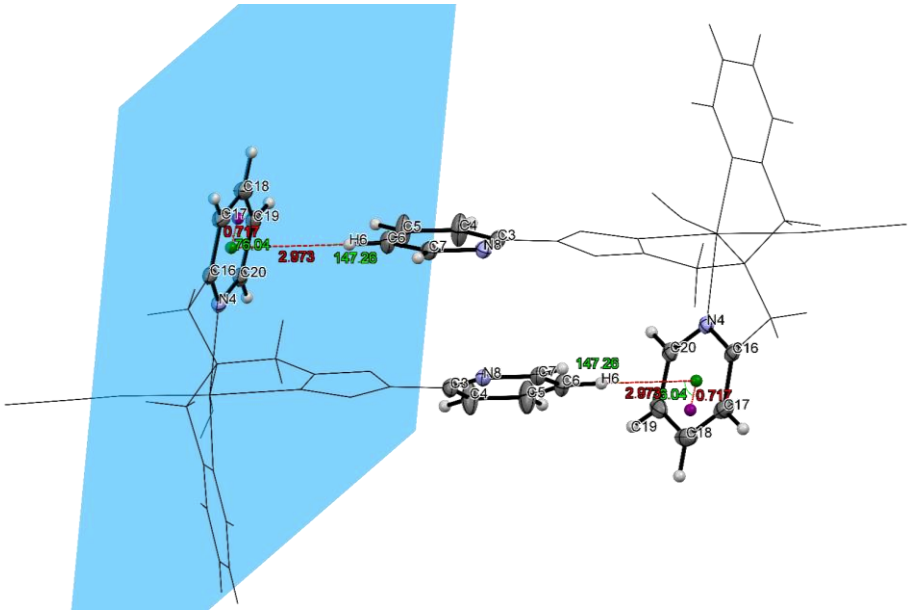


Figure F.39 C-H···π interaction in **C16**·1MeOH. Least-squares plane A is defined by N4, C16, C17, C18, C19 and C20. Interacting C-H fragment is labeled as C6-H6. Green point – center of the aromatic ring in A. Purple point – orthogonal intersection of H6 onto plane A. *Offset r* = 0.717 Å, *interaction distance* d_{QH} = 2.973 Å, α = 147.26 ° and β = 76.04 °. ORTEP representation with atomic displacement parameters set to 50 % probability.

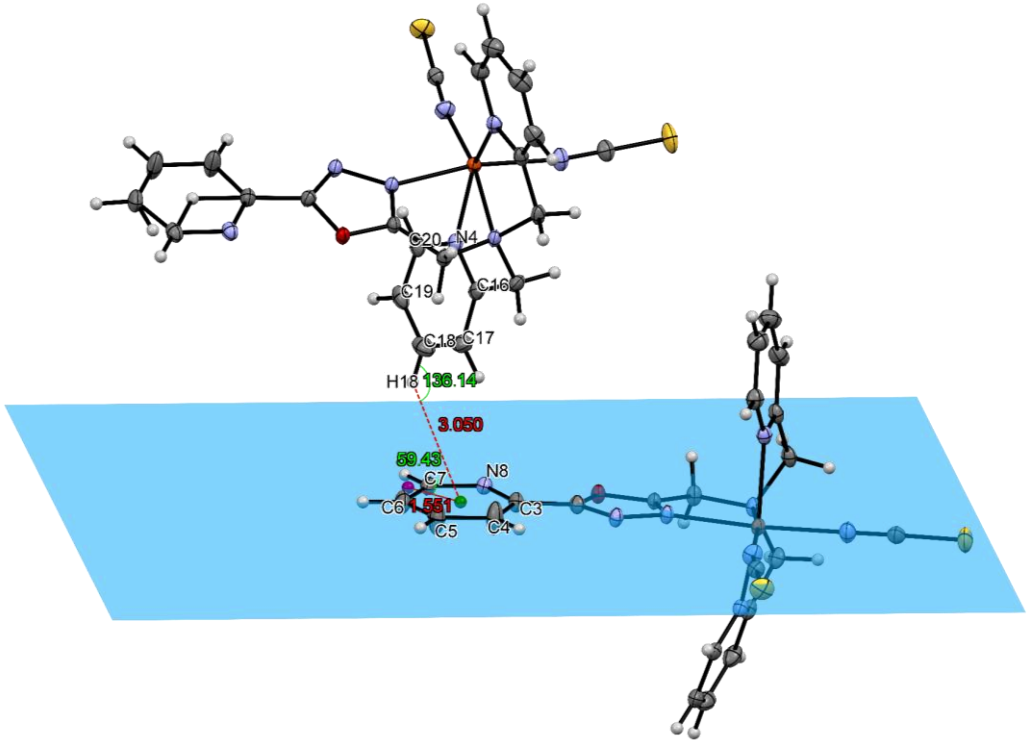


Figure F.40 C-H···π interaction in **C16**·1MeOH. Least-squares plane A is defined by N8, C3, C4, C5, C6 and C7. Interacting C-H fragment is labeled as C18-H18. Green point – center of the aromatic ring in A. Purple point – orthogonal intersection of H6 onto plane A. *Offset r* = 1.551 Å, *interaction distance* d_{QH} = 3.050 Å, α = 136.14 ° and β = 59.43 °. ORTEP representation with atomic displacement parameters set to 50 % probability.

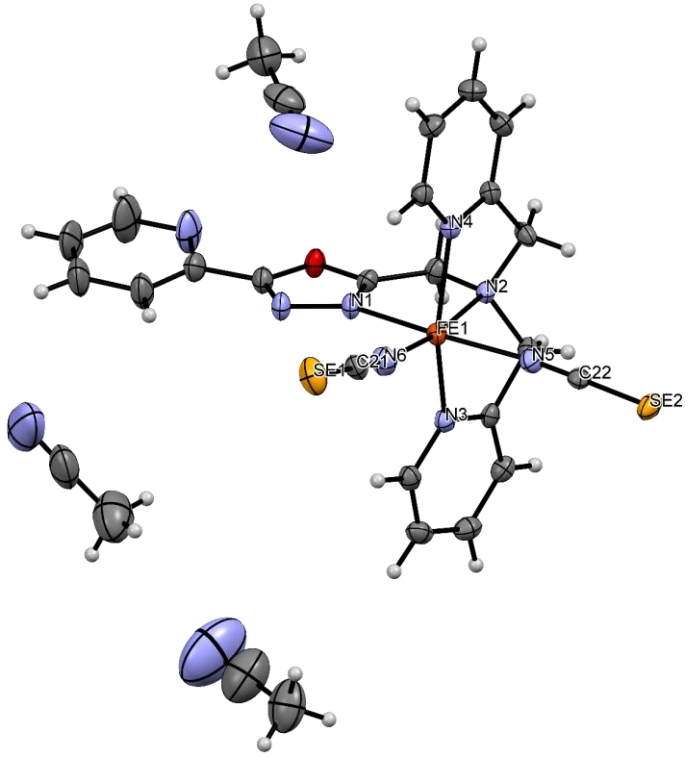


Figure F.41 Asymmetric Unit of **C17**·3MeCN. ORTEP representation with atomic displacement parameters set to 50 % probability.

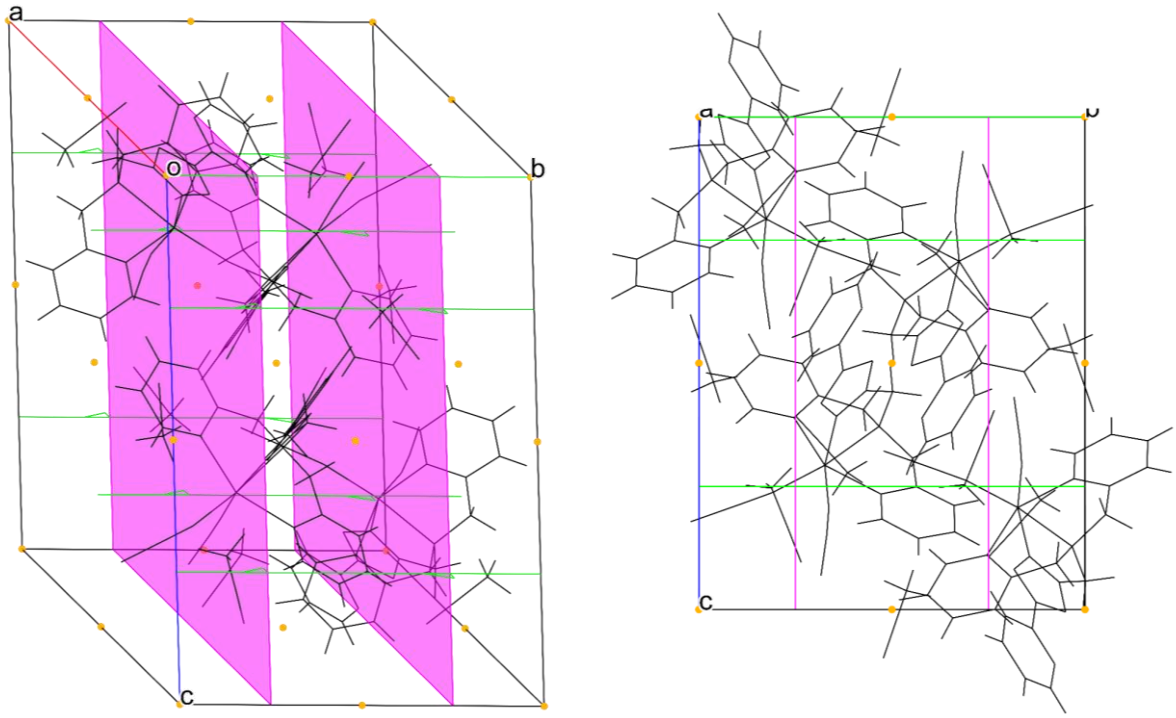


Figure F.42 Unit cell of **C17**·3MeCN with present symmetry elements with perspective view (left) and view along the a-axis (right). Centers of Inversion – yellow dots, Two-fold Axis – green lines, Mirror Glide Planes – purple planes. Molecules are displayed in the wireframe model for better vision.

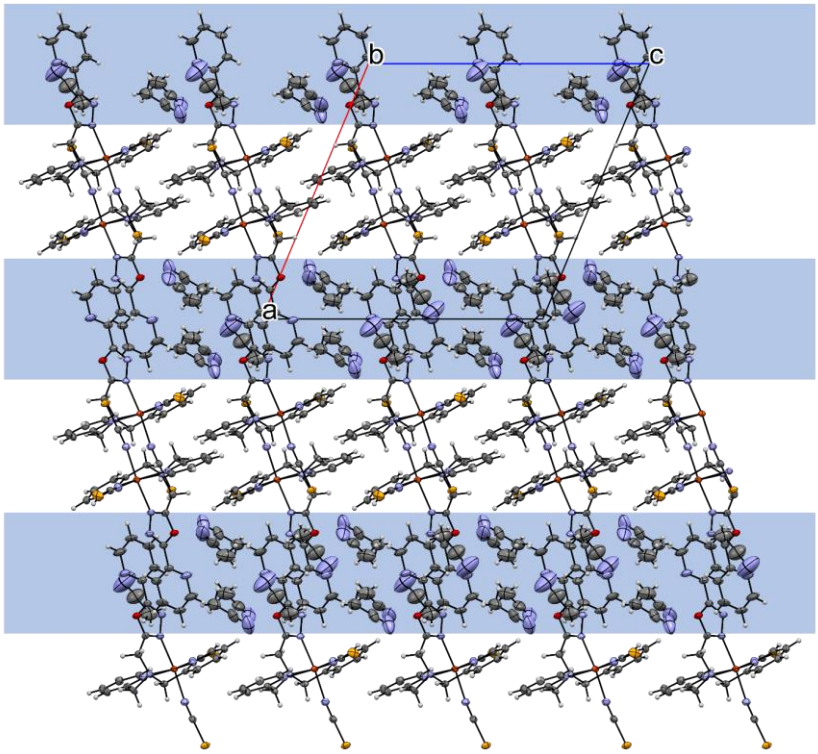


Figure F.43 Packing of **C17**·3MeCN with view along the b-axis. Blue areas illustrate the layers of solvent molecules. ORTEP representation with atomic displacement parameters set to 50 % probability.

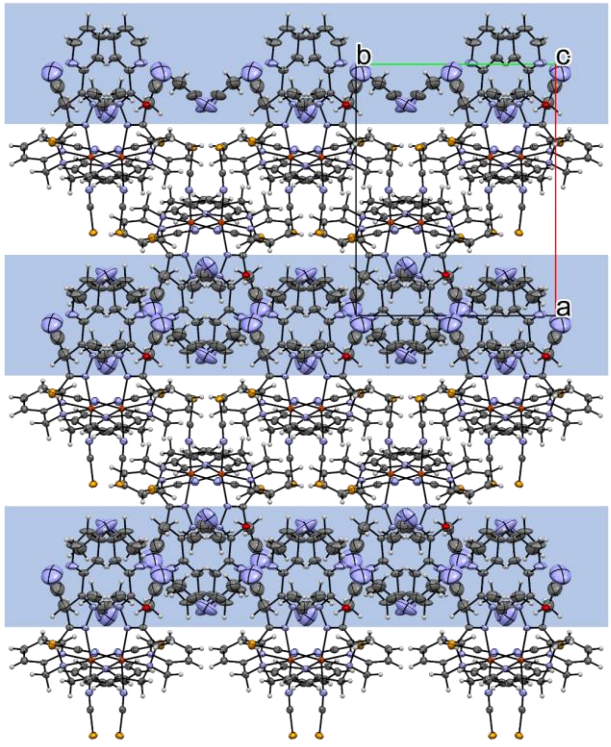


Figure F.44 Packing of **C17**·3MeCN with view along the c-axis. Blue areas illustrate the layers of solvent molecules. ORTEP representation with atomic displacement parameters set to 50 % probability.

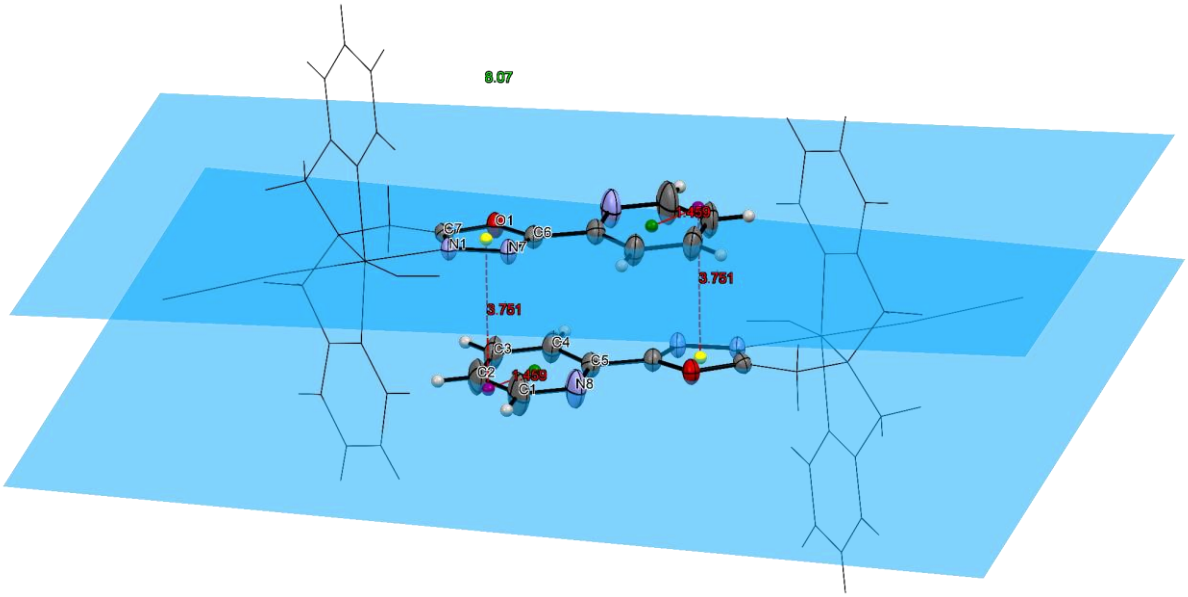


Figure F.45 π-π interaction in **C17**·3MeCN. Least-squares mean plane A is defined by N8, C1, C2, C3, C4 and C5. Plane B is defined by O1, C6, N7, N1 and C7 of an adjacent molecule. Green point – center of the aromatic ring in A. Yellow point – center of the aromatic ring in B. Purple point – orthogonal intersection of the aromatic center in B onto plane A. *Offset* r = 1.459 Å, *interplanar distance* d_{AB} = 3.751 Å, *interplanar angle* θ = 8.07 °. ORTEP representation with atomic displacement parameters set to 50 % probability.

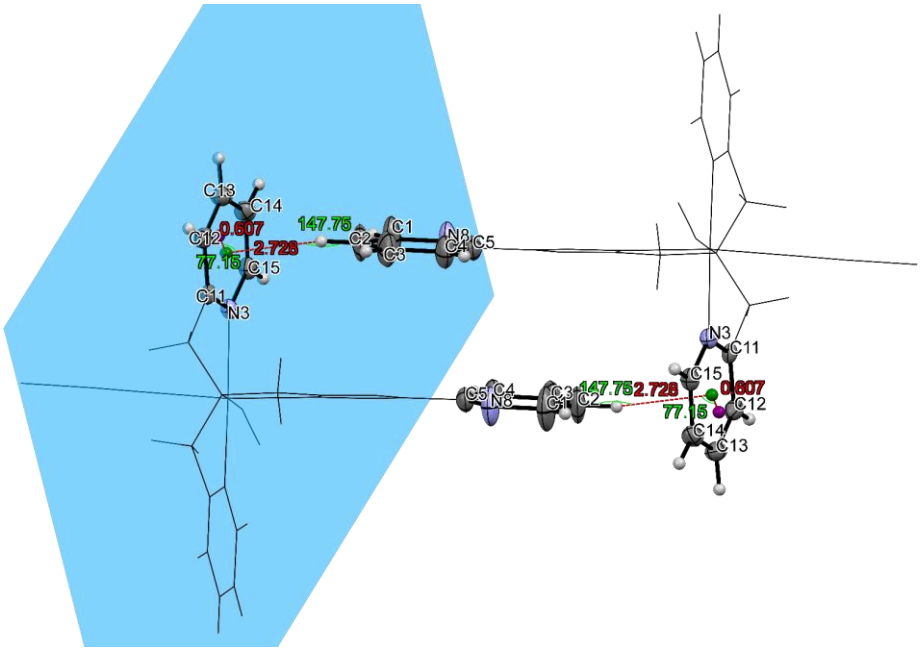


Figure F.46 C-H···π interaction in **C17**·3MeCN. Least-squares plane A is defined by N3, C11, C12, C13, C14 and C15. Interacting C-H fragment is labeled as C2-H2. Green point – center of the aromatic ring in A. Purple point – orthogonal intersection of H2 onto plane A. *Offset* r = 0.607 Å, *interaction distance* d_{QH} = 2.728 Å, α = 147.75 ° and β = 77.15 °. ORTEP representation with atomic displacement parameters set to 50 % probability.

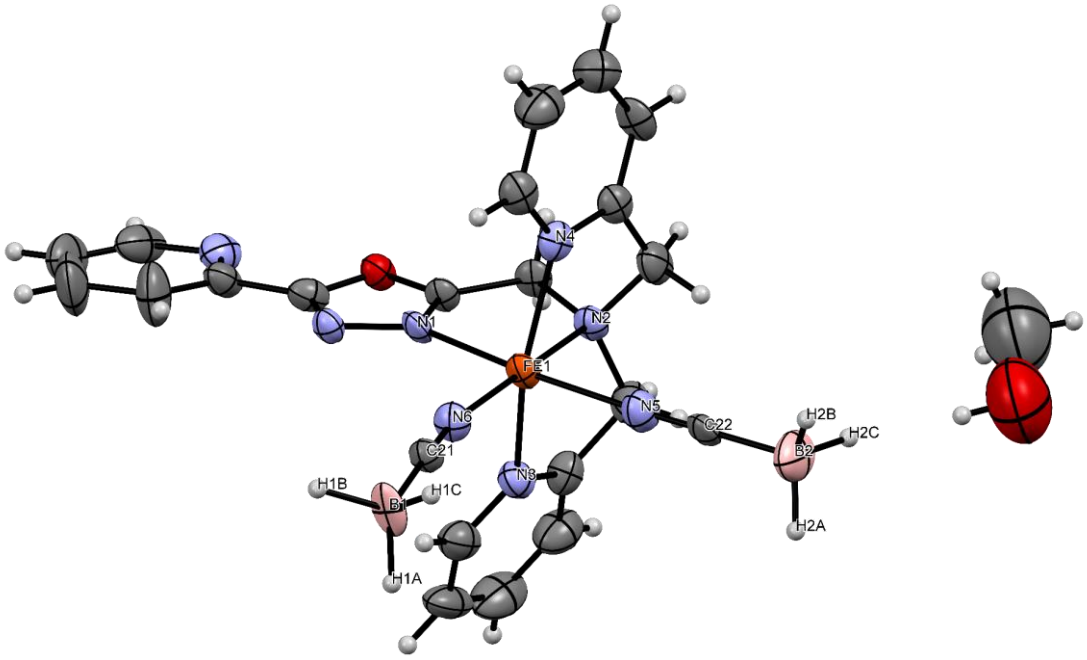


Figure F.47 Asymmetric Unit of **C18**·1MeOH. ORTEP representation with atomic displacement parameters set to 50 % probability.

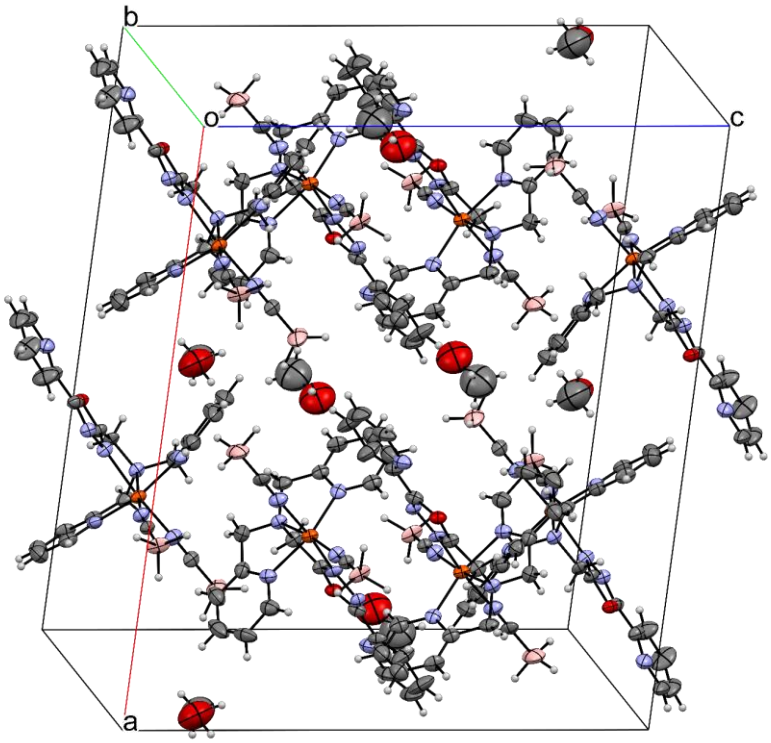


Figure F.48 Perspective view onto the unit cell of **C18**·1MeOH. ORTEP representation with atomic displacement parameters set to 50 % probability.

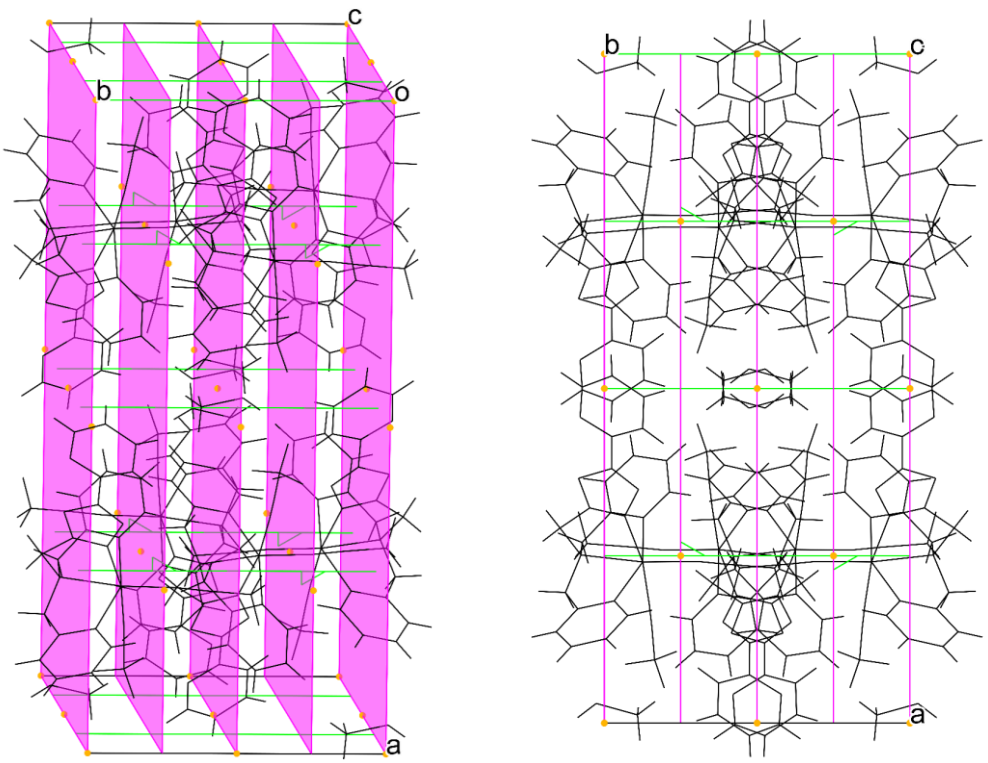


Figure F.49 Unit cell of **C18**·1MeOH with present symmetry elements with perspective view (left) and view along the c-axis (right). Centers of Inversion – yellow dots, Two-fold Axis – green lines, Mirror Glide Planes – purple planes. Molecules are displayed in the wireframe model for better vision.

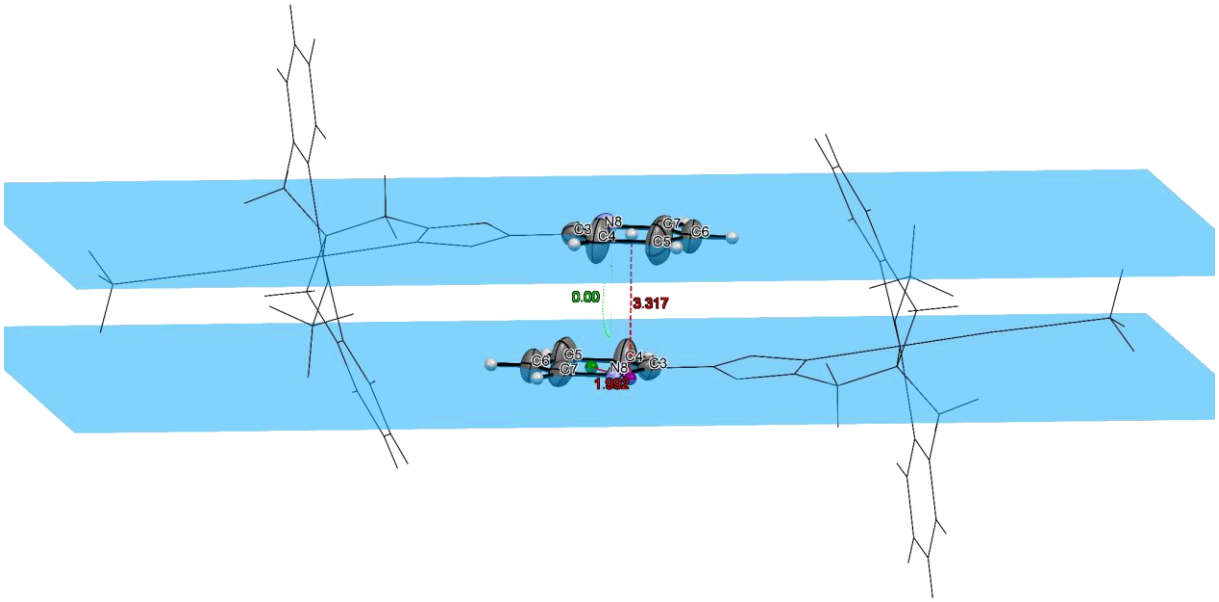


Figure F.50 π-π interaction in **C18**·1MeOH. Least-squares mean plane A is defined by N8, C3, C4, C5, C6 and C7. Plane B is defined by N8, C3, C4, C5, C6 and C7 of an adjacent molecule. Green point – center of the aromatic ring in A. Yellow point – center of the aromatic ring in B. Purple point – orthogonal intersection of the aromatic center in B onto plane A. *Offset r* = 1.992 Å, *interplanar distance* d_{AB} = 3.317 Å, *interplanar angle* θ = 0.00 °. ORTEP representation with atomic displacement parameters set to 50 % probability.

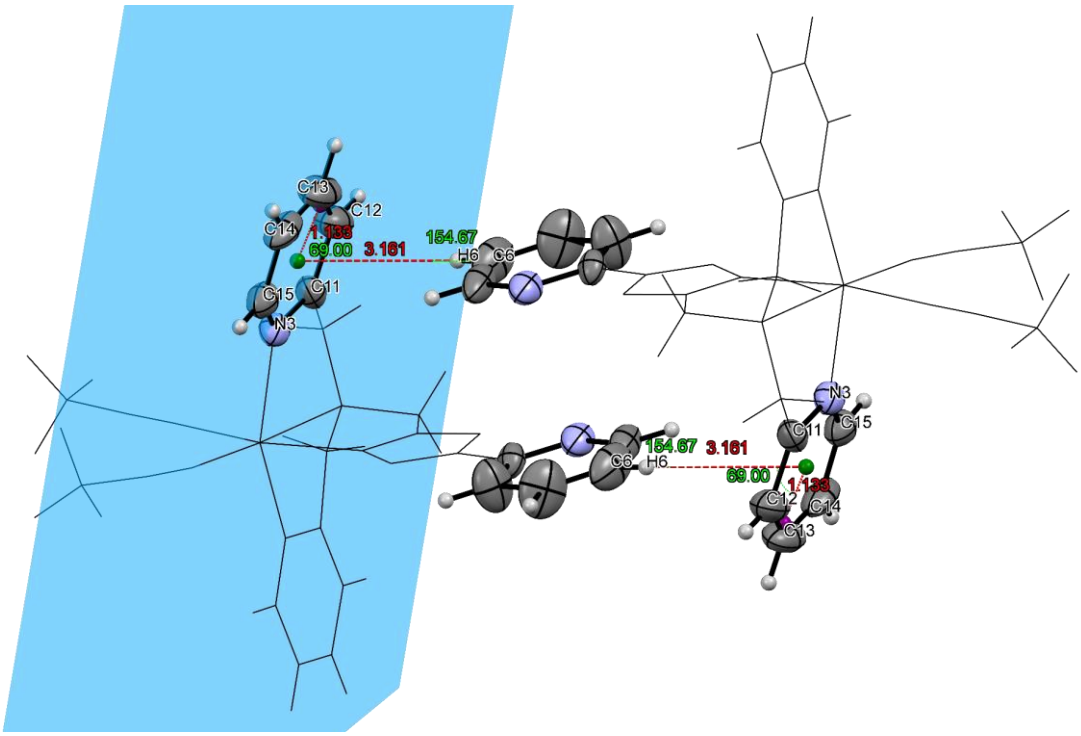


Figure F.51 C-H···π interaction in **C18**·1MeOH. Least-squares plane A is defined by N3, C11, C12, C13, C14 and C15. Interacting C-H fragment is labeled as C6-H6. Green point – center of the aromatic ring in A. Purple point – orthogonal intersection of H6 onto plane A. *Offset* r = 1.133 Å, *interaction distance* d_{QH} = 3.161 Å, α = 154.67 ° and β = 69.00 °. ORTEP representation with atomic displacement parameters set to 50 % probability.

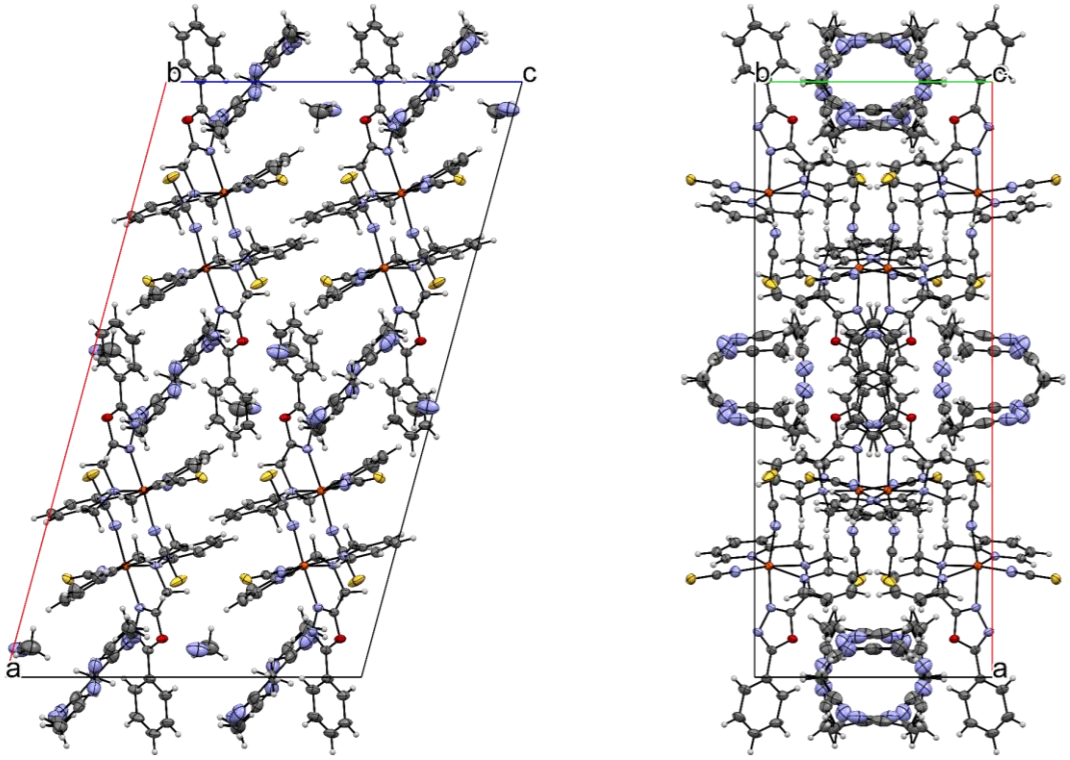


Figure F.52 Unit cell of **C19**·2MeCN with view along the b-axis (left) and view along the c-axis (right). ORTEP representation with atomic displacement parameters set to 50 % probability.

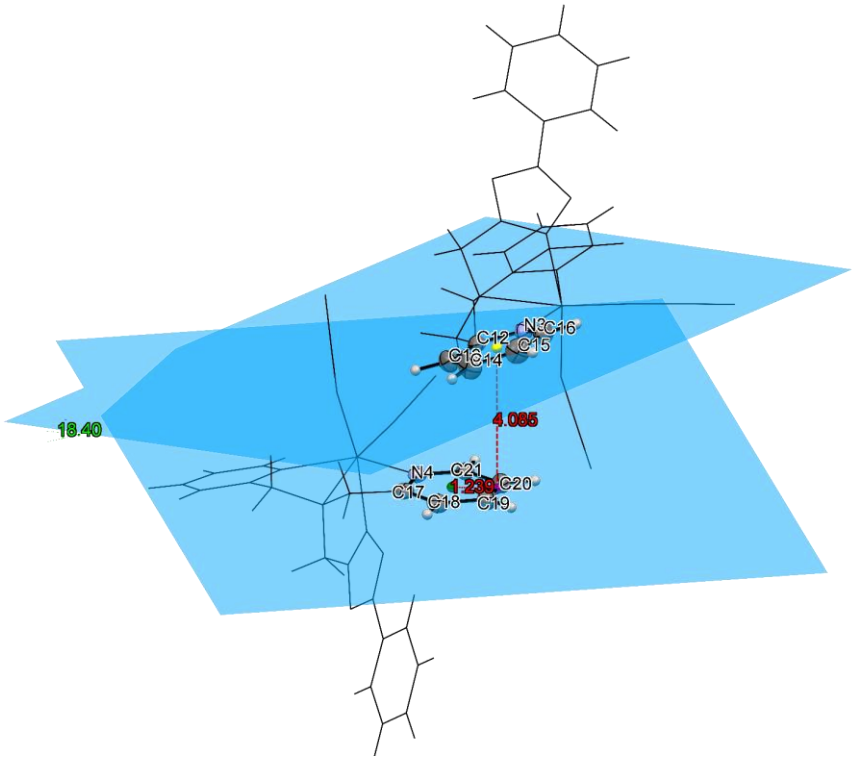


Figure F.53 π-π interaction in **C19**·2MeCN. Least-squares mean plane A is defined by N4, C17, C18, C19, C20 and C21. Plane B is defined by N3, C12, C13, C14, C15 and C16 of an adjacent molecule. Green point – center of the aromatic ring in A. Yellow point – center of the aromatic ring in B. Purple point – orthogonal intersection of the aromatic center in B onto plane A. *Offset* r = 1.239 Å, *interplanar distance* d_{AB} = 4.085 Å, *interplanar angle* θ = 18.40 °. ORTEP representation with atomic displacement parameters set to 50 % probability.

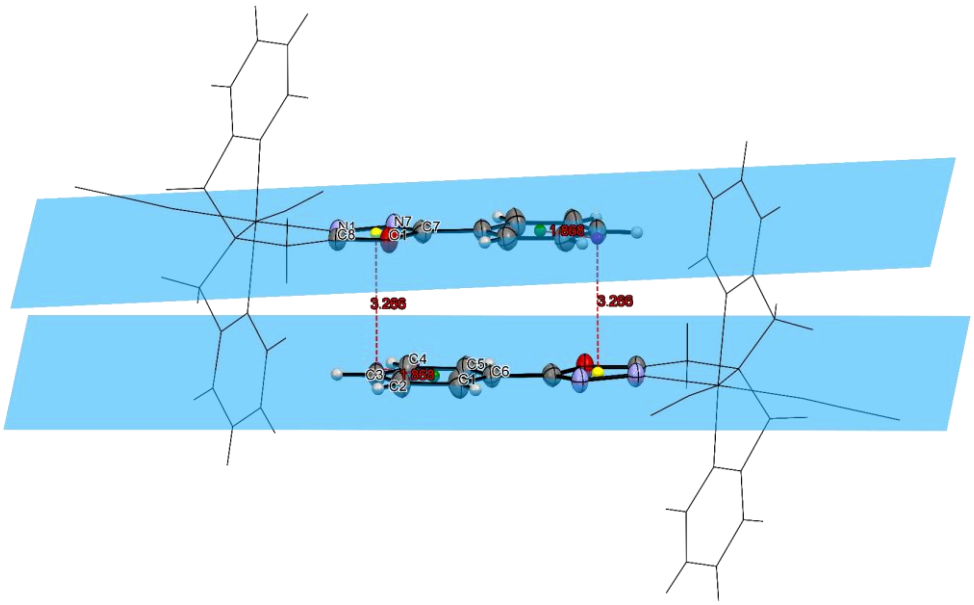


Figure F.54 π-π interaction in **C19**·2MeCN. Least-squares mean plane A is defined by C1, C2, C3, C4, C5 and C6. Plane B is defined by O1, C7, N7, N1 and C8 of an adjacent molecule. Green point – center of the aromatic ring in A. Yellow point – center of the aromatic ring in B. Purple point – orthogonal intersection of the aromatic center in B onto plane A. *Offset* r = 1.868 Å, *interplanar distance* d_{AB} = 3.266 Å, *interplanar angle* θ = 2.7 °. ORTEP representation with atomic displacement parameters set to 50 % probability.

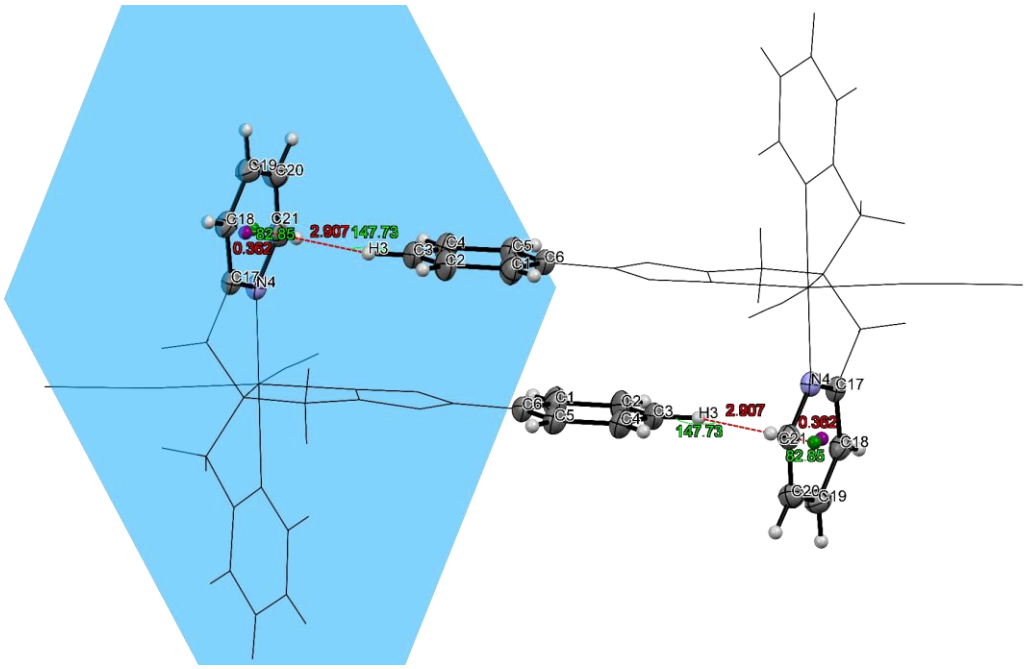


Figure F.55 C-H···π interaction in **C19**·2MeCN. Least-squares plane A is defined by N4, C17, C18, C19, C20 and C21. Interacting C-H fragment is labeled as C3-H3. Green point – center of the aromatic ring in A. Purple point – orthogonal intersection of H13 onto plane A. *Offset* r = 0.362 Å, *interaction distance* d_{QH} = 2.907 Å, α = 147.73 ° and β = 82.85 °. ORTEP representation with atomic displacement parameters set to 50 % probability.

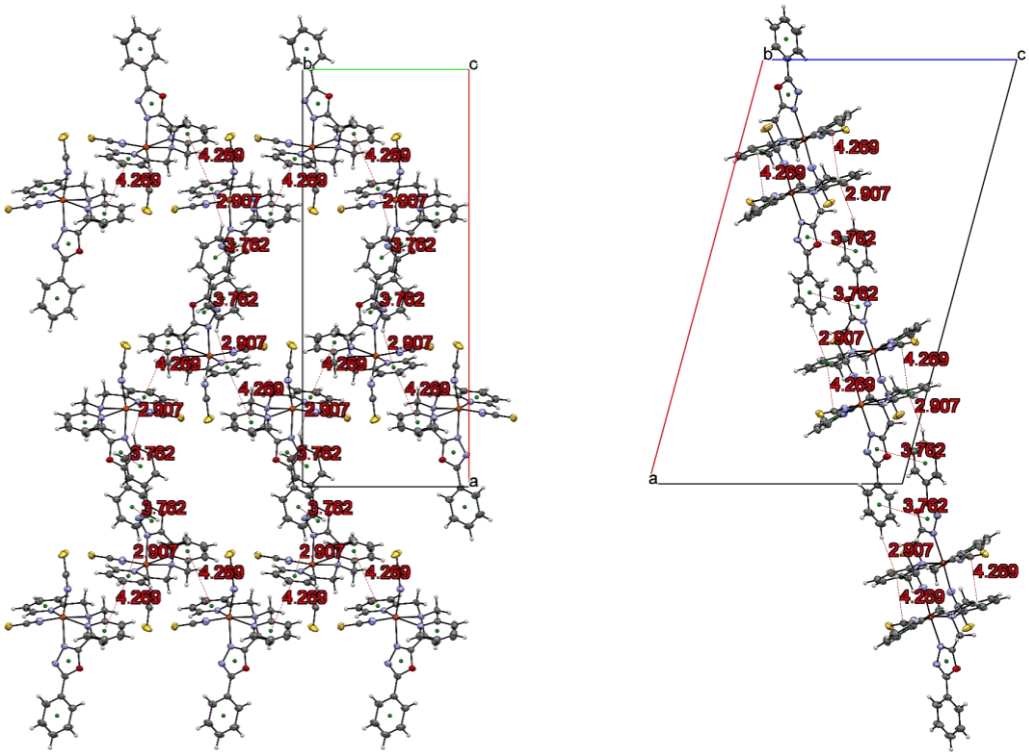


Figure F.56 Two-dimensional network of complex molecules in **C19**·2MeCN due to intermolecular π-π interactions with view along the c-axis (left) and b-axis (right). The centers of involved aromatic rings are displayed as green points. Distances are displayed as red dashed lines and numbers. Solvent molecules are omitted for better vision. ORTEP representation with atomic displacement parameters set to 50 % probability.

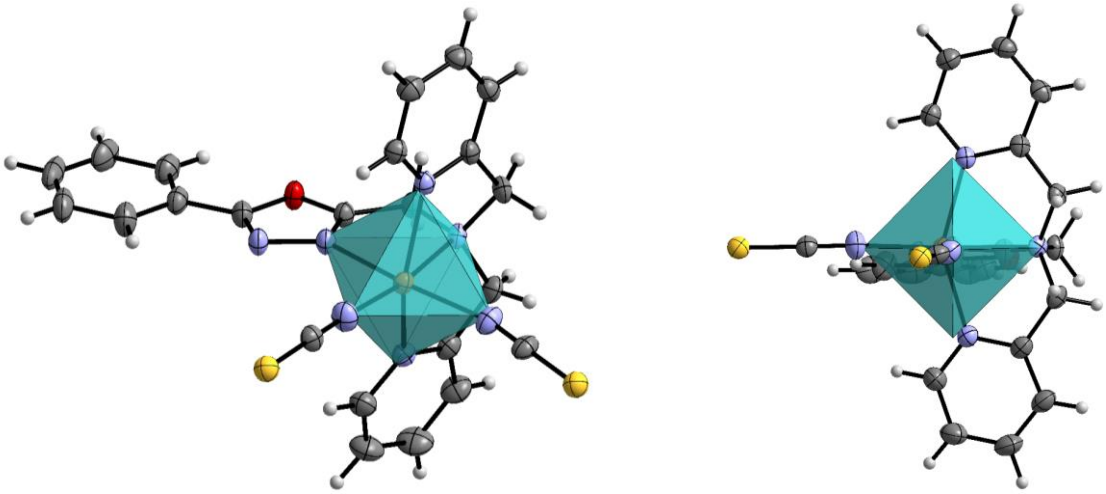


Figure F.57 Molecular structure of **C19**·2MeCN and its ideal coordination octahedron with front view (left) and view along the Fe-N5 axis (right), calculated with SHAPE.[62] ORTEP representation with atomic displacement parameters set to 50 % probability.

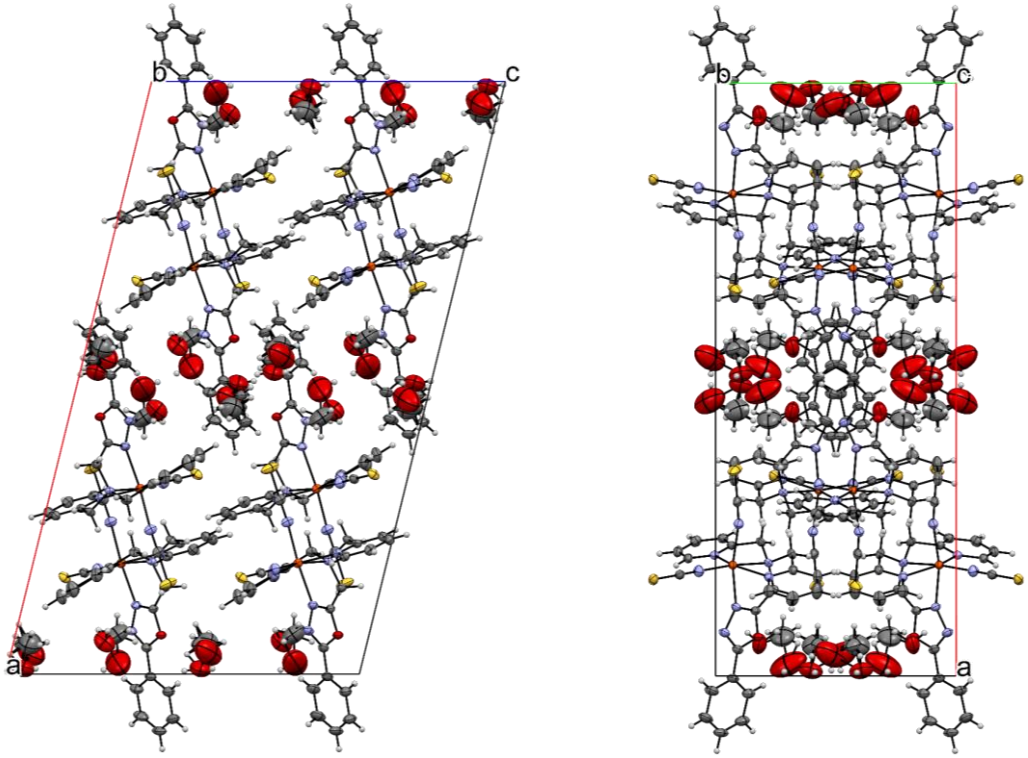


Figure F.58 Unit cell of **C19**·3MeOH with view along the b-axis (left) and view along the c-axis (right). ORTEP representation with atomic displacement parameters set to 50 % probability.

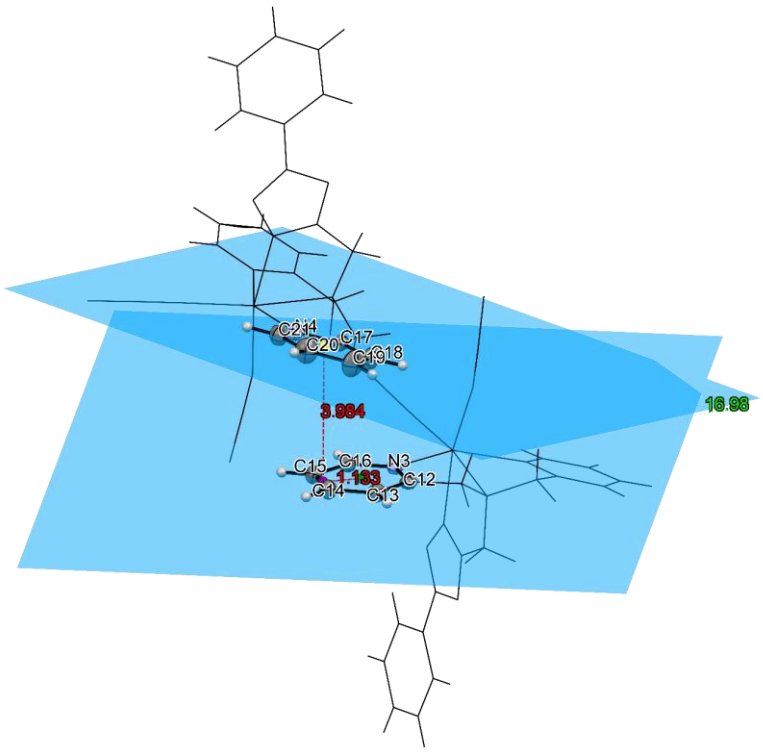


Figure F.59 π-π interaction in **C19**·3MeOH. Least-squares mean plane A is defined by N3, C12, C13, C14, C15 and C16. Plane B is defined by N4, C17, C18, C19, C20 and C21 of an adjacent molecule. Green point – center of the aromatic ring in A. Yellow point – center of the aromatic ring in B. Purple point – orthogonal intersection of the aromatic center in B onto plane A. *Offset r* = 1.133 Å, *interplanar distance* d_{AB} = 3.984 Å, *interplanar angle* θ = 16.98 °. ORTEP representation with atomic displacement parameters set to 50 % probability.

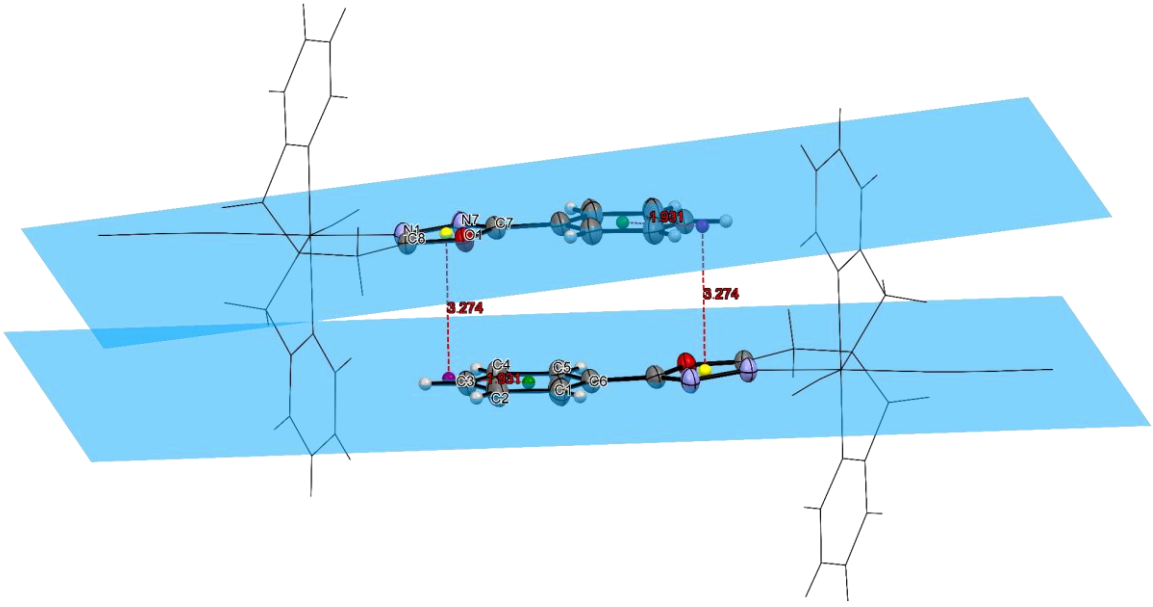


Figure F.60 π-π interaction in **C19**·3MeOH. Least-squares mean plane A is defined by C1. C2. C3. C4. C5 and C6. Plane B is defined by O1, C7, N7, N1 and C8 of an adjacent molecule. Green point – center of the aromatic ring in A. Yellow point – center of the aromatic ring in B. Purple point – orthogonal intersection of the aromatic center in B onto plane A. *Offset r* = 1.931 Å, *interplanar distance* d_{AB} = 3.274 Å, *interplanar angle* θ = 5.6 °. ORTEP representation with atomic displacement parameters set to 50 % probability.

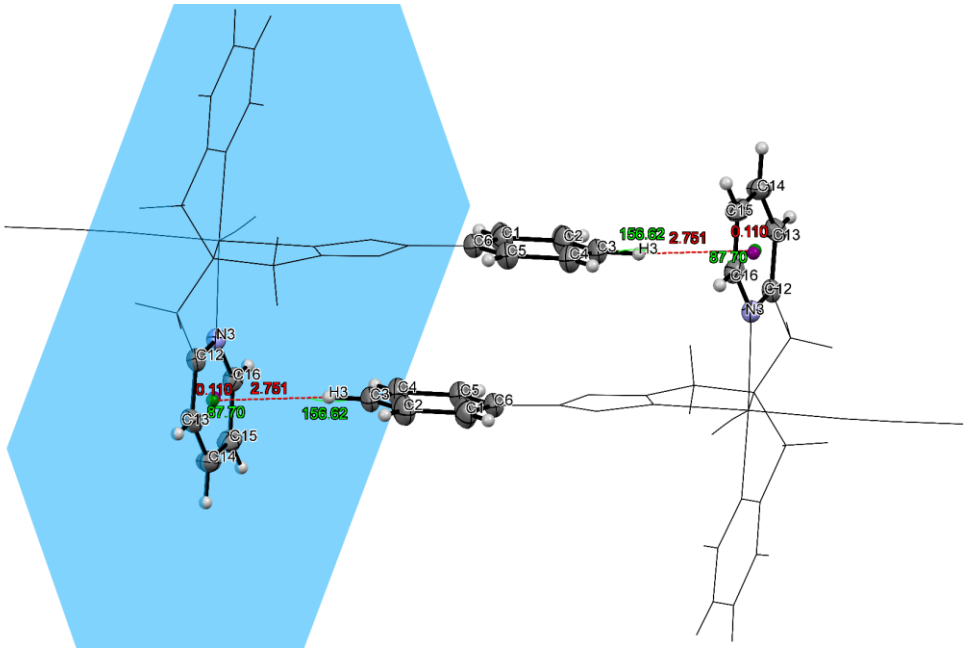


Figure F.61 C-H···π interaction in **C19**·3MeOH. Least-squares plane A is defined by N3, C12, C13, C14, C15 and C16. Interacting C-H fragment is labeled as C3-H3. Green point – center of the aromatic ring in A. Purple point – orthogonal intersection of H13 onto plane A. *Offset* r = 0.110 Å, *interaction distance* d_{QH} = 2.751 Å, α = 156.62 ° and β = 87.70 °. ORTEP representation with atomic displacement parameters set to 50 % probability.

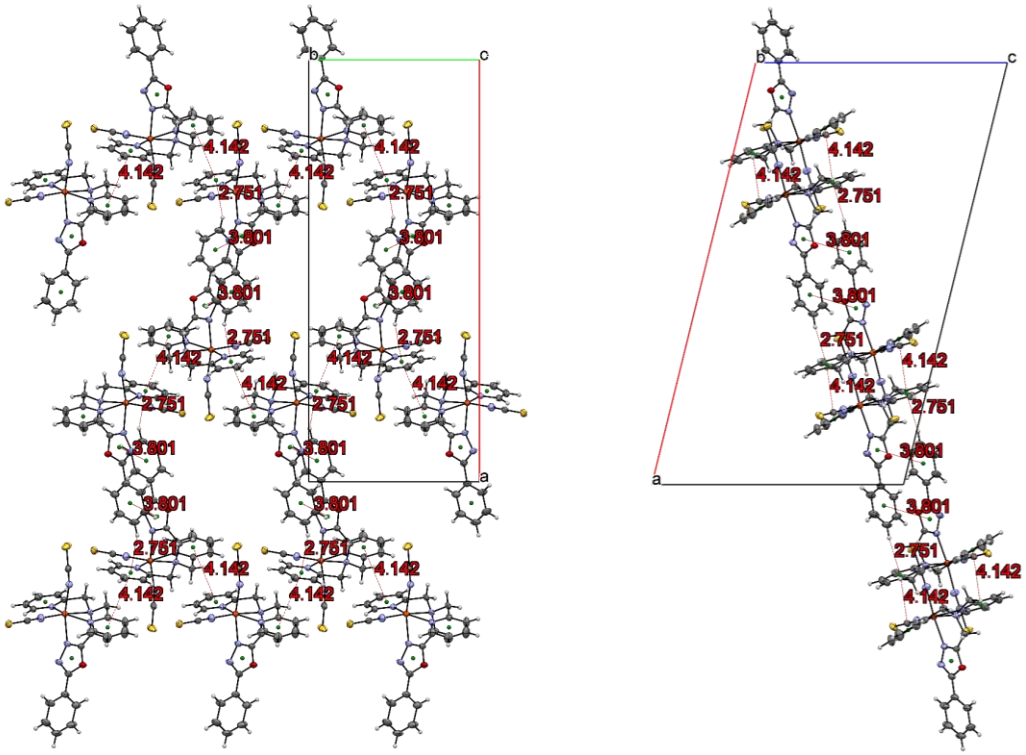


Figure F.62 Two-dimensional network of complex molecules in **C19**·3MeOH due to intermolecular π-π interactions with view along the c-axis (left) and b-axis (right). The centers of involved aromatic rings are displayed as green points. Distances are displayed as red dashed lines and numbers. Solvent molecules are omitted for better vision. ORTEP representation with atomic displacement parameters set to 50 % probability.

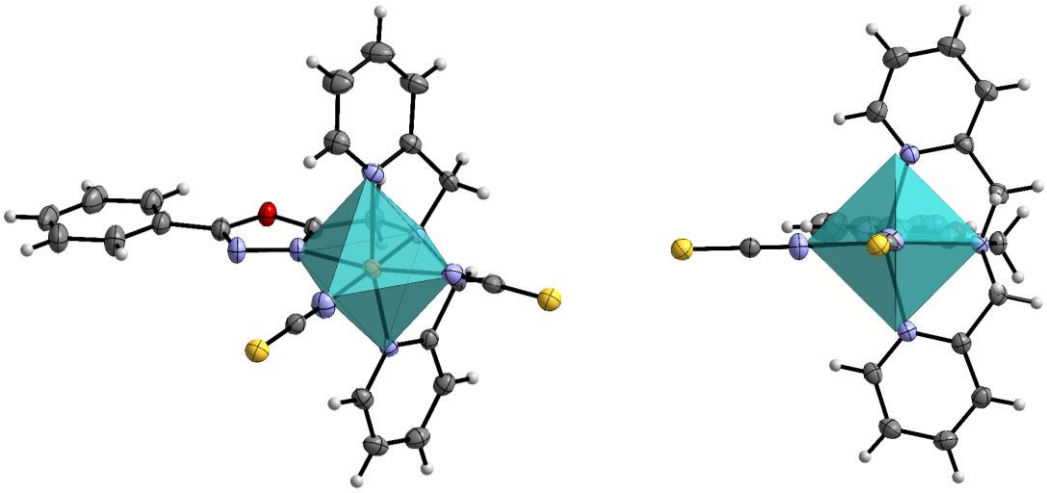


Figure F.63 Molecular structure of **C19**·3MeOH and its ideal coordination octahedron with front view (left) and view along the Fe-N5 axis (right), calculated with SHAPE.[62] ORTEP representation with atomic displacement parameters set to 50 % probability.

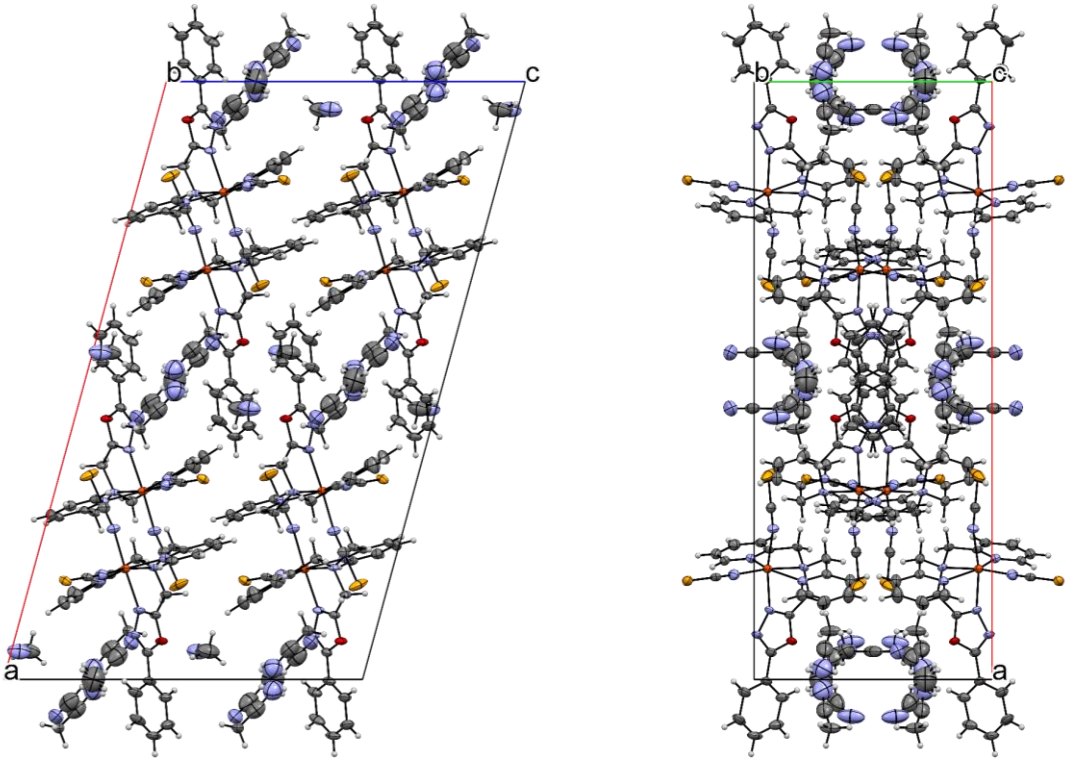


Figure F.64 Unit cell of **C20**·2MeCN with view along the b-axis (left) and view along the c-axis (right). ORTEP representation with atomic displacement parameters set to 50 % probability.

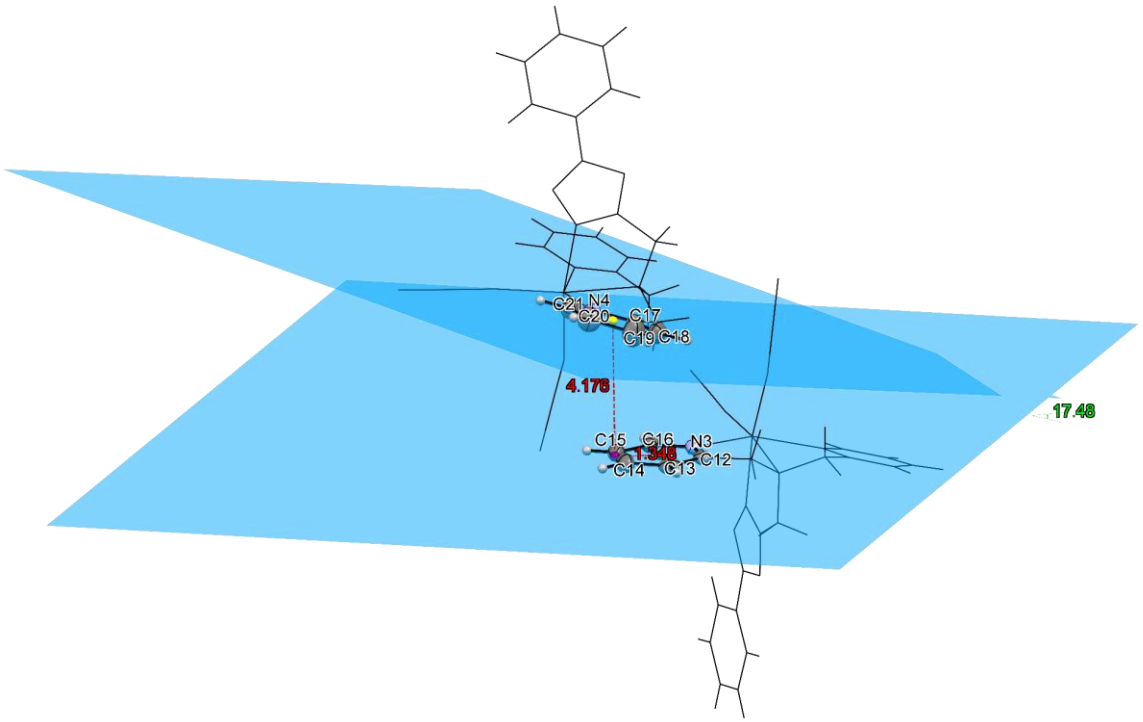


Figure F.65 π-π interaction in **C20**·2MeCN. Least-squares mean plane A is defined by N3, C12, C13, C14, C15 and C16. Plane B is defined by N4, C17, C18, C19, C20 and C21 of an adjacent molecule. Green point – center of the aromatic ring in A. Yellow point – center of the aromatic ring in B. Purple point – orthogonal intersection of the aromatic center in B onto plane A. *Offset* r = 1.348 Å, *interplanar distance* d_{AB} = 4.176 Å, *interplanar angle* θ = 17.48 °. ORTEP representation with atomic displacement parameters set to 50 % probability.

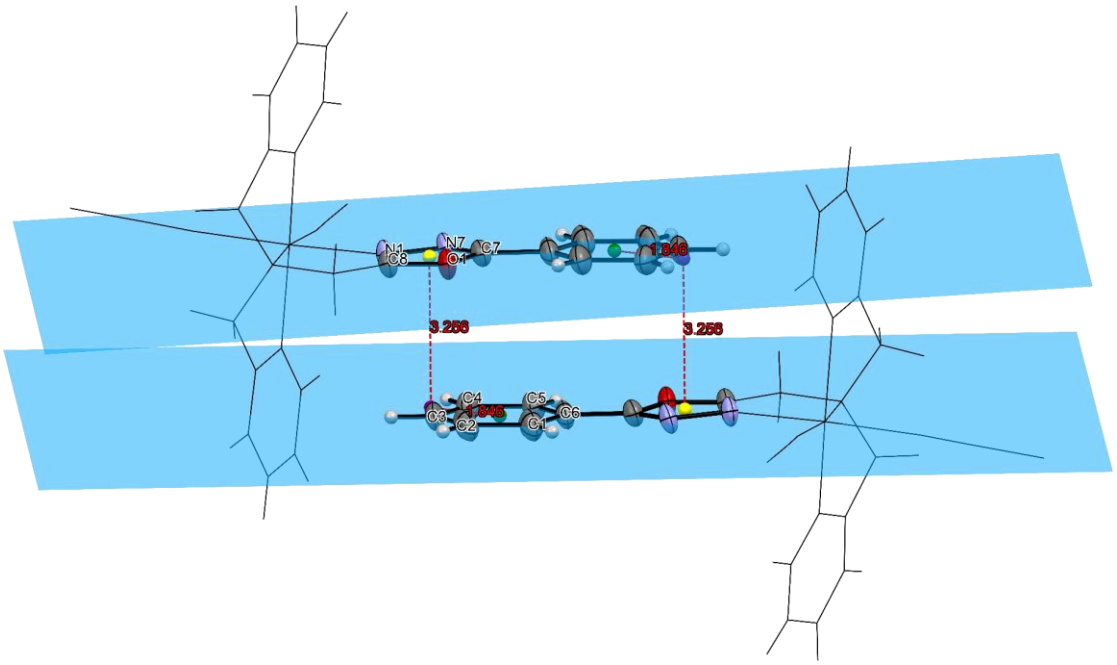


Figure F.66 π-π interaction in **C20**·2MeCN. Least-squares mean plane A is defined by C1. C2. C3. C4. C5 and C6. Plane B is defined by O1, C7, N7, N1 and C8 of an adjacent molecule. Green point – center of the aromatic ring in A. Yellow point – center of the aromatic ring in B. Purple point – orthogonal intersection of the aromatic center in B onto plane A. *Offset* r = 1.846 Å, *interplanar distance* d_{AB} = 3.256 Å, *interplanar angle* θ = 3 °. ORTEP representation with atomic displacement parameters set to 50 % probability.

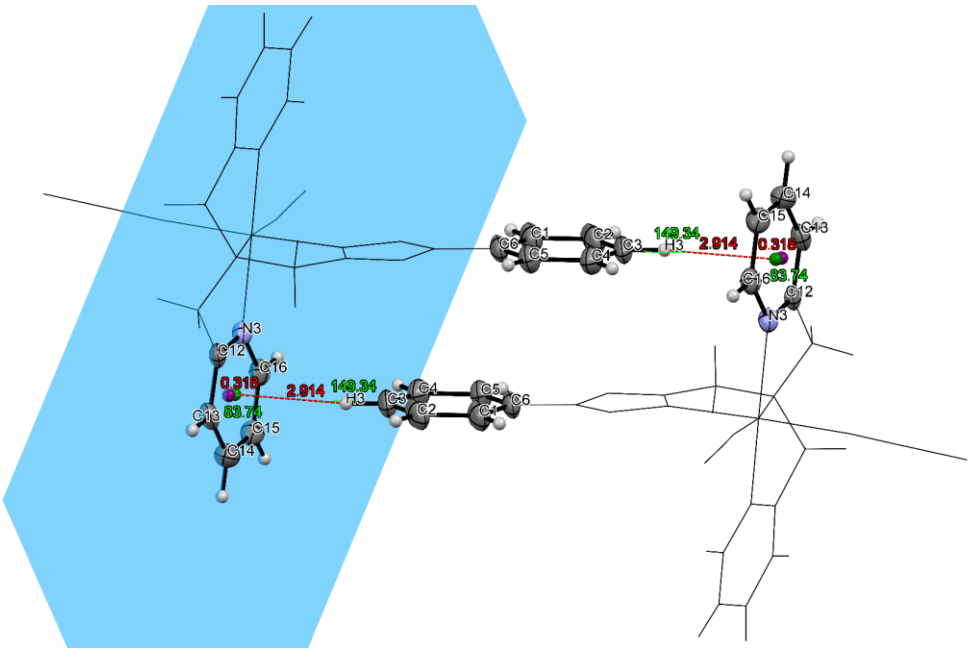


Figure F.67 C-H···π interaction in **C20**·2MeCN. Least-squares plane A is defined by N3, C12, C13, C14, C15 and C16. Interacting C-H fragment is labeled as C3-H3. Green point – center of the aromatic ring in A. Purple point – orthogonal intersection of H13 onto plane A. *Offset* r = 0.318 Å, *interaction distance* d_{QH} = 2.914 Å, α = 149.34 ° and β = 83.74 °. ORTEP representation with atomic displacement parameters set to 50 % probability.

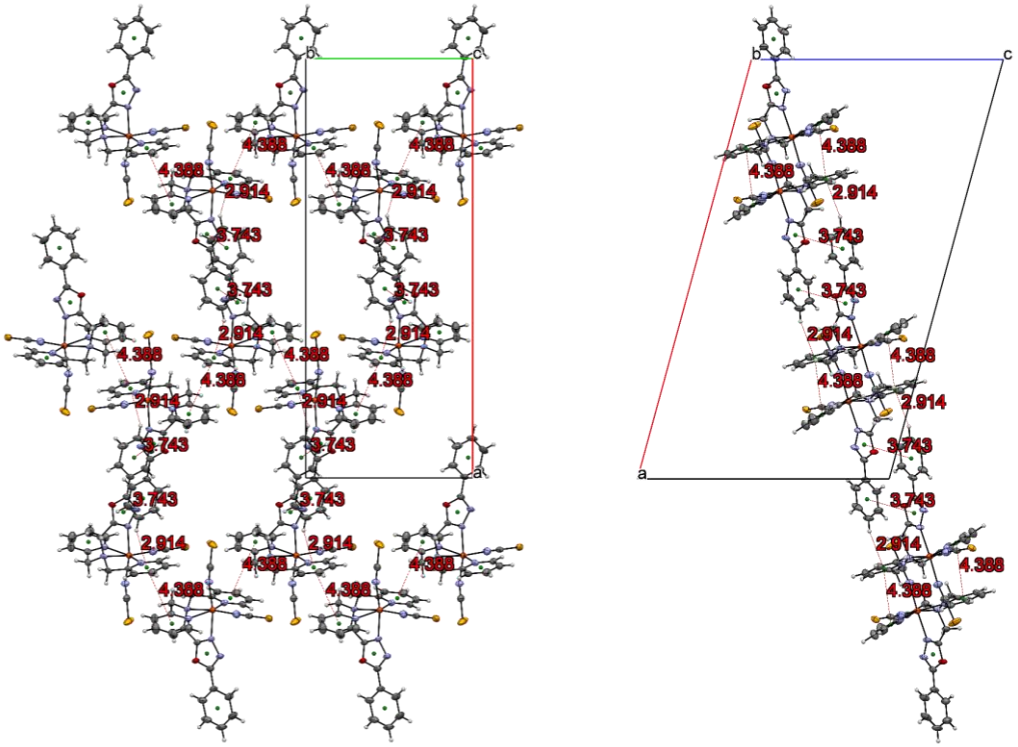


Figure F.68 Two-dimensional network of complex molecules in **C20**·2MeCN due to intermolecular π-π interactions with view along the c-axis (left) and b-axis (right). The centers of involved aromatic rings are displayed as green points. Distances are displayed as red dashed lines and numbers. Solvent molecules are omitted for better vision. ORTEP representation with atomic displacement parameters set to 50 % probability.

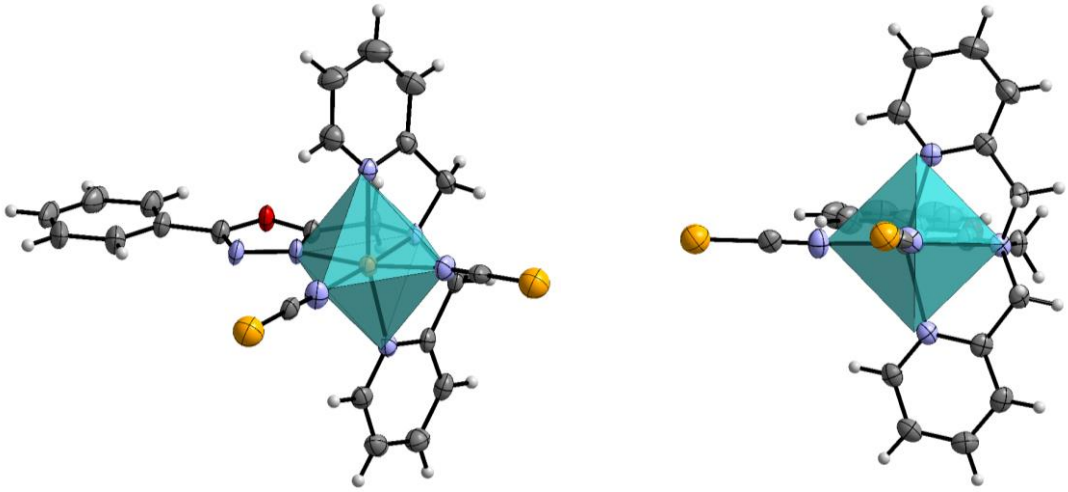


Figure F.69 Molecular structure of **C20**·2MeCN and its ideal coordination octahedron with front view (left) and view along the Fe-N5 axis (right), calculated with SHAPE.[62] ORTEP representation with atomic displacement parameters set to 50 % probability.

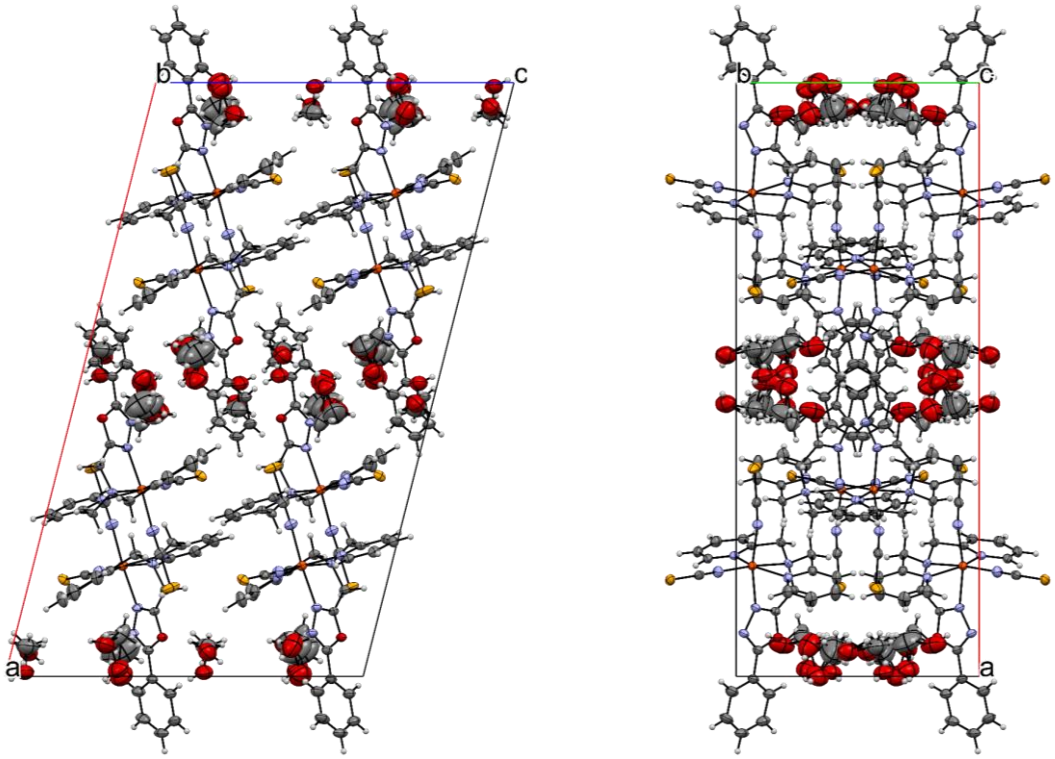


Figure F.70 Unit cell of **C20**·3MeOH with view along the b-axis (left) and view along the c-axis (right). ORTEP representation with atomic displacement parameters set to 50 % probability.

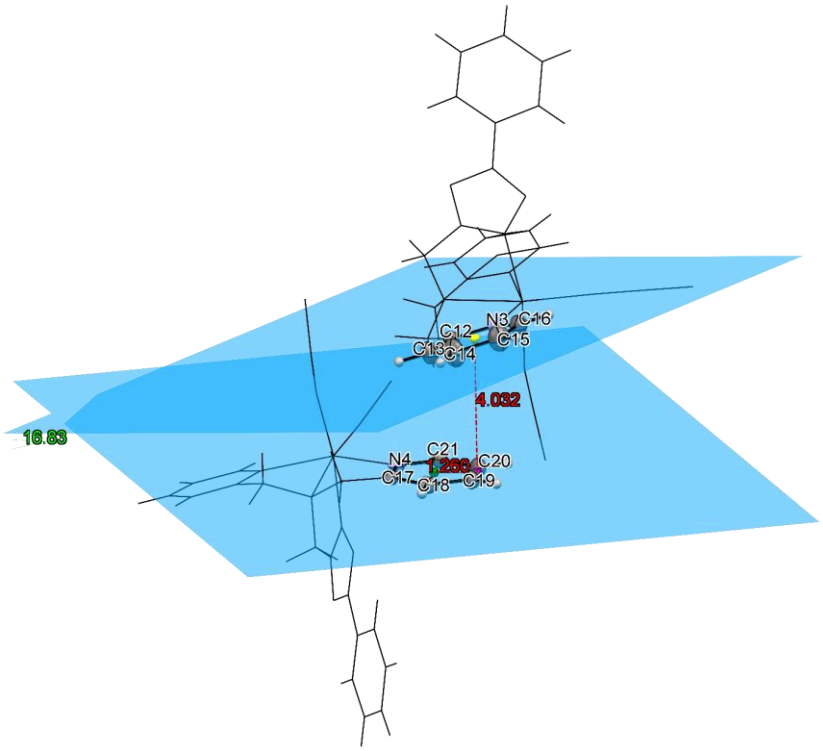


Figure F.71 π-π interaction in **C20**·3MeOH. Least-squares mean plane A is defined by N4, C17, C18, C19, C20 and C21. Plane B is defined by N3, C12, C13, C14, C15 and C16 of an adjacent molecule. Green point – center of the aromatic ring in A. Yellow point – center of the aromatic ring in B. Purple point – orthogonal intersection of the aromatic center in B onto plane A. *Offset r* = 1.260 Å, *interplanar distance* d_{AB} = 4.032 Å, *interplanar angle* θ = 16.83 °. ORTEP representation with atomic displacement parameters set to 50 % probability.

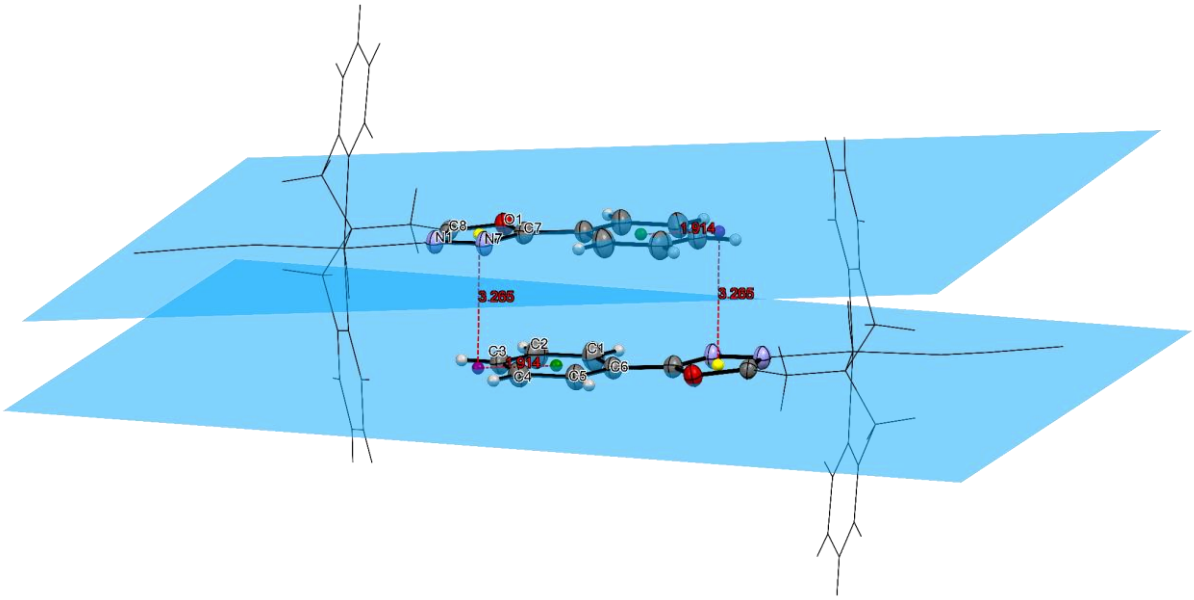


Figure F.72 π-π interaction in **C20**·3MeOH. Least-squares mean plane A is defined by C1, C2, C3, C4, C5 and C6. Plane B is defined by O1, C7, N7, N1 and C8 of an adjacent molecule. Green point – center of the aromatic ring in A. Yellow point – center of the aromatic ring in B. Purple point – orthogonal intersection of the aromatic center in B onto plane A. *Offset r* = 1.914 Å, *interplanar distance* d_{AB} = 3.265 Å, *interplanar angle* θ = 5.9 °. ORTEP representation with atomic displacement parameters set to 50 % probability.

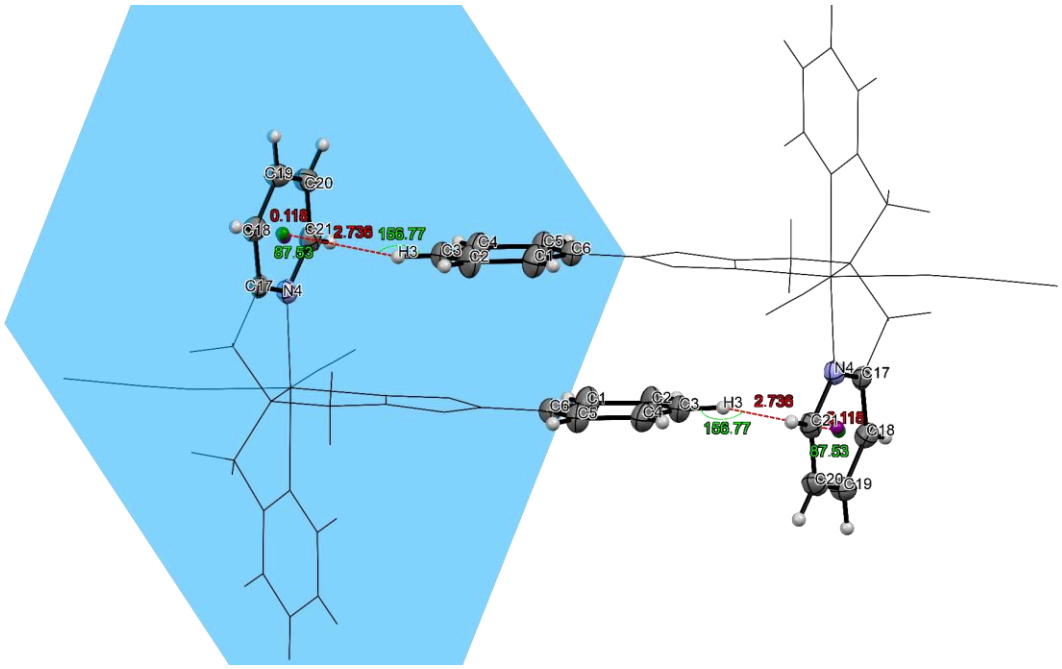


Figure F.73 C-H···π interaction in **C20**·3MeOH. Least-squares plane A is defined by N4, C17, C18, C19, C20 and C21. Interacting C-H fragment is labeled as C3-H3. Green point – center of the aromatic ring in A. Purple point – orthogonal intersection of H13 onto plane A. *Offset* r = 0.118 Å, *interaction distance* d_{QH} = 2.736 Å, α = 156.77 ° and β = 87.53 °. ORTEP representation with atomic displacement parameters set to 50 % probability.

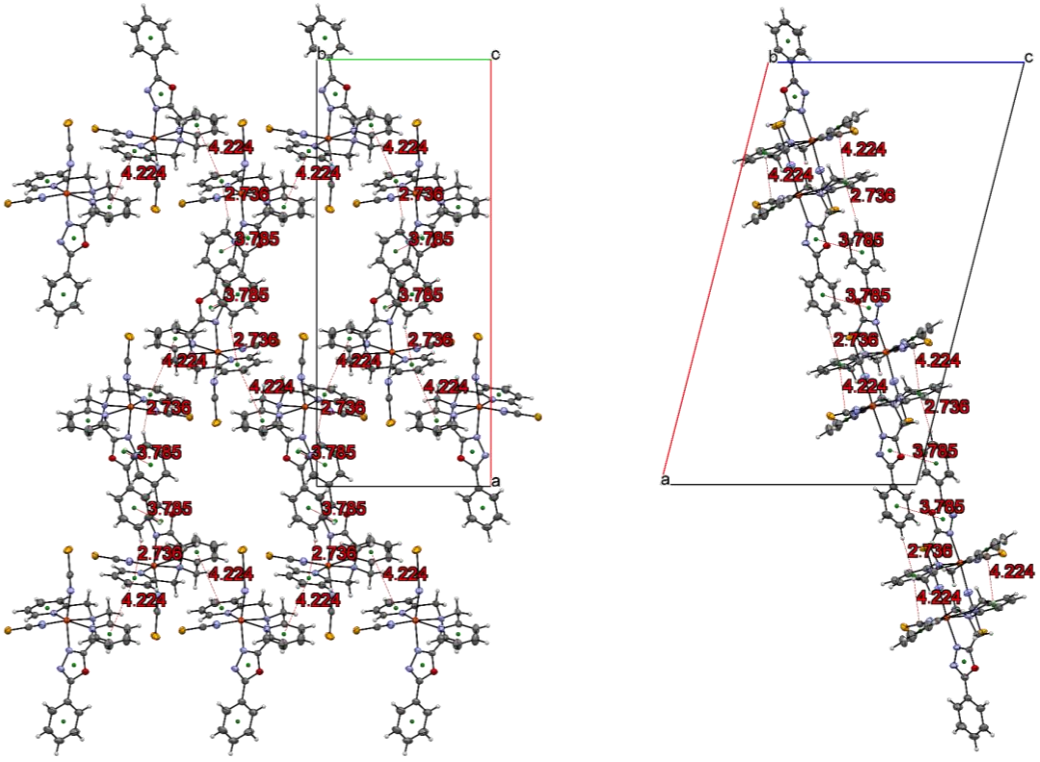


Figure F.74 Two-dimensional network of complex molecules in **C20**·3MeOH due to intermolecular π-π interactions with view along the c-axis (left) and b-axis (right). The centers of involved aromatic rings are displayed as green points. Distances are displayed as red dashed lines and numbers. Solvent molecules are omitted for better vision. ORTEP representation with atomic displacement parameters set to 50 % probability.

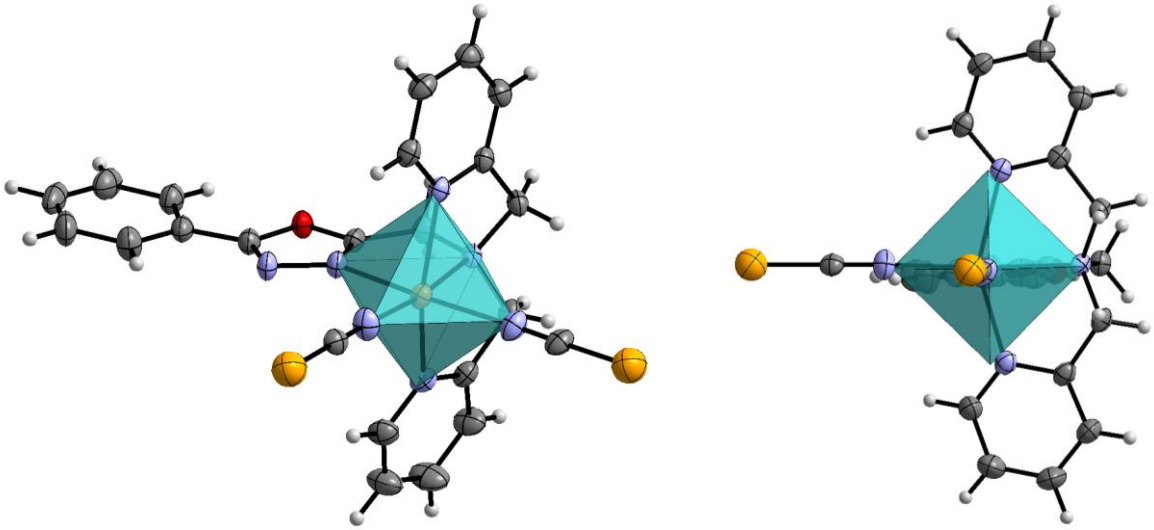


Figure F.75 Molecular structure of **C20**·3MeOH and its ideal coordination octahedron with front view (left) and view along the Fe-N5 axis (right), calculated with SHAPE.[62] ORTEP representation with atomic displacement parameters set to 50 % probability.

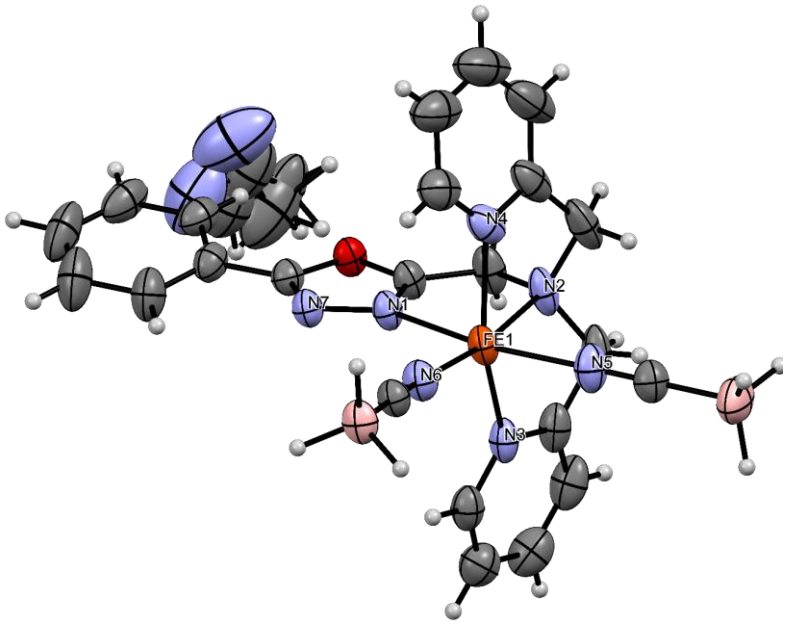


Figure F.76 Asymmetric Unit of **C21**·1MeCN (240 K). ORTEP representation with atomic displacement parameters set to 50 % probability.

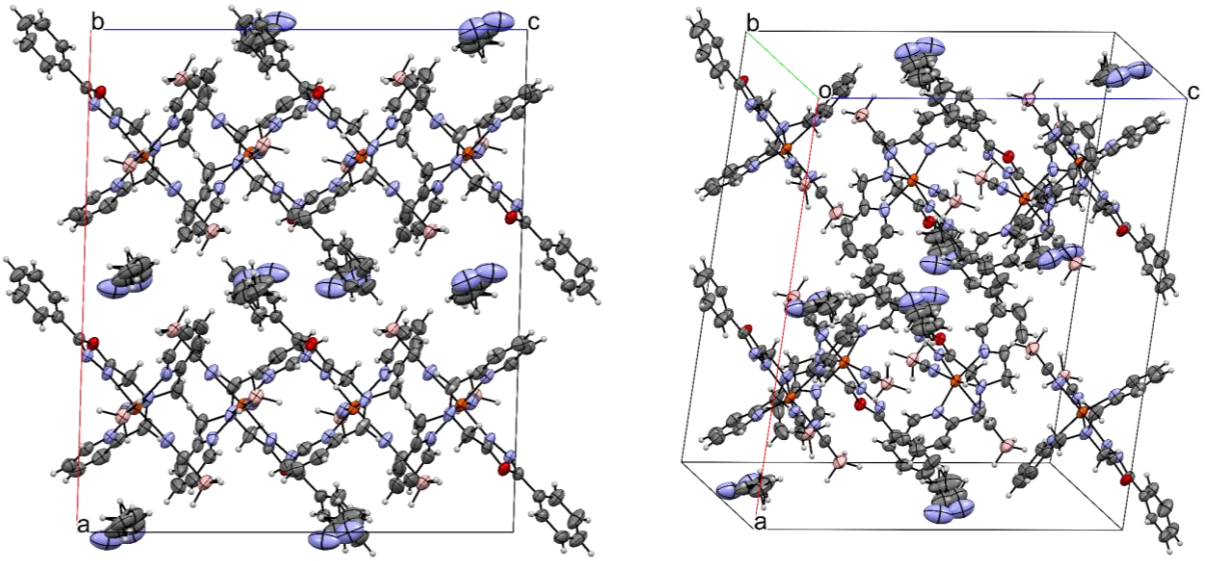


Figure F.77 Unit cell of **C21**·1MeCN (240 K) with view along the b-axis (left) and perspective view (right). ORTEP representation with atomic displacement parameters set to 50 % probability.

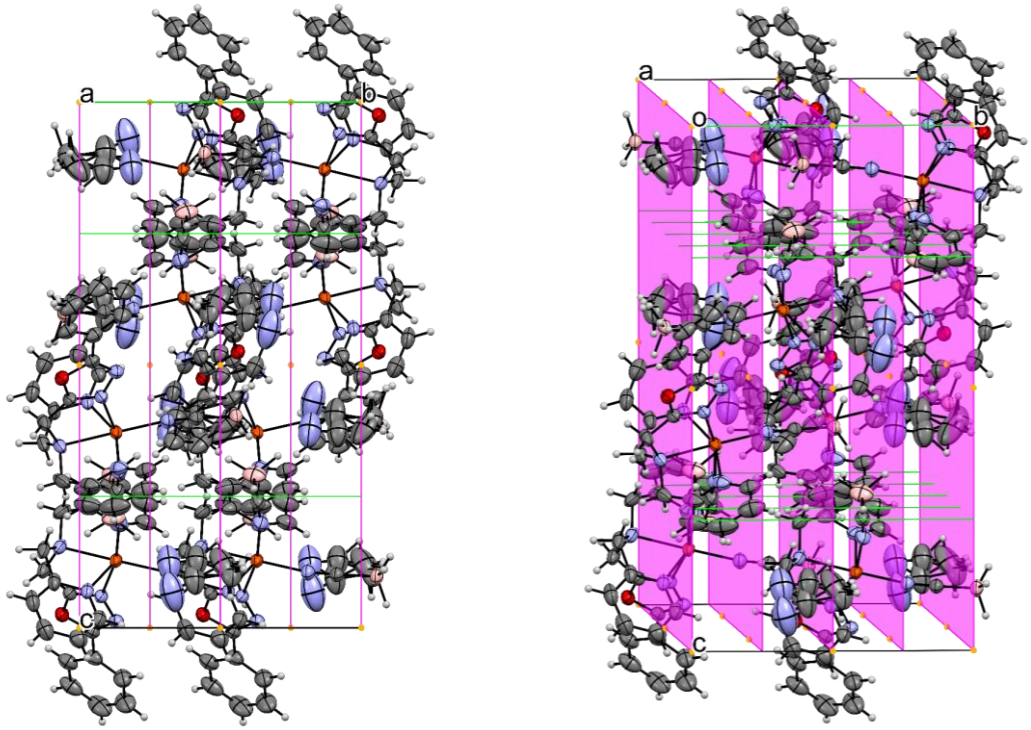


Figure F.78 Unit cell of **C21**·1MeCN (240 K) with present symmetry elements with view along the a-axis (left) and perspective view (right). Centers of Inversion – yellow dots, Two-fold Axis – green lines, Mirror Glide Planes – purple planes.

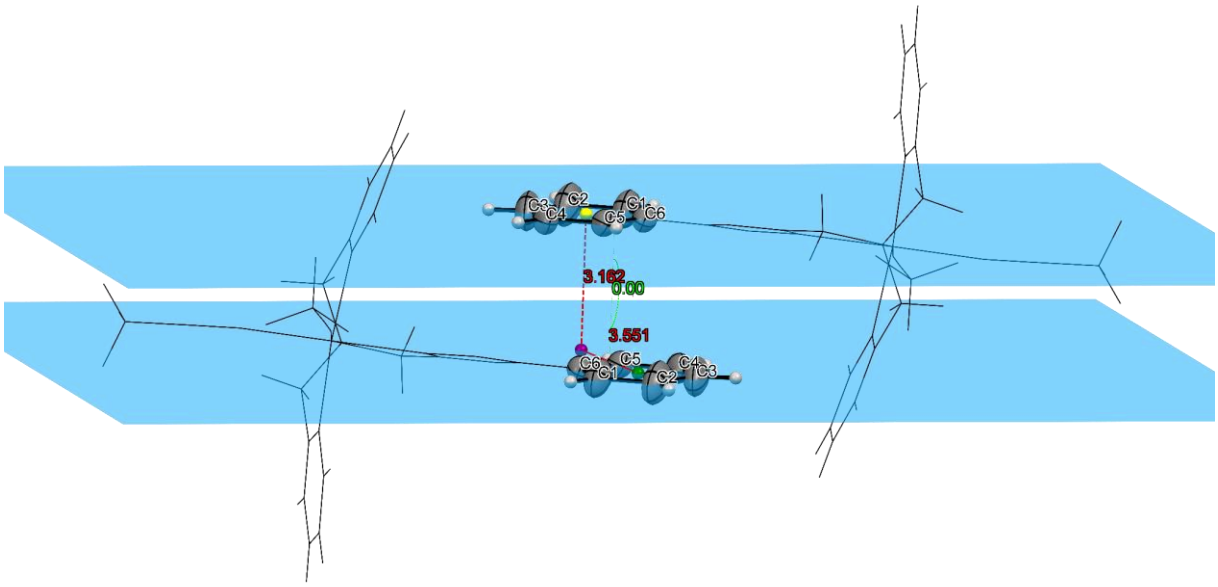


Figure F.79 π-π interaction in **C21**·1MeCN (240 K). Least-squares mean plane A is defined by C1, C2, C3, C4, C5 and C6. Plane B is defined by C1, C2, C3, C4, C5 and C6 of an adjacent molecule. Green point – center of the aromatic ring in A. Yellow point – center of the aromatic ring in B. Purple point – orthogonal intersection of the aromatic center in B onto plane A. *Offset* r = 3.56 Å, *interplanar distance* d_{AB} = 3.16 Å, *interplanar angle* θ = 0 °. ORTEP representation with atomic displacement parameters set to 50 % probability.

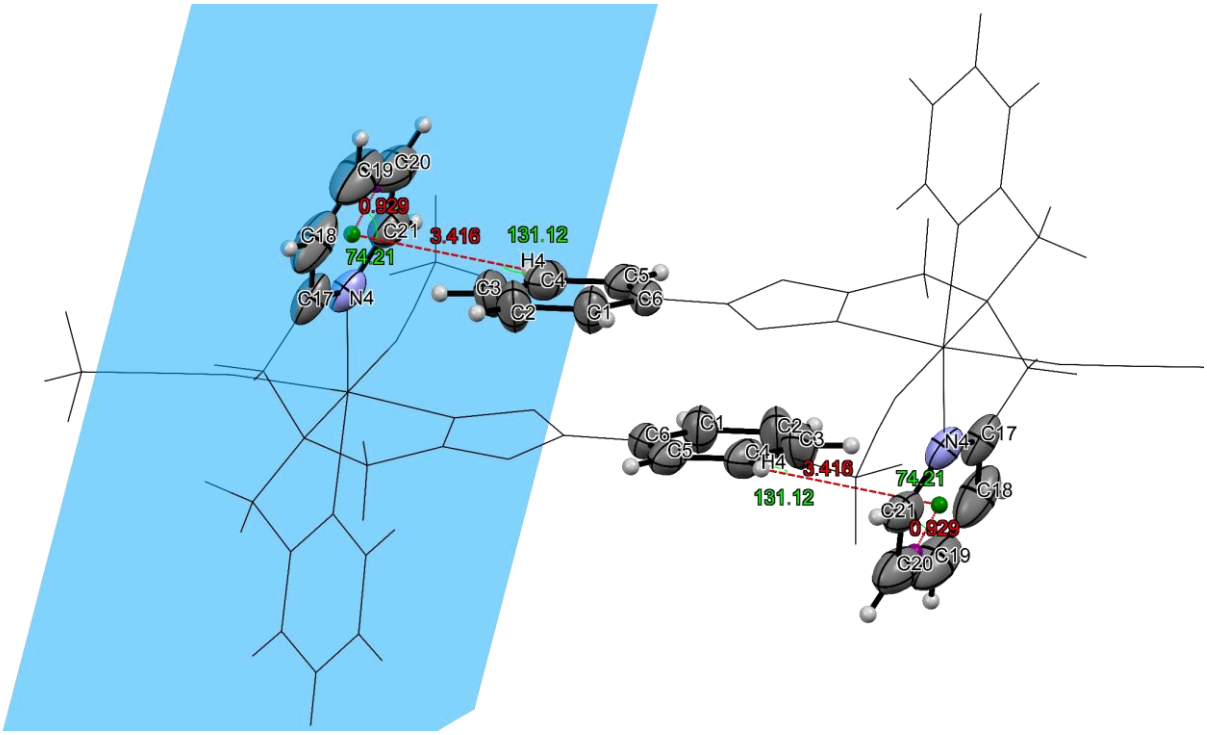


Figure F.80 C-H···π interaction in **C21**·1MeCN (240 K). Least-squares plane A is defined by N4, C17, C18, C19, C20 and C21. Interacting C-H fragment is labeled as C4-H4. Green point – center of the aromatic ring in A. Purple point – orthogonal intersection of H19 onto plane A. *Offset* r = 0.93 Å, *interaction distance* d_{QH} = 3.42 Å, α = 131.1 ° and β = 74.2 °. ORTEP representation with atomic displacement parameters set to 50 % probability.

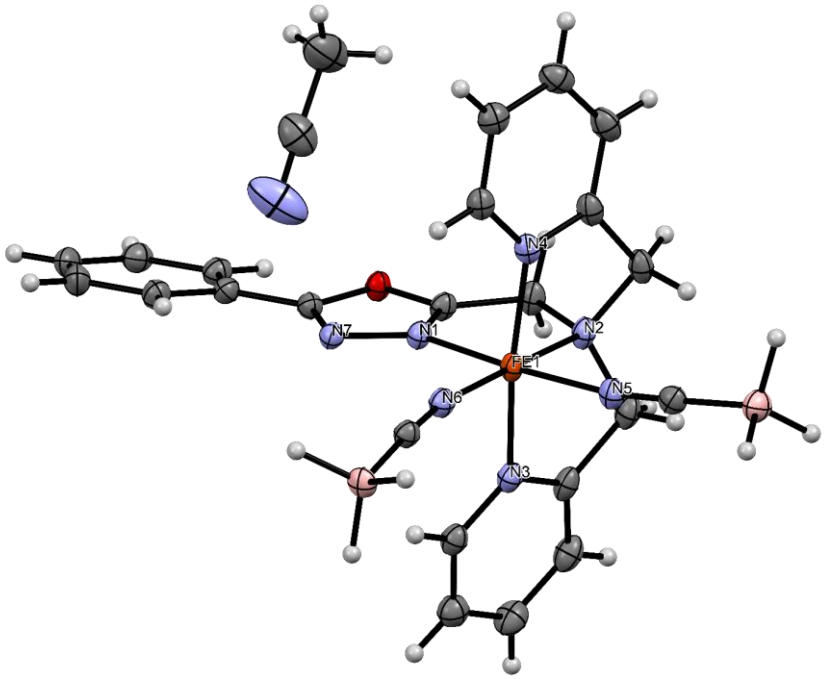


Figure F.81 Asymmetric Unit of **C21**·1MeCN (120 K). ORTEP representation with atomic displacement parameters set to 50 % probability.

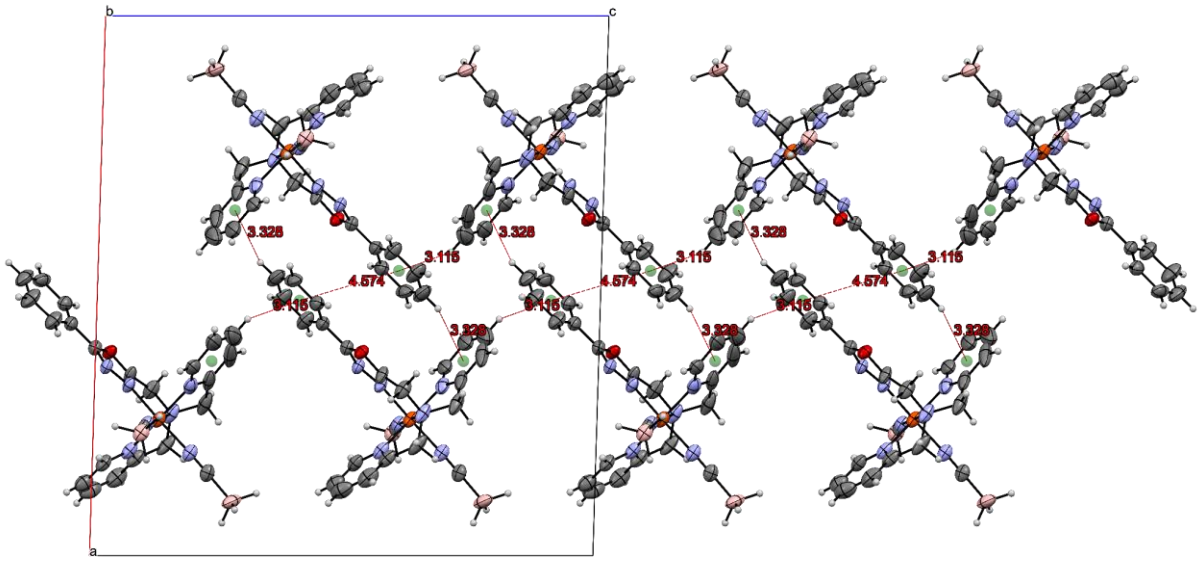


Figure F.82 One-dimensional network of “complex dimers” in **C21**·1.8MeOH. Red dashed lines represent intermolecular distances. ORTEP representation with atomic displacement parameters set to 50 % probability.

Table F.3 Intermolecular π-π interaction in the crystalline phase of **C21**·1.8MeOH with references to the corresponding figures.

π-π interaction	Parameters	Figure reference
Pyridyl-Phenyl- π-π interaction (T-shape) Type V	d_{QH} = 3.12 Å r = 1.49 Å α = 130.3 ° β = 61.3 °	Figure F.83
Phenyl-Phenyl- π-π interaction	d_{AB} = 3.16 Å r = 3.55 Å θ = 0 °	Figure F.84
Phenyl-Pyridyl- π-π interaction (T-shape) Type V	d_{QH} = 3.33 Å r = 1.03 Å α = 129.4 ° β = 71.9 °	Figure F.85

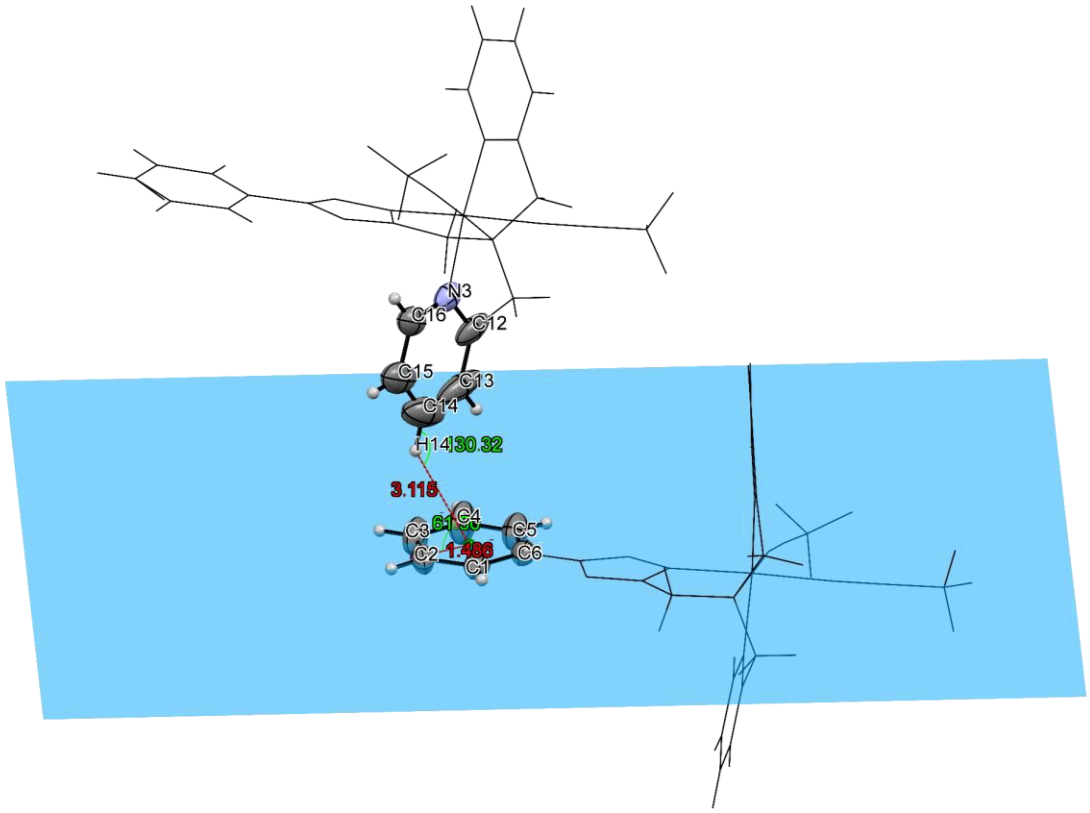


Figure F.83 C-H···π interaction in **C21**·1.8MeOH. Least-squares plane A is defined by C1, C2, C3, C4, C5 and C6. Interacting C-H fragment is labeled as C14-H14. Green point – center of the aromatic ring in A. Purple point – orthogonal intersection of H14 onto plane A. *Offset r* = 1.49 Å, *interaction distance* d_{QH} = 3.12 Å, α = 130.3 ° and β = 61.3 °. ORTEP representation with atomic displacement parameters set to 50 % probability.

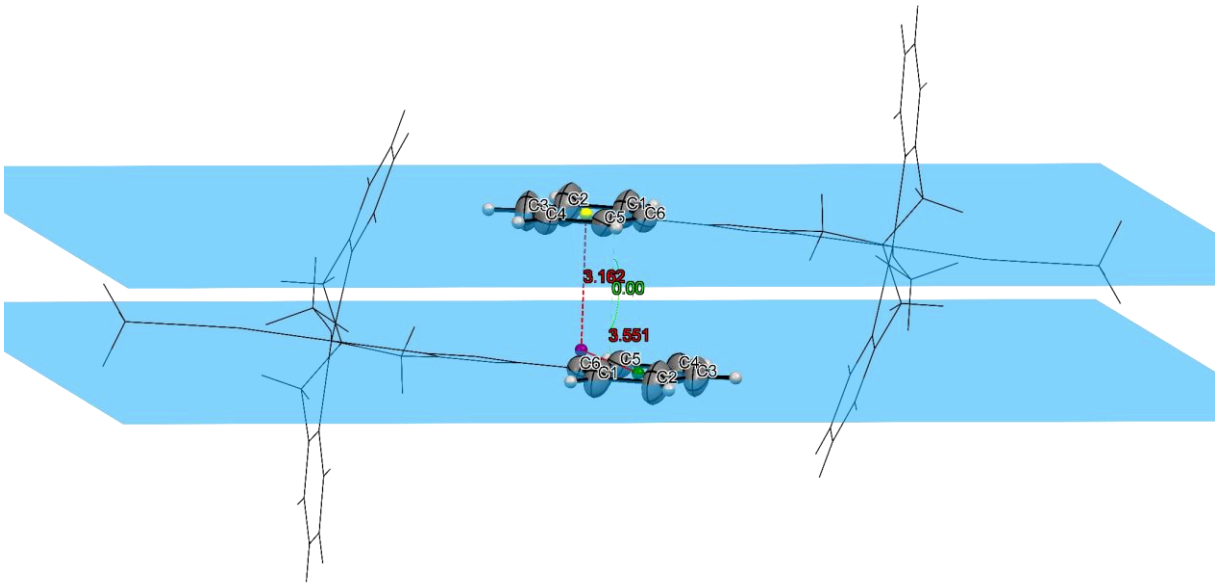


Figure F.84 π-π interaction in **C21**·1.8MeOH. Least-squares mean plane A is defined by C1, C2, C3, C4, C5 and C6. Plane B is defined by C1, C2, C3, C4, C5 and C6 of an adjacent molecule. Green point – center of the aromatic ring in A. Yellow point – center of the aromatic ring in B. Purple point – orthogonal intersection of the aromatic center in B onto plane A. *Offset r* = 3.55 Å, *interplanar distance* d_{AB} = 3.16 Å, *interplanar angle* θ = 0 °. ORTEP representation with atomic displacement parameters set to 50 % probability.

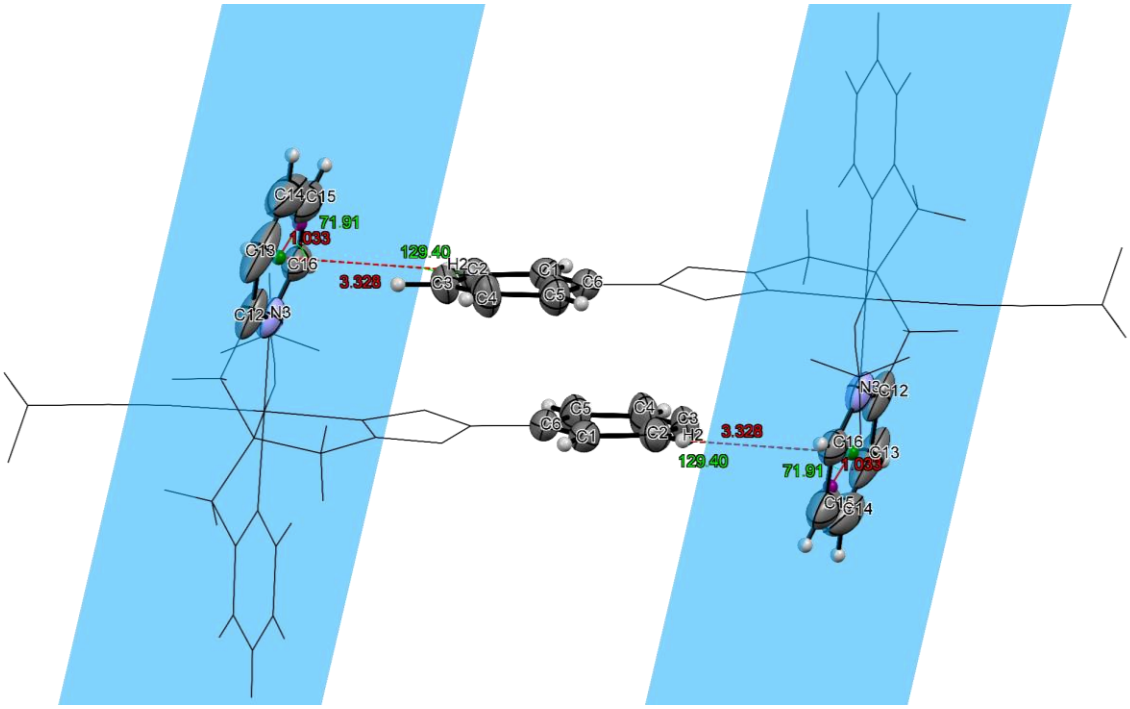


Figure F.85 C-H···π interaction in **C21**·1.8MeOH. Least-squares plane A is defined by N3, C12, C13, C14, C15 and C16. Interacting C-H fragment is labeled as C2-H2. Green point – center of the aromatic ring in A. Purple point – orthogonal intersection of H2 onto plane A. *Offset r* = 1.03 Å, *interaction distance* d_{QH} = 3.33 Å, α = 129.4 ° and β = 71.9 °. ORTEP representation with atomic displacement parameters set to 50 % probability.

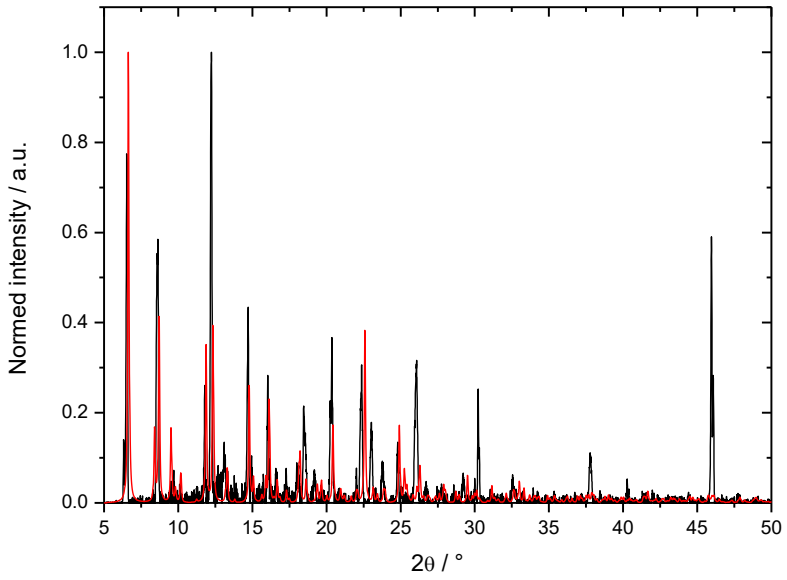


Figure F.86 Powder XRD of **C21**·1.8MeOH. Black solid lines represent experimental data, while the red lines display the calculated pattern.

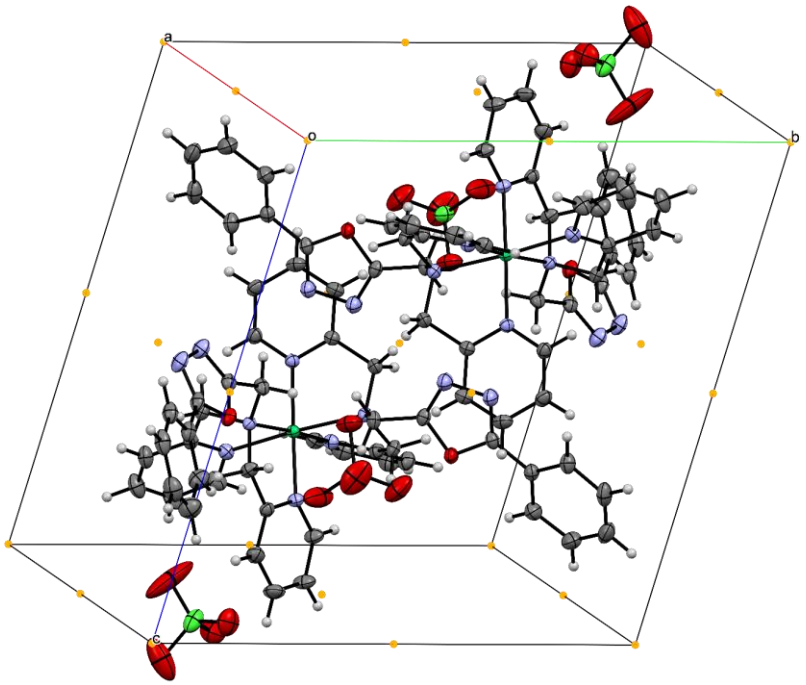


Figure F.87 Unit cell of **C22** with perspective view. Centers of inversion are displayed as yellow circles. ORTEP representation with atomic displacement parameters set to 50 % probability.

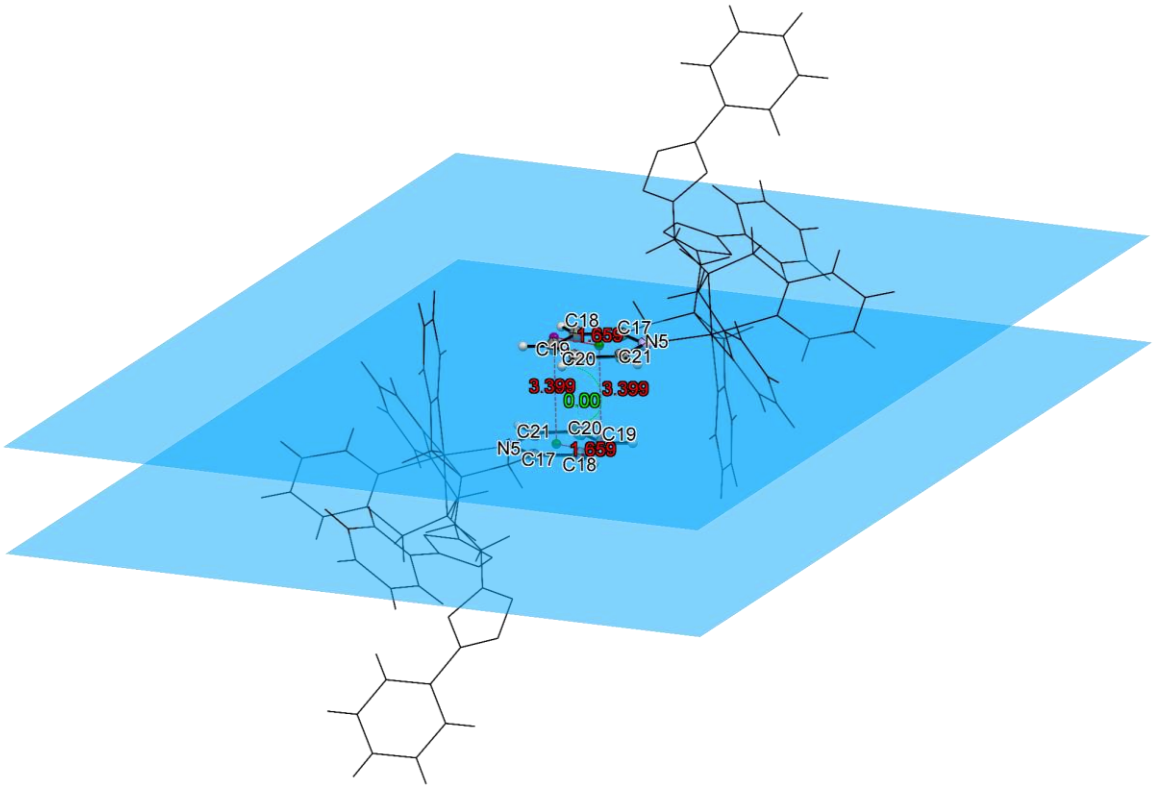


Figure F.88 π-π interaction in **C22-** Least-squares mean plane A is defined by N5, C17, C18, C19, C20 and C21. Plane B is defined by N5, C17, C18, C19, C20 and C21 of an adjacent molecule. Green point – center of the aromatic ring in A. Yellow point – center of the aromatic ring in B. Purple point – orthogonal intersection of the aromatic center in B onto plane A. *Offset r* = 1.66 Å, *interplanar distance* d_{AB} = 3.40 Å, *interplanar angle* θ = 0 °. ORTEP representation with atomic displacement parameters set to 50 % probability.

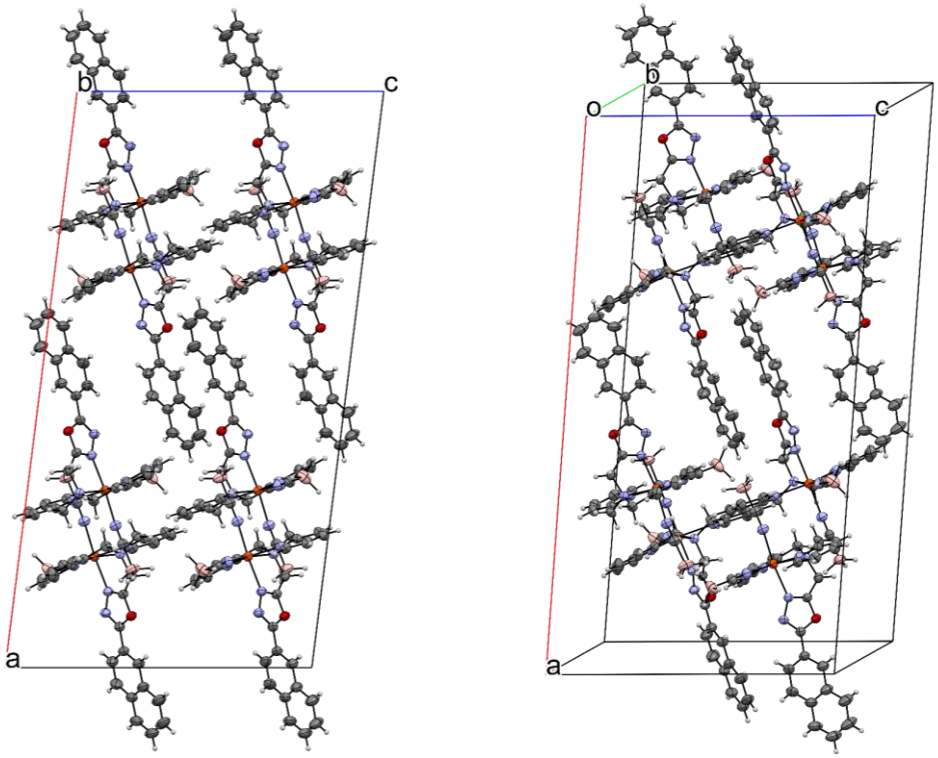


Figure F.89 Unit cell of **C23**·4.5MeCN with view along the b-axis (left) and perspective view (right). ORTEP representation with atomic displacement parameters set to 50 % probability.

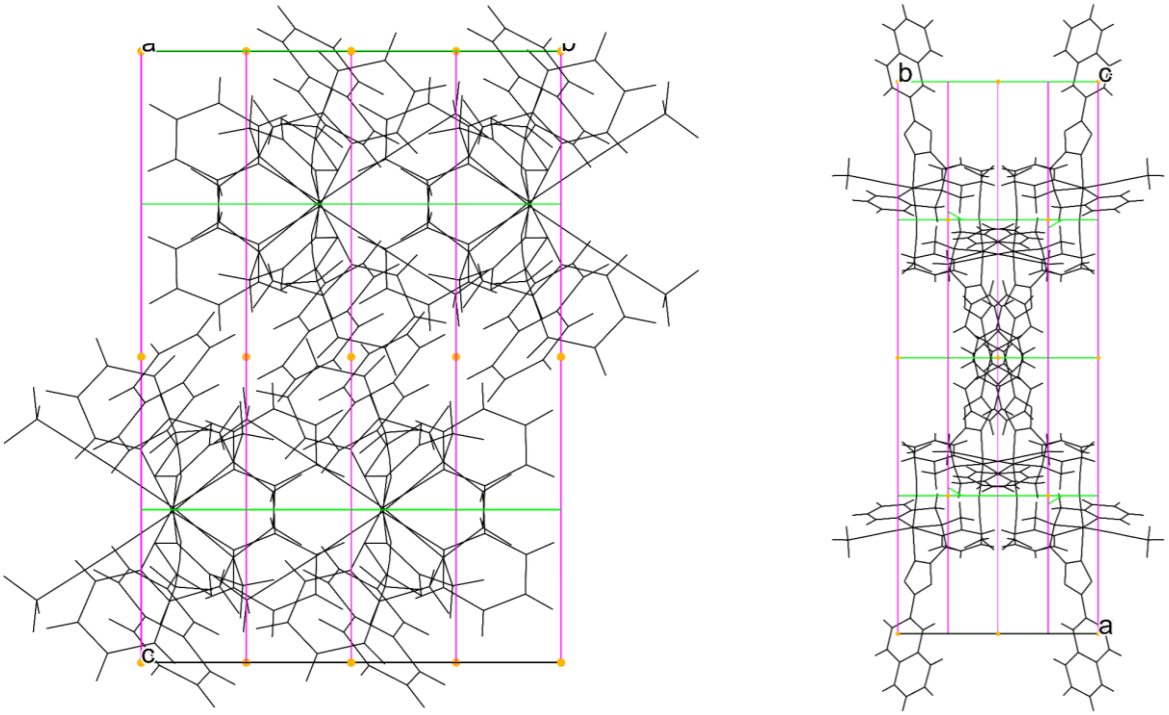


Figure F.90 Unit cell of **C23**·4.5MeCN with present symmetry elements with view along the a-axis (left) and view along the c-axis (right). Centers of Inversion – yellow dots, Two-fold Axis – green lines, Mirror Glide Planes – purple planes. Molecules are displayed in the wireframe model for better vision.

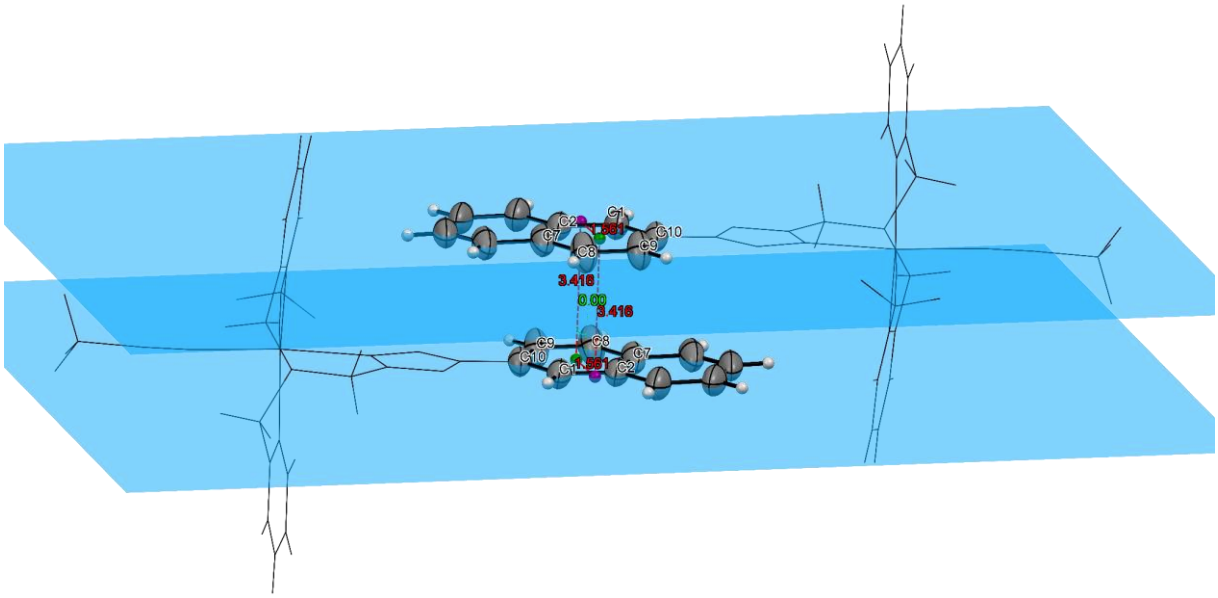


Figure F.91 π-π interaction in **C23**·4.5MeCN Least-squares mean plane A is defined by C1, C2, C7, C8, C9 and C10. Plane B is defined by C1, C2, C7, C8, C9 and C10 of an adjacent molecule. Green point – center of the aromatic ring in A. Purple point – orthogonal intersection of the aromatic center in B onto plane A. *Offset r* = 1.56 Å, *interplanar distance* d_{AB} = 3.42 Å, *interplanar angle* θ = 0 °. ORTEP representation with atomic displacement parameters set to 50 % probability.

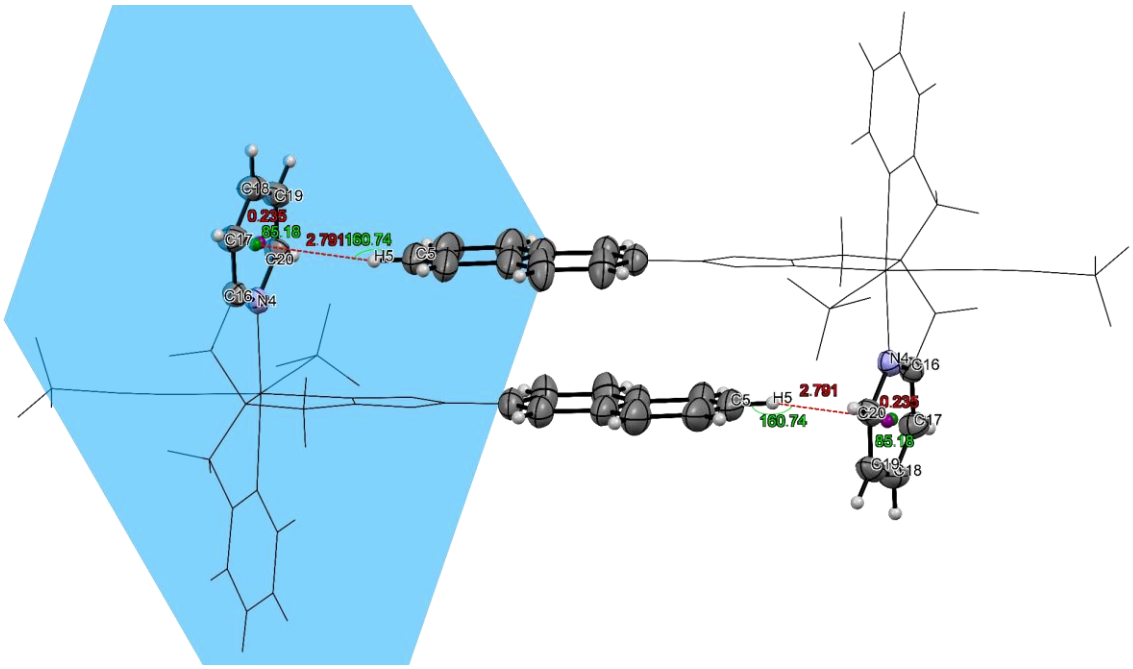


Figure F.92 C-H···π interaction in **C23**·4.5MeCN. Least-squares plane A is defined by N4, C16, C17, C18, C19 and C20. Interacting C-H fragment is labeled as C5-H5. Green point – center of the aromatic ring in A. Purple point – orthogonal intersection of H5 onto plane A. *Offset r* = 0.24 Å, *interaction distance* d_{QH} = 2.79 Å, α = 160.7 ° and β = 85.2 °. ORTEP representation with atomic displacement parameters set to 50 % probability.

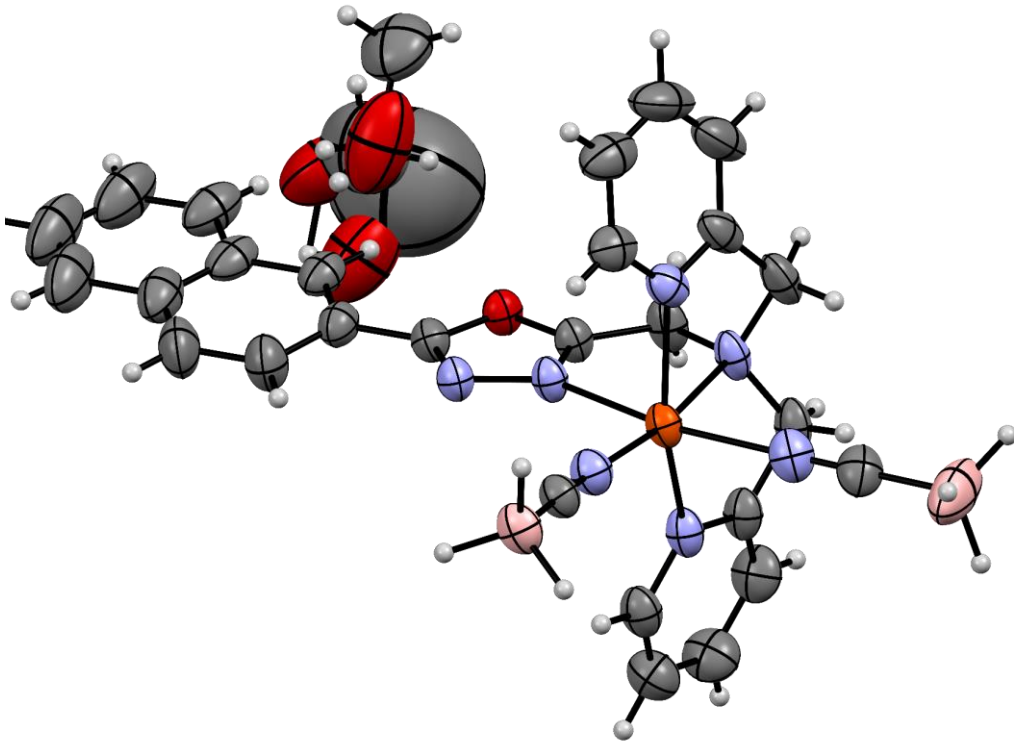


Figure F.93 Asymmetric Unit of **C23**·3MeOH (240 K). ORTEP representation with atomic displacement parameters set to 50 % probability.

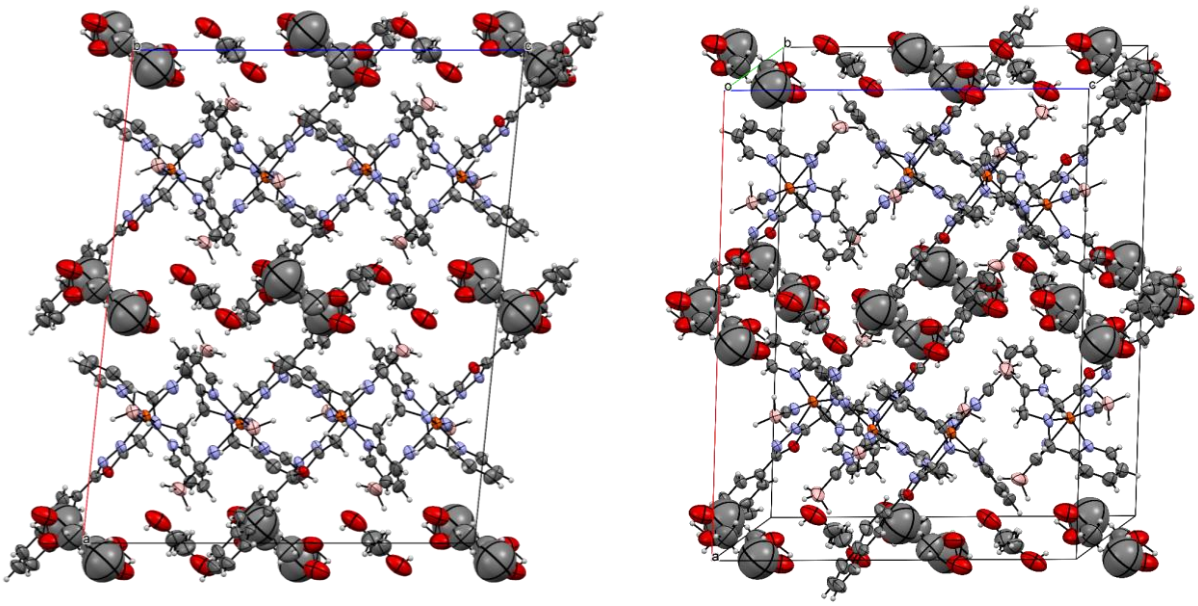


Figure F.94 Unit cell of **C23**·3MeOH (240 K) with view along the b-axis (left) and perspective view (right). ORTEP representation with atomic displacement parameters set to 50 % probability.

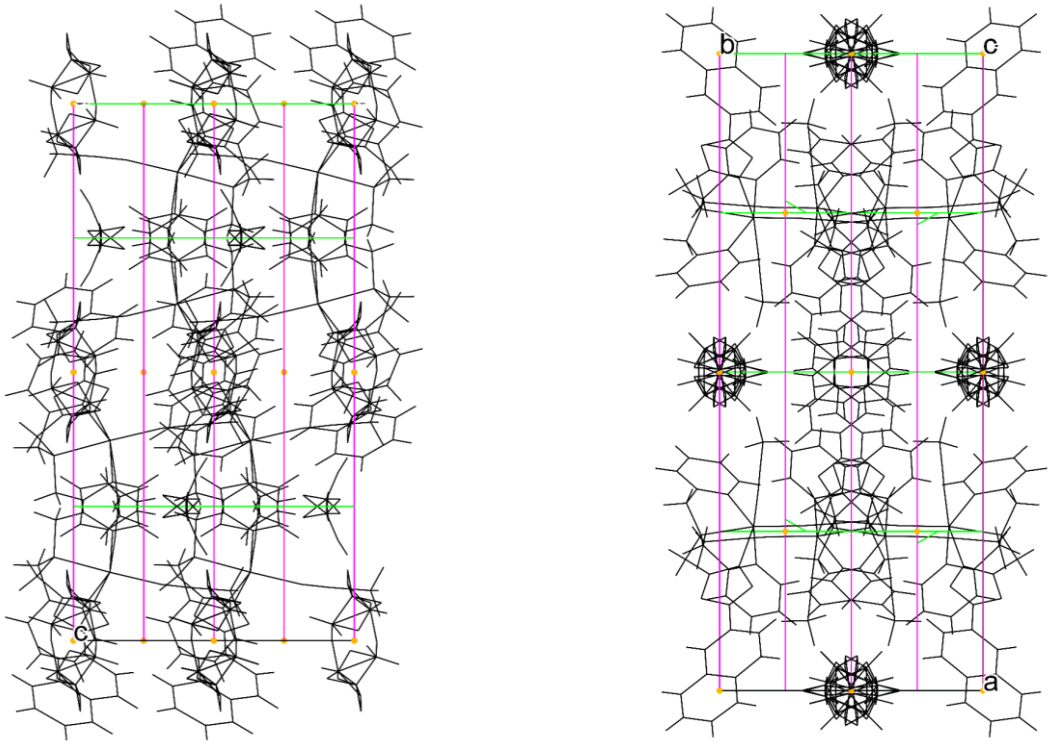


Figure F.95 Unit cell of **C23**·3MeOH (240 K) with present symmetry elements with view along the a-axis (left) and view along the c-axis (right). Centers of Inversion – yellow dots, Two-fold Axis – green lines, Mirror Glide Planes – purple planes. Molecules are displayed in the wireframe model for better vision.

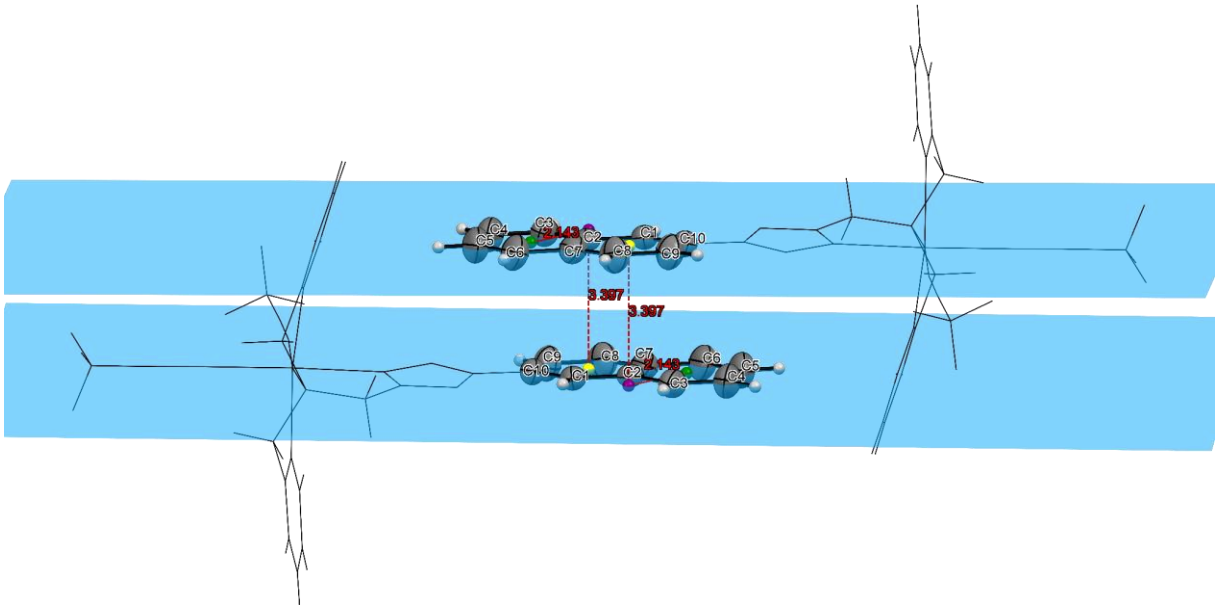


Figure F.96 π-π interaction in **C23**·3MeOH (240 K). Least-squares mean plane A is defined by C2, C3, C4, C5, C6 and C7. Plane B is defined by C1, C2, C7, C8, C9 and C10 of an adjacent molecule. Green point – center of the aromatic ring in A. Purple point – orthogonal intersection of the aromatic center in B onto plane A. *Offset* r = 2.14 Å, *interplanar distance* d_{AB} = 3.40 Å, *interplanar angle* θ = 0 °. ORTEP representation with atomic displacement parameters set to 50 % probability.

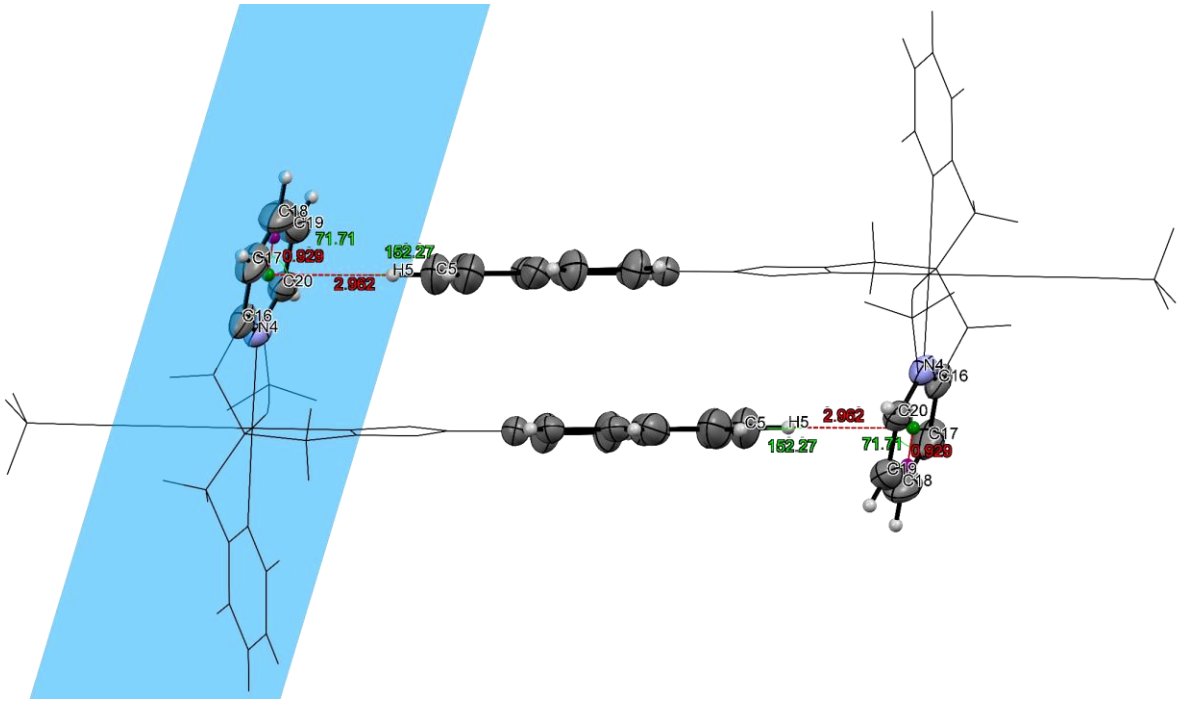


Figure F.97 C-H···π interaction in **C23**·3MeOH (240 K). Least-squares plane A is defined by N4, C16, C17, C18, C19 and C20. Interacting C-H fragment is labeled as C5-H5. Green point – center of the aromatic ring in A. Purple point – orthogonal intersection of H5 onto plane A. *Offset* r = 0.93 Å, *interaction distance* d_{QH} = 2.96 Å, α = 152.3 ° and β = 71.7 °. ORTEP representation with atomic displacement parameters set to 50 % probability.

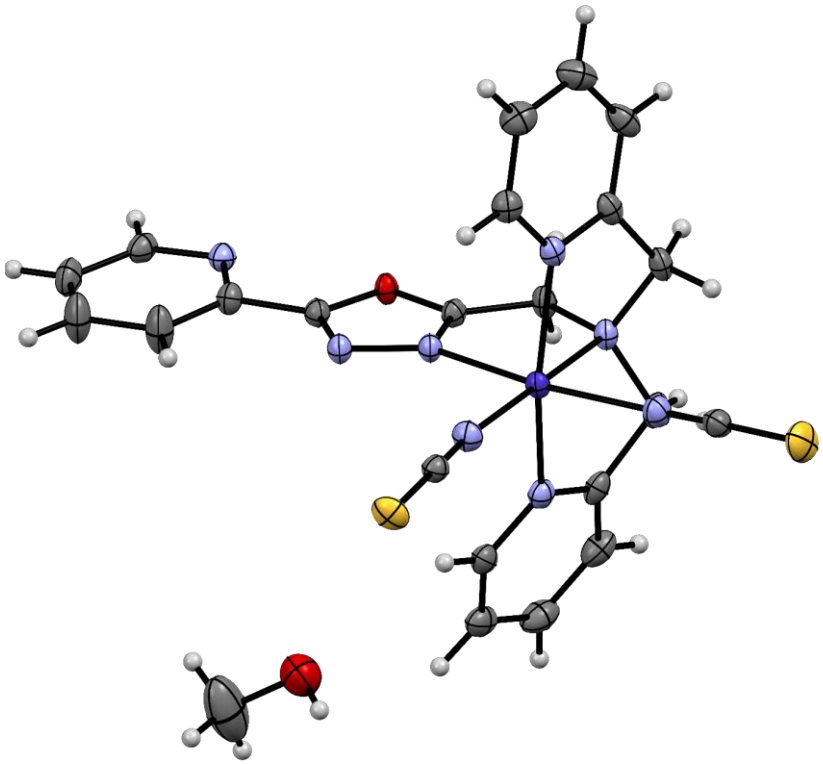


Figure F.98 Asymmetric Unit of **C26**. ORTEP representation with atomic displacement parameters set to 50 % probability.

Table F.4 Intermolecular π-π interaction in the crystalline phase of **C26** with references to the corresponding figures.

π-π interaction	Parameters	Figure reference
Pyridyl-Pyridyl- π-π interaction (T-shape) Type V	d_{QH} = 3.06 Å r = 1.58 Å α = 136.7 ° β = 58.9 °	Figure F.99
Pyridyl-Pyridyl- π-π interaction	d_{AB} = 3.44 Å r = 1.68 Å θ = 22.2 °	Figure F.100
Pyridyl-Pyridyl- π-π interaction (T-shape) Type III	d_{QH} = 2.94 Å r = 0.65 Å α = 147.5 ° β = 77.2 °	Figure F.101

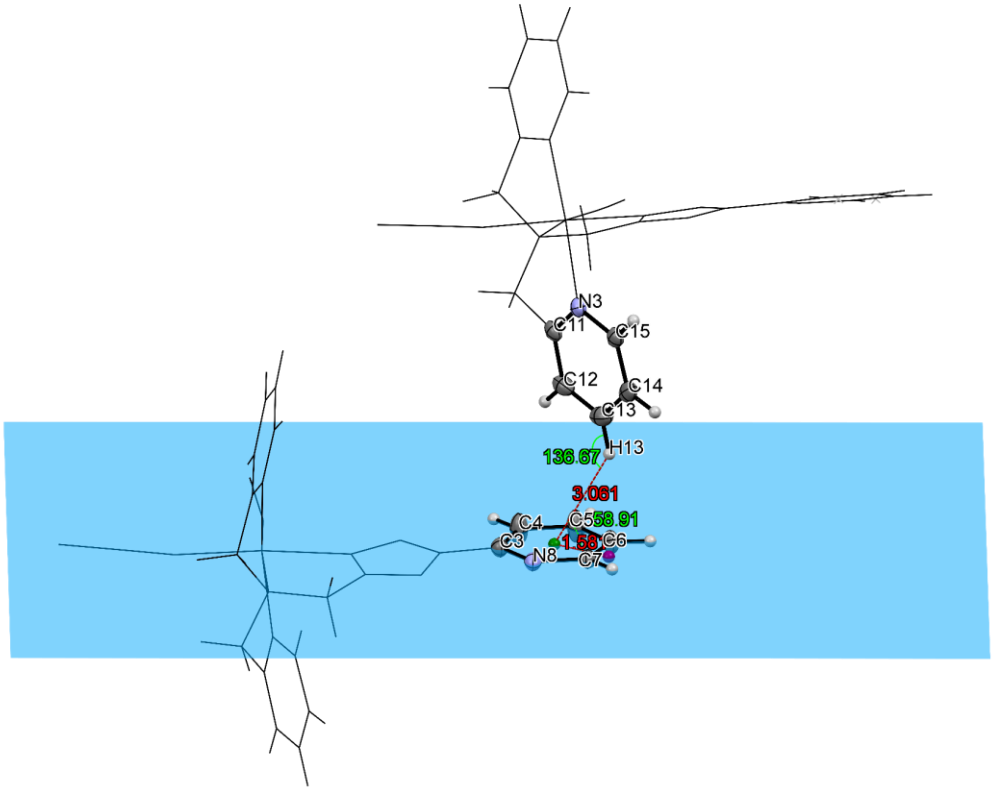


Figure F.99 C-H···π interaction in **C26**. Least-squares plane A is defined by N8, C3, C4, C5, C6 and C7. Interacting C-H fragment is labeled as C13-H13. Green point – center of the aromatic ring in A. Purple point – orthogonal intersection of H13 onto plane A. *Offset r* = 1.58 Å, *interaction distance* d_{QH} = 3.06 Å, α = 136.7 ° and β = 58.9 °. ORTEP representation with atomic displacement parameters set to 50 % probability.

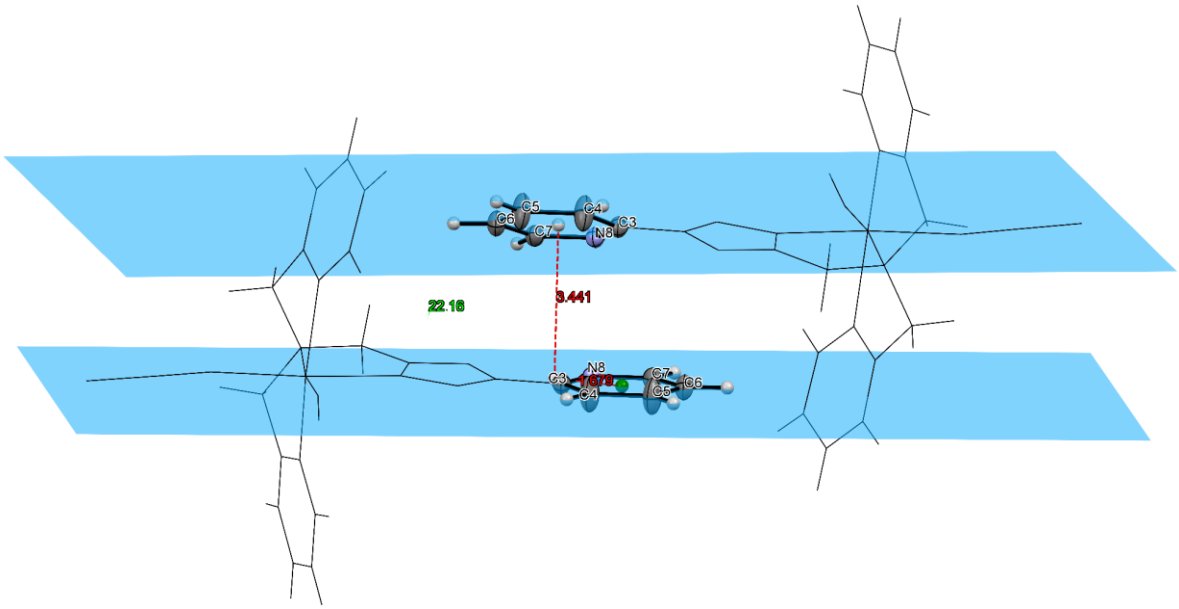


Figure F.100 π-π interaction in **C26**. Least-squares mean plane A is defined by N8, C3, C4, C5, C6 and C7. Plane B is defined by N8, C3, C4, C5, C6 and C7 of an adjacent molecule. Green point – center of the aromatic ring in A. Purple point – orthogonal intersection of the aromatic center in B onto plane A. *Offset r* = 1.68 Å, *interplanar distance* d_{AB} = 3.44 Å, *interplanar angle* θ = 22.2 °. ORTEP representation with atomic displacement parameters set to 50 % probability.

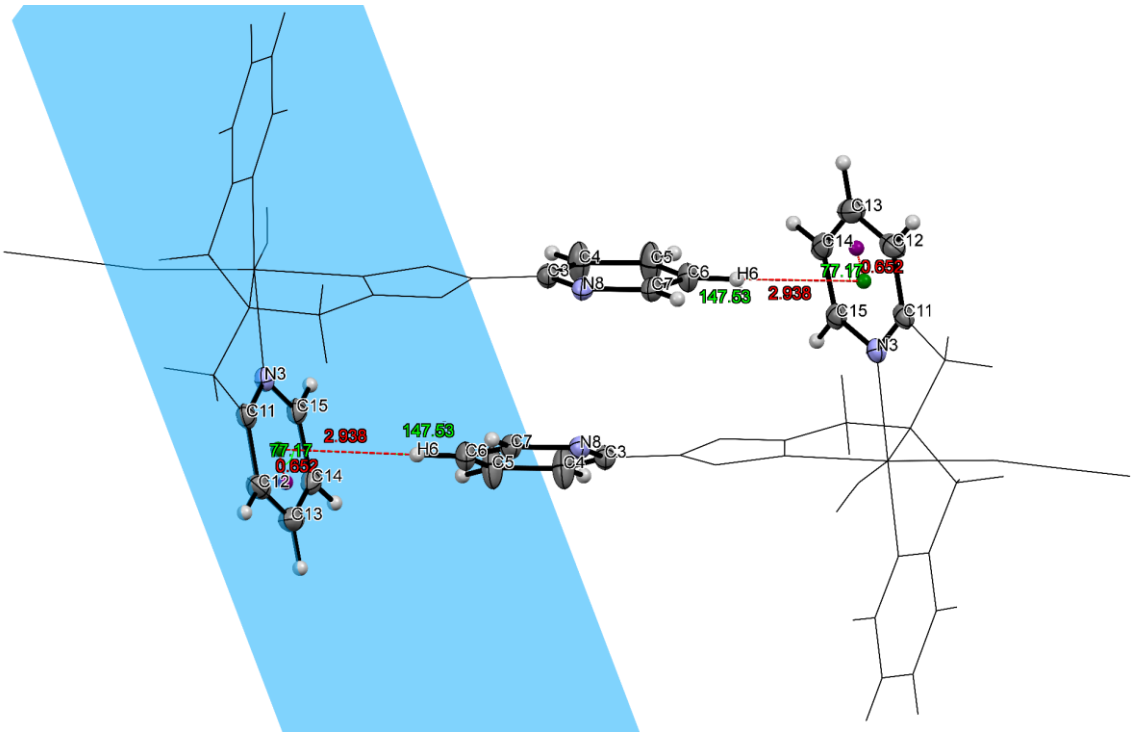


Figure F.101 C-H···π interaction in **C26**. Least-squares plane A is defined by N3, C11, C12, C13, C14 and C15. Interacting C-H fragment is labeled as C6-H6. Green point – center of the aromatic ring in A. Purple point – orthogonal intersection of H13 onto plane A. *Offset r* = 0.65 Å, *interaction distance* d_{QH} = 2.94 Å, α = 147.5 ° and β = 77.2 °. ORTEP representation with atomic displacement parameters set to 50 % probability.

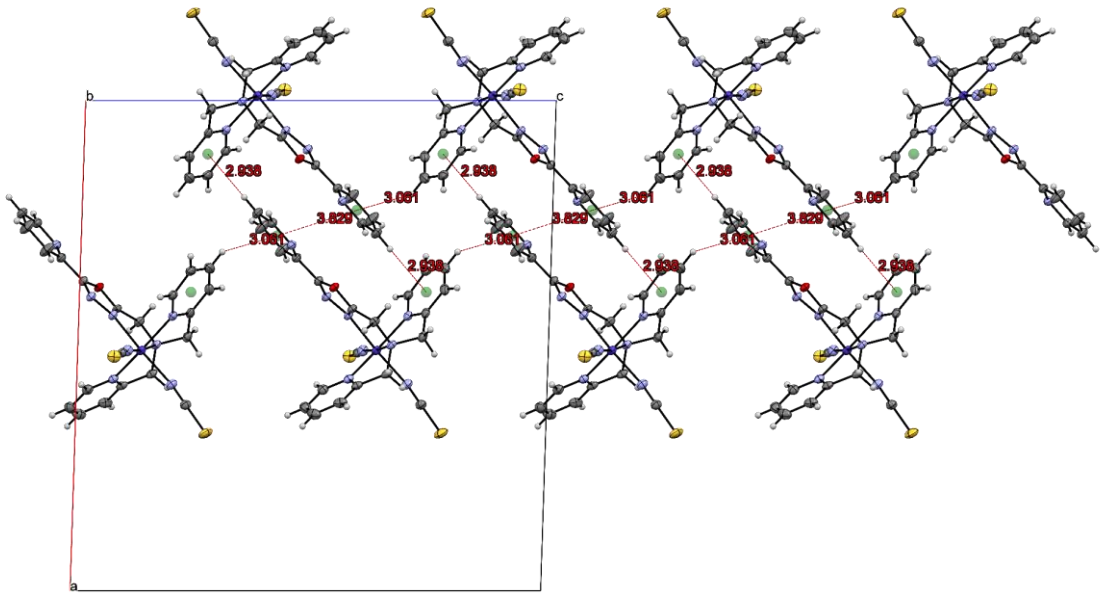


Figure F.102 One-dimensional network of “complex dimers” in **C26**. Red dashed lines represent intermolecular distances. ORTEP representation with atomic displacement parameters set to 50 % probability.

Table F.5 Percentage Composition in the three lowest Kramers doublet states of **26**, calculated with PHI.[201] Major contribution to the two lowest states at zero field are highlighted in bold.

Contribution		Absolute energy (cm^{-1}) of the Kramers doublet states at zero field (H = 0)					
M_S	M_L	-6.38E+02	-6.38E+02	-5.30E+02	-5.30E+02	8.62E+00	8.62E+00
-1.5	-1.0	0.0308042 %		0.0001202 %		1.1886428 %	0.0000111 %
-1.5	**0.0**		0.1296043 %		**93.5720268** %		0.0685007 %
-1.5	1.0	10.8110823 %		0.0346619 %		79.0351436 %	0.0007377 %
-0.5	-1.0		0.0717823 %		6.2148506 %		0.3276995 %
-0.5	**0.0**	**80.3692024** %		0.1736867 %		3.9687014 %	0.0000370 %
-0.5	1.0		8.5875246 %		0.0046537 %	0.0001438 %	15.4103787 %
0.5	-1.0	8.5875246 %		0.0046537 %		15.4103787 %	0.0001438 %
0.5	**0.0**		**80.3692024** %		0.1736867 %	0.0000370 %	3.9687014 %
0.5	1.0	0.0717823 %		6.2148506 %		0.3276995 %	
1.5	-1.0		10.8110823 %		0.0346619 %	0.0007377 %	79.0351436 %
1.5	**0.0**	0.1296043 %		**93.5720268** %		0.0685007 %	
1.5	1.0		0.0308042 %		0.0001202 %	0.0000111 %	1.1886428 %

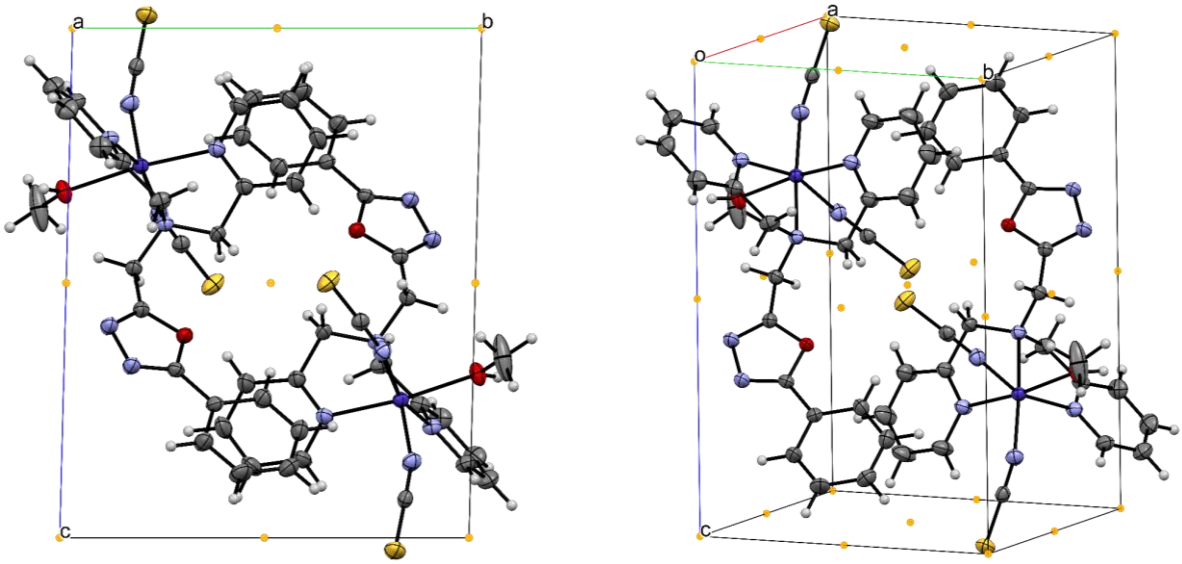


Figure F.103 Unit cell of **C27** with view along the a-axis (left) and perspective view (right). ORTEP representation with atomic displacement parameters set to 50 % probability.

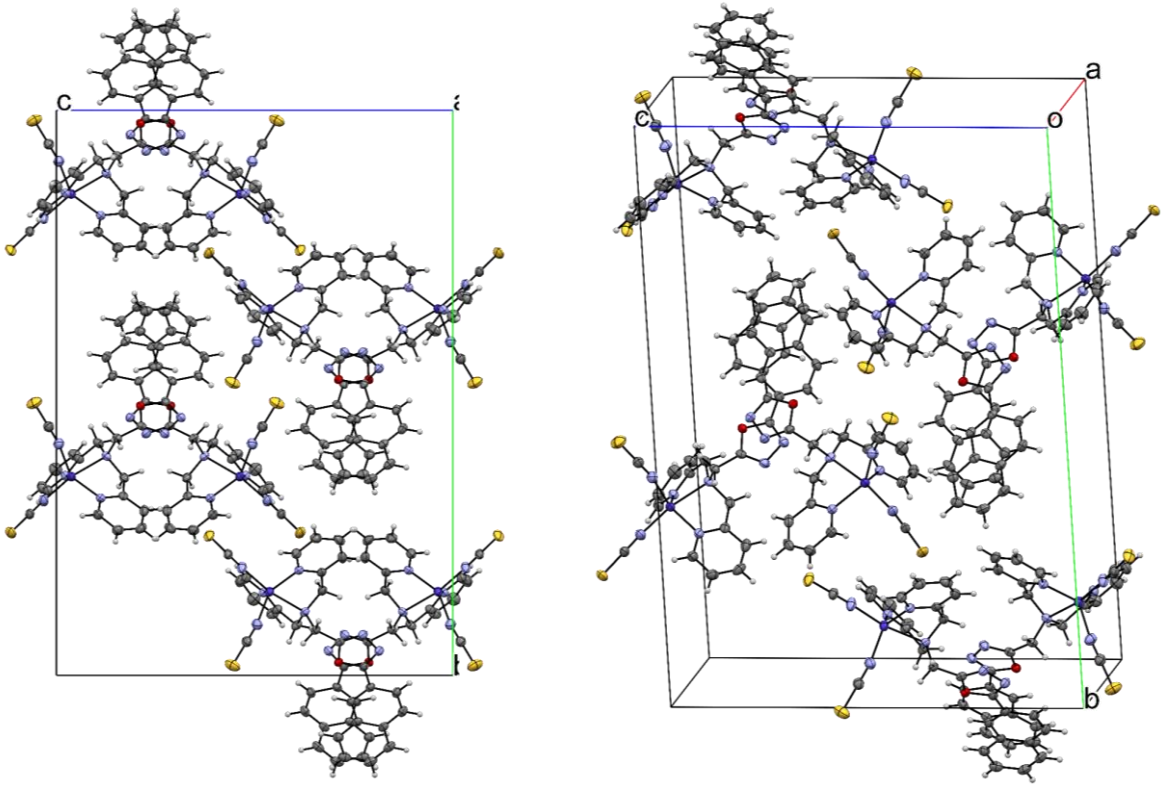


Figure F.104 Unit cell of **C28** with view along the a-axis (left) and perspective view (right). ORTEP representation with atomic displacement parameters set to 50 % probability.

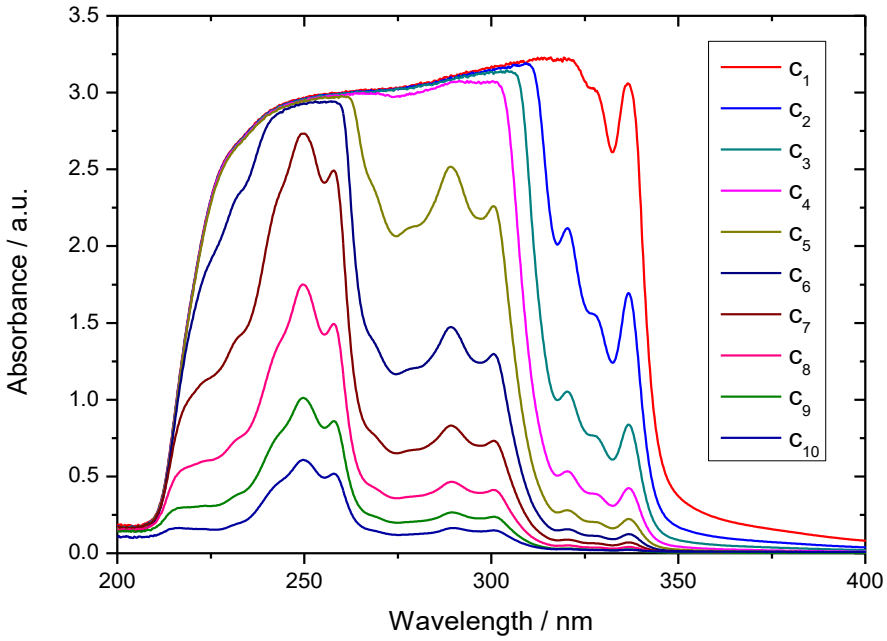
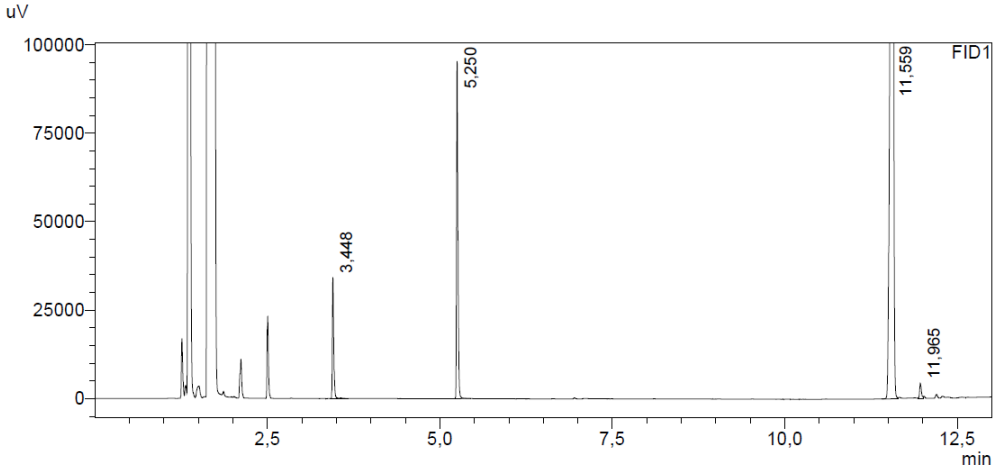


Figure F.105 UV/Vis spectra of $\mathbf{L^{Naph}}$ in n-butyronitril for different concentrations. Starting concentration c_1 is equal to 8 mmol/l. From measurement to measurement, the concentration was bisected. There was no absorption between 400-1000 nm observed.

<Chromatogram>



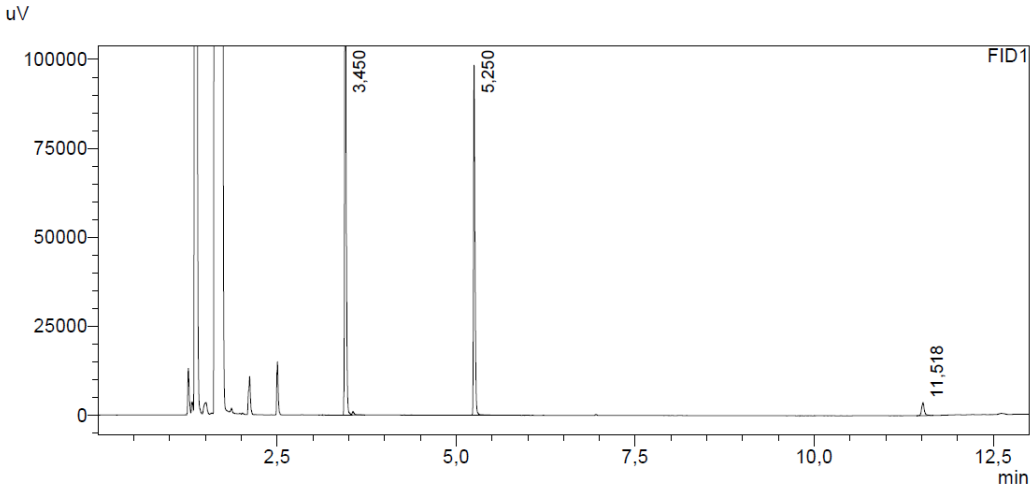
<Peak Table>

FID1

Peak#	Ret. Time	Area	Height	Conc.	Unit	Mark	Name
1	3,448	48846	33650	0,000		S	
2	5,250	134948	93599	0,000			
3	11,559	1072255	413912	0,000			
4	11,965	7577	4246	0,000		V	
Total		1263626	545407				

Figure F.106 Chromatogram of a standard 1 with m(cyclohexanol) = 20 mg and m(nitrobenzene) = 60 mg in 1 ml acetonitrile. The signal at 3.448 min correspond to cyclohexanol, while the one at 5.250 min belongs to nitrobenzene, which served as internal standard.

<Chromatogram>



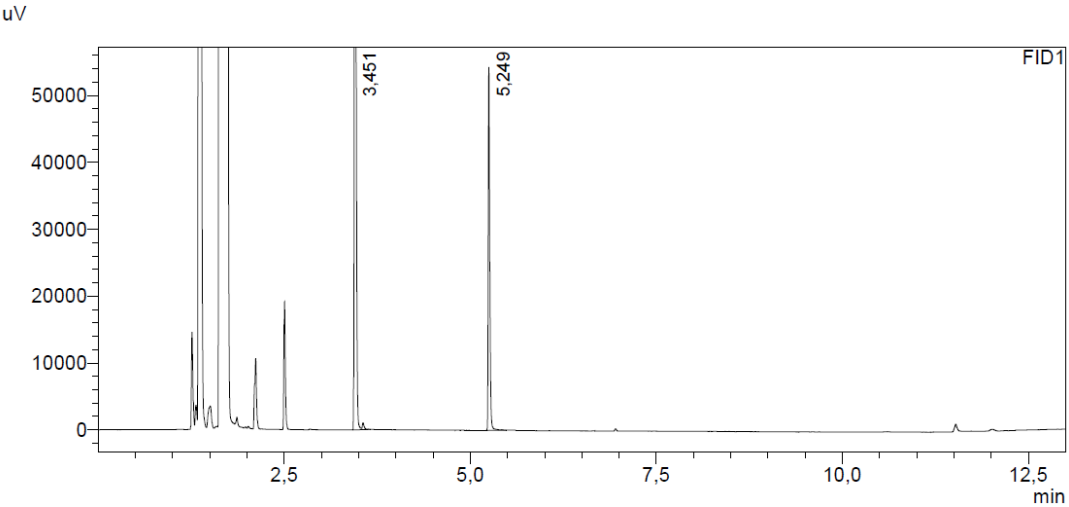
<Peak Table>

FID1

Peak#	Ret. Time	Area	Height	Conc.	Unit	Mark	Name
1	3,450	252229	178528	0,000		S	
2	5,250	139726	94054	0,000		S	
3	11,518	9367	3602	0,000			
Total		401322	276184				

Figure F.107 Chromatogram of a standard 2 with m(cyclohexanol) = 100 mg and m(nitrobenzene) = 60 mg in 1 ml acetonitrile. The signal at 3.450 min correspond to cyclohexanol, while the one at 5.250 min belongs to nitrobenzene, which served as internal standard.

<Chromatogram>



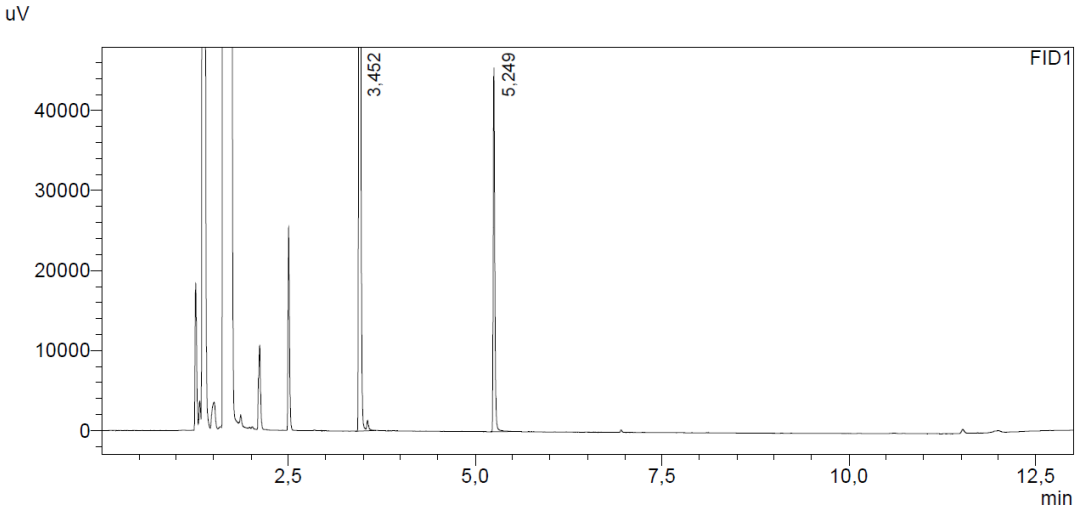
<Peak Table>

FID1

Peak#	Ret. Time	Area	Height	Conc.	Unit	Mark	Name
1	3,451	274134	193925	0,000		S	
2	5,249	78591	53568	0,000		S	
Total		352726	247493				

Figure F.108 Chromatogram of a standard 3 with m(cyclohexanol) = 180 mg and m(nitrobenzene) = 60 mg in 2 ml acetonitrile. The signal at 3.451 min correspond to cyclohexanol, while the one at 5.249 min belongs to nitrobenzene, which served as internal standard.

<Chromatogram>



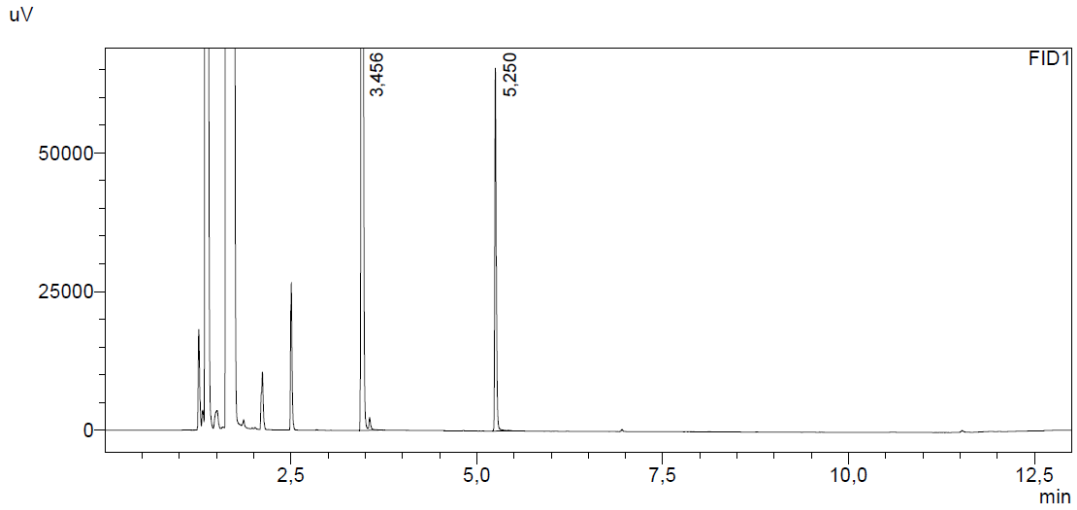
<Peak Table>

FID1

Peak#	Ret. Time	Area	Height	Conc.	Unit	Mark	Name
1	3,452	339268	241561	0,000		S	
2	5,249	66392	44893	0,000		S	
Total		405660	286454				

Figure F.109 Chromatogram of a standard 4 with m(cyclohexanol) = 260 mg and m(nitrobenzene) = 60 mg in 2 ml acetonitrile. The signal at 3.452 min correspond to cyclohexanol, while the one at 5.249 min belongs to nitrobenzene, which served as internal standard.

<Chromatogram>



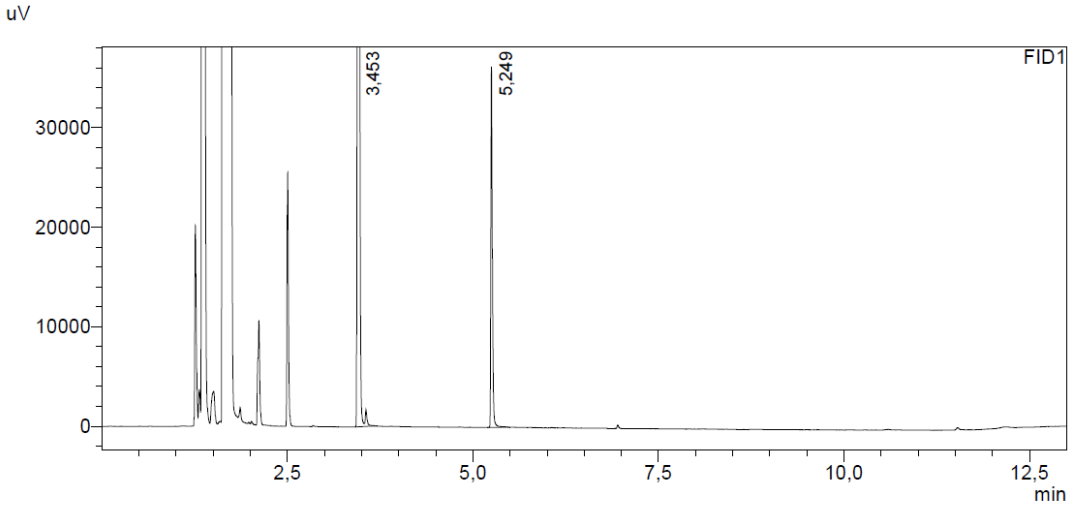
<Peak Table>

FID1

Peak#	Ret. Time	Area	Height	Conc.	Unit	Mark	Name
1	3,456	628405	426415	0,000		S	
2	5,250	94569	64124	0,000		S	
Total		722974	490538				

Figure F.110 Chromatogram of a standard 5 with m(cyclohexanol) = 340 mg and m(nitrobenzene) = 60 mg in 3 ml acetonitrile. The signal at 3.456 min correspond to cyclohexanol, while the one at 5.250 min belongs to nitrobenzene, which served as internal standard.

<Chromatogram>



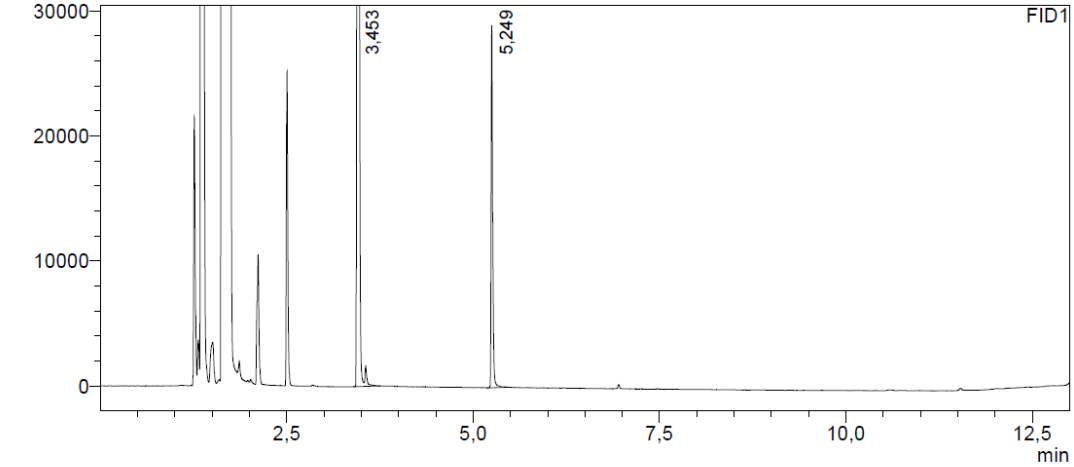
<Peak Table>

FID1

Peak#	Ret. Time	Area	Height	Conc.	Unit	Mark	Name
1	3,453	448045	309752	0,000		S	
2	5,249	53426	35799	0,000		S	
Total		501471	345551				

Figure F.111 Chromatogram of a standard 6 with m(cyclohexanol) = 420 mg and m(nitrobenzene) = 60 mg in 3 ml acetonitrile. The signal at 3.453 min correspond to cyclohexanol, while the one at 5.249 min belongs to nitrobenzene, which served as internal standard.

<Chromatogram>



<Peak Table>

FID1

Peak#	Ret. Time	Area	Height	Conc.	Unit	Mark	Name
1	3,453	436790	304009	0,000		S	
2	5,249	43195	28536	0,000		S	
Total		479984	332545				

Figure F.112 Chromatogram of a standard 7 with m(cyclohexanol) = 500 mg and m(nitrobenzene) = 60 mg in 3 ml acetonitrile. The signal at 3.453 min correspond to cyclohexanol, while the one at 5.249 min belongs to nitrobenzene, which served as internal standard.

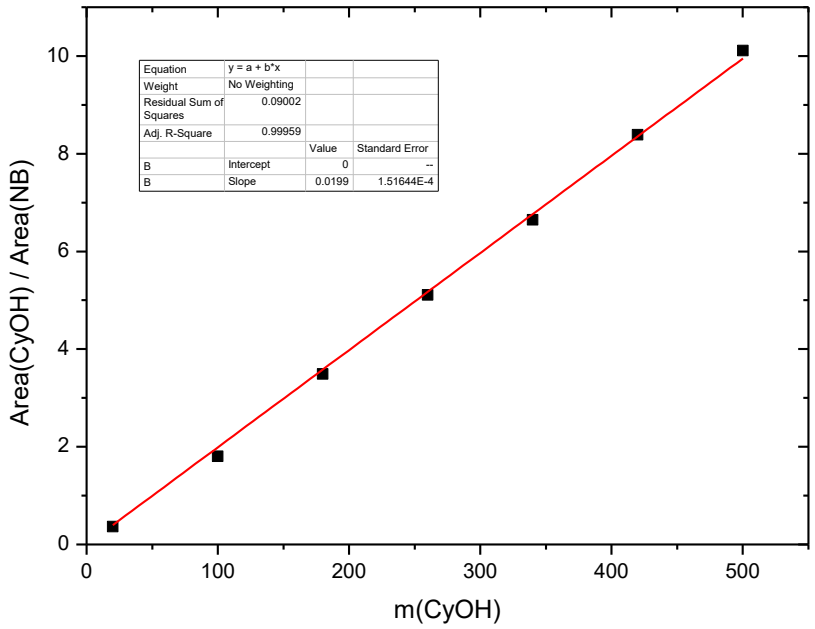
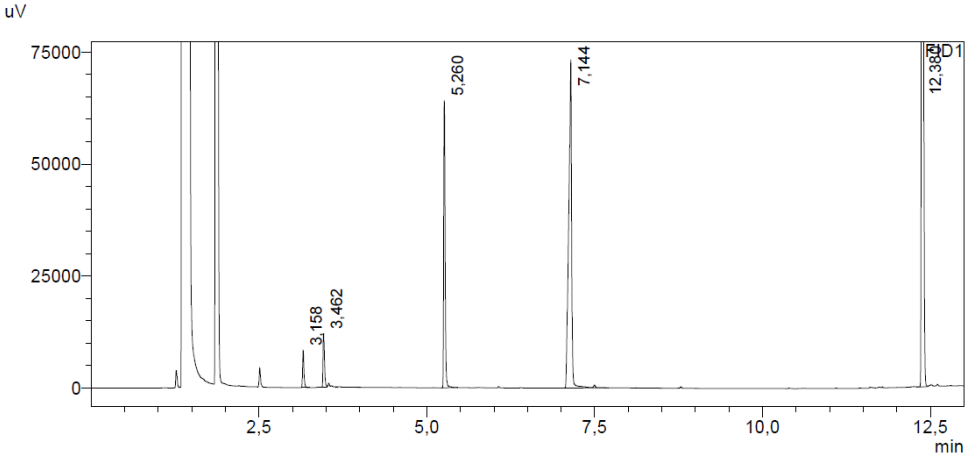


Figure F.113 Calibration curve used for the GC-MS studies described in Chapter 5. The area ratio [area(cyclohexanol)/area(nitrobenzene)] is plotted against the used amount of nitrobenzene of seven different calibration standards.

<Chromatogram>



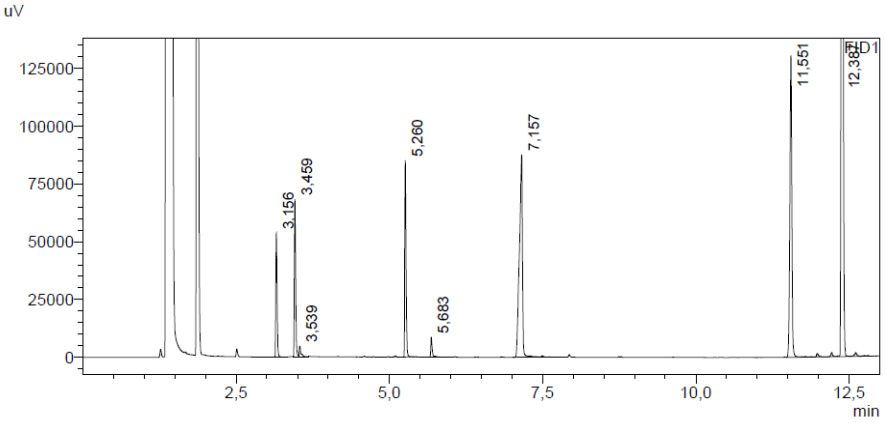
<Peak Table>

FID1

Peak#	Ret. Time	Area	Height	Conc.	Unit	Mark	Name
1	3,158	12167	8216	0,000			
2	3,462	18337	11906	0,000		V	
3	5,260	93107	62070	0,000			
4	7,144	219580	72565	0,000		S	
5	12,380	790253	557361	0,000		V	
Total		1133444	712118				

Figure F.114 Chromatogram of a quenched probe (after 1 hour) of the reaction of cyclohexane with *m*-CPBA to cyclohexanol, catalyzed by **C27** (n = 8 µmol). The signal at 3.462 min correspond to cyclohexanol, while the one at 5.260 min belongs to nitrobenzene, which served as internal standard.

<Chromatogram>



<Peak Table>

FID1

Peak#	Ret. Time	Area	Height	Conc.	Unit	Mark	Name
1	3,156	76208	52160	0,000			
2	3,459	97561	65566	0,000		V	
3	3,539	9082	4493	0,000		V	
4	5,260	121089	81619	0,000		S	
5	5,683	14002	8431	0,000		S	
6	7,157	300041	86851	0,000		S	
7	11,551	290694	128559	0,000		SV	
8	12,387	1530488	982426	0,000		SV	
Total		2439164	1410104				

Figure F.115 Chromatogram of a quenched probe (after 1 day) of the reaction of cyclohexane with *m*-CPBA to cyclohexanol, catalyzed by **C27** (n = 8 µmol). The signal at 3.459 min correspond to cyclohexanol, while the one at 5.260 min belongs to nitrobenzene, which served as internal standard.

G Magnetic Measurements

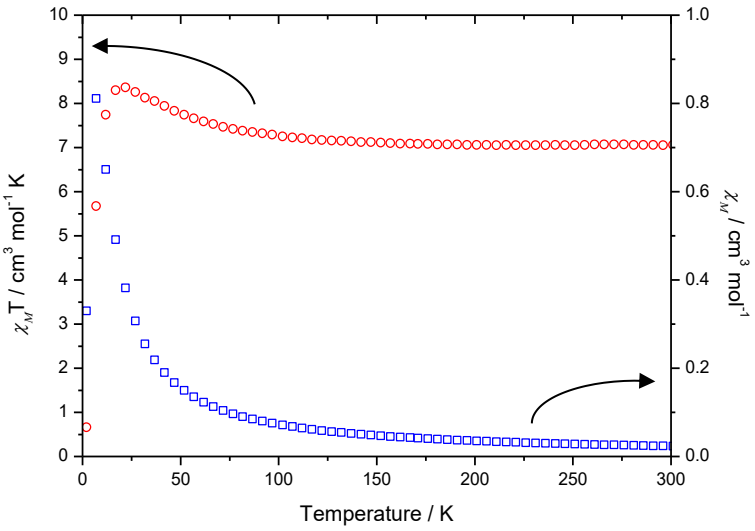


Figure G.1 Temperature dependent magnetic behavior of **C1** in the form of combined $\chi_M T$ *vs*. *T* (left values, red open circles) and χ_M *vs*. *T* plots (right values, blue open squares).

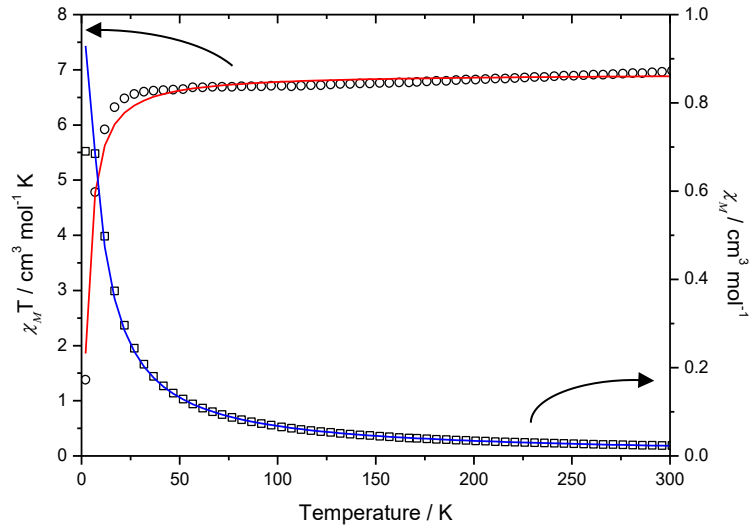


Figure G.2 Temperature dependent magnetic behavior of **C2** in the form of combined $\chi_M T$ *vs*. *T* (left values, open circles) and χ_M *vs*. *T* plots (right values, open squares). Solid lines represent the best fit for $\chi_M T$ *vs*. *T* (red) and χ_M *vs*. *T* (blue), using PHI.[201]

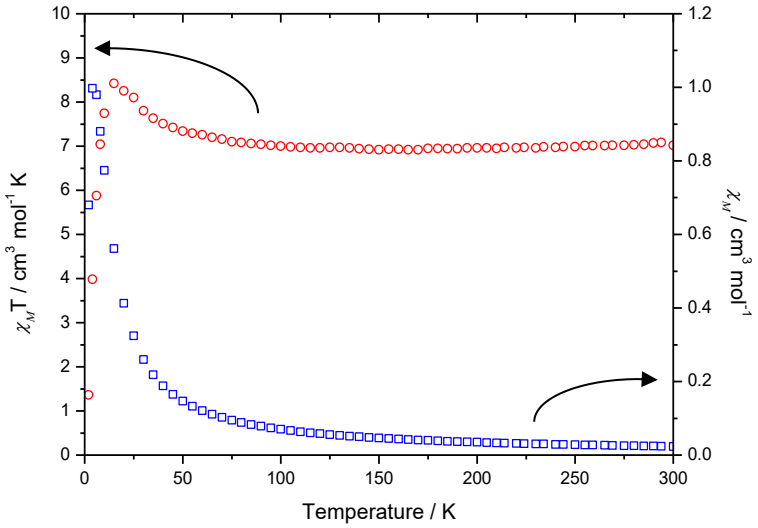


Figure G.3 Temperature dependent magnetic behavior of **C3** in the form of combined $\chi_M T$ *vs*. *T* (left values, red open circles) and χ_M *vs*. *T* plots (right values, blue open squares).

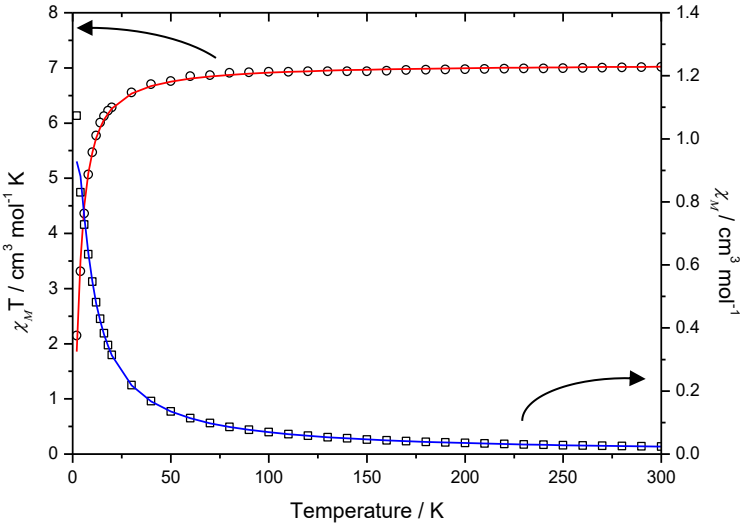


Figure G.4 Temperature dependent magnetic behavior of **C3** (measured in eicosane) in the form of combined $\chi_M T$ *vs*. *T* (left values, open circles) and χ_M *vs*. *T* plots (right values, open squares). Solid lines represent the best fit for $\chi_M T$ *vs*. *T* (red) and χ_M *vs*. *T* (blue), using PHI.[201]

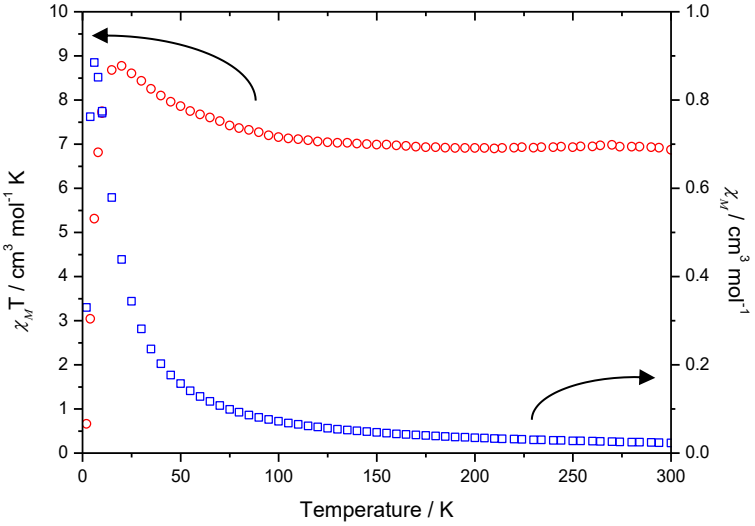


Figure G.5 Temperature dependent magnetic behavior of **C4** in the form of combined $\chi_M T$ *vs*. *T* (left values, red open circles) and χ_M *vs*. *T* plots (right values, blue open squares).

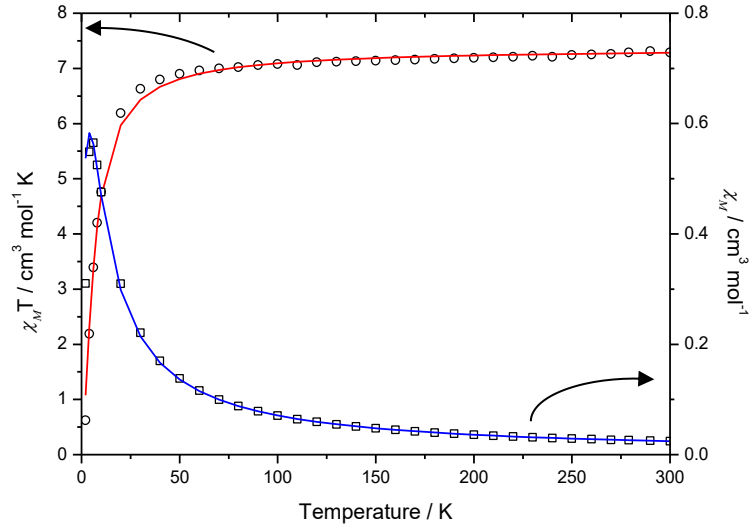


Figure G.6 Temperature dependent magnetic behavior of **C5** in the form of combined $\chi_M T$ *vs*. *T* (left values, open circles) and χ_M *vs*. *T* plots (right values, open squares). Solid lines represent the best fit for $\chi_M T$ *vs*. *T* (red) and χ_M *vs*. *T* (blue), using PHI.[201]

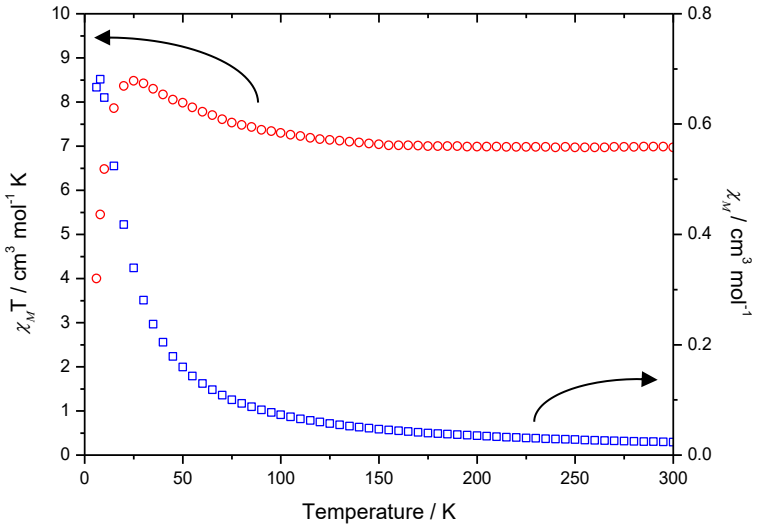


Figure G.7 Temperature dependent magnetic behavior of **C6** in the form of combined $\chi_M T$ *vs*. *T* (left values, red open circles) and χ_M *vs*. *T* plots (right values, blue open squares).

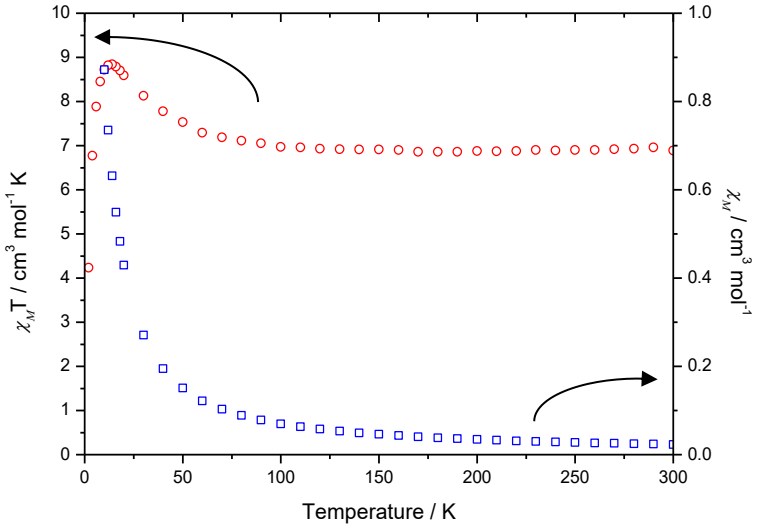


Figure G.8 Temperature dependent magnetic behavior of **C7** in the form of combined $\chi_M T$ *vs*. *T* (left values, red open circles) and χ_M *vs*. *T* plots (right values, blue open squares).

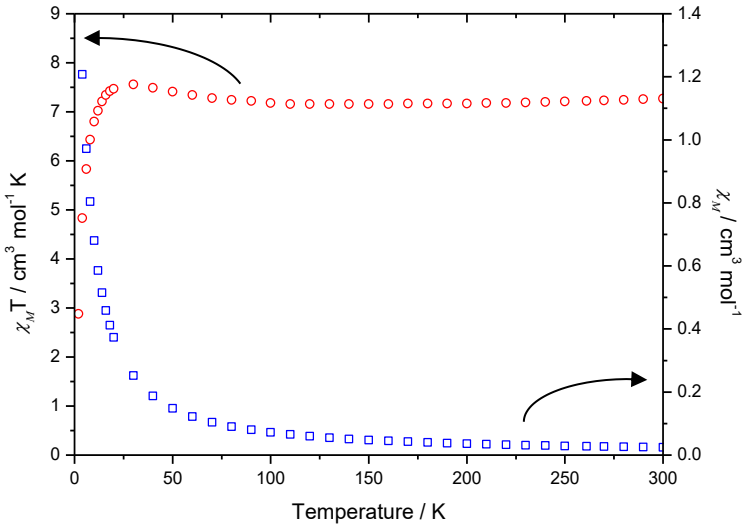


Figure G.9 Temperature dependent magnetic behavior of **C9** in the form of combined $\chi_M T$ *vs*. *T* (left values, red open circles) and χ_M *vs*. *T* plots (right values, blue open squares).

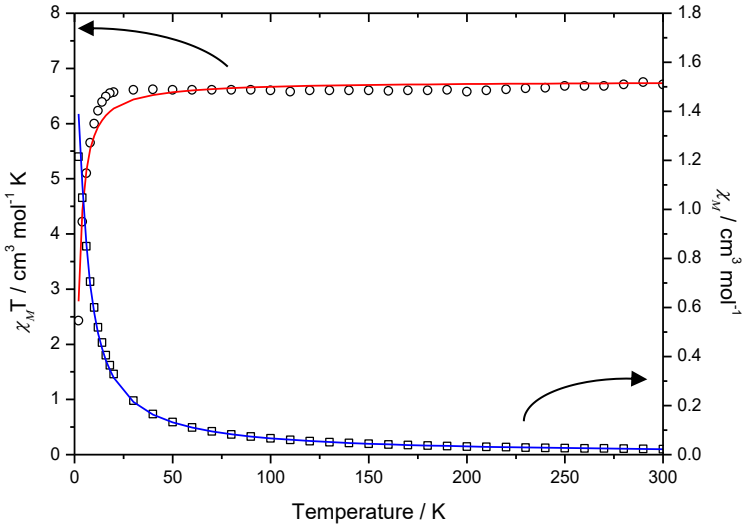


Figure G.10 Temperature dependent magnetic behavior of **C10** in the form of combined $\chi_M T$ *vs*. *T* (left values, open circles) and χ_M *vs*. *T* plots (right values, open squares). Solid lines represent the best fit for $\chi_M T$ *vs*. *T* (red) and χ_M *vs*. *T* (blue), using PHI.[201]

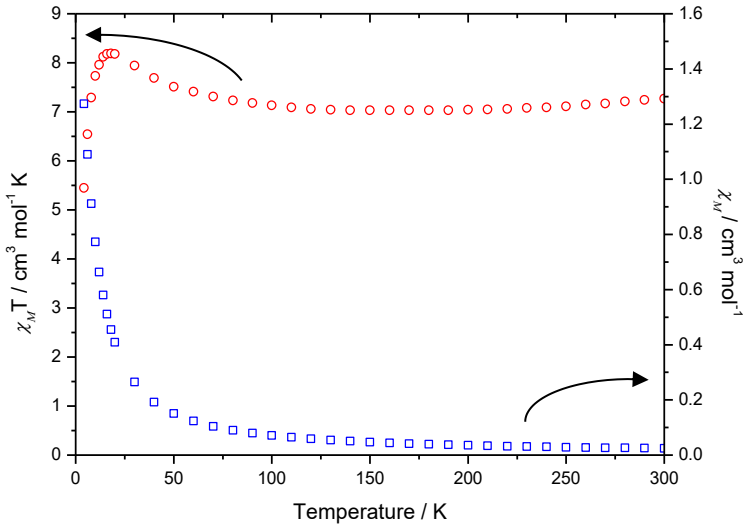


Figure G.11 Temperature dependent magnetic behavior of **C11** in the form of combined $\chi_M T$ *vs*. *T* (left values, red open circles) and χ_M *vs*. *T* plots (right values, blue open squares).

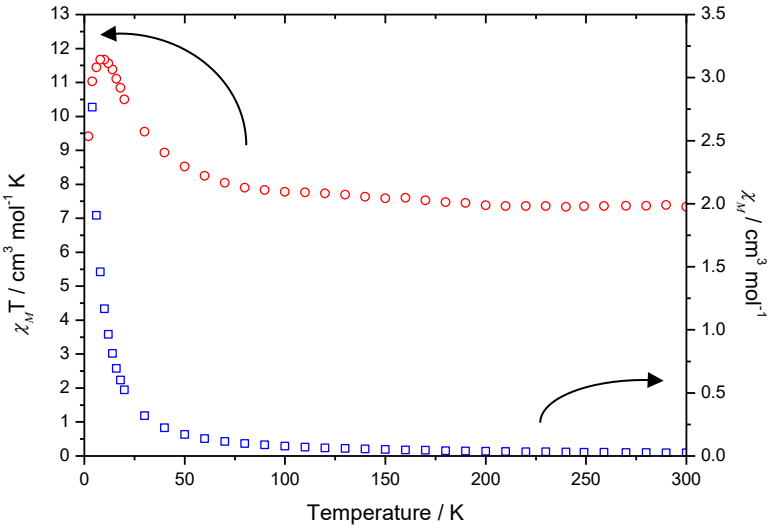


Figure G.12 Temperature dependent magnetic behavior of **C12** in the form of combined $\chi_M T$ *vs*. *T* (left values, red open circles) and χ_M *vs*. *T* plots (right values, blue open squares).

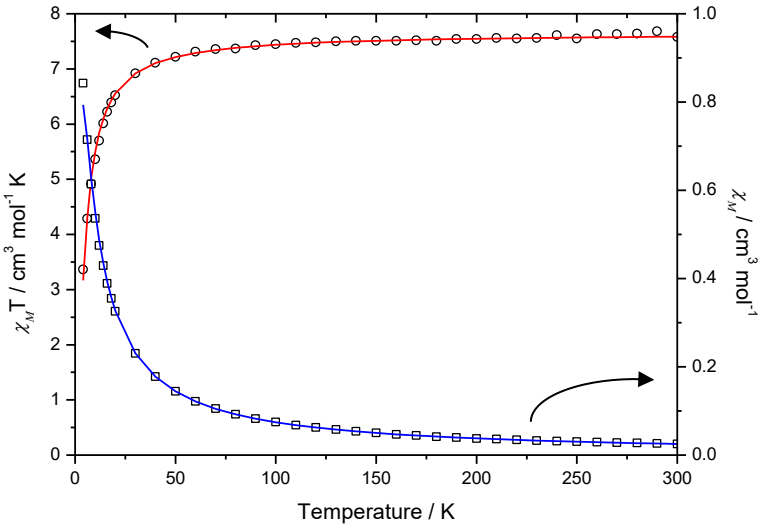


Figure G.13 Temperature dependent magnetic behavior of **C14** in the form of combined $\chi_M T$ *vs*. *T* (left values, open circles) and χ_M *vs*. *T* plots (right values, open squares). Solid lines represent the best fit for $\chi_M T$ *vs*. *T* (red) and χ_M *vs*. *T* (blue), using PHI.[201]

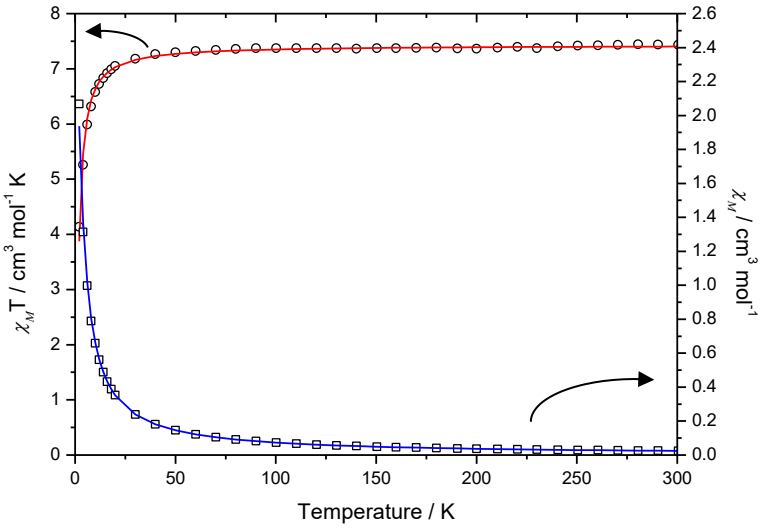


Figure G.14 Temperature dependent magnetic behavior of **C15** in the form of combined $\chi_M T$ *vs*. *T* (left values, open circles) and χ_M *vs*. *T* plots (right values, open squares). Solid lines represent the best fit for $\chi_M T$ *vs*. *T* (red) and χ_M *vs*. *T* (blue), using PHI.[201]

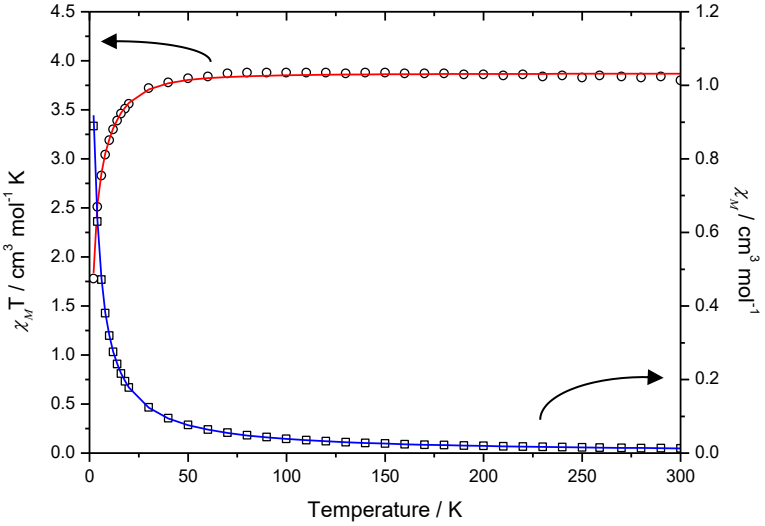


Figure G.15 Temperature dependent magnetic behavior of **C16**·1MeCN in the form of combined $\chi_M T$ *vs*. *T* (left values, open circles) and χ_M *vs*. *T* plots (right values, open squares). Solid lines represent the best fit for $\chi_M T$ *vs*. *T* (red) and χ_M *vs*. *T* (blue), using PHI.[201]

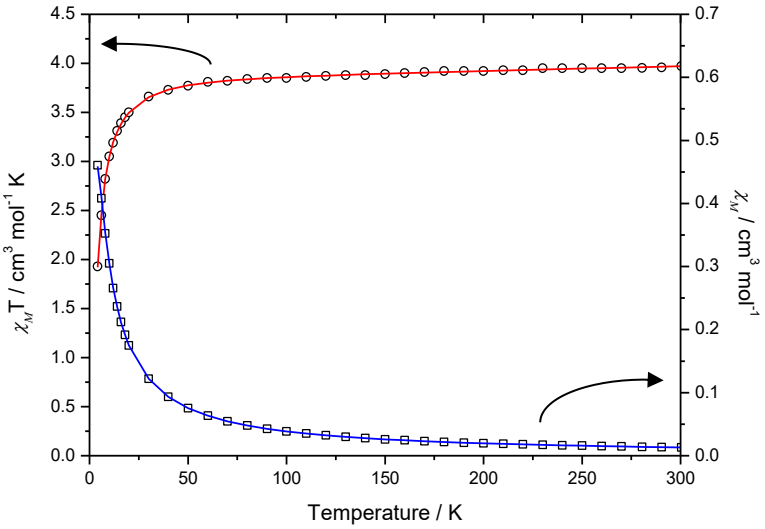


Figure G.16 Temperature dependent magnetic behavior of **C16**·1MeOH in the form of combined $\chi_M T$ *vs*. *T* (left values, open circles) and χ_M *vs*. *T* plots (right values, open squares). Solid lines represent the best fit for $\chi_M T$ *vs*. *T* (red) and χ_M *vs*. *T* (blue), using PHI.[201]

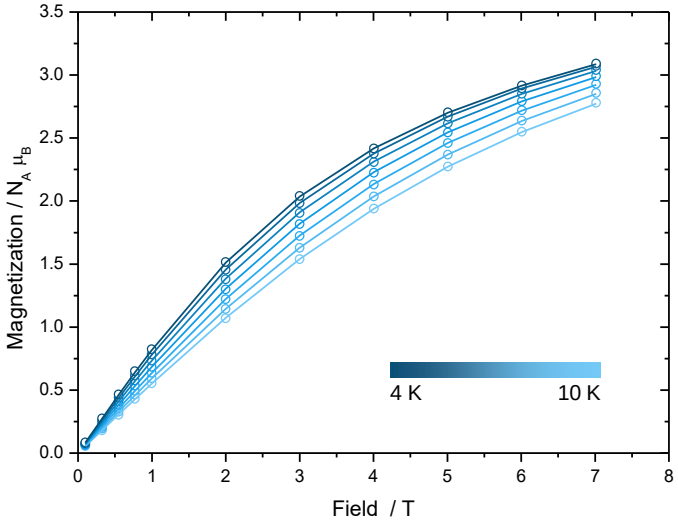


Figure G.17 Temperature and field dependent magnetization data of **C16**·1MeOH in the form of *M vs*. *H* plot (open circles). Solid lines represent the best fit using PHI.[201] Different shades of blue represent different temperatures.

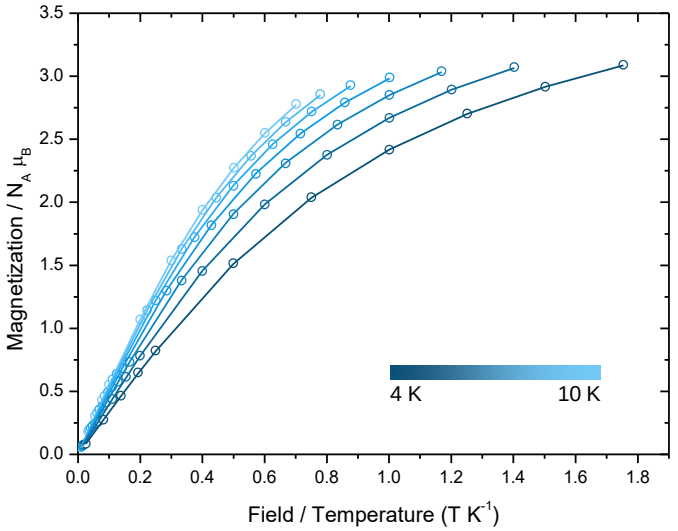


Figure G.18 Temperature and field dependent magnetization data of **C16**·1MeOH in the form of *M vs*. *T*/*H* plot (open circles). Solid lines represent the best fit using PHI.[201] Different shades of blue represent different temperatures.

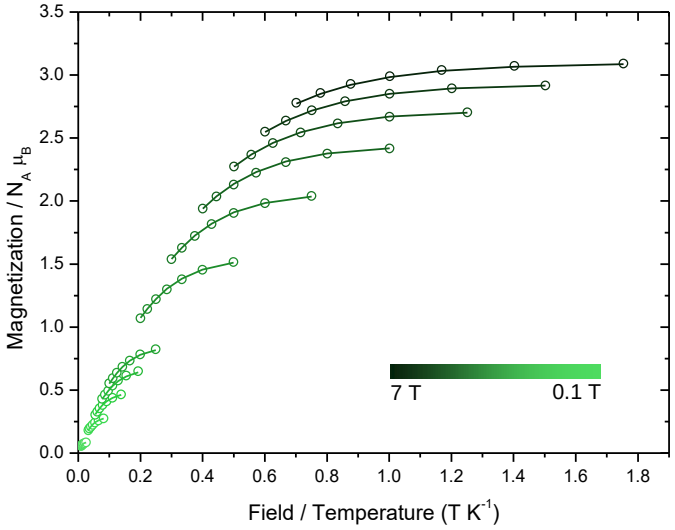


Figure G.19 Temperature and field dependent magnetization data of **C16**·1MeOH in the form of *M vs*. *T*/*H* plot (open circles). Solid lines represent the best fit using PHI.[201] Different shades of green represent different magnetic fields.

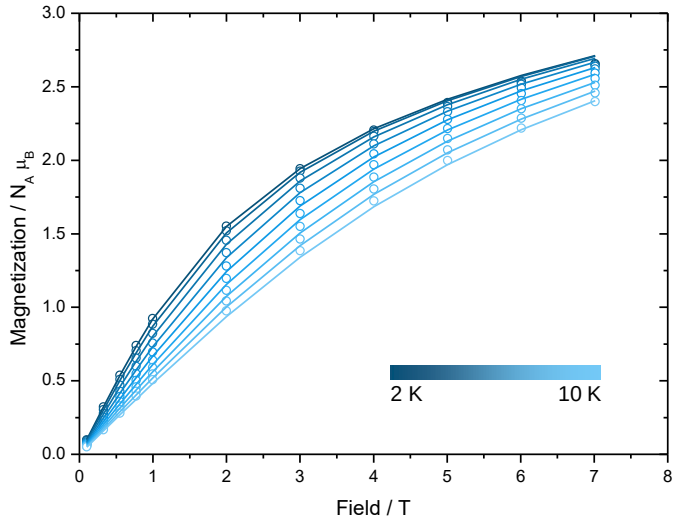


Figure G.20 Temperature and field dependent magnetization data of **C17**·1MeCN in the form of *M vs*. *H* plot (open circles). Solid lines represent the best fit using PHI.[201] Different shades of blue represent different temperatures.

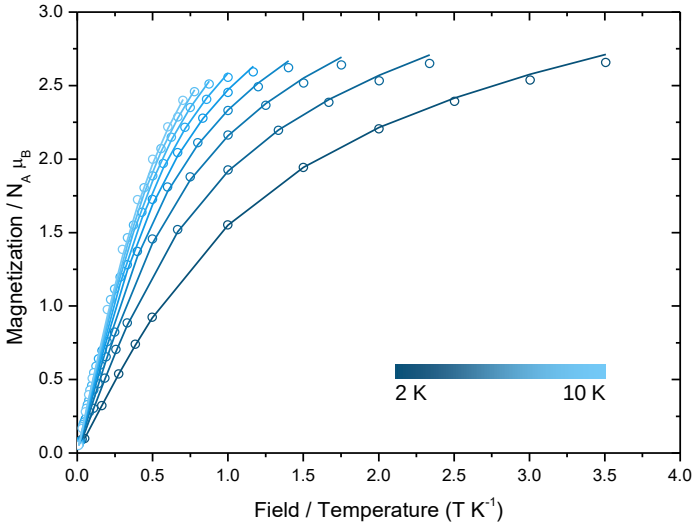


Figure G.21 Temperature and field dependent magnetization data of **C17**·1MeCN in the form of *M vs*. *T*/*H* plot (open circles). Solid lines represent the best fit using PHI.[201] Different shades of blue represent different temperatures.

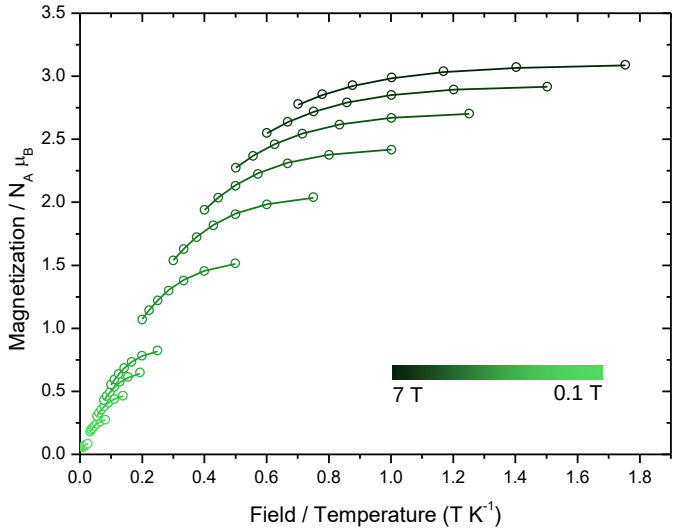


Figure G.22 Temperature and field dependent magnetization data of **C17**·1MeCN in the form of *M vs*. *T*/*H* plot (open circles). Solid lines represent the best fit using PHI.[201] Different shades of green represent different magnetic fields.

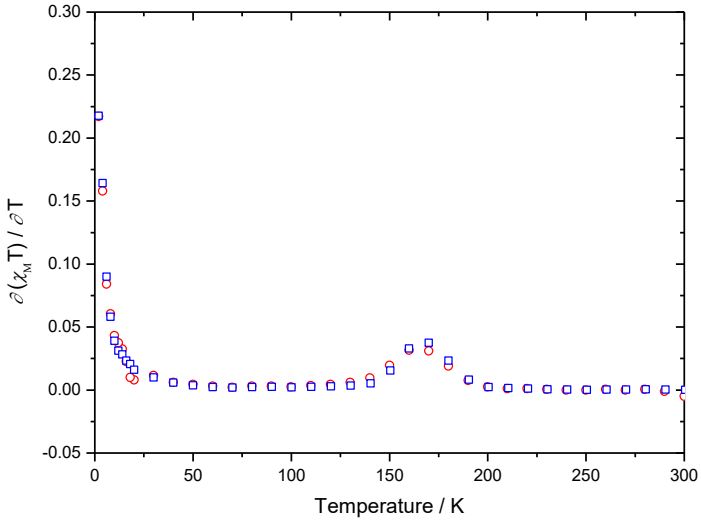


Figure G.23 First derivative of $\chi_M T$ with respect to T for **C18**·1MeOH. Susceptibility was measured from 300 K to 2 K (red open circles) and subsequently from 2 K to 300 K (blue open squares).

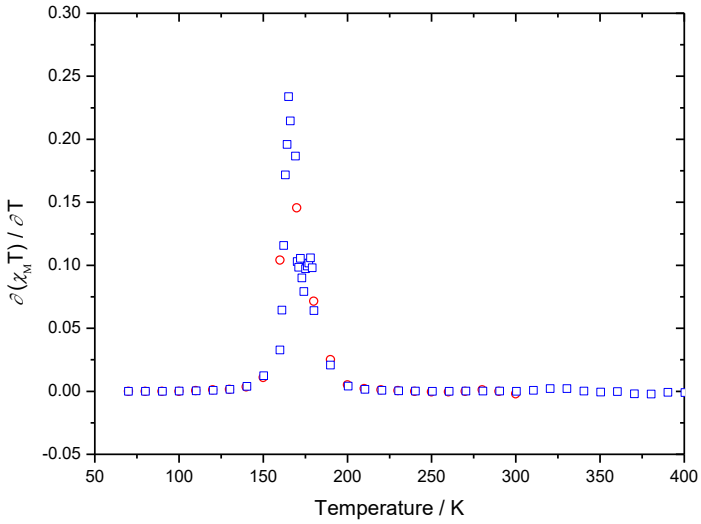


Figure G.24 First derivative of $\chi_M T$ with respect to T for **C18**·1MeOH, measured in mother liquor. Susceptibility was measured from 300 K to 70 K (red open circles) and subsequently from 2 K to 300 K (blue open squares).

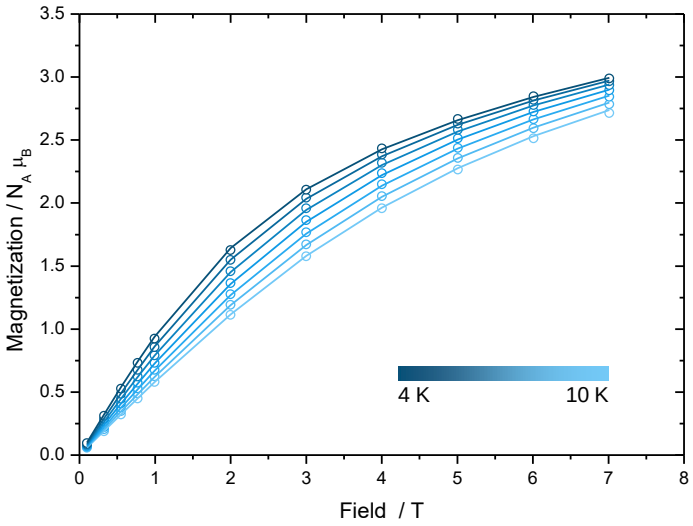


Figure G.25 Temperature and field dependent magnetization data of **C19**·2MeCN in the form of *M vs*. *H* plot (open circles). Solid lines represent the best fit using PHI.[201] Different shades of blue represent different temperatures.

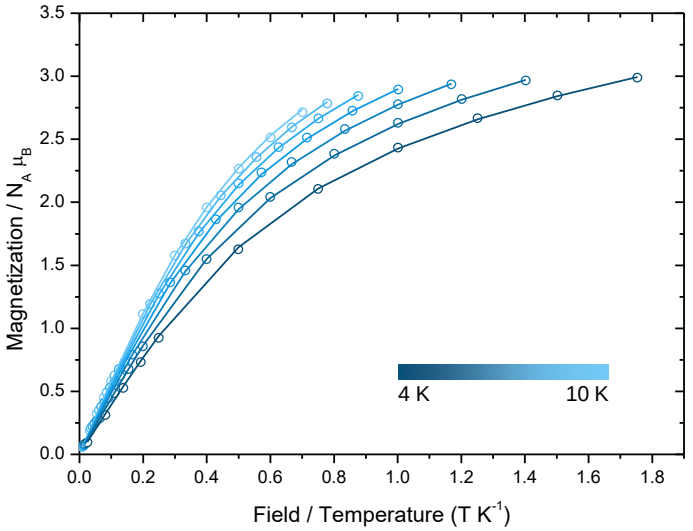


Figure G.26 Temperature and field dependent magnetization data of **C19**·2MeCN in the form of *M vs*. *T*/*H* plot (open circles). Solid lines represent the best fit using PHI.[201] Different shades of blue represent different temperatures.

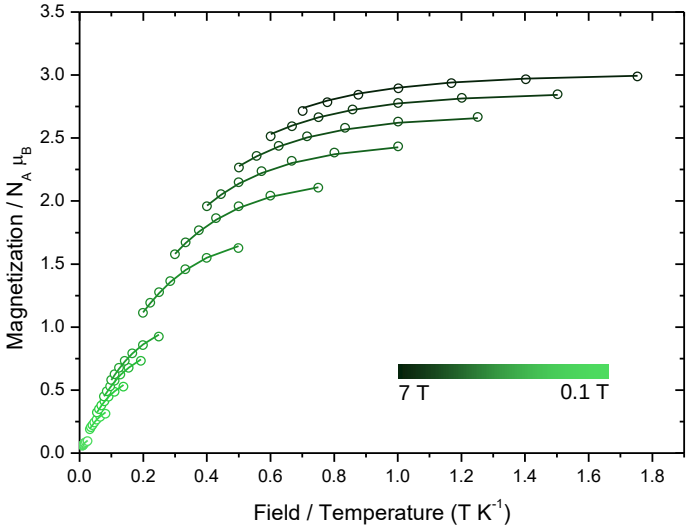


Figure G.27 Temperature and field dependent magnetization data of **C19**·2MeCN in the form of *M vs*. *T*/*H* plot (open circles). Solid lines represent the best fit using PHI.[201] Different shades of green represent different magnetic fields.

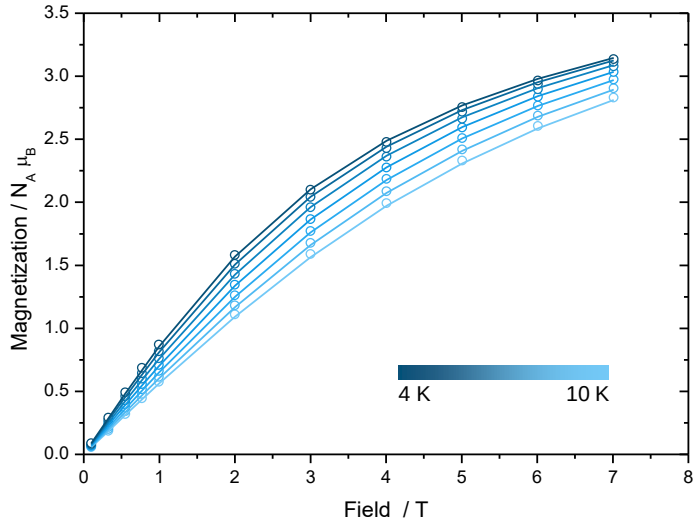


Figure G.28 Temperature and field dependent magnetization data of **C19**·3MeOH in the form of *M vs*. *H* plot (open circles). Solid lines represent the best fit using PHI.[201] Different shades of blue represent different temperatures.

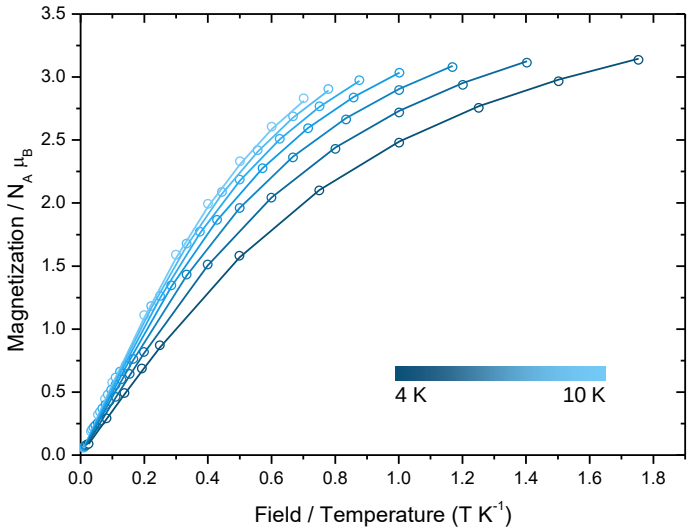


Figure G.29 Temperature and field dependent magnetization data of **C19**·3MeOH in the form of *M vs*. *H* plot (open circles). Solid lines represent the best fit using PHI.[201] Different shades of blue represent different temperatures.

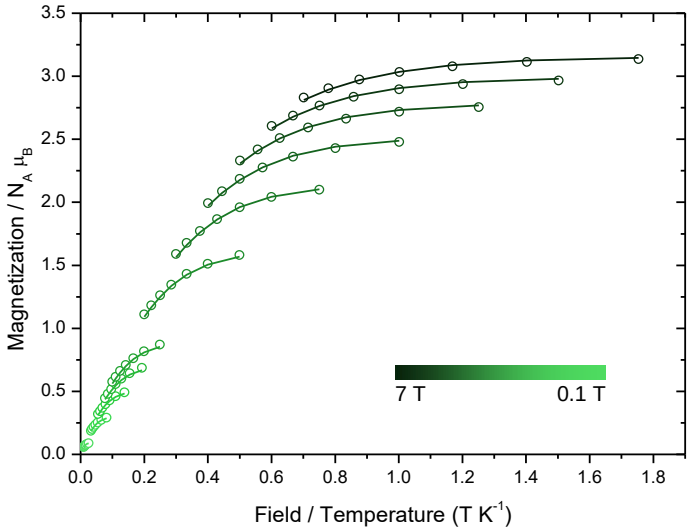


Figure G.30 Temperature and field dependent magnetization data of **C19**·3MeOH in the form of *M vs*. *T*/*H* plot (open circles). Solid lines represent the best fit using PHI.[201] Different shades of green represent different magnetic fields.

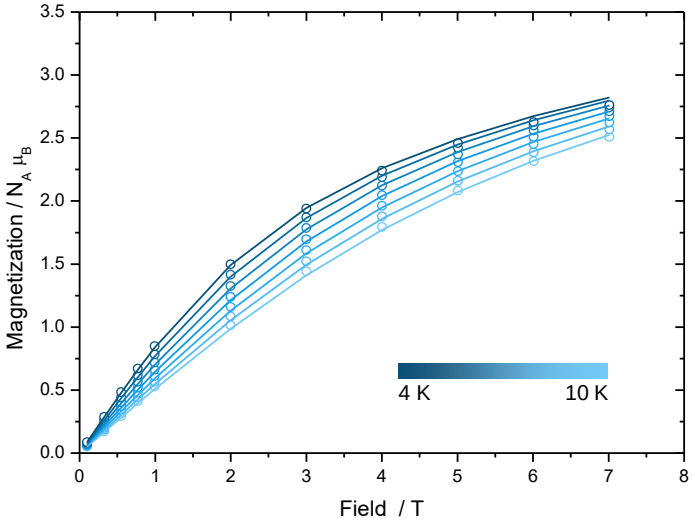


Figure G.31 Temperature and field dependent magnetization data of **C20**·2MeCN in the form of *M vs*. *H* plot (open circles). Solid lines represent the best fit using PHI.[201] Different shades of blue represent different temperatures.

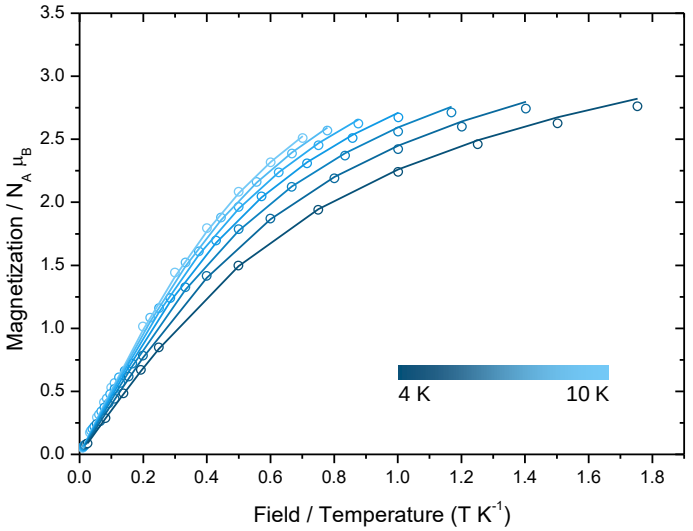


Figure G.32 Temperature and field dependent magnetization data of **C20**·2MeCN in the form of *M vs*. *T*/*H* plot (open circles). Solid lines represent the best fit using PHI.[201] Different shades of blue represent different temperatures.

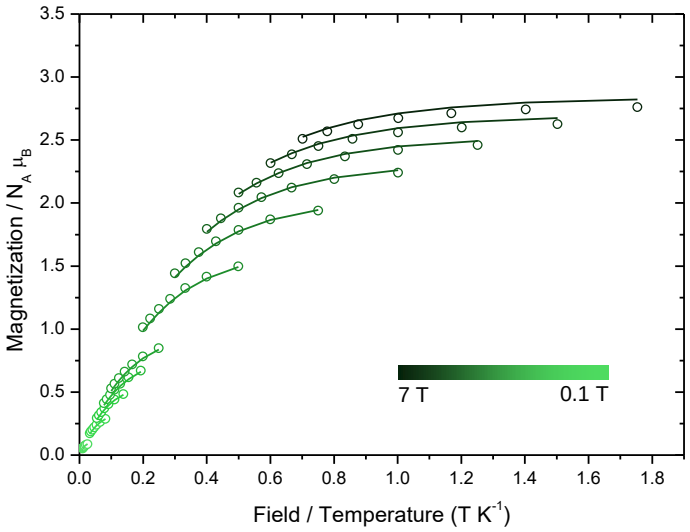


Figure G.33 Temperature and field dependent magnetization data of **C20**·2MeCN in the form of *M vs*. *T*/*H* plot (open circles). Solid lines represent the best fit using PHI.[201] Different shades of green represent different magnetic fields.

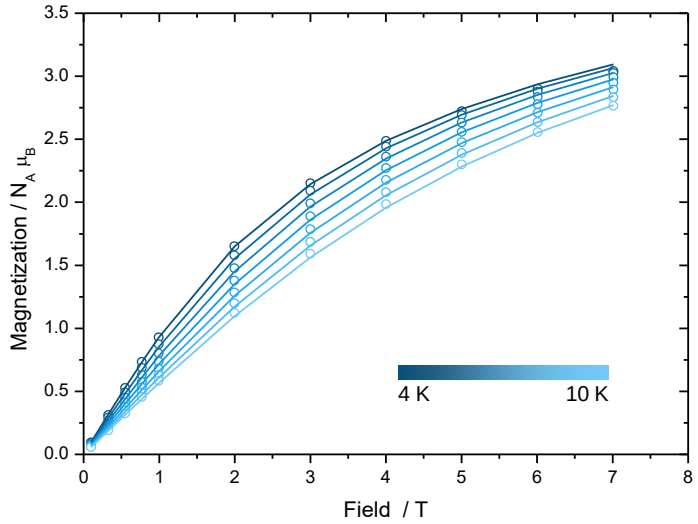


Figure G.34 Temperature and field dependent magnetization data of **C20**·3MeOH in the form of *M vs*. *H* plot (open circles). Solid lines represent the best fit using PHI.[201] Different shades of blue represent different temperatures.

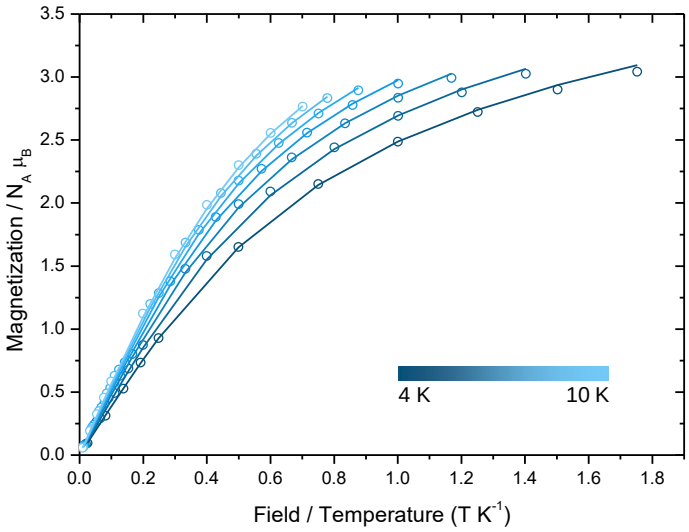


Figure G.35 Temperature and field dependent magnetization data of **C20**·3MeOH in the form of *M vs*. *H* plot (open circles). Solid lines represent the best fit using PHI.[201] Different shades of blue represent different temperatures.

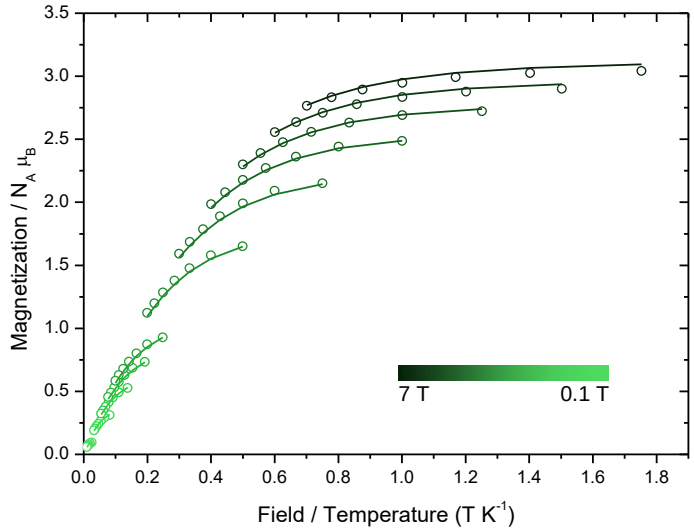


Figure G.36 Temperature and field dependent magnetization data of **C20**·3MeOH in the form of *M vs*. *T*/*H* plot (open circles). Solid lines represent the best fit using PHI.[201] Different shades of green represent different magnetic fields.

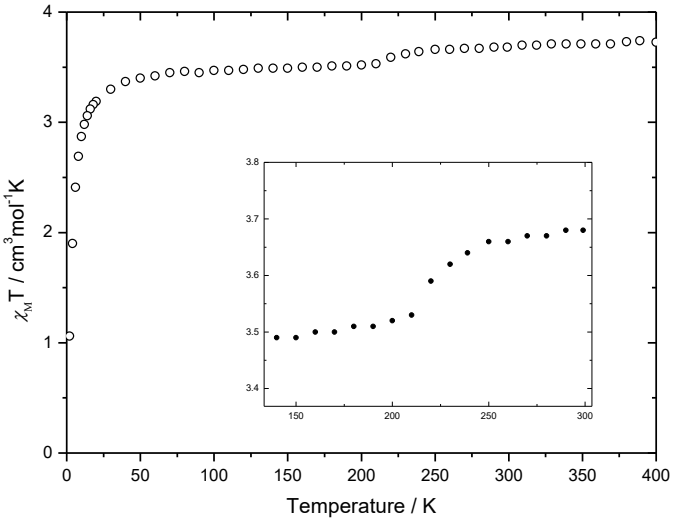


Figure G.37 Temperature dependent magnetic behavior of **C21**·1MeCN in the form of the $\chi_M T$ *vs*. *T* plot. Inset shows the zoom into the temperature region from 130 K to 305 K.

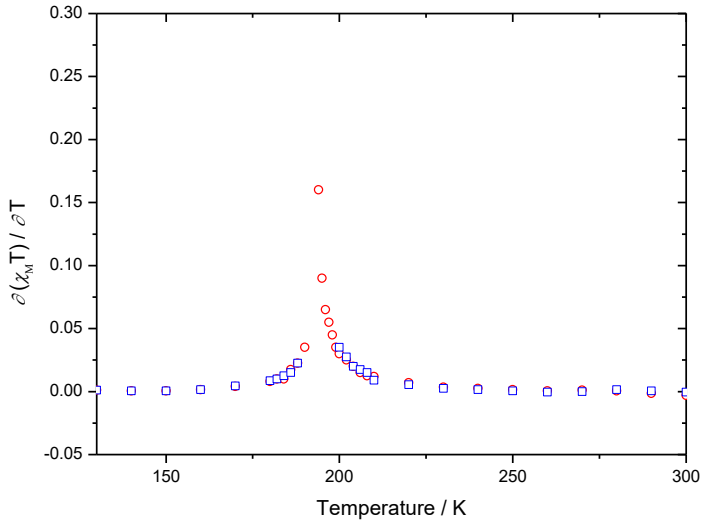


Figure G.38 First derivative of $\chi_M T$ with respect to *T* for **C21**·1MeCN. Susceptibility was measured from 300 K to 130 K (red open circles) and subsequently from 130 K to 300 K (blue open squares).

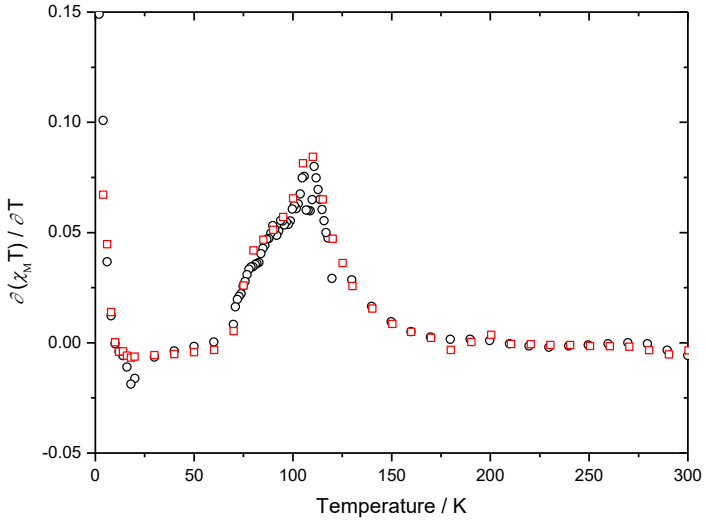


Figure G.39 First derivative of $\chi_M T$ with respect to *T* for **C23**·4.5MeCN. Susceptibility was measured from 300 K to 2 K (black open circles) and subsequently from 2 K to 400 K (red open squares).

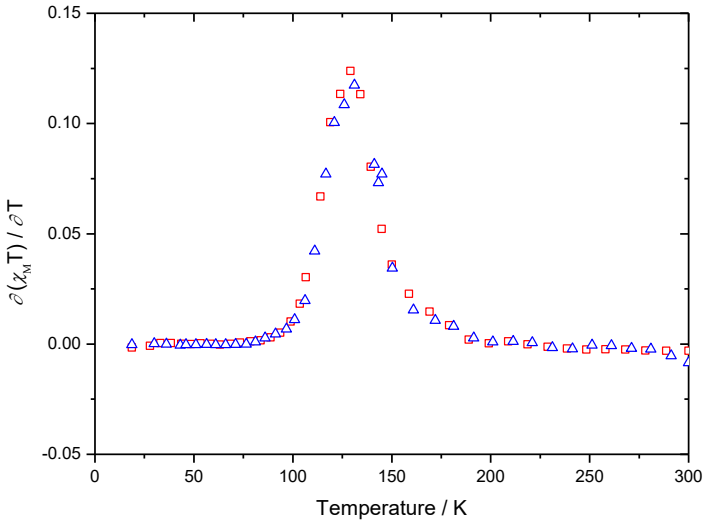


Figure G.40 First derivative of $\chi_M T$ with respect to *T* for **C23**·4.5MeCN, remeasured with freshly prepared single-crystals. Susceptibility was measured from 300 K to 00 K (red open squares) and subsequently from 20 K to 300 K (blue open triangles).

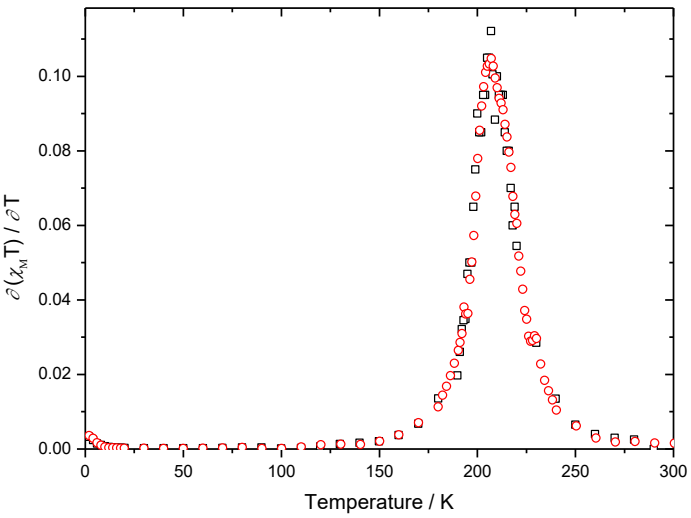


Figure G.41 First derivative of $\chi_M T$ with respect to T for **C23**·3MeOH. Susceptibility was measured from 300 K to 2 K (black open squares) and subsequently from 2 K to 400 K (red open circles).

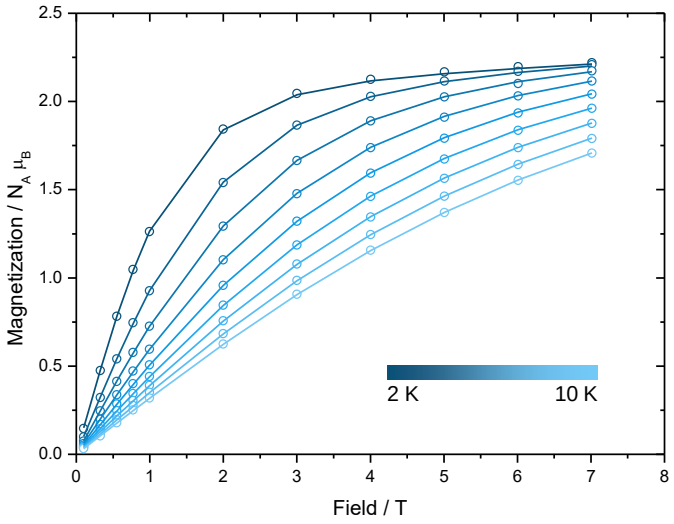


Figure G.42 Temperature and field dependent magnetization data of **C26** in the form of *M vs*. *H* plot (open circles). Solid lines represent the best fit using PHI.[201] Different shades of blue represent different temperatures.

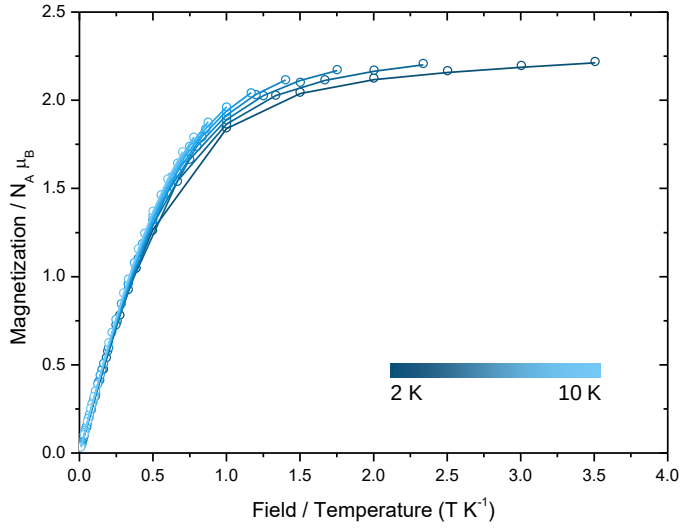


Figure G.43 Temperature and field dependent magnetization data of **C26** in the form of *M vs*. *H* plot (open circles). Solid lines represent the best fit using PHI.[201] Different shades of blue represent different temperatures.

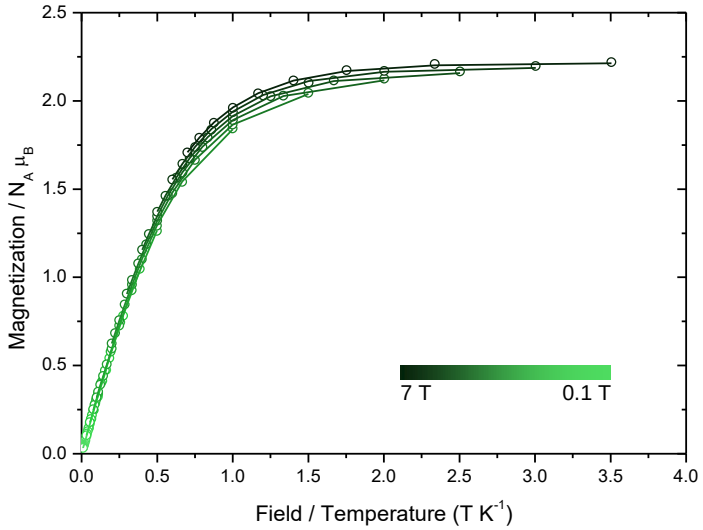


Figure G.44 Temperature and field dependent magnetization data of **C26** in the form of *M vs*. *T*/*H* plot (open circles). Solid lines represent the best fit using PHI.[201] Different shades of green represent different magnetic fields.

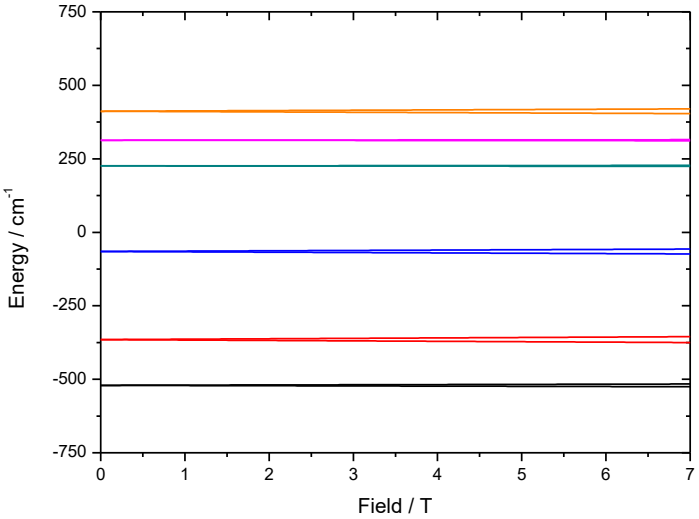


Figure G.45 Simulation of the *Zeeman splitting* in **C27** between 0 and 7 T, calculated with PHI.[201]

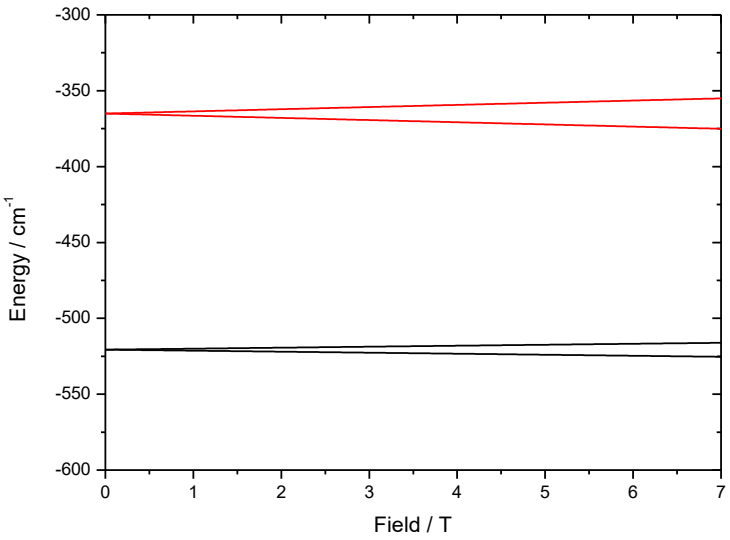


Figure G.46 Zoom into the simulation of the *Zeeman splitting* in **C27** between 0 and 7 T, calculated with PHI.[201]

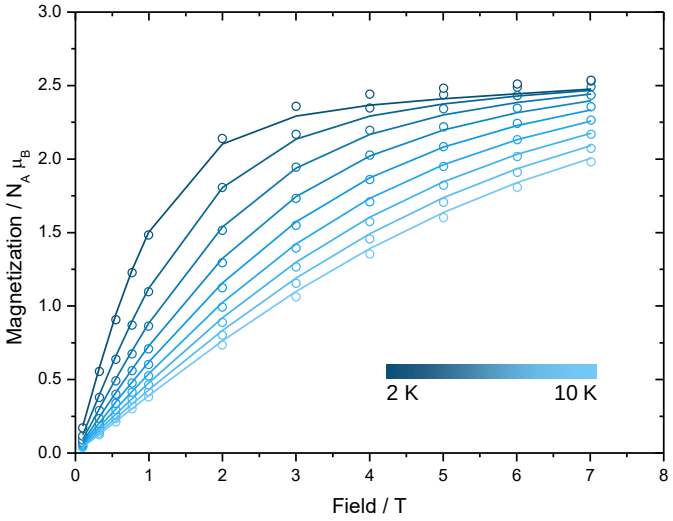


Figure G.47 Temperature and field dependent magnetization data of **C27** in the form of *M vs*. *H* plot (open circles). Solid lines represent the best fit using PHI.[201] Different shades of blue represent different temperatures.

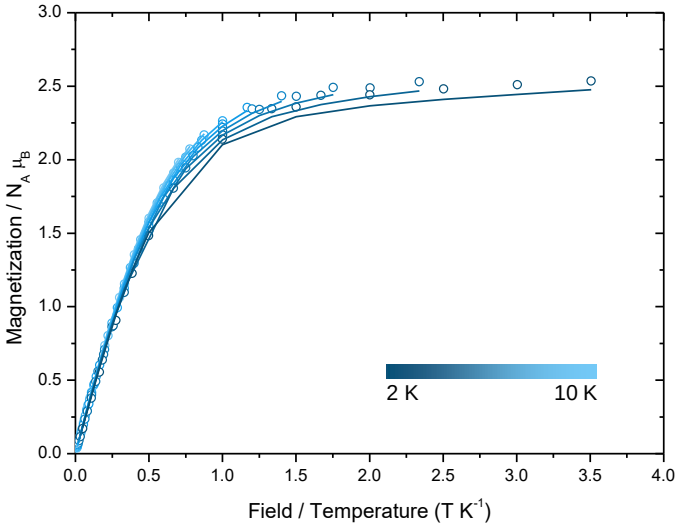


Figure G.48 Temperature and field dependent magnetization data of **C27** in the form of *M vs*. *T*/*H* plot (open circles). Solid lines represent the best fit using PHI.[201] Different shades of blue represent different temperatures.

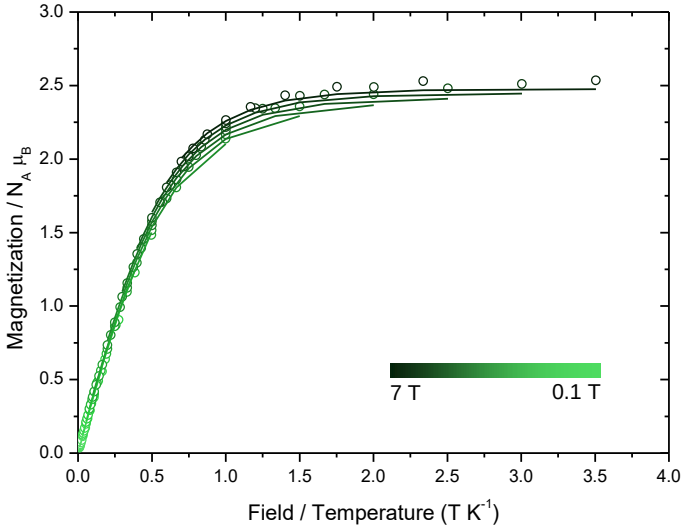


Figure G.49 Temperature and field dependent magnetization data of **C27** in the form of *M vs*. *T*/*H* plot (open circles). Solid lines represent the best fit using PHI.[201] Different shades of green represent different magnetic fields.

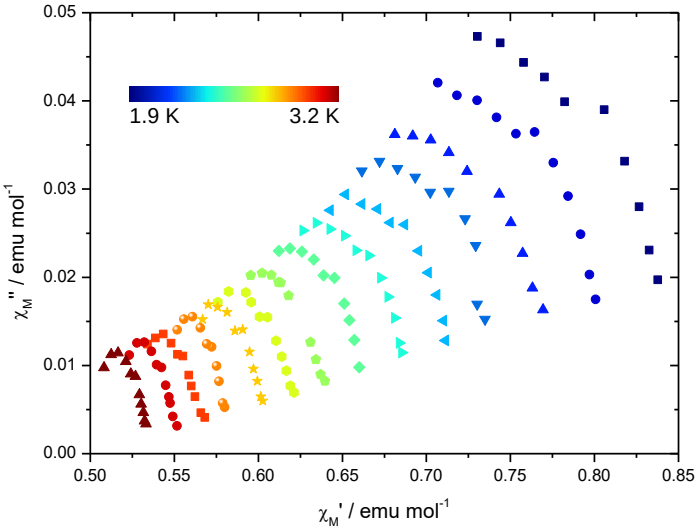


Figure G.50 Cole-Cole plot of **C27** in a temperature range between 1.9 K and 3.2 K at 0.16 T. Frequencies vary between 9 s^{-1} and 1400 s^{-1}.

H Complex coordinates

Table H.1 Cartesian coordinates of **C1**, derived by X-ray structure analysis.

	X	Y	Z		X	Y	Z
Fe	4.499847	6.627534	4.32605	C	2.499049	9.380446	8.65748
N	4.080435	6.402219	2.30353	H	3.316862	9.714406	8.30798
N	4.019524	8.694072	4.58748	C	5.681739	5.075437	6.57367
O	4.179032	10.835969	4.17703	C	2.423653	4.706612	5.25805
N	0.166868	8.992470	4.01013	C	-0.374895	5.952185	7.07252
N	6.214942	7.902107	3.19251	H	-1.143125	5.423743	6.73980
H	7.077002	7.784086	3.68536	H	-0.189068	5.678669	8.00566
N	0.834626	11.107945	5.66035	C	2.175624	9.293241	9.97515
N	4.594677	6.551224	0.17877	H	2.716000	9.557366	10.71049
H	5.048266	6.724134	-0.55521	C	-0.832996	8.011386	8.36162
C	5.011764	6.772646	1.43433	H	-1.489792	8.751547	8.33179
N	-0.545257	10.232257	2.36016	H	-1.152979	7.335859	9.01075
H	-0.807131	10.939510	1.90672	C	5.981647	6.351969	8.34914
N	2.950744	9.344454	5.22082	H	6.190662	6.641200	9.22957
C	-0.022358	8.188821	2.89341	C	5.643271	3.909223	5.64025
H	0.132733	7.252298	2.85648	H	6.544003	3.751297	5.26100
C	4.707159	9.599155	3.98713	H	5.364768	3.094946	6.12963
C	3.019746	5.923471	1.55773	C	3.338066	3.628972	4.78144
H	2.201934	5.589512	1.90723	H	3.387226	2.907165	5.45723
C	-0.162944	10.228480	3.64154	H	2.990596	3.242066	3.93902
C	3.095142	10.597306	4.95716	H	5.023749	3.802597	3.88080
C	5.893690	9.351733	3.14269	F	6.559147	11.678075	5.67096
H	6.661921	9.880174	3.47541	F	7.141906	9.512457	5.94622
H	5.707864	9.625248	2.20955	F	5.465621	10.415504	7.19557
C	3.343172	6.010677	0.24006	F	7.620216	11.030805	7.55114
H	2.802796	5.746551	-0.49527	B	6.694578	10.670088	6.60236
C	6.351792	7.292532	1.85359	F	5.162611	3.432082	1.46668
H	7.008588	6.552371	1.88342	F	5.143813	1.658424	2.87728
H	6.671774	7.968058	1.20446	F	5.946008	1.443324	0.79567
C	-0.462852	8.951948	1.86607	F	3.737734	1.736866	1.14238
H	-0.671866	8.662717	0.98564	B	4.978041	2.059811	1.56611
C	-0.124475	11.394694	4.57496	N	2.997327	9.602141	1.31368
H	-1.025207	11.552620	4.95421	C	2.152131	8.980506	-1.00966
H	0.154027	12.208972	4.08558	H	2.889780	8.602405	-1.53245
C	2.180729	11.674945	5.43377	H	1.808084	9.779635	-1.46070
H	2.131569	12.396753	4.75798	H	1.435430	8.317038	-0.92870
H	2.528199	12.061851	6.27619	C	2.632409	9.340929	0.31764
H	0.495047	11.501321	6.33441	N	1.637766	11.321737	-1.80975
Fe	1.018948	8.676384	5.88916	C	1.675209	8.905259	-1.20820
N	1.438361	8.901698	7.91168	H	0.939227	8.508274	-1.71923
N	1.499271	6.609845	5.62773	H	1.516554	8.772682	-0.25026
O	1.339763	4.467948	6.03818	H	2.518445	8.475353	-1.46223
N	5.351928	6.311448	6.20508	C	1.753550	10.367782	-1.50224
N	-0.696146	7.401811	7.02270	N	1.408598	12.152379	-1.31368
H	-1.558206	7.519831	6.52985	C	2.253793	12.774014	1.00966
N	4.684170	4.195972	4.55486	H	1.516144	13.152114	1.53245
N	0.924118	8.752693	10.03644	H	2.597840	11.974885	1.46070
H	0.470530	8.579784	10.77043	H	2.970494	13.437481	0.92870
C	0.507032	8.531271	8.78088	C	1.773515	12.413591	-0.31764
N	6.064052	5.071661	7.85505	N	2.768159	10.432783	1.80975
H	6.325927	4.364408	8.30849	C	2.730716	12.849260	1.20820
N	2.568052	5.959464	4.99439	H	3.466698	13.246246	1.71923
C	5.541154	7.115096	7.32180	H	2.889370	12.981838	0.25026
H	5.386063	8.051619	7.35873	H	1.887479	13.279167	1.46223
C	0.811637	5.704763	6.22808				

Table H.2 Cartesian coordinates of **C2**, derived by X-ray structure analysis.

	X	Y	Z		X	Y	Z
Fe	8.416613	8.731085	10.59673	N	2.446506	9.902114	14.14871
O	6.068490	11.205135	8.15968	H	1.933525	9.743404	14.84589
N	6.867686	9.959505	9.78214	N	8.899819	9.889907	12.25676
N	5.468738	9.866713	9.78876	N	10.060653	10.308733	14.06529
N	9.521329	10.301134	9.11982	H	10.645073	10.216389	14.71670
H	10.089877	10.909928	9.67309	C	5.355186	6.447484	12.41846
N	2.772881	9.900653	9.22419	C	7.473764	6.584256	12.40842
H	2.186145	10.462956	9.80691	C	3.986301	6.073137	12.84862
N	9.013521	7.591743	8.96612	H	3.886817	6.224454	13.82192
N	10.079894	7.291086	7.08288	H	3.827467	5.113189	12.66594
H	10.592875	7.449796	6.38570	C	8.891627	6.400684	12.80832
N	3.626581	7.303293	8.97483	H	9.160206	5.458703	12.66458
N	2.465747	6.884467	7.16630	H	8.997287	6.609152	13.77034
H	1.881327	6.976811	6.51489	C	2.122461	7.693923	12.98063
C	7.171214	10.745716	8.81313	H	1.221888	7.759721	12.57475
C	5.052636	10.608944	8.82317	H	2.033198	7.255823	13.86393
C	8.540099	11.120063	8.38297	C	2.700842	9.055865	13.14898
H	8.639583	10.968746	7.40968	C	3.130811	11.067057	13.89277
H	8.698933	12.080011	8.56565	H	3.137099	11.851273	14.42891
C	3.634773	10.792516	8.42327	C	3.789762	10.879376	12.73473
H	3.366194	11.734497	8.56701	H	4.351634	11.515765	12.30836
H	3.529113	10.584048	7.46125	C	10.604963	8.190840	12.80333
C	10.403939	9.499277	8.25096	H	10.846748	7.757451	13.65996
H	11.304512	9.433479	8.65684	H	11.438908	8.392740	12.30950
H	10.493202	9.937377	7.36766	C	9.852076	9.444414	13.06291
C	9.825558	8.137335	8.08261	C	9.198023	11.365995	13.89398
C	9.395589	6.126143	7.33883	H	9.120221	12.132038	14.45041
H	9.389301	5.341927	6.80269	C	8.482327	11.100772	12.77777
C	8.736638	6.313824	8.49686	H	7.803709	11.655563	12.41146
H	8.174766	5.677435	8.92323	Cl	6.245726	14.136524	10.06685
C	1.921437	9.002360	8.42826	O	7.425237	13.460522	10.48170
H	1.679652	9.435749	7.57163	O	5.060127	13.391268	10.41365
H	1.087492	8.800460	8.92209	O	6.188129	15.449173	10.47017
C	2.674324	7.748786	8.16868	O	6.328049	14.128031	8.63705
C	3.328377	5.827205	7.33762	Cl	6.227800	13.968065	10.74420
H	3.406179	5.061162	6.78118	O	6.251500	13.895097	12.16776
C	4.044073	6.092428	8.45382	Cl	0.087221	8.452641	4.64747
H	4.722691	5.537637	8.82013	O	0.213913	7.189818	5.34598
Fe	4.109787	8.462115	10.63486	O	1.134867	9.308347	5.03010
O	6.457910	5.988065	13.07191	O	-1.178459	9.002102	4.94757
N	5.658714	7.233695	11.44945	O	0.153361	8.263465	3.26302
N	7.057662	7.326487	11.44283	N	10.276608	12.037183	5.44276
N	3.005071	6.892066	12.11177	C	11.368084	12.240355	5.56788
H	2.436523	6.283272	11.55850	C	12.778456	12.520277	5.71110
N	9.753519	7.292547	12.00740	H	12.950644	12.881180	6.60580
H	10.340255	6.730244	11.42468	H	13.051494	13.176232	5.03615
N	3.512879	9.601457	12.26547	H	13.289734	11.693250	5.58849

Table H.3 Cartesian coordinates of **C3**, derived by X-ray structure analysis.

	X	Y	Z		X	Y	Z
Fe	3.985294	8.287058	8.40666	N	8.525603	5.470667	4.59766
O	5.369894	4.884038	10.53045	H	8.978218	5.599075	3.85398
N	3.027656	3.573364	6.41126	C	3.985441	6.657859	4.44453
N	4.733024	6.389014	9.06277	C	3.398804	8.419702	5.48368
N	3.857372	8.251341	10.86255	C	5.943561	10.366069	7.69307
N	5.102569	5.225163	8.38107	C	7.279181	4.972468	4.69321
N	1.981010	7.876034	8.80236	C	2.927787	9.796691	5.80289
N	5.272244	2.586795	7.70380	H	1.945239	9.803884	5.92383
H	5.875501	1.962658	7.20727	H	3.158960	10.417604	5.06729
N	1.716756	1.878861	6.88243	C	7.070742	9.034753	8.97385
H	1.437042	1.116936	7.22249	H	7.300828	8.288952	9.51545
N	0.349199	7.326633	10.16166	C	4.322484	5.725499	3.33709
H	-0.103416	7.198225	10.90534	H	4.906759	6.180290	2.67991
C	4.889361	6.139441	10.31479	H	3.495625	5.440606	2.87316
C	5.475998	4.377598	9.27564	C	7.953931	5.406859	6.70351
C	2.931240	2.431231	7.06625	H	7.968223	5.490310	7.64973
C	1.595621	7.824832	10.06611	C	8.964406	5.742993	5.87310
C	5.947015	3.000609	8.95643	H	9.810476	6.097248	6.12044
H	6.929563	2.993416	8.83549	C	7.885194	10.077567	8.69278
H	5.715842	2.379696	9.69203	H	8.776558	10.204733	8.99576
C	1.804059	3.762547	5.78548	C	4.879604	10.899883	6.79186
H	1.573974	4.508348	5.24387	H	5.143319	10.762900	5.84751
C	4.552317	7.071801	11.42223	H	4.770982	11.872055	6.94408
H	3.968042	6.617010	12.07942	C	6.453931	4.457069	3.56812
H	5.379177	7.356694	11.88616	H	6.694275	3.514113	3.38595
C	0.920871	7.390441	8.05581	H	6.640216	4.985150	2.75171
H	0.906579	7.306990	7.10959	H	4.619293	3.784046	3.58396
C	-0.089604	7.054307	8.88622	S	4.351270	0.800100	3.78072
H	-0.935674	6.700052	8.63888	F	5.326665	-0.522437	1.72287
C	0.989608	2.719733	6.06654	O	3.967147	1.876225	2.89291
H	0.098244	2.592567	5.76356	O	3.384078	-0.262114	3.89361
C	3.995197	1.897417	7.96747	F	6.688957	0.887032	2.58192
H	3.731482	2.034400	8.91181	O	4.953182	1.215795	5.01696
H	4.103820	0.925245	7.81524	F	6.292258	-0.958940	3.58632
C	2.420871	8.340231	11.19120	C	5.737117	0.005196	2.87653
H	2.180526	9.283187	11.37337	S	-0.945809	5.358089	13.37571
H	2.234586	7.812150	12.00761	O	-1.901279	5.555257	14.44718
H	4.255509	9.013254	11.17536	O	-0.454618	6.597686	12.82416
Fe	4.889508	4.510242	6.35266	F	0.909668	5.536534	15.19335
O	3.504908	7.913262	4.22887	O	-1.281458	4.347038	12.42554
N	5.847146	9.223936	8.34806	F	0.179377	3.564675	14.91397
N	4.141778	6.408286	5.69655	F	1.504279	4.472413	13.44421
N	5.017430	4.545959	3.89677	C	0.497732	4.675954	14.26324
N	3.772233	7.572137	6.37825	C	1.433762	4.051625	9.88581
N	6.893792	4.921266	5.95696	N	2.461678	4.406635	10.15416
N	3.602558	10.210505	7.05552	C	0.107274	3.594992	9.51410
H	2.999301	10.834642	7.55205	H	-0.178133	4.052150	8.69559
N	7.158046	10.918439	7.87689	H	-0.522306	3.796805	10.23748
H	7.437760	11.680364	7.53683	H	0.126568	2.627657	9.35821

Table H.4 Cartesian coordinates of **C4**, derived by X-ray structure analysis.

	X	Y	Z		X	Y	Z
Fe	1.866644	3.425665	0.11736	N	6.719480	6.375680	-1.57644
S	6.682640	6.467799	4.06555	H	7.564549	6.445072	-1.04630
S	2.143982	1.750503	4.31983	N	2.089042	1.517951	-1.23576
O	1.446191	7.029771	2.23883	H	1.894616	0.714815	-0.67260
N	1.983333	5.424556	0.84464	C	5.588488	4.252852	-1.76217
N	5.861830	6.077996	1.69005	C	4.189801	2.669194	-1.54251
N	2.465241	2.413951	1.88871	C	0.722760	3.024716	-2.58956
N	2.907400	6.463426	0.70513	C	0.477406	5.201840	-2.18080
N	0.024708	3.672479	1.57644	H	0.526916	5.998912	-1.66628
H	-0.820361	3.603086	1.04630	C	6.643966	7.523012	-2.51312
N	4.655146	8.530207	1.23576	H	7.053893	8.325113	-2.10239
H	4.849572	9.333343	0.67260	H	7.133759	7.313747	-3.34764
C	1.155700	5.795307	1.76217	C	3.026119	7.969971	-2.37441
C	2.554387	7.378965	1.54251	H	2.240584	7.931097	-1.84155
C	6.021428	7.023442	2.58956	C	6.704171	5.077164	-2.28735
C	6.266782	4.846319	2.18080	H	6.584421	5.226385	-3.25869
H	6.217272	4.049247	1.66628	H	7.564395	4.607168	-2.14876
C	0.100222	2.525147	2.51312	C	5.202142	7.779833	-2.81418
H	-0.309705	1.723045	2.10239	C	3.473037	1.388991	-1.75751
H	-0.389570	2.734411	3.34764	H	3.450214	1.173750	-2.72355
C	3.718069	2.078187	2.37441	H	3.943644	0.656189	-1.28672
H	4.503604	2.117061	1.84155	C	0.005974	5.181323	-3.44964
C	0.040017	4.970995	2.28735	H	-0.308562	5.939673	-3.92763
H	0.159767	4.821773	3.25869	C	1.062036	1.593452	-2.29367
H	-0.820206	5.440990	2.14876	H	1.398920	1.155537	-3.11516
C	1.542046	2.268326	2.81418	H	0.247564	1.113053	-2.00048
C	3.271151	8.659168	1.75751	C	3.013517	8.357189	-3.66811
H	3.293974	8.874409	2.72355	H	2.238351	8.623997	-4.14813
H	2.800544	9.391969	1.28672	F	9.615965	4.056489	7.71894
C	6.738214	4.866835	3.44964	F	8.173348	4.929037	6.21306
H	7.052750	4.108486	3.92763	F	10.361241	5.560728	6.21654
C	5.682152	8.454707	2.29367	F	9.791609	3.484025	5.53904
H	5.345268	8.892621	3.11516	B	9.477845	4.493501	6.41653
H	6.496624	8.935106	2.00048	F	-1.977508	9.045172	0.01934
C	3.730671	1.690969	3.66811	F	-1.110641	8.328351	1.99363
H	4.505837	1.424161	4.14813	F	-0.936986	7.032214	0.15395
Fe	4.877544	6.622493	-0.11736	F	0.281014	8.936802	0.30459
S	0.061548	3.580359	-4.06555	B	-0.928590	8.343741	0.62740
S	4.600206	8.297655	-4.31983	N	3.167451	5.478092	3.96885
O	5.297997	3.018388	-2.23883	C	3.273865	6.158516	4.87653
N	4.760855	4.623602	-0.84464	C	3.415229	7.017245	6.05141
N	0.882358	3.970162	-1.69005	H	3.412893	7.956478	5.77172
N	4.278948	7.634207	-1.88871	H	4.259644	6.813620	6.50517
N	3.836788	3.584732	-0.70513	H	2.667886	6.857205	6.66482

Table H.5 Cartesian coordinates of **C6**, derived by X-ray structure analysis.

	X	Y	Z		X	Y	Z
Fe	2.592393	2.720279	7.33511	N	1.473533	1.917827	5.72194
S	3.186668	4.358692	11.54021	C	6.372552	1.746400	5.62882
S	7.930836	7.256650	7.86908	C	4.784456	0.822132	6.69313
O	2.384236	6.750324	6.15835	C	7.647567	1.990791	4.91365
N	2.839024	4.607719	6.34737	H	7.877583	1.219805	4.37183
N	3.870084	5.224815	5.65056	H	8.362764	2.140755	5.55155
N	0.874376	4.106645	8.19695	C	3.936076	-0.215563	7.32241
H	0.038092	3.596721	8.16524	H	3.784167	-0.941622	6.69738
N	5.713024	6.891406	4.53903	H	4.381014	-0.575662	8.10551
H	5.840878	7.043611	3.57940	C	7.213618	2.848493	2.65124
N	3.230864	3.177769	9.28867	H	7.894161	3.254198	2.09165
N	6.879302	5.368203	6.53034	H	7.262722	1.886993	2.53295
C	1.980283	5.539630	6.62346	C	5.860623	3.334046	2.21963
C	3.568378	6.463897	5.55915	C	3.793093	3.886864	1.10300
C	0.705267	5.295239	7.33863	H	3.058954	4.016499	0.54700
H	0.475252	6.066225	7.88045	C	3.934027	4.422190	2.32748
H	-0.009929	5.145275	6.70074	H	3.284002	4.961435	2.71683
C	4.416758	7.501592	4.92988	C	1.484351	-0.184243	7.00418
H	4.568668	8.227651	5.55490	H	1.682626	-1.098189	6.74672
H	3.971821	7.861692	4.14677	H	0.712199	-0.195550	7.59117
C	1.139217	4.437537	9.60104	C	1.180533	0.628344	5.78647
H	0.458673	4.031832	10.16064	C	0.476512	1.591442	3.67601
H	1.090113	5.399037	9.71933	H	0.143619	1.806721	2.83475
C	2.492211	3.951984	10.03265	C	1.075238	2.466909	4.52110
C	4.559741	3.399166	11.14929	H	1.206306	3.362773	4.30864
H	5.293880	3.269531	11.70528	S	-0.079370	6.130728	3.61483
C	4.418808	2.863840	9.92481	F	-0.186203	4.510307	1.56893
H	5.068833	2.324595	9.53545	F	-1.836888	5.878955	1.68905
C	6.868484	7.470272	5.24811	F	0.092139	6.589538	1.03579
H	6.670209	8.384219	5.50556	O	-0.455503	7.503685	3.80400
H	7.640635	7.481580	4.66111	O	1.327063	5.864909	3.65416
C	7.172301	6.657686	6.46581	O	-0.889977	5.182081	4.35158
C	7.876323	5.694588	8.57627	C	-0.515398	5.756691	1.88287
H	8.209216	5.479308	9.41754	S	5.617493	9.278507	1.87313
C	7.277596	4.819120	7.73118	F	7.015597	9.048611	-0.33619
H	7.146528	3.923257	7.94365	F	7.487093	10.777386	0.85710
Fe	5.760442	4.565750	4.91717	F	8.174389	8.839026	1.46608
S	5.166166	2.927337	0.71207	O	4.695992	10.146880	1.20508
S	0.421998	0.029379	4.38320	O	6.005049	9.699385	3.19664
O	5.968598	0.535706	6.09393	O	5.330836	7.863408	1.76697
N	5.513811	2.678311	5.90491	C	7.157028	9.479707	0.90899
N	4.482750	2.061215	6.60173	N	4.229543	6.686975	8.39044
N	7.478458	3.179385	4.05533	C	4.522472	7.386660	9.23832
H	8.314743	3.689309	4.08704	C	4.892884	8.269315	10.33600
N	2.639811	0.394624	7.71325	H	4.450483	9.114689	10.23010
H	2.511956	0.242418	8.67288	H	5.843523	8.402956	10.33233
N	5.121970	4.108261	2.96362	H	4.628790	7.872094	11.16911

Table H.6 Cartesian coordinates of **C7**, derived by X-ray structure analysis.

	X	Y	Z		X	Y	Z
Fe	10.958860	4.263692	5.91856	N	9.398978	2.552770	6.07877
O	13.617859	7.471090	5.48533	H	9.342858	2.094048	5.19197
O	11.944080	3.046472	-0.12095	N	9.299465	8.851810	7.91890
O	8.774601	11.069949	0.23467	N	11.137504	3.524679	7.91256
N	11.931620	6.171456	6.02930	C	7.323795	6.501102	6.05402
N	11.480060	7.497789	5.98064	C	8.012116	4.500473	6.12877
N	13.259508	3.811253	5.67712	C	6.433363	7.676820	6.19560
H	13.564364	3.293251	6.47634	H	5.971939	7.647659	7.07100
N	11.109461	10.160596	5.69536	H	5.747588	7.669119	5.48162
H	11.165581	10.619318	6.58217	C	8.055254	3.050444	6.42991
N	11.208974	3.861556	3.85524	H	7.366790	2.572656	5.90281
N	9.370935	9.188687	3.86157	H	7.875882	2.896946	7.39136
C	13.184644	6.212264	5.72011	C	7.135003	9.768144	7.28232
C	12.496324	8.212893	5.64537	H	7.280241	10.709879	7.01376
C	14.075077	5.036546	5.57854	H	6.220196	9.694713	7.65359
H	14.536500	5.065706	4.70313	C	9.917626	1.592258	7.06478
H	14.760852	5.044246	6.29251	H	9.168156	1.059825	7.43206
C	12.453185	9.662922	5.34422	H	10.546434	0.970340	6.61990
H	13.141649	10.140710	5.87133	C	8.137230	9.394035	8.34921
H	12.632557	9.816420	4.38278	C	7.893706	9.661194	9.66984
C	13.373437	2.945222	4.49182	H	7.058375	10.025116	9.93869
H	13.228198	2.003487	4.76038	C	8.882445	9.394567	10.61752
H	14.288243	3.018653	4.12055	C	10.095982	8.864485	10.18648
C	10.590813	11.121108	4.70936	H	10.798988	8.685773	10.79996
H	11.340283	11.653541	4.34208	C	10.242794	8.608589	8.84477
H	9.962006	11.743026	5.15423	H	11.065685	8.234929	8.55198
C	12.371210	3.319331	3.42493	C	9.548876	9.400443	12.90706
C	12.614733	3.052172	2.10429	H	9.173281	9.602329	13.78942
H	13.450065	2.688250	1.83544	H	9.807592	8.455923	12.87048
C	11.625995	3.318799	1.15662	H	10.337288	9.961349	12.75152
C	10.412457	3.848881	1.58766	C	10.627870	2.304920	8.19157
H	9.709451	4.027592	0.97418	C	10.795058	1.692929	9.41395
C	10.265645	4.104777	2.92937	H	10.393808	0.849290	9.58655
H	9.442754	4.478437	3.22215	C	11.557678	2.322112	10.39463
C	10.959564	3.312923	-1.13292	C	12.068150	3.591232	10.12415
H	11.335158	3.111037	-2.01528	H	12.566287	4.064639	10.78008
H	10.700848	4.257443	-1.09633	C	11.833885	4.141575	8.88622
H	10.171152	2.752017	-0.97738	H	12.183332	5.006692	8.70745
C	9.880569	10.408446	3.58256	C	12.673668	2.157500	12.50030
C	9.713382	11.020437	2.36018	H	12.744738	1.534426	13.25337
H	10.114631	11.864076	2.18758	H	13.551425	2.259233	12.07652
C	8.950761	10.391254	1.37950	H	12.364871	3.028929	12.82533
C	8.440289	9.122134	1.64999	Cl	14.006949	8.434138	9.11037
H	7.942152	8.648727	0.99405	O	13.563716	9.478842	8.24425
C	8.674554	8.571791	2.88791	O	13.379830	8.548664	10.38151
H	8.325108	7.706674	3.06669	O	15.417378	8.478171	9.28824
C	7.834771	10.555866	-0.72615	O	13.619376	7.203665	8.52277
H	7.763701	11.178940	-1.47923	Cl	9.912955	12.828957	8.30933
H	6.957015	10.454133	-0.30238	O	8.809192	12.405027	7.48009
H	8.143569	9.684437	-1.05119	O	10.288986	14.155095	7.90597
Fe	9.549579	8.449674	5.85557	O	9.536022	12.803515	9.68163
O	6.890581	5.242276	6.28880	O	11.033655	11.941567	8.09780
O	8.564360	9.666894	11.89509	N	12.149247	7.105736	2.96753
O	11.733839	1.643417	11.53947	C	11.746044	7.116142	1.90871
N	8.576819	6.541910	5.74484	C	11.211805	7.131666	0.55931
N	9.028380	5.215577	5.79350	H	11.747673	6.541755	-0.01097
N	7.248932	8.902113	6.09701	H	11.243770	8.045123	0.20582
H	6.944076	9.420115	5.29779	H	10.283240	6.818597	0.57198

Table H.7 Cartesian coordinates of **C8**, derived by X-ray structure analysis.

	X	Y	Z		X	Y	Z
Fe	13.529572	7.405710	11.73094	C	13.226049	4.653943	10.31998
Fe	12.513880	5.052156	15.30577	H	12.396859	4.624716	10.78268
O	16.503478	5.845867	14.21306	C	11.937935	11.427052	12.20089
O	9.554663	6.615740	12.78686	H	11.348802	11.955315	11.67520
O	13.884497	-0.621280	13.04618	C	10.441854	7.757965	18.01616
O	15.154870	2.470168	8.22685	H	9.595187	7.730948	18.44618
O	10.958465	10.008084	18.79197	C	11.248144	8.888611	18.09943
N	11.726640	6.542072	12.49356	C	12.468869	8.903904	17.41176
N	11.406660	5.797452	13.63317	H	13.033156	9.667615	17.43996
O	11.927609	12.992742	14.05052	C	14.836009	3.582712	8.92396
N	14.638484	6.689706	13.40743	C	16.411639	2.453400	7.53646
N	14.329949	5.904876	14.52582	H	16.420584	3.159613	6.85708
N	13.981737	5.781499	10.40994	H	16.535265	1.582633	7.10414
N	12.725793	3.045140	14.57461	H	17.137939	2.606478	8.17636
N	13.223913	9.414010	12.44377	C	9.745111	10.026058	19.56188
N	12.074283	6.671278	16.62216	H	8.982931	9.839358	18.97484
N	11.832204	8.255917	10.37377	H	9.632227	10.908390	19.97316
H	11.949865	7.897734	9.44757	H	9.792759	9.342678	20.26270
N	14.242345	4.128505	16.59156	C	13.407380	-1.045512	11.75868
H	14.162758	4.473945	17.52660	H	13.631926	-0.367666	11.08748
N	15.743838	7.756121	11.14307	H	12.434910	-1.161884	11.79277
H	15.897563	8.738633	11.03800	H	13.829929	-1.896295	11.51778
N	10.283828	4.735708	15.89260	C	10.930954	13.789626	13.37312
H	10.108206	3.755079	15.97935	H	11.313444	14.161371	12.55098
C	10.612622	7.002934	12.03450	H	10.643462	14.520529	13.95925
C	15.449446	5.427546	14.95215	H	10.159905	13.227552	13.14963
C	10.128852	5.886816	13.77256	S	13.048165	3.918962	20.22816
C	15.920664	6.618407	13.26061	O	12.045080	3.512135	19.27528
C	15.150798	5.808618	9.75786	F	12.950794	5.863678	22.05245
C	9.347441	5.305189	14.88624	F	12.578331	6.437344	19.98714
H	8.749960	4.594479	14.54270	O	14.294721	4.279015	19.63377
H	8.787651	6.005508	15.30609	O	13.195752	3.041740	21.35377
C	16.688122	7.231043	12.15761	F	11.076509	5.514245	21.05977
H	17.282848	6.555227	11.74569	C	12.405360	5.460423	20.93744
H	17.249965	7.967400	12.50717	F	13.242615	5.920247	21.85722
C	12.408074	10.210688	11.72997	F	11.374261	5.071276	21.70617
C	13.551601	2.202626	15.24969	F	12.079772	6.372497	20.10211
C	12.046243	9.716814	10.35030	S	13.129174	8.449900	6.79369
H	11.221700	10.168916	10.04072	F	13.488495	6.691057	4.88288
H	12.774665	9.936175	9.71675	O	14.078581	9.102059	7.66908
C	10.480884	7.892741	10.85829	F	15.035478	8.151434	5.07448
H	9.979119	7.430377	10.14099	O	12.526142	9.318055	5.82511
H	9.982186	8.710387	11.10898	F	14.892801	6.552359	6.47285
C	13.626560	9.855419	13.66134	O	12.250521	7.554387	7.45076
H	14.211153	9.306796	14.17098	C	14.195674	7.391226	5.76130
C	15.906312	7.102915	9.82074	S	8.943500	4.278950	10.23588
H	16.867083	6.930996	9.65498	F	10.568123	5.341852	8.47510
H	15.577292	7.710270	9.11155	F	10.538075	3.183432	8.47376
C	15.588044	4.470604	16.07577	O	10.040751	4.144019	11.17285
H	16.047122	3.650632	15.76432	F	8.883636	4.285371	7.62172
H	16.131585	4.875735	16.79725	O	8.291876	5.563740	10.23323
C	10.134105	5.367896	17.22125	O	8.074776	3.137908	10.14367
H	10.464606	4.750251	17.92081	C	9.773342	4.273978	8.62559
H	9.176324	5.546773	17.39665	S	17.019611	8.115644	16.95227
C	10.908992	6.662128	17.28351	O	15.995048	8.300961	15.95849
C	13.438180	0.569531	13.50666	F	15.301084	8.981350	18.73681
C	13.996802	2.681839	16.60584	F	16.948175	7.840292	19.55008
H	13.298938	2.471844	17.27590	F	15.328791	6.846816	18.48795
H	14.826051	2.208611	16.86760	O	17.711223	6.856083	16.87965
C	15.627884	4.729367	9.02043	O	17.848730	9.261595	17.20147
H	16.474498	4.771499	8.59152	C	16.086997	7.942817	18.51611
C	13.935129	0.975254	14.74537	N	10.501900	8.707723	14.45454
H	14.527782	0.416415	15.23419	C	9.970144	9.634699	14.82487
C	12.569881	1.400373	12.81461	C	9.318016	10.835982	15.28633
H	12.206161	1.142012	11.97588	H	8.447805	10.925562	14.84463
C	12.250992	2.621347	13.38938	H	9.874980	11.613182	15.07143
H	11.659760	3.194949	12.91619	H	9.188304	10.785258	16.25638
C	12.348396	11.860198	13.46478	N	15.463574	3.740411	12.59025
C	13.227074	11.064185	14.19504	C	15.961291	2.775858	12.27985
H	13.545452	11.347500	15.04409	C	16.594447	1.511668	11.88729
C	12.831500	7.785928	16.69403	H	16.400501	1.328173	10.94436
H	13.657610	7.800167	16.22515	H	16.241840	0.783968	12.44092
C	13.610134	3.554073	9.58825	H	17.563862	1.578536	12.01437
H	13.050093	2.788467	9.53638				

Table H.8 Cartesian coordinates of **C11**, derived by X-ray structure analysis..

	X	Y	Z		X	Y	Z
Fe	7.982977	8.117204	6.63752	H	9.351857	10.398452	7.41180
Cl	6.550705	9.355383	12.99289	C	10.926314	8.008968	6.65069
Cl	9.680304	1.784501	13.03753	C	11.665480	6.029069	6.76644
O	5.429709	4.834120	6.84962	C	11.128919	3.133402	4.39377
N	7.598079	4.878278	6.53783	C	8.466395	9.954311	4.29262
N	7.113900	6.185556	6.46839	C	12.028035	2.757842	5.54281
N	5.726528	8.514991	6.71309	H	12.973616	2.844550	5.26274
H	5.478465	9.031519	5.89353	H	11.867521	1.813021	5.79110
N	7.563153	8.451789	8.71654	C	11.486371	2.847747	3.08241
N	9.532180	3.400509	8.84907	H	12.333950	2.470965	2.87715
N	8.072592	2.245992	6.87117	C	12.587511	4.864295	6.69853
H	8.156936	1.737308	6.01435	H	13.204677	4.876291	7.47251
C	6.582478	4.126792	6.77545	H	13.126695	4.908037	5.86940
C	5.843313	6.106691	6.65970	C	8.983639	10.763902	5.46104
C	6.379873	9.002358	9.03237	H	8.265432	11.359564	5.79189
C	9.042397	2.181449	9.13353	H	9.737287	11.330968	5.16012
C	5.480757	9.377919	7.88334	C	9.076840	3.957535	3.71634
H	4.535177	9.291210	8.16341	H	8.242303	4.352524	3.94005
H	5.641272	10.322739	7.63505	C	10.847051	9.470148	6.40987
C	6.022422	9.288014	10.34373	H	11.171757	9.681759	5.49889
H	5.174842	9.664795	10.54899	H	11.413222	9.952661	7.06311
C	4.921282	7.271465	6.72761	C	7.450900	8.006072	3.57275
H	4.304115	7.259469	5.95364	H	7.106274	7.142441	3.76733
H	4.382098	7.227723	7.55675	C	10.570140	3.128723	2.08365
C	8.525154	1.371858	7.96510	C	8.458511	10.483147	3.00919
H	9.243360	0.776196	7.63425	H	8.824548	11.341412	2.83052
H	7.771506	0.804792	8.26602	C	9.344050	3.690112	2.38919
C	8.431952	8.178225	9.70980	H	8.708728	3.884628	1.71019
H	9.266489	7.783236	9.48610	C	7.393781	8.466797	2.26924
C	6.661742	2.665613	7.01628	H	7.015835	7.934591	1.57901
H	6.337035	2.454002	7.92725	C	7.901806	9.722185	2.00049
H	6.095570	2.183099	6.36304	S	9.547272	-0.431845	4.48383
C	10.057893	4.129688	9.85340	F	10.013363	-2.171457	2.61054
H	10.402519	4.993319	9.65881	F	8.162610	-1.105805	2.37202
C	6.938653	9.007038	11.34249	O	10.969638	-0.263601	4.68842
C	9.050282	1.652613	10.41696	O	8.977523	-1.515850	5.22882
H	8.684244	0.794348	10.59562	F	10.012074	-0.132767	1.92449
C	8.164743	8.445648	11.03695	O	8.796546	0.792874	4.48696
H	8.800065	8.251132	11.71595	C	9.429732	-0.977205	2.75146
C	10.115012	3.668963	11.15690	S	4.822707	4.187333	3.57325
H	10.492958	4.201169	11.84714	O	5.977107	4.990099	3.86784
C	9.606986	2.413575	11.42565	F	6.093056	3.292428	1.47025
Fe	9.525815	4.018556	6.78862	O	4.835503	2.861525	4.12436
Cl	10.958087	2.780378	0.43326	O	3.568647	4.870346	3.71849
Cl	7.828488	10.351259	0.38862	F	4.945903	5.055509	1.11163
O	12.079083	7.301640	6.57653	F	3.969718	3.145679	1.33380
N	9.910714	7.257483	6.88831	C	4.971241	3.907142	1.78570
N	10.394893	5.950204	6.95775	N	6.718905	5.198341	9.54739
N	11.782264	3.620770	6.71306	C	6.121064	5.377940	10.48256
H	12.030328	3.104241	7.53262	C	5.340899	5.625595	11.69408
N	9.945639	3.683971	4.70961	H	4.413887	5.828955	11.44979
N	7.976613	8.735251	4.57708	H	5.724714	6.385033	12.18023
N	9.436201	9.889768	6.55498	H	5.361191	4.828793	12.26425

Table H.9 Cartesian coordinates of **C12**, derived by X-ray structure analysis..

	X	Y	Z		X	Y	Z
F	10.333932	3.830040	6.52045	H	8.985564	7.654866	10.42301
F	12.244625	2.572058	6.52045	N	5.888122	6.276261	9.29505
F	10.403701	1.942401	5.38072	N	3.382345	7.320715	9.90713
B	10.859184	2.557454	6.52045	C	8.334303	8.364293	7.57804
F	10.403701	1.942401	7.66017	C	8.232028	8.854341	8.97533
F	5.226514	6.278879	13.04090	H	9.027504	9.399481	9.19927
B	5.305102	4.909689	13.04090	H	7.428000	9.423498	9.07376
F	5.504928	4.164372	14.16965	C	7.000378	7.806882	10.81080
F	4.080255	4.471694	12.50692	H	6.874967	8.751441	11.07945
F	6.340896	4.452480	12.27060	H	7.183919	7.276425	11.62630
F	3.862932	4.397342	13.04090	C	5.749245	7.300169	10.15086
F	5.703148	4.478068	11.83305	C	4.492601	7.819858	10.42976
F	6.919206	5.036219	13.04090	H	4.426202	8.562522	11.01843
F	5.156965	4.431444	11.79944	C	3.532183	6.275795	9.08705
F	5.504928	4.164372	11.91214	H	2.758362	5.874634	8.70922
F	4.080255	4.471694	13.57487	C	4.772527	5.759623	8.77035
F	6.340896	4.452480	13.81120	H	4.834311	5.025826	8.17017
F	5.703148	4.478068	14.24874	Fe	7.779144	5.487087	8.76163
F	5.156965	4.431444	14.28235	N	8.363093	7.128484	5.81990
O	7.415369	2.177032	6.52045	N	8.143281	7.703470	3.15473
N	7.386107	4.254216	7.22099	H	8.985564	7.654866	2.61788
N	7.605919	3.679230	9.88616	N	5.888122	6.276261	3.74584
H	6.763636	3.727834	10.42301	N	3.382345	7.320715	3.13376
N	9.861078	5.106439	9.29505	C	8.334303	8.364293	5.46285
N	12.366855	4.061985	9.90713	C	8.232028	8.854341	4.06556
C	7.414897	3.018407	7.57804	H	9.027504	9.399481	3.84162
C	7.517172	2.528359	8.97533	H	7.428000	9.423498	3.96713
H	6.721696	1.983219	9.19927	C	7.000378	7.806882	2.23009
H	8.321200	1.959202	9.07376	H	6.874967	8.751441	1.96144
C	8.748822	3.575818	10.81080	H	7.183919	7.276425	1.41459
H	8.874233	2.631259	11.07945	C	5.749245	7.300169	2.89003
H	8.565281	4.106275	11.62630	C	4.492601	7.819858	2.61114
C	9.999955	4.082531	10.15086	H	4.426202	8.562522	2.02246
C	11.256599	3.562842	10.42976	C	3.532183	6.275795	3.95384
H	11.322998	2.820178	11.01843	H	2.758362	5.874634	4.33167
C	12.217017	5.106905	9.08705	C	4.772527	5.759623	4.27054
H	12.990838	5.508066	8.70922	H	4.834311	5.025826	4.87072
C	10.976673	5.623077	8.77035	Fe	7.874600	5.691350	4.30514
H	10.914889	6.356874	8.17017	Fe	7.779144	5.487087	4.27926
Fe	7.874600	5.691350	8.73576	Fe	7.970056	5.895613	4.27926
Fe	7.970056	5.895613	8.76163	C	13.819451	4.507970	13.04090
N	7.386107	4.254216	5.81990	H	12.872609	4.438058	12.79796
N	7.605919	3.679230	3.15473	H	13.907441	5.030288	13.86542
H	6.763636	3.727834	2.61788	H	14.187683	3.610763	13.18170
N	9.861078	5.106439	3.74584	N	15.167708	5.690371	11.12759
N	12.366855	4.061985	3.13376	C	14.567947	5.186584	11.93878
C	7.414897	3.018407	5.46285	C	17.678949	6.874730	13.04090
C	7.517172	2.528359	4.06556	H	18.625791	6.944642	12.79796
H	6.721696	1.983219	3.84162	H	17.590959	6.352412	13.86542
H	8.321200	1.959202	3.96713	H	17.310717	7.771937	13.18170
C	8.748822	3.575818	2.23009	N	16.330692	5.692329	11.12759
H	8.874233	2.631259	1.96144	C	16.930453	6.196116	11.93878
H	8.565281	4.106275	1.41459	H	18.625791	6.944642	13.28383
C	9.999955	4.082531	2.89003	H	17.590959	6.352412	12.21637
C	11.256599	3.562842	2.61114	H	17.310717	7.771937	12.90009
H	11.322998	2.820178	2.02246	N	16.330692	5.692329	14.95420
C	12.217017	5.106905	3.95384	C	16.930453	6.196116	14.14301
H	12.990838	5.508066	4.33167	H	12.872609	4.438058	13.28383
C	10.976673	5.623077	4.27054	H	13.907441	5.030288	12.21637
H	10.914889	6.356874	4.87072	H	14.187683	3.610763	12.90009
O	8.333831	9.205668	6.52045	N	15.167708	5.690371	14.95420
N	8.363093	7.128484	7.22099	C	14.567947	5.186584	14.14301
N	8.143281	7.703470	9.88616				

Table H.10 Cartesian coordinates of **C13**, derived by X-ray structure analysis..

	X	Y	Z		X	Y	Z
Fe	8.715674	5.682573	7.89376	C	5.282798	3.202211	8.37097
O	6.702519	9.314210	7.36012	C	7.393879	3.072614	8.35864
N	7.273773	7.188072	7.36396	C	3.856373	2.793150	8.32205
N	5.871130	7.281095	7.36858	H	3.607683	2.334779	9.16358
N	9.966079	7.607409	7.59974	H	3.710952	2.165080	7.57074
H	10.520804	7.490352	6.77600	C	8.745836	2.487538	8.24838
N	3.244770	8.034245	7.56562	H	8.802828	1.923419	7.43683
H	2.712029	8.024435	6.71941	H	8.930695	1.917451	9.03638
N	9.305681	6.259337	9.87629	C	2.098029	3.893604	6.98155
N	10.018603	7.250792	12.38349	H	1.823439	2.949601	6.86510
N	3.701247	6.536990	9.82103	H	1.284808	4.431391	7.15348
N	3.156785	7.601952	12.33796	C	10.660262	3.407879	7.03325
C	7.702134	8.408289	7.36763	H	11.514245	3.871034	7.22378
C	5.591053	8.537886	7.37995	H	10.853812	2.446019	6.90112
C	9.128559	8.817350	7.41655	C	2.765568	4.379910	5.72954
H	9.377249	9.275721	6.57502	C	2.426724	3.886743	4.47105
H	9.273980	9.445420	8.16786	H	1.786816	3.187245	4.41002
C	4.239096	9.122962	7.49022	C	3.859207	5.338461	3.50383
H	4.182104	9.687081	8.30176	H	4.260099	5.707745	2.72575
H	4.054237	9.693049	6.70222	C	4.229470	5.841765	4.73908
C	10.886903	7.716896	8.75705	H	4.875020	6.536665	4.79276
H	11.161492	8.660899	8.87350	C	10.041641	3.978884	5.77758
H	11.700124	7.179109	8.58512	C	10.284521	3.439599	4.51989
C	2.324670	8.202621	8.70535	H	10.792209	2.639345	4.45390
H	1.470687	7.739466	8.51482	C	9.128845	5.140595	3.55354
H	2.131120	9.164481	8.83748	H	8.823409	5.600336	2.78033
C	10.219364	7.230590	10.00906	C	8.837695	5.660688	4.79860
C	10.558208	7.723757	11.26755	H	8.311688	6.449110	4.86338
H	11.198115	8.423255	11.32858	Cl	6.688610	9.012616	10.87179
C	9.125725	6.272039	12.23476	O	6.582949	7.594184	10.52519
H	8.724833	5.902755	13.01285	O	5.509082	9.606388	10.34889
C	8.755462	5.768735	10.99952	O	6.618084	9.009527	12.30762
H	8.109912	5.073835	10.94584	O	7.917331	9.562501	10.37975
C	2.943291	7.631616	9.96102	O	5.876119	10.141981	10.37199
C	2.700411	8.170901	11.21871	O	6.368867	7.800677	10.20757
H	2.192723	8.971155	11.28470	O	8.037902	9.347021	10.53556
C	3.856087	6.469905	12.18506	N	1.963325	11.731992	7.24523
H	4.161523	6.010164	12.95827	C	1.146601	11.146800	6.71028
C	4.147237	5.949812	10.94000	C	0.113631	10.361175	6.04118
H	4.673244	5.161390	10.87522	H	0.345079	10.255764	5.09476
Fe	4.269258	5.927927	7.84484	H	-0.747930	10.821938	6.11742
O	6.282413	2.296290	8.37847	H	0.050423	9.478522	6.46230
N	5.711159	4.422428	8.37463	Cl	-0.094540	6.633555	5.17630
N	7.113802	4.329405	8.37002	O	0.781599	7.002362	6.26278
N	3.018853	4.003091	8.13885	O	-1.289689	7.383709	5.33224
H	2.464127	4.120148	8.96260	O	-0.332135	5.213869	5.22918
N	9.740162	3.576255	8.17298	O	0.489079	6.960367	3.94050
H	10.272903	3.586065	9.01919	Cl	-0.030347	6.528317	5.62200
N	3.679251	5.351163	5.86231	O	-0.137529	6.295457	7.01743
N	2.966328	4.359708	3.35510	O	-1.153893	7.208785	5.05022
N	9.283684	5.073510	5.91757	O	1.140972	7.076391	5.32577
N	9.828147	4.008548	3.40064				

Table H.11 Cartesian coordinates of **C14**, derived by X-ray structure analysis..

	X	Y	Z		X	Y	Z
Fe	5.125595	6.122156	5.62002	C	2.115430	6.017660	6.51423
O	8.936040	7.919533	5.69478	C	0.792032	5.681318	6.72778
N	6.833681	7.360631	5.99550	H	0.206848	6.259049	7.20346
N	4.827134	6.745175	3.63228	C	5.453042	9.821197	10.81327
N	7.063204	8.574015	6.64207	C	7.132417	8.400573	10.10204
N	8.044545	10.844756	7.61234	H	7.657574	8.048604	9.39293
N	5.767417	4.544056	6.85931	C	1.239485	3.659305	5.54124
N	6.911411	5.103779	4.39598	H	0.955049	2.823270	5.19104
C	7.953329	7.016885	5.46060	C	7.341333	7.918471	11.37194
C	8.310387	8.857538	6.43768	H	8.002063	7.256118	11.53691
C	8.930289	10.076040	6.93186	C	0.350574	4.466372	6.22028
C	10.253687	10.412382	6.71831	H	-0.551914	4.194630	6.33924
H	10.838870	9.834651	6.24263	C	4.357082	12.408420	7.06831
C	5.592677	6.272503	2.63282	C	2.554098	4.077612	5.37291
C	3.913302	7.693127	3.34405	H	3.158652	3.507976	4.91188
H	3.388145	8.045096	4.05316	C	5.609796	11.605489	5.29459
C	9.806234	12.434395	7.90485	H	6.268532	11.006771	4.96274
H	10.090670	13.270430	8.25505	C	6.568167	8.418872	12.40562
C	3.704385	8.175229	2.07415	H	6.695527	8.114267	13.29641
H	3.043656	8.837582	1.90918	C	5.617339	9.360160	12.12030
C	10.695145	11.627328	7.22581	H	5.066443	9.701508	12.81492
H	11.597633	11.899070	7.10685	C	4.143672	12.377906	8.55688
C	6.688637	3.685280	6.37778	H	3.282108	12.813160	8.77675
C	8.491621	12.016088	8.07318	H	4.866920	12.883715	9.00540
H	7.887067	12.585724	8.53421	C	2.850614	10.329049	8.74022
C	5.435923	4.488211	8.15151	H	2.370590	10.123356	9.58127
H	4.777187	5.086929	8.48335	H	2.284213	10.937568	8.20264
C	4.477552	7.674828	1.04047	C	4.489961	10.927896	10.48654
H	4.350192	7.979433	0.14968	H	4.891026	11.792144	10.75546
C	5.428380	6.733540	1.32579	H	3.663492	10.800997	11.01659
H	5.979276	6.392192	0.63117	C	3.707434	13.310118	6.24143
C	6.902046	3.715794	4.88921	H	3.034024	13.886256	6.58361
H	7.763611	3.280540	4.66934	C	5.026995	12.503936	4.42641
H	6.178799	3.209985	4.44069	H	5.289143	12.534466	3.51381
C	8.195105	5.764651	4.70587	C	4.063612	13.351205	4.90367
H	8.675129	5.970344	3.86482	H	3.639577	13.967030	4.31762
H	8.761506	5.156132	5.24345	F	8.422666	6.178532	8.19283
C	6.555758	5.165804	2.95955	F	9.752312	5.820222	9.97040
H	6.154693	4.301556	2.69063	F	10.330633	5.146701	7.88574
H	7.382226	5.292703	2.42950	F	10.252909	7.358040	8.43819
C	7.338284	2.783582	7.20466	B	9.723445	6.107688	8.63211
H	8.011695	2.207444	6.86248	F	8.561940	10.388145	3.74574
C	6.018724	3.589764	9.01968	F	8.695112	9.147418	1.96768
H	5.756576	3.559234	9.93228	F	7.066917	8.960039	3.57385
C	6.982106	2.742495	8.54242	F	7.054981	10.550949	2.08438
H	7.406142	2.126670	9.12847	B	7.799524	9.742112	2.79734
Fe	5.920123	9.971544	7.82607	F	8.257477	8.461166	2.37845
O	2.109679	8.174167	7.75131	F	7.644232	10.522673	1.70352
N	4.212038	8.733069	7.45059	F	6.479373	9.496925	3.19023
N	6.218585	9.348525	9.81381	O	10.018461	6.131265	1.88566
N	3.982515	7.519685	6.80402	N	10.724388	6.992149	1.43374
N	3.001174	5.248944	5.83375	O	10.870945	7.130684	0.24236
N	5.278302	11.549644	6.58678	C	11.451387	7.891739	2.34118
N	4.134307	10.989921	9.05011	H	10.818431	8.505424	2.76914
C	3.092390	9.076815	7.98549	H	12.111447	8.406383	1.83139
C	2.735332	7.236162	7.00841	H	11.908941	7.363109	3.02790

Table H.12 Cartesian coordinates of **C14'**, derived by X-ray structure analysis – Part 1

	X	Y	Z		X	Y	Z
Fe	17.897495	6.132839	9.79776	C	21.256925	9.659938	5.62541
O	15.194281	7.875847	7.06678	C	20.710747	6.024899	11.20823
N	16.777033	6.800760	11.44483	C	21.818734	5.704363	11.96852
N	16.907858	7.361830	8.34361	H	22.576184	6.276640	12.00435
N	17.201197	8.540951	7.66558	C	20.215818	7.751129	3.96158
N	17.196458	10.740517	6.17771	H	19.834899	7.084361	3.40227
N	18.240468	4.521928	8.48840	C	21.491497	8.234311	3.71569
N	15.739085	5.141996	9.50749	H	21.996041	7.911486	2.97832
C	15.731654	7.007769	7.95985	C	19.569076	12.330982	9.07154
C	16.169780	8.800009	6.93131	C	21.779948	4.508000	12.68029
C	17.279668	7.752666	12.26335	H	22.516030	4.245052	13.22026
H	18.152815	8.086331	12.09366	C	20.656458	3.708540	12.59063
C	15.530885	6.350062	11.67354	H	20.616323	2.884938	13.06241
C	16.077064	9.985101	6.09072	C	22.017120	9.192238	4.55955
C	14.969076	10.305637	5.33043	H	22.892912	9.529760	4.41275
H	14.211627	9.733360	5.29460	C	17.438129	11.561013	9.54852
C	16.571992	8.258871	13.33737	H	16.714616	10.978681	9.34870
H	16.952912	8.925639	13.89668	C	20.723366	12.272433	8.11475
C	15.296313	7.775689	13.58326	H	21.512924	12.711668	8.51944
H	14.791769	8.098514	14.32063	H	20.491687	12.759362	7.28450
C	17.218734	3.679018	8.22742	C	21.765732	10.237402	8.92828
C	15.007862	11.502000	4.61866	H	21.806728	10.868773	9.68971
H	14.271781	11.764949	4.07869	H	22.692444	10.017025	8.65859
C	16.131352	12.301460	4.70832	C	19.583425	4.119101	11.80349
H	16.171487	13.125062	4.23655	H	18.816683	3.560848	11.74909
C	14.770691	6.817762	12.73940	C	21.782415	10.756671	6.51447
H	13.894898	6.480240	12.88620	H	21.721331	11.619001	6.03204
C	19.349681	4.448987	7.75043	H	22.738309	10.584979	6.70651
H	20.073194	5.031319	7.95025	C	19.517268	13.228279	10.12617
C	16.064444	3.737567	9.18420	H	20.253504	13.797418	10.31734
H	15.274886	3.298332	8.77951	C	17.306414	12.455972	10.59459
H	16.296123	3.250638	10.01445	H	16.500317	12.503282	11.09508
C	15.022079	5.772598	8.37067	C	18.368324	13.275140	10.89334
H	14.981082	5.141227	7.60924	H	18.312836	13.874618	11.62822
H	14.095367	5.992975	8.64036	Fe	10.060086	9.953881	-1.00714
C	17.204385	11.890899	5.49546	O	12.683101	8.126036	1.73448
H	17.971127	12.449152	5.54986	N	11.281318	9.382644	-2.61273
C	15.005396	5.253329	10.78448	N	10.697425	7.482097	1.05573
H	15.066480	4.390999	11.26691	N	10.979805	8.715364	0.47897
H	14.049502	5.425021	10.59244	N	10.716537	5.170574	2.35629
C	17.270542	2.781721	7.17278	N	9.608643	11.508853	0.33430
H	16.534306	2.212582	6.98161	N	12.177954	10.982188	-0.55951
C	19.481397	3.554028	6.70436	C	11.816696	5.939166	2.53663
H	20.287493	3.506718	6.20387	C	12.148473	9.053671	0.90321
C	18.419486	2.734860	6.40561	C	11.724891	7.179124	1.78366
H	18.474975	2.135382	5.67073	C	10.845923	8.454097	-3.48883
Fe	18.890316	9.877161	7.50119	H	9.969450	8.103574	-3.38199
O	21.593530	8.134153	10.23217	C	12.893868	5.591525	3.32615
N	20.010777	9.209240	5.85412	H	13.640570	6.170398	3.42536
N	19.879953	8.648170	8.95534	C	12.530226	9.853835	-2.74904
N	19.586614	7.469049	9.63337	C	11.618047	7.992608	-4.53161
N	19.591353	5.269483	11.12124	H	11.276651	7.343979	-5.13597
N	18.547343	11.488072	8.81055	C	11.737005	3.552731	3.79305
N	21.048726	10.868004	7.79146	H	11.685787	2.708156	4.22499
C	21.056156	9.002231	9.33910	C	12.843005	4.358947	3.97156
C	20.618031	7.209991	10.36764	H	13.559875	4.076610	4.52732
C	19.508142	8.257334	5.03560	C	10.698029	3.985930	2.97614
H	18.634995	7.923669	5.20529				

Table H.13 Cartesian coordinates of **C14'**, derived by X-ray structure analysis – Part 2

	X	Y	Z		X	Y	Z
H	9.946196	3.418231	2.85380	C	6.287039	5.693204	-0.57422
C	8.436983	11.557747	0.98031	H	6.290699	5.094302	-1.36250
H	7.752911	10.945589	0.73572	H	5.345436	5.886397	-0.33724
C	12.898103	8.489943	-4.68300	C	6.170302	5.063066	1.80601
H	13.450198	8.196576	-5.39826	H	5.215735	5.195501	1.57937
C	13.356711	9.416666	-3.77926	H	6.253693	4.189705	2.26469
H	14.239196	9.759568	-3.85763	C	8.733185	2.726951	-1.70770
C	10.577304	12.379316	0.66639	H	8.026226	2.146060	-1.96320
C	11.802924	12.362714	-0.20225	C	10.949392	3.542965	-1.99007
H	11.628961	12.881022	-1.02759	H	11.797286	3.510737	-2.41732
H	12.553300	12.794183	0.27825	C	9.938816	2.684189	-2.36243
C	12.850061	10.316796	0.57422	H	10.075742	2.064778	-3.06957
H	12.846401	10.915698	1.36250	F	17.256883	6.125362	5.72815
H	13.791664	10.123603	0.33724	F	17.601256	5.681997	3.52743
C	12.966798	10.946934	-1.80601	F	16.050678	7.182422	4.15209
H	13.921365	10.814499	-1.57937	F	15.715087	4.980439	4.57619
H	12.883407	11.820295	-2.26469	B	16.655552	5.983193	4.49143
C	10.403915	13.283049	1.70770	F	14.206143	10.258904	8.67610
H	11.110874	13.863940	1.96320	F	13.890770	10.651981	10.80435
C	8.187708	12.467035	1.99007	F	12.960888	8.924726	9.81982
H	7.339814	12.499263	2.41732	F	15.229080	9.050917	9.95940
C	9.198284	13.325811	2.36243	B	14.088479	9.679182	9.92901
H	9.061358	13.945222	3.06957	F	15.337032	9.532194	10.59995
Fe	9.077014	6.056119	1.00714	F	13.320397	10.460134	10.76194
O	6.453999	7.883964	-1.73448	F	13.538990	8.370684	9.89299
N	7.855782	6.627356	2.61273	F	13.832118	5.565396	-0.02821
N	8.439675	8.527903	-1.05573	F	15.140037	6.989934	-1.10078
N	8.157295	7.294636	-0.47897	F	12.866105	7.203988	-1.11230
N	8.420563	10.839426	-2.35629	F	13.872547	5.579213	-2.24466
N	9.528457	4.501147	-0.33430	B	13.918296	6.367897	-1.15055
N	6.959146	5.027812	0.55951	F	14.648957	7.578301	-1.10787
C	7.320404	10.070834	-2.53663	F	13.777689	5.789776	0.09275
C	6.988627	6.956329	-0.90321	F	12.683702	6.751673	-1.65187
C	7.412209	8.830876	-1.78366	F	14.482757	5.564003	-2.06274
C	8.291177	7.555903	3.48883	O	11.760013	6.068959	9.04856
H	9.167650	7.906426	3.38199	N	10.984562	6.981225	8.87479
C	6.243232	10.418475	-3.32615	O	10.054001	7.178180	9.62493
H	5.496530	9.839602	-3.42536	C	11.163611	7.866113	7.71774
C	6.606874	6.156165	2.74904	H	10.319062	8.323231	7.52229
C	7.519053	8.017392	4.53161	H	11.435599	7.335718	6.93985
H	7.860449	8.666021	5.13597	H	11.855703	8.530272	7.91842
C	7.400095	12.457269	-3.79305	F	10.280467	10.084523	5.41618
H	7.451313	13.301844	-4.22499	F	10.520379	9.834399	3.17839
C	6.294095	11.651053	-3.97156	F	11.777121	8.628141	4.59725
H	5.577225	11.933390	-4.52732	F	12.102779	10.852362	4.33330
C	8.439071	12.024070	-2.97614	B	11.146229	9.842516	4.38564
H	9.190904	12.591769	-2.85380	F	12.045775	10.393532	3.61027
C	10.700117	4.452253	-0.98031	F	11.313092	10.240252	5.62546
H	11.384189	5.064411	-0.73572	F	9.874307	10.149716	3.86263
C	6.238997	7.520057	4.68300	F	11.211955	8.431218	4.37886
H	5.686902	7.813424	5.39826	N	16.950383	9.070305	-0.00894
C	5.780389	6.593334	3.77926	O	16.098263	9.920292	-0.13097
H	4.897904	6.250432	3.85763	O	17.858308	8.962190	-0.80142
C	8.559796	3.630684	-0.66639	C	16.893778	8.133512	1.12735
C	7.334176	3.647286	0.20225	H	16.683646	8.627101	1.94750
H	7.508139	3.128978	1.02759	H	17.761086	7.688290	1.22718
H	6.583800	3.215817	-0.27825	H	16.198986	7.462213	0.96299

Table H.14 Cartesian coordinates of **C15**, derived by X-ray structure analysis..

	X	Y	Z		X	Y	Z
Fe	5.218541	6.113229	5.61439	H	0.298359	6.200071	7.20311
O	9.018607	7.939010	5.74573	C	5.532360	9.766972	10.92257
N	7.135301	8.569459	6.68910	C	7.264498	8.417578	10.19355
N	6.916136	7.369941	6.01285	H	7.803193	8.091725	9.48212
N	4.897469	6.714047	3.63060	C	4.386997	12.358173	7.20514
N	5.874584	4.520813	6.82053	C	5.667867	11.606549	5.42843
N	8.112954	10.816197	7.72407	H	6.349238	11.035107	5.09425
N	7.030073	5.139567	4.37547	C	0.448293	4.436538	6.17642
C	9.000521	10.063659	7.03189	H	-0.454128	4.161398	6.28789
C	8.383648	8.861750	6.50357	C	7.493392	7.937421	11.46406
C	8.041258	7.041794	5.48410	H	8.180098	7.301244	11.62601
C	10.322683	10.407513	6.82958	C	2.899152	10.235209	8.83345
H	10.909784	9.843129	6.34044	H	2.331809	10.847160	8.30078
C	5.675783	6.276228	2.62097	H	2.413010	10.008598	9.66557
C	3.943645	7.625622	3.34999	C	2.649891	4.070689	5.32344
H	3.404951	7.951475	4.06142	H	3.254892	3.515498	4.84569
C	6.821146	3.685027	6.33840	C	5.713929	9.318741	12.22428
C	5.540276	4.436651	8.11512	H	5.157495	9.644899	12.92179
H	4.858905	5.008093	8.44929	C	4.175313	12.302022	8.69309
C	10.759850	11.606662	7.36712	H	3.310304	12.726605	8.92021
H	11.662271	11.881802	7.25566	H	4.894508	12.807319	9.14864
C	3.714751	8.105779	2.07949	C	1.334660	3.647357	5.47897
H	3.028045	8.741956	1.91753	H	1.050216	2.820699	5.10717
C	8.308991	5.807991	4.71009	C	6.699679	8.402770	12.50174
H	8.876334	5.196040	5.24276	H	6.835311	8.093361	13.38964
H	8.795133	6.034602	3.87797	C	4.503202	10.813598	10.60607
C	8.558252	11.972511	8.22011	H	4.835835	11.693439	10.91484
H	7.953251	12.527702	8.69785	H	3.675186	10.611037	11.10950
C	5.494214	6.724459	1.31926	C	5.064447	12.485283	4.56856
H	6.050648	6.398301	0.62175	H	5.329821	12.532932	3.65763
C	7.032830	3.741178	4.85046	C	3.726553	13.241720	6.38118
H	7.897839	3.316595	4.62333	H	3.044906	13.805655	6.72736
H	6.313635	3.235881	4.39491	C	4.066832	13.296315	5.05266
C	9.873484	12.395843	8.06457	H	3.613569	13.893524	4.46922
H	10.157928	13.222501	8.43637	Cl	7.817782	9.707740	2.82407
C	4.508464	7.640430	1.04181	O	8.580158	10.365287	3.83840
H	4.372832	7.949839	0.15390	O	7.798281	10.529457	1.64688
C	6.704941	5.229602	2.93747	O	8.318922	8.385251	2.46957
H	6.372308	4.349761	2.62870	O	6.407327	9.519955	3.19836
H	7.532957	5.432163	2.43404	O	6.908449	9.011337	3.59747
C	6.143696	3.557917	8.97498	O	8.759763	8.885430	2.17426
H	5.878322	3.510268	9.88591	O	7.274249	10.586619	1.95089
C	7.481590	2.801480	7.16237	Cl	9.891851	6.087785	8.64769
H	8.163237	2.237545	6.81618	O	8.569906	6.190237	8.16888
C	7.141311	2.746885	8.49088	O	9.957617	5.887421	10.07349
H	7.594574	2.149676	9.07432	O	10.638141	7.276409	8.32866
Fe	5.989602	9.929971	7.92915	O	10.537342	4.965419	7.96245
O	2.189536	8.104190	7.79782	O	8.408196	5.965985	8.61248
N	4.072842	7.473741	6.85444	O	10.085588	7.533662	8.63256
N	4.292007	8.673259	7.53070	O	10.433703	5.402018	7.69757
N	6.310674	9.329153	9.91294	O	10.113800	5.564728	9.86116
N	5.333559	11.522387	6.72301	O	10.203070	6.064859	1.92661
N	3.095189	5.227003	5.81947	N	10.873765	6.938636	1.43014
N	4.178070	10.903633	9.16807	O	10.971303	7.094191	0.23950
C	2.207622	5.979541	6.51165	C	11.608144	7.861136	2.31793
C	2.824495	7.181450	7.03997	H	10.981931	8.504966	2.71003
C	3.166885	9.001406	8.05944	H	12.288192	8.340651	1.80023
C	0.885460	5.635687	6.71397	H	12.041920	7.350320	3.03299

Table H.15 Cartesian coordinates of **C16**·1MeCN, derived by X-ray structure analysis.

	X	Y	Z		X	Y	Z
Fe	-0.469359	1.034843	12.03754	H	-0.999016	-3.922306	12.81649
S	4.322347	0.897985	12.96358	C	0.931070	-0.352315	9.73300
S	-1.166135	4.888772	14.78890	H	1.003287	-0.993099	8.98181
O	-3.822510	-0.830594	10.23524	H	1.790801	-0.350182	10.22386
N	-0.165371	-0.759435	10.63894	C	-0.352427	3.081305	9.59718
N	-0.887998	-0.718015	13.33335	H	-0.844724	3.656401	10.17111
N	-2.525857	0.572720	11.31924	C	-1.590084	-0.699959	14.47702
N	-3.855050	0.907373	11.61657	H	-1.737051	0.134702	14.90627
N	-0.034749	1.849907	10.03618	C	-1.049935	3.607969	13.80254
N	-6.541561	-1.177763	10.41681	C	-7.873859	-1.241029	10.30205
N	1.558666	0.950763	12.57930	H	-8.258716	-2.054470	9.99759
N	-0.972498	2.694895	13.09147	C	0.727115	2.710251	7.50789
C	-4.575389	0.064865	10.94842	H	1.003859	3.012187	6.65073
C	-0.655157	-1.911817	12.75053	C	-8.179294	0.995046	11.06148
C	-2.562733	-0.429951	10.50940	H	-8.741122	1.729970	11.27765
C	-6.036811	-0.012354	10.85774	C	-8.722881	-0.189856	10.60132
C	0.637985	1.031679	9.20243	H	-9.662227	-0.280890	10.49251
C	2.708746	0.915926	12.75178	C	-1.908710	-3.064280	14.43161
C	-1.392232	-1.087633	9.86904	H	-2.275244	-3.861613	14.79554
H	-1.525767	-2.068447	9.85196	C	0.008104	3.544726	8.34458
H	-1.297955	-0.770967	8.93580	H	-0.233557	4.419661	8.06427
C	-6.802391	1.097507	11.20370	C	-2.109501	-1.843243	15.05885
H	-6.397863	1.894793	11.52495	H	-2.595193	-1.792749	15.87374
C	0.229163	-1.865217	11.53235	N	-3.147948	1.628123	8.34425
H	1.170763	-1.743112	11.81261	C	-3.745770	2.594334	8.43056
H	0.163320	-2.723729	11.04376	C	-4.509985	3.834575	8.52044
C	1.039871	1.426793	7.93438	H	-3.915821	4.565547	8.79070
H	1.518958	0.831451	7.37000	H	-5.223544	3.731221	9.18422
C	-1.161203	-3.098480	13.26091	H	-4.903759	4.039694	7.64679

Table H.16 Cartesian coordinates of **C16**·1MeOH, derived by X-ray structure analysis.

	X	Y	Z		X	Y	Z
Fe	5.103330	6.450056	5.95478	C	4.150631	8.488156	3.92615
S	5.790518	1.797767	6.95239	H	4.139182	9.356326	3.45050
S	0.290845	5.507175	6.25839	H	3.214222	8.203459	4.07510
O	8.542472	8.875811	5.35000	C	3.993712	9.264402	6.26353
N	11.282483	8.967616	5.45848	H	3.059414	8.953492	6.16106
N	8.484850	6.742471	5.95730	H	4.005501	10.248137	6.15298
N	4.979169	7.646371	7.77282	C	5.098115	7.611416	1.73154
N	4.843947	8.636608	5.22692	H	4.768711	8.373076	1.26909
N	7.176014	7.212243	5.79364	C	5.326259	8.057009	10.10698
N	5.304190	6.374064	3.76750	H	5.608545	7.737692	10.95602
N	2.995343	6.186298	6.00689	C	1.872518	5.920128	6.11579
N	5.557714	4.503159	6.31594	C	5.654529	3.371693	6.57026
C	10.710228	7.787363	5.70719	C	4.836483	9.345453	9.96133
C	6.002832	5.432787	3.10609	H	4.782146	9.925547	10.71169
H	6.315228	4.673905	3.58465	C	6.137022	9.357424	5.08672
C	9.245884	7.753323	5.70058	H	6.146242	10.145264	5.68617
C	5.394900	7.244334	8.98473	H	6.241450	9.676720	4.15546
H	5.750293	6.368197	9.07733	C	11.419503	6.615743	5.94001
C	6.282624	5.530126	1.75496	H	10.968835	5.800667	6.12718
H	6.786042	4.855299	1.31490	C	5.815405	6.628478	1.05733
C	4.501903	8.901636	7.63851	H	5.982707	6.711241	0.12585
C	4.426831	9.779323	8.71040	C	12.805505	6.670366	5.89128
H	4.100006	10.663038	8.58894	H	13.325945	5.892418	6.05379
C	4.872432	7.458314	3.09418	O	8.298267	3.044829	2.23813
C	7.263771	8.449842	5.43462	H	7.772995	2.393513	2.16412
C	12.617198	8.989523	5.40513	C	9.490323	2.762576	1.55959
H	13.043367	9.818358	5.22104	H	9.354130	2.881941	0.59646
C	13.415416	7.877414	5.60198	H	9.757323	1.836974	1.73950
H	14.361239	7.941187	5.53986	H	10.193745	3.371284	1.86794

Table H.17 Cartesian coordinates of **C17**·3MeCN, derived by X-ray structure analysis.

	X	Y	Z		X	Y	Z
Se	5.098338	8.427880	1.08076	C	10.976192	5.316722	2.27544
Se	10.453862	12.589577	2.80791	H	11.732402	5.319285	1.73411
Fe	8.656486	8.306893	4.61343	C	10.262802	4.156361	2.48082
O	10.770671	6.780405	7.95663	H	10.515120	3.367649	2.05753
N	7.776080	6.570130	5.85769	C	9.883399	10.993593	3.37020
N	9.461394	6.514708	3.69247	C	6.704532	11.185123	7.40815
N	7.449691	9.289341	6.13506	H	6.747523	12.100257	7.56809
N	10.164629	7.933482	6.17655	N	12.876310	7.123486	9.62317
N	11.395505	8.427892	6.58951	C	12.871046	7.844144	8.48446
N	7.059610	8.179572	3.24717	C	13.874710	8.693860	8.08451
N	9.523595	9.963401	3.74499	H	13.820821	9.173839	7.28977
C	8.791027	5.376247	3.92461	C	14.991980	8.065437	10.07908
C	6.602230	8.511906	6.84238	H	15.727077	8.122202	10.64590
C	9.857943	6.983483	6.99876	C	14.959788	8.797889	8.91713
C	9.164401	4.178421	3.32593	H	15.667674	9.359453	8.69701
H	8.682409	3.400321	3.49068	C	13.944526	7.256218	10.39834
C	10.544687	6.478290	2.89093	H	13.979517	6.775981	11.19397
H	11.020307	7.264229	2.74611	C	9.750784	9.024087	10.42584
C	6.276589	8.241944	2.40457	N	9.585725	9.427693	9.37911
C	7.592448	5.500709	4.83644	C	9.938870	8.482057	11.75992
H	6.806004	5.699154	4.30443	H	9.443325	7.664346	11.84588
H	7.443196	4.653581	5.28475	H	9.626019	9.115632	12.40978
C	11.697713	7.722874	7.64165	H	10.871554	8.307891	11.90600
C	8.655408	6.140853	6.96665	C	16.635476	8.498152	5.38906
H	8.180421	6.215723	7.80907	N	16.933055	9.235497	6.18689
H	8.909012	5.212779	6.84310	C	16.235647	7.581182	4.37501
C	5.801288	9.028499	7.86505	H	15.832204	8.062738	3.64911
H	5.240219	8.468463	8.35130	H	15.601075	6.959106	4.73822
C	7.495241	10.599970	6.42374	H	17.004247	7.103681	4.05424
H	8.081069	11.140510	5.94467	C	14.459836	6.625736	-0.59774
C	5.852641	10.379934	8.14513	H	15.118334	6.838403	-1.26315
H	5.323440	10.743350	8.81800	H	13.922355	7.401089	-0.42018
C	6.508044	7.073314	6.39097	H	13.899852	5.914581	-0.91753
H	6.238279	6.521868	7.14199	C	15.114331	6.212974	0.60634
H	5.824214	6.999246	5.70701	N	15.639504	5.886408	1.55952

Table H.18 Cartesian coordinates of **C18**·1MeOH, derived by X-ray structure analysis.

	X	Y	Z		X	Y	Z
Fe	5.878290	6.869937	12.90291	C	2.168136	7.725720	15.18982
O	2.923968	4.563457	10.91235	H	1.556834	8.424395	15.24505
N	4.262896	6.225464	11.55170	C	3.321601	7.829065	14.41817
N	3.332987	6.718856	10.63095	H	3.449947	8.610257	13.93014
N	0.772131	4.621930	9.25921	C	7.589278	4.533836	12.03709
N	5.613091	4.650552	13.44150	C	8.434465	3.761711	11.26523
N	4.241066	6.894079	14.33462	H	8.623225	2.885057	11.51172
N	7.314133	5.847878	11.67461	C	9.001807	4.303520	10.11647
N	5.876744	8.882589	12.43537	H	9.573578	3.788489	9.59425
N	7.365275	7.106499	14.40796	C	8.728993	5.554456	9.76363
C	3.970048	4.965515	11.67091	H	9.105224	5.914004	8.99286
C	2.590632	5.757873	10.29316	C	7.870962	6.332970	10.55730
C	1.468601	5.764120	9.33846	H	7.684775	7.207242	10.30065
C	1.191181	6.870815	8.63055	C	5.983948	9.975077	12.37227
H	1.738374	7.618511	8.71062	C	8.182328	7.202257	15.19249
C	0.083605	6.908912	7.77169	B	6.109763	11.605224	12.34350
H	-0.128554	7.670123	7.28134	H	5.508730	12.065756	13.26166
C	-0.669472	5.768830	7.69162	H	5.656355	12.020172	11.32438
H	-1.423747	5.732940	7.14881	H	7.255755	11.916125	12.42351
C	-0.289394	4.696532	8.42123	B	9.306158	7.298784	16.31048
H	-0.810632	3.930677	8.33945	H	8.978404	8.091976	17.13498
C	4.668676	3.900924	12.52633	H	10.331259	7.643444	15.81379
H	4.018672	3.401000	13.04447	H	9.450952	6.233292	16.82047
H	5.160166	3.281934	11.96402	O	11.844248	4.298920	17.34969
C	5.122785	4.693063	14.85155	H	12.197281	4.190009	16.61799
H	5.857177	4.911038	15.44657	C	12.240441	5.780545	17.91425
H	4.776945	3.822611	15.10376	H	11.742134	6.449599	17.43907
C	6.964172	4.093933	13.32328	H	13.179938	5.935347	17.79380
H	6.921483	3.125265	13.35073	H	12.026176	5.825778	18.84895
H	7.506988	4.393877	14.06915	C	11.844248	4.298920	17.34969
C	4.036493	5.729218	14.98476	H	12.310285	3.664801	17.87060
C	2.902467	5.529732	15.78356	H	12.137972	4.269519	16.43456
H	2.782519	4.731335	16.24515	H	10.913452	4.208695	17.41148
C	1.970614	6.536804	15.87187	O	12.240441	5.780545	17.91425
H	1.207210	6.419495	16.38991	H	11.650738	6.038658	18.42257

Table H.19 Cartesian coordinates of **C19**·2MeCN, derived by X-ray structure analysis.

	X	Y	Z		X	Y	Z
Fe	8.422216	5.172779	4.32247	C	15.405118	4.807093	8.33508
S	9.794723	9.034132	1.72642	H	15.813371	4.272003	9.00555
S	4.542348	5.132718	1.47820	C	10.289958	1.084795	2.19615
O	11.446759	4.004558	7.00900	H	10.592202	0.288986	1.77444
N	7.431185	6.015057	6.11642	C	15.516657	6.658312	6.81181
N	9.338677	3.414733	3.34595	H	16.000053	7.386474	6.43954
N	8.010759	3.382363	5.71270	C	14.603858	0.111187	7.96565
N	10.233636	5.080205	5.54096	N	14.497810	1.198863	8.22454
N	11.488584	5.711925	5.58875	C	14.751308	-1.300597	7.69773
N	6.628659	4.849658	3.28458	H	14.480269	-1.487990	6.77479
N	8.995957	6.847551	3.26897	H	14.185763	-1.810911	8.31428
C	10.257770	4.101694	6.37291	H	15.687899	-1.560657	7.82234
C	6.777142	5.137915	6.90170	N	13.622483	-2.466101	4.14942
C	8.870482	2.217258	3.72835	C	12.581190	-2.348823	4.61480
C	6.106206	5.525942	8.05900	C	11.382670	-2.336665	5.28809
H	5.645344	4.885251	8.58778	H	10.844035	-3.106734	5.01016
C	9.151286	3.130662	6.63493	H	10.900307	-1.508991	5.08150
H	9.483520	2.206887	6.50705	H	11.549296	-2.385603	6.25257
H	8.845907	3.220920	7.57233	N	11.734387	0.803110	5.61955
C	5.767746	4.962198	2.53227	C	11.570301	-0.391637	5.49693
C	6.767247	3.706565	6.43393	C	11.310781	-1.812804	5.26223
H	6.671853	3.104923	7.21434	H	10.501058	-1.911657	4.71910
H	5.991441	3.559832	5.83671	H	11.185733	-2.268195	6.12095
C	7.799140	2.242362	4.79300	H	12.071740	-2.210132	4.78954
H	6.909424	2.321590	4.36612	N	12.013563	1.486250	5.41703
H	7.820529	1.395193	5.30480	C	12.917058	1.924956	4.89071
C	12.161976	5.044448	6.46416	C	14.152248	2.567705	4.26173
C	7.450324	7.305247	6.48908	H	14.083427	2.530314	3.30488
H	7.920521	7.927231	5.94636	H	14.198235	3.484155	4.54369
C	6.814941	7.770104	7.62976	H	14.945325	2.106071	4.54369
H	6.851396	8.690151	7.86359	N	14.682013	-2.466101	4.37403
C	13.526168	5.297112	6.92166	C	15.723306	-2.348823	3.90865
C	9.339054	7.753748	2.62976	C	16.921827	-2.336665	3.23537
C	9.317678	1.029201	3.17809	H	17.460461	-3.106734	3.51330
H	8.965506	0.195754	3.46767	H	17.404189	-1.508991	3.44196
C	6.122112	6.862073	8.42629	H	16.755200	-2.385603	2.27089
H	5.668041	7.153575	9.20820	N	16.570109	0.803110	2.90391
C	10.310986	3.449044	2.42784	C	16.734195	-0.391637	3.02653
H	10.668139	4.291675	2.17309	C	16.993716	-1.812804	3.26123
C	14.115156	4.506807	7.89329	H	17.803439	-1.911657	3.80436
H	13.645238	3.765557	8.25690	H	17.118763	-2.268195	2.40251
C	10.816415	2.307951	1.83534	H	16.232756	-2.210132	3.73392
H	11.513049	2.364414	1.19190	N	16.290933	1.486250	3.10642
C	14.227042	6.372594	6.36183	C	15.387439	1.924956	3.63275
H	13.828164	6.902792	5.68191	H	14.221070	2.530314	5.21857
C	16.088758	5.881187	7.79871	H	14.106261	3.484155	3.97977
H	16.961545	6.087006	8.11236	H	13.359171	2.106071	3.97977

Table H.20 Cartesian coordinates of **C19**·3MeOH, derived by X-ray structure analysis.

	X	Y	Z		X	Y	Z
Fe	17.540630	6.750739	12.68369	H	14.567063	9.649590	15.79067
S	16.188005	2.855773	15.21625	C	12.463310	6.768039	9.94610
S	21.747474	6.864235	15.14251	C	15.728130	10.894893	14.71275
O	14.572654	7.992517	9.93084	H	15.419593	11.688528	15.08670
N	18.481164	5.852027	10.89069	C	9.966823	6.176659	8.89556
N	16.706511	8.534256	13.66499	H	9.133356	5.972831	8.53687
N	17.997161	8.506739	11.26385	C	10.697571	7.222663	8.37827
N	14.427542	6.337018	11.39874	H	10.353526	7.725107	7.67537
N	15.702867	6.917046	11.47114	C	11.710988	5.718700	10.47408
N	16.976192	5.079370	13.72845	H	12.044912	5.214494	11.18060
N	19.387785	7.048930	13.67286	C	10.463730	5.430016	9.94199
C	15.734887	7.875545	10.60836	H	9.960891	4.730461	10.29222
C	19.816514	6.271779	8.94887	O	11.354646	13.051974	16.12291
H	20.287655	6.876131	8.42190	H	11.050500	12.828458	16.85087
C	17.159431	9.723414	13.22090	C	12.655655	12.820251	16.09909
C	19.170423	6.697810	10.09944	H	12.907853	12.322064	15.31828
C	20.363806	6.984886	14.28827	H	12.830856	12.295576	16.88429
C	16.882488	8.774091	10.32208	H	13.164221	13.633456	16.13778
H	17.185789	8.633551	9.41149	C	12.592493	12.724823	16.40232
H	16.600359	9.698297	10.40665	H	12.675389	13.316546	15.65091
C	19.235502	8.134406	10.56037	H	13.411950	12.725178	16.90195
H	19.993643	8.250764	11.15415	H	11.874245	13.021394	16.96548
H	19.360840	8.715794	9.79411	O	12.225146	11.561882	15.91591
C	18.231429	9.650513	12.16782	H	11.506969	11.619706	15.52407
H	18.237569	10.473391	11.65425	C	14.078284	2.651697	12.06830
H	19.097793	9.554896	12.59349	H	15.014846	2.612320	12.27765
C	18.411639	4.558195	10.52986	H	13.963081	2.643893	11.11497
H	17.924562	3.972349	11.06318	H	13.633669	1.892296	12.45051
C	16.688357	10.918117	13.71899	H	14.620142	1.867936	11.95087
H	17.011031	11.726782	13.39208	H	14.090191	2.912911	12.99172
C	16.640666	4.153212	14.34464	H	14.427882	3.365454	11.52962
C	19.034215	4.062916	9.39897	O	13.556463	3.743629	12.55548
H	18.973536	3.160858	9.18102	H	14.139781	4.314848	12.63193
C	19.751223	4.938002	8.59564	O	12.739963	2.365792	11.66047
H	20.181600	4.630989	7.83051	H	12.226404	2.566936	12.26674
C	13.800948	6.996557	10.48042	O	10.225196	10.264585	13.37860
C	11.953291	7.532017	8.90506	H	10.231453	10.275937	12.55858
H	12.443728	8.243610	8.56149	C	11.491482	10.125452	13.83590
C	15.742526	8.529231	14.59775	H	11.493116	10.085129	14.79498
H	15.405101	7.712360	14.88720	H	12.013750	10.877285	13.54628
C	15.233489	9.685172	15.14297	H	11.869828	9.317568	13.48106

Table H.21 Cartesian coordinates of **C20**·2MeCN, derived by X-ray structure analysis.

	X	Y	Z		X	Y	Z
Se	9.862818	2.593996	1.66722	H	7.965371	3.837447	6.02922
Se	4.479094	6.619531	1.44097	C	8.961977	9.520266	3.75269
Fe	8.507057	6.579081	4.38129	C	9.454200	10.696589	3.22678
O	11.498994	7.780662	7.06488	H	9.139033	11.519511	3.52406
N	11.553863	6.065135	5.66658	C	10.412346	10.624420	2.26217
N	10.310448	6.686837	5.59595	H	10.723494	11.400279	1.85458
N	8.072234	8.377176	5.73417	C	10.925038	9.384341	1.88785
N	7.488358	5.747972	6.16118	H	11.615487	9.316562	1.26851
N	9.412997	8.315880	3.37105	C	10.378498	8.270225	2.46203
N	9.098838	4.900406	3.32853	H	10.700141	7.437282	2.20195
N	6.734667	6.855687	3.30439	C	9.402017	4.002630	2.66861
C	14.291566	5.424077	6.47587	C	5.852177	6.757467	2.56491
H	13.914537	4.894112	5.81113	N	14.583665	10.649407	8.24546
C	15.571626	5.159112	6.95228	C	14.653660	11.743091	8.00187
H	16.049549	4.438232	6.61050	C	14.738834	13.158741	7.76439
C	16.136484	5.949973	7.92101	H	14.369863	13.361239	6.90157
H	16.997584	5.768487	8.22182	H	15.658409	13.433005	7.79153
C	15.432588	7.015818	8.45294	H	14.245112	13.627091	8.44150
H	15.814880	7.535621	9.12267	N	16.485759	10.730248	2.98147
C	14.149323	7.313874	7.98730	C	15.632596	9.984085	3.43856
H	13.685829	8.045651	8.32583	C	14.222470	9.243518	4.29999
C	13.575200	6.512757	7.02037	H	13.905080	8.609062	3.65320
C	12.223150	6.747387	6.53215	H	14.787274	8.797481	4.93532
C	10.330413	7.669641	6.42147	H	14.722652	9.931390	3.85473
C	9.211528	8.641881	6.67773	H	14.539860	8.609062	4.94678
H	8.904350	8.551647	7.59337	H	13.657666	8.797481	3.66466
H	9.532908	9.548779	6.55468	H	13.722288	9.931390	4.74524
C	6.831536	8.063977	6.45310	N	11.959181	10.730248	5.61850
H	6.073120	8.206350	5.86536	C	12.812344	9.984085	5.16141
H	6.739107	8.660349	7.21251	N	13.702532	14.352940	4.14842
C	7.877963	9.499952	4.79946	C	12.541659	14.237270	4.71735
H	7.887987	10.335782	5.29158	C	11.442136	13.950713	5.33665
H	7.013341	9.415515	4.36795	H	10.693177	14.177346	4.78047
C	6.832165	6.634615	6.93449	H	11.396030	14.450758	6.15483
C	6.157588	6.250371	8.08581	H	11.421485	13.011458	5.53405
H	5.705515	6.881230	8.59821	N	14.742408	14.352940	4.45155
C	6.165036	4.921051	8.46209	C	15.903281	14.237270	3.88263
H	5.720661	4.642114	9.22998	C	17.002805	13.950713	3.26333
C	6.844136	4.018886	7.67609	H	17.751764	14.177346	3.81951
H	6.860777	3.118176	7.90706	H	17.048910	14.450758	2.44514
C	7.499538	4.455316	6.54514	H	17.023455	13.011458	3.06592

Table H.22 Cartesian coordinates of **C20**·3MeOH, derived by X-ray structure analysis.

	X	Y	Z		X	Y	Z
Se	9.761546	9.198816	1.64252	H	5.615220	5.002214	8.52148
Se	4.061178	5.076254	1.70298	C	6.114817	6.950699	8.35359
Fe	8.381847	5.172771	4.28399	H	5.673338	7.248672	9.11596
O	11.312223	3.904056	7.03391	C	6.829767	7.842651	7.55500
N	11.484714	5.582807	5.58765	H	6.878387	8.744816	7.77556
N	10.208755	5.002083	5.49463	C	7.463320	7.356094	6.43021
N	7.912488	3.405783	5.66240	H	7.950364	7.948772	5.90447
N	9.218753	3.413777	3.26989	C	9.275848	7.773515	2.60949
N	7.409249	6.059593	6.05702	C	5.575955	4.958441	2.64133
N	8.950326	6.854086	3.23181	C	11.223984	0.902571	9.26313
N	6.545783	4.910362	3.26032	H	11.152360	0.430174	8.43047
C	14.186861	6.173708	6.55123	H	10.661258	1.679991	9.23941
H	13.863904	6.692191	5.84996	H	10.947097	0.328909	9.98136
C	15.423049	6.441975	7.10737	H	10.744242	1.086633	8.45222
H	15.938836	7.138626	6.77041	H	12.061196	1.372247	9.25326
C	15.894443	5.691767	8.14905	H	10.703309	1.192408	10.01578
H	16.718982	5.895097	8.52808	O	12.477436	1.272103	9.45314
C	15.156664	4.636153	8.64174	H	12.953668	0.927505	8.88142
H	15.492052	4.121225	9.33977	O	11.466122	-0.497390	9.36419
C	13.911129	4.339945	8.09638	H	11.779550	-0.667983	10.10248
H	13.407980	3.630767	8.42622	C	11.664752	9.194616	5.06754
C	13.431166	5.118977	7.05270	H	11.810655	10.034767	4.62656
C	12.094734	4.905339	6.50950	H	11.964706	9.254519	5.97750
C	10.166611	4.038989	6.34884	H	10.728353	8.983675	5.05249
C	9.014551	3.130036	6.60830	O	13.358686	9.451191	5.31943
H	9.300804	2.208162	6.51299	H	14.002933	9.399103	4.81483
H	8.700683	3.255544	7.51750	C	12.170641	9.507670	4.56092
C	7.693804	2.264342	4.74698	H	12.346612	9.217165	3.66320
H	6.830123	2.355359	4.31491	H	11.841061	10.409250	4.54655
H	7.691685	1.437291	5.25382	H	11.513342	8.933340	4.96036
C	6.665441	3.768945	6.36920	O	12.374535	8.197640	4.41078
H	6.542526	3.182732	7.13220	H	11.898431	7.535825	4.32282
H	5.908885	3.650965	5.77370	O	13.638748	1.980936	5.55250
C	8.777644	2.212767	3.70198	H	14.075023	2.317134	4.94530
C	9.268523	1.027816	3.19794	O	12.299862	2.376762	4.80050
H	8.948738	0.212325	3.51039	H	13.003581	2.610002	4.44979
C	10.244168	1.072161	2.22019	C	12.459175	1.317868	5.01672
H	10.577205	0.286365	1.85072	H	12.284068	1.643055	4.13061
C	10.716604	2.295827	1.80035	H	11.704408	1.502717	5.58040
H	11.383473	2.348392	1.15428	H	12.611021	0.370463	4.98572
C	10.185572	3.440692	2.35262	C	12.455073	1.056485	5.38458
H	10.514622	4.264891	2.07455	H	13.145140	0.579281	4.91802
C	6.720177	5.203957	6.83827	H	11.627723	0.575057	5.31174
C	6.072679	5.616701	7.99420	H	12.694999	1.142240	6.31016

Table H.23 Cartesian coordinates of **C21**·1MeCN (120 K), derived by X-ray structure analysis.

	X	Y	Z		X	Y	Z
Fe	16.783612	6.503955	13.13096	H	13.589631	5.319401	16.52389
O	13.990584	4.702042	10.90920	C	13.081700	7.202799	15.98283
N	14.740480	6.795329	10.76015	H	12.336254	7.282346	16.53320
N	15.407780	6.122012	11.78091	C	13.457110	8.248013	15.15796
N	16.383942	4.597065	13.71927	H	12.968672	9.039312	15.14459
N	15.311402	6.968466	14.34967	C	14.575651	8.094651	14.35070
N	18.140478	5.612736	12.01517	H	14.825064	8.794470	13.79128
N	17.101967	8.335690	12.59155	C	18.385238	4.319520	12.37381
N	18.144738	6.681301	14.51847	C	19.225312	3.502995	11.63805
C	13.040745	7.163594	8.31977	H	19.373352	2.622241	11.89738
H	13.681635	7.822311	8.46212	C	19.844221	4.017691	10.50675
C	12.134214	7.279593	7.27091	H	20.411863	3.486616	9.99625
H	12.169586	8.018853	6.70775	C	19.602587	5.337815	10.14922
C	11.176353	6.295480	7.06145	H	20.013460	5.705897	9.40049
H	10.568465	6.383896	6.36321	C	18.738848	6.101359	10.92497
C	11.120377	5.181967	7.88651	H	18.571625	6.981974	10.67705
H	10.480114	4.523828	7.73877	C	17.265902	9.466845	12.45507
C	12.025143	5.052364	8.93614	C	19.021796	6.682297	15.25851
H	11.995309	4.305305	9.48923	B	17.473842	11.042630	12.36864
C	12.978153	6.049749	9.15475	H	16.650110	11.588444	13.03189
C	13.921173	5.920414	10.26270	H	17.369156	11.395094	11.23676
C	14.937708	4.923789	11.83481	H	18.557732	11.322500	12.77264
C	15.389375	3.915692	12.81709	B	20.256575	6.652551	16.25804
H	15.804523	3.165474	12.36349	H	21.181626	6.121615	15.73010
H	14.636608	3.586740	13.33285	H	19.958660	6.047607	17.23867
C	15.850871	4.739727	15.10730	H	20.554279	7.766149	16.55402
H	16.583144	4.852266	15.73342	N	10.824175	2.029637	9.08450
H	15.356391	3.943072	15.35574	C	11.237904	1.075839	8.63472
C	17.694454	3.879529	13.64294	C	11.732801	-0.176039	8.10356
H	17.550374	2.920375	13.63009	H	11.052151	-0.586616	7.56527
H	18.240773	4.097934	14.41413	H	11.964498	-0.761734	8.82803
C	14.943639	5.944644	15.15348	H	12.510020	-0.010208	7.56502
C	13.830357	6.034035	15.97959	H	13.589631	5.319401	16.52389

Table H.24 Cartesian coordinates of **C21**·1MeCN (240 K), derived by X-ray structure analysis.

	X	Y	Z		X	Y	Z
Fe	5.671238	4.110353	7.69997	C	2.854074	5.586733	10.78133
O	8.638897	6.239715	9.83292	H	2.437232	5.240014	11.53693
N	8.069058	4.107299	10.08651	C	3.659197	4.789589	10.00108
N	7.266356	4.693291	9.10715	H	3.777229	3.900089	10.24557
N	6.093596	6.320121	7.16492	C	7.600555	5.130178	5.64024
N	4.281338	5.242634	8.90161	C	8.737802	5.236915	4.85533
N	7.314501	3.988124	6.30025	H	8.928408	6.027274	4.40378
N	5.561876	2.095057	8.15928	C	9.582196	4.150611	4.75541
N	4.178800	3.983648	6.17356	H	10.348876	4.203918	4.23170
C	9.927987	3.845082	12.34780	C	9.288875	2.985590	5.43245
H	9.302253	3.164491	12.24705	H	9.848837	2.245617	5.37084
C	10.917663	3.746686	13.30960	C	8.151446	2.943499	6.19927
H	10.949849	3.004592	13.86921	H	7.953495	2.163535	6.66551
C	11.850391	4.742245	13.43793	C	5.437403	0.963497	8.25304
H	12.533829	4.654043	14.06245	C	3.360619	4.070250	5.40076
C	11.787485	5.871861	12.65281	B	5.241107	-0.603706	8.32932
H	12.414893	6.549076	12.76517	H	4.112467	-0.875385	8.06712
C	10.792644	6.004419	11.69511	H	5.495164	-0.982288	9.42862
H	10.740378	6.771523	11.17194	H	5.967944	-1.132959	7.54962
C	9.877184	4.975853	11.52956	B	2.220331	4.212536	4.32808
C	8.852430	5.044131	10.49800	H	1.162638	4.229806	4.87336
C	7.636630	5.929267	8.99444	H	2.264598	3.290164	3.57732
C	7.064852	6.947559	8.07789	H	2.370494	5.225343	3.72144
H	6.625455	7.640988	8.59460	N	11.946504	9.199862	11.76263
H	7.776678	7.359314	7.56347	C	11.474606	10.071082	12.26960
C	4.773280	6.966905	7.27294	C	10.872906	11.228729	12.86416
H	4.224481	6.719004	6.51249	H	10.092211	11.476464	12.36341
H	4.880014	7.931002	7.26787	H	11.500915	11.954775	12.85775
C	6.595881	6.241415	5.77571	H	10.622687	11.030059	13.76943
H	7.009475	7.084293	5.53196	N	11.557697	9.072491	12.91122
H	5.854104	6.083747	5.17089	C	11.237335	10.168568	13.00837
C	4.098344	6.538259	8.54643	C	11.088316	11.526217	12.50126
C	3.300733	7.394108	9.29673	H	10.909652	11.497842	11.55846
H	3.190700	8.281565	9.04135	H	11.897955	12.017356	12.65887
C	2.673888	6.907479	10.42708	H	10.359146	11.958040	12.95229
H	2.136510	7.463886	10.94338	C	2.854074	5.586733	10.78133

Table H.25 Cartesian coordinates of **C21**·1.8MeOH (173 K), derived by X-ray structure analysis.

	X	Y	Z		X	Y	Z
Fe	16.713794	6.388474	13.43488	C	11.749636	7.069120	7.85148
O	13.925199	4.487173	11.27385	H	11.711296	7.846015	7.34169
N	16.921459	8.249442	12.94260	C	17.794343	3.793734	13.77651
N	14.538996	6.613096	11.15793	H	17.699421	2.829907	13.72244
N	15.295112	5.953848	12.12575	H	18.366981	4.002369	14.53112
N	18.093076	6.606858	14.79926	C	10.890211	6.043425	7.56481
N	18.073885	5.622611	12.23295	H	10.266676	6.129152	6.88016
N	15.256985	6.691641	14.74938	C	19.234780	3.589161	11.71954
N	16.453382	4.429484	13.96175	H	19.417604	2.699138	11.91786
C	13.758238	5.697888	10.65024	C	19.796234	4.203844	10.62151
C	14.873114	4.747620	12.16939	H	20.365499	3.724683	10.06361
C	11.918969	4.740798	9.31762	C	14.997719	5.611080	15.52143
H	11.993080	3.946898	9.79631	C	13.368553	7.815654	15.67180
C	12.762543	5.816586	9.59615	H	12.831969	8.574844	15.69662
C	10.960687	4.873637	8.30850	C	15.989253	4.482219	15.37137
H	10.369403	4.177036	8.13520	H	16.744932	4.626291	15.96220
C	18.407634	4.324716	12.50039	H	15.570381	3.641164	15.61234
C	12.653978	6.985897	8.85541	B	17.304421	10.957087	12.70520
H	13.202309	7.711713	9.04886	H	16.586099	11.513212	13.47401
C	18.636174	6.191688	11.15834	H	17.059462	11.321104	11.59893
H	18.417402	7.073098	10.95794	H	18.437410	11.212326	12.96505
C	17.079870	9.401684	12.80786	C	13.895726	5.656579	16.38659
C	18.923537	6.695555	15.56355	H	13.718184	4.913811	16.91731
C	19.515615	5.537871	10.34347	B	20.100043	6.761370	16.62431
H	19.915010	5.971394	9.62413	H	19.719682	6.329268	17.66593
C	15.462994	3.725850	13.08865	H	20.443992	7.891896	16.76565
H	14.767665	3.319846	13.62956	H	21.019598	6.112348	16.23761
H	15.902301	3.028316	12.57744	C	13.078407	6.729704	16.48596
C	14.454145	7.763482	14.82765	H	12.356342	6.739432	17.07199
H	14.638358	8.500002	14.29052				

Table H.26 Cartesian coordinates of **C22**, derived by X-ray structure analysis.

	X	Y	Z		X	Y	Z
Ni	-0.642080	5.826932	3.86727	H	-2.774551	7.014999	5.82644
O	3.315752	2.497386	3.81528	C	4.949194	10.905026	4.43651
O	3.024345	9.223825	5.60752	H	4.462973	10.337167	3.88332
N	4.106511	1.577303	5.65607	C	6.046528	11.595688	3.93389
N	3.269570	2.656742	6.01833	H	6.280262	11.509844	3.03784
N	0.532928	4.072843	4.48137	C	6.790303	12.411022	4.76908
N	-1.767936	4.223330	3.08975	H	7.539912	12.851233	4.43860
N	-1.490571	5.516343	5.71686	C	6.424243	12.574281	6.09265
N	2.666240	10.582020	7.30757	H	6.924222	13.133240	6.64264
N	1.690634	9.552486	7.33169	C	5.317093	11.911925	6.60973
N	0.518453	7.622766	4.59741	H	5.070216	12.029119	7.49867
N	-1.808790	7.442202	3.13272	C	4.578524	11.065574	5.77333
N	0.466493	6.190721	2.14633	C	3.418222	10.341054	6.29074
C	4.366887	0.385669	2.19881	C	1.943022	8.798334	6.32169
H	3.624518	0.838780	1.86946	C	1.274250	7.527365	5.88012
C	5.050833	-0.519830	1.40423	H	1.951615	6.839215	5.78775
H	4.741122	-0.699494	0.54592	H	0.662648	7.243137	6.57730
C	6.184512	-1.160429	1.86430	C	-0.531380	8.657356	4.78531
H	6.647937	-1.744383	1.30830	H	-0.115150	9.531777	4.84040
C	6.627936	-0.932095	3.15059	H	-0.997946	8.494404	5.61997
H	7.396811	-1.356365	3.45675	C	1.445307	7.987706	3.48939
C	5.935473	-0.075725	3.98746	H	2.347633	7.750048	3.75440
H	6.213437	0.047361	4.86638	H	1.420088	8.950471	3.37388
C	4.812051	0.604650	3.50029	C	-1.514040	8.645644	3.65696
C	4.104375	1.533414	4.37118	C	-2.060104	9.828241	3.16462
C	2.842548	3.156589	4.91057	H	-1.855982	10.642894	3.56409
C	1.971652	4.356609	4.72373	C	-2.907253	9.776881	2.07754
H	2.044748	4.913914	5.51427	H	-3.287160	10.553651	1.73517
H	2.313081	4.868849	3.97410	C	-3.179498	8.551818	1.50889
C	0.381413	3.142401	3.33056	H	-3.735439	8.491524	0.76580
H	0.669848	2.253270	3.58970	C	-2.617312	7.413687	2.05491
H	0.940124	3.439207	2.59528	H	-2.805093	6.592203	1.66145
C	-0.097413	3.505582	5.70483	C	1.155345	7.343050	2.16251
H	0.601217	3.225902	6.31687	C	1.683035	7.908646	1.00448
H	-0.607031	2.717770	5.45876	H	2.158486	8.706944	1.04418
C	-1.056814	3.099306	2.88828	C	1.490686	7.267983	-0.20341
C	-1.620947	1.962698	2.32059	H	1.824701	7.634352	-0.99023
H	-1.109634	1.197411	2.18720	C	0.789562	6.065835	-0.22620
C	-2.956381	1.988817	1.95711	H	0.654301	5.608872	-1.02481
H	-3.345608	1.251216	1.54559	C	0.301299	5.569359	0.96048
C	-3.705441	3.121863	2.21180	H	-0.165876	4.765384	0.94420
H	-4.611151	3.148264	2.00231	Cl	5.181844	6.183709	4.19319
C	-3.081825	4.216437	2.78460	O	5.273759	4.884945	3.59069
H	-3.587478	4.975604	2.96590	O	4.486271	6.073457	5.44701
C	-1.009172	4.474084	6.41509	O	4.448632	7.039266	3.34962
C	-1.381653	4.224217	7.73259	O	6.492414	6.654538	4.42564
H	-1.017992	3.506790	8.19945	Cl	4.461683	10.908631	0.07990
C	-2.302375	5.062111	8.33494	O	3.587575	9.981506	-0.56760
H	-2.560802	4.920161	9.21697	O	5.736438	10.330977	0.31242
C	-2.834076	6.112672	7.61147	O	4.664557	11.986847	-0.89732
H	-3.466054	6.677756	7.99380	O	3.922444	11.428984	1.22280
C	-2.411834	6.309624	6.31200				

Table H.27 Cartesian coordinates of **C23**·4.5MeCN (220 K), derived by X-ray structure analysis.

	X	Y	Z		X	Y	Z
Fe	9.813470	5.143258	4.35276	C	11.240709	3.390333	2.16487
O	12.966742	4.035201	6.89218	H	11.554031	4.205687	1.84562
N	11.720642	5.025378	5.38772	C	15.042079	5.309554	6.70345
N	10.457305	3.383961	3.25122	C	13.671387	5.041100	6.28582
N	8.994768	6.079958	6.16544	C	11.142824	1.026285	1.97643
N	9.479920	3.401864	5.79727	H	11.353107	0.236234	1.53318
N	10.262641	6.832193	3.22138	C	11.601515	2.237252	1.50058
N	7.862755	4.910101	3.49568	H	12.143832	2.275104	0.74602
N	12.973880	5.660156	5.38315	C	15.657687	4.538362	7.66097
C	10.037627	2.198455	3.72646	H	15.207814	3.813344	8.03092
C	8.431654	5.239179	7.05574	C	16.973999	4.843094	8.08656
C	11.769461	4.091937	6.27466	C	15.719848	6.404990	6.12511
C	10.369898	1.001696	3.11560	H	15.302253	6.915710	5.46963
H	10.075599	0.193428	3.46916	C	17.646808	5.946960	7.50343
C	7.929127	5.679572	8.26668	C	17.621062	4.076117	9.08887
H	7.551243	5.079860	8.86870	H	17.195144	3.345915	9.47656
C	8.572812	7.891242	7.66594	C	18.963521	6.270769	7.95142
H	8.628803	8.801233	7.84947	H	19.412441	6.992662	7.57427
C	9.066605	7.382170	6.48042	C	19.563169	5.543450	8.91348
H	9.465100	7.965929	5.87600	H	20.416102	5.774984	9.20293
C	10.540457	7.767499	2.62148	C	18.911334	4.440031	9.48186
C	9.137574	2.251630	4.93228	H	19.346836	3.940019	10.13393
H	8.214744	2.328097	4.64341	C	16.985481	6.715196	6.52604
H	9.226755	1.428996	5.43845	H	17.418995	7.445943	6.14792
C	6.860751	4.944041	2.95055	B	5.482272	5.076929	2.18516
C	8.332185	3.795769	6.63355	H	4.764831	5.812994	2.78503
H	8.299918	3.231535	7.42189	H	4.970622	4.005767	2.10055
H	7.510518	3.662178	6.13562	H	5.674571	5.511993	1.09426
C	7.999013	7.032682	8.56708	B	10.899476	9.070922	1.80082
H	7.660013	7.353511	9.37148	H	10.163146	9.169714	0.87109
C	10.690949	3.128662	6.60968	H	12.021902	8.998258	1.41195
H	10.472673	3.200539	7.55207	H	10.783533	10.025609	2.50188
H	10.998760	2.224643	6.43969				

Table H.28 Cartesian coordinates of **C23**·3MeOH (120 K), derived by X-ray structure analysis.

	X	Y	Z		X	Y	Z
Fe	5.098068	4.199738	13.34620	C	10.570279	3.293934	8.36241
O	8.169215	6.051021	11.56883	H	10.638953	2.492490	7.89563
N	4.933231	2.351339	12.79843	B	4.662859	-0.361146	12.54932
N	7.517544	3.938321	11.34686	H	5.313440	-0.877468	13.40167
N	3.536512	3.980556	14.49858	H	5.039812	-0.731889	11.48313
N	5.331145	6.128651	13.93794	H	3.518521	-0.656172	12.69014
N	6.678372	4.606204	12.24956	C	12.328663	6.580956	8.58543
N	6.330043	3.816618	14.82872	H	12.257932	7.388435	9.04136
N	3.938488	5.012427	11.98022	C	8.260240	3.697832	16.81062
C	4.818763	1.216789	12.64683	H	8.911639	3.659498	17.47328
C	8.368526	4.833006	10.95953	C	13.332105	6.388503	7.66137
C	7.097202	5.813470	12.35092	H	13.941354	7.070601	7.49273
C	2.591351	3.882591	15.14301	C	12.574989	4.158381	7.19005
C	3.533980	4.476320	10.82290	H	12.667177	3.356133	6.72875
H	3.775902	3.600184	10.62605	C	13.442932	5.156315	6.96448
C	9.453269	4.683676	9.99279	H	14.125711	5.039548	6.34390
C	7.078693	2.717379	14.99585	B	1.293221	3.745087	16.03931
H	6.942767	1.994622	14.42660	H	1.483045	4.261947	17.09439
C	6.533105	4.872788	15.65160	H	1.043168	2.592875	16.20128
C	3.593647	6.294734	12.26005	H	0.377760	4.277103	15.49591
C	5.609742	6.036372	15.40902	O	10.229074	0.722609	14.48630
H	4.780524	5.908201	15.89572	H	10.660006	0.556632	13.80868
H	6.022570	6.857190	15.72003	C	11.129077	1.178592	15.53357
C	11.405290	5.534742	8.83356	H	11.997112	1.345785	15.15917
C	10.350820	5.702421	9.78141	H	11.198097	0.503459	16.21257
H	10.271606	6.499140	10.25455	H	10.786203	1.987562	15.92037
C	4.038964	6.786990	13.60727	O	12.392443	0.722609	17.28789
H	4.151303	7.750289	13.58916	H	11.961511	0.556632	17.96551
H	3.373107	6.568854	14.27807	C	11.492440	1.178592	16.24061
C	9.551743	3.464181	9.26798	H	10.624405	1.345785	16.61502
H	8.930404	2.786173	9.40626	H	11.423421	0.503459	15.56162
C	2.767427	5.179535	9.90670	H	11.835314	1.987562	15.85382
H	2.480464	4.773228	9.12091	O	11.493081	9.260022	10.05558
C	8.045244	2.613664	15.98026	H	11.589473	9.612079	10.78986
H	8.539216	1.832185	16.08111	C	10.679763	10.115337	8.50853
C	6.459193	6.825451	13.22372	H	10.557744	10.283227	7.57124
H	6.119262	7.563185	12.69353	H	10.079194	10.668397	9.01355
H	7.100541	7.173269	13.86295	H	10.496949	9.191460	8.69460
C	7.498137	4.839390	16.64690	O	12.055387	10.423669	8.88262
H	7.631054	5.576638	17.19797	H	12.537263	10.347889	8.22362
C	11.511010	4.313556	8.13040	C	11.097387	10.257164	9.09288
C	2.435604	6.494860	10.17871	H	11.508983	10.072733	8.24536
H	1.931874	6.989272	9.57314	H	11.375128	11.122667	9.40173
C	2.866865	7.067610	11.37249	H	10.142652	10.243635	8.99459
H	2.669554	7.954791	11.56968				

Table H.29 Cartesian coordinates of **C23**·3MeOH (220 K), derived by X-ray structure analysis.

	X	Y	Z		X	Y	Z
Fe	5.136887	6.908886	13.18619	H	5.475134	11.976919	11.45466
O	8.331257	4.721962	11.48085	H	5.520737	12.124433	13.39196
N	6.916519	6.298462	12.03654	C	8.568090	6.818179	16.67012
N	5.430364	4.719668	13.77989	H	9.249061	6.753569	17.30018
N	3.934634	5.833730	11.77389	C	13.684269	3.977359	7.86596
N	6.549797	7.016506	14.81241	H	14.250141	3.250502	7.73799
N	7.855025	6.860059	11.15644	C	13.914741	5.160826	7.18624
N	5.154835	8.904770	12.71302	H	14.647339	5.218214	6.61621
N	3.435298	7.103680	14.48140	C	13.112390	6.228673	7.32506
C	8.653607	5.899064	10.84492	H	13.292069	7.012500	6.85788
C	5.089052	10.041946	12.58589	B	1.291881	7.294599	16.13744
C	7.235820	5.063127	12.19258	H	1.218853	8.406938	16.55421
C	6.706050	5.870726	15.51978	H	1.423516	6.538121	17.04672
C	3.677131	4.547680	12.08548	H	0.297179	7.028414	15.54076
C	4.126002	4.104678	13.45325	O	10.687026	10.337697	14.44083
H	3.466495	4.367231	14.11432	H	11.131684	10.706278	13.85873
H	4.206441	3.138229	13.47343	C	11.546690	9.889713	15.48171
C	5.707014	4.791652	15.23393	H	12.341664	10.427812	15.47940
H	6.051899	3.939012	15.54211	H	11.780777	8.972101	15.32427
H	4.883808	4.975197	15.71304	H	11.110196	9.967305	16.33325
C	9.794127	5.948067	9.93604	O	12.825892	10.337697	17.08969
C	11.758588	4.954575	8.91672	H	12.381234	10.706278	17.67178
C	3.506821	6.305442	10.59091	C	11.966228	9.889713	16.04880
H	3.683641	7.192115	10.37310	H	11.171254	10.427812	16.05111
C	10.643556	4.879276	9.79678	H	11.732141	8.972101	16.20624
H	10.489180	4.100464	10.28105	H	12.402722	9.967305	15.19727
C	7.390579	8.030729	15.02215	C	11.442425	-0.627523	9.30158
H	7.285586	8.810309	14.52602	H	12.250921	-1.064543	9.02418
C	2.537926	7.175225	15.16666	H	10.755009	-1.283427	9.43883
C	6.529082	4.065761	13.03173	H	11.600145	-0.152979	10.12106
H	6.167659	3.363258	12.46891	O	12.347117	0.078942	8.77383
H	7.153501	3.662642	13.65502	H	12.620112	-0.651492	9.02746
C	10.002695	7.128823	9.18589	O	11.046765	0.250140	8.33746
H	9.410988	7.841950	9.26499	H	11.602142	0.262256	7.73431
C	3.017529	3.706114	11.20536	C	12.037506	0.859785	9.86867
H	2.869497	2.815654	11.42914	H	11.837383	1.752746	9.57857
C	11.970273	6.153023	8.20289	H	12.785617	0.878793	10.47000
C	2.814563	5.524863	9.68533	H	11.274163	0.491028	10.31914
H	2.511525	5.886025	8.88370	C	13.140488	0.627523	11.71876
C	8.409375	7.964211	15.94809	H	12.331991	1.064543	11.99616
H	8.978556	8.688082	16.07819	H	13.827903	1.283427	11.58151
C	12.626980	3.875709	8.72428	H	12.982767	0.152979	10.89928
H	12.483113	3.080995	9.18538	O	12.235795	-0.078942	12.24651
C	2.581146	4.202278	9.99080	H	11.962800	0.651492	11.99288
H	2.136247	3.650691	9.38855	O	13.536147	-0.250140	12.68288
C	7.711186	5.751901	16.46099	H	12.980770	-0.262256	13.28603
H	7.810345	4.965517	16.94748	C	12.545406	-0.859785	11.15167
C	11.078752	7.219509	8.34219	H	12.745529	-1.752746	11.44177
H	11.217210	8.000439	7.85652	H	11.797295	-0.878793	10.55034
B	4.968838	11.614682	12.46895	H	13.308749	-0.491028	10.70120
H	3.820215	11.926095	12.47229				

Table H.30 Cartesian coordinates of **C26**, derived by X-ray structure analysis.

	X	Y	Z		X	Y	Z
Co	10.980101	4.185467	13.64136	C	12.028780	1.444954	14.15133
S	14.661666	5.142399	16.70578	H	11.951316	0.459263	14.20150
S	11.290311	8.810274	12.41798	H	12.629706	1.745153	14.87857
O	8.156901	1.830516	11.62486	C	9.199548	3.234910	15.83619
N	9.412617	3.499164	12.30854	C	8.096987	3.100033	16.66566
N	8.597791	3.979138	11.27499	H	8.007295	2.345944	17.23645
N	6.293781	1.748468	9.61594	C	7.125404	4.094615	16.64245
N	10.697472	2.057823	14.32127	H	6.362163	4.028269	17.20418
N	9.359673	4.304749	15.03475	C	7.273401	5.179260	15.80020
N	12.320289	3.097634	12.41177	H	6.609881	5.858081	15.76251
N	12.484282	4.465881	15.08213	C	8.407773	5.256373	15.01288
N	11.006591	6.098979	13.02003	H	8.518767	6.004748	14.43833
C	9.114135	2.255763	12.47702	C	12.607872	1.842092	12.81683
C	7.892922	2.965326	10.89779	C	13.419931	1.000146	12.07511
C	6.865962	2.931769	9.85751	H	13.594808	0.114197	12.37010
C	6.519235	4.111222	9.20230	C	13.973172	1.472318	10.89491
H	6.961256	4.928576	9.39993	H	14.542881	0.916521	10.37625
C	5.509631	4.056954	8.25284	C	13.688102	2.758208	10.48061
H	5.251126	4.837681	7.77732	H	14.064091	3.103028	9.67922
C	4.886733	2.848730	8.01067	C	12.843913	3.535631	11.25520
H	4.178794	2.785753	7.38029	H	12.627028	4.411336	10.95752
C	5.315010	1.732606	8.70492	C	13.390000	4.731361	15.75226
H	4.887846	0.903633	8.52370	C	11.117216	7.227277	12.77603
C	9.673668	1.340937	13.51259	O	6.232201	7.625235	13.95460
H	8.946338	1.020943	14.10307	H	6.545268	8.270595	14.39174
H	10.085253	0.553963	13.07515	C	4.928493	7.924112	13.55245
C	10.287209	2.193692	15.73606	H	4.684426	7.359542	12.78950
H	11.063851	2.464363	16.28709	H	4.875302	8.867154	13.29122
H	9.953730	1.325171	16.07456	H	4.310953	7.755358	14.29447

Table H.31 Cartesian coordinates of **C27**, derived by X-ray structure analysis.

	X	Y	Z		X	Y	Z
Co	1.841913	8.875073	10.04581	H	1.604057	6.724699	12.37396
S	-1.132025	6.920864	6.84536	C	5.107035	5.575975	3.76440
S	-0.635228	8.717972	14.11905	H	4.491665	5.371692	4.45873
O	4.207973	7.685831	5.46400	C	3.643611	10.632249	11.77390
O	1.571107	10.954449	9.34849	H	2.827761	10.871322	12.19786
H	2.211171	11.499947	9.42727	C	5.984164	9.953362	10.55534
N	3.615702	9.720949	10.77982	H	6.787650	9.705183	10.11340
N	3.354786	8.215384	8.48160	C	4.812946	11.230581	12.19841
N	2.241740	6.815124	10.49739	H	4.799742	11.876757	12.89467
N	0.725221	9.172087	11.72615	C	2.894950	4.695605	9.60124
N	5.662729	9.122108	4.64393	H	3.234404	4.188987	8.87282
N	0.334668	8.376464	8.72947	C	6.476031	7.169940	2.58870
N	5.000207	9.726643	5.71880	H	6.789860	8.059151	2.47333
C	5.178936	7.925437	4.53682	C	6.008003	10.872284	11.59101
C	5.578170	6.873037	3.61135	H	6.829396	11.251354	11.88103
C	4.768905	9.399023	10.17113	C	6.435368	4.866187	1.89907
C	4.168448	8.857904	6.16531	H	6.731021	4.176927	1.31596
C	2.725160	6.065695	9.48760	C	5.537035	4.579309	2.90112
C	0.161743	8.994573	12.72838	H	5.209428	3.693337	3.00219
C	3.044660	6.791331	8.20405	C	6.911000	6.161731	1.73818
H	3.820829	6.362072	7.76428	H	7.532939	6.357673	1.04731
H	2.271272	6.733753	7.58869	C	2.085020	4.844027	11.83980
C	3.191016	9.062009	7.28456	H	1.863769	4.442695	12.67195
H	3.244351	10.008723	7.56916	C	2.561752	4.076987	10.79392
H	2.279961	8.913726	6.92665	H	2.659565	3.137156	10.89214
C	-0.281968	7.784367	7.93505	C	0.449530	11.629617	8.90756
C	4.702805	8.342875	9.09813	H	-0.089286	11.035283	8.34466
H	5.359913	8.562147	8.39087	H	0.723656	12.413113	8.38661
H	4.960600	7.470869	9.48962	H	-0.081457	11.919433	9.67855
C	1.936286	6.200826	11.65446				

Table H.32 Cartesian coordinates of **C28**, derived by X-ray structure analysis.

	X	Y	Z		X	Y	Z
Co	4.986797	10.428795	9.60170	H	3.235803	13.045345	8.56634
S	6.980755	7.493279	12.76254	C	2.258666	11.360794	9.19099
S	6.907916	14.286706	11.53331	C	3.992538	10.373722	6.82996
O	3.929110	14.129906	5.97822	H	3.876457	10.711391	5.92809
N	4.251303	11.496579	7.75605	H	3.178612	9.914318	7.08954
N	2.967783	10.463504	9.89155	C	6.151705	8.465530	11.76722
N	5.765870	9.300544	8.05663	C	-0.145531	19.099025	5.66048
N	4.270844	13.538659	3.86741	H	-0.504421	19.644151	6.32301
N	5.008629	12.683400	4.71119	C	0.071732	18.569816	3.32554
N	5.571340	9.167604	11.04661	H	-0.155302	18.736872	2.43929
N	5.699603	12.141772	10.24680	C	6.580740	7.717483	5.94774
C	2.158480	16.192794	5.31957	H	6.836193	7.171379	5.23962
H	2.349047	16.001847	6.20957	C	5.557186	8.633535	5.78359
C	1.271210	17.252456	5.00048	H	5.139328	8.729186	4.95828
C	2.739043	15.445547	4.32054	C	2.351750	9.715694	10.82343
C	4.784401	13.069503	5.91742	H	2.846614	9.080430	11.28868
C	3.656638	14.364277	4.65290	C	-0.459703	19.340243	4.30948
C	0.970515	17.511192	3.63143	H	-1.037442	20.034699	4.08850
C	5.245708	12.443428	7.18881	C	6.793284	8.430791	8.19387
H	6.076302	11.969855	7.02530	H	7.229379	8.378386	9.01362
H	5.424891	13.141115	7.83843	C	7.218476	7.617267	7.16025
C	5.158904	9.412616	6.87119	H	7.918491	7.017335	7.28268
C	0.688220	18.062987	6.00586	C	0.905457	11.561314	9.42425
H	0.870389	17.893233	6.90190	H	0.424634	12.184455	8.92884
C	1.578596	16.707568	2.62954	C	6.183479	13.043804	10.78061
H	1.372108	16.861493	1.73592	C	1.017730	9.857674	11.11162
C	2.456053	15.718095	2.94846	H	0.612139	9.327991	11.75957
H	2.868283	15.223122	2.27765	C	0.286447	10.811163	10.41311
C	3.011661	12.184485	8.17957	H	-0.613005	10.945406	10.60770
H	2.448032	12.340307	7.40568				

Curriculum Vitae

Julian Eppelsheimer



Date of Birth	June 02, 1992
Place of Birth	Mainz
Nationality	German

Work Experience:

09/2021 - today	**SAP Consultant and Developer**, DSC Unternehmensberatung und Software GmbH, Schriesheim

Education:

07/2017 - today	**PhD studies in Chemistry**, Johannes Gutenberg University Mainz, Department of Chemistry, Workgroup of [redacted] Subject of PhD thesis: *Multifunctional coordination compounds in Molecular Magnetism – Towards high density data storage*
04/2015 - 06/2017	**Master of Science Chemistry**, Johannes Gutenberg University Mainz, Department of Chemistry Titel of Master thesis: *Eisen(II) Spin-Crossover Verbindungen mit 1,3,4-Oxadiazol – Brückenliganden*
04/2011 - 03/2015	**Bachelor of Science Chemistry**, Johannes Gutenberg University Mainz, Department of Chemistry Titel of Bachelor thesis: *Eisen(II) Spin-Crossover Verbindungen mit 1,3,4-Thiadiazol – Brückenliganden*
09/2002 - 03/2011	**Graduation: Abitur**, Gymnasium am Römerkastell Alzey

Personal Skills and Competences:

Languages	**German** (Nativ)	
	English (Proficient)	
	French (Beginner)	
Programming languages	**ABAP OO**, **Python**, **SQL**, **AutoIT**	
SAP modules	**IS-U**	
GitHub Profile	**https://www.github.com/Julian-E**	
Libraries / APIs	**MySQL**, **NumPy**, **Pandas**, **Matplotlib**, **Scikit-Learn**, **TensorFlow**	
Office	**Microsoft Office**, **Origin**	

Selected Trainings:

2021	**Advanced Data Science with IBM**, *IBM certified online course series, offered by Coursera* (Four courses, covering topics such as Scalable Data Science, Advanced Machine Learning and Applied Deep Learning)
2021	**IBM Data Science – Professional Certificate**, *IBM certified online course series, offered by Coursera* (Ten courses, covering topics such as Data Analysis, Data Mining, Machine Learning, Deep Learning, Databases, SQL)
2021	**GMP Foundation Course**, *TÜV certified online training according to ISO 29990 standard, offered by GMP ACADEMY*
2020	**Python advanced**, *Intensive course Spin+X (SFB/TRR 173)*, Johannes Gutenberg University Mainz, Mainz
2018	**Applied Project Management: Getting a Grip on your PhD**, *Softskill course of the general postgraduate program (GPP)*, Johannes Gutenberg University Mainz, Mainz
2018	**Gekonnt Präsentieren**, *Softskill course of the general postgraduate program (GPP)*, Johannes Gutenberg University Mainz, Mainz
2017	**Prospect of Future Spintronics 2017** *Lorain-Mainz-Tohoku Join Seminar*, Tohoku university, Sendai, Japan
2017	**Workshop Industrial Process Engineering & Process Development,** Johannes Gutenberg University Mainz; BASF Ludwigshafen am Rhein

Conferences & Summer Schools:

2020	**16. Koordinationschemie-Treffen (KCT)**, Albert Ludwigs University Freiburg, Freiburg Poster Presentation
2018	**Molecular Spintronics** *Summer School: Spin+X (SFB/TRR 173)*, Inndependence Hotel, Mainz
2018	**ChemKrist 2018** *Summer School: Kristallographie, 10. Intensivkurs: Grundlagen der Einkristallstrukturbestimmung*, Hardehausen, Warburg
2018	**4th International Conference on Advanced Complex Inorganic Nanomaterials (ACIN 2018)**, Namur, Belgium Poster Presentation
2018	**14. Koordinationschemie-Treffen (KCT)**, University Heidelberg, Heidelberg Poster Presentation
2018	**Molecular Magnetism** *Master Class: Material Science in Mainz (MAINZ)*, Johannes Gutenberg University Mainz, Mainz

J. Eppelsheimer

Julian Eppelsheimer